PHYSICAL MECHANISMS CONTROLLING THE STRENGTH AND DEFORMATION BEHAVIOR OF UNFROZEN AND FROZEN MANCHESTER FINE SAND

by

Christopher Wayne Swan

B.S., Civil Engineering, University of Texas at Austin, 1984
M.S., Civil Engineering, University of Texas at Austin, 1986

Submitted to the Department of Civil and Environmental Engineering in Partial Fulfillment of the Requirements for the Degree of

Doctor of Science in Civil and Environmental Engineering

at the

MASSACHUSETTS INSTITUTE OF TECHNOLOGY

May 1994

Signature of Author.....
Department of Civil and Environmental Engineering, May 13, 1994

Certified by.....
Charles C. Ladd, Professor
Thesis Co–Supervisor

Certified by.....
John T. Germaine, Principal Research Associate
Thesis Co–Supervisor

Accepted by.....
Joseph M. Sussman
Chairman, Departmental Committee on Graduate Studies

PHYSICAL MECHANISMS CONTROLLING THE STRENGTH AND DEFORMATION BEHAVIOR OF UNFROZEN AND FROZEN MANCHESTER FINE SAND

by

Christopher W. Swan

Submitted to the Department of Civil and Environmental Engineering
on May 13, 1994, in partial fulfillment of the requirements for the
Degree of Doctor of Science in Civil and Environmental Engineering

ABSTRACT

The development of physically–based constitutive relationships for modeling the time and temperature dependent behavior of frozen soils first requires careful evaluation of the principal variables that affect frozen soil behavior in order to identify various physical mechanisms controlling strength–deformation properties and to quantify their relative importance. Special testing procedures were developed to enable accurate measurement of axial strains and volumetric strains in high pressure triaxial compression tests from very small (0.001%) to very large axial strains on frozen Manchester Fine Sand (MFS). Prior research by Andersen (1991) evaluated the influence of sand density (from 20 to 100% relative density) and confining pressures (from 0.1 to 10 MPa) on the behavior of frozen MFS at –10° C at three strain rates (from $3x10^{-6}$ to $5x10^{-4}$/sec).

The present research has three major components: 1) extension of the prior program of "conventional" frozen MFS testing to include shearing at different temperatures (–15° C, –20° C and –25° C); 2) development of new testing equipment and procedures to enable consolidation of test specimens prior to freezing to assess the effects of the pre–freezing effective stress level on frozen sand behavior; and 3) performance of high pressure triaxial compression tests on unfrozen MFS to obtain parameters needed to evaluate Ladanyi's dilatancy–hardening model for predicting the peak strength of frozen MFS.

The collective results represent a unique characterization of the complete stress–strain behavior of a frozen sand as a function of relative density (D_r), confining pressure (σ_c), strain rate (ϵ) and temperature (T) and led to the following conclusions. 1) Young's modulus is independent of σ_c, ϵ and T and increases slightly with D_r in a manner consistent with Counto's (1964) isostrain model for composite materials. 2) All "conventional" frozen tests specimens exhibited a distinct upper yield stress (knee in the stress–strain curve occurring at less than 1% axial strain) that is independent of D_r and σ_c, but is strongly dependent on ϵ and T in a fashion similar to that for polycrystalline ice. 3) The post upper yield stress–strain behavior is strongly affected by the D_r and σ_c, and hence by the frictional properties of the sand skeleton. 4) Complex interaction between the sand skeleton and the ice matrix alters their behaviors and invalidates the dilatancy–hardening model. 5) The rate of post peak strain softening is directly related to the rate of volumetric dilation.

Thesis Committee Members
Professor Charles C. Ladd (Co–Chairman)
Dr. John T. Germaine (Co–Chairman)
Professor Lorna J. Gibson

ACKNOWLEDGEMENTS

The writer would like to thank and acknowledge the following persons and groups who have contributed to the success of this research.

Professor Charles C. Ladd who showed extreme interest in and dedicated a significant amount of time working on this project. The writer hopes to someday obtain the same focus and soil (and ice) mechanics insight he possesses.

Dr. John T. (Jack) Germaine for his guidance in designing and constructing the various high–pressure triaxial testing systems. His tireless efforts (e.g., Thanksgiving Eve in 1992) provided a strong inspirational force to the writer.

Professor Lorna J. Gibson who brought the area of materials mechanics more into focus. Her examination of the data from a non–soil mechanics viewpoint provided the necessary balance between soil behavior and material behavior.

Dr. Glen R. Andersen of Tulane University who completed his doctoral work on the research project in 1991. His resilience to the trials of research was an excellent example of the courage necessary to continue the laboratory work.

Arthur and Stephen Rudolph whose unsurpassed mastery with machining tools allowed this research to reach higher standards in laboratory testing.

Doug Cauble whose unselfishness in helping the writer prepare this thesis will not soon be forgotten. Victor Salvador, Ira Beer, Adrian Maung and Muneera Abdul–Rahem for performing some of the laboratory tests and data reductions.

My wife, Mary Hall, who has sacrificed these last five years so that this goal could be pursued. She has provided love, comfort and reassurance and has kept me focused on the "real world".

My parents and family in Texas who taught me to never give up and always pursue your dreams.

Our Lord and Savior, who has been beside me every step of the way and carried me when times were hard.

TABLE OF CONTENT

Abstract 3

Acknowledgements 5

Table of Contents 7

List of Figures 12

List of Tables 33

1. INTRODUCTION 37

1.1 BACKGROUND 37

1.2 OBJECTIVE OF RESEARCH 38

1.2.1 Long Term Objective of M.I.T. Frozen Soil Research 38
1.2.2 Previous M.I.T. Studies on Frozen Sand 39
1.2.3 Current Research Objectives 41

1.3 ORGANIZATION OF THESIS 42

2. LITERATURE REVIEW 47

2.1 UNFROZEN SAND 47

2.1.1 Description of a Sand Mass 47
2.1.2 Saturated Sand and Terzaghi's Principle of Effective Stress 51
2.1.3 Stress–Strain–Strength Behavior of Sand 53
2.1.4 Deformation of Sand 60
2.1.5 The Steady State of Sands 61

2.2 POLYCRYSTALLINE ICE 86

2.2.1 Structure of Polycrystalline Ice 87
2.2.2 Mechanisms of Deformation (Abstracted from Andersen 1991) 89
2.2.3 Mechanical Behavior of Single Ice Crystals 93
2.2.4 Mechanical Behavior of Granular Ice 95
2.2.5 Conclusions and Discussion 113

2.3 FROZEN SAND 114

2.3.1 Description and Structure of Frozen Sand 116
2.3.2 Overview of the Mechanical Behavior of Frozen Sand 123
2.3.3 Effect of Temperature on the Behavior of Frozen Sand 129

2.3.4 Effect of Pre–Freezing Confinement on Frozen Sand Behavior 142

2.4 COMPOSITE/PARTICULATE MODELING OF FROZEN SAND 146

2.4.1 Isostrain Model 146
2.4.2 Dilatancy–Hardening Model 149

3. MATERIALS, EQUIPMENT, EXPERIMENTAL PROCEDURES AND ERROR ANALYSIS 271

3.1 MANCHESTER FINE SAND 272

3.1.1 Description of Manchester Fine Sand 272
3.1.2 Specimen Preparation Techniques 274

3.2 COMMON TESTING COMPONENTS 275

3.2.1 High Pressure Triaxial Cells and Silicon Oil 275
3.2.2 Pressure/Volume Control System 277
3.2.3 Loading Frames 279
3.2.4 Electronic Measuring Devices 280
3.2.5 Central Control Acquisition System 281
3.2.6 Temperature Control and Measurement 282
3.2.7 FATCAT System 286

3.3 EXPERIMENTAL PROCEDURES FOR UNFROZEN TESTS 289

3.3.1 General Test Procedures for Unfrozen MFS Tests 289
3.3.2 Series A Tests 291
3.3.3 Series B Tests 293
3.3.4 Series C Tests 294

3.4 EXPERIMENTAL PROCEDURES FOR CONVENTIONAL FROZEN TESTS 297

3.4.1 Specimen Preparation and Freezing 298
3.4.2 Specimen Trimming and Set–Up for Shear 301
3.4.3 Preshear and Shear Procedures 304

3.5 EXPERIMENTAL PROCEDURES FOR CONSOLIDATE–FREEZE TESTS 306

3.5.1 Procedures for Specimen Preparation and Consolidation 306
3.5.2 Specimen Freezing Procedures 308
3.5.3 Procedures For Shear 311

3.6 DATA COLLECTION AND REDUCTION PROCEDURES 311

3.6.1 Data Reduction for the Unfrozen MFS Testing Program 312
3.6.2 Conventional Frozen MFS Test 318
3.6.3 Consolidate–Freeze Data Reduction 324

3.7 ERRORS 326

3.7.1 Test Parameters Used in Presentation of Test Results 326
3.7.2 Unfrozen MFS Testing Program 330
3.7.3 Frozen MFS Testing Programs 333
3.7.4 Precision of Test Results 335

4. TRIAXIAL COMPRESSION TEST RESULTS ON UNFROZEN MANCHESTER FINE SAND 383

4.1 TRIAXIAL COMPRESSION TESTING OF UNFROZEN MFS 384

4.1.1 Purpose and Scope of Testing Program 384
4.1.2 Overview of Testing Program 385

4.2 SUMMARY OF TRIAXIAL COMPRESSION RESULTS FOR UNFROZEN MFS 388

4.2.1 Consolidation 388
4.2.2 Shear Results 392
4.2.3 Sieve Analysis Results 403

4.3 ANALYSIS OF TRIAXIAL COMPRESSION RESULTS 404

4.3.1 Conditions at Maximum Obliquity 405
4.3.2 Evaluation of Other Shear Properties of Unfrozen MFS 406
4.3.3 Undrained Shear Behavior of MFS 407
4.3.4 Drained Shear Behavior of MFS 409

4.4 STEADY STATE ANALYSIS OF SHEAR RESULTS 410

4.4.1 Review of Steady State Analysis 411
4.4.2 Determination of Steady State Points 411
4.4.3 Steady State Line and State Parameters, Ψ, for MFS 413
4.4.4 Correlation of State Parameter With Undrained Shear Parameters 415
4.4.5 State Parameter and Drained Shear Behavior 415

4.5 CONCLUSIONS 416

5. BEHAVIOR OF FROZEN MANCHESTER FINE SAND IN TRIAXIAL COMPRESSION TESTS 495

5.1 SCOPE OF TESTING PROGRAM 496

5.1.1 Conventional Triaxial Tests on Frozen MFS 496
5.1.2 Consolidate–Freeze Triaxial Tests on Frozen MFS 498

5.2 Conventional Triaxial Test Results 498

5.2.1 Small Strain Behavior 498
5.2.2 Large Strain Behavior 505

5.3 Consolidate–Freeze Triaxial Test Results 525

5.3.1 Consolidation and Freezing of Consolidate–Freeze Tests 526
5.3.2 Shear Results of Consolidate–Freeze Tests 528
5.3.3 Summary and Discussion of Consolidate–Freeze Results 531

6. ANALYSIS OF FROZEN MFS RESULTS 631

6.1 Comparison of Frozen MFS With Previous Frozen Sand Studies 632

6.1.1 Small Strain Behavior 632
6.1.2 Large Strain Behavior 637
6.1.3 Volumetric Strain Behavior 640

6.2 Analysis of Frozen MFS Using Particulate/Composite Models 640

6.2.1 Isostrain Model 641
6.2.2 Dilatancy–Hardening Model 642

6.3 Discussion of Frozen Sand Behavior 648

6.3.1 Small Strain Behavior 649
6.3.2 Large Strain Behavior 651
6.3.3 Frozen Sand Mechanisms as Presented by Ting et al. (1983) 653

6.4 Conceptual Behavior of Frozen Sand as a Composite 654

6.4.1 Small Strain Behavior 656
6.4.2 Large Strain Behavior 658
6.4.3 Concluding Remarks 664

7. SUMMARY, CONCLUSIONS AND RECOMMENDATIONS 689

7.1 SUMMARY 690

7.1.1 Literature Review 690
7.1.2 Material, Equipment and Experimental Procedures 700
7.1.3 Unfrozen MFS Behavior 703
7.1.4 Behavior of Frozen MFS in Triaxial Compression 707
7.1.5 Analysis of Frozen MFS Results 711

7.2 CONCLUSIONS 714

7.3 RECOMMENDATIONS 718

7.3.1 Equipment and Procedures Development 718
7.3.2 Future Testing Program 719

8. BIBLIOGRAPHY 723

APPENDIX A Experimental Procedures 745

APPENDIX B Unfrozen MFS Test Results 749

APPENDIX C Conventional Frozen Test Results 929

APPENDIX D Consolidate–Freeze Test Results 1033

List of Figures

Figure 2.1	Components of Strength in Sands According to Rowe's Equation (after Rowe 1962)	165
Figure 2.2	Behavior of Dry Sand in Direct Shear (from Casagrande 1936)	166
Figure 2.3	Stress–Strain and Volumetric Strain Curves for Sacramento River Sand in Drained Triaxial Compression (from Lee and Seed 1967)	167
Figure 2.4	Mohr's Circles and Failure Envelope for Loose and Dense Sacramento River Sand at Confining Pressures up to 120ksc (from Lee and Seed 1967)	168
Figure 2.5	Undrained Behavior of Banding Sand in Triaxial Compression (from Mohamad and Dobry 1986, Data from Castro 1969)	169
Figure 2.6	Effect of Direction of Loading on ϕ' of Several Sands (from Ladd et al. 1977)	170
Figure 2.7	Effect of Intermediate Principal Stress on the ϕ' of Several Sands (from Ladd et al. 1977)	171
Figure 2.8	Simple Shear Test Results on Steel Balls with a Normal Stress of 20 psi (from Roscoe et al. 1958)	172
Figure 2.9	Critical Void Ratio Lines for Steel Balls and Glass Beads in e–σ' and τ–σ' Space (from Roscoe et al. 1958)	173
Figure 2.10	Critical Void Ratio Line for Banding Sand from Undrained Triaxial Tests Which Liquefied (from Castro 1969)	174
Figure 2.11	Critical Void Ratio Lines for Banding Sand from Undrained and Drained Triaxial Tests (from Castro 1969)	175
Figure 2.12	Steady State Line Developed from Six CIUC Tests on Compacted Sand Specimens (from Poulos et al. 1985)	176
Figure 2.13	Critical Void Ratio Line for Banding Sand using Liquefaction and Limited Liquefaction Test Results (from Castro 1969)	177
Figure 2.14	Schematic Representation of Phase Transformation and Steady State Conditions for Undrained Shear (from Negussey et al. 1988)	178

Figure 2.15	Effective Stress Conditions at Phase Transformation and CSR States for Tailings Sand and Ottawa Sand (from Vaid and Chern 1985)	179
Figure 2.16	Concept of a Collapse Surface (from Sladen et al. 1985)	180
Figure 2.17	Idealized CSR Line and Steady State Envelope for Undrained Compression (from Alarcon–Guzman et al. 1988)	181
Figure 2.18	Definition of the State Parameter (from Been et al. 1991)	182
Figure 2.19	State Diagram and Steady State Line for Kogyuk 350/2 Sand (from Been and Jefferies 1986)	183
Figure 2.20	Steady State Lines for Kogyuk 350 Sand with Various Fines Content (from Been and Jefferies 1985)	184
Figure 2.21	Peak Undrained Strength Ratio, q_{max}/σ'_c Versus State Parameter, Ψ (from Been and Jefferies 1986)	185
Figure 2.22	Drained Angle of Friction, ϕ', versus State Parameter, Ψ (from Been and Jefferies 1985)	186
Figure 2.23	Comparison of Normalized Stress Paths for Samples with the Same State Parameter (from Been and Jefferies 1985)	187
Figure 2.24	Typical Triaxial Compression Tests Results using Various Test Parameters (from Been et al. 1991)	188
Figure 2.25	Effect of Initial State on Steady State Line for Erksak 330/0.7 Sand (from Been et al. 1991)	189
Figure 2.26	Effect of Load–Controlled Versus Strain–Controlled Triaxial Tests on the SSL for Banding Sand (from Casagrande 1975)	190
Figure 2.27	Effect of Load–Controlled Versus Strain–Controlled Triaxial Tests on the SSL for Leighton Buzzard Sand (from Hird and Hassona 1990)	191
Figure 2.28	Interpretation of Effect of Strain Rate on Strain–Controlled Triaxial Tests (from Hird and Hassona 1990)	192
Figure 2.29	Effect of Load–Controlled Versus Strain–Controlled Triaxial Tests on the SSL for Syncrude Tailings Sand (from Poulos et al. 1988)	193

Figure 2.30	Effect of Load–Controlled Versus Strain–Controlled, CIUC with $+\Psi$, Triaxial Tests on the SSL for Erksak 330/0.7 Sand (from Been et al. 1991)	194
Figure 2.31	Effect of Specimen Preparation Technique on the SSL for Erksak 330/0.7 Sand (from Been et al. 1991)	195
Figure 2.32	Schematic Representation of the Effect of Initial State for Consolidated–Undrained Triaxial Tests on Sands (from Konrad 1990b)	196
Figure 2.33	Effect of Initial State on Steady State Condition of Consolidated–Undrained Triaxial Tests on Normally Consolidated Dune Sand (from Konrad 1990a)	197
Figure 2.34	Effect of Consolidated Undrained Stress Path on the Steady State Condition for Loose Ottawa Sand (from Vaid et al. 1990)	198
Figure 2.35	Triaxial Compression and Extension Behavior of Loose Ottawa Sand (from Vaid et al. 1990)	199
Figure 2.36	Effect of Hydrostatically Consolidated Undrained Stress Path on the Steady State Condition for Two Sands (from Been et al. 1991)	200
Figure 2.37	Basic Structure of Ice Ih (from Sanderson 1988)	201
Figure 2.38	Schematic Representation of Development of Bjerrum Defects in Ice Lattice (from Sanderson 1988)	202
Figure 2.39	Idealized Representation of Deformation Mechanisms (after Sanderson 1988)	203
Figure 2.40	Young's Moduli for Single Ice Crystal (from Dantl 1969)	204
Figure 2.41	Creep Data from Monocrystals in Easy and Hard Glide and for Polycrystalline Ice (from Duval et al. 1983)	205
Figure 2.42	Stress–strain Curves for Single Ice Crystals in Basal and Nonbasal Glide (from Higashi 1969)	206
Figure 2.43	Small Strain Elastic Properties of Granular Ice (from Sinha 1989)	207
Figure 2.44	Idealized Creep and Stress–strain Curves for Polycrystalline Ice Tested in Compression (from Shyam Sunder 1993)	208

Figure 2.45	Stress–Strain Curves for Fine–grained Polycrystalline Ice at –5° C and Various Strain Rates (from Mellor and Cole 1982)	209
Figure 2.46	Stress–strain Curves From Uniaxial Tension Tests on Polycrystalline Ice (from Hawkes and Mellor 1972)	210
Figure 2.47	Schematic Log Stress – Log Strain Rate Response Highlighting the Effects of Strain Rate on the Behavior of Ice (from Shyam Sunder 1993)	211
Figure 2.48	Log Applied Stress versus Log Minimum Strain Rate for Creep Tests on Granular Ice at –5° C (from Cole 1985)	212
Figure 2.49	Stress/Strain–Rate Relationship for Uniaxial Test on Granular Ice at –7° C (from Mellor 1980)	213
Figure 2.50	Applied Axial Stress versus Minimum Strain Rate for Creep Tests on Granular Ice (data from Jacka 1984)	214
Figure 2.51	Minimum Strain Rate versus the Reciprocal of Absolute Temperature for Creep Tests on Polycrystalline Ice with Applied Stress of 6 bars (from Glen 1955)	215
Figure 2.52	Minimum Strain Rate versus 1/T for Creep Tests on Granular Ice with σ_a = 1.18 MPa (from Mellor and Testa 1969)	216
Figure 2.53	Minimum Strain Rate versus 1/T for Creep Tests on Granular Ice (data from Jacka 1984)	217
Figure 2.54	Idealize Stress–strain Curve for "Moderate" Strain–rate Compression Test on Polycrystalline Ice (from Mellor and Cole 1982)	218
Figure 2.55	Minimum Strain Rate versus Applied Stress for Creep Tests on Granular Ice at Different Temperatures (from Barnes et al. 1971)	219
Figure 2.56	Peak Compressive Strength versus Applied Strain Rate from Strength Tests on Granular Ice (data from Sayles and Epanchin 1966)	220
Figure 2.57	Unconfined Compressive Strength versus Temperature for Granular Ice (from Haynes 1979)	221
Figure 2.58	Unconfined Compressive Strength for Granular Ice as a Function of Strain Rate and Temperature (from Schulson 1990)	222
Figure 2.59	Uniaxial Tensile Strength versus Temperature for Granular Ice (from Haynes 1979)	223

Figure 2.60	Log Stress versus Log Strain Rate for Creep and Strength Tests on Granular Ice Performed by Various Researchers	224
Figure 2.61	Effect of Confining Pressure on the Peak Strength of Granular Ice (from Jones 1982)	225
Figure 2.62	Peak Strength versus Strain Rate for Strength Tests on Granular Ice for Zero and 10 MPa Confinement Levels (data from Jones 1982)	226
Figure 2.63	Effect of Grain Size on the Unconfined Compression Strength of Granular Ice (from Schulson 1990)	227
Figure 2.64	Peak Strength versus Confining Pressure for Triaxial Tests on Granular Ice (data from Murrell et al. 1989)	228
Figure 2.65	Effect of Temperature and Strain Rate on the Compressive Strength of Polycrystalline Ice Based on Glen's Creep Law	229
Figure 2.66	Proposed Structure of Frozen Sand (from Ting et al. 1983)	230
Figure 2.67	Alternative Structure of Frozen Sand (from Andersen 1991)	231
Figure 2.68	Phase Diagram for Water Ice (from Nadreau and Michel 1986)	232
Figure 2.69	Proposed Mechanism Map for Unconfined Compressive Strength of Frozen Ottawa Sand (from Ting et al. 1983)	233
Figure 2.70	Idealized Stress–Strain and Volumetric Behavior for Frozen Manchester Fine Sand at –10° C (from Andersen et al. 1992)	234
Figure 2.71	Variation in Upper Yield Stress with Confining Pressure for Uniform Ottawa Sand at –10° C	235
Figure 2.72	Peak Deviator Stress Versus Volume Fraction of Sand	236
Figure 2.73	Peak Deviator Stress Versus Dry Density for Frozen Ottawa Sand (from Baker and Kurfurst 1985)	237
Figure 2.74	Peak Deviator Stress Versus Confining Pressure for Tests on "Saturated" Dense Sands at Low to Moderate Confining Pressures	238
Figure 2.75	Effect of Strain Rate on the Unconfined Compressive Strength of Dense Sands at –10° C	239

Figure 2.76	Failure Strain as a Function of a) Relative Density, b) Temperature and c) Strain Rate (from Baker and Kurfurst 1985, Bourbonnais and Ladanyi 1985 and Bragg and Andersland 1980)	240
Figure 2.77	Stress–Strain and Volumetric Responses for Dense Frozen Ottawa Sand at Moderate Confining Pressure (from Chamberlain et al. 1972)	241
Figure 2.78	Young's Modulus and Poisson's Ratio for Peabody Gravelly Sand (from Kaplar 1963)	242
Figure 2.79	Young's Modulus and Poisson's Ratio for Ottawa 16–100 Sand in Freshwater (from Baker and Kurfurst 1985)	243
Figure 2.80	Stress–Strain Curves for Unconfined Compression Tests on Frozen Dense Ottawa Sand at Temperatures from –2 to –15° C (from Parameswaran 1980)	244
Figure 2.81	Unconfined Compressive Strength versus Temperature for Several Frozen Granular Materials (from Bourbonnais and Ladanyi 1985)	245
Figure 2.82	Compressive Peak Strength versus Applied Strain Rate for Frozen Ottawa Sand at Temperatures from –3 to –30° C (tests by Sayles and Epanchin 1966)	246
Figure 2.83	Unconfined Compressive Peak Strength versus Applied Strain Rate for Frozen Ottawa Sand at Temperatures from –2 to –15° C (from Parameswaran 1980)	247
Figure 2.84	Unconfined Compressive Peak Strength versus Applied Strain Rate for Tests on Frozen Silica Sand at Temperature from –2 to –15° C (from Bragg and Andersland 1982)	248
Figure 2.85	Stress–Strain Curves for Unconfined Compression Tests on Frozen Ottawa Sand at Temperatures from –6.7 to –160° C (from Bourbonnais and Ladanyi 1985)	249
Figure 2.86	Stress–Deviatoric Strain and Volumetric Strain Curves for Frozen Toyoura Sand at Temperatures from –2 to –50° C (from Shibata et al. 1985)	250
Figure 2.87	Peak Strength versus Applied Strain Rate for Tests on Frozen Toyoura Sand at Different Temperatures (data from Shibata et al. 1985)	251
Figure 2.88	Effect of Temperature on Measured Peak Strength of Frozen Toyoura Sand (from Shibata et al. 1985)	252

Figure 2.89	Stress–Strain Curves from Unconfined Compression Tests on Frozen Karlsrude Sand at Temperature from –2 to –20° C (from Orth 1985)	253
Figure 2.90	Peak Deviator Stress versus Applied Strain Rate for Frozen Karlsrude Sand (from Orth 1985)	254
Figure 2.91	Stress–Strain Curves from Unconfined Compression Tests on Frozen Lanzhau Sand at Temperatures from –2 to –15° C (from Yuanlin et al. 1988)	255
Figure 2.92	Unconfined Compressive Peak Strength versus Applied Strain Rate for Frozen Lanzhau Sand at Temperatures from –2 to –15° C (data from Yuanlin et al. 1988)	256
Figure 2.93	Uniaxial Tensile Strength of Frozen Dense Penn Sand (from Perkins and Reudrich 1973)	257
Figure 2.94	Strain at Failure versus Strain Rate from Unconfined Compression Tests on Frozen Lanzhau Sand at Temperatures from –2 to –15° C (tests by Yuanlin et al. 1988)	258
Figure 2.95	Derived Parameters for Arrhenius–Type Formulation (from Anderson and Andersland 1978)	259
Figure 2.96	Derived Parameters for Strength–Strain Rate Power Law Formulation	260
Figure 2.97	Yield Pressure versus Confining Pressure for Frozen Quartz Sand (from Goodman 1975)	261
Figure 2.98	Peak Strength versus Applied Strain Rate for Quartz Sand (tests by Sego et al. 1982)	262
Figure 2.99	Stress–Strain Curves Which Show the Effect of Specimen Preparation Technique on Frozen Manchester Fine Sand (after Andersen 1991)	263
Figure 2.100	Schematic Diagram of Counto's (1964) Isostrain Composite Material Model Applied to Frozen Sand	264
Figure 2.101	Schematic Representation of Total and Effective Stress Paths for Unfrozen Dense Sand at Low Effective Consolidation Stress and Zero Back Pressure	265
Figure 2.102	Schematic Representation of Total and Effective Stress Paths for the Dilatancy–Hardening Model (after Andersen et al. 1992)	266
Figure 2.103	Comparison of Dense Frozen Ottawa Sand Results with the Dilatancy–Hardening Model in MIT p'–p–q Space	267

Figure 2.104	Force Equilibrium of Sand Particle In Frozen Sand (after Andersen 1991)	268
Figure 3.1	Mechanical Dry Sieve Analysis on Manchester Fine Sand	362
Figure 3.2	Schematic Diagram of Multiple Sieve Pluviation for Unfrozen MFS and Consolidate–Freeze Specimens (from Andersen et al. 1992)	363
Figure 3.3	Details of the Modified High Pressure Triaxial Cell (from Andersen et al. 1992)	364
Figure 3.4	Details of Internal Modifications for the Various Testing Programs	365
Figure 3.5	Schematic Drawing of Mechanical Portion of Pressure/Volume Controller (from Andersen et al. 1992)	366
Figure 3.6	Schematic Diagram of Pressure/Volume Controller System (from Andersen 1991)	367
Figure 3.7	Details of On–Specimen Axial Strain Device (from Andersen et al. 1992)	368
Figure 3.8	Plan View of MIT Cold Room Facility (from Andersen et al. 1992)	369
Figure 3.9	Schematic View of Environmental Chamber and Triaxial Cell (from Andersen et al. 1992)	370
Figure 3.10	Component of Temperature Measurement System	371
Figure 3.11	Schematic Drawing of Specimen Preparation Molds (after Martin et al. 1981)	372
Figure 3.12	Temperature Inside the Environmental Chamber and Triaxial Cell During Shear of FRS100.	373
Figure 3.13	Pore Volume Expelled and Temperature Changes During Specimen Freezing Phase of CF02	374
Figure 3.14	Idealized Stress–Strain Behavior and Graphical Construction Techniques (from Andersen et al. 1992)	375
Figure 3.15	The Effects of Leakage on the Measured Volumetric Strain During Consolidation of Unfrozen MFS Test C–13	376

Figure 3.16	Examples of On–Specimen Strain Responses for Unfrozen MFS Tests	377
Figure 3.17	Range in Stress–Strain Responses for Unfrozen MFS Test C–15	378
Figure 3.18	Examples of ACDT Agreement Qualifiers (from Conventional Frozen Tests)	379
Figure 3.19	Examples of Specimen Stability Qualifiers (from Andersen 1991)	380
Figure 3.20	Examples of Initial Stress–Strain Responses for Unfrozen MFS Tests	381
Figure 4.1	Void Ratio versus Effective Stress for Consolidation of MFS: $\sigma'_c = 2$ MPa	436
Figure 4.2	Void Ratio versus Effective Stress for Consolidation of MFS: $\sigma'_c = 5$ MPa	437
Figure 4.3a	Void Ratio versus Effective Stress for Isotropic Consolidation of MFS: $\sigma'_c = 10$ MPa, Series B Tests	438
Figure 4.3b	Void Ratio versus Effective Stress for Isotropic Consolidation of MFS: $\sigma'_c = 10$ MPa, Series C Tests	439
Figure 4.4	Void Ratio versus Effective Stress for Isotropic Consolidation of MFS: $\sigma'_c = 12.5$ MPa	440
Figure 4.5	Void Ratio versus Vertical Effective Stress for Anisotropic Consolidation of MFS	441
Figure 4.6	Deviator Stress and Excess Pore Pressure versus Axial Strain for Unfrozen CIUC Tests with $\sigma'_c = 0.1$ MPa: Series B and C Tests	442
Figure 4.7	Effective Stress Paths for Unfrozen MFS CIUC Tests with $\sigma'_c = 0.1$ MPa: All Series	443
Figure 4.8	Deviator Stress and Excess Pore Pressure versus Axial Strain for Unfrozen CIUC Tests with $\sigma'_c = 2$ MPa: Series B and C Tests	444
Figure 4.9	Effective Stress Paths for Unfrozen MFS CIUC Tests with $\sigma'_c = 2$ MPa: All Series	445
Figure 4.10	Deviator Stress and Excess Pore Pressure versus Axial Strain for Unfrozen CIUC Tests with $\sigma'_c = 5$ MPa: Series B and C Tests	446

Figure 4.11	Effective Stress Paths for Unfrozen MFS CIUC Tests with σ'_c = 5 MPa: Series B and C Tests	447
Figure 4.12	Deviator Stress and Excess Pore Pressure versus Axial Strain for Unfrozen CIUC Tests with σ'_c = 10 MPa: Series B and C Tests	448
Figure 4.13	Effective Stress Paths for Unfrozen MFS CIUC Tests with σ'_c = 10 MPa: Series B and C Tests	449
Figure 4.14	Deviator Stress and Excess Pore Pressure versus Axial Strain for Unfrozen CIUC Tests with σ'_c = 12.5 MPa: Series C Tests	450
Figure 4.15	Effective Stress Paths for Unfrozen MFS CIUC Tests with σ'_c = 12.5 MPa	451
Figure 4.16	Deviator Stress and Excess Pore Pressure versus Axial Strain for Unfrozen CAUC Tests	452
Figure 4.17	Effective Stress Paths for Unfrozen MFS CAUC Tests	453
Figure 4.18	Deviator Stress and Volumetric Strain versus Axial Strain for Unfrozen CIDC Tests with σ'_c = 0.1 MPa: Series C Tests	454
Figure 4.19	Effective Stress Paths for Unfrozen MFS CIDC Tests with σ'_c = 0.1 MPa: Series C Tests	455
Figure 4.20	Deviator Stress and Volumetric Strain versus Axial Strain for Unfrozen CIDC Tests with σ'_c = 2, 5 and 10 MPa: Series C Tests	456
Figure 4.21	Effective Stress Paths for Unfrozen MFS – CIDC Tests with σ'_c = 2 to 10 MPa: Series C Tests	457
Figure 4.22	Post–Shear Particle Size Distributions of Unfrozen MFS for CIUC Tests at σ'_c = 0.1 MPa	458
Figure 4.23	Post–Shear Particle Size Distributions of Unfrozen MFS for CIUC Tests at σ'_c = 2 MPa	459
Figure 4.24	Post–Shear Particle Size Distributions of Unfrozen MFS for CIUC Tests at σ'_c = 5 MPa	460
Figure 4.25	Post–Shear Particle Size Distributions of Unfrozen MFS for CIUC Tests at σ'_c = 10 MPa	461
Figure 4.26	Post–Shear Particle Size Distributions of Unfrozen MFS for CIUC Tests at σ'_c = 12.5 MPa	462

Figure 4.27	Post–Shear Particle Size Distributions of Unfrozen MFS for CAUC Tests	463
Figure 4.28	Post–Shear Particle Size Distributions of Unfrozen MFS for CIDC Tests at $\sigma'_c = 0.1$ MPa	464
Figure 4.29	Post–Shear Particle Size Distributions of Unfrozen MFS for CIDC Tests at $\sigma'_c = 2$ to 10 MPa	465
Figure 4.30	Mobilized Friction Angles at Maximum Obliquity for Undrained Triaxial Compression Tests	466
Figure 4.31	Mobilized Friction Angles at Maximum Obliquity for Drained Triaxial Compression Tests	467
Figure 4.32	Mobilized Friction Angles at Maximum Obliquity for Undrained Triaxial Compression Tests: $\sigma'_c = 0.1$ MPa	468
Figure 4.33	Effective Friction Angle at Maximum Obliquity versus Relative Density for Undrained MFS Tests	469
Figure 4.34	Effective Friction Angle at Maximum Obliquity versus Effective Confining Stress for Undrained MFS Tests	470
Figure 4.35	Young's Modulus, E_s, versus Relative Density for Unfrozen MFS	471
Figure 4.36	Young's Modulus, E_s, versus Effective Confining Stress for Unfrozen MFS	472
Figure 4.37	Upper Yield Stress versus Relative Density for Undrained Triaxial Compression Tests	473
Figure 4.38	Upper Yield Stress versus Effective Confining Stress for Undrained Triaxial Compression Tests	474
Figure 4.39	Peak Strength versus Relative Density for Undrained Triaxial Compression Tests	475
Figure 4.40	Peak Strength versus Effective Confining Stress for Undrained Triaxial Compression Tests	476
Figure 4.41	Stress–Strain and Pore Pressure Responses for Undrained Tests at Similar Relative Density	477
Figure 4.42	Effective Stress Paths for Unfrozen Undrained Tests at Similar Relative Densities	478
Figure 4.43	Stress–Strain and Pore Pressure Response for Unfrozen CIUC Tests with Similar Confinement: 0.1 MPa	479

Figure 4.44	Effective Stress Paths for Unfrozen CIUC Tests with Similar Confinement: 0.1 MPa	480
Figure 4.45	Stress–Strain and Pore Pressure Response for Unfrozen CIUC Tests with Similar Confinement: 2 MPa	481
Figure 4.46	Effective Stress Paths for Unfrozen CIUC Tests with Similar Confinement: 2 MPa	482
Figure 4.47	Stress–Strain and Volumetric Strain Response for Unfrozen CIDC Tests with Similar Relative Densities	483
Figure 4.48	Effective Stress Paths of Unfrozen CIDC Tests with Similar Relative Densities	484
Figure 4.49	Stress–Strain and Volumetric Strain Responses for Unfrozen CIDC Tests at Similar Confinement: 0.1 MPa	485
Figure 4.50	Effective Stress Paths Showing the Effects of Relative Density on CIDC Tests at $\sigma'_c = 0.1$ MPa	486
Figure 4.51	Steady State Condition for Four Undrained Triaxial Compression Tests	487
Figure 4.52	Steady State Points as Determined by Undrained Triaxial Compression Tests from Series B and Series C Tests	488
Figure 4.53	Steady State Line and Parameters as Determined by Undrained Tests from Series B and Series C Tests	489
Figure 4.54	A_f versus State Parameter from CIUC Tests on Unfrozen MFS	490
Figure 4.55	Undrained Strength Ratio, q/I'_c versus State Parameter from CIUC Tests on Unfrozen MFS	491
Figure 4.56	Comparison of Steady State LIne, as Determined by Undrained Tests, and Drained Behavior in Triaxial Compression	492
Figure 5.1	Young's Modulus versus Relative Density for Conventional Frozen MFS Tests at Different Temperatures (Includes All Confining Pressures and Strain Rates)	547
Figure 5.2	Young's Modulus versus Confining Pressure for Conventional Frozen MFS Tests at Different Temperatures	548
Figure 5.3	Young's Modulus versus Temperature for Conventional Frozen MFS Tests	549

Figure 5.4	Yield Offset Stress at 10^{-4} Strain versus Relative Density for Conventional Frozen MFS Tests at Low and High Confinement, Moderate Strain Rate and Different Temperatures	550
Figure 5.5	Yield Offset Stress at 10^{-4} Strain versus Confining Pressure for Conventional Frozen MFS Tests at Moderate Strain Rate and Different Temperatures	551
Figure 5.6	Yield Offset Stress at 10^{-4} Strain versus Strain Rate for Conventional Frozen MFS Tests at Low and High Confinement	552
Figure 5.7	Yield Offset Stress at 10^{-4} Strain versus Temperature for Conventional Frozen MFS Tests at Low and High Confinement	553
Figure 5.8	Upper Yield Stress versus Specimen Length for Conventional Frozen MFS Tests at Different Temperatures	554
Figure 5.9	Initial Stress–Strain Curves Showing the Effect of Relative Density on Upper Yield Stress for Conventional Frozen MFS Tests at Moderate Strain Rate and Low Confinement	555
Figure 5.10a	Upper Yield Stress versus Relative Density for Conventional Frozen MFS Tests at Moderate Strain Rate and Different Temperatures and Confining Pressures	556
Figure 5.10b	Upper Yield Stress versus Relative Density for Conventional Frozen MFS Tests at Fast Strain Rates and Different Temperatures and Confining Pressures	557
Figure 5.11	Initial Stress–Strain Curves Showing the Effect of Confinement on the Upper Yield Stress for Conventional Frozen MFS Tests on Loose Specimens at Moderate Strain Rates	558
Figure 5.12a	Upper Yield Stress versus Confining Pressure for Conventional Frozen MFS Tests at Moderate Strain Rate and Different Temperatures	559
Figure 5.12b	Upper Yield Stress versus Confining Pressure for Conventional Frozen MFS Tests at Various Strain Rates and Different Temperatures	560

Figure 5.13	Initial Stress–Strain Curves Showing the Effect of Strain Rate on Upper Yield Stress for Conventional Frozen MFS Tests on Loose Specimens at High Confinement	561
Figure 5.14	Upper Yield Stress versus Strain Rate for Conventional Frozen MFS Tests at Different Temperatures	562
Figure 5.15	Initial Stress–Strain Curves Showing the Effect of Temperature on Upper Yield Stress on Conventional Frozen MFS Tests on Loose Specimens at High Confinement	563
Figure 5.16	Upper Yield Stress versus Temperature for Conventional Frozen MFS Tests at Different Strain Rates	564
Figure 5.17	Axial Strain at Q_{uy} versus Relative Density for Conventional Frozen MFS Tests at Different Strain Rates and Different Temperatures	565
Figure 5.18	Axial Strain at Q_{uy} versus Confining Pressure for Conventional Frozen MFS Tests at Different Temperatures	566
Figure 5.19	Axial Strain at Q_{uy} versus Strain Rate for Conventional Frozen MFS Tests at Different Temperatures	567
Figure 5.20	Axial Strain at Q_{uy} versus Temperature for Conventional Frozen MFS Tests	568
Figure 5.21	Basic Types of Stress–Strain Curves from Conventional Triaxial Compression Tests on Frozen MFS	569
Figure 5.22a	Normalized Stress–Strain Curves Showing the Effect of Relative Density for Conventional Frozen MFS Tests at Moderate Strain Rate, Low Confinement and T=–10° C	570
Figure 5.22b	Normalized Stress–Strain Curves Showing the Effect of Relative Density for Conventional Frozen MFS Tests at Moderate Strain Rate, Low Confinement and T=–15° C	571
Figure 5.22c	Normalized Stress–Strain Curves Showing the Effect of Relative Density for Conventional Frozen MFS Tests at Moderate Strain Rate, Low Confinement and T=–20° C	572
Figure 5.22d	Normalized Stress–Strain Curves Showing the Effect of Relative Density for Conventional Frozen MFS Tests at Moderate Strain Rate, Low Confinement and T=–25° C	573

Figure 5.23	Normalized Stress–Strain Curves Showing the Effect of Relative Density for Conventional Frozen MFS Tests at Moderate Strain Rate, High Confinement and T=–10° C	574
Figure 5.24a	Normalized Stress–Strain Curves Showing the Effect of Confinement for Conventional Frozen MFS Tests on Loose Specimens at Moderate Strain Rate and T=–10° C	575
Figure 5.24b	Normalized Stress–Strain Curves Showing the Effect of Confinement for Conventional Frozen MFS Tests on Dense Specimens at Moderate Strain Rate and T=–10° C	576
Figure 5.25a	Stress–Strain Curves Showing the Effect of Strain Rate for Conventional Frozen MFS Tests on Loose Specimens at Low Confinement and T=–10° C	577
Figure 5.25b	Stress–Strain Curves Showing the Effect of Strain Rate for Conventional Frozen MFS Tests on Loose Specimens at Low Confinement and T=–20° C	578
Figure 5.25c	Stress–Strain Curves Showing the Effect of Strain Rate for Conventional Frozen MFS Tests on Loose Specimens at Low Confinement and T=–25° C	579
Figure 5.26a	Stress–Strain Curves Showing the Effect of Strain Rate for Conventional Frozen MFS Tests on Loose Specimens at High Confinement and T=–10° C	580
Figure 5.26b	Stress–Strain Curves Showing the Effect of Strain Rate for Conventional Frozen MFS Tests on Loose Specimens at High Confinement and T=–15° C	581
Figure 5.26c	Stress–Strain Curves Showing the Effect of Strain Rate for Conventional Frozen MFS Tests on Loose Specimens at High Confinement and T=–20° C	582
Figure 5.26d	Stress–Strain Curves Showing the Effect of Strain Rate for Conventional Frozen MFS Tests on Loose Specimens at High Confinement and T=–25° C	583
Figure 5.27a	Stress–Strain Curves Showing the Effect of Strain Rate for Conventional Frozen MFS Tests on Dense Specimens at Low Confinement and T=–10° C	584
Figure 5.27b	Stress–Strain Curves Showing the Effect of Strain Rate for Conventional Frozen MFS Tests on Dense Specimens at Low Confinement and T=–20° C	585

Figure 5.28a	Stress–Strain Curves Showing the Effect of Strain Rate for Conventional Frozen MFS Tests on Dense Specimens at High Confinement and T=–10° C	586
Figure 5.28b	Stress–Strain Curves Showing the Effect of Strain Rate for Conventional Frozen MFS Tests on Dense Specimens at High Confinement and T=–15° C	587
Figure 5.29a	Stress–Strain Curves Showing the Effect of Temperature on Conventional Frozen MFS Tests on Loose Specimens at Low Confinement and Slow Strain Rate	588
Figure 5.29b	Stress–Strain Curves Showing the Effect of Temperature on Conventional Frozen MFS Tests on Loose Specimens at Low Confinement and Moderate Strain Rate	589
Figure 5.29c	Stress–Strain Curves Showing the Effect of Temperature on Conventional Frozen MFS Tests on Loose Specimens at Low Confinement and Fast Strain Rate	590
Figure 5.30a	Stress–Strain Curves Showing the Effect of Temperature on Conventional Frozen MFS Tests on Loose Specimens at High Confinement and Slow Strain Rate	591
Figure 5.30b	Stress–Strain Curves Showing the Effect of Temperature on Conventional Frozen MFS Tests on Loose Specimens at High Confinement and Moderate Strain Rate	592
Figure 5.30c	Stress–Strain Curves Showing the Effect of Temperature on Conventional Frozen MFS Tests on Loose Specimens at High Confinement and Fast Strain Rate	593
Figure 5.31a	Stress–Strain Curves Showing the Effect of Temperature on Conventional Frozen MFS Tests on Dense Specimens at Low Confinement and Slow Strain Rate	594
Figure 5.31b	Stress–Strain Curves Showing the Effect of Temperature on Conventional Frozen MFS Tests on Dense Specimens at Low Confinement and Moderate Strain Rate	595
Figure 5.32	Stress–Strain Curves Showing the Effect of Temperature on Conventional Frozen MFS Tests on Dense Specimens at High Confinement and Slow Strain Rate	596

Figure 5.33	Peak Strength versus Relative Density for Conventional Frozen MFS Tests at Moderate Strain Rate, Low Confinement and Different Temperatures	597
Figure 5.34	Peak Strength versus Relative Density for Conventional Frozen MFS Tests at Slow and Fast Strain Rate, Low Confinement and Different Temperatures	598
Figure 5.35	Peak Strength versus Relative Density for Conventional Frozen MFS Tests at Moderate Strain Rate, High Confinement and Different Temperatures	599
Figure 5.36	Peak Strength versus Relative Density for Conventional Frozen MFS Tests at Slow and Fast Strain Rate, High Confinement and Different Temperatures	600
Figure 5.37	Peak Strength versus Confining Pressure for Conventional Frozen MFS Tests at Moderate Strain Rate, Low Confinement and T=–10° C (from Andersen, 1991)	601
Figure 5.38	Peak Strength versus Confining Pressure for Conventional Frozen MFS Tests on Dense Specimens at Moderate Strain Rate and Different Temperatures	602
Figure 5.39	Peak Strength versus Strain Rate for Conventional Frozen MFS Tests on Loose and Dense Specimens at Low Confinement and Different Temperatures	603
Figure 5.40	Peak Strength versus Strain Rate for Conventional Frozen MFS Tests on Loose and Dense Specimens at High Confinement and Different Temperatures	604
Figure 5.41	Comparison of Peak Strength versus Strain Rate Results of Loose Specimens At Low and High Confinement	605
Figure 5.42	Peak Strength versus Temperature for Conventional Frozen MFS Tests on Loose Specimens at Low and High Confinement	606
Figure 5.43	Peak Strength versus Temperature for Conventional Frozen MFS Tests on Dense Specimens at Low and High Confinement	607
Figure 5.44a	Axial Strain to Peak Strength versus Relative Density for Conventional Frozen MFS Tests at Different Temperatures and Moderate Strain Rate	608

Figure 5.44b	Axial Strain to Peak Strength versus Relative Density for Conventional Frozen MFS Tests at Slow and Fast Strain Rate and Different Temperatures	609
Figure 5.45a	Axial Strain at Q_p versus Confining Pressure for Conventional Frozen MFS Tests on Loose Specimens at Different Temperatures	610
Figure 5.45b	Axial Strain at Q_p versus Confining Pressure for Conventional Frozen MFS Tests on Dense Specimens at Different Temperatures	611
Figure 5.46a	Axial Strain to Peak Strength versus Strain Rate for Conventional Frozen MFS Tests on Loose and Dense Specimens at Low Confinement and Different Temperatures	612
Figure 5.46b	Axial Strain to Peak Strength versus Strain Rate for Conventional Frozen MFS Tests on Loose and Dense Specimens at High Confinement and Different Temperatures	613
Figure 5.47	Axial Strain to Peak Strength versus Temperature for Conventional Frozen MFS Tests at Low and High Confinement	614
Figure 5.48	Maximum Rate of Dilation versus Relative Density for Conventional Frozen MFS Tests at Low and High Confinement, Various Strain Rates and Different Temperatures	615
Figure 5.49	Maximum Rate of Dilation versus Confining Pressure for Conventional Frozen MFS Tests on Loose and Dense Specimens at Various Strain Rates and Different Temperatures	616
Figure 5.50	Maximum Rate of Dilation versus Temperature for Conventional Frozen MFS Tests on Loose and Dense Specimens at Various Strain Rates	617
Figure 5.51	Volumetric Strain at ϵ_a=20% versus Relative Density for Conventional Frozen MFS at Low and High Confinement, Various Strain Rates and Different Temperatures	618
Figure 5.52	Volumetric Strain at ϵ_a=20% versus Confining Pressure for Conventional Frozen MFS on Loose and Dense Specimens at Various Strain Rates and Different Temperatures	619

Figure 5.53	Volumetric Strain at ϵ_a=20% versus Temperature for Conventional Frozen MFS on Loose and Dense Specimens at Various Strain Rates	620
Figure 5.54	Void Ratio and Relative Density versus Effective Stress for Isotropically Consolidated Consolidate–Freeze Tests	621
Figure 5.55	Efficiency of Specimen Freezing versus Elapsed Freezing Time for Consolidate–Freeze Tests on Dense Specimens	622
Figure 5.56	Small Strain Parameters versus Confining Pressure for Consolidate–Freeze and Conventional Frozen Tests on Dense Specimens at T=–10° C	623
Figure 5.57	Initial Stress–Strain Curves Showing the Upper Yield Region for Consolidate–Freeze tests on Dense Specimens at Moderate Strain Rate and T=–10° C	624
Figure 5.58	Comparison of Stress–Strain Curves for Consolidate–Freeze on Dense Specimens at Moderate Strain Rate and T=–10° C	625
Figure 5.59	Comparison of Stress–Strain Curves for Consolidate–Freeze and Conventional Frozen Tests on Dense Specimens at Moderate Strain Rate and T=–10° C	626
Figure 5.60	Peak Strength versus Confining Pressure for Consolidate–Freeze and Conventional Tests on Dense Specimens at Moderate Strain Rate and T=–10° C	627
Figure 5.61	Comparison of Stress–Strain Curves for Consolidate–Freeze Tests and Conventional Frozen Tests on Wet Tamped Specimens at Moderate Strain Rate and T=–10° C	628
Figure 6.1	Comparison of Magnitude and Rate Sensitivity of Q_{uy} for Conventional Frozen MFS and Calculated Peak Strength of Polycrystalline Ice	668
Figure 6.2	Comparison of Peak Strength versus Applied Strain Rate for Various Sands and Frozen MFS on Dense Specimens at No or Low Confinement	669
Figure 6.3	Comparison of Peak Strength versus Applied Strain Rate for Various Sands and Frozen MFS on Dense Specimens at High Confinement	670
Figure 6.4	Comparison of Predicted Initial Modulus from Isostrain Model and Measured Initial Modulus from Conventional Frozen MFS Tests	671

Figure 6.5	Critical Confining Pressure Line of Unfrozen MFS Based on Steady State Analysis of CIUC Tests	672
Figure 6.6	Peak Strength versus Strain Rate Equations for Polycrystalline Ice Developed from Results by Jones (1982)	673
Figure 6.7	Calculated Peak Strengths of Polycrystalline Ice Used in the Dilatancy–Hardening Model Compared with Results by Murrell et al. (1989)	674
Figure 6.8	Peak Strength versus Strain Rate Comparing Measured Results from Conventional Frozen Tests on Loose Specimens at Low Confinement with Predicted Results from Dilatancy–Hardening Model	675
Figure 6.9	Peak Strength versus Strain Rate Comparing Measured Results from Conventional Frozen Tests on Dense Specimens at Low Confinement with Predicted Results from Dilatancy–Hardening Model	676
Figure 6.10	Peak Strength versus Strain Rate Comparing Measured Results from Conventional Frozen Tests on Loose Specimens at High Confinement with Predicted Results from Dilatancy–Hardening Model	677
Figure 6.11	Peak Strength versus Strain Rate Comparing Measured Results from Conventional Frozen MFS Tests on Dense Specimens at High Confinement with Predicted Results from Dilatancy–Hardening Model	678
Figure 6.12	Comparison of Peak Strength versus Relative Density from Dilatancy–Hardening and Peak Strength and Upper Yield Stress from Conventional MFS Tests at Moderate Strain Rate and Different Temperatures	679
Figure 6.13	Ratio of Predicted Peak Strength from Dilatancy–Hardening Model to Measured Peak Strength versus Temperature for Conventional Frozen MFS Tests	680
Figure 6.14	Schematic Representation of Frozen MFS	681
Figure 6.15	Conceptual Composite Behavior of Conventional Frozen MFS – Initial Response and Upper Yield Region	682
Figure 6.16a	Conceptual Composite Behavior of Frozen MFS at Low Confinement – Post–Upper Yield Behavior	683
Figure 6.16b	Conceptual Composite Behavior of Frozen MFS at Low Confinement – Large Strain Behavior	684

Figure 6.17a	Conceptual Composite Behavior of Frozen MFS at High Confinement – Post–Upper Yield Behavior	685
Figure 6.17b	Conceptual Composite Behavior of Frozen MFS at High Confinement – Large Strain Behavior	686
Figure 6.18	Rate of Strain Softening versus Maximum Rate of Dilation for All Testing Conditions	687

List of Tables

Table 2.1	Factors Affecting the Steady State Condition of Sands	158
Table 2.2	Possible Deformational Mechanisms in Polycrystalline Ice (Abstracted from Andersen, 1991)	159
Table 2.3	Mechanisms of Strength for Frozen Sand	161
Table 2.4	Overview of Testing Programs to Measure Large Strain Behavior of Frozen Sand (abstracted from Andersen, 1991)	162
Table 3.1	Dry Mechanical Sieve Analysis on Manchester Fine Sand	340
Table 3.2a	Unfrozen MFS Testing Program: Series A Tests Set–up Characteristics and Specimen History	341
Table 3.2b	Unfrozen MFS Testing Program: Series B Tests Set–up Characteristics and Specimen History	342
Table 3.2c	Unfrozen MFS Testing Program: Series C Tests Set–up Characteristics and Specimen History	343
Table 3.3	Conventional Frozen MFS Tests: Set–up Characteristics and Specimen History	345
Table 3.4	Consolidate–Freeze Testing Program: Set–up Characteristics and Specimen History	347
Table 3.5	Measured Leakage Rates and Area Correction Calculation Factors for Unfrozen MFS Tests	348
Table 3.6	Correction Factors for Volumetric Strain and Specimen Area for Conventional Frozen MFS Tests	350
Table 3.7	Conventional Frozen MFS Tests: Temperature Fluctuations Inside the Triaxial Cell During Shear	352
Table 3.8	Summary of Measured Testing Temperatures	355
Table 3.9	Corrections for Volumetric Strain and Specimen Area For Consolidate–Freeze Tests	356
Table 3.10	Consolidate–Freeze Tests: Temperature Fluctuations Inside the Triaxial Cell During Shear	357
Table 3.11	Specimen Freezing Characteristics: Consolidate–Freeze Tests	358

Table 3.12	Range in Stress Strain Parameters for Repeatability Tests at –10° C (from Andersen 1991)	359
Table 3.13	Range in Stress Strain Parameters for Repeatability Tests from Current Research: Unfrozen MFS Tests	360
Table 3.14	Range in Stress Strain Parameters for Repeatability Tests from Current Research: Conventional Frozen MFS Tests	361
Table 4.1	Consolidation and Shear History of Consolidated –Undrained and Drained Triaxial Compression Tests on Unfrozen Manchester Fine Sand: Series B and C	418
Table 4.2	Consolidation Characteristics – Series B and C	420
Table 4.3	Shear Characteristics – Shearing Conditions and Descriptions: Series B and C	422
Table 4.4	Shear Characteristics – Series B and C CIUC Tests: Conditions at Maximum Obliquity	424
Table 4.5	Shear Characteristics – Series B and C: Conditions at Peak Shear Strength	426
Table 4.6	Shear Characteristics – Series C CIDC Tests: Conditions at Peak Shear Strength (= Conditions at Maximum Obliquity)	428
Table 4.7	Shear Characteristics – Modulus and Stress Properties	429
Table 4.8	Shear Characteristics – Series B and C: Conditions At or Near Steady State	431
Table 4.9	Shear Characteristics – Series B and C: Steady State Parameters	433
Table 4.10	Shear Characteristics – Series C CIDC Tests: Steady State Parameters	435
Table 5.1	Scope of Triaxial Testing on Frozen MFS: Conventional and Consolidate–Freeze Tests	533
Table 5.2	Summary of Available Tests for Presentation	534
Table 5.3	Measured Conventional Frozen Tests Results: Test Results at –10, –15, –20 and –25° C	535
Table 5.4	Summary of Small Strain Behavior	540
Table 5.5	Summary of Large Strain Behavior	542

Table 5.6	Summary of Volumetric Strain Behavior	543
Table 5.7	Consolidate–Freeze Tests – Consolidation Characteristics	544
Table 5.8	Consolidate–Freeze Tests – Specimen Freezing Characteristics	545
Table 5.9	Consolidate–Freeze Test Results	546
Table 6.1	Comparison of Measured Frozen Initial Modulus Results With Prior Testing Programs on Frozen Sands	666
Table 6.2	Variables Used in Dilatancy Hardening Analysis	667

CHAPTER 1
INTRODUCTION

1.1 BACKGROUND

Frozen soils exist in Arctic regions as permafrost (perennially frozen ground) that underlies nearly 20% of the land surface of the earth. In addition, artificial ground freezing may be employed for temporary support of excavations and tunnels. However, in spite of its abundance, frozen soils represent perhaps the most complex and least understood of all "geomaterials". The complexity is due not only to the behavior of the soil skeleton and the behavior of the pore ice, but also to the interaction between these two components. Knowledge and understanding of the fundamental behavior of frozen soils is required in order to develop rational design practices. However, acquiring this understanding has proven to be a difficult challenge to the scientific and engineering community since description of frozen soil behavior involves (but is not limited to) the disciplines of soil mechanics, ice mechanic and material mechanics to varying degrees.

At present, engineers, in general, rely on empirically–based behavioral models and procedures to predict the response of frozen soils. These methods use correlations between various parameters such as temperature, strain rate, creep stress, peak strength, minimum creep rate, or time to minimum creep rate determined from laboratory tests. Unconfined compression tests have been used most often as a means of estimating frozen soil responses. These laboratory tests generally involve much shorter times than appropriate for modeling field which may lead to a considerable amount of uncertainty in the predicted frozen soil response.

In contrast to the typical laboratory program, the actual states of stress and

deformation constraints in the field are very complex. To capture these complex field conditions, it would be necessary to conduct sophisticated laboratory testing programs where various principal stress levels are applied to the frozen specimens. For the case of deep permafrost or ground freezing, the effects of the pre–frozen effective stresses on the behavior of the frozen soil would also require examination. Laboratory testing equipment and procedures to study these "field" conditions are not commonplace and would be costly. Therefore, simple tests are performed with a significant factor of safety (factor of ignorance) imposed to reduce the risk of an unconservative design.

The lack of fundamental understanding of the strength and deformation mechanisms of frozen soils leads to empirically–based procedures which are limited in their range of application and mask inherent uncertainties in the analyses. If a more elemental approach is undertaken, one which is built from an understanding of the physical mechanisms involved in frozen soil behavior, predictions of behavior would be more reliable and engineering designs more cost effective. Therefore, research of these mechanisms is paramount to the development of more rational design procedures.

1.2 OBJECTIVE OF RESEARCH

1.2.1 Long Term Objective of M.I.T. Frozen Soil Research

The ultimate objective of the M.I.T. research effort on frozen soils is to develop physically–based constitutive relations for frozen soil behavior. In essence, these physically–based constitutive relations are behavioral models which describe the physical mechanisms controlling the strength and deformation of the frozen soil. It is hoped that these relations will aid in the development of rational design techniques which in turn will lead to more cost effective designs.

An understanding of the fundamental behavior of frozen soils is essential to develop these constitutive relationships. To this end, the current frozen soil research effort at M.I.T. attempts to identify the major physical mechanisms involved in the behavior of frozen soils and to quantify their relative importance. This is the primary thrust of this thesis.

To date, these mechanisms can be broadly classified in three areas (Ting et al. 1983): strength mechanisms predominantly associated with the soil skeleton; strength mechanisms predominantly associated with the pore ice; and mechanisms associated with the interaction between the soil particles and the pore ice. At present, results from direct, "micro–structure" measurements of the behavior of either the soil skeleton or the pore ice in a frozen soil are not available. In addition, a direct assessment of frozen soil behavior based on effective stress principles is not currently possible. Therefore, indirect methods which measure the macro–structure behavior of frozen soils are used to evaluate possible physical, micro–structure mechanisms.

The first part of this indirect approach is to fully characterize the stress–strain–strength and deformation behavior of a frozen soil. This requires sophisticated testing techniques in order to measure stress–strain–strength behavior from very small to very large strains. The second component of the indirect method is to compare existing behavioral models, used to estimate certain aspects of frozen soil behavior, with the measured behavior. In conjunction with the evaluation of existing models, the measured behavior of frozen soils should also be compared to the "known" behaviors of its individual components; namely the soil skeleton (and its individual particles) and the pore ice.

1.2.2 Previous M.I.T. Studies on Frozen Sand

During the early 1980's, frozen sand research at M.I.T. was conducted on

frozen Manchester Fine Sand at various densities and ice saturations (see Ting et al. 1983). The focus of this prior research was on the uniaxial compression creep behavior of the sand. Possible mechanisms controlling the behavior of frozen soils were proposed and evaluated in this study. These mechanisms formed the reference base of M.I.T.'s continued research effort in frozen soil behavior.

Andersen (1991) and Andersen et al. (1992) present the results of triaxial compression tests on frozen Manchester Fine Sand (MFS) tested at one temperature (–10° C). The behavior of frozen Manchester Fine Sand as measured in Andersen's research represented the most complete set of data describing the triaxial compression behavior of any frozen soil which has been presented in the literature. This research presented, for the first time, a complete characterization of the stress–strain behavior of a frozen material from very small strains (10^{-4}), which captured the initial elastic behavior, to very large strains which captured the yielding behavior and subsequent strain hardening or strain softening.

The parameters studied by Andersen et al. included the relative density, strain rate and confining pressure. Other variables included the method of preparation of the sand specimens and the effect of specimen end conditions. One test was conducted at a different temperature ($\approx$ –15° C). A major contribution of the research was the construction of a sophisticated triaxial testing system and development of careful testing procedures. Specimen preparation via multiple sieve pluviation and exacting specimen set–up procedures lead to uniform sand specimens and high–caliber measurements of stress–strain strength behavior. On–specimen axial strains were measured using a specially designed displacement yokes, and lubricated end platens were used to achieve uniform specimen strains throughout the course of the deformation.

Andersen et al. (1992) also presents analyses comparing the results from the

frozen MFS program with two behavioral models. One model, adapted from work by Counto (1964) on a composite material (concrete), was used to estimate the elastic behavior (Young's modulus) of the frozen MFS. A second model, proposed by Ladanyi (1985), attempts to estimate the strength behavior of a frozen sand system based on the contributions of the soil skeleton (via dilatancy–hardening) and the pore ice (via tensile stresses and compressive strength). This particulate model considers the nature of the sand skeleton in a frozen sand system and attempts to describe its behavior in terms of unfrozen undrained behavior. Studies with both of these models indicated that the adaptation of Counto's isostrain model showed promise while Ladanyi's dilatancy–hardening model may be deficient in describing the strength behavior

1.2.3 Current Research Objectives

The major components of the current research have expanded on the work of Andersen (1991) in three principal areas. The first area included a study of the effects of temperature on frozen MFS behavior. Additional frozen MFS tests have been performed at various relative densities, confining pressures and strain rates at nominal temperatures of –15° C, –20° C and –25° C. Analyses using the isostrain and dilatancy–hardening models have also been extended to include this new data set.

Secondly, extensive triaxial compression tests were conducted on *unfrozen* MFS specimens. Consolidated–undrained and consolidated–drained tests were performed for a variety of relative densities and effective consolidation stresses. These results are used for direct comparison to the frozen MFS results and are analyzed using steady state concepts, specifically the state parameter Ψ as proposed by Been and Jefferies (1985). Results of the steady state analysis are used in the analysis of the dilatancy–hardening model.

Specimens for the frozen MFS tests conducted by Andersen et al. and in the current extension of his research were prepared and frozen under atmospheric conditions. For the third area in the current research, a new triaxial device was developed where unfrozen, saturated specimens are first consolidated to an effective consolidation stress, and then frozen with the consolidation stresses maintained during the freezing process. These "consolidate–freeze" tests attempt to study the effects of an pre–existing effective stress on the frozen MFS behavior. Though only preliminary, the consolidate–freeze tests exhibit a significantly different behavior from the "conventional" frozen MFS tests.

1.3 ORGANIZATION OF THESIS

Chapter 2 presents background information, via an extensive literature review, on the behavior of unfrozen sand, polycrystalline ice and frozen sand. This review is intended to give the reader an appreciation for the complexity of frozen sand behavior by considering the complex behavior of its constituents and how they might interact as a composite system. A description of the isostrain and dilatancy–hardening models are also presented in Chapter 2.

Chapter 3 describes the materials, equipment and testing procedures used in the three testing programs, i.e., the unfrozen tests, conventional frozen tests and consolidate–freeze tests. Components of the high–pressure triaxial testing systems are described along with special design considerations. The scope of each testing program is summarized as well as the general procedures used in test set–up. The chapter also presents the data reduction procedures and possible errors associated with each testing program.

The measured unfrozen test results are presented and discussed in Chapter 4. This presentation includes a summary of the scope of the testing

program and a presentation of consolidation and shear results. The chapter also presents comparisons of measured stress–strain behaviors and summary plots of particular shear parameters. A steady state analysis, based on the state parameter Ψ, is also presented with particular attention given to how steady state conditions were derived for the unfrozen MFS tests and correlations of Ψ with measured shear parameters.

Chapter 5 presents the measured behavior of frozen Manchester Fine Sand in triaxial compression. First, the scopes of the conventional frozen and consolidate–freeze testing programs are described, followed by presentation of the conventional frozen results and then the consolidate–freeze results. The effects of relative density, confining pressure, strain rate and temperature on the stress–strain and volumetric behavior of the conventional frozen tests are treated in detail. This presentation includes both the results from the current research and those by Andersen (1991). Summary plots of small strain, large strain and volumetric strain parameters, as well as stress–strain and volumetric strain curves, are presented and used for discussion. Only 10 consolidate–freeze tests have been performed; therefore, presentation is limited to display of the stress–strain and volumetric responses and comparison of test parameters with conventional frozen results which were performed under similar conditions.

Chapter 6 is an analysis of the measured data. This is done in four sections. In the first section, the measured conventional frozen test results are compared to results found in the literature. In the second section, a complete evaluation of the isostrain and dilatancy–hardening models is presented using the measured conventional frozen and consolidate–freeze results. The third section presents a discussion of the mechanisms involved with the strength and deformation behavior of frozen sand. This presentation follows the frame work first proposed by Ting et

al. (1983). Finally, a proposed conceptual model is presented which attempts to explain the behavior of the frozen MFS based on mechanisms associated with the sand skeleton and pore ice and the interaction between the two components.

Chapter 7 presents a summary of this research, conclusions, and recommendations for continued research.

CHAPTER 2
LITERATURE REVIEW

This chapter provides background information based on review of the available literature. The chapter is divided in four sections. The first three sections review the behavior of unfrozen sand, polycrystalline ice and frozen sand, respectively. Portions of these sections have been abstracted from the work of Andersen (1991), but additional information also has been included, especially with respect to steady state concepts for unfrozen sands and temperature effects on polycrystalline ice and frozen sand behavior. The fourth section summarizes two models which will be used to describe frozen Manchester Fine Sand (MFS) behavior.

2.1 UNFROZEN SAND

This section presents a summary of the behavior of unfrozen sand as well as a detailed review of the steady state (ultimate state, critical state) concept for unfrozen sands. Portions of the summary of unfrozen sand behavior were abstracted from material presented in Andersen's doctoral thesis (1991). The first part of this section covers the parameters used to describe a sand mass; Terzaghi's principle of effective stress and pore water–sand skeleton interaction; possible mechanisms of deformation and strength; and the effects of density and confining stress on stress–strain behavior. The second part of this section presents a detailed review of the steady state concept for monotonic loading of sands.

2.1.1 Description of a Sand Mass

(portions abstracted from Andersen 1991)

Sands can be described based on their particle size, mineral composition, angularity, shape, size and gradation. Sands may also be characterized by properties of the sand mass such as void ratio, relative density and sand structure. Each of these descriptors are briefly discussed below.

2.1.1.1 Particle Size

According to the Unified Soil Classification System, sand size is defined as those soil particles fine enough to pass through the #4 sieve (i.e., < 4.76 mm) and coarse enough to be retained on the #200 sieve (i.e., > 0.074 mm). This corresponds to particle diameters ranging from 4.76 mm to 0.074 mm. Other classification systems have slightly different limits. For example, in the MIT Classification System sand size particles range from 2 mm to 0.06 mm in diameter.

2.1.1.2 Mineral Composition

The mineral composition of a sand can vary widely and is affected by such factors as the composition of the parent rock material, method of formation, amount of weathering and transportation distance. Pettijohn (1975) lists quartz and feldspars as comprising the major fraction of sand size particles in most sand deposits. Micas and other minerals compose approximately 10% or less of the remaining grains. The actual percentages of these constituents will vary widely between sand masses.

2.1.1.3 Particle Angularity

The angularity or roundness of individual particles is affected by the amount and nature of weathering which has occurred and also can be affected by the mineral type and depositional environment. Sand particles can be

visually classified as angular, subangular, subrounded, rounded or well–rounded (Pettijohn, 1975).

2.1.1.4 Particle Shape

Sand particles can also be classified according to shape. Koerner (1970) described the shape of particles by their sphericity which is the ratio of projected particle area to the projected area of the smallest sphere which circumscribes the particle. Other researchers have used a ratio between the length and the width of a sand particle as a measure of shape (Oda 1972, and Ochai and Lade 1983). However, such measurements can be somewhat uncertain because of the difficulty in identifying the major and minor principal axis of irregularly shaped grains.

2.1.1.5 Gradation

The grain size distribution of a sand is termed its gradation. A gradation analysis consists of passing a representative quantity of sand through standardized square mesh openings (sieves) and weighing the amount of material that is retained on each sieve. Based on this gradation or sieve analysis the sand may be classified as well–graded (substantial amounts of sands on a wide range of sieve sizes), poorly–graded (predominantly one particle size) or gap–graded (some intermediate grain sizes missing).

Based on the Unified Classification System, two coefficients are used to define a sand based on gradation analysis results. The coefficient of uniformity, C_u, is defined as

$$C_u = d_{60}/d_{10} \qquad 2.1$$

where d_{60} and d_{10} are the grain sizes for which 60% and 10% of the particles are finer by weight, respectively. C_u is a measure of the uniformity of grain sizes for a given sand. The coefficient of curvature, C_c, is defined as

$$C_c = \frac{d_{30}^2}{d_{60} \cdot d_{10}} \qquad 2.2$$

where d_{30} is the grain size for which 30% of the particles are finer by weight. C_c is a measure of the shape of the gradation curve between the d_{60} and d_{10} sizes.

2.1.1.6 Void Ratio and Relative Density

The void ratio (e) of a sand equals the volume of the voids (V_v) divided by the volume of the solids (V_s)

$$e = V_v/V_s \qquad 2.3$$

Standard procedures, developed by ASTM, are used to determine the maximum void ratio, e_{max}, (i.e., the loosest state) and the minimum void ratio, e_{min}, (i.e., the densest state) for a sand. In general, the these reference states that a sand mass can assume will depend on the shape, gradation and angularity of the grains comprising the sand. They also apply only to sands at relatively low confining stresses.

The relative density (D_r) describes (on a percentage scale) the degree of compactness of a sand and is defined as

$$D_r = \frac{e_{max} - e}{e_{max} - e_{min}} \qquad 2.4$$

where e is the current void ratio. Thus, void ratio and relative density are interrelated.

It must be noted that the D_r of a sand alone can not predict the stress–strain behavior of sand. The effects of sand "structure" (defined below) and confining pressure (discussed in Section 2.1.3) also must be considered.

2.1.1.7 Sand Structure

A sand mass can be classified according to its "structure". As defined

in Lambe and Whitman (1969), "structure" refers "to the orientation and distribution of particles in a soil mass (also called fabric and architecture) and the forces between adjacent soil particles". Brewer (1964) defined the soil fabric as "The physical constitution of a soil material as expressed by the spatial arrangement of the solid particles and associated voids". Oda (1972) states that there are principally two types of fabric, homogeneous fabric and heterogeneous fabric. The homogeneous fabric is that as described by Brewer while heterogeneous fabric consists of "submasses" of homogeneous fabric. For the case of heterogeneous fabric, Oda states that within a granular mass the "Three–dimensional orientations of these homogeneous submasses and their mutual relationships must be the most important fabric feature prevailing in the heterogeneous granular mass."

Ladd et al. (1977) state that for "cohesionless soils, fabric and structure are closely related because interparticle contacts will largely govern the soil's fabric". This is consistent with the observation by Oda (1981) that the behavior of sand is affected both by the preferential alignment of nonspherical particles parallel to the horizontal (orientation of particles) and by the concentration of the unit normal vectors at the points of contact in preferred directions (interparticle contacts). Numerous researchers note that in naturally occurring sands and laboratory specimens prepared by pluviation through air or water, the homogeneous sand fabric is usually cross–anisotropic. The sand particles tend to orient themselves with their contact point unit normals closer to the vertical depositional direction [Oda (1981), Ochai and Lade (1983) and Mitchell (1976)].

2.1.2 Saturated Sand and Terzaghi's Principle of Effective Stress

Terzaghi (1925) presented a method of partitioning stresses in a

saturated soil mass commonly known as the principle of effective stress. As a result of experimental measurements, Terzaghi proposed that the total stress acting on a soil element be partitioned into the effective stresses acting on the skeleton and the pore water pressure according to the following equation

$$\sigma = \sigma' + u \qquad 2.5$$

where σ is the total stress, σ' is the effective soil skeleton stress and u is the pore water pressure.

When considering the interaction between the effective stresses acting on the soil skeleton and the pore water pressures, it is important to consider the case of an incremental change in total stress occurring under conditions where the pore water is not free to drain out of the soil. Skempton (1954) introduced a pore pressure parameter to quantify the amount of stress sharing which occurs between the soil skeleton and the pore water under these conditions. This parameter is known as Skempton's B–value and is defined

$$B = \Delta u/\Delta\sigma \qquad 2.6$$

where Δu is the increment in pore pressure caused by $\Delta\sigma$ which is an increment in total applied (hydrostatic) stress.

Skempton proposed that the magnitude of the B–value is dependent on the porosity of the soil (the ratio of the volume of the voids to the total volume), the bulk compressibility of the soil skeleton and the compressibility of the pore fluid (water). Bishop (1973) summarized Skempton's earlier work and extended his analysis to include the effect of the compressibility of the individual sand grains. He concluded that the B–value could be expressed

$$B = \frac{1}{1 + n\cdot(C_w - C_s)/(C - C_s)} \qquad 2.7$$

where n is the porosity, C_w is the bulk compressibility of the pore fluid, C_s is the bulk compressibility of the solid material forming the porous medium,

and C is the bulk compressibility of the porous medium (skeleton) under drained conditions. Therefore, a saturated sand will exhibit a lower B–value as the sand density increases because the skeleton's bulk compressibility decreases with density. Lambe and Whitman (1969, Table 26.1) state B–values for saturated loose and dense sand as 0.998 and 0.992, respectively.

Skempton (1954) also proposed that, for fully saturated soils, the partitioning of applied, non–hydrostatic stresses between the soil skeleton and pore water could be represented by the A–parameter.

$$A = \frac{\Delta u - \Delta \sigma_3}{\Delta \sigma_1 - \Delta \sigma_3} \qquad 2.8$$

where Δu is the change in pore pressure induced by changes in the applied major and minor principal stresses, $\Delta \sigma_1$ and $\Delta \sigma_3$, respectively.

2.1.3 Stress–Strain–Strength Behavior of Sand

This section presents a review of the stress–strain–strength behavior of unfrozen sand. First an overview of the shear behavior is presented followed by a presentation of measured shear results.

2.1.3.1 Rowe's Postulate of the Strength of Sand

Rowe (1962) proposed that the peak drained friction angle of a sand (ϕ_p) can be divided into three components: that due to sliding friction between particles (ϕ_u); that due to interference of particles as they move around each other during large deformations (ϕ_i); and that due to the dilation of the skeleton (ϕ_d). Figure 2.1 presents a schematic plot of these three components of ϕ versus D_r. The value ϕ_f represents the combined frictional and interference components of strength, i.e. $\phi_f = \phi_u + \phi_i$.

As illustrated in Figure 2.1 the difference between ϕ_p and ϕ_f is the dilatancy component of strength (ϕ_d) which is due to the expansion of the soil skeleton as it "loosens up" to accommodate the imposed deformations.

This results in a greater expenditure of energy to cause deformation and thus leads to an increase in strength. The friction between particles (ϕ_u), which Rowe termed true physical friction, depends on the nature of the mineral forming the sand, the surface properties and the roughness and size of the particles. This component of strength is constant for all D_r, but will supposedly decrease with increasing pressure and particle size according to Rowe (1971). The interference component of strength (ϕ_i) is associated with the amount of energy necessary to change the particle assembly.

One can predict the shear and deformation behavior of sand using Figure 2.1. For a dense sand sheared at a low confining pressure under drained conditions, the peak strength is reached at small strains and the peak friction angle is due to dilatancy and interparticle friction with little or no particle interference component of strength. If the "dense" sand specimen is sheared to large strains, an ultimate state is reached where the sand will reach a constant volume friction angle, ϕ_{cv} ($= \phi_u + \phi_i$). This constant volume condition, also referred to as the critical state or steady state condition, is independent of the initial density of the sand. For a "loose" sand, the peak friction angle equals ϕ_{cv}, with very little dilation component involved in the sand's strength. At intermediate sand densities, the peak strength is due to a combination of dilatancy, interference and sliding friction. For undrained shear conditions, the dilative tendency of dense sands leads to a reduction in pore water pressure, and hence an increase in effective stress. For loose sands, the contractive tendency leads to an increase in pore water pressure, and thus a decrease in effective stress. The development of constant pore pressures with continued deformation for undrained conditions is analogous to the constant volume deformation in the drained condition.

To calculate ϕ_f, Rowe derived the following equation for the peak principal stress ratio, R_p

$$R_p = \left[\frac{\sigma'_1}{\sigma'_3}\right]_p = (1 + \frac{\Delta\epsilon_v}{\Delta\epsilon_1})\cdot\tan^2(45 + \frac{\phi'_f}{2}) = (1 + D)\cdot R_f \qquad 2.9$$

where σ'_1 and σ'_3 are the major and minor principal effective stresses and ϕ'_f and R_f represent the combined frictional (ϕ_u) and interference (ϕ_i) components of strength. The rate of dilation, D, is defined as the ratio of the change in volumetric strain ($\Delta\epsilon_v$) with the change in strain in the direction of the major principal stress ($\Delta\epsilon_1$). Volumetric strain is defined as the ratio of the change in specimen volume (ΔV) and the initial volume (V_o)

$$\epsilon_v = \Delta V/V_o \qquad 2.10$$

Note that a negative volumetric strain represents a decrease in specimen volume. The dilatancy factor (1 + D) is a measure of the effect of dilation (ϕ_d) on the peak shear strength (ϕ_p).

Under drained conditions, the peak stress ratio and peak strength ($\sigma'_1 - \sigma'_3$) of a sand occur at the same strain; however, R_p and peak strength do not necessarily occur at the same strain under undrained conditions where, by definition, D = 0.

2.1.3.2 Measured Drained Shear Behavior

Casagrande (1936) summarized the results of direct shear tests on sands with varying densities by stating that "during shearing tests, we find that dense sand expands and very loose sand reduces its volume". Figure 2.2 reproduces sketches which qualitatively illustrate his observations. The expansion of dense sand during shear is referred to as dilation, which "loosens up the structure" of the sand resulting in a net volume increase. In loose sands, the structure collapses during shear to a more stable configuration.

Lee and Seed (1967) performed a series of drained triaxial compression

loading tests on processed Sacramento River Sand. The grain size ranged from 0.149 to 0.297 mm and the sand was tested at initial relative densities ranging from 38 to 100% and effective confining stresses (σ'_c) ranged from 1 to 140 ksc. Results of their tests are presented in Figure 2.3. Tests results are presented in terms of the principal stress ratio, R, and volumetric strain, ϵ_v, versus axial strain, ϵ_a ($= \epsilon_1$). The principal stress ratio is defined as

$$R = \sigma'_1/\sigma'_3 = \frac{\sigma'_c + (\sigma'_1 - \sigma'_3)}{\sigma'_c} = 1 + (\sigma_1 - \sigma_3)/\sigma'_c \qquad 2.11$$

where σ'_1 and σ'_3 are the major and minor principal effective stresses, respectively, and $(\sigma_1 - \sigma_3)$ is commonly called the deviator stress. In the Figure 2.3, "σ_3" is the effective confining stress (σ'_c) for each test. The principal stress ratio is related to the effective friction angle by

$$\phi' = \arcsin\left[\frac{R - 1}{R + 1}\right] = \arcsin\left[\frac{\sigma'_1 - \sigma'_3}{\sigma'_1 + \sigma'_3}\right] \qquad 2.12$$

As illustrated in Figure 2.3, Lee and Seed (1967) observed that Sacramento River Sand tested under drained conditions in triaxial compression can exhibit either brittle type behavior with significant strain softening after peak strength, or ductile type behavior with no strain softening. This change in behavior depends both on the relative density and on the magnitude of the effective confining stress. For example, Figure 2.3b shows dense sand specimens prepared with an initial (preconsolidation) void ratio of 0.61 (D_r = 100%) and tested at various confining stresses. The test with the lowest confining stress, σ'_c = 1 ksc exhibited the largest principal stress ratio at peak deviator stress and the most post peak strain softening (brittle behavior). As σ'_c increases, the principal stress ratio (and hence ϕ') at peak decreased and the strain to peak increased leading to a more ductile type behavior. The specimens tested under lower confining pressures also exhibited the greatest dilation. It is important to note that for the specimens which

exhibited some tendency for dilation (i.e., $\sigma'_c < 20$ ksc), the maximum rate of dilation occurred near the peak strength as predicted by Rowe (1962). The rate of dilation in triaxial compression tests is defined as $\Delta\epsilon_v/\Delta\epsilon_a$.

Figure 2.3a shows loose sand specimens prepared at an initial void ratio of 0.87 ($D_r = 38\%$). The effect of increasing the effective confining pressure was the same as for the dense sand, i.e., a decrease in peak principal stress ratio and an increase in the strain to failure with increasing σ'_c. However, these loose sands did not exhibit strain softening. All loose specimens with $\sigma'_c > 2$ ksc exhibited volume decreases during shear, with the greatest decrease in volume occurring for the test with the largest effective confining stress.

The results in Figure 2.3 also show that the stress–strain behavior of the dense sand sheared at a high effective confining pressure is qualitatively similar to a loose sand sheared at a low effective confining pressure. Thus, the effect of an increase in effective confining stress is similar to a decrease in density.

Figure 2.4 presents the Mohr–Coulomb representation of Lee and Seed's drained triaxial compression tests results on Sacramento River Sand. The figure shows Mohr's circles representing the state of stress at peak strength for confining pressures up to 120 ksc. Note that the failure envelope is not linear, but exhibits a decreasing slope as the effective stress increases.

2.1.3.3 Measured Undrained Shear Behavior

Undrained shear behavior is illustrated using results by Castro (1969). Castro performed a series of stress–controlled, consolidated–undrained triaxial compression tests to study the effect of relative density and confining pressure on the undrained response of several sands. One of these sand was uniform

Ottawa Banding Sand with particle sizes ranging from 0.4 to 0.07 mm and preshear relative densities ranging from 16 to 96%. Effective confining pressure varied from 0.3 to 10 ksc. Summary plots of some of Castro's data, presented by Mohamad and Dobry (1986), are reproduced as Figure 2.5. In the figure, q is defined as

$$q = (\sigma_1 - \sigma_3)/2 \qquad 2.13$$

and $\bar{p}$ (= p′) is defined as

$$\bar{p} = p' = (\bar{\sigma}_1 + \bar{\sigma}_3)/2 \qquad 2.14$$

The effect of effective confining stress ($\bar{\sigma}_{3c} = \sigma'_c$) on the undrained response of a medium dense sand is illustrated in Figure 2.5a. These tests were conducted at a preshear relative density of 42% and effective confining pressures of 0.3, 4 and 10 ksc. Figure 2.5b presents the effect of relative density on the undrained behavior of the Banding sand. All the specimens were isotropically consolidated to 4 kg/cm^2, but at relative densities ranging from 37 to 96%.

Based on these measured results, the behavior of sand in undrained shear can be summarized as follows. In terms of changes in σ'_c, sands at a "moderate" relative density and "low" confining stress (e.g., Test No. 3 in Fig. 2.5a) will continuously strain hardening during shear. The stress path reaches the K_f–line early in straining and then continuously climbs up the K_f–line. The K_f–line is the locus of points on the q–$\bar{p}$ diagram representing the failure envelope (maximum principal stress ratio). Though initially positive, negative pore pressures predominate during shear, and it is difficult/impossible to reach the peak undrained strength of the specimen. The same sand with the same relative density tested at a "high" confining stress (e.g. Test No. 1) will exhibit brittle type behavior with a peak

undrained strength at very low axial strains, followed by a significant amount of strain softening to a very low strength at large strains. This stress–strain behavior is generally termed liquefaction. This strain softening is caused by the generation of large positive pore pressures.

In terms of changes in D_r, a "dense" sand at a "moderate" confining stress (Test Nos. 5 and 6) will reach the K_f–line at very low axial strains and continuously climb up the K_f–line through the generation of negative pore pressures, while a "loose" sand (Test No. 4) will exhibit liquefaction and significant post peak strain softening caused by the generation of large positive pore pressures. Thus qualitatively for undrained shear, a decrease in relative density has the same effect as an increase in confining stress.

In Figure 2.5 the stress paths for Test Nos. 2 and 5 have what are called "elbows" where the stress path changes from a decreasing p' direction to an increasing p' direction. Ishihara et al. (1975) called this transition stress ratio (q/p') the angle of phase transformation. At phase transformation, the shear response of a sand changes from contractive to dilative. That is, the generated pore pressures reach a maximum positive level and become less positive as shear continues.

2.1.3.4 Other Factors Affecting Shear Strength of Sands

In addition to the density, effective confining stress and drainage conditions during shear, sand strength is also influenced by the sand's anisotropic fabric and the intermediate principal stress. Anisotropy can be inherent as a result of the depositional process or induced as a result of prior straining (e.g., Wong and Arthur 1985). Ladd et al. (1977) present triaxial test results for three sands where the angle (β) between the direction of deposition and the direction of loading (major principal stress, σ_1) was varied.

Test results are presented in Figure 2.6. Generally the strength (as well as stiffness) is greater if the major principal stress is oriented in the direction of deposition or in the direction of the major principal stress of prior loadings.

The magnitude of the intermediate principal stress influences the behavior of sand. This effect can be expressed in terms of the b–value

$$b = \frac{\sigma'_2 - \sigma'_3}{\sigma'_1 - \sigma'_3} \qquad 2.15$$

where σ'_1, σ'_2 and σ'_3 are the major, intermediate and minor principal stresses, respectively. The b–value ranges from zero (triaxial compression) to one (triaxial extension). Figure 2.7 shows the results of several testing programs that evaluated the effect of b on the drained strength of sands (Ladd et al. 1977). In general, the strengths in plane strain (b = 0.2 to 0.4) are higher than those in triaxial compression, especially for dilative specimens. Tests results beyond b = 0.5 may be questionable due to possible experimental errors.

2.1.4 Deformation of Sand

Sands deform by various mechanisms including the elastic and plastic straining of individual particles at points of contact, crushing of particles and the rearranging of particles within the sand mass. Bishop (1966) notes that crushing is initially concentrated at the particle contact points, but as shear stresses and confining pressures increase, particles will ultimately shatter. Vesic and Clough (1968) and Lee (1977) present triaxial compression results which indicate that the crushing of grains is more prevalent in sands that have undergone both hydrostatic compression and shear deformations as opposed to having only undergone hydrostatic compression.

Rearranging of the sand particles may be accomplished by both sliding and rolling motions. There is debate as to the relative importance of sliding

versus rolling although most researchers believe that sliding is predominant. Several researchers (Horne 1965; Oda and Konishi 1974; Athanasiou–Grivas and Harr 1980) postulate that deformations occur due to the relative motions of instantaneously "rigid groups" of particles, such that slip (and rolling) occurs at a relatively few locations at any instant in time and is not proceeding generally throughout the granular mass. Discrete element modeling of idealized granular media (Cundall et al. 1982) supports the hypothesis that deformations in granular materials are accommodated by the rigid body motion of groups in particles which continuously group and regroup during shear.

2.1.5 The Steady State of Sands

The steady/critical/residual state of a sand has been a topic of research and controversy since the pioneering studies by Casagrande (1936). Casagrande (1936) found that dense and loose sands in drained direct shear tests tend to come to the same density and shear stress at large strains. This condition signified a state of continuous deformation at constant volume and constant shear and normal stresses. It is this concept of constant volume deformation that has been the basis of the steady/critical/residual state analysis of granular materials.

The following presents a general review of steady state concepts as they pertain to granular materials. For purposes of consistency, the writer will use the term of "steady state" in the following discussion, as opposed to "critical state" or "residual state" which also may be found in the literature. It should be noted that the concepts of critical state soil mechanics, developed by Roscoe et al. (1958) and Schofield and Wroth (1968), may be valid for steady state conditions; however, a detailed discussion on critical

state soil mechanics would be far too broad in scope for this report. Methodologies which use steady state concepts to analyze sand behavior are also summarized with particular emphasis on the state parameter (Ψ) as developed by Been and Jefferies (1985). Given the wealth of research in this area of soil mechanics, discussion is limited to steady state behavior due to static or monotonic loading. Steady state behavior of sands due to cyclic loading, shock (earthquake) loading or other transient loading conditions will not be discussed.

2.1.5.1 Steady State Concepts

The early beginnings of what the writer terms steady state can be traced back to Casagrande's experiments in the early 1930's. As stated previously, various terms have been used to describe the steady state condition: critical void ratio, critical state, residual state and ultimate state are common examples. While researchers believe that a condition of constant volume deformation exists for sands, they disagree on what defines this state and if the steady state is the same as or different from the critical state or critical void ratio state. The following discusses various steady state concepts for sands and the differences, if any, between these concepts.

Definition of Critical Void Ratio

As noted previously, Casagrande (1936) observed that dense sands have a tendency to expand and loose sands to contract during drained shear. He also noted that at large strains, sands sheared under drained conditions will deform to a state where there is no additional volume change and no change in stresses with continued straining. He found in his experiments that a dense sand and loose sand, subjected to drained shear under identical vertical normal stresses, would ultimately end up at the same density (void ratio) and

shear stress. Casagrande called the void ratio at this state the critical void ratio and explained that sands in this state have reached a condition at which continuous deformation is possible at constant shear stress.

The concept of a critical void ratio was also analyzed by Roscoe et al. (1958) in their presentation of critical state soil mechanics. Similar to the definition prescribed by Casagrande, they proposed that in a drained test, the critical void ratio state can be characterized by a condition that "any arbitrary further increment of shear distortion will not result in any change in void ratio". In their paper, Roscoe et al. present results of simple shear tests on 1 mm diameter steel balls and glass beads as being representative granular media. Figure 2.8 reproduces the void ratio versus shear displacement results for a set of tests on steel balls where a normal stress of 20 psi was applied to specimens of various ball packings. As shown in the figure, the critical void ratio state, reached for these tests, represents a unique condition independent of the initial conditions. However, they noted that the critical void ratio is defined by both the void ratio and the stresses acting on the steel balls. If the applied stress is changed, the critical void ratio will also change. They then noted that plotting the critical void ratio points versus applied stress forms a critical void ratio (CVR) line. The CVR lines for the steel balls and glass beads are reproduced in Figure 2.9. The CVR lines are plotted in shear stress – normal stress ($\tau - \sigma'$) space and void ratio – normal stress ($e - \sigma'$) space. Roscoe et al. believed that the CVR line for a soil would lie on or near its drained failure surface. For soils sheared under undrained conditions, they state that "the sample remains at a constant voids ratio, but the mean normal effective stress will alter to bring the sample into an ultimate state such that the particular voids ratio, at

which it is compelled to remain during shear, becomes the critical voids ratio". They state that these two conditions in the drained and undrained tests may or may not be identical; i.e, give the same CVR line.

Based on these observations/hypotheses, the existence of a constant volume – constant stress deformation condition in sands in widely accepted. However, while researchers agree that a critical state condition exists, they disagree about the structure of the sand in this condition and whether or not it is unique and independent of the initial state or loading conditions (see Section 2.1.5.3).

Concept of a Flow Structure

During his tenure at Harvard University, Casagrande expanded the critical void ratio concept and developed the hypothesis of a "flow" structure. Casagrande (1975) states that granular materials can develop a structure during shear such that "each grain is constantly rotating in relation to all surrounding grains so as to offer a minimum of frictional resistance". This flow structure is only present during the liquefaction (undrained deformation) of the sand; once flow stops, the sand grains revert back to a more stable structure. Casagrande believed that the flow condition was initiated at one point in the soil mass and would quickly spread through the mass via chain reaction. Casagrande also stated that this flow condition could be best demonstrated in the laboratory using load–control testing techniques with undrained shearing conditions since he believed that the applied loading must be sustained to induce the flow structure in monotonic testing.

The early work by Casagrande and Roscoe et al. used direct shear or simple shear apparati to develop the critical void ratio concept. However, the state of stress in these devices cannot be defined. Therefore, other

devices, predominantly the triaxial apparatus, have become the preferred tool used in subsequent research. One of the pioneering triaxial–based studies was performed by Castro (1969). He conducted a series of undrained and drained triaxial compression tests (previously presented in Section 2.1.3, Figure 2.5) to support the hypothesis of a flow structure. In undrained triaxial testing, the flow structure is characterized by an increase in pore pressure, along with a rapid loss in strength, while undergoing very rapid deformations (strain rates in the 100,000's %/hour). After the rapid strength loss, the shear strength, pore pressure and normal effective stresses remain constant with continued deformation. This test condition is illustrated by Tests No. 1 and 4 and Figure 2.5. Castro (1969) performed 27 undrained triaxial tests and, based on his results, developed a flow line (F–line). Figure 2.10 shows this line (denoted as the $\bar{e}_f$–line), along with measured test results, plotted in void ratio–log effective confining stress (e–log σ'_{3f}) space. Figure 2.11 shows the CVR line for strain–controlled, drained tests performed by Castro (1969) on the same sand used for developing the F–line. The applied strain rate for these tests was 60%/hour. This line is designated the S–line. Casagrande (1975) states that test performed under drained conditions would not develop the flow condition but would develop a large strain, constant–volume–deformation condition. These results imply that the behavior of drained and undrained tests will lead to different steady state conditions. Castro (1969) stated that there may be two critical void ratios of a sand; one characterized by a flow structure, leading to the F–line, and the other characterized by a "normal structure" leading to the S–line. The difference between these two lines may depend not only on drainage conditions but also on strain rate. [See Section 2.1.5.3.]

The Steady State of Deformation

Poulos (1981), Poulos et al. (1985) and Poulos et al. (1988) have expanded on the flow structure concept and hypothesize that an unique condition of sand exists which can be described as "The Steady State of Deformation". Poulos (1981) defines this condition as "that state in which the [sand] mass is continuously deforming at constant volume, constant normal effective stress, constant shear stress, and constant velocity. The steady state of deformation is achieved only after all particle orientation has reached a statistically steady–state condition and after all particle breakage, if any, is complete so that the shear stress needed to continue deformation and the velocity of deformation remain constant". Poulos et al. (1985 and 1988) further state that the undrained strength at steady state is a function of the soil's in–situ void ratio and is independent of the method or rate of loading and its initial structure. Poulos (1981) states that the concept of critical state referred to by Roscoe et al. (1958) does not meet the definition of steady state deformation since their critical state can be reached without a continuation of deformation. Schofield and Wroth (1968) provide a definition of critical state which includes continued deformation but ignores the structure of the soil in this state. Poulos (1981) states that the steady state of deformation institutes a complete remolding or destruction of the sand's previous structure. Rowe (1962) also considers the structure of granular material at large deformation to be remolded. Rowe describes remolding as a condition where half of the particles are in contact, resisting the applied shear stress, and the other half are not in contact but are forming new contacts. As deformations continue, particles break contacts and form new ones. Poulos agrees that Rowe's remolding concept is compatible with the steady

state of deformation but states that the provision for constant velocity is missing from Rowe's concept.

The steady state condition is often assumed to be unique for a given sand (e.g., Poulos et al. 1985) and is characterized in e – log σ' space or "state diagram" by a steady state line (SSL) which is analogous to the F–line presented by Castro (1969). Figure 2.12 shows a steady state line developed from consolidated–undrained tests on compacted sand specimens. Poulos et al. (1985) claim that the steady state condition can be reached from either drained or undrained conditions and its position is extremely sensitive to the gradation and angularity of the sand. Poulos et al. (1988) state that the steady state condition may not be achievable for dense sands in triaxial compression and can be best achieved for clean narrowly graded sands that exhibit entirely contractive behavior and are strained in excess of 20% to 30%. In the majority of research programs, the steady state condition is typically studied using undrained triaxial compression tests on "loose" sands, where the critical state parameters are usually developed from drained tests on dense sands (e.g., Been et al. 1991).

Concept of a Collapse Structure

Alarcon–Guzman et al. (1988) describe a concept they call "structural collapse" to describe the undrained shear behavior of contractive sands. They state that for a very loose (contractive) sand, the structure is metastable and collapsive. Such a structure only requires small shear strains to induce a sudden rearrangement of grains and a momentary loss of contact at grain–to–grain interfaces. This loss of grain–to–grain contact causes the load being carried by the sand skeleton to be transferred to the pore water; producing a sharp increase in pore pressure, sharp decrease in effective stress

and rapid loss in sand strength. Alarcon–Guzman et al. go on to state "that the pore water pressure response of sand specimens in undrained shear does not depend only on the potential [for] volume changes, as determined by the critical void ratio line, but also on the tendency to collapse". It is this tendency for collapse that allows sands to reach the steady state condition. They further hypothesize that if a sand's structure is not "inherently brittle", no collapse will take place and the steady state conditions of the F–line (from undrained tests) and S–line (from drained tests) will tend to be the same (i.e., Castro's "normal structure" hypothesis). However, if the sand consists of smoother, rounder and finer particles of uniform gradation, the potential of collapse is higher and the F–line and S–line will be further apart.

Pseudo–Steady State Conditions

The steady state of deformation has become the preferred definition for the constant volume deformation of sands. However, for some sands ascertaining this condition can be difficult, if not impossible, using conventional laboratory tests (e.g., triaxial tests). In addition, not all testing conditions lead to a steady state condition as illustrated by Test Nos. 2 and 5 in Fig. 2.5 which show initially contractive behavior but then show dilative responses.

Castro (1969), when developing the F–line from tests which experienced full liquefaction, also presented results of load–controlled, undrained tests where full liquefaction was not reached (e.g., Test No. 2 in Fig. 2.5). This "limited liquefaction" condition is similar to the flow condition in that there is a significant and rapid loss of sand strength after reaching the "peak" strength; however, after some limited amount of deformation, the sand begins to gain strength and may even exceed the initial "peak" strength. Figure

2.13 recreates Figure 2.10 but includes those tests which exhibited limited liquefaction (plotting the minimum σ'_3 measured during shear) and shows that tests with limited liquefaction plot along the same F–line as full liquefaction tests. This implies that a full, continuous flow condition is not required to reach the flow line. Vaid and Chern (1985) present strain–controlled, undrained triaxial compression tests results on an angular, tailings sand and rounded, Ottawa sand which indicate that the liquefaction and limited liquefaction rest results could be grouped together. However, they state that while the limited liquefaction test results plot along the steady state line, they do not constitute a steady state condition.

Phase Transformation and Critical Stress Ratio

Vaid and Chern (1985) found that the mobilized effective friction angle at steady state ϕ'_{ss} and at phase transformation ϕ'_{pt} are identical. As noted in Section 2.1.3, the phase transformation signals the change from a contractive response to a dilative response. Figure 2.14 shows the stress paths, deviator stress and pore pressures versus axial strain for contractive and dilative specimens sheared under undrained conditions. As shown in the figure, the contractive specimen reaches the steady state condition without phase transformation occurring. On the other hand, the stress path of the dilative specimen reaches the phase transformation "elbow", then shows an increase in stresses and finally curves back around to the steady state condition which has the same friction angle as the phase transformation point.

Vaid and Chern state that this equality is unique for a given sand and independent of initial stress state or void ratio. Negussey et al. (1988) expand on this hypothesis of equality by concluding that the friction angle at constant volume (ϕ'_{cv}) for drained tests also equals the friction angle at

steady state, ϕ'_{ss} (= ϕ'_{pt}), for undrained tests. Negussey et al. performed drained shear tests using a ring shear device on a variety of granular materials including Ottawa sand, tailing sands, lead shot, glass beads and copper beads. Applied normal stresses ranged from 0.01 to 1.4 MPa. Test results indicate that ϕ'_{cv} is independent of confining pressure and void ratio and is equal to the friction angle mobilized at steady state in undrained tests. Vaid and Chern (1985) also found that a sand specimen will exhibit either a slightly contractive or a dilative response based on the level of axial strain needed to reach phase transformation. If the ϵ_a level to phase transformation is small (less than $2^1/_2$ % for the sands they tested), then the specimen would exhibit a strong dilative response (i.e., strain hardening) with no contractive response. However, if the ϵ_a level to phase transformation was large, then the specimen would exhibit a "slightly contractive" (some strain softening followed by strain hardening) behavior during shear. Only tests which were slightly contractive to fully contractive were used in their development of the $\phi'_{pt} = \phi'_{ss}$ concept.

Vaid and Chern (1985) also noted that the initiation of large contractive behavior for loose sands occurs at the peak deviator stress. They noted that for undrained compression tests the stress ratio (σ'_1/σ'_3) at peak deviator stress ($\sigma_1 - \sigma_3$) was the same for all tests which undergo liquefaction, regardless of the sands initial state. This stress ratio is called the critical stress ratio (CSR). Figure 2.15 shows the CSR lines, along with the phase transformation (PT) line, in q–p′ space for the angular tailings sand and rounded Ottawa sand they tested. Note that their CSR lines are linear and fall below the steady state and "failure" (maximum obliquity) envelopes for the sands [note: "failure" does not imply a peak strength condition].

Also note that both the CSR and PT lines are shown to extend to the origin. Vaid and Chern note that the zone between the PT and CSR lines denotes the region of contractive response.

Sladen et al. (1985) introduced a similar concept to the CSR which they called the collapse surface. The collapse surface, schematically shown in Figure 2.16a, is a plane in the e–q–p′ space which represents the locus of peak deviator stresses for loose (contractive) sands that reach the steady state condition. It should be noted that in Figure 2.16 $q = (\sigma_1 - \sigma_3)$ and $p' = (\sigma'_1 + \sigma'_2 + \sigma'_3)/3$. Sladen et al. state that the "collapse surface can be imagined as the locus of soil states at which destruction of a metastable sensitive soil structure is initiated by static loading until the steady state" is obtained. They also state that the collapse surface may be reached by either undrained or drained loading, but that actual liquefaction (collapse) will only occur if drainage is impeded.

The collapse surface may also be represented as a line in normalized stress space where the normalizing parameter, P'_{ss}, is the p′ at the steady state condition for any particular void ratio. Such a plot is presented in Figure 2.16c using Castro's (1969) tests results on Banding sand. The normalized peak strengths for Castro's tests form a line in normalized stress space which represents the location of the collapse surface at any particular void ratio. This collapse surface line extends back to the steady state point for each void ratio. Note that the stress path for a test may extend above the collapse surface but the final state of stress will be at the steady state point.

Alarcon–Guzman et al. (1988) also note that in stress space, the CSR for loose (contractive) sands signifies the initiation of structural collapse.

Figure 2.17 schematically illustrates the CSR lines and steady state envelope for a series of undrained tests at a constant void ratio but different initial stress states. It can be seen that, unlike Vaid and Chern (1985), the value of the CSR is not a constant but is dependent on the level of stress. Alarcon–Guzman et al. also state that the CSR is dependent on the void ratio as well. It should also be noted that in Figure 2.17 the CSR line does not extend to the origin but to the steady state point; similar to the collapse surface concept of Sladen et al. (1985). The writer believes it may be impossible to obtain CSR points below (i.e., to the left of) the steady state points since the CSR line represents the behavior of contractive sands. Only sands which are dilative (e.g., curve A in Fig. 2.17) will have stress paths to the left of the steady state point.

2.1.5.2 The State Parameter for Sands

Definition of State Parameter

Using the steady state concept as a basis, Been and Jefferies (1985) introduced the state parameter (Ψ) as a measure of the physical condition (state) of a sand in terms of its initial void ratio and the initial state of stress with respect to the conditions at steady state. Figure 2.18 illustrates the definition of the state parameter as defined by Been and Jefferies. The steady state line (SSL) is presented in the void ratio – log mean normal effective stress (e – log I'_1) space where the mean normal effective stress is the effective octahedral stress defined as

$$I'_1 = (\sigma'_1 + \sigma'_2 + \sigma'_3)/3 \qquad 2.16$$

In this space, the slope of the SSL is defined by λ_{ss}. As illustrated in Figure 2.18, the Ψ parameter is defined as the vertical distance from the initial state to the SSL expressed in units of void ratio. A sand which has

an initial state that plots above the SSL has a $+\Psi$ and would exhibit a contractive response during shear. A sand which has an initial state that plots below the SSL has a $-\Psi$ and would exhibit a dilative response during shear.

Been and Jefferies assume that all specimens of a given sand tend to approach the same final state irrespective of the initial state. They adopt the concept of "The Steady State of Deformation" as proposed by Poulos (1981). However, they explain that the state parameter Ψ "does not depend on the nature of the sand structure at the steady state. Rather is depends on there being a unique, repeatable particle arrangement at the steady state condition". Therefore, it appears that this particle arrangement may be the completely remolded structure, as hypothesized by Rowe (1962) and Poulos (1981), the collapse structure described by Alarcon–Guzman et al. (1988) or some other structure which may be unique and repeatable. The writer believes that all of these hypothesized structures are, from a macroscopic viewpoint, essentially the same and appropriate. However, Been and Jefferies do state that the overall behavior of a granular material must be described by both a state parameter and an as yet developed fabric parameter.

Been and Jefferies (1985) present the results of 43 stress–controlled (load–controlled) triaxial compression tests on Kogyuk 350 sand; a uniform quartzitic sand with a mean grain diameter of 350 μm. The fines content of the sand was varied from 0 to 10 percent in an attempt to model actual field sand gradations and to evaluate the effect of fines on the steady state condition. Lubricated end platens were used to minimize specimen non–uniformities during shear. Figure 2.19 reproduces the SSL developed from their testing on Kogyuk 350/2 sand (the second number denotes fines

content in percent). As can be seen in the figure, the SSL was defined from both $-\Psi$ and $+\Psi$ tests, but mostly $+\Psi$ tests. Figure 2.20 shows the SSL's from the tests of Kogyuk 350 sand at different fine contents. It can be seen that an increase in fines content leads to a steepening of the SSL line. Been and Jefferies contribute this steepening of the SSL to an increase in sand compressibility with increased fines content.

Use of the State Parameter

The state parameter, as developed by Been and Jefferies, represents the first attempt to quantify the overall behavior of sands as a function of both the initial density and the effective stress level. The state parameter's usefulness lies in its ability to correlate various shear parameters, such as undrained shear strength and effective friction angles regardless of the absolute magnitude of the e or σ'_c. Figure 2.21 shows a plot of peak undrained strength ratio versus $+\Psi$ for their Kogyuk and other sands. The plot shows a consistent reduction in normalized strength with an increase in Ψ. Figure 2.22 shows the peak drained effective friction angle (ϕ') versus Ψ for a variety of sands. The figure shows that all data fall within a fairly narrow band with a general trend for ϕ' to decrease with increasing Ψ.

The state parameter can also be used to illustrate normalized effective stress paths during undrained shear of sands. Figure 2.23 plots several normalized stress paths for specimens tested undrained at various relative densities and effective confining pressures, but with similar Ψ parameters. The deviator stress and the mean stress (I'_1) have both been normalized by the mean normal effective stress at the steady state line (I'_{ss}). Specimens #103 and #108 have different σ'_c (50 kPa and 300 kPa, respectively) and D_r (33% and 50%, respectively) but similar Ψ parameter and, therefore

almost identical dilative normalized stress paths, and specimens #45 and #112 with positive values of Ψ exhibit similar contractive normalized stress paths.

Uniqueness of Steady State Line

Been et al. (1991) expanded on the universality of the state parameter by performing 56 triaxial tests on Erksak 330/0.7 sand using a variety of test conditions. The testing program included triaxial tests performed using different loading rates (load–controlled versus strain–controlled), drainage conditions (drained versus undrained), stress paths (compression versus extension) and specimens preparation techniques (moist compaction versus wet pluviation). A variety of initial void ratios (some at $D_r < 0\%$) and stress states (σ'_c up to 8.1 MPa) were employed. Lubricated ends were used to limit specimen non–uniformities during shear, and special procedures, including corrections for membrane penetration and post–shear freezing of specimens, were employed to measure accurate void ratios. Figure 2.24 reproduces typical undrained and drained test results for which the steady state condition was judged to exist at the end of the test.

Figure 2.25 shows the SSL (which they now denote as the critical state line) developed from their tests. Two observations worth noting are that:

1) The SSL is a bi–linear curve with the line becoming steeper at $I'_1 \approx 1$ MPa. Been et al. contribute the break in the SSL to the breakage of sand grains thus creating a change in the sand's mineralogy and particle size distribution. They present data on Leighton Buzzard sand which show a similar curvature in the steady state line at higher stresses.

2) A unique SSL was developed from a variety of specimen

preparation techniques, loading methods, stress paths and drainage conditions.

Given that the SSL was obtainable from a variety of testing conditions, they claim that the SSL for Erksak 330/0.7 sand is a unique entity independent of the testing variables employed (i.e., undrained versus drained tests, compression versus extension). This suggests that the steady state line for undrained tests (F–line) and the critical state line for drained tests (S–line) are identical. However, Been et al. acknowledge that this conclusion is contrary to other steady state research endeavors with other sands. (See Section 2.1.5.3).

Alternative Uses of the Steady State Line

Though the first to quantify overall sand behavior with the state parameter, Been and Jefferies were not the only researchers to recognize the value of the steady state concept. Poulos et al. (1985 and 1988) developed design procedures for stability analyses using the concept of steady state but did not realize the usefulness of a state parameter nor try to correlate other shear parameters with the steady state conditions.

A surprising coincidence is the work of Sladen et al. (1985) who present a view of the state parameter parallel to that of Been and Jefferies (1985). They performed a series of strain–controlled and load–controlled, undrained triaxial compression tests on Nerlerk sand and Leighton Buzzard sand. They used critical state concept to examine the behavior of sands at the steady state condition claiming that the steady state and critical state condition were identical; a conclusion later concurred by Been et al. (1991). As in the Been and Jefferies paper, Sladen et al. also plot the steady state line in the $e - \log I'_1$ space and state that "The difference between the initial void ratio

and the void ratio at the critical state at the same normal stress has been termed the state parameter." They claim the concept of a state parameter stems from the work of "equivalent pressures" first developed by Hvorslev (1937) and extended by Roscoe and Poorooshab (1963). Sladen et al. also present normalized stress paths and state that "stress paths will be geometrically similar for samples with the same [state parameter]". This behavior was also obtained by Been and Jefferies (1985) as previously shown in Figure 2.23. However, Sladen et al. did not pursue the use of the state parameter for correlation with other shear parameters. However, they did note (indirectly) the comparison between normalized stress paths for tests with similar state parameters.

Konrad (1990a and 1990b) further expands on the steady state concept by suggesting that there are two steady state lines: an upper flow line (UF) and lower flow line (LF). Whether a sand reaches the UF line or LF line is based on its initial state (Ψ_i) prior to shear. Konrad found that the strength at steady state and the minimum undrained strength for a sand also could be related to the initial Ψ (see following discussion).

2.1.5.3 Factors Affecting the Steady State Line

Numerous researchers have examined the effects of various factors on the position and slope of the steady state line. These factors, for undrained shear tests include:

1) sand grain characteristics, including sand mass compressibility and gradation;
2) strain rate;
3) initial fabric, as developed by the specimen's preparation technique;

4) initial state or Ψ_i; and

5) applied stress path, i.e. compression versus extension.

Table 2.1 summarizes the effect that these factors can have on the steady state condition. Examination of these factors have lead to differing opinions as to whether some factors do or do not affect the position or uniqueness of the steady state line. These factors and differing opinions are briefly discussed in the following section.

Sand Grain Characteristics

As noted previously, Poulos et al. (1985) stated that sand grain characteristics greatly affect the steady state. Specifically, they note that the slope of the SSL becomes flatter as the sand grains becomes rounder. They also note that the SSL moves vertically with minute changes in grain size distribution. Hird and Hassona (1990) state that the SSL moves up and to the right as grain angularity increases and that angular sand particles are less susceptible to liquefaction at a given void ratio, than rounded particles. They claim this is because a higher void ratio (higher void space) is needed for angular particles to develop the flow structure. As noted previously in Section 2.1.5.2, Alarcon–Guzman et al. (1988) hypothesis that sand grain smoothness, angularity, size and gradation will dictate whether one or several SSL's are possible.

Changes in the fines content of the sand mass will also effect the position of the SSL. As previously shown in Figure 2.20, Been and Jefferies (1985) find that an increase in fines content causes a steepening of the SSL. Similar trends were noted by Sladen et al. (1985) and Hird and Hassona (1986 and 1990). Hird and Hassona claim that the increased slope of the SSL with increased fines content is due to an overall increase in

compressibility for the sand; the same conclusion noted by Been and Jefferies.

Effect of Strain Rate

Controversy exists on whether the strain rate during shear affects the position of the SSL. As discussed earlier, Castro (1969) presented two SSL's for his tests; one for load–control undrained tests and the other for strain–controlled drained tests. He states that part of the difference in behavior may be due to the different strain rates applied to the specimens. Casagrande (1975) expands on this hypothesis by presenting load–controlled and strain–controlled undrained test results, for Banding sand, which have different SSL's. Figure 2.26 reproduces these results showing the SSL (F–line) from load controlled tests on Banding sand and the SSL (E_{sc}–Line) from strain–controlled tests. Casagrande believed that there could be numerous E_{sc} lines; all dependent on the strain rate used. Casagrande further stated that strain–controlled drained tests (the S–Line in Castro's work) plot even further to the right of the E_{sc} Line and that this was because a flow structure could not develop under drained loading.

Hird and Hassona (1990) present undrained triaxial compression test results (all with $+\Psi$'s) which concur with Casagrande's hypothesis. Figure 2.27 shows the SSL's for Leighton Buzzard sand using load–controlled triaxial tests and strain–controlled triaxial tests. Hird and Hassona further state that load–controlled tests which experience limited liquefaction would plot at the SSL for load–controlled tests but, with further straining, would travel to the right and end at the SSL for strain–controlled tests. Figure 2.28 presents a schematic of this behavior. It can be hypothesized that the specimen goes first to the load–control SSL because upon the initiation of liquefaction, strain rates are high and a temporary flow structure is developed. However, this

rapid deformation is quickly arrested and continued strains occur at a rate more common to strain–controlled tests. Thus, with the specimen's condition more like that of strain–controlled tests, the steady state point moves to the strain–control SSL.

As previously discussed in Section 2.1.5.2, Alarcon–Guzman et al. (1988) hypothesized that the difference in SSL's with applied strain rate is due to the sand's potential to develop "structural collapse". The lower the potential for a structural collapse, the more likely that one SSL will describe the steady state condition of the sand. Conversely, the higher the structural collapse potential, the higher the chance different SSL's will be developed for different strain rates.

In contrast to the above findings, Poulos et al. (1985), in describing their design procedure for the stability analysis of liquefiable soils, note that the undrained steady–state shear strength of a soil "is not dependent on the soil structure or the method or rate of loading." Poulos et al. (1988) present the results of load–controlled and strain–controlled triaxial tests on a Syncrude tailings sand which indicate no difference in SSL due to the different loading methods. Their results are reproduced as Figure 2.29. In their design procedure, Poulos et al. (1985) recommended that strain–controlled triaxial tests be used for determining the SSL. As previously presented, Been and Jefferies (1985) and Been et al. (1991) performed both load–controlled and strain–controlled tests and found that the SSL was the same for both loading methods. Figure 2.30 presents steady state conditions and the SSL for Erksak 330/0.7 sand from both load–controlled and strain–controlled triaxial tests and shows that no difference in SSL position exists. A closer look at this figure reveals that a

direct comparison of load–controlled and strain–controlled is valid only for the SSL at low stresses ($I'_1 \leq 1$ MPa) because no load–controlled tests are plotted at the higher stresses, i.e., along the steeper slope of the SSL. Given these diverse viewpoints, this phenomenon deserves further study.

Effect of Initial Fabric

It is well documented that a sand's initial fabric will have a great influence on the stress–strain–strength characteristics of the sand (Oda 1972; Arthur and Mendezies 1972; Wong and Arthur 1985). Oda (1972) found that different specimen preparation techniques will lead to different initial fabrics. However, Poulos (1981) and Poulos et al. (1985) claim that the method of specimen preparation does not affect the steady state condition of a sand. Hird and Hassona (1990) performed load–controlled triaxial compression tests on Leighton Buzzard sand. Specimens were prepared by moist compaction and pluviation. Their results indicate that the same SSL was obtained using either specimen preparation technique. However, Hird and Hassona did note that pluviated specimens were less susceptible to liquefaction than specimens which were compacted to the same density, especially if the fines content of the sand was increased. Been et al. (1991) used moist compacted and wet pluviated specimens to develop the SSL previously presented as Figure 2.25. Figure 2.31 presents this same SSL showing the steady state points for tests prepared by the two specimen preparation techniques. As illustrated in the figure, the different preparation methods have no effects on SSL location. Closer examination of Figure 2.31 indicates that moist compacted specimens can be prepared in a broader range of densities than pluviated specimens, and, therefore, can reach steady state conditions (drained or undrained) from a much broader range of initial states (void ratio and mean normal stress)

than pluviated specimens. This difference in specimen preparation techniques is similar to that noted by Hird and Hassona (1990). While for triaxial compression, there appears not to be an effect of specimen preparation technique on the steady state condition, a different view may be concluded in triaxial extension (see following discussion).

Effect of Initial State

Most researchers assume the existence of one steady state line for undrained shearing. A second line may also exist for drained shearing (i.e., the S–line). Konrad (1990a and 1990b) states that two steady state lines, the UF–line and LF–line, exist for sands, and which line is reached in steady state is a function of the sand's initial state, Ψ_i. Figure 2.32 presents a schematic state diagram and undrained stress–strain curves of the proposed behavior. The state diagram (Fig. 2.32a) is divided into five regions by four initial state parameter lines: Ψ_{UF}, Ψ^{+}_{LF}, Ψ^{-}_{LF}, and Ψ_S. Sands with an initial $\Psi_i > \Psi_{UF}$ (Region 1); e.g., the stress–strain curves label A and B in Fig. 2.32b, reach the steady state condition on the UF line (point a in Fig. 2.32a). These two tests, which exhibit a highly contractive response (strain softening), would also have the same steady state strength. Sands with $\Psi_{UF} > \Psi_i > \Psi^{+}_{LF}$ (Region 2); e.g., curve C, will also reach their steady state point at the UF line, but have a lower steady state strength than sands with $\Psi_i > \Psi^{+}_{LF}$. For $\Psi^{+}_{LF} > \Psi_i > \Psi^{-}_{LF}$, the steady state condition is reached at the LF line. Tests within this region may exhibit a contractive response (curve D where $\Psi_i \approx \Psi^{+}_{LF}$) or exhibit a "limited flow" condition (curve E where $\Psi_i \approx \Psi^{-}_{LF}$). It should be noted that the steady state strength for curve D represents the minimum undrained strength since tests at lower initial Ψ's will exhibit some dilation which leads to a higher strength. If

$\Psi_{LF} > \Psi_i$ (Regions 4 and 5), the sand exhibits a dilative response (e.g., curves F and G) and steady state can not be reached except at very large strains. However, conditions at phase transformation (points f and g) will fall between the LF and UF lines.

Konrad (1990a) presents results from undrained triaxial compression tests on loose, normally consolidated specimens of angular dune sand. Figure 2.33 presents these test results in e – log I'_1 space. Tests with initial $\Psi_i > \Psi_{UF}$ (i.e., initial state above the Ψ_{UF} line) reach steady state conditions at the UF line while tests with $\Psi_i < \Psi_{UF}$ will reach steady state conditions at the LF line.

Effect of Stress Path

Vaid et al. (1990) present undrained triaxial compression and extension test results for a rounded Ottawa sand (ASTM designation C–109) and state that the SSL for compression is not the same as for extension. They state further that the steady state condition in extension changes with void ratio, thus creating a range of extension SSL's. Figure 2.34 shows the typical response of undrained triaxial compression and extension tests on the Ottawa sand and the stress conditions at phase transformation, CSR and steady state. All tests were prepared by wet pluviation. Vaid et al. found that the undrained ϕ'_{ss} $(= \phi'_{pt})$ is identical for compression and extension, independent of all state variables, but their strengths may vary significantly (up to 90% reduction from compression to extension strengths for a loose sand). They also found that the CSR lines for compression and extension also differ with numerous CSR lines existing for extension loading, each dependent on the depositional void ratio, e_i. Figure 2.35 reproduces the SSL's in e–log σ'_3 space and illustrates the non–uniqueness of the steady

state conditions between compression and extension. The figure also shows that various extension SSL's are developed, each based on e_i. They also state that Ottawa sand specimens at the same void ratio are more likely to develop a contractive response in extension than in compression. Vaid et al. hypothesize that the difference in compression and extension behaviors is due to the anisotropic nature of the initial fabric of the sand. The greater compressibility of the sand in extension leads to more pronounced contractive response and large induced pore pressures. These observations suggest that the uniqueness of the SSL is invalid.

In contrast, Been et al. (1991) present results from undrained triaxial compression and extension tests and conclude there is no difference in steady state conditions. Figure 2.36 shows the SSL for Erksak 330/0.7 sand from both extension and compression tests. All extension tests were prepared by moist compaction. Figure 2.36 also presents similar results for Toyoura sand. For both sands, there is no effect of stress path on the position of the SSL.

Vaid and Pillai (1992), in discussing the Been et al. (1991) paper, note that the extension tests performed by Been et al. were on specimens compacted to D_r below 0%, and, in turn, called Been et al. observations improbable and invalid. In response, Been et al. (1992) state that the difference in behavior Vaid et al. noted was due to the use of "quasi–steady state" conditions (i.e., phase transformation and limited liquefaction) to evaluate conditions at steady state; which Been et al. claim is invalid. Again, given the conflicting views, it is clear that addition research is needed in this area.

2.1.5.4 Limitations to Steady State Analysis

The state parameter Ψ, and the steady state concept in particular, have

been the source of considerable controversy in the literature. As indicated above, the universality of this approach has not been conclusively demonstrated. In addition, various experimental difficulties in the testing of sands must be overcome, such as the ability to measure the true undrained steady state strength of highly dilative sands, compensation for membrane compliance effects and the control on non–uniform specimen deformations.

Andersen (1991) summarized some possible limitations to the use of the steady state analysis for sands. These limitations include:

1) The uniqueness of the SSL for a given sand is called into question given the difficulty in reaching the same SSL with specimens that have large $-\Psi$ parameters. Researchers have tended to rely on undrained testing of sands with $+\Psi$ parameters to locate the SSL.

2) An accurate measure of the void ratio at the steady state is important in determining the SSL. There can be a significant redistribution in the void ratio during shear, especially if frictional end platens are used with "dense" sand, because significant bulging may occur or a failure plane may develop. This can lead to significant errors in the position of the SSL.

3) The effects of membrane compliance on the behavior of both drained and undrained tests can be significant for coarse to medium sands. Changes in the amount of membrane penetration occurring during shear can significantly influence the accuracy of the volume change measured in drained tests and the "zero volume change" condition in undrained tests.

4) It may not be possible for deformations to occur during the undrained shear of dense sands without a local redistribution of void ratio. Casagrande (1936) postulated that for undrained tests on dense sands the measured strength would be due to cleavage of the individual particles. This would seem to indicate that the strength of dense sands might be less dependent on the effective stress level and more dependent on the cleavage strength of the sand particles, thus violating the state parameter assumption that the large strain behavior of sands is dependent only on the effective stress level and void ratio of the sand.

These limitations concern themselves to testing/laboratory related issues.

The first and second limitations can be addressed by using sophisticated testing techniques such as lubricated end platens and specimen preparation techniques which create repeatedly uniform test specimens. The redistribution of void ratio at the end of the test may also be measured using careful sectioning techniques. The third limitation can be mitigated by studying a very fine sand or a sand with a significant, but relatively constant, fines content.

2.2 POLYCRYSTALLINE ICE

This section presents a summary of polycrystalline ice behavior as described in the literature. A complete review of ice behavior is beyond the scope of this research. Therefore, particular focus will be given to the behavior of ice as it may pertain to frozen soils. As will be discussed in the following section, it is the view of the majority of researchers that ice in the pores of frozen soils is polycrystalline in nature; therefore, this review will highlight the deformation and strength behaviors of polycrystalline ice.

The following summary is divided into four parts. The first part presents a brief description of the structure of polycrystalline ice. The second section presents a summary of possible deformation mechanisms which can occur in ice. These mechanisms also influence the strength of ice. The third section describes the mechanical behavior of single ice crystals as well as factors which effect their behavior such as crystal orientation and the presence of impurities in the crystal lattice. The fourth section presents a review of the mechanical behavior of polycrystalline ice. In general, the behavior, as observed in prior research programs, ranges from ductile flow to brittle fracture and is strongly influenced by applied stresses, strain rate,

temperature, confining pressure, grain size and presence of impurities. Possible deformation and strengthening mechanisms which play a role in the overall behavior of polycrystalline ice are also discussed in this section.

2.2.1 Structure of Polycrystalline Ice

Andersen (1991) states that "Ice Ih is the stable form of solid water encountered in most engineering applications. It is normally encountered at homologous temperatures of 0.9 or greater." The homologous temperature is the actual temperature divided by the melting temperature, both expressed in absolute temperature (°K). The basic building structure of ice Ih, illustrated in Fig. 2.37, is a tetrahedron formed by the five oxygen atoms of five water molecules. Three tetrahedrons combine, each sharing two oxygen atoms, to form a hexagonal ring of oxygen atoms. This hexagonal ring of oxygen atoms lie in a slightly distorted plane that forms the basal plane. The axis normal to the basal plane is referred to as the c–axis. An ice crystal consists of numerous layers of these hexagonal rings bonded by a relatively weak hydrogen bond. The density of ice in this arrangement is 0.917 Mg/m^3 at 0 ^oC (Hobbs 1974). Ice has a naturally anisotropic structure because the oxygen atoms are packed more densely along the basal plane than they are along the c–axis direction. Slip along the basal plane is referred to as easy glide and slip in other directions is referred to as hard glide.

The lattice is disordered in ice due to the random disorder of hydrogen protons between oxygen atoms. This gives rise to ionization defects when either two or no protons are located between adjacent oxygen atoms; the Bjerrum D–defect and Bjerrum L–defect, respectively. Figure 2.38 illustrates the creation of these defects as a dislocation (defect) travels through the ice crystal.

Polycrystalline ice covers a wide range of ice types. Isotropic polycrystalline ice, the main focus of this review, consists of a conglomeration of individual ice grains which have randomly oriented c–axes. This form of polycrystalline ice is commonly referred to as granular (or sometimes type T_1) ice. Columnar–grained ice is a form of polycrystalline ice where the c–axes of individual grains are all oriented in the same direction, leading to higher anisotropic properties.

Mellor (1980) describes the "initial anisotropy" of polycrystalline ice in terms of its texture and fabric. Texture refers to the shape and assembly of the grains, and fabric refers to the orientation of the c–axes in the ice crystals. Anisotropy can also be "induced" during loading and straining processes. For example, as will be discussed in Section 2.2.2, the texture of a polycrystalline ice can evolve with time and the fabric can evolve under different loading conditions as the grains change shape, as the boundaries between the grains migrate and/or as recrystallization takes place [see Glen (1963); Mellor and Testa (1969a); Mellor (1980); Wilson and Russell–Head (1982); Jacka (1984); Cole (1986, 1987)].

With regards to the structure of ice in frozen soils, many researchers [e.g. Ladanyi (1981a); and Ting et al. (1983)] assume that the pore ice is polycrystalline in nature with random c–axis orientation (i.e., granular ice). However, the grain size of the pore ice in frozen sand greatly differs from the grain size of polycrystalline ice commonly encountered in nature and tested in the laboratory. Andersen (1991) notes that "Ice crystals in nature can have grain diameters which range from just under 1 mm to 10's of cm or larger. The grain sizes of granular ice which have been routinely tested in the laboratory range from just under 1 mm to 10 mm." Martin et al. (1981)

performed an analysis on frozen Manchester Fine Sand to estimate the ice grain diameter which may exist in the sand's pore space. They estimated that the maximum grain diameter of the pore ice would range from 0.03 mm to 0.08 mm, which is significantly smaller than the grain sizes normally found in nature or tested in the laboratory.

Sayles (1989) suggests that the pore ice may be columnar in nature following a tortuous path through the pore space. He cites work by Gow (1975) on ice lenses in frozen silt which had columnar ice crystals with their c–axes randomly oriented in a plane parallel to the surface of the lense. However, Sayles does state that the pore ice may also be granular with random c–axis orientations. Different frozen soil behavior would be expected given these two different possible pore ice structures. Additional research is required in this area.

2.2.2 Mechanisms of Deformation (Abstracted from Andersen 1991)

Numerous possible explanations exist to describe the deformation mechanisms for polycrystalline ice. However, a complete review of these explanations is beyond the scope of this section. Accordingly, this review summarizes some of the possible deformation mechanisms. For additional information, the reader is referred to the work of Langdon (1973), Goodman et al. (1981) and Duval et al. (1983) as well as the review by Andersen (1991).

Many of the following deformation mechanisms occur on a micro–level, i.e., the single crystal; however, they are commonly used to explain observed behavior of polycrystalline ice. Mechanisms of deformation in polycrystalline ice can be broadly classified into five groups: elastic processes; anelastic processes; plastic deformation processes, evolving microstructure processes and

internal fracturing processes. Nine classes of proposed deformation mechanisms are briefly discussed below. Table 2.2, reproduced from Andersen (1991), presents a summary of each proposed mechanism. Figure 2.39 presents an idealized view of some of these deformation processes.

Figure 2.39a schematically illustrates the elastic deformation of an ice crystal. In describing elastic deformation processes, Andersen (1991) states "Elastic deformation processes involve the elastic straining of the hydrogen bonds holding the H_2O molecules in the ice lattice. The molecules move to slightly distorted positions under the influence of external forces. Upon removal of these forces they return to their original positions. Elastic deformations can be observed under all loading conditions so long as sufficient care is taken to make high quality measurements (Hobbs 1974; Cole 1990)."

Anelastic or time dependent "elastic" deformations in ice lead to decreasing strain rates during primary (transient) creep and strain recovery during unloading. These are caused by the motion of a certain population of mobile dislocations under the influence of both short range and long range internal stress fields. Short range internal stress fields may be caused by interactions between dislocations and lead to isotropic (non–directional) hardening. Long range stress fields may be caused by the pile up of dislocations at grain boundaries which lead to kinematic (directional) hardening. Duval (1978) observed anelastic deformations in monotonic creep tests upon removal of the load, and Cole (1990) observed anelastic deformations in cyclic tests as a hysteretic behavior. Anderson (1991) notes that "Anelasticity will occur under all loading conditions so long as there is sufficient time for the build up of the internal stress field. In monotonic loading and unloading creep tests, the anelastic strain can be more than an

order of magnitude greater than the corresponding elastic strain (Duval et al. 1983)."

Diffusional flow, grain boundary sliding and dislocation gliding and climbing processes have been grouped under plastic deformation mechanisms. Diffusional flow is associated with the interstitial motions of intact water molecules to point vacancies either through the crystal lattice, a pathway proposed by Coble (1963), or along grain boundaries, a pathway proposed by Nabarro (1947) and Herring (1950) (Fig. 2.39b). The diffusion of point defects also accommodates grain boundary sliding. These diffusional type mechanisms lead to a Newtonian fluid type behavior. Diffusional type mechanisms dominate the deformation behavior only at very low stresses or strain rates such as those that occur during the flow of glaciers (Langdon 1973).

The slipping of adjacent sections of a given crystal lead to dislocation gliding and climbing mechanisms (Fig. 2.39c). Dislocations are linear defects in the crystalline lattice. The plastic strain rate of the crystal can be related to the velocity of these dislocations along their glide planes, the density of dislocations and the length of the dislocation's Burger vector (the distance and direction needed to close a circuit drawn around a dislocation center). Duval et al. (1983) suggest that four independent slip systems must be available in order for a crystal of ice to undergo an arbitrary change in shape. The basal plane, which is the preferred slip plane in ice, provides two independent slip systems. Therefore, the motion of dislocations on non–basal planes (e.g., prismatic or pyramidal planes) or the climbing motions of dislocations out of their slip planes must accompany the movements in the basal glide. Dislocations travel at velocities which are linearly proportional to

the effective stresses acting on them. Andersen (1991) notes that "researchers have made observations of dislocations gliding along the basal plane in ice (Jones and Gilra 1975; Fukuda et al. 1987 and Sinha 1978). Nonbasal glide and climbing motions have been much more difficult to observe. Research by Langdon (1973) and Duval et al. (1983) suggests that these gliding and climbing motions of dislocations dominate the behavior of polycrystalline ice in the power law creep region" (see Section 2.2.4).

The texture and fabric of polycrystalline ice can evolve via the processes of grain boundary migration and grain growth, termed dynamic recrystallization (Fig. 2.39d). Cole (1986 and 1987) noted that these processes can take place during periods of storage or under applied stresses. Duval et al. (1983) explain that dynamic recrystallization and accompanying grain boundary migration occur due to changes in the strain energy between adjacent grains. This changing strain energy field causes the nucleation of a "bulge" at the grain boundary with the "new" crystals dominating the behavior of the polycrystal. Wilson and Russell–Head (1982) have observed these processes through careful thin sectioning studies after shear and at various levels of imposed deformations. Anderson (1991) summarizes the strain and time dependent effects of dynamic recrystallization and grain growth as follows: "These (processes) might dominate the behavior at strain rates in the range of 10^{-9} to 10^{-7}/sec and are more important for finer grained specimens where there are a larger number of potential nucleation sites and a relatively short amount of time is necessary for the grain boundary of these 'new' crystals to migrate so that they occupy most of the polycrystalline mass."

Internal fracturing and cracking processes dominate the behavior of

polycrystalline ice at faster strain rates or lower temperatures (Fig. 2.39e). Under these conditions significant contributions from the other deformation mechanisms are reduced. Cole (1988) suggests that there are two mechanisms responsible for cracking. Andersen (1991), in summarizing these mechanisms, states "One (mechanism) is strain, or time, dependent and is associated with the pile up of dislocations at grain boundaries. This dislocation pile up mechanism requires a certain amount of time for the dislocations to travel to the pile up. The second is strain independent and is associated with elastic stresses developed from the anisotropy of the individual crystals." Cole (1988) directly observed both cracking phenomenon through careful sectioning techniques of specimens after shear deformations. Cole and St. Lawrence (1981) used acoustic emission detection to study the onset and rate of cracking. Andersen (1991) notes that a lower limit of strain rate for which this mechanism may apply is approximately 10^{-4}/sec. Cracking causes volumetric straining of polycrystalline ice and therefore is sensitive to confining pressures. Jones (1982) found that confining pressures in excess of 10 MPa appear to be sufficient to suppress internal fracturing activity.

2.2.3 Mechanical Behavior of Single Ice Crystals

The study of the behavior of single ice crystals has focused on the elastic properties and the differences in strength for shearing at various orientations to the c–axis. Some work has also been performed with respect to the effects of impurities.

2.2.3.1 Elastic Behavior

The Young's modulus and Poisson's ratio can be used to describe the elastic behavior of ice. Dantl (1969) reported values of these parameters from the measured elastic properties of single ice crystals using ultrasonic

measurement techniques. Laboratory–grown single ice crystals, 10 cm in diameter and 25 cm in length were tested, the c–axis being parallel to the length. Dantl reports Young's moduli for five orientations; two longitudinal (C_{11} and C_{33}), two transverse (C_{44} and C_{13}) and one quasi–longitudinal (C_{12}) to the c–axis. Figure 2.40 presents his results for these five moduli for a temperature range of 0 to –140° C. As can be seen in the figure, the moduli parallel to the c–axis (C_{11} and C_{33}) are the highest with values of $13.5\pm0.5\text{x}10^{10}$ dyn/cm^2 (10^{10} dyn/cm^2 = 1 GPa), and the modulus parallel to the basal plane (C_{44}) is the lowest ($\approx$ 2.8 GPa). The moduli for all five orientations tend to increase with decreasing temperature.

2.2.3.2 Strength–Deformation Behavior

The fabric (orientation of the c–axis) of single ice crystals affects their strength–deformation behavior. This is illustrated in the log σ –log $\dot{\epsilon}$ plot reproduced in Fig. 2.41 which shows the results of single ice crystals strained in hard glide and easy glide orientations. Andersen (1991) states that "For a given creep rate, a single crystal constrained to deform in hard glide requires a creep stress that is at least 60 times larger than that for easy glide. If constrained to deform in easy glide under constant stress, the creep rate will continuously accelerate." Higashi (1967 and 1969) reports that under constant rates of strains, easy glide crystals exhibit strain softening after the first yield, while hard glide crystals exhibit strain hardening after the first yield (Fig. 2.42).

Various ionic impurities incorporated into the ice lattice (e.g., hydrogen fluoride, HF, and hydrochloric acid, HCl) can lead to an increased mobility of dislocations and thus lower strength. Glen (1968) proposed that if the presence of these impurities increases the number of mobile ionization defects

(Bjerrum L– and D–defects), this might serve to increase the dislocation mobility and decrease dislocation drag (a strengthening mechanism). Thus, the increased dislocation mobility leads to a decrease in the strength.

In contrast, other ionic impurities may increase the strength of ice crystals. Jones and Glen (1969 a and b) observed that ammonia (NH_3), when incorporated into the ice lattice, increased the peak strength of polycrystalline ice from 3.2 MPa to 5.0 MPa. They postulated that this increased strength was due to a decrease in the mobility of dislocations. They further hypothesize that if the dislocation core attracts Bjerrum D–defects, the number of proton reorientations ahead of the dislocation line will decrease if the number of mobile Bjerrum L–defects are reduced. If an impurity, such as NH_3, causes such a decrease, then the drag stresses increase and the dislocation velocities decrease. This leads to an increase in strength.

2.2.4 Mechanical Behavior of Granular Ice

2.2.4.1 Elastic Behavior

Sinha (1989) used Dantl's results from single crystals to develop equations for the modulus of randomly–oriented granular ice. Sinha used an averaging technique appropriate for a system of hexagonal crystals to compute Young's modulus (E), shear modulus (G) and Poisson's ratio (μ) for granular ice for a temperature range of 0 to –50° C. Figure 2.43 shows these results for granular polycrystalline ice. As illustrated in the figure, these elastic properties show a slight tendency to increase with decreasing temperature.

2.2.4.2 General Stress–Strain Behavior

The mechanical behavior of polycrystalline ice ranges from ductile (creep) to brittle (fracture). In general, unconfined compression and tension tests are used to study ice behavior. Two types of tests are predominant;

constant stress or creep tests where the applied load (or stress) is held constant with time and constant strain rate or strength tests where the rate of deformation is maintained constant during shear.

Figure 2.44 shows schematic representations of creep and strength tests. For creep tests (Fig. 2.44a), the strain versus time (ϵ–t) plots show four distinct regions: an initial elastic response, primary creep (decelerating creep rate or strain hardening), secondary creep (transition or constant creep rate) and tertiary creep (accelerating creep rate or strain softening). The minimum creep (or strain) rate, i.e., the minimum slope of the ϵ–t curve, occurs during secondary creep. In general, increases in applied stress lead to increased minimum strain rates.

For strength tests at about –10° C, four curve types are shown in Fig. 2.44b: brittle fracture ($\dot{\epsilon} > 10^{-2}$/sec), peak strength followed by significant strain softening ($10^{-3} < \dot{\epsilon} < 10^{-2}$/sec), peak strength followed by moderate to low strain softening ($10^{-5} < \dot{\epsilon} < 10^{-4}$/sec) and ductile behavior signified by continuous strain hardening ($\dot{\epsilon} < 10^{-6}$/sec). In general, the range in strain rates for which a curve type will occur tends to decrease with decreasing temperature.

Figure 2.45 shows stress–strain curves for unconfined compression tests performed by Mellor and Cole (1982) on granular ice specimens at –5° C and different strain rates. At fast strain rates (10^{-4}/sec), the initial yield stress and peak strength coincide and is followed by very pronounced strain softening (e.g., Test Nos. 16, 22 and 23CD in Fig. 2.45a) Moderate strain rates ($\approx 10^{-5}$/sec) lead to strain hardening after initial yielding up to the peak strength and then strain softening (e.g., Test No. 39 in Fig 2.45a). At slow strain rates ($\approx 10^{-6}$/sec or less) the amount of strain hardening after the

initial yield decreases until the initial yield stress again represents the maximum strength (Fig. 2.45b). But compared to the behavior at high strain rates, there is less strain softening.

Polycrystalline ice exhibits a different behavior in uniaxial tension than in compression. Figure 2.46 shows the stress–strain response of two constant strain rate tensile tests performed by Hawkes and Mellor (1972). As illustrated in the figure, tensile specimens fail by brittle fracture even at relatively low strain rates (3.4×10^{-6}/sec). Murrell et al. (1989) show a similar behavior for granular ice in uniaxial tensile but note that a ductile failure in tension was obtained for tests at strain rates below 10^{-7}/sec.

Mellor and Cole (1982) report on a correspondence established experimentally between the results of constant load (creep) tests and constant strain rate (strength) tests. The stress/strain–rate correspondence is a relationship between the applied stress and minimum strain rate ($\sigma_a/\dot{\epsilon}_{min}$) in a creep test and the peak strength and applied strain rate ($Q_p/\dot{\epsilon}_a$) in a strength test. Andersen (1991) states that "So long as the mechanical properties of the ice do not change under these two loading conditions," then the results of creep tests and strength tests will plot along the same line or flow curve in a log σ – log $\dot{\epsilon}$ plot.

Figure 2.47 shows a schematic diagram highlighting the effects of strain rate on the measured behavior of polycrystalline ice at –10° C. The log stress – log strain rate plot shows the "flow curve" of ice from ductile to brittle regimes. In the ductile region, the linear portion of the flow curve is commonly called the region of power law creep. As seen in Fig. 2.47 the ductile region for compression extends to higher strain rates than that for tension (approximately 5×10^{-5}/sec to 2×10^{-7}/sec, respectively). At faster

strain rates ($> 10^{-2}$/sec) the ice behaves in a brittle manner with significant cracking and fracturing occurring during shear. A transition zone exists between the ductile and brittle regimes which involves attributes from both regions. Figure 2.48 shows strength tests results by Cole (1985) for tests on granular ice specimens (grain diameter d = 1.5 mm) at strain rates between 10^{-6}/sec and 10^{-2}/sec and a temperature of –5° C. This figure clearly illustrates the behavior previously described. The following sections discuss the behavior and possible mechanisms involved in each region.

2.2.4.3 Behavior in the Ductile Region

Effect of Strain Rate

Andersen (1991) describes this region as "that portion of the flow curve where the correspondence can be described by a simple power law equation of the form

$$\dot{\epsilon} = k\sigma^n \qquad 2.17$$

where $\dot{\epsilon}$ is the strain rate, σ is the stress, k is a constant and n is the power law coefficient (the slope of the line in log $\dot{\epsilon}$ – log σ space)." The power law coefficient typically ranges from 3 to 4.5 for strain rates between 10^{-7}/sec to 10^{-4}/sec; rates often of interest to engineers. At slower strain rates, such as for glacial flow, the power law coefficient tends to decrease to near 1 indicating a Newtonian fluid behavior. However, experimental evidence is lacking to verify that a n = 1 is possible (Mellor, 1980).

This general ductile region behavior is illustrated in the results from compression and tension tests on polycrystalline ice by Hawkes and Mellor (1972). Figure 2.49 shows the flow curve for tests at –7° C for both tensile strength tests (strain rates of 10^{-5}/sec to 1/sec) and compressive strength and creep tests (strain rates from 10^{-11}/sec to 10^{-2}/sec). The figure shows that

the compressive strength of ice is rate dependent at strain rates less than 10^{-3}/sec. A mean power law coefficient (inverse slope of the flow curve) of 4.6 can be calculated for compressive test results at strain rates between 10^{-7}/sec and 10^{-4}/sec.

Jacka (1984) presents a more recent set of creep tests performed on isotropic polycrystalline ice specimens with grain diameters of 1.7 ± 0.2 mm. Applied axial stresses ranged from 1.1 to 25.5 bars (0.11 to 2.55 MPa) with temperatures of –5, –10.6, –17.8 and –32.5° C used in testing. Test durations of 10,000's of hours were required to reach minimum strain rate points for tests at the lowest applied stress and higher temperature levels. Figure 2.50 presents a log–log plot of the minimum strain rate versus the applied stress for Jacka's tests. As illustrated, an average power law coefficient of 2.95 describes the log σ – log $\dot{\epsilon}_{min}$ relationship for tests at –5, –10.6 and –17.8° C. A lower power law coefficient of 2.27 is calculated for all tests at –32.5° C; however, this lower n–value may be misleading. In reality, the data set at –32.5° C may be represented more appropriately by a curved line with the power law coefficient being lower (the slope of the curve being steeper) at the lowest $\dot{\epsilon}_{min}$, then increasing as the applied stress increases. As discussed earlier, very slow strain rates create a condition where the ice starts to approach the behavior of a Newtonian fluid (n = 1).

Effect of Temperature

Glen (1955) used the Arrhenius equation to describe the temperature–dependent behavior of polycrystalline ice. This equation relates the temperature and strain rate in the following manner

$$\dot{\epsilon} = A \cdot \exp(-Q/RT) \qquad 2.18$$

where $\dot{\epsilon}$ is the strain rate, A is a constant varying with stress, Q is the

activation energy (units of J/mole), R is the gas constant (8.31 J/mole°K) and T is absolute temperature in °K. If the value of A is constant (i.e., constant applied stress), a plot of natural log $\dot{\epsilon}$ versus 1/T would be linear for a constant value of Q. The slope of the line in this space is equal to –Q/R.

Creep tests have been the predominant form of testing used in the study of the effect of temperature on polycrystalline ice behavior. Glen (1955) reported the results of creep tests on polycrystalline ice specimens under applied stresses from 1 to 10 bars (0.1 to 1 MPa) and at temperatures from –0.02 to –12.8° C. Figure 2.51 reproduces a plot of log $\dot{\epsilon}_{min}$ versus 1/T (1/°K) for four test results at an applied stress of 6 bars (0.6 MPa) at temperatures of –0.02°, –1.5°, –6.7° and –12.8° C. As illustrated in the figure, the creep test results at –1.5°, –6.7° and –12.8° C form an approximate straight line with a linear decrease in $\dot{\epsilon}_{min}$ with decreasing temperature. Glen associated the result of the test at –0.02° C to poor temperature control and localized melting during the test. Based on the three lower temperature tests, Glen, using Eq. 2.18, calculated an activation energy of 133 kJ/mole for this temperature range.

Mellor and Testa (1969b) investigated the effect of temperature on the behavior of isotropic polycrystalline ice by conducting a series of creep tests on specimens of approximately 1mm grain size at temperatures ranging from 0° C to –60° C and an axial stress of 1.18 MPa. Figure 2.52 presents a log $\dot{\epsilon}_{min}$ – 1/T plot of their results on these polycrystalline ice specimens. As in Glen's data, Mellor and Testa also observed a decrease in the minimum strain rate with a decrease in temperature. It also can be noted in the plot that the curve is linear for temperatures below –10° C, but is non–linear for

higher temperatures. For temperatures from –10° C to –60° C, the Arrhenius equation describes the change in minimum strain rate with temperature using a constant activation energy of 68.8 kJ/mole. This activation energy is approximately one–half of that from Glen's work. This discrepancy is due to the different temperature ranges used in determining the activation energies. In fact, Glen (1958) states that the range in test temperatures for his 1955 study was too small and that the testing temperatures were too high; therefore, he calls into question his earlier activation energy. However, Mellor and Testa's results also show a similarly high activation energy at higher temperatures (> –10° C), but the non–linear behavior they show indicates that the activation energy is changing (since all other variables in Eq. 2.18 are constant). Thus the use of the Arrhenius equation may not be applicable at temperatures greater than –10° C for polycrystalline ice.

Barnes et al. (1971) reviewed the results of previous creep and hardness tests on both monocrystals and polycrystals of ice. They found that the activation energy ranged from 120 to 136 kJ/mole for temperatures above –12° C, but ranged from 68 to 85 kJ/mole for temperatures less than –10° C [Mellor and Testa's (1969) work is included in the latter range]. Weertman (1983) also reviewed prior data on measured activation energies in polycrystalline ice. For temperatures less than –10° C, the activation energies are generally in the range of 55 to 85 kJ/mole. Above –10° C, there is a wider range in activation energies ranging from 122 to 200 kJ/mole.

Figure 2.53 presents a plot of log $\dot{\epsilon}_{min}$ versus 1/T produced from the test results by Jacka (1984). This plot also shows a decreasing trend in activation energies with decreasing temperature. However, there is also an effect of applied stress level. Creep tests performed at temperatures at or

above –17.8° C indicate an approximately linear portion of the log $\dot{\epsilon}_{min}$ – 1/T response. These higher temperature test results yield activation energies between 80 and 111 kJ/mole with the value of Q reducing as the applied stress level reduces. For temperatures below –17.8° C, activation energies between 27 and 61 kJ/mole are calculated, again with the value of Q decreasing with a decrease in applied stress level. The writer notes that these activation energies are based on bi–linear regression lines for, at most, four data points. Therefore, these activation energies may be inappropriately derived. However, the noted behavior does indicate that the activation energy may not only be temperature dependent, but also applied stress dependent. This phenomenon warrants further study.

Based on these studies, except the data by Jacka, the temperature dependency of polycrystalline ice in the ductile region can be described by the Arrhenius equation with a constant activation energy for temperatures less than –10° C, which indicates a similar deformation mechanism for this range. For temperatures warmer than –10° C, the Arrhenius equation breaks down because of changes in the activation energy and may indicate that the deformation mechanisms are changing.

Combined Strain Rate and Temperature Effects

Glen (1955) combined the power law equation (Eq. 2.17) and the Arrhenius equation (Eq. 2.18) to estimate the combined effects of temperature, stress and strain rate. Referred to in the literature as Glen's creep law, Glen's original equation was of the form

$$\dot{\epsilon} = B \cdot \exp(-Q/RT) \cdot \sigma^n \qquad 2.19$$

where B is a constant, σ is the applied stress, n is the power law coefficient and the other variables are as previously defined. This form of the equation

allows an estimate the minimum strain rate for creep tests. Subsequently, using the correspondence principal, Glen's creep law equation has been extended to estimate the combined effects of temperature, peak strength (Q_p) and applied strain rate (ϵ_a) for constant rate of strain tests, a form more germane to the present studies. Shyam Sunder and Wu (1989) present a form of the combined equation as

$$Q_p = V_o \cdot \exp(Q/nRT) \cdot (\dot{\epsilon}_a/\dot{\epsilon}_o)^{1/n} \qquad 2.20$$

where V_o is a temperature–independent constant (with units of stress), $\dot{\epsilon}_o$ is a reference strain rate (set to one for convenience) and the other variables are a previously defined.

Glen's creep law in this form allows the direct calculation of the peak strength from constant strain rate tests, but Glen's creep law, in either form, should not be considered as a complete constitutive relationship. However, it does quantify the relationship between temperature and strain rate as long as the deformation regime is not changing (i.e., where n is not changing).

2.2.4.4 Ductile–to–Brittle Transition

The ductile–to–brittle transition region represents one of the most complex areas in ice behavior given that mechanisms from both the ductile and brittle regions occur to varying degrees. Within this region, strain rate has a complex effect on the behavior of polycrystalline ice, especially the compressive behavior. As mentioned previously, the power law coefficient is between 3 and 4.5 for strain rates within the ductile region of deformation ($10^{-7} < \dot{\epsilon} < 10^{-4}$/sec for tests at –10° C). At higher strain rates, the coefficient increases to infinity, i.e., the ice becomes rate insensitive, and in some cases becomes negative. This behavior is referred to as power law breakdown. Aspects of this behavior are seen both in Figs. 2.48 and 2.49.

It is interesting to note the tensile strength behavior shown in Fig. 2.49. The plot shows that the tensile strength of polycrystalline ice is essentially insensitive to strain rate for rates greater than 10^{-6}/sec. Although Hawkes and Mellor did not conduct tensile tests at strain rates below strain rates of 10^{-6}/sec, it can be inferred that the behavior in tension and compression coincide at slower strain rates (i.e. both are in the ductile regime). This suggests that the transition between ductile and brittle behavior occurs over a relatively short range in strain rates for tensile strengths.

For the compressive strength, the behavior is more varied and occurs over a wider range of strain rates. Fig. 2.54 presents an idealized stress–strain curve for compressive strength tests in the transition region. Three zones can be identified. The first zone is the essentially linear stress–strain behavior to an initial yield point. This yield point coincides with the onset of internal cracking. After the initial yield there is strain hardening to the peak strength and thereafter strain softening to an ultimate condition of constant stress at large strains. As previously illustrated in Fig. 2.45, actual stress–strain curves may exhibit little strain softening after initial yield, depending on the applied strain rate and temperature.

Power Law Formulations

Many researchers describe the behavior in the transition region by extending the methods previously described for the ductile region, i.e., the combined power law equation (Eqs. 2.19 and 2.20). Barnes et al. (1971) present results from a series of unconfined compression creep tests on granular ice specimens with average grain sizes of 1 to 2 mm in diameter. Test temperatures varied between –2 to –48° C, and applied stresses varied from

0.1 to 10 MPa. Figure 2.55 reproduces the plot of log σ_a – log $\dot{\epsilon}_{min}$ for the creep tests at different temperatures. Barnes et al. found that Glen's creep law was inappropriate at higher stresses indicating power law breakdown. Therefore, they used a variation of Glen's creep law equation in which the strain rate is equated to the stress times a hyperbolic sine function

$$\dot{\epsilon} = A \exp(-Q/RT) [\sinh(\alpha\sigma)]^n \qquad 2.21$$

where α is an experimentally determined constant having units of 1/stress. The α term was chosen such that $\sinh(\alpha\sigma) = \sigma$ at lower stresses, thus preserving Glen's original formulation. Based on their test results, Barnes et al. found that the power law coefficient was 3.04±0.12 and α was 0.262±0.014 for the entire temperature range tested, but two distinct activation energies were found; Q = 120 kJ/mole for temperatures between –2 and –8° C and Q = 78.1 kJ/mole for temperatures between –8 and –45° C. [Using Glen's original creep law, Q = 121.4 kJ/mole for temperatures between –2 and –8° C and Q = 74.5 kJ/mole for temperatures between –8 and –45° C with n = 3.12±0.04 for the entire temperature range.]

Sayles and Epanchin (1966) performed unconfined, constant rate of strain tests on granular ice specimens at temperatures of –3.5 and –10° C. Strain rates varied from 4.1×10^{-4} to 1.7×10^{-2}/sec. Figure 2.56 presents a plot of log σ_p – log $\dot{\epsilon}_a$ for the test results which suggest that the tests are in the power law breakdown region of the flow curve. As illustrated in the plot, a relatively large amount of scatter exists in the test results; however, the general trend of the results, represented by regression lines, indicate that the peak strength is essentially insensitive to the applied strain rate; n = –12.6 and 46 for tests at –3.5 and –10° C, respectively. However, peak strength is strongly dependent on temperature with significantly higher strengths reported

for tests at –10° C than for the tests at –3.5° C.

Haynes (1979) presents the results of unconfined compression tests on fine–grained, polycrystalline ice specimens. The temperature ranged from –0.1 to –54° C with an average ice grain size of 0.6 mm. Deformation rates of 0.847 mm/sec and 84.7 mm/sec were used in the testing program which correspond to approximate strain rates of 2.0×10^{-3}/sec and 1.5×10^{-1}/sec, respectively; again both of these strain rates are in the power law breakdown region. A plot of temperature versus compressive strength, reproduced as Fig. 2.57, illustrates that there is little effect of applied strain rate on the strength of ice, but there is a general increase in strength with lower temperature.

Schulson (1990) reports unconfined compression data on granular ice specimens at temperatures between –10 and –50° C. Grain diameters ranged from 1 to 10 mm. Strain rates ranged from 10^{-3}/sec to 10^{-1}/sec. Figure 2.58 shows some of his test results, again signifying brittle behavior during shear and power law breakdown. Schulson's results show that the compressive strength increases with decreasing temperature (Fig. 2.58a), but decreases with increases in applied strain rate (Fig. 2.58b).

Haynes also presents the results of tensile strength tests at different temperatures for the same approximate strain rates. Figure 2.59 reproduces a plot of tensile strength versus temperature. The plot shows that the tensile strength is rate insensitive which corroborates the results presented by Hawkes and Mellor (1972) (see Fig. 2.49). However, in contrast to the compressive strength results, there also appears to be little to no effect of temperature on the tensile strength of polycrystalline ice at these strain rates.

Summary of Effect of Strain Rate and Temperature

The consistency of the overall behavior of granular ice from the ductile to brittle regions can be best evaluated by comparing a large set of results available in the literature. Figure 2.60 presents a log σ – log $\dot{\epsilon}$ plot summarizing the results from compressive creep and strength tests on granular ice performed by various researchers. The results in Fig. 2.60 are limited to unconfined tests on fresh water specimens with grain diameters of approximately 1 to 2 mm. Many of the referenced results have been previously cited in the preceding discussion.

As can be seen in Fig. 2.60, the test results follow similar trends of increasing power law coefficients with increasing strain rate and/or decreasing temperature. The results by Barnes et al. (1971) are represented by lines based on both the original Glen's creep law (Eq. 2.19) and their suggested sinh–function alternative (Eq. 2.21). [Note that the plotted lines represent the limits of the actual data as shown in Fig. 2.55.] It can be seen that the sinh–function equation provides a better fit to the results at higher temperatures ($T > -7^\circ C$),but insufficient results exist at lower temperatures to develop a definitive conclusion.

The results by Jacka (1984) at different temperatures fall near those found by Barnes et al. Closer examination of Jacka's results at $-32.5^\circ C$ does indicate that the slope of the flow curve decreases (i.e., value of n is increasing) even in the "ductile" region of deformation. A similar behavior can also be noted for tests at $-5^\circ C$.

2.2.4.5 Other Factors Which Affect Granular Ice Behavior

Effect of Confining Pressure

Jones (1978 and 1982) performed triaxial tests on polycrystalline ice at

$-11.5 \pm 1°C$ to measure the effect of confining stress on ice behavior. Confining pressures ranged from 0 (unconfined) to 85 MPa with strain rates ranging from 10^{-7} to 10^{-1}/sec. Andersen (1991) summarizes this behavior as follows: "Confining pressure can have both a strengthening and weakening effect on isotropic polycrystalline ice depending on the strain rate and stress level. (Figure 2.61 illustrates this phenomenon.) At very low strain rates there is no effect. For strain rates greater than about 10^{-5}/sec, an increase in confining pressure from 0 to 10 MPa leads to an increase in the peak strength and this effect increases with strain rate. For confining pressures greater than 10 to 40 MPa, the beneficial effect of confinement at high strain rates is lost and increasing the confining pressure can actually lead to a decrease in strength."

Figure 2.62 shows a log Q_p – log $\dot{\epsilon}$ plot of Jones' results for unconfined tests (also shown in Fig. 2.61) and tests at σ_c = 10 MPa. Regression lines through the data lead to a power law coefficient of 5.43 for unconfined tests and 4.62 for tests at σ_c = 10 MPa; thus, it appears that increased confinement (up to 10 MPa) leads to a more ductile behavior.

Jones (1982) states that the strength gain for increases in confining pressure from 0 (unconfined) to 10 MPa is primarily due to the suppression of cracks by the increased confining pressure. This increased confinement causes an increase in the stress required to nucleate a crack as well as increases the frictional resistance along cracks which develop. Hence, the strength of the ice is increased. It should be noted that this strengthening effect increases when internal cracking is an important deformation mechanism, i.e., the faster strain rates (and presumably lower temperatures).

Jones also notes that at confining pressures greater than 10 MPa and at

temperatures warmer than –10° C, pressure melting can occur at grain boundaries and intersections. Pressure melting reduces the high contact stresses between grains, thus reducing the shear resistance of the boundaries and enhancing grain boundary sliding.

Murrell et al. (1989) details a comprehensive program of unconfined and triaxial compression and tension tests on isotropic polycrystalline ice with a uniform grain size of 1mm. Cylindrical specimens, 10 cm in length and 4 cm in diameter, were tested at various temperatures (–5, –10, –20 and –40° C), strain rates (from 10^{-7}/sec to 10^{-2}/sec) and confining pressures (from 0 to 30 MPa). In addition to the strength testing, the level of cracking during shear was measured using acoustic emissions and by visual observation. However, in their paper, they only present a small portion of the test results with the majority of presented test results for strain rates greater than 10^{-4}/sec, i.e., in the transition or brittle regions of behavior. The available results do provide some information to evaluate trends in granular ice behavior. In general, the compressive strength results indicate that a decrease in temperature leads to an increase in strength, all other variables held constant. Triaxial compression tests also show that an increase in confinement leads to little change in ice strength if specimen deformation was ductile (a yield stress followed by strain hardening to peak strength and then strain softening). However, the compressive strength of ice was more dependent on confinement if a brittle failure occurred. This observed trend is illustrated in Fig. 2.63 which plots the peak strength versus confining pressure for tests at –20 and –40° C and strain rates of 10^{-4} and 10^{-2}/sec. As seen in the figure, the level of confinement has the greatest effect on tests at –40° C and strain rate of 10^{-2}/sec; tests which failed in a brittle mode.

Murrell et al. (1989) also note that the level of cracking was suppressed with an increase in confining pressure. In general, they note an even distribution of visible cracks throughout the specimen. However, they state that an uneven distribution of cracks was noticeable for tests at high temperatures (–5° C) and higher confining pressures which they claimed was evidence of pressure melting of the ice.

Effect of Grain Size

Grain size may also influence the deformation behavior of polycrystalline ice. For example, polycrystalline ice strength can increase due to a decrease in grain size from the coarse (10mm) to the fine (1mm). Schulson (1990) presents compressive strength results for granular ice specimens with grain diameters (d) from 1 mm to 10 mm. Figure 2.64 shows plots of strength versus $1/\sqrt{d}$ for tests at strain rates of 10^{-3} to 10^{-1}/sec and temperatures of –10° C, –30° C and –50° C. The plot clearly shows an increase in strength with decreasing grain size (increasing $1/\sqrt{d}$). Schulson and Cannon (1984) and Schulson (1987) present the results of compressive strength tests at fast strain rates (10^{-4} and 10^{-3}/sec) on granular ice specimens with diameters from 0.8 to 9 mm. These test results also show that there is a tendency for the strength of polycrystalline ice to increase with decreasing grain size.

Li (1963) explains this strengthening using a grain boundary source theory which assumes that the grain boundaries act as sources of dislocations. Therefore, a smaller grain, with a larger surface–area–to–volume ratio, will have a higher dislocation density. This leads to an increase in the internal stresses (increase in hardening) and increases the strength. Andersen (1991) notes that internal cracking theories (e.g., Cole 1988 and Shyam Sunder and Wu 1990) also predict an increase in strength with decrease in grain size.

However, Cole (1987) found a different behavior at the very slow strain rates in creep tests. This apparent change in behavior may be due to the evolving texture and fabric permitted at the lower strain rates (see following discussion).

Armstrong (1970) hypothesizes that a decrease in grain size from the fine (1mm) to the ultra fine (<<1mm) range may result in a significant decrease in the strength. This could be due to enhanced grain boundary sliding and greater diffusional processes along grain boundaries. Cole (1987) observed that finer grained ice specimens offer a greater number of potential nucleation sites for dynamic recrystallization processes, and thus will have lower strengths.

Effect of Impurities

The presence of impurities and gases in ice can significantly influence the behavior by affecting the mobility of dislocations and changing the orderly arrangement of the water molecules. Andersen (1991) states that "Impurities present in the water before freezing will tend to concentrate at the boundaries of the grains during the freezing process because they are not easily accommodated into the lattice." Mellor (1980) hypothesized that high concentrations of impurities at the grain boundaries decreases the melting point and creates a liquid like film between adjacent crystals. The presence of the liquid–like film may enhance grain boundary sliding and diffusional flow processes which will decrease the ice strength. In addition, as for the case of pressure melting, the film will decrease the strength of polycrystalline ice by decreasing the stress concentrations between grains and thus decreasing the shear strength of the interface.

In contrast, Jones (1982) noted the presence of air bubbles (0.6% by

volume) in specimens of polycrystalline ice tested at –11° C. He found no change in peak strength due to the presence of the air and concluded that their presence did not significantly affect the "flow of ice".

Effect of Texture and Fabric

The texture and fabric of the ice can significantly affect its behavior. The initial fabric of granular ice provides a fundamental strengthening mechanism, when compared to monocrystals sheared in easy glide, due to the random orientation of its grains. As shown previously in Fig. 2.41, there is a significant difference in the strength of monocrystals in easy glide and in hard glide. Andersen (1991) states that as granular ice is strained, grains oriented in easy glide directions reach maximum resistance first with additional loading to be taken by grains with hard glide orientations. This transfer mechanism allows the matrix of granular ice to reach higher strengths than single grains in easy glide.

However, as noted previously in Section 2.2.2, the fabric of polycrystalline ice (orientation of the c–axis) can evolve during deformations (see Jacka 1984, Cole 1987, and Duval et al. 1983). In describing this evolving fabric, Andersen (1991) states "The tendency is for crystals oriented in easy glide directions to begin to dominate stress–strain behavior. This can be due either to the preferred growth of favorably oriented crystals (easy glide) at the expense of unfavorably oriented crystals (hard glide) or the nucleation of new crystals at grain boundaries (dynamic recrystallization) and subsequent grain boundary migration. When a larger population of crystals are oriented in easy glide directions due to these processes, the polycrystalline mass weakens."

2.2.5 Conclusions and Discussion

The behavior of polycrystalline ice is complex based on the available data presented herein. However, the effects of strain rate and temperature in the ductile region can be described using an Arrhenius–type equation or combined power law equation (e.g., Eq. 2.20). But the applicability of this equation is limited to certain strain rates, temperatures and stress ranges where ductile (creep) deformation processes dominate ice behavior.

It is possible to quantitatively examine the effects of strain rate and temperature, within the ductile region, by calculating the change in strength, from a reference condition, solely caused by either a change in strain rate or change in temperature. Assuming a reference condition, consisting of results from an unconfined compression test from Murrell et al. (1989) (i.e., Q_p = 2.5 MPa, $\dot{\epsilon}_a = 10^{-6}$/sec and T = −10° C) and a power law coefficient of three and activation energy (Q) of 70 kJ/mole lead to a V_o of 5.77×10^{-3} MPa for $\dot{\epsilon}_o$ = 1/sec, based on Eq. 2.20. The complete equation can now be used to develop changes in Q_p due to changes in strain rate (T held constant) and changes in temperature ($\dot{\epsilon}$ held constant). Figure 2.65 presents the curves from this analyses. Noted that strain rate is plotted on a $\log_{10}$ scale. It can be clearly seen in the figure that the effects of a decrease in temperature or increase in strain rate lead to similar parabolic increases in peak strength. Therefore, a correspondence between strain rate and temperature is shown for the ductile region (for constant values of n and Q), and this correspondence provides an alternative means to estimate the effects of temperature (or strain rate) on the behavior of polycrystalline ice if strain rate (or temperature) is the only testing variable.

With respect to the ductile–to–brittle transition, Murrell et al. (1989)

show that as the temperature decreases (all other variables held constant), the stress–strain response becomes more brittle. A similar behavior is displayed if the strain rate is increased (see, e.g., Fig. 2.45). In the writer opinion, it could be inferred that the dominate deformation processes involved in the case of decreasing temperature are the same processes involved in the case of increasing strain rate; similar to the case for the ductile region. Most researchers agree that internal fracturing processes dominate deformation in the brittle region. However, the cause of internal fracturing may be different in the case of decreasing temperature from the case of increasing strain rate. For example, the internal fracturing caused by a increase in strain rate may be due (predominantly) to the pile–up of dislocation at the grain boundaries (a rate dependent phenomenon). For fracturing caused by a decrease in temperature, the fracturing mechanisms may be caused by stresses developed from the anisotropic structure of polycrystalline ice (a rate independent phenomenon). This possible difference in deformation phenomenon deserves more study.

2.3 FROZEN SAND

The behavior of frozen sands is extremely complex. This is due not only to the complex, individual behavior of the sand skeleton and the pore ice, presented in Sections 2.1 and 2.2, respectively, but also due to the interaction of the sand skeleton and the pore ice matrix. Although a complete understanding of frozen soil behavior is lacking, previous research has demonstrated some of the aspects of the "macrostructural" behavior of frozen sands as a function of sand density, confining pressure, strain rate, temperature, degree of saturation and sand type. However, the

"microstructural" interaction between the sand and pore ice, as well as the effect of unfrozen water and air voids, are poorly understood.

Andersen's (1991) work with frozen Manchester Fine Sand (MFS) represents a substantial contribution to the "macrostructural" behavior of frozen sand as a function of relative density, confining pressure and strain rate. The current research extends Andersen's work by evaluating the effect of temperature, along with the other three variables, on frozen MFS. Chapter 5 presents an integration of the results of the current research as well those presented in Andersen (1991) and Andersen et al. (1992). Therefore, this background section will focus on research efforts performed by others. However, conclusion and behaviors noted in Andersen and Andersen et al. will be presented where appropriate.

The following review of frozen sand behavior will specifically address variables which pertain directly to the present research. Therefore, the section is divided into four parts. The first part presents a general summary of the description and structure of frozen sand. As was the case in the review of unfrozen sand and ice behavior, the majority of this part was abstracted from the review presented in Andersen (1991). The second section presents an overview of the mechanical behavior of frozen sands. This review is based primarily on the behavior observed from other testing programs. The third section presents a more detailed review of the effects of temperature on the behavior of frozen sand. The effects of a pre–freezing effective stress on the behavior of frozen soils is presented in the final section.

2.3.1 Description and Structure of Frozen Sand

2.3.1.1 Classification

Classification of frozen soils was addressed by Sayles et al. (1987). They suggest the soil phase in a frozen soil be classified according to the Unified Soil Classification System. The ice in a frozen soil is classified on whether it is visible to the naked eye, if it is well–bonded with the soil, and if there is "excess" ice (i.e., increased pore space in the soil due to the freezing process). If the pore ice is visible, then it is described in terms of its macroscopic features; e.g., orientation of grains, color, hardness, thickness, spacing and length.

Frozen soils are also described in terms of the unfrozen water content and the degree of saturation. The amount of unfrozen water is expressed as a ratio of the weight of unfrozen water to the weight of the soil particles. The unfrozen water content is highly temperature dependent, with lower temperatures leading to lower unfrozen water contents. Andersen (1991) defines the degree of saturation as "a measure of the amount of ice and water that is present in the pore spaces as a percentage of the total void space. The condition of 100% saturation means that there is no air in the voids and a condition of 0% saturation means that there is no unfrozen water or ice in the pores. He states that "the degree of saturation can be computed from the following equation

$$S = \frac{\gamma_t(w_u + w_i/G_i)}{\gamma_w(w + 1) - \gamma_t/G_s} \times 100\% \qquad 2.22$$

where S is the degree of saturation expressed as a percentage, γ_t is the total frozen density, γ_w is the density of water, w is the total water content (both ice and unfrozen water), w_u is the unfrozen water content (taken as 0.001 for frozen MFS at $T \leq -10°C$), w_i is the ice content (equal to the difference

between the total water content and the unfrozen water content), G_i is the specific gravity of ice and G_s is the specific gravity of the soil particles." The specific gravity of ice and density of water are also temperature dependent parameters where G_i ranges between 0.9164 and 0.9193 for $0°C > T > -30°C$ (Hobbs 1974) and γ_w ranges between 0.9970 to 0.9895 g/cm^3 for $-5°C > T > -25°C$ (Zheleznyi 1969).

2.3.1.2 Structure of Frozen Sand

Ting et al. (1983) present a possible, idealized structure for frozen sand which is presented in Fig. 2.66. They postulate that in this structure: 1) solid contacts exist between most of the sand particles; 2) a continuous unfrozen water film surrounds the silicate particles and is present to very low temperatures; 3) the unfrozen water in this film is mobile parallel to the surface of the particles, but strong tensile and moderate shear adhesional forces can be transmitted between the pore ice and the silicate particles; 4) there are no direct ice to soil contacts; and 5) the macroscopic structure of the ice in the pores is polycrystalline (granular) and the maximum grain size is limited to the size of the individual pores. The applicability of each of these postulates is discussed below. In contrast to the proposed structure presented in Fig. 2.66, Andersen (1991) suggested an alternative structure which he felt was more representative of a single plane passing through a frozen sand. A schematic of this structure is presented as Fig. 2.67.

Solid Contacts

In a careful experimental program, Singh et al. (1982) measured the effect of freezing and thawing on the structure of a clean sand (no fines) using cyclic triaxial tests. All specimens had the same initial effective stress ($\approx$ 0.05 MPa). Before performing the cyclic triaxial tests, some specimens

were subjected to a cycle of uni–directional freezing and thawing. Pore water was allowed to drain freely out of or into the specimen during the freeze–thaw process. A comparison of the cyclic response of tests with and without the freeze–thaw cycle showed that the freezing and thawing cycle had no effect on the cyclic response of the sand. Based on this observation, Singh et al. concluded that the structure of the sand is preserved during the freeze–thaw process if drainage is allowed. Consequently, their results indicate that the solid contacts between most adjacent particles in an unfrozen sand are still maintained when the sand is subjected to open freezing and thawing. Singh's et al. testing program will be further discussed in Section 2.3.4.

Unfrozen Water Film

Hoekstra and Chamberlain (1964), who performed electro–osmosis experiments on frozen New Hampshire silts and Wyoming bentonite clays, and Hoekstra (1965), who performed a series of electrical conductance experiments on frozen bentonite pastes, present data which clearly demonstrated the presence of an unfrozen water film around soil particles. Corte (1962) performed experiments with individual silicate particles placed on top of a freezing front in water. He observed that the particles "floated" on top of the ice as the freezing front slowly advanced. He concluded that only the presence of a continuous unfrozen water film around the particle could allow this behavior to occur and that this film was continually "replenished" as freezing occurred at the advancing front.

Andersen (1991) states that "the amount of unfrozen water present in a frozen soil is strongly affected by the temperature, the specific surface area of the soil particles, the surface chemistry, the presence of ionic impurities, and

changes in confining pressure (see Anderson and Morgenstern 1973)."

Strength of Ice–Silicate Interface

Ting et al. (1983) suggested that the strength of the ice–silicate interface in a frozen soil followed the behavior measured from a series of experiments reported by Jellinek (1962). Jellinek's experiments consisted of direct shear and direct tension tests on snow ice frozen to a fused quartz surface. Jellinek noted that for a temperature of –4.5° C, the tensile adhesional strength was one to two orders of magnitude greater than the shear adhesional strength, and this tensile adhesional strength of the ice–silicate interface was greater than the tensile strength of the pure snow ice (> 1 MPa). However, Jellinek (1962) attributed the large tensile strength of the interface to surface tension forces between the unfrozen water film and the atmosphere at the exposed edges of the ice and quartz interface; a condition not likely in a saturated frozen soil (no atmosphere exposure) therefore casting doubt on the applicability of Jellinek's tensile strength data to frozen sand behavior.

Other qualitative models have been proposed to predict the behavior at the ice–water–silicate interface. One possible explanation is Martin's (1960) ball–bearing–on–magnetic–surface type model where the absorbed water on the sand surface exhibits behavior similar to a steel ball on a magnetic surface; no shear strength but strong tensile strength. The reader is referred to Anderson and Morgenstern (1973) for a review of various other theories. Andersen (1991) notes that "The actual structure of this interface and its strength and deformation behavior are still poorly understood."

Direct Ice–Soil Contact

The presence of absorbed water on the surface of the silicate will

generally prohibit direct ice to soil contact in frozen sands. Water may be absorbed to silicate surfaces by hydrogen bonding, cation hydration, orientation of H_2O dipoles in an electric field, osmotic pressure and van der Waal's forces. Strong forces are required to remove the next to last molecular layer of adsorbed water from a silicate surface. Work by Steinfink and Gebhart (1962) indicates that a normal stress in excess of 200 MPa is required for this removal. This stress is much larger than the compressive strength of ice. However, ice can still exist under this pressure at low temperatures. Figure 2.68 presents a phase diagram for water which indicates that at a pressure of 200 MPa, ice Ih will exist at temperatures lower than –22° C. Therefore, frozen soils deformed at temperatures below –22° C may have ice grains come into direct contact with soil grains. However, the condition of the ice when this direct contact occurs is unknown.

Granular Pore Ice

Ice in frozen soils exists as normal hexagonal ice Ih. However, debate exists as to whether the fabric and texture is isotropic polycrystalline ice or of some other structure. As noted in Section 2.2.1, Ting et al. (1983) suggested that the pore ice in frozen sands is polycrystalline with the maximum grain size equal to the maximum pore size. In contrast, experimental work by Gow (1975) and Colbeck (1982, 1985) gives credence to the view that the pore ice may consist of single crystals extending in a tortuous path through several pores. Sayles (1989) argue that the ice structure could be either of theses forms. This postulate requires additional study.

2.3.1.3 Mechanisms of Strength

Mechanisms of strength in frozen sand will be presented in terms of the

Ting et al. (1983) hypothesis as summarized in Table 2.3 and Fig. 2.69. They considered that the frozen sand could be modeled as a particulate material and described the strengthening mechanisms as being derived from three components: the pore ice, the sand skeleton and the ice–sand interaction. The strength of the sand skeleton and ice have been previously addressed in Sections 2.1 and 2.2, respectively. The following discusses the ice–sand interaction component of strength which include the following: 1) ice strengthening due to changes in structure, state of stress, deformation constraints and/or strain rate; 2) tension in the unfrozen water film; and 3) soil strengthening due to dilation and structural hindrance. Each of these components are discussed below.

Ice Strengthening

In general, researchers have concluded that the behavior of the pore ice tends to dominate the behavior of frozen soils at small strains up to first yielding and the behavior of the soil skeleton tends to dominate at large strains [e.g., see Parameswaran (1980), Bragg and Andersland (1980) and Andersland (1989)].

The structure of ice in the pore space could govern the strength of frozen sand. As noted previously, Colbeck (1985) hypothesizes that the pore ice strength may be different from that of normally tested isotropic ice due to a decrease in the grain size. Sayles (1989) suggests that the pore ice may be represented by single tortuous crystals filling several pore spaces which may introduce anisotropic strength behavior of the frozen sand.

In analyzing Ting et al. (1983) model, Andersen (1991) notes that "the state of stress and deformation constraints in the pore ice are different from those imposed during uniaxial compression or tension tests. In addition, the

stress concentrations occurring between the ice and silicate particles may be complicated by the presence of the unfrozen water film. Because of these complications, a linear extrapolation of ice strength versus V_s to all D_r (as shown in Fig. 2.69) may not be valid."

Goughnour and Andersland (1968) postulated that the pore ice is deformed at an "enhanced" strain rate compared to the overall imposed strain rate on the frozen sand system. If this process occurs, the higher strain rate leads to a higher pore ice strength.

Tension in the Unfrozen Water Film

The tension in the unfrozen water film may also serve to strengthen the frozen sand. However, its effect relies on the effective stress principle which may not apply to frozen soils. For their model, Ting et al. (1983) concluded that this strengthen effect would be small.

Soil Strengthening

However, the development of tensile stresses in the pore ice, caused by dilatancy of the sand skeleton, can serve as a significant strengthening mechanism in frozen sand. Ladanyi (1985) and Ladanyi and Morel (1990) have attempted to quantify the effect of dilatancy by developing a dilatancy hardening model. This model relies on the assumption that the effective stresses acting on the sand skeleton in a frozen sand are identical to those acting on an unfrozen sand skeleton in an undrained test. Section 2.4 presents a detailed review of this model.

Ting et al. (1983) proposed another mechanism that might enhance the strength of a frozen sand called structural hindrance. They explained that structural hindrance is analogous to the application of lateral support to a slender member to maintain stability. In terms of frozen sand, the pore ice

applies lateral resistance to the sand grains thus preventing the "collapse" of the soil skeleton. They state that this interaction can be synergistic in nature.

2.3.2 Overview of the Mechanical Behavior of Frozen Sand

Most previous testing programs have used unconfined or triaxial compression tests either at constant strain rate (strength test) or constant stress (creep test) to study the behavior of frozen sands. Based on these studies, the strength and deformation behavior of frozen sands have been found to depend on numerous variables such as strain rate, confining pressure, temperature, relative density, degree of saturation, and the presence of ionic impurities. Andersen (1991) reviewed the results of several testing programs that studied the influence of these variables and this review is summarized below. In contrast to Andersen's review, this summary is limited to test results from saturated (or near–saturated), freshwater specimens.

The summary is divided into two parts, small strain behavior and large strain behavior. Andersen (1991) presents idealized stress–strain curves from his triaxial compression testing on frozen Manchester Fine Sand to show the major features of the behavior. These curves are reproduced as Fig. 2.70. The small strain behavior is depicted in Figs. 2.70a and b. In Fig. 2.70a, the initial, small strain response becomes non–linear beginning at axial strain levels on the order of 0.01%. The "knee" in the stress–strain curve (Fig. 2.70b) has been designated as the *upper yield* point in recognition of the significant yielding which occurs prior to that point. This idealized small strain behavior, particularly the upper yield behavior, is primarily based on data obtained from Andersen's work since most published stress–strain curves do not define the initial small strain response or the distinct upper yield

behavior. This lack of stress–strain detail may be due to inadequate axial strain measurement techniques.

Figure 2.70c depicts the large strain behavior. In general, frozen sands may exhibit either post–upper yield strain hardening or strain softening depending on the relative density, confining pressure, strain rate and temperature. Volumetric behavior, shown in Fig. 2.70d, generally shows expansion at low confinement levels. The following section presents an overview of the small strain and large strain behavior as measured in prior frozen sand testing programs.

2.3.2.1 Small Strain Behavior

Elastic Response

A number of testing programs have attempted to measure the small strain "elastic" properties of Young's modulus and Poisson's ratio. Baker and Kurfurst (1985) used acoustic wave propagation techniques and on–specimen axial strain measurements to measure the effect of relative density on the Young's modulus and Poisson's ratio of frozen Ottawa sand. Kaplar (1963) used resonant beam tests on frozen Peabody gravelly sand to measure the Young's modulus and Poisson's ratio. Vinson (1978) presents Young's modulus results from cyclic triaxial tests on frozen Ottawa sand at different levels of confinement, but his results are questionable since they may involve significant level of plastic straining. Parameswaran (1980) reports initial moduli for frozen Ottawa sand specimens based on external displacement measurements. The current testing program of frozen MFS uses on–specimen axial strain techniques to measure the Young's modulus. These results will be discussed in Chapters 5 and 6.

In summary, a review of these various programs results indicates the

following:

1) The Young's modulus varied from a low of 0.52 to 4.8 GPa (measured by Parameswaran) to a high of 34.5 to 47.1 GPa (measured by Kaplar). Baker and Kurfurst found the Young's modulus to vary from 24 to 30 GPa for acoustic wave propagation techniques and from 26 to 45 GPa for on–specimen axial strain measurements. Vinson measured moduli from 5 to 13 GPa (probably low due to the previously mentioned plastic straining).

2) The Young's modulus increases moderately with increasing dry density, and perhaps increases with increasing confining pressure. Baker and Kurfurst found the modulus to increase approximately 20% for an increase in D_r from 20 to 100%. Vinson measured a 60% increase in modulus for a density change from a sand–ice mixture ($D_r < 0\%$) to a dense frozen sand.

3) The Poisson's ratio increases slightly with decreasing temperature and increases slightly with increasing dry density. These results are from the testing programs of Kaplar and Baker and Kurfurst which will be examined in more detailed in Section 2.3.3.

Upper Yield Region

Limited data exist on the upper yield stress behavior. Chamberlain et al. (1972) presents test results on a dense, frozen Ottawa banding sand at a strain rate of 10^{-3}/sec and confining pressures up to 280 MPa. They note a distinctive "yield point" which increased with increasing confining pressure. Parameswaran and Jones (1981) presents results on dense frozen Ottawa sand tested at a strain rate of 7.7×10^{-5}/sec and confining pressures from 0.1 to 75

MPa. [Note: In these tests, the confining pressure was allowed to increase during axial loading.] Parameswaran and Jones also note a distinct "yield stress" in their tests which also increased with increasing confining pressure. The results of both Chamberlain et al. and Parameswaran and Jones are illustrated in Fig. 2.71 for confining stresses up to 20 MPa. The work with frozen MFS, discussed in Chapter 5, suggests that confining pressure has little effect on the upper yield stress.

2.3.2.2 Large Strain Behavior

This section reviews the large strain behavior with respect to the behavior at the peak deviator stress or peak strength (Q_p) and the axial strain at peak strength (ϵ_p). The presentation summarizes the effects of relative density or volume fraction of sand, confining pressure and strain rate. The effects of temperature are presented in Section 2.3.3. Table 2.4, reproduced from Andersen (1991), summarizes the principal testing programs used to evaluate and illustrate the large strain behavior of frozen sand. For continuity, Andersen's letter designations have been retained. Based on the reviewed literature, the effect of some of these variables on the stress–strain behavior is still in question. Andersen's work, and the work in this thesis, represent a significant advance in this regard and are detailed in Chapter 5.

Peak Deviator Stress

Sand content or relative density has a profound effect on the peak deviator stress. Unconfined compression tests by Goughnour and Andersland (1968) and Jones and Parameswaran (1983) are summarized in Fig. 2.72. These tests were conducted at temperatures from –4 to –12° C and at strain rates from 2.2×10^{-6} to 7.7×10^{-5}/sec. Andersen (1991) summarizes this behavior as follows: "... in the range of sand volume fractions from 0 to

40%, there is a linear increase in strength above that of pure ice. At 40% sand by volume, the particles begin to come into contact and the rate of strengthening increases dramatically but is still approximately linear."

Baker and Kurfurst (1985) present a study of the effect of sand relative density on the peak strength. Their tests were conducted at a temperature of –10° C and at a strain rate of 1.7×10^{-4}/sec. Figure 2.73 presents a summary plot of strength versus D_r for their results. At low relative densities, they found that the peak strength coincided with the upper yield stress. This peak strength was unaffected by the relative density. At higher relative densities, strain hardening occurred after the initial yielding, and the strength was strongly affected by sand density.

Results from testing programs by Chamberlain et al. (1972), Alkire and Andersland (1973), Sayles (1973), Parameswaran and Jones (1981) and Shibata et al. (1985) show that increasing the confining pressure (σ_c) from 0 to 10 MPa generally leads to an increase in peak strength. Figure 2.74 presents a summary plot of Q_p versus confining pressure from these testing programs. Temperatures for these programs ranged from –4 to –12° C and strain rates from 4.5×10^{-6} to 1.1×10^{-2}/sec. The results from Alkire and Andersland (1973) exhibit a linear increase with confinement while Sayles (1973) test results show a pronounced curvature. For the results in Fig. 2.74, the total stress friction angle ranged from 0° to 28°.

The effects of strain rate on the peak strength is illustrated from tests from the following testing programs: Bragg and Andersland (1982), Orth (1985), Parameswaran (1980), Sayles and Epanchin (1966), Shibata et al. (1985) and Yuanlin (1988). Figure 2.75 presents a summary plot of the strain rate versus peak deviator stress results from these six testing programs.

All tests were unconfined compression tests at a temperature of –10°C. Strain rates for these programs varied from 10^{-7} to 10^{-1}/sec. It can be concluded that strain rate effects can be described by a simple power law relationship, i.e., $Q_p = k \cdot \dot{\epsilon}^{1/n}$. The results indicate that the power law coefficients generally range from 7 to 16. Test results from Bragg and Andersland (1980) and Yuanlin et al. (1988) show that above a certain strain rate, the strength of frozen sand becomes insensitive to changes in strain rate. It was previously stated in Section 2.2 that a similar behavior is also noted for polycrystalline ice at fast strain rates.

Axial Strain at Peak Strength

The axial strain at the peak deviator stress (ϵ_p) is strongly dependent of the deformation behavior after the upper yield. If strain hardening occurs after upper yield, then ϵ_p increases with relative density and appears to be strain rate independent. If the peak strength and upper yield stress coincide, the ϵ_p is insensitive to relative density, temperature and strain rate. These trends in ϵ_p, as affected by D_r, temperature and strain rate, are shown in the results from the testing programs by Baker and Kurfurst (1985), Bourbonnais and Ladanyi (1985) and Bragg and Andersland (1980), respectively; reproduced in Fig. 2.76.

2.3.2.3 Volumetric Strain Behavior

Little information exist on the measured volumetric strain response of frozen soils. Chamberlain et al. (1972) measured volumetric response for their tests on frozen Ottawa banding sand. Figure 2.77 shows the stress–strain and volumetric responses for three tests on dense specimens at confining pressures of 0.5, 1 and 2.5 kips/in^2 (1 kip/in^2 = 6.9 MPa). Note that the volumetric response shows a net dilation ($+\epsilon_v$) at the end of all tests.

However, the amount of dilation decreases with increasing confinement.

Shibata et al. (1985) also present volumetric strain responses for their tests on dense frozen Toyoura sand. These responses also show no net volume change or net dilation for all conditions, but dilation is suppressed at higher confining pressures (for more discussion, see Section 2.3.3.2).

2.3.3 Effect of Temperature on the Behavior of Frozen Sand

Temperature strongly effects the behavior of frozen sand beyond the "elastic" region. The following presents a review of available literature on the effects of temperature on the behavior of frozen sand. Both small strain and large strain behaviors are presented. A number of studies have been performed where frozen sand was tested under different temperatures. The results of studies which show the greatest relevance to the current research (i.e., constant rate of strain testing) are presented and examined below. As in the previous discussion, the presentation is limited to saturated or nearly saturated ($S \geq 90\%$), freshwater specimens.

2.3.3.1 Small Strain Behavior

Initial Elastic Response

Work by Kaplar (1963) and Baker and Kurfurst (1985), two of the test programs previously summarized in Section 2.3.2, illustrate the effects of temperature on the Young's modulus and Poisson's ratio. Kaplar (1963) performed resonant beam tests on Peabody gravelly sand at temperatures between –1.1 and –27.8° C. Figure 2.78 reproduces the results of Young's modulus and Poisson's ratio versus temperature. The results clearly illustrate an increasing trend in both Young's modulus and Poisson's ratio with decreasing temperature with the most significant increase in modulus occurring between 0° and –5° C.

Baker and Kurfurst (1985) performed acoustic wave propagation experiments on Ottawa 16–100 sand. Two testing temperatures of –3.2 and –10° C were used on sand specimens of different dry densities. Figure 2.79 reproduces the Young's modulus and Poisson's ratio results for the two testing temperatures. As illustrated in the figure, there appears to be a consistent increase in Poisson's ratio with decreasing temperature, but there is virtually no change in Young's modulus with decreasing temperature.

Upper Yield Stress

Review of the upper yield behavior is limited because most researchers either did not use appropriate measuring techniques to adequately define an upper yield stress, or they presented only peak strength results and chose to ignore the behavior at the upper yield stress. Parameswaran (1980) presents results from a series of unconfined compression tests on dense frozen Ottawa sand (ASTM C–109). Temperatures ranged from –2 to –15° C and strain rates ranged from 10^{-7} to 10^{-2}/sec. Cylindrical specimens (5 cm in diameter and 10 cm in length) were compacted to an optimum density of 1.7 g/cm^3 and a water content of 14% and subsequently saturated to a water content of 20%. Although considered dense, the final range in relative densities was not presented nor the range in degree of saturation. Figure 2.80 reproduces sets of stress–strain curves for different temperatures. Parameswaran noted that tests at high temperatures (–2 and –6° C) and low strain rates (10^{-7} to 10^{-5}/sec) exhibited little to no "yield stress", but a distinct yield stress, possibly followed by a drop in stress, was noticeable at lower temperatures. He reasoned that the distinct yield point was a function of both the strain rate and temperature. If a slow enough strain rate was applied, the yield point could become nonexistent. He attributed the drop in stress after yield

at the higher strain rates and lower temperatures to a yielding of the ice matrix. Once yield is reached in the ice, lower stresses are required to continue deformation. He also reasoned that the drop in stress after initial yield for frozen sand may be due to the "rupture" of the pore ice matrix which could be mitigated by application of a confining stress. The subsequent increase in stress after the yield drop (strain hardening) was due to the frictional component of the frozen sand beginning to control strength. The initiation of this frictional component, and hence the overall yield behavior, was considered to be strain rate dependent.

Orth (1985) performed uniaxial compression tests on very dense frozen Karlsrude sand. Testing temperatures ranged from –2 to –20° C, and strain rates ranged from 1.7×10^{-7} to 3.3×10^{-4}/sec. Nearly saturated (S = 91%), cylindrical specimens, 10 cm in diameter and 10 cm in length, were used. Orth also notes that a distinct yield point is exhibited for his tests at the lowest temperature and fastest strain rate. However, he states that the drop in stress after yield is due to dynamic recrystallization caused by the initial pressure melting of ice near sand particle contact points, movement of water to locations of lower stress and then re–freezing of water at the lower stress point. A similar view of the upper yield behavior was suggested by Bragg and Andersland (1980). The writer believes that dynamic recrystallization could not have occurred at the faster strain rates since this pore ice deformation mechanisms is predominant at slow strain rates, i.e., in the ductile region of granular ice behavior (see Section 2.2.2).

Bourbonnais and Ladanyi (1985) note an initial yield behavior in their test of a frozen Ottawa sand (ASTM designation C–778). Cylindrical specimens (10 cm in diameter and 15 cm in diameter) were compacted in

molds, saturated and frozen prior to testing. The average degree of saturation was 92%. Testing temperatures ranged from –6.7 to –160° C. Strain rates of $3x10^{-5}$, $3x10^{-4}$ and $3x10^{-3}$/sec were used during shear. They note that at a strain rate of $3x10^{-5}$/sec the initial yield behavior is followed by strain hardening at high temperatures (–6.7° C) but is followed by strain softening at lower temperatures (< –43.8° C). In the latter case, the upper yield point coincides with the peak strength. This strain hardening/softening behavior is also apparent in the failure strain behavior which is presented in Fig. 2.76. It is interesting to note that the strain corresponding to initial yield in this figure is essentially the same for all temperatures.

2.3.2.2 Large Strain Behavior

The effects of temperature on the large strain behavior of frozen sands will be examined via results from several testing programs. The testing programs cited in this review are also summarized in Table 2.4. The majority of these programs consist of unconfined compression tests, although the effects of confinement have also been studied. Testing temperatures ranged from near 0 to –180° C, but emphasis will be placed on results from 0 to –30° C. The presentation will describe the effects of temperature on the behavior in the peak strength region.

Where possible, stress–strain curves from the various programs will be classified according to the system used in the current research. This system, more fully described in Chapter 5 and Fig. 5.25, classifies the stress–strain curve response as one of four possible curves types; Type A, B, C or D. Type A stress–strain curves have the peak strength coincident with the upper yield stress ($\epsilon_p \approx 1\%$) beyond which the curve exhibits significant strain softening with continued deformation. Type B curves may also have the

peak strength coincident with the upper yield stress but the curve tends to "levels out" at larger strains. Type C curves exhibit their peak strength at moderate strain levels ($\epsilon_p \approx 3$ to 7%) followed by strain softening. Type D curves exhibit strain hardening to a peak strength at large strains (typically $\epsilon_p > 15\%$).

Peak Strength Behavior

Numerous testing programs have studied the effects of temperature on the peak strength behavior of frozen sands. Bourbonnais and Ladanyi (1985) present a plot of unconfined compressive strength versus temperature from ten testing programs. This plot is reproduced as Fig. 2.81. In general, all tests show an increase in strength with decreasing temperature for temperatures above –40° C. At temperatures lower than –40° C, the strength of saturated frozen sands tends to level off.

Sayles and Epanchin (1966) present the results of unconfined compression tests on frozen dense Ottawa sand (ASTM designation C–109). Cylindrical specimens (7.0 cm in diameter and 15.2 cm in length) were vibrated to an average dry density of 1.71 g/cm^3, saturated and then uni–directionally frozen. Testing temperatures were –3, –6.5, –10 and –30° C, and strain rates ranged from 3.8×10^{-5} to 2.4×10^{-2}/sec. Figure 2.82 shows a log–log plot of compressive strength versus applied strain rate for the tests performed at the four testing temperatures. The figure clearly shows that the strength of the frozen sand increased with decreasing temperature. The figure also shows that the flow curves for each series of tests are linear and nearly parallel, i.e., the power law coefficients (n) are similar for the four sets of tests ranging from 8.47 to 11.2.

As previously mentioned, Parameswaran (1980) presents the results from

unconfined compression tests on frozen Ottawa sand at temperatures of –2 to –15° C. Figure 2.80 showed a series of stress–strain curves for tests at temperatures of –2, –6, –10 and –15° C and strain rates between 1.32×10^{-5} and 5.53×10^{-4}/sec. These stress–strain responses range from Type C curves at slower strain rates and higher temperatures to Type A curves at faster strain rates and/or lower temperatures. While not consistent, in general the figure shows that the peak strength increases with decreasing temperature, as well as with increasing strain rate. Figure 2.83 shows a log–log plot of compressive strength versus applied strain rate for all tests. For tests at –6, –10 and –15° C, power law coefficients range from 13.5 to 15.7 for the full range of tested strain rates. However, tests at –2° C only show a trend of increasing strength up to a strain rate of 10^{-5}/sec above which the frozen sand becomes strain rate insensitive. A power law coefficient of 4.6 is calculated for those –2° C tests with strain rates below 6×10^{-6}/sec. This n–value is close to the range of n–values for pure polycrystalline ice, i.e., 3 to 4.5 (see Section 2.2). Parameswaran associates the transition in peak strength behavior at the strain rate of 10^{-5}/sec for the –2° C tests to a higher unfrozen water content and pressure melting at sand grain contact points during deformation. He also hypothesized that the lower power law coefficient for –2° C tests indicates that the pore ice controls the peak strength behavior at higher temperatures. However, in the writer's opinion, a set of tests at different relative densities would be needed to verify the ice–controlling aspect of peak strength behavior.

Bragg and Andersland (1980) performed a series a unconfined compression tests on dense frozen silica sand. Cylindrical specimens, 3.6 cm in diameter and 7.2 cm in length, were prepared with sand volume fractions

of approximately 64% and degrees of saturation between 96 and 100%. Testing temperatures ranged from –2 to –15° C, and strain rates ranged from $5.7x10^{-7}$ to $1.8x10^{-3}$/sec. Figure 2.84 reproduces a log–log plot of compressive strength versus applied strain rate for tests at –2, –6, –10 and –15° C. The results show a clear trend of increasing strength with decreasing temperature and increasing strain rate up to a strain rate of 10^{-5}/sec; then the compressive strength becomes insensitive to the applied strain rate at all tested temperatures. Bragg and Andersland state that, at lower strain rates, their results follow the simple power law with power law coefficients ranging from 8.4 to 12.7 for temperatures less than –6° C. For tests at –2° C, the power law coefficient is 3.3, which is within the range of values for pure polycrystalline ice. Bragg and Andersland suggest that this change in power law coefficient indicates a change in the pore ice behavior. They suggest that the ability of the pore ice, which experiences pressure melting during shear, to undergo dynamic recrystallization is reduced or eliminated at higher temperatures; therefore, the unfrozen water content increases leading to a relatively weaker frozen sand whose peak strength behavior is governed by the strength of the pore ice. Again, in the writer opinion, dynamic recrystallization (or lack thereof) is not an appropriate mechanism to explain rate insensitivity at faster strain rates.

Bourbonnais and Ladanyi (1985) present the results of unconfined compression tests on dense frozen Ottawa sand which were discussed earlier. Figure 2.85 reproduces a plot of stress versus strain for four tests at a strain rate of $3x10^{-5}$/sec but different temperatures. The test at –6.7° C appears to exhibit a Type C stress–strain curve response while the responses at lower temperatures are Type A. The figure clearly illustrates the increase in

strength in the frozen sand for temperature down to –109.6° C; however, the strength decreases as the temperature is further lowered (test SCU–28 at –160° C).

Shibata et al. (1985) present results from a comprehensive series of triaxial compression tests on dense frozen Toyoura sand. Specimens 5 cm in diameter and 10 cm in length were tested at strain rates of 4.5×10^{-6} to 4.5×10^{-4}/sec, temperatures from –2 to –50° C and confining stresses of 0, 4.9 and 9.8 MPa. The degree of saturation was not stated but is assumed to be near or at 100%. Volumetric strains were also measured by on–specimen lateral strain indicators. Figure 2.86 reproduces the stress versus deviatoric strain (= axial strain – 1/3 volumetric strain) for tests at temperatures of –2, –10, –30 and –50° C; strain rates of 4.5×10^{-6} and 4.5×10^{-4}/sec and confining pressures of 0 to 100 ksc (9.8 MPa). The following curve responses can be noted: Type A (generally at faster strain rate and/or lower temperatures and low confinement), Type B (faster strain rate, –30° C and high confinement), Type C (slower strain rate, higher temperatures and low confinement) and Type D (higher temperatures and higher confinement). The figures also show an increase in peak strength with decreasing temperature, increasing strain rate and increasing confinement. As noted in Section 2.3.2, the figure also shows an increase in volumetric strain with a decrease in temperature, increase in strain rate and decrease in confinement.

Figure 2.87 plots these results in terms of peak strength versus applied strain rate. Power law coefficients range from 13.9 to 28.0 exhibiting an inconsistent variation with temperature and confinement. Figure 2.88 shows the effect of temperature on the peak strength as a function of strain rate and confining stress. Shibata et al. note that the increase in peak strength is

linear for almost all strain rates and confining stresses (only results at the zero confining stress and slowest strain rate shows a clear non–linear behavior). From this they conclude that the slope of the peak strength versus temperature lines are independent of both strain rate and confining stress. In addition, they note that the slope of the peak strength versus temperature lines almost equals the slope of similar results on polycrystalline ice. Therefore, they conclude that the the strength gain with temperature in frozen soil is mainly due to the increase in ice strength. The writer notes that since the tests by Shibata et al. were performed at only one density, the effects of sand's frictional resistance on peak strength can not be evaluated. Therefore, the conclusion that changes in the peak strength of frozen sand with temperature is due solely to a change in ice strength may be questionable.

Orth (1985) presents results from a series of unconfined compression tests on a dense sand which were described earlier (see Section 2.3.3.1). Figure 2.89 reproduces plots of axial stress versus axial strain for tests at a strain rate of 0.01%/min (1.7×10^{-6}/sec) and temperatures of –2, –10, –15 and –20° C illustrating that the strength increases with decreasing temperature. Though all of these tests exhibit Type C curves, tests at $\dot{\epsilon} = 3.3 \times 10^{-4}$/sec and –20° C exhibited a Type A response. Figure 2.90 plots the log peak strength – log strain rate relationships for Orth's tests. Power law coefficients range from 5.6 (for –2° C tests) to 12.0 (for –20° C tests). Again, the power law coefficient for –2° C tests is similar to that found for pure polycrystalline ice.

Yuanlin et al. (1988) present the results of unconfined compression tests on dense frozen Lanzhau sand. The sand was compacted to a dry density of

1.8 g/cm^3 with average water contents and degree of saturations of 14% and 93%, respectively. Testing temperatures ranged from –2 to –15° C and strain rates from 4.92x10^{-7} to 6.41x10^{-4}/sec. Figure 2.91 reproduces the set of stress strain curves for tests at temperatures of –2, –5, –10 and –15° C. All curves exhibit Type C responses. Figure 2.92 plots the peak strength versus strain rate in log–log space for Yuanlin's et al. test results and shows that the log Q_p – log $\dot{\epsilon}$ relationships follow the power law equation with Q_p increasing with increasing strain rate for all temperatures and strain rates up to 3x10^{-4}/sec. Power law coefficients increase with decreasing temperature with n–values ranging from 5.22 to 9.54. For higher strain rates, the peak strength appear to become strain rate insensitive. Similar to the results of Parameswaran (1980), Bragg and Andersland (1980) and Orth (1985), the power law coefficient for the tests at –2° C (n = 5.22) approaches that found for polycrystalline ice.

Tensile Strength Behavior

Perkins and Ruedrich (1973) present the results of uniaxial tensile strength tests on frozen quartz Penn sand. Cylindrical specimens (4 cm in diameter by 5 cm in length) were formed in a special mold which created radial protrusions at the ends of the specimen so that the specimens could by clamped and pulled. Specimens were compacted to a total density of 1.92 g/cm^3; other specimen parameters such as the degree of saturation and relative density were not provided. Figure 2.93 reproduces their results for tensile tests at strain rates between 1.67x10^{-6} to 1.67x10^{-3}/sec and temperatures between –1.1 to –13.3° C. The plot shows that for strain rates up to 1.67x10^{-3}/sec (0.1/min) there is a strain rate dependence on the tensile strength of the sand at all tested temperatures. The plot also shows that for

a given strain rate the tensile strength of the frozen sand becomes temperature independent as the temperature decreases. The temperature at which this temperature insensitivity occurs increases as the strain rate increases.

Strain at Peak Strength

The effect of temperature on the strain at peak strength can be seen in Fig. 2.76 which shows the results of unconfined tests from Bourbonnais and Ladanyi (1985) and Bragg and Andersland (1980). As illustrated, the results of Bourbonnais and Ladanyi (Fig. 2.76b) show that the failure strain is essentially constant at 0.5% and coincides with the strain at upper yield for nearly all test temperatures and strain rates (indicative of Type A responses). Only the test at the slowest strain rate (3.0×10^{-5}/sec) and highest temperature (–6.7° C) has a higher strain at failure. The test results from Bragg and Andersland (Fig. 2.76c) show that the failure strain is essentially the same for their tests ($\approx$ 4%) at temperatures of –2 to –15° C for strain rates at or below 1×10^{-4}/sec (indicative of Type C responses). As the strain rate increases, the failure strain reduces to 0.5 – 1% at a strain rate of 2×10^{-4}/sec for tests at –10 and –15° C (Type A response). The change in failure strain indicates a ductile–brittle transition in stress–strain response of the frozen sand.

Yuanlin et al. (1985) also examined the strain at peak strength. Figure 2.94 plots the strain at failure for all of their reported tests previously shown in Figs. 2.91 and 2.92. As illustrated, there is little evidence of an abrupt change in ϵ_p behavior with strain rate for their tests.

2.3.2.3 Methods of Calculating the Peak Strength of Frozen Sand

The following discusses three methods that have been proposed to

estimate the peak strength of frozen sands as a function of temperature. The first method follows an Arrhenius–type equation which considers the peak strength of frozen soils to involve thermally–activated processes. The second and third methods assume that the peak strength follows a power law–type formation between strength and temperature and between the strength and strain rate, respectively.

Arrhenius–Type Formulation

Anderson and Andersland (1978) propose that the relationship between strength and temperature of frozen sands closely follows Glen's (1955) creep law (see Section 2.2.3) as follows

$$Q_p = \sigma_{c0} \cdot \exp\left[\frac{Q\theta}{273 \cdot nR(273-\theta)}\right] \cdot (\dot{\epsilon}_a/\dot{\epsilon}_c)^{1/n} \qquad 2.23$$

where Q_p is the peak strength, Q is the apparent activation energy, θ is the temperature in degrees below zero in Celsius (°C), n is the power law coefficient, R is the universal gas constant, $\dot{\epsilon}_a$ is the applied strain rate, $\dot{\epsilon}_c$ is a reference strain rate (selected as 1.67×10^{-7}/sec) and σ_{c0} is the strength at a temperature of 0°C and $\dot{\epsilon}_a = \dot{\epsilon}_0$. Evaluation of the input parameters (i.e. n and σ_{c0}) are illustrated in Fig. 2.95. The value of n is determined in the usually manner from the top diagram. The value of σ_{c0} is determined from the intercept of a plot of log strength versus temperature at the reference strain rate $\dot{\epsilon}_c$. The apparent activation energy is determined as for the case of pure ice, i.e., from a plot of strain rate versus 1/T and conditions of constant stress.

Parameswaran (1980) applied a form of Glen's creep law to his frozen sands in an attempt to describe the effect of temperature on peak strength behavior. This equation was as follows

$$\dot{\epsilon} = C \cdot \sigma^n \cdot \exp(-Q/RT) \qquad 2.24$$

where $\dot{\epsilon}$ is the strain rate, C is a temperature–independent constant, σ is the stress, T is the absolute temperature (°K) and the other variables are as described previously.

Strength–Temperature Power Law

A second method to estimate the peak strength of frozen sands as a function of temperature is the use of a direct "power law" relationship between temperature and peak strength. Tsytovich (1975) presents a form of this equation as

$$Q_p = a + b\theta^s \qquad 2.25$$

where a and b are temperature–dependent constants, θ is the degrees Celsius below freezing (absolute value of temperature in °C) and s is an experimentally determined parameter. This s parameter may vary with strain rate.

Strength–Strain Rate Power Law

Anderson and Andersland (1978) present a third method to estimate the peak strength of frozen sands based on a power law relationship of the form

$$\sigma_{max} = \sigma_{c0} \cdot [1 + \theta/\theta_c]^{\omega} \cdot (\dot{\epsilon}_a/\dot{\epsilon}_c)^{1/n} \qquad 2.26$$

where θ_c is an arbitrary temperature (e.g. 1°C) and ω is obtained from the slope of a line in a log–log plot of $\sigma_{c\theta}$ strength versus $(1+\theta/\theta_c)$,

$$\omega = \frac{\Delta \log \sigma_{c\theta}}{\Delta \log(1+\theta/\theta_c)} \qquad 2.27$$

For small temperature intervals, $\omega \approx 1$ and the power law formulation reduces to

$$\sigma_{max} = \sigma_{c0} \cdot [1 + \theta/\theta_0] \cdot (\dot{\epsilon}_a/\dot{\epsilon}_c)^{1/n} \qquad 2.28$$

where σ_{c0} and θ_0 are the strength and temperature intercepts, respectively, in a linear plot of strength versus temperature. Evaluation of these derived parameters is presented in Fig. 2.96.

The writer notes that none of these methods include the effects of relative density or sand volume fraction in their formulations. In addition, these methods do not consider the number and the applicable range of deformation processes involved at peak strength. If the upper yield and peak strength coincide, the predominant deformation processes could be those most associated with the the pore ice. However, if the strain at peak strength is significantly different from the strain at upper yield, the controlling deformation processes may be a combination of ones of the pore ice and ones of the sand skeleton. A more complete procedure to estimate the peak strength of frozen sands must incorporate temperature, strain rate, confining pressure and relative density or sand volume.

2.3.4 Effect of Pre–Freezing Confinement on Frozen Sand Behavior

In the current research program, triaxial tests were performed on Manchester Fine Sand specimens which were initially saturated and consolidated to a desired effective stress prior to freezing and subsequent shear. These tests have been termed *consolidated – freeze* (CF) tests. Essentially all of the earlier testing programs, including that of Andersen (1991), performed tests on specimens which had been prepared in a mold, saturated and frozen under atmospheric conditions. These "conventional" tests would best simulate the condition of sands frozen under little or no overburden. However, the behavior of frozen deep beneath the surface may be best modeled by consolidate – freeze testing.

This section is divided into two parts. The first part presents a review of the available literature relevant to pre–freezing confinement on frozen sands. Unlike the previous sections, a review of the literature revealed that no published testing programs exist which have compared the effects of

confinement on the behavior of frozen sands using both conventional and consolidate–freeze testing methods. However, a few researchers have studied sands which were frozen after the application of a confining pressure, and their findings will be briefly discussed. The second part hypothesizes on the possible effect of pre–freezing confinement on the behavior of frozen sand.

2.3.4.1 Previous Research with Pre–Freezing Confinement

Three programs will be reviewed which confined the sand specimen prior to freezing. As mentioned in Section 2.3.1, Singh et al. (1982) performed cyclic triaxial tests on unfrozen sand specimens which were initially consolidated to a known stress level then frozen and subsequently thawed prior to testing. The objective of this testing was to evaluate the effect of freezing on the undisturbed sampling of sands. The unidirectional freezing was performed under a hydrostatic effective confining stress of 0.56 ksc with a backpressure of 1.5 ksc. As noted earlier, measurements of the volume change during freezing and thawing were conducted and found to be essentially the same and as theoretically predicted. However, Singh et al. did not perform any tests on the frozen sand so the effects of confinement on the behavior of frozen sands cannot be analyzed.

Goodman (1975) performed a series of unfrozen and frozen test on a quartz sand. Cylindrical specimens 7.6 cm in diameters and 15.2 cm in height were prepared by forming the specimens in a plasticized polyvinyl chloride (PVC) "membrane" with a wall thickness of 0.64 cm. The specimens were compacted/consolidated by a combination of 1) side tamping while being poured in the PVC membrane and 2) application and subsequent cycling of a hydrostatic confining pressure. Final effective confining pressures ranged from 0.86 to 3.44 MPa with cycling pressures ranging from 0 to 1.03

MPa. Back pressures during consolidation/compaction and freezing ranged from 0 to 0.69 MPa. Unidirectional freezing was performed by circulating freezing fluid through a coiled tube wrapped around the specimen and through the top cap. The testing temperature was $-7\pm1^{\circ}$C. Specimen densities and degrees of saturation were not reported.

The testing procedure consisted of the incremental application of load with the measurement of axial deformations with time under each load increment (i.e., incremental creep tests). If the deformation rate had decreased to zero for a time period of 45 minutes, another increment of load was added. The "yield pressure" of a test was the stress at which the specimen deformed at a constant rate with time. Figure 2.97 reproduces a plot of yield pressure versus confining pressure for both frozen and unfrozen sand specimens and shows that the yield surface for both materials is the same. Based on this measured behavior, Goodman suggested that the yield stress is dependent only on the sand skeleton with no influence of the ice. He does note however, that his results are at slow strain rates and results at higher strain rates may be differ. Andersen et al. (1992) suggest that the PVC membrane may have also produced a condition closer to that of confined (one–dimensional) compression and not triaxial compression. Thus, it is not possible to draw fruitful conclusions from the data.

Sego et al. (1982) present test results on a concrete mortar sand which was first consolidated and then frozen and sheared. However, the process was not continuous. Cylindrical specimens 10 cm in diameter and 18 cm in length were formed in a PVC mold at a water contents of 30%. Salt concentrations of the pore fluid ranged from 0 to 30 mg/liter (note: only the test results with no salinity will be discussed). After being vibrated to an

appropriate density, the specimens were one–dimensionally consolidated in the molds under an axial stress of 0.08 MPa, placed in a room set at +1° C and subsequently frozen from the bottom to the top with a base temperature maintained at –75° C. The consolidation stress was also maintained during the freezing process. At the end of the freezing process (24 hours), the specimen was removed from the consolidation apparatus and stored until needed for strength testing.

Unconfined compression tests of pre–frozen specimens were performed at a temperature of –7° C and strain rates ranged from 5.5×10^{-6} to 1.4×10^{-3}/sec. Figure 2.98 shows a log–log plot of peak strength versus strain rate for the tests with no salt concentration. The linear relationship in the plot shows that the peak strength behavior of these tests follows a simple power law equation with a power law coefficient of 5.52. These test results suggest that the behavior of conventional and consolidate–freeze tests may be similar. However, it must be noted that the effective confining stress on these specimens prior to freezing was relative small. In addition, the confining stress was relieved prior to shearing. Thus, the effect of maintaining the effective confining pressure on the specimen during the freezing and shearing processes can not be evaluated.

2.3.4.2 Possible Effect of Pre–Freezing Confinement on Behavior

Andersen et al. (1992) present results from tests on frozen Manchester Fine Sand which may indicate what effects confinement prior to freezing can have on the behavior of frozen sands. They compare the stress–strain results from two tests prepared to similar densities (D_r = 90%) and tested under similar strain rates (3×10^{-5}/sec), confining pressure (2 MPa) and temperatures (–10° C). However, one test was prepared by wet tamping (compaction) while

the other was prepared using multiple sieve pluviation (see Chapter 3 for description of these methods). Figure 2.99 shows the stress–strain response of these two tests. The figure shows that the test which was compacted (FRS26) has a significant increase in the post upper yield strain hardening and in peak strength, as well as a decrease in the strain at failure when compared to the pluviated specimen (FRS55). One possible explanation for this behavior is that the sand skeleton of the compacted specimen retained some of the "locked in" stresses imposed during compaction and that these stresses were preserved during freezing. These locked in stresses may be similar to the case of a pre–freezing effective stress on the sand skeleton.

2.4 COMPOSITE/PARTICULATE MODELING OF FROZEN SAND

This section describes two models which can be used to analyze frozen sand. The first model is an isostrain model which considers the sand particles to be imbedded in an ice matrix. This model has been previously described by Andersen et al. (1992) and was found to be most appropriate for modeling the small strain behavior (especially the initial modulus) of frozen MFS. The second model, called the dilatancy–hardening model, consists of equations based on well established unfrozen soil mechanic principles that account for the dilatancy and soil strengthening mechanisms discussed in the previous Section 2.3. This model attempts to estimate the peak strength of dense frozen sands.

2.4.1 Isostrain Model

Counto (1964) developed an isostrain model for the initial modulus of concrete considering the aggregate to be embedded in a matrix of cement. Andersen (1991) and Andersen et al. (1992) adopted this model in an

attempt to model the initial modulus of frozen MFS. The model considers the frozen soil as a composite of aggregate encased in an ice matrix. As illustrated in Fig. 2.100, the model can be described as a cube–in–a–cube, although the equations can also be derived from a cylinder–in–a–cylinder framework. In this model, a prism of silicate mineral (sand) is embedded in a cube of matrix material which represents the ice phase. The presence of air or unfrozen water is neglected. Counto recommended that the composite be of unit volume and that the ratio of height to cross–sectional area be unity. The aggregate prism should have the same dimensional characteristics as the composite cube such that the volume of the aggregate can be represented as V_a, which is the volume fraction of aggregate in the composite material.

Counto (1964) outlined several of the assumptions upon which this model is based. The major assumptions are:

1) The composite material consists of two phases, the aggregate (sand particles) and matrix (pore ice).

2) The sand particles exhibit only elastic deformations; no time dependent behavior can occur.

3) Only the matrix is allowed to exhibit yielding behavior. In the derivation of composite yielding, an effective modulus of the matrix is used which is a function of the level of strain applied to the composite.

4) A "perfect bond" exists between the aggregate and matrix. Thus, strain compatibility between the silicate prism and the ice matrix is assured.

The model equations are developed based on three horizontal sections of the composite; two pure ice ends and a central section which includes all of the sand and the surrounding ice (see Fig. 2.100). From an applied axial

force, the corresponding deformation of each section is computed from the "known" elastic moduli of the pore ice and sand particles. In the central composite section, the isostrain condition between the silicate prism and the surrounding ice allows for a partitioning of the stresses between the sand and ice. For the condition that the silicate prism is stiffer than the ice matrix, higher stresses exist on the silicate.

The composite modulus is computed from the deformation of the three section using the moduli of the individual components and the volume fraction each components occupies in the composite material. The resulting equation for the composite modulus using the height to area ratio of unity is

$$\frac{1}{E_c} = \frac{1 - \sqrt{V_s}}{E_i} + \frac{1}{\left[\frac{1 - \sqrt{V_s}}{\sqrt{V_s}}\right] E_i + E_s} \qquad 2.29$$

where E_c is the composite Young's Modulus, E_i is the Young's Modulus of the ice, E_s is the Young's Modulus of the individual sand particles (not the sand skeleton), and V_s is the volume fraction of the sand.

Andersen (1991) also presented an equation for the assumption that the geometry of the silicate prism is that of a perfect cube

$$\frac{1}{E_c} = \frac{1 - \sqrt[3]{V_s}}{E_i} + \frac{1}{\left[\frac{1 - \sqrt[3]{V_s^2}}{\sqrt[3]{V_s}}\right] E_i + E_s \sqrt[3]{V_s}} \qquad 2.30$$

where E_c, E_i, E_s and V_s have the same meaning as previously defined. If this cubic geometry is adopted, the model predicts a slightly higher elastic modulus (approximately 20%) (Andersen et al. 1992).

Andersen (1991) and Andersen et al. (1992) showed that Eq. 2.29 worked well with their results of frozen MFS at a temperature of –10° C. An examination of how the model compares to frozen MFS tests over a range of

temperatures is presented in Chapter 6.

2.4.2 Dilatancy–Hardening Model

The dilatancy and soil strengthening mechanisms in frozen soils (mechanisms previously discussed in Section 2.3) can be evaluated using a dilatancy–hardening model. This behavioral model and its basis were developed principally by Ladanyi in a series of papers (Ladanyi 1981a and b; Ladanyi 1985; and Ladanyi and Morel 1990), and equates the strength of a frozen sand to 1) the development of higher effective stresses on the sand skeleton provided by the tensile strength of the pore ice; and 2) the additional shear strength provided by the pore ice. The following sections discuss the genesis of the model's formulation and its use for dense frozen sands.

2.4.2.1 Description of Pore Stresses in Unfrozen and Frozen Soils

Ladanyi (1981 a and b) describes how the pore stresses in soils are developed during shear and how different pore fluid's or pore matrix materials will behave. Figure 2.101 shows a schematic drawing of total and effective stress paths for a consolidated–undrained test on unfrozen dense sand in the M.I.T. q–p–p′ space, i.e., $q = 0.5 \cdot (\sigma_1 - \sigma_3)$, $p = 0.5 \cdot (\sigma_1 + \sigma_3)$ and $p' = 0.5 \cdot (\sigma'_1 + \sigma'_3)$. Initially, there is no shear stress on the sand ($q = 0$) with both the effective stress path (ESP) and total stress path (TSP) starting at point O. As the sand is sheared, the ESP follows a curved shape with the path joining and climbing up along the failure envelope (K_f–line) with continued shear. The TSP follows a constant 1:1 slope up and to the right. The difference between the two paths is the pore pressure generated during shear

$$\Delta u = p_{TSP} - p'_{ESP} \qquad 2.31$$

where p_{TSP} and p'_{ESP} are the average normal stresses of the TSP and ESP, respectively, at the same level of shear stress (q). As illustrated in the figure, due the dilative response of the sand, the ESP crosses the TSP leading to the development of negative pore pressure. The stress paths continue to travel upwards until the developed negative pore pressure causes the pore fluid to cavitate (at magnitude T), at which point the maximum shear strength (q_{max}) of the sand is reached at point B. If the sand is tested with an initial back pressure, the shear strength will continue to increase as the ESP is able to travel further up the K_f–line before the pore fluid cavitates or until the specimen reaches the critical state point.

The fact that negative (tensile) stresses in bulk pore water above approximately one atmosphere ($\approx$ 0.1 MPa) can lead to cavitation is well known. Ladanyi extended this observation to the case where the pore fluid was ice. As discussed in Section 2.2, the tensile strength of ice can reach maximum stress levels of approximately 2 MPa (Hawkes and Mellor 1972, Haynes 1978) for strain rates greater than 10^{-6}/sec and temperatures from –1° C to –35° C. With this increased tensile strength, a higher sand strength can be realized due to the "dilatancy–hardening" of the sand.

Along with the increased soil strength developed from dilatancy–hardening, the ice also provides additional shear strength to overall frozen soil's strength. Ladanyi proposed that this strength, q_i, could be added directly to the enhanced soil strength leading to the final strength of the frozen soil.

2.4.2.2 Dilatancy–Hardening Model

Ladanyi (1985) and Ladanyi and Morel (1990) present a model to describe the dilatancy–hardening or internal confinement provided by the pore

ice for dense, ice–saturated sands. The model draws on an analogy between the undrained behavior of an unfrozen sand and the shearing at constant volume of a frozen sand. Its purpose was to show how the pore ice affects the strength of frozen sands by increasing the effective stresses the sand can reach and adding "cohesion" to the overall frozen sand strength. The basic concepts are:

1) both systems (unfrozen and frozen) are subjected to the same strain path; i.e., specimens are loaded axially at a constant confining pressure and constant volume; and
2) the sand skeleton in both systems starts from the same "state" (density and effective stress).

As discussed earlier, unfrozen dense sand sheared under undrained conditions at low confinement will want to dilate. This resulting development of negative pore pressures increase the effective stresses acting on the sand skeleton,leading to increased frictional resistance (dilatancy–hardening). Ladanyi and Morel (1990) list the following assumptions for the model:

1) All of the pore water in the sand is considered to be frozen.
2) The behavior of the sand skeleton is a function of its initial density and consolidation stress which can be described by the state parameter Ψ as introduced by Been and Jefferies (1985) and described in Section 2.1.2.
3) The frozen sand is considered "unconsolidated".
4) The sand in the composite sand–ice material behaves "undrained" as long as the pore ice is continuous and unbroken during shear. The sand behaves "drained" when the pore ice fails, i.e., breaks up.
5) It is assumed that, provided the pore ice remains continuous and unbroken, the dilatancy–hardening principles, such as established by Bishop and Edlin (1950) and Seed and Lee (1967), for unfrozen sands are applicable for frozen sands as long as the pore

ice matrix is taken into account.

As discussed previously, it has been observed that for a dense, unfrozen sand sheared under undrained conditions from a low consolidation stress the sand exhibits a tendency to dilate causing the pore water pressure to decrease and the effective stresses to increase on the sand skeleton until one of two conditions occurs: either the pore water pressure cavitates, or the effective stresses increase until the "state point" reaches the Critical Void Ratio Line (CVRL) or steady state line (SSL).

The transition between the cavitation regime (where the test terminates due to cavitation of the pore water) and where the state point of the sand is reached is determined by the critical consolidation stress, σ'_{3crit}, and the magnitude of the tensile stress increment which can be supported by the pore fluid. The critical consolidation stress was defined by Seed and Lee (1967) as that consolidation stress for a given void ratio which results in no net volume change at peak strength in a drained triaxial compression test on unfrozen sand or no net change in pore pressure at peak strength for an undrained triaxial compression test. Ladanyi and Morel (1990) adopted a different criterion in that the critical consolidation stress is defined as the stress at which the rate of dilation at the peak strength is zero for drained shearing or rate of pore pressure change is zero for undrained shearing.

The cavitation and non–cavitation regimes are graphically described in Fig. 2.102. This figure, using the MIT q–p–p′ format, shows that the strength of the unfrozen soil (q_{us}) is defined by the effective stress failure envelope (K_f–line) which starts at the origin and has a slope $q_f/p'_f = \tan \alpha' = \sin \phi'$. The total stress (failure) envelope, TSE (FS = us (unfrozen

sand) + fs (frozen sand)), has an initial slope identical to the K_f–line, but translated to the left by an amount equal to the tensile strength of the pore fluid. Note that the beginning of this TSE does not intersect the vertical (q) axis but begins at the point in the q–p–p′ space where q = p = p′ = tensile strength of the pore fluid.

The transition point between the cavitating and noncavitating regimes occurs at a confining pressure (total stress) of

$$\sigma_c = \sigma'_{3crit} - T \qquad 2.32$$

where T is the tensile strength of the pore fluid. For pore water, $T = T_w$ which is $\cong$ 1 atm (or 0.1 MPa); for pore ice $T = T_i$ where $T_i >> 1$ atm. For a confining pressure greater than $\sigma'_{3crit} - T$, i.e., for an initial p ($= \sigma_c$) greater than p_2 in Fig. 2.102, the total stress envelope, assuming an undrained test condition, becomes horizontal with a value of $q = q_{fs}$. The predicted strength of the soil skeleton in this region is therefore solely controlled by the magnitude of the critical consolidation stress and can be calculated as

$$q_{fs} = 0.5 \cdot \sigma'_{3crit} \cdot (R'_f - 1) \qquad 2.33$$

where R'_f is equal to $1/K_f = (\sigma'_1/\sigma'_3)_f = \tan^2(45 + \phi'/2)$. For a confining pressure less than $\sigma'_{3crit} - T$, the strength of the sand is governed by the applied confining pressure ($\sigma_3 = \sigma_c$) and the tensile strength of the pore matrix, so that

$$q_{fs} = 0.5 \cdot (\sigma_3 + T) \cdot (R'_p - 1) \qquad 2.34$$

Since pore ice can support both tensile and shear stresses, Ladanyi and Morel (1990) propose that the shear strength of the ice can be added directly to the shear strength of the sand skeleton, which also has been increased by the tensile strength of the pore ice. Using Ladanyi and Morel's methodology,

the strength of the frozen sand is represented by a total stress line, TSL (FS = fs + ice), where the additional ice strength is added to the sand skeleton strength directly above the effective stress envelope (ESE). For example, for the non–cavitating case, the soil skeleton ends up at point B on the ESE. The shear strength of the ice, q_i, is then added to obtain point C which defines the break in the TSL (FS) envelope. In contrast, the MIT methodology would use the TSE (FS) which represents the actual end points of measured total stress paths.

The total shear strength of the frozen "system" can now be described for both the cavitating and non–cavitating case. In the noncavitating region, the shear strength of the frozen sand can be determined as

$$q_{FS} = 0.5 \cdot \sigma'_{3crit} \cdot (R'_f - 1) + q_i \qquad 2.36$$

where σ'_{3crit} is the critical confining pressure for the given initial void ratio (density) of the sand skeleton. This equation predicts that the strength of the frozen sand is independent of the actual confining pressure.

For the cavitating case, i.e., $\sigma_3 < \sigma_{crit}–T_i$, the shear strength of the frozen sand (q_{FS}) is determined as

$$q_{FS} = q_{fs} + q_i = 0.5 \cdot (\sigma_3 + T_i) \cdot (R'_f - 1) + q_i \qquad 2.35$$

where σ_3 is the cell pressure, T_i is the tensile strength of ice, R'_f is $(\sigma'_1/\sigma'_3)_f$, and q_i is the shear strength of the pore ice. Hence the shear strength in this region increases linearly at slope K_f with the confining pressure.

Ladanyi and Morel (1990) present the results of drained triaxial compression tests on unfrozen sand and "conventional" triaxial compression tests on frozen specimens of 20–30 Ottawa sand to validate the dilatancy–hardening model. Tests were performed on dense, saturated

specimens (D_r = 79 to 96%) at nominal strain rates between 2.0×10^{-3} to 2.3×10^{-3}/sec. Confining pressures (or effective consolidation stresses) prior to shear ranged from 0.1 to 0.3 MPa. The temperature for frozen tests was –5° C. For both the frozen and unfrozen tests, the strain at failure ranged from approximately 1 to 2%.

Figure 2.103 shows a plot of the measured and predicted strengths of the frozen sand in q–p space. The pertinent parameters used in dilatancy–hardening model were:

1) Effective friction angle, ϕ' = 32° as determined from consolidated–drained tests on unfrozen specimens (Ladanyi and Morel note that consolidated–undrained tests would have been more appropriate for determining effective stress paths). This led to an R'_f = 3.25.

2) Tensile strength of the ice, T_i = 1.5 to 1.8 MPa. These values were chosen as representative of the ice tensile strength and fall within range (if not somewhat below) the tensile strength of polycrystalline measured by others (e.g., Hawkes and Mellor 1972, Haynes 1978)

3) An ice strength, Q_i (= $2 \cdot q_i$) of 4.5 MPa. This value is from two tests performed by the authors on polycrystalline ice specimens. These tests were performed at a similar strain rate and temperature as the frozen sand tests.

Based on these parameters, Ladanyi and Morel found excellent agreement between the calculated and measured peak strength results. The applicability of the dilatancy–hardening model to frozen MFS is presented in Chapter 6.

2.4.2.3 Discussion of Dilatancy–Hardening Model

The dilatancy–hardening model assumes that the effective stresses acting on the sand skeleton are identical in both the frozen and unfrozen states after accounting for the greater tensile strength of ice compared to water. Andersen (1991) and Andersen et al. (1992) noted that some possible deficiencies exist with this model, namely;

1) This model adds directly the shear strength of pore ice to that of the unfrozen sand skeleton as found on the ESE [i.e. the TSL (FS)]. If this methodology is followed, the final total stresses will not lie on the total stress line. This was previously illustrated in Fig. 2.102, but can be circumvented using the MIT methodology and the TSE (FS + ice) line.

2) The level of axial strain required to mobilized the peak strength of a dense, dilative unfrozen sand (large – Ψ) will be much higher than that reached in mobilizing the peak strength of a frozen sand. [This will be the case for dense unfrozen MFS at low confinement which reaches a peak strength at $\epsilon_a \approx 22\%$.] This represents a significant strain incompatibility.

Andersen et al. (1992) suggest that the intergranular contact forces acting on individual silicate particles in frozen sand will not, in and of themselves, be in equilibrium. In frozen soils, the external forces on individual sand particles are produced by contact forces between grains of the sand skeleton and by forces transferred through the ice–silicate interfaces. Figure 2.104 presents a two–dimensional, free–body diagram of an silicate particle and the applied forces on it's faces. The figure shows that a state of force equilibrium is not normally reached in frozen sands by considering the intergranular forces alone or by considering the ice–silicate forces alone. Andersen (1991) states "Consideration of the equilibrium of an individual sand particle in a frozen sand matrix indicates that in all but the most

specialized cases, the intergranular contact forces do not constitute an equilibrium stress state when considered separately from the ice–silicate interface forces. This means that a quantitative evaluation of the strength and deformation behavior of frozen sands in terms of the intergranular effective stresses may not be appropriate." Based on this consideration, the use of "effective stresses" to describe frozen sand behavior is limited to only special cases.

TABLE 2.1 FACTORS AFFECTING THE STEADY STATE CONDITION OF SANDS

Factor	Descriptors	Effect on Steady State Line	REFERENCES
Sand Grain Characteristics	Particle Shape, Grain Size Distribution, Fines Content	Rounder particles lead to flatter SSL's and are more subceptible to liquefaction. Uniform sand masses are more subsceptible to liquefaction than well-graded sands. Increased fines content leads to higher compressibility and steeper SSL's.	Poulos et al. (1985) Alarcon-Guzman et al. (1988) Been and Jefferies (1985) Sladen et al. (1985) Hird and Hassona (1990)
Strain Rate	Load-controlled vs Strain-controlled Testing Techniques	Increased strain rate causes lower SSL due to development of flow structure. May be due to grain characteristics.	Castro (1969) Casagrande (1975) Hird and Hassona (1990) Alarcon-Guzman et al. (1988)
		No effect of strain rate on position of SSL	Poulos et al. (1985 and 1988) Been and Jefferies (1985) Been et al. (1991)
Initial Fabric	Pluviatied vs Compacted Specimen Preparation Techniques	Should not effect steady state condition since initial fabric does not effect large strain behavior. However, compacted specimens are more likely to liquefy than pluviated specimens at the same initial state.	Poulos (1981) Poulos et al. (1985) Hird and Hassona (1990) Been et al. (1991) Vaid et al. (1990) Verdugo (1992)
Initial State	ψ parameter based on upper steady state line	Have upper and lower steady state lines. Steady state line reached based on initial ψ	Konrad (1990a and b)
Effective Stress Path	Triaxial Compression vs Extension	Compression SSL is different from extension SSL with multiple SSL's for extension possible.	Vaid et al. (1990) Vaid and Pillai (1992)
		No difference between compression and extension.	Been et al. (1991) Been et al. (1992)

TABLE 2.2 POSSIBLE DEFORMATIONAL MECHANISMS IN POLYCRYSTALLINE ICE (page 1/2)
Abstracted from Andersen (1991)

CATEGORY	NAME	DESCRIPTION	RANGE OF APPLICABILITY	REFERENCES
Elastic	Elastic Straining of Crystal Lattice	Distortion of lattice due to elastic straining of hydrogen bonds	Occurs under all loading conditions. May dominate behavior in the absence of other mechanisms.	Cottrell (1953) Hobbs (1974) Cole (1990) Hertzberg (1989)
Anelastic	Anelasticity	Motion of a population of mobile dislocations under internal stresses	Under all loading conditions with sufficient time to build up internal stresses	Duval et al. (1983) Duval (1978) Cole (1990)
Plastic	Diffusional Flow	Diffusion of vacancies either the lattice or along the grain boundaries.	At very low stresses or strain rates or high homologous temperatures (n=1)	Coble (1963) Nabarro (1947) Herring (1950)
	Grain Boundary Sliding with Diffusional Accommo-dation	Combined diffusion along boundaries or through lattice to accommodate discon-tinuities during sliding.	At low stresses or strain rates or high homologous temperatures (n=1)	Raj and Ashby(1971) Ignat and Frost 1987)
	Dislocation Gliding and Climbing	Gliding and climb-ing motions of dis-locations either along or between slip planes	Considered dominant mech-ism controlling power law creep for n = 3 to 4.5	Hertzberg (1989) Duval et al. (1983) Weertman (1983) Langdon (1973) Sinha (1978)

TABLE 2.2 POSSIBLE DEFORMATIONAL MECHANISMS IN POLYCRYSTALLINE ICE (page 2/2)
From Andersen (1991)

CATEGORY	NAME	DESCRIPTION	RANGE OF APPLICABILITY	REFERENCES
Evolving Micro-Structure	Grain Boundary Migration	Motion of grain boundaries as individual crystals grow and consume adjacent crystals	During periods of storage or under low stresses and strain rates at the lower end of the power law regime	Cole (1986,1987) Duval et al. (1983) Gold (1963)
	Dynamic Recrystallization and Grain Boundary Migration	Nucleation and growth of new grains along existing grain boundaries due to strain energy gradients	Lower end of power law regime as coefficient approaches 1	same as above
Internal Cracking and Fracture	Transcrystalline Fracture	Nucleated cracking due to the pileup of dislocations against grain boundaries	Higher end of power law regime up to strain rates of approximately 10^{-4}/sec	Ashby et al. (1979) Cole (1987, 1988)
	Grain Boundary Fracture	Cracking along boundaries between adjacent grains due to elastic anisotropy	Higher end of power law regime and in the region of power law breakdown	Cole (1988) Zener (1948) Sunder and Wu (1990)

TABLE 2.3
MECHANISMS OF STRENGTH FOR FROZEN SAND

Possible Mechanisms from Ting et al. (1983)	Conclusions from Ting et al. (1983)
(1) Ice Strength Function of $\dot{\epsilon}$, T, σ_c, grain fabric	• Thought to dominate at low strains.
(2) Soil Strength Cited Rowe (1962) for drained strength of cohesionless soil having three components: • Sliding between grains • Particle inference • Dilatancy (volume increase against σ'_c)	• Thought to dominate at large strains.
(3) Interaction Between Ice and Soil	
(a) Ice strengthening-due to altered i) Structure ii) State of stress & deformational constraints iii) Strain rate (higher)	• Thought to dominate at low strains.
(b) Soil strengthening	• Thought to dominate at large strains.
i) Increased dilatancy	• Increase σ' due to strong tensile adhesional soil-ice interface forces resisting expansion of soil skeleton.
ii) Structural hindrance	• Synergistic mechanical interaction due to strong bonding between the ice matrix and soil skeleton.
(c) Tension in unfrozen water film	• Probably not very significant (e.g., decreasing ice saturation leads to much lower strength).

TABLE 2.4
OVERVIEW OF TESTING PROGRAMS TO MEASURE LARGE STRAIN BEHAVIOR OF FROZEN SAND (page 1/3)
(abstracted from Andersen, 1991)

INVESTIGATOR(S) (PROGRAM LETTER)	MATERIAL TESTED	TYPE OF TEST	STRAIN RATE (s^{-1})	RANGES IN TESTING VARIABLES				
				TEMP (°C)	σ_c (MPa)	DENSITY	SATURATION (%)	SALINITY
Bragg and Andersland (1980) (A)	Wedron Silica Sand ϕ-0.105-0.595 mm C_u = 1.5	Unconfined Compression	6×10^{-7} to 2×10^{-3}	-2 -6 -10 -15	0	Medium Dense $\frac{V_s}{V_t}$=0.64	96.1 to 99.9	Distilled Water
Parameswaran (1980) (B)	Ottawa 30 - 100 Sand D_{50} = 0.37mm C_u = 1.9	Unconfined Compression	10^{-7} to 10^{-2}	-2 -6 -10 -15	0	Dense w = 20% e≈ 0.53	Not Reported (95-100 ?)	Distilled Water
Parameswaran and Roy (1982) (C)	Ottawa 30 - 100 Sand, D_{50}=0.37mm C_u = 1.9	Unconfined Compression	5×10^{-7} to 10^{-2}	-30°C	0	Dense w = 20% e≈ 0.53	Not Reported (95-100 ?)	Distilled Water
Orth (1985) (D)	Karlsruhe Sand D_{50} = 0.6mm C_u = 2.4	Unconfined Compression	1.7×10^{-7} to 3.3×10^{-4}	-2 -6 -10 -20	0	Dense w=18.3% e= 0.54	91	Distilled Water
Yuanlin et al. (1988) (E)	Lanzhau Medium Sand D_{50} = 0.3mm C_u = 2.5	Unconfined Compression	5×10^{-7} to 7×10^{-3}	-2 -5 -10 -15	0	Dense w = 14% e= 0.47	93	Not Reported

TABLE 2.4
OVERVIEW OF TESTING PROGRAMS TO MEASURE LARGE STRAIN BEHAVIOR OF FROZEN SAND (page 2/3)
(abstracted from Andersen, 1991)

INVESTIGATOR(S) (PROGRAM LETTER)	MATERIAL TESTED	TYPE OF TEST	STRAIN RATE (s^{-1})	RANGES IN TESTING VARIABLES				
				TEMP (°C)	σ_c (MPa)	DENSITY	SATURATION (%)	SALINITY
Bourbonnais and Ladanyi (1985) (F)	LeSueur 16-30 rounded silica sand, $D_{50} \approx 1mm$ $C_u < 1.5$	Unconfined Compression	3×10^{-5} to 3×10^{-3}	-6.7 -43.8 -109.6 -20	0	Medium Dense w=20.5% e= 0.63	92	Distilled Water
Chamberlain et. al. (1972) (G)	Ottawa 100 - 200 Sand $D_{50} = 0.13_{mm}$ $C_u < 1.5$	Triaxial Compression	1×10^{-3}	-10	3.5 to 282	Medium Dense e=0.60	100	Not Reported
Sayles (1973, 1974) (H)	Ottawa 20 - 30 $D_{50} \approx 0.7_{mm}$ $C_u < 1.5$	Triaxial Compression	6.7×10^{-5} 8.3×10^{-3}	-3.85	0.34 to 8.2	Medium Dense e=0.59	Saturated	Distilled Water
Shibata et al. (1985) (I)	Toyoura Sand	Triaxial Compression	4.5×10^{-4} to 4.5×10^{-6}	-2 -10 -30 -50	0 4.0 9.8	Dense e=0.65 D_r=94%	Not Reported (100?)	Not Reported Distilled ?
Alkire and Andersland(1973) (J)	Ottawa 20 - 30 D_{50} = 0.7mm C_u = 1.9	Triaxial Compression	4.4×10^{-5}	-12	0 to 6.89	Medium Dense e ≈ 0.58	97 and 55	Distilled Water
Perkins and Reudrich (1973) (K)	Penn 80 - 200 Sand	Triaxial Compression	1.1×10^{-5}	-7.8	0 to 11.5	Dense	Not Reported (90-100?)	Distilled Water

TABLE 2.4
OVERVIEW OF TESTING PROGRAMS TO MEASURE LARGE STRAIN BEHAVIOR OF FROZEN SAND (page 3/3)
(abstracted from Andersen, 1991)

INVESTIGATOR(S) (PROGRAM LETTER)	MATERIAL TESTED	TYPE OF TEST	STRAIN RATE (s^{-1})	RANGES IN TESTING VARIABLES				
				TEMP (°C)	σ_c (MPa)	DENSITY	SATURATION (%)	SALINITY
Parameswaran and Jones (1981) (L)	Ottawa 30-100 D_{50} = 0.37mm C_u = 1.9	Triaxial Compression σ_3 not constant	$7.7x10^{-5}$	-10	0 to 76	Medium Dense w = 20% e=0.59	Not Reported (90-100?)	Distilled Water
Goughnour and Andersland (1968) (M)	Ottawa 20 - 30 D_{50} = 0.7mm C_u < 1.5	Triaxial Compression	$2.2x10^{-6}$ and $4.4x10^{-6}$	-4 -12	0 to 0.69	Ice, Sand-Ice, Dense Sand(60%)	Not Reported (90-100?)	Distilled Water
Jones and Parameswaran (1983) (N)	Ottawa 30-100 D_{50} = 0.37mm C_u = 1.9	Triaxial Compression	$7.7x10^{-5}$	-11	0.1 to 82	10-67% Sand by Weight e=24-1.56	Not Reported (90-100?)	Distilled Water
Baker (1979) (O)	Ottawa ASTM C-109 Fine Sand 16-100; D_{50}=0.4mm C_u = 2	Uniaxial Compression	10^{-2} to 10^{-7}	-5.5	--	D_r=74.8% Dense	97	Distilled Water
Sayles and Epanchin (1966) (P)	Ottawa ASTM C-109;16-100 D_{50}=0.4mm C_u = 2	Uniaxial Compression	$1.37x10^{-2}$ to $3.83x10^{-5}$	-3 -6.5 -10 -30	--	Dense to Very Dense D_i 60-100%	≈ 100 88.4-100	?

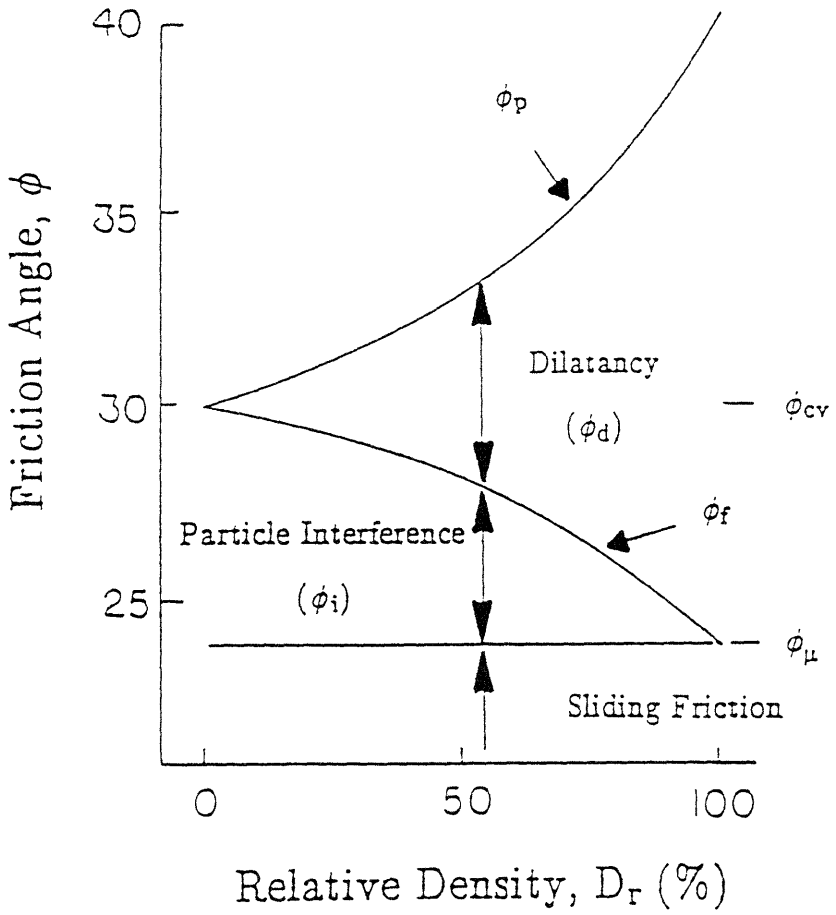

Figure 2.1 Components of Strength in Sands According to Rowe's Equation (after Rowe 1962)

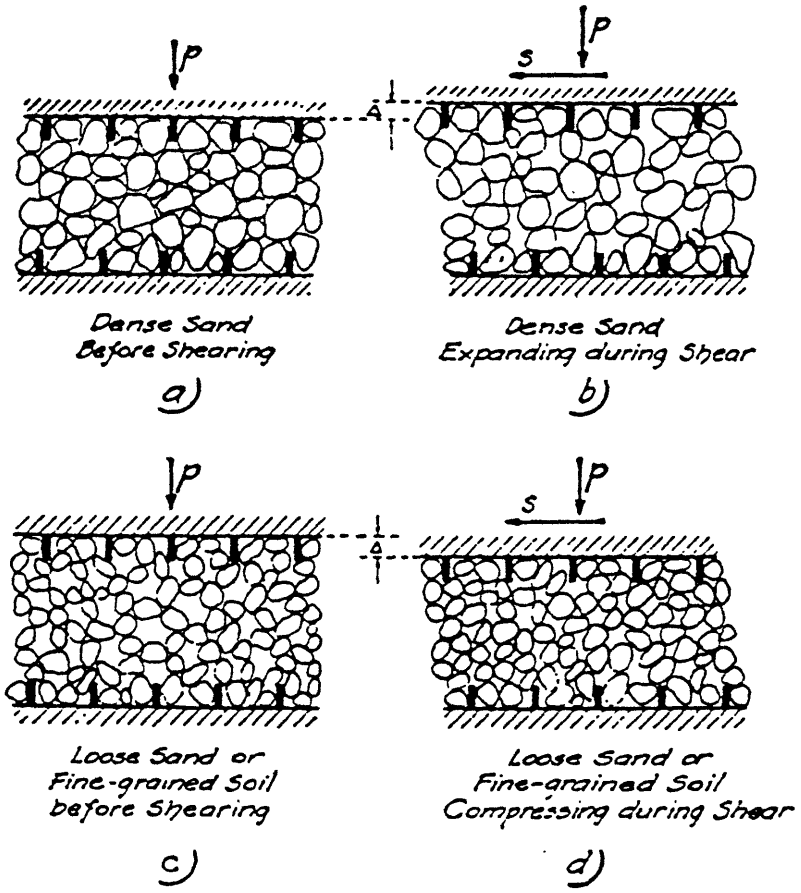

Figure 2.2 Behavior of Dry Sand in Direct Shear (from Casagrande 1936)

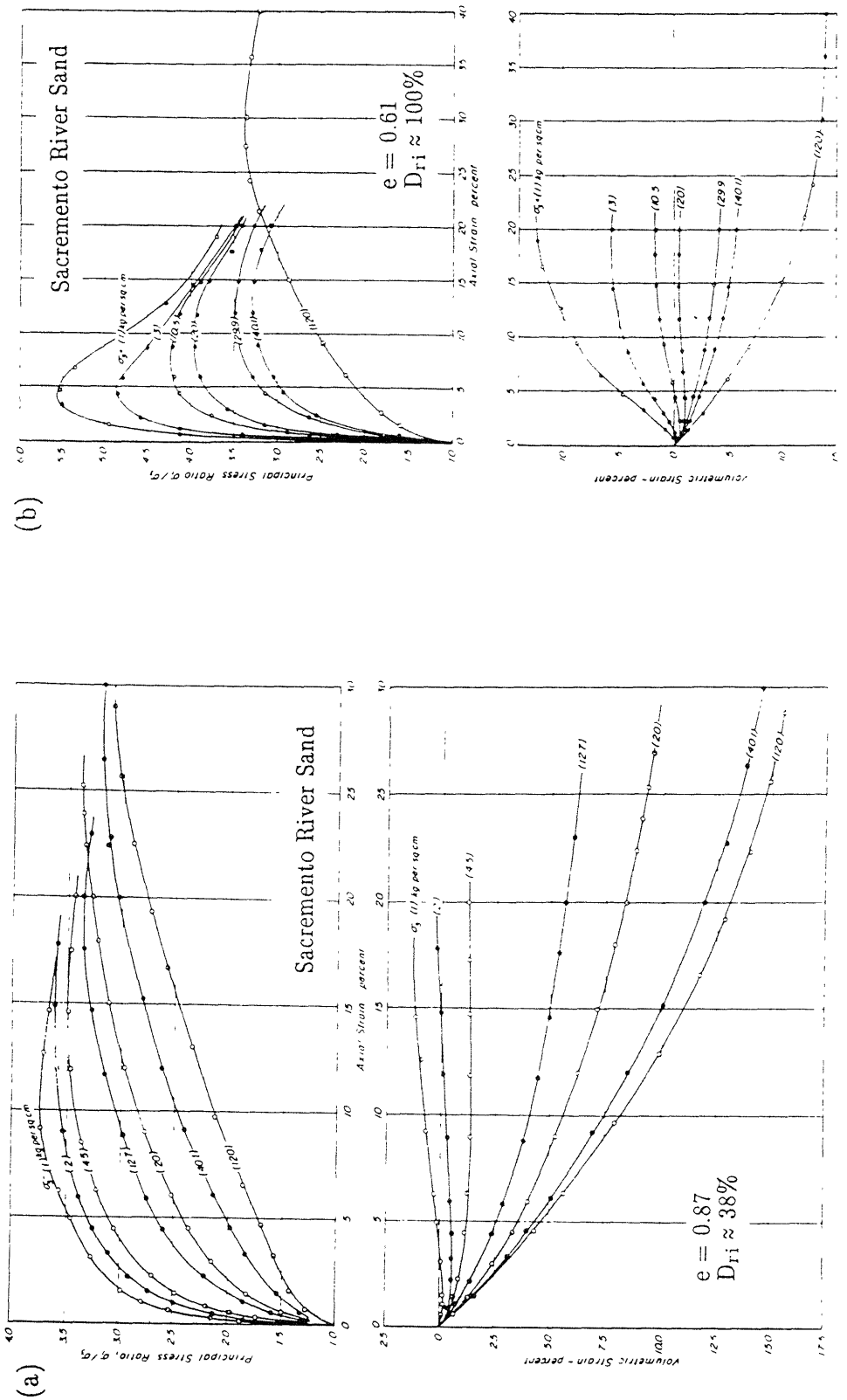

Figure 2.3 Stress–Strain and Volumetric Strain Curves for Sacramento River Sand in Drained Triaxial Compression (from Lee and Seed 1967)

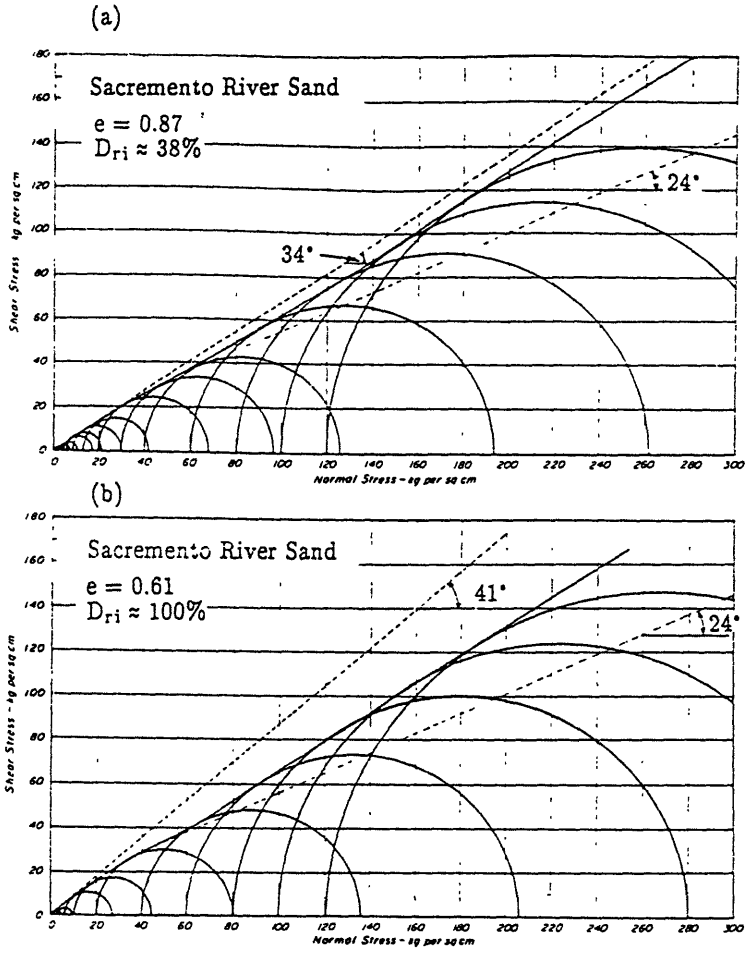

Figure 2.4 Mohr's Circles and Failure Envelope for Loose and Dense Sacremento River Sand at Confining Pressures up to 120ksc (from Lee and Seed 1967)

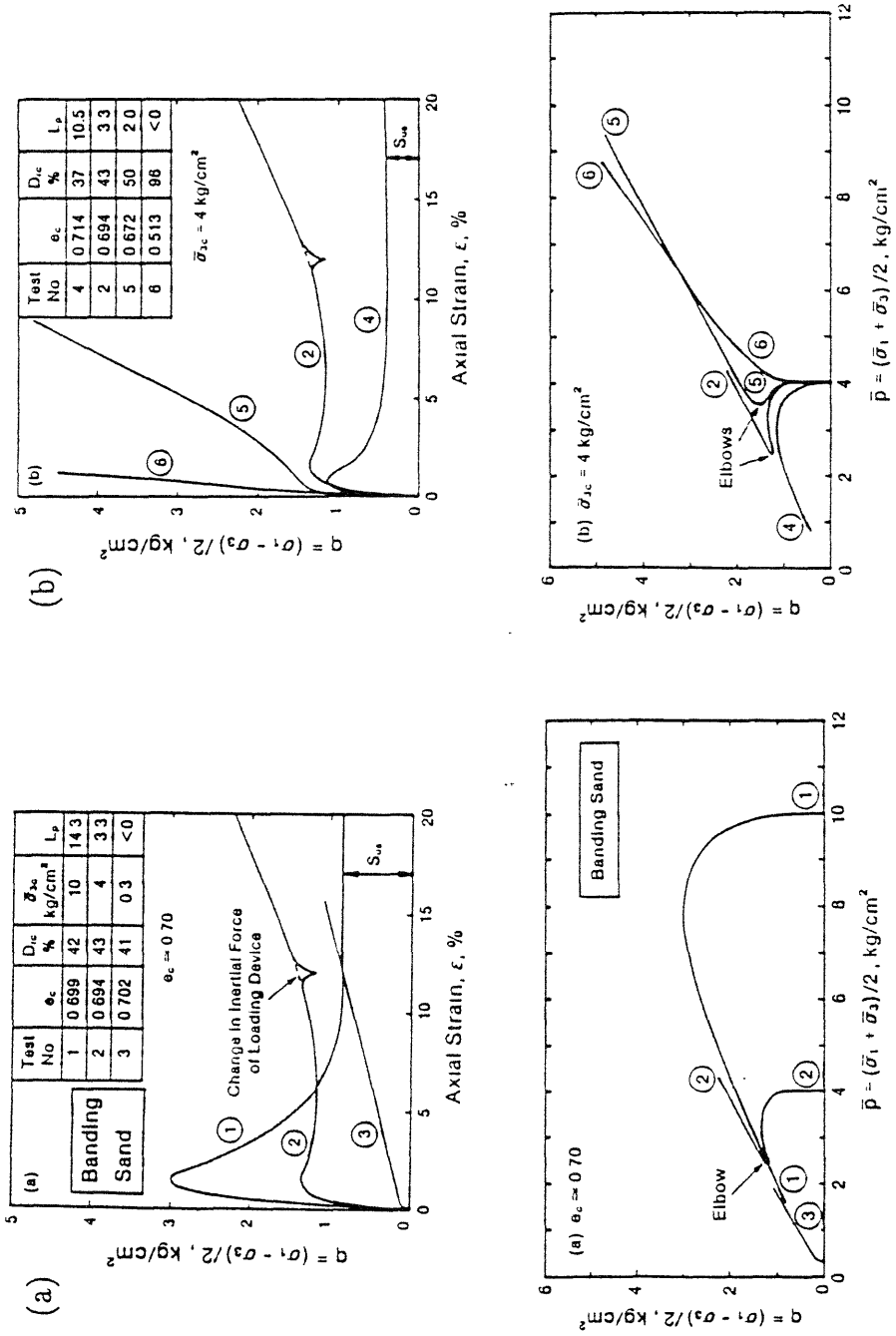

Figure 2.5 Undrained Behavior of Banding Sand in Triaxial Compression (from Mohamad and Dobry 1986, Data from Castro 1969)

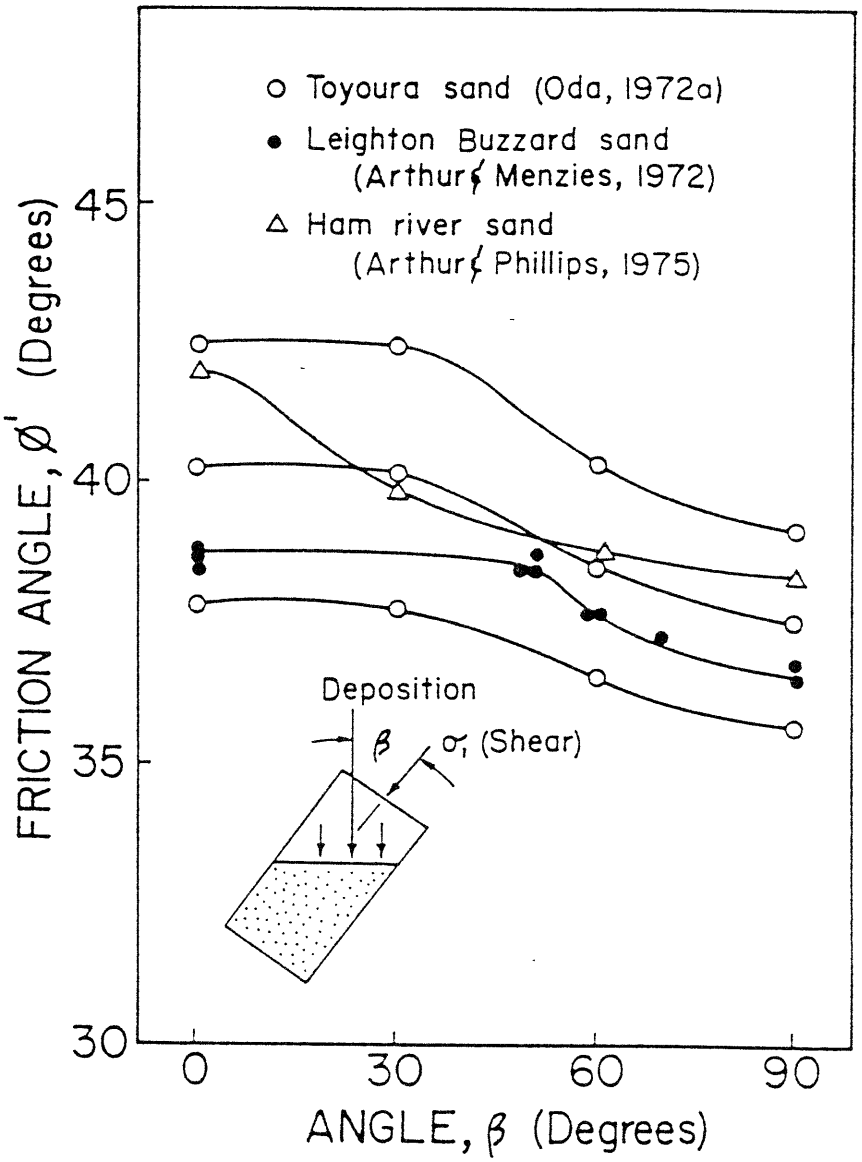

Figure 2.6 Effect of Direction of Loading on ϕ' of Several Sands (from Ladd et al. 1977)

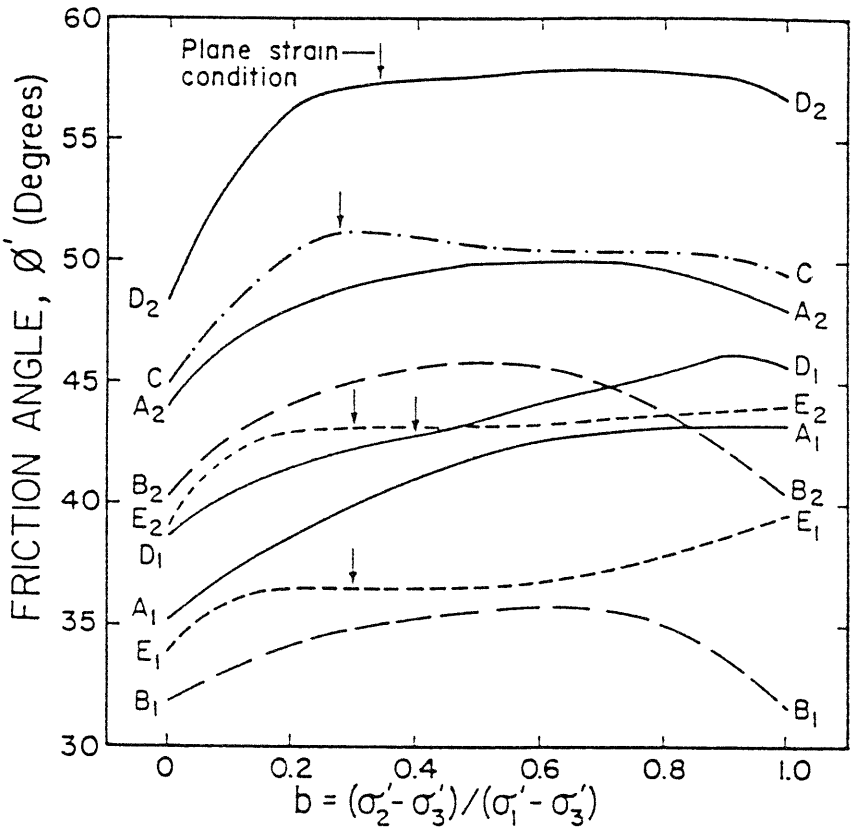

LINE	SAND	D_r (%)	REFERENCE
A_1	Ottawa	med. loose	Ko and Scott (1968)
A_2		med. dense	
B_1	Med Fine Loch Aline	30	Sutherland and Mesdary (1969)
B_2		80	
C	River Welland	dense	Proctor and Barden (1969)
D_1	Monterey No. 0	27	Lade and Duncan (1973)
D_2		98	
E_1	Ham River	loose	Reades and Green (1974)
E_2		dense	

Figure 2.7 Effect of Intermediate Principal Stress on the ϕ' of Several Sands (from Ladd et al. 1977)

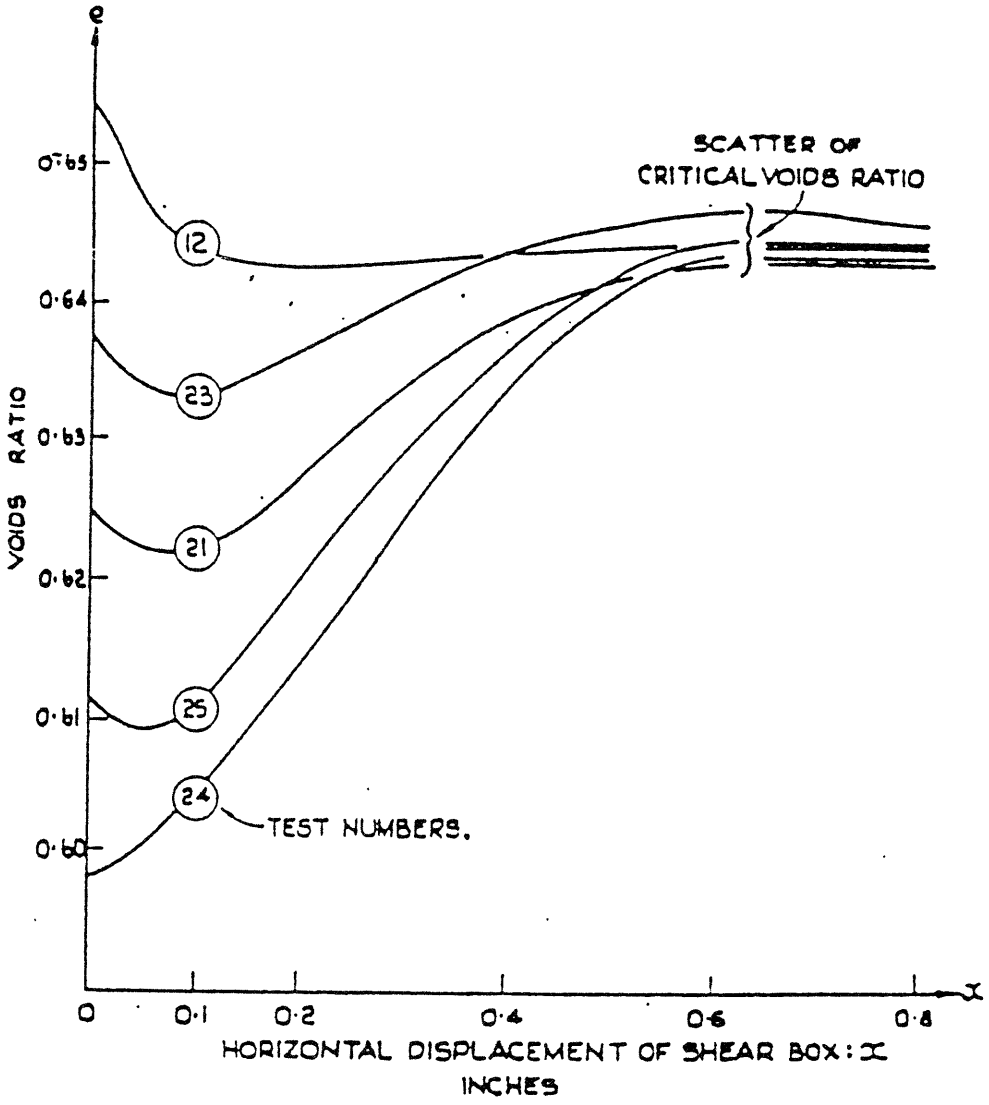

Figure 2.8 Simple Shear Test Results on Steel Balls with a Normal Stress of 20 psi (from Roscoe et al. 1958)

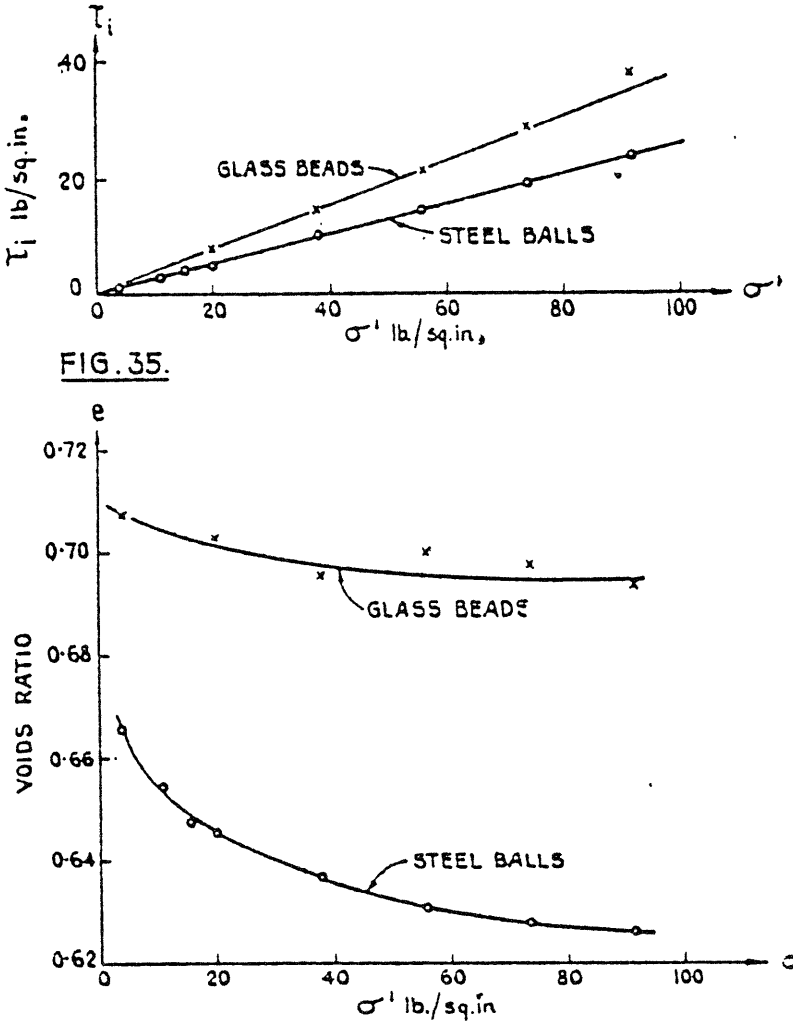

Figure 2.9 Critical Void Ratio Lines for Steel Balls and Glass Beads in e–$\sigma'$and τ–σ'Space (from Roscoe et al. 1958)

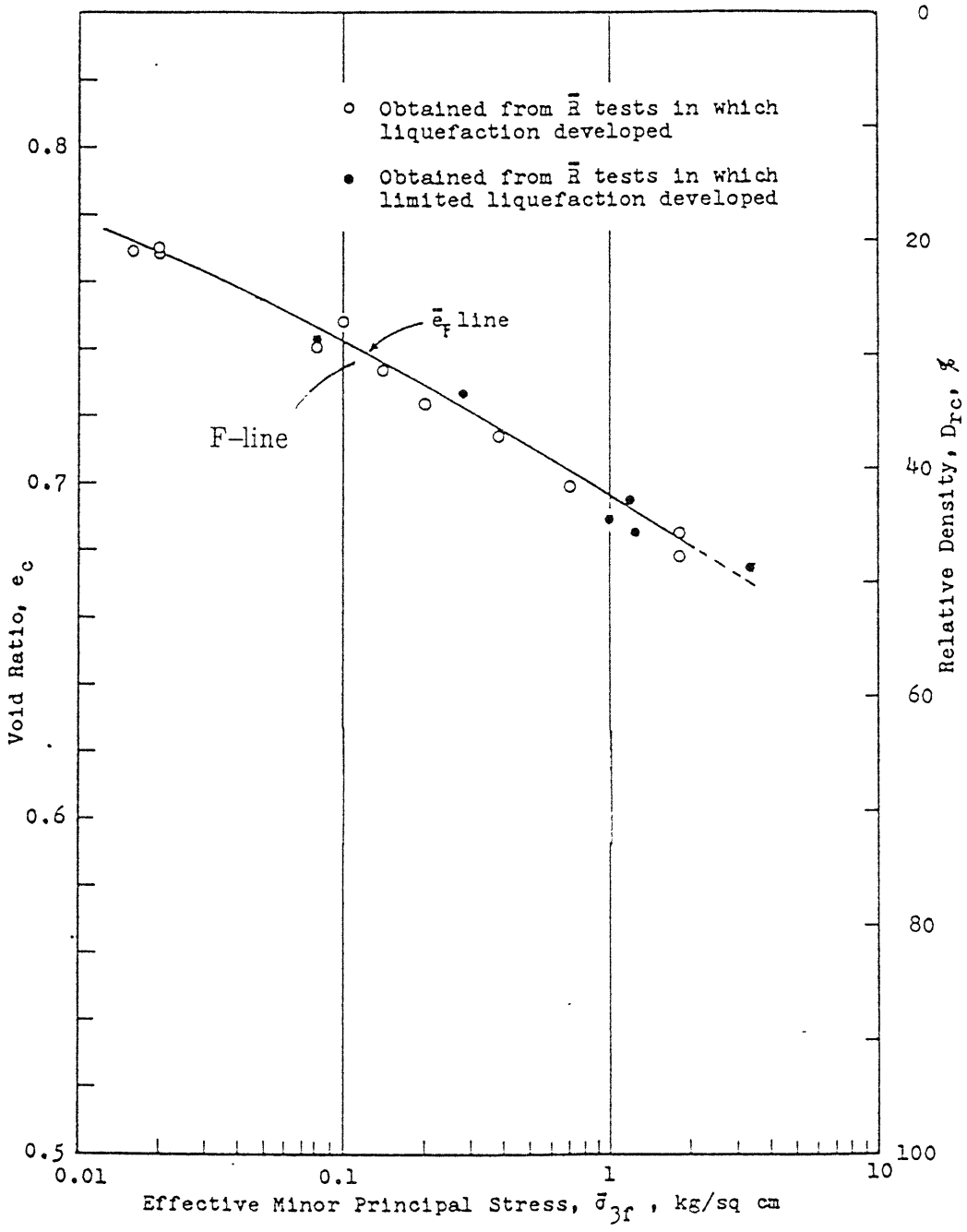

Figure 2.10 Critical Void Ratio Line for Banding Sand from Undrained Triaxial Tests Which Liquefied (from Castro 1969)

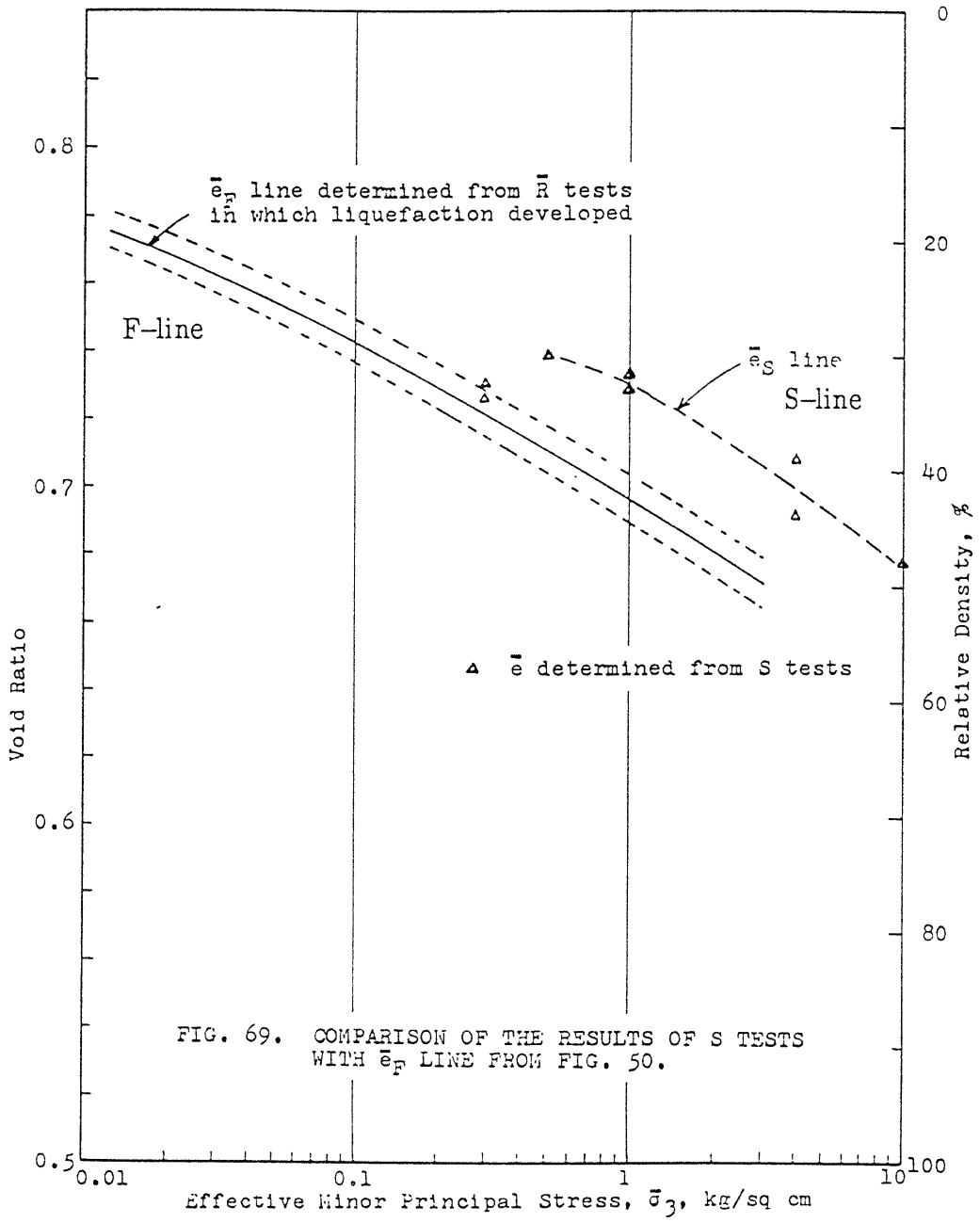

FIG. 69. COMPARISON OF THE RESULTS OF S TESTS WITH $\bar{e}_F$ LINE FROM FIG. 50.

Figure 2.11 Critical Void Ratio Lines for Banding Sand from Undrained and Drained Triaxial Tests (from Castro 1969)

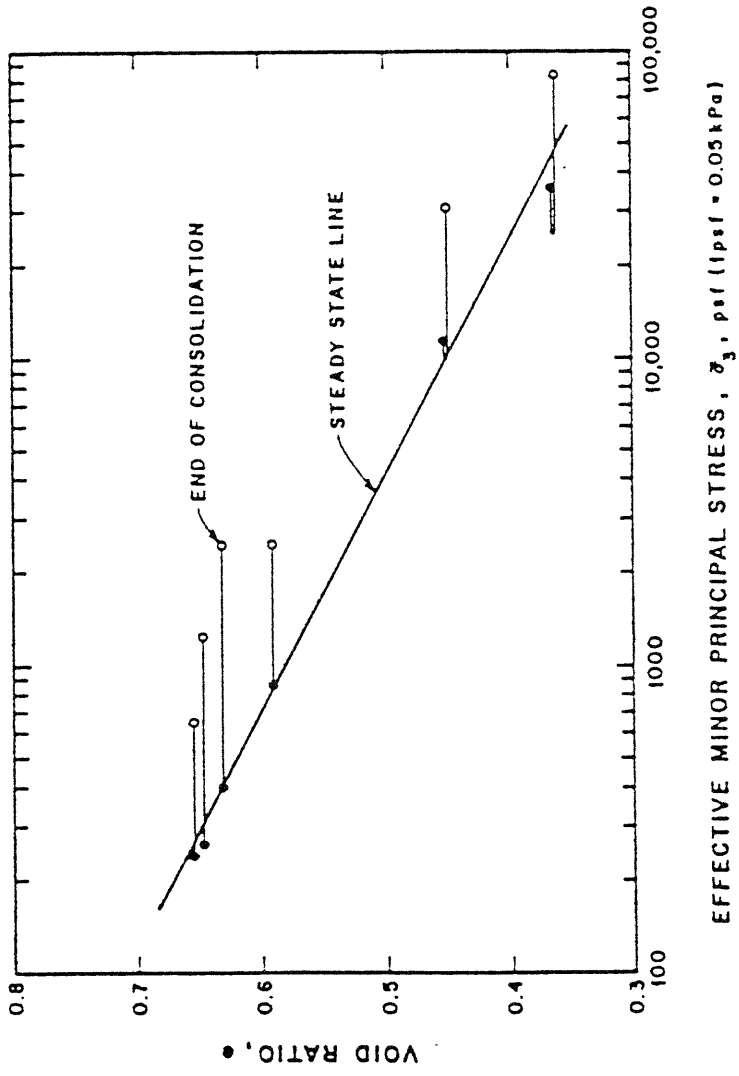

Figure 2.12 Steady State Line Developed from Six CIUC Tests on Compacted Sand Specimens (from Poulos et al. 1985)

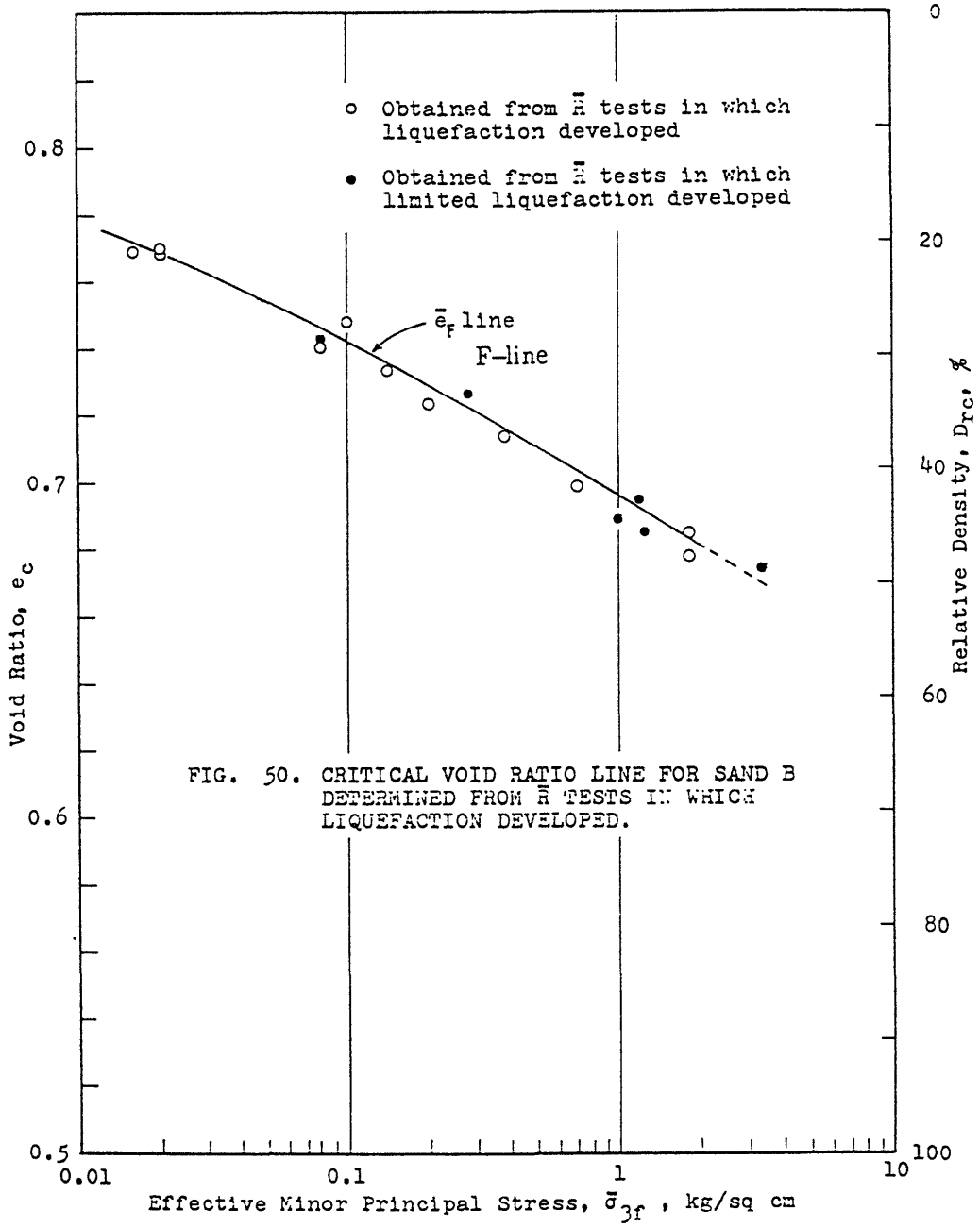

FIG. 50. CRITICAL VOID RATIO LINE FOR SAND B DETERMINED FROM R̄ TESTS IN WHICH LIQUEFACTION DEVELOPED.

Figure 2.13 Critical Void Ratio Line for Banding Sand using Liquefaction and Limited Liquefaction Test Results (from Castro 1969)

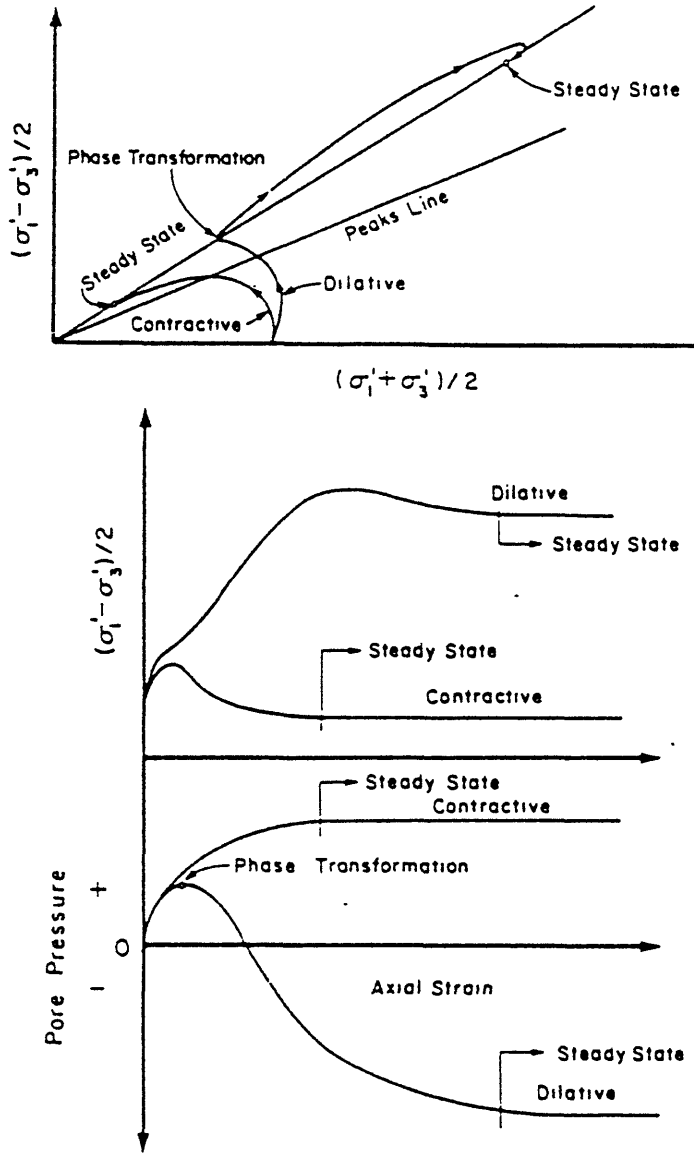

Figure 2.14 Schematic Representation of Phase Transformation and Steady State Conditions for Undrained Shear (from Negussey et al. 1988)

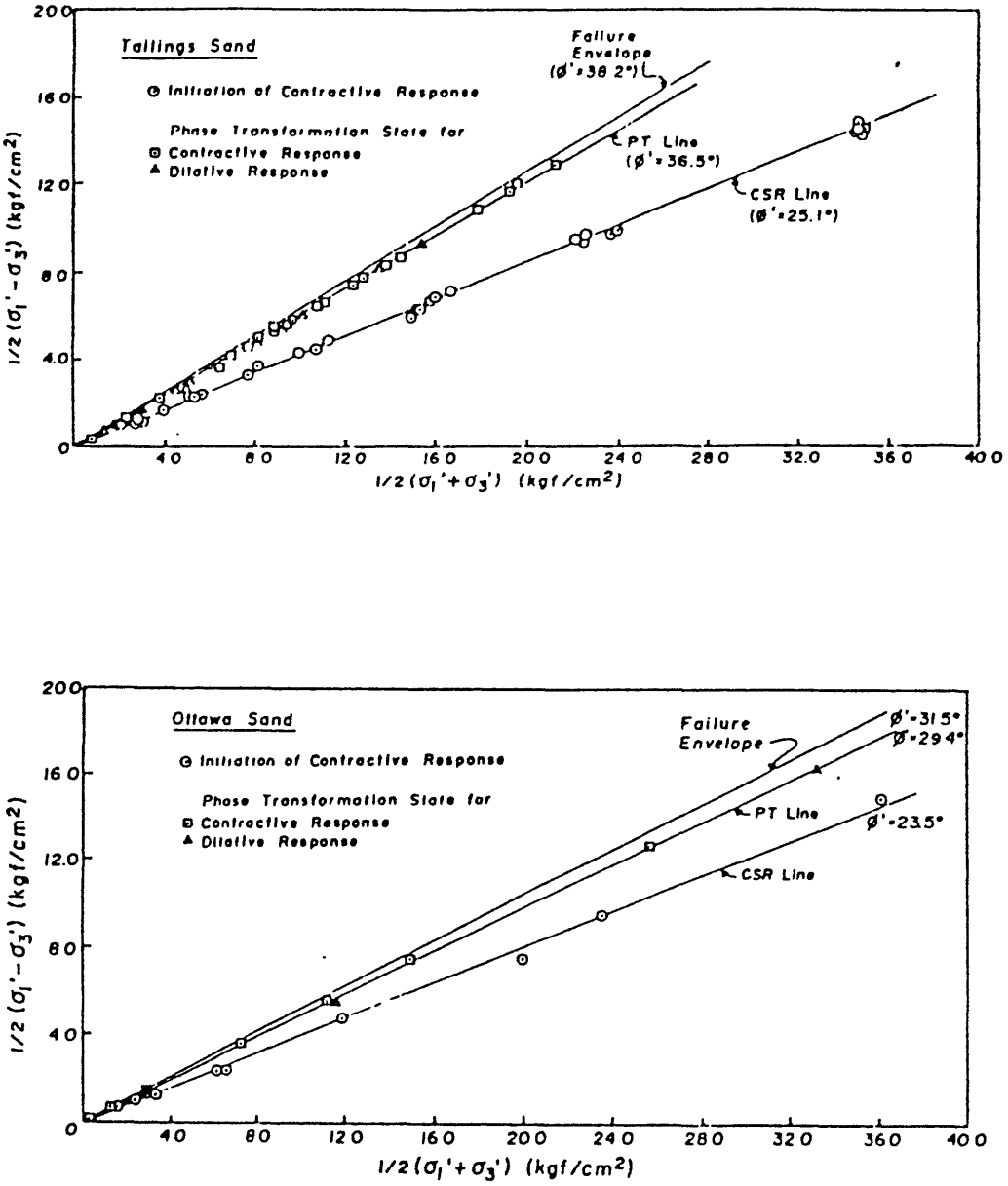

Figure 2.15 Effective Stress Conditions at Phase Transformation and CSR States for Tailings Sand and Ottawa Sand (from Vaid and Chern 1985)

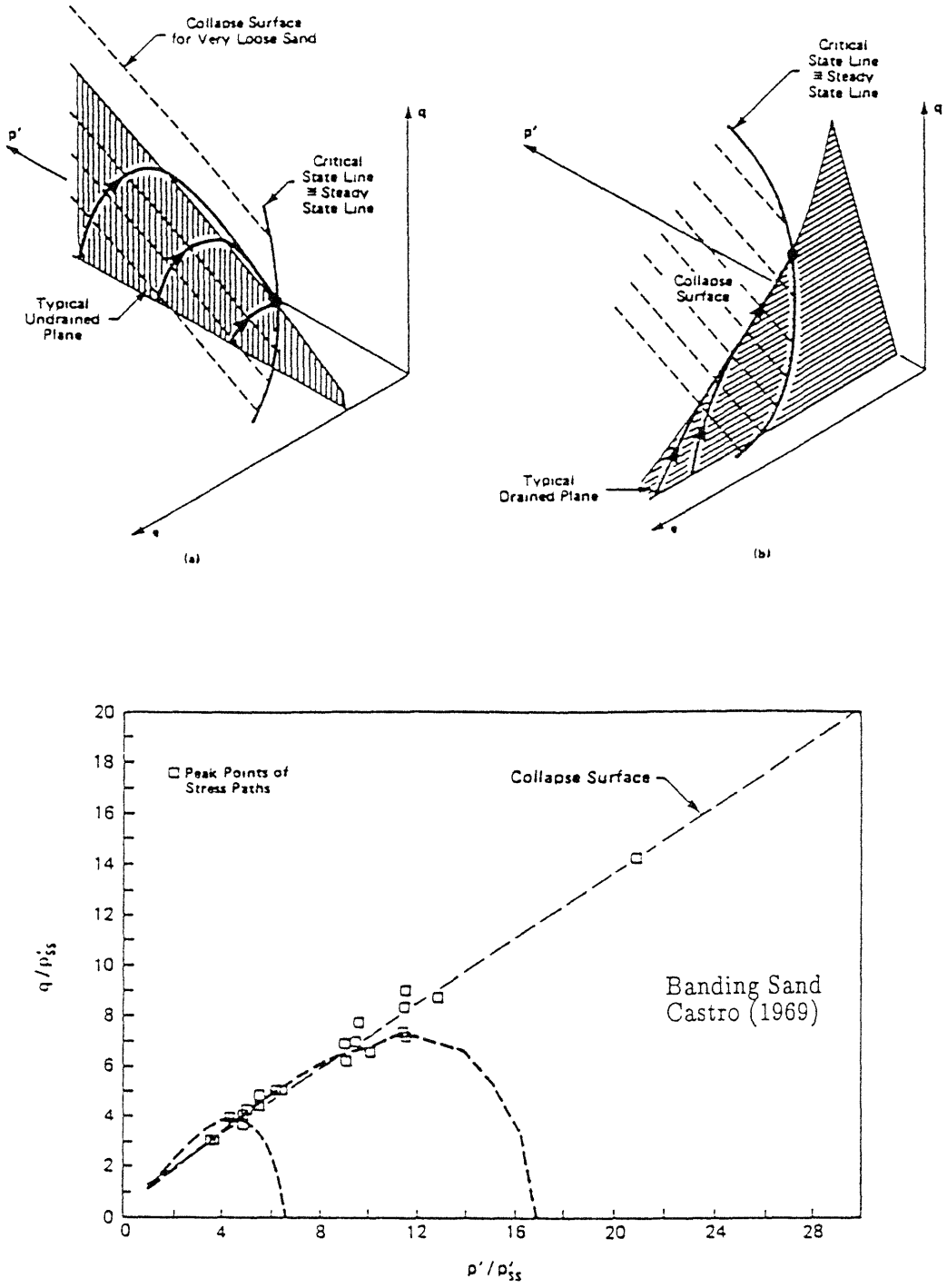

Figure 2.16 Concept of a Collapse Surface (from Sladen et al. 1985)

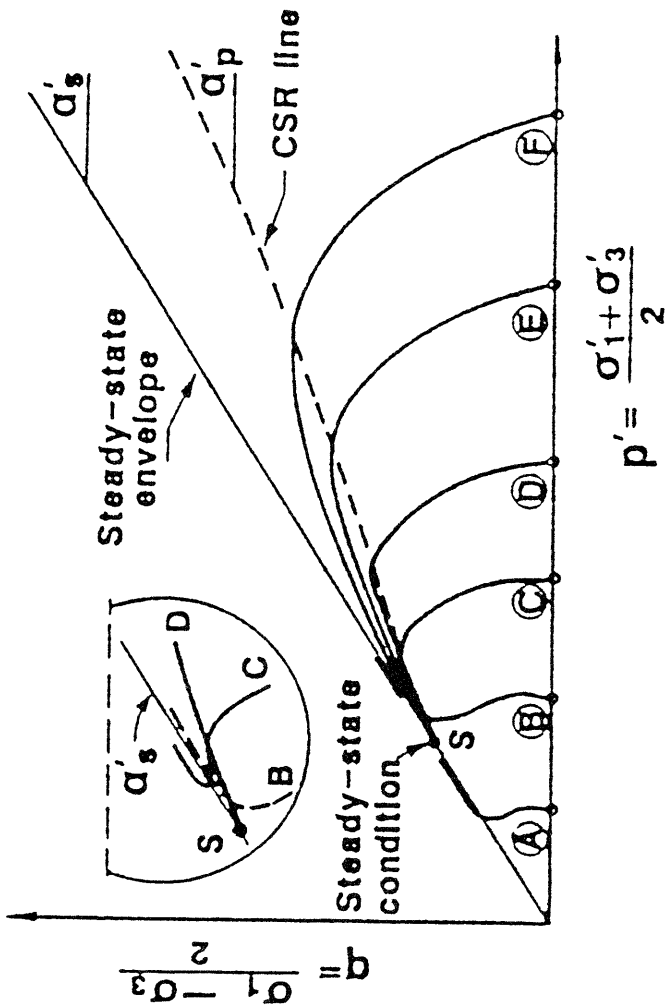

Figure 2.17 Idealized CSR Line and Steady State Envelope for Undrained Compression (from Alarcon–Guzman et al. 1988)

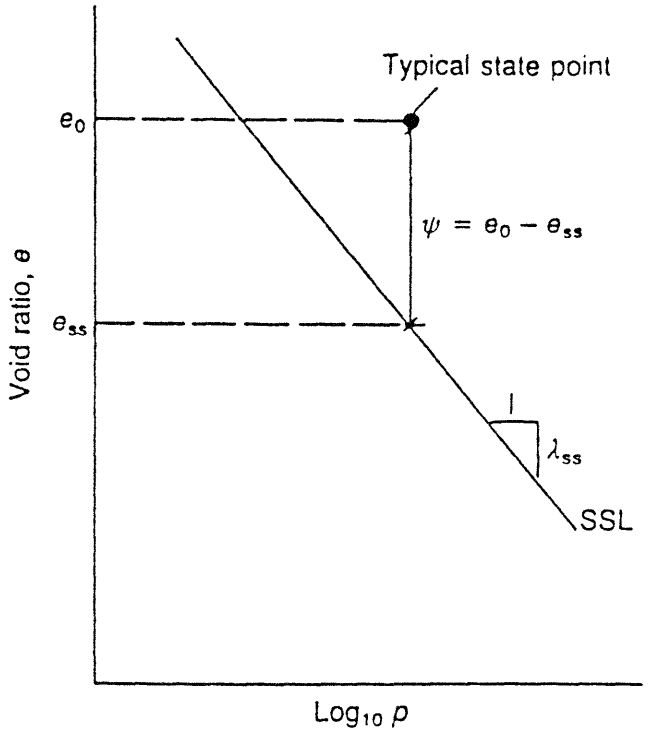

Figure 2.18 Definition of the State Parameter (from Been et al. 1991)

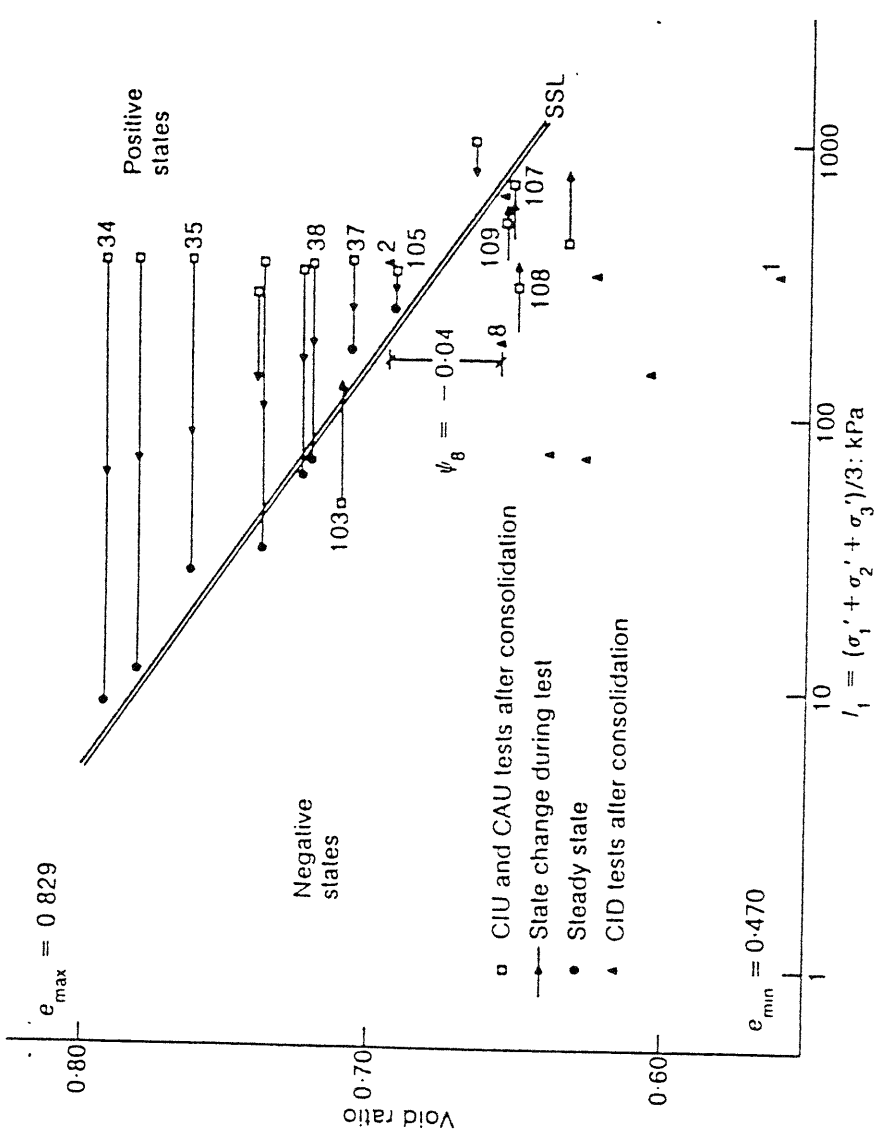

Figure 2.19 State Diagram and Steady State Line for Kogyuk 350/2 Sand (from Been and Jefferies 1986)

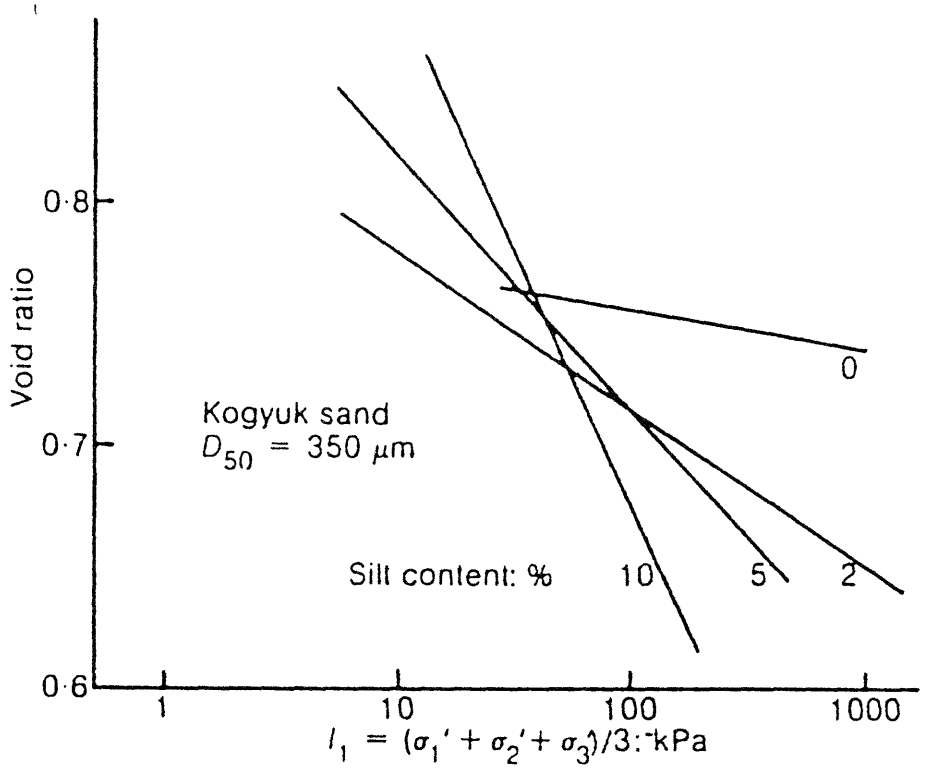

Figure 2.20 Steady State Lines for Kogyuk 350 Sand with Various Fines Content (from Been and Jefferies 1985)

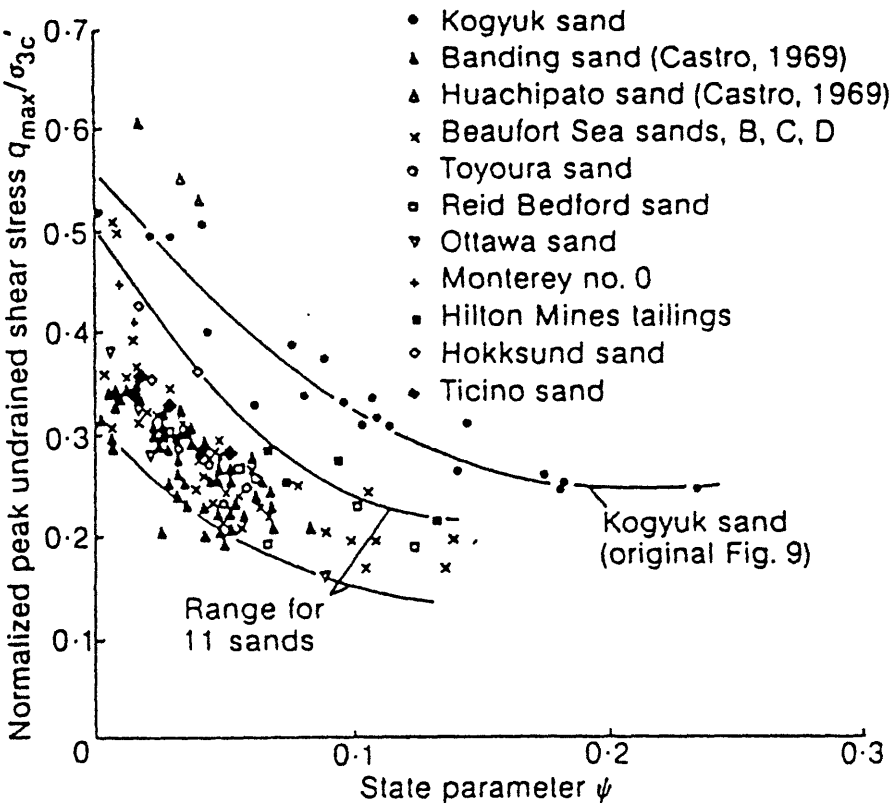

Figure 2.21 Peak Undrained Strength Ratio, q_{max}/σ'_c Versus State Parameter, Ψ (from Been and Jefferies 1986)

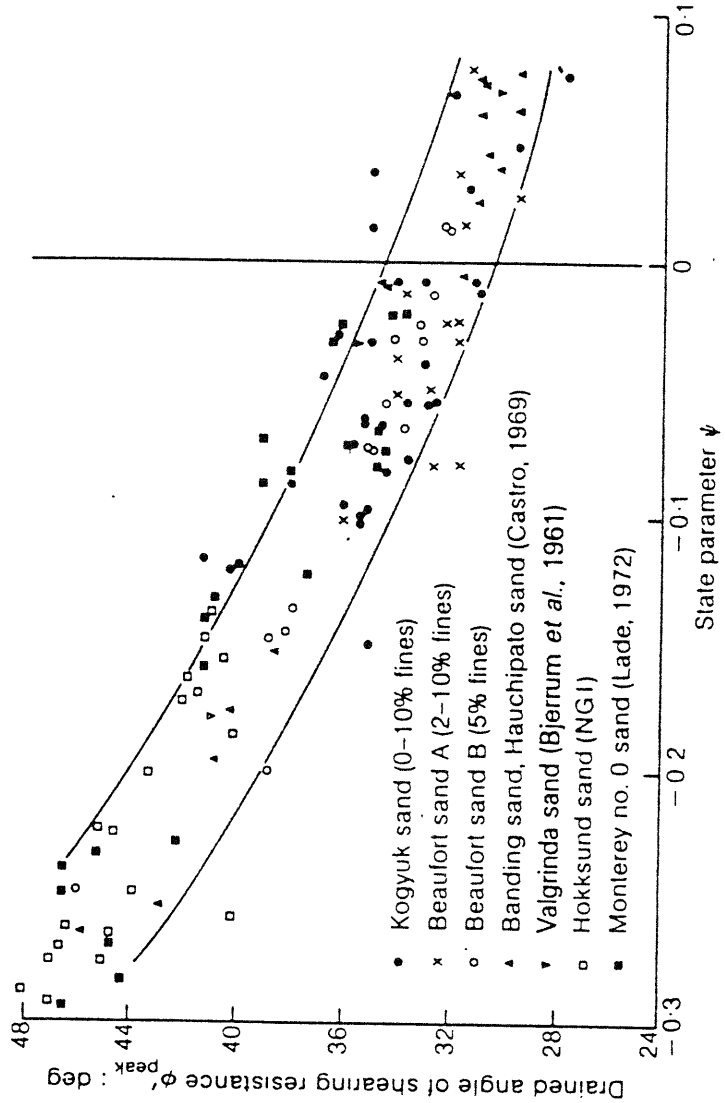

Figure 2.22 Drained Angle of Friction, ϕ', versus State Parameter, Ψ (from Been and Jefferies 1985)

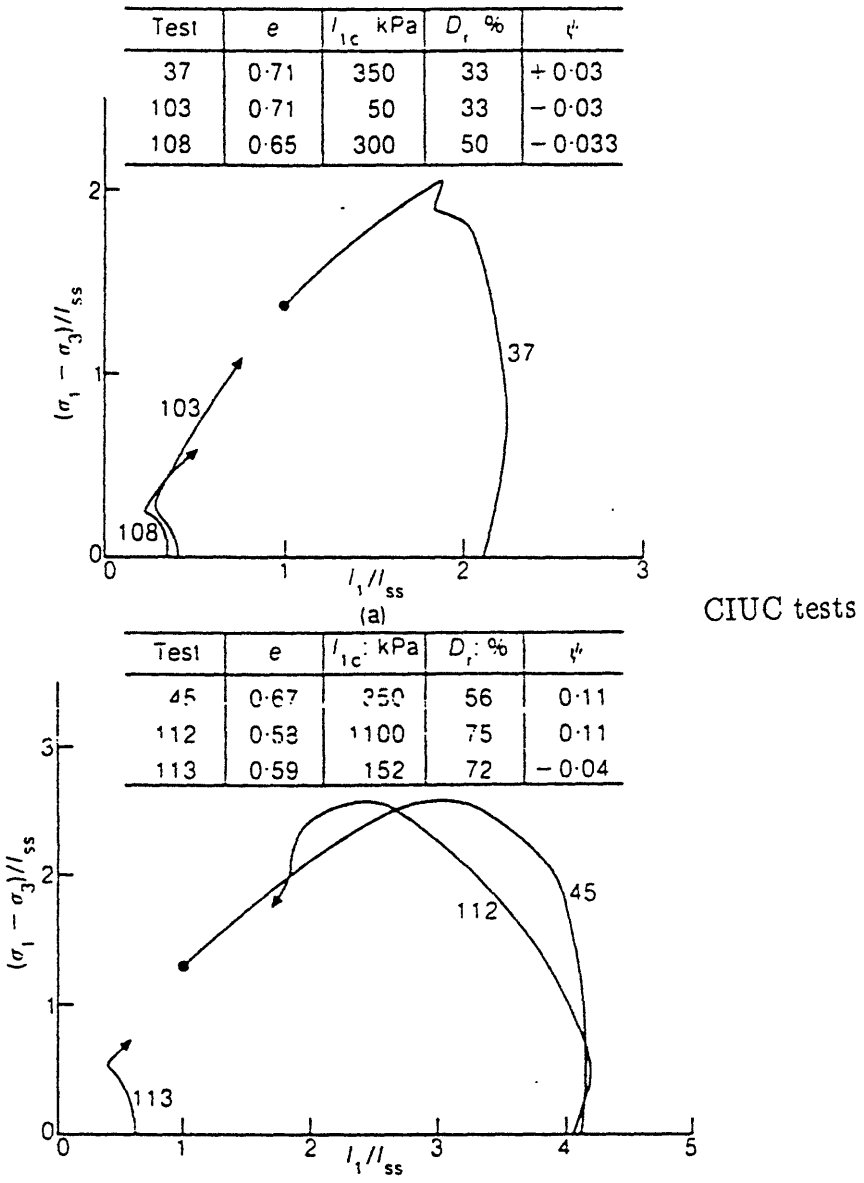

Figure 2.23 Comparison of Normalized Stress Paths for Samples with the Same State Parameter (from Been and Jefferies 1985)

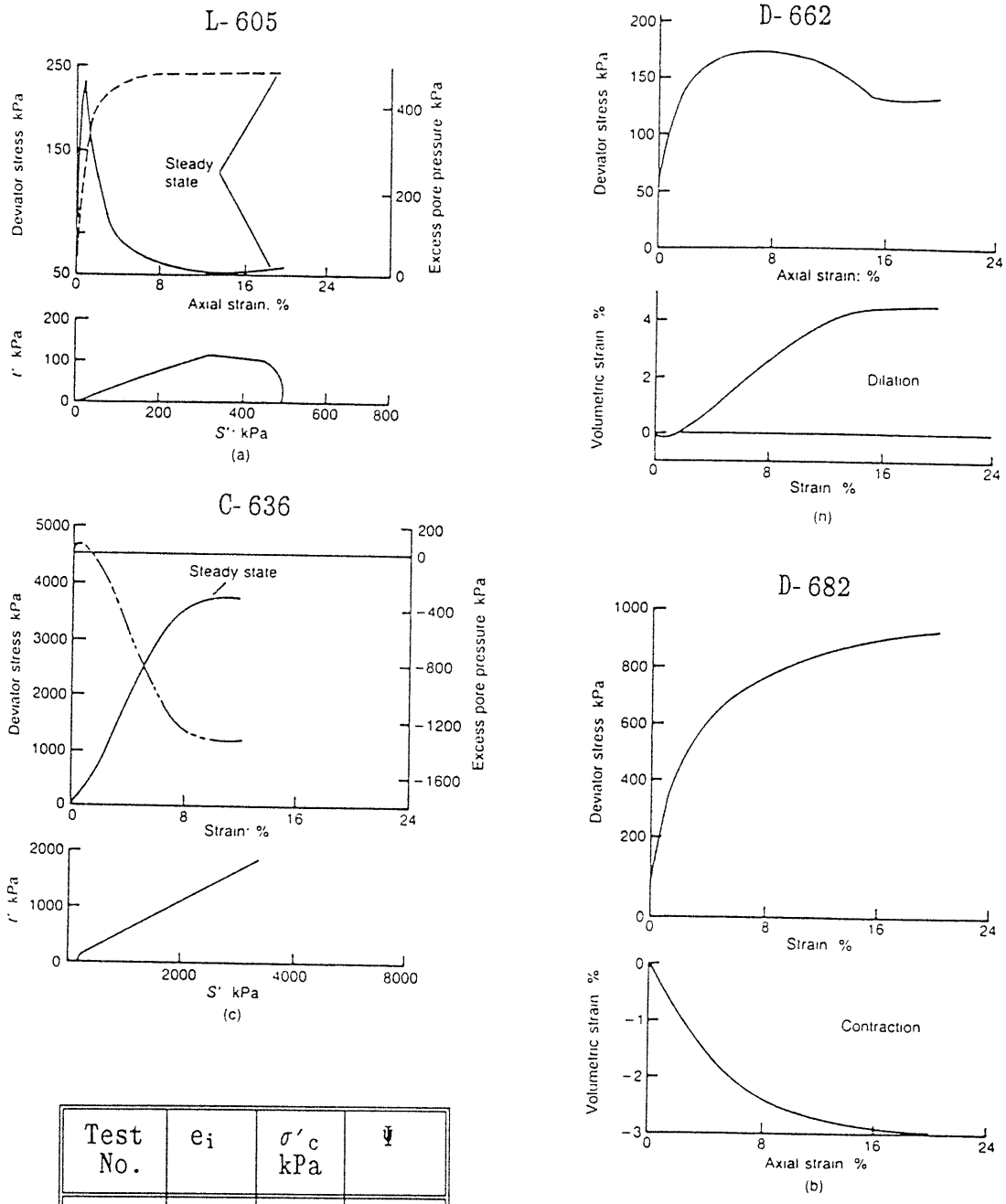

Test No.	e_i	σ'_c kPa	Ψ
L-605	0.771	500	+0.039
C-636	0.618	200	-0.126
D-682	0.776	500	+0.044
D-662	0.677	60	-0.084

Figure 2.24 Typical Triaxial Compression Tests Results using Various Test Parameters (from Been et al. 1991)

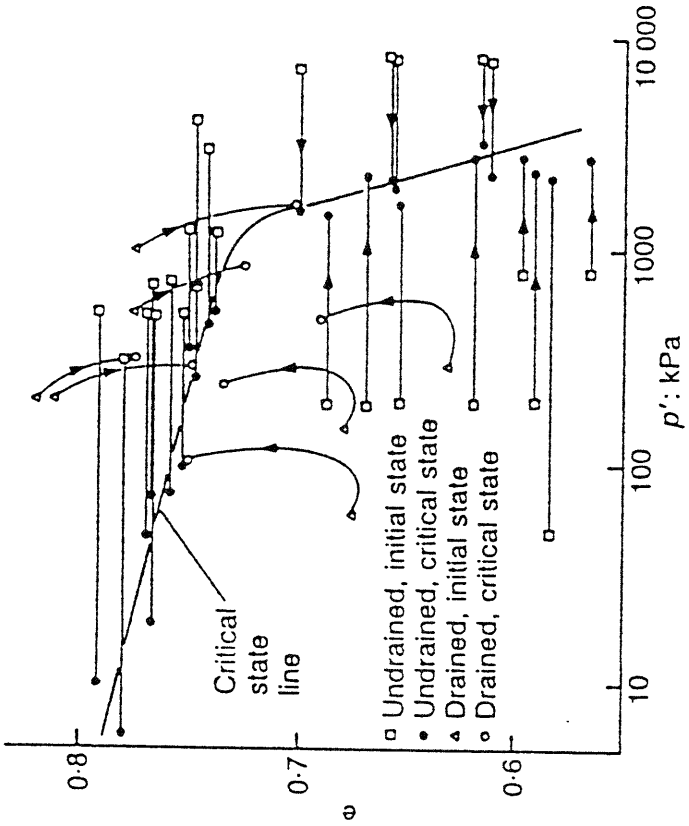

Figure 2.25 Effect of Initial State on Steady State Line for Erksak 330/0.7 Sand (from Been et al. 1991)

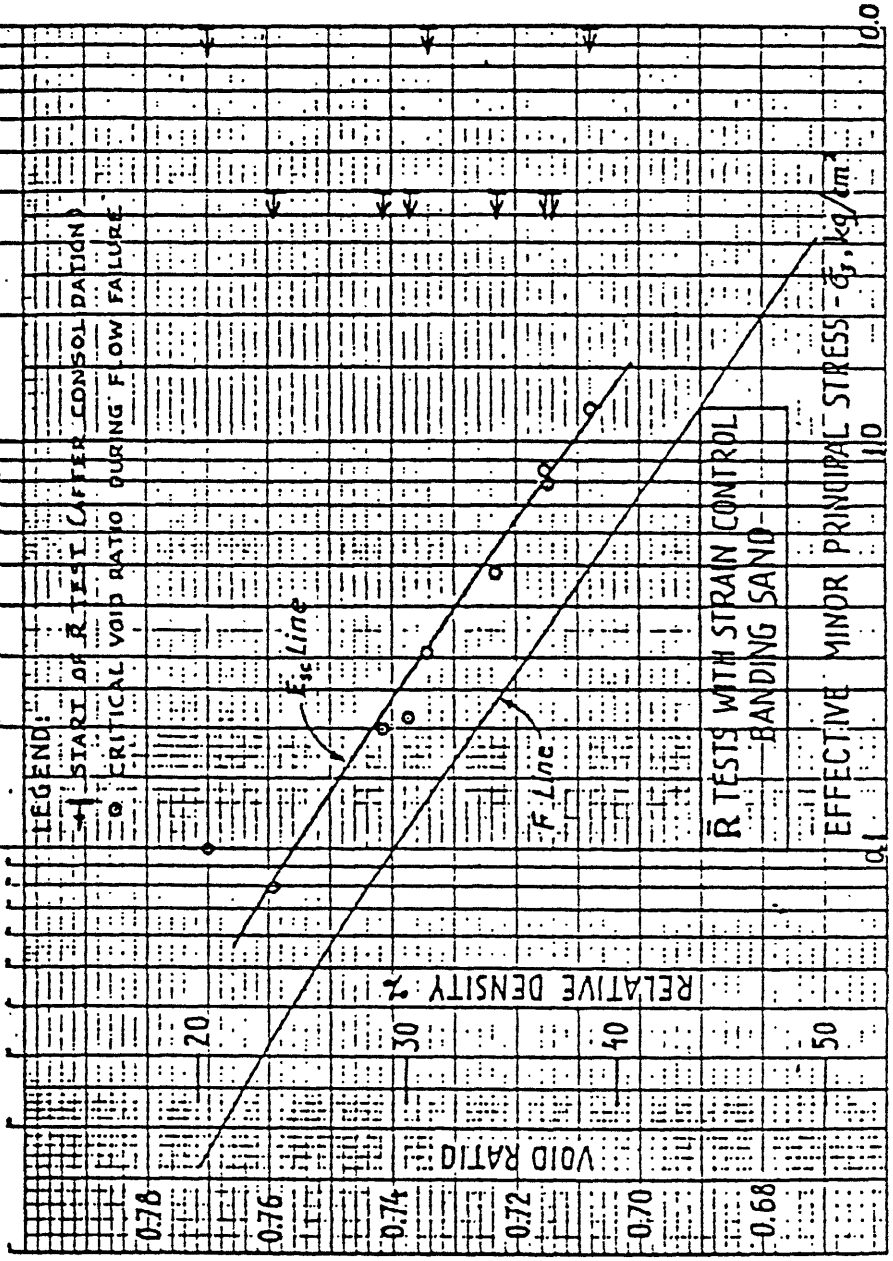

Figure 2.26 Effect of Load–Controlled Versus Strain–Controlled Triaxial Tests on the SSL for Banding Sand (from Casagrande 1975)

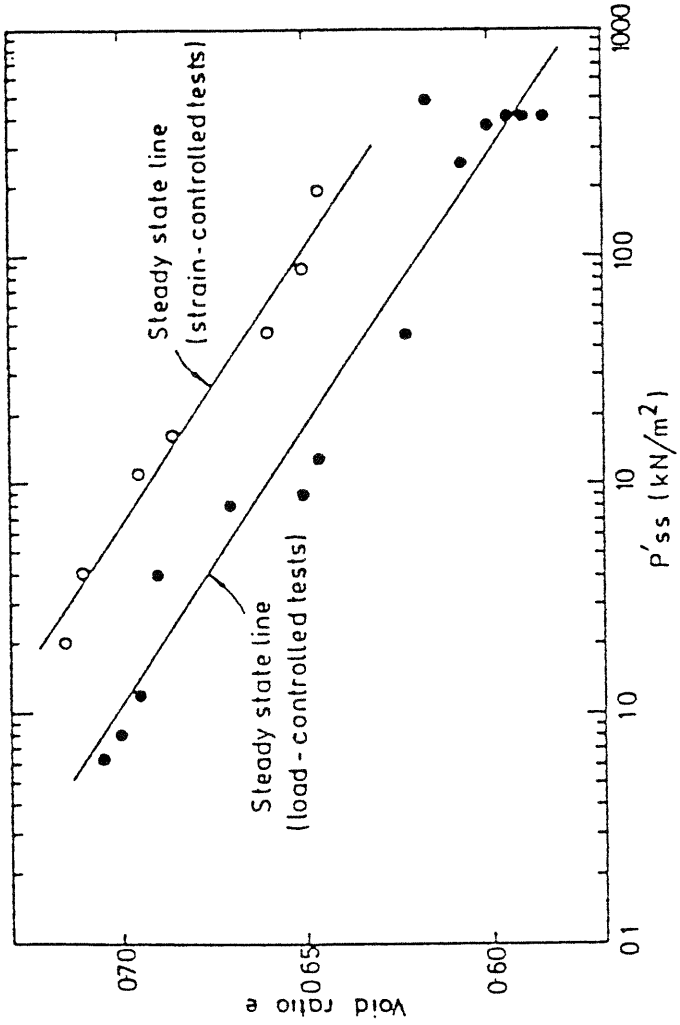

Figure 2.27 Effect of Load–Controlled Versus Strain–Controlled Triaxial Tests on the SSL for Leighton Buzzard Sand (from Hird and Hassona 1990)

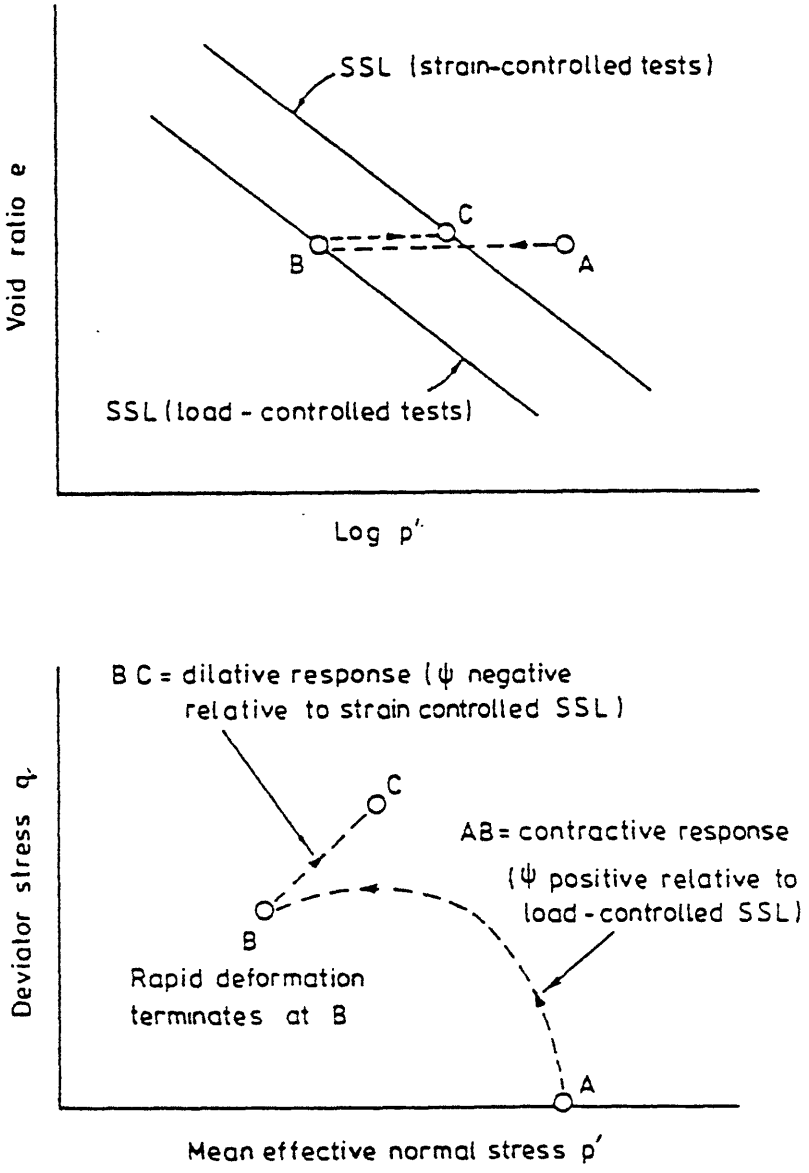

Figure 2.28 Interpretation of Effect of Strain Rate on Strain–Controlled Triaxial Tests (from Hird and Hassona 1990)

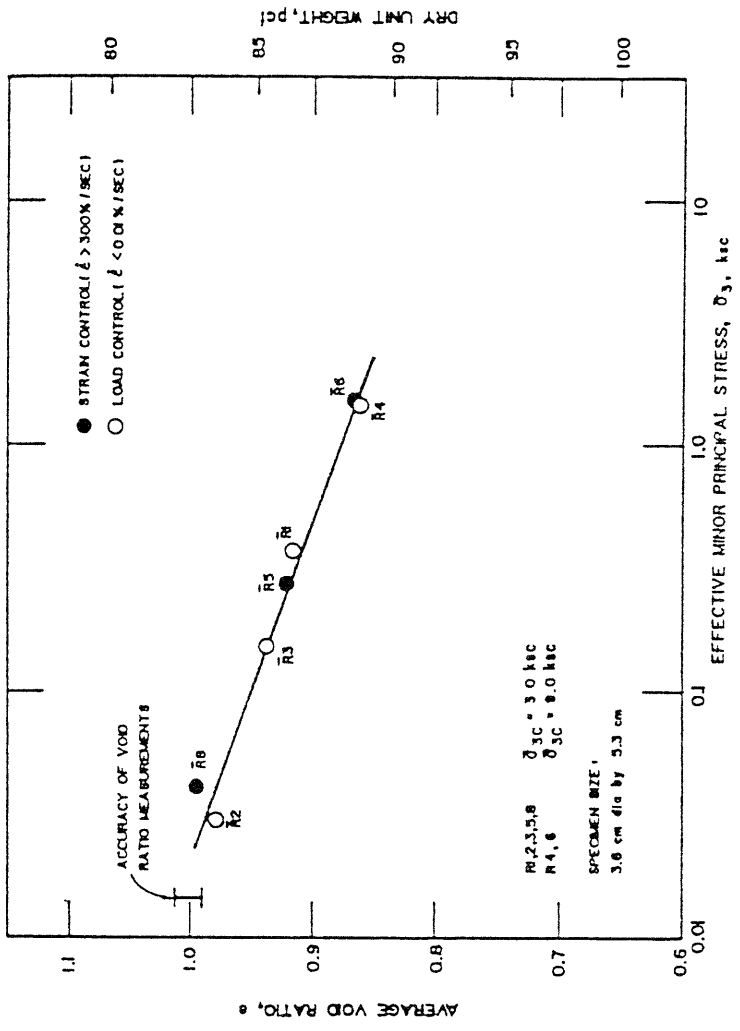

Figure 2.29 Effect of Load–Controlled Versus Strain–Controlled Triaxial Tests on the SSL for Syncrude Tailings Sand (from Poulos et al. 1988)

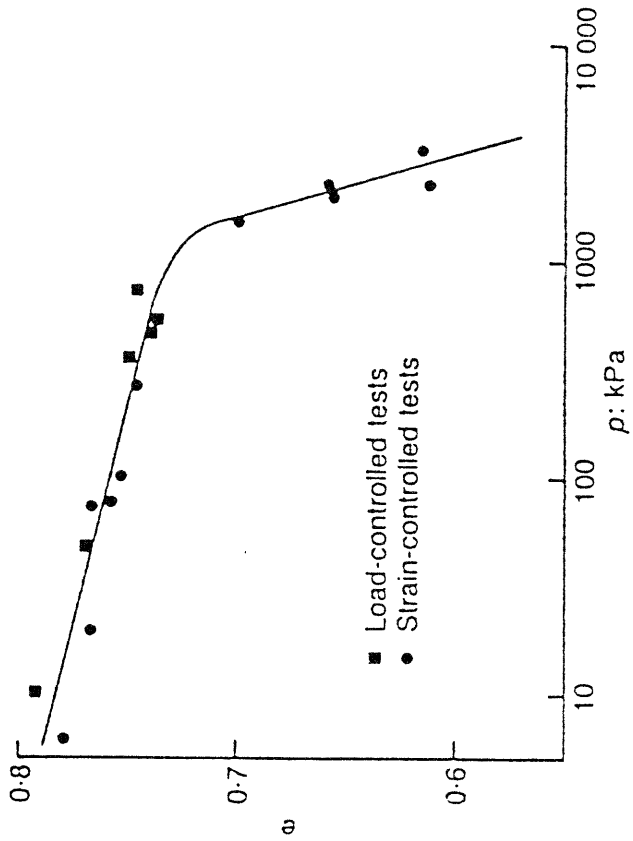

Figure 2.30 Effect of Load–Controlled Versus Strain–Controlled, CIUC with $+\Psi$, Triaxial Tests on the SSL for Erksak 330/0.7 Sand (from Been et al. 1991)

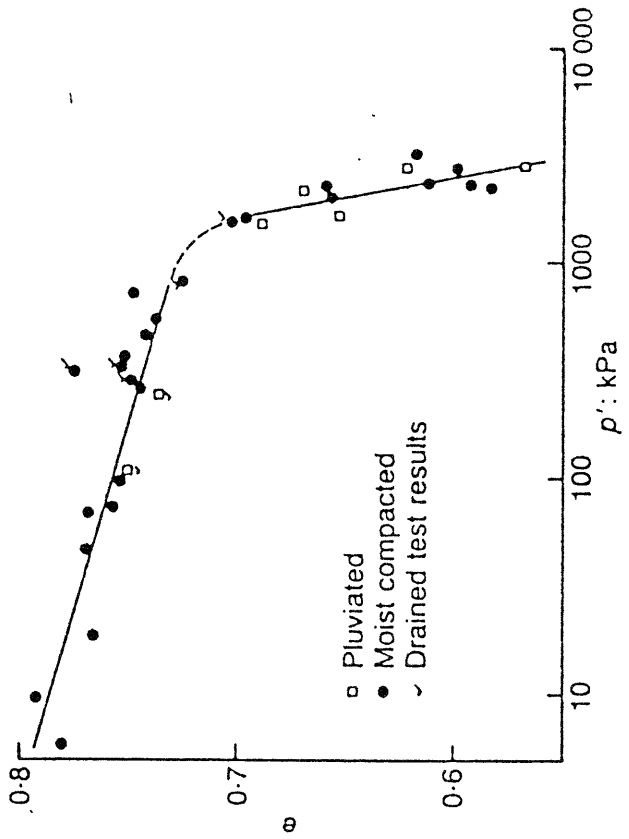

Figure 2.31 Effect of Specimen Preparation Technique on the SSL for Erksak 330/0.7 Sand (from Been et al. 1991)

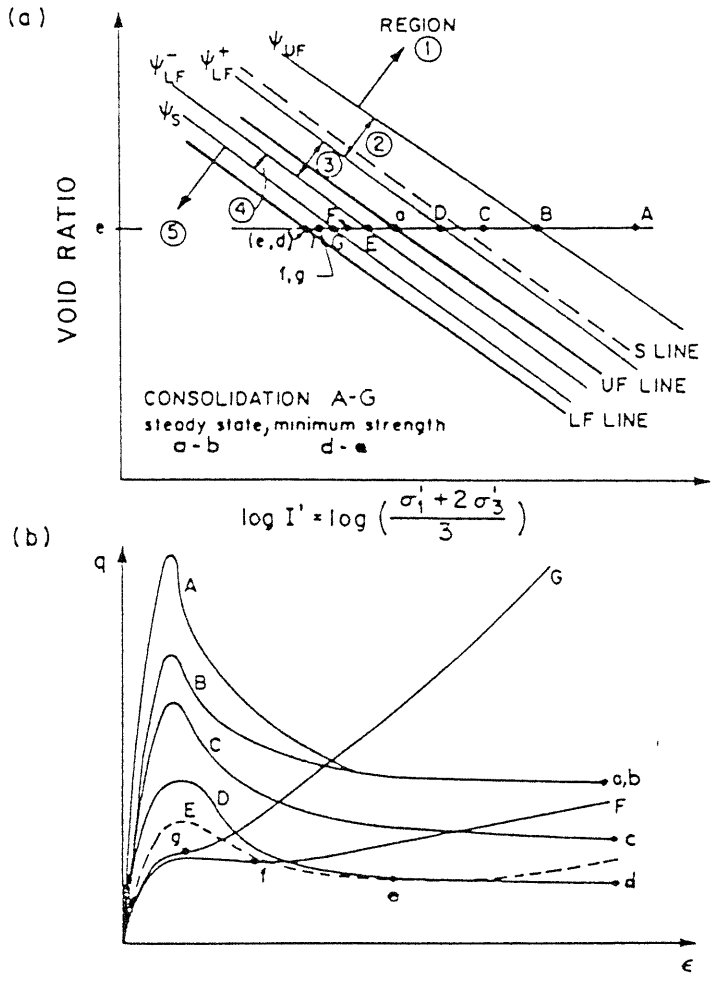

Figure 2.32 Schematic Representation of the Effect of Initial State for Consolidated–Undrained Triaxial Tests on Sands (from Konrad 1990b)

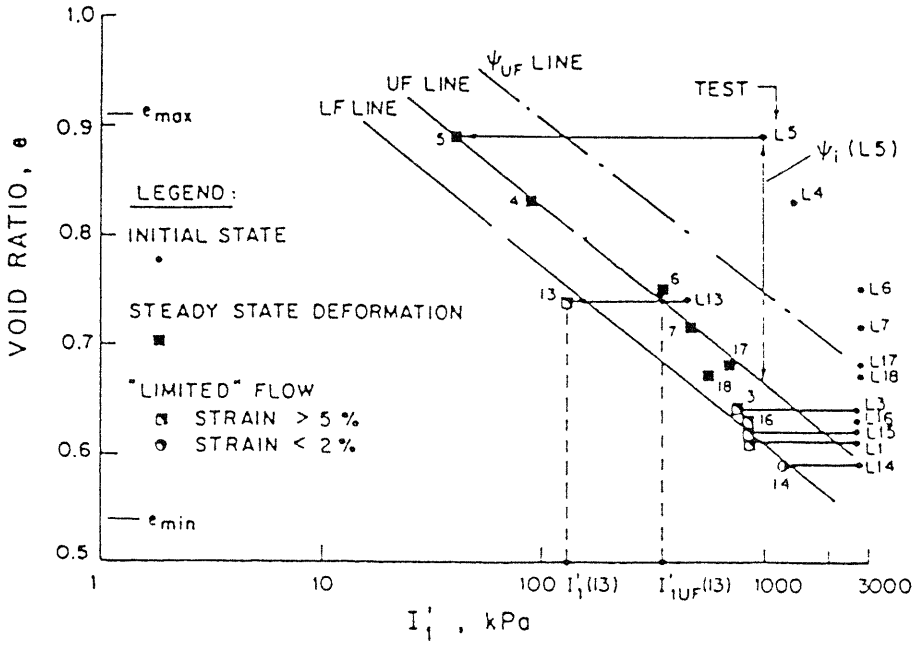

Figure 2.33 Effect of Initial State on Steady State Condition of Consolidated–Undrained Triaxial Tests on Normally Consolidated Dune Sand (from Konrad 1990a)

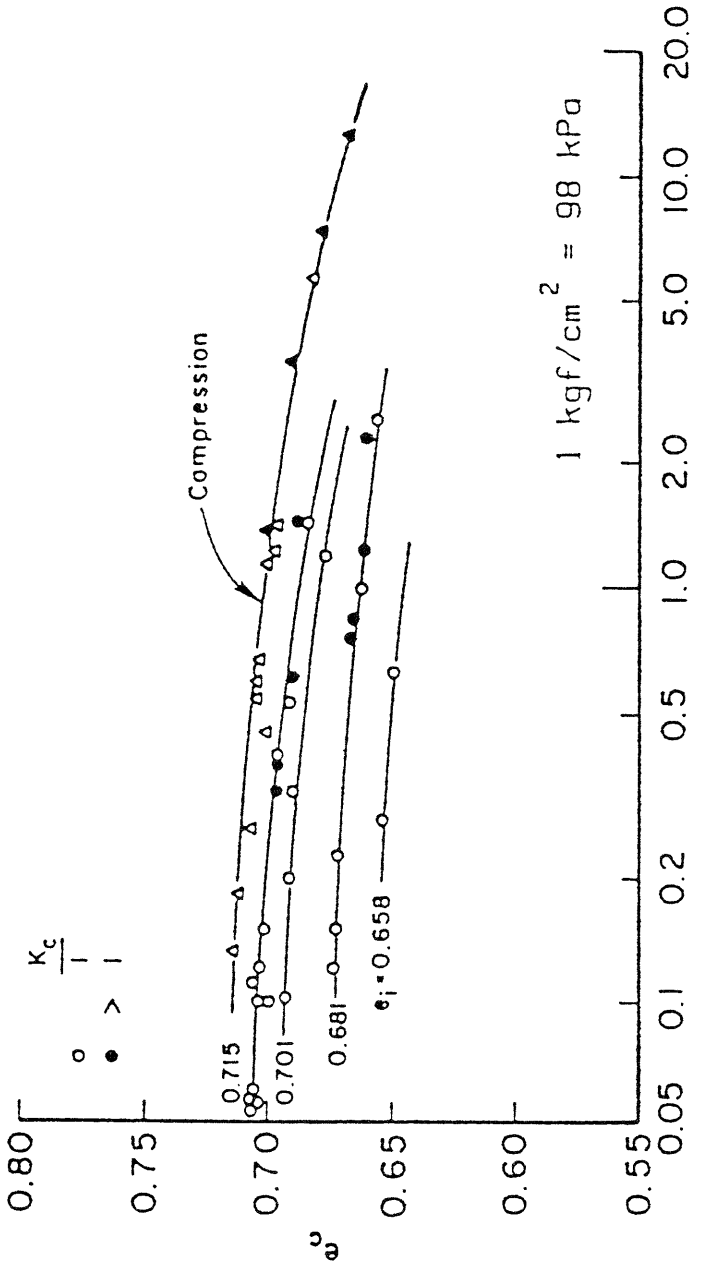

Figure 2.34 Triaxial Compression and Extension Behavior of Loose Ottawa Sand (from Vaid et al. 1990)

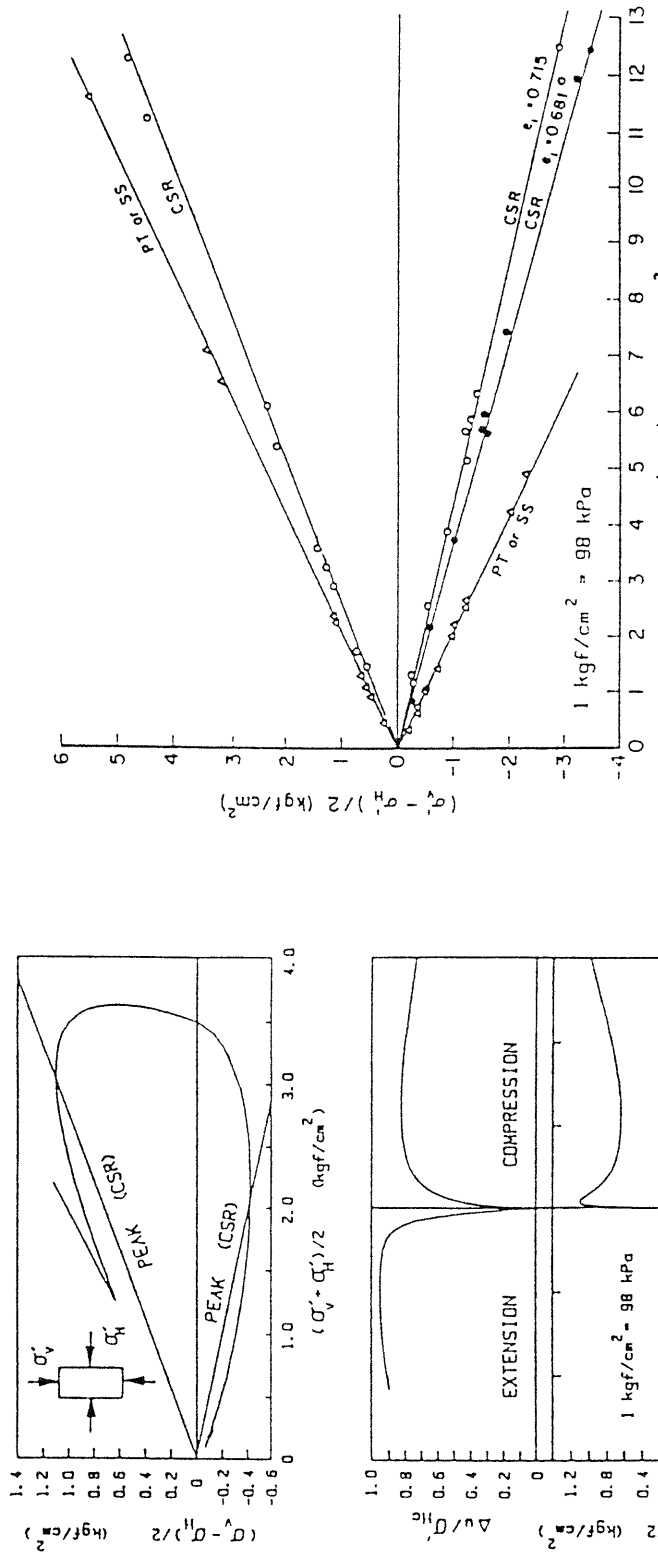

Figure 2.35 Effect of Consolidated Undrained Stress Path on the Steady State Condition for Loose Ottawa Sand (from Vaid et al. 1990)

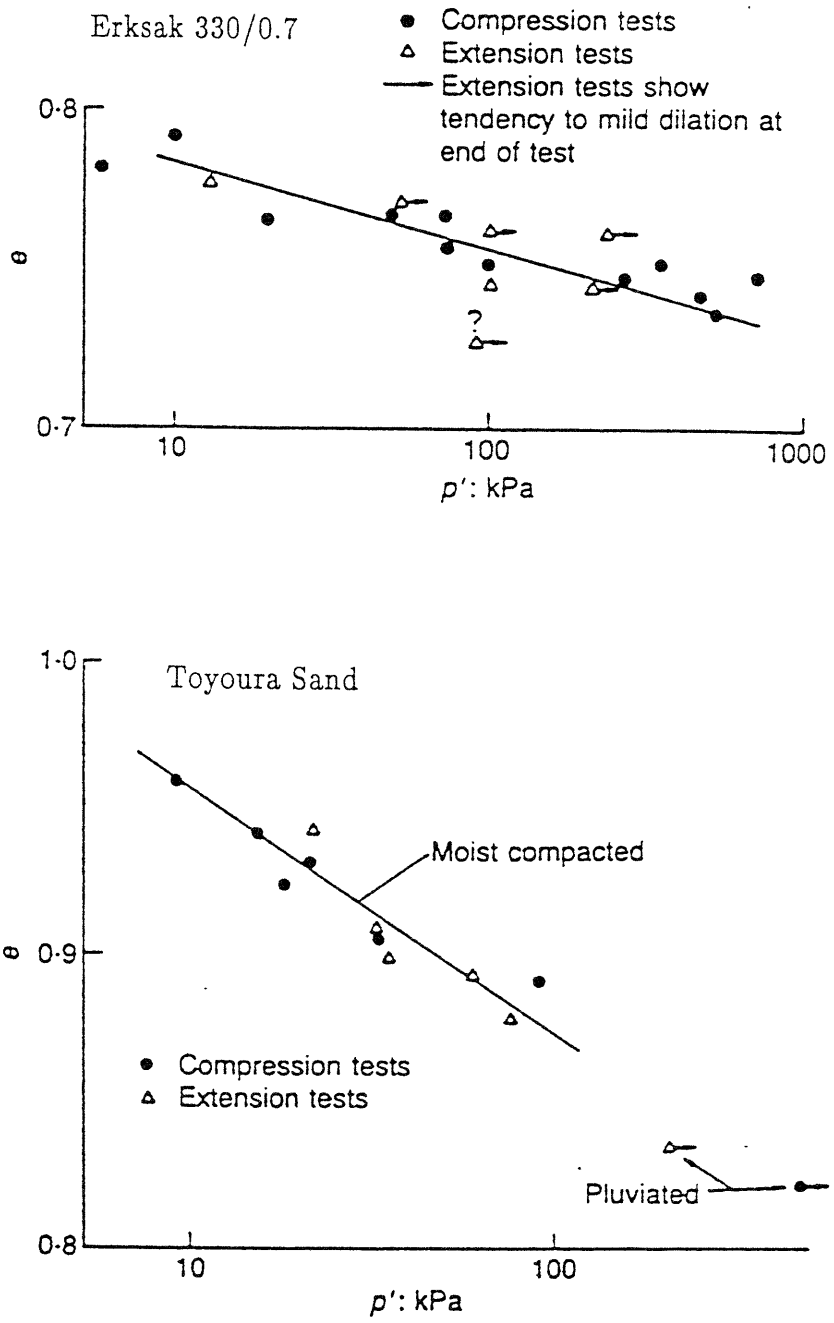

Figure 2.36 Effect of Hydrostatically Consolidated Undrained Stress Path on the Steady State Condition for Two Sands (from Been et al. 1991)

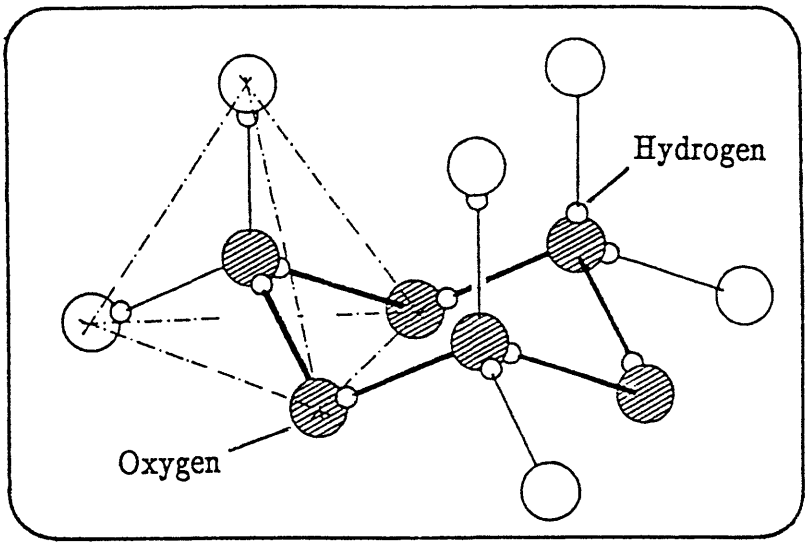

a. Formation of Basal Plane (hatched oxygen molecules)

b. Looking at ice lattice along c–axis

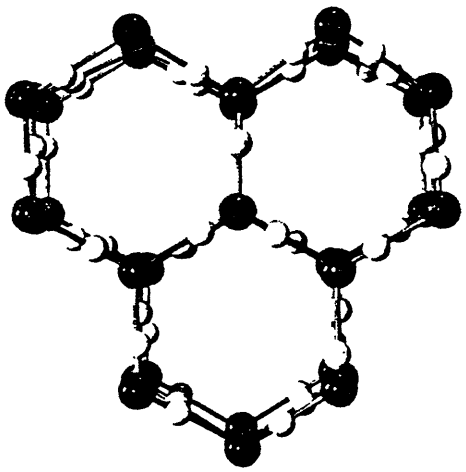

c. Looking at ice lattice along basal plane

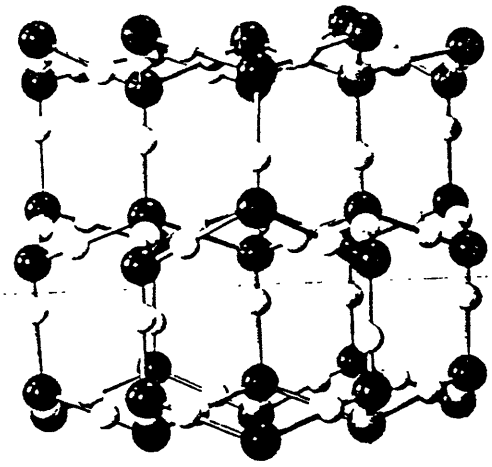

Figure 2.37 Basic Structure of Ice Ih (from Sanderson 1988)

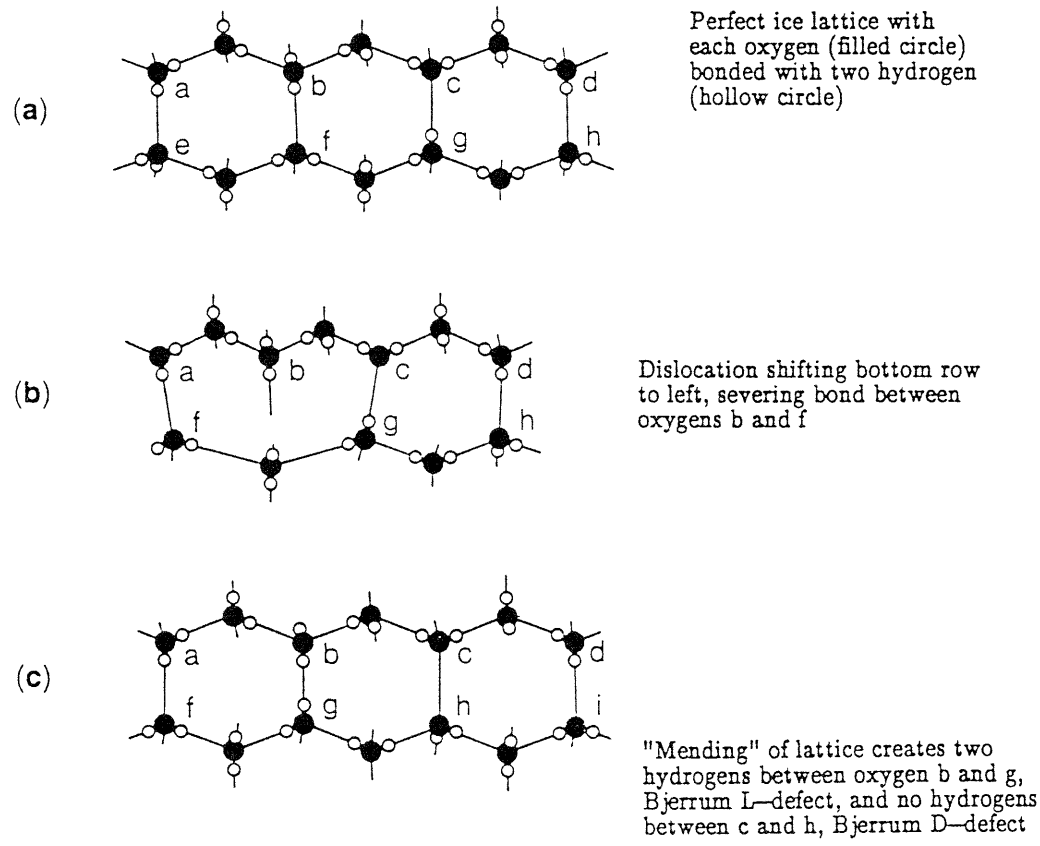

Figure 2.38 Schematic Representation of Development of Bjerrum Defects in Ice Lattice (from Sanderson 1988)

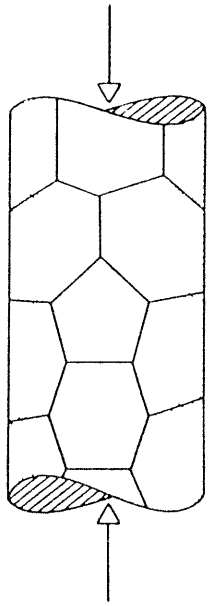

Idealized Polycrystalline
under Uniaxial Compression

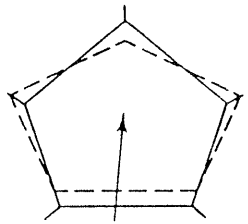

(a) Elastic Deformation

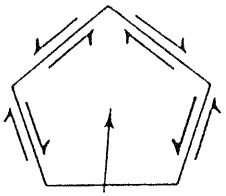

(b) Diffussional Flow

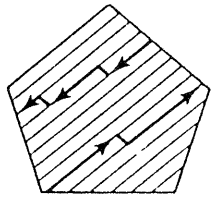

(c) Dislocation Mobility

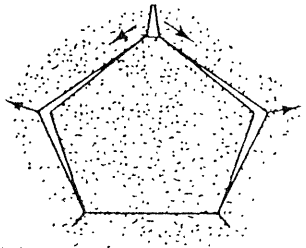

(e) Internal Fracturing

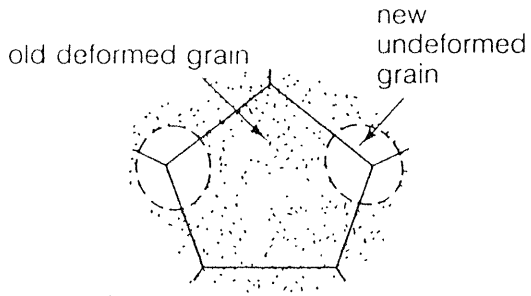

(d) Dynamic Recrystallization

Figure 2.39 Idealized Representation of Deformation Mechanisms (after Sanderson 1988)

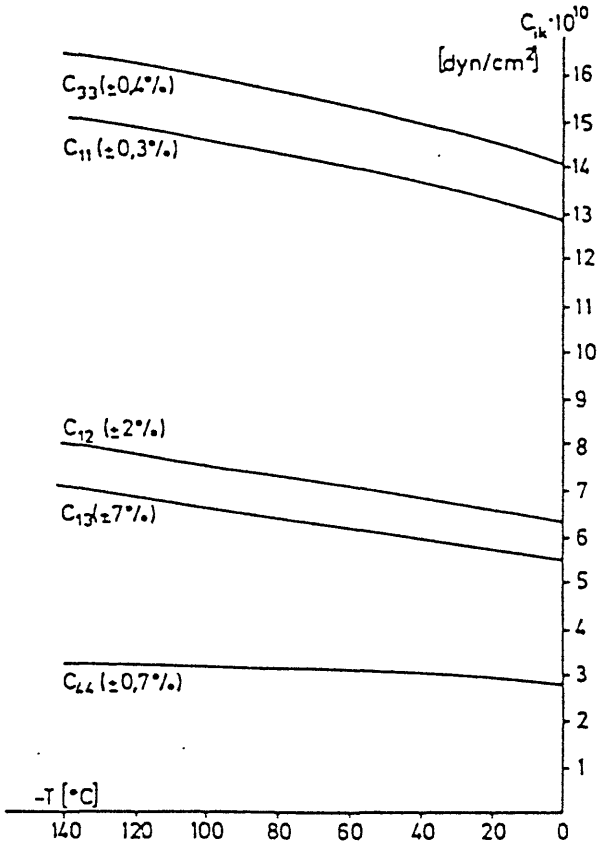

Figure 2.40 Young's Moduli for Single Ice Crystal (from Dantl 1969)

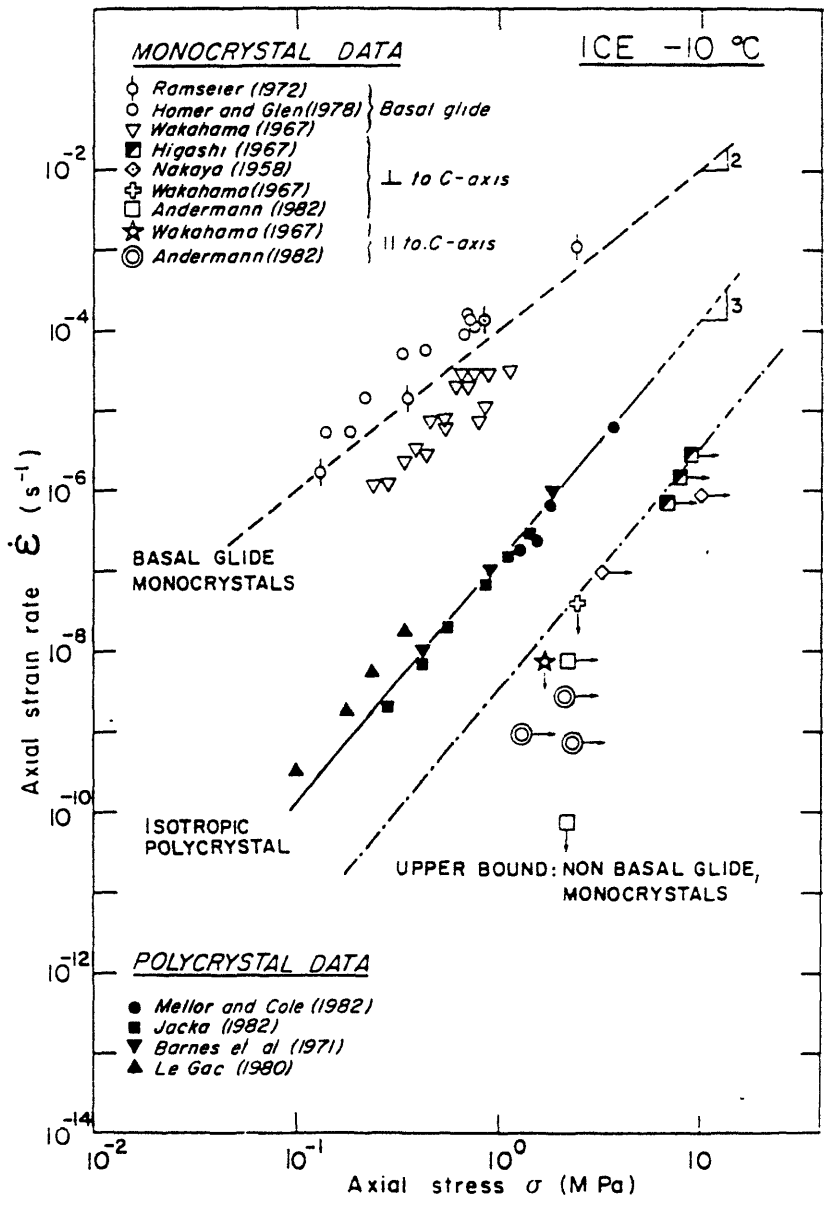

Figure 2.41 Creep Data from Monocrystals in Easy and Hard Glide and for Polycrystalline Ice (from Duval et al.1983)

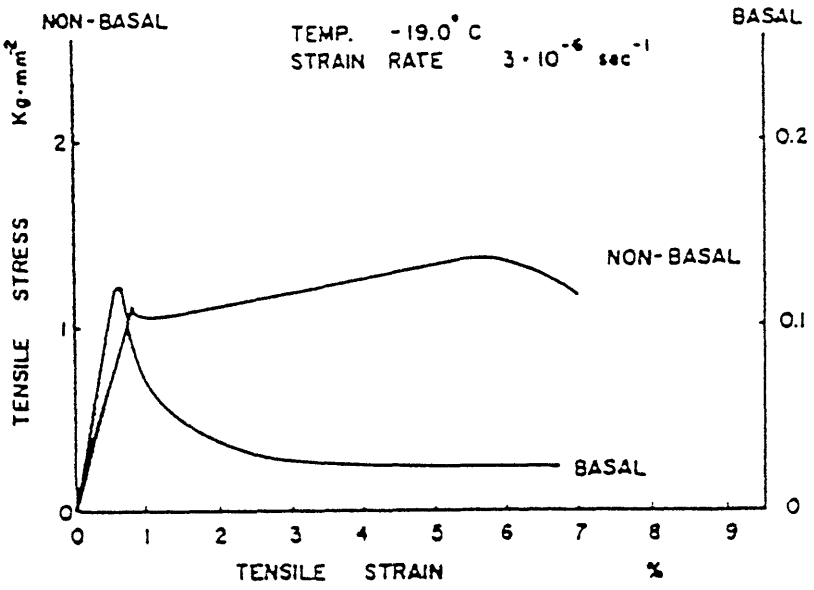

Figure 2.42 Stress–strain Curves for Single Ice Crystals in Basal and Nonbasal Glide (from Higashi 1969)

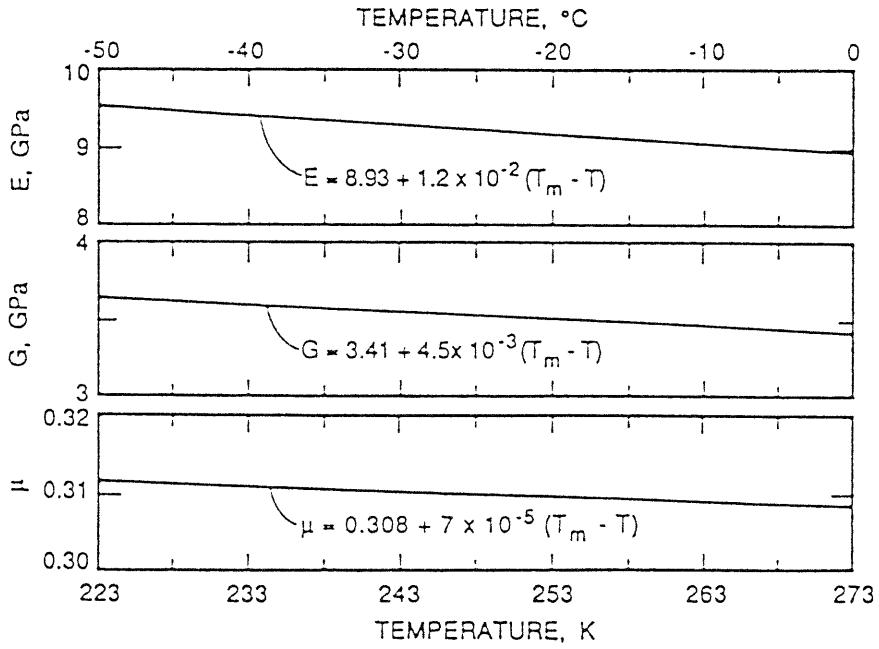

Figure 2.43 Small Strain Elastic Properties of Granular Ice (from Sinha 1989)

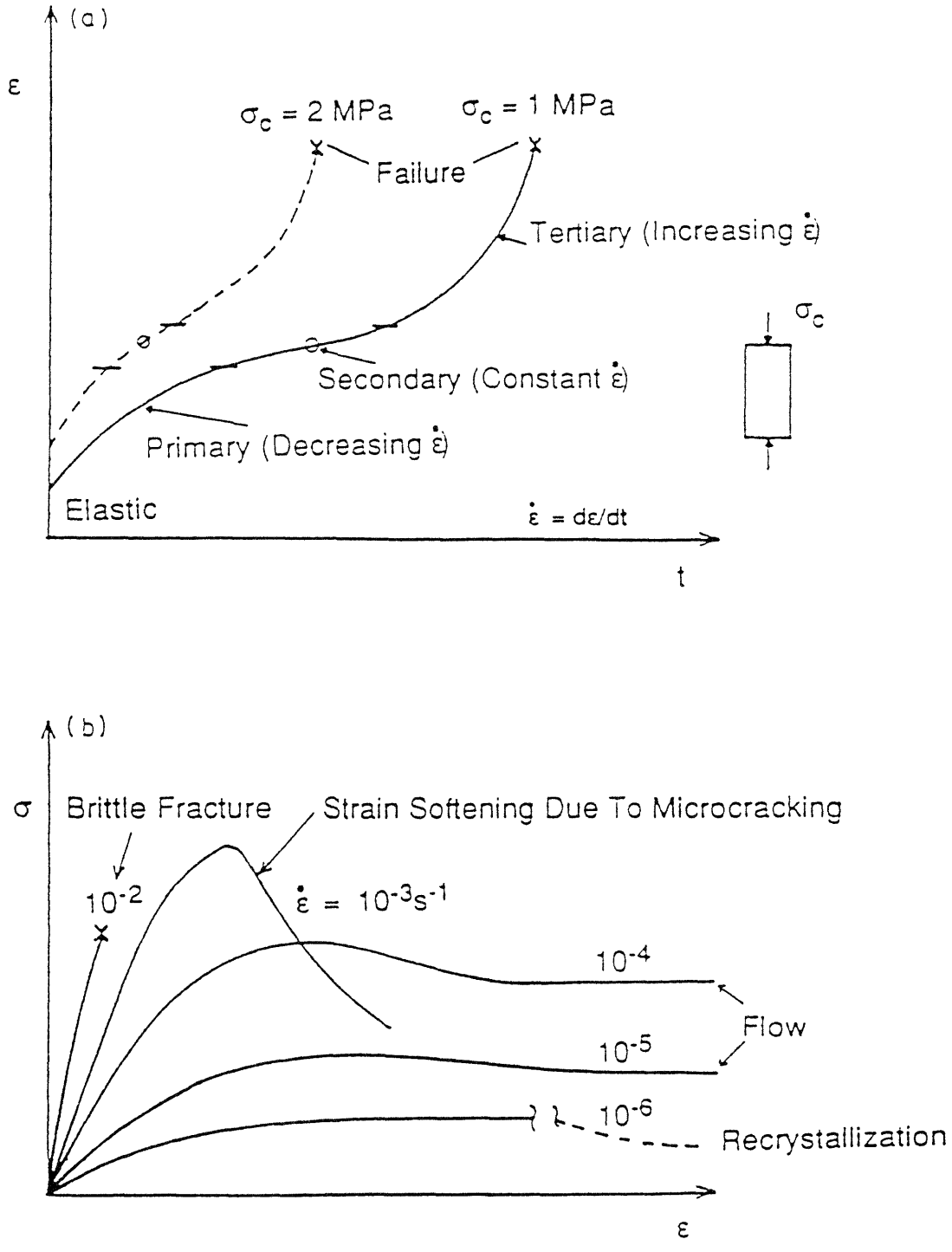

Figure 2.44 Idealized Creep and Stress–strain Curves for Polycrystalline Ice Tested in Compression (from Shyam Sunder 1993)

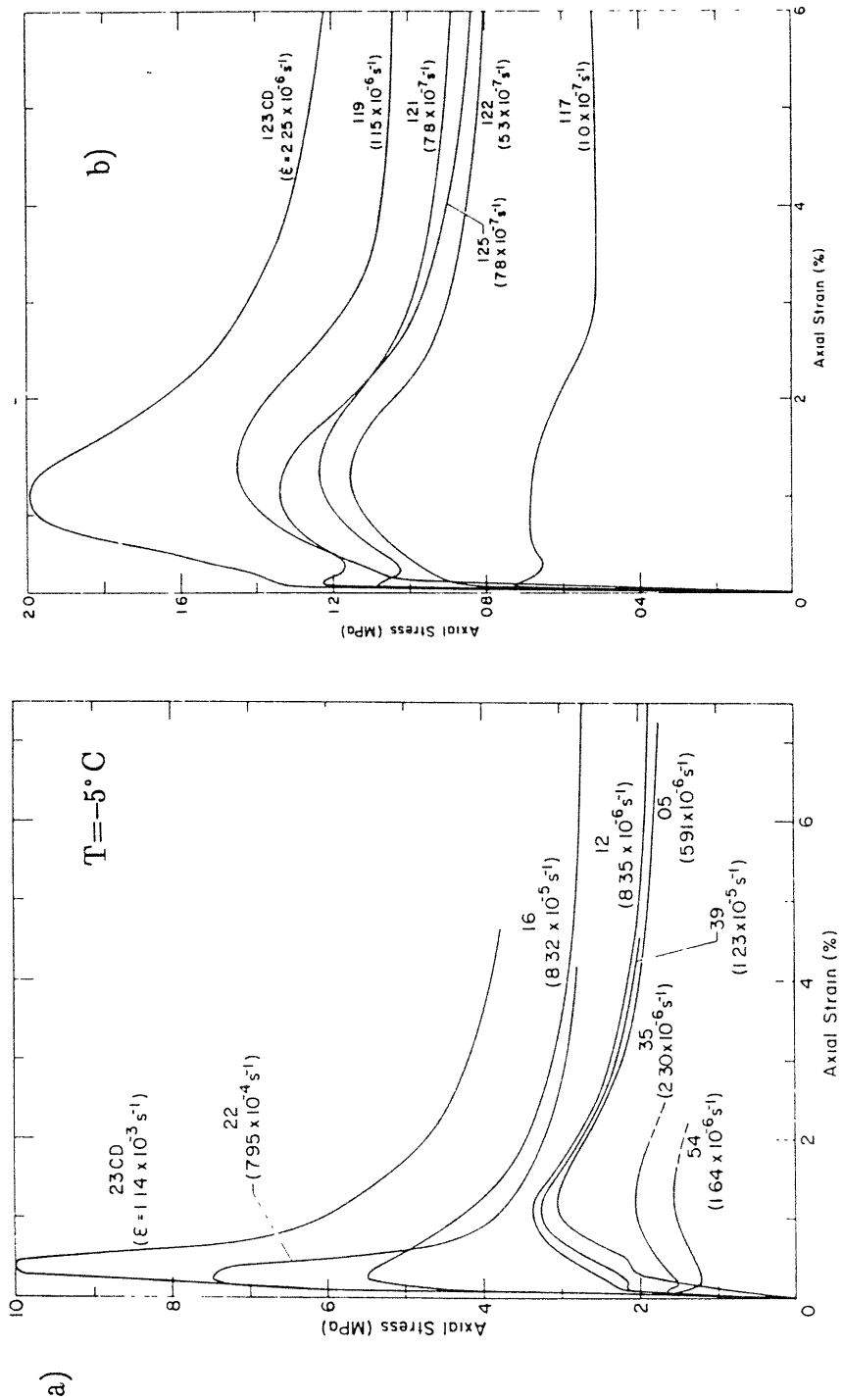

Figure 2.45 Stress–Strain Curves for Fine–grained Polycrystalline Ice at –5°C and Various Strain Rates (from Mellor and Cole 1982)

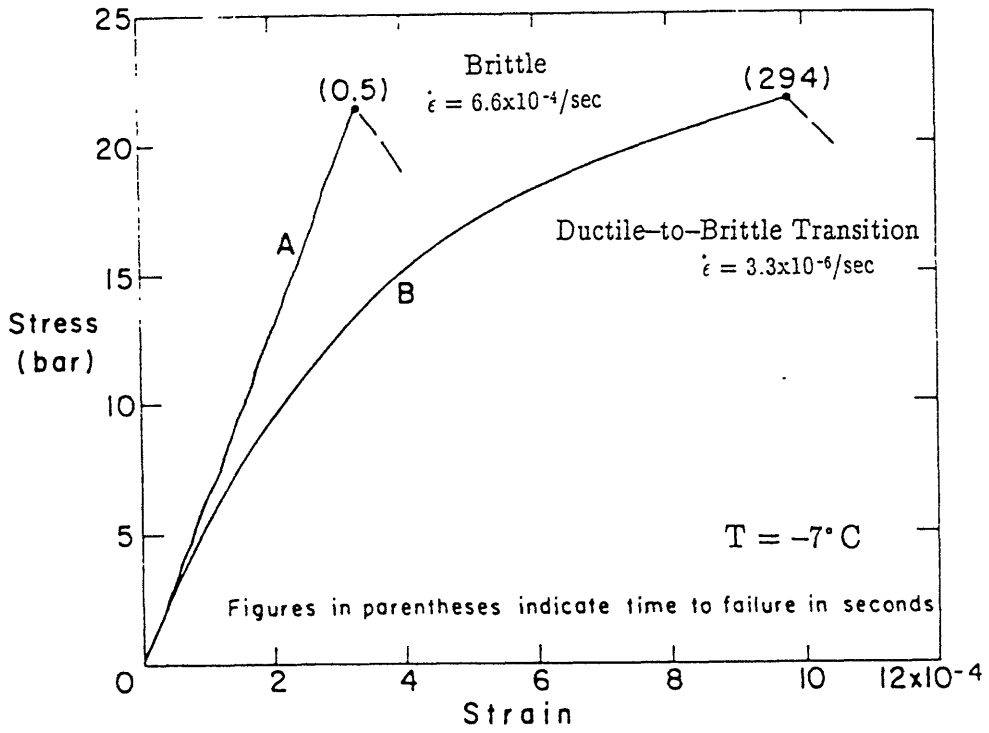

Figure 2.46 Stress–strain Curves From Uniaxial Tension Tests on Polycrystalline Ice (from Hawkes and Mellor 1972)

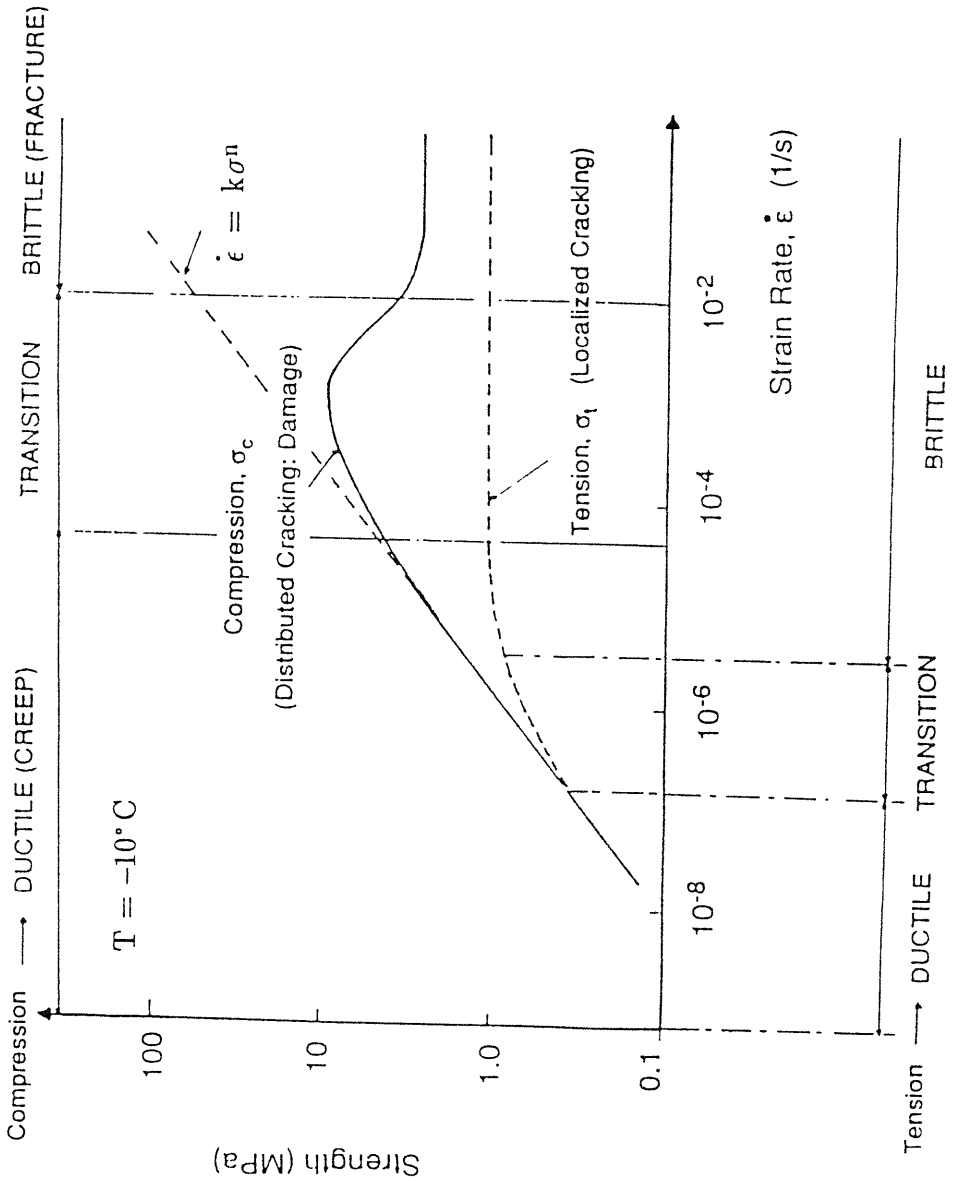

Figure 2.47 Schematic Log Stress – Log Strain Rate Response Highlighting the Effects of Strain Rate on the Behavior of Ice (from Shyam Sunder 1993)

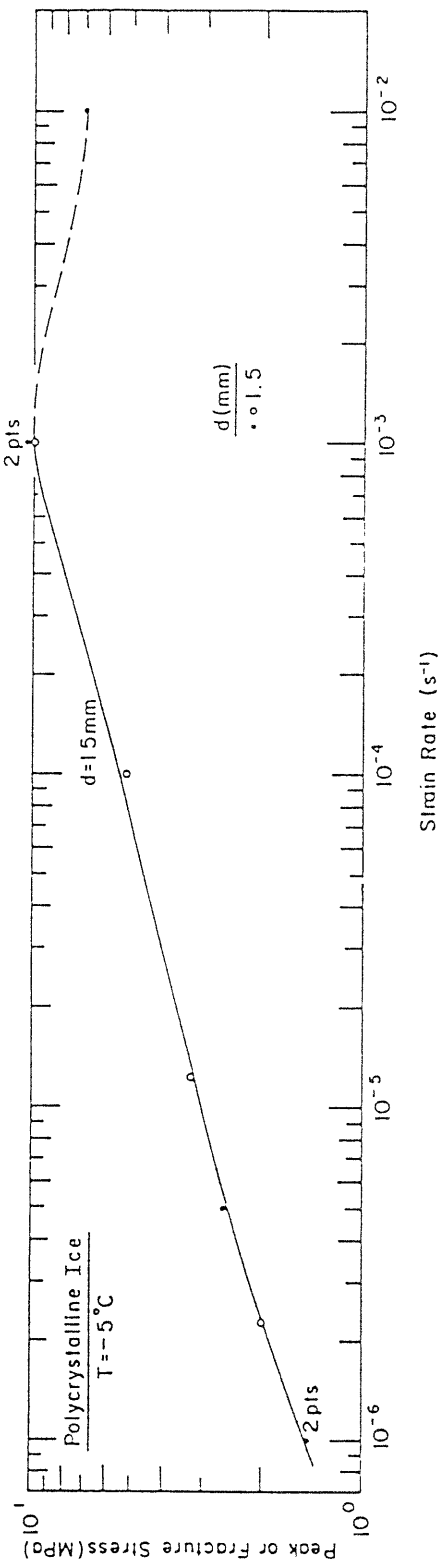

Figure 2.48 Log Applied Stress versus Log Minimum Strain Rate for Creep Tests on Granular Ice at −5° C (from Cole 1985)

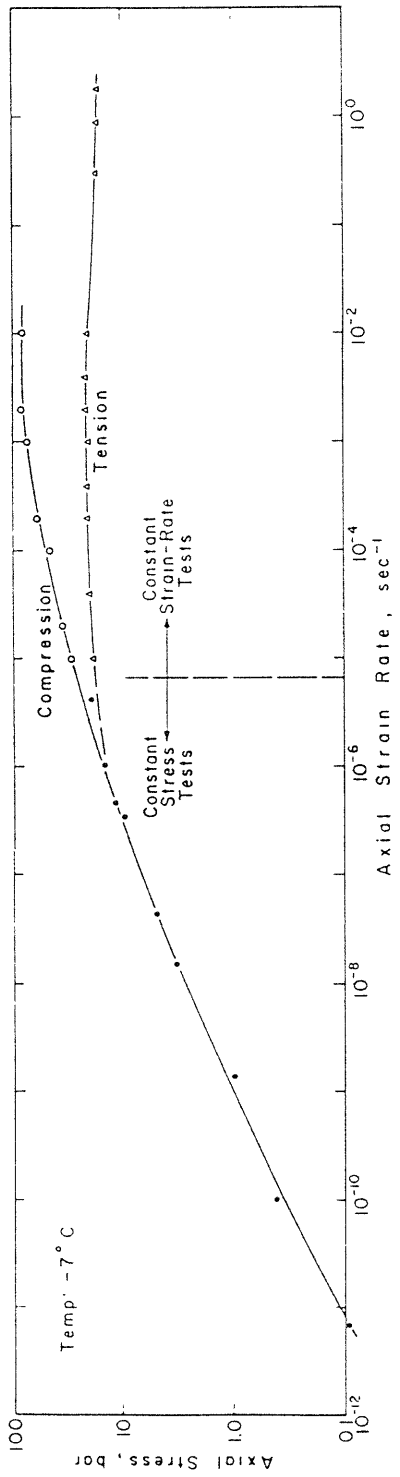

Figure 2.49 Stress/Strain–Rate Relationship for Uniaxial Tests on Granular Ice at –7° C (from Mellor 1980)

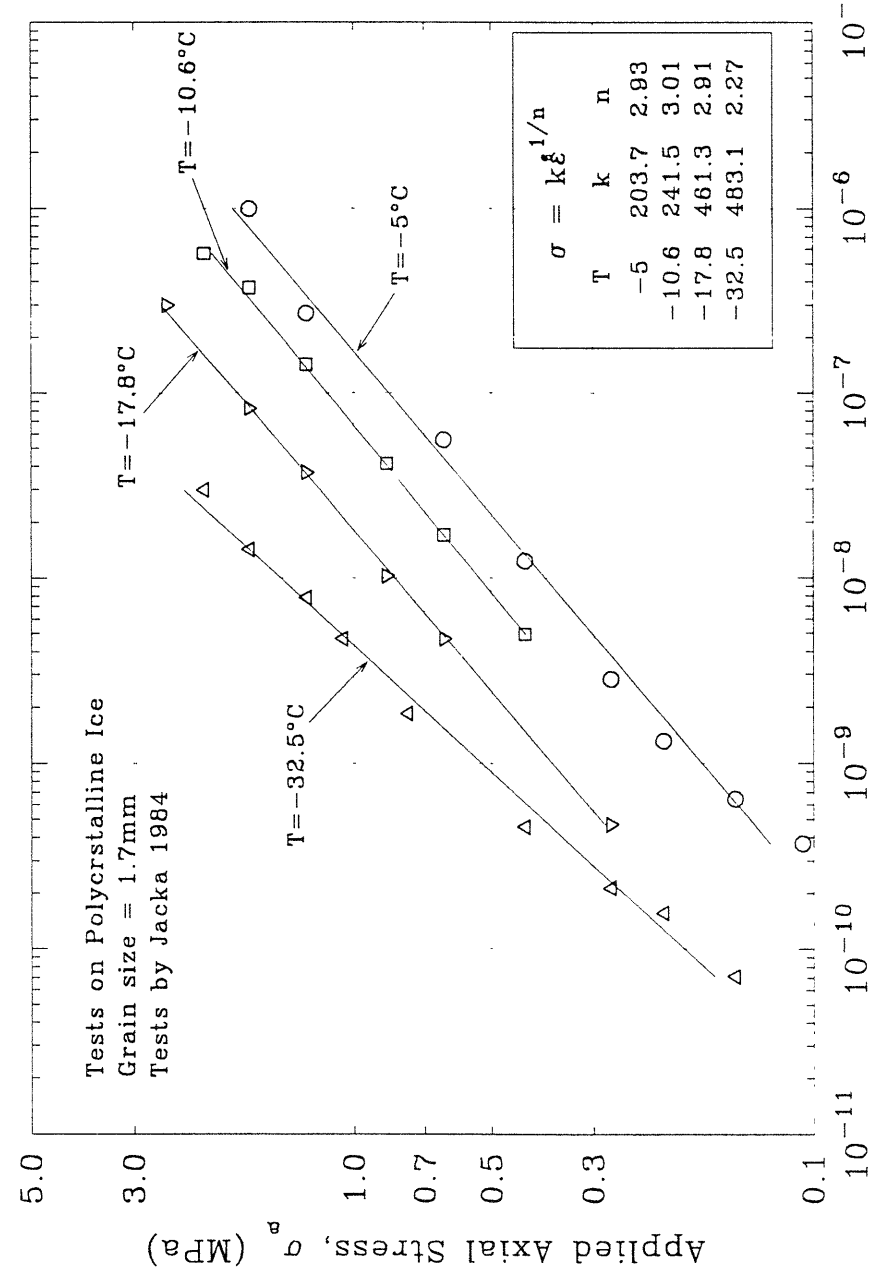

Figure 2.50 Applied Axial Stress versus Minimum Strain Rate for Creep Tests on Polycrystalline Ice (tests by Jacka 1984)

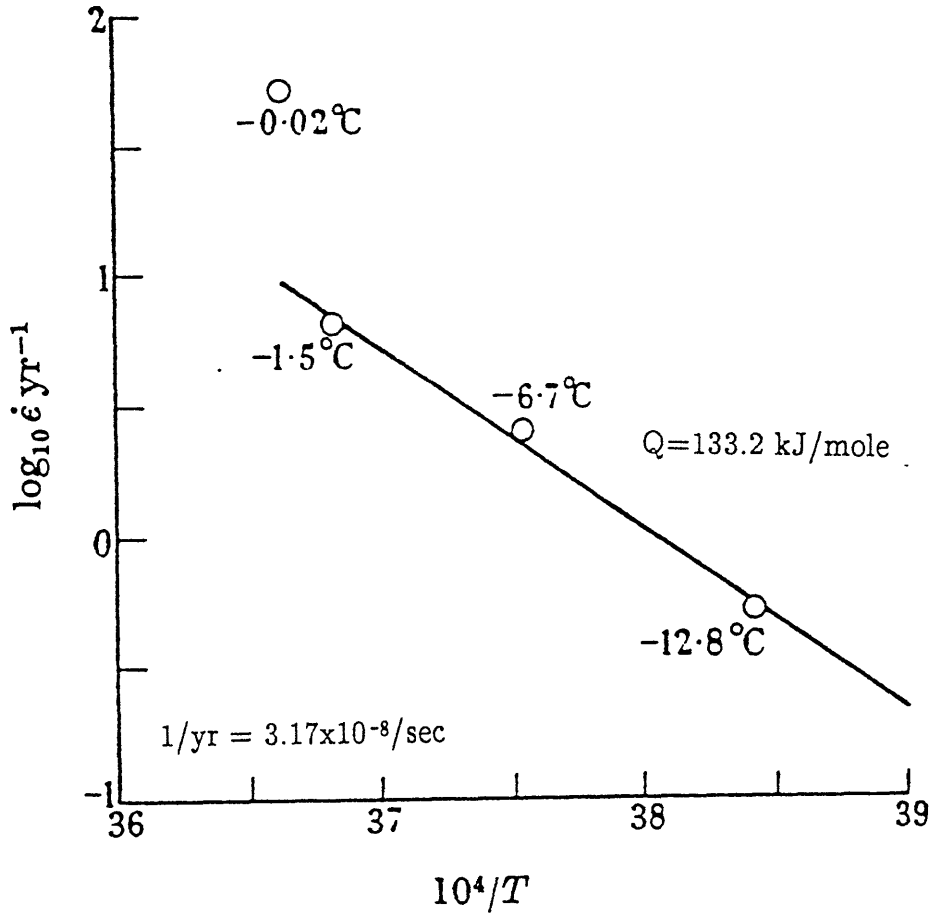

Figure 2.51 Minimum Strain Rate versus the Reciprocal of Absolute Temperature for Creep Tests on Polycrystalline Ice with Applied Stress of 6 bars (from Glen 1955)

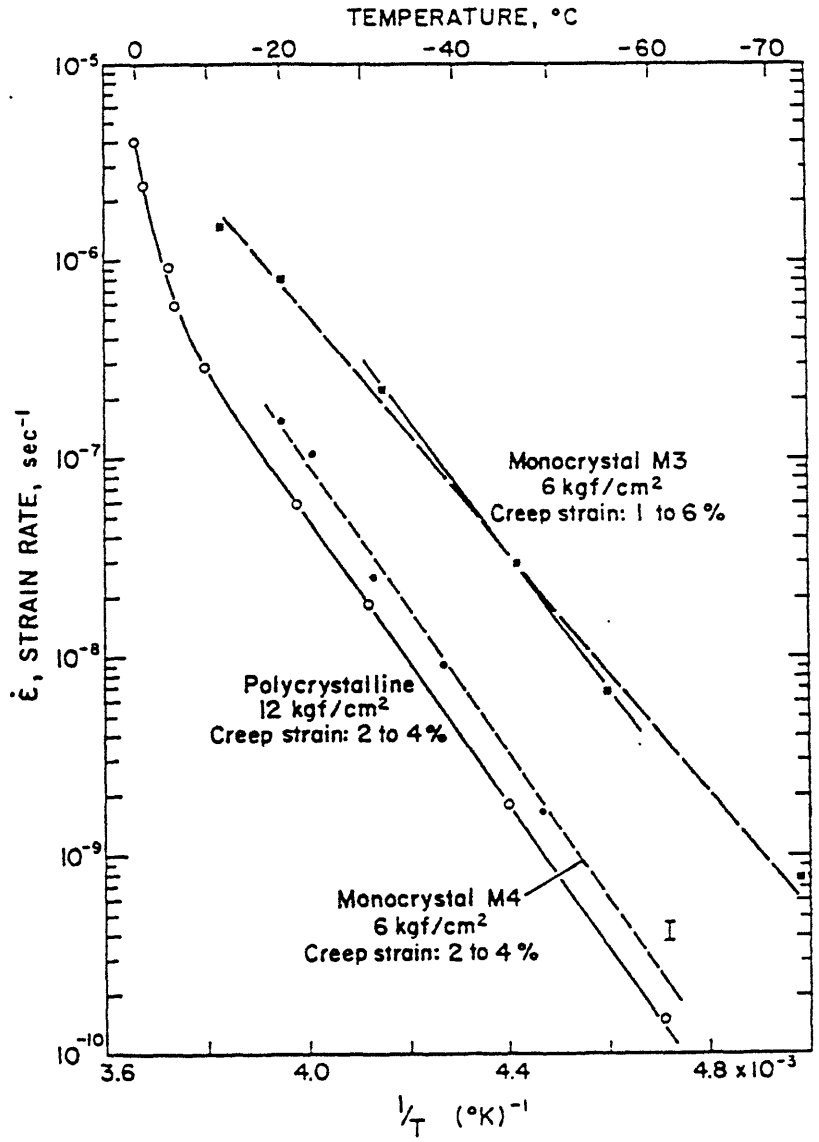

Figure 2.52 Minimum Strain Rate versus 1/T for Creep Tests on Polycrystalline Ice with σ_a = 1.18 MPa (from Mellor and Testa 1969)

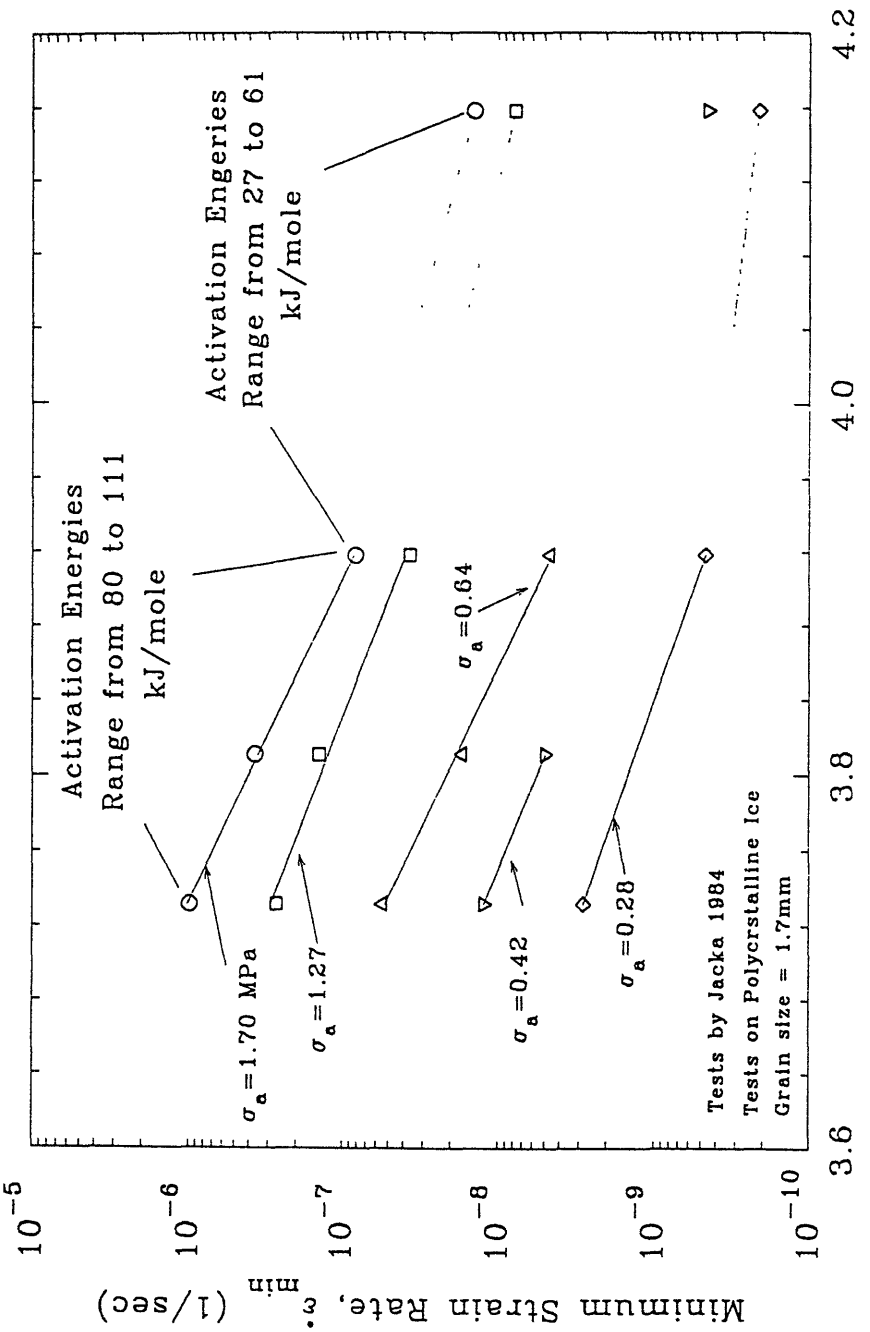

Figure 2.53 Minimum Strain Rate versus 1/T for Creep Tests on Polycrystalline Ice (tests by Jacka, 1984)

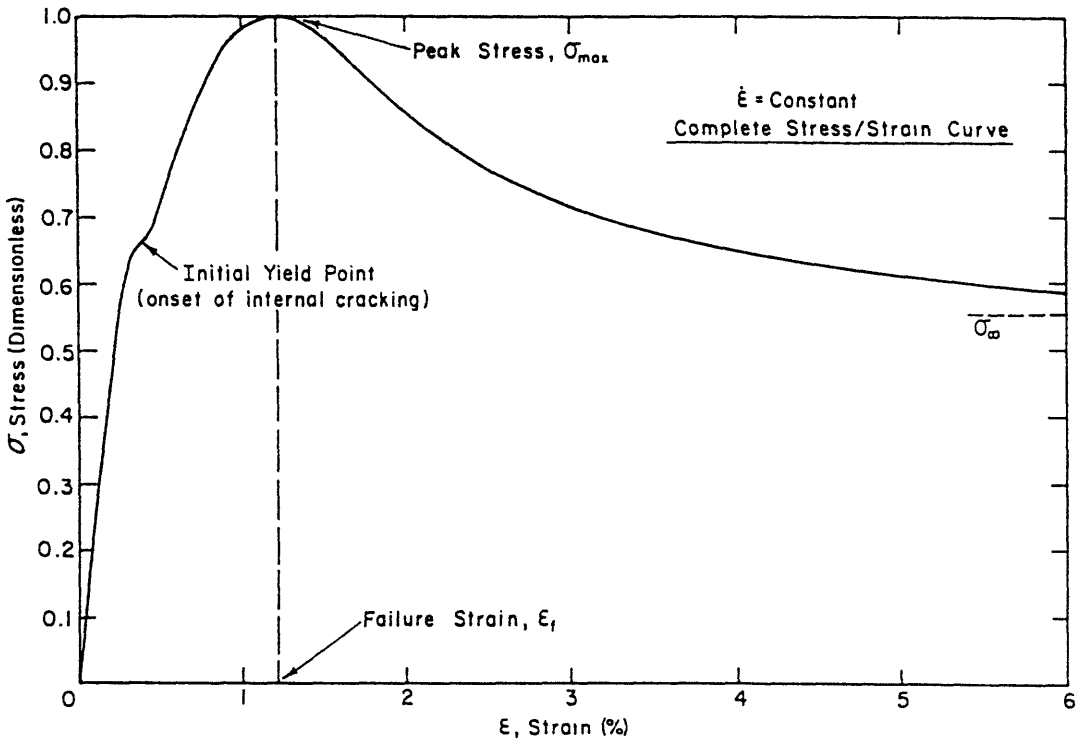

Figure 2.54 Idealize Stress–strain Curve for "Moderate" Strain–rate Compression Test on Polycrystalline Ice (from Mellor and Cole 1982)

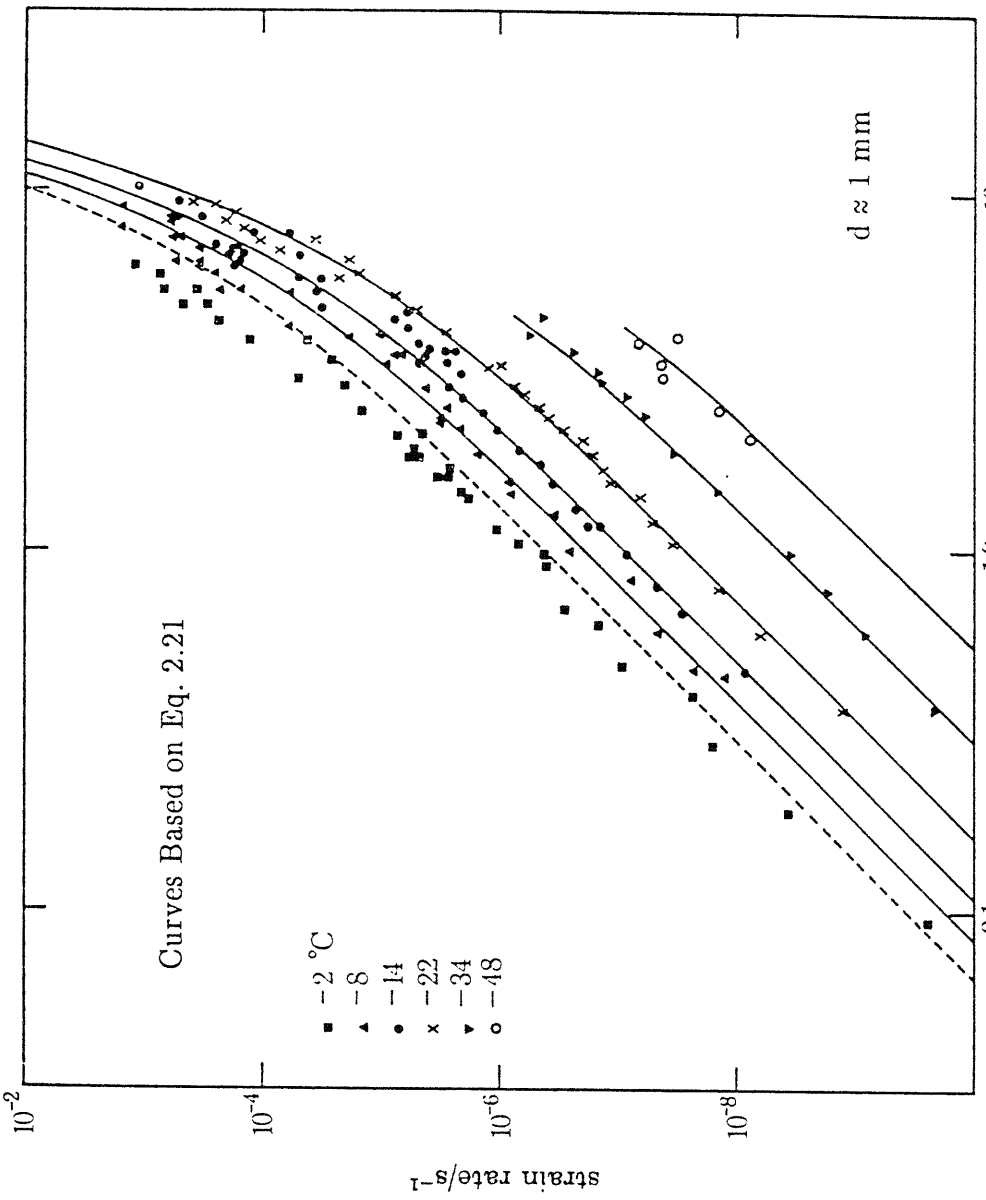

Figure 2.55 Minimum Strain Rate versus Applied Stress for Creep Tests on Polycrystalline Ice at Different Temperatures (from Barnes et al. 1971)

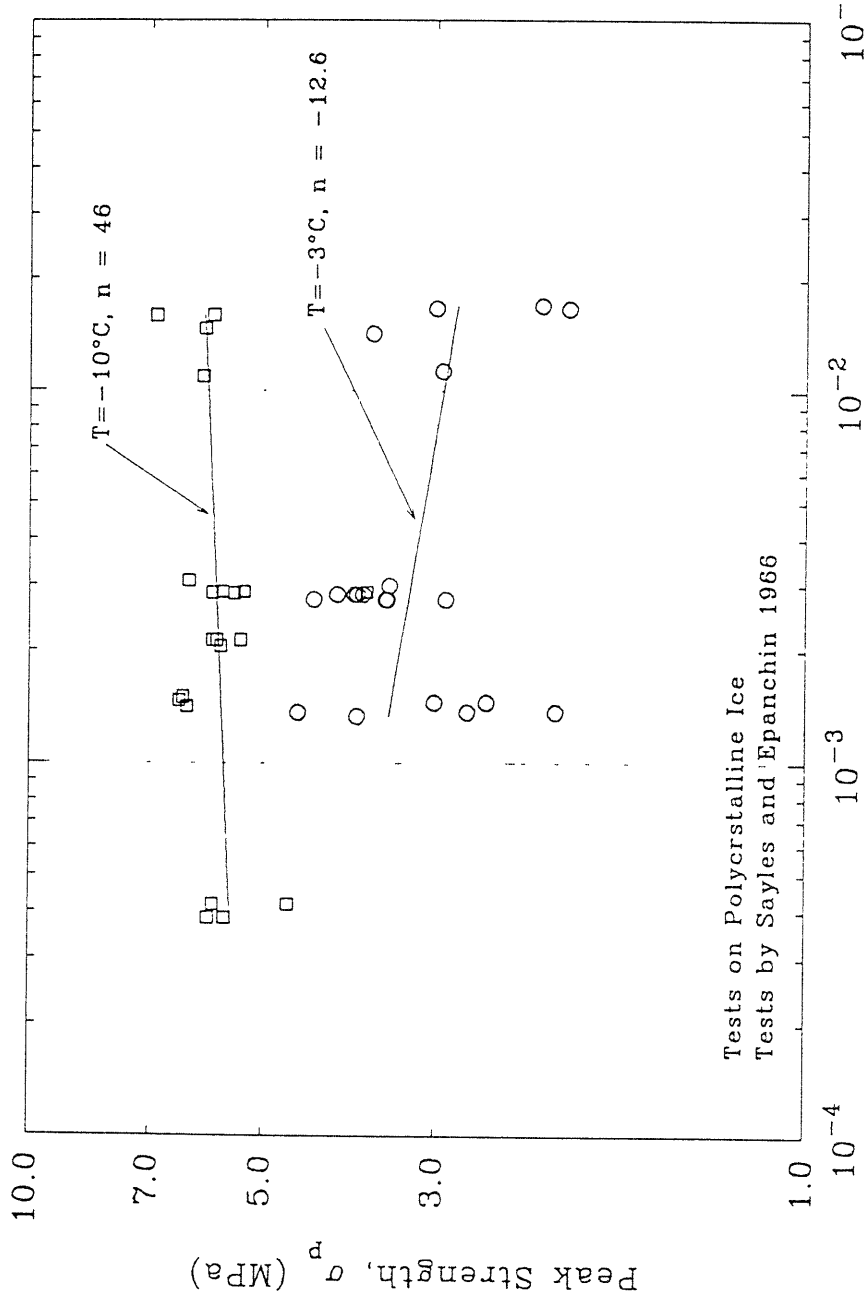

Figure 2.56 Peak Compressive Strength versus Applied Srain Rate from Strength Tests on Polycrystalline Ice (tests by Sayles and Epanchin, 1966)

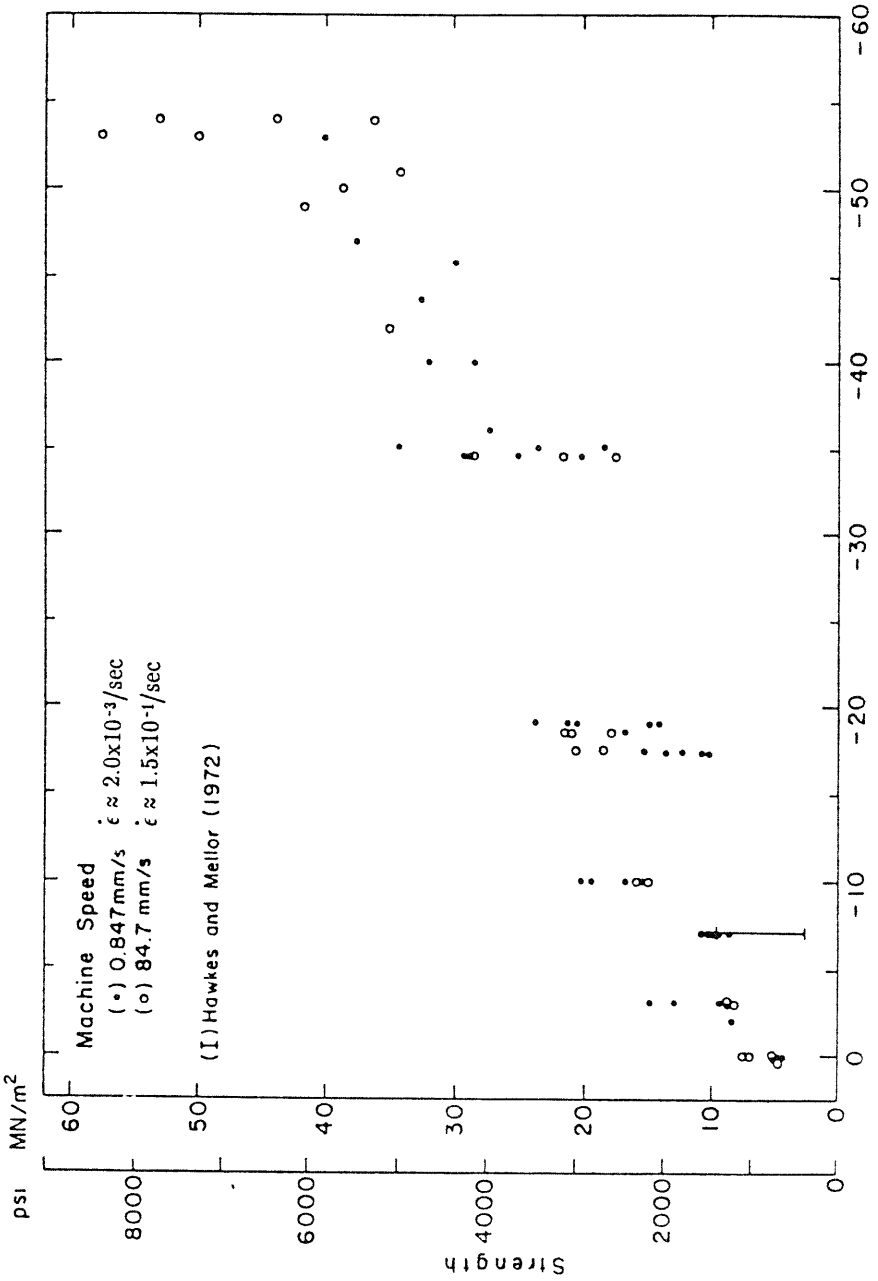

Figure 2.57 Unconfined Compressive Strength versus Temperature for Granular Ice (from Haynes 1979)

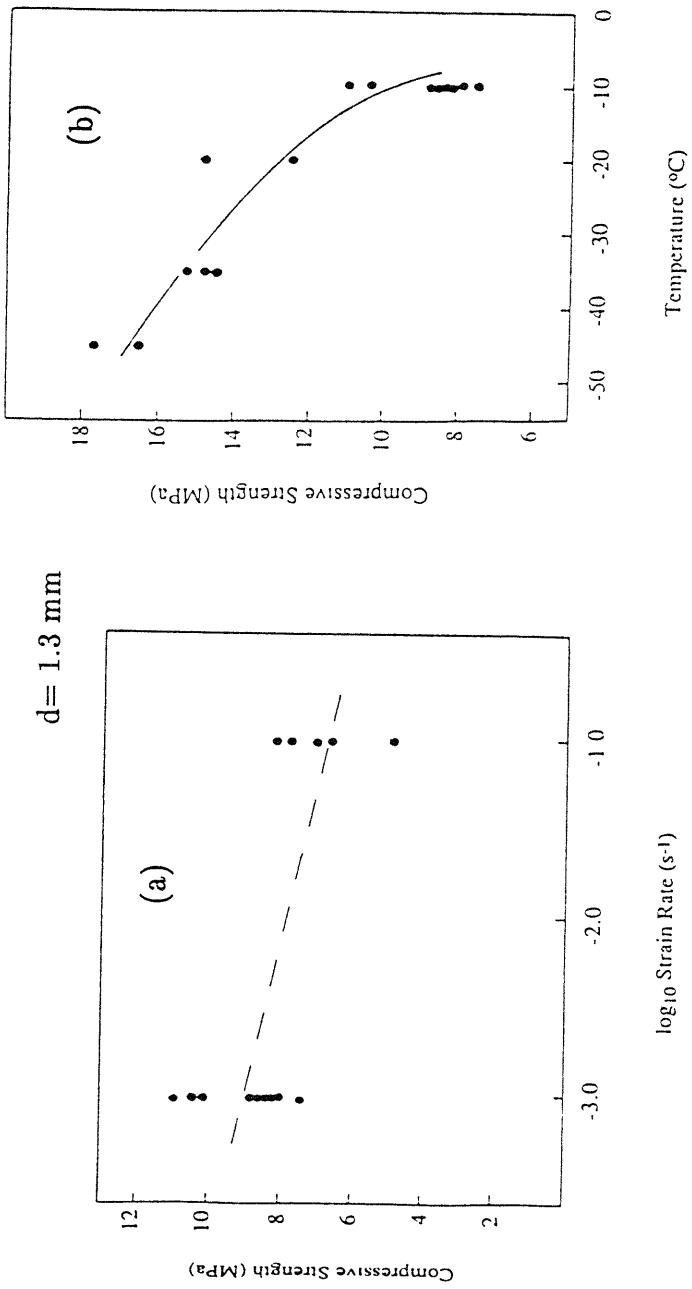

Figure 2.58 Unconfined Compressive Strength for Granular Ice as a Function of Strain Rate and Temperature (from Schulson 1990)

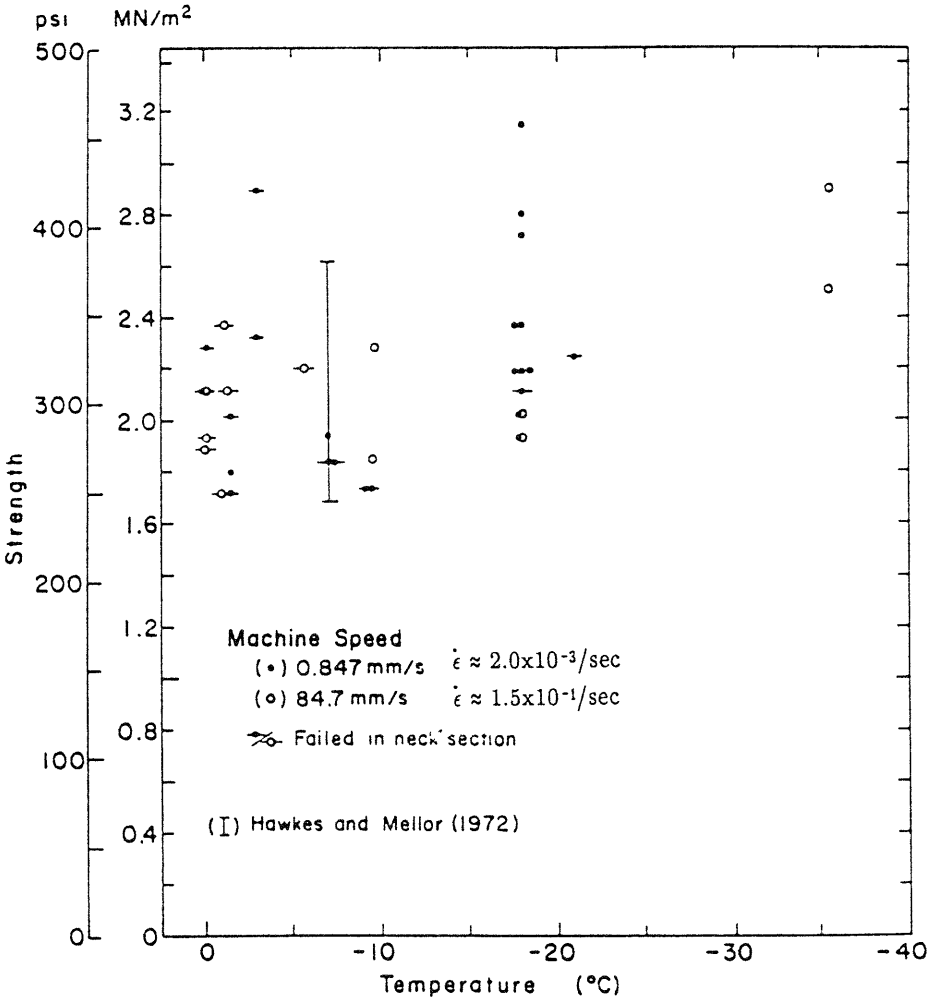

Figure 2.59 Uniaxial Tensile Strength versus Temperature for Granular Ice (from Haynes 1979)

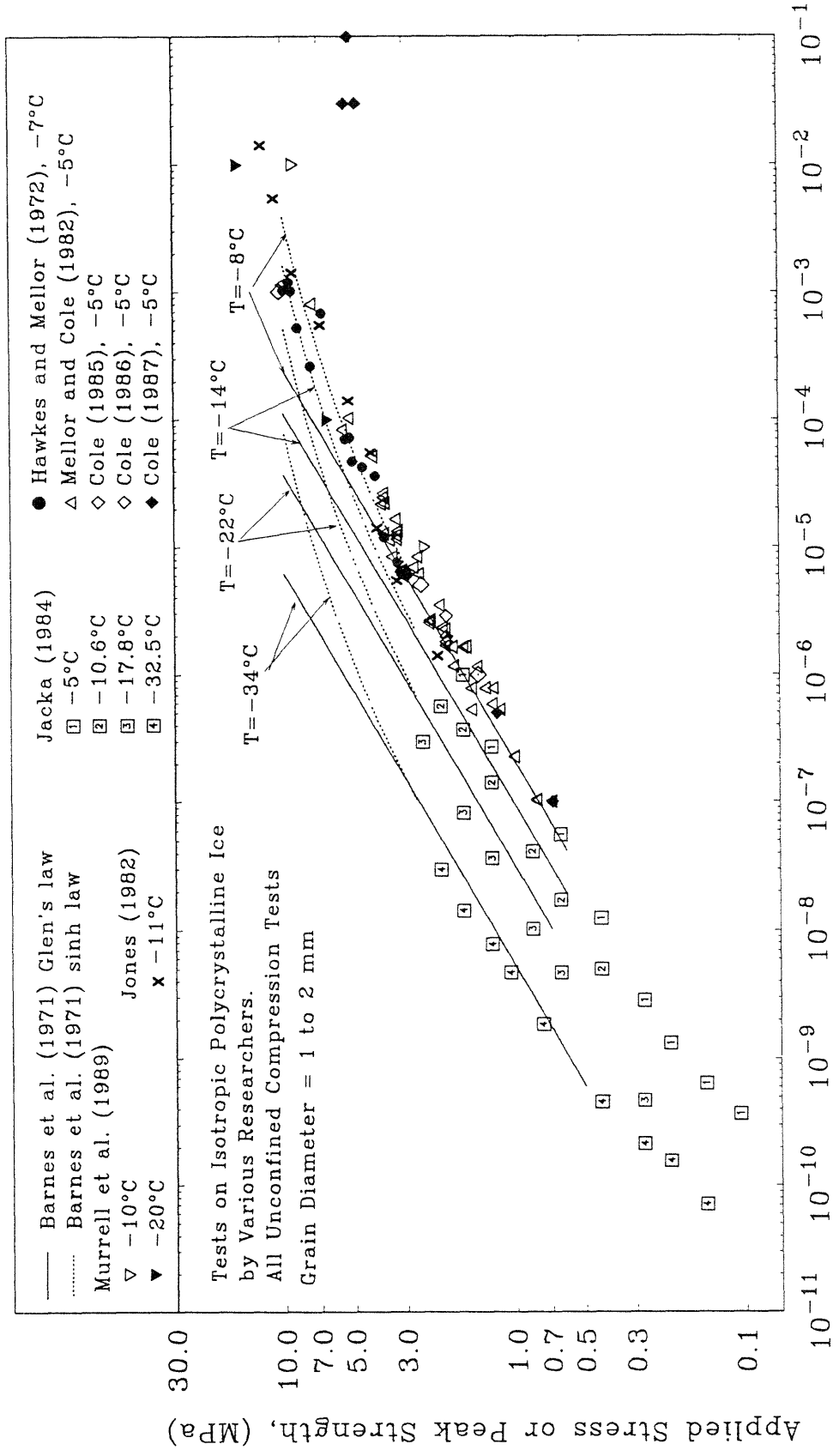

Figure 2.60 Stress versus Strain Rate for Creep and Strength Tests on Isotropic Polycrystalline Ice

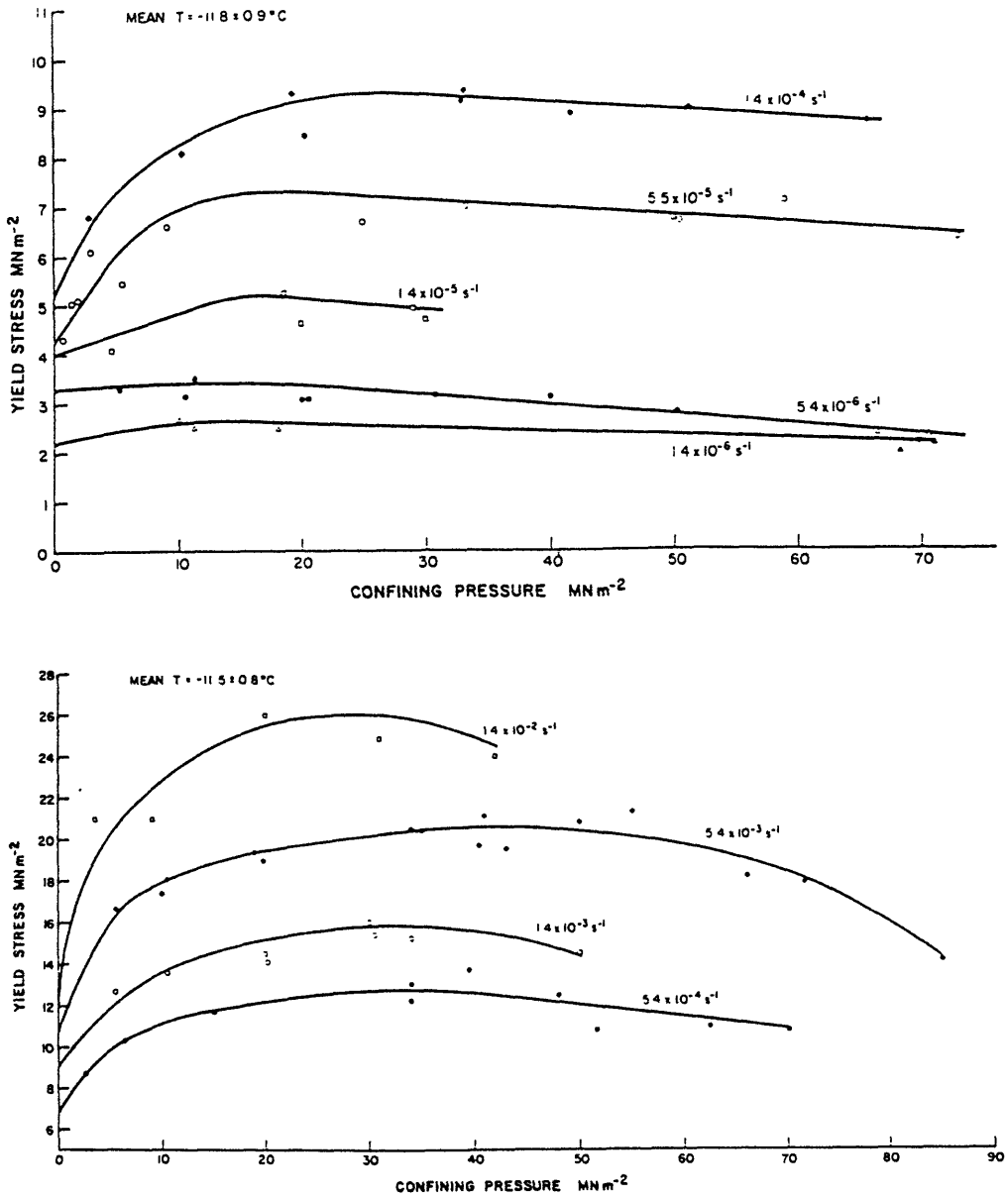

Figure 2.61 Effect of Confining Pressure on the Peak Strength of Granular Ice (from Jones 1982)

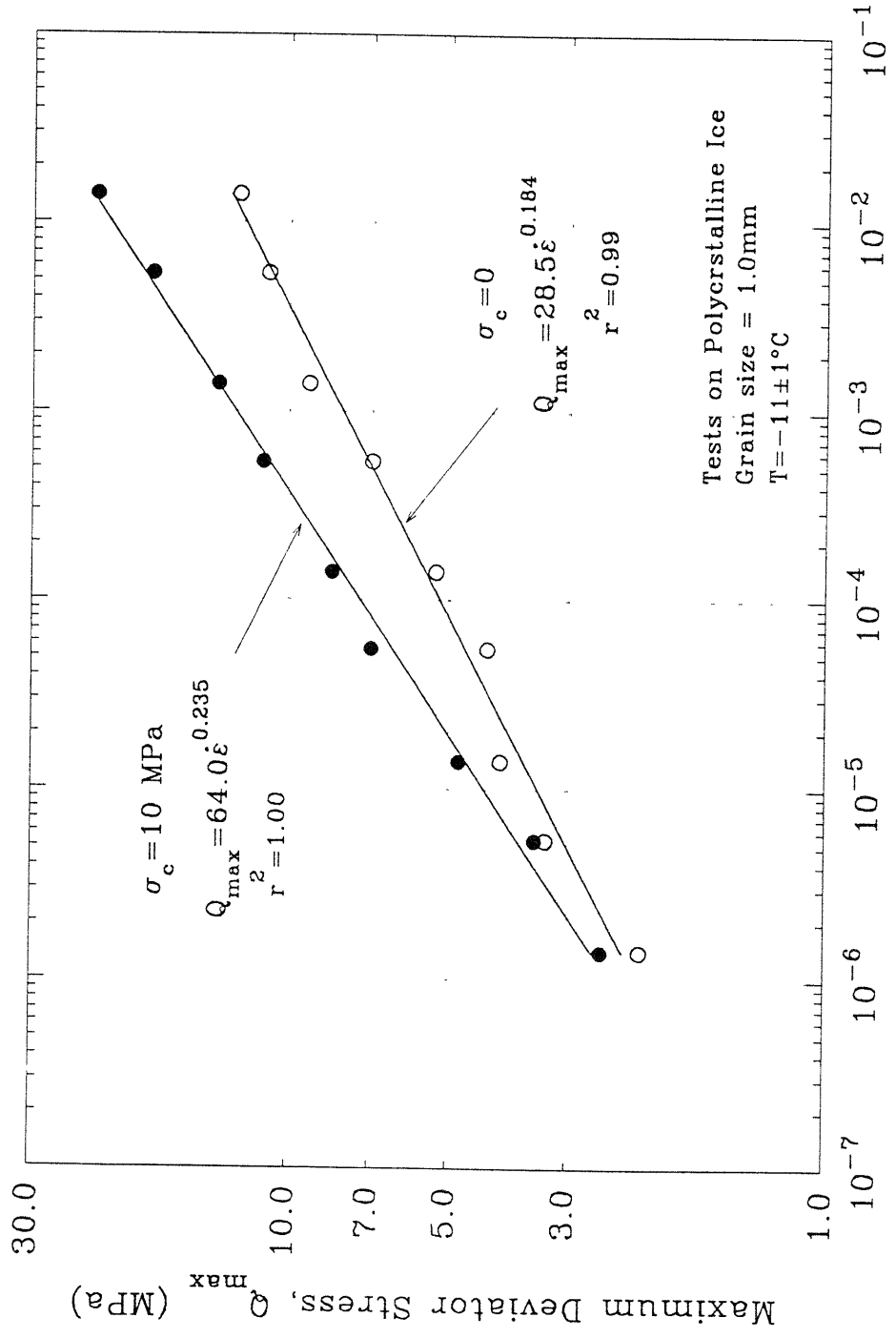

Figure 2.62 Maximum Deviator Stress versus Applied Strain Rate for Constant Rate of Strain Tests on Polycrystalline Ice (tests by Jones, 1982)

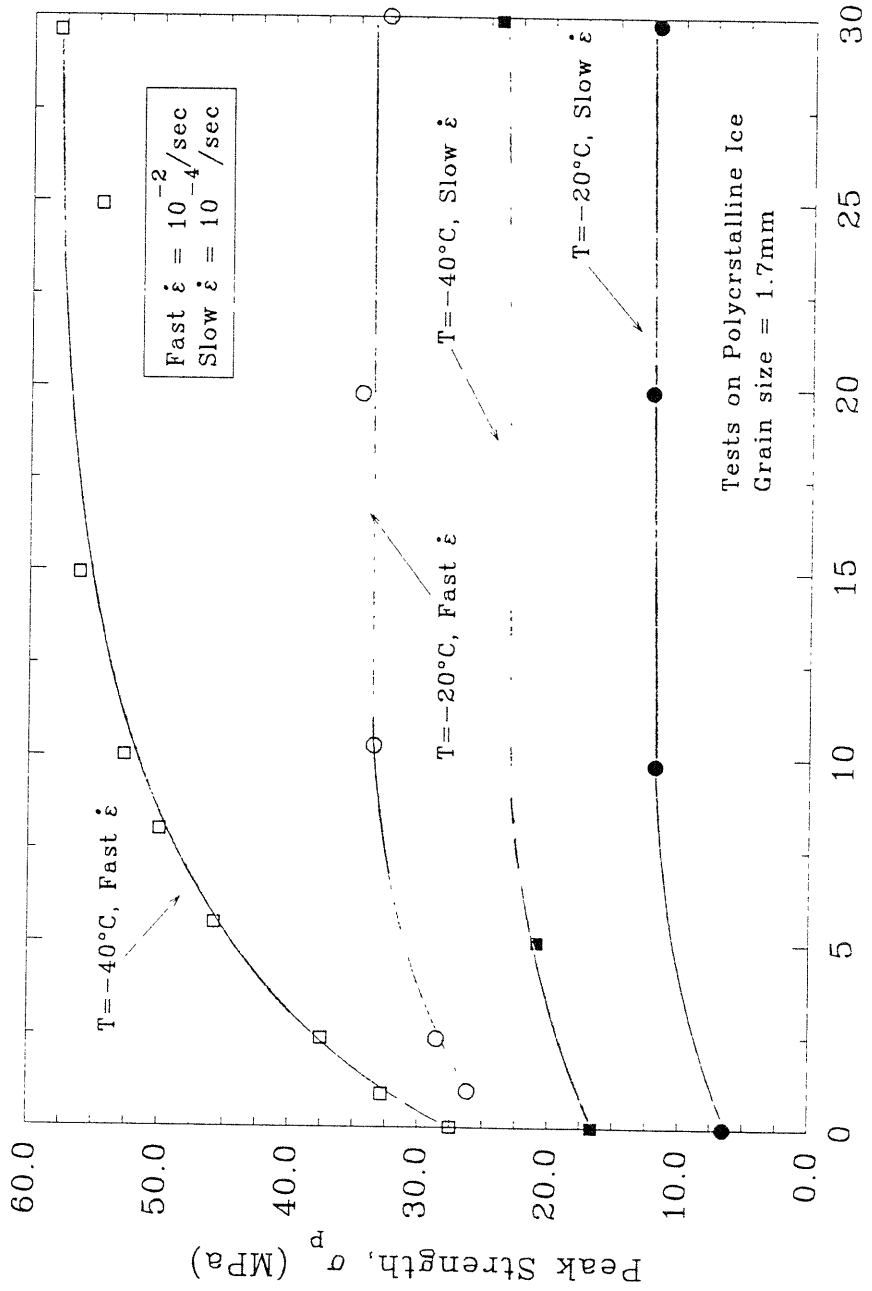

Figure 2.63 Peak Strength versus Confining Stress for Strength Tests on Polycrystalline Ice (tests by Murrell et al. 1989)

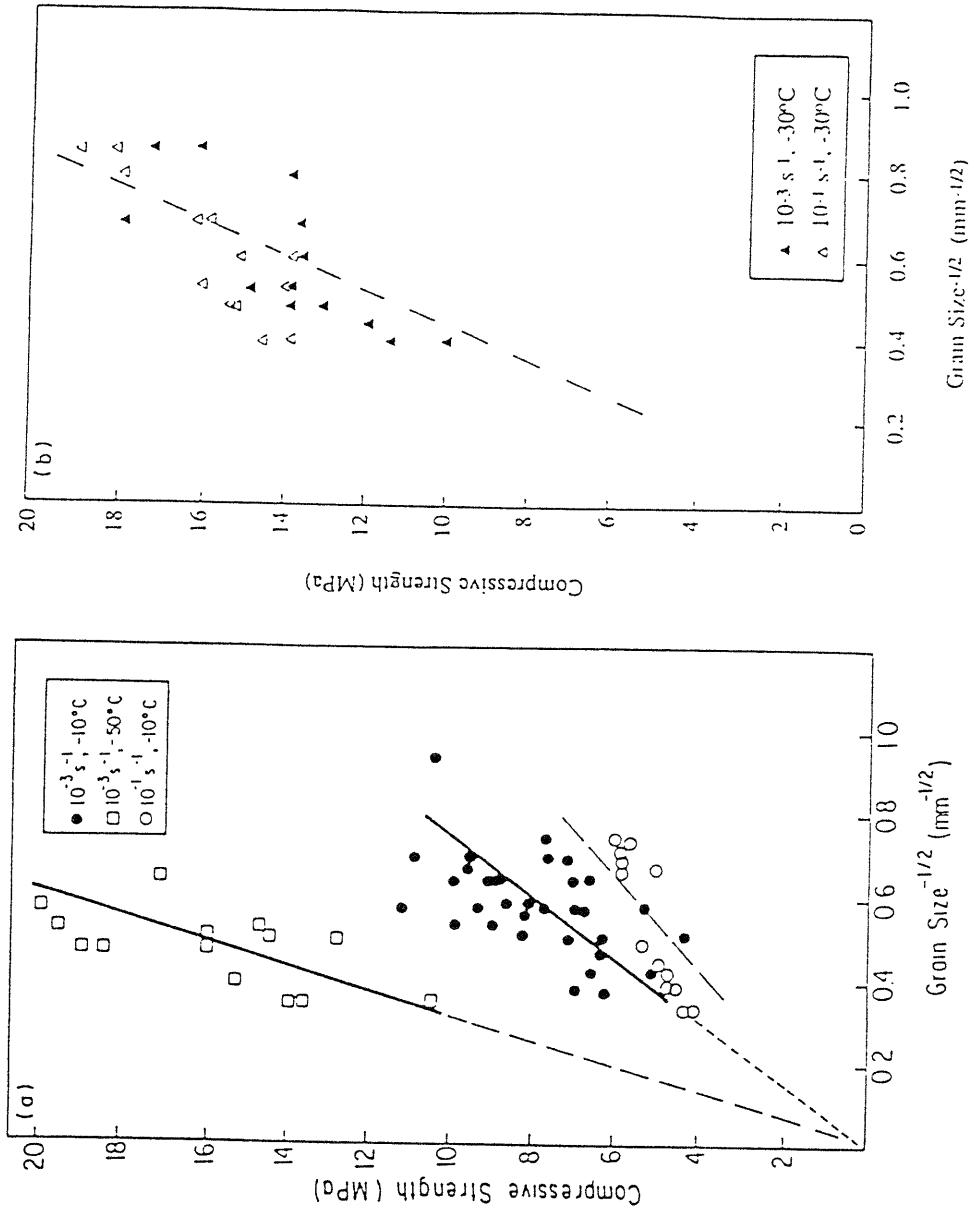

Figure 2.64 Effect of Grain Size on the Unconfined Compression Strength of Granular Ice (from Schulson 1990)

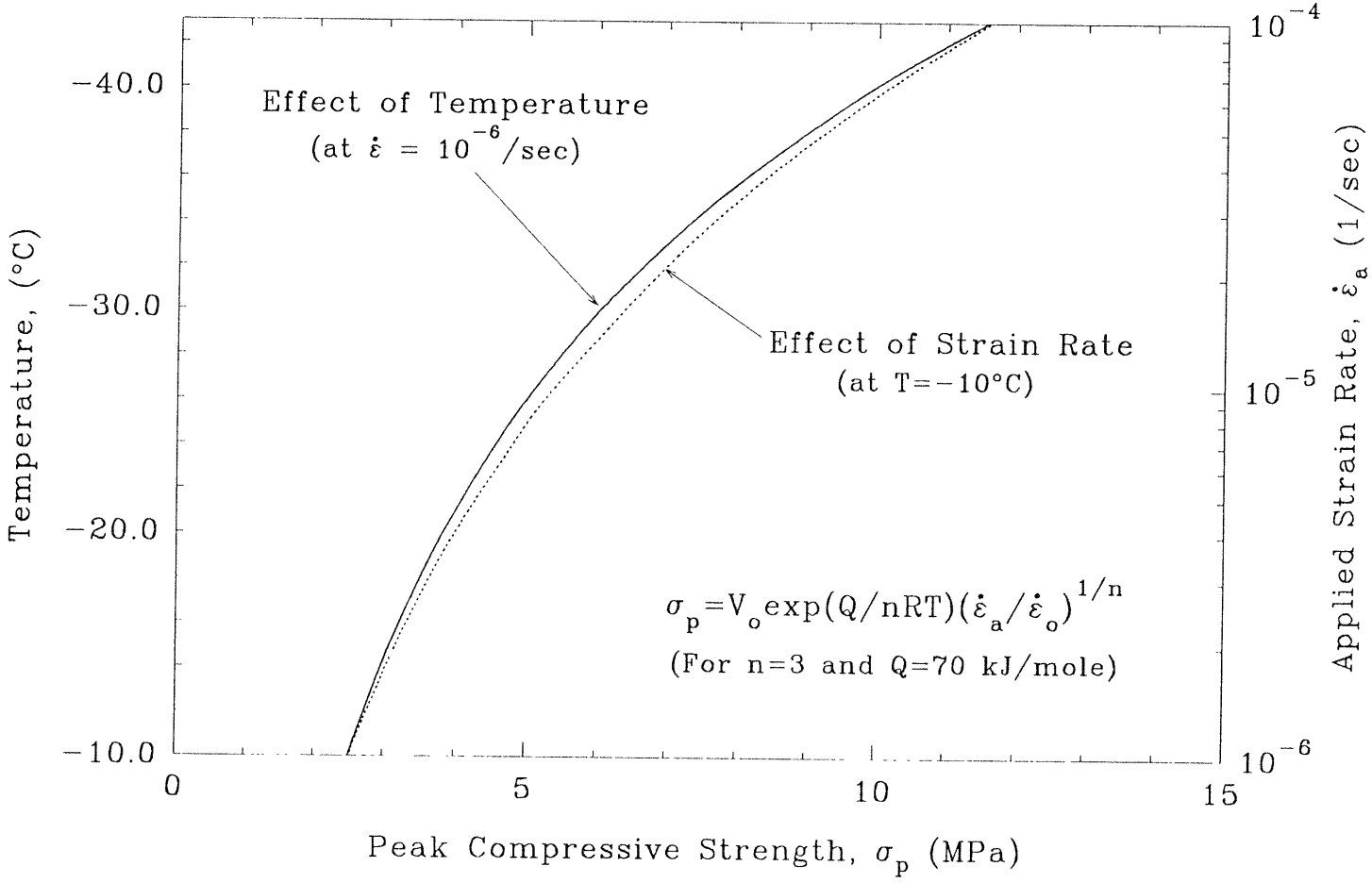

Figure 2.65 Effect of Temperature and Strain Rate on the Compressive Strength of Polycrystalline Ice Based on Glen's Creep Law

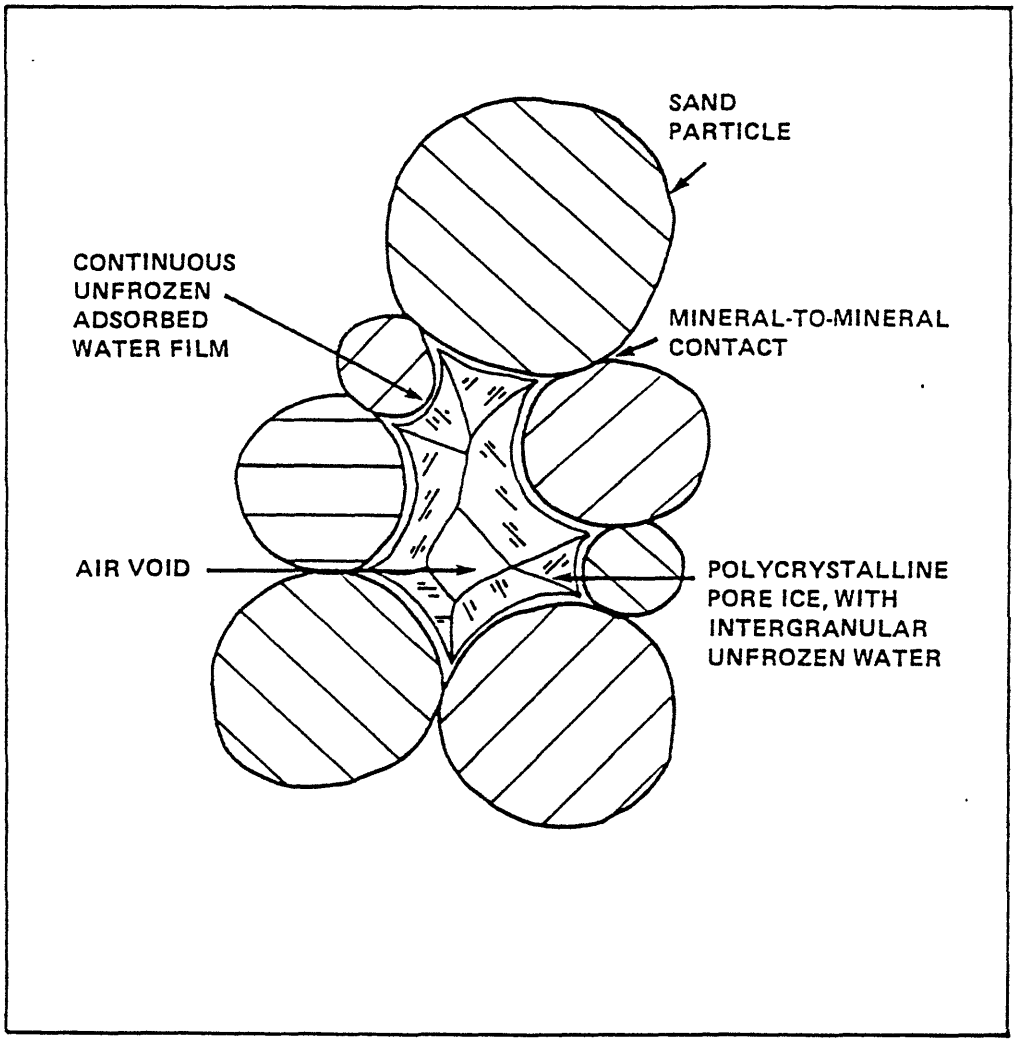

Figure 2.66 Proposed Structure of Frozen Sand (from Ting et al. 1983)

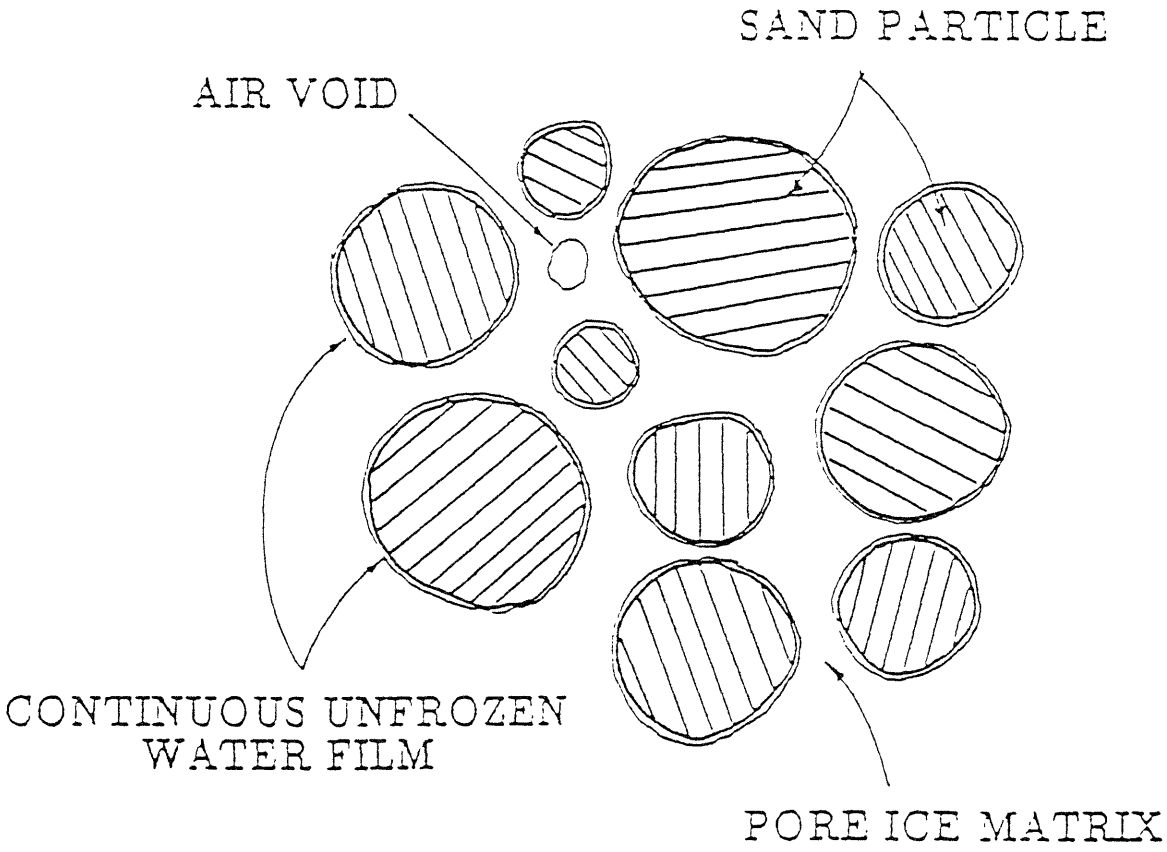

Figure 2.67 Alternative Structure of Frozen Sand (from Andersen 1991)

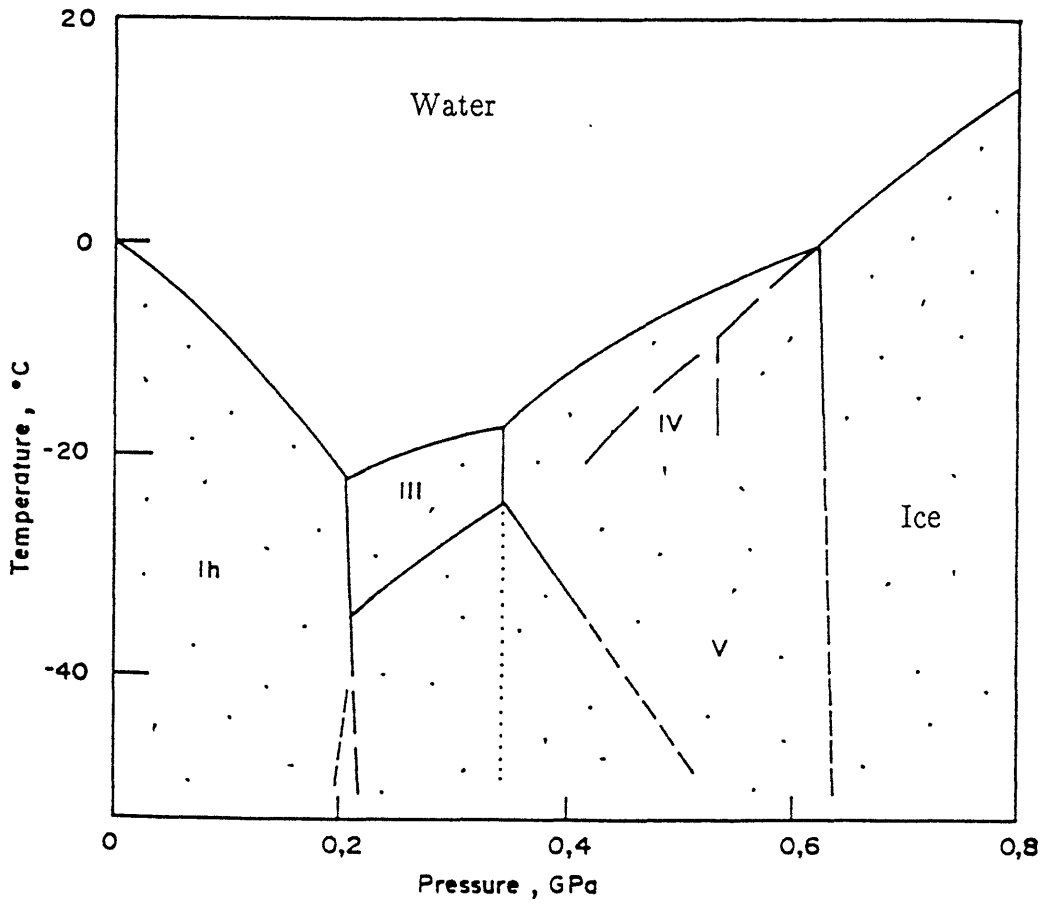

Figure 2.68 Phase Diagram for Water/Ice (from Nadreau and Michel 1986)

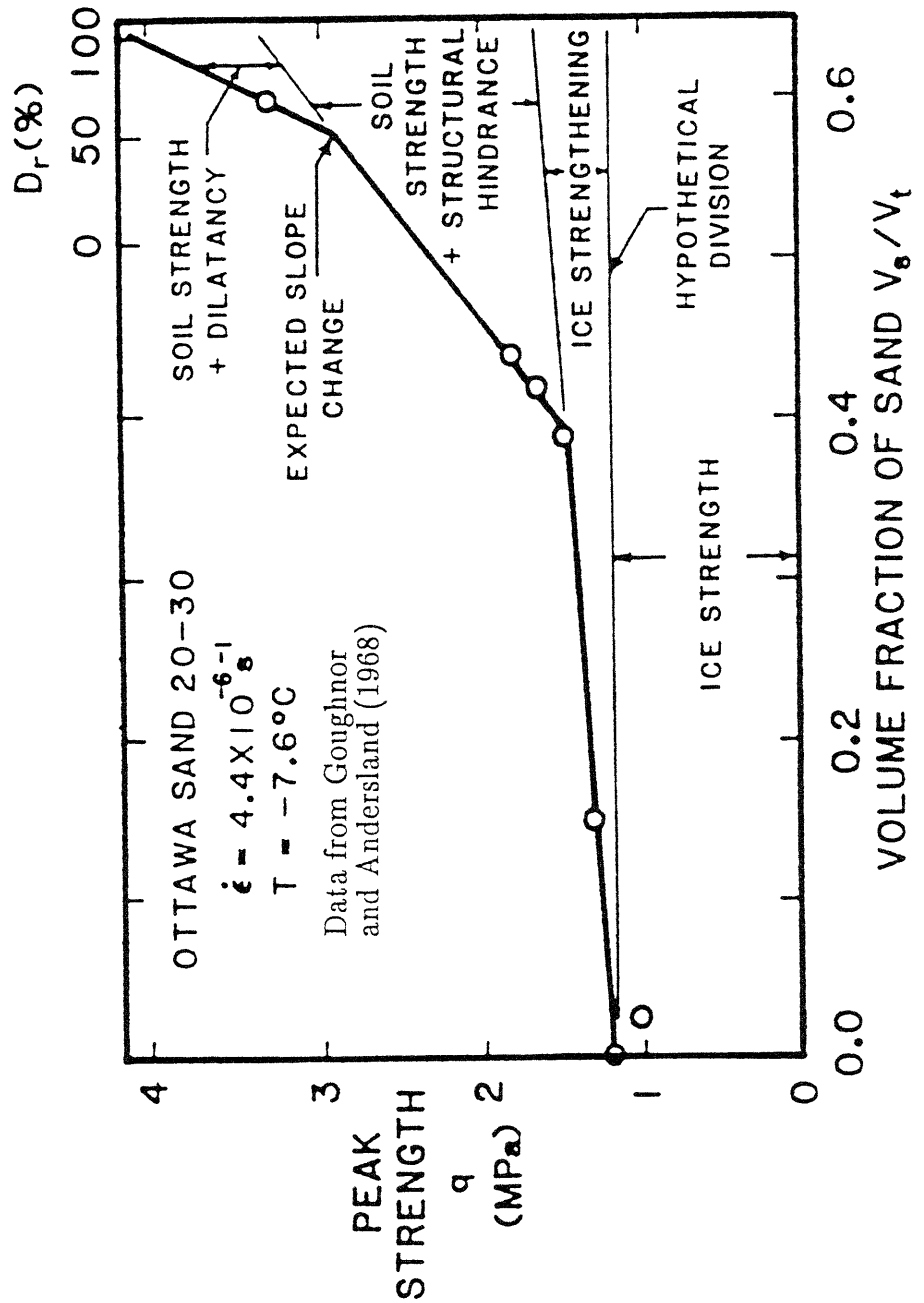

Figure 2.69 Proposed Mechanism Map for Unconfined Compressive Strength of Frozen Ottawa Sand (from Ting et al. 1983)

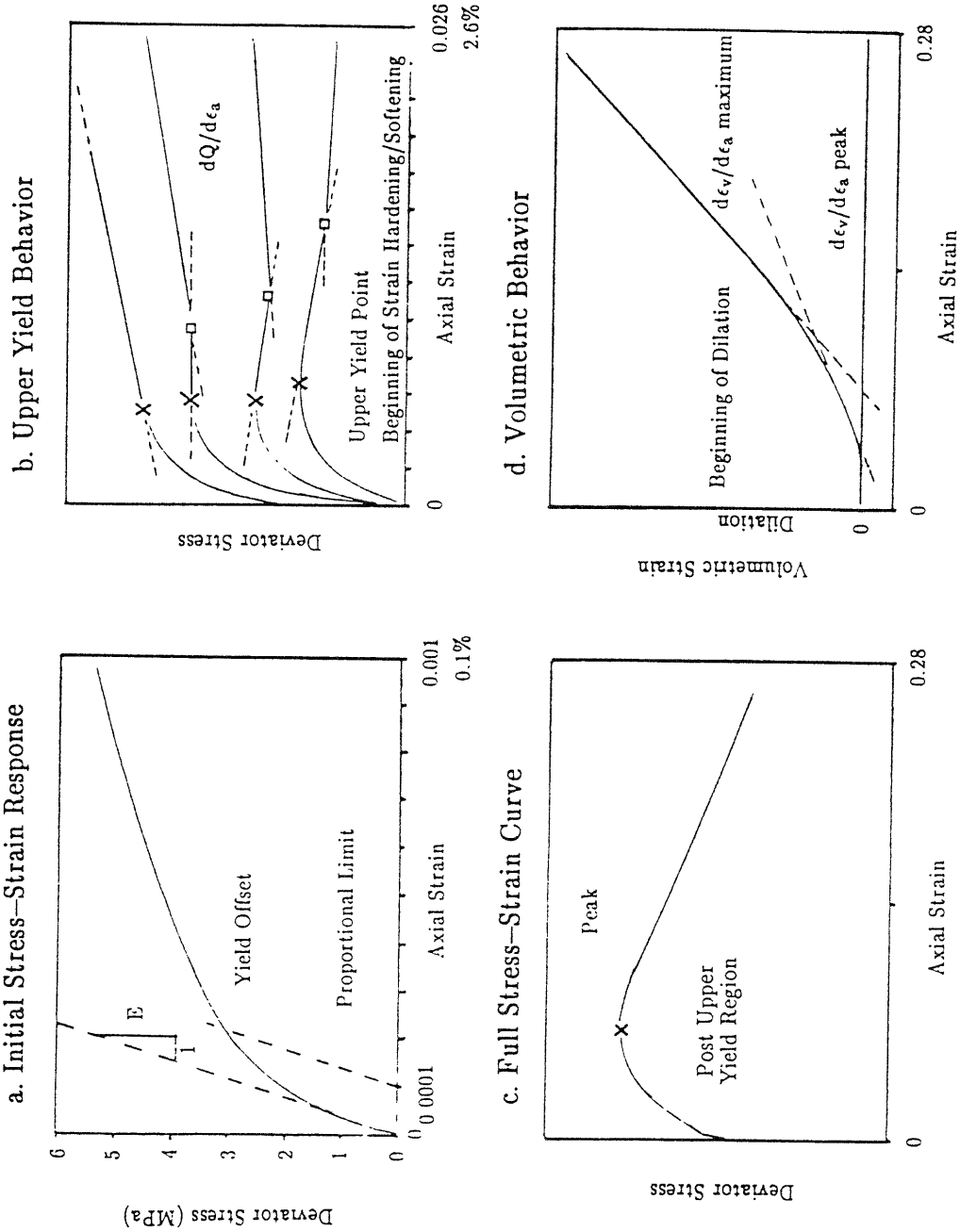

Figure 2.70 Idealized Stress–Strain and Volumetric Behavior for Frozen Manchester Fine Sand at −10°C (from Andersen et al. 1992)

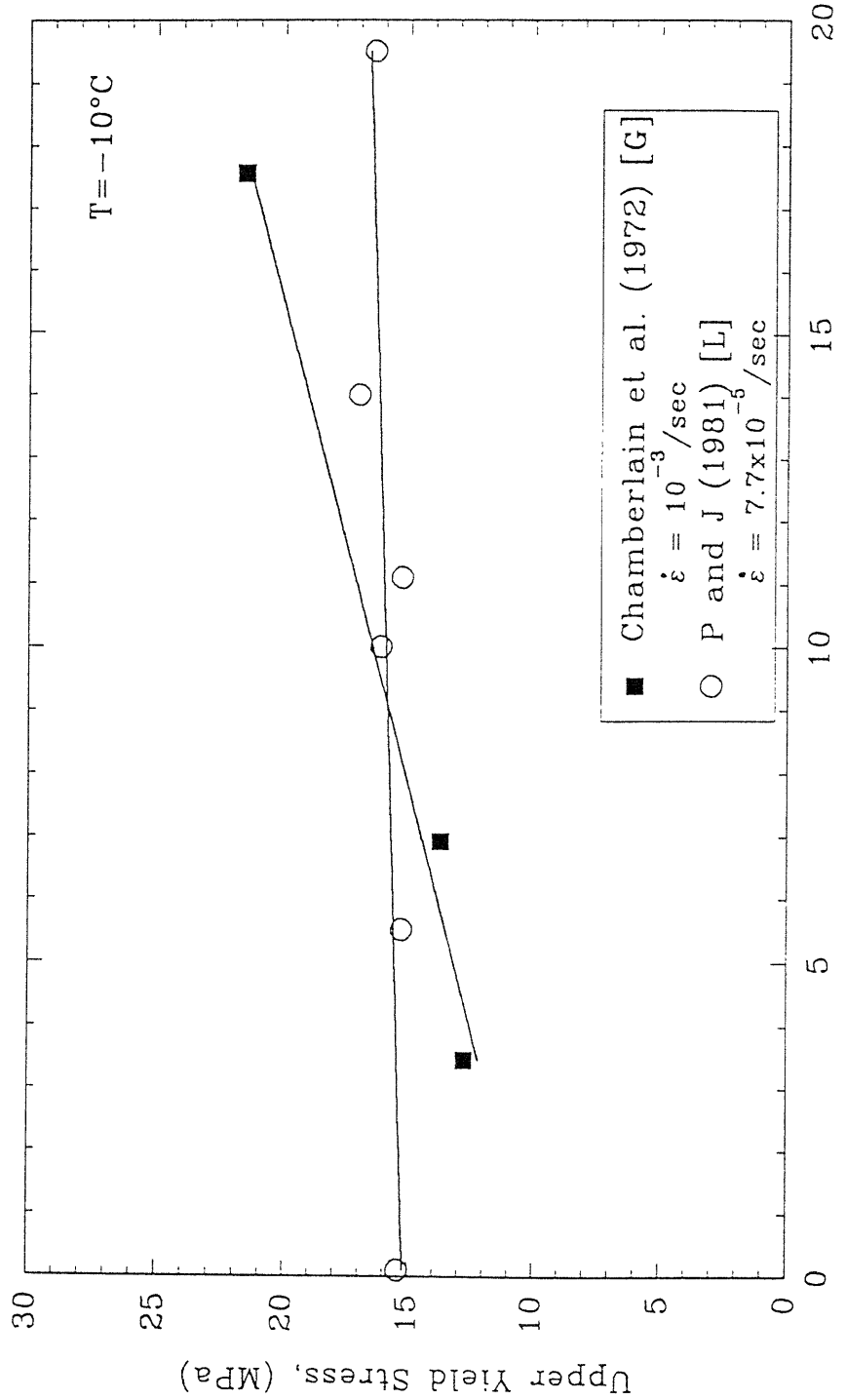

Figure 2.71 Variation in Upper Yield Stress with Confining Pressure for Uniform Ottawa Sand at −10°C

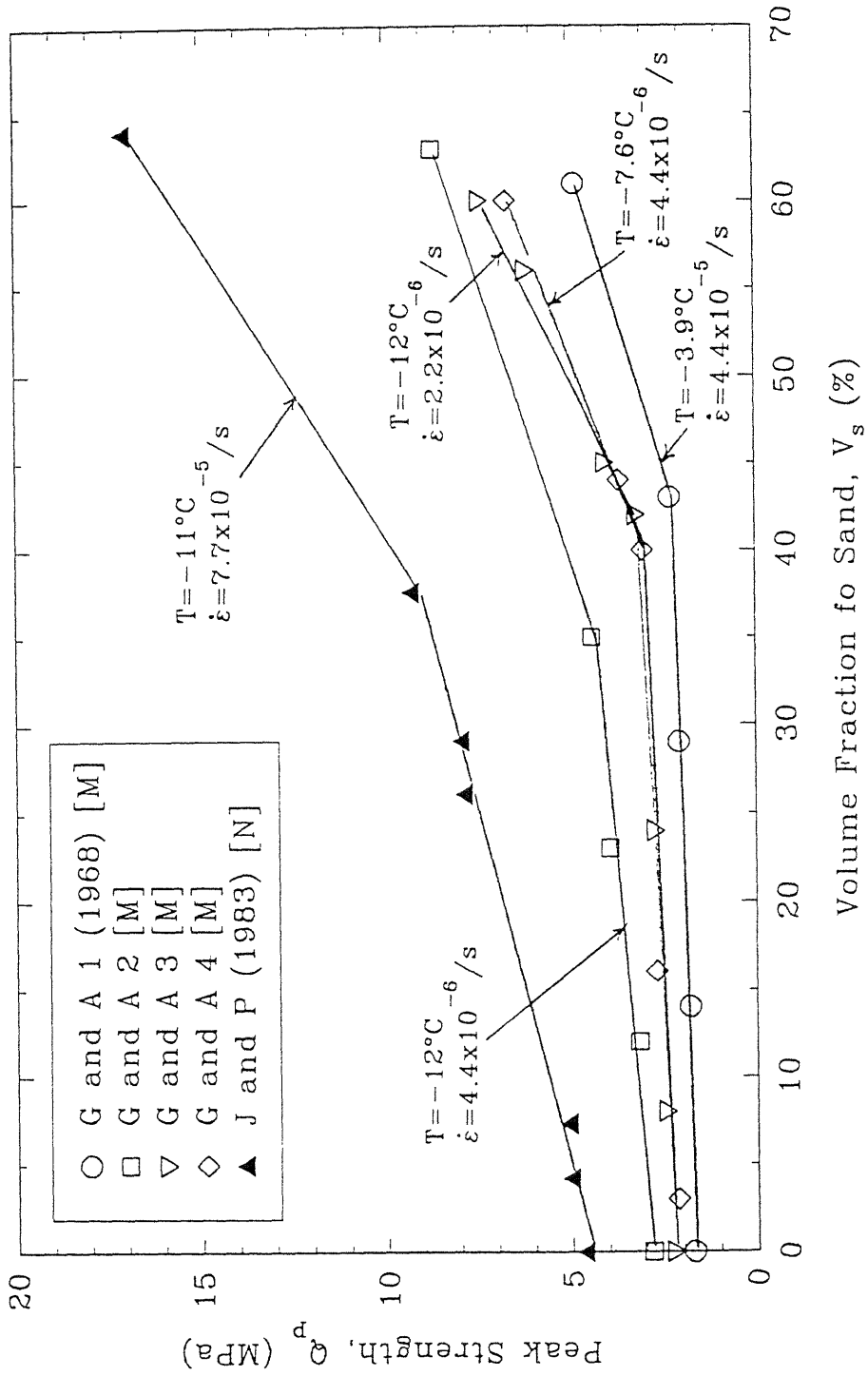

Figure 2.72 Peak Strength versus Volume Fraction of Sand

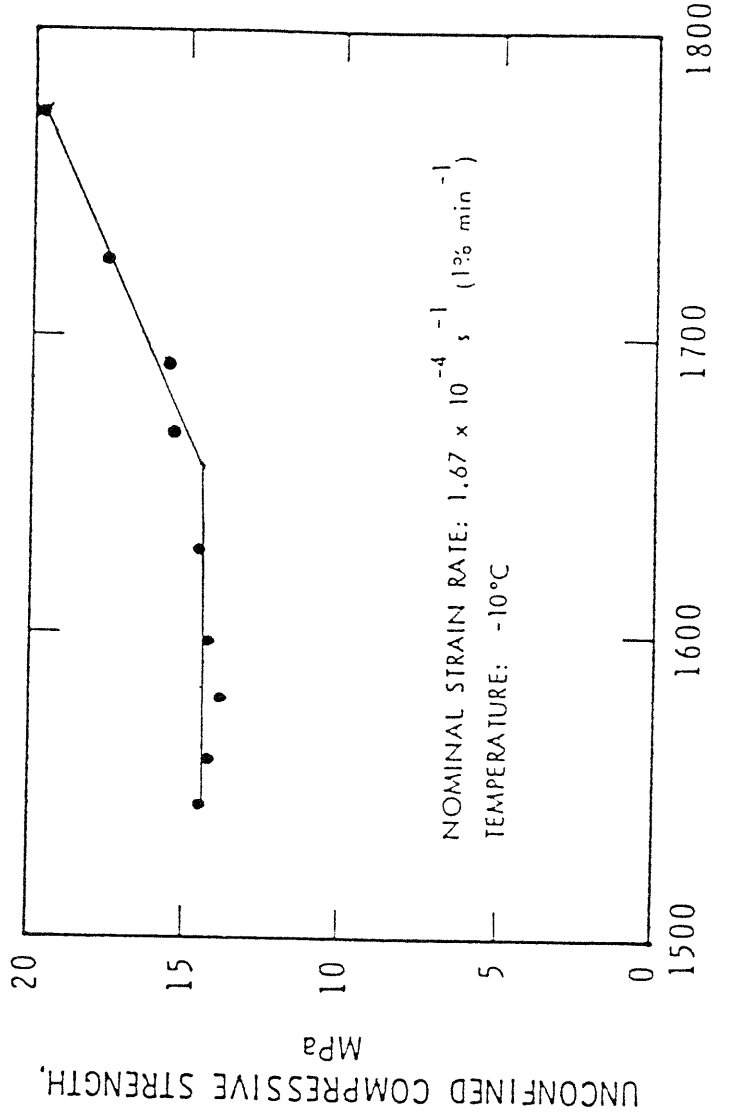

Figure 2.73 Peak Deviator Stress Versus Dry Density for Frozen Ottawa Sand (from Baker and Kurfurst 1985)

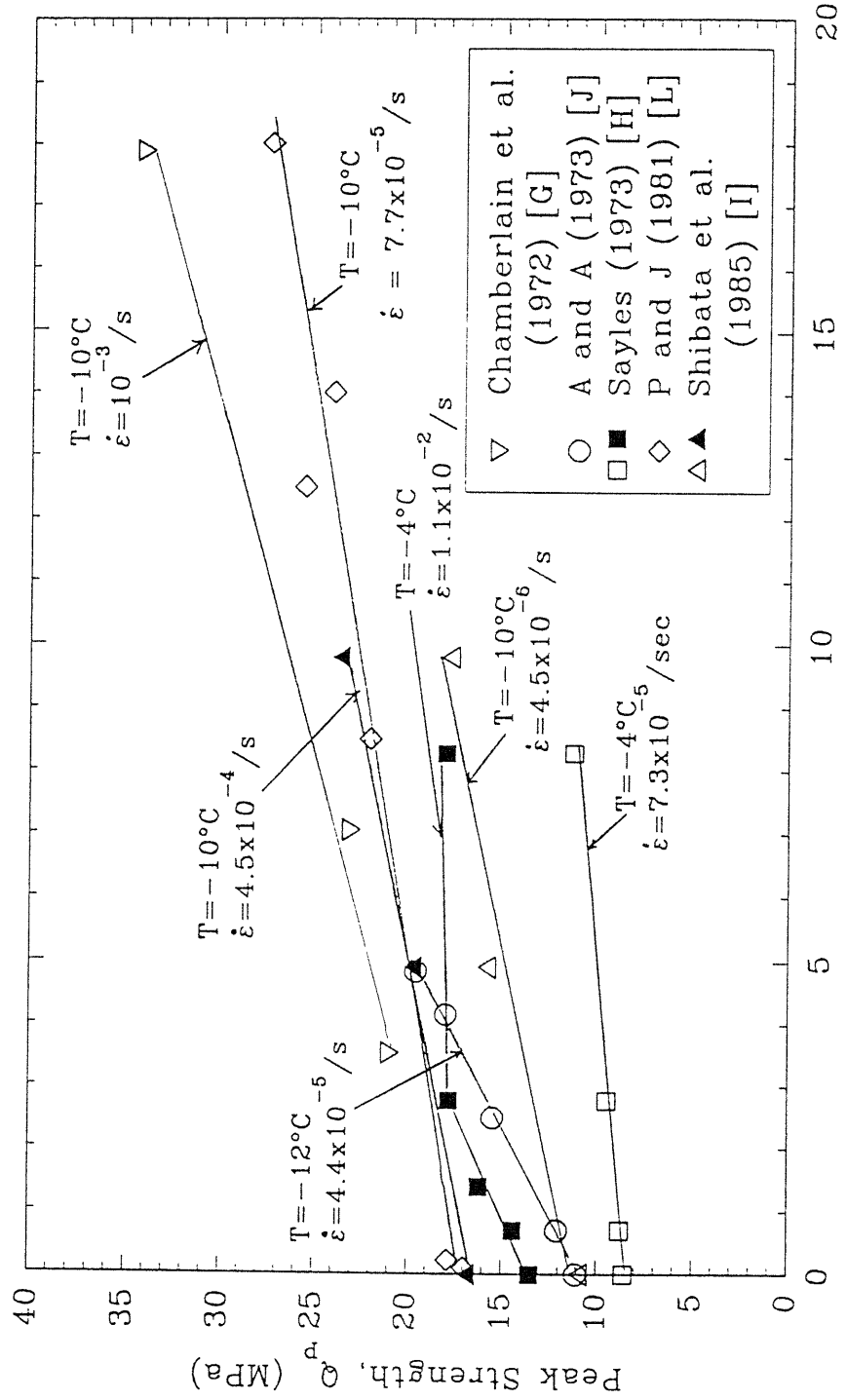

Figure 2.74 Peak Strength verus Confining Pressure for Tests on "Saturated" Dense Sands at Low to Moderate Confining Pressures

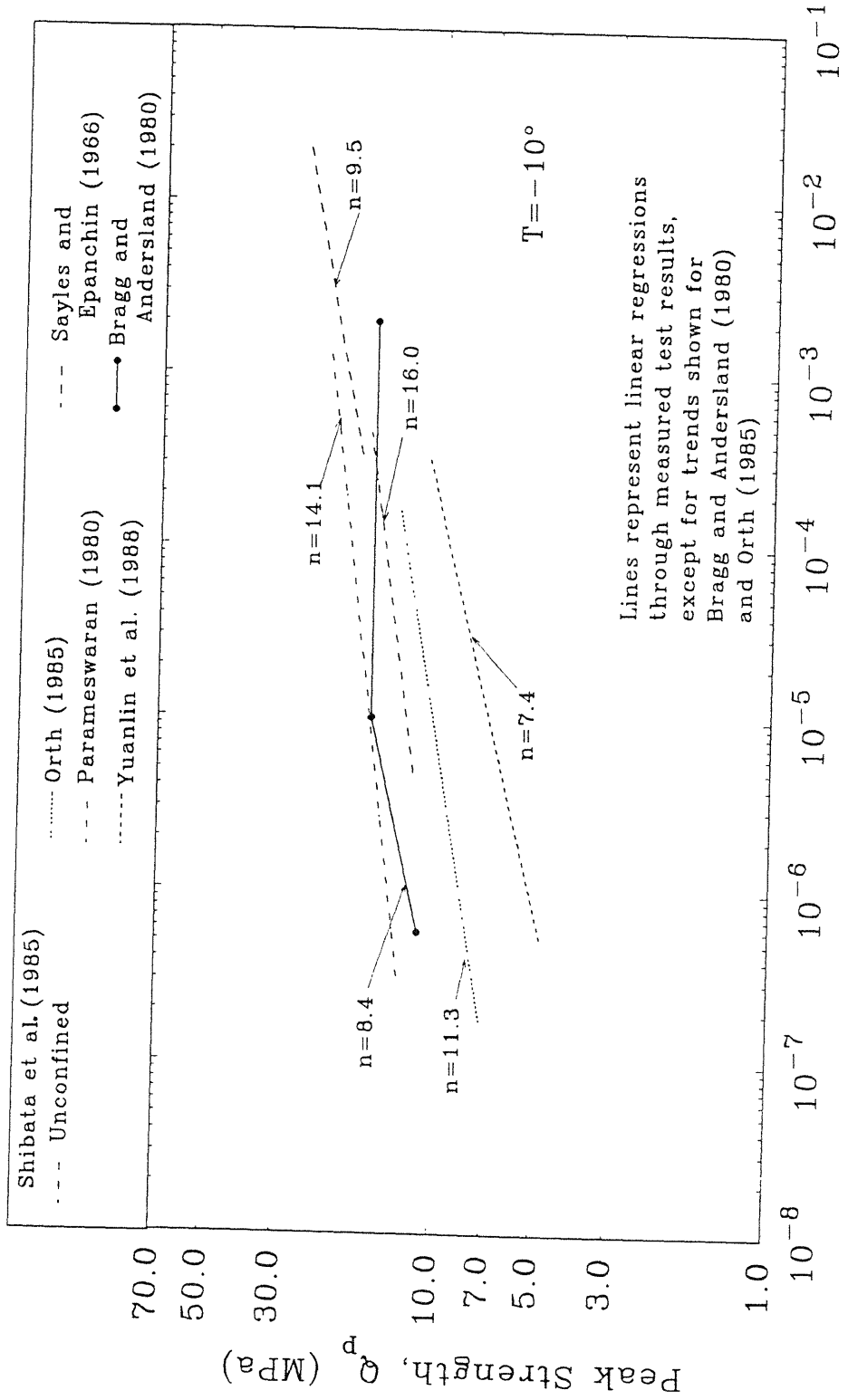

Figure 2.75 Effect of Strain Rate on the Unconfined Compressive Strength of Dense Sands at −10°C

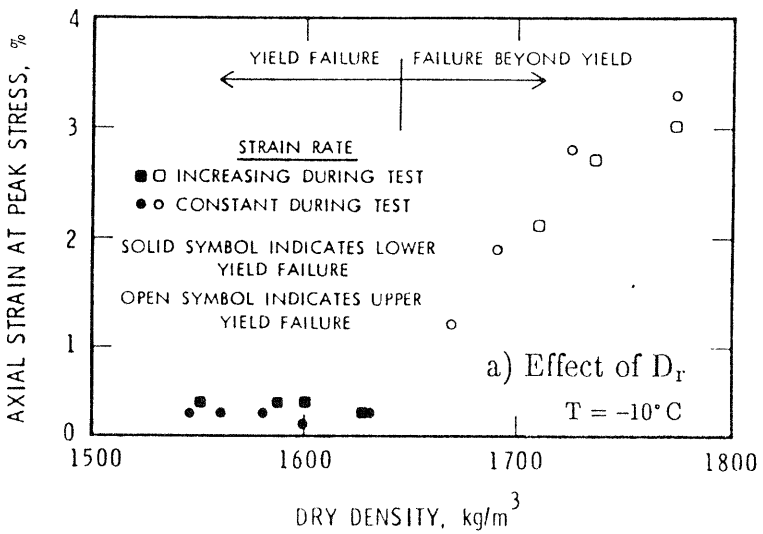

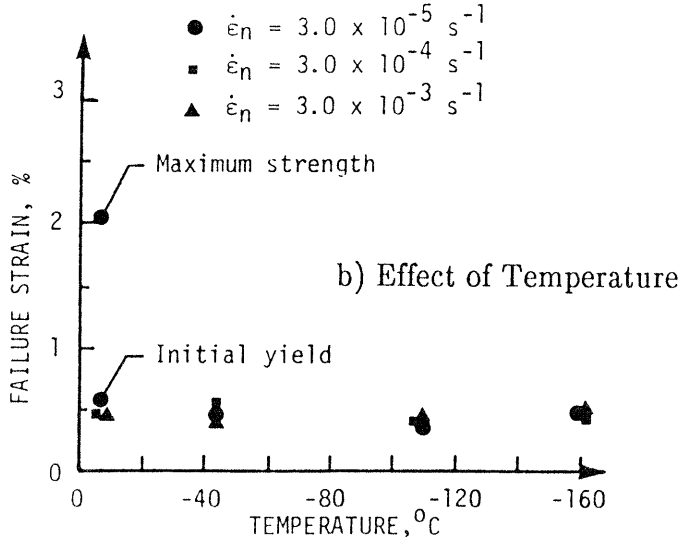

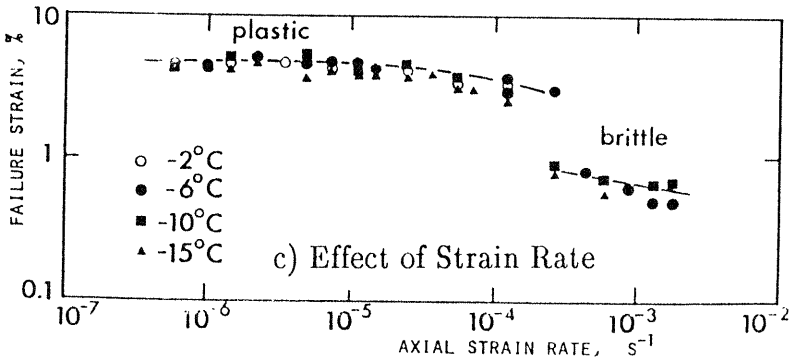

Figure 2.76 Failure Strain as a Function of a) Relative Density, b) Temperature and c) Strain Rate (from Baker and Kurfurst 1985, Bourbonnais and Ladanyi 1985, and Bragg and Andersland 1980)

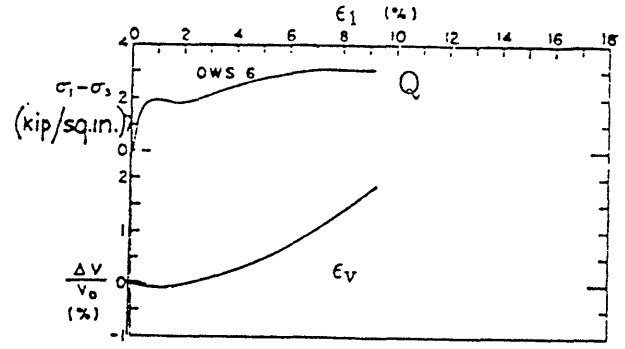

(a) $\sigma_c = 0.5$ ksi

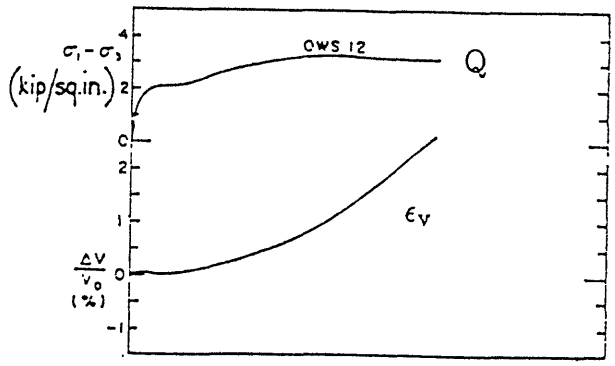

(b) $\sigma_c = 1.0$ ksi

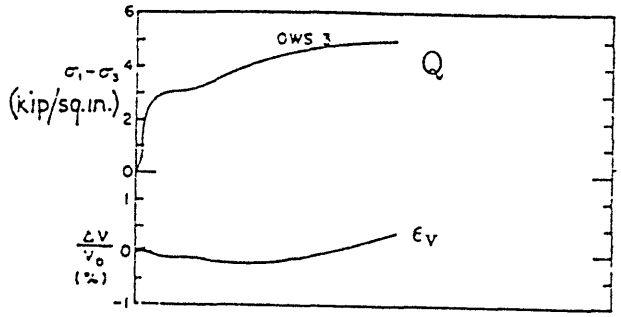

(c) $\sigma_c = 2.5$ ksi

$T = -10°C$

$\dot{\epsilon} = 10^{-3}$/sec

Figure 2.77 Stress–Strain and Volumetric Responses for Dense Frozen Ottawa Sand at Moderate Confining Pressure (from Chamberlain et al. 1972)

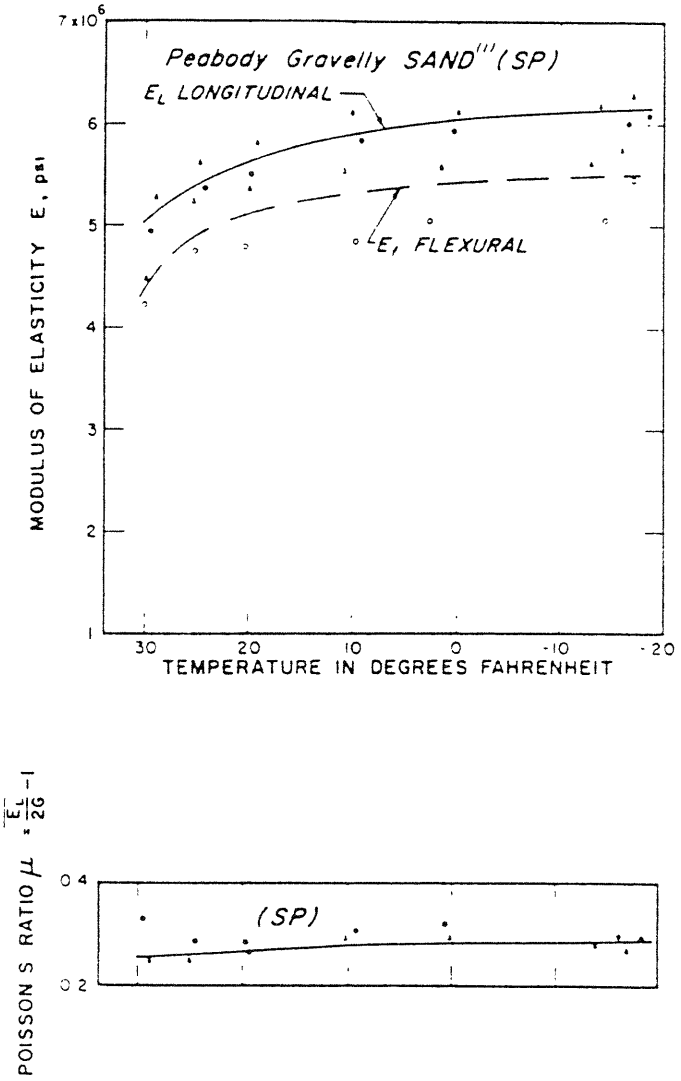

Figure 2.78 Young's Modulus and Poisson's Ratio for Peabody Gravelly Sand (from Kaplar 1963)

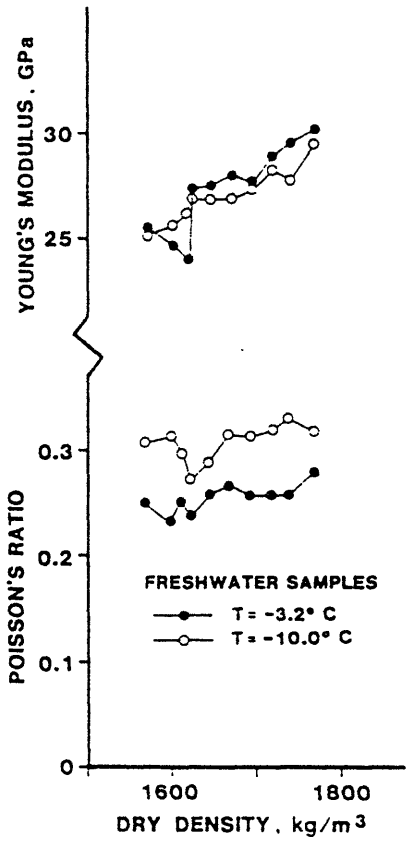

Figure 2.79 Young's Modulus and Poisson's Ratio for Ottawa 16–100 Sand in Freshwater (from Baker and Kurfurst 1985)

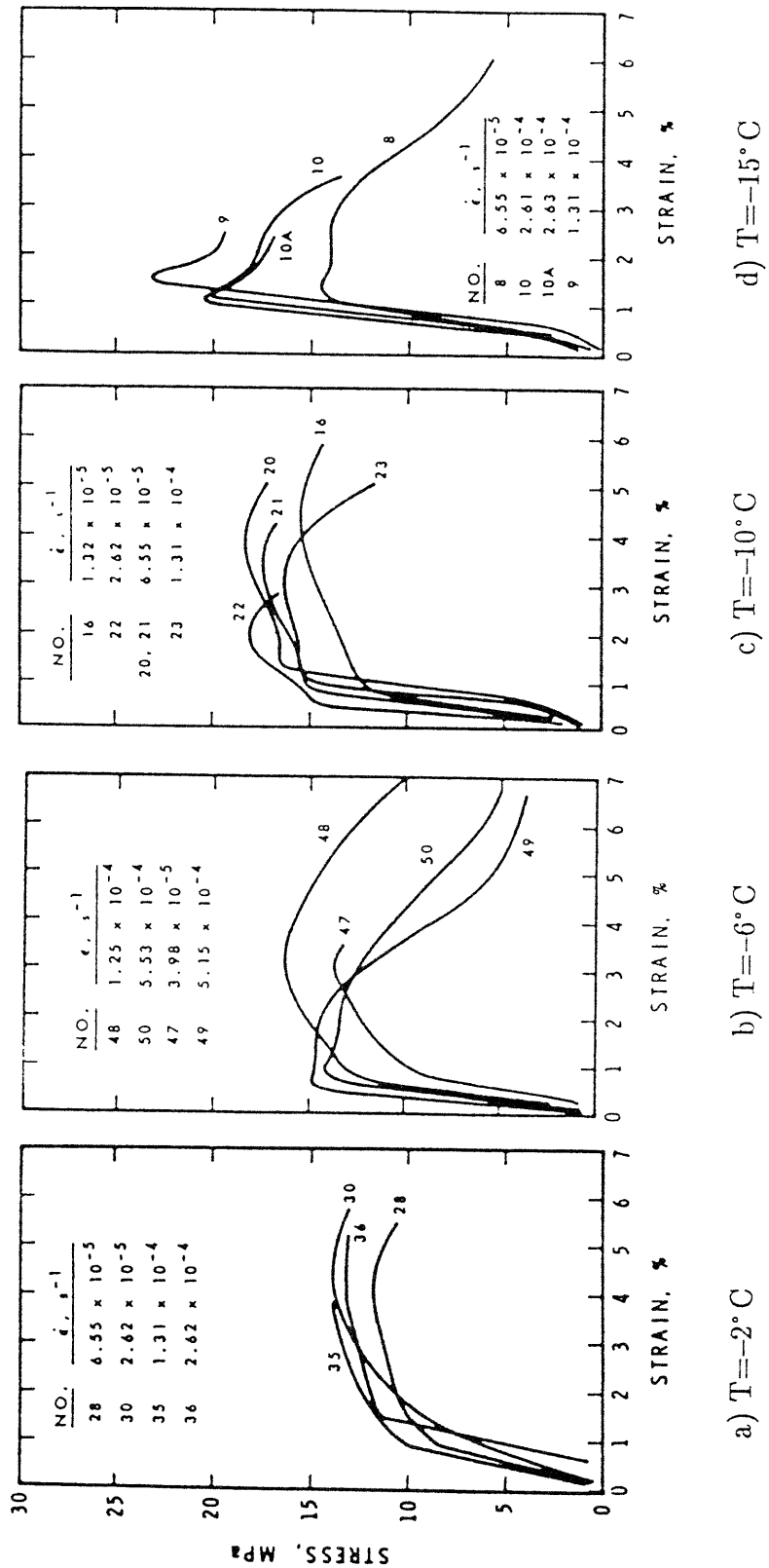

a) T=−2°C b) T=−6°C c) T=−10°C d) T=−15°C

Figure 2.80 Stress–Strain Curves for Unconfined Compression Tests on Frozen Dense Ottawa Sand at Temperatures from −2 to −15°C (from Parameswaran 1980)

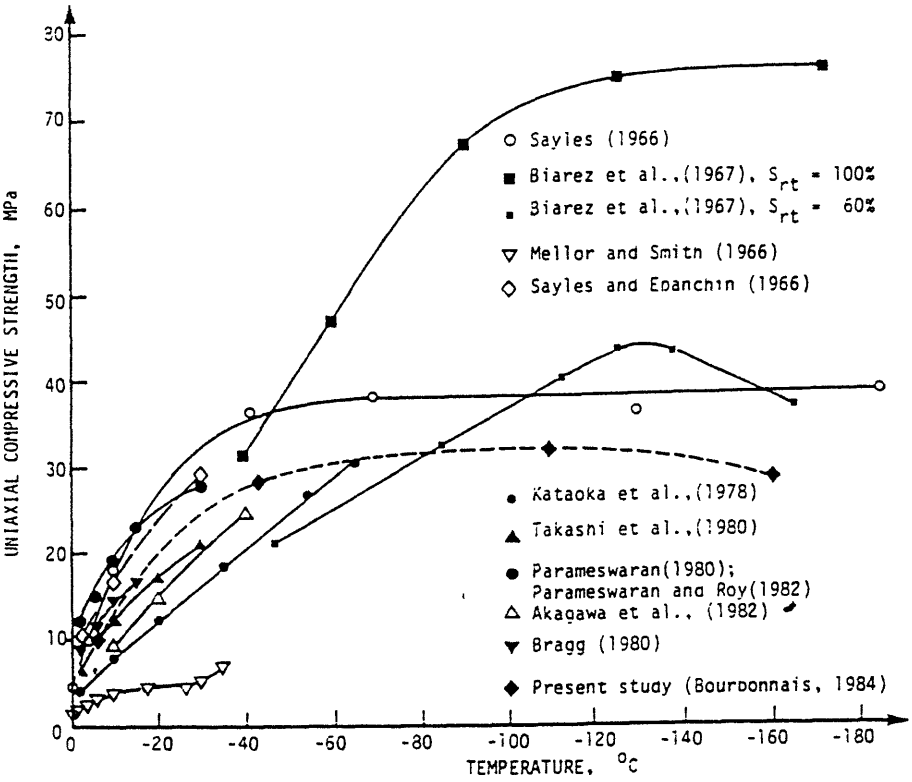

Author(s)	Sand Type	Grain size (%)				Dry Density	Total Water Content	Total Degree of Saturation	Loading Rate
		Clay <5μ	Silt 5-74μ	Fine sand 74-420μ	Sand 420-2000μ	g/cm³	(%)	(%)	
Sayles (1966)	Ottawa 20-30	-	-	-	100	1.65	21.2	100	5.1 mm/min 3%/min
Sayles and Epanchin (1966)	Ottawa C-109	-	-	70	30	1.71	18.8	100	2%/min
Mellor and Smith (1966)	Concrete	-	-	-	-	1.5	16.5	60-70	146 mm/min
Biarez et al. (1967)	Fontainebleau	-	-	-	-	-	-	60-100*	-
Kataoka et al. (1978)	-	-	-	100	-	1.5	29.6	100	1%/min
Takashi et al. (1980)	Toyoura	-	-	100	-	1.51	26	98	0.8%/min
Bragg (1980)	Wedron	-	-	91	9	1.69	19.3	98	0.7-3.5%/min
Parameswaran (1980) et Param. and Roy (1982)	Ottawa C-109	-	-	70	30	1.70	20.0	100	0.6-3.9%/min
Akagawa et al. (1982)	#S-5	1	2	54	43	1.52	25.4	95	1%/min
	#S-4	6	8	86	-	1.45	30.0	100	1%/min
	#S-1	-	1	97	2	1.47	30.4	100	1%/min
Present study Bourbonnais (1984)	Le Sueur ASTM-C-778	-	-	-	100	1.63	20.4	91.8	1.8%/min

* State (frozen or unfrozen) for which the physical properties are supplied by the author is uncertain
Note: For all other cases, properties correspond to the frozen state.

Figure 2.81 Unconfined Compressive Strength versus Temperature for Several Frozen Granular Materials (from Bourbonnais and Ladanyi 1985)

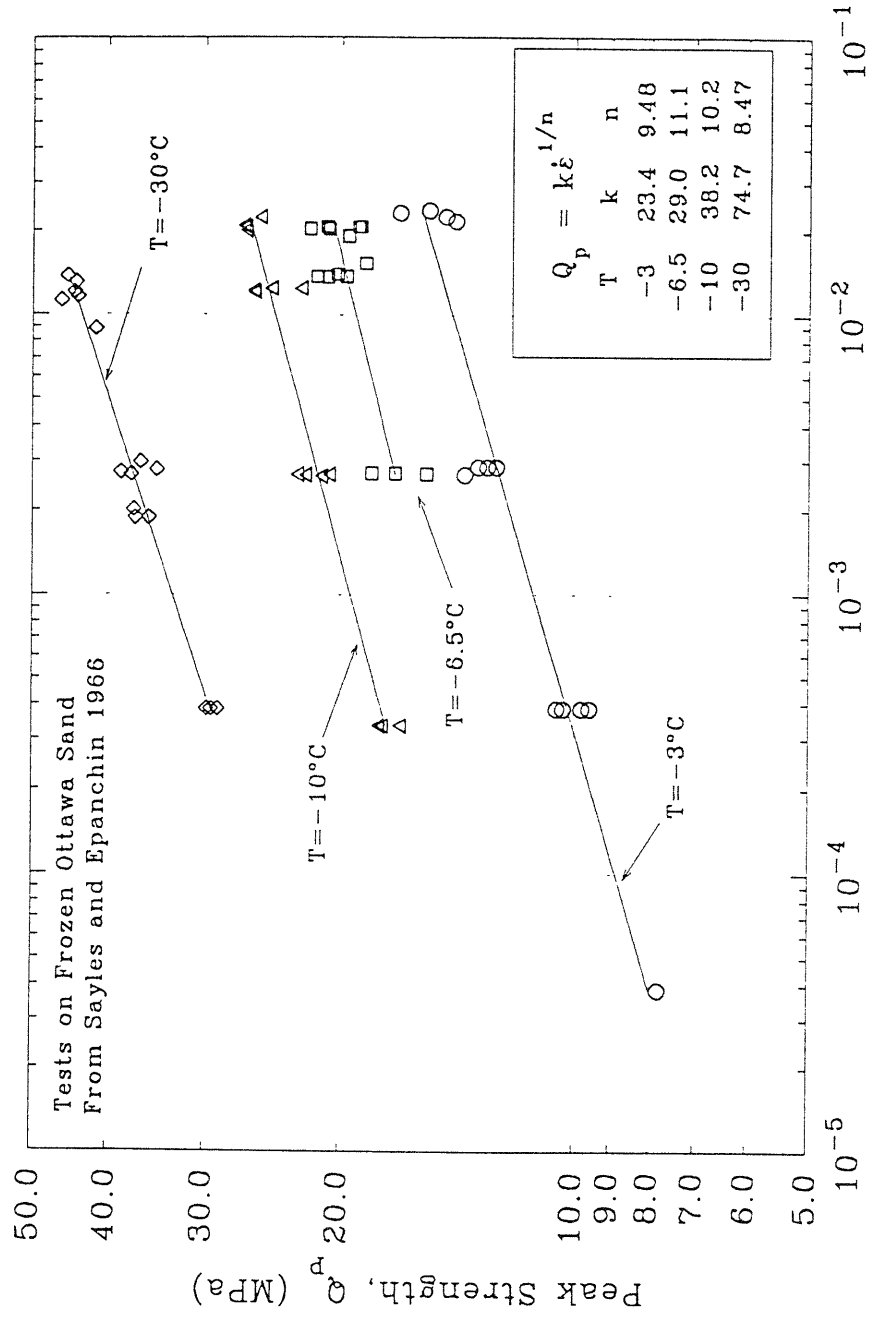

Figure 2.82 Unconfined Compressive Peak Strength versus Applied Strain Rate for Frozen Ottawa Sand at Temperatures from −2 to to −30°C (tests by Sayles and Epanchin, 1966)

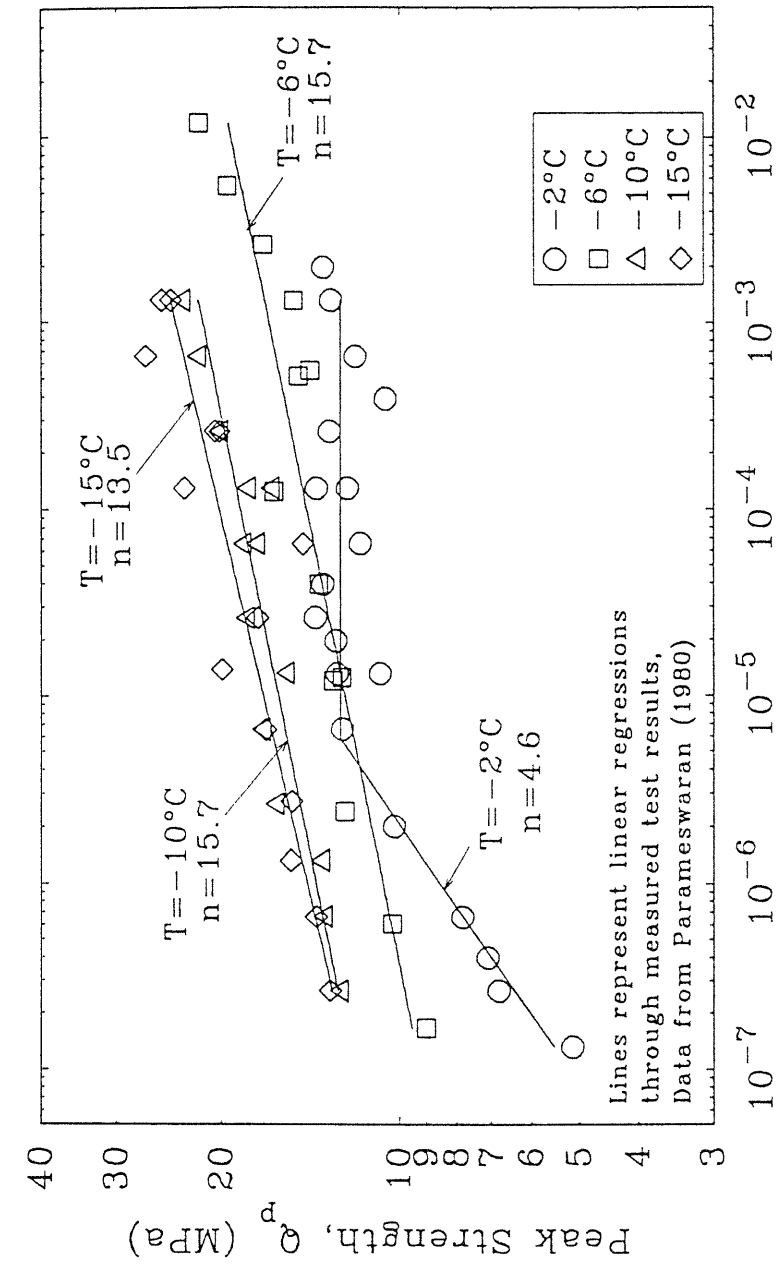

Figure 2.83 Unconfined Compressive Strength versus Applied Strain Rate for Dense Frozen Ottawa Sand at Temperatatures from −2 to to −15°C (Data from Parameswaran, 1980)

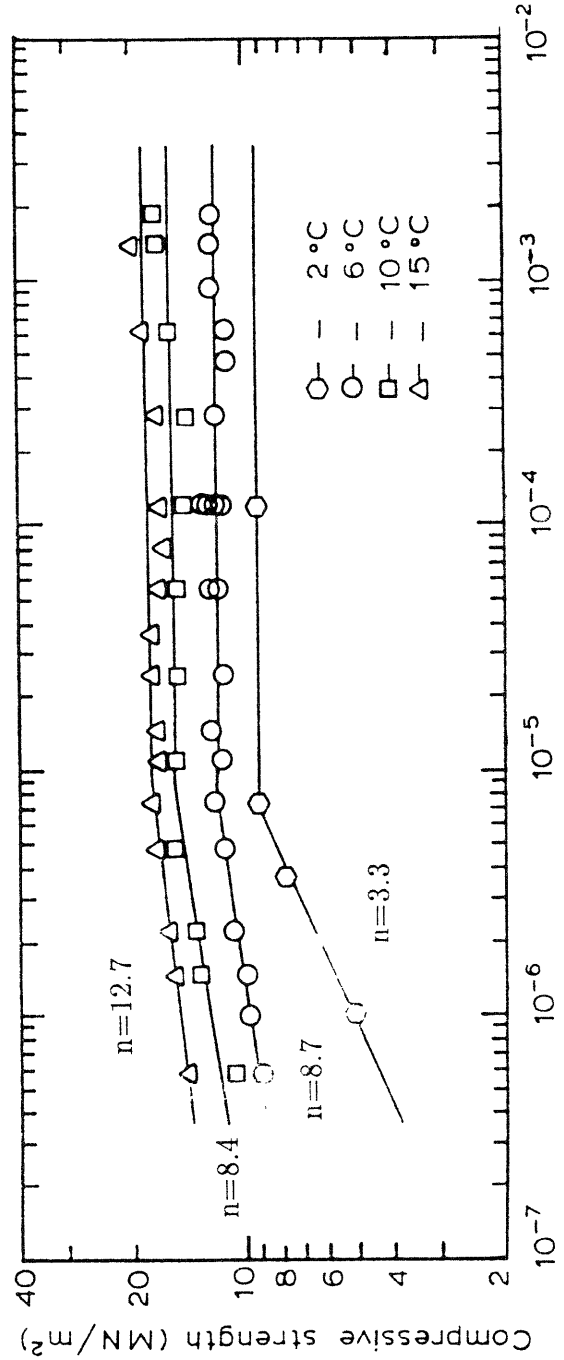

Figure 2.84 Unconfined Compressive Peak Strength versus Applied Strain Rate for Tests on Frozen Silica Sand at Temperature from −2 to −15°C (from Bragg and Andersland 1980)

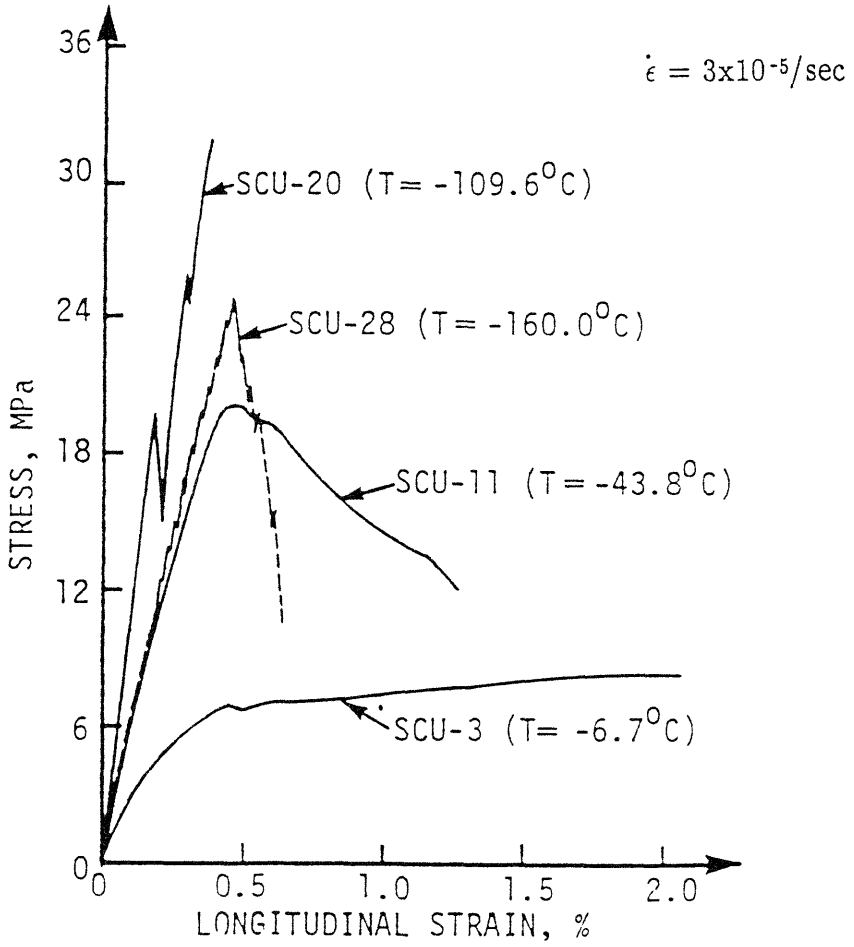

Figure 2.85 Stress–Strain Curves for Unconfined Compression Tests on Frozen Ottawa Sand at Temperatures from –6.7 to –160° C (from Bourbonnais and Ladanyi 1985)

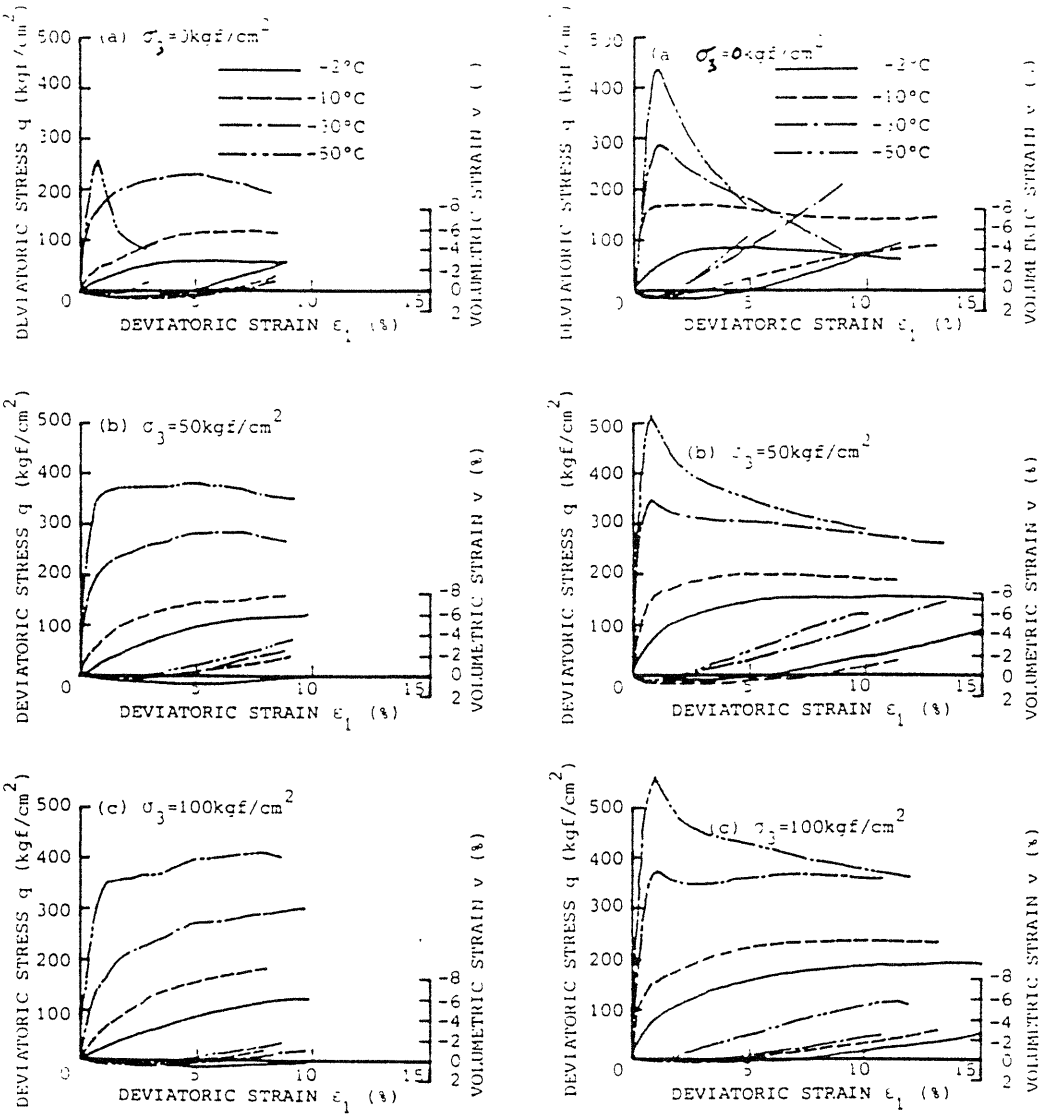

a) $\dot{\epsilon} = 0.027\%/\text{min} = 4.5\text{x}10^{-6}/\text{sec}$

b) $\dot{\epsilon} = 2.7\%/\text{min} = 4.5\text{x}10^{-4}/\text{sec}$

Figure 2.86 Stress–Deviatoric Strain Curves for Frozen Toyoura Sand at Temperatures from –2 to –50° C (from Shibata et al. 1985)

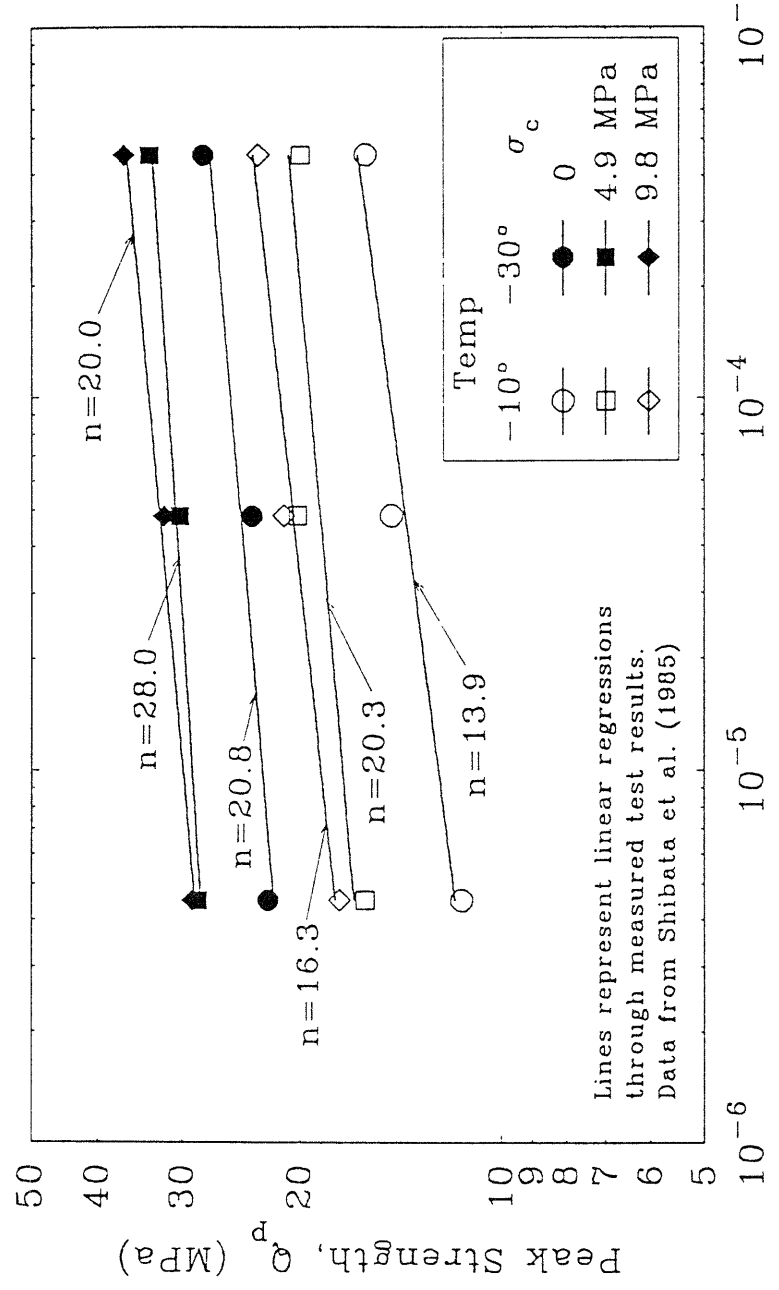

Figure 2.87 Compressive Peak Strength versus Applied Strain Rate for Dense Frozen Toyoura Sands at Temperatatures from −2 to −50°C

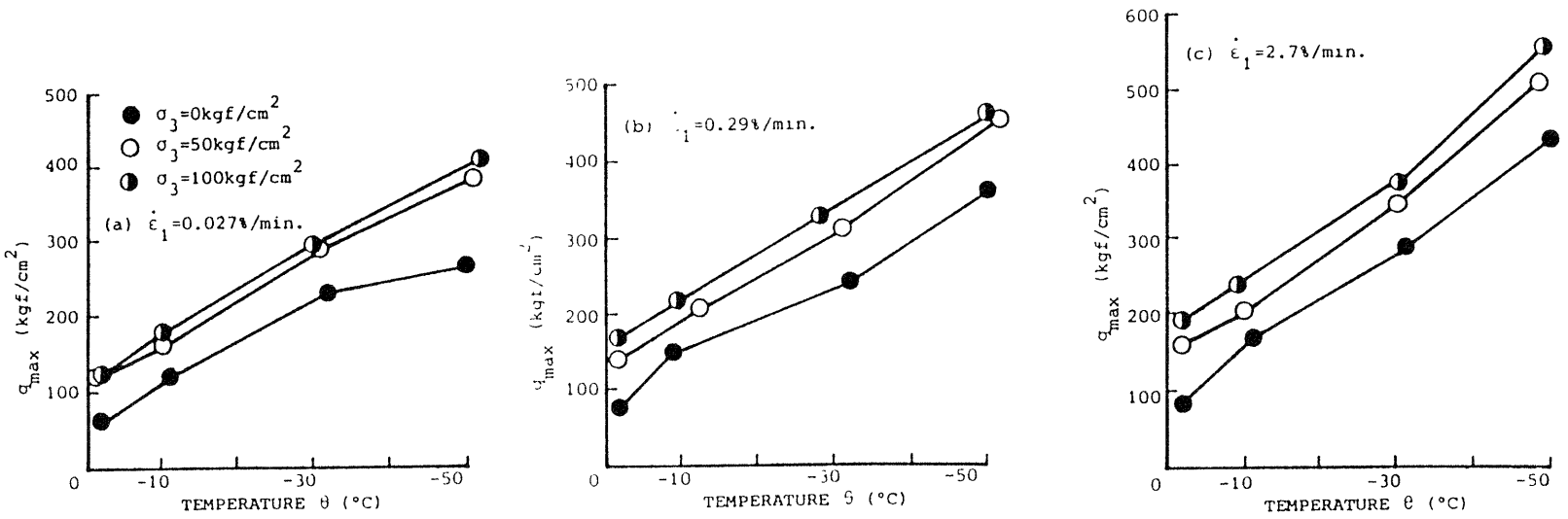

Figure 2.88 Effect of Temperature on Measured Peak Strength of Frozen Toyoura Sand (from Shibata et al. 1985)

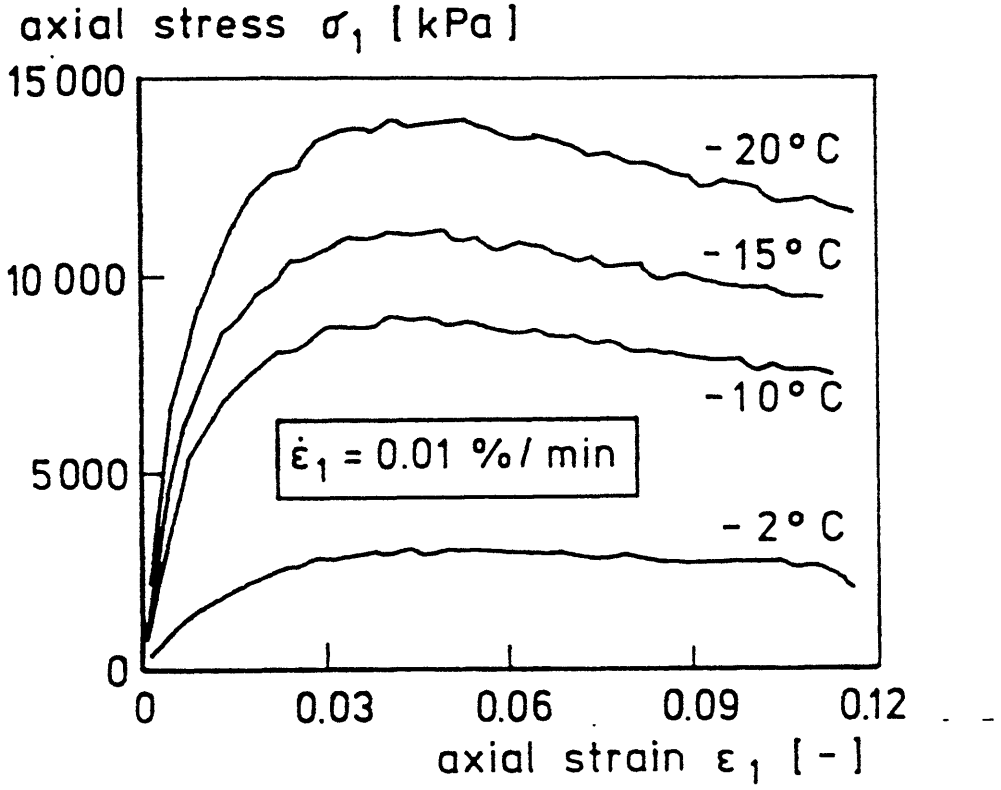

Figure 2.89 Stress–Strain Curves from Unconfined Compression Tests on Frozen Karlsrude Sand at Temperature from –2 to –20° C (from Orth 1985)

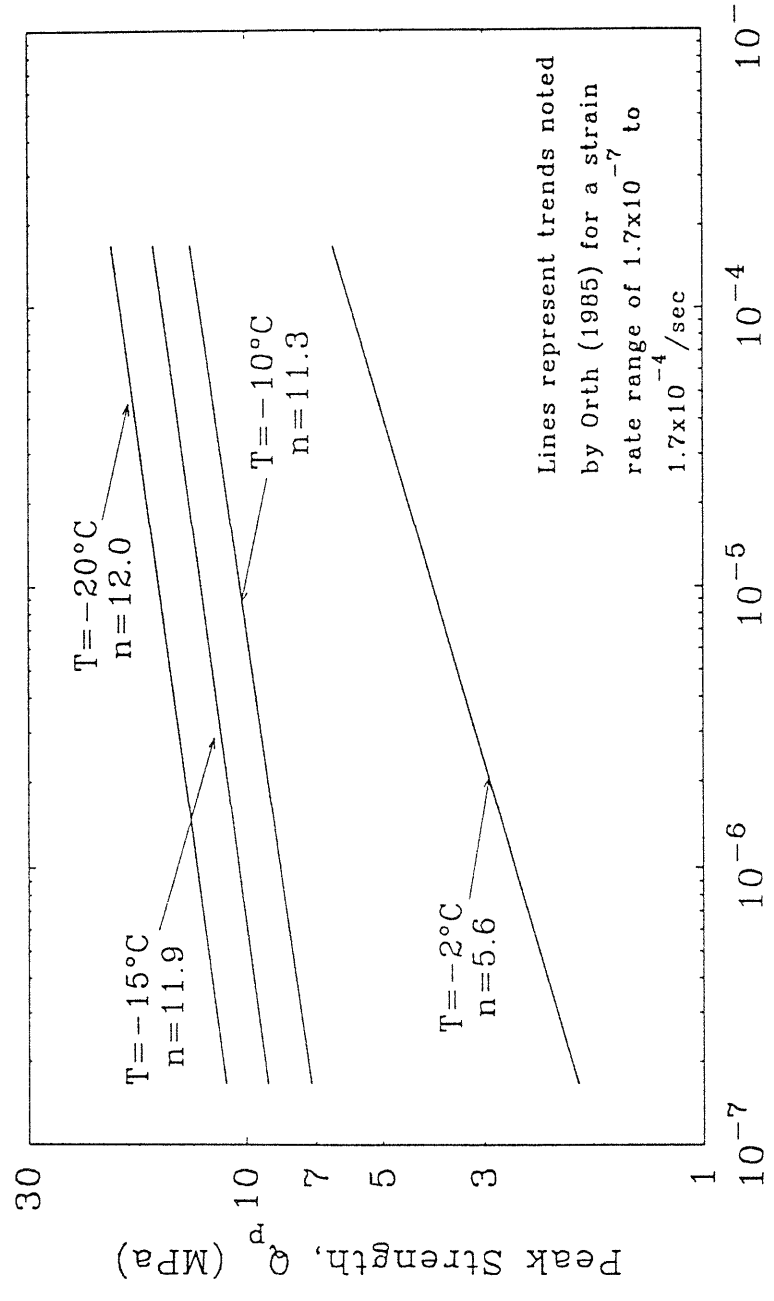

Figure 2.90 Unconfined Compressive Strength versus Applied Strain Rate for Frozen Karlsrude Sand at Temperatures from −2 to −20°C

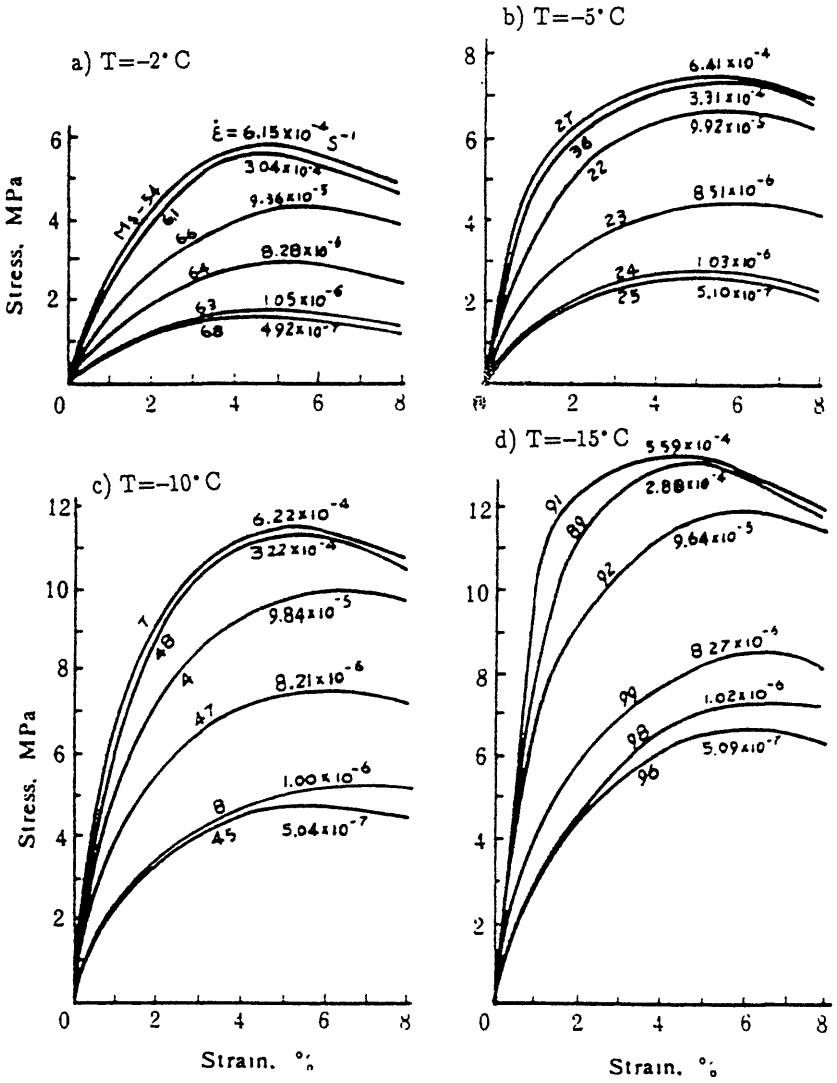

Figure 2.91 Stress–Strain Curves from Unconfined Compression Tests on Frozen Lanzhau Sand at Temperatures from –2 to –15° C (from Yuanlin et al. 1988)

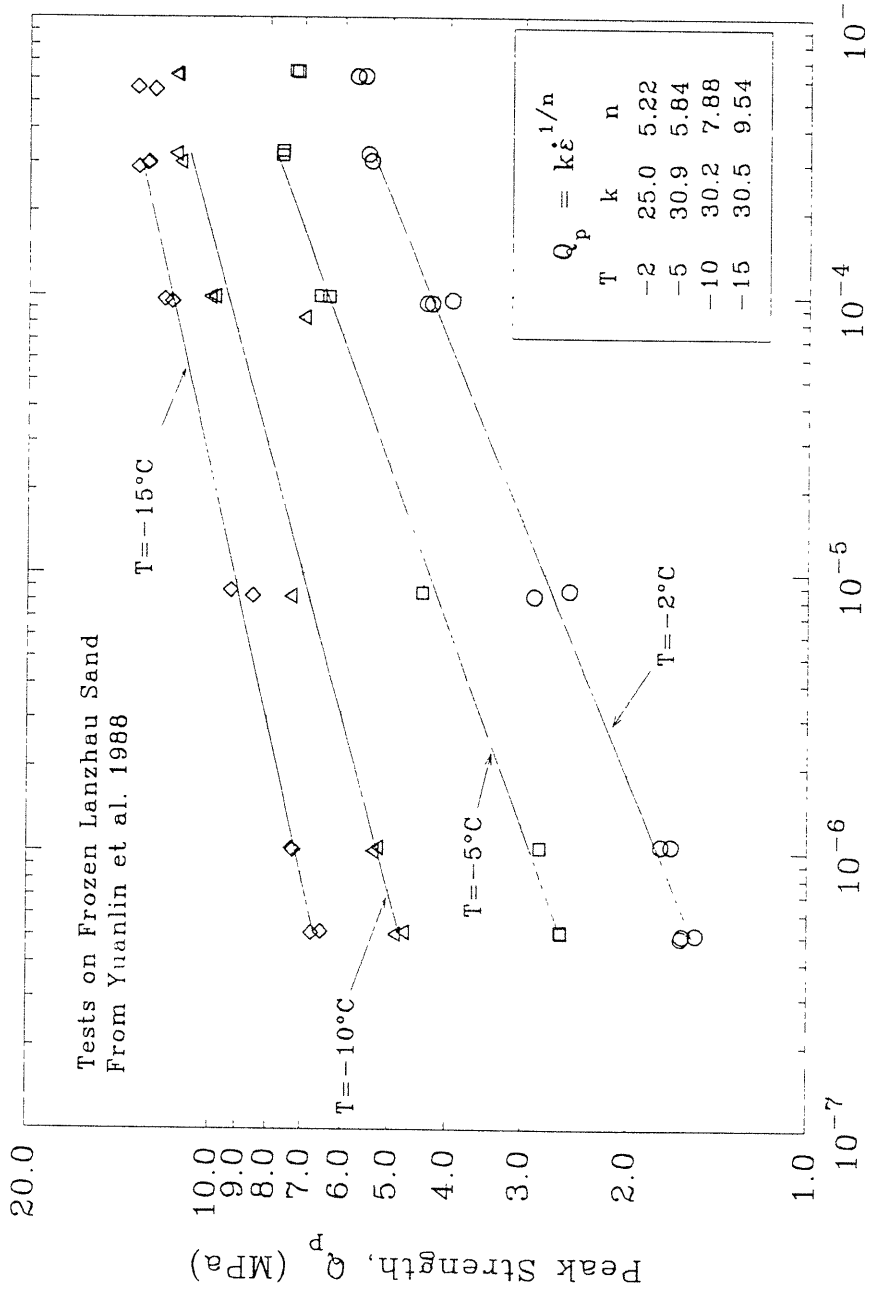

Figure 2.92 Unconfined Compressive Peak Strength versus Applied Strain Rate for Frozen Lanzhau Sand at Temperatures from −2 to −15°C (tests by Yuanlin et al. 1988)

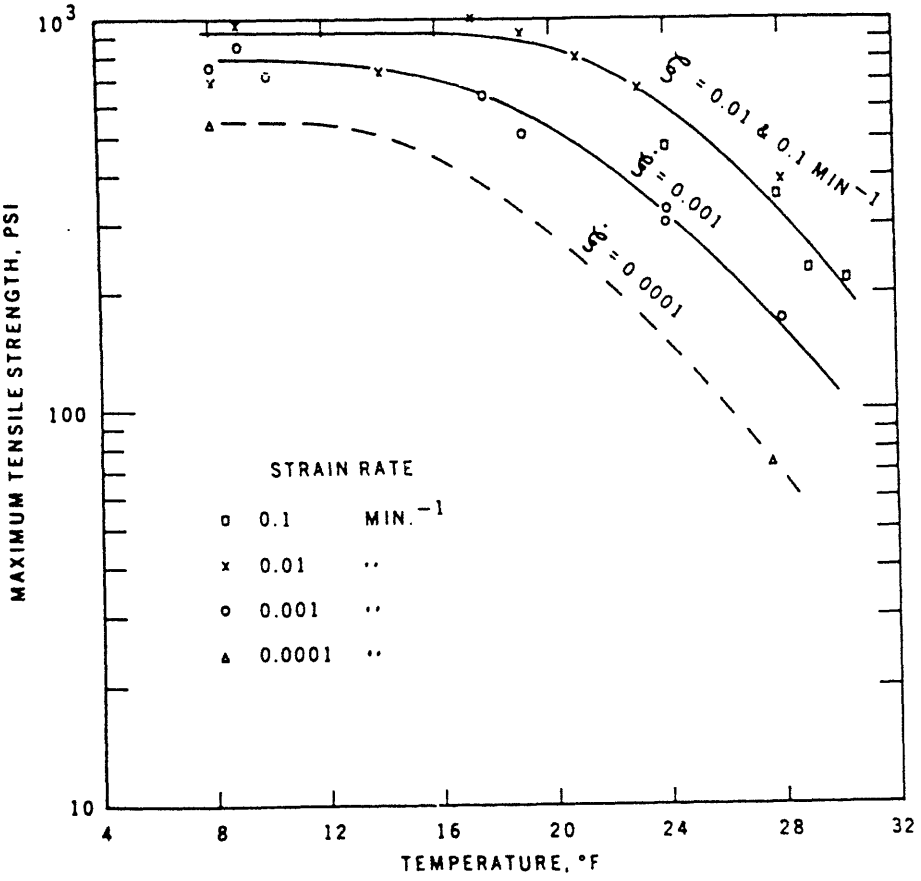

Figure 2.93 Uniaxial Tensile Strength of Frozen Dense Penn Sand (from Perkins and Reudrich 1973)

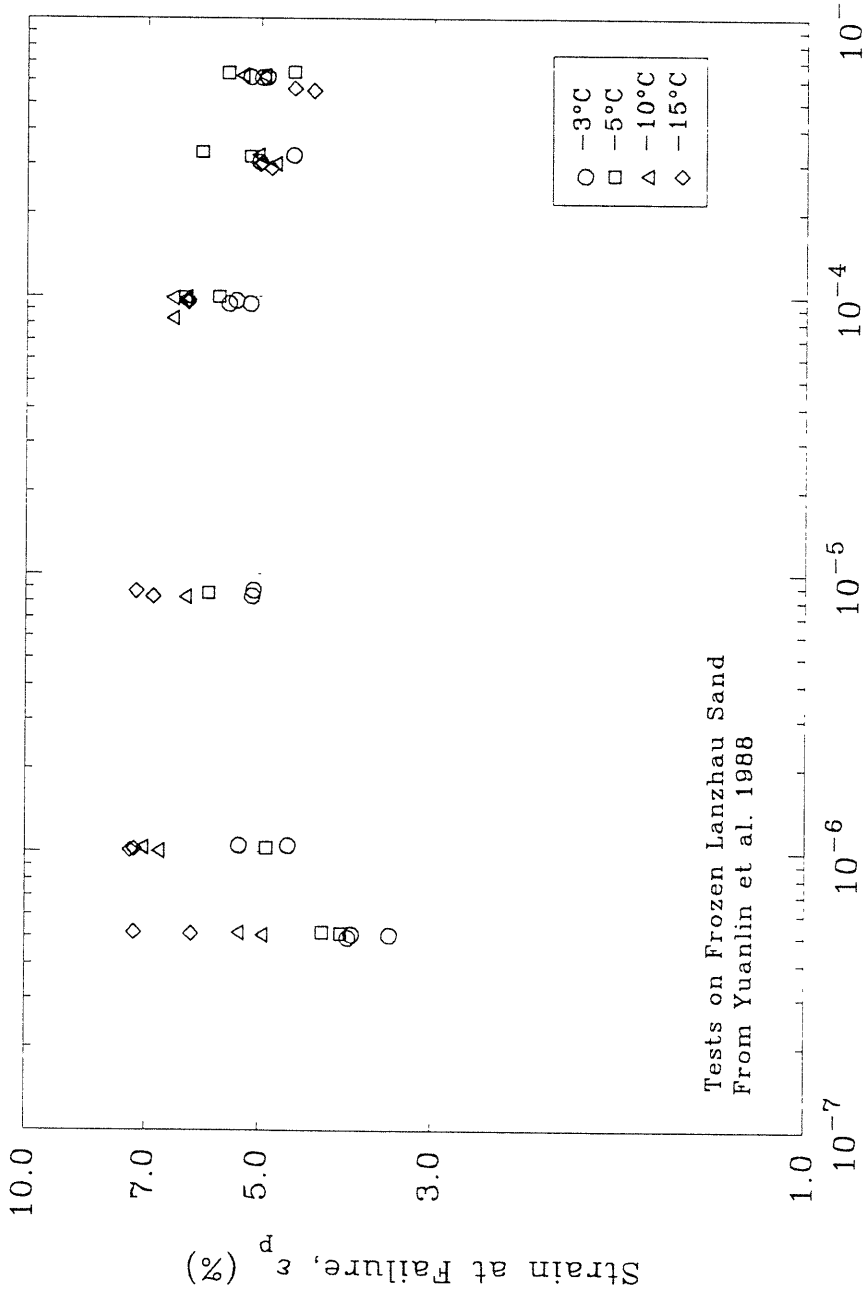

Figure 2.94 Strain at Failure versus Applied Strain Rate for Frozen Lanzhau Sand at Temperatures from −2 to −15°C (tests by Yuanlin et al. 1988)

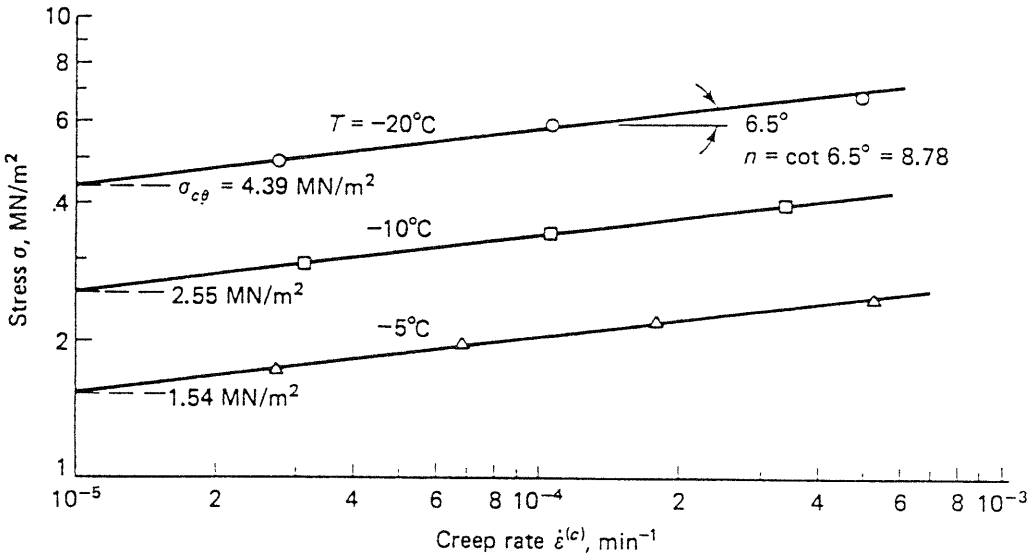

$$Q_p = \sigma_{c0} \cdot \exp\left[\frac{Q\theta}{273 \cdot nR(273-\theta)}\right] \cdot \left(\dot{\epsilon}_a / \dot{\epsilon}_c\right)^{1/n}$$

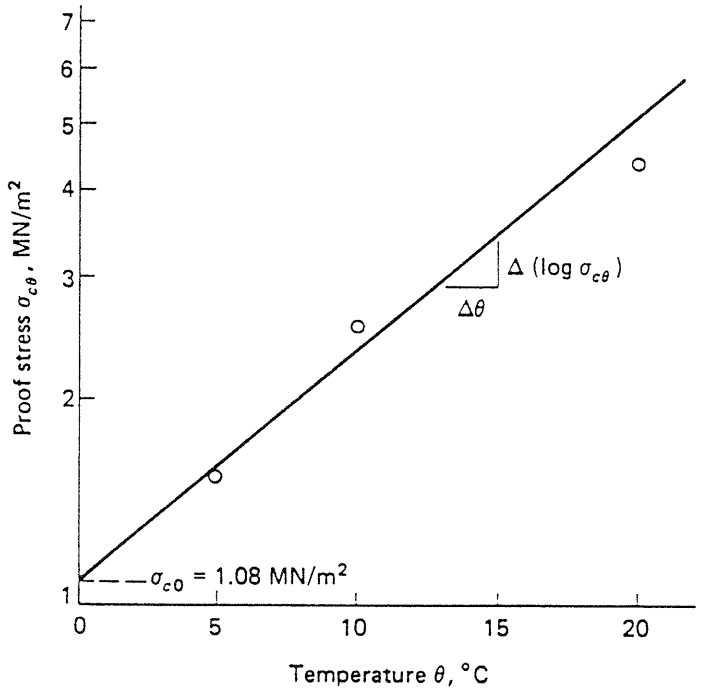

Figure 2.95 Derived Parameters for Arrhenius–Type Formulation (from Anderson and Andersland 1978)

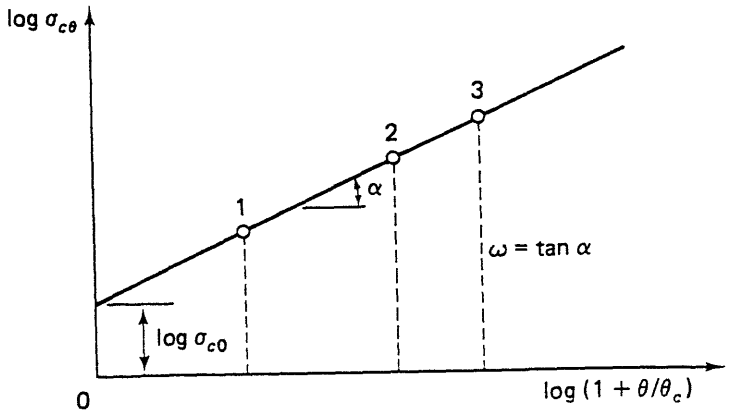

$$\sigma_{max} = \sigma_{c0} \cdot [1 + \theta/\theta_c]^{\omega} \cdot (\dot{\epsilon}_a/\dot{\epsilon}_c)^{1/n}$$

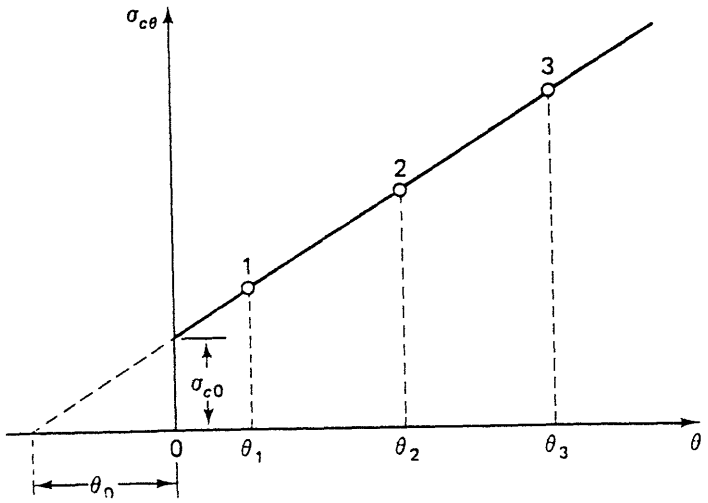

$$\sigma_{max} = \sigma_{c0} \cdot [1 + \theta/\theta_0] \cdot (\dot{\epsilon}_a/\dot{\epsilon}_c)^{1/n}$$

Figure 2.96 Derived Parameters for Strength–Strain Rate Power Law Formulation

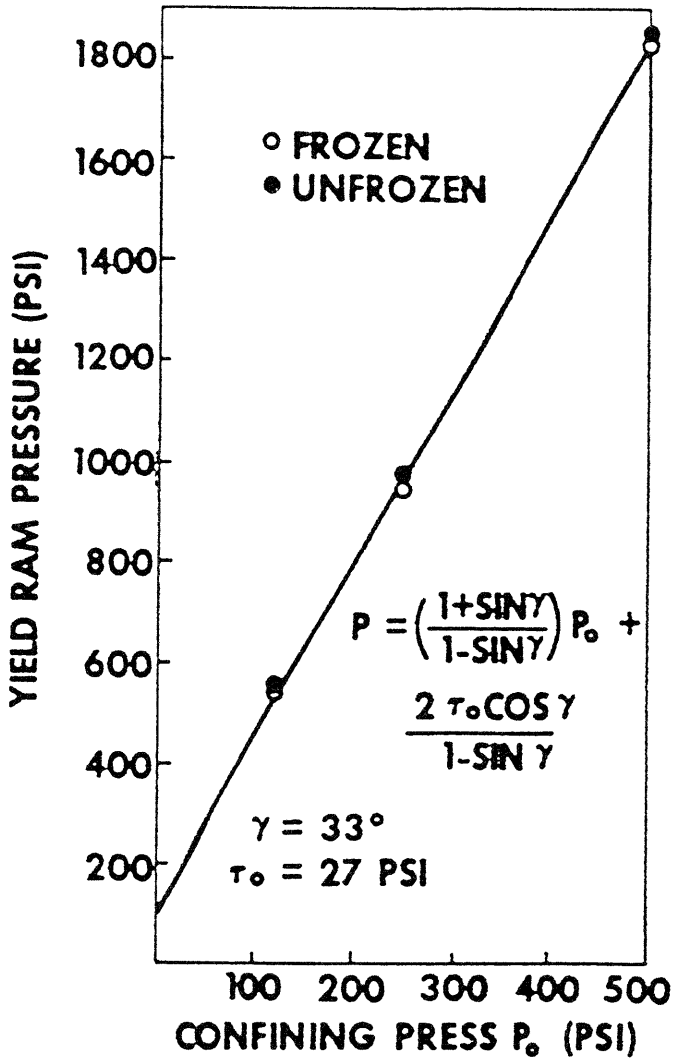

Figure 2.97 Yield Pressure versus Confining Pressure for Frozen Quartz Sand (from Goodman 1975)

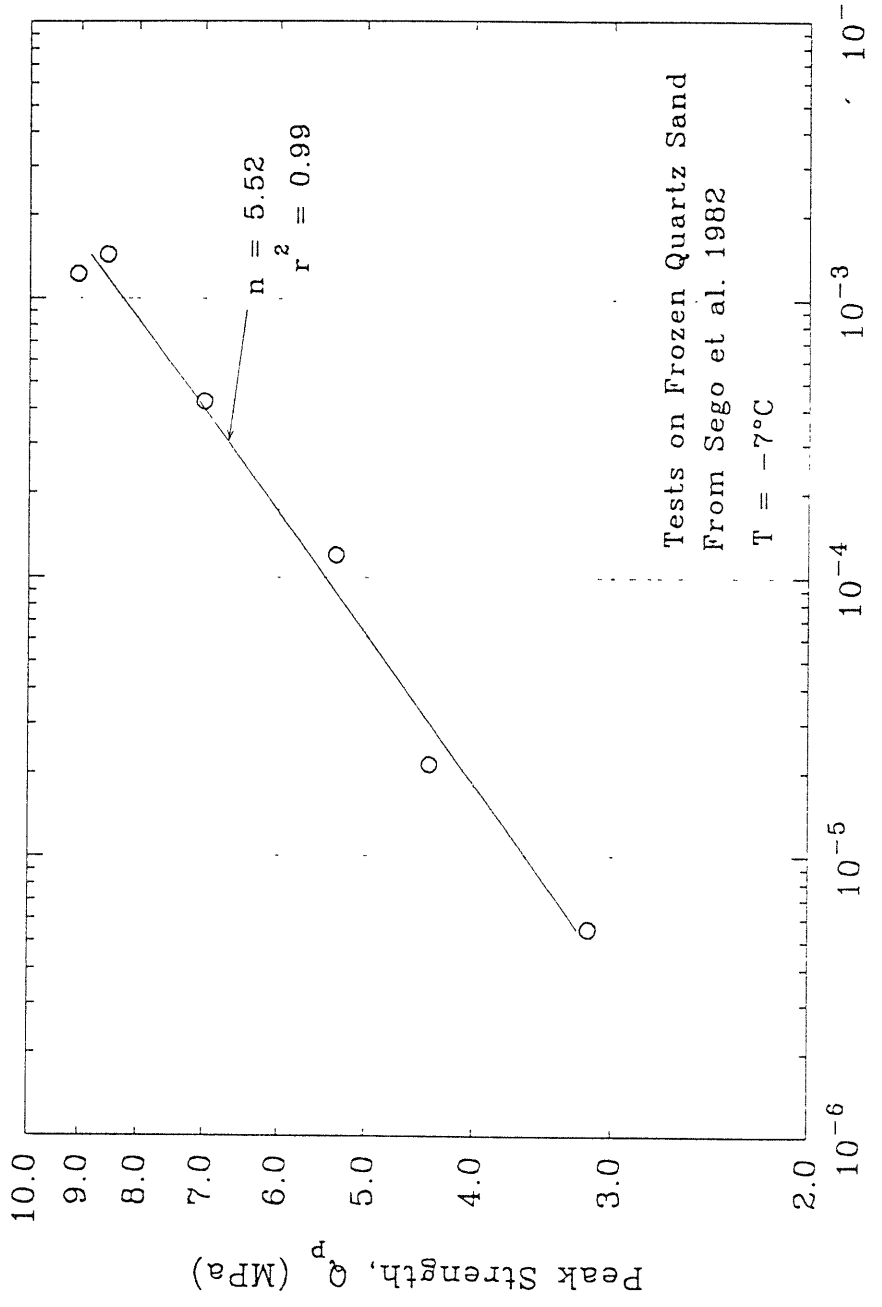

Figure 2.98 Peak Strength versus Applied Strain Rate for Frozen Quartz Sand (tests by Sego et al. 1982)

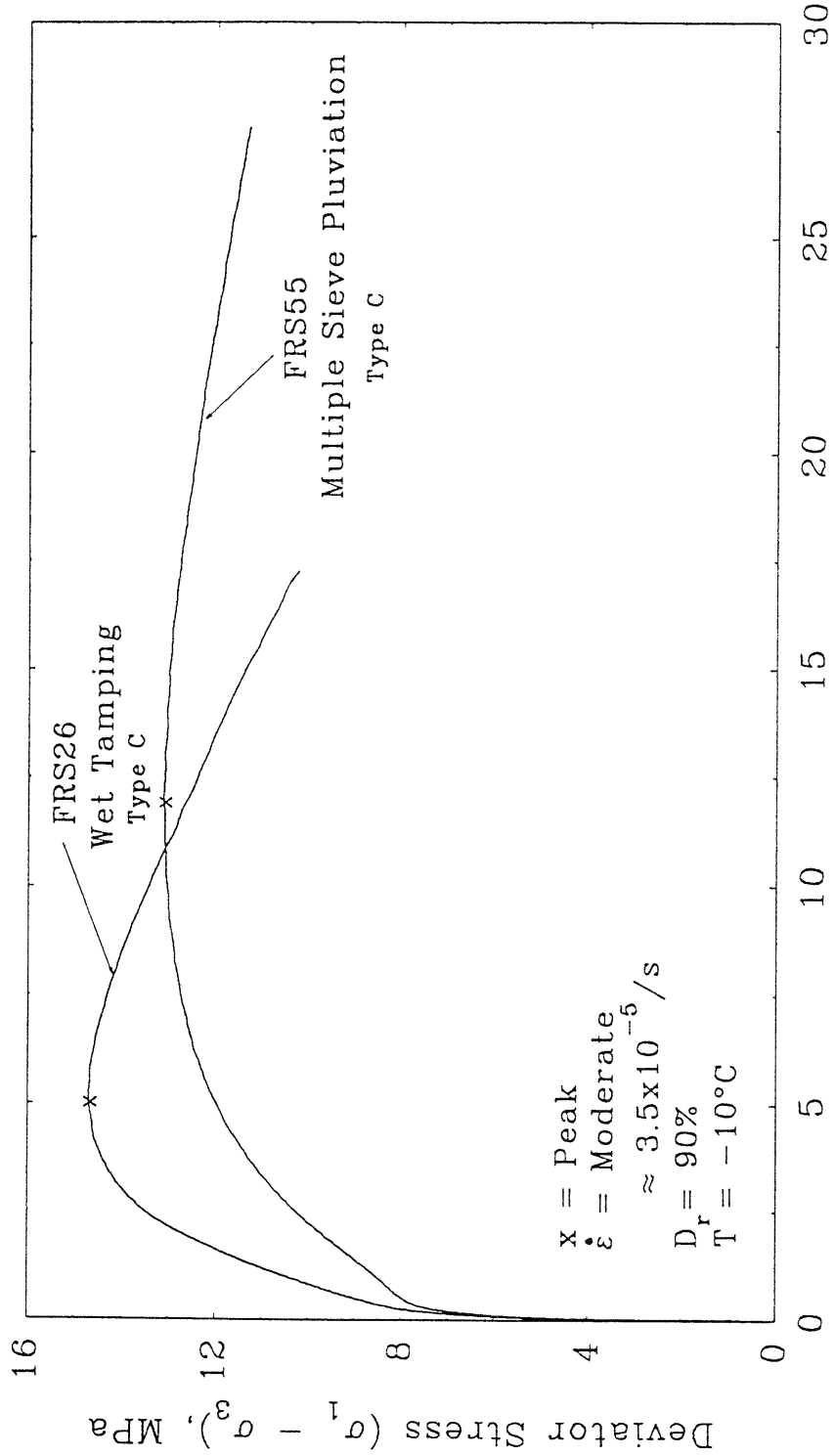

Figure 2.99 Stress–Strain Curves Which Show the Effect of Specimen Preparation Techniquie on Frozen Manchester Fine Sand

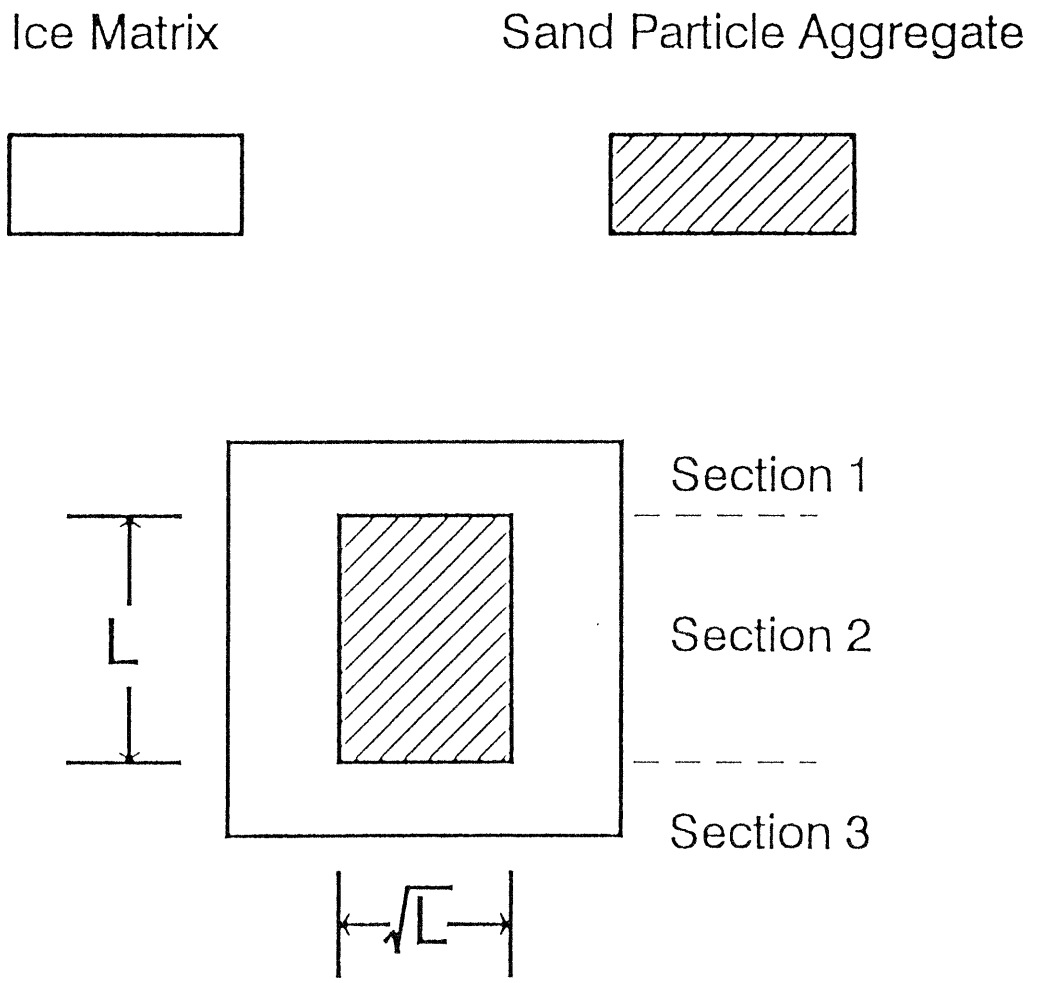

Figure 2.100 Schematic Diagram of Counto's (1964) Isostrain Composite Material Model Applied to Frozen Sand

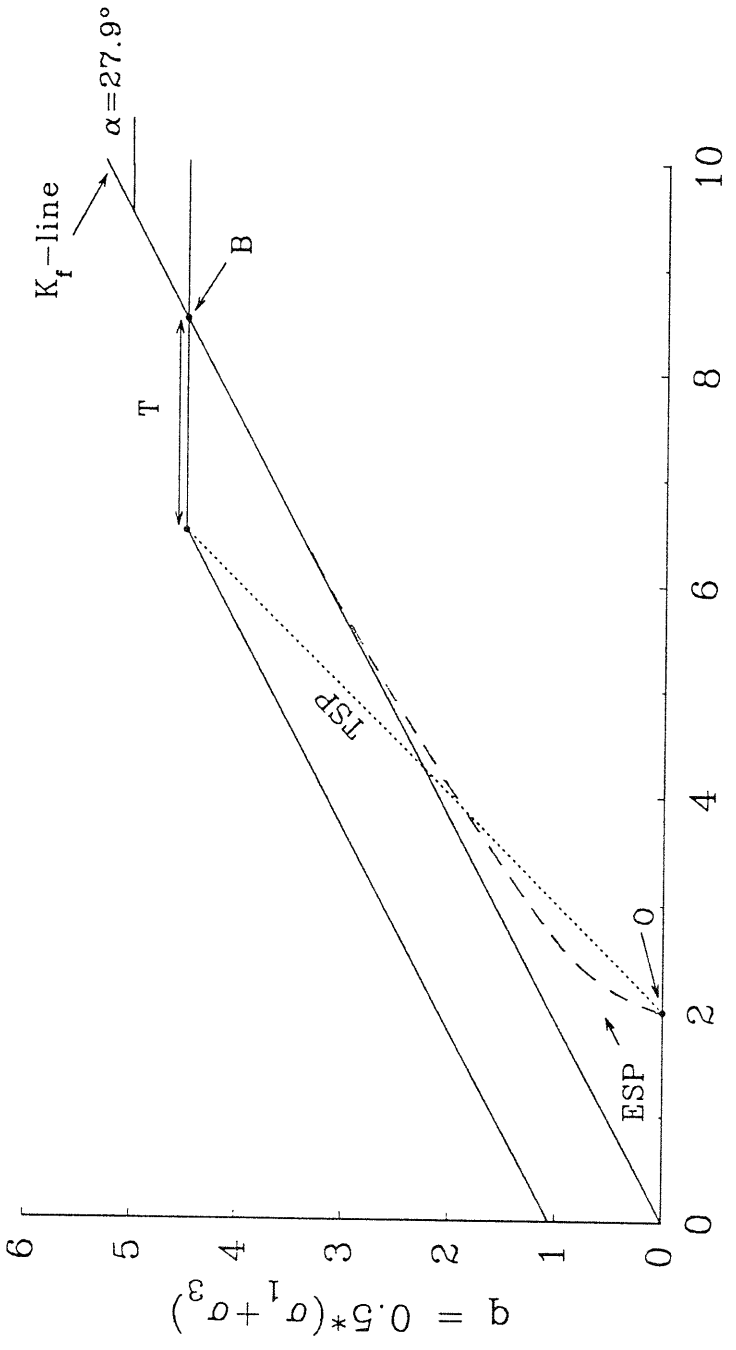

Figure 2.101 Schematic Representation of Total and Effective Stress Paths for Dense Sand at Low Effective Confining Pressure

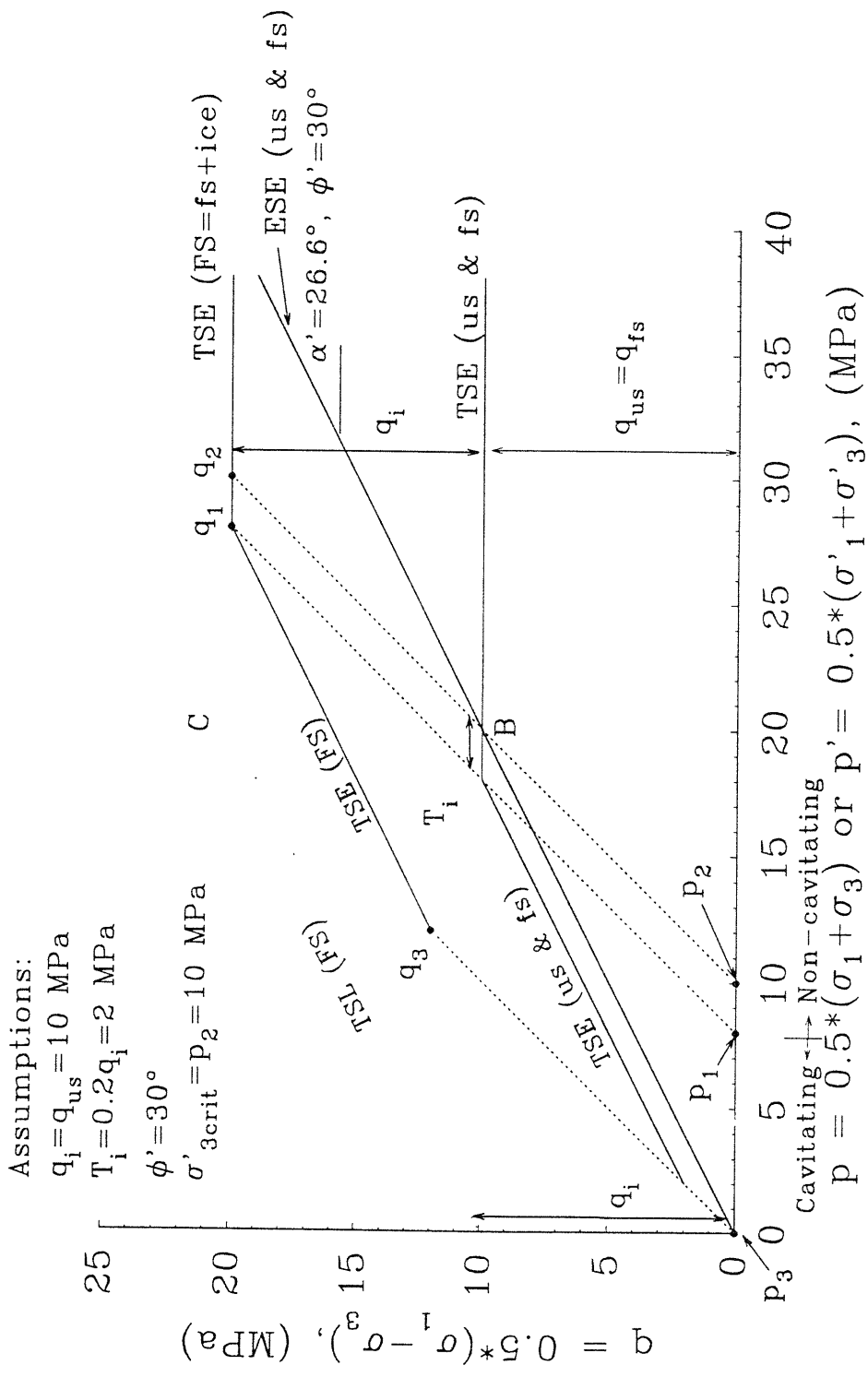

Figure 2.102 Schematic Representation of Total and Effective Stress Paths for the Dilatancy–Hardening Model (after Andersen et al. 1992)

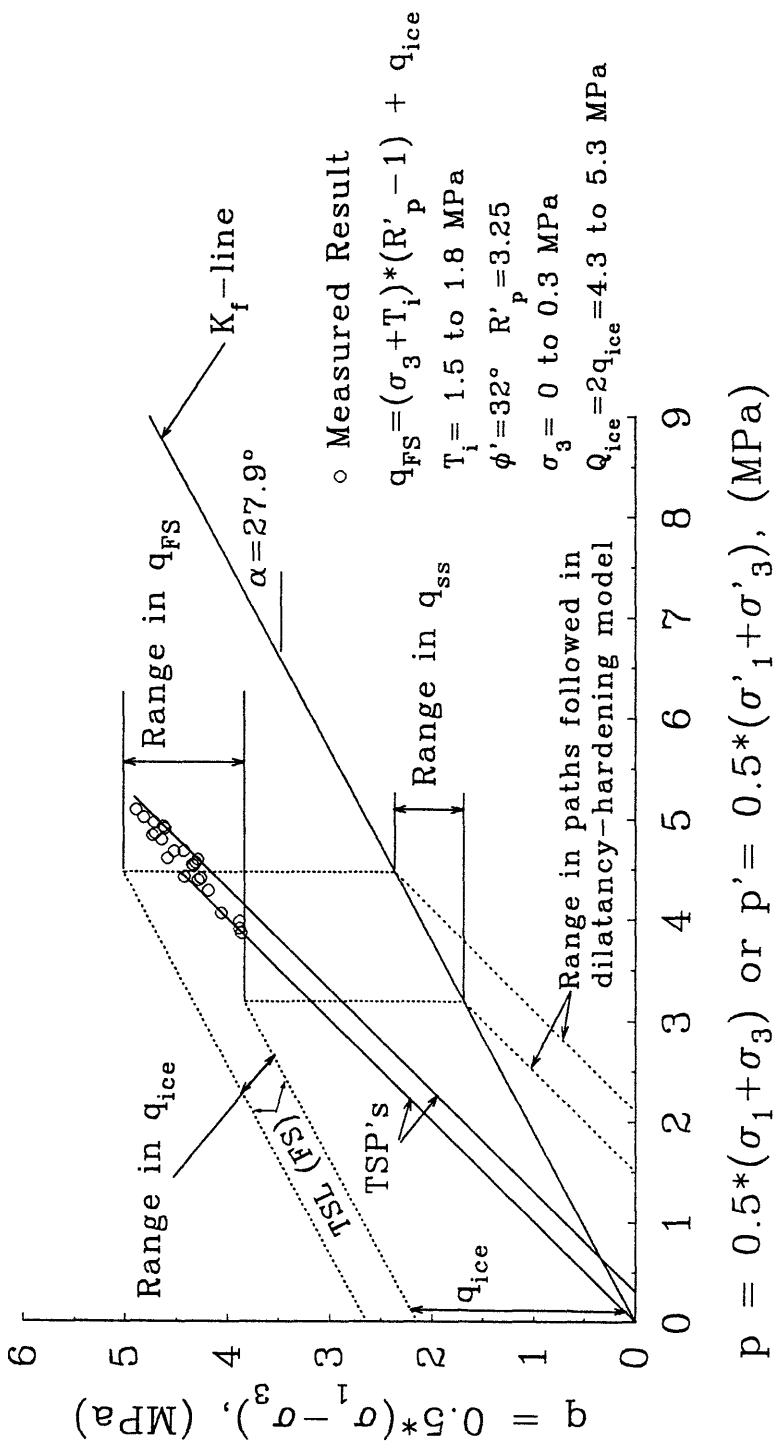

Figure 2.103 Comparison of Dense Frozen Ottawa Sand Results with the Dilatancy−Hardening Model in MIT p'−p−q Space (Data from Ladanyi and Morel 1990)

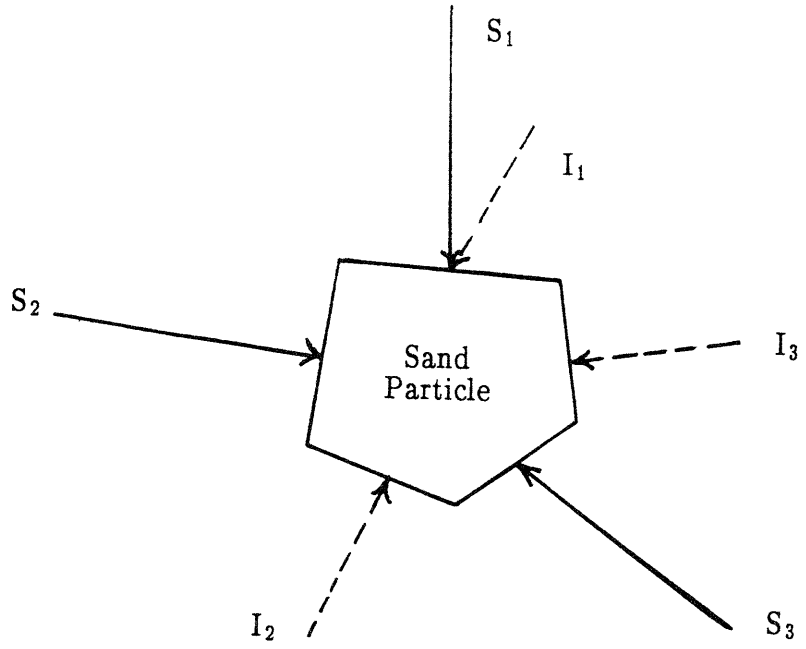

FORCE POLYGONS

Sand Intergranular Contact Forces, S_i

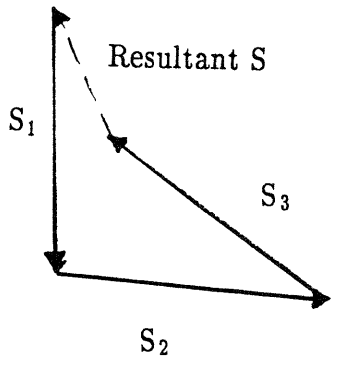

Ice–Silicate Interface Forces, I_i

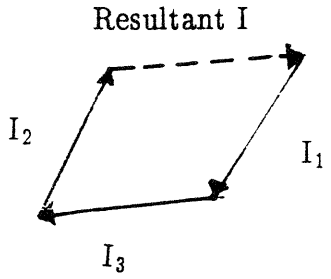

Figure 2.104 Force Equilibrium of Sand Particle In Frozen Sand (after Andersen 1991)

CHAPTER 3
MATERIALS, EQUIPMENT, EXPERIMENTAL PROCEDURES AND ERROR ANALYSIS

This chapter describes the materials, equipment, and testing procedures used in the unfrozen and frozen testing programs. This chapter also presents the data reduction methods and a presentation of possible errors associated with the test results for each program. The chapter is divided into seven sections. The first, Section 3.1, presents a description of Manchester Fine Sand (MFS), the soil used for both the unfrozen and frozen testing programs. Section 3.2 describes the common equipment used in performing the unfrozen and frozen MFS testing programs. Significant improvements in the measurement of temperature are highlighted in discussion of the frozen MFS testing programs. In addition, special emphasis will be given to the use of the Flexible Automated Technology for Computer–Assisted Testing (FATCAT), MIT's state–of–the–art testing capability to control applied pressures and volumes via DC–servo motor–driven mechanisms.

Sections 3.3, 3.4 and 3.5 describe the testing procedures used in the unfrozen MFS, conventional frozen MFS and the consolidate–freeze testing programs, respectively. Various procedures were used in the unfrozen testing program leading to a division of the test results into three series: Series A, B and C. The procedures used for conventional frozen tests are essentially identical to those developed during the previous frozen MFS testing program at a temperature of –10° C performed by Andersen (1991) (also see Andersen et al. 1992). The majority of the tests in the current research were

performed at temperatures of –15° C, –20° C and –25° C. The procedures for the consolidate–freeze testing program involved a combination of procedures from the unfrozen MFS and conventional frozen MFS testing programs. In particular, this section describes the procedures used to freeze consolidated MFS specimens while maintaining the applied consolidation stresses.

Section 3.6 presents the data collection and reduction procedures used to develop test results. In particular, the discussion focuses on the various correction methods used in calculating stresses and strains acting on the specimen as well as specimen volume changes. Section 3.7 discusses the possible errors associated with experimental measurement and the evaluation of each program's test results.

It is the intention of this Chapter to summarize descriptions of the testing procedures and to highlight unique testing equipment and procedures, e.g., temperature measurement, the FATCAT technology and development of the consolidate–freeze testing capabilities.

3.1 MANCHESTER FINE SAND

3.1.1 Description of Manchester Fine Sand

Manchester Fine Sand (MFS) was used in all three testing programs. Andersen et al. (1992) presented a description of this material which was also used for his conventional frozen tests. The following discussion presents information abstracted from Andersen's work along with additional information developed during the current research.

The MFS used in the tests was collected from the Plourde Sand and Gravel Company in Hooksett, New Hampshire. The sand is a river bed deposit with nearly horizontal bedding planes. Based on a mineralogical

analysis performed by Martin et al. (1981) on a similar MFS, the sand particles consist primarily of sub–angular quartz and feldspar with some mica flakes.

Field samples of the sand were collected from different beddings and combined to form a representative material. Subsequently, the field samples were processed, using a #200 sieve (0.075 mm), to remove excess fines (initial fine contents were as high as 21%) and re–mixed to form a relatively uniform sand. All sand particles pass the #40 sieve (0.425 mm) with approximately 7% passing the #200 sieve. Based on the Unified Soil Classification System, the processed MFS is classified as SP–SM; a poorly graded fine sand with 7% non–plastic silt size particles.

Andersen (1991) conducted five dry sieve analyses to establish an initial gradation curve of the processed MFS and to serve as benchmarks for after–test sieve results. Four additional dry sieves were conducted during the current research program to supplement those by Andersen. Table 3.1 presents the results of these nine sieve analysis. An average gradation curve is presented as Fig. 3.1 along with the standard deviation of the results at each sieve used in the analyses. Based on the average curve, the following parameters can be determined:

Particle diameter at 10 percent passing, $d_{10} = 0.083$ mm

Particle diameter at 30 percent passing, $d_{30} = 0.132$ mm

Particle diameter at 50 percent passing, $d_{50} = 0.179$ mm

Particle diameter at 60 percent passing, $d_{60} = 0.195$ mm

Coefficient of uniformity, $C_u = d_{60}/d_{10} = 2.35$

Coefficient of concavity, $C_c = \frac{d_{30}^2}{d_{60} \cdot d_{10}} = 1.08$

These values closely match those presented by Andersen (1991).

Andersen et al. (1992) also presented the following additional parameters for MFS:

Maximum Dry Density, γ_{dmax} = 1.701 g/cc (by ASTM Standard D4253, Method 1.A)

Minimum Dry Density, γ_{dmin} = 1.408 g/cc (by ASTM Standard D4254, Method A)

Maximum void ratio, e_{max} = 0.909

Minimum void ratio, e_{min} = 0.580

Specific Gravity, G_s = 2.688 ± 0.003

where the void ratio (e) is the (volume of voids, V_v)/(volume of solids, V_s).

3.1.2 Specimen Preparation Techniques

Unfrozen and consolidate–freeze specimens were prepared to different set–up relative densities, D_r, where

$$D_r = \frac{e_{max} - e}{e_{max} - e_{min}} \cdot 100\ (\%) \qquad 3.1$$

These specimens were subsequently consolidated to lower pre–shear relative densities. Conventional frozen tests were prepared at their intended preshear D_r.

The majority of the frozen and unfrozen MFS specimens were prepared using a multiple sieve pluviation (MSP) technique. Figure 3.2 illustrates the technique. The pluviator consists of a funnel resting on top of a long, plexiglas cylinder which rests on a series of four screens encased in plexiglas dividers. Two screens openings approximately the size of U.S. standard No. 10 sieves (2 mm openings) and the other two have openings approximately the size of U.S. standard No. 20 sieves (0.9 mm openings). Oven dried MFS is poured into the funnel with the sand passing through, and randomly bouncing off of, the screens to form the specimen. The funnel uses

interchangeable cork stoppers in which a small diameter opening have been bored. The rate of falling sand, which is a function of the size of the funnel's opening, determines the density of the specimen with faster rates (larger openings) leading to looser specimens. Funnel openings ranged from 0.20 cm (for dense specimens) to 1.27 cm (loose specimens).

Specimens for the Series B and C unfrozen tests and all consolidate–freeze tests used MSP and were prepared directly on the base pedestal of the triaxial cell (see next section for cell description). For conventional frozen tests, specimens were prepared in molds, saturated and frozen prior to set–up in the triaxial cell (see Section 3.4). Only specimens for Series A tests did not use MSP (see Section 3.3.2 for techniques used).

3.2 COMMON TESTING COMPONENTS

Many of the test components used in the various testing programs can be considered universal since they were identical (i.e., the same design) and could be interchanged between testing programs. Five components common to the three test programs were 1) a modified triaxial cell with silicon oil used as the cell fluid, 2) pressure/volume control systems, 3) a load frame, 4) electronic measuring devices and 5) a central control acquisition system. The following sections describe these various components used in the testing programs. Other testing components such as temperature control and measurement techniques and Flexible Automated Technologies for Computer Assisted Testing (FATCAT) systems are discussed in Sections 3.2.6 and 3.2.7, respectively.

3.2.1 High Pressure Triaxial Cells and Silicon Oil

Two high pressure triaxial cells were used in the testing programs.

Both cells were modifications to existing high pressure cells manufactured by Wykeham Farrance, Inc. A schematic of the triaxial cell is presented in Figure 3.3. One cell was used for unfrozen MFS tests, the other for both conventional and consolidate–freeze tests. Each cell consists of two parts: a cell base and upper shell. The cell base was modified to include an enlarged, smooth brass pedestal (4.0 cm in diameter) to allow radial expansion of the specimens ($\approx$ 3.5 cm initial diameter) during testing. The upper shell of the triaxial cell, which houses the loading piston, was extended so as to accommodate the use of an internal load cell, thereby eliminating the variable component of piston friction in axial load measurements. Electrical feedthrough connections were installed in both parts of the triaxial cell.

For unfrozen and consolidate–freeze tests, the cell base was further modified to include internal and external drainage lines for transfer of specimen pore water. These internal modifications to the cell are illustrated in Fig. 3.4. Also shown in the figure is the enlarged top cap used to transfer load from the loading piston to the specimen. The top cap was fitted with a drainage connection to connect to the internal drainage line. A cylindrical seating piece, attached to the load cell, exists between the load cell and top cap. This piece is in contact with the entire flat top of the top cap and has a small circular lip with an inside taper to provide a guide during test set–up when the load cell and piston are lowered onto the top cap. The lip also prevents lateral motion and rotation of the top cap during shear.

For consolidate–freeze testing, a small annular chamber was machined inside the base pedestal to facilitate specimen freezing. This chamber, also illustrated in Fig. 3.4, is approximately 2.5 cm in depth and 1 cm in width.

The chamber is accessed through two ports which exit the pedestal through the base of the cell, thereby allowing freezing fluid (ethylene glycol) to circulate through the pedestal while the cell and pore water back pressures are maintained on the specimen.

Silicon oil was used as the cell fluid in all testing programs. This oil provided a relatively constant viscosity over a wide range of temperatures and was non–conductive; an attribute necessary for use of the internal electronic devices. The oil was also highly compatible with the prophylactic membranes used to surround both unfrozen and frozen MFS specimens. In addition, the oil's relatively large molecular structure virtually eliminates leakage through the membrane.

3.2.2 Pressure/Volume Control System

Cell and back pressures are controlled using MIT–designed pressure/volume controllers. Figure 3.5 presents a schematic drawing of a controller. The controller, driven by DC servomotors, is also used for measuring specimen volume changes and, if computer–assisted testing is implemented, the controller also is used to develop axial loads and displacements. As shown in the figure, the controller consists of a pressurizing piston which is moved into or out of a fluid–filled reservoir via connection to a ball–screw actuator. DC–servomotors are used to drive the ball–screw actuator. To increase pressures, the pressurizing piston is inserted into the reservoir; to decrease pressures the piston is drawn out of the reservoir.

The controller is used for measuring specimen volume changes by two different methods. For unfrozen tests and for the unfrozen phase of testing in consolidate–freeze tests, specimen volume changes were directly measured

using the pore water back pressure controller. During shear of frozen MFS, specimen volume changes were measured indirectly using the cell pressure controller and the movement of silicon oil into and out of the cell. Volume measurements are made using a direct–current–in–direct–current–out (DC–DC), linear variable differential transformer (LVDT) mounted on the pressurizing piston. The LVDT measures displacement of the piston into or out of the reservoir from which the volume change can be calculated using the measured displacement and the area of the pressurizing piston (see Section 3.6 for the methods used to calculate specimen volume changes in the various testing programs).

For the initial unfrozen tests (known as Series A and Series B tests) and all conventional frozen tests, the controllers were an integral part of a closed–loop analog system to control cell and back pressures. This closed–loop system was a precursor to the FATCAT systems implemented for later unfrozen tests and the consolidate–freeze tests. Figure 3.6 present a schematic of how the closed–loop analog system works. In brief, the analog signal from pressure transducer (increased by a factor of 100) is compared with a manually set reference signal corresponding to the desired pressure. The difference between the two signals is called the error signal which may be negative (factored transducer signal > reference voltage) or positive (reference voltage > factored transducer signal). To increase the sensitivity, the error signal can then be amplified and sent as an analog command to the motor control card. Based on this analog command, the control card then sends a velocity command to the DC–servomotor connected to the pressure/volume controller causing the applied pressure to increase (if the error signal was positive) or decrease (if the error signal was negative). The

change in applied pressure changes the pressure transducer signal and the process is started again.

The closed–loop system allows for continual change in conditions until the target pressure is met. [Note: The target pressure is never perfectly met so a small error signal will be generated continuously.] The level of error signal amplification controls the speed of pressure correction; a lower amplification yields a smaller motor velocity command leading to a slower pressure correction.

3.2.3 Loading Frames

Axial loads and displacements were applied using two types of loading frames. Screw–driven, displacement rate loading frames (Wykeham Farrance Model T–57) were used for the initial unfrozen MFS tests (Series A and Series B) and all conventional frozen MFS tests. These loading frames have a nominal capacity of 10,000 lb (44.4kN) and 30 displacement rates ranging from 0.0037 to 46 cm/hour. Due to compliance in the loading frames and triaxial cell components, the strain rate experienced by the specimens was not constant. Measurement of the initial deformation ($< 0.5\%$ axial strain) found the strain rate to be an one order of magnitude below final nominal values (see Andersen, 1991, Chapter 3).

Later unfrozen tests (known as Series C tests) and the consolidate–freeze tests used hydraulically–driven loading frames developed and constructed at MIT. These hydraulic loading frames have an 8,000 lb (35.6kN) capacity with a variable displacement rate ranging from 0.38 to 38 cm/hour for the unfrozen tests; 0.076 to 7.6 cm/hour for the consolidate–freeze tests. These loading frames have the added capability to be computer–controlled (see discussion on FATCAT in Section 3.2.7).

3.2.4 Electronic Measuring Devices

This section provides a summary of the electronic devices used to measure displacement, load and pressures. As mentioned previously, DC–DC LVDTs are used to measured the displacement of the pressurizing piston on the cell pressure and back pressure controllers. These LVDT's have linear displacement ranges from 10 to 15 cm. Axial displacements are measured by a separate DC–DC LVDT mounted on the exterior of the cell. These LVDTs have a smaller linear displacement range of approximately 2.5 cm.

Specimen axial strains up to approximately 3% are also measured internally using the on–specimen strain device as illustrated in Fig. 3.7. The device consists of two independently–acting yokes, which have three points of contact to the specimen, that are held onto a specimen via spring loading and friction. The yokes house two small displacement transducers, set diametrically opposite each other, which are used to measure axial displacements. Unlike the previous displacement transducers, these LVDT's receive and send alternating currents (AC–AC). The AC output had to be converted (demodulated) to a DC output to be compatible with the data acquisition system. Separate power supply units and voltage demodulators were used so that the small strain measurements could be obtained and recorded by the central control acquisition system in the same manner as the other electronic devices. The on–specimen strain device provided the best means available to monitor the specimen during the unfrozen or consolidate–freeze testing processes of saturation and consolidation since the triaxial cells do not have viewing ports for specimen observation.

Axial Loads on the specimens were measured using strain–gage–type load cells. These load cells have shear beam designs making them less

sensitive to eccentric loading conditions. Load cells with 2.2kN (500 lb) and 8.8kN (2000 lb) capacities were used in the unfrozen testing while a 44.5kN (10,000 lb) load cell was used for conventional and consolidate–freeze tests.

Cell pressures and specimen pore pressures were measured using interchangeable pressure transducers with transducer capacities of 1.38 MPa (200 psi), 13.8 MPa (2000 psi) and 34.5 MPa (5000 psi) used in testing.

All electronic measuring devices, except the on–specimen ACDTs, were powered using a direct current voltage source. One power source, set at +5.5 volts, was used for each testing program. In addition, a revised electronic wiring scheme eliminated the voltage line drops which were a part of Andersen's (1991) work.

3.2.5 Central Control Acquisition System

The MIT Geotechnical Laboratory Central Control Acquisition System is used to collect the output signals from the various electronic devices. The system is a 140 channel network and connects to every room in the laboratory complex. The laboratory room where both the frozen and unfrozen tests were conducted currently occupies 30 channels on this network. The system is designed around the Hewlett Packard 3477A data acquisition unit which is a very low noise integrating analog–to–digital converter. The acquisition/control unit has 17 bit precision in taking readings resulting in a one micro volt sensitivity. The system also uses an auto–ranging capability so that an electronic device which has a range in output from millivolts to volts can be used without any signal conditioning or voltage amplification/de–amplification.

The acquisition unit is controlled by a 286–based personal computer running a "Windows type" user friendly program developed by Dr. J.T.

Germaine of MIT in collaboration with R.S. Ladd of Woodward–Clyde Consultants. The program collects data for user–assigned tasks. Minimum task readings of 1 second are allowed. Raw data from the tasks are stored in the computers hard drive and converted to ASCII–formatted files which can be down–loaded to a floppy disk and manipulated in subsequent data reduction.

3.2.6 Temperature Control and Measurement

Temperatures during certain phases of testing were controlled during the conventional frozen MFS and consolidate–freeze testing programs. These testing programs were also performed in a specially–designed low temperature testing facility. The following sections describe this facility and the temperature control methods used in testing as well as the equipment used to measure temperatures.

3.2.6.1 Low–Temperature Facility and Environmental Chambers

The conventional and consolidate–freeze tests were performed inside the MIT Low–Temperature Testing Facility. This facility, constructed in 1988, is located inside a laboratory at room–temperature and consists of three separate rooms with independent temperature control: the vestibule; the growth room; and the testing room. Figure 3.8 shows a plan view of the facility. The vestibule is used as a temperature buffer between the outside laboratory and the inner rooms. It cuts down on the amount of humidity that reaches the two inner rooms and also serves as a staging area for trimming frozen specimens. It normally has a temperature of –4 to –5° C for conventional frozen tests, but was set to +5° C for the consolidate–freeze tests. The growth room, located to the rear of the vestibule and maintained at a temperature of 0° C, is used for the preparation and freezing of specimens for

conventional frozen MFS tests. The testing room contains the triaxial apparatus, loading frame and the environmental chamber (see description below). It can be regulated to –40° C, and is normally maintained at a temperature approximately 3° C to 5° C colder than the desired temperature for a particular triaxial test.

Each room of the facility is composed of sheet metal walls with styrofoam insulation. The testing room has a double–paned glass window which allows observation of the testing equipment from the outside, room–temperature laboratory. This window is heated to prevent icing. The testing and growth rooms are fitted with feed–through ports to allow for the passage of cables for the electronic devices, as well as hoses for air, water or freezing fluid.

Andersen (1991) measured the temperature inside the testing room as a function of time and found that the air temperature fluctuated about the desired set point (–15° C) by about ±1.5° C. The period of fluctuation was typically about 7 to 10 minutes. The testing room has programmable defrost cycles which are required for continuous operation. These defrost cycles produce temperature spikes of about 3° C above the normal cyclic oscillation and can last as long as 20 minutes. While no direct measurements were performed during the current research, fluctuations about the different set–points used in testing were assumed to be similar.

Specially–constructed environmental chambers were used to control the ambient temperatures surrounding the triaxial apparatus for tests in all three testing programs except for the Series A and Series B unfrozen tests which were performed under open laboratory conditions. For the conventional frozen tests, the chamber enclosed the cell pressure controller and loading platform

of the load frame. Figure 3.9 shows a schematic of the environmental chamber for the conventional frozen test setup. All components of the testing system (hydraulic load frame, triaxial cell and the three controllers) were enclosed within the chamber for the Series C unfrozen tests and all consolidate–freeze tests. The environmental chambers were essentially wood–frame boxes with walls constructed of styrofoam insulation sandwiched between plywood panels. The chamber's front door consisted of two sheets of plexiglas attached to an aluminum frame thereby allowing observation of the testing equipment during operation.

Temperature inside the chamber was maintained using a thermoregulator system. As can be seen in Fig. 3.9, two thermoregulator systems were used for the conventional frozen and consolidate–freeze tests; only one unit was used for unfrozen tests. Each system is composed of four components; a fan, a heat source, a mercury contact switch and power source. The first three components of the thermoregulator system sit inside the chamber, while the power source sits outside the chamber in the room–temperature laboratory. The fan, which operates continuously at a flow rate of 45 cubic feet (1.3 m^3) per minute, and the heat source, a 100 watt light bulb, are mounted inside a small metal box located inside the environmental chamber. The fan and heat source are powered by a relay circuit which is controlled (opened or closed) by a mercury contact switch. The contact switch hung freely near the top of the environmental chamber and was preset for the appropriate testing temperature. For unfrozen tests, a contact switch preset at a temperature of +25° C was used; for conventional frozen tests, contact switches preset to temperatures of –15° C, –20° C and –25° C were used. Consolidate–freeze tests used two contact switches; one preset to +3° C for the unfrozen and freezing

phases of testing, the other preset to –10° C for the frozen phase of testing. If the temperature in the environmental chamber falls below the preset temperature, the relay circuit closed and power is supplied to the heat source until the temperature raises above the preset point, at which point the relay circuit opens and power to the heat source is discontinued. Since the thermoregulator systems can only supply heat, the ambient room temperature surrounding the environmental chamber is keep below the contact switch's preset temperature so that heat would be lost from the warmer environmental chamber, thus allowing the heat source to cycle on and off as needed. The level of temperature control is discussed in Section 3.6.

3.2.6.2 Temperature Measurement

The temperature measurement system used in the current research consists of three components: epoxy–beaded, wafer thermistors; a Wheatstone bridge circuit; and an input voltage source. These components are schematically illustrated in Fig. 3.10. Essentially, the system is an electrical circuit with the thermistor acting as a variable resistor. The thermistor's resistance varies significantly with temperature, thus changing the bridge circuit's voltage output (potential) which is measured across points a and b (see Fig. 3.10).

The thermistors are interchangeable wafer thermistors accurate to within ±0.2 °C at higher temperatures (–5 °C) and decreasing to ±0.4 °C at lower temperatures (–40 °C). The Wheatstone bridge circuit consists of four resistors arranged such that the resistance of an unknown resistor (thermistor) can be calculated using the resistances of the other known resistances (R_2, R_3 and R_4). The resistance of the thermistor, R_t, can be measured very accurately if the tolerances of the known resistances are very low. In

developing the bridge circuits, metal film resistors, with tolerances of 0.01%, were used. The known resistors were set at approximately 20 KΩ. With this circuit, it is possible to measure voltage reading corresponding to a ±0.01° C temperature fluctuations.

An input DC–voltage source is needed to power the circuit. A voltage of 0.25 volts or less across the thermistor reduces the thermistor's self–heating to less than 0.001° C, an error well below measuring accuracies. However, it is also desirable to use the same input voltage used by the other electronic equipment (5.5 volts for the load cell, pressure transducers, etc.); therefore, an additional resistor, R_1, was placed in series with the bridge circuit to act as a voltage "sink". The R_1 resistor, with a resistance of approximately 380 KΩ, allows the complete thermistor circuit to operate under an input power of 5.5 volts with approximately 5.25 volts "dropped" through R_1.

The entire system is connected to the central control acquisition system so that the change in voltage (potential) across bridge circuit points a and b, as well as the input voltage, can be recorded.

For the conventional tests, four thermistors were used; two within the environmental chamber and two inside the triaxial cell. The two thermistors in the environmental chamber were located near the top and bottom of the triaxial cell (see Fig. 3.9). The two thermistors inside the triaxial cell were located near the top and bottom of the specimen. For consolidate–freeze tests, a third thermistor was added inside the cell near the middle of the specimen.

3.2.7 FATCAT System

Flexible Automated Technologies for Computer–Assisted Testing (FATCAT) was used in unfrozen MFS tests (Series C) and the

consolidate–freeze tests. The system converts existing, manually–controlled tasks of the triaxial tests to computer–automated tasks by converting conventional triaxial equipment for computer control. The reader is referred to Sheahan and Germaine (1992) for additional background information. In the current research, FATCAT allows computer control of all three axes of test stresses; cell pressure, backpressure and axial stress/displacement. With control of these axes, a flexible array of stress and strain conditions can be developed and applied to test specimens.

For the unfrozen MFS testing program, the FATCAT system components consists of a computer, motor control unit, pressure/volume controllers with DC–servomotors and electronic measuring devices. An IBM–compatible personal computer, using an 8086 microprocessor, acts as the "brain" of the system. The computer takes readings from the electronic measuring devices, performs calculations and relays commands to motors to change the existing test conditions (i.e., stresses or strains). The computer is outfitted with both analog–to–digital (A/D) and digital–to–analog (D/A) conversion boards. The A/D board, designed and constructed at MIT, has a 22–bit resolution with an integration time which can be varied between 16.7 to 167 milliseconds (the reader is referred to Sheahan, 1991, for more information). The D/A conversion board was manufactured by Strawberry Tree Inc. and can convert up to four digital signals. In simple terms, these boards allow the computer to receive the analog (voltage) signals from the electronic devices via the A/D board and then send back commands to the DC–servomotors via the D/A board.

The motor control unit houses control boards and electronics used to run the DC–servomotors. The control boards act as interpreters of the

computer's analog commands to the DC–servomotors, converting the analog command to a motor velocity command. Therefore, the motors rotate in proportion to the analog command signal from the computer. The motor control unit has been designed to allow manual control of the DC–servomotors.

In brief, the system follows a continuous process with the computer sending commands to the DC–servo motors to increase/decrease pressures and/or increase/decrease axial load or displacement. Initially, the computer takes a set of voltage readings from the triaxial cell's instrumentation that includes the load cell, axial and volumetric displacement transducers and cell pressure and back pressure transducers. These analog readings are then converted to digital signal via the computer's A/D conversion board. Once the analog signal is converted, the computer calculates the present conditions (stresses and strains) on the specimen. These calculated conditions are then compared to a target set of conditions which depend on the current test task (e.g. saturation, consolidation, shear, etc.). The difference between the current conditions and target conditions leads to the calculation of a new set of analog command signals which are transferred, via the electronic motor control boards, to the three DC–servomotors. These commands are first converted from digital to analog signals via the D/A conversion board with the analog signals going to the motor control unit. The motor control unit then converts the computer's analog command to a motor velocity command causing the DC–servomotors to proceed forward or to reverse; moving the pressurizing piston on the pressure/volume controller in or out to increase or decrease pressures. The electronic devices measure the changes in stresses and/or displacement which occur due the controller's movements and transmit

a new set of readings to the computer, thus initiating a new set of computer calculations.

3.3 EXPERIMENTAL PROCEDURES FOR UNFROZEN TESTS

The unfrozen testing program was performed, intermittently, from 1990 to 1993 with a total of 83 tests attempted. Numerous adjustments and alterations have occurred in the unfrozen MFS test procedures, especially with respect to specimen preparation techniques and the later use of the FATCAT system. Therefore, the program has been divided into three series: Series A, B and C. The following sections describe the general set of procedures used for all unfrozen tests, then testing procedures unique to a each series.

3.3.1 General Test Procedures for Unfrozen MFS Tests

Although the unfrozen MFS testing program is divided into three series, general testing procedures were followed for all tests. A typical unfrozen MFS test consists of four stages; 1) cell and specimen preparation, 2) specimen saturation, 3) consolidation and 4) shear of the specimen. A sieve analysis of the specimen is performed after shearing. The time between initiation and completion of a test is usually one to three days.

Prior to preparing a specimen, the cell base and the internal and external drainage lines are flushed first with water then pressurized air. The cleaned cell base is wiped dry and appropriate "lubricated ends" (described later) are placed on the base pedestal and top cap. A thick membrane (thickness = 0.3 mm) is placed around the pedestal with three o–rings. A prophylactic (thin membrane) is then placed around the pedestal and over two of the o–rings. A fourth o–ring is then placed on the pedestal between the two o–rings covered by the prophylactic. This assemble of membranes is

then encased in a split–mold, called the membrane expander/specimen former, which is clamped onto the base pedestal. The thick membrane passes through the cylindrical opening of the expander/former and is folded over the top of the former/expander. A small vacuum ($\approx$ 0.05 MPa) is then applied to the space between the inner wall of the expander/former and the thick membrane creating a cylindrical space to create the MFS specimen. Initial specimen dimensions were typically 3.5 cm in diameter and 7.6 cm in length.

Once the specimen has been prepared (see Section 3.1.2 for preparation methods), the top cap is placed on top of the specimen using an alignment device to insure proper vertical alignment. The thick membrane is then removed from the expander/former and placed around the top cap and sealed with two o–rings. An internal drainage line is connected to the top cap leading to an exit port in the cell base. With the specimen completely sealed, a 0.1 MPa vacuum is applied to the specimen through a drainage port as an initial effective stress thus creating a stable specimen. The expander/former is then removed and initial specimen dimensions (diameter and length) are measured using an optical scope with a veneer that has a direct read out of 0.025 mm.

The thin, prophylactic membrane is then rolled up from the base pedestal, over the specimen and onto the top cap. An o–ring from the pedestal is also brought up to the top cap to seal the thin membrane against the top cap. The on–specimen strain device is then placed around the specimen with the top and bottom yokes located at approximately the specimen third points. Initial gage lengths between the top and bottom yokes are measured using the optical scope.

The upper shell of the triaxial cell is then lowered over the cell base

and the two cell components are bolted together. A large o–ring is used as a seal between the two components. The complete cell is then placed in the loading frame and filled with silicon oil. An initial cell pressure, equal to the applied vacuum, is applied while the vacuum is removed. The specimen, now open to the atmosphere, is flushed with carbon dioxide, CO_2, (for approximately 15 minutes) and then water (approximately 200+ cm^3). The cell and back pressure are then increased while maintaining the initial effective stress level ($\approx$ 0.1 MPa) and these pressures are held overnight. Typical back pressures of 1.0 to 1.3 MPa were used for most tests except dense undrained tests at low confinements which had back pressures of 3.2 MPa (to prevent cavitation of pore water during shear).

The overnight back–pressure saturation is followed by a B–value evaluation where an increase in cell pressure is applied and the corresponding increase in specimen pore pressure measured, i.e., $B = \Delta u/\Delta\sigma$ (see Section 2.1). The specimen was then consolidated and sheared. Specimens sheared at low confinement (σ'_c = 0.1 MPa) were not subject to further consolidation. The majority of specimens (44 of 55 or 80%) were sheared under undrained conditions. After shear, the cell is dismantled; the specimen frozen; then the specimen is removed from the cell base and placed in an oven to obtain a dry mass. A sieve analysis is performed on the specimen after drying.

3.3.2 Series A Tests

The Series A unfrozen MFS tests consist of the first 17 unfrozen MFS tests. Tests were attempted with effective confining pressures (σ'_c) of 0.1, 1, 2, 4 and 5 MPa. All except one test was sheared under undrained conditions (CIUC tests). Preshear relative densities (D_r) ranged from 14 to 106 percent.

A nominal strain rate of 2.3×10^{-5}/sec (8.4%/hour) was used for all tests. It should be noted that 24 specimens were actually prepared in this series but the first seven tests rarely proceeded beyond back–pressure saturation. In addition, of these 17 tests; only six provide useful shear results. Initial specimen characteristics for Series A tests are summarized in Table 3.2a.

Based on the low success rate, it is evident that significant difficulties were encountered performing Series A tests and that Series A tests should be considered as the "learning curve" in the unfrozen MFS testing program. The reasons for this "learning curve" center around the novelty of the testing program. Many of the experimental techniques used in the testing program had never been attempted for a sand at MIT. The triaxial cell had just recently been modified and had not been proof–tested. The combination of lubricated end platens, internal axial load cell, high capacity pressure/volume controllers and on–specimen axial strain measurements also was being tried for the first time.

Series A tests used three end platen lubrication techniques: teflon lubrication alone, teflon lubrication and a rubber membrane cut to the diameter of the test specimen and a rubber membrane with high vacuum grease. The specimen preparation techniques used for Series A tests included open–air raining of MFS into the split mold and vibratory densification of rained specimens. As will be discussed later in the sections on consolidation and shear, these preparation techniques lead to erratic and questionable test results.

Isotropic (hydrostatic) consolidation was performed for tests with effective confining stresses greater than 0.1 MPa. Consolidation of test specimens essentially consisted of maintaining a constant back pressure while

manually increasing the cell pressure by changing the reference voltage in the closed–loop pressure control system. The cell pressure was increased up to the desired effective stress. Specimen axial strains were measured using both the on–specimen strain device and the external LVDT. On–specimen strains could be measured during the consolidation process as the specimen shortened; however, strains measured by the external LVDT were performed by manually raising the platen of the loading frame after consolidation until the load cell once again contacted the specimen.

An average strain rate of 2.3×10^{-5}/sec was used for specimen shearing. Undrained tests were performed by closing the back pressure valve at the cell before initiating loading via the loading frame. For drained tests, the back pressure valve was not closed and the back pressure was held constant. Most tests exhibited erratic and/or questionable shear results. The most common anomalies in the tests were:

1) the axial load on the specimen would suddenly drop to near zero with a coincidental jump in measured pore pressure, and

2) a predominant failure surface would develop in the specimen causing the measured pore pressures and axial stress to vary erratically.

These anomalies are attributed mainly to non–uniformities in the specimens which are due, in large part, to the use of various specimen preparation techniques.

3.3.3 Series B Tests

Series B consisted of 24 undrained (CIUC) tests. Preshear relative densities ranged from 44 to 104% and effective confining pressures were 0.1, 2, 5 and 10 MPa. All tests were sheared at a nominal strain rate of 2.3×10^{-5}/second. Eighteen of the 24 Series B tests provide useful shear

results. Specimen characteristics of Series B tests are summarized in Table 3.2b.

Various combinations of teflon lubrication, rubber membrane, and high vacuum grease were again tried to obtain lubricated end platen conditions with varying degrees of success. Greased membranes provided the best lubrication, but often led to over lubrication so that specimens would slide at the top cap and/or bottom pedestal often creating an S–shaped sheared specimen.

As noted in Section 3.1.2, multiple sieve pluviation was used for all Series B tests. It is believed that the use of multiple sieve pluviation greatly increased the success rate of Series B tests. In fact, of the six tests which do not provide useful shear results, five do so because of known mechanical or human errors.

Specimen consolidation was performed as previously described for Series A tests; however, Series B tests were consolidated up to a pressure of 10 MPa. For consolidation to 10 MPa, a liquid latex adhesive was applied to the outside of the specimen's membrane at the junction of the specimen and the pedestal and top cap. This added "membrane" thickness helped prevent membrane rupture during consolidation. Undrained shear (CIUC) occurred in the same manner as Series A tests.

3.3.4 Series C Tests

Series C consisted of 35 unfrozen tests with 22 sheared under undrained conditions and 13 in drained conditions. [The reader should note that the first 16 Series C tests were previously referred to as Series B Test #25 to #40 in Andersen et al (1992).] Pre–shear relative densities ranged from 31 to 90% for drained tests and 56 to 115% for undrained tests. Twenty–four

tests were consolidated beyond 0.1 MPa; 21 isotropically and three anisotropically with final K_c values (ratio of effective minor principal consolidation stress to effective major principal consolidation stress, $\sigma'_{1c}/\sigma'_{3c}$) of 0.51, 0.56 and 0.59 obtained. Effective confining pressures for isotropically–consolidated shear tests were, 0.1, 2, 5, 7.5, 10 and 12.5 MPa. Effective minor principal stresses were 5.6 (K_c = 0.59), 7.0 (K_c = 0.51) and 7.6 (K_c = 0.56) MPa. Nominal strain rates varied from 2.8×10^{-5} to 3.3×10^{-4}/sec (10.2 to 120 %/hour). Of the 35 tests performed, 31 provide useful shear results. Specimen characteristics of Series C tests are summarized in Table 3.2c.

Series C tests are different from the previous testing series due to 1) the use of a FATCAT system, 2) the use of higher confining pressure and faster strain rates and 3) an increase in the time allowed for secondary compression at the final effective consolidation stress (σ'_c) . Each of these factors are highlighted in the discussion below.

The use of FATCAT techniques allowed the saturation, consolidation and shear tasks to be performed under more controlled conditions, thus eliminating many of the problems encountered in Series A and Series B tests. Computer–assisted testing also allows better control for testing a wider variety of testing conditions for unfrozen MFS, such as anisotropic consolidation and drained tests using constant p′ ($= 0.5 \cdot (\sigma'_1 - \sigma'_3)$) stress paths. These testing conditions would have been extremely difficult using the manual set–up in Series A and Series B.

Test specimens were set–up in the same manner as Series B tests (i.e., using multiple sieve pluviation, various lubricated end methods, etc.). Unlike previous test series, a small pre–stress (approximately 20 to 50 kPa) was

applied to the specimen so as to maintain specimen alignment during the saturation and consolidation phases of testing. The change in specimen length due to this preload was measured and accounted for in data reduction.

Isotropic (hydrostatic) consolidation was performed using one of two methods. For the first four tests in this series, consolidation consisted of incrementally increasing the cell pressure while maintaining a constant back pressure. For subsequent tests, consolidation consisted of subjecting the specimen to an axial displacement rate and requiring the cell pressure to increase so as to maintain hydrostatic conditions on the specimen (i.e., keep the deviator stress at prestress levels). Anisotropic consolidation was performed by setting effective stress target values for the axial (major principal) and radial (minor principal) stresses to be applied to the specimen. In addition, continuous measurement of the axial strains via piston displacement by the external LVDT was now possible given that the initial deviator stress on the specimen was maintained during the consolidation process.

Once targeted effective stress levels were reached, the effective stresses were held to allow secondary compression (or drained creep) of the specimen to occur. Series A and Series B tests had essentially no secondary compression prior to shear. The time for secondary compression for Series C tests ranged from one to 48 hours. Secondary compression was allowed to occur because the Series B tests, which provided the first high ($\sigma'_c \geq 5$ MPa) consolidation stress results, indicated that the level of drained creep became significant after reaching the final effective stress for high consolidation stresses. It was found that for some Series B tests, if drainage was stopped prematurely prior to shear, excess pore pressure would develop

without an increase in applied axial load or cell pressure. These creep–developed pore pressures caused slight to moderate reductions in effective confining pressure and interfered with small strain measurements in the test.

For Series C tests, shearing of specimens was performed at slightly higher strain rates than tests in previous series; from 2.3×10^{-5}/sec to 2.8×10^{-5}/sec (8.4 to 10.2%/hr). Two undrained tests were sheared at strain rates an order of magnitude higher (3.3×10^{-4}/sec or 120%/hr) than all previous tests; however, this is believed to be of minor significance with respect to shear results (see Chapter 4 for corroborating results). Drained shear tests were performed at constant mean effective stress (constant p') during shear. For some of the drained tests, axial strains in excess of 30% were developed in an attempt to reach steady state conditions.

3.4 EXPERIMENTAL PROCEDURES FOR CONVENTIONAL FROZEN TESTS

For the current research effort, 79 specimens were prepared for use in testing; however only 61 specimens were used in testing. Table 3.3 summarizes the histories for the 61 specimens. As can be noted in the table, specimen numbering is not sequential (indicating an un–used specimen) nor was specimen testing chronological. In addition, seven specimens either provided erroneous or highly questionable test results. Of the remaining 54 useful specimens, 17 were tested at a nominal temperature (T) of –15° C; 19 were tested at T = –20° C and 13 were tested at T = –25° C. Additional tests were also performed at approximate temperatures of –5° C, –14° C, –23° C, –24° C and –28° C; however, temperature control for these tests are

suspect. Tests were prepared to preshear relative densities between 33 and 93% with the majority of specimens at two D_r, ≈ 35% and ≈ 90%. Nominal confining pressures of either 0.1 and 10 MPa were used for all tests, and the three strain rates used by Andersen (1991) were again used; namely, slow ($3x10^{-6}$/sec), moderate ($3.5x10^{-5}$/sec) and fast ($5x10^{-4}$/sec).

The conventional test procedures closely follow those developed by Andersen (1991). Tests procedures are divided into three stages; specimen preparation and freezing, specimen trimming and set–up, and shearing. Each of these stages are described below. Much of this discussion was abstracted from Andersen (1991) and Andersen et al. (1992).

3.4.1 Specimen Preparation and Freezing

3.4.1.1 General Procedure

For conventional frozen MFS tests, sand is first deposited in molds, saturated with de–aired water and frozen. The molds used for the preparation and freezing of specimens were obtained from CRREL and originally had been used by Martin et al. (1981) in earlier MIT frozen soil research. Figure 3.11 presents a series of schematic drawings of a mold in different stages of operation. The mold features a thin, inner split–sleeve of plexiglas surrounded by a thick outer sleeve of plexiglas, both sandwiched between brass top and bottom caps. Prepared specimens have approximate dimensions of 3.5 cm diameter by 8.1 cm length. Dry sand is deposited inside the plexiglas sleeves and then saturated with water. The molds are designed so that water can be circulated through the prepared specimens through porous elements fitted into the top and bottom caps. Filter paper is used between the sand and porous elements to prevent the migration of fines out of the specimen during the preparation process. At the end of

saturation, part of the top cap is removed and replaced by a freezing cap. Freezing fluid is circulated through this freezing cap creating top–to–bottom uniaxial freezing of the specimen. Excess pore water can leave through the bottom cap during the freezing process.

3.4.1.2 Preparation Method

Multiple sieve pluviation (MSP), as previously described in the Section 3.1.2, was used to form all conventional frozen specimens in the current research effort. Although capable of producing uniform specimens at varying relative densities, the majority of specimens were either loose ($D_r \approx 35\%$) or dense ($D_r \approx 95\%$). A few specimens were formed at intermediate densities ($D_r \approx 50\%$ and 80%). The procedure for preparing the specimens in the freezing molds is similar to that for the unfrozen tests. The pluviator is placed over the freezing mold and sand is poured into the funnel and through the four screens. Five molds are prepared and taken into the growth room which is maintained at 0° C. The top caps of the molds are connected, in parallel, to a stationary reservoir which is connected to a vacuum source. The bottom caps are directly connected, also in parallel, to this vacuum source. A vacuum, approximately 28 inch Hg (95 kPa), is drawn on the prepared specimens and then the vacuum source is closed off to the specimens to check for possible leaks in the molds and connections. Once a non–leak condition is established, a movable reservoir, filled with deaired deionized distilled water, is connected to the bottom caps of the molds and the vacuum is re–applied to the entire setup including both reservoirs. The movable reservoir is then raised above the molds so that the water then flows through the molds, from bottom to top, to the stationary reservoir. A head of approximately one meter of water is used for this initial specimen saturation.

After several pore volumes of water pass through the specimens (usually less than 1 hour after initiation), the movable reservoir is placed at the same elevation as the stationary reservoir such that their water levels are above the specimens (i.e., a no flow condition) and the vacuum is held overnight.

3.4.1.3 Specimen Freezing

The following morning, the vacuum is slowly removed from the specimens, and the movable reservoir is placed at the elevation of the top of the specimens. The brass top caps of the molds are removed and replaced with freezing caps. The filter paper between the top cap and specimen is retained and the freezing caps are placed in direct contact with the filter paper. The freezing fluid (ethylene glycol) is circulated through the freezing caps at –15° C and the specimens are frozen from the top down, while allowing for drainage through the base of the molds and into the reservoir. Freezing is assumed to be complete when water droplets freeze on the base of the mold. In general, the freezing process lasts approximately four to six hours.

3.4.1.4 Storage

After freezing, the top and bottom caps are removed and the specimens, along with their thin plexiglas split–sleeve, are extruded from the thick outer sleeves using a hydraulic jacking assembly. The specimen and inner sleeve are then prepared for storage in a freezer. First, the exposed ends of the specimen and the split–seam of the plexiglas sleeve are covered with vacuum grease. The specimen is then wrapped in saran wrap and placed in a plastic bag with pieces of ice. The specimens are then stored in a freezer set at –20° C until needed for testing.

3.4.2 Specimen Trimming and Set–Up for Shear

The specimens must be trimmed prior to being set–up in the triaxial cell. The trimming process consists of removing frozen MFS from both ends of the specimens creating smooth ends which are nearly perfectly perpendicular to the frozen sand cylinder. The trimming also shortens the specimens to increase stability during shear as well as removes the filter paper, greases and any specimen irregularities such as sand or ice gaps created by the segregation and densification of the sand during specimen preparation. Specimen trimming occurs in the vestibule room of the cold room facility which is maintained at –4 to –5° C. Trimming is done by hand with sharpened steel knives with trimming proceeding in 10 minute cycles; five minutes of trimming in the vestibule followed by five minutes of temperature equilibration in the testing room which is set between –18° C and –28° C, depending upon the selected testing temperature. This process prevents melting of the specimen due to the continued handling during trimming. Each end of the specimen is separately trimmed by extruding approximately 0.7 cm out of the split–sleeve and clamping the specimen firmly into place in the split–sleeve. In order to obtain a trimmed specimen with a near–perfect right circular cylinder shape, the specimen is placed on a flat metal stand which has a spring loaded depth gage sensitive to 0.025 of an millimeter. The trimmed specimen ends are then placed in contact with the depth gage at various locations to check for levelness and smoothness of the trimming. The difference in readings over the trimmed surface is held to within a 0.025 mm tolerance.

Once the ends of the specimen are trimmed, the diameter of the specimen is measured at eight locations; one reading at each end and

specimen third points performed in two directions, each 90° to the other. The measurements are performed using a hand held micrometer with a direct readout to 0.001 of an inch. Four measurements of the specimen's length are also performed, one measurement at four locations spaced at roughly 90° around the circumference. These diameter and length measurements are used to estimate the specimen volume. The trimmed specimen is then weighed on an electronic scale sensitive to ±0.01 g.

For the current research, all specimens were tested with "lubricated" ends, i.e., an ice cap was formed on each end by open–air freezing of distilled water. After freezing, the ends were re–trimmed to the same tolerance level as the frozen MFS. After trimming, measurement of the specimen length and weight are again made as described previously to compute the thickness of the ends. Small diameter holes, approximately 1 mm in diameter and 3 mm in depth, are then bored into the ends of the specimen. These holes, which will mate with 1 mm pins in the top cap and pedestal of the triaxial cell, aid in both aligning the specimen between the base pedestal and floating top cap of the triaxial cell and in increasing (slightly) the specimen's stability during shear.

Components of the triaxial cell are then prepared by covering both the base pedestal and top cap with high–vacuum silicone grease. Two prophylactic membranes are placed, still rolled, on the base pedestal with two o–rings, both of which will be used to seal the specimen against the cell fluid. The specimen (top end up) is placed and seated on the base pedestal, then the top cap is lowered onto the top of the specimen using a specially–designed alignment device which is mounted directly on the base of the triaxial cell. Excess grease on the specimen and the pedestal and top

cap is forced out by applying a small axial force through the alignment device. This axial force also brings the top cap, specimen and pedestal into better initial alignment. Any excess grease is then removed and the two prophylactic membranes are rolled from the base pedestal over the specimen and onto the top cap. One o–ring is also rolled from the base pedestal to the top cap so that both ends of the membranes are secured.

The on–specimen strain device is placed around the specimen and plugged into the electrical feedthroughs in the cell base. The top and bottom yokes rest at roughly the third points along the specimen so that the active gage length includes the central portion of the specimen. The two internal thermistors are then set in place, both on the same side with one near the top and the other near the bottom of the specimen. With the internal devices in place, the posts in the on–specimen strain device are removed and the initial gage lengths between the top and bottom yokes are measured with the optical device.

The specimen alignment device is then removed from the cell base and the upper shell of the triaxial cell is lowered onto the cell base using the guide stand. Care is taken not to accidentally disturb the on–specimen strain device during the lowering of the upper shell. The loading piston, with the attached load cell, is then gently lowered onto the top cap and the top and base of the triaxial cell are bolted together. The loading piston is then locked into position. The entire triaxial cell is then placed in the loading frame. Before the cell is filled with silicone oil, each of the internal electronic devices are connected to appropriate power supplies as well as the data acquisition system, and device output levels are checked for satisfactory reading, i.e. readings within the normal range. In addition, a slight preload

is applied to the specimen through a manual crank on the loading frame. It is reapplied at various times throughout the preshear stage of the test because it gradually reduces over time.

The triaxial cell is filled with silicone oil using a diaphragm pressure reservoir located inside the cold room. The filling process occurs in two stages, the first being a relatively fast stage where oil in the reservoir is placed under pressure (approximately 2 kPa) and allowed to quickly flow into the triaxial cell from the bottom up. Once oil exits the top exit port of the cell, the pressure is removed from the reservoir, and the oil is allowed to flow under gravity. This slower second stage removes any small air pockets which may have been trapped in the triaxial cell during the more rapid cell filling stage. External electronic devices are connected and checked for appropriate reading levels during the filling process.

3.4.3 Pre–shear and Shear Procedures

Once the cell is filled and all electronic devices are properly set, the environmental chamber is sealed and the thermoregulating unit is switched on. Voltage readings, representing initial or "zero" conditions, are taken of the cell pressure and the displacement transducer that measures volume. A target voltage for the cell pressure transducer is then calculated using the cell pressure zero reading, the input power voltage, the target cell pressure and appropriate calibration factors. Two nominal cell pressures were used for all testing, 0.1 MPa and 10 MPa. These pressures were applied using the cell pressure/volume controller and the set–point (= target voltage) of the closed–loop analog feedback system. The specimen is allowed to sit in the triaxial cell under the applied pressure until both the temperature and the leakage rate of oil out of the triaxial cell (e.g., around loading piston or

through the electrical feedthroughs) stabilize. Measurement of a constant preshear leakage rate occurs for a period equal to or longer than the time required for shear; usually overnight for moderate and fast strain rate tests and over two days for slow strain rate tests (see Section 3.6 for use of leakage rate).

Once a constant leakage rate has been established, the compressibility of the cell fluid is measured by cycling the cell pressure about the target value and measuring the change in volume as a function of the change in cell pressure. Just prior to shearing, the small preload on the specimen is removed and a "zero" reading of the load cell is recorded. The load frame is set to the appropriate deformation speed and shearing of the specimen begins. Three nominal strain rates; $3x10^{-6}$/sec (slow), $3.5x10^{-5}$/sec (moderate) and $5x10^{-5}$/sec (fast) were used in testing. During shear, more data are recorded at the beginning to better record small strain behavior. In general, the specimens are sheared to axial strains in excess of 20%.

After shearing, the cell pressure is relieved and cell fluid is forced back into the oil reservoir under 200 kPa pressure. External devices and connections are removed and the triaxial cell is removed from the loading frame and disassembled. The specimen is photographed and then removed from the base pedestal. The final diameter is measured near the ends and at third points along the length. The specimen is then placed in an oven and dried. A post–shear dry weight is recorded to compare with the specimen preparation weights. In addition, a post–shear sieve analysis is performed on the dried MFS. If required, oil cleaning of the oven–dried sand is performed on approximately one–half the specimen with the sieve analysis performed on the oil–cleansed material.

3.5 EXPERIMENTAL PROCEDURES FOR CONSOLIDATE–FREEZE TESTS

The consolidate–freeze tests represent a unique testing condition where specimens are first consolidated and then frozen while under a desired effective confining stress. Ten consolidate–freeze tests were performed as part of the current research on dense specimens under four confining pressures, 0.1, 2, 5 and 10 MPa. All tests were performed at moderate strain rate (3.5×10^{-5}/sec) and T = –10° C. Table 3.4 summarizes the initial specimen characteristics of the consolidate–freeze tests. Note that tests were not performed sequentially.

In essence, the consolidate–freeze test procedures essentially combine the procedures of the unfrozen and conventional frozen MFS testing programs. A major addition is a specimen freezing phase of testing. The following sections briefly describe the consolidate–freeze test procedures, highlighting the differences between these procedures and those from the unfrozen and conventional tests and the procedures used for specimen freezing.

3.5.1 Procedures for Specimen Preparation and Consolidation

The procedures for the specimen preparation and the initial phase of testing (i.e., saturation and consolidation) are essentially the same as those for unfrozen tests. The cell base is flushed with water and air dried prior to specimen preparation. Thick and thin rubber membranes are attached to the base pedestal and the specimen former/membrane expander (Fig. 3.2) is used to form the cylindrical opening for the specimen. Thick, greased rubber membranes are used as lubricated ends, and multiple sieve pluviation is used in forming all test specimens. The top cap and internal drainage lines are

installed; a vacuum is placed on the specimen ($\approx$ 0.1 MPa); and initial measurements are made as described in the unfrozen test procedures. The on–specimen strain device is placed around the specimen, and three thermistors (rather than two) are also placed around the specimen. Thermistors are placed near the top, bottom and middle of the specimen with the middle thermistor diametrically opposite the ones at the top and bottom. These thermistors are used to measure temperatures during both the freezing process and during shear. Once all internal electronic devices are in place and final measurements are made, the upper shell of the triaxial cell is lowered and secured onto the cell base.

The triaxial cell is then transferred to the hydraulic loading frame in the testing room of the Low–Temperature Testing Facility. After checking the internal devices for appropriate output levels, the triaxial cell is filled with oil. The vacuum on the specimen is maintained throughout both the cell transfer and subsequent filling processes. An initial cell pressure, equal to the applied vacuum, is applied to the specimen while the vacuum is removed from the specimen. Drainage lines to the specimen are then opened and the specimen is flushed with CO_2, and then with deaired deionized distilled water. Approximately 500 ml of water is passed through the specimen prior to initiating overnight back–pressure saturation. For the overnight saturation, the cell and back pressures are set at 0.3 and 0.2 MPa, respectively. These pressures are significantly lower than those commonly used in the unfrozen tests (1.0 to 1.3 MPa).

A B–value evaluation is performed after overnight saturation. After a successful B–value check (i.e, B $\geq$ 0.97), the cell and back pressure are simultaneously decreased to 0.2 and 0.1 MPa, respectively. The lower back

pressure aids in the specimen freezing phase of the testing. For effective confining stresses higher than 0.1 MPa, the specimen is consolidated to the higher stress level with at least 4 hours of secondary compression allowed prior to freezing.

3.5.2 Specimen Freezing Procedures

Prior to specimen freezing, the specimen has been saturated and consolidated at a temperature of +3° C. Freezing fluid is now circulated through the base pedestal to cause bottom–to–top freezing of the specimen while the cell pressure and back pressure are maintained constant. During saturation and consolidation, movement of specimen pore water is restricted through only the port in the center of the base pedestal; however, this port is frozen once specimen freezing begins. Therefore, prior to freezing, the line connected to the back pressure/volume controller is connected to the port in the top cap via the triaxial cell's internal drainage line. Freezing fluid can now be circulated through the pedestal as excess specimen pore water exits through the top cap. The freezing fluid is maintained at –8° C during the freezing process. During the freezing process, the temperature inside the environmental chamber (i.e., around the triaxial cell) is maintained at +3° C.

Temperature measurements are recorded during the freezing process using the three thermistor located near the specimen. The amount of pore water expelled during freezing is measured via the back pressure controller. The freezing process is ended when the top thermistor registers zero degrees and/or there is no measured outflow of water. In general, approximate freezing time is 4 hours.

Once specimen freezing is complete, the cell pressure is reduced approximately 0.1 MPa (the existing back pressure level) to equal the final

effective confining stress on the specimen. The temperature inside the testing room is then reduced to –13° C, and a mercury contact switch with a set–point of –10° C is now used inside the environmental chamber. To hasten the decrease in temperature within the environmental chamber, its door is opened to allow the lower testing room temperature to directly decrease the temperature in the environmental chamber. After the heat source in the thermoregulator is switched on, the door to the environmental chamber is closed. While the temperature is decreasing in the chamber, the back pressure/volume controller is removed from the environmental chamber and placed in the vestibule room, which is now set at +5° C. All pore water lines are opened to the atmosphere and the pore pressure transducer is removed. These precautions prevent rupture of the water–filled components caused by the freezing of the water. The temperature is allowed to equilibrate through all components in the environmental chamber before the preshear leakage rate is measured.

3.5.2.1 Earlier Methods of Specimen Freezing

Other methods of specimen freezing and volume measurement were also attempted during the consolidate–freeze testing program but proved less successful. Initially, the freezing process was to occur from the top down with freezing fluid being circulated through a specially designed cap that would fit over the floating top cap. Excess pore water would then exit through the port in the base pedestal. However, the flow of freezing fluid through the designed top cap was insufficient to create a strong enough cooling source; therefore, the base pedestal was redesigned so that the freezing fluid would circulate through it.

Another change in the freezing process was an increase in freezing fluid

temperature. Freezing for the first four consolidate–freeze tests used a freezing fluid temperature of –15° C, the same as that used in freezing conventional test specimens. However, the measured volume change was found to be significantly lower than anticipated, i.e., the theoretical expansion of the pore water was calculated to be 3 to 5 times higher than that measured (this is discussed further in Section 3.6). It was believed that the low freezing fluid temperature was not only freezing the specimen but also freezing the exit point for the excess pore water. For subsequent tests, the temperature of the freezing fluid was increased to –8° C. In addition, a small heat source (6 volt light bulb) was placed beneath the exit port of the internal drainage line to further deter the premature freezing of exiting water.

3.5.2.2 Modification of Pore Water Volume Measurement

Another redesign led to more reliable measurement of expelled pore water during the freezing process. Initially, the back pressure was reduced to zero and the exterior port to the top cap's internal drainage line was connected to an open–ended graduated tube with 0.1 cc divisions. As specimen freezing progressed, excess pore water would travel through the top cap and internal drainage line and into the graduated tube. Readings were taken manually at a variety of intervals with shorter intervals (as low as 3 minutes) early in the freezing process and longer intervals (30 minutes to an hour) as the rate of out flow decreased. This measurement method was used for the first five consolidate–freeze tests. For subsequent tests, the measurement method was performed as previously described, i.e., using the pressure/volume controller and computer automation. Pore water volume could then be measured via the back pressure controller while maintaining a back pressure of 0.1 MPa (or less) during the freezing process.

Initially, the internal drainage line used in the tests consisted of two separate pieces of copper tubing; one coiled–shape piece which was "wrapped" around the top cap and another straight piece which connected the coiled tubing to the exit port in the cell base (see Fig. 3.4). Although not directly observed, it is believed that a leak developed in the connection between the two drainage line pieces caused by the expanding water which became trapped inside the internal drainage line during the freezing process. The connection's sealing capability apparently deteriorated with continued use so that pressurized cell fluid was able to enter the internal drainage line during specimen consolidation and the freezing process (thus, volume changes during consolidation are also erroneous). Once this design flaw was discovered, the two–piece drainage line was replaced by a continuous piece of tubing, effectively preventing leakage of the cell fluid into the drainage line.

3.5.4 Procedures For Shear

Once the temperatures in the environmental chamber have equilibrated and a constant leakage rate is determined, the test procedures follow those for conventional frozen tests. Cell fluid compressibility and shear tests are performed after which the cell pressure is relieved, the cell fluid removed and the triaxial cell taken out of the loading frame and disassembled. Final specimen dimensions are taken as described for conventional tests. Post–shear sieve analyses are performed after drying.

3.6 DATA COLLECTION AND REDUCTION PROCEDURES

This section describes the data collection and calculation procedures used to reduce raw data. For all test programs, voltage readings from the electronic measuring devices were recorded using the Central Data Control

Acquisition System. Voltages were then converted to engineering units using conversion factors which are relationships between a known pressure (or load, displacement, etc.) of a device and the output voltage of a device normalized by the input voltage. These engineering units were then used to calculate various testing parameters associated with the different phases of testing. All data reduction was performed on 286–based personal computers using Lotus 123 spreadsheet software. The following sections briefly describe the data reduction methods used in the testing programs and the testing parameters developed from the reduced results.

3.6.1 Data Reduction for the Unfrozen MFS Testing Program

For unfrozen tests, data collection was performed in five tasks: 1) zero voltage values (voltages prior to test initiation), 2) overnight back–pressure saturation, 3) B–value evaluation, 4) consolidation, and 5) shear. The consolidation and shear tasks required the most complex reduction procedures and are therefore discussed separately.

The zero voltage task was used to collect initial voltage readings ("zero" values) of the electronic devices prior to testing for use in the subsequent reduction of raw test data. Raw data from the saturation task chronicles the effective stresses on the specimen, volume changes during both the initial pressuring up sequence and the overnight maintenance of the cell and back pressures, and any changes in specimen length during the saturation process. The saturation results were used to calculate a leakage rate from the drainage system. It should be noted that this leakage rate incorporates both external (e.g., leakage at connections to the cell) and internal (e.g., leakage through the membrane and under the o–rings) components, though the internal component is thought to be negligible.

For B–value evaluation, raw data was collected in short time intervals since it was anticipated that the specimen's pore pressure response would be relatively instantaneous. Only cell pressure and back pressure measurements were needed for B–value evaluation.

3.6.1.1 Reduction of Consolidation Results

The reduction of consolidation raw data provided changes in effective stress, specimen volume and specimen lengths during the consolidation process. Post–saturation specimen dimensions were used in reducing the consolidation data. Cell and back pressure calculations were based on previous zero values, but specimen displacements and volume changes are calculated considering zero to be at the initiation of consolidation.

Axial strains (ϵ_a) were calculated based on the following equation

$$\epsilon_a = \Delta L/L_o \qquad 3.2$$

where ΔL is the measured axial displacements of the specimen and L_o is the initial specimen length, which in this case was the length after saturation. Where possible, specimen displacements were based on the on–specimen ACDT measurements which are deemed more reliable than the external strain measurement; however, use of the external LVDT for axial strain was necessary for some tests where the ACDTs malfunctioned prior or during consolidation. For Series A and Series B tests, external measurement of specimen strains during consolidation was not possible (i.e., no axial prestress maintained during). For these cases; external strain measurements are estimated based on the external axial strain LVDT reading recorded at the start of consolidation and the LVDT reading just prior to shear. For Series C tests, external specimen displacements during consolidation could be continually measured and directly compared to those from the on–specimen

ACDTs.

For all unfrozen testing series, a leakage rate correction was included in calculating the changes in specimen volume during consolidation. The correction used the leakage rate (LR) measured during overnight back pressure saturation and was calculated as

$$\Delta V = \Delta V_m + LR \cdot \Delta t \qquad 3.3$$

where ΔV is the corrected change in specimen volume, ΔV_m is the measured change in specimen volume from the back pressure/volume controller and Δt is the elapsed time since the beginning of consolidation. In this equation, the leakage rate (LR) is assumed positive for a leak "out" of the system. Table 3.5 lists the leakage rate measured for the unfrozen tests. Given the rapid application of consolidation stresses, especially for the Series A and Series B tests, correction for leakage rate has only minor effects on calculated void ratios. However, for tests with substantial periods of secondary compression, such as those in Series C, the effect of leakage could be significant (see Section 3.7 for more discussion).

Some researchers (e.g., Nicholson et al. 1992; Kramer et al. 1990; and Frydman et al. 1973) have shown that a correction to specimen volume is warranted due to the tendency of the membrane to penetrate into the outer voids of the specimen with the increase in confining pressure. Under low stress conditions, a correction for membrane compliance would not apply to the MFS used in this study due to the relatively small sizes of the sand particles (all particles are smaller than the #40 sieve) and the relatively high fines content. However, at higher stresses (i.e., 10 MPa), membrane compliance might influence measured volume changes. The magnitude of the compliance was not measured in this program and was not taken into account

in the calculations of volume change.

3.6.1.2 Reduction of Shear Results

Shear data reduction provided various shear parameters including: axial displacements, cell pressure, axial loads and specimen pore pressure changes (undrained tests) or specimen volume changes (drained tests). These results were then used to calculate test parameters such as the principal effective stresses (σ'_1 and σ'_3), the stress difference ($\sigma'_1 - \sigma'_3$), stress path components p′ ($= \frac{\sigma'_1+\sigma'_3}{2}$) and q ($= \frac{\sigma'_1-\sigma'_3}{2}$), obliquity ($R = \sigma'_1/\sigma'_3$) and Skempton's pore pressure response ($A = \frac{\Delta u - \Delta \sigma_3}{\Delta \sigma_1 - \Delta \sigma_3}$).

Axial Strain

The reduction consisted of first converting the raw data of each axial displacement measuring device (one LVDT and two ACDTs) to values of axial strain (ϵ_a). Strains are calculated from specimen dimensions and yoke gage lengths corresponding to the end of consolidation (or the end of saturation if no consolidation was performed). These individual axial strain measurements were then combined into one quantity for future calculations. Typically, overall specimen axial strains were developed by first averaging the strains from the two on–specimen ACDTs up to $\epsilon_a \approx 3\%$, then calculating subsequent increases in ϵ_a using the average strain rate computed from the external LVDT and the elapsed time.

Prior to determining the strain rate from the external LVDT, the measured external strains were corrected for compliance of the loading piston and cell base. This correction was determined using an aluminum dummy substituted for the sand specimen. The dummy specimen was subjected to axial loads, and the axial strains were measured via the external LVDT and the internal ACDTs. A comparison of the strains measured by the two

methods indicated that a significant amount of compliance existed in the loading system of the triaxial cell during shear. Based on these dummy tests, formulae were developed for two specimen end conditions. One formula was for an end condition where no rubber membrane was used and is expressed as

$$\epsilon_{a_{corr}} = \epsilon_{a_{meas}} - 0.325 \cdot F_{ax} \qquad 3.4$$

where $\epsilon_{a_{corr}}$ is the corrected axial strain, $\epsilon_{a_{meas}}$ is the measured axial strain and F_{ax} is the measured axial force in MN. A second formula considers the case where thick rubber membranes were used as lubricated ends and is expressed as

$$\epsilon_{a_{corr}} = \epsilon_{a_{meas}} - 0.875 \cdot F_{ax} \qquad 3.5$$

with the same variables as in Eq. 3.3. Note the higher compliance for lubricated ends with rubber membranes.

Specimen Area

A correction was used for the change in specimen area during shear. In general, the specimen area was corrected using a combination of the widely used right circular cylinder and parabolic correction formulae. The right circular cylinder correction is expressed as (Germaine and Ladd 1988)

$$A_c = A_0 \cdot \left[\frac{1 + \epsilon_v}{1 - \epsilon_a}\right] \qquad 3.6$$

where A_c is the current specimen area, A_0 is the initial specimen area, and ϵ_a and ϵ_v are the axial strains (positive for axial shortening) and volumetric strains (positive for expansion), respectively. The parabolic correction formula is expressed as

$$A_c = A_0 \cdot \left[-\frac{1}{4} + \frac{\sqrt{25 - 20\epsilon_a - 5\epsilon_a^2}}{4(1-\epsilon_a)} \right] \qquad 3.7$$

with the same definitions as for the right circular cylinder formula. Note

that this formula applies to undrained ($\epsilon_v = 0$) conditions. However, it was also applied to the drained tests in the testing program (i.e., volume changes were ignored). Table 3.5 list the contributions (in percent) of Eq. 3.6 and 3.7 used in area correction calculations for Series B and Series C tests which provided useful shear results. The reader is referred to Section 3.7 for further discussion of the area correction calculation.

Membrane Compliance

A correction due to membrane compliance was also made to the measured axial stress. This membrane compliance was calculated based on the following equation (see Germaine and Ladd 1988)

$$\Delta\sigma_a = -\frac{4bE_r}{D_i}\cdot(\epsilon_a + {}^2/_3\epsilon_v) \qquad 3.8$$

where $\Delta\sigma_a$ is the change in axial stress due to the membrane, b is the membrane thickness, D_i is the initial diameter of the specimen ($\approx$ diameter of membrane), E_r is the elastic modulus of rubber ($\approx$ 1.4 MPa), ϵ_a is the axial strain and ϵ_v is the volumetric strain of the specimen during shear. For most tests a thick (b = 0.036 cm) and thin membrane (b = 0.0008 cm) were used. Ultimately, this axial stress correction proved to be negligible given the relatively high applied loads in the tests, except for drained tests at low confinement. No correction for radial stress was applied since the correction would be negligible, especially for tests with relatively high effective confining stresses. A correction to the axial load for the "spring" force exerted by the rigid, internal drainage line connected to the top cap also was considered negligible.

Volumetric Strain

A correction for leakage in volumetric strain calculations, as given in Eq. 3.3, was used for specimens sheared under drained conditions. As with

consolidation, a correction for membrane penetration into or out of the specimen was deemed negligible.

3.6.2 Conventional Frozen MFS Test

3.6.2.1 Data Reduction Related to Shear Results

Data reduction for conventional frozen tests did not require as many tasks as the unfrozen tests. Data collection and reduction is divided into three areas: preshear leakage rate, cell fluid compressibility and specimen shear. During preshear, silicon oil leaked from the lines and connections between the triaxial cell and cell pressure controller as well as from around the piston and through the electrical feedthrough connections. This leakage rate was calculated from the preshear data with a constant leakage rate occurring over a period of time greater than the duration of the tests. After a constant leakage rate was established, the cell fluid compressibility was measured by cycling the cell pressure ± 10% about the current confining pressure and measuring the change in cell fluid volume. A successful compressibility test consisted of a linear relationship between the change in cell fluid volume and the change in applied cell pressure as well as an instantaneous response in the volume change with applied cell pressure. Both phenomenon indicate the absence of air bubbles which distort compressibility results. The slope of the cell pressure versus cell fluid volume relationship was taken as the fluid compressibility (C_p) for that test.

Similar to the reduction of shear results for unfrozen tests, data reduction of conventional frozen test shear data lead to measurements of specimen displacements, cell pressures, axial loads and changes in cell fluid volume. These measurements were converted to axial strains, applied stresses and specimen volumetric strains. Axial strains were calculated in a manner

similar to that for unfrozen tests; i.e., the strains of the individual devices were first calculated, then the average of the internal ACDTs were used to an $\epsilon_a \approx 3\%$ and the average strain rate calculated from the external LVDT was used to calculate the remaining strain levels. Correction of the external strain measurement for loading piston compliance and base flexure were also included. The following correction was used for all conventional tests

$$\epsilon_{a_{corr}} = \epsilon_{a_{meas}} - 0.051 \cdot F_{ax}{}^{0.645} \qquad 3.9$$

where $\epsilon_{a_{corr}}$ is the corrected external axial strain, $\epsilon_{a_{meas}}$ is the measured axial strain and F_{ax} is the axial load. As was the case for the unfrozen tests, Eq. 3.9 was developed from a test on an aluminum dummy. However, ice caps were not placed on the dummy prior to testing so the effects of ice cap compliance is not included in this correction. This equation is also based on a calibration performed at a temperature of –20° C. The effects of temperature on the measured compliance, while not measured, is assumed to be negligible. The writer notes that the exponential (0.645) in Eq. 3.9 leads to a better fit between the equation and the measured results from the aluminum dummy calibration.

To calculate axial stress, the axial load was divided by the area of the specimen. However, unlike unfrozen tests, a modified right circular cylinder formula was used to estimate the specimen area. The formula was of the following form (Andersen 1991)

$$A_c = A_o \left[\frac{1 + \epsilon_v}{1 - \alpha\epsilon_a}\right] \qquad 3.10$$

where A_c is the corrected area, A_o is the initial specimen area and ϵ_a is the axial strain (in corrected form), ϵ_v is the volumetric strain and α is a factor to account for bulging of the middle of the specimen or flaring out at the specimen ends. An α factor of 1 reverts Eq. 3.10 to the right circular

cylinder formula (Eq. 3.6). An α less than 1 indicates that some flaring of the specimen ends occurred during shear and an α greater than 1 indicates that some bulging in the middle of the specimen occurred during shear. In essence, a small α (< 1) leads to a smaller specimen cross–sectional area than if a right circular cylinder was assumed during shear and a large α (> 1) leads to a larger specimen cross–sectional area than from right circular cylinder formulation. The α factors used in the reduction of conventional frozen shear tests are presented in Table 3.6. Based on all tests results, α factors ranged from 0.81 to 1.29 with an average value of 1.02±0.097.

The method to calculate volumetric strains of the specimen follows that proposed by Andersen (1991). This indirect method incorporates a number of corrections that account for leakage of oil from the cell, compressibility of the cell fluid and volume changes caused by the flexure of the cell base due to the axial force. The formula used in calculating the volume change of the specimen in conventional frozen tests was as follows

$$\Delta V_s = -\Delta L_{cp}A_{cp}-\Delta L_{tp}A_{tp}+LR\Delta t+\Delta\sigma_c C_p+F_{ax}C_{ax} \qquad 3.11$$

where

ΔV_s = the change in volume of the specimen (positive means dilation)

ΔL_{cp} = the distance that the pressurizing piston travels <u>into</u> the cell fluid reservoir

A_{cp} = the area of the pressurizing piston of the cell pressure controller

ΔL_{tp} = the distance that the loading piston travels into the triaxial cell

A_{tp} = the area of the loading piston of the triaxial cell

LR = the leakage rate of fluid out of the triaxial cell

Δt = the time from the start of the test

$\Delta\sigma_c$ = the change in cell fluid pressure from the start of shear

C_p = the measured compressibility of the cell fluid and triaxial cell including transmission lines

F_{ax} = the change in axial force during shear acting on the base of the triaxial cell through the specimen

C_{ax} = coefficient relating the volume change due to base flexure of the triaxial cell and the applied axial load

The correction for leakage rate ($LR\Delta t$) is based on leakage rates measured for each test. These leakage rates are presented in Table 3.6. As can be seen in the table, the leakage rate is influenced by the magnitude of the cell pressure with leakage generally increasing with increased cell pressure. For 0.1 MPa tests, the leakage rate was 0.0020 ± 0.0015 cc/min; for 10 MPa tests, the leakage rate was 0.0044 ± 0.0016 cc/min. Measured leakage rates varied from a high of 89.5×10^{-3} cc/min for test FRS117 (an anomalous value) to a low of 0 cc/min for test FRS79.

The correction for cell fluid compressibility ($\Delta\sigma_c C_p$) is also as proposed by Andersen. Table 3.6 also presents the fluid compressibility measured for each test. As can be noted in the table, the general trend is for fluid compressibility to decrease by an order of magnitude as the cell pressure increases. A cell pressure "smoothing" procedure was used in the

compressibility correction where a "moving" average of three cell pressures; one at, one above and one below the current point, was used in the calculation of $\Delta\sigma_c$.

The correction for base flexure ($F_{ax}C_{ax}$) used by Andersen was also used for each test. Since the same cell base is used in both the current research and in the research by Andersen, the correction factor C_{ax} = 10.2 cc/MN developed in Andersen's work was used for all tests. Andersen also included a correction in measured volume change to account for the change in diameter of the pressurizing piston on the cell pressure controller. This correction was not used in this research because that pressurizing piston was replaced with a precision–milled piston grounded to within 0.0001 of an inch (0.0025 mm) tolerance in diameter.

Andersen (1991) reports an accuracy of ±0.2% for volumetric strain measurements. This accuracy was based on calibration tests in which no specimen was used. By measuring the volumetric strain, which should be zero, an accuracy of the measurement procedure was derived. No such calibration was performed in the current research; therefore, a similar measurement accuracy is assumed. Volumetric strains during shear of frozen MFS are reported to the nearest 0.1% (see Andersen 1991).

3.6.2.2 Data Reduction of Temperature Results

Temperature measurements were made during both the preshear and shear phases of conventional frozen tests. Measurements were recorded at four locations; two outside the cell in the environmental chamber, and two inside the cell near the top and bottom of the specimen. Raw data, which included the output voltages of each thermistor circuit and the common input voltage (power), were collected by the Central Control Acquisition System.

To summarize the reduction procedure, the output voltages from each thermistor circuit were first converted into resistances using the input voltage and the other known resistances in the thermistor circuit. These resistances were then used in general resistance–to–temperature equations which govern the temperatures characteristics of the thermistors. The resulting calculated temperature from these equations were corrected using calibration factors determined in calibration tests performed at each temperature. The reduction and calibration procedures are discussed in more detail in Appendix A.

Figure 3.12 shows a plot of temperature versus time for test FRS100. This test was sheared at a temperature of –20° C over 2.5 hours (i.e., a moderate strain rate test). The behavior illustrated in the figure is indicative of the behavior in tests at all temperatures and strain rates. The measured temperature results show that the individual thermistors located in the environmental chamber show larger temperature fluctuations than the thermistors located inside the triaxial cell, thus clearly illustrating the buffering capability of the silicon oil in reducing temperature fluctuations. The figure also shows that a temperature gradient exists both outside and inside the triaxial cell, with warmer temperatures near the top. The gradient outside the cell (in the environmental chamber) is due to the natural phenomenon that warmer air will exist over cooler air. Andersen (1991) noted a reversed gradient inside the environmental chamber which he suggested was due to poor air circulation and the use of one thermoregulating unit near the bottom of the environmental chamber. The changed direction of the gradient in the current research is an indication of the enhanced temperature control inside the environmental chamber.

The gradient inside the triaxial cell, though partly due to the gradient

outside the cell, is predominantly produced by the heat generated by the internal electronic devices, i.e., the on–specimen ACDTs and internal load cell. A similar gradient inside the triaxial cell was noted by Andersen (1991) for tests at –10° C which he also attributed to heat from internal devices. For test FRS100, the temperature difference between the the top and bottom of the specimen inside the cell averaged 0.73° C. Table 3.7 presents a summary of the temperatures measured inside the triaxial cell for each test (these are used as the actual testing temperature). Temperature measurements are reported to the nearest 0.01° C. Table 3.8 summarizes the average measured temperatures and the temperature gradients for the tests at the nominal –10° C, –15° C, –20° C and –25° C. The values for –10° C are from Andersen (1991).

3.6.3 Consolidate–Freeze Data Reduction

As was the case for the consolidate–freeze testing procedures (Section 3.5), the data reduction procedures for consolidate–freeze tests combine those from the unfrozen and conventional frozen MFS programs. For the unfrozen phase of consolidate–freeze testing, the data collection and reduction procedures followed those for unfrozen tests (Section 3.6.1), and, once the specimen was frozen, the data collection and reduction procedures followed those for shearing in the conventional frozen tests (Section 3.6.2). Table 3.9 lists the parameters used in reducing consolidate–freeze tests. Table 3.10 summarizes the measured temperature results during testing.

Additional data collection and reduction procedures were developed for the specimen freezing phase of testing. Data collected during the specimen freezing phase included the volume of excess water expelled from the specimen and temperature changes during the freezing process. Figure 3.13

shows a plot of temperature changes and volume of excess water measured for test CF02 (the last test performed), which was consolidated to 10 MPa effective confining stress. Based on the temperature of the thermistor near the top of the specimen (T1), total freezing time was approximately 235 minutes. The pore fluid measurement for this specimen shows a steadily decreasing rate of excess pore water leaving the specimen until the measured outflow stops at approximately 205 minutes, 30 minutes before the top thermistor indicates the specimen is frozen. However, it must be noted that the top thermistor is not located inside the specimen, but in the cell fluid; therefore, a "lag time" may exist between when the thermistor indicates the specimen is frozen and when the outflow of excess water actually stops.

Table 3.11 summarizes the freezing characteristics of the ten consolidate–freeze tests. As can be noted in the table, the time when pore fluid outflow stopped was not coincident with the time the top thermistor indicated a completely frozen specimen. Also noted in the table and discussed earlier in Section 3.5, the procedures used in the freezing process underwent several changes during the testing program. For three tests (CF06, CF07 and CF09) leakage of cell oil into the internal drainage line led to initially large and erroneous volume change results in both specimen consolidation and freezing calculations. Where possible, a rate of oil leakage into the internal drainage line was back–calculated using measured "pore fluid" volume changes which occurred <u>after</u> freezing of the specimen was expected to have been completed (temperature results were used to estimate when freezing was complete). These internal leakage rates were then used to correct measured volume changes during freezing as well as consolidation.

3.7 ERRORS

This section discusses the possible errors associated with particular aspects of the testing programs, including specimen preparation and test results. However, first the test parameters which will be used in presenting consolidation results, where applicable, and shear results from the various testing programs need to be defined. Then the errors associated with each of the testing programs are presented and discussed in Section 3.7.2 and 3.7.3. Finally, Section 3.7.4 presents an analysis on the precision of the test results from the unfrozen MFS and conventional frozen MFS testing programs. The unfrozen MFS test results are presented in Chapter 4, and the conventional frozen and consolidate–freeze tests are presented in Chapter 5.

3.7.1 Test Parameters Used in Presentation of Test Results

This section describes the various parameters developed from the reduction of the raw test data. For all testing programs, the stress–strain results from the shear phase of testing are described by a set of parameters which follow those described in Andersen et al. (1992). These parameters are described below. The volumetric strain behavior of frozen tests (conventional and consolidate–freeze) during shear also follow those previously described by Andersen et al. Additional parameters are used to describe the shear results of unfrozen tests and are also presented below. Finally, parameters used to describe the consolidation behavior from unfrozen and consolidate–freeze tests are also detailed.

3.7.1.1 Test Parameters to Describe Shear Results

Andersen et al. (1992) presented test parameters used to describe the shear results of conventional frozen tests. These parameters were also developed for the unfrozen tests and consolidate–freeze tests of the current

research. Figure 3.14 presents schematic stress–strain ($Q–\epsilon_a$) and volumetric strain ($\epsilon_v–\epsilon_a$) responses which illustrate these parameters. The parameters related to the $Q–\epsilon_a$ results are summarized below where $Q = (\sigma_1 - \sigma_3)$.

Axial strain, ϵ_a – the change in specimen length (ΔL) during shear divided by the specimen length prior to shear (L_o);

Young's modulus, E – the slope of the initial linear portion of the $Q–\epsilon_a$ curve (see Fig. 3.14a).

Yield offset stress, Q_{yo} – the stress determined from the intersection of a line drawn parallel to the initial slope of the $Q–\epsilon_a$ curve, but offset 10^{-4} (0.01%) strain, and the $Q–\epsilon_a$ curve (see Fig. 3.14a).

Upper yield point, Q_{uy}, and corresponding strain, ϵ_y – these parameters represents the upper yield region where significant non–linear $Q–\epsilon_a$ behavior first occurs. The upper yield point represents the point where the slope of the $Q–\epsilon_a$ curve ($dQ/d\epsilon_a$) reaches it minimum positive value before significant strain hardening or strain softening behavior occurs. The four $Q–\epsilon_a$ responses shown in Fig. 3.14b illustrate where the Q_{uy} point would be for cases of post–upper yield strain hardening or strain softening.

Peak strength (deviator stress), Q_p, and corresponding strain, ϵ_p – these parameters represent the peak strength region of the $Q–\epsilon_a$ curve and are illustrated in Fig. 3.14c.

The Young's modulus, yield offset stress and the upper yield stress and corresponding strain represent small strain results. The peak strength and corresponding strain represent large strain results.

The volumetric strain results, presented in Fig. 3.14d, are more

representative of the conventional frozen and consolidate–freeze test results. Two parameters used to describe the volumetric response of these frozen tests are: the maximum rate of dilation, $(\Delta\epsilon_v/\Delta\epsilon_a)_{max}$, which is the maximum slope of the ϵ_v–ϵ_a response; and the volumetric strain at an axial strain of 20%, ϵ_{v20}.

3.7.1.2 Additional Parameters Used for Unfrozen Tests

Additional parameters are used to describe the shear behavior of unfrozen MFS tests. For undrained tests, characteristics were developed for two conditions: the point of maximum obliquity, $R_{max} = (\sigma'_1/\sigma'_3)_{max}$, and peak deviator stress, $Q_p = (\sigma_1 - \sigma_3)_{max}$. For both conditions the following parameters are presented.

Normal effective stress, p′ – the average of the effective major and minor principal stresses, $p' = 0.5\cdot(\sigma'_1+\sigma'_3)$;

Shear stress, q – one half the deviator stress at the particular condition, $q = 0.5\cdot(\sigma_1-\sigma_3) = 0.5\cdot Q$;

Excess pore pressure, u_e – the excess pore pressure developed during shear which equals the measured change in pore pressure minus any change in the cell pressure, $u_e = \Delta u - \Delta\sigma_3$;

Pore pressure parameter, A – a parameter which relates the change in excess pore pressure with changes in applied stress, $A = (\Delta u-\Delta\sigma_3)/(\Delta\sigma_1-\Delta\sigma_3)$ [note that at the peak strength condition, the pore pressure parameter is denoted as A_f];

Effective friction angle, ϕ' – the angle described by the effective stresses at that point, $\phi' = \sin^{-1}(q/p')$ [note that at maximum obliquity, ϕ' is at a maximum];

Obliquity, R – the ratio of the major and minor effective principal stresses, $R = \sigma'_1/\sigma'_3$ or $R = q/p'$; and

Normalized shear stress, q/σ'_c – ratio of the given shear stress to the initial effective confining stress.

For drained tests, the conditions at maximum obliquity and peak strength are coincident, thus requiring only one set of test results. In addition, pore pressures are held constant during shear and specimen volume changes are measured. Therefore, the excess pore pressure and A–parameter are not relevant. However, other parameters are developed, namely:

Volumetric strain, ϵ_v – the change in specimen volume (ΔV) during shear divided by the specimen volume prior to shear (V_o);

Void ratio at failure, e_f – the void ratio at the peak strength (= maximum obliquity) condition; and

The rate of dilation at peak strength, $(\Delta\epsilon_v/\Delta\epsilon_a)_p$ – the slope of the line in $\epsilon_v - \epsilon_a$ space at the peak strength.

Consolidation results were produced for the unfrozen and consolidate–freeze tests. Parameters used to describe consolidation behavior are described below.

Changes in specimen volume, ΔV – the volume of pore water expelled during the consolidation process;

Changes in void ratio, Δe – void ratio changes are calculated from changes in specimen volume;

Axial strain, ϵ_a – the total change in specimen length divided by the

initial specimen length prior to consolidation (measurement from both the on–specimen ACDTs and external LVDT are presented);

Volumetric strain, ϵ_v – the total change in specimen volume divided by the initial volume of the specimen prior to consolidation.

Virgin compression index, C_c – the slope of the linear portion of the consolidation curve in e – log σ'_c space, i.e. $C_c = \Delta e/\Delta \log \sigma'_c$. For MFS, C_c–values were only determined for specimens isotropically consolidated to nominal effective confining stresses $\geq$ 10 MPa or for the anisotropically consolidated specimens where σ'_{1c} replaces σ'_c.

Consolidation stress ratio, K_c – the ratio of the major and minor principal consolidation stresses, $K_c = \sigma'_{3c}/\sigma'_{1c}$. This parameter is only presented for the the anisotropically–consolidated specimens.

3.7.2 Unfrozen MFS Testing Program

There are several errors, both mechanical and computational, which can occur in the unfrozen MFS testing program. Most of the mechanical errors were rectified by experience (learning curve) or by trail and error. However, some errors in testing procedures and data reduction may still have occurred. These errors involve initial specimen dimensions measurement, volumetric corrections to consolidation results and area corrections during specimen shear.

3.7.2.1 Initial Specimen Dimensions

Measurement of the initial specimen dimensions could be a significant error; however, effort was made to minimize this error by taking specimen diameter and height measurements at many points. For Series A tests, three diameter and two length measurements were taken during specimen set–up. Diameter measurements were increased to eight and length measurements to four for Series B and Series C tests. However, errors in initial specimen

dimensions are still possible since specimens dimensions could have changed from the point of measurement during set–up to the initiation of back pressure saturation. Some of the possible causes of dimension changes include the movement and/or jarring of the triaxial cell while being placed onto the loading frame, the application of an initial cell pressure which may be higher or lower than the vacuum initially applied to the specimen, the initial flushing of water through the specimen which may allow previously stable particle arrangements to become unstable and "slip" into a more stable condition, and an application of an initial preload prior to data collection. In analysis, these potential causes are viewed as having minor or negligible effects on specimen dimensions.

As an approximation of the error in initial relative density due to limitations in existing measurement capabilities, calculations were made on a hypothetical, newly formed specimen; 3.450 cm in diameter and 7.480 cm in length. The initial dry soil weight is 110.00 g. These values are typical of unfrozen MFS specimens (see Table 3.2). The resolutions of these measurements, based on the tolerances of the appropriate measuring equipment, are ±0.0025 cm for both the diameter and length and ±0.01 g for the weight. The upper and lower bound in calculated D_r, based solely on these resolutions, are 60.0% and 61.9% with an average of 60.9%. This translates to an approximate error of 3.2% in measured D_r values. In the following Chapters, relative densities are reported to the nearest 0.1%, and void ratios are reported to the nearest 0.001.

3.7.2.2 Specimen Volume Change During Consolidation

As noted in Section 3.6.1, the leakage rate can affect the measured specimen volume changes during consolidation, especially when long periods of

secondary compression are allowed, as for Series C tests. Figure 3.15 presents the ϵ_v versus log time results of the consolidation of test C–13 (isotropically consolidated to a nominal σ'_c = 5 MPa) where leakage is and is not taken into account. As illustrated in the figure, the calculated volumetric strain is too low if leakage is not taken into account in data reduction. Thus, leading to an increase in the calculated final void ratio for this test, where the uncorrected final void ratio is 0.619 and the corrected void ratio is 0.617. The use of the leakage rate in data reduction is also corroborated by axial strain measurements from the on–specimen ACDTs. Figure 3.15 also plots the ϵ_a versus log time for test C–13. As illustrated in Fig. 3.15b, the measured (on–specimen) axial strains indicate a more similar strain versus time slope to that of the corrected volumetric strain than to that of the uncorrected volumetric strain.

3.7.2.3 Area Correction During Shear

Extreme care has been taken in determining an appropriate area correction for each unfrozen MFS test. As described in Section 3.6.1, the area correction for unfrozen tests involves a partitioning of the equations for right circular cylinders (Eq. 3.6) and parabolic (Eq. 3.7) specimen shapes. To evaluate the weight to assign to each equation, the response of the on–specimen ACDTs were compared to the external LVDT strain measurements. This comparison focused on the strain measurements beyond the initial response, i.e., $\epsilon_a > 1\%$. Figure 3.16 presents measured responses of the on–specimen ACDTs for three tests along with the external LVDT response. [Though only used up to $\epsilon_a \approx 3\%$, the on–specimen strains could provide accurate ϵ_a measurements in excess of 10%. This behavior was common for the majority of tests which provided useful shear results.] As

noted in Fig. 3.16c, if the on–specimen ACDTs exhibited an increasing or faster strain rate than that indicated by the external LVDT, more weight was given to the parabolic formula to calculate the area correction for the specimen. On the other hand, if the on–specimen ACDTs exhibited a similar strain rate to that indicated by the external LVDT, as for case (a) in Figure 3.16a, more weight was give to the right–circular cylinder formula. Intermediate cases, such as shown in Fig. 3.16b, shared equal contributions from the formulae to calculate the area correction.

Figure 3.17 presents three Q–ϵ_a responses for test C–15. One Q–ϵ_a response is based on using only the parabolic formula, one based on using only the right–circular cylinder formula, and the third is the actually reported response using a combination of the two formulae based on the on–specimen ACDT behavior and after–test specimen shape. For this third response, the area correction is based on 50% of the right–circular cylinder equation (Eq. 3.6) and 50% of the parabolic equation (Eq. 3.7). As illustrated in the figure, the difference in calculated Q–ϵ_a response between the three curves is negligible at small strains; however, at larger strains the difference is quite significant causing changes in undrained peak shear stress. This figure clearly illustrates why care was taken in applying an appropriate area correction to the shear results.

3.7.3 Frozen MFS Testing Programs

3.7.3.1 Conventional Frozen MFS Testing Program

The current research effort of conventional frozen MFS tests represents a continuation of the test program performed by Andersen (1991). Andersen (1991) presents an error analysis for the relative density and degree of saturation based on a second order approximation to the variance (Ang and

Tang 1975). Using appropriate average and standard deviations, Andersen computed an estimated standard deviations in D_r of 2.0% and in S_r of 0.55%. Though not performed for the current results, it is expected that similar errors exist in the reported D_r and S_r values since similar test procedures were performed in both programs.

Fewer problems were encountered in performing the conventional frozen tests than the unfrozen tests. However, some notable problems did occur, most of which were mechanical in nature. One problem was rupture of the prophylactic membranes which sealed the specimen against the cell fluid. Membrane rupture, though not common, could lead to erroneous volumetric strain measurements. Membrane rupture also led to oil–stained specimens which required cleaning prior to obtaining the specimen's dry weight. Andersen (1991) also reported membrane rupture problems.

Another problem concerned the measurement of volumetric strains for tests at T = –15° C. For these conventional tests, a new component of the triaxial cell's upper shell was first used. The new component consisted of a new guide for the loading piston which also contained additional electrical feedthrough connections and ports for the circulation of freezing fluid around the top cap (see consolidate–freeze discussion, Section 3.5). Small fluctuations in leakage around the loading piston occurred during specimen shearing due to improper o–ring sealing design. Thus, some of the measured volumetric strain results for tests at –15° C are, at best, questionable if not completely erroneous. Erroneous volumetric strain measurements occur mostly for high confinement tests where leakage rate effects are strongest.

3.7.3.2 Consolidate–Freeze Testing Program

The most novel aspect of consolidate–freeze testing centered around the

specimen freezing phase of testing. Since the freezing of soil under high triaxial confining stresses is unique, problems associated with design and implementation of the freezing process were not unexpected. The major problems encountered in performing the specimen freezing have been discussed in Sections 3.5.2 and 3.6.2.

Another difficulty in testing was specimen stability during shear. Unlike conventional frozen tests, the frozen specimen is not trimmed to have a near–perfect right circular cylinder shape prior to shear nor are steel pins used to enhance specimen stability. Although a small preload is maintained on the specimen during saturation, consolidation and freezing, specimen non–uniformities may lead to eccentric alignments of the specimen, base pedestal and loading piston. Initial misalignment will lead to specimen instability as well as to rubbing of the load cell against the inside of the triaxial cell. Specimen instability also led to a weaker specimen causing the measured load to decrease or decrease more rapidly than if the specimen were stable.

3.7.4 Precision of Test Results

The precision is the degree of mutual agreement among individual measurements made under similar conditions (ASTM E111–82). Andersen (1991) evaluated the precision of his frozen MFS results by examining the repeatability of tests at similar conditions. Similar analyses are presented for the unfrozen MFS tests and the additional conventional frozen MFS tests in the current research.

3.7.4.1 Review of Previous Analysis

Andersen (1991) and Andersen et al. (1992) present results of error analyses on the conventional frozen MFS tests performed at –10° C. Andersen

presents the results of seven test conditions which were repeated. For analysis, the coefficient of variation (COV) was calculated for these repeated conditions as well as the mean and standard deviation of the COV's found for all seven conditions. Table 3.12 reproduces Andersen's results. He noted that the variability of his quantities may be due to several factors including "natural variations in the intrinsic properties of the (frozen) sand, unobserved external variables, and observable external variables." He noted that two observable variables; namely, the on–specimen ACDT behavior and the specimen stability, had the most significant effect on the measured results.

On–Specimen Strain Measurement Behavior

Andersen (1991) presented three qualitative classifications for the on–specimen strain response; "good", "fair" and "poor". These classifications are illustrated in Fig. 3.18. In brief, a "good" on–specimen strain response (Fig. 3.18a) signifies that the two ACDTs are in excellent agreement, with respect to strain measurement, during initial specimen shearing. A "poor" response (Fig. 3.18c) indicates that each ACDT may exhibit opposite behavior, i.e., one showing specimen compression with the other showing expansion. A "fair" classification (Fig. 3.18b) corresponds to an intermediate response. Of Andersen's 51 tests, 30 exhibited a "good" response, five "fair" and 16 "poor".

Based on his repeatability analysis (see Table 3.12), Andersen found that "good" and "fair" on–specimen responses produced the best results for the small strain parameters of E, Q_{yo} and ϵ_y. Therefore, he removed tests with "poor" on–specimen strain responses from his analyses of these parameters. He found that the Q_{uy} was not as affected by the on–specimen response and therefore all tests may be used to evaluate the upper yield

stress.

Specimen Stability

Specimen stability would have it's greatest effect on large strain parameters such as Q_p, ϵ_p and the volumetric strain parameters. Andersen notes that the steel pin centrally located in the top cap and base pedestal did not always insure specimen stability during shear. He evaluated the stability of his frozen MFS tests, based on final specimen shapes, and developed four stability qualifiers; "good", "fair", "poor" and "very poor". Figure 3.19 reproduces photographs of four specimens from Andersen's previous work illustrating the four different qualifiers. As with the on–specimen strain response, these qualifiers are subjective, but do provide a basis for classifying test results. Of Andersen's tests, 19 test were classified with "good" stability, 18 "fair", 11 "poor" and two "very poor".

Andersen noted that, based on the COV's of the repeated tests, the parameters describing the peak strength region (i.e., Q_p and ϵ_p) were not affected by specimen stability. However, he does state that their was insufficient data to make a thorough comparison (no "very poor" results in repeatability analysis). Therefore, he chose to remove tests classified as "very poor" from consideration in analysis. In terms of the volumetric parameter, Andersen found that tests classified as "poor" or "very poor" should not be included in future data analyses.

3.7.4.2 Analysis of Current Results

Similar analyses on repeated tests have been performed for the unfrozen MFS and conventional frozen MFS testing programs conducted in the current research. No analysis is presented for the consolidate–freeze testing program given its small data set (10 tests). Seven conditions were repeated in the

unfrozen testing program. Table 3.13 presents the repeatability analysis (COV's) results from these seven repeated conditions. For the additional conventional frozen tests, six conditions were repeated. Table 3.14 presents the repeatability analysis for these six conditions. The writer realizes, as did Andersen in his original analysis, that these analyses were performed on relatively small data sets.

The results of the error analyses on the current tests lead to the same conclusions as previously found by Andersen (1991). Therefore, only tests which meet the appropriate on–specimen ACDT and stability qualifiers (as presented in Section 3.7.4.1) will be presented in Chapters 4 and 5.

3.7.4.3 Qualification of Initial Q–ϵ_a Response for Unfrozen Tests

A third qualification for the unfrozen tests is proposed for the initial stress–strain response since an unfrozen test may have "good" on–specimen ACDT agreement, but still exhibit a poor initial stress–strain response. Unlike conventional frozen tests which were carefully trimmed and "seated" prior to shear, the unfrozen tests experienced relatively severe seating problems. In general, tests which did not have a preload prior to shear (i.e., all Series B tests) and/or were consolidated to relatively high confining stresses most consistently exhibited this seating problem. In the writer's opinion, the seating problem was probably due to 1) an induced misalignment caused by consolidation, and/or 2) high secondary compression (creep) rates which induced deformations just prior to the initiation of the deviator stress (axial loading).

Figure 3.20 presents three initial stress–strain responses for the unfrozen MFS tests. These initial responses have been qualitatively classified as "good", "fair" and "poor". Tests with "good" responses exhibit a smooth

curve from the initiation of axial loading with the slope ($dQ/d\epsilon_a$) consistently positive, but decreasing with continued deformation. A "poor" initial response has a severe seating problem, with the slope increasing (as shown), and then decreasing with continued deformation. There is an initial "lag" in a "fair" response followed by a behavior similar to that of a "good" initial response. These qualifiers for the initial $Q-\epsilon_a$ response allow for further delineation of the small strain parameters of E, Q_{yo} and ϵ_y. For unfrozen MFS results presented in Chapter 4, only tests with "good" and "fair" initial stress–strain responses are used in the presentation of these small strain parameters.

TABLE 3.1
DRY MECHANICAL SIEVE ANALYSIS ON MANCHESTER FINE SAND

SOURCE	PERCENT FINER THAN U.S. STANDARD SIEVE NUMBER (mesh size in μm)							
	#45 (355)	#60 (250)	#80 (180)	#100 (149)	#120 (125)	#140 (105)	#170 (90)	#200 (74)
Current Research								
1	98.7	86.6	50.0	44.1	27.8	22.7	15.1	7.6
2	99.0	88.6	55.0	45.6	29.3	22.1	14.7	7.5
3	98.5	86.3	51.5	43.1	26.3	19.0	12.3	6.1
4	99.1	90.9	61.7	50.7	33.1	24.4	16.0	7.5
Andersen (1991)								
1	98.9	84.5	39.7	34.0	17.4	14.6	10.2	
2	98.8	84.8	49.9	42.2	24.6	19.2	12.8	
3	99.0	86.9	53.3	45.4	26.8	21.1	14.1	
4	98.8	88.5	50.5	43.1	25.6	20.1	13.5	6.8
5	98.9	90.4	50.5	43.2	25.7	20.2	13.4	7.4
Average	98.9	87.4	51.3	43.5	26.3	20.4	13.6	7.2
Std Dev	0.2	2.3	5.8	4.4	4.2	2.8	1.7	0.6

TABLE 3.2a
UNFROZEN MFS TESTING PROGRAM
Series A Tests
Set-up Characteristics and Specimen History

Test No. A-	Date Set-up	Init. Dims. L_o (cm)	Init. Dims. D_o (cm)	Init. Dims. V_o (cm^3)	W_s [1] (g)	Dry Unit Weight (g/cc)	D_r (%)	e	Specimen Prep. Tech.	Type of End Condn. [2]	Comments on Tests
01-07*	NO RELIABLE INFORMATION										
08*	6-13-90	7.55	3.44	70.23	113.04	1.61	72.7	0.670	Raining	T	Lost load at 5% strain.
09*	6-18-90	7.49	3.38	67.33	103.05	1.53	46.5	0.756	Raining	T	Erratic σ-ϵ and Δu behavior, early failure.
10*	6-19-90	7.58	3.48	71.91	113.31	1.58	61.8	0.706	Raining	T	Erratic stress-strain and pore pressure.
11	6-20-90	7.58	3.47	71.88	120.68	1.68	93.7	0.601	Vibration	T	Useful results to 17.6% ϵ_a.
12	6-27-90	7.58	3.42	69.46	100.29	1.44	14.4	0.862	Raining	T	Useful results to 14.9% ϵ_a.
13	6-28-90	7.59	3.47	71.78	109.89	1.53	46.6	0.756	Raining	T	Useful results to 19.9% ϵ_a.
14*	7-2-90	7.49	3.46	70.55	106.32	1.51	38.2	0.784	Raining	G & R	Erratic shear behavior.
15*	7-3-90	7.54	3.4	71.79	115.81	1.61	73.9	0.666	Vibration	G & R	Erroneous consolidation results.
16*	7-4-90	7.51	3.47	70.84	108.97	1.54	49.2	0.747	Raining	G & R	Consolidation problems: poor records.
17	7-9-90	7.54	3.48	71.85	113.23	1.58	61.9	0.706	Vibration	G & R	Useful results to 14.6% ϵ_a.
18*	7-11-90	7.51	3.46	70.63	113.70	1.61	72.8	0.670	Vibration	G & R	No Good. Cell leak during consolidation.
19*	7-12-90	7.57	3.48	71.96	115.47	1.60	71.1	0.675	Vibration	G & R	Questionable results; poor data acq records.
20	7-13-90	7.5	3.4	70.21	101.8	1.45	17.0	0.853	Raining	T & R	No on-specimen strain measurement.
21*	7-17-90	7.6	3.4	72.05	121.1	1.68	94.3	0.599	Vibration	T	Erratic shear behavior.
22*	7-19-90	7.5	3.4	69.96	106.4	1.52	43.2	0.767	Raining	T & R	Erratic shear behavior.
23	7-23-90	7.4	3.3	67.59	98.89	1.46	21.8	0.837	Raining	G & R	No on-specimen strain measurement.
24*	7-25-90	7.44	3.40	67.45	99.75	1.48	27.8	0.818	Raining	G & R	Erratic shear behavior.

NOTES:

[1] - Weight of solids (W_s) taken from after test weights except for tests 10, 17, 18, 22 which were taken from the initial set-up weight

[2] - End Condition Key: T - teflon spray; G - vacuum grease; R - rubber membrane

* - No useful shear results

TABLE 3.2b
UNFROZEN MFS TESTING PROGRAM
Series B Tests
Set-up Characteristics and Specimen History

(Specimens Prepared by Multiple Sieve Pluviation)

Test No. B-	Date Set-up	Init. Dims. L_o (cm)	D_o (cm)	V_o (cm^3)	W_s[1] (g)	Dry Unit Weight (g/cc)	D_r (%)	e	Type of End Condn.[2]	Comments on Tests
01	9-17-90	7.50	3.41	68.50	103.68	1.51	40.5	0.776	T & R	
02	9-30-90	7.60	3.47	71.81	118.90	1.66	86.9	0.623	T	
03*	9-24-90	7.54	3.45	70.31	109.58	1.56	56.1	0.725	G & R	Lost load during early part of shear.
04	10-2-90	7.55	3.47	71.22	109.93	1.54	51.0	0.741	G & R	Useful results to 16.3% ϵ_a.
05	10-9-90	7.64	3.48	72.58	117.01	1.61	73.5	0.667	G & R	
06	10-13-90	7.55	3.45	70.70	108.03	1.53	45.6	0.759	G & R	
07	10-15-90	7.64	3.49	72.94	119.12	1.63	80.0	0.646	G & R	
08	10-16-90	7.65	3.47	72.30	118.75	1.64	82.9	0.637	G & R	Pore water cavitation, limited results.
09	10-19-90	7.61	3.47	71.90	118.09	1.64	82.9	0.637	G & R	Pore water cavitation, limited results.
10	10-22-90	7.59	3.44	70.75	107.72	1.52	43.7	0.765	G & R	
11	10-23-90	7.60	3.44	70.76	109.63	1.55	53.0	0.735	G & R	
12	10-24-90	7.61	3.45	71.28	117.73	1.65	85.7	0.627	G & R	
13	11-4-90	7.58	3.41	69.21	103.24	1.49	32.6	0.802	G & R	
14	11-5-90	7.60	3.46	71.50	115.14	1.61	72.9	0.669	G & R	Useful results at 16.9% ϵ_a.
15	11-12-90	7.60	3.46	71.38	115.04	1.61	73.4	0.668	G & R	
16*	12-4-90	7.61	3.41	69.55	107.48	1.55	51.6	0.739	G & R	⎫ Unsuccessful shearing
17*	12-6-90	7.61	3.46	71.32	112.51	1.58	62.4	0.704	G & R	⎬← due to problems with
18*	12-10-90	7.60	3.45	70.97	113.62	1.60	70.0	0.679	G & R	⎭ load cell wiring.
19	12-12-90	7.59	3.39	68.39	102.80	1.50	36.8	0.788	G & R	
20*	12-14-90	7.59	3.45	70.85	111.08	1.57	59.2	0.715	G & R	Load cell wiring problems.
21*	12-15-90	7.58	3.42	69.68	106.57	1.53	46.1	0.758	G & R	Load cell wiring problems.
22	12-17-90	7.60	3.48	72.49	121.62	1.68	93.3	0.602	G & R	
23	12-30-90	7.59	3.45	70.98	110.01	1.55	53.2	0.734	G & R	
24	1-11-91	7.67	3.38	68.95	104.62	1.52	41.8	0.772	T	

NOTES:
[1] - Weight of solids (W_s) taken from after test weights except for tests 03, 04, 17, 18, 20, 21 which were taken from the initial set-up weight
[2] - End Condition Key: T - teflon spray; G - vacuum grease; R - rubber membrane
* - No useful shear results

TABLE 3.2c (page 1 of 2)
UNFROZEN MFS TESTING PROGRAM
Series C Tests
Set-up Characteristics and Specimen History

(Specimens Prepared by Multiple Sieve Pluviation)

Test No. C-	Date Set-up	Init. Dims. L_o (cm)	D_o (cm)	V_o (cm^3)	W_s [1] (g)	Dry Unit Weight (g/cc)	D_r (%)	e	Type of End Condn. [2]	Comments on Tests
01	8-23-91	7.62	3.41	69.66	104.28	1.50	34.5	0.796	G & R	
02	9-23-91	7.60	3.41	69.62	103.84	1.49	32.5	0.802	G & R	
03	10-21-91	7.65	3.44	70.96	105.09	1.48	28.6	0.815	T	
04	12-4-91	7.51	3.43	69.53	104.96	1.51	39.1	0.781	R	
05*	12-8-91	7.51	3.46	70.46	107.51	1.53	44.8	0.762	R	No Good. Bad pore pressure transducer.
06*	12-10-91	7.55	3.45	70.48	107.57	1.53	45.0	0.761	R	No Good. Bad pore pressure transducer.
07*	12-15-91	7.53	3.43	69.47	106.34	1.53	46.5	0.756	G & R	Erroneous consolidation results.
08*	12-16-91	7.51	3.43	69.51	108.44	1.56	56.6	0.723	R	Membrane rupture during shear.
09	12-30-91	7.52	3.44	69.94	104.24	1.49	32.1	0.803	R	
10	1-13-92	7.55	3.46	71.14	107.65	1.51	40.3	0.776	R	
11	1-15-92	7.56	3.48	71.88	111.85	1.56	55.3	0.727	G & R	
12	1-17-92	7.56	3.48	71.68	116.54	1.63	77.8	0.653	G & R	
13	1-19-92	7.54	3.47	71.24	112.78	1.58	64.2	0.698	R	
14	1-21-92	7.59	3.48	72.39	119.58	1.65	85.7	0.627	G & R	
15	2-4-92	7.49	3.43	69.14	103.25	1.49	33.2	0.800	R	
16	2-6-92	7.53	3.46	70.94	109.81	1.55	52.5	0.736	R	
17	3-5-92	7.48	3.40	68.04	101.04	1.49	30.1	0.810	G & R	
18	3-9-92	7.51	3.47	70.86	105.09	1.48	29.4	0.813	G & R	
19	3-23-92	7.50	3.42	68.67	102.16	1.49	31.1	0.807	G & R	
20	4-20-92	7.59	3.49	72.46	117.83	1.63	77.9	0.653	G & R	
21	4-30-92	7.61	3.50	73.13	120.45	1.65	84.3	0.632	G & R	

NOTES:
[1] - Weight of solids (W_s) taken from after test weights except for tests 07, 08, 10, 11, 12, which were taken from the initial set-up weight
[2] - End Condition Key: T - teflon spray; G - vacuum grease; R - rubber membrane
* - No useful shear results

TABLE 3.2c (page 2 of 2)
UNFROZEN MFS TESTING PROGRAM
Series C Tests
Set-up Characteristics and Specimen History

(Specimens Prepared by Multiple Sieve Pluviation)

Test No. C-	Date Set-up	Init. Dims. L_o (cm)	D_o (cm)	V_o (cm^3)	W_s[1] (g)	Dry Unit Weight (g/cc)	D_r (%)	e	Type of End Condn.[2]	Comments on Tests
22	6-2-93	7.53	3.46	70.37	108.38	1.53	47.4	0.753	G & R	
23	6-7-93	7.53	3.42	69.22	104.50	1.51	39.1	0.783	G & R	
24	6-11-93	7.52	3.45	70.24	106.30	1.51	40.6	0.776	G & R	
25		7.59	3.49	72.46	117.83	1.63	77.9	0.653	G & R	
26	8-9-93	7.53	3.48	71.55	114.24	1.60	68.6	0.684	G & R	
27	7-13-93	7.51	3.42	68.92	104.23	1.51	40.0	0.777	G & R	
28	6-30-93	7.50	3.43	69.28	104.46	1.51	38.4	0.783	G & R	
29	7-15-93	7.49	3.40	68.14	102.11	1.50	35.0	0.794	G & R	
30	7-21-93	7.53	3.47	71.01	114.94	1.62	75.6	0.661	G & R	
31	7-23-93	7.51	3.48	71.25	113.32	1.59	66.6	0.683	G & R	
32	8-6-93	7.51	3.48	71.25	109.80	1.53	46.9	0.755	G & R	
33		7.53	3.47	71.44	116.44	1.63	79.0	0.649	G & R	
34	8-4-93	7.54	3.48	71.59	120.29	1.68	94.0	0.600	G & R	
35	8-25-93	7.39	3.43	68.46	104.43	1.53	44.7	0.762	G & R	

NOTES:
1 - Weight of solids (W_s) taken from after test weights except for tests 07, 08, 10, 11, 12, which were taken from the initial set-up weight
2 - End Condition Key: T - teflon spray; G - vacuum grease; R - rubber membrane

TABLE 3.3 (page 1 of 2)
CONVENTIONAL FROZEN MFS TESTS
Set-up Characteristics and Specimen History

(Specimens Prepared Using Multiple Sieve Pluvation)

Test[1] Number	Date of Test[1]	Init. Dimens. L_o (cm)	D_o (cm)	V_o (cm^3)	γ_t (g/cc)	γ_d (g/cc)	D_r (%)	w (%)	S_r (%)	Test Conditions σ_c (MPa)	ϵ[2]	T (°C)	Comments on Test
FRS70	7-28-92	6.88	3.52	67.15	2.003	1.647	84.4	21.6	101.6	0.1	F	-20	Some crushing at top.
FRS71	7-22-92	7.02	3.56	69.72	2.006	1.667	90.3	20.3	98.7	0.1	M	-20	
FRS72	7-20-92	6.67	3.55	66.06	2.003	1.672	91.7	19.8	97.0	10	S	-20	
FRS74	7-30-92	6.48	3.51	62.81	1.891	1.493	33.2	26.6	98.7	10	S	-20	Questionable small ϵ data.
FRS75	8-8-91	7.12	3.52	69.14	1.920	1.535	48.0	25.1	99.2	0.1	M	-20	Load cell rubbed against side.
FRS76	8-9-91	7.42	3.54	73.08	1.908	1.513	40.3	26.1	99.9	0.1	M	-20	Load cell rubbed against side.
FRS77	8-13-91	7.48	3.51	72.55	1.893	1.503	36.8	25.9	97.3	0.1	M	-15	Poor temperature control.
FRS78	8-14-91	7.28	3.51	70.52	1.898	1.508	38.5	25.8	98.8	0.1	M	-25	No Good. Specimen unstable during shear.
FRS79	8-17-91	7.07	3.51	68.58	1.892	1.520	42.9	24.4	95.0	0.1	M	-23	Poor temperature control.
FRS80	11-20-91	6.77	3.51	65.35	1.895	1.518	42.0	24.8	95.1	0.1	M	-5	Poor temperature control.
FRS81	10-23-91	6.48	3.55	63.99	1.891	1.522	43.4	24.3	93.5	0.1	M	-5	Poor temperature control.
FRS83	1-3-92	6.97	3.51	67.28	1.892	1.508	41.0	24.9	96.8	0.1	M	-28	Poor temperature control.
FRS84	1-9-92	7.06	3.52	68.52	1.897	1.527	45.1	24.2	94.6	0.1	M	-15	No Good. Electrical problems.
FRS85	7-8-92	7.11	3.54	69.97	1.982	1.625	77.5	22.0	99.9	0.1	M	-20	
FRS86	5-28-92	7.19	3.51	69.34	1.903	1.504	37.0	26.5	100.0	10	M	-20	
FRS87	6-24-92	7.30	3.52	70.83	1.923	1.542	50.4	24.7	98.7	0.1	M	-20	
FRS88	6-10-92	7.50	3.51	72.62	1.894	1.499	35.4	26.3	98.6	0.1	S	-20	
FRS89	6-13-92	6.74	3.50	65.03	1.889	1.504	37.1	25.6	96.5	0.1	F	-20	Specimen crushed during shear.
FRS92	7-17-92	7.20	3.51	69.79	1.897	1.500	35.6	26.4	99.2	10	F	-20	
FRS93	7-10-92	6.96	3.52	67.57	1.977	1.625	77.4	21.7	98.6	10	F	-20	Exceeded capacity of load frame.
FRS94	6-17-92	7.17	3.55	70.91	2.016	1.677	93.2	20.2	99.8	0.1	S	-20	No small ϵ_a results.
FRS95	6-19-92	7.37	3.53	71.95	2.002	1.645	86.3	21.1	100.2	0.1	M	-20	Slight crushing during shear.
FRS96	7-2-92	7.25	3.52	70.72	1.997	1.659	87.9	20.4	97.7	10	S	-20	No temperature control.
FRS97	6-23-92	7.39	3.52	71.72	1.898	1.500	35.7	26.5	99.5	0.1	M	-20	
FRS98	6-26-92	7.41	3.52	71.93	1.895	1.496	34.3	26.7	99.4	10	S	-20	Poor small ϵ data.
FRS99	7-7-92	7.47	3.51	72.15	1.900	1.502	36.3	26.5	99.7	0.1	F	-20	
FRS100	8-5-92	6.84	3.51	66.34	1.992	1.640	82.2	21.4	100.8	10	M	-20	
FRS101	9-23-92	7.26	3.55	71.95	1.900	1.503	36.7	26.4	100.5	0.1	M	-24	Poor temperature control.
FRS102	10-2-92	6.96	3.52	67.60	1.930	1.549	52.7	24.6	100.3	0.1	F	-25	
FRS103	10-5-92	6.97	3.51	67.43	1.901	1.500	35.5	26.8	101.3	0.1	S	-25	

Notes:
1 Tests not necessarily performed in chronological order
2 S = slow strain rate, M = moderate strain rate, F = fast strain rate

TABLE 3.3 (page 2 of 2)
CONVENTIONAL FROZEN MFS TESTS
Set-up Characteristics and Specimen History

(Specimens Prepared Using Multiple Sieve Pluvation)

Test[1] Number	Date of Test[1]	Init. Dimens. L_o (cm)	D_o (cm)	V_o (cm^3)	γ_t (g/cc)	γ_d (g/cc)	D_r (%)	w (%)	S_r (%)	Test Conditions σ_c (MPa)	ϵ[1]	T (°C)	Comments on Test
FRS104	10-6-92	6.89	3.51	66.77	1.905	1.504	36.9	26.7	101.6	0.1	M	-25	
FRS105	10-17-92	6.68	3.54	65.91	1.901	1.501	36.1	26.6	100.9	10	S	-25	No results. Mechanical malfunction.
FRS106	10-10-92	6.95	3.51	67.22	2.012	1.662	88.7	21.1	102.6	0.1	S	-25	
FRS107	10-13-92	6.81	3.55	67.26	2.009	1.668	90.4	20.5	100.7	10	S	-25	Slight crushing during shear.
FRS109	10-26-92	6.87	3.53	67.08	1.970	1.615	74.5	22.0	99.4	0.1	M	-25	Slightly crushed at bottom.
FRS110	10-27-92	6.98	3.55	68.99	2.007	1.662	88.6	20.8	101.3	0.1	M	-25	
FRS111	10-20-92	6.77	3.51	65.46	1.898	1.498	34.9	26.7	100.8	10	M	-25	
FRS113	10-25-92	6.88	3.51	66.40	1.930	1.547	52.0	24.8	100.8	0.1	M	-25	
FRS114	10-28-92	6.80	3.51	65.61	1.913	1.516	41.2	26.2	101.5	0.1	F	-25	Slightly crushed at top.
FRS115	10-24-92	6.69	3.51	64.75	1.912	1.521	43.1	25.7	100.3	10	S	-25	
FRS116	11-18-92	6.88	3.51	66.42	1.909	1.511	39.4	26.4	101.3	0.1	F	-25	
FRS117	12-4-92	6.80	3.54	66.90	1.901	1.501	36.1	26.6	101.0	10	F	-25	
FRS121	1-28-93	6.80	3.51	65.75	2.014	1.672	91.7	20.4	99.6	10	F	-15	
FRS122	1-19-93	6.55	3.51	63.31	1.988	1.665	89.7	19.4	93.3	10	F	-15	No Good. Load cell malfunction.
FRS123	1-21-93	6.80	3.55	67.14	2.009	1.669	90.7	20.4	98.8	10	S	-15	Poor ϵ_v results.
FRS124	1-27-93	6.77	3.51	65.54	2.009	1.665	89.7	20.7	99.6	10	F	-15	No Good. Specimen unstable during shear.
FRS126	1-20-93	6.80	3.51	65.73	1.926	1.536	48.3	25.4	100.2	10	F	-15	
FRS127	1-24-93	6.62	3.51	64.06	1.903	1.499	35.4	26.9	100.4	10	S	-15	Poor ϵ_v and small ϵ_a results.
FRS128	2-2-93	6.78	3.54	66.79	1.931	1.547	52.1	24.8	99.6	10	M	-15	Poor ϵ_v results.
FRS129	2-3-93	6.38	3.51	61.63	1.921	1.534	47.7	25.2	99.2	10	F	-15	
FRS130	2-10-93	6.78	3.51	65.62	1.903	1.507	38.2	26.3	99.1	10	S	-15	Poor ϵ_v and small ϵ_a results.
FRS131	2-4-93	6.97	3.51	67.55	1.985	1.656	86.9	19.9	94.4	10	S	-15	Poor ϵ_v results.
FRS133	2-13-93	6.74	3.51	65.11	1.996	1.632	79.8	22.3	101.9	10	M	-15	Poor ϵ_v results.
FRS134	2-16-93	6.76	3.51	65.55	2.003	1.652	85.8	21.2	100.3	10	S	-15	Poor ϵ_v results.
FRS135	2-27-93	6.74	3.51	65.30	1.997	1.651	85.5	20.9	98.7	10	M	-15	
FRS136	3-10-93	6.81	3.51	65.80	1.947	1.575	61.7	23.6	98.8	0.1	M	-15	
FRS138	3-11-93	6.82	3.54	67.11	1.985	1.627	78.0	22.0	99.8	0.1	M	-15	
FRS141	2-11-93	6.82	3.51	66.00	1.909	1.513	40.3	26.2	99.6	10	M	-15	Poor ϵ_v results.
FRS142	3-12-93	6.69	3.50	64.52	1.911	1.514	40.5	26.2	99.9	0.1	M	-15	
FRS146	2-24-93	6.73	3.51	65.16	2.016	1.673	91.9	20.5	100.1	10	M	-15	Poor ϵ_v results.
FRS148	3-5-93	6.83	3.51	66.22	2.013	1.671	91.5	20.4	99.5	0.1	M	-15	

Notes:
1 Tests not necessarily performed in chronological order
2 S = slow strain rate, M = moderate strain rate, F = fast strain rate

TABLE 3.4
CONSOLIDATE-FREEZE TESTING PROGRAM
Set-up Characteristics and Specimen History

(Specimens Prepared Using Multiple Sieve Pluviation)

Test No.[1] CF-	Date Set-up[1]	Init. Dims. L_o (cm)	D_o (cm)	V_o (cm^3)	W_s[2] (g)	Dry Unit Weight (g/cc)	D_r (%)	e	Type of End Condn.[3]	Comments on Tests
01	8-16-93	7.55	3.46	70.87	119.90	1.69	97.4	0.594	G & R	Ice layer around top half of specimen.
02	8-31-93	7.52	3.43	69.54	104.12	1.50	34.6	0.795	G & R	
03	7-9-93	7.61	3.48	72.46	120.11	1.66	87.4	0.621	G & R	
04	7-12-93	7.50	3.44	69.67	106.85	1.53	47.6	0.753	G & R	
05	7-16-93	7.52	3.43	69.35	103.09	1.49	30.7	0.808	G & R	
06	8-2-93	7.52	3.46	71.25	112.82	1.58	64.3	0.698	G & R	Leakage into internal drainage line.
07	8-5-93	7.52	3.47	72.94	114.34	1.61	72.9	0.669	G & R	Leakage into internal drainage line.
08	8-9-93	7.55	3.46	71.11	115.97	1.63	79.3	0.648	G & R	
09	8-12-93	7.54	3.42	69.15	114.04	1.65	84.9	0.630	G & R	Leakage into internal drainage line.
10	8-26-93	7.54	3.46	70.86	112.49	1.59	65.6	0.693	G & R	Poor stability→limited reliable data.

NOTES:
[1] - Tests not necessarily performed in chronological order, e.g., CF-01 an CF-02 were performed (for the second time) after most other tests.
[2] - Weight of solids (W_s) taken from after test weights except for test 01
[3] - End Condition Key: G - vacuum grease; R - rubber membrane

TABLE 3.5 (page 1 of 2)
MEASURED LEAKAGE RATES AND AREA CORRECTION CALCULATION FACTORS FOR UNFROZEN MFS TESTS

Test No.	Leakage Rate ($x10^{-4}$ cc/min)	Area Correction Calculation	
		% RCC	% P
A-08	NA	NA	NA
A-09	NA	NA	NA
A-10	NA	NA	NA
A-11	NA	NA	NA
A-12	NA	NA	NA
A-13	NA	NA	NA
A-14	NA	NA	NA
A-15	NA	NA	NA
A-16	NA	NA	NA
A-17	34.93	NA	NA
A-18	10.26	NA	NA
A-19	NA	NA	NA
A-20	NA	NA	NA
A-21	6.184	NA	NA
A-22	NA	NA	NA
A-23	7.051	NA	NA
A-24	5.057	NA	NA
B-01	NA	0	100
B-02	10.59	10	90
B-03	8.477	NA	NA
B-04	26.68	30	70
B-05	4.212	90	10
B-06	3.765	90	10
B-07	4.706	50	50
B-08	5.719	50	50
B-09	3.573	100	0
B-10	2.200	100	0
B-11	3.307	90	10
B-12	5.452	100	0
B-13	1.183	25	75
B-14	17.66	90	10
B-15	3.631	75	25
B-16	2.771	NA	NA
B-17	134.2	NA	NA
B-18	13.53	NA	NA
B-19	7.063	90	10
B-20	4.617	NA	NA
B-21	3.728	NA	NA

NA - Not Available
* RCC = Right Circular Cylinder, Eq. 3.6
P = Parabolic, Eq. 3.7

TABLE 3.5 (page 2 of 2)
MEASURED LEAKAGE RATES AND AREA CORRECTION CALCULATION FACTORS FOR UNFROZEN MFS TESTS

Test No.	Leakage Rate ($\times 10^{-4}$ cc/min)	Area Correction Calculation*	
		% RCC	% P
B-22	1.146	90	10
B-23	3.715	90	10
B-24	NA	20	80
C-01	NA	80	20
C-02	0.105	80	20
C-03	0.658	0	100
C-04	0	70	30
C-05	1.032	NA	NA
C-06	1.368	NA	NA
C-07	NA	NA	NA
C-08	0.901	NA	NA
C-09	3.417	100	0
C-10	2.944	100	0
C-11	1.346	90	10
C-12	0.808	80	20
C-13	1.113	100	0
C-14	1.052	10	90
C-15	0	50	50
C-16	1.279	90	10
C-17	4.896	10	90
C-18	2.010	10	90
C-19	3.687	10	90
C-20	4.743	10	90
C-21	4.400	10	90
C-22	6.603	30	70
C-23	1.039	70	30
C-24	2.435	30	70
C-25	0.666	95	5
C-26	0.438	50	50
C-27	0.397	20	80
C-28	2.572	20	80
C-29	1.453	90	10
C-30	1.136	80	20
C-31	0.910	10	90
C-32	0.382	25	75
C-33	1.553	50	50
C-34	3.630	50	50
C-35	0.981	85	15

NA - Not Available
* RCC = Right Circular Cylinder, Eq. 3.6
P = Parabolic, Eq. 3.7

TABLE 3.6 (page 1 of 2)
CORRECTION FACTORS FOR VOLUMETRIC STRAIN AND
SPECIMEN AREA FOR CONVENTIONAL FROZEN MFS TESTS

Test No.	σ_c (MPa)	T °C	LR Leakage Rate (x10^{-3} cc/min)	C_c Fluid Comp. (cc/MPa)	a Area Corr.
FRS70	0.1	-20	1.34	48.8	1[1]
FRS71	0.1	-20	6.43	202	1.02
FRS72	10	-20	4.37	1.43	1.05
FRS74	10	-20	5.93	1.41	1.13
FRS75	0.1	-20	1.54	34.0	1[1]
FRS76	0.1	-20	2.98	34.7	1[1]
FRS77	0.1	-15	0.71	42.6	1[1]
FRS79	0.1	-23	0	45.2	1[1]
FRS80	0.1	-5	0.92	24.3	1[1]
FRS81	0.1	-5	0.39	24.2	1[1]
FRS83	0.1	-28	7.01	28.3	1[1]
FRS85	0.1	-20	3.01	25.6	1.12
FRS86	10	-20	7.85	1.40	1.03
FRS87	0.1	-20	1.31	34.3	1.00
FRS88	0.1	-20	0.58	28.8	1.01
FRS89	0.1	-20	1.27	33.8	1[1]
FRS92	10	-20	5.53	1.34	1.14
FRS93	10	-20	78.4	1.49	0.81
FRS94	0.1	-20	0.59	23.4	0.94
FRS95	0.1	-20	3.90	39.0	1[1]
FRS97	0.1	-20	2.03	34.3	1.22
FRS98	10	-20	7.73	1.39	0.99
FRS99	0.1	-20	2.35	28.4	1.00
FRS100	10	-20	6.73	1.40	1.02
FRS101	0.1	-24	1.47	34.9	1.10
FRS102	0.1	-25	1.48	24.9	0.92
FRS103	0.1	-25	2.72	13.9	1.05

Note: [1] an a factor was not calculated for this test so value of 1 was assumed.

TABLE 3.6 (page 2 of 2)
CORRECTION FACTORS FOR VOLUMETRIC STRAIN AND
SPECIMEN AREA FOR CONVENTIONAL FROZEN MFS TESTS

Test No.	σ_c (MPa)	T °C	LR Leakage Rate (x10^{-3} cc/min)	C_c Fluid Comp. (cc/MPa)	a Area Corr.
FRS104	0.1	-25	1.78	34.4	0.96
FRS106	0.1	-25	2.12	32.6	1.15
FRS107	10	-25	5.62	1.42	0.92
FRS109	0.1	-25	1.57	30.9	1.00
FRS110	0.1	-25	1.82	31.4	1.07
FRS111	10	-25	4.82	1.47	1.02
FRS113	0.1	-25	1.74	28.8	1.02
FRS114	0.1	-25	1.18	27.9	0.81
FRS115	10	-25	4.12	1.52	1.01
FRS116	0.1	-25	2.60	37.7	0.84
FRS117	10	-25	89.5	1.65	1.00
FRS121	10	-15	2.96	1.56	0.98
FRS123	10	-15	3.42	1.51	1.19
FRS126	10	-15	5.02	1.50	1.02
FRS127	10	-15	3.22	1.46	1.29
FRS128	10	-15	3.80	1.45	1.07
FRS129	10	-15	3.09	1.48	1.04
FRS130	10	-15	3.20	1.48	1.06
FRS131	10	-15	3.51	1.52	1[1]
FRS133	10	-15	2.62	1.49	0.98
FRS134	10	-15	2.80	1.50	0.93
FRS135	10	-15	3.47	1.57	1.04
FRS136	0.1	-15	2.24	33.1	0.93
FRS138	0.1	-15	1.85	34.8	0.91
FRS141	10	-15	2.81	1.60	1.01
FRS142	0.1	-15	1.41	31.0	1.04
FRS146	10	-15	4.06	1.52	1.11
FRS148	0.1	-15	0.77	18.1	1.04

TABLE 3.7 (page 1 of 3)
CONVENTIONAL FROZEN MFS TESTS
TEMPERATURE FLUCTUATIONS INSIDE THE TRIAXIAL CELL DURING SHEAR

Test	AVG TEMP (°C)	TEMPERATURE NEAR BASE OF SPECIMEN (°C)			TEMPERATURE NEAR TOP OF SPECIMEN (°C)			ΔT top-base
		max.	min.	mean	max.	min.	mean	
FRS70	-20.20	-20.42	-20.62	-20.47	-19.73	-20.11	-19.92	0.55
FRS71	-20.56	-20.79	-20.92	-20.84	-20.21	-20.33	-20.27	0.57
FRS72	-20.55	-20.77	-20.89	-20.83	-20.23	-20.31	-20.27	0.56
FRS74	-20.46	-20.66	-20.74	-20.70	-20.14	-20.27	-20.22	0.48
FRS75	-20.41	-20.34	-20.47	-20.43	-20.29	-20.42	-20.39	0.04
FRS76	-20.29	-20.23	-20.35	-20.29	-20.25	-20.36	-20.29	0.00
FRS85	-20.15	-20.46	-20.53	-20.48	-19.80	-19.85	-19.82	0.66
FRS86	-20.50	-20.76	-20.90	-20.83	-20.11	-20.20	-20.17	0.56
FRS87	-20.16	-20.38	-20.53	-20.45	-19.82	-19.94	-19.86	0.59
FRS88	-20.28	-20.50	-20.60	-20.58	-19.91	-20.05	-19.97	0.61
FRS89	-19.92	-20.15	-20.35	-20.28	-19.47	-19.64	-19.56	0.72
FRS92	-20.28	-20.37	-20.66	-20.52	-19.90	-20.04	-20.04	0.48
FRS94	-20.09	-20.34	-20.45	-20.40	-19.65	-19.84	-19.78	0.62
FRS95	-20.39	-20.51	-20.65	-20.59	-20.06	-20.13	-20.08	0.51
FRS97	-19.93	-20.22	-20.26	-20.24	-19.57	-19.63	-19.61	0.63
FRS98	-20.14	-20.34	-20.49	-20.39	-19.75	-19.81	-19.78	0.61
FRS99	-20.09	-20.48	-20.57	-20.53	-19.57	-19.78	-19.65	0.88
FRS100	-19.96	-20.28	-20.36	-20.31	-19.45	-19.69	-19.58	0.73

TABLE 3.7 (page 2 of 3)
CONVENTIONAL FROZEN MFS TESTS
TEMPERATURE FLUCTUATIONS INSIDE THE TRIAXIAL CELL DURING SHEAR

Test	AVG TEMP (°C)	TEMPERATURE NEAR BASE OF SPECIMEN (°C)			TEMPERATURE NEAR TOP OF SPECIMEN (°C)			ΔT top-base
		max.	min.	mean	max.	min.	mean	
FRS102	-25.21*	-25.16	-25.26	-25.21	NA	NA	NA	NA
FRS103	-25.35	-25.47	-25.61	-25.53	-25.11	-25.21	-25.16	0.37
FRS104	-25.38	-25.56	-25.60	-25.58	-25.16	-25.22	-25.18	0.40
FRS106	-25.34	-25.46	-25.63	-25.51	-25.11	-25.24	-25.17	0.34
FRS107	-25.33	-25.47	-25.58	-25.52	-25.10	-25.20	-25.14	0.38
FRS109	-25.36	-25.54	-25.59	-25.56	-25.15	-25.19	-25.16	0.40
FRS110	-25.51*	NA	NA	NA	-25.47	-25.56	-25.51	NA
FRS111	-25.26	-25.38	-25.49	-25.43	-25.06	-25.13	-25.09	0.34
FRS113	-25.35	-25.53	-25.59	-25.56	-25.15	-25.19	-25.16	0.42
FRS114	-25.25	-25.40	-25.53	-25.48	-24.86	-25.15	-25.01	0.47
FRS115	-25.35	-25.46	-25.59	-25.53	-25.15	-25.22	-25.18	0.45
FRS116	-25.32	-25.51	-25.61	-25.57	-24.95	-25.16	-25.07	0.50
FRS117	-25.78	-25.78	-26.08	-25.94	-25.46	-25.77	-25.61	0.33

NA - Not Available
* - Average temperature based on one thermistor

TABLE 3.7 (page 3 of 3)
CONVENTIONAL FROZEN MFS TESTS
TEMPERATURE FLUCTUATIONS INSIDE THE TRIAXIAL CELL DURING SHEAR

Test	AVG TEMP (°C)	TEMPERATURE NEAR BASE OF SPECIMEN (°C)			TEMPERATURE NEAR TOP OF SPECIMEN (°C)			ΔT top-base
		max.	min.	mean	max.	min.	mean	
FRS121	-15.44	-15.62	-15.78	-15.69	-15.02	-15.36	-15.19	0.50
FRS123	-15.56	-15.71	-15.80	-15.75	-15.28	-15.42	-15.36	0.39
FRS124	-15.49	-15.59	-15.79	-15.69	-15.14	-15.42	-15.28	0.41
FRS126	-15.50	-15.67	-15.83	-15.74	-15.14	-15.40	-15.25	0.49
FRS127	-15.55	-15.68	-15.78	-15.73	-15.35	-15.40	-15.36	0.37
FRS128	-15.60	-15.76	-15.82	-15.79	-15.32	-15.50	-15.40	0.39
FRS129	-15.48	-15.67	-15.77	-15.71	-15.11	-15.39	-15.24	0.47
FRS130	-15.79*	-15.74	-15.83	-15.79	NA	NA	NA	NA
FRS131	-15.61	-15.74	-15.86	-15.79	-15.39	-15.46	-15.43	0.36
FRS133	-15.58	-15.72	-15.84	-15.77	-15.32	-15.44	-15.38	0.39
FRS134	-15.51	-15.67	-15.81	-15.73	-15.21	-15.34	-15.29	0.44
FRS135	-15.85	-16.03	-16.16	-16.09	-15.55	-15.66	-15.60	0.49
FRS136	-15.74	-15.93	-16.05	-15.99	-15.45	-15.54	-15.49	0.50
FRS138	-15.74	-15.94	-16.02	-15.97	-15.44	-15.55	-15.50	0.47
FRS141	-15.55	-15.72	-15.78	-15.75	-15.29	-15.42	-15.35	0.40
FRS142	-15.74	-15.95	-16.05	-15.99	-15.44	-15.54	-15.49	0.50
FRS146	-15.84	-16.04	-16.97	-16.09	-15.54	-15.62	-15.59	0.50
FRS148	-15.81	-15.99	-16.12	-16.05	-15.52	-15.63	-15.57	0.48

NA - Not Available
* - Average temperature based on one thermistor

TABLE 3.8
SUMMARY OF MEASURED TESTING TEMPERATURES

Nominal (°C)	Mean Temperature for All Tests, °C	Temperature Gradient, °C (warmer near top)
-10	-9.55 ± 0.05	0.34 ± 0.05
-15	-15.62 ± 0.12	0.42 ± 0.12
-20	-20.24 ± 0.21	0.55 ± 0.21
-25	-25.35 ± 0.18	0.32 ± 0.15

Notes:
Numbers stated are the mean ± standard deviation
Results for -10°C from Andersen (1991)

TABLE 3.9
CORRECTIONS FOR VOLUMETRIC STRAIN AND SPECIMEN AREA
FOR CONSOLIDATE-FREEZE TESTS

Test No.	σ'_c or σ_c (MPa)	UNFROZEN STAGE Back Pressure LR (10^{-6} cc/min)	FROZEN STAGE Cell Fluid LR (10^{-3}cc/min)	FROZEN STAGE Cell Fluid Comp. C_c (cc/MPa)	α
CF01	0.1	10.7	0.17	0	1.04
CF02	10	68.6	2.75	1.41	1.00
CF03	0.1	30.4	0.38	11.5	0.74
CF04	10	19.5	3.74	1.49	1.02
CF05	10	23.5	3.31	1.46	0.88
CF06	5	44.9	3.70	1.69	0.89
CF07	2	52.4	0.71	1.89	1.10
CF08	2	31.1	0.70	1.80	0.76
CF09	2	20.4	0.71	1.94	1.14
CF10	5	41.2	1.57	1.63	0.91

TABLE 3.10
CONSOLIDATE-FREEZE TESTS
TEMPERATURE FLUCTUATIONS INSIDE THE TRIAXIAL CELL DURING SHEAR

Test	AVG TEMP (°C)	TEMPERATURE NEAR BASE OF SPECIMEN (°C)			TEMPERATURE NEAR TOP OF SPECIMEN (°C)			ΔT top-base
		max.	min.	mean	max.	min.	mean	
CF01	-10.30	-10.43	-10.52	-10.46	-10.11	-10.19	-10.14	0.32
CF02	-10.33	-10.47	-10.59	-10.51	-10.12	-10.21	-10.15	0.36
CF03	-9.84	-9.88	-10.03	-9.94	-9.70	-9.79	-9.74	0.20
CF04	-9.99	-10.08	-10.16	-10.11	-9.85	-9.90	-9.87	0.24
CF05	-10.01	-10.11	-10.18	-10.15	-9.85	-9.90	-9.87	0.28
CF06	-10.20	-10.25	-10.36	-10.30	-10.05	-10.11	-10.09	0.21
CF07	-10.47*	-10.44	-10.50	-10.47	NA	NA	NA	NA
CF08	-10.14	-10.35	-10.44	-10.39	-9.68	-10.04	-9.89	0.50
CF09	-10.20	-10.35	-10.45	-10.40	-9.93	-10.09	-10.00	0.40
CF10	-10.06	-10.28	-10.31	-10.29	-9.80	-9.88	-9.83	0.46

NA - Not Available
* - Average temperature based on one thermistor

TABLE 3.11
SPECIMEN FREEZING CHARACTERISTICS
CONSOLIDATE-FREEZE TESTS

Test No.[1]	Nom. σ'_c MPa	Measured Volume Change cc	Elapsed Time (min) Temp = 0°C	Flow Stopped	Freezing Temperature °C	Comments
CF01	0.1	0.46	90		-8	Excess ice noted around top
CF02	10	1.42	235	205	-8	
CF03	0.1	0.60	65	60 to 105	-15	Manual Δvolume measurement
CF04	10	1.11	70	120+	-15	Manual Δvol. measure, premature stop?
CF05	10	1.03	90	90	-15	Manual Δvolume measurement
CF06	5	0.48	120	?	-15	Oil leak into drainage line
CF07	2	1.91	180	?	-8	Oil leak? Prematurely stop?
CF08	2	1.74	200	240+	-8	Oil leak?
CF09	2	1.91	200	?	-8	Oil leak into drainage line
CF10	5	1.90	800	500	-8	

Notes:
[1] - Tests not performed sequentially, see Table 3.4 for order

TABLE 3.12
RANGE IN STRESS STRAIN PARAMETERS FOR REPEATABILITY TESTS AT -10°C
(from Andersen 1991)

NOMINAL TESTING CONDITIONS σ_c ϵ (F,M,S)	TEST #	D_r (%)	SMALL STRAIN PARAMETERS (COV) Initial E (GPa)	Initial Q-ϵ_a Q_{vo} (MPa)	Upper Yield Q_{uy} (MPa)	Upper Yield ϵ_{uy} (%)	ACDT g f p	LARGE STRAIN PARAMETERS (COV) Q_p (MPa)	LARGE STRAIN PARAMETERS (COV) ϵ_p (%)	VOLUMETRIC PARAMETERS Maximum $d\epsilon_v/d\epsilon_a$	VOLUMETRIC PARAMETERS ϵ_{v20}	STAB g f p vp
	18	48.4	28.6	2.7	7.2	0.43	g	13.4	24.9	0	-	f
10 MPa	19	49.4	21.4	2.7	7.2	0.43	g	13.1	18.4	0.03	0.004	p
m	63	51.1	24.0	3.0	8.2	0.50	p	14.4	26.4	0.01	0.001	g
			(14.8)	(6.2)	(7.7)	(8.9)		(5.0)	(18.3)	(114.6)	(84.9)	
	20	76.3	20.7	3.2	8.6	0.50	g	16.7	16.5	0.05	0.004	f
10 MPa	21	74.4	20.0	3.0	8.2	0.52	g	15.9	14.8	0.04	0.003	p
m	22	80.3	25.0	3.0	8.2	0.51	g	16.3	13.5	0.05	0.004	p
			(12.4)	(3.8)	(2.8)	(2.0)		(2.5)	(10.1)	(12.4)	(15.7)	
10 MPa	48	96.3	25.0	2.7	4.9	0.34	g	13.0	13.0	-	-	vp
s	54	94.0	26.3	2.8	5.4	0.44	g	16.0	21.9	0.04	0.005	g
			(3.6)	(2.6)	(6.9)	(18.1)		(14.6)	(36.1)			
0.1 MPa	38	94.3	41.2	4.1	8.5	0.44	p	11.6	5.2	0.47	0.074	vp
m	56	92.8	46.7	3.8	9.5	0.49	p	13.1	5.2	0.61	0.084	f
			(8.8)	(7.9)	(7.9)	(7.6)		(8.6)	(0)	(18.3)	(9.0)	
0.1 MPa	32	80.3	28.0	3.9	8.3	0.42	p	10.9	6.1	0.50	0.066	p
m	66	83.0	35.6	4.3	8.4	0.27	g	12.1	5.1	0.46	0.067	f
			(16.9)	(6.9)	(0.8)	(30.7)		(7.4)	(12.6)	(5.9)	(1.1)	
10 MPa	51	80.0	31.6	3.3	8.8	0.52	p	17.9	23.4	0.04	0.005	f
m	64	82.7	22.2	3.3	7.9	0.48	g	17.8	24.0	0.02	0.002	f
			(24.7)	(0)	(7.6)	(5.7)		(0.4)	(1.8)	(47.1)	(60.6)	
5 MPa	23	56.2	23.1	3.1	7.4	0.46	g	12.6	17.6	0.04	0.006	p
m	62	54.2	25.9	3.4	8.3	0.43	g	12.8	21.4	0.06	0.004	g
			(8.1)	(6.5)	(8.1)	(4.8)		(1.1)	(13.8)	(28.3)	(28.3)	
2 MPa	60	54.2	31.8	3.5	9.2	0.43	f	11.4	8.0	0.22	0.028	f
m	25	52.8	26.1	3.4	7.6	0.48	f	10.9	12.1	0.17	0.020	p
			(13.9)	(2.0)	(13.5)	(7.8)		(3.2)	(28.8)	(18.1)	(23.6)	
0.1 MPa	46	92.0	40.0	3.3	5.1	0.26	g	8.5	7.2	0.57	0.078	f
s	58	93.7	14.3	1.8	5.6	0.49	p	9.3	6.8	0.67	0.083	p
			(66.9)	(41.6)	(6.6)	(43.4)		(6.4)	(4.0)	(11.4)	(4.4)	
Ave. COV ± S.D.	all	all	18.9 ±19.0	8.3 ±12.7	6.9* ±3.6	14.3 ±14.0	g,f p	5.5 ±4.4	13.9 ±12.2	11.9 ±6.2	4.8 ±4.0	g,f, p,vp
Best COV ± S.D.			9.5 ±4.6	3.7 ±2.0	6.9* ±3.6	8.2 ±7.0	g,f	3.7 ±2.6	12.8 ±9.1	8.7 ±3.9	2.8 ±2.3	g,f p

* Includes all test results

TABLE 3.13
RANGE IN STRESS STRAIN PARAMETERS FOR REPEATABILITY TESTS FROM CURRENT RESEARCH
UNFROZEN MFS TESTS

NOMINAL TESTING CONDITIONS σ_c CIUC CIDC	TEST #	D_r (%)	SMALL STRAIN PARAMETERS (COV) Initial E (GPa)	Initial Q-ϵ_a Q_{yo} (MPa)	Upper Yield Q_{uy} (MPa)	Upper Yield ϵ_{uy} (%)	ACDT g f p	LARGE STRAIN PARAMETERS (COV) Q_p (MPa)	LARGE STRAIN PARAMETERS (COV) ϵ_p (%)	STAB g f p vp
0.1 MPa CIUC	B-22	94.0	0.23	0.08	0.15	0.38	g	4.81	22.0	p
	C-34	94.9	0.31	0.10	0.12	0.08	g	5.48	16.5	g
			(19.8)	(19.2)	(16.3)	(91.3)		(9.2)	(20.2)	
2 MPa CIUC	B-06	65.4	0.93	0.15	1.23	0.92	f	2.57	18.7	f
	B-11	67.2	1.19	-	1.43	1.13	g	3.09	16.2	p
	C-27	63.6	0.70	0.53	1.05	-	g	2.15	26.4	g
			(26.1)	(79.0)	(15.6)	(14.3)		(18.2)	(26.0)	
2 MPa CIUC	B-07	96.1	-	-	1.50	0.72	f	5.82	17.2	g
	C-33	93.4	1.16	-	-	-	p	5.53	19.5	f
			(-)	(-)	(15.6)	(32.8)		(3.6)	(8.8)	
5 MPa CIUC	B-01	72.7	1.07	0.90	2.48	1.50	p	3.19	21.4	g
	B-04	75.7	2.36	-	3.26	1.20	g	5.63	11.3	p
	C-23	75.4	1.36	-	2.55	1.47	p	2.98	17.1	p
			(42.3)	(-)	(15.6)	(11.9)		(37.4)	(30.4)	
5 MPa CIUC	B-05	91.5	0.86	-	3.47	1.59	p	5.63	11.2	f
	B-14	92.5	2.50	1.05	3.39	1.21	f	5.84	12.1	f
	B-15	94.3	1.30	-	3.70	1.56	g	6.95	13.9	p
			(54.9)	(-)	(4.6)	(14.5)		(11.6)	(11.2)	
10 MPa CIUC	C-01	82.7	1.02	-	4.87	1.97	p	4.87	1.97	vp
	C-02	82.7	1.16	-	5.08	2.12	f	5.08	2.12	vp
			(9.4)	(-)	(3.1)	(5.2)		(3.1)	(5.2)	
0.1 MPa CIDC	C-14	86.1	0.31	0.09	-	-	g	0.31	5.7	g
	C-21	84.3	0.17	0.08	-	-	g	0.17	4.7	g
			(40.6)	(12.3)	(-)	(-)		(41.4)	(13.2)	
Ave. COV ± S.D.	all	all	32.2 ±16.7	36.9 ±36.7	11.0 ±6.6	27.4 ±35.9	g,f p	17.8 ±15.7	16.5 ±9.4	g,f, p,vp
Best COV ± S.D.			35.2 ±13.1	45.6 ±47.2	11.0* ±6.6	- -	g,f	20.2 ±15.6	18.3 ±8.7	g,f p

* Includes all test results

TABLE 3.14
RANGE IN STRESS STRAIN PARAMETERS FOR REPEATABILITY TESTS FROM CURRENT RESEARCH
CONVENTIONAL FROZEN MFS TESTS

NOMINAL TESTING CONDITIONS σ_c, ϵ, T	TEST #	D_r (%)	SMALL STRAIN PARAMETERS (COV) Initial E (GPa)	Initial Q-ϵ_a Q_{yo} (MPa)	Upper Yield Q_{uy} (MPa)	Upper Yield ϵ_{uy} (%)	ACDT	LARGE STRAIN PARAMETERS (COV) Q_p (MPa)	LARGE STRAIN PARAMETERS (COV) ϵ_p (%)	VOLUMETRIC PARAMETERS Maximum $d\epsilon_v/d\epsilon_a$	VOLUMETRIC PARAMETERS ϵ_{v20} (%)	STAB
10 MPa Slow -15°	123	90.7	22.8	3.2	7.9	0.55	f	17.3	15.0	-	-	f
	131	86.9	14.2	1.9	9.0	0.54	p	17.0	8.6	-	-	vp
	134	85.8	18.9	2.5	7.9	0.46	g	17.4	14.2	-	-	p
			(23.1)	(25.6)	(7.7)	(9.5)		(1.2)	(27.6)			
10 MPa Fast, -15°	126	48.7	24.3	4.9	20.3	0.94	g	20.3	0.94	0.07	1.2	g
	129	47.7	26.9	5.3	20.4	0.94	g	20.4	0.94	0.14	2.0	g
			(7.2)	(5.6)	(0.4)	(0)		(2.5)	(10.1)	(47.1)	(35.3)	
10 MPa Slow, -15°	127	35.4	-	-	7.8	1.09	p	11.4	22.1	-	-	g
	130	38.2	22.9	-	7.6	0.68	g	10.8	21.3	-	-	f
			(-)	(-)	(1.8)	(32.8)		(3.8)	(2.6)			
10 MPa Slow, -20°	74	33.2	21.7	0.8	11.5	0.65	p	14.0	19.6	0.11	0.6	f
	98	34.3	-	-	10.5	0.34	f	14.1	19.6	0.12	2.1	g
			(-)	(7.9)	(3.9)	(44.3)		(0.5)	(0)	(6.1)	(78.6)	
0.1 MPa Mod., -20°	71	90.3	31.3	6.6	18.0	1.00	g	20.6	4.7	0.64	8.2	f
	95	86.3	18.3	4.1	16.4	0.90	NA	18.9	4.3	0.38	6.3	vp
			(35.3)	(33.0)	(6.6)	(7.4)		(6.1)	(7.4)	(36.0)	(18.5)	
0.1 MPa Fast, -20°	89	37.1	25.7	8.1	24.8	0.68	g	24.8	0.68	0.50	7.0	f
	99	36.3	25.8	8.8	26.7	0.74	f	26.7	0.74	0.47	6.3	f
			(0.3)	(5.9)	(5.2)	(6.0)		(5.2)	(6.0)	(4.4)	(7.4)	
Ave. COV ± S.D.	all	all	16.5 ±15.8	17.5 ±14.0	4.3 ±2.8	16.7 ±17.6	g,f p	2.9 ±2.5	7.3 ±10.4	23.4 ±21.4	35.0 ±31.2	g,f, p,vp
Best COV ± S.D.			6.9 ±6.5	9.6 ±6.7	4.3* ±2.8	6.2 ±6.3	g,f	1.3 ±1.7	1.6 ±1.9	26.6 ±29.0	57.0 ±30.6	g,f p

* Includes all test results

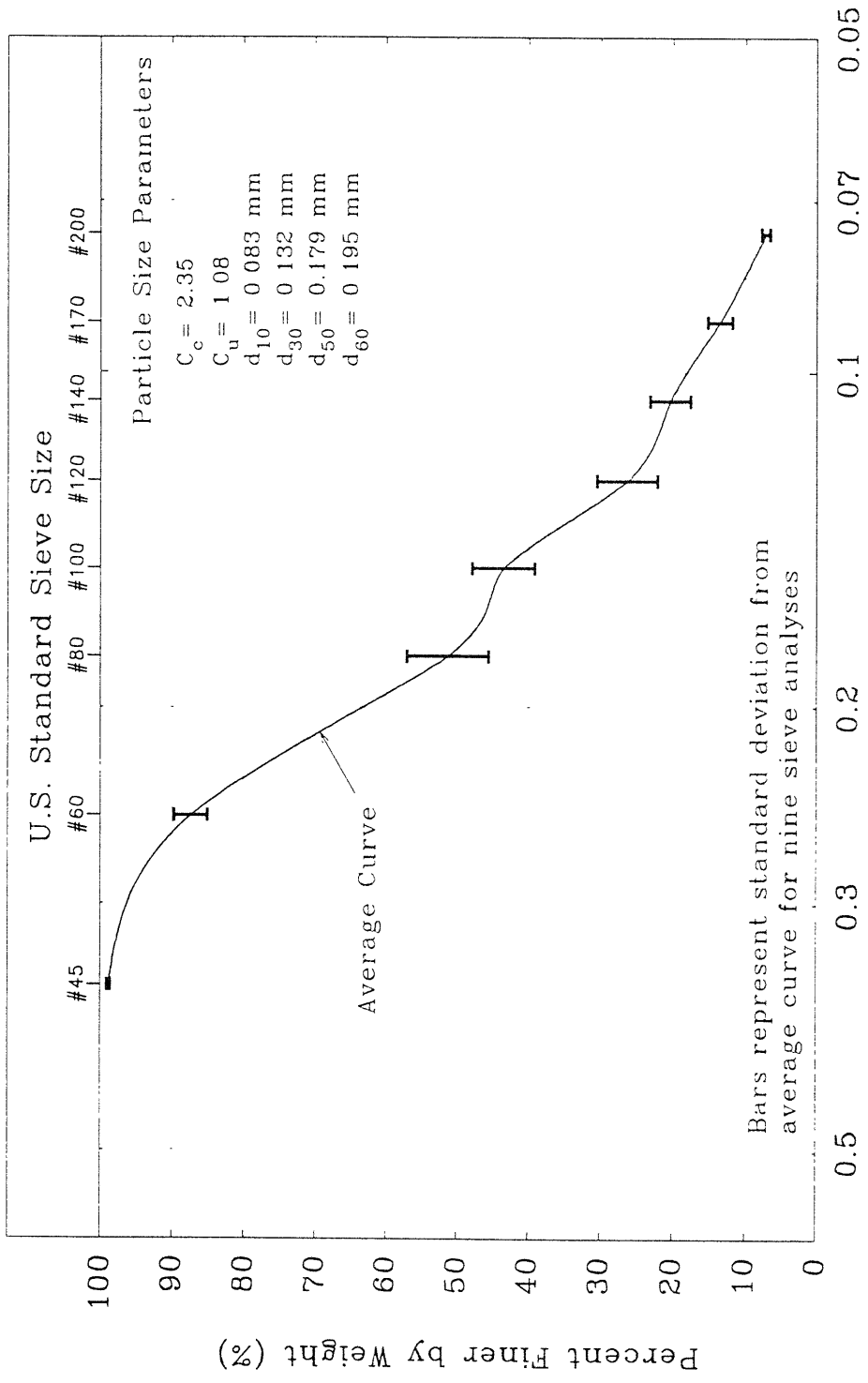

Figure 3.1 Mechanical Dry Sieve Analysis of Manchester Fine Sand

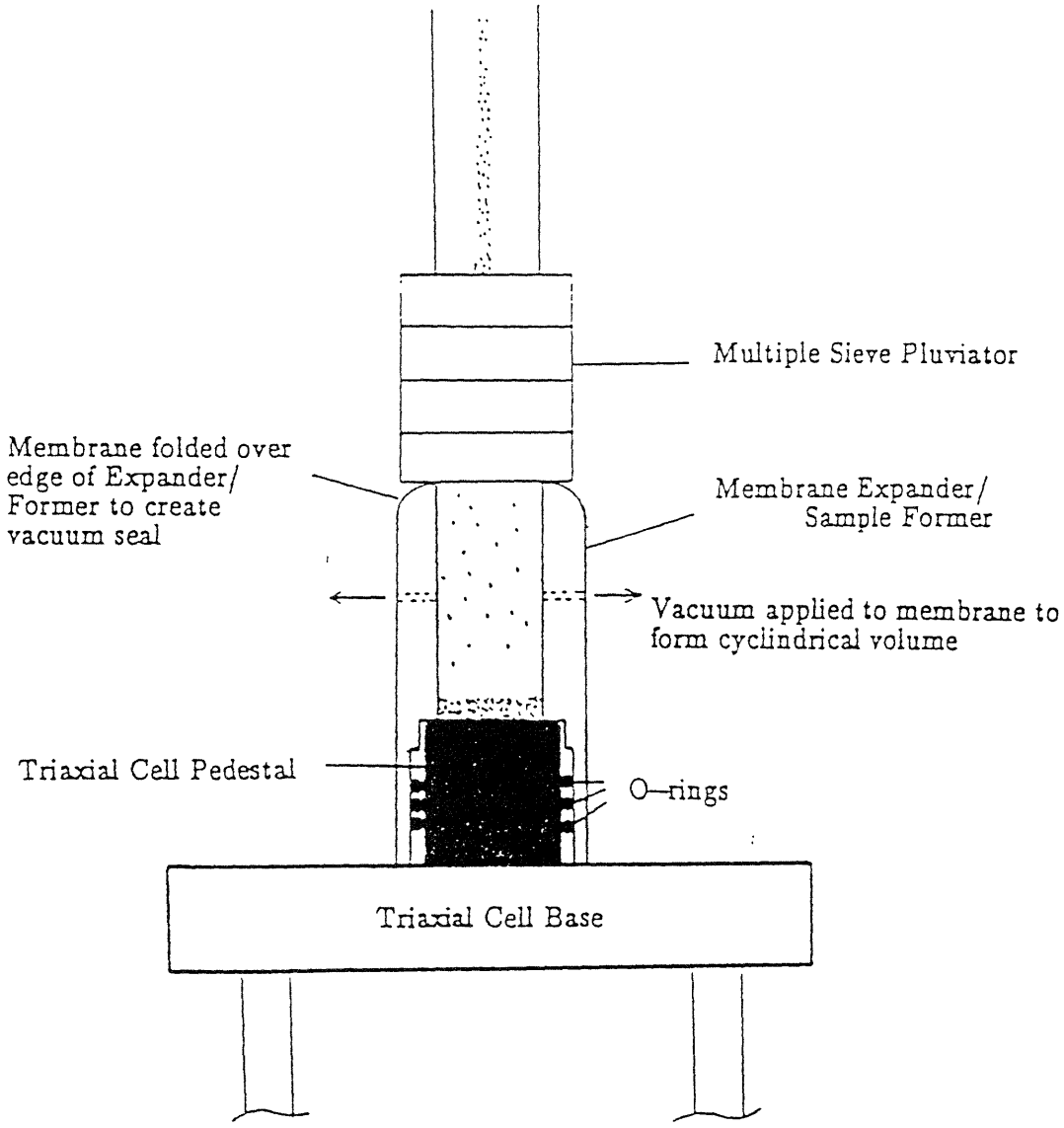

Figure 3.2 Schematic Diagram of Multiple Sieve Pluviation for Unfrozen MFS and Consolidate–Freeze Specimens (from Andersen et al. 1992)

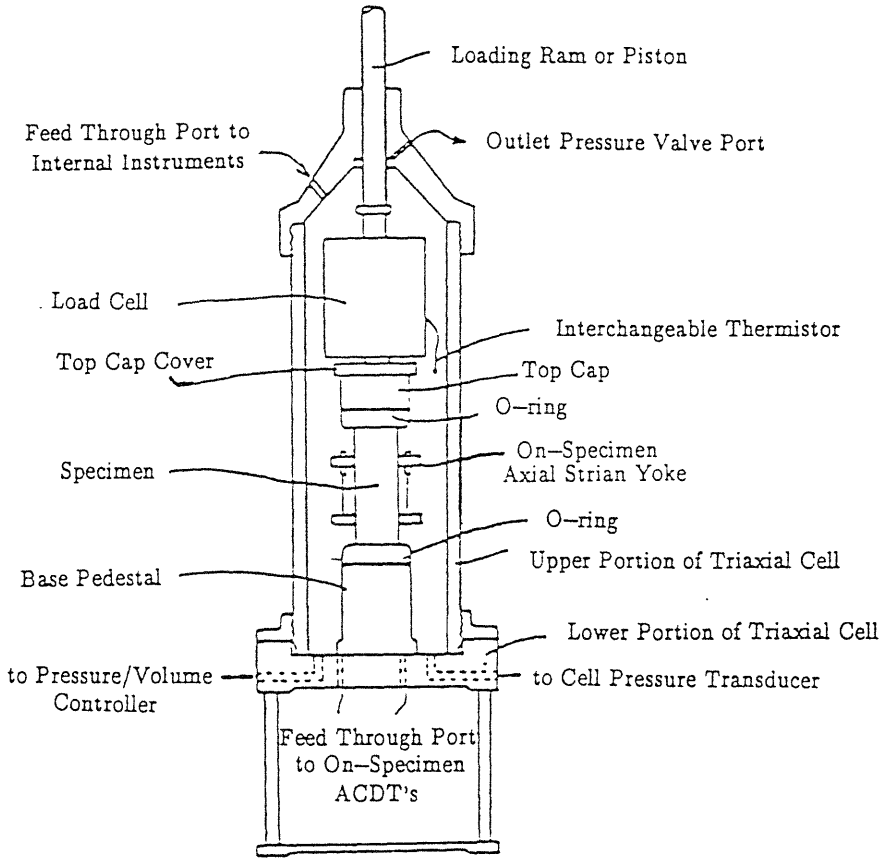

Figure 3.3 Details of the Modified High Pressure Triaxial Cell (from Andersen et al. 1992)

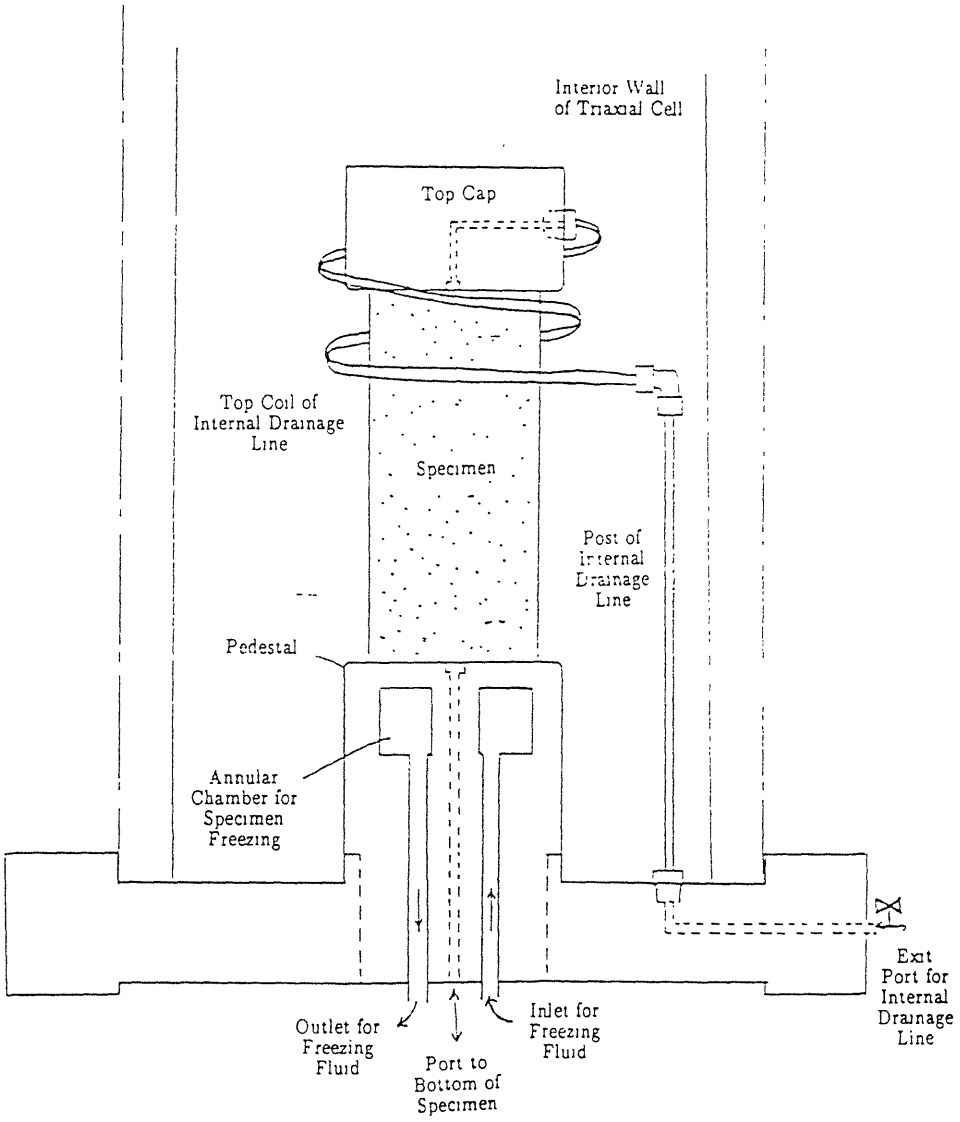

Figure 3.4 Details of Internal Modifications for the Various Testing Programs

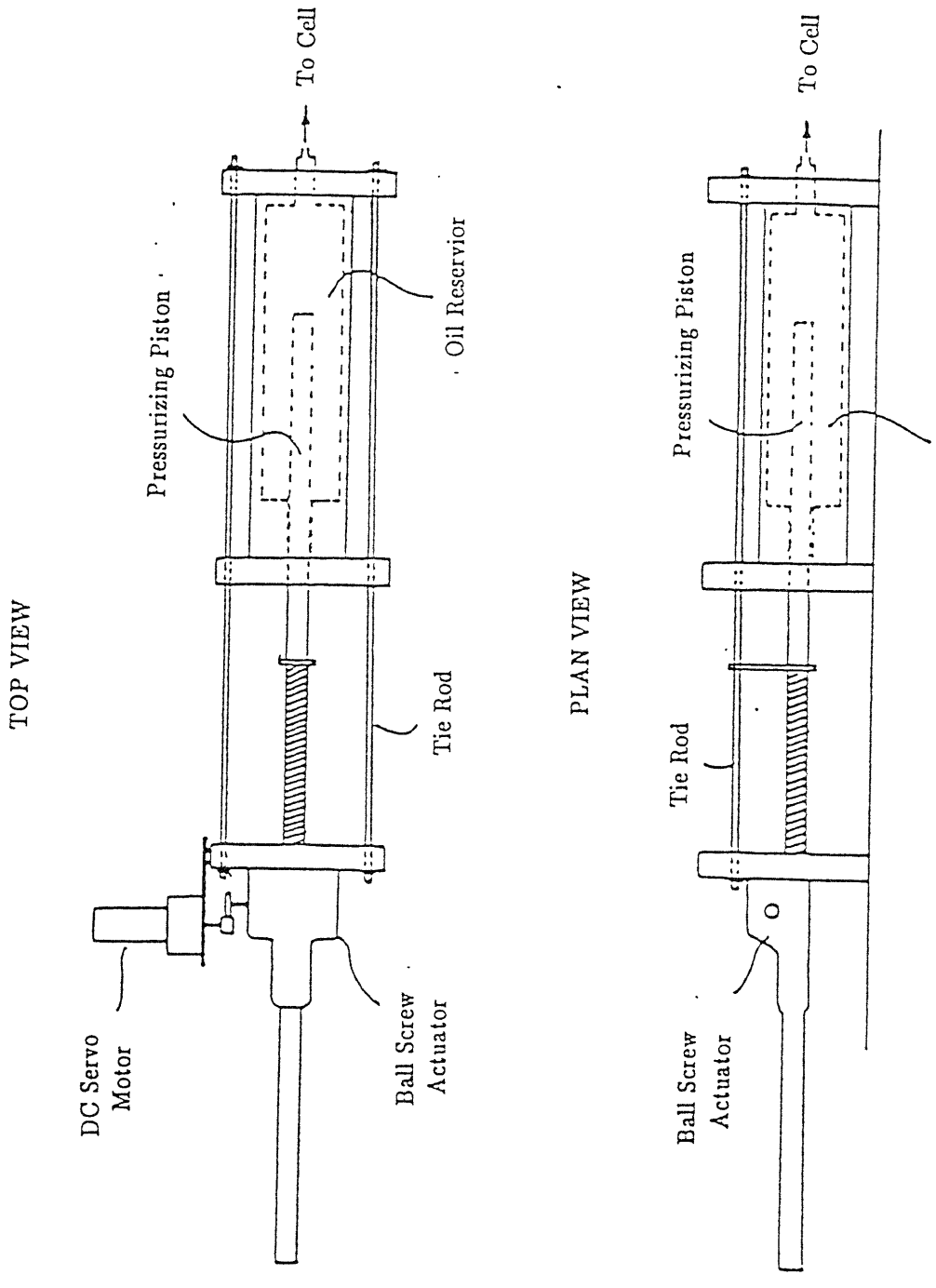

Figure 3.5 Schematic Drawing of Mechanical Portion of Pressure/Volume Controller (from Andersen et al. 1992)

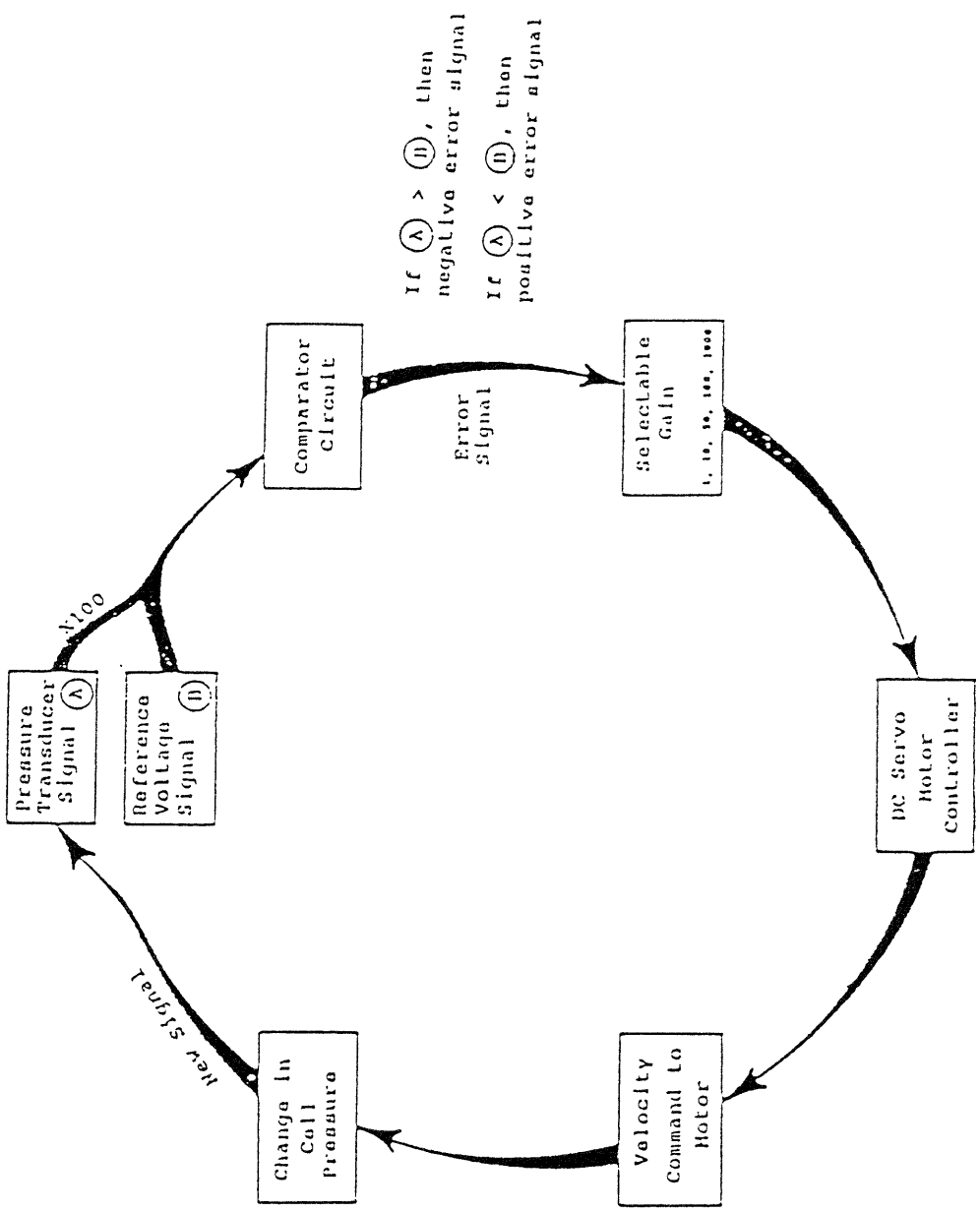

Figure 3.6 Schematic Diagram of Pressure/Volume Controller System (from Andersen 1991)

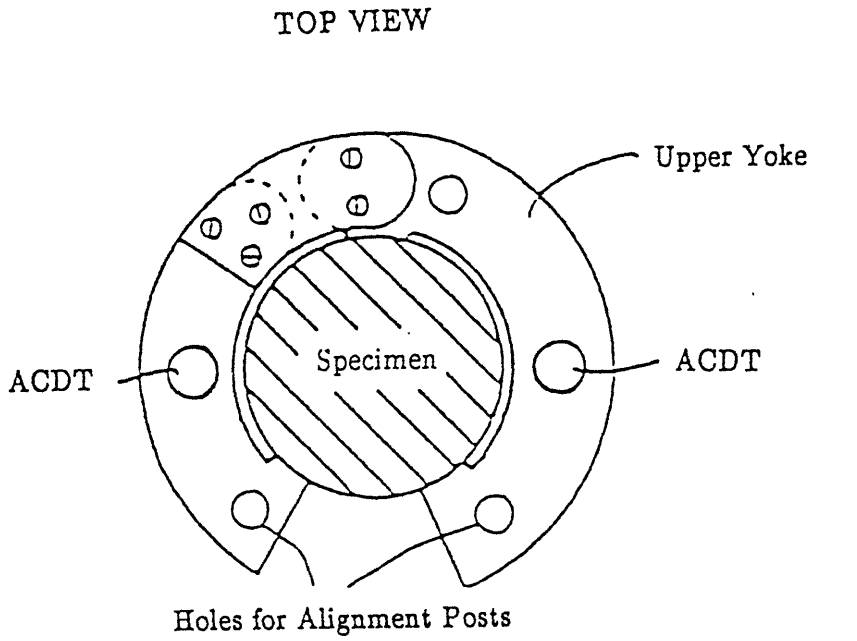

Figure 3.7 Details of On–Specimen Axial Strain Device (from Andersen et al. 1992)

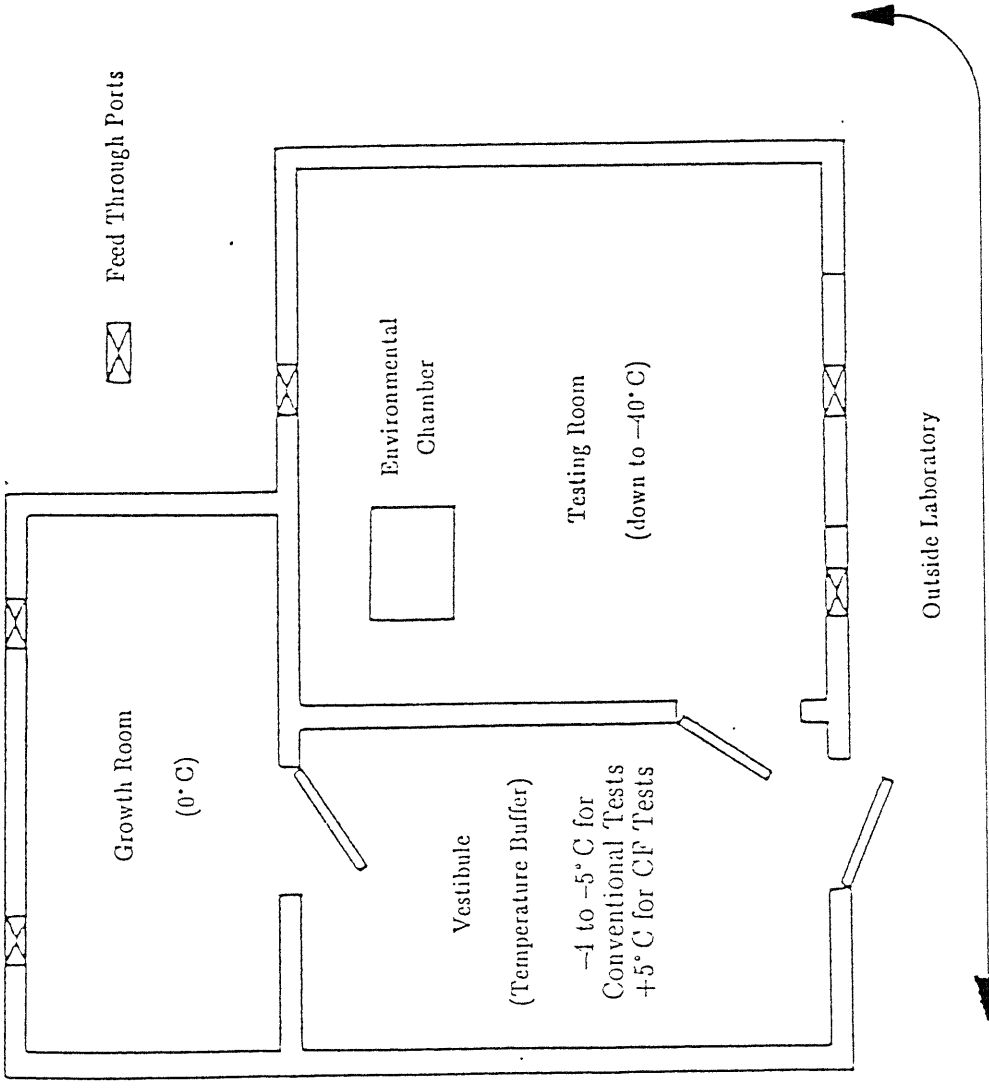

Figure 3.8 Plan View of MIT Cold Room Facility (from Andersen et al. 1992)

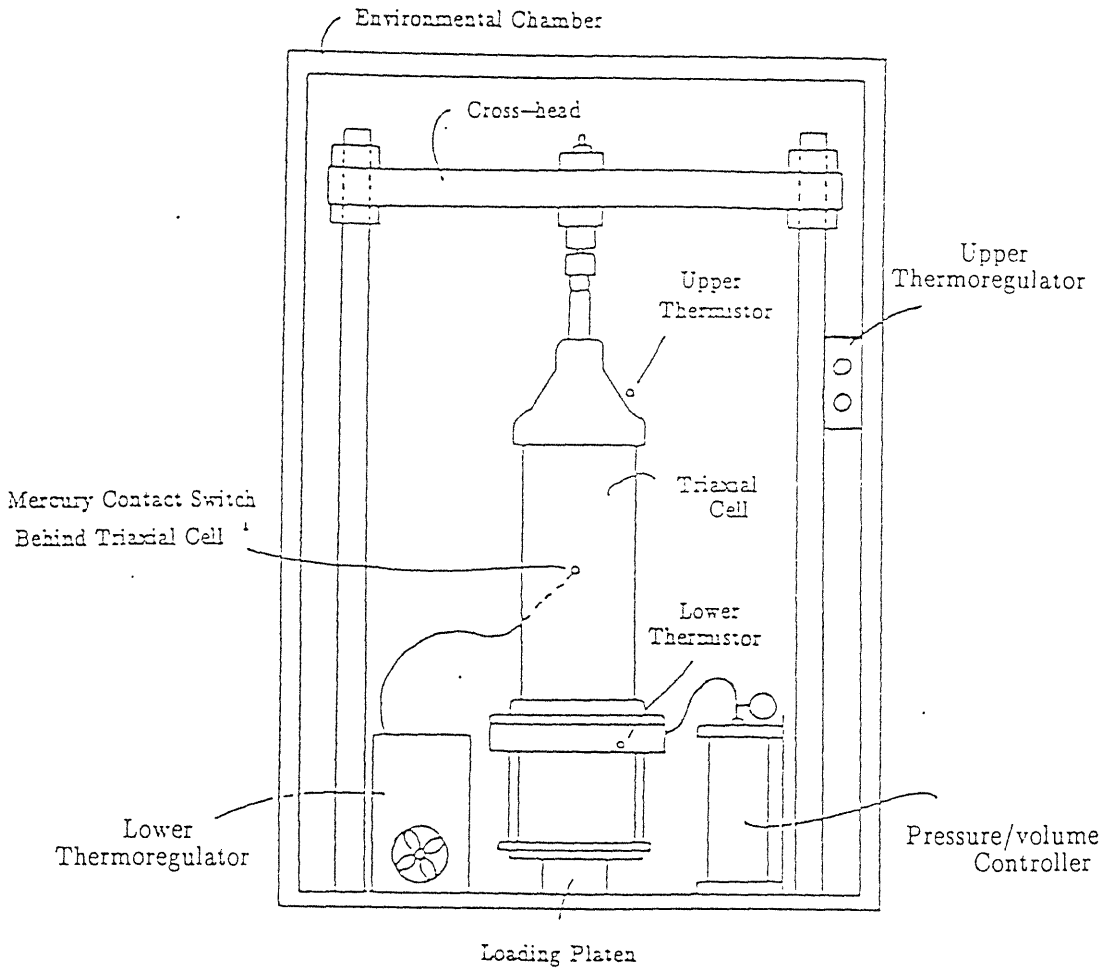

Figure 3.9 Schematic View of Environmental Chamber and Triaxial Cell (from Andersen et al. 1992)

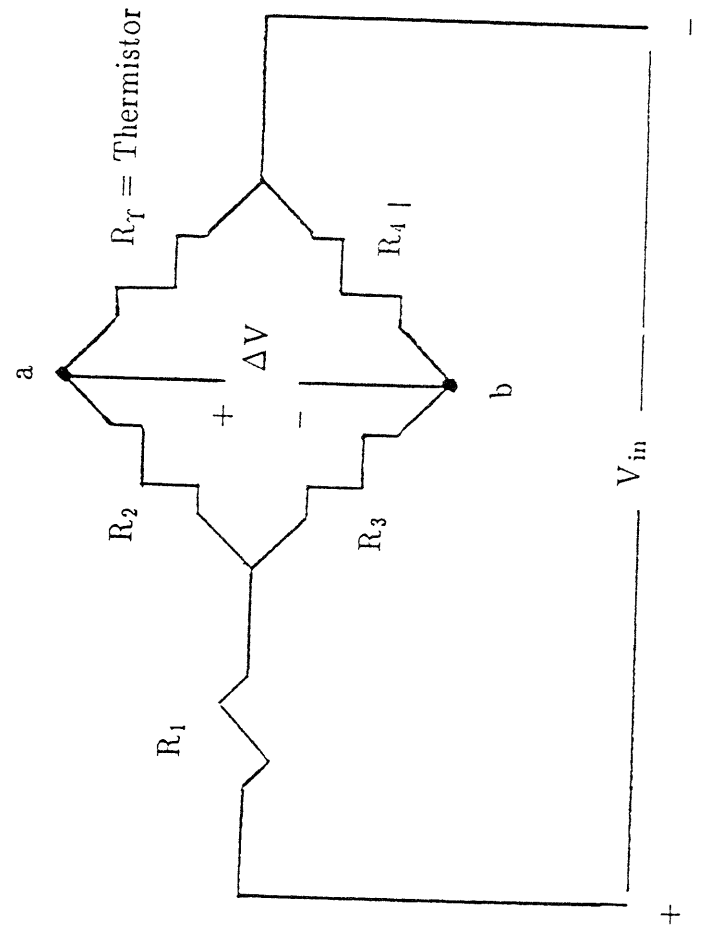

V_{in} = input voltage
ΔV = measured output
R_1, R_2, R_3 and R_4 = known resistances
R_T = thermistor resistance which varies with temperature

Figure 3.10 Component of Temperature Measurement System

1 Plexiglas Split Sleeve
2 Plexiglas Hollow Cylinder
3 Porous Stone
4 Filter Paper
5 Drainage Lines
6 Brass Collar
7 Knife Edge Aliminum Guide
8 Brass Base
9 Bolt
10 Freezing Cap
11 Inlet for Freezing Fluid
• O–rings

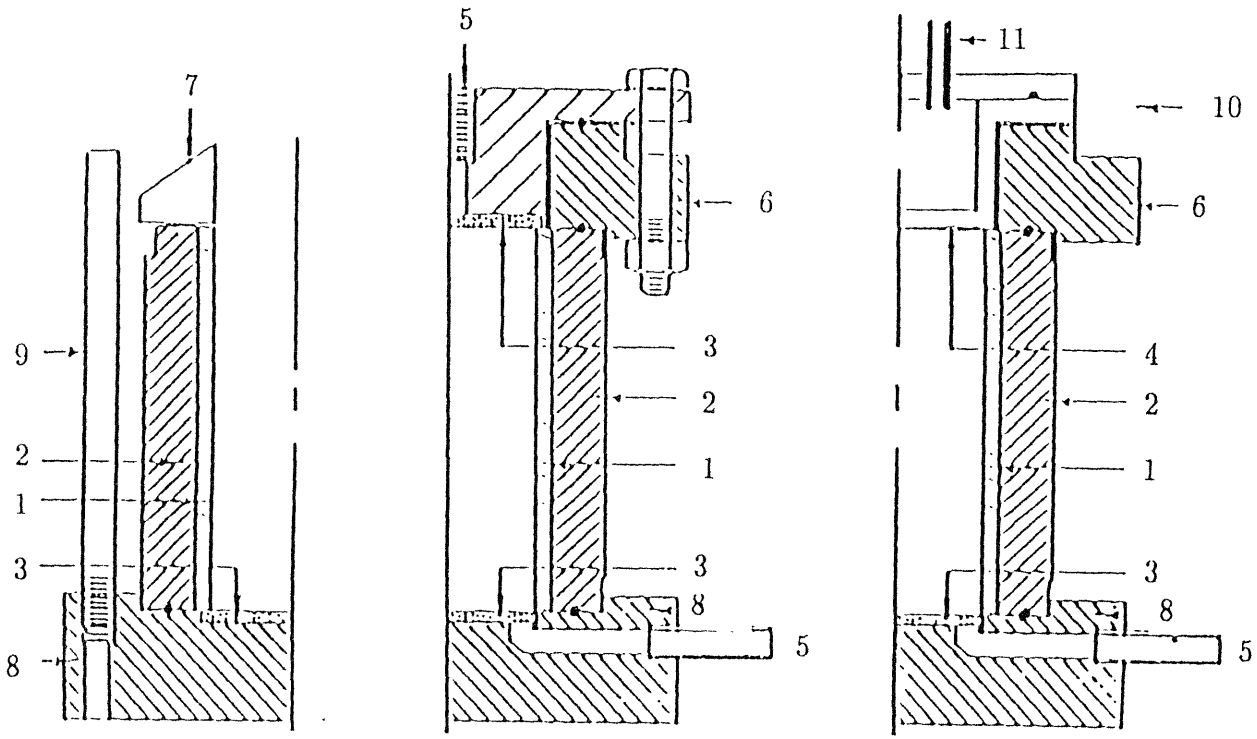

a) MSP Mode b) Saturation Mode c) Freezing Mode

Figure 3.11 Schematic Drawing of Specimen Preparation Molds (after Martin et al. 1981)

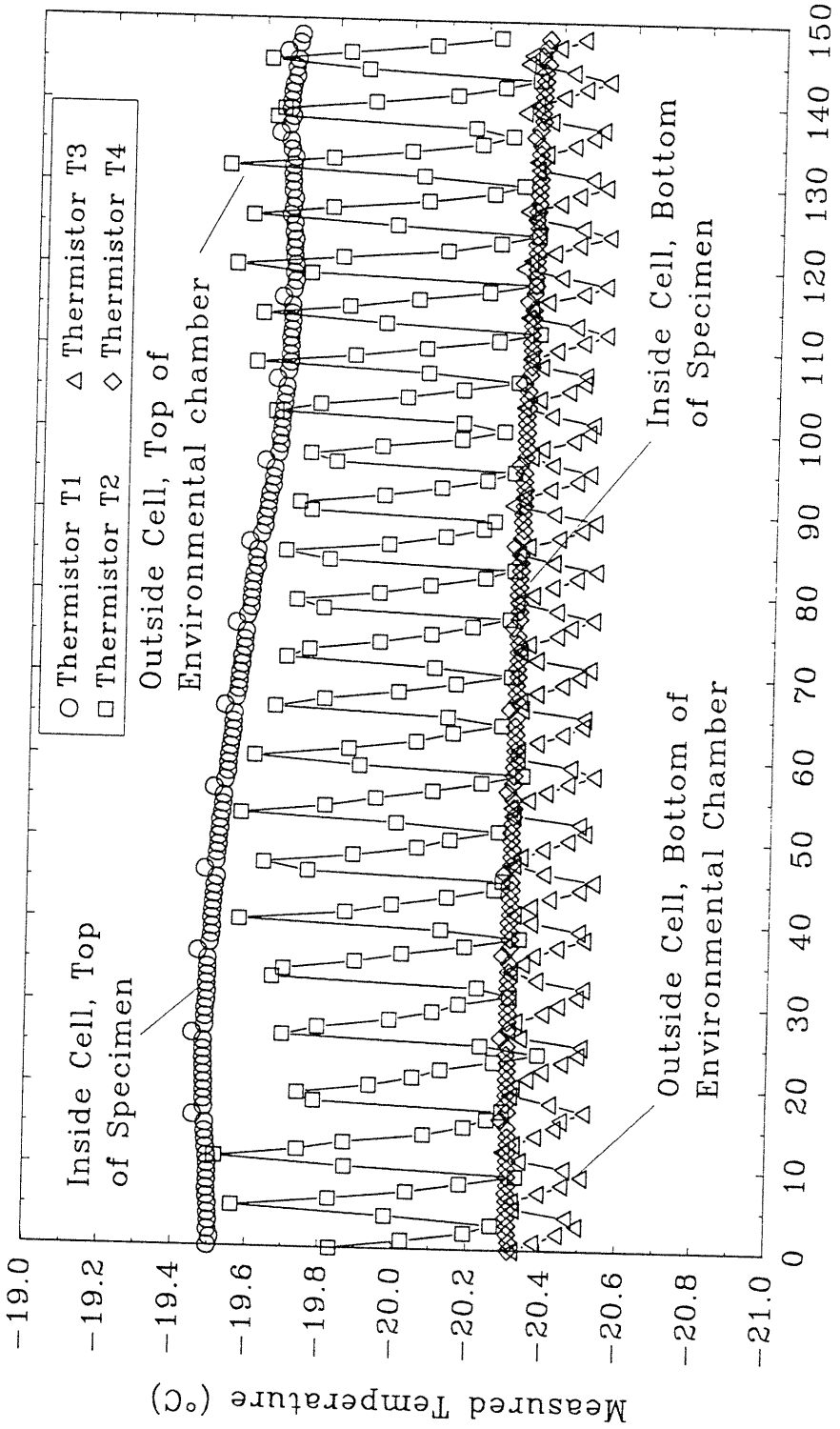

Figure 3.12 Temperature Inside the Environmental Chamber and Triaxial Cell During Shear of FRS100

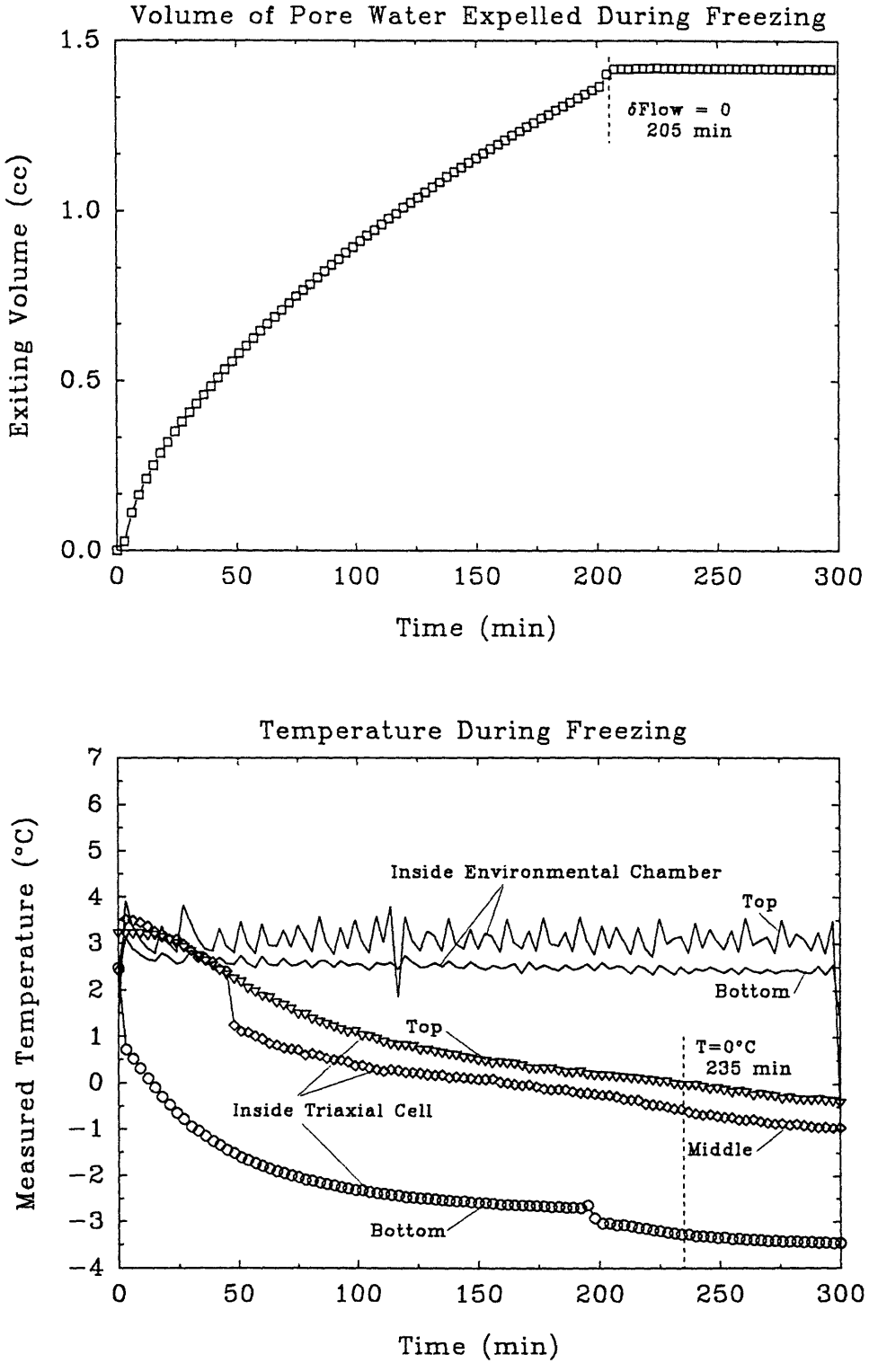

Figure 3.13 Pore Volume Expelled and Temperature Changes During Specimen Freezing Phase of CF02

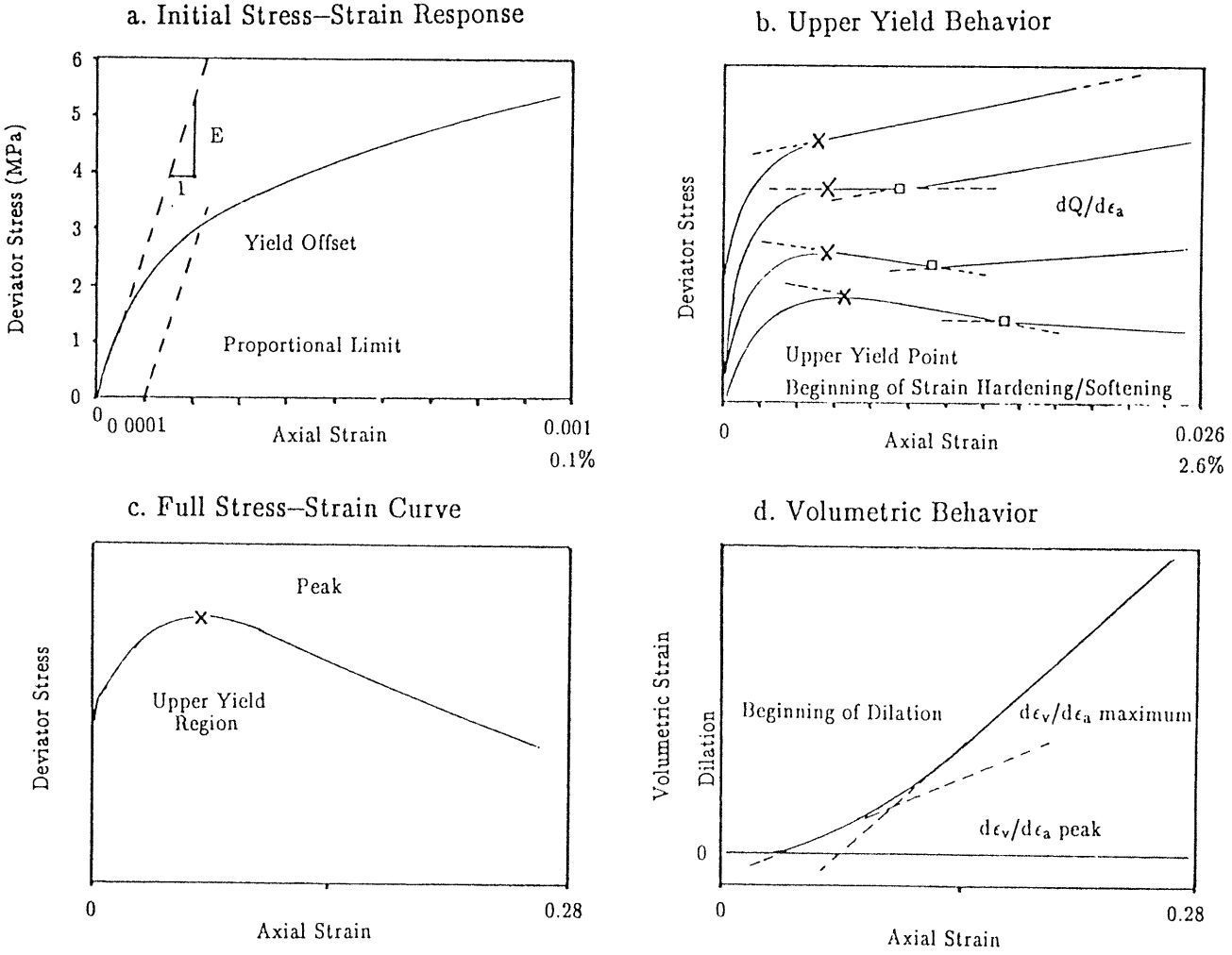

Figure 3.14 Idealized Stress–Strain Behavior and Graphical Construction Techniques (from Andersen et al. 1992)

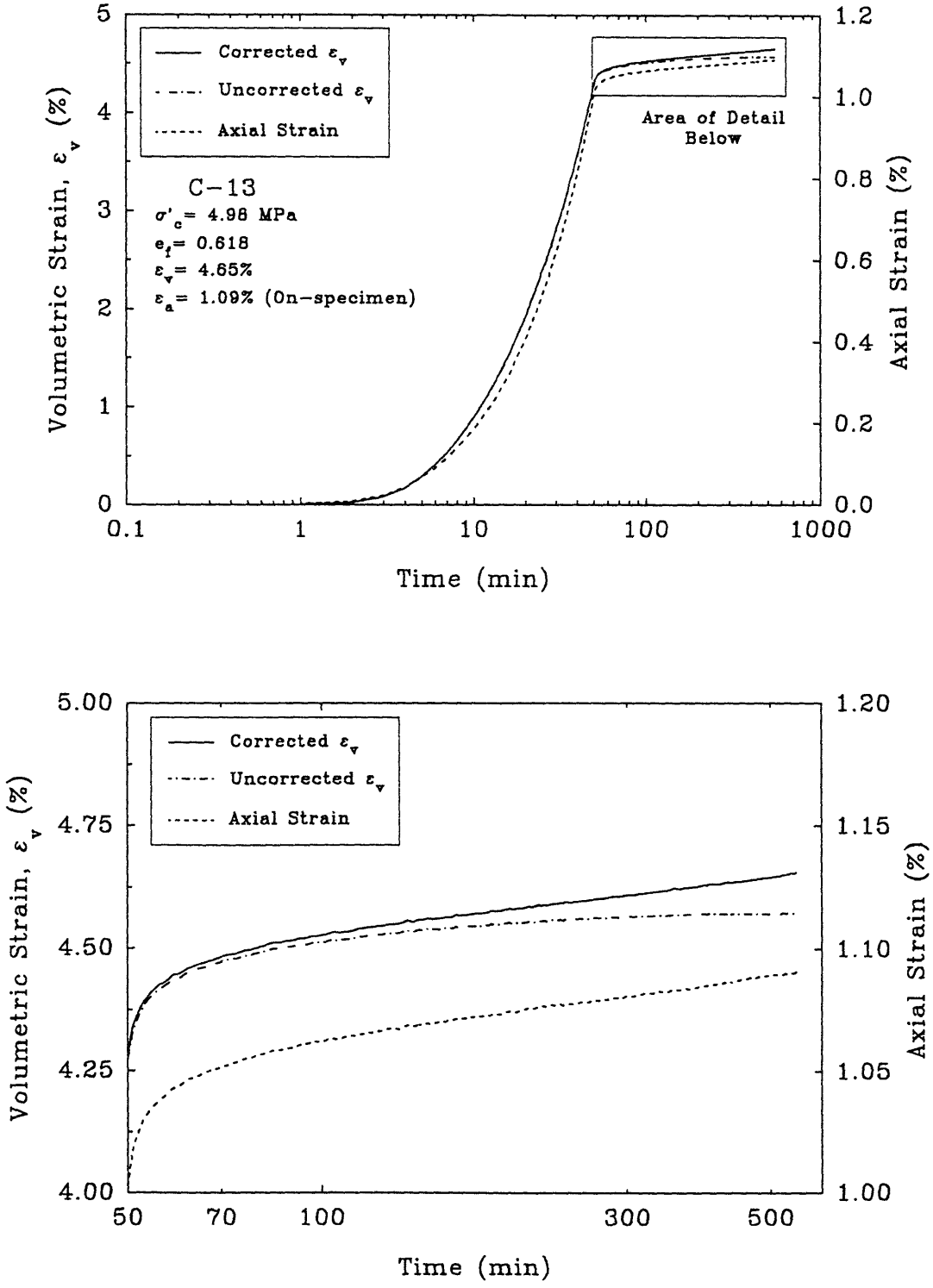

Figure 3.15 The Effects of Leakage on the Measured Volumetric Strain During Consolidation of Unfrozen MFS Test C-13

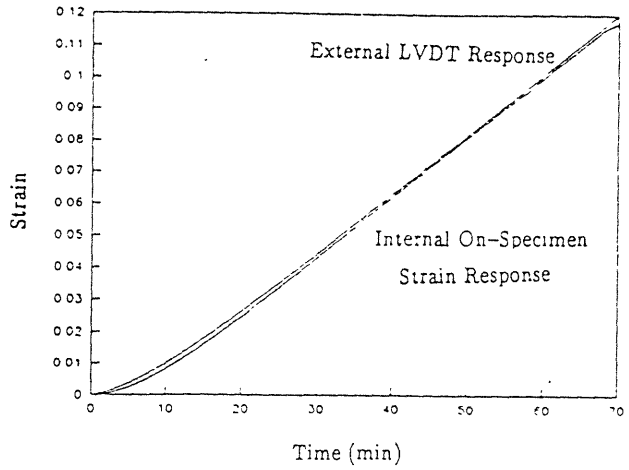

a) Initial Strain Behavior Indicative of Right Circular Cylinder Deformation

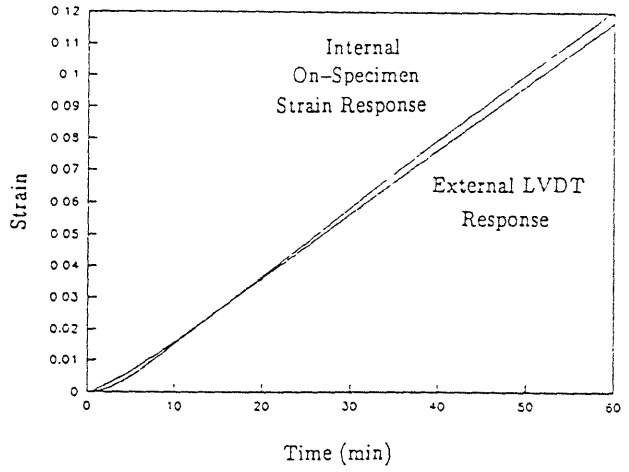

b) Initial Strain Behavior Indicative of Combined Right Circular Cylinder and Parabolic Deformation

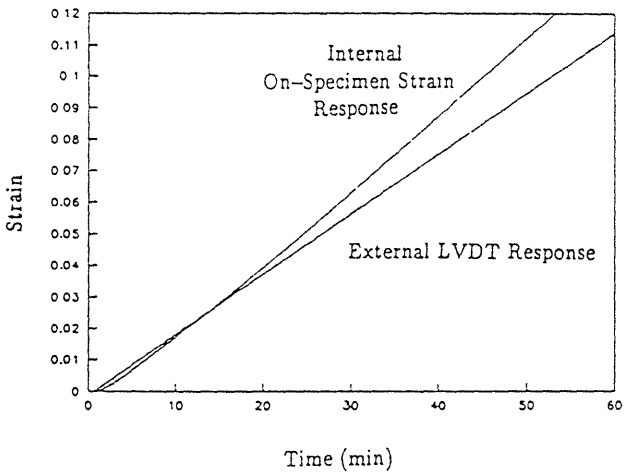

c) Initial Strain Behavior Indicative of Parabolic Deformation

Figure 3.16 Examples of On-Specimen Strain Responses for Unfrozen MFS Tests

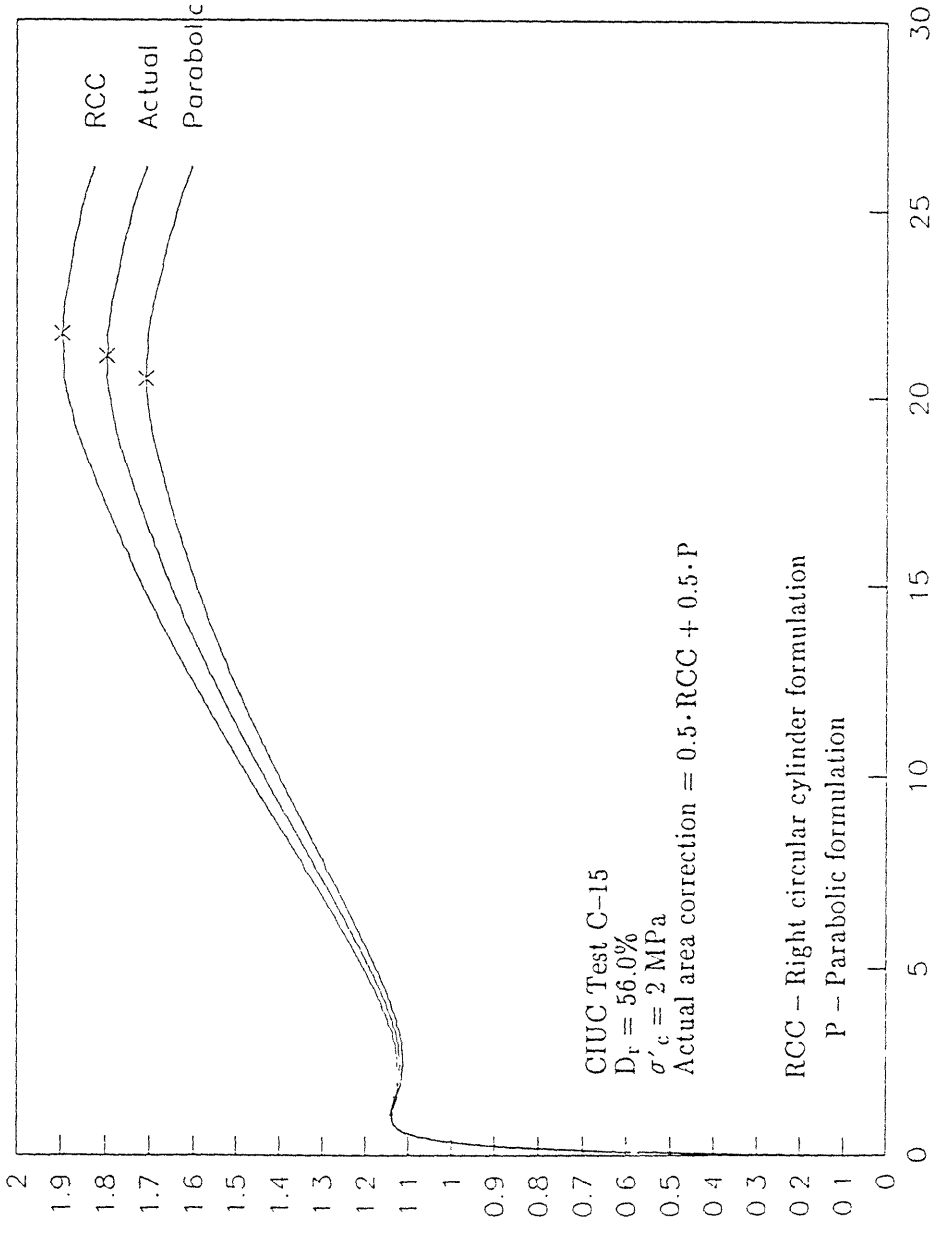

Figure 3.17 Range in Stress–Strain Responses for Unfrozen MFS Test C–15

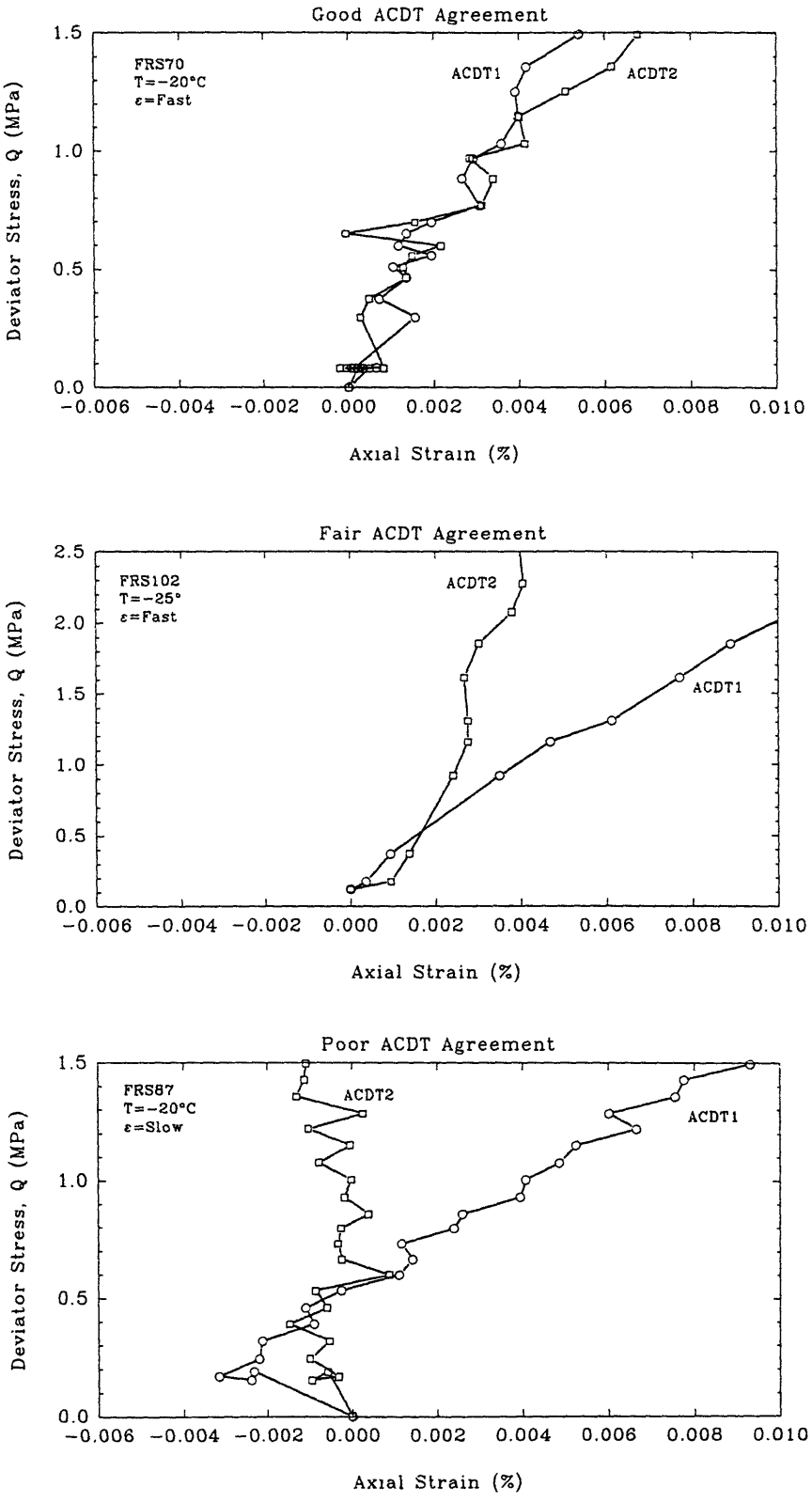

Figure 3.18 Examples of ACDT Agreement Qualifiers (from Conventional Frozen Tests)

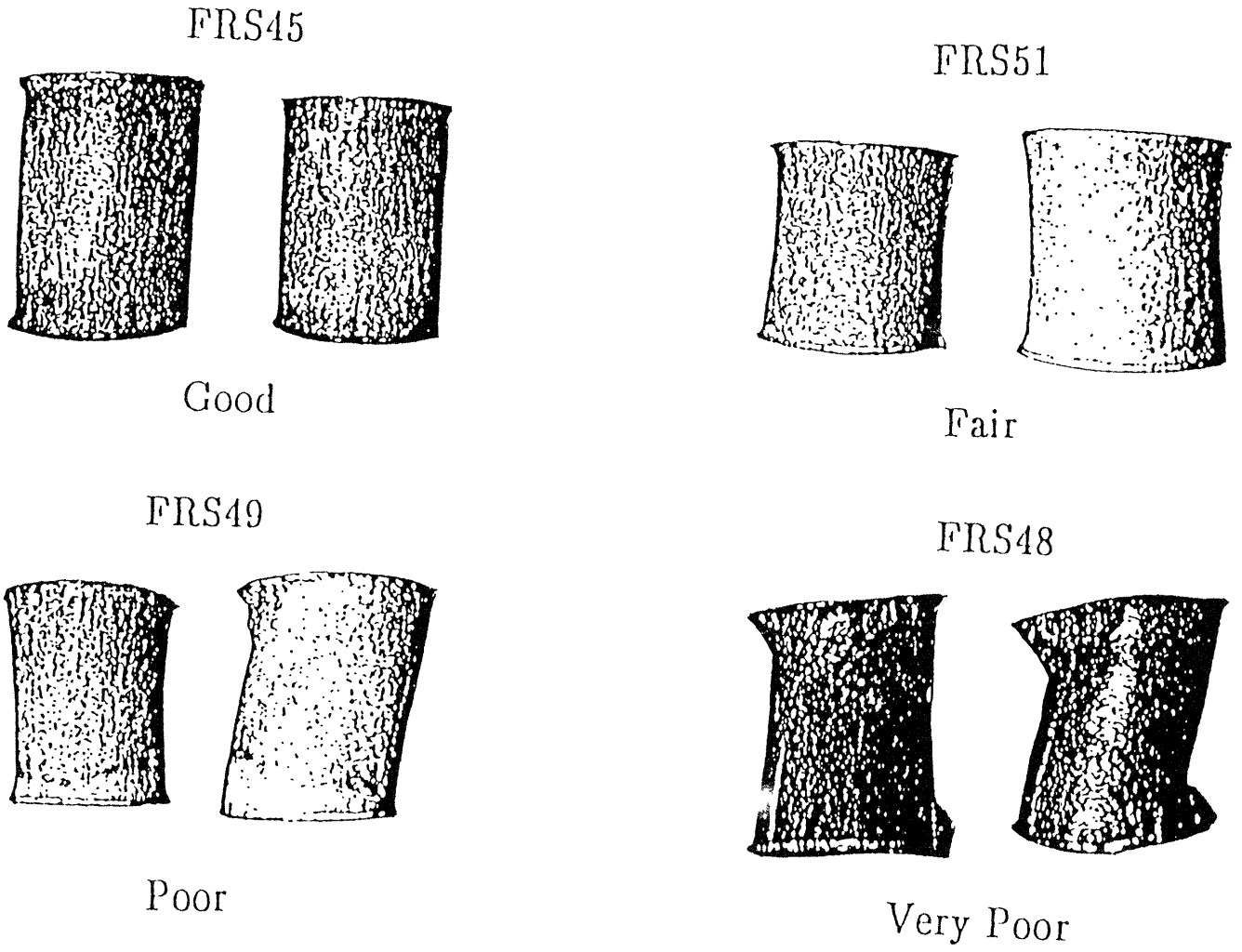

Figure 3.19 Examples of Specimen Stability Qualifiers (from Andersen 1991)

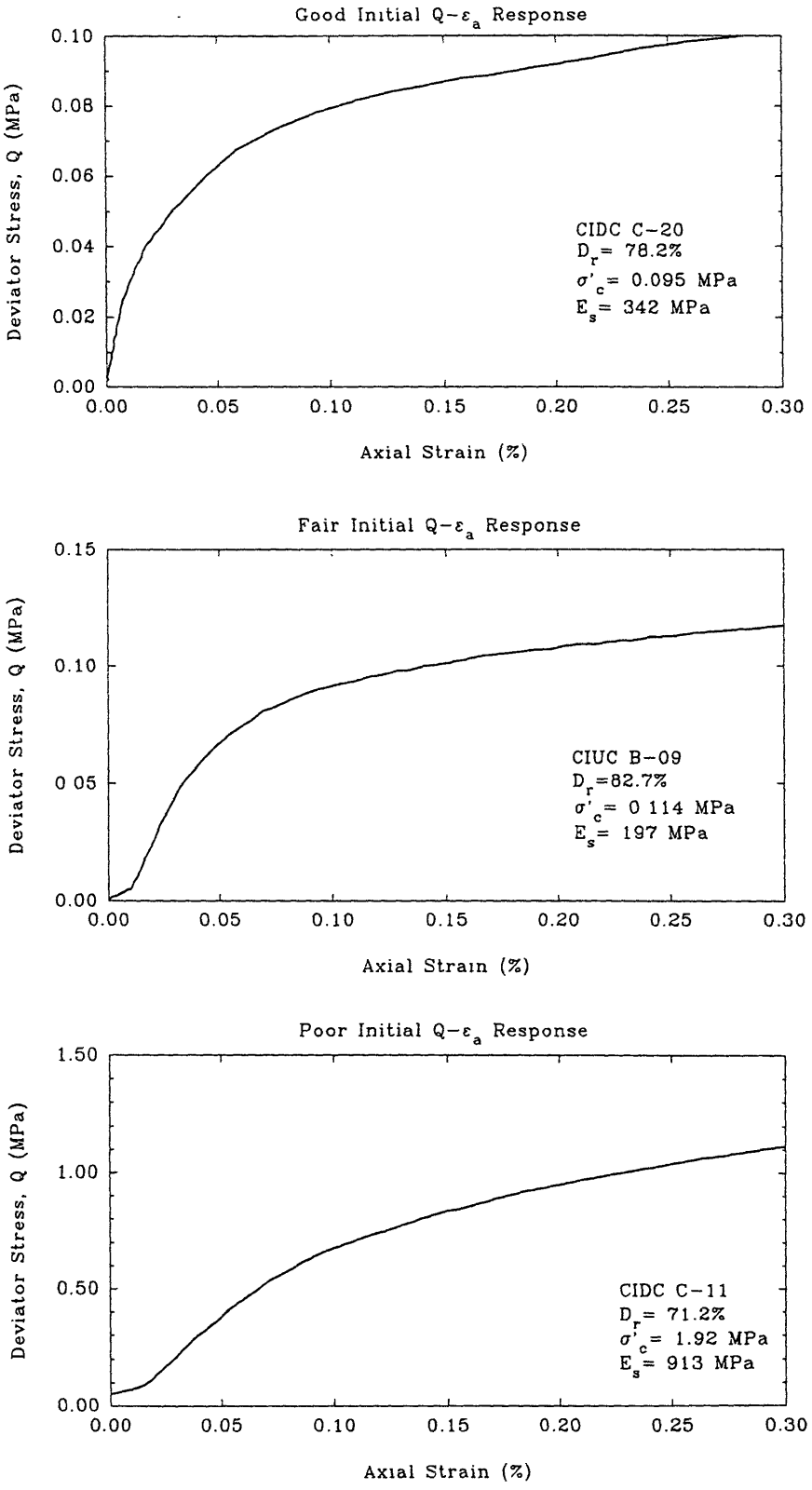

Figure 3.20 Examples of Initial Stress-Strain Responses for Unfrozen MFS Tests

CHAPTER 4
TRIAXIAL COMPRESSION TEST RESULTS ON UNFROZEN MANCHESTER FINE SAND

This chapter presents the results of triaxial compression tests on unfrozen MFS. A complete and detailed characterization of unfrozen MFS is beyond the scope of the present research. Therefore, the scope of this program mirrored that for the conventional frozen MFS; namely, the majority of tests were consolidated–undrained (CIUC) or consolidated–drained (CIDC) tests performed at effective confining stresses (σ'_c) from 0.1 to 10 MPa. Preshear relative densities (D_r) ranged from 43.8% to 104% for this range in confining stresses. The analysis of the unfrozen MFS results includes an evaluation of the stress–strain–strength and deformation behavior of unfrozen MFS, and the development of shear parameters which may be directly compared to those of frozen MFS.

In addition, this chapter presents the results of a steady state analysis based on the state parameter (Ψ) procedure as outlined by Been and Jefferies (1985). This analysis provides a means to correlate the behavior of unfrozen MFS to that of other sands. This analysis also aids in the implementation of the dilatancy–hardening model for frozen soil (see Chapter 6).

The chapter is divided into five sections. Section 4.1 presents the purpose and scope of the unfrozen testing program and the various testing variables and conditions used in each of the three testing series which comprise the testing program (see Chapter 3, Section 3.3 for discussion of testing series). Section 4.2 presents summary plots of the consolidation and

shear results from the unfrozen MFS testing program, although the latter is discussed in the greatest detail. This presentation is restricted to Series B and Series C test results. Presentation of individual test results for Series B and Series C tests are presented in Appendix B.

Section 4.3 presents an analysis of the undrained and drained behavior of unfrozen MFS with respect to the effects of σ'_c and D_r on measured stress–strain, excess pore pressure/volumetric strain and effective stress path behavior. This section also summarizes the effects of σ'_c and D_r on the mobilized friction angle as well as testing parameters used in describing frozen MFS behavior; i.e., the initial modulus, upper yield stress and peak strength (see Chapter 5 for frozen MFS results). Section 4.4 presents the results of the steady state analysis of the unfrozen tests in terms of the state parameters, Ψ. Section 4.5 presents conclusions of the current research effort on unfrozen MFS and discusses the general analysis of the unfrozen MFS test results as well as the analysis of steady state conditions. Section 4.5 also evaluates how these analyses may be applied to the understanding of frozen soil.

4.1 TRIAXIAL COMPRESSION TESTING PROGRAM ON UNFROZEN MFS

4.1.1 Purpose and Scope of Testing Program

The primary purpose of the unfrozen MFS testing program was to develop an unfrozen MFS data base to compare with the data base for conventional frozen MFS results. A secondary purpose was to develop an understanding of the stress–strain–strength and deformation behavior of an unfrozen sand at high confining stresses. Andersen (1991) previously

presented a frozen MFS data base for tests at a temperature of –10 °C. However, a lack of unfrozen MFS data did not allow a comparison of frozen and unfrozen MFS behavior. Andersen et al. (1992) presented a summary of conventional frozen and unfrozen MFS tests conducted at that time, but little direct comparison of results was performed. However, Andersen et al. (1992) used the available unfrozen MFS results to define parameters for evaluation of the dilatancy–hardening model for frozen soils proposed by Ladanyi (1985). State parameter concepts, developed by Been and Jefferies (1985), were used to develop these unfrozen sand parameters.

The unfrozen MFS testing program was performed intermittently from 1990 to 1993. To accomplish the primary purpose of the program, the initial scope of the unfrozen MFS testing program consisted of eight isotropically – consolidated undrained triaxial compression (CIUC) tests at four effective confining stresses (σ'_c) of 0.1, 2, 5 and 10 MPa and two relative densities (D_r) of 55% and 95%. However, this limited testing scope was expanded significantly to include a total of 49 "useful" tests: 35 CIUC tests, 11 isotropically–consolidated drained triaxial compression tests (CIDC) and three anisotropically–consolidated undrained triaxial compression (CAUC) tests. The term "useful" signifies that the tests provide reliable shear results for analysis. This expanded scope of unfrozen MFS testing created a larger data base to compare to the conventional frozen MFS test data and a more detailed evaluation of the tests via the steady state concepts.

4.1.2 Overview of Testing Program

As described in Chapter 3, the testing program has been divided into three series; Series A, Series B and Series C. This division was due, in part, to the intermittent nature of test performance and relatively long duration of

the testing program as well as to the numerous modifications and alterations to testing equipment and procedures that occurred. Chapter 3 describes the testing procedures used in the testing series. The following summarizes the scope of the testing series. Additional information on Series B and Series C tests is presented in Appendix B.

4.1.2.1 Series A Tests

The Series A tests consist of the first 17 unfrozen MFS tests. Tests were attempted with effective confining stresses (σ'_c) of 0.1, 1, 2, 4 and 5 MPa. All except one test was sheared under undrained conditions. Pre–shear D_r ranged from 14 to 106%. A nominal strain rate of 8.3 %/hour was used for all tests. It should be noted that 24 specimens were actually prepared in this series, but the first seven tests rarely proceeded beyond back–pressure saturation. In addition, of these 17 tests cited, only six provide shear results; a success rate of 25% (6 out of 24). As stated in Chapter 3, Series A tests are considered the "learning curve" in the unfrozen MFS testing program. Given this "learning curve" status and the poor success rate of tests in Series A, these tests will be excluded from future analysis and discussion.

4.1.2.2 Series B Tests

Series B consisted of 24 undrained triaxial compression tests sheared at a nominal strain rate of 8.3%/hour. [The reader should note that in Andersen et al. (1992), these tests were referred to as the Series B Tests #01 to #24.] Pre–shear D_r ranged from 43.8 to 104.3% with effective confining stresses of 0.1, 2, 5 or 10 MPa used for all tests. Nineteen tests were consolidated under hydrostatic stresses (note that tests with σ'_c = 0.1 MPa were not further consolidated prior to shear).

The number of "useful" shear results increased substantially with 18 of the 24 Series B tests providing reliable shear results; a success rate of 75 percent. Specimen histories of Series B tests are summarized in Table 4.1. Final axial strain levels during shear ranged from 8.5% to 25.9%. Of the six tests which do not provide useful shear results, five tests (B–16 to B–18, B–20 and B–21) had mechanical problems with a faulty load cell that provided erroneous readings during shear. Test B–03 may have also had load cell problems in that all load was lost during the early stages of shear (less than 5% axial strain). Although not useful for shear, these six tests do provide useful consolidation results.

4.1.2.3 Series C Tests

Series C consisted of 35 tests; 22 sheared under undrained conditions and 13 under drained conditions. [The reader should note that the first 16 Series C tests were previously reported as Series B Test #25 to #40 in Andersen et al. (1992).] Pre–shear D_r ranged from 29.8 to 115%. A wider range of strain rates were also employed with nominal strain rates varying from 10.2%/hour to 120%/hour. Specimen histories of Series C tests are also summarized in Table 4.1.

Twenty–three tests were consolidated to $\sigma'_c > 0.1$ MPa. Twenty tests were consolidated under hydrostatic stresses with final σ'_c value ranging from 2 to 12.5 MPa. Three tests were anisotropically consolidated with final K_c values (ratio of effective minor principal stress to effective major principal stress, σ'_3/σ'_1) of 0.51, 0.56 and 0.59.

Series C tests produced a success rate of 89% with 31 of the 35 tests performed providing useful shear results. Final axial strain levels for these useful tests ranged from 22.1% to 36.9%. Two of the four unsuccessful tests

(C–05 and C–06) were previously reported as being successful (Andersen et al. 1992), but upon further review, it was determined that these tests had a faulty pore pressure transducer. Test C–07 experienced mechanical problems during consolidation. For test C–08, a leak in the membrane developed during shear, excluding it from the useful shear results.

4.2 SUMMARY OF TRIAXIAL COMPRESSION RESULTS FOR UNFROZEN MFS

This section presents a summary of the consolidation and shear results from Series B and Series C tests. A summary of material properties and post–shear grain size distributions are also presented. The results are grouped according to final effective consolidation stress. Differences, if any, in results between tests from Series B and Series C are examined, and possible reasons for these differences provided.

4.2.1 Consolidation

Consolidation was performed on 42 tests prior to shear (or attempted shear). Consolidation procedures are discussed in Section 3.3. Consolidation consisted of primary consolidation, which corresponds to volume changes during increases in cell pressure (and axial load for CAUC tests) to the final effective stress level, and secondary compression which is the measure of specimen volume changes after the final effective consolidation stress (σ'_c) has been reached. For Series B and C tests, pre–consolidation void ratios ranged from 0.621 to 0.811 (D_r of 27.1% to 86.9%).

Consolidation times for Series B and Series C tests varied significantly. Primary consolidation for Series B tests was usually completely in under 10 minutes and secondary compression was limited to under 30 minutes. For

Series C tests, where consolidation was computer–controlled, primary consolidation times were significantly increased, ranging from 16 to 92 minutes. Times for secondary compression for Series C tests were also increased, with times ranging from one to 48 hours. Table 4.2 summarizes pertinent consolidation characteristics including the initial and final consolidation stress, specimen volume, and void ratio for each test as well as the measured axial and volumetric strains (see Section 3.6) and the times allowed for primary consolidation and secondary compression.

The following sections present the isotropic consolidation results at σ'_c values of 2, 5, 10 and 12.5 MPa since the majority of tests were consolidated at these four stresses. Anisotropic consolidation results are presented in Section 4.2.1.5. Discussion is limited to the void ratio versus effective stress response. Summary plots of void ratio versus log effective stress are presented for each of the five above–mentioned groupings as Figs. 4.1 though 4.5. Appendix B presents additional consolidation results for individual tests.

4.2.1.1 Consolidation to 2 MPa

A total of 8 tests were consolidated to a nominal pressure of 2 MPa; three from Series B and five from Series C. Actual σ'_c values ranged from 1.93 to 2.04 MPa. Figure 4.1 shows the void ratio versus effective consolidation stress for all σ'_c = 2 MPa tests. It can be seen that the initial portion of the e–log σ'_c curves are relatively flat with the curves slowly rounding downward as the consolidation pressure increases. The largest changes in void ratio during consolidation occur for the loosest specimens (e.g. test C–15 of Series C where Δe is 0.074) and the initially dense specimens experience a smaller void ratio change (test C–12 of Series C where Δe is 0.037). The amount of secondary compression was generally

small for this σ'_c, although test B–07 shows a marked decrease in void ratio at constant σ'_c.

4.2.1.2 Consolidation to 5 MPa

A total of 12 tests were consolidated to 5 MPa; nine from Series B and three from Series C. Final effective consolidation stresses ranged from 4.89 to 5.19 MPa. Figure 4.2 shows the void ratio versus effective consolidation stress for all $\sigma'_c = 5$ MPa tests. The curves follow behavior similar to that described for the tests consolidated to 2 MPa, with the curves rounding downward more as the σ'_c increases. Again, looser specimens generally have the larger change in void ratio. The effects of secondary compression are generally small as for the 2 MPa case.

4.2.1.3 Consolidation to 10 MPa

Fifteen tests were consolidated to a nominal σ'_c of 10 MPa: seven tests from Series B and eight tests from Series C. Final effective consolidation stresses ranged from 9.36 to 10.16 MPa. Figure 4.3 shows the void ratio versus σ'_c response for these tests. While the trend in consolidation behavior is similar to that for specimens consolidated to 2 and 5 MPa, the amount of curvature in the e–log σ'_c response is more pronounced. The anomalous behavior of test B–17 cannot be explained. Secondary compression is more noticeable than for the lower σ'_c tests, especially in the Series C tests where the time allowed for secondary compression ranged from one to 48 hours.

While not true for the first three Series C tests, subsequent tests provide evidence that computer–assisted testing can produce a much smoother e–log σ'_c curve. For example, compare tests B–16 and B–20 with C–16. The continuous "stepping down" of the curve for test B–20 is due to the onset of secondary compression caused by the stop–and–start application of

cell pressure during specimen consolidation while the much smoother curve of Test C–16 results from the continuous application of cell pressure during consolidation.

The tests consolidated to 10 MPa also provide the first opportunity to obtain a virgin compression index ($C_c = \frac{\Delta e}{\Delta \log \sigma_c'}$) for isotropically consolidated MFS. [However, it should be noted that it is questionable if a consistent virgin compression line was reached for MFS in this testing program.] Excluding the anomalous test B–17, the C_c values ranged from 0.136 to 0.208, with the Series C tests exhibiting the most consistent data (values from 0.169 to 0.208).

4.2.1.4 Consolidation to 12.5 MPa

Three tests from Series C were consolidated to a σ'_c of 12.5 MPa. Figure 4.4 shows a plot of void ratio versus log σ'_c for tests C–25, C–30 and C–35. As expected, these tests exhibit the largest change in void ratio for isotropically consolidated tests with Δe values ranging from 0.129 to 0.193. Like the tests consolidated to 10 MPa, a virgin compression index could be determined from these tests with C_c values ranging from 0.155 to 0.228. It is interesting to note that Tests C–25 and C–35, with initial void ratios of 0.763 and 0.733, respectively, exhibit nearly identical void ratio changes while Test C–30, with the lowest initial void ratio of 0.660, exhibits a relatively small void ratio change. It should also be noted that all tests were consolidated to void ratio levels below the minimum void ratio (e_{min} = 0.580).

4.2.1.5 Anisotropic Consolidation

Anisotropic consolidation was performed on three tests from Series C; tests C–28, C–29 and C–32. Unlike isotropic consolidation where the applied

axial load is maintained near zero values, both the cell pressure and axial load are increased until targeted stress levels are reached. The final vertical effective consolidation stress ($= \sigma'_{1c}/K_c$ ($= \sigma'_{3c}/\sigma'_{1c}$) values were: C–28, 13.33/0.57; C–29, 13.64/0.52 and C–32, 9.45/0.59. Figure 4.5 shows a plot of void ratio versus log σ'_{1c} for these tests where σ'_{1c} is the vertical effective stress.

Changes in void ratio for these tests ranged from 0.121 to 0.207 (the highest for all tests) with the smallest change occurring for the initially denser specimen which also was consolidated to the lowest σ'_{1c}. Test C–29 experienced the largest change in void ratio due in part to its lower K_c value. Virgin compression indices for these tests ranged from 0.157 to 0.289 with test C–29 exhibiting the highest value.

4.2.2 Shear Results

Of the 59 Series B and Series C tests which were initiated, 49 provide "useful" shear results. Of the 49 useful tests, 38 were sheared under undrained conditions (35 CIUC and 3 CAUC tests) and 11 were sheared under drained conditions (CIDC) at constant p′. Approximately 90% of these useful tests provide shear characteristics to axial strains greater than 20%.

Table 4.3 summarizes pertinent pre–shear, shear and post–shear conditions and descriptions for the 49 useful tests. Pre–shear conditions include the test's initial effective confining stress (σ'_c) and the specimen void ratio (e_c) just prior to shear. Table 4.3 also indicates the type of shear test performed, level of axial strain which provides useful shear results and test strain rates as measured by the external LVDT and the internal ACDT's.

Description of the specimen after shear includes the behavior of the

lubricated ends, the specimen's shape, if sliding occurred at the top cap and/or pedestal and if a rupture surface developed during shear and the amount of lateral deformation at the specimen's ends. These subjective post–shear observations are predominantly controlled by the behavior of the lubricated ends during shear.

The following sections present the shear results for the unfrozen MFS testing program. To simplify the following presentation, CIUC, CAUC and CIDC test results will be presented separately.

4.2.2.1 CIUC Tests

The 35 CIUC tests are presented in five sets based on their effective confining stress;

1) eight tests at 0.1 MPa
2) six tests at 2 MPa
3) 10 tests at 5 MPa
4) one test at 7.5 MPa and seven at 10 MPa
5) three tests at 12.5 MPa

Shear characteristics at maximum obliquity are summarized in Table 4.4; shear characteristics at maximum shear stress are summarized in Table 4.5.

In the following discussion, test results are summarized via three plots; deviator stress ($\sigma_1 - \sigma_3$) versus axial strain, excess pore pressure versus axial strain and effective stress paths. These plots, presented as Figs. 4.6 through 4.15, are discussed for each effective confining stress noted above. Test results for each individual tests are presented in Appendix B.

0.1 MPa Tests

For tests at σ'_c of 0.1 MPa, the pre–shear relative densities ranged from 43.8% to 94.9% (void ratios from 0.597 to 0.765). Five tests were

performed in Series B and three tests were performed in Series C. Two tests (B–08 and B–09) were stopped at lower strains due to the possibility of pore water cavitation.

Deviator stress versus axial strain (Q–ϵ_a) responses for 0.1 MPa tests are shown in Fig. 4.6a. All tests exhibited very strong dilative responses (i.e., strain hardening) for all densities; the responses being strongest for denser specimens, and there is a general trend of increased peak strength (i.e., maximum deviator stress) with increase in density. In general, the Q–ϵ_a behavior at large axial strains ($\epsilon_a > 20\%$) exhibited a decrease with continued straining. This behavior may be indicative of sliding of the specimen at the top cap or pedestal and/or a weakening of the specimen due to the relatively large strains and high deviator stresses. The large strain Q–ϵ_a behavior of test B–22 appears to indicate the development of a rupture surface, thus the severe change in stress–strain response (curve becomes concave upwards).

The excess pore pressure response is illustrated in Fig. 4.6b. All tests exhibited initial increases in pore pressure followed by significant decreases to negative values. The general trend is for more negative values for denser specimens. Pore pressures tend to "level out" at large strains, e.g. tests B–10, B–12 and C–34.

The effective stress paths, illustrated in Fig. 4.7, more clearly indicate the previously–noted strong dilative response in that specimens quickly reach and then proceed up and along the failure envelope. The stress paths tend to curve downward as they travel up along the failure envelope. The denser specimens tend to travel further along the failure envelope. At higher strains, the stress paths deviate downward from the failure envelope and

ultimately "loop back" underneath themselves. This "looping back" behavior may be actual undrained sand behavior; an artifact of the experimental procedures (i.e., a problem with specimen stability); or a combination of both.

2 MPa Tests

A total of six tests were performed at σ'_c = 2 MPa; three each from Series B and C. Pre–shear D_r ranged from 56.0% to 96.1% (void ratios from 0.593 to 0.725.

The Q–ϵ_a curves, illustrated in Fig. 4.8a, show an initial yield behavior at small strains followed by strain hardening. Test C–15 (the loosest 2 MPa test) first exhibits strain softening after reaching the yield point but strain hardens with continued straining. There is a better defined change in yield stresses as a function of density for the 2 MPa tests than for the 0.1 MPa tests. As with 0.1 MPa tests, there is a general trend of increased peak strength with increased density and, at large axial strains, the decrease in stress may be indicative of sliding and/or weakening of the specimen.

Excess pore pressure responses for 2 MPa tests are shown Fig. 4.8b. In contrast to 0.1 MPa tests, a more patterned response versus density can be noted at lower strains with pore pressures increasing then decreasing with continued strain. Denser specimens (tests B–07 and C–33) exhibit both positive and negative pore pressures while looser specimens maintain net positive pressures during shear. Pore pressures tend to level out with continued shearing.

Figure 4.9 shows the effective stress paths for 2 MPa tests. As with 0.1 MPa tests, all tests travel up to and then along a failure envelope. However, "elbowing" of stress paths (phase transformation) becomes noticeable and is most significant at lower densities. Denser specimens travel further up

the failure envelope, and all stress paths loop (or begin to loop) beneath themselves at larger strains/higher stresses.

5 MPa Tests

At a σ'_c of 5 MPa, ten tests were performed, eight from Series B and two from Series C. Pre–shear D_r ranged from 64.5% to 104.9% (void ratios from 0.564 to 0.697).

Based on the deviator stress–strain behavior, shown in Fig. 4.10a, 5 MPa tests exhibit even higher yield stresses than 2 MPa tests, with the difference in yield stress levels increasing with increased density. The amount of strain hardening tends to increase with density. However, tests B–01, C–23 and C–24 exhibit slight strain softening behaviors after yielding but strain hardening with continued straining. As for the tests at lower effective confining stresses, deviator stresses tend to decrease, after reaching a peak value, with continued straining. This stress reduction is indicative of sliding and/or weakening of the specimen.

Two tests also present some questionable results. Test B–04 has a D_r = 75.7%, yet has a stress–strain curve comparable to Test B–05 with a D_r = 91.5%. However, C–23, which has an D_r = 75.4%, exhibits a more expected Q–ϵ_a response plotting near B–01 (D_r = 72.7%); thus, providing evidence that test B–04 may be in error.

Test B–19 (D_r = 70.0%) has a D_r lower than Test B–01, yet acts significantly denser by exhibiting a significantly greater strength (peak strength of B–19 is 44% higher than that of B–01).

Figure 4.10b illustrates the excess pore pressure response of 5 MPa tests. All specimens exhibit a significant increase in pore pressure with initial shearing, with the excess pore pressure remaining positive in all cases.

However, excess pore pressures generally reach maximum value within 5% axial strain and thereafter generally decrease with continued straining with a larger decrease occurring for denser specimens. As with the 0.1 and 2 MPa tests, the excess pore pressures at large strain begin to become constant.

As with the Q–ϵ_a curves, the excess pore pressure responses also present some questionable results. Test B–04 exhibits the lowest peak pore pressure yet is looser than one–half of the other 5 MPa tests. Test B–19 exhibits a significantly lower pore pressure response than B–01 although B–19 is looser.

The effective stress paths for the 5 MPa tests are shown in Fig. 4.11. In general, looser specimens exhibit significant rounding to the left, but, with an increase in density, stress path "elbows" (phase transformation) become less pronounced. In addition, increase in specimen density increases the travel of the stress path along the failure envelope. All tests except B–01 and C–24 demonstrate the "looping–back–underneath" phenomenon at high strains. Tests B–04 and B–19 again present questionable/contradictory results in that both tests indicate a much lower failure envelope (i.e., friction angle) than the other tests. In light of their overall anomalous behavior, tests B–04 and B–19 will be excluded in future analysis.

10 MPa Tests

The tests at σ'_c = 10 MPa proved to be the most difficult to perform with only seven out of 13 tests providing useful shear results. Of these seven useful tests, two are from Series B and five are from Series C. Pre–shear D_r range from D_r = 77.3% to 104.3% (void ratios from 0.566 to 0.655). In addition to the 10 MPa tests, test C–04 (σ'_c = 7.5 MPa) is also included in the following presentation, but only for purposes of illustration.

The Q–ϵ_a responses for 10 MPa tests (and the 7.5 MPa test),

illustrated in Fig. 4.12a, exhibit still higher yield stresses than the 0.1, 2 or 5 MPa tests with the value of the yield stress generally increasing with density. However, all tests exhibit strain softening after yield. In fact, the yield stress is also the peak strength for tests C–01, C–02 and C–03 ($D_r \approx 77$ to 83%). Only tests C–03, C–16 and C–22 did not have clearly distinguishable rupture surfaces. For other tests, rupture surface formation is indicated by abrupt change in Q–ϵ_a behavior at large strains (as well as post–shear observation). For B–23, sliding of the specimen at the top cap significantly reduces the measured strength of specimen beyond an axial strain of 10%.

Figure 4.12b illustrates the highly contractive excess pore pressure responses for the 10 MPa tests. In all tests excess pore pressures reach their highest positive levels within the first 5% of specimen axial strain, then the pressures essentially level off or slightly decrease with larger strains. However, unlike tests at lower σ'_c values, the excess pore pressure response does not necessarily follow a trend of increasing response with decreasing density. For example, the response of test B–24 is slightly higher than C–03 although C–03 is looser (e = 0.627 versus 0.655 for tests B–24 and C–03, respectively). Rupture surfaces (such as for B–23, B–24, and C–01) cause significant increases in pore pressure at larger axial strains.

The effective stress paths for the 10 MPa tests are shown in Fig. 4.13. The curvature of the stress paths to the left illustrates the strongly contractive response of the sand. Most of the travel to the left occurs within the first 6% of axial strain. The sudden downward break of the stress paths for tests B–23, C–01, and C–02 is indicative of sliding and/or the development of a rupture surface. Tests B–24, C–16 and C–22 exhibit the "climbing along the failure envelope" behavior but to a lesser extent than

tests at lower confining stresses. It is interesting to note that all three of these tests did not slide at the top cap or pedestal. It is also interesting to note that test C–22 falls within the trends of the other 10 MPa tests, but was sheared at a strain rate one order of magnitude higher than the other tests. The friction angles of tests B–24 and C–16 are significantly higher than the other tests.

12.5 MPa Tests

Three Series C tests were performed at an σ'_c of 12.5 MPa. Pre–shear D_r ranged from 100.4% to 114.8% (void ratios from 0.531 to 0.579). Figure 4.14a shows the deviator stress versus axial strain response for these tests. The Q–ϵ_a response is similar to that of the 10 MPa tests; an increase in stress up to a yield point then strain softening followed by relatively constant deviator stresses with continued straining. This pattern is not followed by test C–30 which exhibits significant strain hardening after the yield point. This behavior may be due to the low pre–shear void ratio (e = 0.531) and the fact that the specimen was consolidated from an already dense state (the void ratio at end of saturation was 0.660 or D_r = 75.7%).

The excess pore pressure response and effective stress paths, illustrated in Figs. 4.14b and 4.15, respectively, illustrate the contractive nature of MFS at this σ'_c. The excess pore pressure response is similar to that for 10 MPa tests in that the pore pressures increase sharply within the first 5% axial strain then become nearly constant with continued straining. The effective stress paths, illustrated in Fig. 4.15c, also exhibit similar behavior to the 10 MPa tests in that the stress paths initially curve strongly to the left then show only a modest attempt to climb up the failure envelope (except for test C–30 which has a stronger dilative response).

4.2.2.2 CAUC Tests

Three anisotropically–consolidated, undrained tests were performed in the Series C tests; namely, C–28, C–29 and C–32. Pre–shear D_r = 83.8 to 98.5% (e = 0.633 to 0.585). Shear characteristics for CAUC tests are included along with CIUC characteristics in Tables 4.4 and 4.5. Individual test results are presented in Appendix B. Figure 4.16a shows the Q–ϵ_a response for these tests. All of the Q–ϵ_a curves reach the yield stress at very low strains (< 1%) and then strain softening with continued straining. For tests C–28 and C–29, this yield stress also represents the peak strength of the specimen. After the initial strain softening, the deviator stress tends to remain constant or slightly increase with continued shear. It is interesting to note the "kink" in the Q–ϵ_a curve for test C–29 at an axial strain of approximately 2%. This behavior may be due to the fact that the test was performed at a $\dot{\epsilon} \simeq$ 120%/hour, ten times the rate of the other two CAUC tests.

The excess pore pressure response of the CAUC tests, illustrated in Fig. 4.16b, is similar to that of the 10 MPa and 12.5 MPa CIUC tests. However, the magnitude of the excess pore pressures is much less than those for the CIUC tests. As with the Q–ϵ_a curve for test C–29, the excess pore pressure response also shows a "kink" in its curve at $\epsilon_a \approx 2\%$.

The effective stress paths for the CAUC tests show a very strong contractive response during shear. Figure 4.17 shows the effective stress paths for the CAUC tests. Unlike the CIUC tests at 10 and 12.5 MPa, tests C–28 and C–29 do not show a tendency to "climb up the failure envelope" but rather tend to proceed downward along the failure envelope. Test C–32, at a lower initial p′, does exhibit the "climbing" along the failure envelope

behavior and ultimately loops back underneath itself.

4.2.2.3 CIDC Tests

Given that only 11 CIDC tests were performed, test results will be presented in two sets; one set for 0.1 MPa tests and another set for all other tests. Six of the 11 CIDC tests were performed with σ'_c = 0.1 MPa, two at 2 MPa, one at 5 MPa and two at 10 MPa. All tests are from Series C and were sheared under constant p′ stress paths. Shear characteristics of CIDC tests at maximum obliquity (= maximum shear stress) are presented in Table 4.6. In the following discussion, CIDC tests results will be presented via three plots; deviator stress versus axial strain, volumetric strain versus axial strain and effective stress paths (p' vs q). Individual test results are presented in Appendix B.

0.1 MPa Tests

For CIDC tests at a nominal σ'_c of 0.1 MPa, actual pre–shear effective confining stresses ranged from 0.095 to 0.160 MPa. Pre–shear D_r = 29.8% to 86.1% (e = 0.626 to 0.811).

The deviator stress versus strain behavior for 0.1 MPa tests is illustrated in Fig. 4.18a. There is a consistent trend in higher shear strength with increase in density. As illustrated by test C–14, the effect of an increase in effective confining stress is significant. For all tests, the Q–ϵ_a curve initially increases to a peak strength value then gradually reduces with continued strain to near constant values. Unlike the undrained tests, there is no definitive yield point in the tests.

Figure 4.18b illustrates the volumetric strain response of the 0.1 MPa tests. There is a general trend for an increase in dilative volumetric strain with increase in specimen density. However, the effect of σ'_c is again

illustrated in Test C–14 where the ϵ_v is lower than should be expected due to the increased confinement. Dense specimens (Test C–14, C–20 and C–21) dilate immediately upon loading with the rate of dilation ($d\epsilon_v/d\epsilon_a$) quickly becoming constant at low axial strains (< 5%). With continued shear, the rate of dilation reduces. Loose specimens (Tests C–17, C–18 and C–19) initially contract upon loading then dilate. The maximum rate of dilation occurs during the dilative phase of shearing. As with dense tests, the rate of dilation reduces with continued shear. The maximum rate of dilation for all tests occurred near the peak strength in accordance to Rowe's (1962) hypothesis (Section 2.1.3).

The effective stress paths, shown in Fig 4.19, indicate the difficulty in maintaining a constant p′ value during shear. As shown for all tests, the stress path would travel up on an irregular pattern, reach the peak strength, then proceed to decrease and move to the left. The denser specimens illustrate the most erratic behavior while moving along the stress path. The increases in σ'_c of test C–14 leads to an increase in peak shear stress.

2 to 10 MPa Tests

A limited number of CIDC tests were performed at elevated σ'_c levels. Specifically, tests C–11 and C–12 were performed at an σ'_c of 2 MPa; C–13 was performed at 5 MPa and C–09 and C–10 were performed at 10 MPa. Pre–shear D_r ranged from 71.2% to 91.2% (e = 0.609 to 0.675). However, four of the five tests were conducted at D_r between 87.6% and 91.2%.

Figure 4.20a shows the Q–ϵ_a behavior of these tests. As evident in the figure, there is a significant effect of confinement on the magnitude of measured shear stresses. There is an increase in shear stress with an increase in density, as signified best by Tests C–11 and C–12 at 2 MPa. As with

the 0.1 MPa CIDC tests, there is no definable yield point with specimens deforming continuously with continued strain. The strain to peak strength increases with increase in σ'_c for high D_r specimens, as expected.

The volumetric strain response is shown in Fig. 4.20b. As indicated in the figure, an increase in confining pressure causes a decrease in volumetric strain. All tests initially contract upon loading but with continued shear, tests at a σ'_c of 2 MPa (C–11 an C–12) begin to dilate and reach net expansion (positive ϵ_v), while tests at 10 MPa show contractive behavior throughout shear (negative ϵ_v). The rate of dilation for the tests at 2 MPa start negative, become positive at low ϵ_a ($< 5\%$), increase with increasing strains to a peak value, and then start to decrease slightly at large ϵ_a ($> 15\%$). For Test C–13 at 5 MPa, the rate of dilation starts negative but becomes essentially zero at ϵ_a above 5%. A similar condition of zero rate of dilation is almost reached in C–11. As for 0.1 MPa tests, the maximum rate of dilation occurs near the peak strength for these tests. For the 10 MPa tests (C–09 and C–10), the rate of dilation begins and remains negative, but becomes less negative with continued strains.

Figure 4.21 shows the effective stress paths for the 2 to 10 MPa CIDC tests. In comparison to the 0.1 MPa tests, these higher σ'_c tests demonstrate better "controlled" $p' =$ constant stress paths during shear. As noticed for the deviatoric stress behavior, for a particular σ'_c, an increase in specimen density increases the peak shear strength as seen for tests at 2 MPa. Table 4.6 shows that the obliquity (friction angle) decreases with the increase in σ'_c.

4.2.3 Sieve Analysis Results

Sieve analyses were performed for all tests but only those tests which

provide useful shear characteristics will be presented. As in the presentation of the shear results, sieve analyses for CIUC, CAUC and CIDC tests are presented separately. The sieve analyses for each CIUC test set, i.e., σ'_c = 0.1, 2, 5, 10 and 12.5 MPa, are plotted in Figs. 4.22 through 4.26, respectively. Also plotted in these figures is the range of sieve analysis results from "control" sieves on MFS (presented as Figure 3.1). Sieve analyses from CAUC tests are presented in Fig. 4.27. Sieve analyses for CIDC tests are presented in Fig. 4.28 for 0.1 MPa tests and Fig. 4.29 for the 2 to 10 MPa tests.

A general observation from these figures is that particle breakage, indicated by an increase in percent finer, is not significant for CIUC tests at σ'_c values of 0.1, 2 and 5 MPa and CIDC tests at 0.1 MPa. However, particle breakage is evident for CIUC and CIDC tests at higher σ'_c values as well as for the CAUC tests. This increase is more apparent for tests which also reach higher shear stresses, such as the 12.5 MPa CIUC tests, the CAUC tests and the 5 and 10 MPa CIDC tests. The largest change in percent finer by weight generally occurs for particle sizes between about 0.1 mm and 0.2 mm.

4.3 ANALYSIS OF TRIAXIAL COMPRESSION RESULTS

This section presents the analysis of the unfrozen MFS test results. First, a summary of conditions at maximum obliquity (i.e., the effective stress envelope) are presented followed by an evaluation of the tests based on testing parameters used in frozen MFS analyses. The undrained and drained behaviors are then analyzed based on comparisons of test results under conditions of constant D_r with varying σ'_c, or varying D_r with constant σ'_c.

The discussion will focus on the undrained behavior of MFS since the majority of useful shear results from Series B and C are CIUC tests (36 of the 47).

4.3.1 Conditions at Maximum Obliquity

The effective stress envelope in q–p′ space represents the stresses at maximum obliquity, $R_{max} = (\sigma'_1/\sigma'_3)_{max}$. Figure 4.30 presents plots of p′ [$= 0.5\cdot(\sigma'_1 + \sigma'_3)$] versus q [$= 0.5\cdot(\sigma_1 - \sigma_3)$] which correspond to the conditions at the point of R_{max} for undrained tests. The effective friction angles, ϕ'_{max}, range from 32.3° to 56.4° but the majority of the test results have ϕ' within the range of 32° to 37°. Concentrating on the tests with $\sigma'_c > 0.1$ MPa, the majority of tests fall within a linear trend; however, two tests at $\sigma'_c = 10$ MPa (B–24 and C=–16) lie above this general trend. Excluding these two points (and the points at a σ'_c of 0.1 MPa) yields an average failure envelope with an ϕ'_{max} of 34.9±1.4°.

Figure 4.31 plots q vs p′ at R_{max} for the CIDC tests. Drained test results below a σ'_c of 5 MPa fall within the linear trend of the undrained test results; however, CIDC tests at 10 MPa show a marked deviation from this linear trend. The measured ϕ'_{max} for these tests were 29.1° and 32.2°, and, if the failure envelope is extended to these points, a downward curvature of the failure envelope is noted. Therefore, curvature of the failure envelope of MFS does occur at higher p′ levels.

Higher ϕ'_{max} values occur for CIUC and CIDC tests at low σ'_c (0.1 MPa). Figure 4.32 shows the q and p′ at R_{max} for these low confinement tests. A linear regression line through the results indicates a similar friction angle ($\phi'_{max} = 36.2°$) as the higher confinement tests but also a small intercept, $c' \approx 0.017$ MPa. Figures 4.33 and 4.34 present plots of the

effective friction angle, ϕ'_{max}, versus D_r and σ'_c, respectively, for the undrained MFS tests. Figure 4.33 shows that the effect of D_r on the ϕ'_{max} is most evident for low confinement tests, and as the σ'_c level increases the effect of D_r reduces. Figure 4.34 shows that, along with the effect of D_r, the value ϕ'_{max} also decreases with increasing σ'_c level.

4.3.2 Evaluation of Other Shear Properties of Unfrozen MFS

This section presents results of the unfrozen test program in terms of the parameters which have been used to describe frozen MFS behavior. The specific properties evaluated include the initial modulus, E_s, the upper yield stress, Q_{uy}, and the peak strength, Q_p. Section 3.7 (Fig. 3.14) describes these properties. Table 4.7 summarizes these parameters for the unfrozen MFS tests.

Although the characterization of the unfrozen MFS shear results in this manner is unusual, this analysis parallels that performed for the frozen MFS testing program presented by Andersen (1991) and Andersen et al. (1992) and is presented in Chapter 5. However, the extent of the analysis has been limited to the aforementioned properties because these properties can be readily obtained from the unfrozen MFS results. This form of analysis may also be beneficial in the future modeling of frozen MFS as a composite material of ice and unfrozen sand.

4.3.2.1 Initial Modulus

The initial modulus of test specimens were determined from $Q-\epsilon_a$ curves at small strains as illustrated in Figure 3.14a. In order to differentiate the quality of the small strain measurements, the initial $Q-\epsilon_a$ curve for each test was ranked on their smoothness and continuity (see Section 3.7). The initial $Q-\epsilon_a$ qualifier, as well as the qualifiers for ACDT agreement and stability are

presented in Table 4.7. Tests with good or fair ACDT agreement and $Q-\epsilon_a$ response are plotted versus D_r and σ'_c in Fig. 4.35 and 4.36, respectively. These figures include both undrained and drained test results with the vertical effective stress (σ'_{1c}) used for CAUC tests. In general, as shown in the figures, E_s mainly increases with an increase in σ'_c.

4.3.2.2 Upper Yield Stress

Upper yield stress (Q_{uy}) behavior was only evident in undrained tests (both CIUC and CAUC). Upper yield stresses, determined for 36 undrained tests, are also presented in Table 4.7. Plots of Q_{uy} versus D_r and Q_{uy} versus σ'_c are presented as Figures 4.37 and 4.38, respectively. All data, regardless of ACDT, initial $Q-\epsilon_a$, or stability qualification are presented in the figures. As indicated in the figures, there is a strong dependence of Q_{uy} on both D_r and σ'_c with the dependence strongest for Q_{uy} versus σ'_c.

4.3.2.3 Peak Strength

The peak strength (peak deviator stress) behavior is also restricted to undrained tests because of the differences in the magnitude of Q_p between undrained and drained shear behavior and the relatively limited number of CIDC tests. Plots of Q_p versus D_r and Q_p versus σ'_c are presented as Figures 4.39 and 4.40, respectively. Again, all data are presented regardless of qualification. Like the results of Q_{uy}, there is a dependence of Q_p on the D_r and σ'_c. However, the relative importance of density and confining stress are now reversed. That is, Q_p is now almost a unique function of D_r (Fig. 4.39), whereas the increase in Q_p with increasing σ'_c (at constant density) is rather modest (Fig. 4.40).

4.3.3 Undrained Shear Behavior of MFS

Shear results from CIUC tests will be mainly used to evaluate the

undrained shear behavior of MFS. However, presentation will include some CAUC tests to illustrate the effects of anisotropic consolidation.

4.3.3.1 Effect of Effective Confining Stress

Figure 4.41 presents plots of deviator stress and excess pore pressure versus axial strain for five CIUC tests and one CAUC test at different effective confining stresses yet at similar pre–shear relative densities (D_r ranges from 92.5% to 100.4%). As illustrated in the figure, C–34 (σ'_c = 0.1 MPa) exhibits a strong dilative response but a very low stiffness at small strains. The negative pore pressures increase the effective stresses, thereby strengthening the sand as straining continues. In contrast, C–22 (10 MPa) and C–25 (12.5 MPa) develop large positive pore pressures, i.e., a strong contractive response. But these tests are much stiffer at small strains. Anisotopic consolidation (C–29) produces an even stiffer small strain response.

Figure 4.42 presents the effective stress paths of these same tests. The dilative response of test C–34 causes its stress path to climb along the failure envelope until it reaches the peak stress at large strains. For tests at higher effective confining stresses, the stress path moves more to the left before climbing the failure envelope until, for tests with $\sigma'_{1c} \geq 10$ MPa, the stress paths show little or no capacity to proceed up along the failure envelope.

4.3.3.2 Effect of Relative Density

Figure 4.43 presents plots of deviator stress and excess pore pressure versus axial strain for four of the CIUC tests at an σ'_c of 0.1 MPa previously shown in Fig. 4.6. As would be expected, the lower the preshear D_r, the weaker the sand's dilative response (generation of less negative excess pore pressures), thus creating a lower effective stress which leads to lower strength. This trend in lower strength can also be noted in the effective

stress paths for the four tests plotted in Fig. 4.44. In this figure, the stress path for test B–10 travels a relatively short distance along the failure envelope before looping back, while the stress path for test C–34 exhibits much stronger dilative response by traveling a significant distance along the failure envelope before beginning to loop back.

Figures 4.45 and 4.46 present similar trends for CIUC tests at σ'_c = 2 MPa. Increases in D_r cause enhanced strain hardening after the upper yield stress due to development of lower excess pore pressures.

4.3.4 Drained Shear Behavior of MFS

Though only a relatively few drained tests were conducted, an analysis of drained tests behavior can be performed. Both the condition of constant void ratio with different σ'_c and different void ratio with constant σ'_c are examined.

4.3.3.1 Effect of Effective Confining Stress

The effects of σ'_c on the drained shear behavior of MFS is illustrated in Fig. 4.47, which shows deviator stress and volumetric strain (ϵ_v) versus axial strain (ϵ_a) responses of four tests at different effective confining stresses (0.1, 2, 5, and 10 MPa) but at similar preshear relative densities (D_r = 88.7±2.6%). Test C–14 at σ'_c = 0.16 MPa exhibits the lowest strength and the most expansion (dilation) during shear. As the confinement increases, the strength increases and dilation decreases until at high confinement (Test C–10) the specimen exhibits the highest strength but exhibits predominantly contractive behavior.

In Andersen et al. (1992), it was previously concluded that the ϵ_v behavior of test C–14 was erroneous due to the sudden change in the rate of dilation ($\Delta\epsilon_v/\Delta\epsilon_a$) for this test. However, subsequent tests at σ'_c = 0.1

MPa indicate that this behavior is to be expected for dense MFS at this confinement. This behavior is illustrative of the specimen's attempt to approach constant volume conditions.

The effective stress paths for these tests, shown in Fig. 4.48, clearly illustrates the curvature of the failure envelope with increased stress, as first illustrated in Fig. 4.21.

4.3.3.2 Effect of Void Ratio

The effect of varying the void ratio at one σ'_c is illustrated in Fig. 4.49 which shows deviator stress and volumetric strain responses for three CIDC tests at 0.1 MPa confinement. Although the variety of relative densities is limited, it can be seen that a decrease in relative density (i.e., the looser the specimen) produces a lower strength and reduced volumetric expansion during shear. In addition, the ϵ_v behavior for these tests illustrates an initially high rate of dilation, which reduces with continued straining. The effective stress paths for these tests, presented as Fig. 4.50, also show that the denser the specimen, the higher the strength.

4.4 STEADY STATE ANALYSIS OF SHEAR RESULTS

In Section 2.1.5, numerous views and methods were reviewed to evaluate steady/critical state conditions for sands. The following steady state analysis is based on the state parameter concept prescribed by Been and Jefferies (1985). In Andersen et al. (1992), a similar steady state analysis was performed on the unfrozen triaxial compression test results available at that time (CIUC tests). The following evaluation expands on that steady state analysis focusing on the undrained (CIUC and CAUC) test results. The applicability of steady state concepts to the CIDC tests will also be

discussed.

4.4.1 Review of Steady State Analysis

A detailed review of the steady state concepts was presented in Section 2.1. To briefly review, Been and Jefferies (1985) introduced the state parameter, Ψ, as a measure of the physical state of a sand. The Ψ parameter is defined as the vertical distance (Δe) from the initial state to the steady state line, SSL (see Fig. 2.18). The steady state line is determined from a plot of steady state points (SSP) from tests which have reached steady state conditions. The criteria for the steady state condition are (from Poulos 1981 and Section 2.1.5, p. 66):

1) constant shear stress,
2) constant mean effective stress (constant pore pressure),
3) constant volume (void ratio), and
4) constant velocity.

A sand which has an initial state that lies above the SSL has a $+\Psi$ and one that has an initial state that lies below the SSL has a $-\Psi$.

4.4.2 Determination of Steady State Points

The above criteria for evaluating the steady state condition were used to determine SSP's for the undrained MFS test results. Since all tests were performed at constant volume under constant rates of deformation, these two criteria are consistently met. To analyze the other criteria, the deviator stress, excess pore pressure and mean effective stress ($I'_1 = \frac{\sigma'_1 + \sigma'_2 + \sigma'_3}{3}$) responses versus axial strain for each test were reviewed to determine if and when the other criteria for steady state are satisfied. Appendix B presents plots of these three parameters versus axial strain for each undrained test.

Based on a review of the available 36 CIUC and CAUC tests (again, tests B–04 and B–19 are excluded), it is debatable if any of them rigorously meet all four criteria. Ten tests appear closest to meeting these criteria; namely, tests B–01, B–23, C–01, C–02, C–16, C–24, C–28, C–29, C–34 and C–35. Figure 4.51 shows a plot of deviator stress, excess pore pressure and mean effective stress versus axial strain for tests B–01, B–23, C–28 and C–34. These tests, and the other six which have been deemed as reaching steady state conditions, represent a wide range of tests from both CIUC and CAUC stress conditions. The initial state conditions for these tests ranged from effective confining stresses of 0.1 MPa to 12.5 MPa and D_r from 73% to 112% (e = 0.537 to 0.670). Table 4.8 summarizes the shear characteristics of tests which reach the steady state condition.

The questioned validity of steady state condition for these unfrozen MFS tests centers on whether the chosen SSP represents a sustained state condition or only a temporary or transient one. No test achieved a state of liquefaction developed in load–controlled tests by Castro (1969); i.e., a significant and rapid loss in strength, with associated increase in excess pore pressure, with conditions sustained under continuous deformation. Tests C–28, C–29 and C–35 appear closest to approaching liquefaction conditions in that constant stresses and pressures are maintained for significant amounts of axial strain (5 to 10%), after post upper yield stress strain softening. However, in other tests, such as B–01 and C–34, the criteria for steady state conditions are not met until the last few data points of the test, or, as for test B–23, the steady state condition is assumed to occur at a relatively small strain ($\approx$ 8%) prior to the onset of questionable results.

For the remaining 26 tests, the steady state criteria were not met;

however, one or two criteria, specifically constant pore pressure and/or constant mean effective stress, were ascertained for 20 tests which will be termed "near steady state" tests. Table 4.8 also includes the shear characteristics of these undrained tests at this "near" steady state condition. In general these tests reached and maintained constant mean effective stress conditions before a constant excess pore pressure condition was reached. Constant shear stress conditions were not met in any of these tests. Tests B–24 and C–27; 10 MPa and 2 MPa tests, respectively, had not reached a notably constant stress or pressure condition at the end of shear. However, for these two tests, shear characteristics at the conditions closest to steady state have been taken as the SSP and are included in Table 4.8.

4.4.3 Steady State Line and State Parameters, Ψ, for MFS

Based on the above summary of SSP determination, a total of 33 tests reach or nearly reach the steady state condition during shear. Figure 4.52 plots the void ratio versus log mean effective stress at the steady state condition (I_{ss}) for these tests. The figure also shows the initial mean effective stress and stress path taken during shear for each test. As can be seen, the SSP's appear to form a gradually descending trend of decreasing void ratio with increasing I'_1 . This trend is fairly linear up to a I'_1 of approximately 4.5 to 5 MPa at which point the SSP's become much steeper with further increases in I'_1. This change in SSP slope at $I'_1 \simeq 4.5$ MPa also corresponds to a void ratio close to $e_{min} = 0.580$ ($D_r = 100\%$).

Steady state points which lead to the steeper slope also exhibit an increase in fines content (minus #200 sieve) measured in post–shear sieve analysis. In Section 2.1.2, it was noted that numerous researchers have found that the slope of the SSL becomes steeper with an increase in fines content

(e.g., Been and Jefferies 1985; Poulos et al. 1985, Hird and Hassona 1990). Been et al. (1991) note that the steady state line for Erksak 330/0.7 sand is curved with a distinctive break (steepening) at an I'_{ss} of 1 MPa (Fig. 2.25). They suggested that this break may be due to an increase in fines content caused by particle crushing at higher stresses.

In light of this previously established behavior, the SSPs for the unfrozen MFS tests were segregated according to the amount of fines determined from post–shear sieve analyses. A post–shear fines content of 10% was used as the dividing point. The set of results which had little or no change in fines content (or < 10% total fines) during shear included all CIUC tests at a σ'_c = 0.1, 2 , all but one 5 MPa test and test C–04 tested at 7.5 MPa. The set of test results which experienced an increase in fines content (or ≥ 10% total fines) during shear included the one CIUC test at a σ'_c of 5 MPa (B–02) and all CIUC tests at 10 or 12.5 MPa and the CAUC tests. Both sets of data are plotted in Fig. 4.53.

For the set of data with little change in fines content, a linear steady state line (SSL) can be determined in e – log I'_{ss} space and is shown in Fig. 4.53. This steady state line has a slope λ_{ss} = 0.254 with a coefficient of determination, r^2 = 0.954. A linear SSL would not be appropriate for the SSPs which had significant changes in fines content given the sensitivity of the steady state line to fines contents and the fines content is different for each test. It would be more appropriate the represent the steady state line as a curved line which would encompass both sets of results. However, for the purposes of this research, the linear steady state line in Fig. 4.53 provides sufficient information for analyses applying the dilatancy–hardening model (see Chapter 6). This linear line is only appropriate so long as there are no

appreciable changes in fines content.

It is important to note that the SSP's for the linear SSL were developed from initial states to the left ($-\Psi$) and to the right ($+\Psi$) of the established trend. The tests which had not fully reached steady state conditions are thought to agree reasonably will with the SSL in Fig. 4.53.

State parameters, Ψ's, were determined for those tests which should correspond to the linear SSL in Fig. 4.53, i.e. no appreciable change in fines content (< 10%). Tests B–08, B–09 and B–22 were also included even though these tests were not used in defining the SSL. Ψ–values calculated from the SSL are presented in Table 4.9 along with "measured" I'_{ss}.

4.4.4 Correlation of State Parameter With Undrained Shear Parameters

The state parameter can be correlated to undrained shear parameters such as the A–parameter at failure (A_f) and the undrained strength ratio (q_{max}/I'_c). These quantities are presented in Table 4.9. Figure 4.54 shows the relationship between A_f and Ψ, and it can be seen that a clear trend exists for A_f to increase with an increase in Ψ. Figure 4.55 shows the relationship between log q_{max}/I'_c and Ψ, and a well defined linear trend exists showing a decrease in undrained strength ratio with an increase in Ψ.

4.4.5 State Parameter and Drained Shear Behavior

The stress paths, in e–log I'_1 space, of the 11 CIDC tests are presented in Fig. 4.56 along with the SSL from the undrained tests. The directions these paths were taking at the end of shear are also plotted in the figure. Two CIDC tests (C–11 and C–13) end very close to the SSL determined from the undrained tests. However, based on the criteria for the steady state condition, only test C–13 is judged to have reached a true steady state condition at the end of shear (Fig. 4.20 and 4.47), whereas the end–of–test

condition for test C–11 appears to be very close to a steady state condition. However, although certainly not conclusive, these two tests appear to validate the use of the SSL for both drained and undrained MFS tests. Table 4.10 tabulates Ψ values based on the SSL in Fig. 4.53.

Another interesting behavior of the drained tests is the direction of the state paths of the looser tests at a σ'_c of 0.1 MPa. Tests C–17, C–18 and C–19 with $e_0 \approx 0.8$ clearly exhibit dilative behavior as the paths travel upwards, but still no approaching the linear SSL. These tests appear to substantiate the existence of a curved SSL at very low stress levels. However, more testing at higher void ratios is necessary before a more definitive conclusion can be reached.

4.5 CONCLUSIONS

The following conclusions can be made regarding the consolidated–undrained and drained triaxial compression testing program on unfrozen MFS.

1) The testing program represents a significant contribution to the shear behavior of sands, especially with regards to undrained testing at elevated confining stresses.

2) The consolidation behavior of MFS exhibits a continuously curving line in e – log σ'_c space as the consolidation stress increases (Figs. 4.1 through 4.5). While "virgin" compression indices are determined for high stress tests, a consistent virgin consolidation line is not defined. Consolidation to much higher stresses would be required to do this.

3) The undrained shear behavior of MFS generally compares well

with established behavior. The deviator stress and pore pressure responses exhibit expected trends in behavior with changes in relative density and consolidation stress (Figs. 4.41, 4.43 and 4.45). Effective stress paths also change from being strongly dilative to strongly contractive as expected with decreasing D_r and increasing σ'_c (Figs. 4.42 and 4.46). The effective stress failure envelope for undrained tests exhibits initial downward curvature at low stresses (0.1 MPa), but thereafter remains fairly linear for a large range of stresses (Fig. 4.30).

4) The drained shear behavior of MFS also compares well to expected behavior. Peak shear strengths increase and rates of dilation decrease with increasing σ'_c (Fig. 4.47). Conversely, both the peak strengths and rates of dilation increase with increasing D_r (Fig. 4.49). The effective stress paths clearly illustrate the curvature of the failure envelope with increasing p'_f (Fig. 4.48).

5) The steady state analysis of the undrained shear results indicates that a linear approximation for the steady state line is appropriate for conditions where little or no increase of fines content was observed in post–shear sieve analyses (Fig. 4.53).

6) Good correlations exist between the state parameter (Ψ) and the pore pressure parameter at failure and the undrained strength ratio (Figs. 4.54 and 4.55, respectively).

TABLE 4.1 (page 1 of 2)
CONSOLIDATION AND SHEAR HISTORY OF CONSOLIDATED-UNDRAINED
AND DRAINED TRIAXIAL COMPRESSION TESTS ON UNFROZEN MANCHESTER FINE SAND
SERIES B

Spec. No.	Set-up			Pre-shear			Test Type	Consol. Results ?	Useful Shear ϵ_a	Remarks
	Date	e	D_r (%)	σ'_{1c} (MPa)	e	D_r (%)				
B-01	9-17-90	0.776	40.5	4.98	0.670	72.7	CIUC	YES	24.9%	
B-02	9-30-90	0.623	86.9	5.01	0.564	104.9	CIUC	YES	22.9%	
B-03	9-24-90	0.725	56.1	5.08	0.614	89.7	NA	YES	NA	Lost load prematurely
B-04	10-2-90	0.741	51.0	4.98	0.660	75.7	CIUC	YES	16.3%	
B-05	10-9-90	0.667	73.5	5.01	0.608	91.5	CIUC	YES	21.6%	
B-06	10-13-90	0.759	45.6	2.04	0.694	65.4	CIUC	YES	25.3%	
B-07	10-15-90	0.646	80.0	2.03	0.593	96.1	CIUC	YES	24.9%	
B-08	10-16-90	0.637	82.9	0.104	0.636	83.0	CIUC	NA	8.5%	Shear stopped due to
B-09	10-19-90	0.637	82.9	0.114	0.637	82.9	CIUC	NA	11.0%	possible cavitation
B-10	10-22-90	0.765	43.7	0.102	0.765	43.8	CIUC	NA	25.7%	
B-11	10-23-90	0.735	53.0	2.01	0.688	67.2	CIUC	YES	24.1%	
B-12	10-24-90	0.627	85.7	0.110	0.626	86.1	CIUC	NA	24.8%	
B-13	11-4-90	0.820	32.6	5.19	0.697	64.7	CIUC	YES	21.5%	
B-14	11-5-90	0.669	72.9	5.01	0.605	92.5	CIUC	YES	16.9%	
B-15	11-12-90	0.668	73.4	5.03	0.599	94.3	CIUC	YES	24.6%	
B-16	12-4-90	0.739	51.6	10.10	0.592	96.4	NA	YES	NA	Bad load cell wiring
B-17	12-6-90	0.704	62.4	10.09	0.654	77.6	NA	YES	NA	" " " "
B-18	12-10-90	0.679	70.0	10.07	0.566	104.3	NA	YES	NA	" " " "
B-19	12-12-90	0.788	36.8	5.05	0.679	70.0	CIUC	YES	25.4%	
B-20	12-14-90	0.715	59.2	9.72	0.582	99.5	NA	YES	NA	Bad load cell wiring
B-21	12-15-90	0.758	46.1	10.14	0.614	89.7	NA	YES	Na	" " " "
B-22	12-17-90	0.602	93.3	0.122	0.600	94.0	CIUC	NA	25.9%	
B-23	12-30-90	0.734	53.2	10.16	0.616	89.1	CIUC	YES	8.4%	Very poor stability
B-24	1-11-91	0.772	41.8	9.94	0.627	85.8	CIUC	YES	21.9	

TABLE 4.1 (page 2 of 2)
CONSOLIDATION AND SHEAR HISTORY OF CONSOLIDATED-UNDRAINED
AND DRAINED TRIAXIAL COMPRESSION TESTS ON UNFROZEN MANCHESTER FINE SAND
SERIES C

Spec. No.	Set-up			Pre-shear				Consol. Results ?	Final Shear ϵ_a	Remarks
	Date	e	D_r (%)	σ'_{1c} (MPa)	e	D_r (%)				
C-01	8-23-91	0.796	34.5	9.36	0.637	82.7	CIUC	YES	24.0%	
C-02	9-23-91	0.802	32.5	9.96	0.637	82.7	CIUC	YES	23.1%	
C-03	10-21-91	0.815	28.6	10.10	0.655	77.3	CIUC	YES	26.7%	
C-04	12-4-91	0.781	39.1	7.48	0.631	84.6	CIUC	YES	25.2%	
C-05	12-8-91	0.762	44.8	Not available			NA	NO		Faulty pressure trans.
C-06	12-10-91	0.761	45.0	Not available			NA	NO		" " "
C-07	12-15-91	0.756	46.5	Not available			NA	NO		Consolidation no good.
C-08	12-16-91	0.723	56.6	10.00	0.609	91.2	NA	YES		Membrane rupture
C-09	12-30-91	0.803	32.1	10.03	0.621	87.6	CIDC	YES	23.5%	
C-10	1-13-92	0.776	40.3	9.98	0.609	91.2	CIDC	YES	25.7%	
C-11	1-15-92	0.727	55.3	1.92	0.675	71.2	CIDC	YES	26.1%	
C-12	1-17-92	0.653	77.8	2.00	0.614	89.7	CIDC	YES	24.2%	
C-13	1-19-92	0.698	64.2	4.97	0.618	88.5	CIDC	YES	24.9%	
C-14	1-21-92	0.627	85.7	0.16	0.626	86.1	CIDC	NA	25.5%	
C-15	2-4-92	0.800	33.2	1.94	0.725	56.0	CIUC	YES	26.1%	
C-16	2-6-92	0.736	52.5	9.96	0.566	104.3	CIUC	YES	24.6%	
C-17	3-5-92	0.810	30.1	0.117	0.807	31.0	CIDC	NA	26.8%	
C-18	3-9-92	0.813	29.4	0.102	0.811	29.8	CIDC	NA	30.3%	
C-19	3-23-92	0.807	31.1	0.097	0.805	31.7	CIDC	NA	36.9%	
C-20	4-20-92	0.653	77.9	0.095	0.652	78.2	CIDC	NA	29.1%	
C-21	4-30-92	0.632	84.3	0.095	0.633	84.3	CIDC	NA	35.1%	
C-22	6-2-93	0.753	47.4	9.96	0.596	95.2	CIUC	YES	26.5%	
C-23	6-7-93	0.783	39.1	5.00	0.661	75.4	CIUC	YES	32.1%	
C-24	6-11-93	0.776	40.6	4.96	0.642	81.2	CIUC	YES	25.7%	
C-25	9-2-93	0.778	40.0	12.52	0.579	100.4	CIUC	YES	25.7%	
C-26	8-9-93	0.684	68.6	0.106	0.683	68.7	CIUC	NA	25.7%	
C-27	7-13-93	0.777	40.0	1.960	0.700	63.6	CIUC	YES	27.1%	
C-28	6-30-93	0.783	38.4	13.33	0.606	92.2	CAUC	YES	22.1%	
C-29	7-15-93	0.794	35.0	13.64	0.585	98.5	CAUC	YES	22.3%	
C-30	7-21-93	0.661	75.6	12.49	0.531	115.0	CIUC	YES	24.6%	
C-31	7-23-93	0.683	66.6	0.115	0.688	67.2	CIUC	NO	25.4%	
C-32	8-6-93	0.755	46.9	7.57	0.633	83.8	CAUC	YES	26.5%	
C-33	8-2-93	0.649	79.0	2.03	0.602	93.3	CIUC	YES	25.3%	
C-34	8-4-93	0.600	94.0	0.077	0.597	94.9	CIUC	NA	25.6%	
C-35	8-24-93	0.762	44.7	12.48	0.540	112.2	CIUC	YES	26.6%	

TABLE 4.2 (page 1 of 2)
CONSOLIDATION CHARACTERISTICS - SERIES B

Test Group	Test No.	Eff. Stress Init. MPa	Eff. Stress Final MPa	Volume Init. cc	Volume Final cc	Volume ΔV cc	Void Ratio, e Init.	Void Ratio, e Final	Void Ratio, e Δe	Axial Strain DCDT %	Axial Strain ACDT %	Vol. Strain %	Consol. Time Prim. min	Consol. Time Sec. min	C_c
2 MPa Tests	B-06	0.131	2.02	70.57	68.09	2.48	0.756	0.694	0.062	1.90	0.34	3.51	4.0	11.0	
	B-07	0.102	2.04	73.04	70.58	2.46	0.648	0.593	0.055	0.84	0.73	3.37	2.0	24.6	
	B-11	0.105	2.02	70.75	68.86	1.89	0.735	0.688	0.047	0.46	0.46	2.67	2.0	13.1	
5 MPa Tests	B-01	0.038	5.01	68.16	64.42	3.74	0.767	0.670	0.097	2.20	0.51	5.49	7.0	17.1	
	B-02	0.102	5.02	71.70	69.20	2.50	0.621	0.564	0.057	1.25	0.09*	3.49	5.5	26.4	
	B-03	0.111	5.08	70.31	65.79	4.52	0.727	0.614	0.113	1.47	0.30	6.54	5.5	14.4	
	B-04	0.012	4.89	71.22	67.90	3.32	0.741	0.660	0.081	1.11	0.27*	4.66	4.0	13.3	
	B-05	0.058	5.03	72.58	69.99	2.59	0.669	0.608	0.059	0.63	0.69	3.57	8.5	9.1	
	B-13	0.093	5.19	69.21	65.16	4.05	0.802	0.697	0.105	1.94	2.98*	5.85	10.3	9.9	
	B-14	0.098	5.00	71.52	68.76	2.76	0.670	0.605	0.065	1.27	0.45	3.86	6.0	9.3	
	B-15	0.031	5.03	71.20	68.43	2.77	0.664	0.599	0.065	1.25	0.97	3.89	8.5	5.0	
	B-19	0.119	5.05	68.42	64.23	4.19	0.789	0.679	0.110	2.26	1.55	6.12	7.0	8.0	
10 MPa Tests	B-16	0.081	10.10	69.17	63.67	5.50	0.730	0.592	0.138	3.54	2.18*	7.95	6.7	23.8	0.146
	B-17	0.184	10.09	71.37	69.21	2.16	0.705	0.654	0.051	2.02	1.12	3.02	10.2	11.3	0.068
	B-18	0.092	10.07	71.02	66.19	4.83	0.680	0.566	0.114	2.73	0.67	6.81	7.2	11.1	0.136
	B-20	0.038	9.72	71.07	65.37	5.70	0.720	0.582	0.138	NA	4.24	8.02	11.5	7.0	NA
	B-21	0.116	10.14	69.44	64.00	5.44	0.751	0.614	0.137	3.22	NA	7.83	10.2	9.6	0.183
	B-23	0.115	10.16	70.95	66.14	4.81	0.734	0.616	0.118	1.73	1.45	6.78	10.0	9.4	0.143
	B-24	0.108	10.03	68.95	63.32	5.63	0.772	0.627	0.145	2.84	0.69*	6.78	10.0	8.7	0.172

Notes: * - ACDT Strains based on one ACDT recording
NA - Not available

TABLE 4.2 (page 2 of 2)
CONSOLIDATION CHARACTERISTICS - SERIES C

Isotropic Consolidations

Test Group	Test No.	Eff. Stress Init. MPa	Eff. Stress Final MPa	Volume Init. cc	Volume Final cc	Volume ΔV cc	Void Ratio, e Init.	Void Ratio, e Final	Void Ratio, e Δe	Axial Strain DCDT %	Axial Strain ACDT %	Vol. Strain %	Consol. Time Prim. min	Consol. Time Sec. min	C_c
2 MPa Tests	C-11	0.110	1.925	71.86	69.71	2.15	0.727	0.675	0.052	1.25	0.46	2.99	28.0	271.0	
	C-12	0.189	2.000	71.57	70.00	1.57	0.651	0.614	0.037	1.04	0.50	2.20	30.0	632.5	
	C-15	0.116	1.948	69.09	66.27	2.82	0.799	0.725	0.074	1.14	0.91	4.09	31.5	550.4	
	C-27	0.104	1.960	68.85	66.03	2.82	0.773	0.700	0.073	1.66	0.79	4.10	33.0	135.0	
	C-33	0.144	2.030	71.41	69.31	2.10	0.643	0.602	0.041	2.31	0.63	2.50	16.0	189.0	
5 MPa Tests	C-13	0.148	4.975	71.19	67.88	3.31	0.697	0.618	0.079	1.70	1.09	4.65	51.0	497.0	
	C-23	0.125	4.989	69.19	64.57	4.62	0.780	0.661	0.119	2.06	1.27	6.67	48.0	1507.0	
	C-24	0.113	4.966	70.22	65.19	5.03	0.769	0.642	0.127	1.62	1.87	7.17	38.0	1322.0	
7.5 MPa Test	C-04	0.232	7.495	69.48	63.69	5.79	0.779	0.631	0.148	2.55	1.95	8.33	41.3	568.2	
10 MPa Tests	C-01	0.099	9.359	69.66	63.50	6.16	0.796	0.637	0.159	2.51	2.43	8.84	57.8	66.6	0.169
	C-02	0.467	9.856	69.36	63.23	6.13	0.796	0.637	0.159	2.90	1.96	8.84	57.5	123.7	0.204
	C-03	0.252	10.027	70.79	64.68	6.11	0.811	0.655	0.156	3.19	2.69	8.63	44.0	124.8	0.195
	C-08	0.122	10.00	69.39	62.72	6.67	0.780	0.609	0.171	2.72	1.84	9.61	81.0	298.0	0.195
	C-09	0.155	9.953	69.84	62.86	6.98	0.801	0.621	0.180	2.62	1.77	9.99	82.0	277.5	0.205
	C-10	0.133	9.985	71.12	64.49	6.63	0.776	0.609	0.167	3.14	2.24	9.32	92.0	65.0	0.202
	C-16	0.128	9.953	70.88	63.97	6.91	0.735	0.566	0.169	2.41	1.72	9.75	78.0	2915.0	0.178
	C-22	0.107	9.966	70.45	64.33	6.12	0.747	0.596	0.151	2.47	2.43	8.68	66.0	606.8	0.208
12.5 MPa Test	C-25	0.107	12.465	67.27	60.27	7.00	0.763	0.579	0.184	3.32	3.38	10.41	51.0	189.0	0.201
	C-30	0.103	12.375	70.97	65.49	5.48	0.660	0.531	0.129	2.73	2.00	7.73	77.0	214.0	0.155
	C-35	0.096	12.533	67.33	59.82	7.45	0.733	0.540	0.193	3.07	2.67	11.16	62.0	140.0	0.228

Anisotropic Consolidations

Test No.	Effective Stresses, MPa Initial σ'_1	Initial σ'_3	Final σ'_1	Final σ'_3	Final K_c	Volume Init. cc	Volume Final cc	Volume ΔV cc	Void Ratio, e Init.	Void Ratio, e Final	Void Ratio, e Δe	Axial Strain DCDT %	Axial Strain ACDT %	Vol. Strain %	Consol. Time Prim. min	Consol. Time Sec. min	C_c
C-28	0.110	0.098	13.329	7.567	0.56	69.28	63.19	6.09	0.761	0.606	0.155	6.85	6.16	8.79	148.0	345.0	0.199
C-29	0.139	0.139	13.641	7.033	0.51	68.08	60.21	7.87	0.792	0.585	0.207	1.25	9.93	11.56	230.0	130.0	0.289
C-32	0.121	0.113	9.449	5.540	0.59	71.67	66.75	4.92	0.754	0.633	0.121	5.56	5.08	6.86	65.0	173.0	0.157

TABLE 4.3 (page 1 of 2)
SHEAR CHARACTERISTICS - SHEARING CONDITIONS AND DESCRIPTIONS: SERIES B

Test Group	Test No.	PRE-SHEAR Void Ratio e	PRE-SHEAR σ'_c (MPa)	SHEAR Test Type	SHEAR Final Strain (%)	SHEAR Nominal $\dot{\epsilon}$ DCDT %/min	SHEAR Nominal $\dot{\epsilon}$ ACDT %/min	POST-SHEAR Description of Sheared Specimen End Behavir	Spec. Shape	Sliding? Top Cap	Sliding? Pedestal	Surf. Rupt?	Lat. Exp.
0.1 MPa Tests	B-08	0.636	0.104	CIUC	8.54	0.1401	0.1126	LU	RC	NO	NO	NO	S
	B-09	0.637	0.114	CIUC	11.00	0.1356	0.1204	LU	RC	YES	NO	NO	S
	B-10	0.765	0.102	CIUC	25.74	0.1446	0.0773	CS-LU	RC-B	YES	NO	YES	M
	B-12	0.626	0.110	CIUC	24.78	0.1405	0.1296	OL	RC-S	YES	NO	NO	L
	B-22	0.600	0.122	CIUC	25.87	0.1464	0.1245	OL	RC-S	YES	NO	YES	L
2 MPa Tests	B-06	0.694	2.035	CIUC	25.28	0.1453	0.1377	LU-OL	RC-S	YES	NO	NO	L
	B-07	0.593	2.030	CIUC	24.92	0.1422	0.1275	LU-OL	RC-S	NO	NO	NO	L
	B-11	0.688	2.013	CIUC	24.13	0.1436	0.1511	OL	RC-S	YES	YES	NO	L
5 MPa Tests	B-01	0.670	4.983	CIUC	24.94	0.1455	0.1711	CS	B	NO	NO	NO	N-S
	B-02	0.564	5.005	CIUC	22.82	0.1397	0.1422	VC	B	NO	NO	NO	N
	B-04	0.660	4.982	CIUC	16.03	0.1415	0.1526	OL	RC-S	YES	NO	YES	L
	B-05	0.608	5.010	CIUC	21.55	0.1417	0.1316	OL	RC-S	YES	YES	NO	M
	B-13	0.697	5.185	CIUC	21.45	0.1470	0.1305	OL	RC-S	YES	YES	YES	L
	B-14	0.605	5.006	CIUC	16.86	0.1425	0.1323	OL	RC-S	YES	NO	NO	M
	B-15	0.599	5.034	CIUC	24.61	0.1442	0.1345	OL	RC-S	YES	NO	YES	L
	B-19	0.679	5.049	CIUC	25.41	0.1459	0.1363	OL	RC-S	YES	YES	YES	M
10 MPa Tests	B-23	0.616	10.16	CIUC	25.20	0.1456	0.1359	OL	RC-S	YES	YES	YES	M
	B-24	0.626	9.937	CIUC	21.92	0.1446	0.1634	CS	RC-B	NO	NO	YES	S

KEY:

Description of Sheared Specimen
End Behavior
- VC - Very constrained at ends
- CS - Constrained at ends
- LU - Lubricated to allow expansion
- OL - Over lubricated at ends

Specimen Shape
- RC - Right cylinder dominant
- B - Barrel-shape dominant
- S - S-shaped sample due to sliding

Lateral Expansion (specimen ends)
- N - No lateral expansion
- S - Slight expansion
- M - Moderate expansion
- L - Large expansion

TABLE 4.3 (page 2 of 2)
SHEAR CHARACTERISTICS - SHEARING CONDITIONS AND DESCRIPTIONS: SERIES C

Test Group	Test No.	PRE-SHEAR Void Ratio e	PRE-SHEAR σ'_c σ'_{1c} (MPa)	SHEAR Test Type	SHEAR Final Strain (%)	SHEAR Nominal $\dot{\epsilon}$ DCDT %/hr	SHEAR Nominal $\dot{\epsilon}$ ACDT %/hr	POST-SHEAR Description of Sheared Specimen: End Behavir	Spec. Shape	Sliding? Top Cap	Sliding? Pedestal	Rupt. Surf?	Lat. Exp.
0.1 MPa Tests	C-14	0.626	0.160	CIDC	25.48	11.01	12.74	- Not Identifiable -- Specimen Disturbed -					
	C-17	0.807	0.117	CIDC	26.83	11.44	14.29	- Not Identifiable -- Specimen Disturbed -					
	C-18	0.811	0.102	CIDC	30.33	12.51	15.13	- Not Identifiable -- Specimen Disturbed -					
	C-19	0.805	0.097	CIDC	36.88	10.87	13.87	VCS	B	NO	NO	NO	N
	C-20	0.652	0.095	CIDC	29.08	12.71	17.59	VCS	B	NO	NO	NO	N
	C-21	0.632	0.095	CIDC	35.10	12.83	17.33	VCS	B	NO	NO	NO	N
	C-26	0.683	0.106	CIUC	25.71	13.34	12.59	CS	RC-B	YES	NO	YES	S
	C-31	0.688	0.115	CIUC	25.40	12.25	11.48	VCS	B	NO	NO	NO	N
	C-34	0.597	0.077	CIUC	25.63	12.13	11.91	CS	B	NO	NO	YES	M
2 MPa Tests	C-11	0.675	1.919	CIDC	26.07	12.50	13.09	LU	RC-B	YES	NO	NO	L
	C-12	0.614	1.997	CIDC	24.23	9.96	10.17	LU	RC	NO	NO	YES	L
	C-15	0.725	1.937	CIUC	26.14	12.08	12.93	LU	RC-B	YES	NO	NO	L
	C-27	0.700	1.959	CIUC	27.07	12.91	14.87	CS	RC-B	NO	NO	NO	S
	C-33	0.602	2.031	CIUC	25.32	15.77	14.66	LU	RC-S	YES	NO	NO	M
5 MPa Test	C-13	0.618	4.969	CIDC	24.85	11.29	11.03	LU	RC-S	NO	NO	NO	L
	C-23	0.661	4.999	CIUC	32.11	13.57	11.87	OL	RC-S	YES	YES	NO	M
	C-24	0.642	4.959	CIUC	25.65	12.15	14.57	CS	RC-B	NO	NO	NO	M
7.5 MPa Test	C-04	0.631	7.483	CIUC	25.18	12.56	13.87	OL	RC-S-B	YES	YES	YES	L
								OL	RC-S	YES	YES	YES	L
	C-02	0.637	9.911	CIUC	23.06	11.72	11.65	OL	RC-S	YES	YES	YES	L
	C-03	0.655	10.10	CIUC	26.69	13.15	15.65	CS	B	NO	NO	YES	S
	C-09	0.621	10.03	CIDC	23.46	10.84	9.15	LU	RC-S	NO	NO	NO	L
	C-10	0.609	9.978	CIDC	25.65	11.14	11.05	LU	RC-S	NO	NO	NO	L
	C-16	0.566	9.961	CIUC	24.58	11.42	11.69	LU	RC-B	NO	NO	NO	L
	C-22	0.596	9.960	CIUC	26.49	122.9	133.8	CS	RC-B	NO	NO	NO	M
12.5 MPa Test	C-25	0.579	12.52	CIUC	25.67	13.96	12.14	LU	RC	NO	NO	NO	L
	C-30	0.531	12.49	CIUC	24.55	12.13	11.54	OL	RC-S	YES	YES	YES	L
	C-35	0.540	12.50	CIUC	26.62	14.35	12.71	LU	RC	NO	NO	NO	L
Anisotropic Tests	C-28	0.606	13.33	CAUC	22.09	13.82	17.77	LU	RC-B	NO	NO	NO	M
	C-29	0.585	13.64	CAUC	22.29	139.0	129.7	LU	RC	NO	NO	NO	L
	C-32	0.633	9.45	CAUC	26.51	14.25	13.96	LU	RC-B	YES	NO	NO	M

Note: [1] For tests #11 and #19 only one ACDT was functioning
For key see page 1.

TABLE 4.4 (page 1 of 2)
SHEAR CHARACTERISTICS - SERIES B: CIUC TESTS
Conditions at Maximum Obliquity

Test Group	Test No.	D_r (%)	e	σ'_c (MPa)	Strain (%)	p (MPa)	q (MPa)	I_1 (MPa)	Δu (MPa)	A	ϕ'	R	q/σ'_c
0.1 MPa Tests	B-08	83.0	0.636	0.104	1.83	0.273	0.176	0.214	0.008	0.022	40.1	4.628	1.69
	B-09	82.7	0.637	0.114	3.57	0.566	0.353	0.448	-0.100	-0.142	38.5	4.307	3.10
	B-10	43.8	0.765	0.102	7.26	0.494	0.300	0.394	-0.090	-0.150	37.5	4.107	2.93
	B-12	86.1	0.626	0.110	0.84	0.157	0.119	0.117	0.035	0.146	49.4	7.290	1.08
	B-22	94.0	0.600	0.122	0.50	0.164	0.137	0.118	0.094	0.344	56.4	10.986	1.12
2 MPa Tests	B-06	65.4	0.694	2.035	12.20	2.044	1.150	1.661	1.100	0.478	34.2	3.569	0.57
	B-07	96.1	0.593	2.030	7.19	3.358	1.964	2.703	0.606	0.154	35.8	3.818	0.97
	B-11	67.2	0.688	2.013	6.81	2.012	1.182	1.895	1.120	0.474	36.0	3.848	0.59
5 MPa Tests	B-01	72.7	0.670	4.982	11.68	2.555	1.444	2.073	3.922	1.358	34.4	3.599	0.29
	B-02	104.9	0.564	5.017	6.74	4.849	2.839	3.903	3.006	0.329	35.8	3.825	0.57
	B-04	75.7	0.660	4.982	8.05	5.133	2.712	4.229	2.545	0.469	31.9	3.240	0.54
	B-05	91.5	0.608	5.009	8.02	4.671	2.644	3.789	2.991	0.566	34.5	3.609	0.53
	B-13	64.5	0.697	5.184	6.39	2.368	1.442	1.888	4.201	1.457	37.5	4.111	0.28
	B-14	92.5	0.605	5.001	7.45	4.532	2.648	3.650	3.137	0.593	35.7	3.809	0.53
	B-15	94.3	0.599	5.003	9.75	5.778	3.268	4.688	2.538	0.388	34.5	3.605	0.65
	B-19	70.0	0.679	5.047	10.87	4.411	2.281	3.651	2.848	0.625	31.1	3.141	0.45
10 MPa Tests	B-23	89.1	0.616	10.174	8.44	5.050	2.851	4.100	8.030	1.408	34.4	3.593	0.28
	B-24	85.8	0.627	10.027	9.94	4.241	2.779	3.315	8.694	1.564	41.0	4.803	0.28

TABLE 4.4 (page 2 of 2)
SHEAR CHARACTERISTICS - SERIES C
Conditions at Maximum Obliquity

CIUC Tests

Test Group	Test No.	D_r (%)	e	σ'_c (MPa)	Strain (%)	p (MPa)	q (MPa)	I_1 (MPa)	Δu (MPa)	A	ϕ'	R	q/σ'_c
0.1 MPa Tests	C-26	68.7	0.683	0.106	1.30	0.137	0.095	0.105	0.075	0.392	44.1	5.570	0.90
	C-31	67.2	0.688	0.115	2.40	0.353	0.220	0.279	-0.020	-0.050	38.6	4.314	1.91
	C-34	94.9	0.597	0.077	0.53	0.140	0.094	0.108	0.025	0.138	42.5	5.155	1.23
2 MPa Tests	C-15	56.0	0.725	1.937	9.04	1.121	0.694	0.890	1.522	1.123	38.2	4.247	0.36
	C-27	63.6	0.700	1.960	12.32	1.472	0.840	1.192	1.327	0.808	34.8	3.659	0.43
	C-33	93.3	0.602	2.031	5.17	2.518	1.478	2.026	0.996	0.340	35.6	3.843	0.73
5 MPa Tests	C-23	75.4	0.661	4.999	7.90	2.579	1.377	2.120	3.790	1.392	32.3	3.291	0.28
	C-24	81.2	0.642	4.959	13.09	3.191	1.790	2.593	3.554	1.009	34.1	3.557	0.36
7.5 MPa Test	C-04	84.6	0.631	7.483	10.19	3.619	2.158	2.900	6.040	1.445	36.6	3.955	0.29
10 MPa Tests	C-01	82.7	0.637	9.362	8.63	4.329	2.322	3.555	7.494	1.628	32.5	3.315	0.25
	C-02	82.7	0.637	9.961	8.11	4.206	2.412	3.402	8.101	1.690	35.0	3.689	0.24
	C-03	77.3	0.655	10.099	9.61	4.198	2.475	3.373	8.270	1.679	36.1	3.874	0.25
	C-16	104.3	0.566	9.961	13.92	5.130	3.242	4.050	8.093	1.252	39.2	4.433	0.33
	C-22	95.2	0.596	9.960	14.36	5.811	3.188	4.749	7.416	1.172	33.3	3.430	0.32
12.5 MPa Test	C-25	100.4	0.579	12.515	14.50	5.438	3.033	4.427	10.112	1.683	33.9	3.522	0.24
	C-30	115.0	0.531	12.487	12.62	7.756	4.376	6.297	9.110	1.045	34.4	3.590	0.35
	C-35	112.2	0.540	12.498	18.97	5.535	3.188	4.472	10.152	1.614	35.2	3.717	0.26

CAUC Tests

Test No.	D_r (%)	e	σ'_{1c} (MPa)	σ'_{3c} (MPa)	K_c	Strain (%)	p (MPa)	q (MPa)	I_1 (MPa)	Δu (MPa)	ϕ'	R	q/σ'_{1c}
28	92.2	0.606	13.329	7.556	1.76	11.03	5.539	3.067	4.517	5.076	33.6	3.482	0.23
29	98.5	0.585	13.641	6.968	1.95	12.79	5.799	3.270	4.709	4.602	34.3	3.586	0.24
32	83.8	0.633	9.449	5.572	1.70	10.12	4.556	2.552	3.705	3.567	34.1	3.548	0.27

TABLE 4.5 (page 1 of 2)
SHEAR CHARACTERISTICS - SERIES B: CIUC TESTS
Conditions at Peak Shear Strength

Test Group	Test No.	D_r (%)	e	σ'_c (MPa)	Strain (%)	p (MPa)	q (MPa)	I_1 (MPa)	Δu (MPa)	A	ϕ'	R	q/σ'_c
0.1 MPa Tests	B-08[1]	83.0	0.636	0.104	*8.54*	*1.768*	*1.088*	*1.405*	*-0.575*	*-0.264*	*38.0*	*4.202*	*10.46*
	B-09[1]	82.7	0.637	0.114	*11.00*	*2.82*	*1.676*	*2.262*	*-1.031*	*-0.308*	*36.5*	*3.928*	*14.70*
	B-10	43.8	0.765	0.102	22.50	1.236	0.693	1.005	-0.440	-0.318	34.1	3.554	6.77
	B-12	86.1	0.626	0.110	16.90	3.470	2.003	2.802	-1.409	-0.352	35.3	3.731	18.24
	B-22	94.0	0.600	0.122	16.50	4.534	2.405	3.732	-2.016	-0.419	32.0	3.259	19.68
2 MPa Tests	B-06	65.4	0.694	2.035	18.74	2.344	1.283	1.916	0.925	0.361	33.2	3.419	0.63
	B-07	96.1	0.593	2.030	17.24	5.173	2.908	4.203	-0.262	-0.041	34.2	3.568	1.43
	B-11	67.2	0.688	2.013	16.17	2.794	1.547	2.279	0.699	0.226	33.6	3.480	0.77
5 MPa Tests	B-01	72.7	0.670	4.982	21.38	2.891	1.597	2.358	3.727	1.167	33.5	3.469	0.32
	B-02	104.9	0.564	5.017	16.95	6.443	3.616	5.238	2.176	0.301	34.1	3.558	0.72
	B-04	75.7	0.660	4.982	11.31	5.407	2.815	4.469	2.373	0.421	31.4	3.172	0.57
	B-05	91.5	0.608	5.009	11.21	5.076	2.814	4.138	2.766	0.491	33.7	3.487	0.56
	B-13	64.5	0.697	5.184	9.92	2.542	1.525	2.034	4.132	1.354	36.9	4.000	0.29
	B-14	92.5	0.605	5.001	12.07	5.138	2.920	4.165	2.805	0.481	34.6	3.632	0.58
	B-15	94.3	0.599	5.003	13.93	6.304	3.476	5.146	2.221	0.320	33.5	3.458	0.69
	B-19	70.0	0.679	5.047	13.64	4.506	2.308	3.736	2.769	0.600	30.8	3.100	0.46
10 MPa Tests	B-23	89.1	0.616	10.174	8.44	5.050	2.851	4.100	8.030	1.408	34.4	3.593	0.28
	B-24	85.8	0.627	10.027	14.11	4.391	2.845	3.443	8.587	1.509	40.4	4.680	0.28

Notes:
[1] - Represents end of test and not peak strength conditions; i.e., stresses were still increasing at end of shear. Results are *italicized* for convenience

TABLE 4.5 (page 2 of 2)
SHEAR CHARACTERISTICS - SERIES C
Conditions at Peak Shear Strength

CIUC Tests

Test Group	Test No.	D_r (%)	e	σ'_c (MPa)	Strain (%)	p (MPa)	q (MPa)	I_1 (MPa)	Δu (MPa)	A	ϕ'	R	q/σ'_c
0.1 MPa Tests	C-26	68.7	0.683	0.106	22.83	2.511	1.395	2.046	-0.996	-0.357	33.7	3.500	13.16
	C-31	67.8	0.688	0.115	22.75	2.399	1.314	1.961	-0.968	-0.374	33.2	3.421	11.43
	C-34	94.9	0.596	0.077	21.99	4.885	2.740	3.971	-2.065	-0.377	34.1	3.556	35.59
2 MPa Test	C-15	56.0	0.725	1.937	21.10	1.520	0.898	1.220	1.329	0.754	36.2	3.888	0.46
	C-27	63.6	0.700	1.959	26.40	1.974	1.076	1.615	1.070	0.506	33.0	3.397	0.55
	C-33	93.3	0.602	2.031	19.54	4.871	2.765	3.950	-0.068	-0.012	34.6	3.625	1.36
5 MPa Tests	C-23	75.4	0.661	4.999	17.06	2.855	1.491	2.358	3.624	1.228	31.5	3.186	0.30
	C-24	81.2	0.642	4.959	21.80	3.478	1.920	2.838	3.394	0.897	33.5	3.465	0.39
7.5 MPa Test	C-04	84.6	0.631	7.483	11.98	3.691	2.181	2.964	5.985	1.417	36.2	3.888	0.29
10 MPa Tests	C-01	82.7	0.637	9.362	1.97	5.894	2.433	5.083	6.036	1.251	24.4	2.406	0.26
	C-02	82.7	0.637	9.961	2.12	6.045	2.540	5.198	6.378	1.263	24.9	2.450	0.25
	C-03	77.3	0.655	10.099	1.63	6.362	2.601	5.495	6.237	1.205	24.1	2.383	0.26
	C-16	104.3	0.566	9.961	19.71	5.232	3.299	4.133	8.046	1.223	39.1	4.414	0.33
	C-22	95.2	0.596	9.960	18.46	5.939	3.243	4.858	7.345	1.140	33.1	3.406	0.33
12.5 MPa Test	C-25	100.4	0.575	12.515	18.69	5.535	3.071	4.511	10.054	1.652	33.7	3.493	0.24
	C-30	114.8	0.531	12.487	13.43	7.807	4.391	6.343	9.069	1.037	34.2	3.571	0.35
	C-35	112.8	0.537	12.498	1.36	8.420	3.288	7.324	7.365	1.135	23.0	2.282	0.26

CAUC Tests

Test No.	D_r (%)	e	σ'_{1c} (MPa)	σ'_{3c} (MPa)	K_c	Strain (%)	p (MPa)	q (MPa)	I_1 (MPa)	Δu (MPa)	ϕ'	R	q_{max}/σ'_{1c}
C-28	92.2	0.606	13.329	7.556	1.76	0.34	9.763	3.578	8.571	1.358	21.5	2.157	0.27
C-29	98.5	0.585	13.641	6.986	1.95	0.39	10.117	4.014	8.779	0.893	23.4	2.315	0.29
C-32	83.8	0.633	9.449	5.572	1.70	16.53	4.749	2.628	3.950	3.453	33.6	3.479	0.28

TABLE 4.6
SHEAR CHARACTERISTICS - SERIES C: CIDC TESTS
Conditions at Peak Shear Strength (= Conditions at Maximum Obliquity)

Test Group	Test No.	D_r (%)	e	σ'_c (MPa)	p (MPa)	q (MPa)	ϵ_a (%)	ϵ_v (%)	e_f	$\Delta\epsilon_v/\Delta\epsilon_a$ (%)	ϕ'	R	q/σ'_c
0.1 MPa Tests	C-14	86.1	0.626	0.160	0.192	0.159	5.72	2.48	0.666	0.649	56.0	10.550	0.99
	C-17	31.0	0.807	0.117	0.134	0.077	10.18	0.29	0.813	0.140	35.0	3.689	0.66
	C-18	29.8	0.811	0.102	0.115	0.077	10.20	0.33	0.825	0.142	42.0	5.049	0.75
	C-19	31.7	0.805	0.097	0.101	0.061	8.77	0.87	0.821	0.166	37.5	4.107	0.63
	C-20	78.2	0.652	0.095	0.111	0.081	5.33	2.78	0.699	0.755	47.0	6.427	0.85
	C-21	84.3	0.632	0.095	0.117	0.087	4.74	2.79	0.677	0.789	48.0	6.780	0.92
2 MPa Tests	C-11	71.2	0.675	1.919	1.966	1.187	12.90	0.62	0.686	0.151	37.1	4.048	0.62
	C-12	89.7	0.614	1.997	2.048	1.293	8.79	1.06	0.632	0.289	39.1	4.424	0.65
5 MPa Test	C-13	88.5	0.618	4.969	5.096	2.945	13.24	-1.14	0.599	0.036	35.3	3.738	0.59
10 MPa Tests	C-09	87.6	0.621	10.027	10.140	4.929	13.77	-4.65	0.553	-0.161	29.1	2.892	0.49
	C-10	91.2	0.609	9.978	10.195	5.425	19.56	-5.57	0.520	-0.119	32.2	3.274	0.54

TABLE 4.7 (page 1 of 2)
SHEAR CHARACTERISTICS - Modulus and Stress Properties

SERIES B

Test Group	Test No.	D_r (%)	e	σ'_c (MPa)	E_i (MPa)	Q_{uy} (MPa)	Q_p (MPa)	ACDT Agmt	Q-ϵ_a Qual.	Stab. Qual.
0.1 MPa Tests	B-08[1]	83.0	0.636	0.104	122	0.126	2.176	F	F	G
	B-09[1]	82.7	0.637	0.114	197	0.110	3.352	F	P	G
	B-10	43.8	0.765	0.102	NA	0.145	1.386	P	P	P
	B-12	86.1	0.626	0.110	503	0.165	4.006	F	F	P
	B-22	94.0	0.600	0.122	234	0.150	4.810	G	P	P
2 MPa Tests	B-06	65.4	0.694	2.035	935	1.229	2.566	F	P	F
	B-07	96.1	0.593	2.030	NA	1.498	5.816	F	P	F
	B-11	67.2	0.688	2.013	1192	1.434	3.094	G	P	P
5 MPa Tests	B-01	72.7	0.670	4.982	1070	2.482	3.194	P	P	G
	B-02	104.9	0.564	5.017	3000	3.638	7.754	G	P	G
	B-04	75.7	0.660	4.982	2356	3.260	5.630	G	P	P
	B-05	91.5	0.608	5.009	857	3.468	5.628	P	P	F
	B-13	64.5	0.697	5.184	1768	2.654	3.050	P	P	P
	B-14	92.5	0.605	5.001	2502	3.389	5.840	F	F	F
	B-15	94.3	0.599	5.003	1298	3.699	6.952	G	P	P
	B-19	70.0	0.679	5.047	2017	2.607	4.616	P	P	P
10 MPa Tests	B-23	89.1	0.616	10.174	1669	5.644	5.702	F	P	VP
	B-24	85.8	0.627	10.027	2235	5.503	5.690	P	P	G

SERIES C

Test Group	Test No.	D_r (%)	e	σ'_c (MPa)	E_i (MPa)	Q_{uy} (MPa)	Q_p (MPa)	ACDT Agmt	Q-ϵ_a Qual.	Stab. Qual.
0.1 MPa Tests	*C-14*	*86.1*	*0.626*	*0.160*	*314*	*NA*	*0.318*	*G*	*P*	*G*
	C-17	*31.0*	*0.807*	*0.117*	*350*	*NA*	*0.154*	*G*	*F*	*G*
	C-18	*29.8*	*0.811*	*0.102*	*292*	*NA*	*0.154*	*G*	*F*	*G*
	C-19	*31.7*	*0.805*	*0.097*	*453*	*NA*	*0.122*	*NA*[2]	*F*	*G*
	C-20	*78.2*	*0.652*	*0.095*	*342*	*NA*	*0.162*	*G*	*G*	*G*
	C-21	*84.3*	*0.632*	*0.095*	*174*	*NA*	*0.174*	*G*	*P*	*G*

Note: [1] - Q_p represents end of test conditions since stresses were still increasing at end of shear.
[2] - Only one ACDT functional during tests; therefore, ACDT agreement not appropriate
CIDC tests are in italics
KEY: ACDT, Initial Q-ϵ_a, and Stability Qualifiers
VP - Very Poor P - Poor F - Fair G - Good

TABLE 4.7 (page 2 of 2)
SHEAR CHARACTERISTICS - Modulus and Stress Properties

SERIES C continued

Test Group	Test No.	D_r (%)	e	σ'_c (MPa)	E_i (MPa)	Q_{uy} (MPa)	Q_p (MPa)	ACDT Agmt	Q-ϵ_a Qual.	Stab. Qual.
0.1 MPa Tests	C-26	68.7	0.683	0.106	78	NA	2.790	F	P	P
	C-31	67.2	0.688	0.115	250	0.122	2.628	G	F	G
	C-34	94.9	0.597	0.077	310	0.119	5.481	G	G	G
2 MPa Tests	*C-11*	*71.2*	*0.675*	*1.919*	*913*	*NA*	*2.374*	*NA*[2]	*P*	*F*
	C-12	*89.7*	*0.614*	*1.997*	*1804*	*NA*	*2.586*	*F*	*F*	*G*
	C-15	56.0	0.725	1.937	1738	1.141	1.796	G	F	F
	C-27	63.6	0.700	1.959	700	1.048	2.150	G	P	G
	C-33	93.3	0.602	2.031	1160	NA	5.530	F	P	P
5 MPa Test	*C-13*	*88.5*	*0.618*	*4.969*	*4875*	*NA*	*5.890*	*F*	*P*	*F*
	C-23	75.4	0.661	4.999	1360	2.551	2.982	P	P	P
	C-24	81.2	0.642	4.959	3261	2.816	3.840	G	P	G
7.5 MPa Test	C-04	84.6	0.631	7.483	2543	4.213	4.362	G	F	P
10 MPa Tests	C-01	82.7	0.637	9.362	1016	4.866	4.866	P	P	VP
	C-02	82.7	0.637	9.961	1160	5.081	5.081	F	P	VP
	C-03	77.3	0.655	10.10	2359	5.201	5.201	G	P	F
	C-09	*87.6*	*0.621*	*10.03*	*2131*	*NA*	*9.858*	*G*	*P*	*F*
	C-10	*91.2*	*0.609*	*9.978*	*2500*	*NA*	*10.850*	*G*	*P*	*F*
	C-16	104.3	0.566	9.961	748	5.929	6.598	P	P	F
	C-22	95.2	0.596	9.960	3784	5.720	6.486	F	G	G
12.5 MPa Tests	C-25	100.4	0.579	12.49	11130	5.783	6.142	F	P	G
	C-30	114.8	0.531	12.49	3550	7.362	8.782	G	P	P
	C-35	112.8	0.540	12.50	3784	6.577	6.577	P	P	G

CAUC Tests

Test No.	D_r (%)	e	σ'_{1c} (MPa)	σ'_{3c} (MPa)	K_c	E_i (MPa)	Q_{uy} (MPa)	Q_p (MPa)	ACDT Agmt.	Q-ϵ_a Qual.	Stab. Qual.
C-28	92.2	0.606	13.329	7.556	1.95	3880	7.160	7.160	G	G	G
C-29	98.5	0.585	13.641	6.986	1.70	2559	8.030	8.030	G	G	G
C-32	83.8	0.633	9.449	5.572	1.76	2205	5.106	5.256	F	G	F

See page 1 for notes

TABLE 4.8 (page 1 of 2)
SHEAR CHARACTERISTICS - SERIES B
Conditions At or Near Steady State

Test Group	Test No.	D_r (%)	e	I_c (MPa)	Strain (%)	p′ (MPa)	q (MPa)	I_{ss} (MPa)	Δu (MPa)	A	ϕ'	q/I_c
0.1 MPa Tests	10	43.8	0.765	0.102	25.27	1.209	0.648	0.993	-0.460	-0.355	32.4	6.33
	12	86.1	0.626	0.110	22.53	3.353	1.859	2.788	-1.494	-0.402	33.6	16.93
2 MPa Tests	06	65.4	0.694	2.035	25.28	2.291	1.210	1.960	0.837	0.346	30.9	0.59
	07	96.1	0.593	2.030	24.92	4.979	2.616	4.147	-0.406	-0.078	31.4	1.29
	11	67.2	0.688	2.013	22.58	2.619	1.429	2.308	0.585	0.205	30.9	0.71
5 MPa Tests	**01**	**72.7**	**0.670**	**4.982**	**22.40**	**2.888**	**1.595**	**2.371**	**3.714**	**1.164**	**33.4**	**0.32**
	02	104.9	0.564	5.017	22.82	6.356	3.403	5.221	2.038	0.299	32.4	0.68
	05	91.5	0.608	5.009	17.58	5.039	2.618	4.174	2.584	0.493	31.3	0.52
	13	64.5	0.697	5.184	23.09	2.399	1.241	1.986	3.986	1.605	31.2	0.24
	14	92.5	0.605	5.003	16.18	5.154	2.812	4.216	2.652	0.472	33.1	0.56
	15	94.3	0.599	5.033	23.74	6.086	3.027	5.077	1.978	0.327	29.8	0.60
10 MPa Tests	**23**	**89.1**	**0.616**	**10.174**	**8.44**	**5.050**	**2.851**	**4.100**	**8.030**	**1.408**	**34.4**	**0.28**
	24	85.8	0.627	10.027	18.79	4.316	2.673	3.425	8.484	1.587	38.3	0.27

Conditions "at" steady state are highlighted by **boldface** type

TABLE 4.8 (page 2 of 2)
SHEAR CHARACTERISTICS - SERIES C
Conditions at or near Steady State

CIUC Tests

Test Group	Test No.	D_r (%)	e	I_c (MPa)	Strain (%)	p′ (MPa)	q (MPa)	I_{ss} (MPa)	Δu (MPa)	A	ϕ'	q/I_c
0.1 MPa Tests	C-26	68.7	0.683	0.106	22.83	2.511	1.395	2.046	-0.996	-0.357	33.7	13.16
	C-31	67.2	0.688	0.115	24.79	2.423	1.306	1.988	-0.999	-0.388	32.6	11.36
	C-34	**94.9**	**0.597**	**0.077**	**25.63**	**4.911**	**2.700**	**4.011**	**-2.131**	**-0.395**	**33.4**	**35.06**
2 MPa Tests	C-15	56.0	0.725	1.948	26.14	1.517	0.853	1.233	1.289	0.770	34.2	0.44
	C-27	63.5	0.700	1.972	27.04	1.980	1.073	1.622	1.064	0.505	32.8	0.55
	C-33	93.4	0.602	2.031	22.43	4.863	2.678	3.970	-0.147	-0.028	33.4	1.32
5 MPa Tests	C-23	75.5	0.661	5.010	18.08	2.868	1.490	2.371	3.614	1.226	32.4	0.30
	C-24	**81.2**	**0.642**	**4.979**	**25.04**	**3.494**	**1.908**	**2.859**	**3.361**	**0.894**	**33.1**	**0.38**
7.5 MPa Test	C-04	84.6	0.631	7.529	23.08	3.554	1.889	2.924	5.834	1.602	32.1	0.25
10 MPa Tests	**C-01**	**82.7**	**0.637**	**9.375**	**10.04**	**4.331**	**2.316**	**3.559**	**7.481**	**1.630**	**32.3**	**0.25**
	C-02	**82.7**	**0.637**	**9.921**	**8.50**	**4.208**	**2.411**	**3.404**	**8.101**	**1.691**	**35.0**	**0.24**
	C-03	77.3	0.655	10.108	19.08	4.392	2.505	3.557	8.147	1.635	34.8	0.25
	C-16	**104.3**	**0.566**	**9.968**	**19.71**	**5.232**	**3.299**	**4.133**	**8.046**	**1.223**	**39.1**	**0.33**
	C-22	95.3	0.596	9.991	24.10	5.943	3.187	4.881	7.321	1.157	32.4	0.32
12.5 MPa Test	C-25	100.4	0.579	12.534	25.67	5.384	2.934	4.406	10.073	1.733	33.0	0.23
	C-35	**113.2**	**0.540**	**12.527**	**20.64**	**5.535**	**3.182**	**4.474**	**10.152**	**1.617**	**35.1**	**0.25**

CAUC Tests

Test No.	D_r (%)	e	I_c (MPa)	K_c	Strain (%)	p′ (MPa)	q (MPa)	I_{ss} (MPa)	Δu (MPa)	ϕ'	q/I_c
C-28	**92.1**	**0.606**	**9.480**	**1.76**	**14.95**	**5.573**	**3.072**	**4.549**	**5.503**	**33.5**	**0.41**
C-29	**98.5**	**0.585**	**9.204**	**1.95**	**15.10**	**5.803**	**3.259**	**4.716**	**4.607**	**34.2**	**0.47**
C-32	83.9	0.633	7.529	1.70	23.08	4.764	2.604	3.896	3.412	33.1	0.47

Conditions "at" steady state are highlighted by boldface type

TABLE 4.9 (page 1 of 2)
SHEAR CHARACTERISTICS - SERIES B
Steady State Parameters

Test Group	Test No.	D_r (%)	e	I'_c (MPa)	Measured I'_{ss} (MPa)	Calculated I'_{ss} (MPa)	Cal. Ψ	Shear Parameters ϕ'_{max}	A_f	q_{max}/I'_c
0.1 MPa Tests	B-08	83.0	0.636	0.104	NA	3.081	-0.373	40.1	NA	NA
	B-09	82.7	0.637	0.114	NA	3.054	-0.362	38.5	NA	NA
	B-10	43.8	0.765	0.102	0.993	0.956	-0.246	37.5	-0.318	6.77
	B-12	86.1	0.626	0.110	2.788	3.574	-0.377	49.4	-0.352	18.24
	B-22	94.0	0.600	0.122	NA	4.272	-0.392	56.4	-0.419	19.68
2 MPa Tests	B-06	65.4	0.694	2.035	1.960	1.820	0.020	34.2	0.361	0.63
	B-07	96.1	0.593	2.030	4.147	4.553	-0.089	35.8	-0.045	1.43
	B-11	67.2	0.688	2.013	2.308	1.920	0.005	36.0	0.226	0.77
5 MPa Tests	B-01	72.7	0.670	4.982	2.371	2.263	0.087	34.3	1.167	0.32
	B-05	91.5	0.608	5.009	4.174	3.973	0.026	34.5	0.491	0.56
	B-13	64.5	0.697	5.184	1.986	1.771	0.118	37.5	1.354	0.29
	B-14	92.5	0.605	5.003	4.216	4.083	0.022	35.7	0.481	0.58
	B-15	94.3	0.599	5.033	5.077	4.311	0.017	34.5	0.320	0.69

TABLE 4.9 (page 2 of 2)
SHEAR CHARACTERISTICS - SERIES C
Steady State Parameters

CIUC Tests

Test Group	Test No.	D_r (%)	e	I'_c (MPa)	Measured I'_{ss} (MPa)	Calculated I'_{ss} (MPa)	Cal. Ψ	Shear Parameters ϕ'_{max}	A_f	q_{max}/I'_c
0.1 MPa Tests	C-26	68.7	0.683	0.106	2.046	2.011	-0.324	44.1	-0.357	13.16
	C-31	67.2	0.688	0.115	1.988	1.922	-0.310	38.6	-0.374	11.43
	C-34	94.9	0.597	0.077	4.011	4.390	-0.445	42.5	-0.377	35.59
2 MPa Tests	C-15	56.0	0.725	1.948	1.233	1.374	0.038	38.2	0.754	0.46
	C-27	63.5	0.700	1.972	1.622	1.724	0.015	34.8	0.505	0.55
	C-33	93.4	0.602	2.031	3.970	4.195	-0.080	35.6	-0.012	1.36
5 MPa Tests	C-23	75.5	0.661	5.010	2.371	2.456	0.079	32.3	1.228	0.30
	C-24	81.2	0.642	4.979	2.859	2.918	0.059	34.1	0.894	0.39
7.5 MPa Test	C-04	84.6	0.631	7.529	2.924	3.225	0.093	36.6	1.417	0.29

TABLE 4.10
SHEAR CHARACTERISTICS - SERIES C: CIDC TESTS
Steady State Parameters

Test Group	Test No.	D_r (%)	e	I'_c (MPa)	Measured I'_{ss} (MPa)	Calculated I'_{ss} (MPa)	Cal. Ψ	Shear Parameters ϕ'_{max}	Shear Parameters $(\Delta\epsilon_v/\Delta\epsilon_a)_{max}$ (%)
0.1 MPa Tests	C-14	86.1	0.626	0.163	NA	3.374	-0.334	56.0	0.649
	C-17	31.0	0.807	0.125	NA	0.653	-0.182	35.0	0.140
	C-18	29.8	0.811	0.106	NA	0.629	-0.196	42.0	0.142
	C-19	31.7	0.805	0.099	NA	0.665	-0.211	37.5	0.166
	C-20	78.2	0.652	0.096	NA	2.665	-0.366	47.0	0.755
	C-21	84.3	0.632	0.098	NA	3.195	-0.383	48.0	0.789
2 MPa Tests	C-11	71.2	0.675	1.936	NA	2.163	-0.012	37.1	0.151

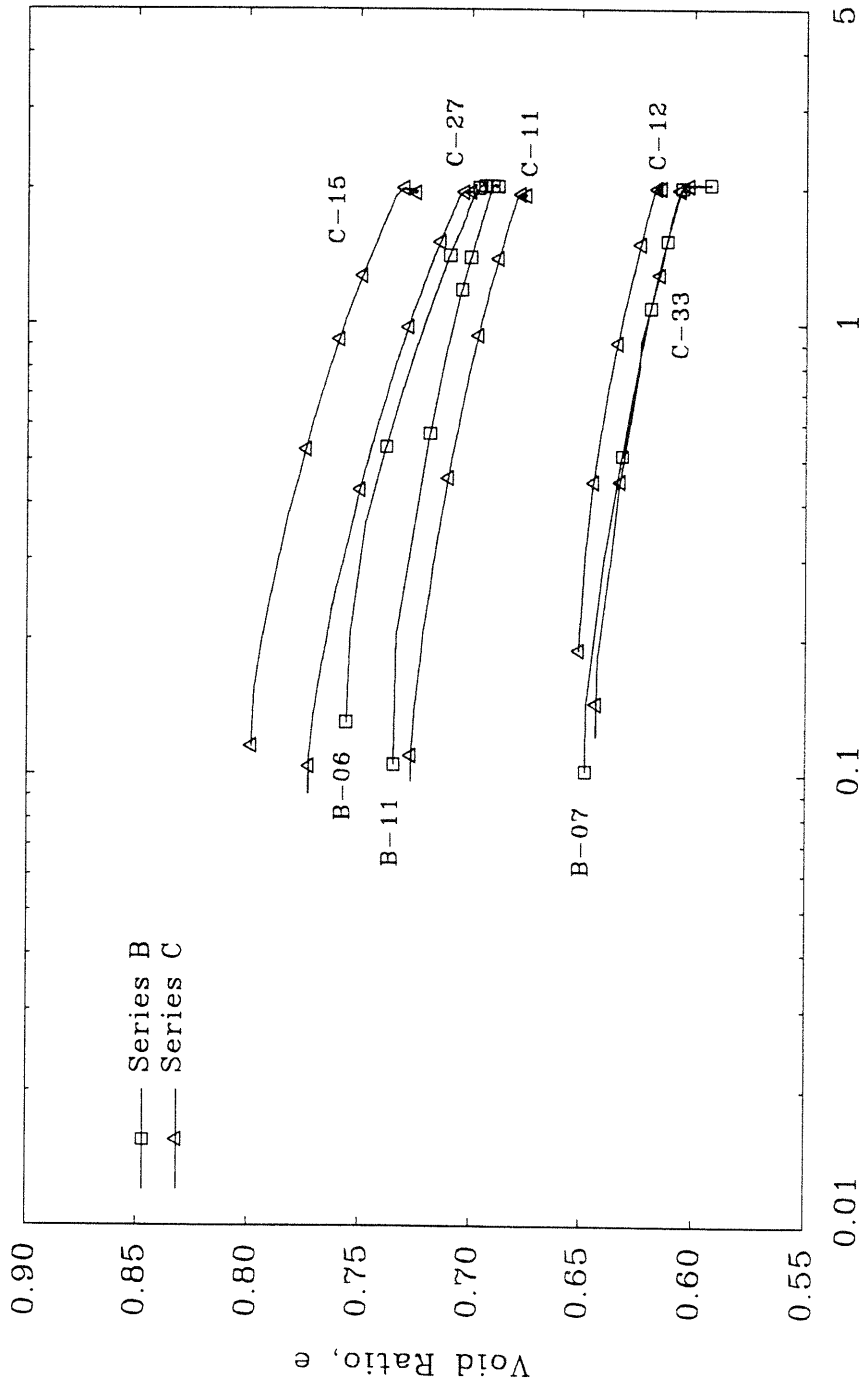

Figure 4.1 Void Ratio versus Effective Stress for Consolidation of MFS: σ'_c = 2 MPa

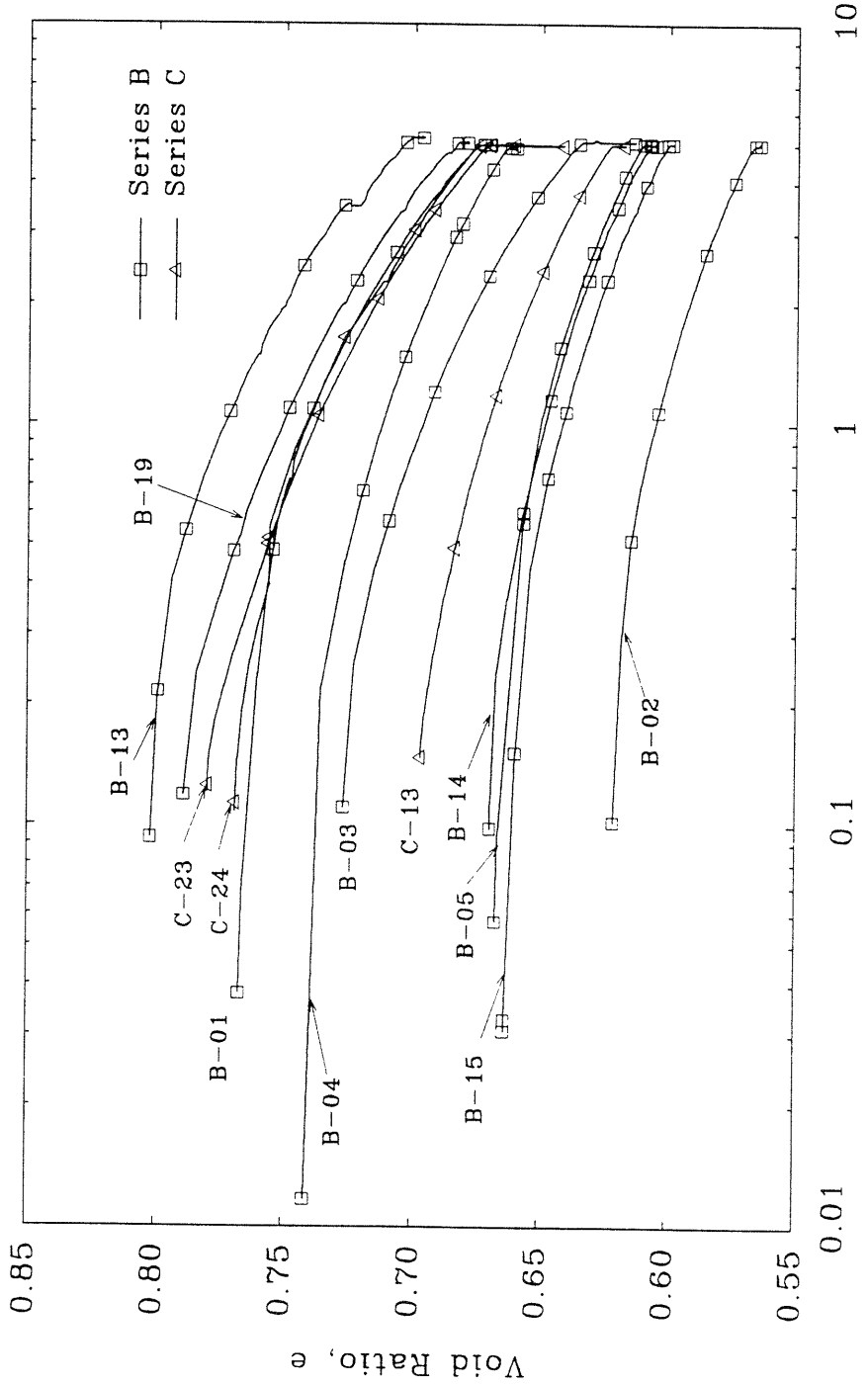

Figure 4.2 Void Ratio versus Effective Stress for Consolidation of MFS: σ'_c = 5 MPa

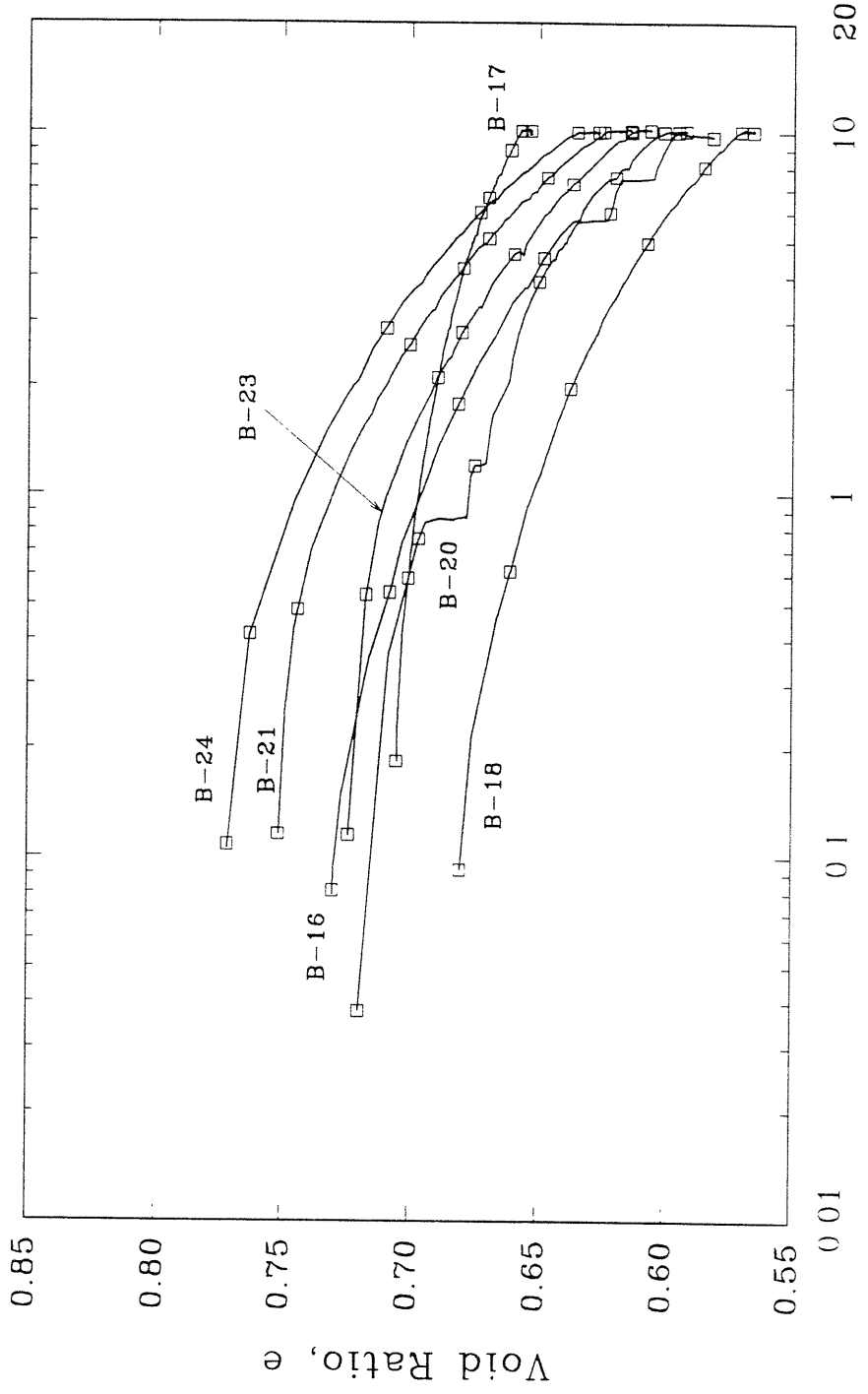

Figure 4.3a Void Ratio versus Effective Stress for Isotropic Consolidation of MFS: σ'_c = 10 MPa, Series B Tests

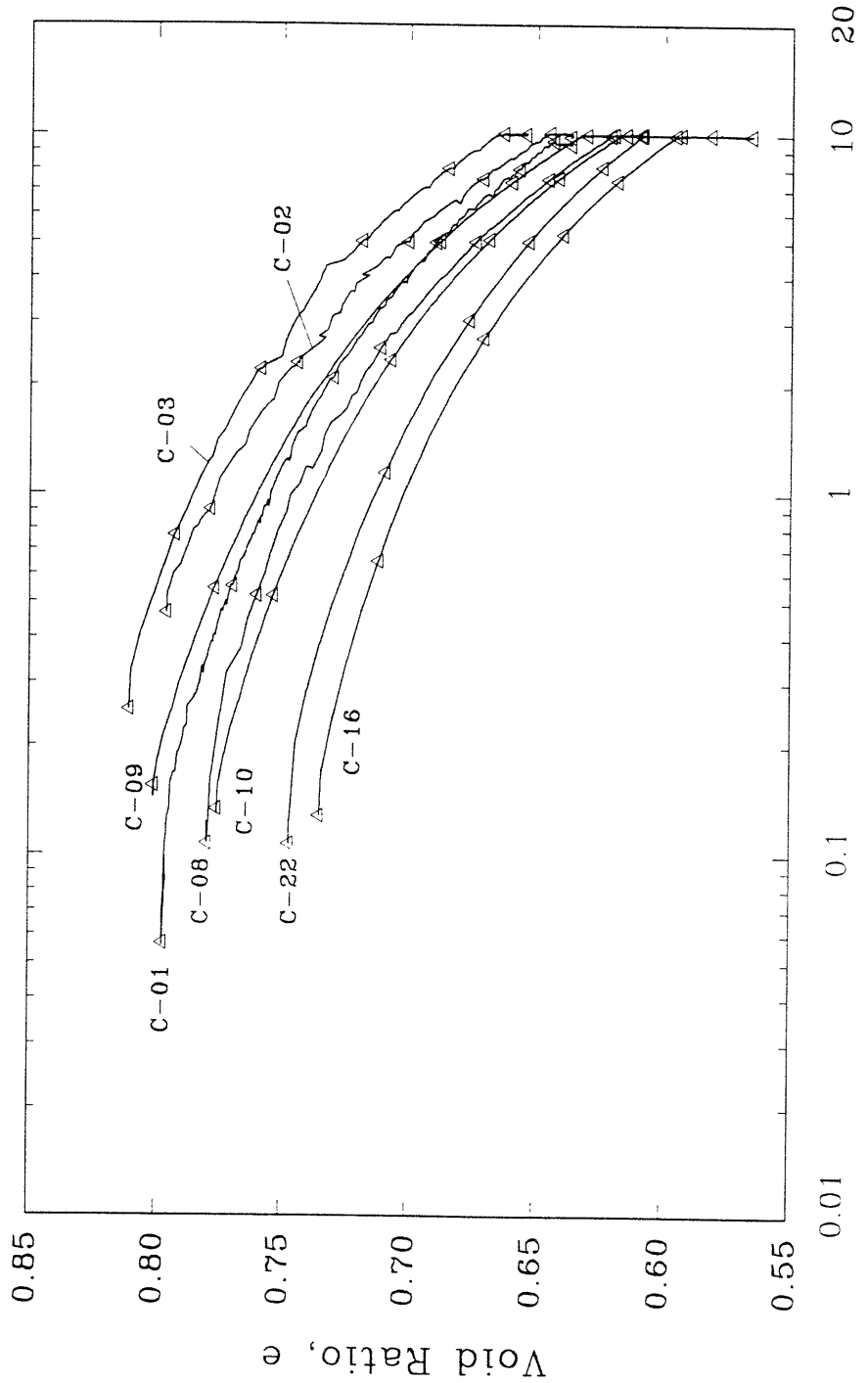

Figure 4.3b Void Ratio versus Effective Stress for Isotropic Consolidation of MFS: σ'_c = 10 MPa, Series C Tests

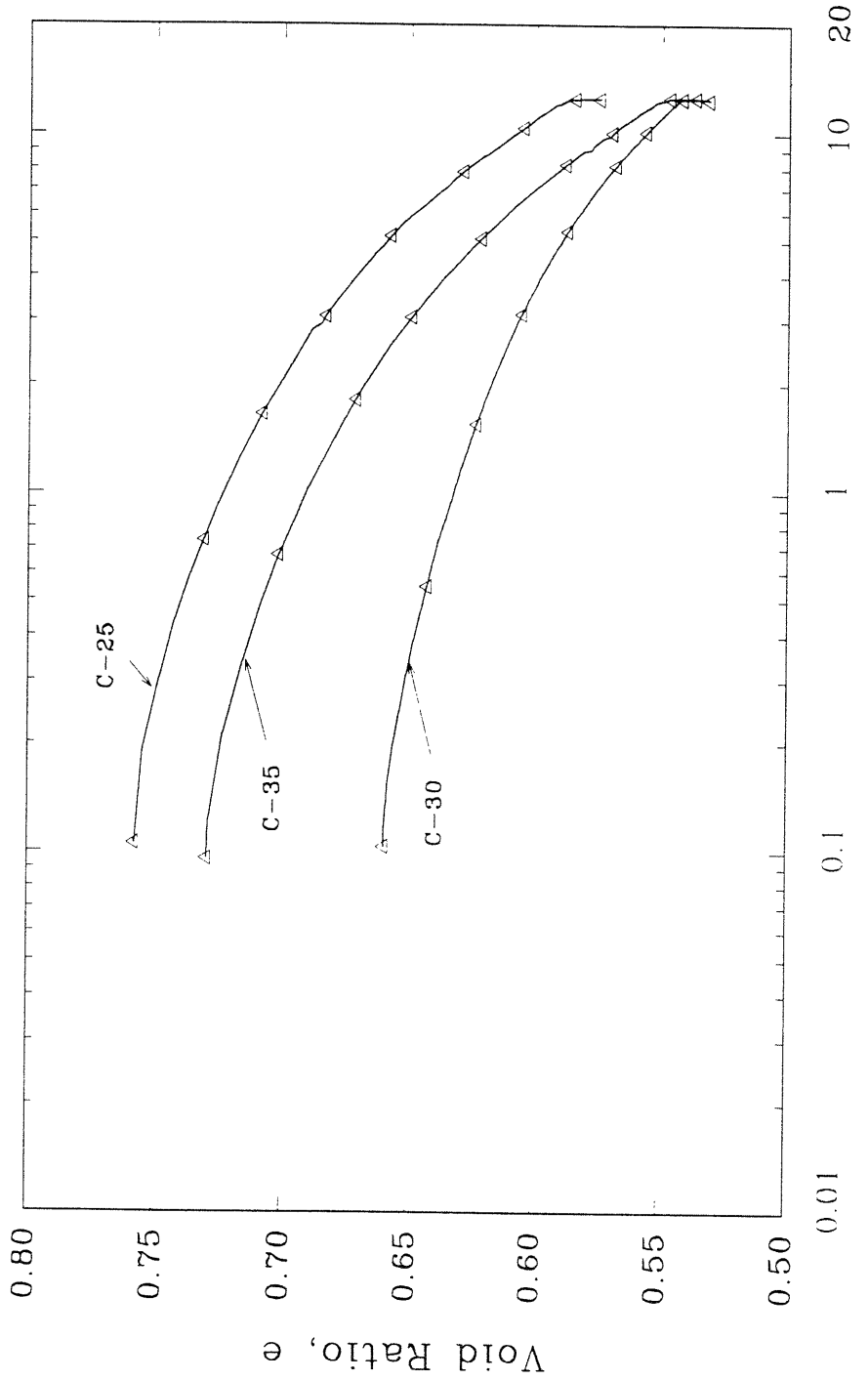

Figure 4.4 Void Ratio versus Effective Stress for Isotropic Consolidation of MFS: σ'_c = 12.5 MPa

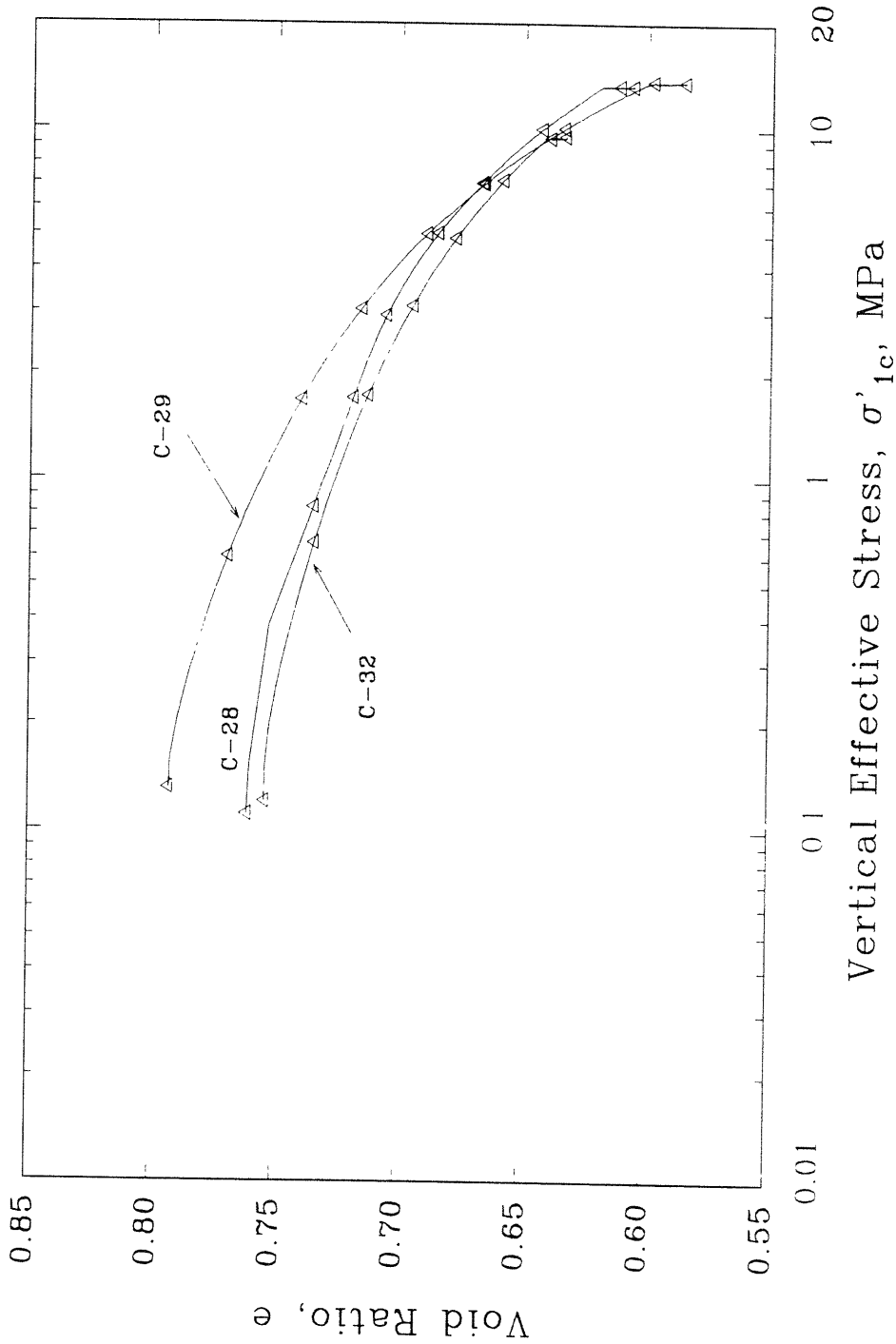

Figure 4.5 Void Ratio versus Vertical Effective Stress for Anisotropic Consolidation of MFS

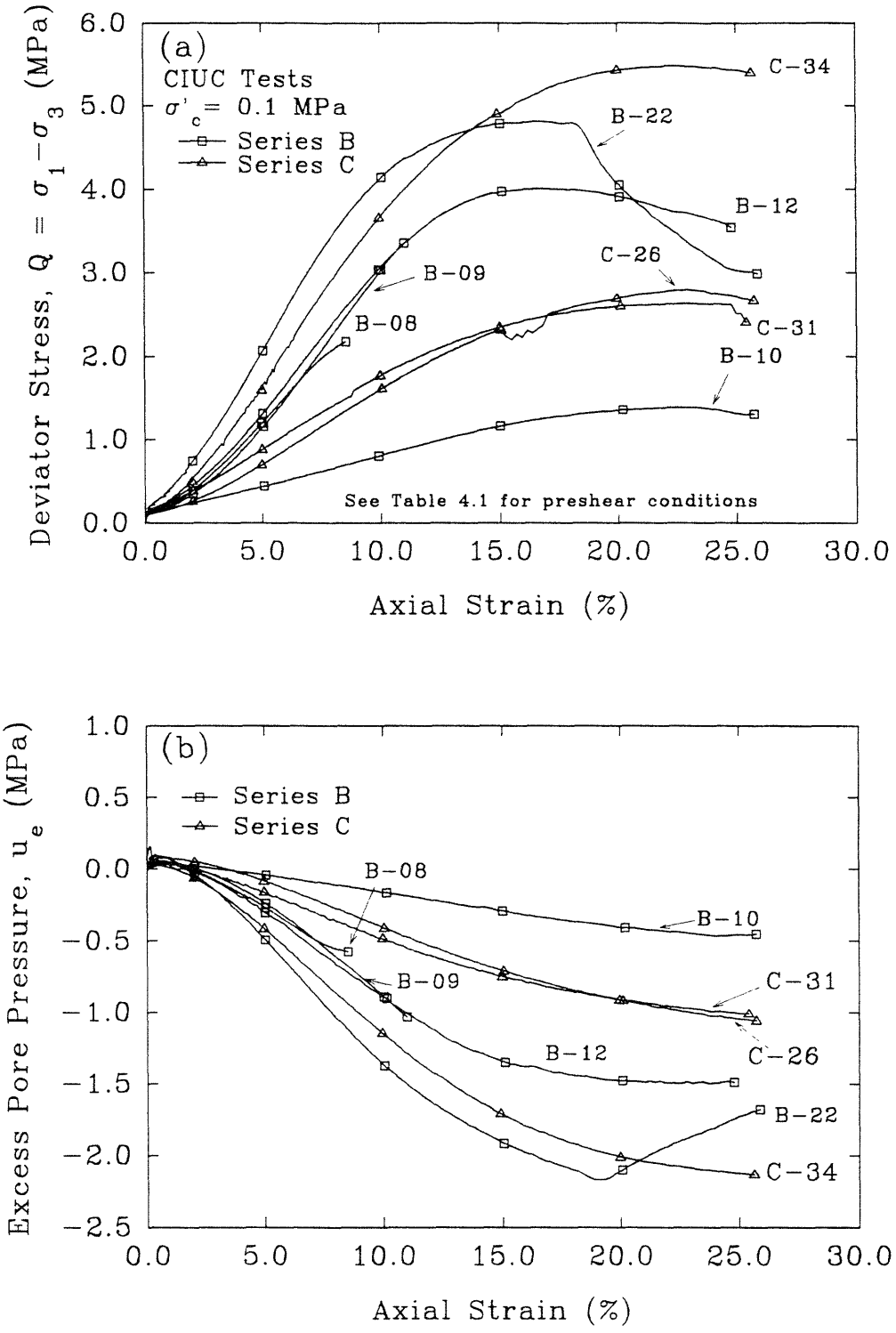

Figure 4.6 Deviator Stress and Excess Pore Pressure versus Axial Strain for Unfrozen CIUC Tests with σ'_c = 0.1 MPa: Series B and C Tests

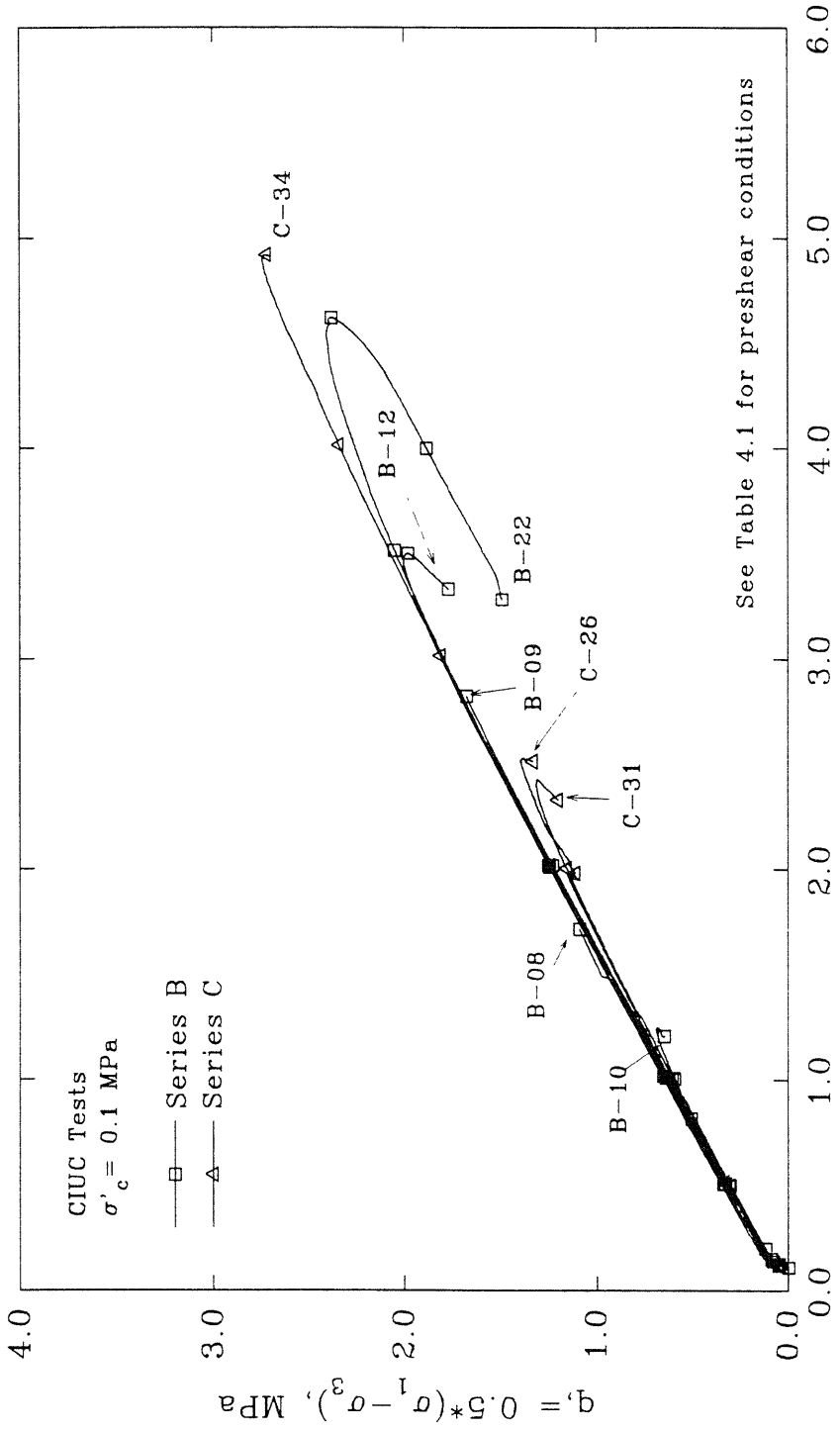

Figure 4.7 Effective Stress Paths for Unfrozen MFS
CIUC Tests with σ'_c = 0.1 MPa : All Series

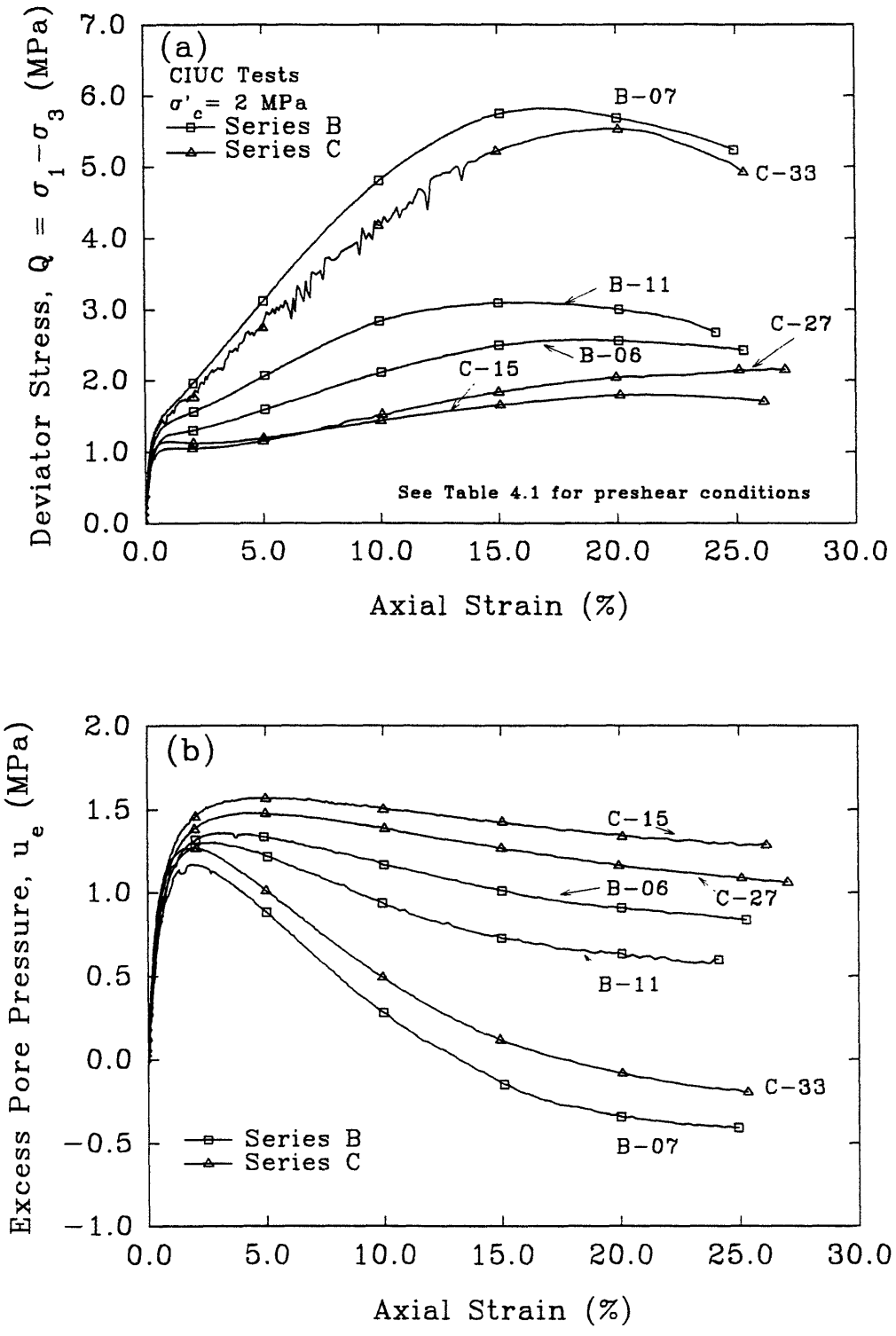

Figure 4.8 Deviator Stress and Excess Pore Pressure versus Axial Strain for Unfrozen CIUC Tests with σ'_c = 2 MPa: Series B and C Tests

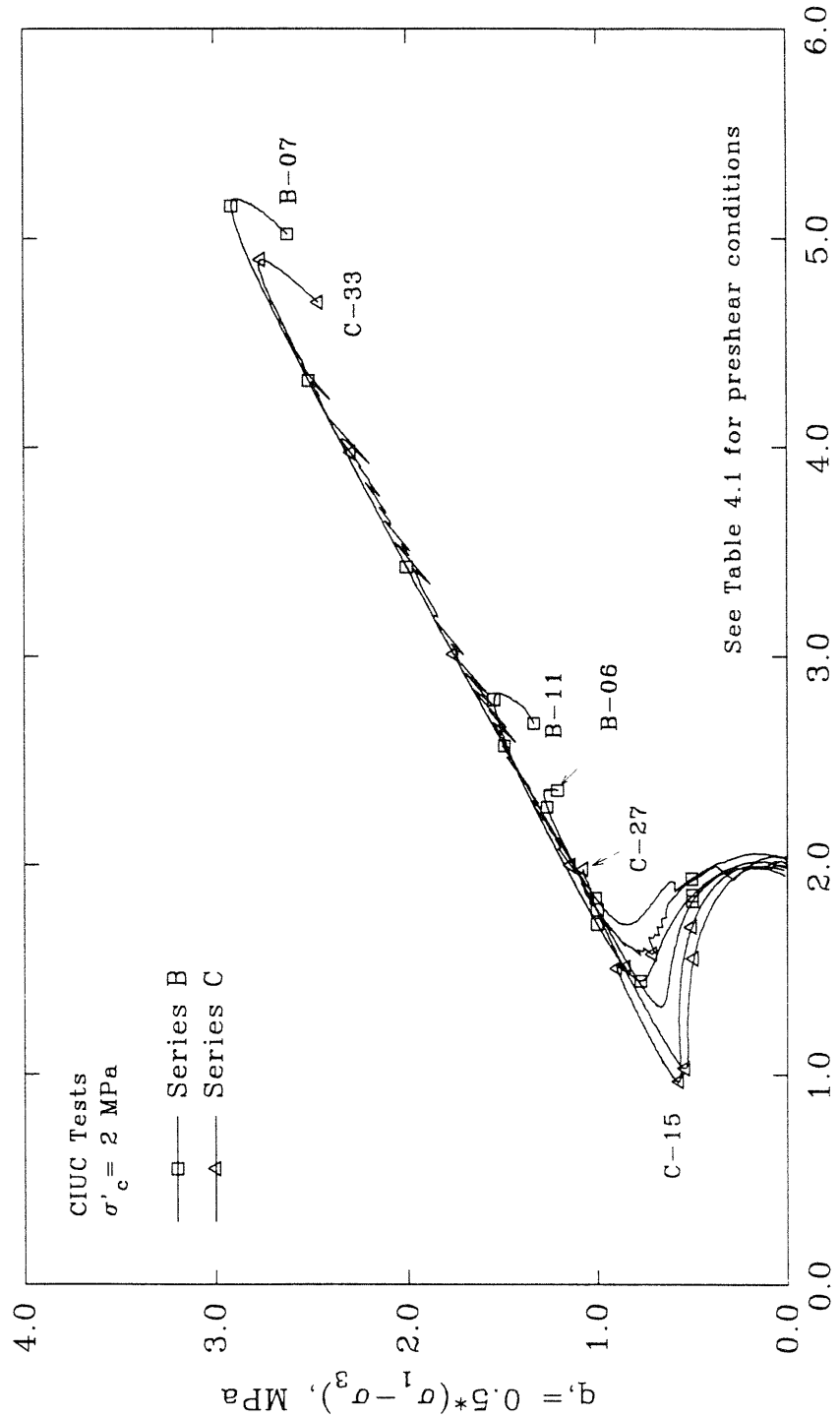

Figure 4.9 Effective Stress Paths for Unfrozen MFS CIUC Tests with σ_c' = 2 MPa : All Series

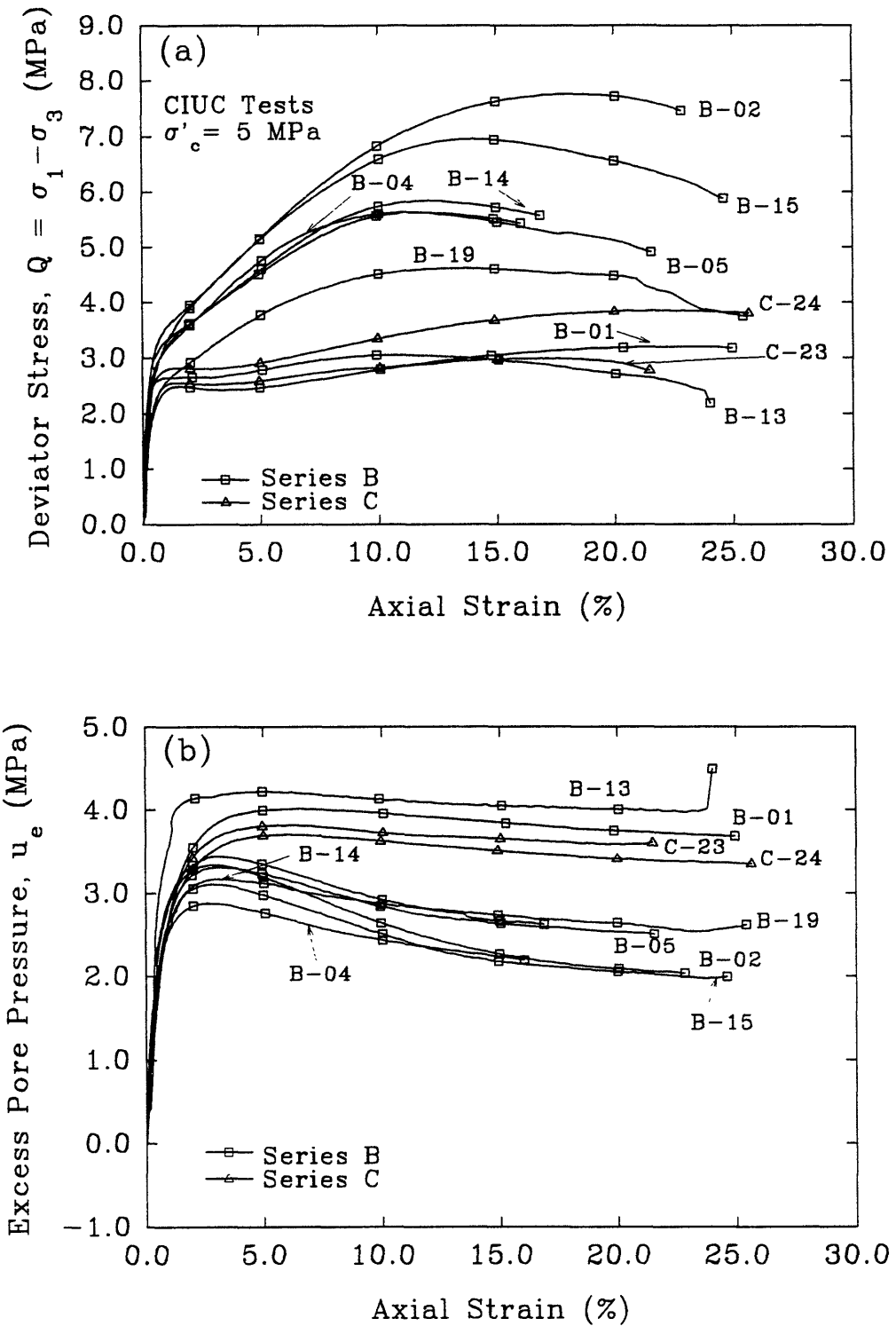

Figure 4.10 Deviator Stress and Excess Pore Pressure versus Axial Strain for Unfrozen CIUC Tests with σ'_c= 5 MPa: Series B and C Tests

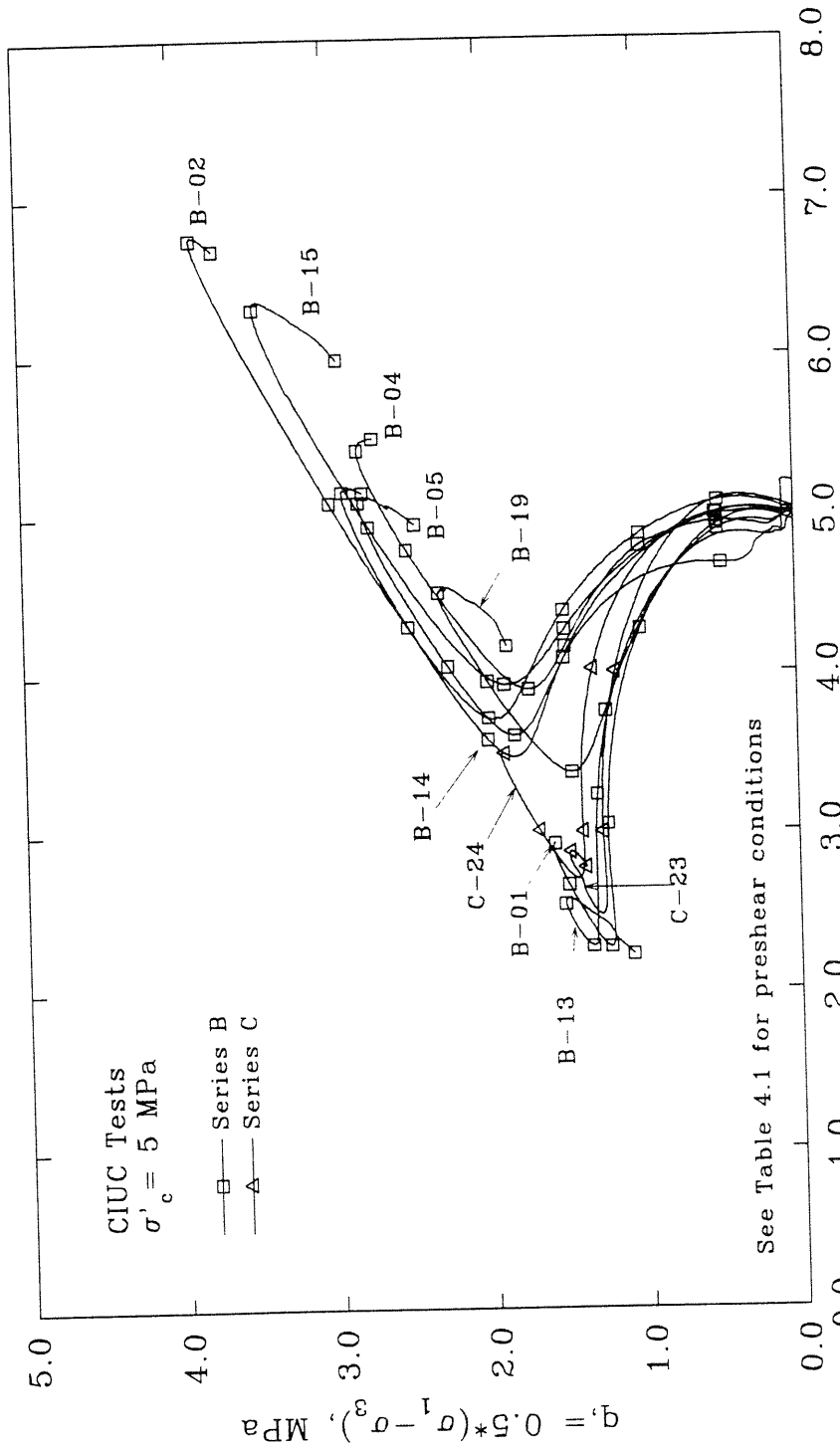

Figure 4.11 Effective Stress Paths for Unfrozen MFS CIUC Tests with σ'_c = 5 MPa : Series B and C Tests

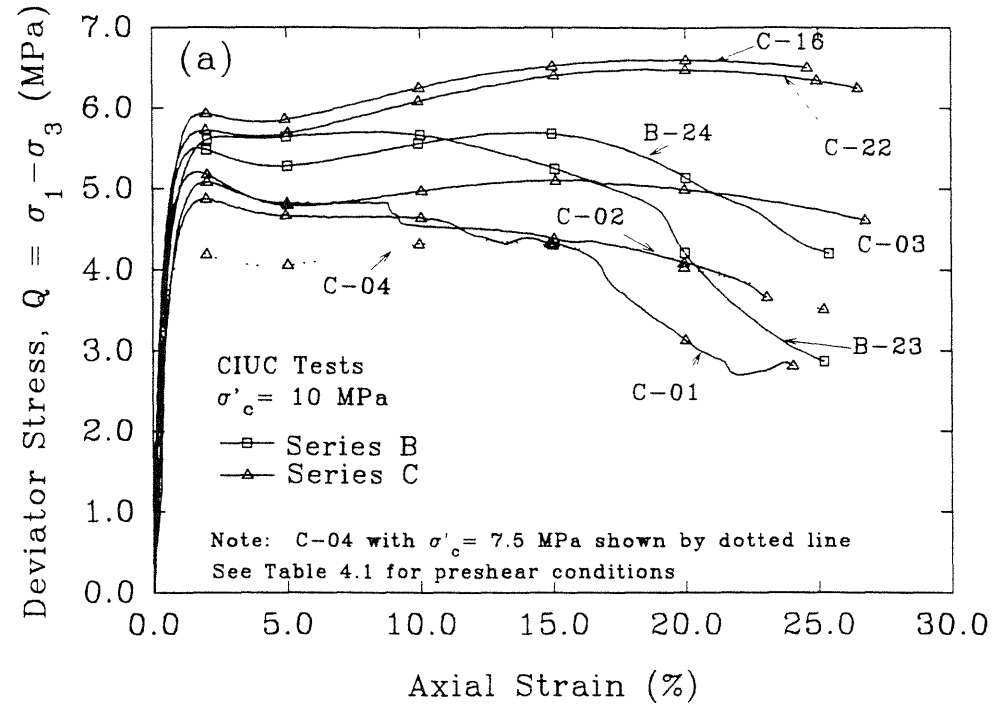

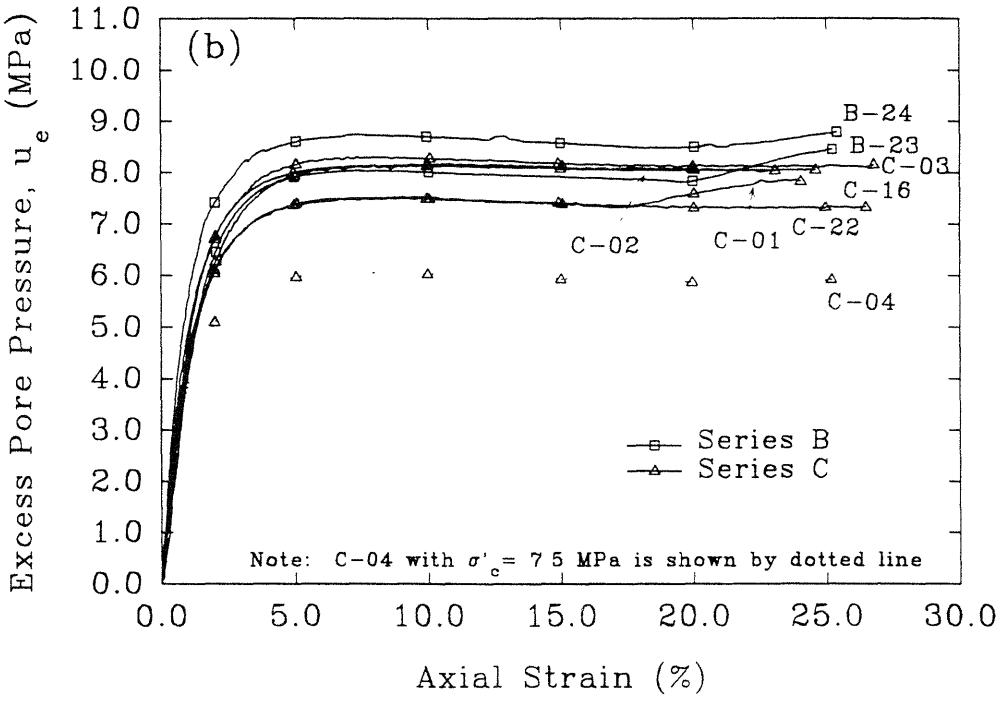

Figure 4.12 Deviator Stress and Excess Pore Pressure versus Axial Strain for Unfrozen CIUC Tests with σ'_c= 10 MPa: Series B and C Tests

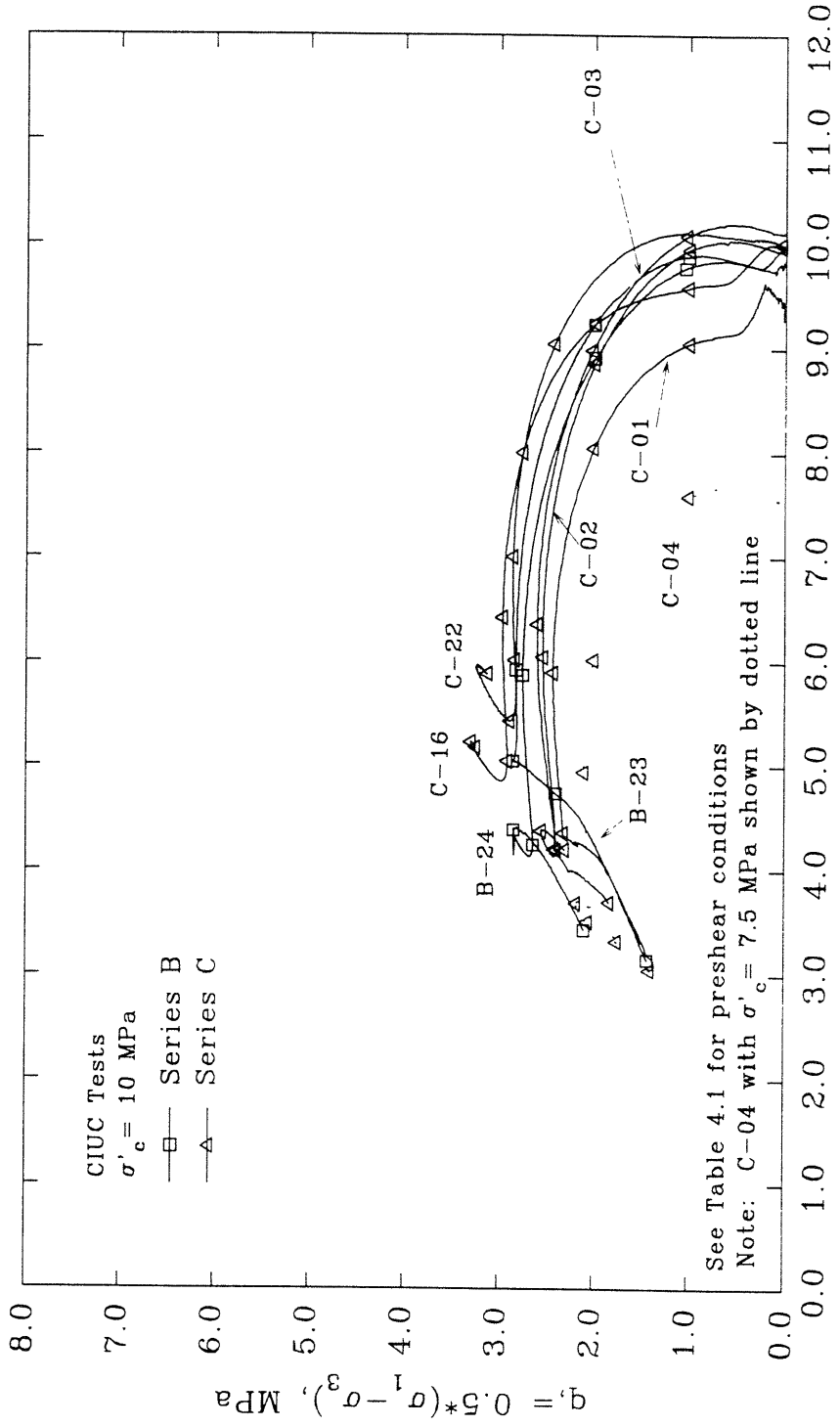

Figure 4.13 Effective Stress Paths for Unfrozen MFS CIUC Tests with σ'_c = 10 MPa: Series B and C Tests

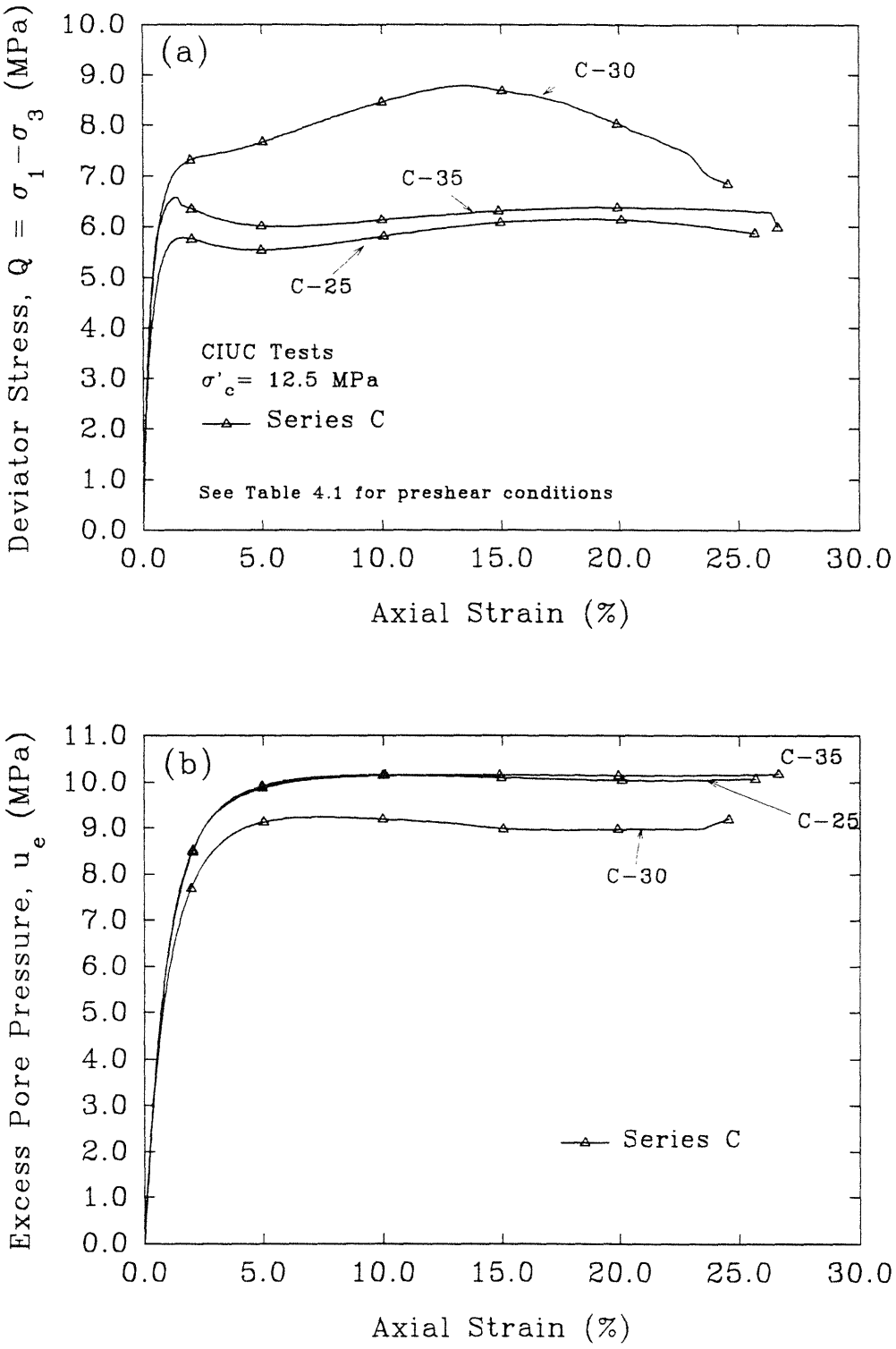

Figure 4.14 Deviator Stress and Excess Pore Pressure versus Axial Strain for Unfrozen CIUC Tests with σ'_c = 12.5 MPa: Series C Tests

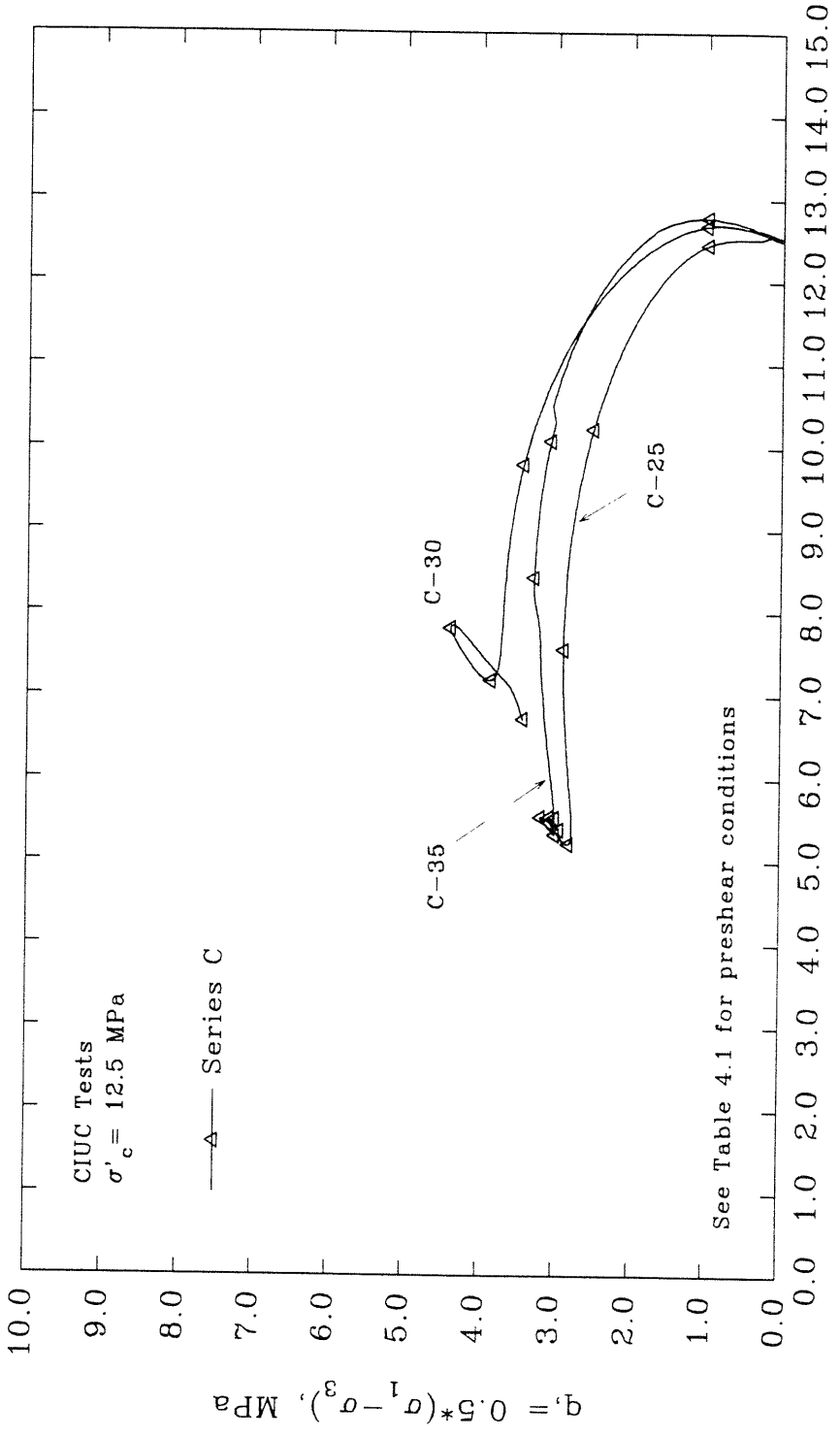

Figure 4.15 Effective Stress Paths for Unfrozen MFS CIUC Tests with σ'_c = 12.5 MPa

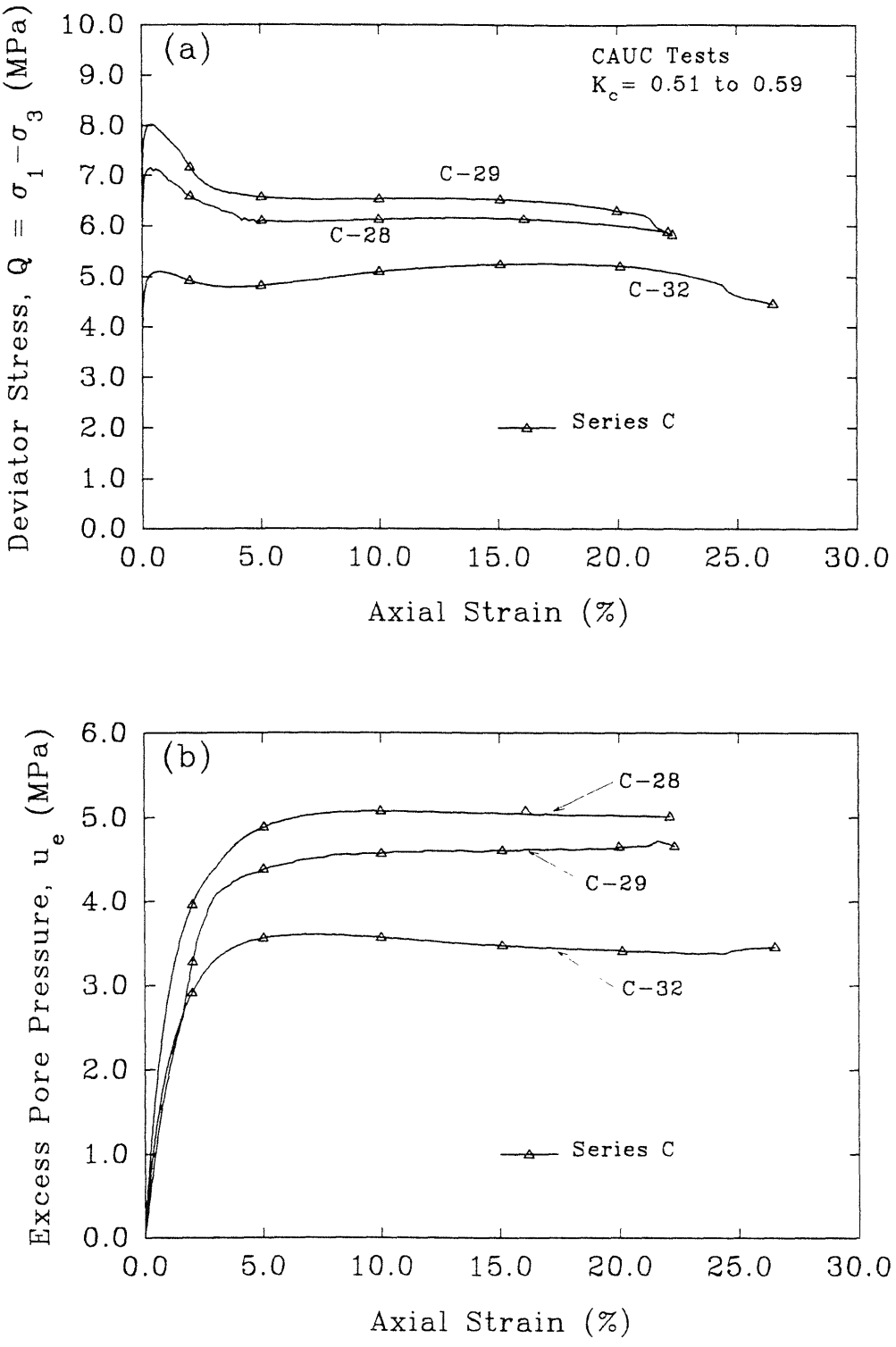

Figure 4.16 Deviator Stress and Excess Pore Pressure versus Axial Strain for Unfrozen CAUC Tests

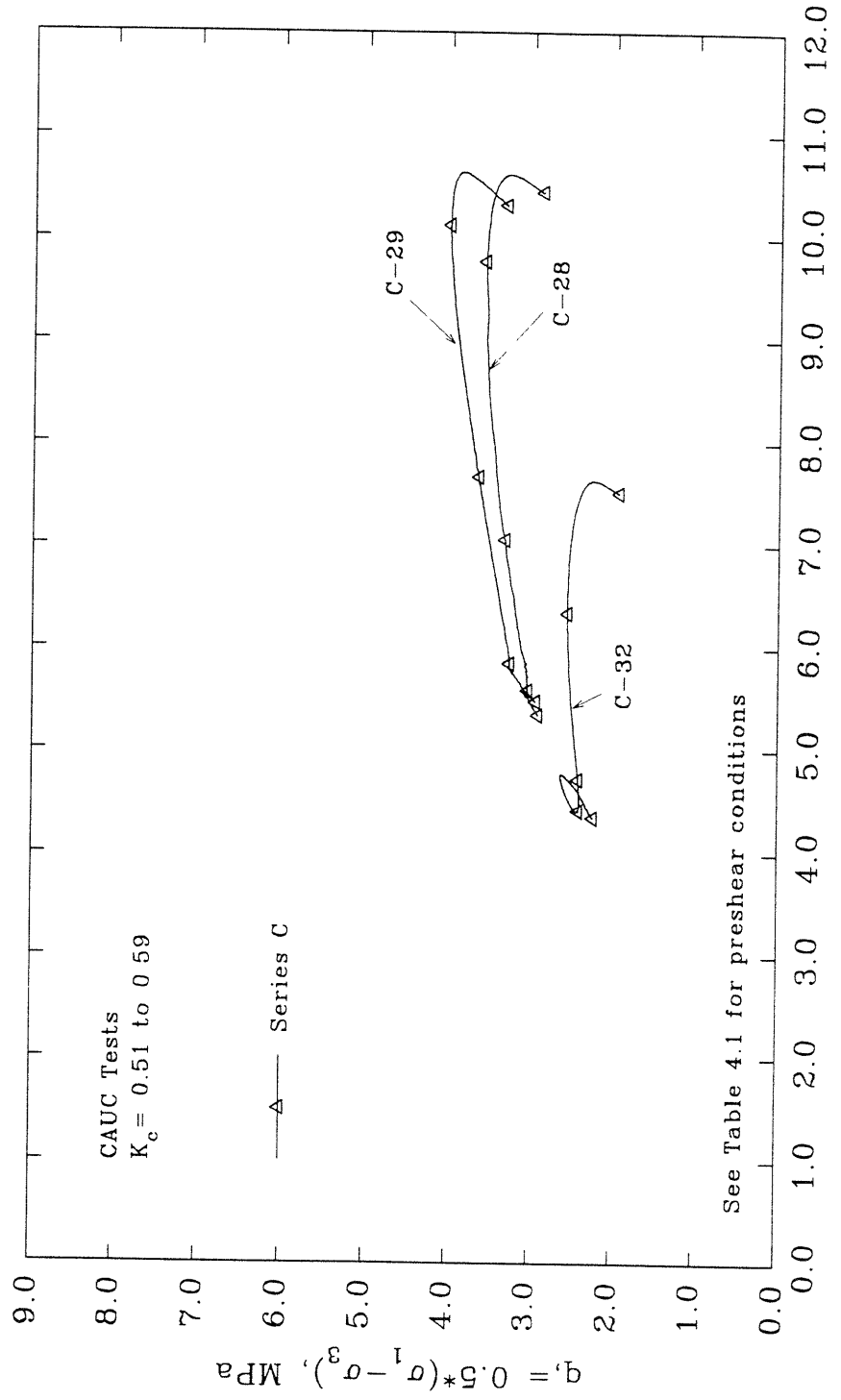

Figure 4.17 Effective Stress Paths for Unfrozen MFS CAUC Tests

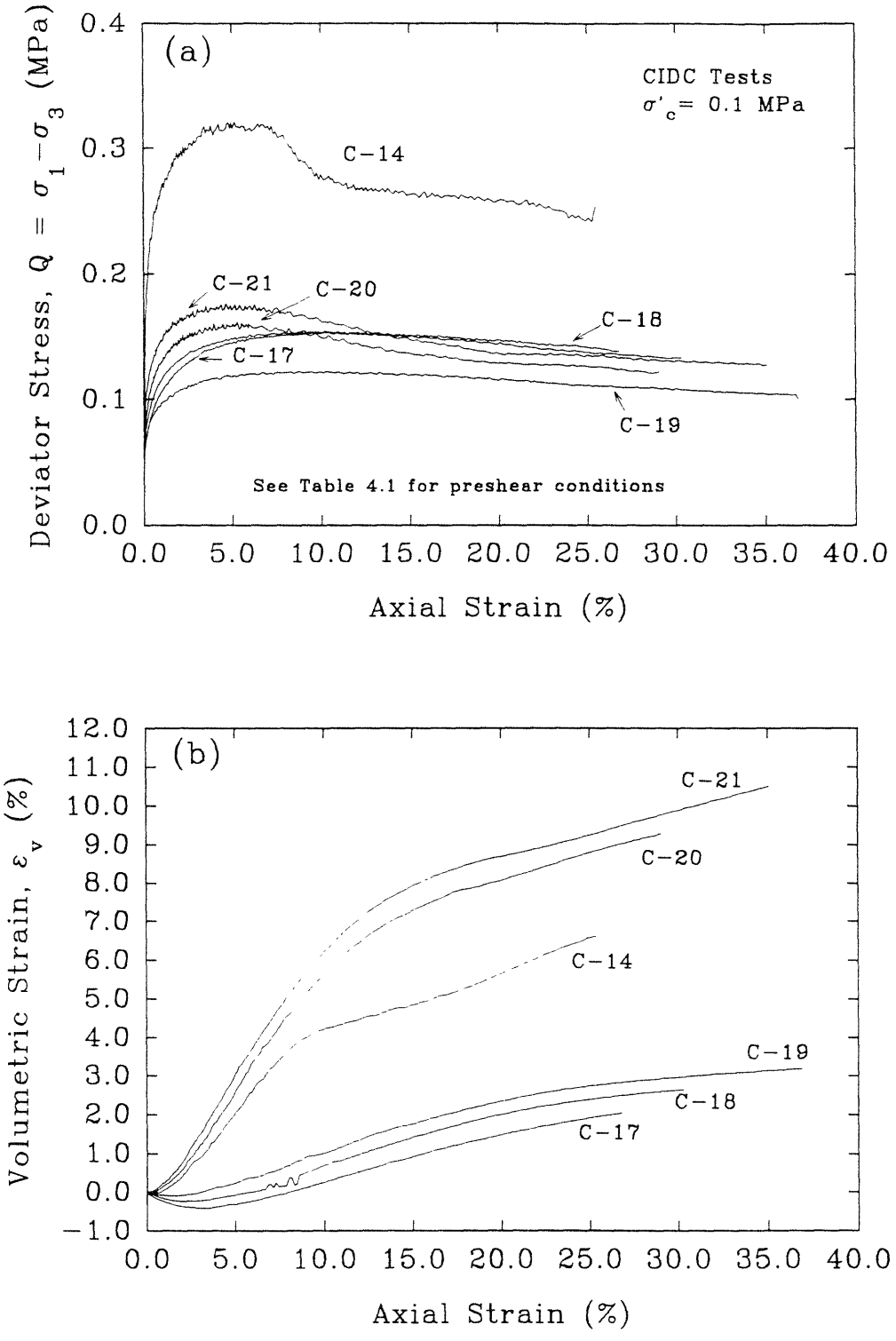

Figure 4.18 Deviator Stress and Volumetric Strain versus Axial Strain for Unfrozen CIDC Tests with σ'_c= 0.1 MPa: Series C Tests

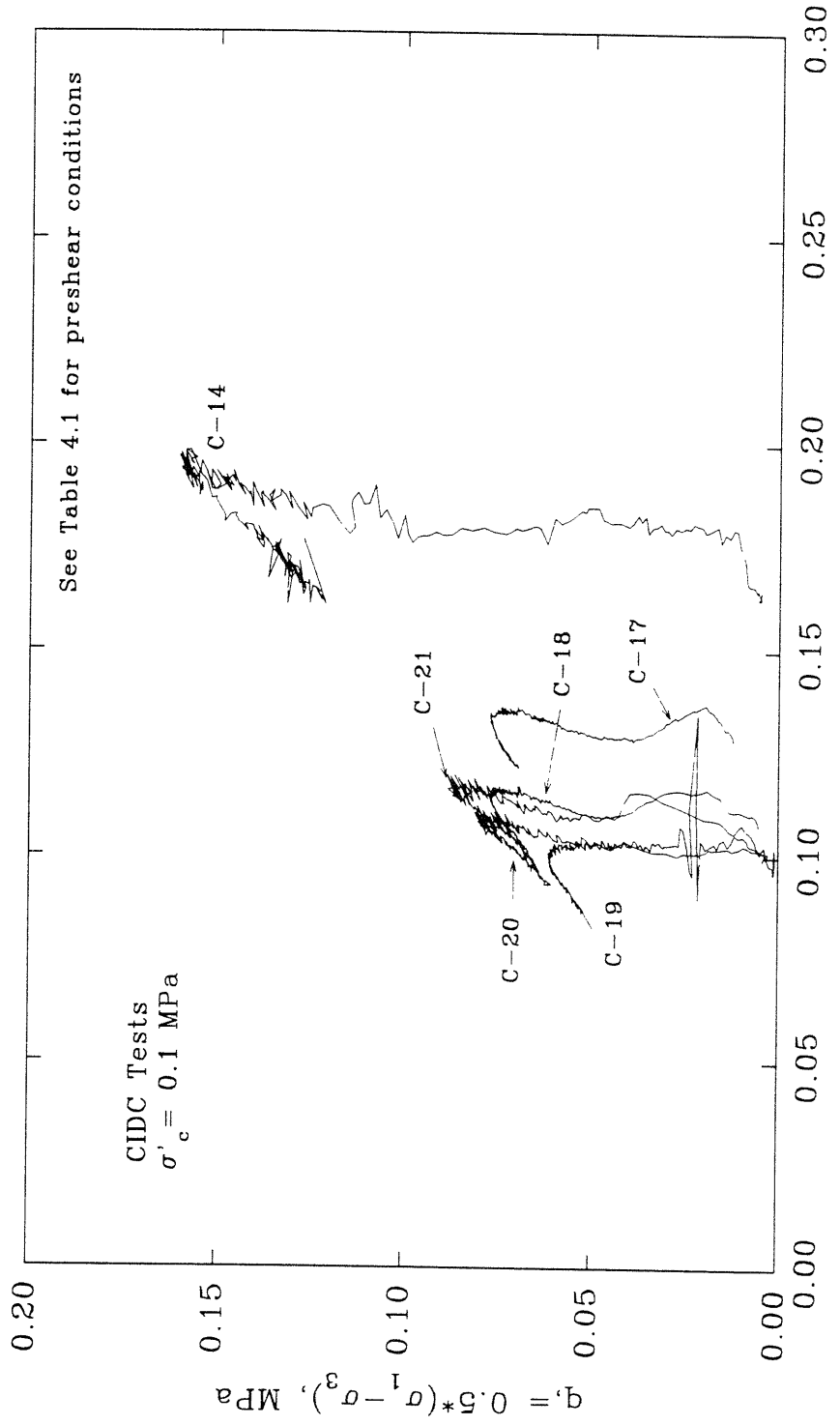

Figure 4.19 Effective Stress Paths for Unfrozen MFS CIDC Tests with σ_c' = 0.1 MPa : Series C Tests

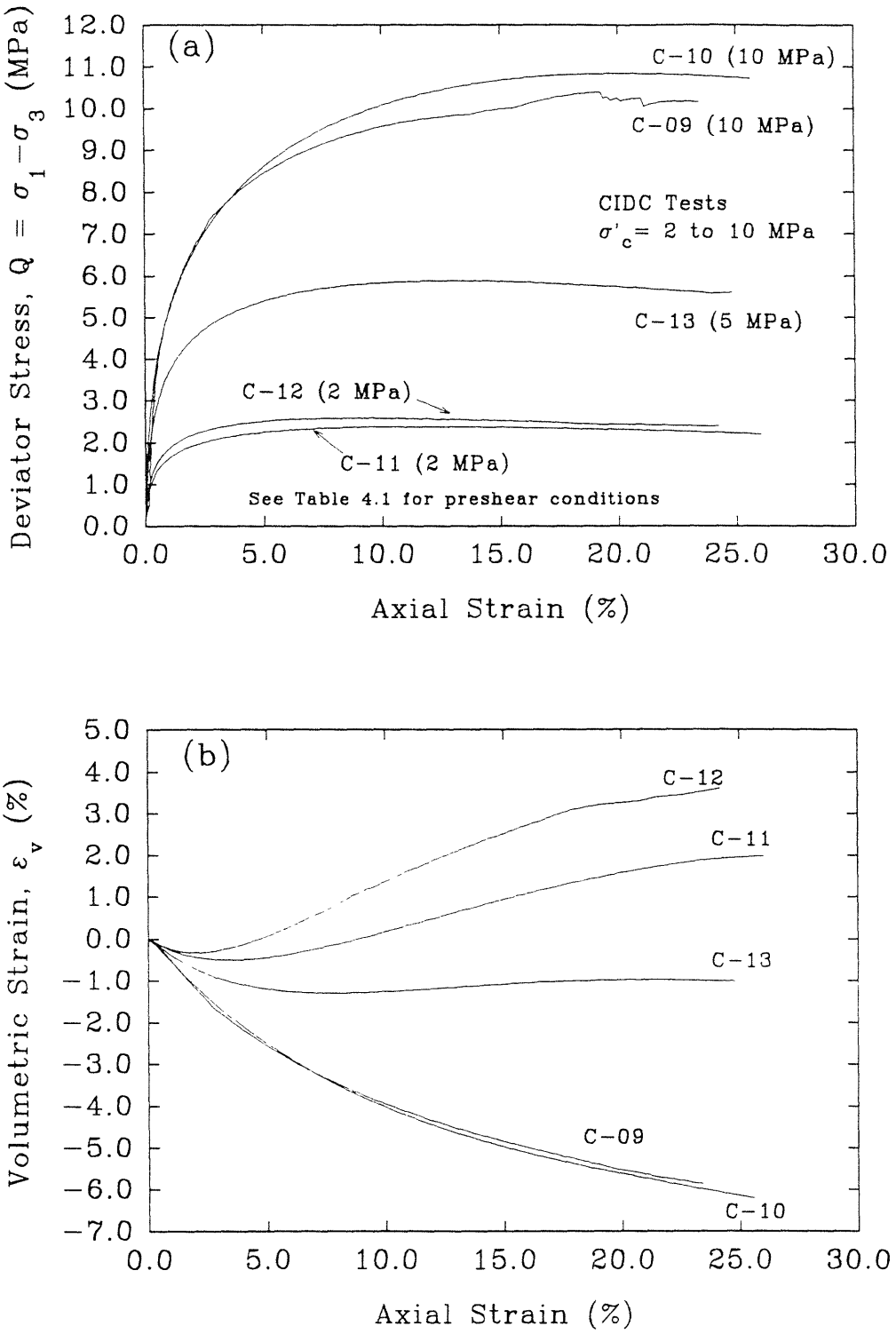

Figure 4.20 Deviator Stress and Volumetric Strain versus Axial Strain for Unfrozen CIDC Tests with σ'_c= 2, 5 and 10 MPa: Series C Tests

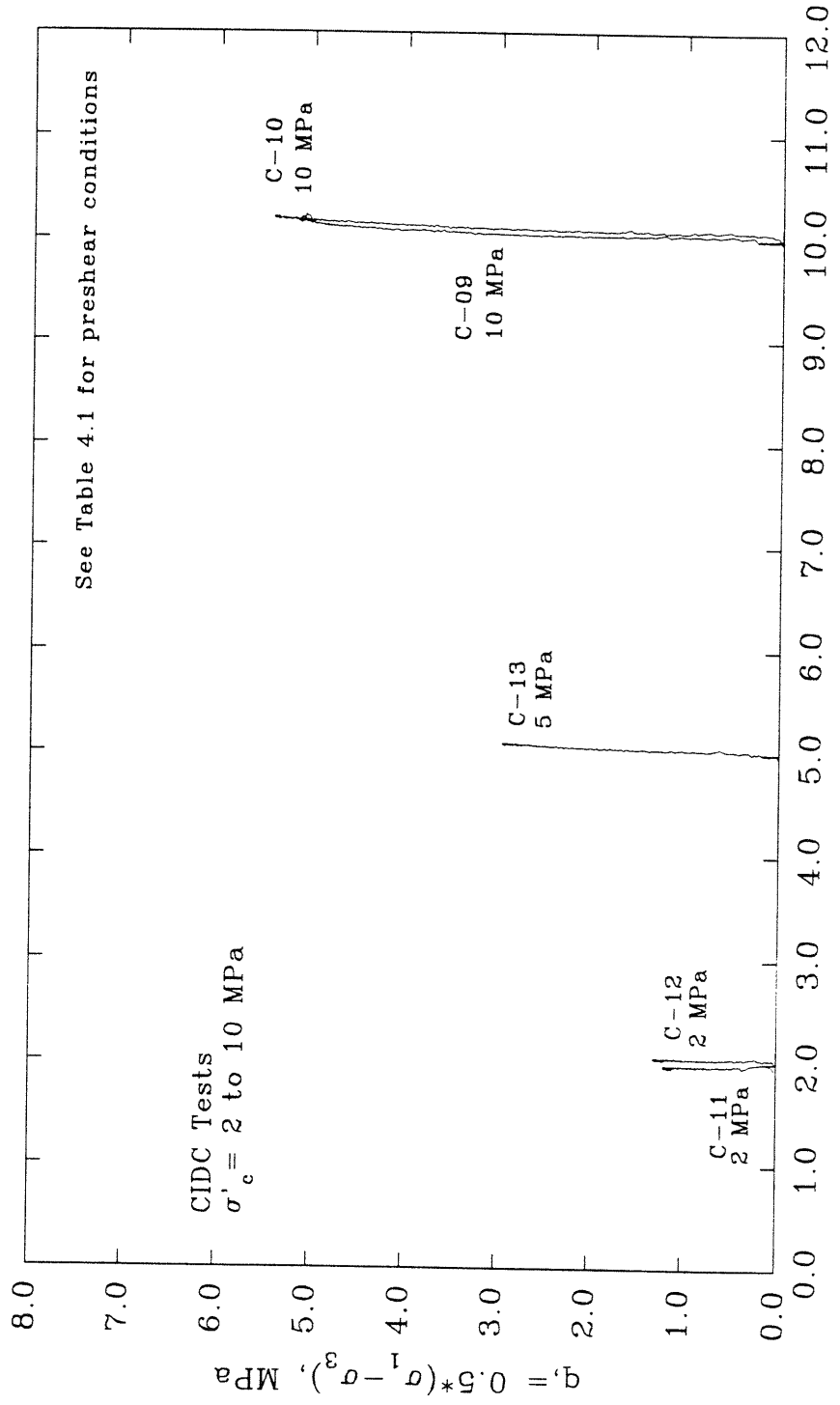

Figure 4.21 Effective Stress Paths for Unfrozen MFS – CIDC Tests with σ_c' = 2 to 10 MPa : Series C Tests

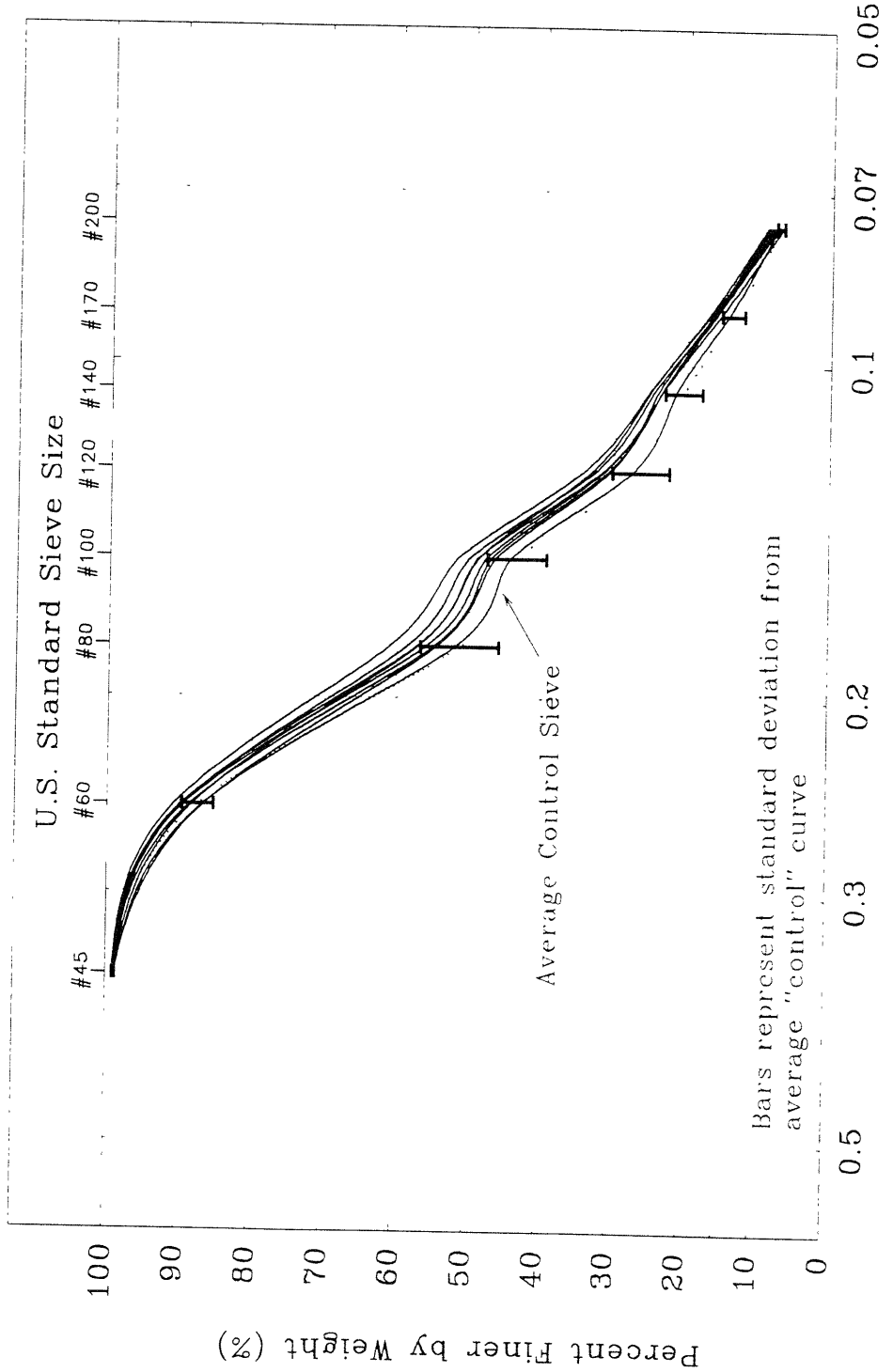

Figure 4.22 Post–Shear Particle Size Distributions of Unfrozen MFS for CIUC Tests at σ'_c = 0.1 MPa

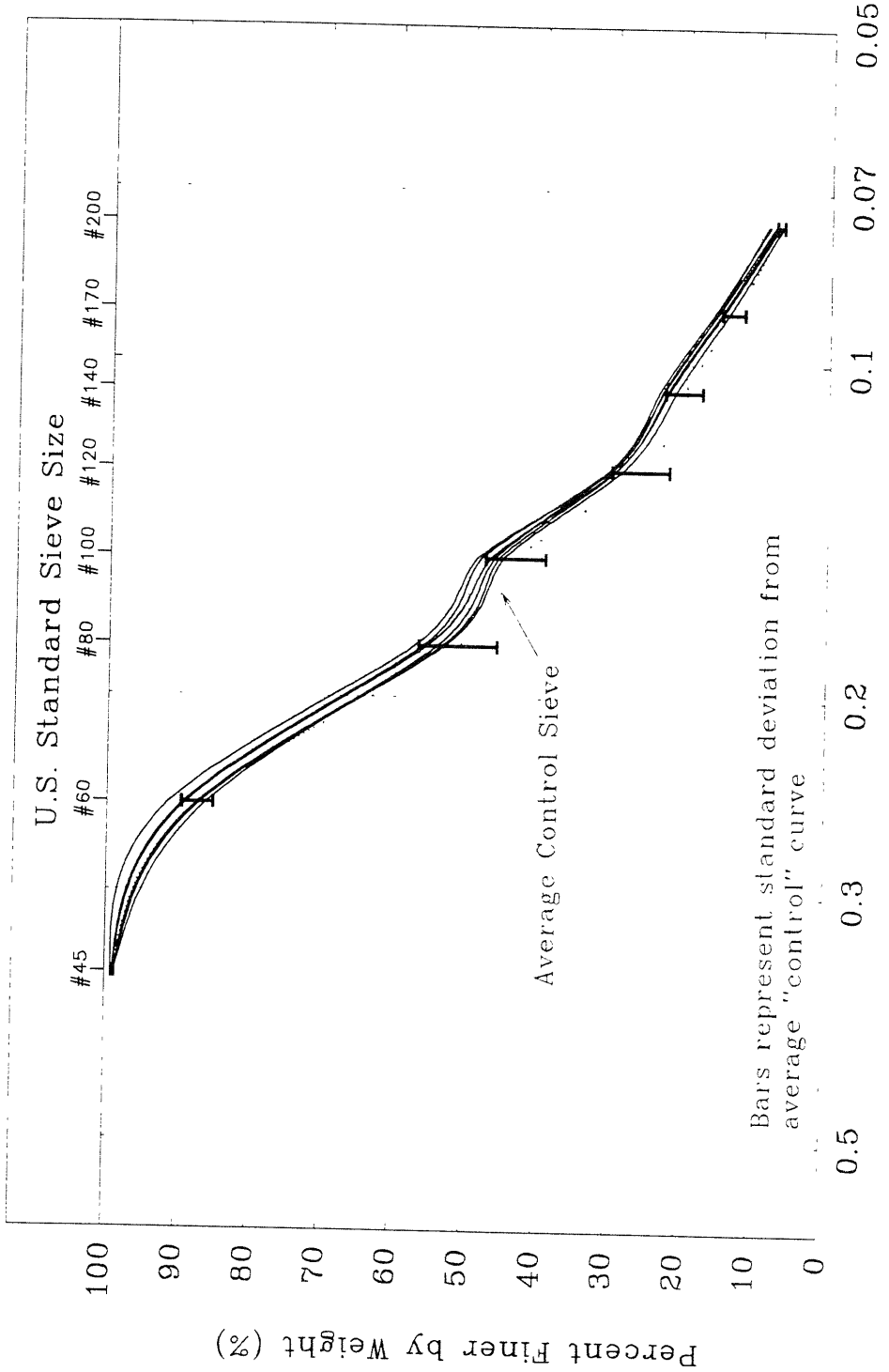

Figure 4.23 Post–Shear Particle Size Distributions of Unfrozen MFS for CIUC Tests at $\sigma'_c = 2$ MPa

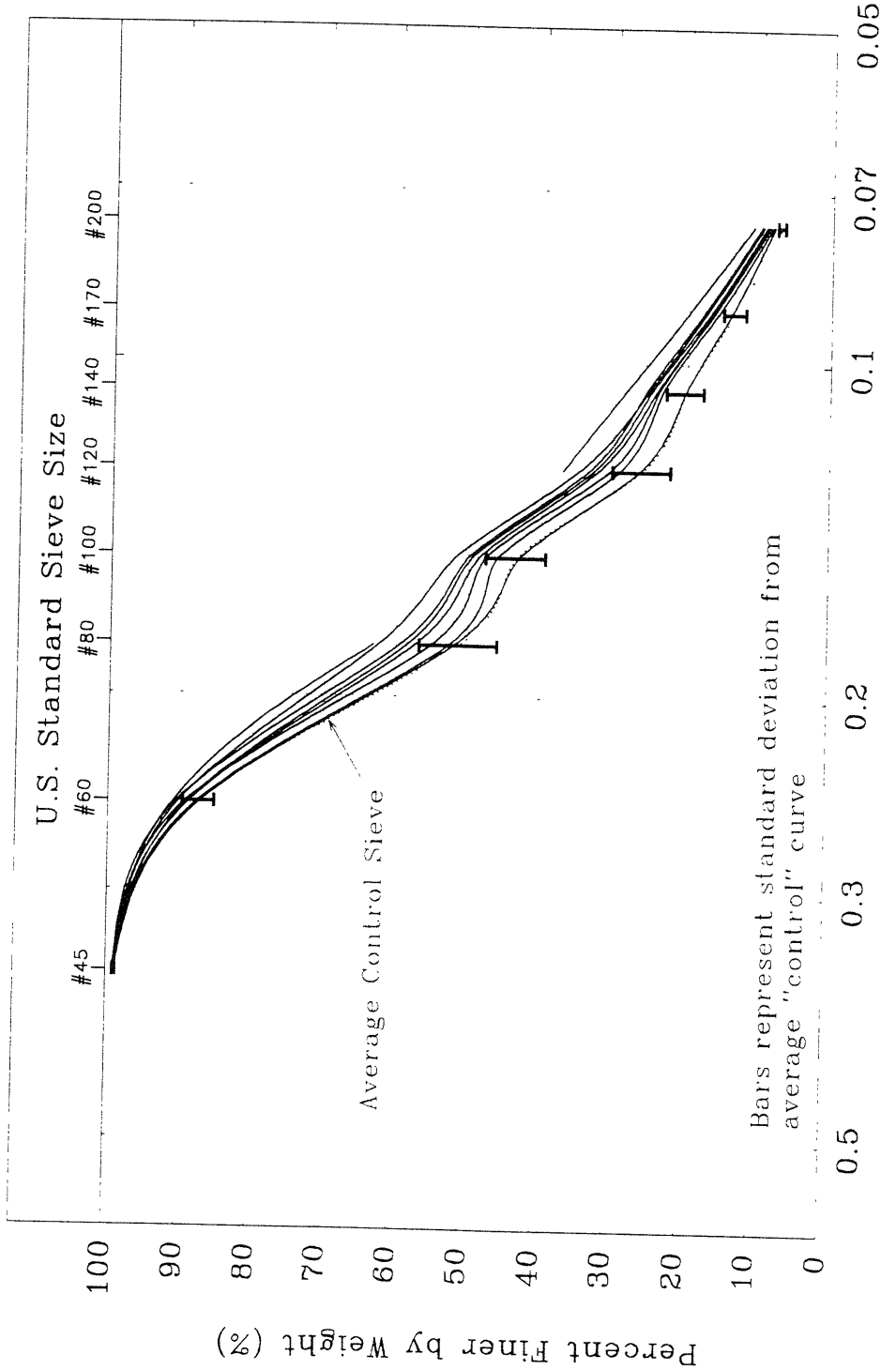

Figure 4.24 Post–Shear Particle Size Distributions of Unfrozen MFS for CIUC Tests at $\sigma'_c = 5$ MPa

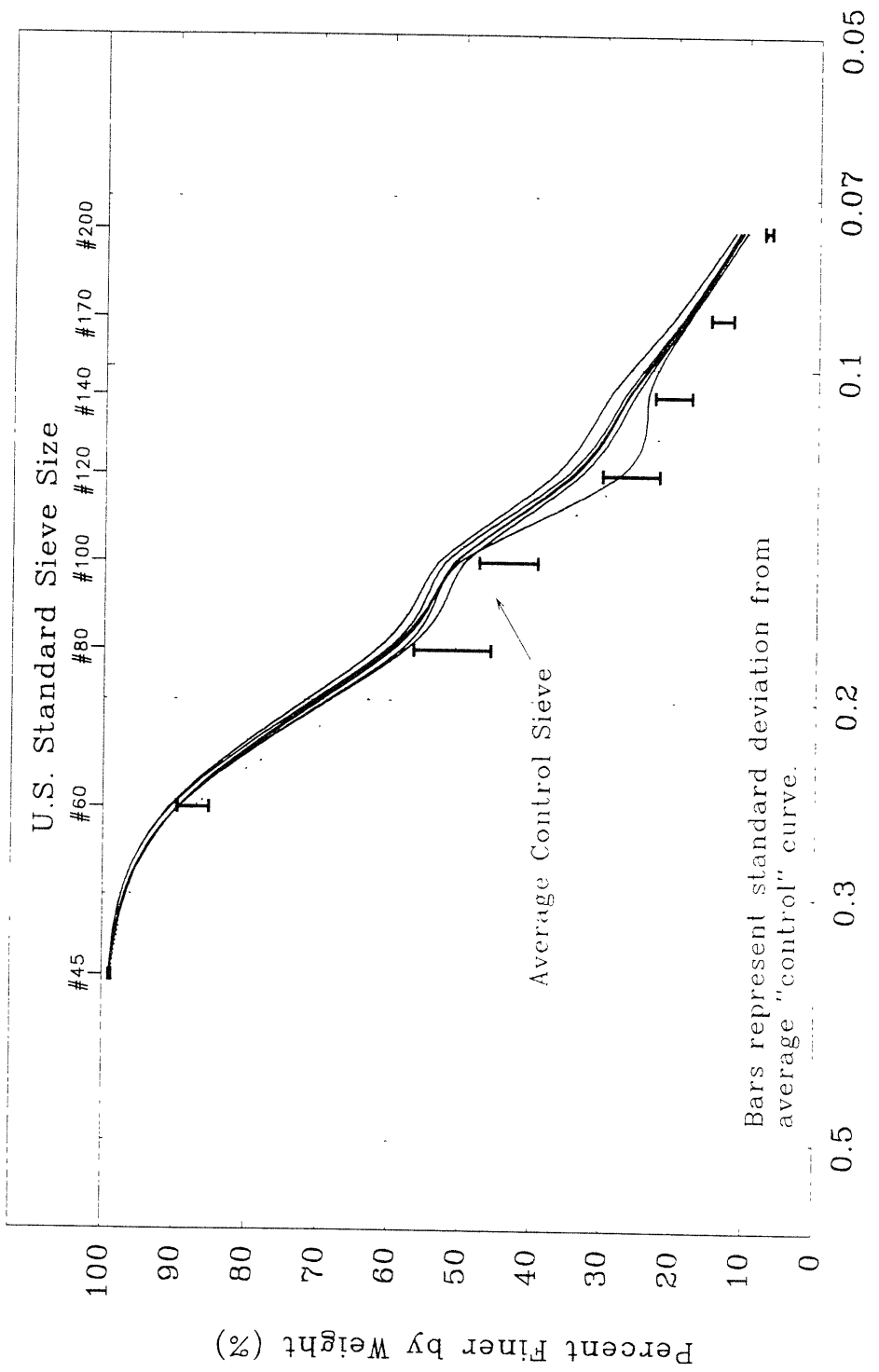

Figure 4.25 Post–Shear Particle Size Distributions of Unfrozen MFS for CIUC Tests at σ'_c = 10 MPa

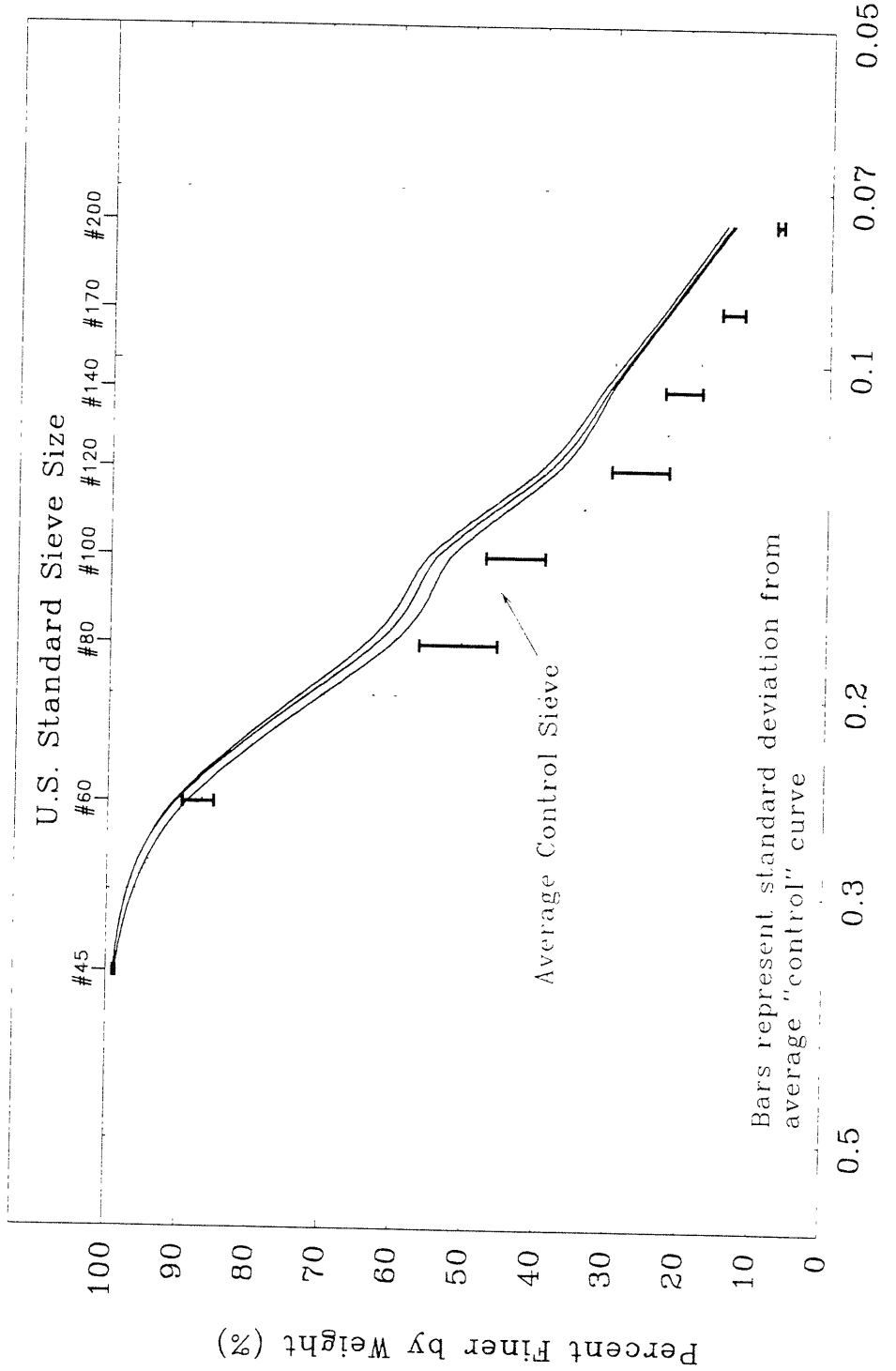

Figure 4.26 Post–Shear Particle Size Distributions of Unfrozen MFS for CIUC Tests at σ'_c = 12.5 MPa

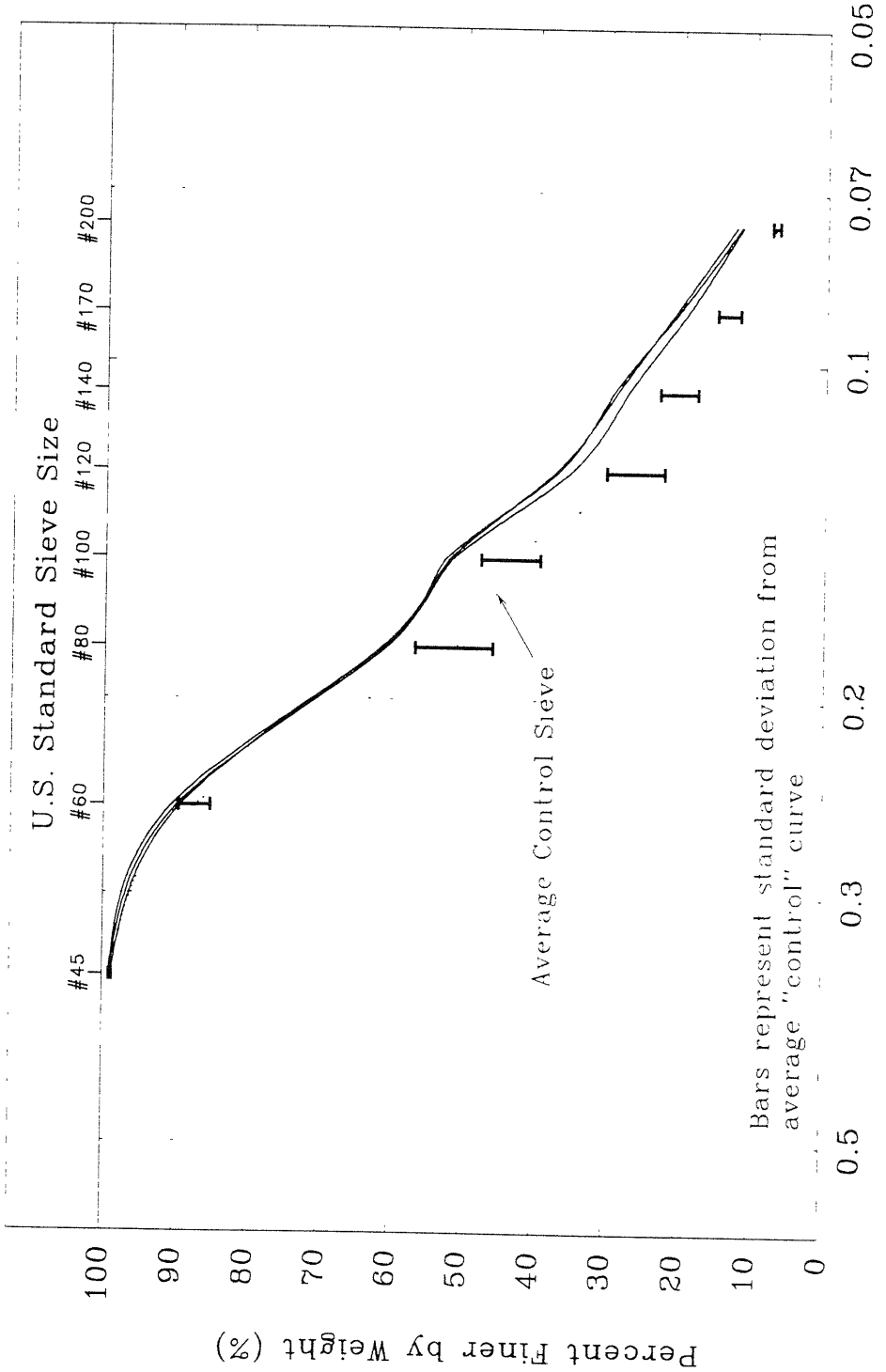

Figure 4.27 Post-Shear Particle Size Distributions of Unfrozen MFS for CAUC Tests

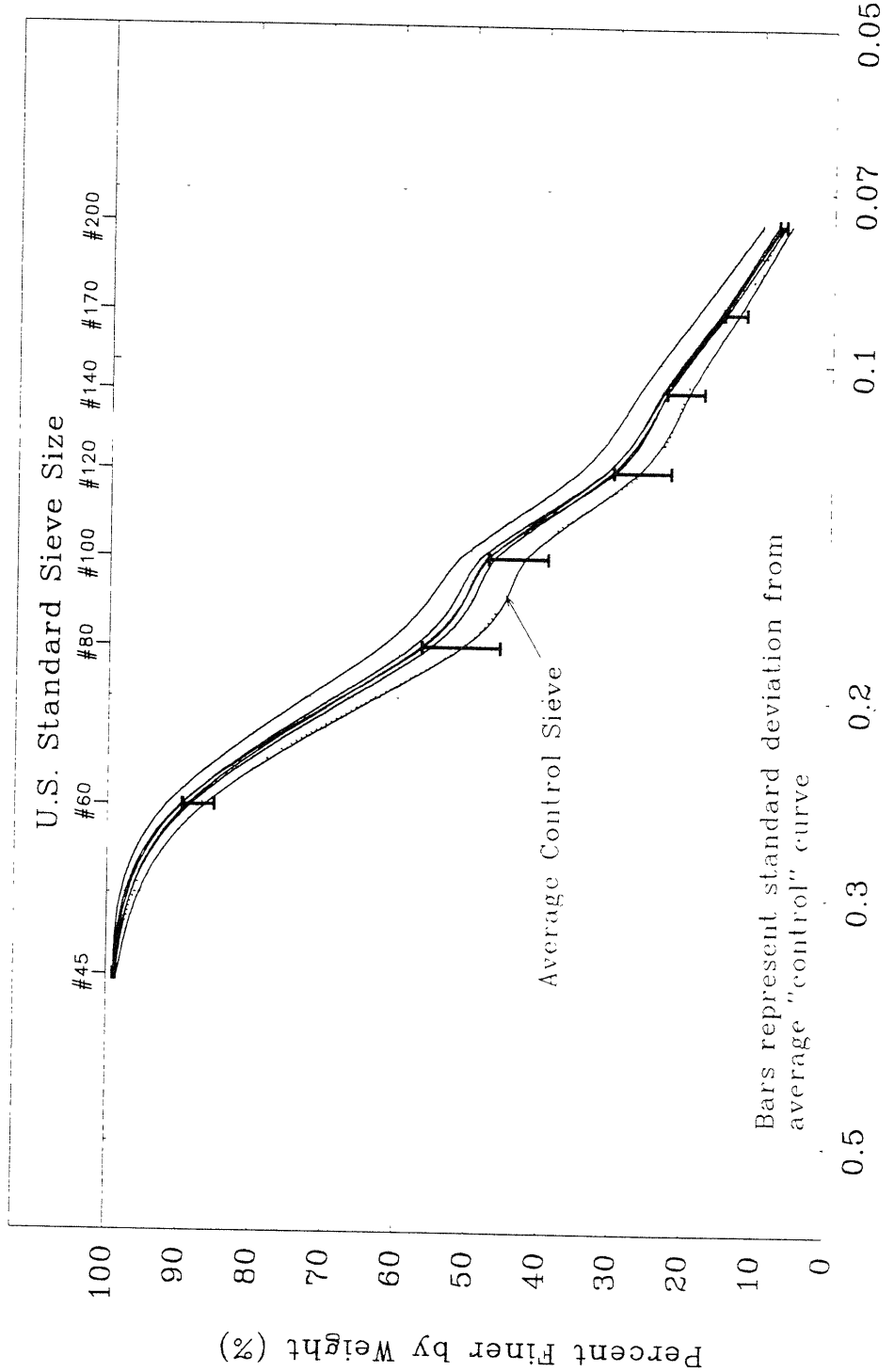

Figure 4.28 Post–Shear Particle Size Distributions of Unfrozen MFS for CIDC Tests at $\sigma'_c = 0.1$ MPa

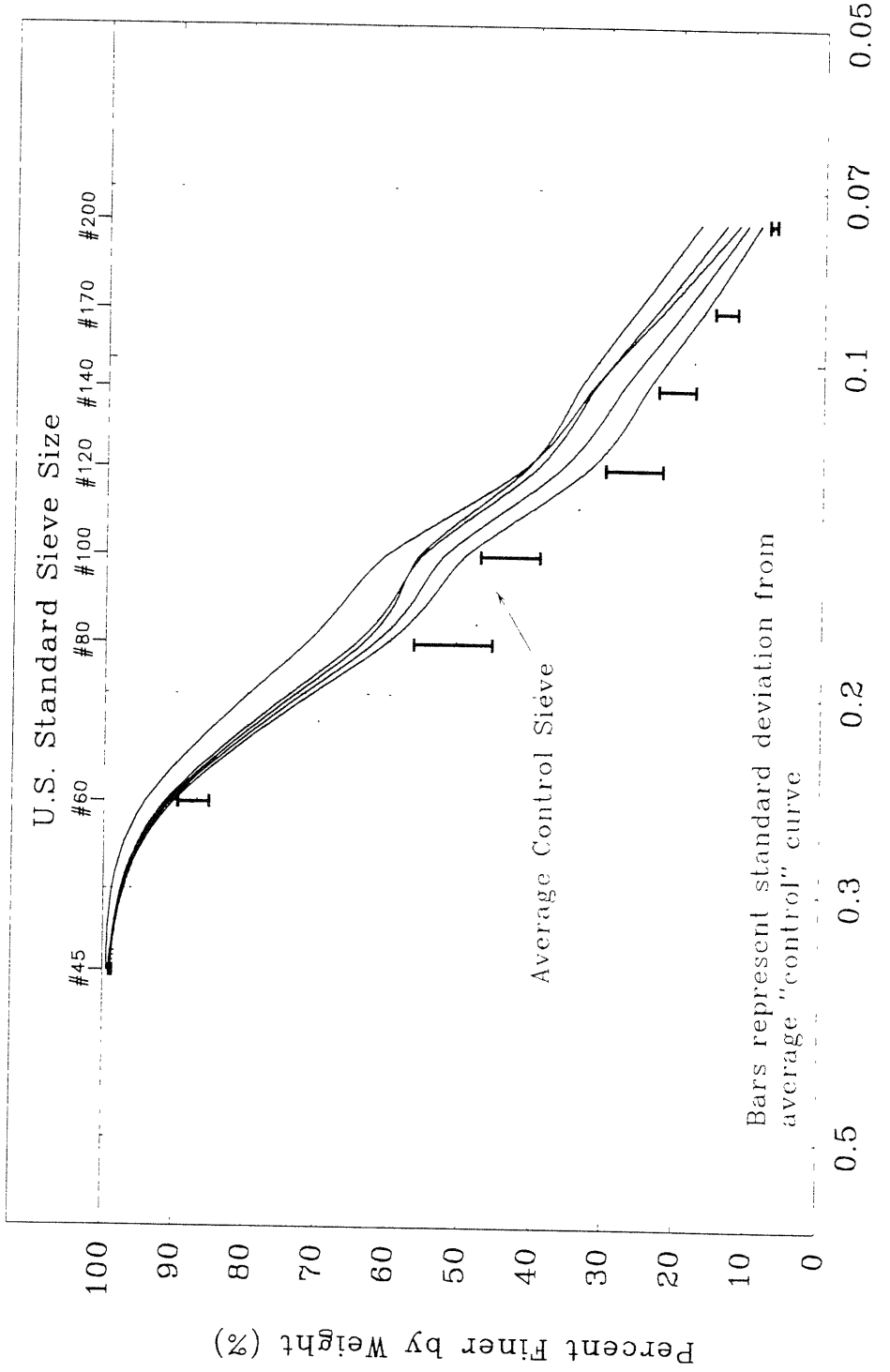

Figure 4.29 Post–Shear Particle Size Distributions of Unfrozen MFS for CIDC Tests at σ'_c = 2 to 10 MPa

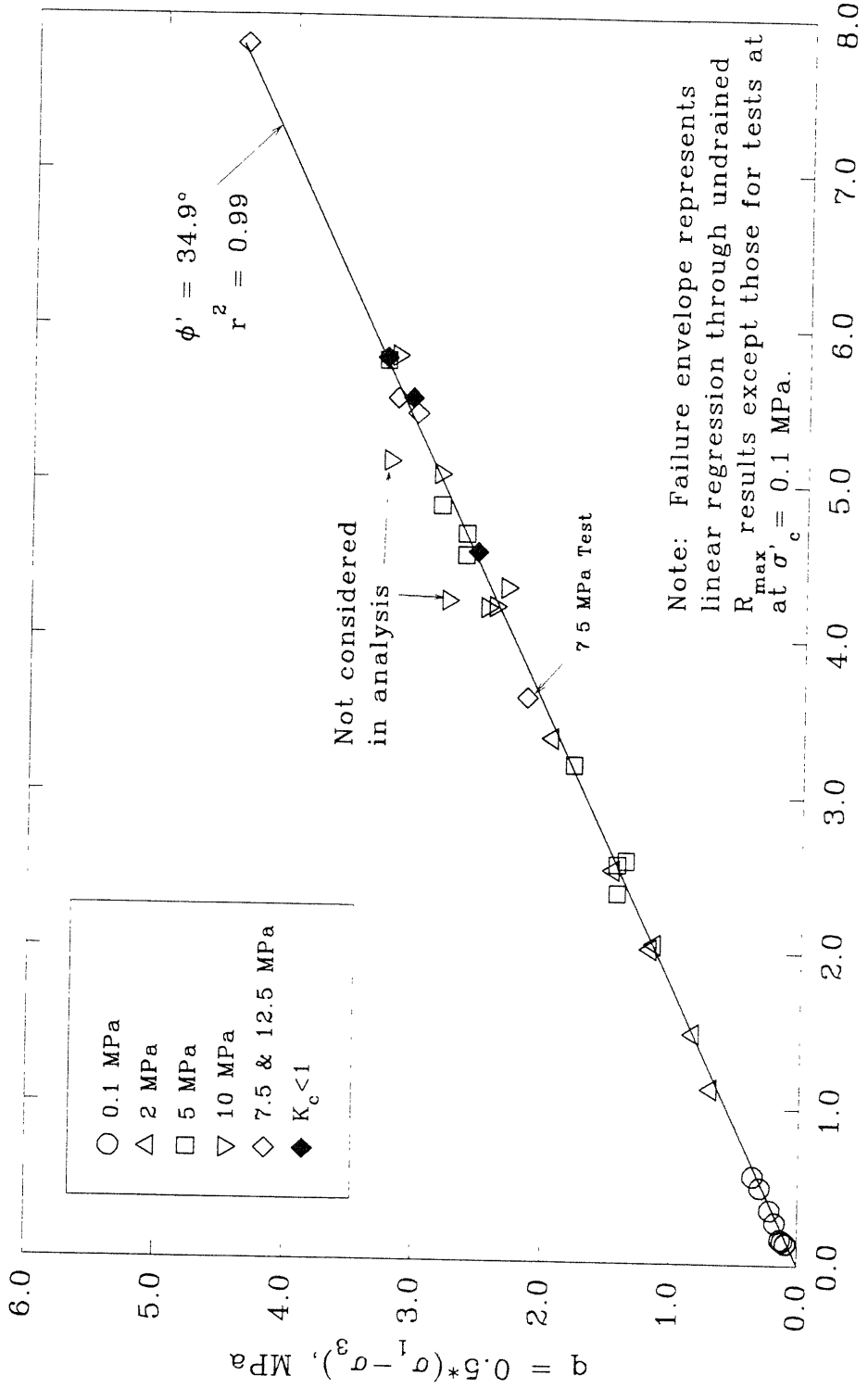

Figure 4.30 Mobilized Friction Angles at Maximum Obliquity for Undrained Triaxial Compression Tests

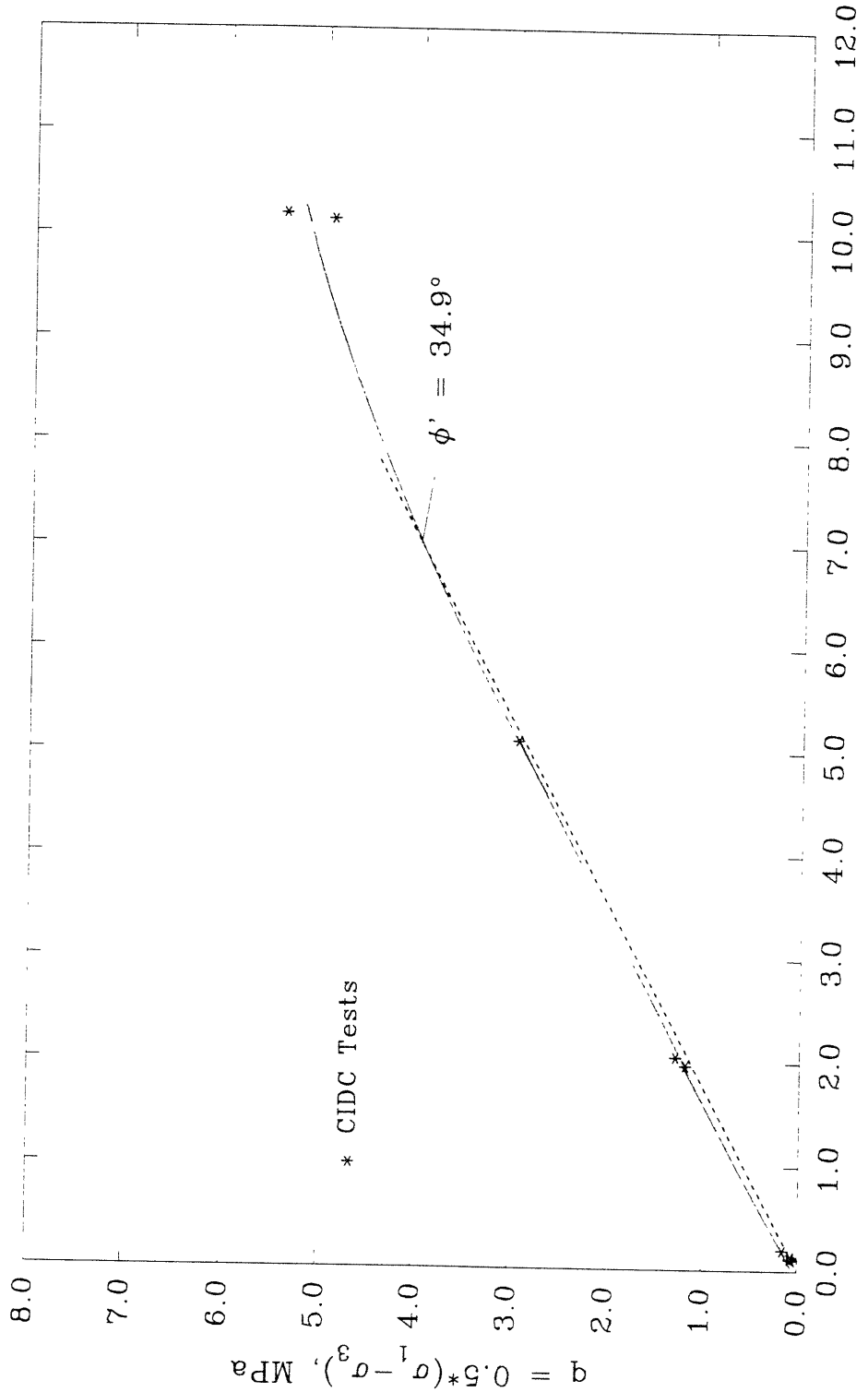

Figure 4.31 Mobilized Friction Angles at Maximum Obliquity for Drained Triaxial Compression Tests

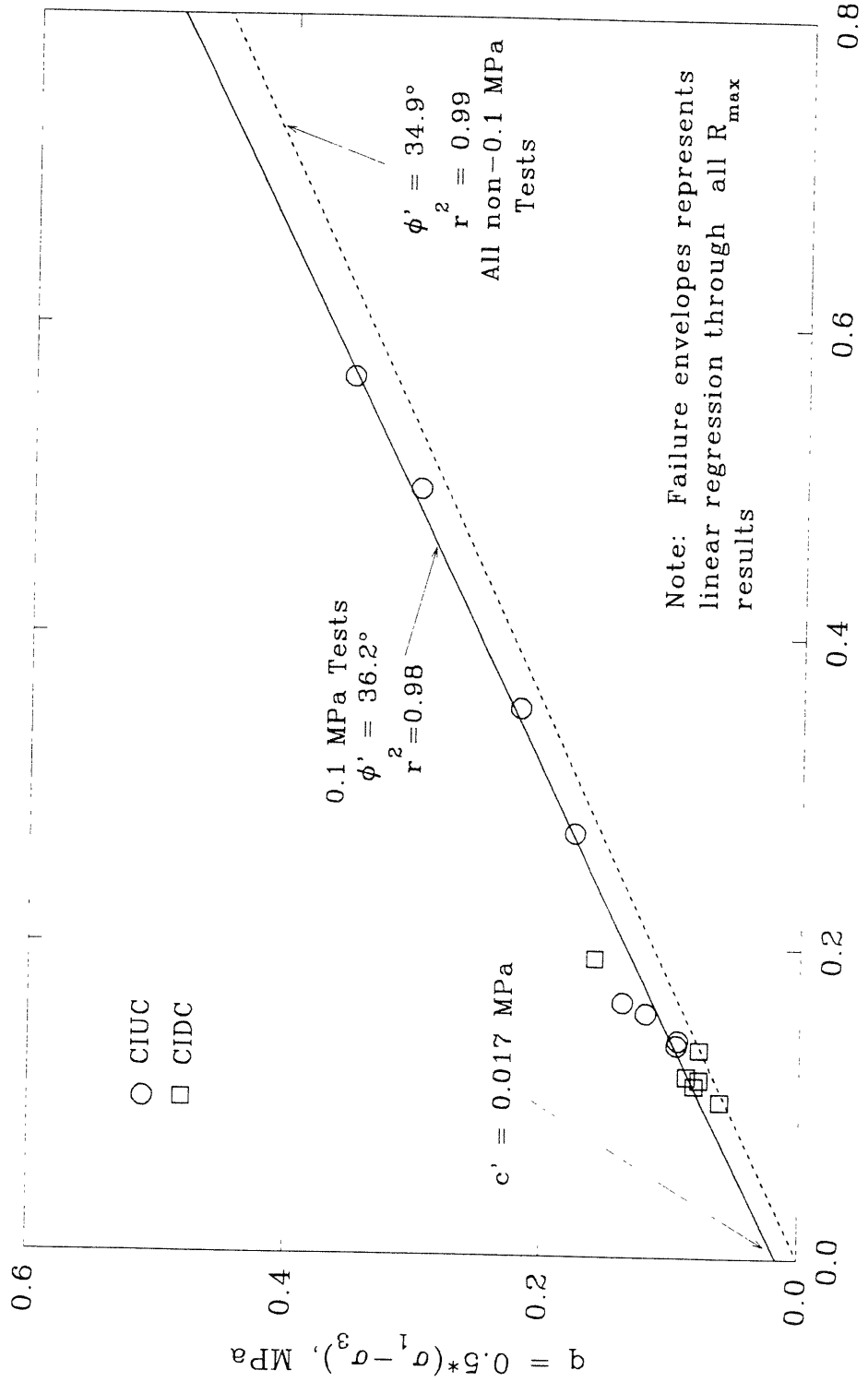

Figure 4.32 Mobilized Friction Angles at Maximum Obliquity for Undrained Triaxial Compression Tests: σ'_c = 0.1 MPa

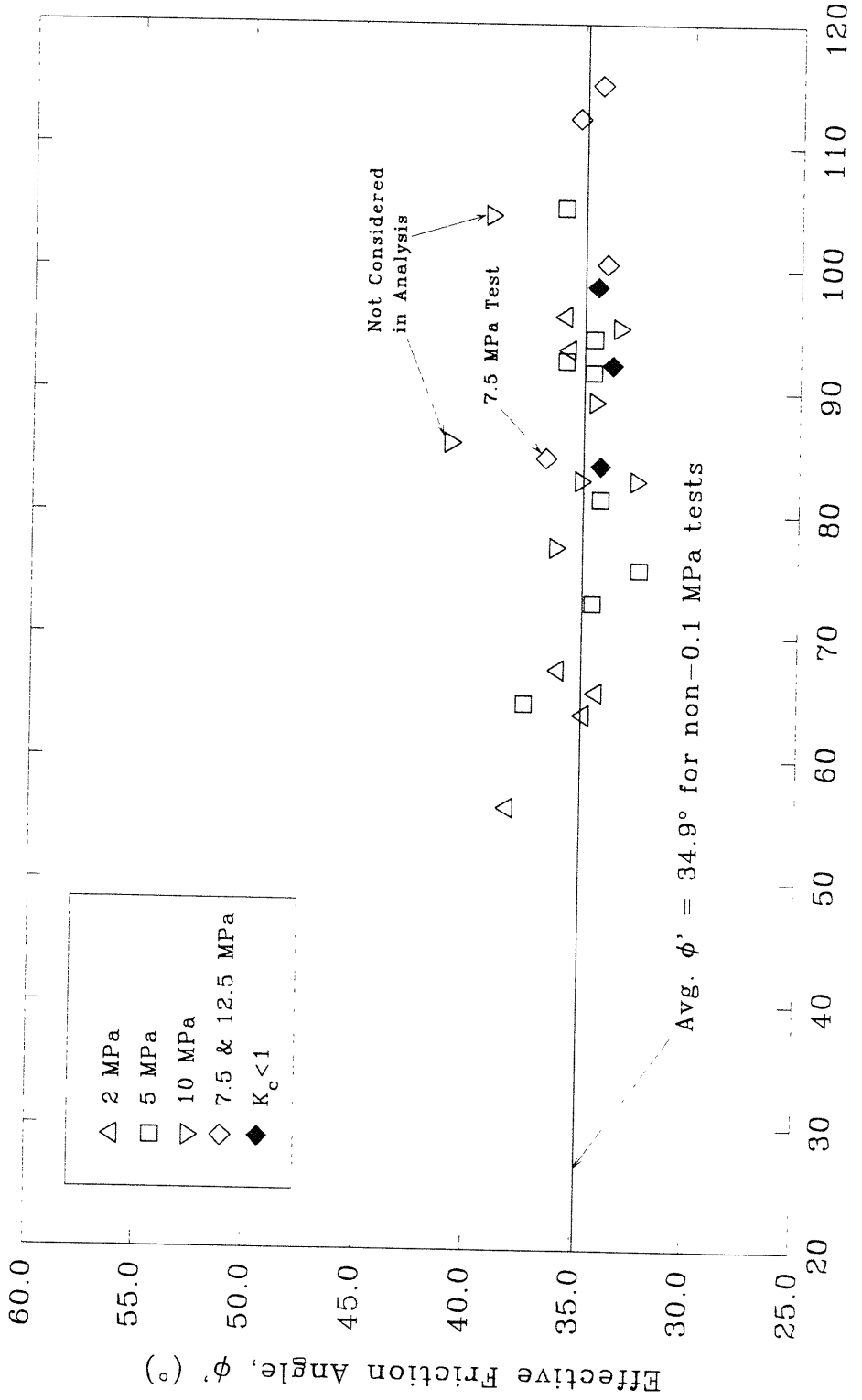

Figure 4.33 Effective Friction Angle at Maximum Obliquity versus Relative Density for Undrained MFS Tests

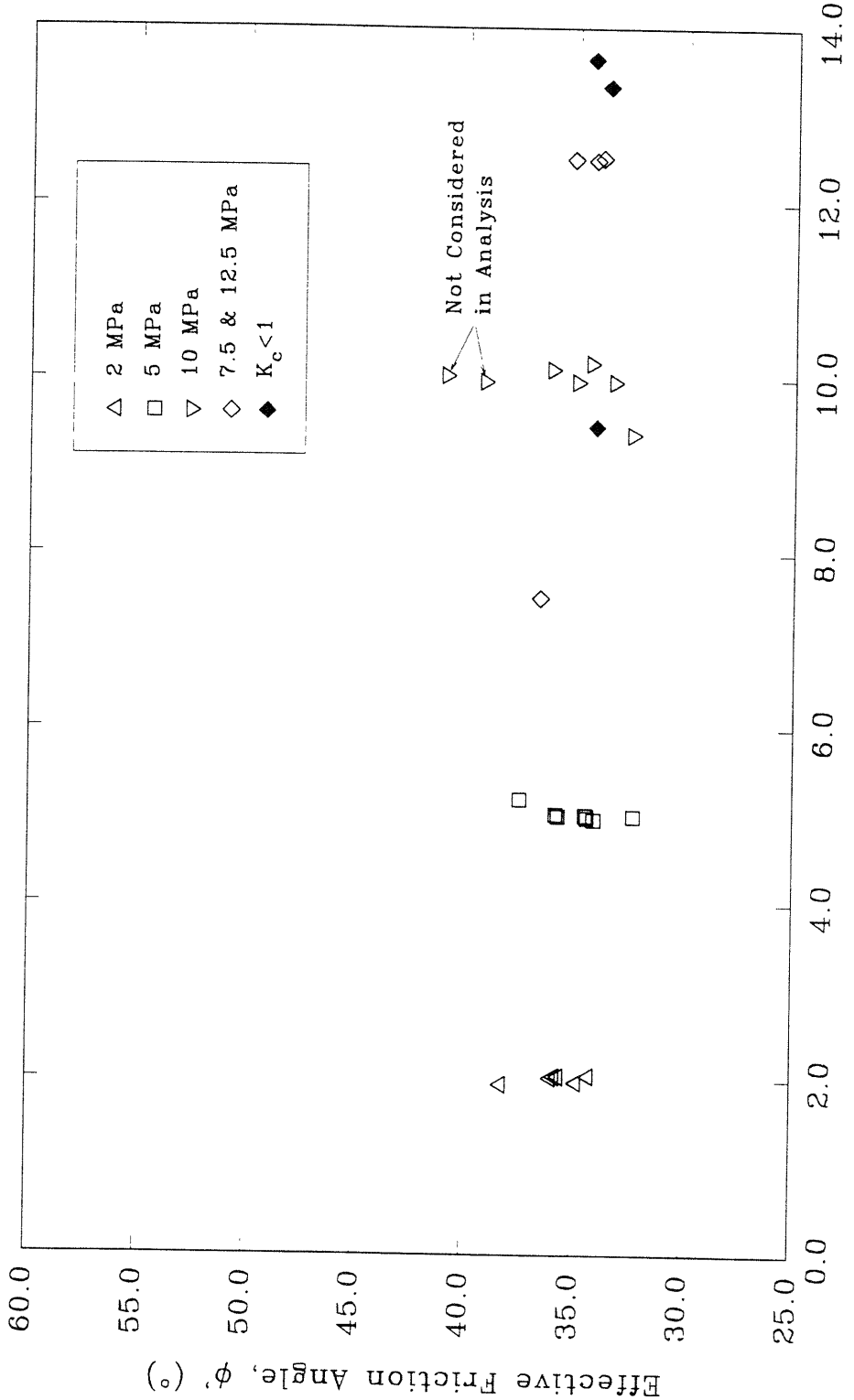

Figure 4.34 Effective Friction Angle at Maximum Obliquity versus Effective Confining Stress for Undrained MFS Tests

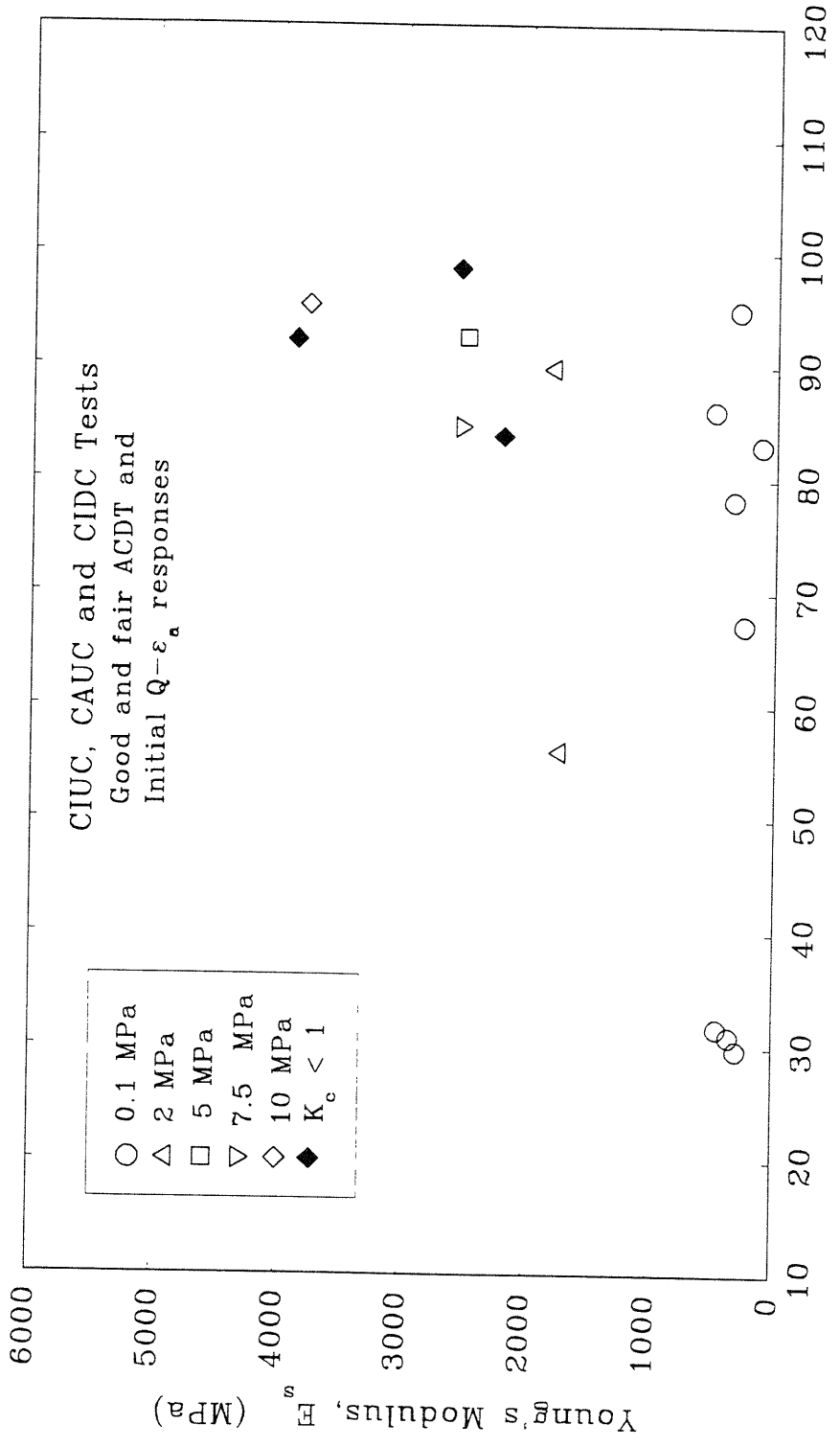

Figure 4.35 Young's Modulus, E_s, versus Relative Density for Unfrozen MFS

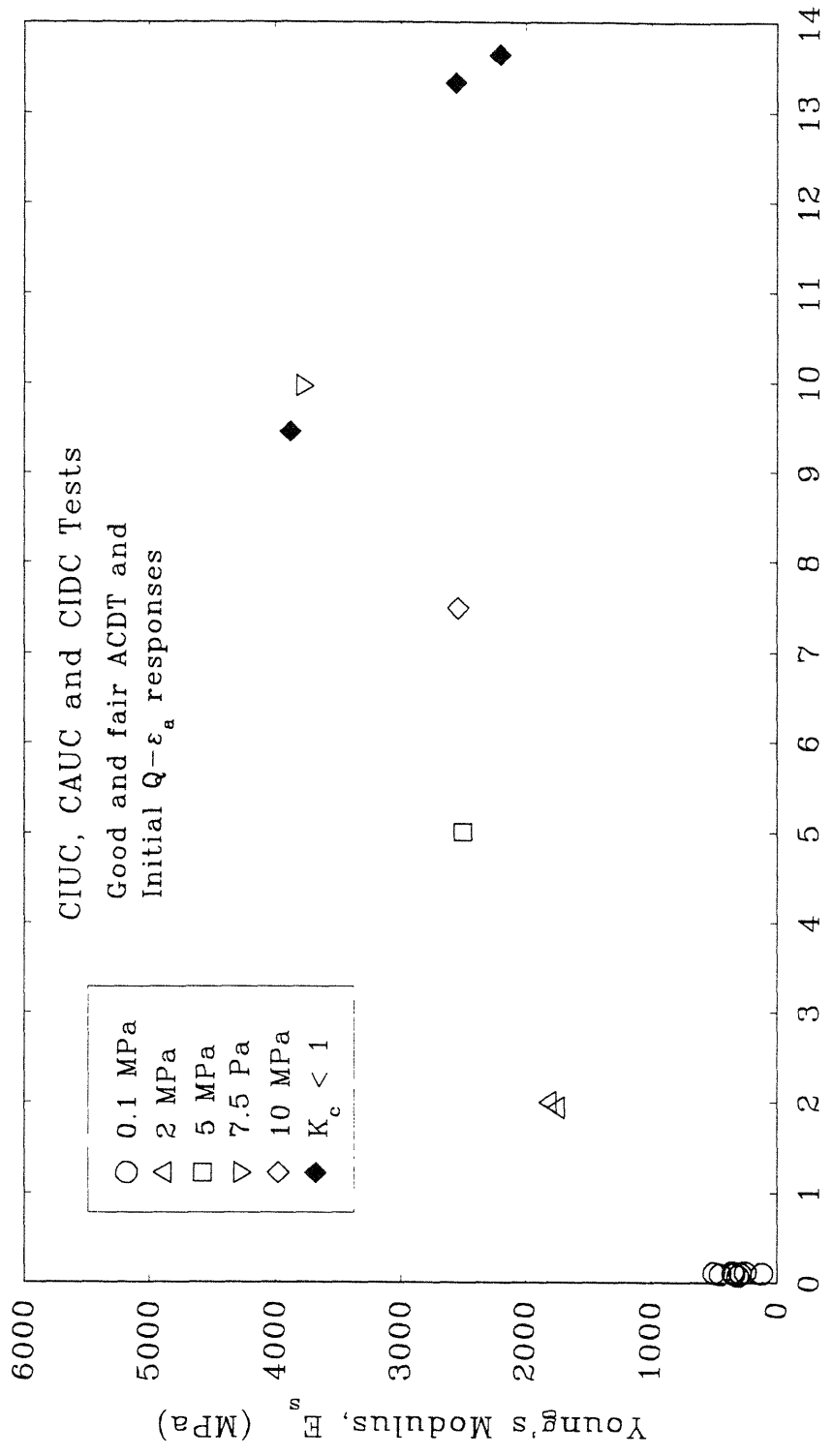

Figure 4.36 Young's Modulus, E_s, versus Effective Confining Stress for Unfrozen MFS

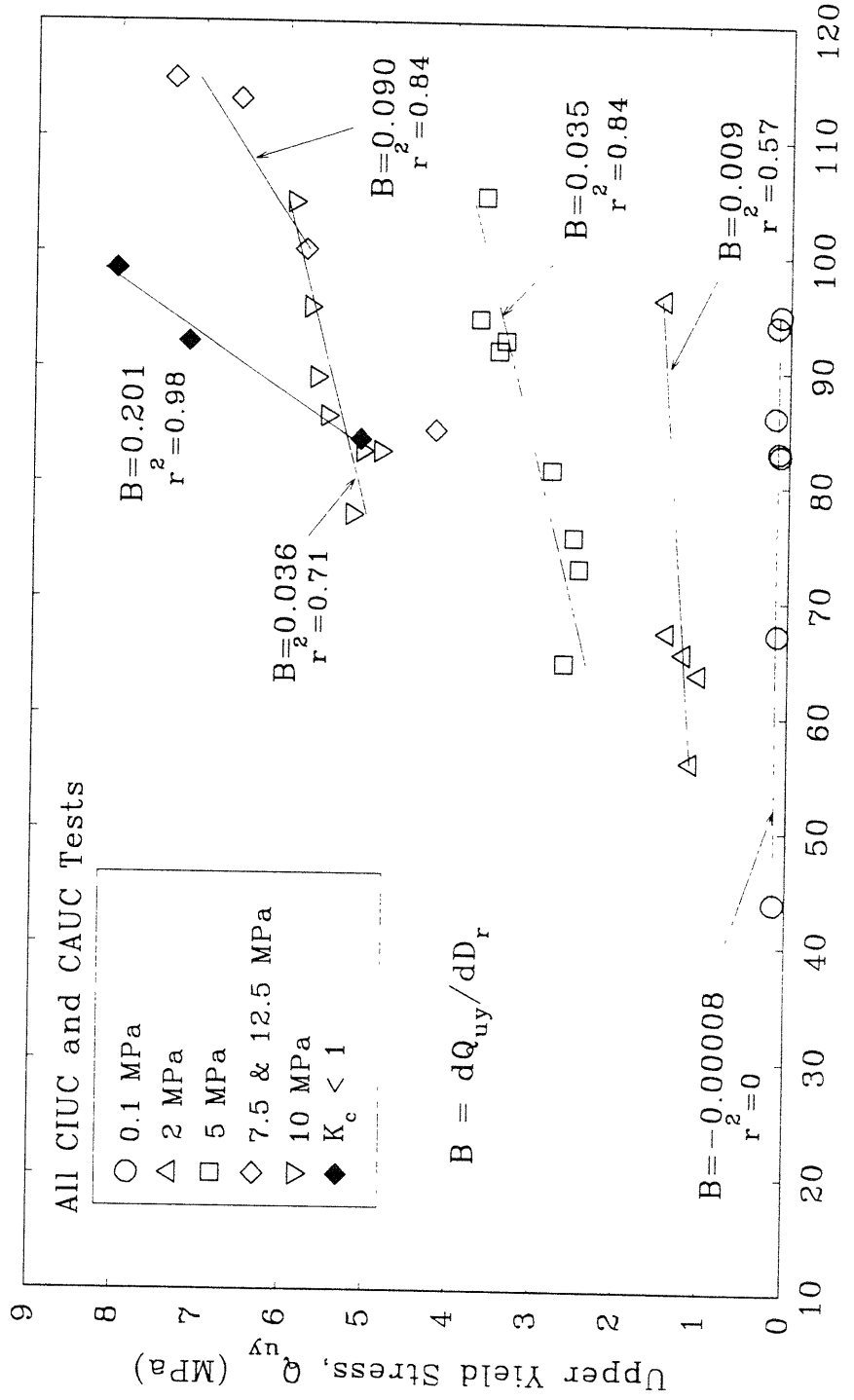

Figure 4.37 Upper Yield Stress versus Relative Density for Undrained Triaxial Compression Tests

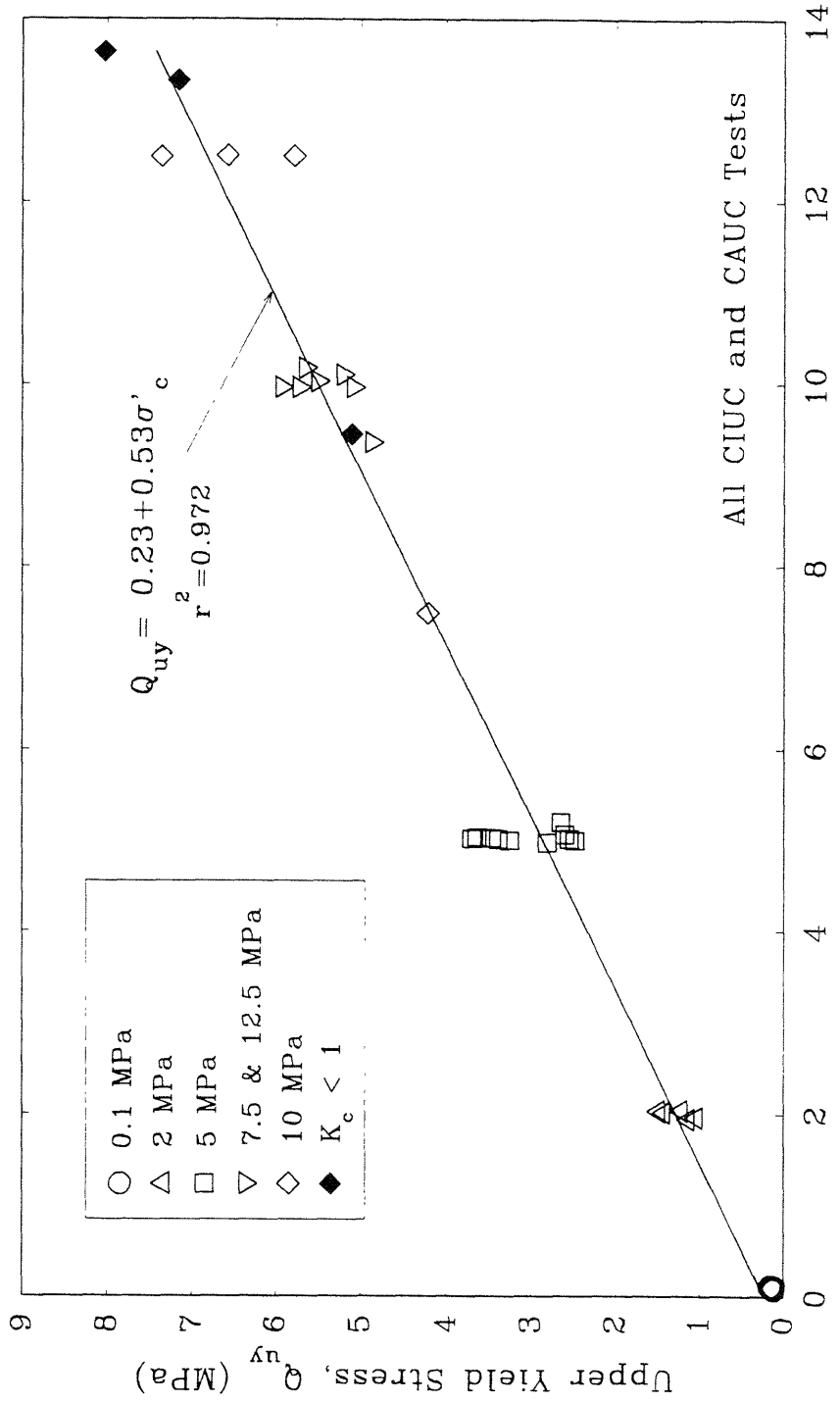

Figure 4.38 Upper Yield Stress versus Effective Confining Stress for Undrained Triaxial Compression Tests

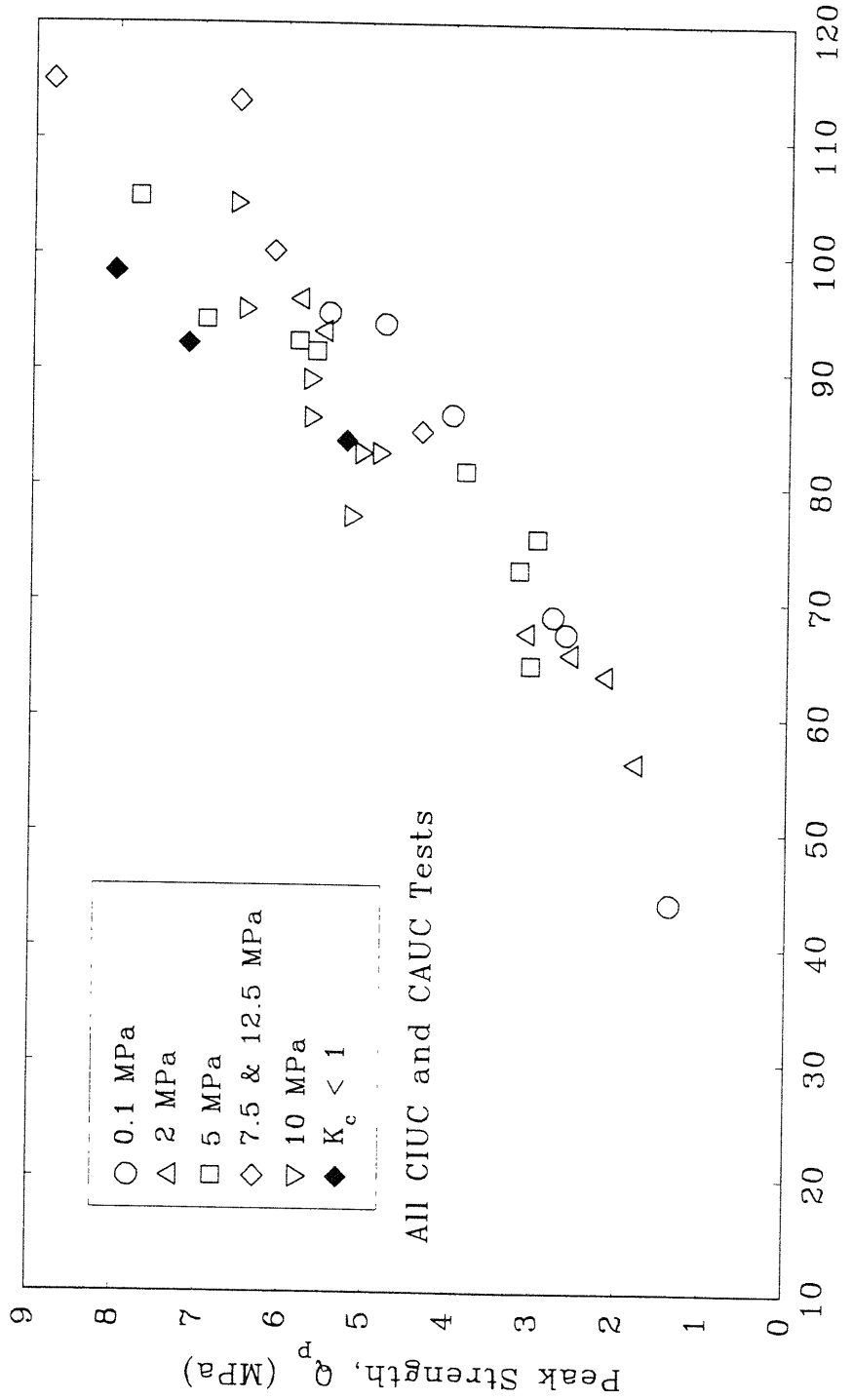

Figure 4.39 Peak Strength versus Relative Density for Undrained Triaxial Compression Tests

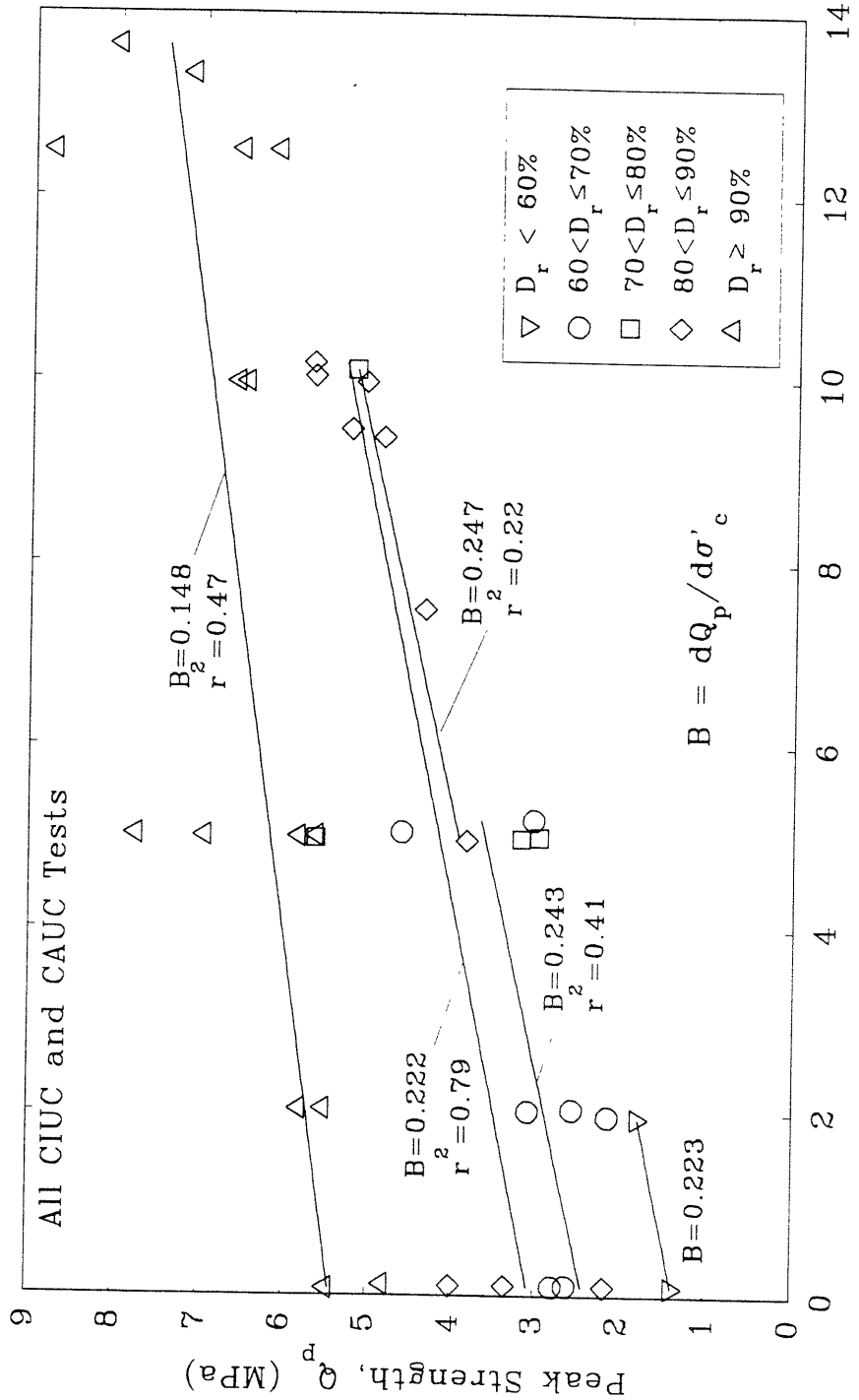

Figure 4.40 Peak Strength versus Effective Confining Stress for Undrained Triaxial Compression Tests

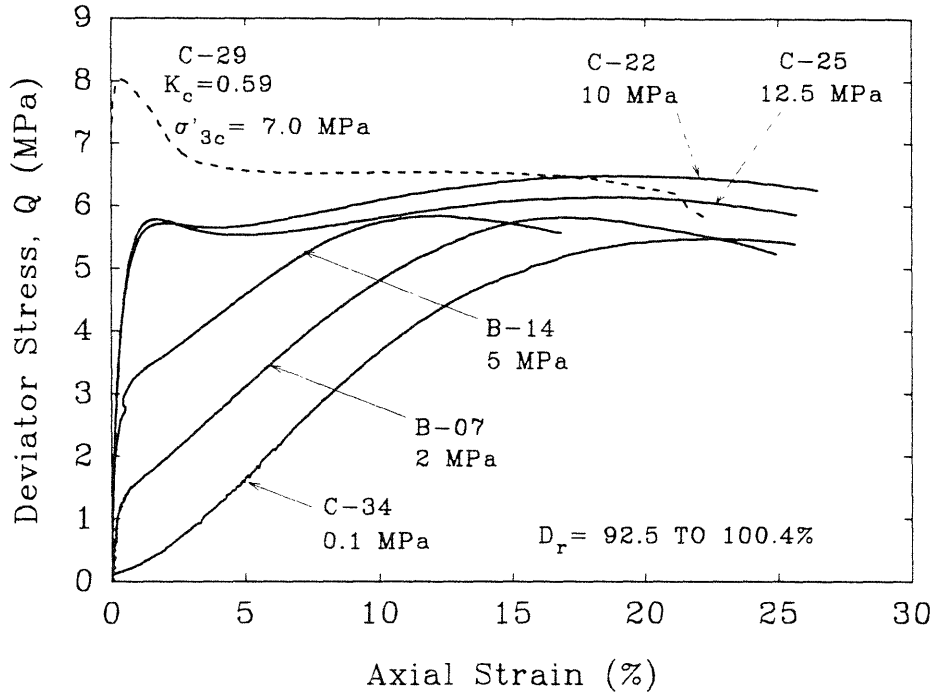

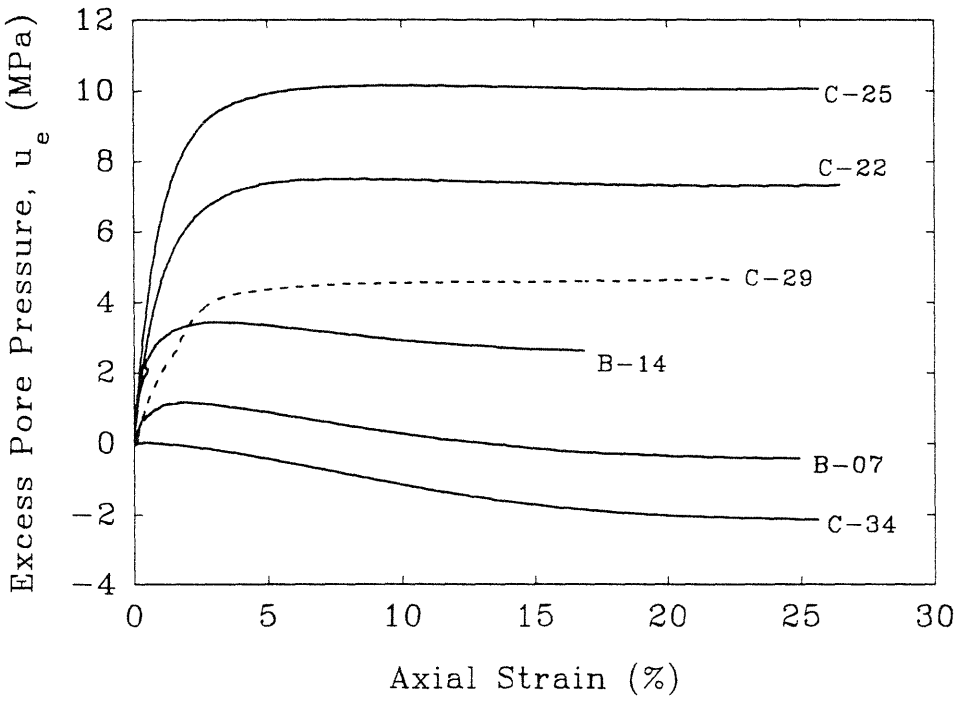

Figure 4.41 Stress–Strain and Pore Pressure Responses for Undrained Tests at Similar Relative Density

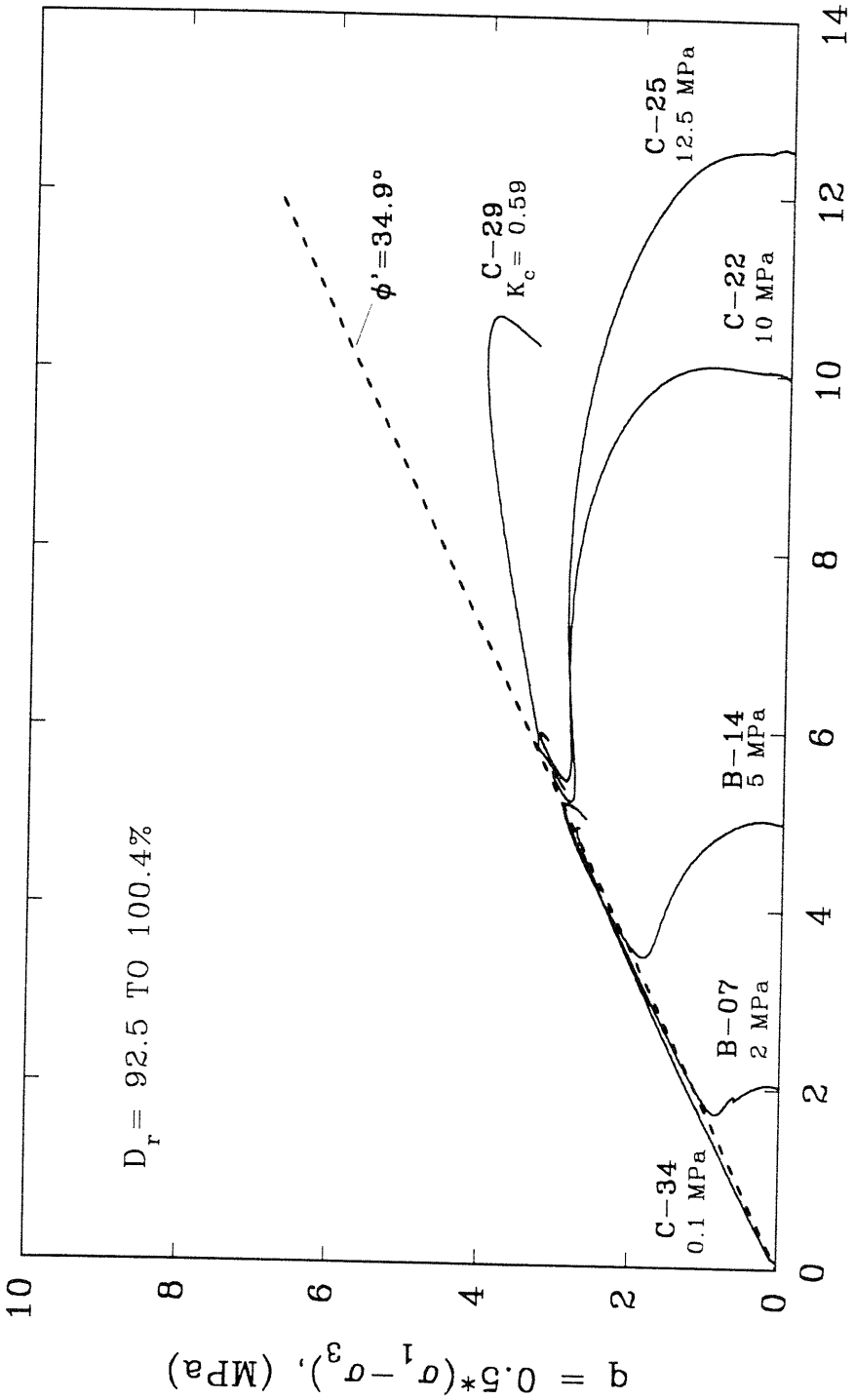

Figure 4.42 Effective Stress Paths for Unfrozen Undrained Tests at Similar Relative Densities

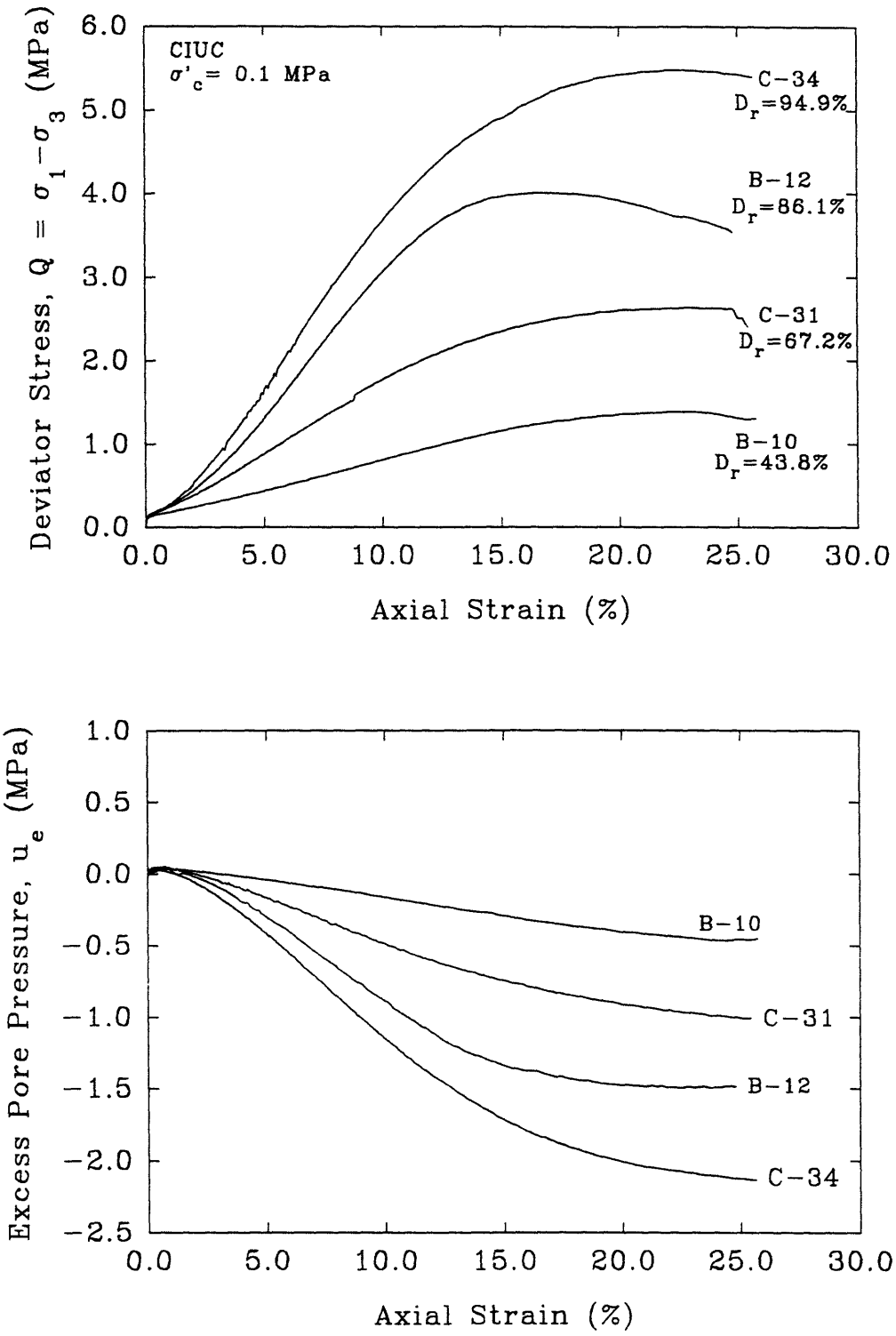

Figure 4.43 Stress–Strain and Pore Pressure Response for Unfrozen CIUC Tests with Similar Confinement: 0.1 MPa

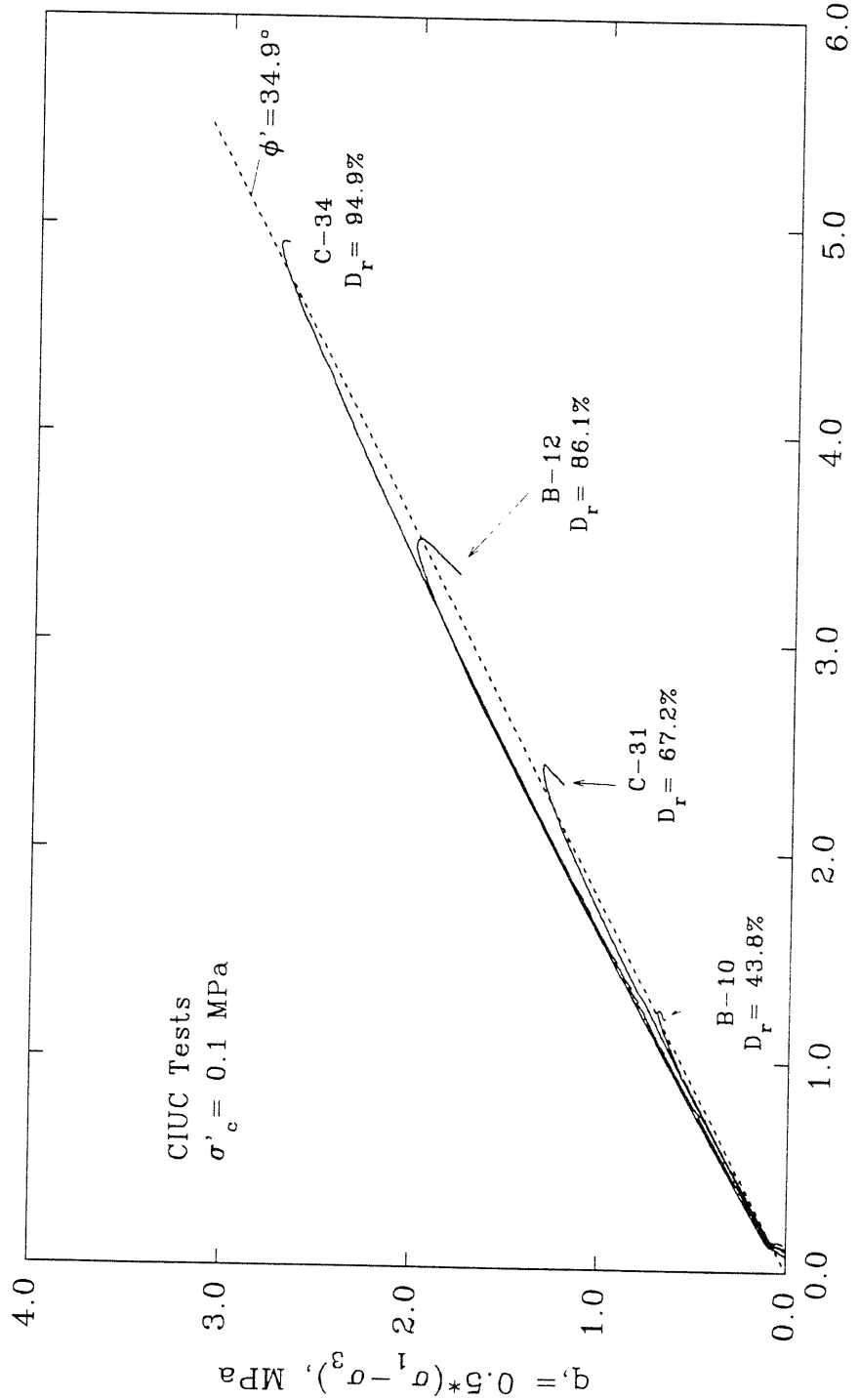

Figure 4.44 Effective Stress Paths for Unfrozen CIUC Tests with Similar Confinement: 0.1 MPa

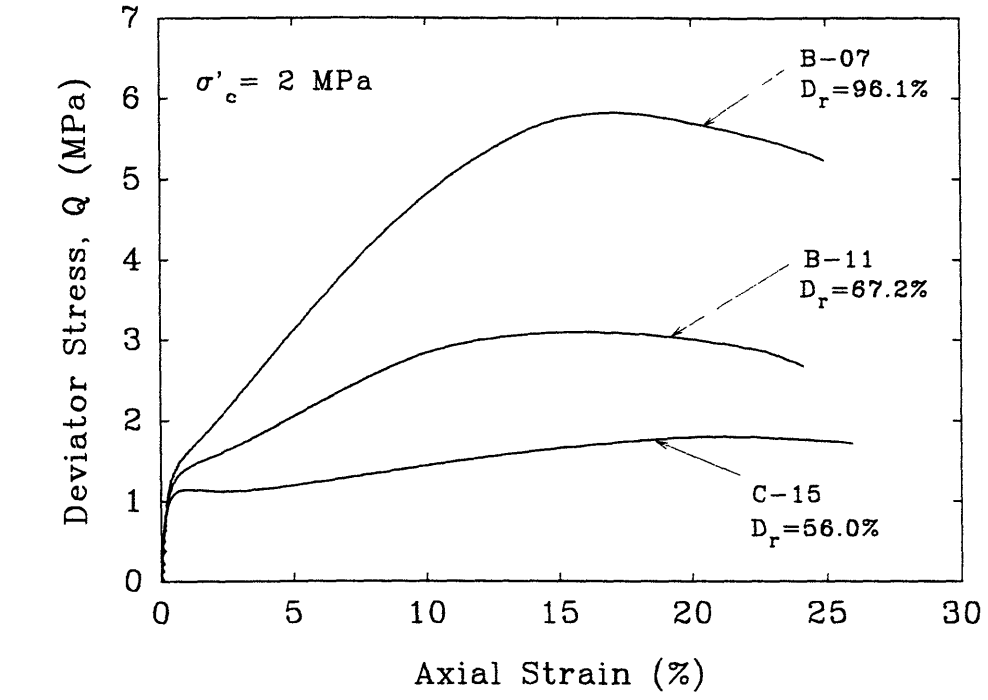

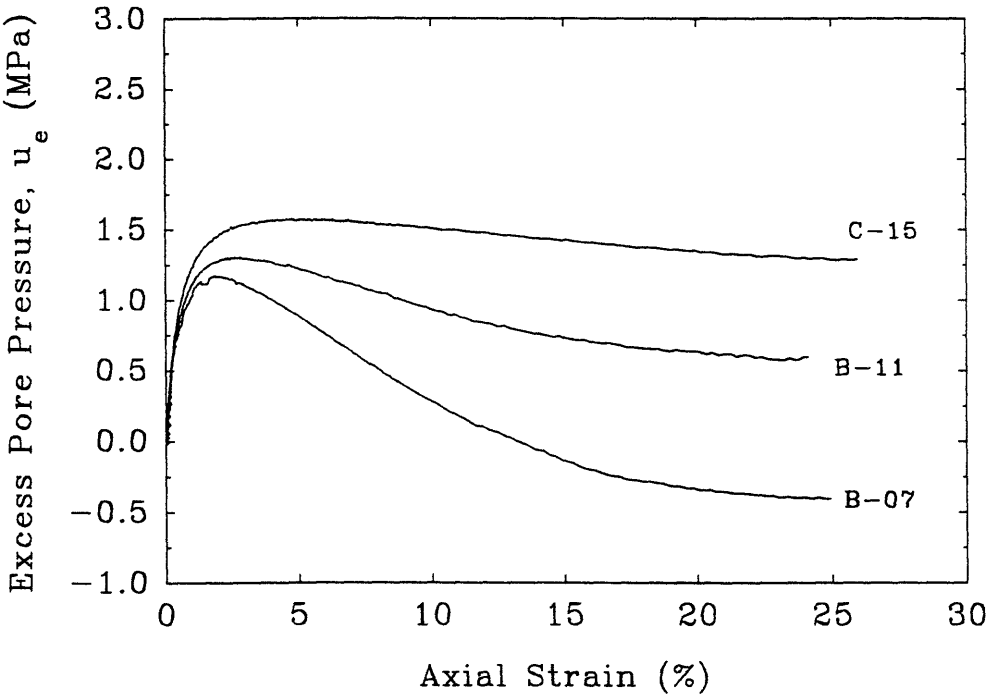

Figure 4.45 Stress–Strain and Pore Pressure Response for Unfrozen CIUC Tests with Similar Confinement: 2 MPa

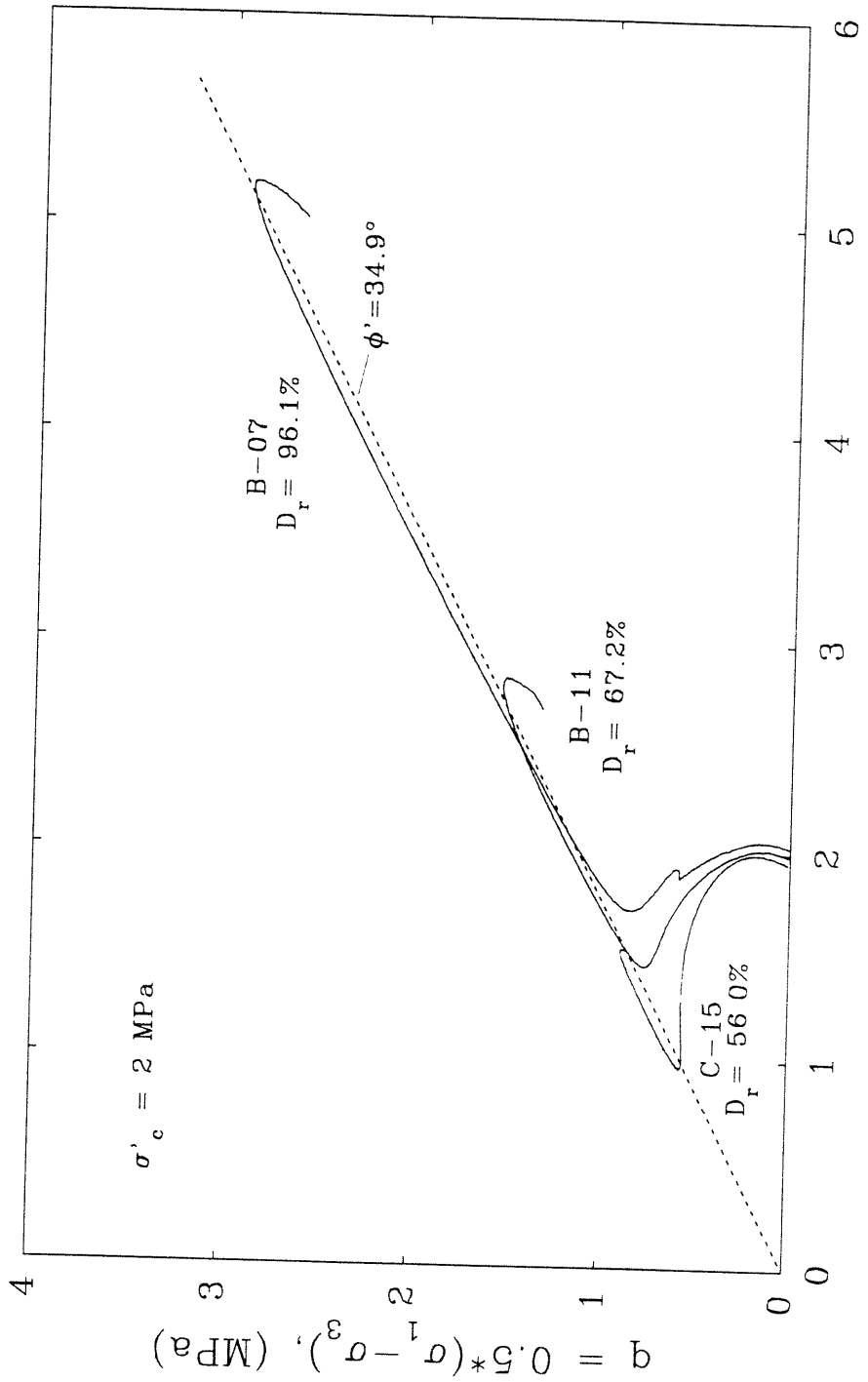

Figure 4.46 Effective Stress Paths for Unfrozen CIUC Tests with Similar Confinement: 2 MPa

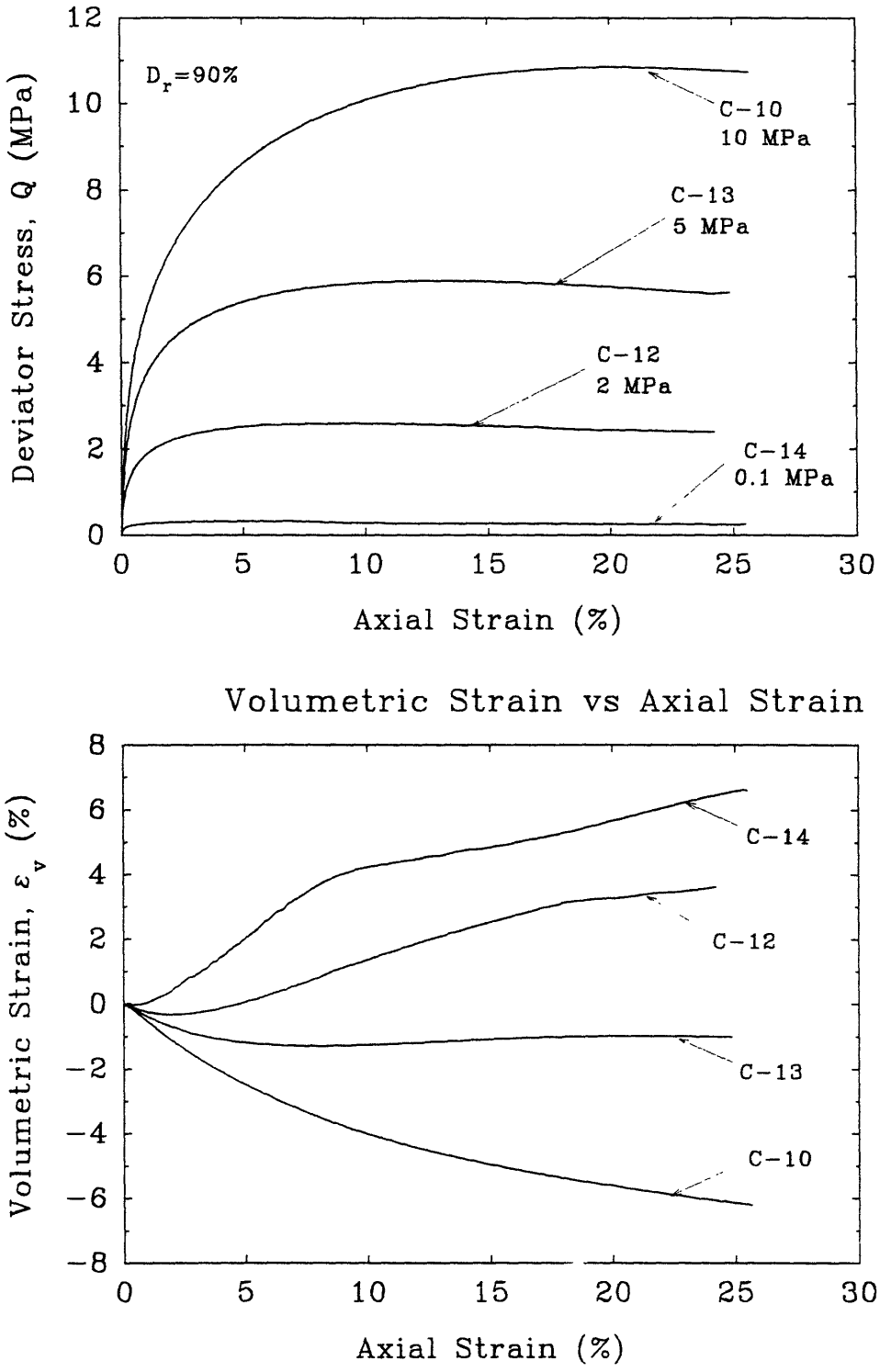

Figure 4.47 Stress–Strain and Volumetric Strain Responses for Unfrozen CIDC Tests with Similar Relative Densities

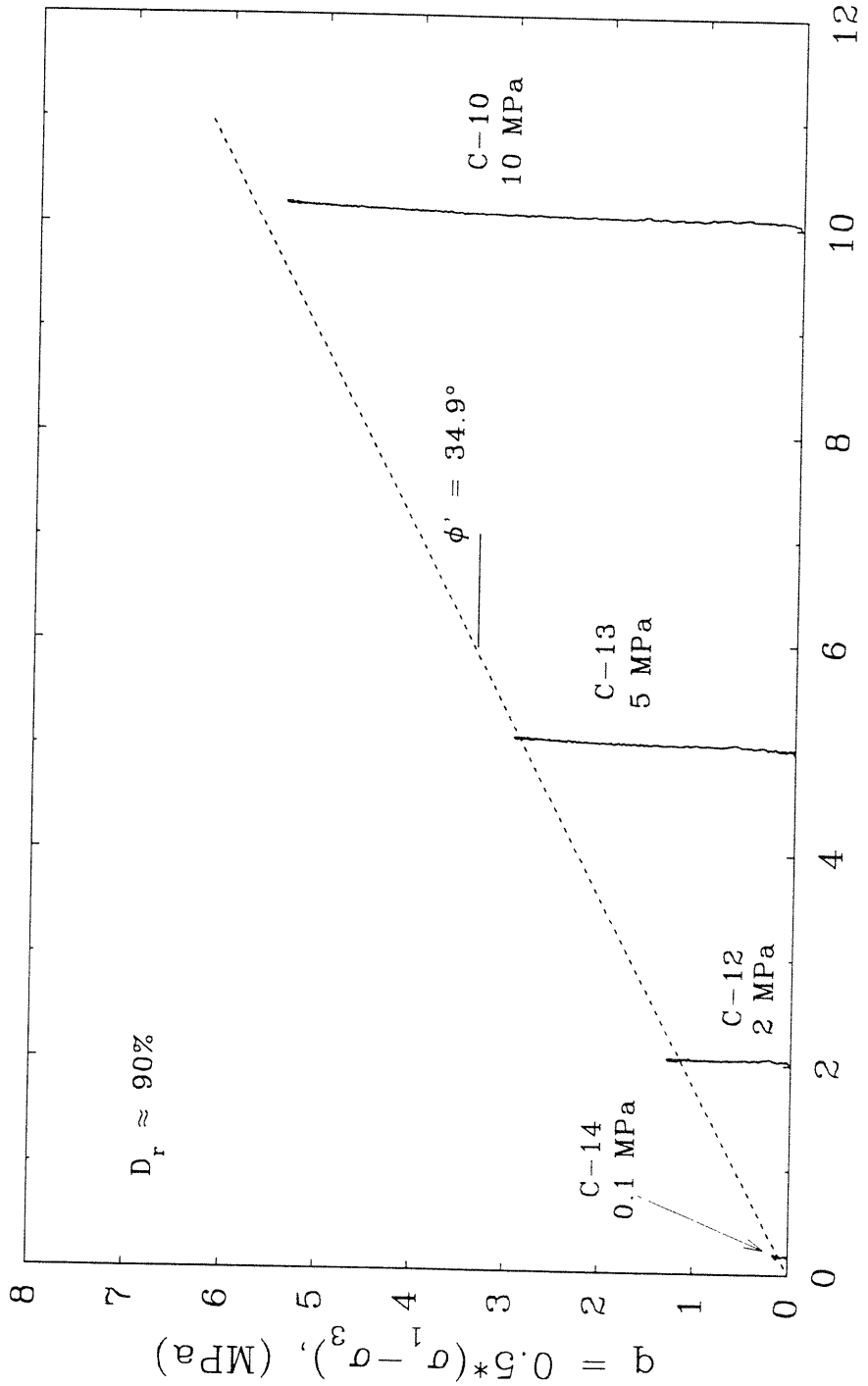

Figure 4.48 Effective Stress Paths of Unfrozen CIDC Tests withve Similar Relative Densities

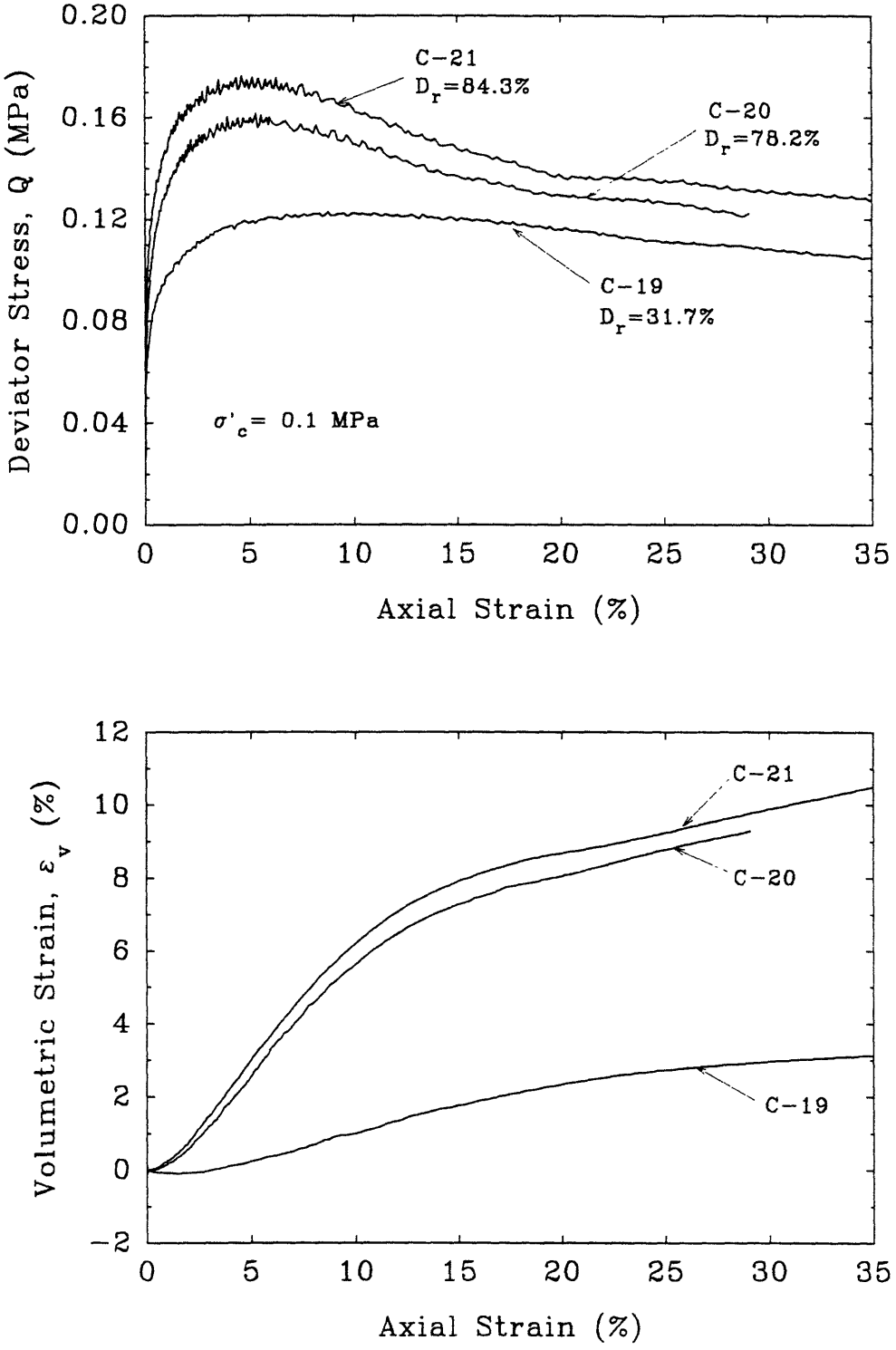

Figure 4.49 Stress–Strain and Volumetric Strain Responses for Unfrozen CIDC Tests at Similar Confinement: 0.1 MPa

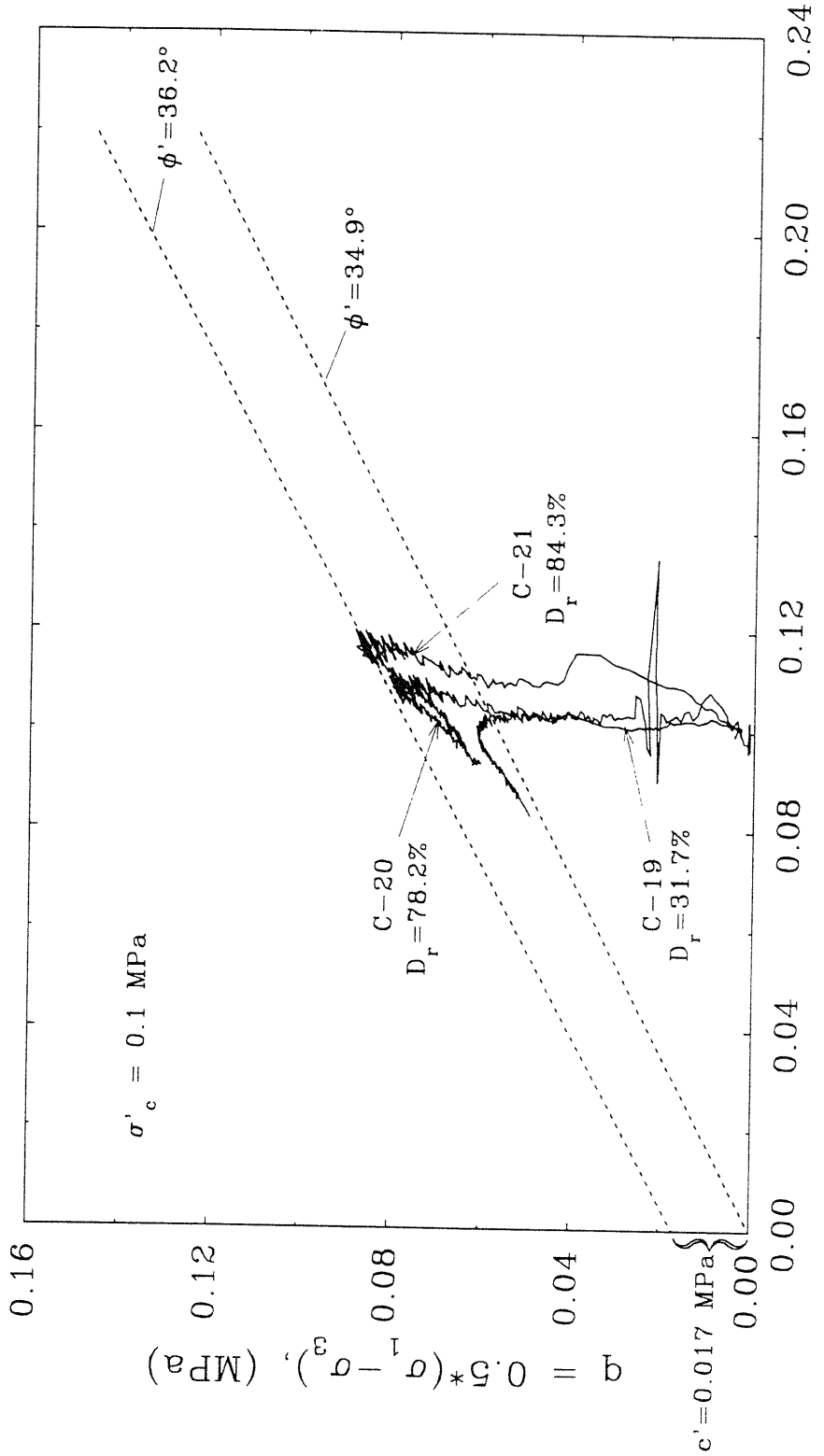

Figure 4.50 Effective Stress Paths Showing the Effects of Relative Density on CIDC Tests at σ'_c = 0.1 MPa

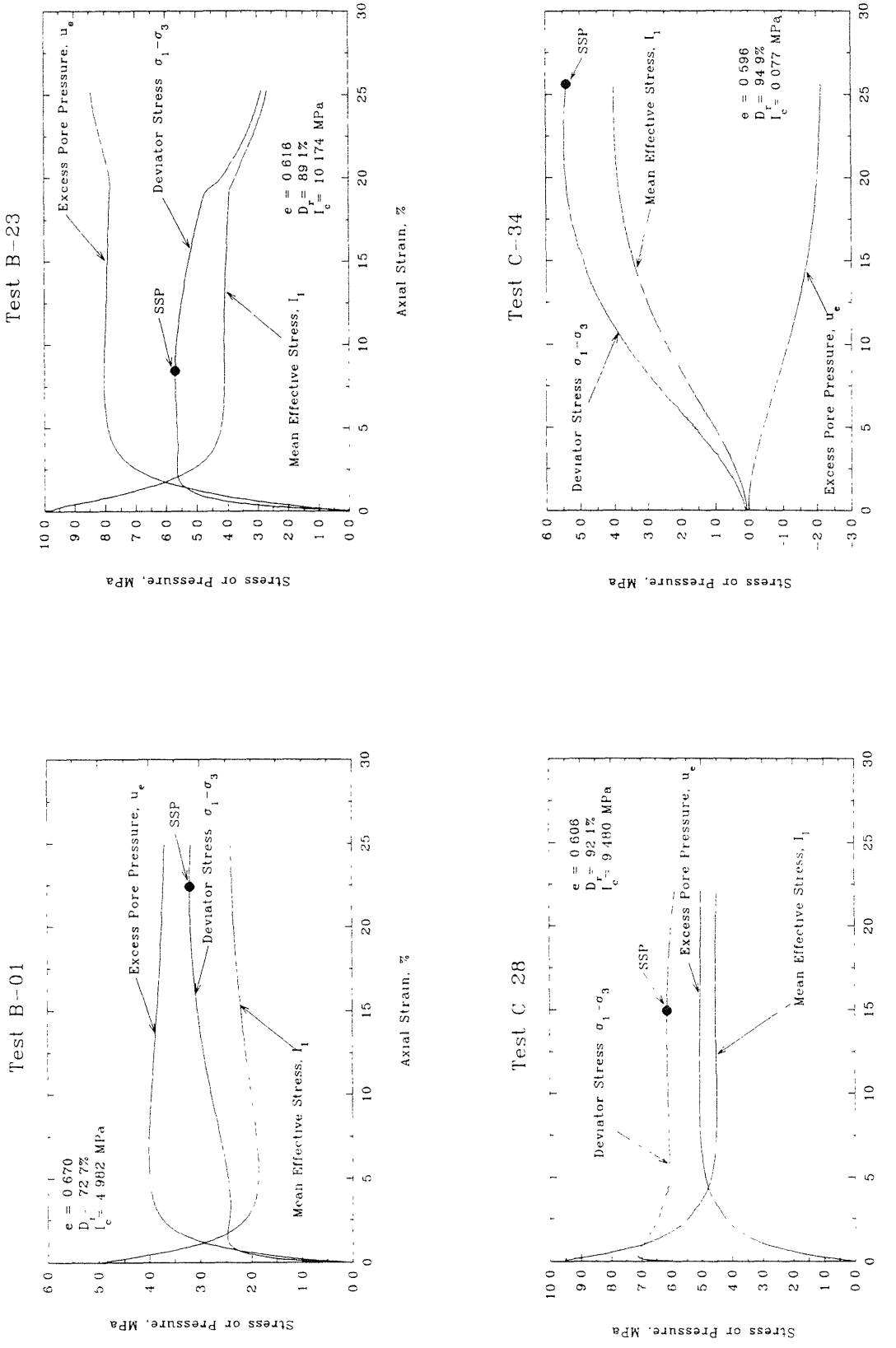

Figure 4.51 Steady State Condition for Four Undrained Triaxial Compression Tests

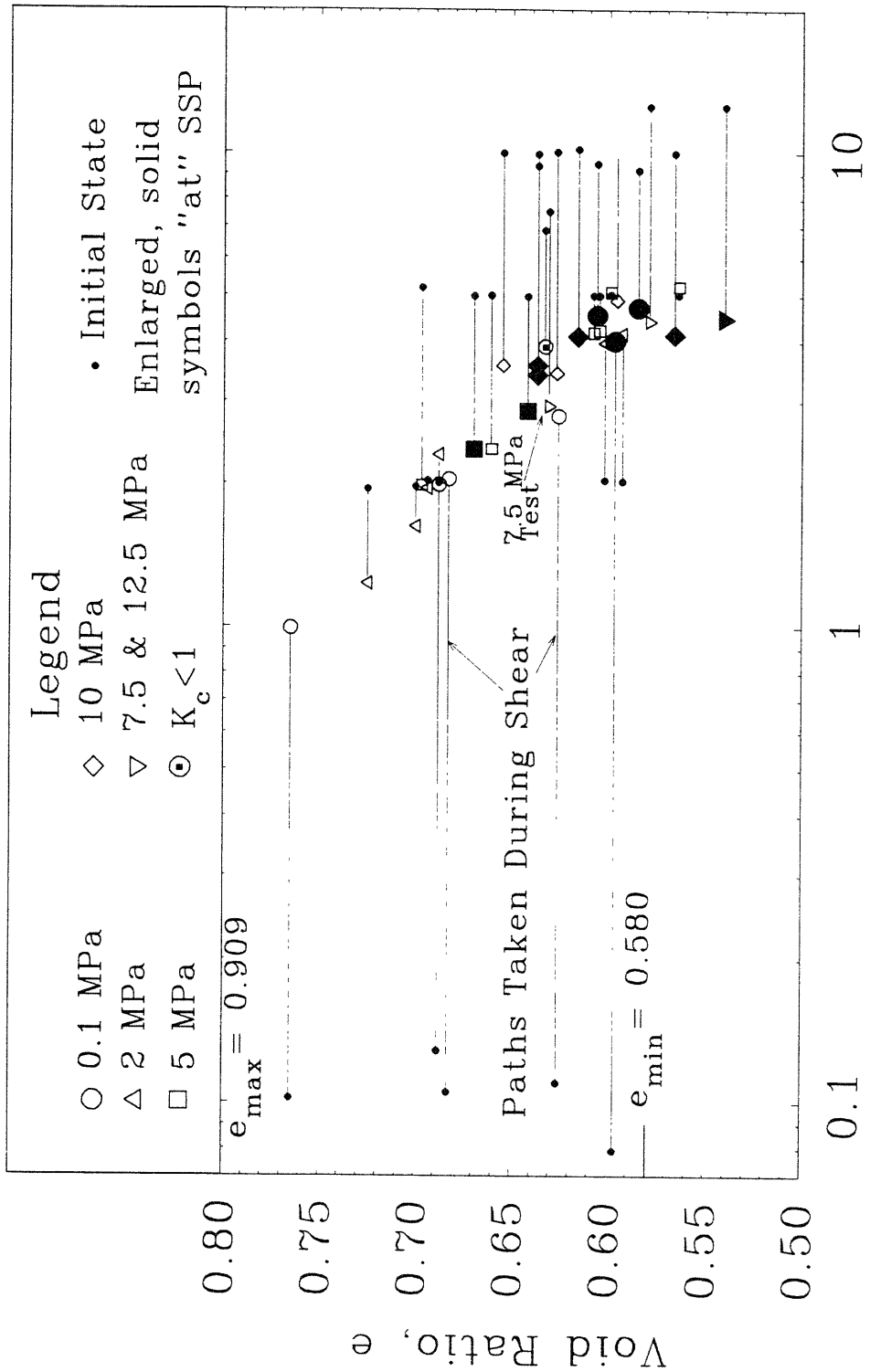

Figure 4.52 Steady State Points as Determined by Undrained Triaxial Compression Tests from Series B and Series C Tests

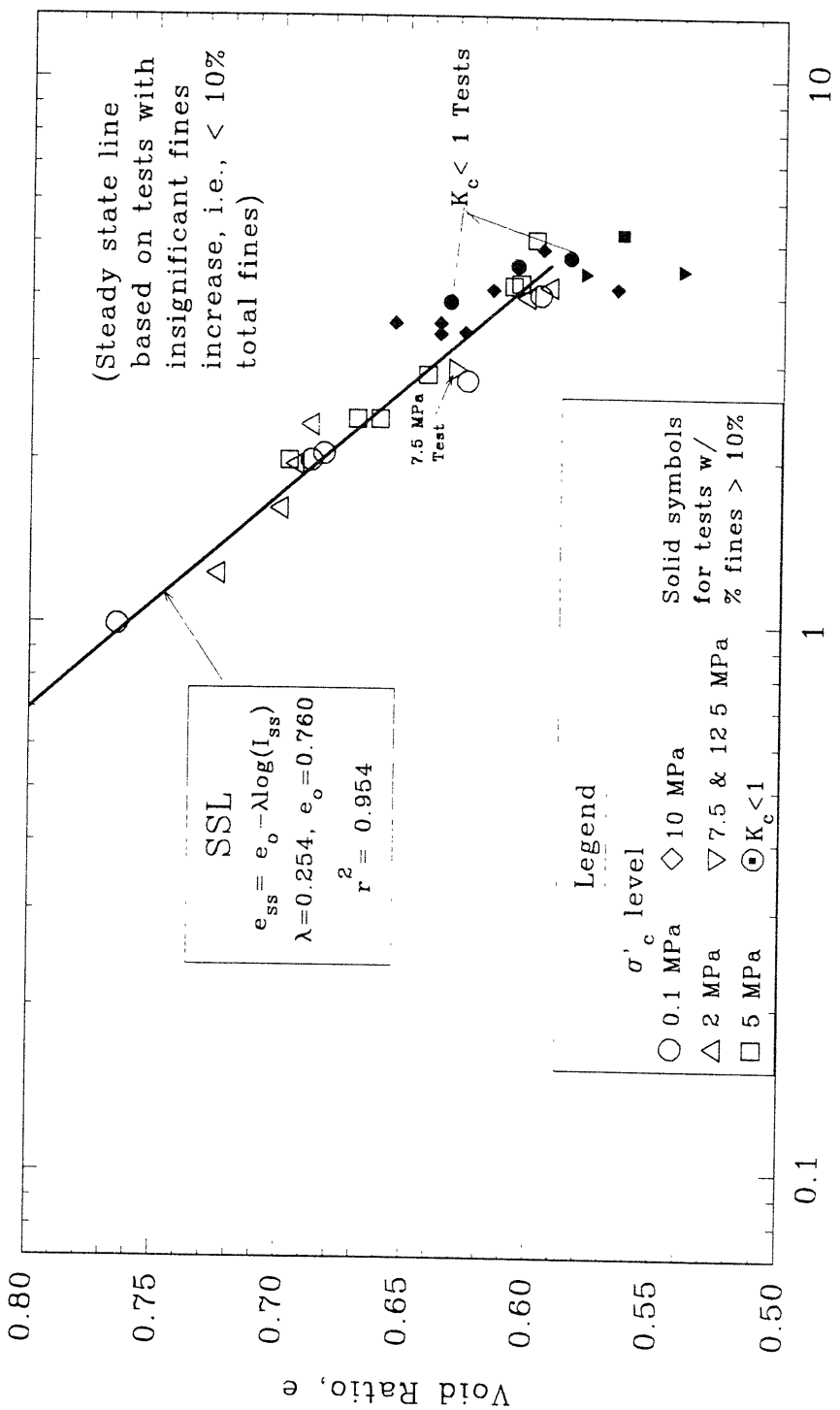

Figure 4.53 Steady State Line and Parameters as Determined by Undrained Tests from Series B and Series C Tests

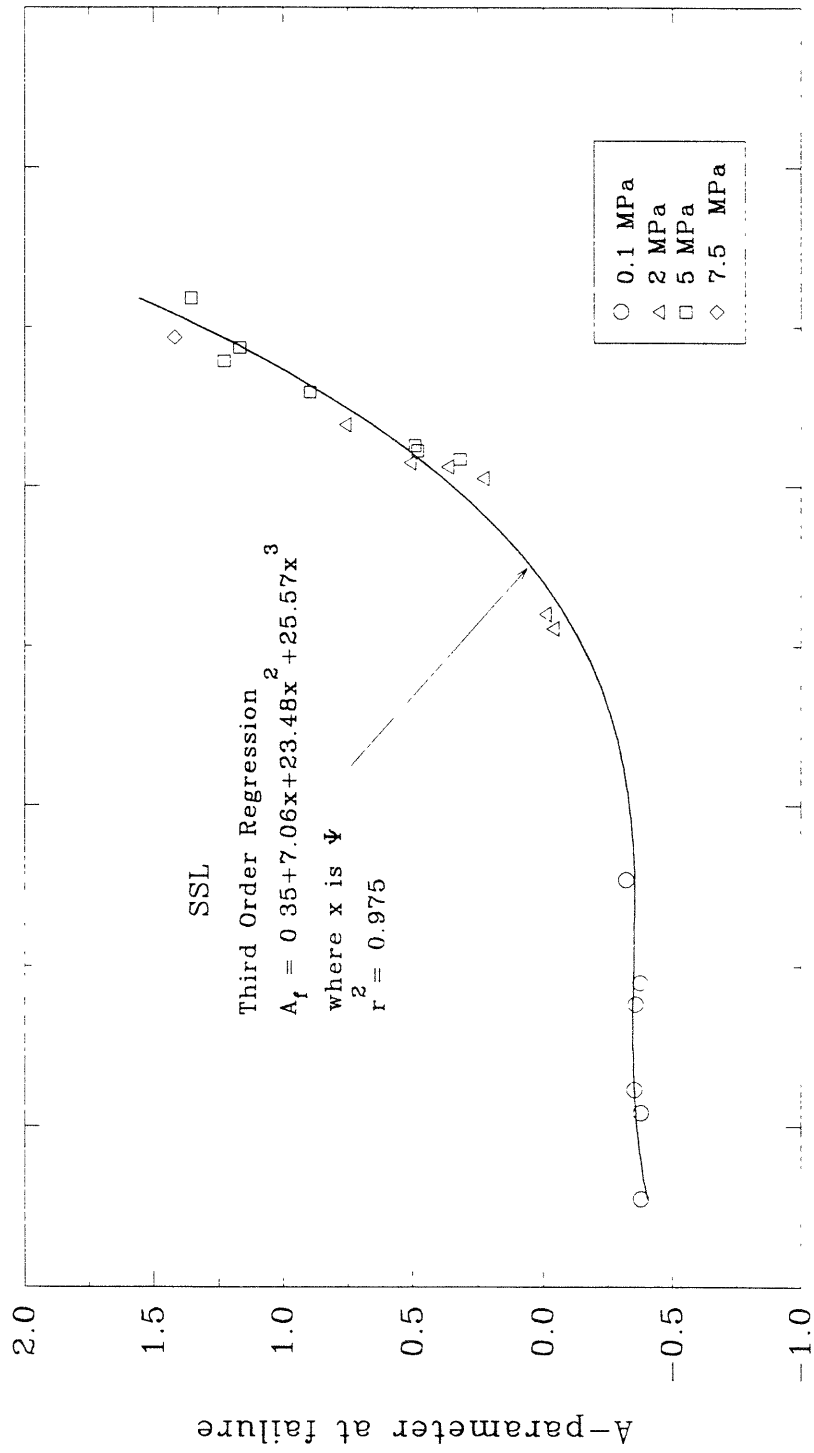

Figure 4.54 A_f versus State Parameter from CIUC Tests on Unfrozen MFS

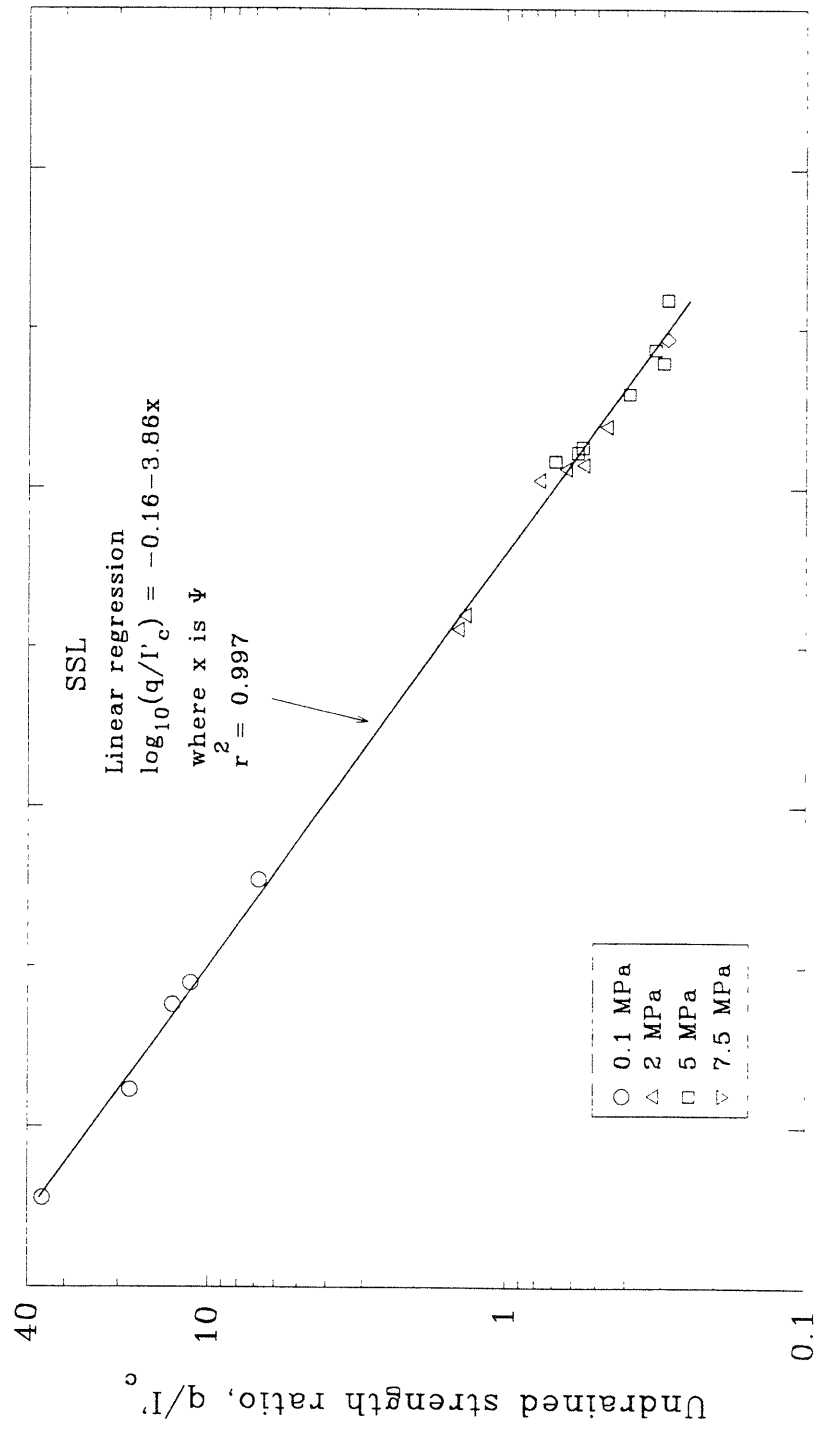

Figure 4.55 Undrained Strength Ratio, q/I'_c, versus State Parameter for CIUC Tests on Unfrozen MFS

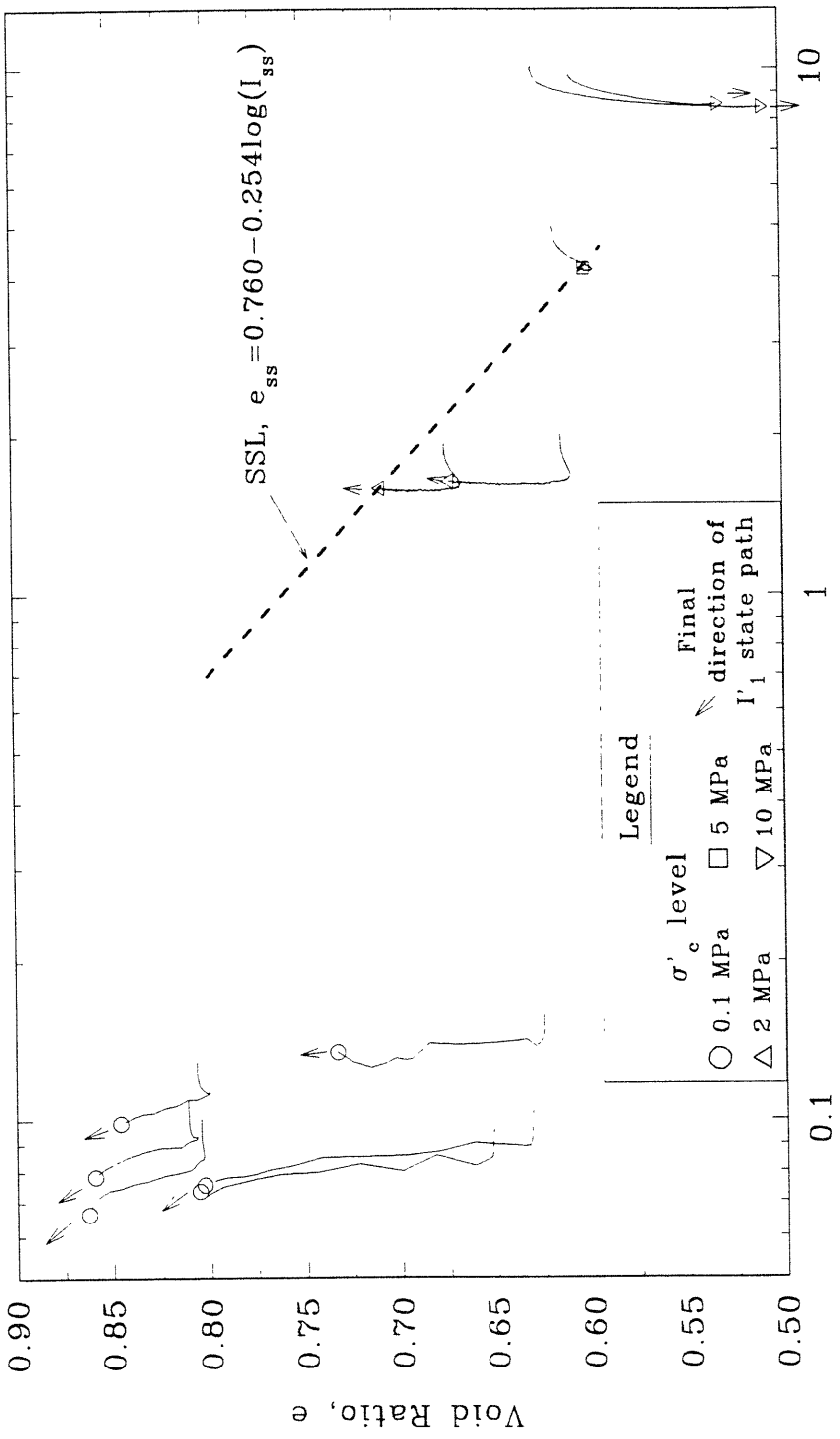

Figure 4.56 Comparison of Steady State Line, as Determined by Undrained Tests, and Drained Behavior in Triaxial Compression

CHAPTER 5
BEHAVIOR OF FROZEN MANCHESTER FINE SAND IN TRIAXIAL COMPRESSION TESTS

This chapter presents the results of the conventional frozen (specimens frozen in molds) and consolidate–freeze (specimens frozen under stress) triaxial compression tests performed on frozen Manchester Fine Sand. This presentation will encompass both the conventional tests performed by Andersen (1991) at –10° C as well as the conventional tests performed during the current research at temperatures of –15° C, –20° C and –25° C and the limited consolidate–freeze tests performed at T = –10° C.

The presentation will first focus on the effects of relative density (D_r), confining pressure (σ_c), strain rate ($\dot{\epsilon}$) and temperature (T) on the stress–strain and volumetric strain response of frozen MFS in conventional triaxial tests. Though all four testing variables are examined, the effect of temperature will be the principal variable throughout the presentation. After outlining the scope of the conventional frozen MFS testing program, the stress–strain behavior is presented in two major sections: small strain behavior and large strain behavior. The small strain behavior is described with respect to the Young's modulus (E), the yield offset stress at 10^{-4} (0.01%) strain (Q_{yo}) and the behavior in the upper yield region (the upper yield stress, Q_{uy}, and the strain to the upper yield stress, ϵ_y). The large strain behavior is evaluated in terms of the behavior in the peak strength region (the peak strength, Q_p, and the strain to peak strength, ϵ_p) and the volumetric behavior (maximum rate of dilation, $(d\epsilon_v/d\epsilon_a)_{max}$, and volumetric strain at 20% axial strain, ϵ_{v20}).

A presentation of all stress–strain and volumetric strain plots for all tests

would be too cumbersome. Therefore, this chapter presents representative stress–strain curves and detailed plots showing how the four testing variables affect the parameters that describe the behavior at small and large strains. Appendix C contains stress–strain and volumetric strain responses for each conventional test.

The presentation of consolidate–freeze triaxial tests results will focus on the effects of varying the pre–freezing confinement on the stress–strain and volumetric strain response of frozen MFS. The results of 10 consolidate–freeze tests are presented; all with similar relative densities and performed at the same strain rate (moderate) and temperature (–10° C). Similar to the presentation of the conventional tests, the presentation summarizes the results in terms of small and large strain behavior.

5.1 SCOPE OF TESTING PROGRAM

5.1.1 Conventional Triaxial Tests on Frozen MFS

Conventional tests on frozen MFS have been conducted in two phases at MIT. In the first phase of testing, a total of 50 "useful" conventional tests were conducted on frozen MFS specimens. These tests form the basis of the work by Andersen (1991). Table 5.1 presents a summary of this first testing program. The predominant testing temperature was –9.55±0.3° C, taken as a nominal –10° C. As shown in the table, tests were conducted at relative densities (D_r) ranging from 20 to 100% at nominal confining pressures (σ_c) of 0.1, 2, 5 and 10.0 MPa. The vast majority of tests were conducted at one of three nominal axial strain rates ($\dot{\epsilon}$): $3x10^{-6}$/sec (termed "slow"), $3x10^{-5}$/sec ("moderate") and $4x10^{-4}$/sec ("fast").

The second phase of testing, which is also summarized in Table 5.1 and is part of the current research effort, consisted of 49 "useful" conventional tests performed at three additional temperatures; –15° C (17 tests), –20° C (19 tests) and

–25° C (13 tests), to specifically study the effect of temperature on the behavior of frozen MFS. Actual average testing temperatures were –15.6° C, –20.3° C and –25.4° C for the tests. As with the first testing program, a range of relative densities was used in testing but the majority of testing was limited to relatively loose ($D_r \approx 35\%$) and dense ($D_r \approx 90\%$) specimens. The range in nominal confining pressures was also limited to only low (0.1 MPa) and high (10 MPa) confinement levels. The three nominal strain rates (slow, moderate, and fast) used in the first testing program were also used in this second testing program. In addition to these 49 tests, one test was performed at each of the following approximate temperature; –5° C, –14° C, –23° C, –24° C and –28° C. However, accurate temperature control for these tests is questionable and/or non–existent; therefore, these tests are not reported in the following presentation.

A combined total of 99 conventional tests on frozen MFS from the two phases will be used to evaluate the effects of the testing variables on the behavior of frozen MFS. However, as presented in Chapter 3 (Section 3.7), each test has also been categorized according to its performance during testing, i.e., the agreement between on–specimen ACDT's and the overall stability of the specimen during shear. Table 5.2 presents a summary of the performance criteria and specimen conditions needed for a test to be used in analysis. To ensure the use of the best quality data and most appropriate results, certain tests will be excluded in the evaluations that follow. For example, the presentation of small strain results is limited to specimens which had good to fair agreement between the on–specimen ACDT's. For the large strain presentation, tests prepared by wet tamping and/or which used utilized frictional ends conditions (grease or emery cloth) as opposed to lubricated end conditions (ice caps) are excluded.

Lines from linear regression analyses are frequently used to illustrate trends

of the data with respect to the testing variables (i.e., D_r, σ_c, $\dot{\epsilon}$ and T). The equations describing the regression line are given in the figures along with the coefficients of regression (r^2). In cases where a trend is constant with respect to a testing variable, a line representing the mean value of the result is shown with the mean and standard deviation (SD) stated.

5.1.2 Consolidate–Freeze Triaxial Tests on Frozen MFS

Ten consolidate–freeze tests were performed on dense specimens (D_r = 84.9 to 102.5%). Table 5.1 also presents a summary of the consolidate–freeze testing program. Tests were conducted at nominal effective confining stresses (σ'_c) of 0.1, 2, 5 and 10 MPa. Additional consolidation, prior to freezing, to higher confining stresses was performed for tests at σ'_c = 2, 5 and 10 MPa. All tests were sheared at moderate strain rate and at a nominal temperature of –10.12±0.16° C.

5.2 CONVENTIONAL TRIAXIAL TEST RESULTS

5.2.1 Small Strain Behavior

The graphical construction techniques used by Andersen (1991) to obtain various stress–strain parameters was presented in Fig. 2.70, but is more fully discussed in Section 3.7 and Figure 3.14. Figure 3.14a illustrates the derivation of the small strain parameters of Young's modulus (initial slope of the stress–strain curve) and the yield offset stress at 10^{-4} strain (intersection point of the stress–strain curve and a line with a slope of the Young's modulus translated by 10^{-4} strain). Figure 3.14b illustrates the upper yield region. The upper yield stress (Q_{uy}) and strain at upper yield stress (ϵ_y) represent the occurrence of significant plastic strains. Table 5.3 presents a tabulation of these small strain parameters for all conventional frozen tests on MFS, including those which have "poor" ACDT agreement. These parameters and how they are affected by the testing variables of D_r, σ_c, $\dot{\epsilon}$ and T are discussed below.

5.2.1.1 Young's Modulus, E

The Young's modulus for frozen MFS is found to be independent of $\dot{\epsilon}$ and T and only slightly dependent on D_r and σ_c. An average Young's modulus of 26.5 ±4.0 SD GPa is measured for 69 tests having good and fair ACDT agreement. Figure 5.1 plots Young's modulus versus relative density and shows that there is a slight increase in Young's modulus with increasing D_r (approximately 15% over tested D_r range), but the scatter in results ($r^2 = 0.06$) suggest an average value of Young's modulus equally represents the results. Note that no tests with "poor" ACDT agreement are used in the evaluation.

Figure 5.2 illustrates the effect of confining pressure on the Young's modulus for all tests. The figure indicates a decrease in modulus as the confining pressure increases from 0.1 to 10 MPa. The average decrease is approximately 10% between these two confinement levels. Figure 5.3 presents the measured Young's modulus versus temperature. The results indicate a very slight increase in modulus with decreasing temperature, but the scatter suggests that an average value of the modulus over the tested temperature range is equally valid.

5.2.1.2 Yield Offset at 10^{-4} Strain, Q_{yo}

Figure 5.4 plots Q_{yo} versus relative density for tests conducted at low and high confinement and moderate strain rate and shows that for each temperature Q_{yo} is independent of relative density at both confinement levels. However, there is a relatively strong influence of temperature on Q_{yo}, with the average value for tests at one temperature increasing as the test temperature decreases. There is also more scatter in the results as testing temperature decreases.

Figure 5.5 shows a plot of Q_{yo} versus confining pressure for moderate strain rate tests. In the figure, the offset stress tends to decrease with increasing confining pressure for temperatures of –10° C and –15° C, with the percent decrease

ranging from 24% to 29% for confining pressures between 0.1 and 10 MPa.

Figure 5.6 shows the effects of strain rate on Q_{yo} for tests at low and high confinement. Again, low confinement tests at –15° C were conducted only at the moderate strain rate so no trend can be analyzed. In addition, it should be noted that the strain rates used in this presentation represent the rates which are occurring at the Q_{yo} point, which are approximately an order of magnitude less than the nominal strain rate (see Table 5.3) For test at low confinement (Fig. 5.6a), the results at –10° C and –25° C exhibit similar rate sensitivities with power law coefficients of 11.2 to 13.7, respectively, and tests at –25° C have significantly higher Q_{yo} values. The tests at –20° C show a greater rate sensitivity with a power law coefficient of 6.7. Tests at high confinement (Fig. 5.6b) exhibit almost identical rate sensitivities with power law coefficients ranging from 8.9 to 13.6 for all four test temperatures. The increase in Q_{yo} with a decrease in temperature is clearly evident in the results.

Figure 5.7 shows the effect of temperature on Q_{yo} for tests at low and high confinement. As illustrated in the figure, Q_{yo} for both confinement levels increases with decreasing temperatures at all strain rates. In addition, the rate of change in Q_{yo} with decreasing temperature (dQ_{yo}/dT) increases with increasing strain rate for tests at both low and high confinement.

5.1.2.3 Behavior in the Upper Yield Region

On–specimen strain measurements provide, for the first time, an opportunity for a comprehensive evaluation of the upper yield region in terms of relative density, confining pressure, strain rate and temperature. The following presentation uses summary plots showing the effect of these four testing variables on the upper yield stress (Q_{uy}) and strain at upper yield stress (ϵ_y).

Andersen (1991) noted for tests at –10° C that the initial specimen length

may have affected Q_{uy}. Figure 5.8 reproduces a plot of the measured Q_{uy} versus initial specimen length for the set of tests at each temperature and shows that for tests at T = –10° C (Fig. 5.8a) Q_{uy} decreases as the initial length increased for all strain rates. Andersen (1991) reasoned that the reduction in Q_{uy} was due to the decrease in the "true" strain rate caused by the increased specimen length. Since the loading apparatus is displacement–controlled, the true strain rate of a specimen depends on its initial length. Longer specimens will have a slower "true" strain rate, and hence lower Q_{uy} values, than shorter specimens tested at the same nominal strain rate. Andersen used the regression lines in Fig. 5.8a to correct the Q_{uy} values for all tests to a length of 7.5 cm. Similar regression analyses were performed for tests at T = –15° C, –20° C and –25° C (Figs. 5.8 b, c and d, respectively). However, similar correspondences of decreasing Q_{uy} with increasing specimen length are not always evident. In fact, some Q_{uy}–specimen length correlations led to an increase in measured Q_{uy} with increasing length (e.g., slow strain rate tests at T = –25° C). In addition, a limited number of data points are available for some of these new correlations leading one to further question their validity. Given the questionable and contradictory nature of the specimen length correlations for tests at the lower temperatures, measured Q_{uy} values at all temperatures will be used in the following presentation.

Upper Yield Stress, Q_{uy}

Figure 5.9 shows the initial deviator stress versus strain ($Q - \epsilon_a$) responses (i.e., the response up to ϵ_a of 2%) of two tests at each of the four different temperatures; the tests are at different D_r but are at the same strain rate (moderate) and confining pressure (0.1 MPa). The figure illustrates that while for each set of tests the post–upper yield behavior is different, the Q_{uy} points are essentially the same and occur at nearly the same strain level. Figure 5.10a

presents a summary plot of Q_{uy} versus D_r for tests performed at moderate strain rate and all σ_c levels and temperatures. The figure, which includes all tests regardless of ACDT or stability quality, clearly shows that the Q_{uy} is independent of relative density for each of the tested temperatures and that Q_{uy} is strongly dependent on temperature. As illustrated in Fig. 5.10b, Q_{uy}'s independence of D_r also holds for tests at the slow and fast strain rates.

Figure 5.11 shows four sets of initial $Q - \epsilon_a$ responses for two tests at different σ_c levels but similar D_r ($\approx$ 35%) and $\dot{\epsilon}$ (moderate). For each set of tests the post–yield $Q - \epsilon_a$ responses differ but the upper yield region of the tests show similar Q_{uy} values for the tests at nearly identical strain levels. Figure 5.12a shows a plot of Q_{uy} versus confining pressure for all tests performed at the moderate strain rate. For tests at T = –10° C, regression analysis indicates that there is a slight decrease ($\approx$ 8%) in Q_{uy} with increases in confining pressure from 0.1 to 10 MPa. A smaller decrease ($\approx$ 2%) is noted for tests at T = –15° C. At T = –20° C and –25° C, Q_{uy} is essentially constant with confining pressure. Figure 5.12b shows plots of Q_{uy} versus σ_c for tests at slow and fast strain rates. For the slow and fast strain rates Q_{uy} may decrease (up to $\approx$ 4%) or increase (up to $\approx$ 10%) with increases in σ_c from 0.1 to 10 MPa. Based on the small and contradictory (increasing and decreasing trends) changes in the Q_{uy} with respect to confinement, it can be concluded that confining pressure has relatively little effect on Q_{uy}.

Figure 5.13 show four sets of initial $Q - \epsilon_a$ curves for tests at different strain rates but similar D_r ($\approx$ 35%) and confinement (σ_c = 10 MPa). It can be clearly seen that increased strain rate causes a significant increase in Q_{uy}. Figure 5.14 shows a log–log plot of Q_{uy} versus strain rate for tests at each temperature. The data points represent tests at all relative densities and confining pressures. These results closely follow a simple power law, with power law coefficients

consistently increasing with decreasing temperature and ranging from 4.62 at T = –10° C to 6.54 at T = –25° C. The increasing coefficient indicates a decrease in the rate sensitivity of the frozen MFS with decreasing temperature.

Figure 5.15 shows three sets of initial Q – ϵ_a curves for tests at different temperatures but with similar D_r and σ_c; one for each strain rate. The figure shows, that similar to the case for increasing $\dot{\epsilon}$, decreasing temperature also causes an increase in Q_{uy}. Figure 5.16 shows a plot of Q_{uy} versus temperature for tests at all D_r and σ_c. As illustrated in the figure, the lowest Q_{uy} values are for the slow strain rate tests at T = –10° C, and the highest Q_{uy} values are for the fast strain rate tests at T = –25° C. It is also evident that the rate of increase in Q_{uy} with decreasing temperature (dQ_{uy}/dT) increases with increasing strain rate with dQ_{uy}/dT = –0.58 MPa/° C for slow strain rate tests, dQ_{uy}/dT = –0.77 MPa/° C for moderate strain rate tests and dQ_{uy}/dT = –0.97 MPa/° C for fast strain rate tests.

Axial Strain at Q_{uy}, ϵ_y

Figure 5.17 shows three plots of the axial strain at upper yield stress, ϵ_y, versus D_r; one plot for each strain rate. Only tests with good or fair ACDT agreement were used in these summary plots. As was the case for Q_{uy}, the ϵ_y is essentially independent of D_r.

Figure 5.18 shows three plots of ϵ_y versus σ_c; one for each strain rate. The figure indicates that ϵ_y is also independent of confining pressure for tests at slow and moderate $\dot{\epsilon}$ and different temperatures. However, the tests at the fast strain rate indicate a slight global increase in ϵ_y at the higher σ_c level (trend not plotted).

Figure 5.19 presents a log–log plot of ϵ_y versus $\dot{\epsilon}$ for each temperature and shows that the ϵ_y – $\dot{\epsilon}$ relationships also are of a simple–power–law–type with "power law coefficients" increasing slightly for T = –10° C to T = –20° C tests (n =

5.54 to 7.02, respectively), then increasing substantially for tests at T = –25° C (n = 25.2). The decrease in rate sensitivity with lower temperatures coincides with the increased occurrence of the $Q_{uy} = Q_p$, even at moderate strain rates. This trend in ϵ_y behavior is indicative of the influence of the pore ice in the overall behavior of frozen MFS.

Figure 5.20 plots ϵ_y versus temperature and shows that ϵ_y increases with decreasing temperature for slow and moderate strain rate tests. Tests at fast strain rate appear to be relatively independent of temperature, which might be expected given the convergence of the linear regression lines in Fig. 5.19 at the fast strain rate.

5.2.1.4 Summary of Small Strain Behavior

Elastic Properties

Table 5.4 summarizes the effects of relative density, confining pressure, strain rate and temperature on the small strain behavior of frozen MFS. A change in relative density causes virtually no change in Young's modulus and yield offset stress for all testing conditions. Therefore, relative density or sand volume fraction (at this range of volume fractions) does not have an effect on the small strain behavior of frozen MFS. However, given the comparative Young's moduli for frozen MFS (26.5 GPa) and polycrystalline ice (≈ 9 GPa based on Sinha 1989), it would be erroneous to assume that the sand particles do not contribute to the small strain behavior (see Section 6.2 for application of isostrain model).

An increase in confining pressure leads to a slight decrease in the measured elastic parameters at temperatures of –10°, –15° C and –20° C. The trend in modulus results is completely opposite to the behavior measured in the unfrozen MFS testing program where increases in confinement led to large increases in Young's modulus (see Fig. 4.36). This suggests that the pore ice dominates frozen

MFS behavior at small strains. There are no reliable data on the effects of confining pressure on ice to compare with this small strain frozen MFS behavior.

The effects of strain rate and temperature are complex. Given that the behavior of ice is strongly influenced by strain rate and temperature, the increase in yield offset stress with increasing strain rate or decreasing temperature (Figs. 5.6 and 5.7) again suggests that the pore ice strongly influences the behavior of frozen MFS at very small strains. However, the Young's modulus is essentially insensitive to these same changes in strain rate and temperature. It appears as though an increase in strain rate or decrease in temperature causes an "extension" of the initially steep portion of the $Q - \epsilon_a$ curve (leading to increases in Q_{yo}) without changing the slope of the initial linear portion (leading to constant modulus).

Upper Yield Region

Table 5.4 also summarizes the behavior in the upper yield region. The upper yield region shows an even stronger influence of the pore ice. The magnitude of Q_{uy} is found to be independent of D_r and essentially independent of σ_c; variables which have great influence on the behavior of unfrozen MFS (e.g., Figs. 4.37 and 4.38). However, Q_{uy} is strongly influenced by strain rate and temperature; variables which have significant influence on the behavior of ice (see Section 2.2). This suggests that the physical mechanisms controlling the yield behavior of frozen sand are similar to those controlling the behavior of ice. It is also interesting to note that, in general, a larger ϵ_y is necessary to reach Q_{uy} as the strain rate increases or temperature decreases (Figs. 5.19 and 5.20).

5.2.2 Large Strain Behavior

This section discusses the large strain behavior of frozen MFS as described by the peak strength, Q_p; corresponding strain, ϵ_p; and the volumetric strain

behavior represented by the maximum rate of dilation, $(d\epsilon_v/d\epsilon_a)_{max}$, and volumetric strain at 20% axial strain, ϵ_{v20}. Tables 5.5 and 5.6 present a summary of these large strain parameters for conventional frozen MFS tests.

The large strain parameters were schematically illustrated in Fig. 3.14 c and d. Both strain softening and strain hardening occur after the upper yield stress is reached. Strain hardening leads to a peak strength higher than the upper yield stress. A number of tests exhibited both post–yield softening and then hardening similar to the distinct "double yield" behavior sometimes found for fine–grained polycrystalline ice (see Section 2.2, Fig. 2.45). A few test exhibited only strain softening after yielding. For these tests, the upper yield and peak strength coincide.

5.2.2.1 Types of Stress–Strain Curves

Figure 5.21 presents four basic types of stress–strain curves exhibited for conventional triaxial compression tests on frozen MFS. Note that the deviator stress in this figure has been normalized by the upper yield stress. As previously shown, Q_{uy} is essentially independent of D_r and σ_c but strongly dependent on $\dot{\epsilon}$ and temperature. For convenience, the following discussion uses normalized $Q - \epsilon_a$ curves when highlighting the effects of D_r and σ_c on the behavior of frozen MFS in conventional tests. Referring to Fig. 5.21 the four curve types may be described as follows.

Type A: The upper yield stress and peak strength coincide for this curve type. The $Q_{uy} = Q_p$ point is then followed by significant strain softening.

Type B: There is slight to moderate strain softening after reaching the upper yield point. The specimen then either maintains that stress or undergoes slight strain hardening to where Q_p at larger strains is approximately equal to Q_{uy}. There is no strain softening at large strains.

Type C: Rapid and significant post–Q_{uy} strain hardening occurs for this curve type. Upon reaching peak strength at moderate strain

levels, the $Q - \epsilon_a$ curve exhibits significant strain softening to stress levels near or below the upper yield stress.

Type D: The $Q - \epsilon_a$ curve exhibits significant strain hardening after the upper yield point with the peak strength occurring at large strains (i.e., $\epsilon_a > 10$ to 15%); no post peak strain softening.

Type A curves are most likely to occur for loose specimens at faster strain rates and low confinement at all temperatures used in this research. Type B curves develop for loose specimens at slower strain rates, low confinement and lower temperatures (i.e., $T \leq -25^\circ C$); or loose specimens at the fast strain rate, high confinement and all temperatures. Type C curves typically occur for dense specimens under low confinement at slow to moderate strain rates and all temperatures. This curve type can also occur for loose specimens under low confinement and slow to moderate strain rates and high temperatures. Type D curves exist for dense specimens under high confinement and all temperatures. Looser specimens under high confinement, slow strain rate and high temperatures may also exhibit Type D curves.

There are "transition" curves which do not fall fully into one of these four classifications. The most common case is for tests which exhibit a peak strength slightly higher than the upper yield stress; a condition which may occur for Type B and Type C curves. Therefore, two "hybrid" curve types, Type B_y and C_y, are used for stress–strain curves where $Q_p/Q_{uy} \leq 1.03$. In the following presentation, stress–strain responses will be classified according to these curve types.

5.2.2.2 Effect of Testing Variables on Stress–Strain Behavior

The general influence of the relative density, confining pressure, strain rate and temperature on the behavior of frozen MFS is first examined by comparing the stress–strain ($Q - \epsilon_a$) and volumetric strain (ϵ_v) responses of tests which have all but one of these testing variables held constant. Figures 5.22 through 5.32 present such comparison plots to illustrate the effects of D_r, σ_c, $\dot{\epsilon}$ and T on the large strain

behavior of frozen MFS. As stated earlier, D_r and σ_c have virtually no effect on the Q_{uy}; therefore, the $Q - \epsilon_a$ curves in comparison plots highlighting the effect of D_r and σ_c have been normalized by Q_{uy}. The $Q - \epsilon_a$ comparison plots illustrating the effects of strain rate and temperature are not presented in this normalized manner. Unlike analyses to correlate properties versus testing variables, all stress–strain curves will be used in these figures, regardless of ACDT agreement or stability classification. The effects of these variables on the $Q - \epsilon_a$ and ϵ_v responses are summarized below.

Effect of Relative Density, D_r

Figures 5.22 a, b, c and d illustrate the effect of D_r on frozen soil behavior for tests at temperatures of –10° C, –15° C, –20° C and –25° C, respectively. All tests were performed at moderate strain rate and low confinement. As illustrated in the figures, an increase in D_r causes a significant increase in the rate of post–Q_{uy} strain hardening (and hence peak strength) which is followed by strain softening (Type C curves). However, at lower temperatures (T = –20° C and –25° C) loose specimens exhibit strain softening after reaching the upper yield stress (Type A curves). Except for $Q - \epsilon_a$ curves where Q_{uy} and Q_p coincide, axial strains at peak strength are approximately the same for all D_r for tests at any one temperature. The volumetric strain response for all temperatures shows that an increase in D_r always leads to increased expansion of the specimen.

Figure 5.23 compares tests at different D_r for high confinement at T = –10° C. Similar to the tests at low confinement, the figures show an increase in peak strength for an increase in D_r. All $Q - \epsilon_a$ curves are Type D. The volumetric strain for tests at high confinement also show increased dilative response for increases in D_r, but at much smaller levels than low confinement tests.

Virtually all of the conventional tests on frozen MFS exhibited a dilative

response except for loose specimens at slow strain rate, high confinement and T = –10° C that exhibited essentially no change in volume during deformation. This expansive behavior of frozen sands is like that for drained tests on unfrozen sands under low confinement (Fig. 4.19); however, the expansive behavior under high confinement indicates that mechanisms other than those associated with the sand skeleton are also governing volumetric strain behavior.

Effect of Confining Pressure, σ_c

The effect of σ_c on the behavior of frozen MFS is best illustrated in Figures 5.24 a and b, which show the effect of a range of confining pressures on frozen MFS tests performed on loose and dense specimens, respectively, at moderate strain rate and T = –10° C. Both figures clearly show that an increase in σ_c also causes a large increase in the rate of post–Q_{uy} strain hardening and hence peak strength. However, the axial strain to peak strength increases with increasing confinement for both loose and dense specimens. Increasing confinement also leads a change in curves from Type C to Type D. As should be expected, the dilative volumetric strain response is also significantly reduced with increasing confining pressure for both loose and dense specimens. Since confining pressures were limited to only 0.1 MPa and 10 MPa for tests at T = –15° C, –20° C and –25° C, comparison plots showing the effect of σ_c are not presented for these temperatures.

Effect of in Strain Rate, $\dot{\epsilon}$

Figures 5.25 a, b, and c illustrate the effect of strain rate on the stress–strain responses of loose specimens at low confinement for temperatures of –10° C, –20° C and –25° C, respectively. In all three figures, it can be clearly seen that the upper yield stress increases with increasing strain rate and along with this increase in Q_{uy} there is an increase in Q_p. For all three temperatures, the increase in strain rate causes a change in stress–strain curve type from Type B or C for

slow strain rate tests to Type A for moderate or fast strain rate tests. These changes in response are indicative of a ductile–to–brittle transition in frozen soil behavior and leads to a decrease in the axial strain at peak strength until, at faster strain rates, the upper yield stress and peak strength coincide ($Q_p = Q_{uy}$ and $\epsilon_y = \epsilon_p$). For tests at T = –10° C, the magnitude of the dilative volumetric strain response increases with increasing strain rate.

Loose specimens under high confinement are illustrated in Fig. 5.26 a, b, c and d for temperatures of –10° C, –15° C, –20° C and –25° C, respectively. For all temperatures, the $Q - \epsilon_a$ curves show a change from Type D to Type B with increasing strain rate due to the decrease in post–Q_{uy} strain hardening. At lower temperatures, fast strain rate tests have $Q_p = Q_{uy}$ followed initially by significant strain softening. This strain softening is followed by a "leveling out" of deviator stress with continued deformation. The volumetric strain response shows a tendency for increased dilation with increased strain rate.

Figure 5.27 a and b illustrate the effect of strain rate for tests on dense specimens at low confinement and T = –10° C and –20° C, respectively. As was the case for loose specimens at low confinement, an increase in strain rate causes an increase in Q_{uy} and Q_p. For tests at T = –10° C (Fig. 5.27a) the amount of post–Q_{uy} strain hardening decreases with increasing strain rate although the $Q - \epsilon_a$ responses remain Type C. For tests at T = –20° C (Fig. 5.27b) the $Q - \epsilon_a$ curves change to Type A at the fast strain rate. For both temperatures, all tests exhibit similar large dilation responses regardless of the strain rate.

Figures 5.28 a and b show the effect of strain rate on dense specimens under high confinement at T = –10° C and –15° C, respectively. In both figures, both Q_{uy} and Q_p increase with increasing strain rate with $Q - \epsilon_a$ responses for these tests remaining Type D for all strain rates and temperatures except for the fast strain

rate test at T = –15° C which is Type C. It is likely that at faster strain rates or lower temperatures, the Q – ϵ_a responses would become Type B or even Type A. Tests at T = –10° C indicate that the volumetric strain responses show an increase in dilation with increasing strain rate.

Effect of Temperature, T

Figure 5.29 a, b and c shows the effect of temperature on frozen MFS behavior for loose specimens at low confinement and at slow, moderate, and fast strain rates, respectively. In all three figures, the Q_{uy} and Q_p increase with decreasing temperature. For tests at the slow strain rate (Fig. 5.29a), the curves essentially remain Type C curves for all temperatures. At the moderate strain rate (Fig. 5.29b), the curves change from Type C to Type A as the temperature decreases, while at the fast strain rate (Fig. 5.29c) the curves are all Type A. The volumetric response for tests at the slow strain rate indicates an increase in specimen dilation with decreasing temperature; however, at the moderate and fast strain rates, the ϵ_v response remains essentially the same.

Figure 5.30 a, b and c illustrate the effect of temperature on loose specimens at high confinement and slow, moderate, and fast strain rates, respectively. As was the case for low confinement tests, both the Q_{uy} and Q_p increase with decrease in temperature. For slow strain rate tests (Fig. 5.30a), all curves are Type D; however, there is a more pronounced change in post–Q_{uy} Q – ϵ_a behavior with decreasing temperature. For moderate strain rate tests (Fig. 5.30b), the curves change from Type D at T = –10° C to Type B at T = –25° C. At fast strain rates (Fig. 5.30c), the curves are all classified as Type B, but the amount of strain softening before the deviator stress becomes constant increases as the temperature decreases. For all three strain rates, the volumetric strain responses show an increase in dilation with decreasing temperature.

The study of the effects of temperature on dense specimens is restricted to slow and moderate strain rates due to the limited capacity of the load frame. Figure 5.31 a and b show the effect of temperature on dense specimens at low confinement and slow and moderate strain rates, respectively. In both figures, both the Q_{uy} and Q_p increase with decreasing temperature with all tests exhibiting significant post–Q_{uy} strain hardening. At both strain rates, the curves are Type C with the strain at peak strength being essentially the same for all temperatures. The volumetric strain responses are similar at all temperatures and strain rates. Figure 5.32 illustrates the effect of temperature for dense tests at high confinement and slow strain rate. As can be seen in the figure, the upper yield stress and peak strength both increase with decrease in temperature. All stress–strain curves are Type D with the strain at peak strength exhibiting a decreasing trend with decreasing temperature. The volumetric strain responses show an increase in dilation with decrease in temperature.

5.2.2.3 Effect of Testing Variables on Peak Strength Parameters

Based on the $Q - \epsilon_a$ curves in Figs. 5.22 to 5.32, it is clear that all testing variables affect the behavior at peak strength. The following material presents plots of the data to quantify the effects of D_r, σ_c, $\dot{\epsilon}$ and T on the peak strength (Q_p) and the strain at peak strength (ϵ_p). Tests performed on MSP–prepared specimens with lubricated ends, good to poor ACDT agreement and good to poor (but not very poor) stability are used for the evaluation of peak strength. However, all tests where Q_p and Q_{uy} coincide (Type A or B curves) are used regardless of specimen preparation or end conditions and ACDT and stability qualification. Table 5.5 contains a summary of the trends.

Peak Strength, Q_p

Effect of D_r. Figure 5.33 plots Q_p versus D_r for tests at low confinement, moderate strain rate and different temperatures. The results show an increase in peak strength with increasing D_r for all temperatures except for tests at T = –20° C and –25° C where Q_p is constant over a lower range of D_r. This linear trend is characterized by Type C curves. For looser specimens at these lower temperatures, relative density has essentially no effect on the peak strength because $Q_p = Q_{uy}$ or exceeds Q_{uy} by a very small amount ($Q_p/Q_{uy} \leq 1.03$). These conditions are identified in Fig. 5.33 as A and y, respectively. For test results which did not exhibit this behavior, a linear regression line has been used to describe the $Q_p - D_r$ relationship for each temperature. As illustrated in the figure, these linear regression lines suggest that the rate of increase in Q_p with respect to D_r (dQ_p/dD_r) increases with decreasing temperature. Given the occurrence of "Type A" $Q - \epsilon_a$ curves for tests at T = –20° C and –25° C, a bi–linear relationship can be used with a constant Q_p (= Q_{uy} for that temperature) representing the lower limit of Q_p. The intersection of the linear regression line and constant Q_p line occurs at D_r = 63% for T = –20° C and at D_r = 72% for T = –25° C.

For other strain rates, the majority of tests were performed on loose ($D_r \approx$ 35%) or dense ($D_r \approx$ 95%) specimens. Figure 5.34 plots Q_p versus D_r for low confinement tests at slow and fast strain rates. Again, it should be noted that there are no results for tests at T = –15° for these strain rates. The trends of Q_p for these tests have been developed as described earlier for the moderate strain rate results which are also plotted in Fig. 5.34. For tests at the slow strain rate (Fig. 5.34a), which are all Type C $Q - \epsilon_a$ curves, dQ_p/dD_r is essentially the same for all temperatures. For fast strain rate tests (Fig. 5.34b), given the predominance of

Type A curves, the effect of relative density is either small or non–existent. It should be noted that for fast strain rate tests at T = –10° C, the loose specimen exhibited a Type A Q – ϵ_a curve while the dense specimens exhibited Type C curves. Andersen (1991), in his analysis of these results, concluded that the Q_p – D_r relationship followed a bi–linear trend and hypothesized that dQ_p/dD_r for the denser specimens was similar to that for moderate strain rate tests. Andersen's bi–linear relationship is plotted in Fig. 5.34b where the intersection of the constant Q_p (= Q_{uy}) line and assumed dQ_p/dD_r line occurs at a $D_r \simeq 75\%$.

Figure 5.35 plots Q_p versus D_r for moderate strain rate tests under high confinement (σ_c = 10 MPa) at different temperatures. The Q – ϵ_a curves for these tests are Type D. Linear regression lines for each set of tests at the different temperatures (T = –10° C, –15° C and –20° C) show that the rate of increase in Q_p with increasing D_r is essentially the same for all temperatures (dQ_p/dD_r = 0.12).

Figure 5.36 shows plots of Q_p versus D_r for high confinement tests at slow and fast strain rates. Like moderate strain rate tests, all slow strain rate tests at high confinement (Fig. 5.36a) exhibit Type D curves, and the dQ_p/dD_r values are 0.12. Fast strain rate tests (Fig. 5.36b) at –10° C and –15° C also exhibit Type D curves with dQ_p/dD_r equal to 0.12. However, at T = –20° C, the Q – ϵ_a curves are Type B with $Q_p = Q_{uy}$ and dQ_p/dD_r is flat (zero). These results at high confinement show that the increase in strength with D_r is strongly dependent on curve type with Type D curves showing a constant increase in strength for all temperature and strain rate conditions while Type B curves exhibit no change in Q_p with D_r.

Effect of σ_c. The effect of confining pressure has been indirectly presented in the previous discussion on the effect of D_r where both low and high confinement test conditions were presented. An evaluation of the effects of confinement using a

wide range of pressure was best demonstrated in Andersen (1991) for tests at T = –10° C. Figure 5.37 plots Q_p versus confining pressure for moderate strain rate tests at three different densities for this temperature. The data points represent values from linear regressions of the $Q_p - D_r$ data. The figure shows that for loose (D_r = 35%) specimens, increased confinement leads to an increase in strength up to σ_c = 5 MPa, where the peak strength is similar to the upper yield stress. The $Q - \epsilon_a$ curves for loose specimens are Type C. In this plotting format, the friction angle ϕ may be calculated as

$$\phi = \sin^{-1}\left(\frac{dQ_p/d\sigma_c}{dQ_p/d\sigma_c + 2}\right) \qquad 5.1$$

For loose specimens, the ϕ angle ranges from 11.2° at low confinement to 1.6° for higher confinement. For dense specimens (D_r = 95%), where the $Q - \epsilon_a$ curves were Type C to Type D, an increase in σ_c causes a near linear increase in peak strength. For dense specimens, a constant ϕ of 15.6° is calculated over the entire confining pressure range.

It is not possible to adequately evaluate the effect of σ_c for tests at T = –15° C, –20° C and –25° C since they were performed at only σ_c = 0.1 MPa and 10 MPa. However, given the linear $dQ_p/d\sigma_c$ line for dense specimens at T = –10° C in Fig. 5.37, it can be assumed that a linear $dQ_p/d\sigma_c$ relationship exist for tests on dense specimens at lower temperatures. Figure 5.38 shows a plot of Q_p versus σ_c for tests on dense specimens at the moderate strain rate at other temperatures. Data could only be developed for T = –15° C and –20° C based on the linear regressions in Figs. 5.33 and 5.35. As shown in the figure, the ϕ angle reduces from 15.6° to 9.1° as the temperature decreases from T = –10° C to –20° C. However, the data at lower temperatures may be insufficient to prove if these trends are representative $dQ_p/d\sigma_c$ relationships over the entire range of confining pressure. That is, a reduction in ϕ, as shown for looser specimens at T = –10° C in Fig. 5.37,

may be occurring for tests on dense specimens at lower temperature. Additional data at intermediate confining pressures are needed for more conclusive analysis.

Effect of Strain Rate, $\dot{\epsilon}$. Figure 5.39 plots Q_p versus strain rate for loose and dense specimens under low confinement. Note that there are no results presented for T = –15° C since tests were only performed at the moderate strain rate. As shown in Fig. 5.39a, the strength of loose specimens increases significantly with increasing strain rate for all temperatures. The power law coefficients are similar for the three presented temperatures ranging from 5.9 to 7.1. For dense specimens (Fig. 5.40b), the peak strength also increases with increase in strain rate. The power law coefficient of 7.9 for dense tests at T = –10° C is slightly higher than that for loose specimens (n = 6.4). The power law coefficients for the tests at T = –20° C and –25° C also show an increase from their loose specimen counterparts with the increase becoming more significant as the temperature decreases. These higher power law coefficients indicate that the dense specimens are less rate sensitive than the loose specimens. This behavior should be expected given the increased contribution of the sand skeleton to Q_p for dense specimens. It is also interesting to note that for loose specimens tested at the moderate and fast strain rates and T = –20° C and –25° C, the $Q - \epsilon_a$ curves are Type A ($Q_p = Q_{uy}$) while dense specimens at all temperatures have Type C $Q - \epsilon_a$ curves. Therefore, since the Q_{uy} behavior is strongly influenced by the pore ice, loose specimens should (and do) show an increase in rate sensitivity over that of the dense specimens.

Figure 5.40 shows a plot of Q_p versus $\dot{\epsilon}$ for loose and dense specimens under high confinement. As shown in Fig. 5.40a, loose specimens at T = –10° C show a slightly less rate sensitivity than specimens at T = –15° C, –20° C and –25° C. The power law coefficient for the T = –10° C tests is 9.8 while the n–value ranges from

7.4 to 8.0 for tests at lower temperatures. Similar to the low confinement tests on loose specimens, tests at the fast strain rate and T = –20° C and –25° C have Type B Q – ϵ_a curves with $Q_p = Q_{uy}$; however, at the slow and moderate strain rates, the Q – ϵ_a curves are predominantly Type D. For dense specimens under high confinement (Fig. 5.40b), regression lines can only be developed for tests at T = –10° C and –15° C. The power law coefficients are similar for both temperatures with n = 11.4 for T = –10° C tests and n = 12.5 for T = –15° C. As for the tests at low confinement, the results for tests at high confinement show that the rate sensitivity of frozen MFS decreases with sand density.

To evaluate the coupled effects of confinement and strain rate, Figure 5.41 presents a log–log plot of Q_p versus $\dot{\epsilon}$ for loose specimens at low and high confinement for T = –10° C, –20° C and –25° C. For all three temperatures the greatest difference in Q_p, with respect to the level of confinement, occurs at the slow strain rate. This Q_p difference decreases as the temperature decreases. Tests at the slow strain rate exhibited Type C or Type D curves. As the strain rate increases, the difference between low and high confinement Q_p values decreases to where at T = –25° C the low and high confinement tests have essentially the same peak strength. It can be reasoned that the difference in Q_p between low and high confinement tests at slow strain rate is because at high confinement, the peak strength is developed at large strains where the contribution of the sand skeleton predominates. As shown for unfrozen MFS, increased confinement leads to an increase in Q_p. At faster strain rates, the contribution of the sand friction is minimal or non–exist as the peak strength is near or coincides with the ice–controlled Q_{uy}. It is also interesting to note that the power law coefficients for the loose specimens at T = –10° C range from 6.4 at low confinement to 9.8 at high confinement; both n–values higher than that for Q_{uy} (n = 4.6). This decrease in

rate sensitivity of the peak strength of frozen MFS compared to that of the upper yield stress illustrates the influence of the rate–insensitive sand skeleton on the Q_p $\dot{\epsilon}$ behavior.

Effect of Temperature, T. Figure 5.42 shows plots of Q_p versus temperature for tests on loose specimens at low and high confinement. For both levels of confinement, the figure shows a linear dependence of Q_p on temperature with an overall increase in Q_p with increasing strain rate. For low confinement tests (Fig. 5.42a), the rate of increase in Q_p with decreasing temperature (dQ_p/dT) increases with strain rate from –0.55 MPa/° C for slow strain rate tests to –1.02 MPa/° C for fast strain rate tests. As noted in the figure, all fast strain rate tests results are from tests with Type A $Q - \epsilon_a$ curves; therefore, dQ_p/dT for fast strain rate tests should be similar to dQ_{uy}/dT for fast strain rate tests (= –0.97 MPa/° C; see Fig. 5.16). The non–equality is due to the inclusion of all tests in the Q_{uy} derivation. For the slow and moderate strain rate results, the dQ_p/dT values are slightly lower than their dQ_{uy}/dT counterparts. For fast strain rate results at high confinement (Fig. 5.42b), a similar condition of $dQ_p/dT \approx dQ_{uy}/dT$ exists where dQ_p/dT =–1.05 MPa/° C; although one of these fast strain rate tests did not have a Type A curve, that test at T = –10° C had a Q_p only 0.4 MPa higher than Q_{uy}. Both the moderate and slow strain rate test results show smaller dQ_p/dT values than at low confinement. Comparison of the trends observed in Figs. 5.16 and 5.42 leads to the general conclusion that the difference between Q_p and Q_{uy} for loose specimens increases with increase in confinement, decrease in strain rate and increase in temperature.

Figure 5.43 shows the effect of temperature for tests on dense specimens at low and high confinement. It was not possible to evaluate the full range of temperatures and strain rates for dense tests given the limited capacity of the

loading frame. However, the available results do show the expected trend of increasing Q_p with decreasing temperature and increasing strain rate. For tests at low confinement (Fig. 5.43a), the slow and moderate strain rate results have similar dQ_p/dT values, –0.62 versus –0.67 MPa/°C, respectively. The limited results for tests at high confinement (Fig. 5.43b) also have similar dQ_p/dT values, if the moderate strain rate results are considered as an anomaly, with $dQ_p/dT \approx$ –0.6 MPa/°C. Note that all of the dQ_p/dT values are less than or approximately equal to their dQ_{uy}/dT counterparts; namely, dQ_{uy}/dT = –0.77 MPa/°C for moderate strain rate tests and dQ_{uy}/dT = –0.58 MPa/°C for slow strain rate tests. Based on the limited data, the rate of increase in Q_p with decreasing temperature is approximately the same for tests on dense specimens regardless of confinement or strain rate (i.e., dQ_p/dT = –0.6±0.05 MPa/°C). However, these variables do cause significant changes in the magnitude of Q_p.

Axial Strain at Peak Strength, ϵ_p

Figure 5.44a plots the strain at peak strength (ϵ_p) versus relative density for moderate strain rate tests at low and high confinement. Only tests with good to fair stability (i.e., excluding poor and very poor) are considered in this evaluation unless Q_p and Q_{uy} are coincident for which all tests are used (i.e., same conditions as for ϵ_y). It can be seen that the ϵ_p is essentially constant ($\epsilon_p = 4.9 \pm 1.2\%$ SD) for all D_r and all temperatures at low confinement, excluding tests with Type A $Q - \epsilon_a$ curves where $\epsilon_p \approx 1\%$. Note that the Type A curves occur for tests at lower temperatures and D_r. At high confinement, ϵ_p increases with both decreasing D_r and increasing temperature. It should be noted that the $Q - \epsilon_a$ responses for low confinement tests are generally Type C while the response for high confinement is generally Type D. Figure 5.44b shows plots of ϵ_p versus D_r for slow and fast strain rate tests. The trends obtained above for moderate strain

rate tests are shown for comparison. Although there are a limited number of data points, especially for fast strain rate tests, the ϵ_p results follow similar patterns as those for moderate strain rate tests, i.e., a constant ϵ_p for low confinement, non–Type A curve tests and increasing ϵ_p with decreasing D_r and increasing temperature for high confinement tests.

Figure 5.45a shows plots of ϵ_p versus confining pressure for slow, moderate and fast strain rate tests on loose specimens and shows that for all non–Type A $Q - \epsilon_a$ curve results, ϵ_p increases with σ_c. For slow strain rate tests, the rate of increase in ϵ_p with σ_c ($d\epsilon_p/d\sigma_c$) ranges from 1.5 to 1.8 %/MPa for tests at T = –10° C, –20° C and –25° C. For moderate strain rate tests, the two determinable $d\epsilon_p/d\sigma_c$ values are 2.45 %/MPa for T = –10° C tests and 2.00 %/MPa for T = –15° C. No trends in data could be determined from the fast strain rate tests. Figure 5.45b shows plots of ϵ_p versus σ_c for slow and moderate strain rate tests on dense specimens. Again, limited data are available for tests on dense specimens; however, the data do show that the ϵ_p increases with increased confinement.

Figure 5.46a shows the effect of strain rate on ϵ_p for tests at low confinement. For loose or dense specimens with non–Type A $Q - \epsilon_a$ curves, the general trend considering tests at all temperatures is for ϵ_p to decrease with increasing strain rate. Figure 5.46b shows the effect of strain rate on ϵ_p for tests at high confinement. As for tests at low confinement, high confinement tests on loose or dense specimens with non–Type A $Q - \epsilon_a$ curves show a general trend of decreasing ϵ_p with increasing strain rate. Note that the trend shown for dense specimens is based on the results at T = –15° C.

Figure 5.47 shows plots of ϵ_p versus temperature for tests at low and high confinement. For tests at low confinement, it may be concluded that temperature has little effect on ϵ_p with $\epsilon_p = 4.9 \pm 1.2\%$ SD for all non–Type A curve tests.

However, insufficient data exist to strongly support this trend. For tests at high confinement, the various test conditions produce a number of $d\epsilon_p/dT$ trends which, in general, show a decrease in ϵ_p with decreasing temperature.

5.2.2.4 Volumetric Strain Behavior

Previously, Figs. 5.22 to 5.32 illustrated the effects of D_r, σ_c, $\dot{\epsilon}$ and temperature on the volumetric strain (ϵ_v) response. As previously discussed in Section 5.2.2.2, the overall ϵ_v behavior is very different from unfrozen sand in that virtually all specimens exhibited expansion during shear. Some additional aspects of the volumetric strain behavior are:

1) The ϵ_v response for all tests follows a similar pattern; essentially no ϵ_v prior to the upper yield point and then followed by volumetric expansion (dilation) with continued shear. However, the amount of dilation is suppressed very significantly by increases in confining pressure (σ_c). This general response is observed for all four types of $Q-\epsilon_a$ curves.

2) The peak strength does not occur at the maximum rate of dilation, $(d\epsilon_v/d\epsilon_a)_{max}$ as it does for drained tests on unfrozen sands (see Section 4.2, Figs 4.18 and 4.20).

3) For loose specimens under low confinement and fast strain rate or lower temperature, the level of volumetric expansion creates a condition where the overall specimen relative density drops below 0% after large axial strains. Such a condition cannot be reached in the unfrozen state; therefore, a significant contribution to dilation must be from the pore ice matrix.

As illustrated in Figs. 5.22 through 5.32, the effects of the testing variables on the ϵ_v behavior can be summarized as follows.

Effect of D_r (Figs. 5.22 a, b, c, d and 5.23): For tests at low confinement, an increase in D_r from loose to dense, leads to a two–fold increase in ϵ_v based on values at large axial strains ($\epsilon_a \geq 15$ to 20%). This two–fold increase occurred for all tested temperatures (for moderate strain rate). Tests on loose and dense specimens at high confinement also suggest an increase in ϵ_v by two–fold.

Effect of σ_c (Figs. 5.24 a and b): Level of confinement has a very significant effect on ϵ_v. For both loose and dense specimens, there is an approximately twelve–fold decrease in ϵ_v from low to high confinement.

Effect of $\dot{\epsilon}$ (Figs. 5.25 to 5.28): The effect of $\dot{\epsilon}$ on ϵ_v is generally much smaller compared to the effects of D_r and σ_c. In addition, strain rate effects are more complex. For example, loose specimens tested at low confinement and T = –10° C (Fig. 5.25a) show a two–fold increase in ϵ_v with increasing $\dot{\epsilon}$ while similar tests at lower temperatures (Figs. 5.25 b and c) show virtually no change in ϵ_v as the $\dot{\epsilon}$ increases.

Effect of T (Figs. 5.29 to 5.32): Similar to the effects of $\dot{\epsilon}$, the effects of temperature are also complex. For example, for loose specimens at low confinement (Fig. 5.29a), a decrease in temperature leads to a two–fold increase in ϵ_v for slow strain rate tests but there is virtually no change in ϵ_v with temperature for tests at moderate and fast strain rates (Figs. 5.29 b and c).

The effect of the testing variables on the volumetric strain behavior can be quantified by using the maximum rate of dilation, $(d\epsilon_v/d\epsilon_a)_{max}$, and the volumetric strain at 20% axial strain, ϵ_{v20}. The methods used to obtain both of these quantities were illustrated in Fig. 3.14d.

Maximum Rate of Dilation, $(d\epsilon_v/d\epsilon_a)_{max}$

Figure 5.48 shows plots of $(d\epsilon_v/d\epsilon_a)_{max}$ versus D_r for tests at low and high confinement. Tests with lubricated ends, good to poor ACDT agreement and good to poor stability were considered for this evaluation. For tests at low confinement (Fig. 5.48a), there is a generally a strong trend of increasing $(d\epsilon_v/d\epsilon_a)_{max}$ with increasing D_r. The rate of increase in $(d\epsilon_v/d\epsilon_a)_{max}$ with D_r is essentially the same. For tests at high confinement (Fig. 5.48b), the rate of increase in $(d\epsilon_v/d\epsilon_a)_{max}$ with D_r becomes much less.

The effects of confinement on $(d\epsilon_v/d\epsilon_a)_{max}$ are illustrated in Fig. 5.49 for tests on loose and dense specimens. In both figures, it can be seen that increased confinement leads to a significant reduction in $(d\epsilon_v/d\epsilon_a)_{max}$. The rate of decrease in $(d\epsilon_v/d\epsilon_a)_{max}$ with increasing σ_c is larger for dense specimens than for loose specimens. Figure 5.50 plots $(d\epsilon_v/d\epsilon_a)_{max}$ versus temperature considering loose and dense specimens separately. As illustrated in the figure, $(d\epsilon_v/d\epsilon_a)_{max}$ increases slightly with decreasing temperature for loose specimens but is essentially constant with temperature for dense specimens.

Volumetric Strain at $\epsilon_a = 20\%$, ϵ_{v20}

Figure 5.51 plots ϵ_{v20} versus D_r for tests at low and high confinement. For tests at all strain rates and temperatures, ϵ_{v20} increases with increasing D_r for tests at low confinement (Fig. 5.51a), but ϵ_{v20} is essentially constant for tests at high confinement (Fig. 5.51b). The effect of σ_c on ϵ_{v20} is illustrated in Fig. 5.52 for tests on both loose and dense specimens. For both specimen densities, the plots shows that ϵ_{v20} decreases with increasing confinement. The rate of decrease in ϵ_{v20} is larger for dense specimens versus loose specimens. Figure 5.53 presents a plot of ϵ_{v20} versus temperature for loose and dense specimens. Similar to the case for $(d\epsilon_v/d\epsilon_a)_{max}$, the ϵ_{v20} increases with decreasing temperature for loose specimens

but is essentially constant for dense specimens.

5.2.2.5 Summary of Large Strain Behavior

Section 5.2.1.4 concluded that Q_{uy} was independent of D_r and σ_c (both of which effect the behavior of unfrozen sand) and increased with increasing $\dot{\epsilon}$ and temperature (both of which effect the behavior of ice). In contrast to the small strain behavior, the large strain behavior is influenced by all four variables, i.e., both the pore ice and sand skeleton become important.

Table 5.5 summarizes the effects of the testing variables on the behavior in the peak strength region (both Q_p and ϵ_p). For Type A and B curves, Q_p is essentially not affected by D_r and σ_c since $Q_p \approx Q_{uy}$; however, for Type C and D curves D_r and σ_c strongly effect Q_p results. Both Type A and B curves occur for loose frozen MFS sheared at the fast strain rate, but also occur at moderate strain rate at lower temperatures. With respect to Type C and D curves, Type C curves are predominant at low confinement while Type D curves are predominant at high confinement. The rate of change in Q_p with D_r (dQ_p/dD_r) increases from 0.06 for Type C (low confinement) tests to 0.12 for Type D (high confinement) tests (see Figs. 5.35 and 5.36). The rate of change in Q_p with σ_c ($dQ_p/d\sigma_c$) decreases with decreasing density, especially at higher levels of confinement (see Fig. 5.37).

For Type A and B curves, the effects of strain rate and temperature are similar to those on Q_{uy} to where Q_p ($\approx Q_{uy}$) exhibits similar strain rate and temperature sensitivities as Q_{uy}. For Type C and D curves, the sand skeleton contributes a significant amount of frictional resistance to the Q_p development leading to lower rate and temperature sensitivities of Q_p (i.e., higher n–values and lower dQ_p/dT values).

Table 5.6 summarizes the volumetric strain behavior as represented by $(d\epsilon_v/d\epsilon_a)_{max}$ and ϵ_{v20}. The sand skeleton affects the volumetric strain behavior

since increases in D_r always led to increases in the amount of dilation. In addition, increases in the level of confinement always led to a decrease in the amount of dilation. However, the pore ice also contributes to the measured volumetric expansion as the pore ice cracks during shearing. It can be hypothesized that the level of cracking increases as testing variables lead to more "brittle" failure conditions for the pore ice, i.e., lower temperatures and/or faster strain rates. This increased cracking activity probably accounts for the greater dilation in tests on loose specimens which can expand to values of $D_r < 0\%$ at low confinement. However, for dense specimens, strain rate and temperature have little effect on ϵ_v behavior; thus it appears that the sand skeleton has increased control of the ϵ_v behavior as sand density increases.

An additional characteristic worth noting concerns the post–shear sieve analyses performed on conventional frozen MFS tests. Similar to the unfrozen MFS testing program, sieve analyses were performed on all tests in the current research. These post–shear analysis indicate no appreciable change in the gradation curve for all testing conditions.

5.3 CONSOLIDATE–FREEZE TRIAXIAL TEST RESULTS

Consolidate–freeze tests involve three distinct phases: unfrozen consolidation, specimen freezing, and subsequent shearing of the frozen specimen. Results from these three phases are discussed below. The writer notes that a complete evaluation of the consolidate–freeze results may be premature given the comparatively small set of results (10 tests compared to 99 conventional tests). Based on these limitations, analyses and conclusions have been made as far is possible. Emphasis of the presentation is on the shear results of the frozen specimens.

5.3.1 Consolidation and Freezing of Consolidate–Freeze Tests

5.3.1.1 Consolidation Characteristics

Consolidation was performed on eight specimens with a nominal, final effective confining stress (σ'_c) $\geq$ 2 MPa. As was the case for the unfrozen MFS testing program, low confinement tests, i.e. nominal σ'_c = 0.1 MPa, were not consolidated. Furthermore, the goal of consolidation was to develop specimens with similar final densities for subsequent freezing and shear regardless of the final σ'_c. Consolidation of consolidate–freeze tests proceeded in a manner similar to that in the unfrozen MFS testing program. Pertinent consolidation characteristics of the eight tests are summarized in Table 5.7. Figure 5.54 plots void ratio versus effective stress for these specimens. As should be expected, the consolidation curves exhibit similar behavior as noted in the unfrozen MFS testing program, i.e., larger changes in void ratio for the initially looser specimens consolidated to the higher σ'_c levels. For three tests (CF06, CF07 and CF09), the consolidation curves represent a best estimate of results because leakage of cell fluid into the internal drainage lines caused erroneous measurement of the specimen's change in volume during consolidation (see Section 3.5). Though this leakage rate was not directly determined, estimation of the rate was obtained from measurements of "volume flow" from the specimen after freezing was complete. Final void ratios ranged from 0.572 to 0.629, which correspond to relative densities from 85.2 to 102.4%.

5.3.1.2 Specimen Freezing

Freezing of the specimens proved to be the most difficult task in performing consolidate–freeze tests. As discussed in Section 3.5, specimen freezing was intended to be uniaxial (from bottom to top) with excess water allowed to freely drain from the top as the freezing front advanced upwards through the specimen.

However, due to the triaxial cell's internal drainage line configuration, premature freezing of the exit port for the free–draining water caused the excess water to be trapped in the specimen thus creating excess ice in the frozen specimen. Remedial measures, discussed in Section 3.5, lead to a better freezing process by allowing more water to exit the specimen, but also increasing the time needed for freezing. Figure 5.55 plots the "efficiency" of the freezing process versus the elapsed freezing time. The efficiency is defined as the measured volume change during freezing divided by the calculated volume change if all excess water exits the specimen, and hence, no net change in total specimen volume occurs during freezing. The calculated volume change is based on the approximate increase in volume caused by the change of pore water to pore ice, taken as a 9% volume increase. The elapsed freezing time is based on the temperature measured by the near–specimen thermistors located at the top of the specimen. These freezing characteristics are summarized in Table 5.8. As seen in Fig. 5.55, the efficiency of the freezing process increases as the elapsed time for freezing increases; however, 100% efficiency is not obtained for any specimen. Reasons for efficiencies below 60% nay include premature closing of the exit port or specimen freezing which was too rapid to allow un–interrupted flow of excess water out of the specimen. However, for specimens with higher efficiencies, the measured volume change and temperature records indicate that the flow of excess water continued until the temperature near the top of the specimen indicated freezing was complete, i.e., all available excess water had exited the specimen (see Fig. 3.13). Possible reasons for not measuring 100% efficiency in these cases include errors in the measurement of water expelled from the specimen (especially for those tests with an oil leak problem) and an actual volume increase of the pore water, as it changes to pore ice, which was smaller than the estimated 9%. Further tests and analysis of the specimen freezing

process are required before definitive conclusion can be made.

5.3.2 Shear Results of Consolidate–Freeze Tests

Consolidate–freeze shear results are presented in a similar fashion to the conventional frozen MFS tests (i.e., summary tables and plots); however, only the effects of σ'_c can be presented. The following presentation includes both small and large strain results for consolidate–freeze tests. A summary of test parameters are presented in Table 5.9. Review of the table indicates that many of the consolidate–freeze tests do not provide useful small strain and/or large strain results. Therefore, given the limited number of test results available for evaluation, all tests will be used in the following presentation regardless of their performance criteria (i.e., ACDT agreement or stability qualifiers). While this may diminish the quality of the presented results, it allows for an increased evaluation of the test parameters. In addition, throughout the following presentation the consolidate–freeze results will be compared to the conventional frozen test results at T = –10° C. The performance criteria for presentation of conventional tests results remain as detailed in Table 5.2.

5.3.2.1 Small Strain Results

Small strain results are presented in terms of the Young's modulus, yield offset stress and the behavior in the upper yield region. Figure 5.56 plots E and Q_{yo} versus σ'_c and σ_c for all consolidate–freeze tests along with the results from conventional tests. For the case of Young's modulus (Fig 5.56a), only six consolidate–freeze tests provide useful results. For conventional tests, the regression line shown in Fig. 5.2 for tests all D_r, σ_c, $\dot{\epsilon}$ and temperatures is presented in the figure. As shown in the figure, the Young's modulus for consolidate–freeze tests shows a slight decrease with increasing confining pressure,

a behavior similar to that for conventional tests. However, based on the regression lines, the consolidate–freeze moduli are approximately 2.5 GPa lower than those of conventional tests. For Q_{yo} versus σ'_c and σ_c (Fig. 5.56b), the consolidate–freeze tests are essentially constant yet do not significantly deviate from the decreasing trend noted for the the conventional test results first shown in Fig. 5.5.

The upper yield region represents one of the unexpected aspects of the consolidate–freeze tests compared to the conventional tests. While consolidate–freeze tests at low confinement (σ'_c = 0.17 and 0.27 MPa) exhibit a distinct yield point, tests consolidated prior to freezing to the higher stresses ($\sigma'_c \geq$ 2 MPa) exhibit no distinguishable upper yield point. This phenomenon is illustrated in Fig. 5.57 which plots the initial Q – ϵ_a curves of consolidate–freeze and conventional tests, one at each confining pressure. As shown in the figure, consolidate–freeze tests at $\sigma'_c \geq$ 2 MPa show no abrubt change in curvature signifying a yield point as shown for conventional tests. Also note that the consolidate–freeze tests exhibit a stiffer small strain response with increasing confinement when compared to the responses of conventional tests which are all similar. For the two tests at low confinement, Q_{uy} equaled 7.7 and 8.6 MPa which is comparable to the Q_{uy} from all conventional tests under similar conditions (8.3 ± 0.6SD MPa). The axial strains to Q_{uy} for these two consolidate–freeze tests were 0.5% to 0.8%, which is also within the range of ϵ_y for conventional tests under similar test conditions (0.46 ± 0.06SD %).

5.3.2.2 Large Strain Behavior

Figure 5.58 shows the Q – ϵ_a and ϵ_v responses for all consolidate–freeze tests. As illustrated in the figure, all consolidate–freeze tests exhibit Type C curves, with the peak strength increasing with increasing confinement until the test at σ_c (σ'_c) = 10 MPa where the peak strength is approximately the same as that

for the test at $\sigma'_c = 5$ MPa. The axial strain to peak strength for these tests also reduces with higher confinement until σ'_c reaches the 10 MPa level where ϵ_p shows a, slight increase above that for the test at $\sigma'_c = 5$ MPa.

Figure 5.59 compares four consolidate–freeze tests to four conventional tests performed at the different confinement levels. The consolidate–freeze tests presented in the figure represent what the writer considers to be the "best" test for a particular confining pressure. The writer realizes that the designation of the a "best" test is subjective given the limited data set and aforementioned problems in the testing program. However, review of all stress–strain curves (Fig. 5.58) suggests that the presented tests appropriately represent the currently available data set. In contrast to the consolidate–freeze results, the $Q - \epsilon_a$ curves of conventional tests change from Type C at low confinement to Type D at higher confinement. Axial strains to peak strength for conventional tests increase with higher confinement; a trend opposite to that for the consolidate–freeze tests.

Figure 5.59 shows a plot of Q_p versus σ_c and σ'_c for all consolidate–freeze tests and the trend previously noted for comparable conventional tests (see Fig. 5.37). The consolidate–freeze results exhibit two distinct behaviors. For consolidate–freeze tests consolidated to $\sigma'_c \leq 5$ MPa, the $Q_p - \sigma_c$ relationship is similar to that for the conventional tests, but with a slightly higher ϕ value (18.4°). However, at the higher confinement, the Q_p for the consolidate–freeze test falls below that for the conventional tests that show a linear increase in strength over all σ_c levels.

The volumetric strain results for consolidate–freeze tests, as illustrated in Figs. 5.58 and 5.59, represent one of the weaker aspects of the testing program due to the lack of results at higher axial strains and the poor to very poor stabilities exhibited by nearly tests. However, based on the available results, the volumetric

responses do show a decrease with increasing confinement (Fig. 5.58). In addition, the ϵ_v responses for a particular consolidate–freeze test is slightly higher than its conventional test counterpart (Fig. 5.59). Further examination of the volumetric strain behavior will require additional testing.

5.3.3 Summary and Discussion of Consolidate–Freeze Results

The consolidate–freeze tests represent the first known attempt to measure the effect of an effective confining stress applied prior to freezing on the behavior of frozen sand. Although the number of tests are limited, the available results show that the pre–freezing σ'_c has little effect on very small strain behavior (i.e. E and Q_{yo}) and a modest increase in the dilatancy. An upper yield point, consistently found in conventional tests, becomes non–existent at higher σ'_c levels (Fig. 5.57). The Q_p, while similar to conventional tests, occurs at a similar strain level for low confinement tests (Type C curves for both FRS and CF tests) but at a significantly lower axial strain level for tests at higher confinement (Type C versus Type D curves for FRS and CF tests, respectively).

One obvious explanation for the difference in behaviors is the level of initial stressing of the sand skeleton prior to freezing. For conventional tests, the sand is not "preloaded" prior to freezing; therefore, during shear the sand can develop significant additional resistance at large axial strains. In contrast, consolidate–freeze specimens have already experienced significant stresses during consolidation which are "locked in" during the freezing process. This prestressing leads to an initially stiffer $Q - \epsilon_a$ response and peak strength at lower axial strain levels; a behavior similar to that exhibited by unfrozen MFS (e.g., see Figs. 4.12 and 4.41). However, the post–Q_p strain softening behavior of consolidate–freeze tests with continued shear does not follow the behavior of unfrozen MFS or the conventional tests.

This hypothesis of "locked in" stresses can also be used to explain the behavior of the conventional tests prepared by wet tamping. Figure 5.61 shows Q ϵ_a and ϵ_v responses of conventional tests prepared by wet tamping and comparable consolidate–freeze tests. The figure shows that wet tamping, which required a significant compaction effort in order to achieve $D_r \approx 95\pm5\%$, also produces Type C stress–strain curves and that the initial stiffness is very similar to that measured in the consolidate–freeze tests with $\sigma'_c = 2$ MPa. However, the conventional wet tamped tests do exhibit an upper yield point, which is not present in the consolidate–freeze tests for $\sigma_c \geq 2$ MPa, and the corresponding values of Q_{uy} agree reasonably well with those for conventional tests run on specimens prepared by MSP. This phenomenon can not currently be explained.

It also must be noted that the consolidate–freeze tests were performed under limited test conditions, i.e. only one specimen density, strain rate and temperature were evaluated. Therefore, although the available consolidate–freeze results do provide some insight into the influence of pre–shear effective stress on the behavior of frozen MFS in triaxial compression, definitive conclusions on the differences in behavior of these two types of frozen MFS tests over a wider range of testing conditions would be premature. It is recommended that additional testing with other testing variables be performed.

TABLE 5.1
SCOPE OF TRIAXIAL TESTING ON FROZEN MFS
Conventional Frozen and Consolidate-freeze Tests

Nominal Temperature (°C)	Confining Pressure σ_c (MPa)	SLOW (3×10^{-6}/s) Range in D_r (%)			MODERATE (3.5×10^{-5}/s) Range in D_r (%)			FAST (5×10^{-4}/s) Range in D_r (%)			Total Number of FRS Tests
		≈35	50-80	≈95	≈35	50-80	≈95	≈35	50-80	≈95	
-10	0.1	•		•	•	•	• ω	•		•	50 FRS + 10 CF
	2				•	•	• ω				
	5				•	•	• ω				
	10	•		•	•	•	• ω	•		•	
-15	0.1				•	•	•				17
	10	•		•	•	•	•	•		•	
-20	0.1	•		•	•	•	•	•		•	19
	10	•		•	•	•		•	•		
-25	0.1	•		•	•	•	•	•	•		13
	10	•		•	•			•			

Notation: • = Conventional (FRS) tests ω = Consolidate-Freeze (CF) tests
One specimen tested at a strain rate of 1.2×10^{-4}/sec at T = -10°C
Specimen preparation techniques: All tests prepared by Multiple Sieve Pluviation (MSP) except for seven tests at T = -10°C prepared by Wet Tamping
Specimen end conditions: All tests at T = -15°C, -20°C and -25°C had ice caps and grease. At -10°C, all but seven tests had ice caps and grease; the other seven tests had only greased ends (6 tests) or emery cloth (1 test). Consolidate-freeze tests had greased rubber membranes as ends.

TABLE 5.2
SUMMARY OF AVAILABLE CONVENTIONAL TESTS FOR EVALUATION

Test Parameter	Specimen Conditions and Performance Criteria											Number of Available Tests				
	Prep		Ends		ACDT's			Stability				-10°C	-15°C	-20°C	-25°C	Total
	MSP	WT	Lub	Fric	g	f	p	g	f	p	vp					
E	√	√	√	√	√	√		√	√	√	√	34	12	12	11	69
PL	√	√	√	√	√	√		√	√	√	√	34	11	12	11	68
Q_{yo}	√	√	√	√	√	√		√	√	√	√	34	11	12	11	68
Q_{uy}	√	√	√	√	√	√	√	√	√	√	√	50	17	19	13	99
ϵ_y	√	√	√	√	√	√		√	√	√	√	34	12	13	11	70
Q_p	√		√		√	√	√	√	√	√		36	15	17	10	78
ϵ_p	√		√		√	√	√	√	√			28	13	13	8	62
$(d\epsilon_v/d\epsilon_a)_{max}$	√		√		√	√	√	√	√	√		35	7	17	10	69
ϵ_{v20}	√		√		√	√	√	√	√	√		34	6	15	9	64

Notes:
√ - This condition/criterion must be satisfied
MSP = Multiple Sieve Pluviation; WT = Wet Tamping
Lub = Lubricated ends (ice caps); Fric = Frictional ends (grease or emery cloth)
ACDT's Agreement: g - good, f - fair, p - poor
Stability: g - good, f - fair, p - poor, vp - very poor

TABLE 5.3 (page 2 of 5)
MEASURED CONVENTIONAL FROZEN TESTS RESULTS
Test Results at T = -10 °C (from Andersen 1991)

FRS Test #	D_r %	σ_c MPa	TEMP (°C)	STRAIN RATE /sec @Q_{yo} x10^7	STRAIN RATE /sec Nom. x10^7	SMALL STRAIN RESPONSE E GPa	SMALL STRAIN RESPONSE Q_{yo} MPa	UPPER YIELD REGION Q_{uy} MPa	UPPER YIELD REGION ϵ_y %	PEAK STRENGTH REGION Q_p MPa	PEAK STRENGTH REGION ϵ_p %	Q - ϵ_a Curve Type	VOLUMETRIC BEHAVIOR Max. $d\epsilon_v/d\epsilon_a$ x10^2	VOLUMETRIC BEHAVIOR ϵ_{v20} %	S*	A*
40	37.4	10.13		400	5420	25.7	4.7	15.0	0.83	15.4	16.5	B	4	0.5	f	g
41[2]	96.0	0.102		180	5380	*38.5*	*4.7*	16.6	*0.89*	*17.1*	*3.6*	C	67	9.8	g	p
42[2]	93.4	10.13		19	362	25.0	3.1	8.2	0.50	*18.8*	*17.3*	D	8	0.8	g	g
43[2]	90.8	0.102		16	342	*25.9*	*4.2*	8.8	*0.50*	*12.4*	*5.2*	C	64	8.6	g	p
44	36.3	0.102		17	366	25.7	4.1	8.2	0.48	9.3	3.9	C	36	3.9	f	g
45	38.1	0.102		1.6	30.9	*28.6*	*3.0*	5.0	*0.28*	6.6	8.2	C	33	3.0	g	p
46	92.0	0.101		1.3	24.3	40.0	3.3	5.1	0.26	8.5	7.0	C	57	7.8	f	g
47	43.5	10.03		1.9	29.2	*20.0*	*2.7*	4.8	*0.36*	9.1	24.4	D	NA	0	g	p
48	96.3	10.04		2.0	27.2	25.0	2.7	4.9	0.34	*13.1*	*12.8*	D	NA	NA	vp	g
49	96.9	10.01		370	4380	24.3	4.3	15.4	0.85	22.0	*14.9*	D	11	1.8	p	g
51	80.0	10.02		20	370	*31.6*	*3.3*	8.8	*0.52*	17.9	23.2	D	4	0.5	f	p
52	90.8	10.04		27	355	*20.7*	*2.8*	8.2	*0.48*	19.0	23.4	D	6	0.7	f	p
53	92.5	5.03		15	352	35.3	2.9	8.5	0.51	16.5	*18.8*	D	13	1.6	p	f
54	94.0	10.04		3.1	32.5	26.3	2.8	5.4	0.44	16.0	21.7	D	4	0.5	g	g
55	88.1	2.00		24	382	*26.1*	*3.4*	7.9	*0.44*	13.1	11.9	D	27	3.2	f	p
56	92.8	0.101		12	371	*46.7*	*3.8*	9.5	*0.49*	13.1	4.8	C	61	8.4	f	p
57	35.6	0.101		18	384	25.0	3.3	8.7	0.54	9.6	3.9	C	35	3.9	g	g
58	93.7	0.100		0.7	32.9	*14.3*	*1.8*	5.6	*0.49*	9.3	6.8	C	67	8.3	g	p
59	30.1	5.01	-9.60	23	333	29.2	3.5	8.9	0.44	11.5	19.6	D	6	0.4	f	f
60	54.2	2.01	-9.50	20	339	31.8	3.5	9.2	0.43	11.4	8.3	C	22	2.8	f	f
61	33.4	10.02	-9.57	2.8	28.9	21.7	2.9	5.1	0.34	9.0	24.6	D	2	0.1	g	f
62	54.2	5.00	-9.47	19	335	25.9	3.4	8.3	0.43	12.8	21.3	D	6	0.4	g	g
63	51.1	10.03	-9.53	28	335	*24.0*	*3.0*	8.2	*0.50*	14.4	26.4	D	1	0.1	g	p
64	82.7	10.02	-9.50	23	338	24.3	3.3	7.9	0.48	17.8	23.8	D	2	0.2	f	g
65	95.7	0.102	-9.54	290	4990	26.3	5.0	15.8	0.82	16.8	*4.1*	C	60	9.1	p	g
66	83.0	0.102	-9.57	18	235	35.6	4.3	8.4	0.27	12.1	5.1	C	46	6.7	f	g
67	33.1	2.01	-9.62	26	339	25.0	3.6	8.0	0.42	10.2	12.4	D	15	1.9	g	g

See page 1 for notes

TABLE 5.3 (page 1 of 5)
MEASURED CONVENTIONAL FROZEN TESTS RESULTS
Test Results at T = -10 °C (from Andersen 1991)

FRS Test #	D_r %	σ_c MPa	TEMP (°C)	STRAIN RATE /sec @Q_{yo} x10^7	STRAIN RATE /sec Nom. x10^7	SMALL STRAIN RESPONSE E GPa	SMALL STRAIN RESPONSE Q_{yo} MPa	UPPER YIELD REGION Q_{uy} MPa	UPPER YIELD REGION ϵ_y %	PEAK STRENGTH REGION Q_p MPa	PEAK STRENGTH REGION ϵ_p %	Q - ϵ_a Curve Type	VOLUMETRIC BEHAVIOR Max. $d\epsilon_v/d\epsilon_a$ x10^2	VOLUMETRIC BEHAVIOR ϵ_{v20} %	S* g f p vp	A* g f p
15	31.6	10.15		31	336	21.4	2.8	7.3	0.50	11.6	27.7	D	NA	NA	f	g
18	48.4	10.18		27	329	28.6	2.7	7.2	0.43	13.4	24.5	D	NA	NA	f	g
19	49.4	10.18		24	344	21.4	2.7	7.2	0.43	13.1	*18.4*	D	3	0.4	p	g
[1]20	76.3	10.18		31	299	20.7	3.2	8.6	0.50	16.7	16.3	D	5	0.4	f	g
[1]21	74.4	10.18		27	311	20.0	3.0	8.2	0.52	16.0	*15.2*	D	4	0.3	p	g
[1]22	80.3	10.15		22	320	25.0	3.0	8.2	0.51	16.3	*13.3*	D	5	0.4	p	g
23	56.2	5.12		19	330	23.1	3.1	7.4	0.46	12.7	*17.8*	D	4	0.6	p	g
[1]24	90.5	5.12		19	303	*33.3*	*3.2*	8.9	*0.54*	15.8	8.5	C	12	1.5	f	p
25	52.8	2.05		21	336	26.1	3.4	7.6	0.48	10.9	*12.1*	D	17	2.0	p	f
[1]26	94.0	2.08		18	300	31.8	3.7	9.2	0.53	14.7	*5.0*	C	23	NA	p	g
[1][2]27	90.5	2.07		15	348	*33.3*	*3.8*	9.0	*0.53*	*15.1*	*5.6*	C	31	NA	g	p
[1][2]28	99.2	0.103		15	386	*21.2*	*3.2*	9.1	*0.44*	*14.6*	*3.5*	C	42	NA	g	p
29	56.2	0.106		15	334	25.9	3.8	8.2	0.47	10.1	6.2	C	29	NA	f	g
30	21.8	0.106		17	339	25.9	4.2	8.4	0.50	8.5	5.9	B_y	26	3.7	g	g
[2]31	23.0	0.106		12	352	29.2	3.8	8.3	0.50	*8.6*	*4.9*	B_y	29	3.8	g	g
32	80.3	0.102		16	344	*28.0*	*3.9*	8.3	*0.42*	10.9	*6.1*	C	50	6.6	p	p
33	60.6	0.103		22	337	29.2	3.4	8.5	0.53	10.2	4.9	C	42	5.5	f	g
34	36.7	0.102		24	358	23.5	4.9	8.7	0.47	9.4	6.6	C	33	3.7	g	g
35	36.3	0.101		53	1070	25.8	4.3	10.6	0.65	10.6	0.65	A	35	4.2	g	g
36	36.7	0.101		230	4950	25.0	5.2	15.0	0.74	15.0	0.81	A	39	5.4	f	g
37	96.9	0.101		180	4790	30.3	5.1	15.4	0.83	16.4	*4.0*	C	60	9.5	p	g
38	94.3	0.101		14	322	*41.2*	*4.1*	8.5	*0.44*	*11.7*	*5.4*	C	47	7.4	vp	p
[2]39	92.8	10.11		260	5360	*29.0*	*4.4*	16.1	*1.02*	*21.6*	*13.1*	D	12	1.8	g	p

Numbers in *italics* not used in presentations (see Table 5.2 for summary of conditions)
[1] = Specimens formed by Wet Tamping
[2] = Specimens with non-lubricated ends
S* = Stability Qualifiers
A* = ACDT Qualifiers
NA = Not Available
See Fig. 5.21 for Curve Types

TABLE 5.3 (page 3 of 5)
MEASURED CONVENTIONAL FROZEN TESTS RESULTS
Tests Results at T = -15 °C

FRS Test #	D_r %	σ_c MPa	TEMP (°C)	STRAIN RATE /sec @Q_{yo} x10^7	STRAIN RATE /sec Nom. x10^7	SMALL STRAIN RESPONSE E GPa	SMALL STRAIN RESPONSE Q_{yo} MPa	UPPER YIELD REGION Q_{uy} MPa	UPPER YIELD REGION ϵ_y %	PEAK STRENGTH REGION Q_p MPa	PEAK STRENGTH REGION ϵ_p %	Q - ϵ_a Curve Type	VOLUMETRIC BEHAVIOR Max. $d\epsilon_v/d\epsilon_a$ x10^2	VOLUMETRIC BEHAVIOR ϵ_{v20} %	S* g f p vp	A* g f p
121	91.7	9.99	-15.4	286	4480	23.1	4.4	21.7	1.04	25.5	7.69	C	15	2.7	f	f
123	90.7	9.94	-15.6	1.9	34.6	22.8	3.2	7.9	0.55	17.3	15.0	D	NA	NA	f	f
126	48.7	9.99	-15.5	230	4340	24.3	4.9	20.3	0.94	20.3	0.94	B	7	1.2	g	g
127	35.4	9.96	-15.5		35.3	NA	NA	7.8	*1.09*	11.4	22.1	D	NA	NA	g	p
128	52.1	9.97	-15.6	19	394	26.9	2.8	12.2	0.76	16.5	21.1	D	NA	NA	g	f
129	47.7	9.91	-15.5	201	4480	26.9	5.3	20.4	0.94	20.4	0.94	B	14	2.0	g	g
130	38.2	9.86	-15.8		35.7	22.9	NA	7.6	0.68	10.8	21.3	D	NA	NA	f	g
131	86.9	9.94	-15.6	2.5	34.6	*14.2*	*1.9*	9.0	*0.54*	*17.0*	*8.61*	D	NA	NA	vp	p
133	79.8	10.02	-15.6	18	403	*28.9*	*3.1*	12.9	*0.70*	*19.6*	*10.7*	D	NA	NA	vp	p
134	85.8	9.96	-15.5	1.9	34.0	18.9	2.5	7.9	0.46	17.4	*14.2*	D	NA	NA	p	g
135	85.5	10.02	-15.6	20	372	*21.6*	*4.8*	14.1	*0.82*	21.3	13.0	D	NA	NA	f	p
136	61.7	0.099	-15.7	15	381	25.6	5.2	12.6	0.78	13.7	7.02	C	35	5.4	f	g
138	78.0	0.099	-15.7	15	377	26.5	5.5	13.1	0.60	15.2	4.60	C	56	7.4	f	g
141	40.3	9.94	-15.5	23	397	22.0	4.0	12.3	0.70	15.5	22.3	D	NA	NA	g	f
142	40.5	0.100	-15.7	14	384	25.4	4.6	12.9	0.75	13.1	2.59	C_y	40	4.8	f	f
146	91.9	9.99	-15.8	20	388	21.3	4.0	11.4	0.55	21.5	12.6	D	NA	NA	f	f
148	91.5	0.099	-15.8	11	387	*33.0*	*5.0*	13.0	*0.50*	16.6	*4.91*	C	49	NA	p	p

See page 1 for notes

TABLE 5.3 (page 4 of 5)
MEASURED CONVENTIONAL FROZEN TESTS RESULTS
Tests Results at T = -20 °C

FRS Test #	D_r %	σ_c MPa	TEMP (°C)	STRAIN RATE /sec @Q_{yo} x10^7	STRAIN RATE /sec Nom. x10^7	SMALL STRAIN RESPONSE E GPa	SMALL STRAIN RESPONSE Q_{yo} MPa	UPPER YIELD REGION Q_{uy} MPa	UPPER YIELD REGION ϵ_y %	PEAK STRENGTH REGION Q_p MPa	PEAK STRENGTH REGION ϵ_p %	Q - ϵ_a Curve Type	VOLUMETRIC BEHAVIOR Max. $d\epsilon_v/d\epsilon_a$ x10^2	VOLUMETRIC BEHAVIOR ϵ_{v20} %	S* g f p vp	A* g f p
70	84.4	0.100	-20.2	118	4090	25.9	8.2	25.7	0.76	25.7	0.76	A	65	8.5	p	g
71	90.3	0.100	-20.6	18	346	31.3	6.6	18.0	1.00	20.6	4.74	C	64	8.2	f	g
72	91.7	10.06	-20.6	18	34.6	31.9	5.5	11.4	0.43	21.2	15.9	D	5	0.7	g	g
74	33.2	9.99	-20.5	1.5	35.8	21.7	0.8	11.1	0.65	14.0	19.6	D	11	0.6	f	p
75	48.0	0.101	-20.4	9.4	368	27.5	4.6	15.8	0.89	15.9	*3.44*	C_y	24	4.0	p	f
76	45.7	0.101	-20.3	14	355	29.2	5.1	15.3	0.89	15.6	*4.13*	C_y	28	4.1	p	f
85	77.5	0.102	-20.2	11	375	32.1	6.7	16.7	0.76	18.6	4.52	C	43	6.7	f	g
86	37.0	10.06	-20.5	25	364	20.7	4.6	15.9	0.91	18.3	16.8	D	5	0.8	g	g
87	50.4	0.102	-20.2		358	22.9	NA	15.6	0.68	15.8	3.06	C_y	33	4.5	f	p
88	35.4	0.101	-20.3	1.3	32.2	31.2	4.1	9.8	0.37	11.3	4.44	C	35	3.9	g	f
89	37.1	0.102	-19.9	180	5940	25.7	8.1	24.8	0.68	24.8	0.68	A	50	7.0	vp	g
92	35.6	10.05	-20.3		5440	NA	NA	28.1	*0.70*	28.1	0.70	B_y	16	2.4	g	p
93	77.5	10.02	-20.4	27	5860	33.2	8.4	28.9	0.99	28.9	0.99	A	23	NA	g	g
94	93.2	0.101	-20.1		33.3	NA	NA	10.1	*0.35*	14.7	*4.62*	C	58	8.6	p	NA
95	86.3	0.100	-20.3	14	363	*18.8*	*4.1*	16.4	*0.90*	*18.9*	*4.27*	C	38	6.3	vp	NA
97	35.7	0.101	-19.9	14	353	23.1	5.4	16.3	0.87	16.3	0.87	A	27	3.9	g	g
98	34.3	10.03	-20.1		31.3	NA	NA	10.5	0.34	14.1	19.6	D	12	2.1	g	f
99	36.3	0.102	-20.1	253	5310	25.8	8.8	26.7	0.74	26.7	0.74	A	47	6.3	f	f
100	82.2	10.03	-19.9	231	367	*30.5*	*3.3*	17.2	*0.73*	23.6	12.3	D	13	NA	f	p

See page 1 for notes

TABLE 5.3 (page 5 of 5)
MEASURED CONVENTIONAL FROZEN TESTS RESULTS
Tests Results at T = -25 °C

FRS Test #	D_r %	σ_c MPa	TEMP (°C)	STRAIN RATE /sec @Q_{yo} x10^7	STRAIN RATE /sec Nom. x10^7	SMALL STRAIN RESPONSE E GPa	SMALL STRAIN RESPONSE Q_{yo} MPa	UPPER YIELD REGION Q_{uy} MPa	UPPER YIELD REGION ϵ_y %	PEAK STRENGTH REGION Q_p MPa	PEAK STRENGTH REGION ϵ_p %	Q - ϵ_a Curve Type	VOLUMETRIC BEHAVIOR Max. $d\epsilon_v/d\epsilon_a$ x10^2	VOLUMETRIC BEHAVIOR ϵ_{v20} %	S* g f p vp	A* g f p
102	52.7	0.101	-25.0	171	4430	29.0	9.7	30.9	0.82	30.9	0.82	A	45	NA	vp	f
103	35.5	0.148	-25.4	1.5	34.8	24.2	5.4	14.5	0.59	15.6	6.34	B	48	6.6	g	g
104	36.9	0.100	-25.4	13	394	22.2	7.7	21.1	0.83	21.1	0.83	A	51	4.3	f	f
106	88.8	0.100	-25.3	1.1	34.9	26.4	6.6	15.0	0.87	19.0	4.85	C	61	7.9	g	f
107	90.4	9.96	-25.3	1.7	34.5	33.9	6.1	15.0	0.94	*23.4*	*12.6*	D	11	2.0	vp	g
109	74.5	0.100	-25.4	17	389	26.2	7.0	20.6	0.99	21.0	*3.99*	C_y	40	6.0	p	g
110	88.6	0.099	-25.3	16	382	*25.0*	*5.9*	21.2	*1.00*	23.0	5.63	C	53	7.7	g	p
111	34.9	9.95	-25.3	26	378	28.1	8.0	20.5	0.84	20.5	0.84	B_y	12	1.8	g	g
113	52.0	0.101	-25.4	15	386	*26.0*	*7.4*	20.1	*0.79*	20.1	*0.79*	A	62	5.0	f	p
114	41.2	0.098	-25.2	206	4600	27.5	8.0	28.7	0.77	28.7	0.77	A	49	7.2	vp	f
115	43.1	10.00	-25.4	2.2	34.6	27.2	5.8	13.6	0.55	17.0	24.0	D	5	0.9	g	f
116	39.4	0.094	-25.3	175	4420	29.6	8.6	30.8	0.86	30.8	0.86	A	45	5.9	p	f
117	36.1	10.02	-25.8	303	4350	26.0	8.5	31.6	0.97	31.6	0.97	B_y	12	2.2	f	g

See page 1 for notes

TABLE 5.4 (page 1 of 2)
SUMMARY OF SMALL STRAIN BEHAVIOR

Small Strain Parameter		Effect of			
		Increasing D_r	Increasing σ_c	Increasing $\dot{\epsilon}$	Decreasing T
Young's Modulus, E	Figure	5.1	5.2	None	5.3
	Trends	Slight Increase For all conditions E_{avg} = 26.5±4 GPa	Decrease Slight decrease in collective results	None	Constant Varies with temperature but all means within overall SD
Yield Offset Stress, Q_{yo}	Figure	5.4	5.5	5.6	5.7
	Trends	Constant Q_{yo} constant for results at a particular temperature	Decrease Based on data at T = -10° and -15°	Increase Power law coefficients fairly constant for all temperatures	Increase Rate of increase increases with increasing strain rate

TABLE 5.4 (page 2 of 2)
SUMMARY OF SMALL STRAIN BEHAVIOR

Small Strain Parameter		Effect of			
		Increasing D_r	Increasing σ_c	Increasing $\dot{\epsilon}$	Decreasing T
Upper Yield Stress, Q_{uy}	Figures	5.10	5.12	5.14	5.16
	Trends	Constant Constant of given $\dot{\epsilon}$ and T	Constant But can show slight decrease or increase with increasing σ_c	Increase Power law coefficient increases w/ decreasing T	Increase Rate increases with increasing $\dot{\epsilon}$
Axial Strain at Q_{uy}, ϵ_y	Figures	5.17	5.18	5.19	5.20
	Trends	Constant Essentially constant for given $\dot{\epsilon}$ and T	Constant Essentially constant for given $\dot{\epsilon}$ and T	Increase Increase is proportional to increase in Q_{uy}	Complex Increase is proportional to increase in Q_{uy}

TABLE 5.5
SUMMARY OF LARGE STRAIN BEHAVIOR

Large Strain Parameter		Effect of			
		Increasing D_r	Increasing σ_c	Increasing $\dot{\epsilon}$	Decreasing T
Peak Strength, Q_p	Figures	5.22-5.23, 5.33-5.36	5.24, 5.37, 5.38	5.25-5.28, 5.39-5.40	5.29-5.32, 5.42-5.43
	Trends	Complex Increases at moderat $\dot{\epsilon}$ and T (Type C and D curve), but constant for faster ϵ and/or lower T. dQ_p/dD_r = 0 for Type A and B curves; ≈ 0.06 for Type C; ≈ 0.12 for Type D	Increase Generally increases except at low D_r/ high σ_c, or lower T. $dQ_p/d\sigma_c \approx$ constant for dense sand (Type C and D) at constant ϵ and T; decreases with increasing σ_c at lower D_r; = 0 for Type A and B curves	Increase Power law coefficient increases for increasing D_r & σ_c; complex trend with T	Increase For loose specimens, dQ_p/dT increases w/ increasing $\dot{\epsilon}$ which lead to Type A curve For dense specimens, dQ_p/dT constant
Axial Strain at Q_p, ϵ_p	Figures	5.22-5.23, 5.44a & b	5.24, 5.45 a and b	5.25-5.28, 5.46a & b	5.29-5.32, 5.47
	Trends	Complex Constant for low σ_c (Type C curve), but decreases at high σ_c (Type D to C curve)	Increase Increases for all conditions except constant at $Q_p=Q_{uy}$ (Type A or B curve)	Decrease Type A or B curves at higher $\dot{\epsilon}$ cause decrease	Complex Constant for low σ_c, decreasing for high σ_c

TABLE 5.6
SUMMARY OF VOLUMETRIC STRAIN BEHAVIOR

Volumetric Strain Parameter		Effect of			
		Increasing D_I	Increasing σ_c	Increasing $\dot{\epsilon}$	Decreasing T
Max. Rate of Dilation, $(d\epsilon_v/d\epsilon_a)_{max}$	Figures	5.48	5.49		5.50
	Trends	Increase Rate decreases significantly with increasing σ_c	Decrease Decrease is non-linear	None	Complex Increases for low D_I but constant for high D_r
ϵ_v @ 20% ϵ_a, ϵ_{v20}	Figures	5.22-5.23, 5.51	5.24, 5.52	5.25-5.28, 5.51-5.52	5.29-5.32, 5.53
	Trends	Increase Rate decreases to zero± at high σ_c	Decrease Decrease is non-linear	Increase At fast $\dot{\epsilon}$ versus slow and moderate	Complex Increases for low D_r but constant for high D_r

TABLE 5.7
CONSOLIDATION CHARACTERISTICS
CONSOLIDATE-FREEZE TESTS

Test No.	Eff. Stress		Volume			Void Ratio, e			Axial Strain		Vol. Strain (%)	Consol. Time		Final D_r (%)
	Init. (MPa)	Final (MPa)	Init. (cc)	Final (cc)	ΔV (cc)	Init.	Final	Δe	DCDT (%)	ACDT (%)		Prim. (min)	Sec. (min)	
CF02	0.084	9.938	69.48	63.09	6.39	0.794	0.629	0.165	2.73	3.50	9.19	49	239	85.2
CF04	0.088	10.09	69.65	62.49	7.16	0.752	0.572	0.180	2.01	2.71	10.27	59	309	102.5
CF05	0.083	9.946	69.31	62.51	6.80	0.803	0.626	0.177	3.03	3.24	9.82	39	182	84.9
CF06	0.098	4.992	70.78	67.14[1]	3.64	0.686	0.600[1]	0.086	1.02	1.12	5.14[1]	23	190	94.1[1]
CF07	0.090	2.010	70.98	67.73[1]	3.25	0.669	0.592[1]	0.077	0.58	0.83	4.58[1]	13	131	96.4[1]
CF08	0.089	1.993	71.09	69.17	1.92	0.648	0.603	0.045	0.52	0.71	2.70	17	174	93.0
CF09	0.100	1.980	69.15	66.80[1]	2.35	0.630	0.575[1]	0.065	0.45	0.93	3.40[1]	18	70	101.7[1]
CF10	0.059	4.980	70.81	67.28	3.53	0.686	0.601	0.085	1.49	1.34	5.00	30	244	91.7

Notes:
NA - Not available
[1] Value represents best estimate due to leakage of oil into internal drainage line

TABLE 5.8
SPECIMEN FREEZING CHARACTERISTICS
CONSOLIDATE-FREEZE TESTS

Test No.	Nominal σ'_c (MPa)	Freezing Temperature °C	Initial Volumes V[1] (cc)	V_s[2] (cc)	V_w (cc)	Volume Change Meas. (cc)	Calc. (cc)	Eff. (%)	Elapsed Time (min)	Comments
CF01	0.1	-8	70.80	44.60	26.20	0.46	2.35	20	100	Excess ice noted around top
CF02	10	-8	63.08	38.74	24.35	1.42	2.19	65	230	
CF03	0.1	-15	72.44	44.68	27.76	0.60	2.50	24	105	Manual Δvolume measurement
CF04	10	-15	62.49	39.75	22.74	1.11	2.05	54	120	Manual Δvolume measurement
CF05	10	-15	62.51	38.35	24.16	1.03	2.17	47	90	Manual Δvolume measurement
CF06	5	-15	67.14	41.97	25.27	0.48[3]	2.27	21	120	Oil leak into drainage line
CF07	2	-8	67.73	42.54	25.19	1.91[3]	2.27	84	180	Oil leak, stopped prematurely
CF08	2	-8	69.17	43.14	26.03	1.74	2.34	74	240	
CF09	2	-8	66.80	42.43	24.37	1.91[3]	2.19	87	200	Oil leak into drainage line
CF10	5	-8	67.28	41.85	25.43	1.90	2.29	83	500	

Notes:
[1] V = Total volume after consolidation
[2] V_s = Volume of solids based on after test weight
[3] Measured volume change represents best estimate due to leakage of oil into internal drainage line

TABLE 5.9
CONSOLIDATE-FREEZE TESTS RESULTS

CF Test No.	D_r (%)	σ_c (MPa)	TEMP (°C)	NOMINAL STRAIN RATE (/sec) x10^6	SMALL STRAIN RESPONSE		UPPER YIELD REGION		PEAK STRENGTH REGION		Q - ϵ_a Curve Type	VOLUMETRIC BEHAVIOR		S[4]	A[5]
					E (GPa)	Q_{yo} (MPa)	Q_{uy} MPa	ϵ_y (%)	Q_p (MPa)	ϵ_p (%)		Max. $d\epsilon_v/d\epsilon_a$ x10^2	ϵ_{v10} (%)	g f p vp	g f p
01	97.4	0.265	-10.3	30.6	26.5	2.7	8.6	0.50	13.3	6.6	C	NA	NA	f	f
02	85.2	10.00	-10.3	36.4	23.6	3.2	NA	NA	17.2	4.4	C	38	NA	p	p
03	87.6	0.170	-9.84	31.1	NA	NA	7.7	0.80	11.3	6.5	C	443	1.5	vp	f
04	102.5	10.19	-9.99	33.7	NA	NA	NA	NA	16.3	5.2	C	63	0.6	vp	p
05	84.9	10.02	-10.0	36.2	22.2	3.5	NA	NA	16.4	5.8	C	48	0.4	p	p
06	94.1[1]	4.99	-10.2	38.1	20.8	4.0	NA	NA	16.7	3.7	C	57	0.7	p	p
07	96.4[1]	2.02	-10.5[2]	29.5	NA	NA	NA	NA	13.6	3.3	C	236	1.5	vp	p
08	93.0	2.03	-10.1	39.4	22.5	3.5	NA	NA	14.6	5.4	C	233	1.2	vp	f
09	101.7[1]	2.01	-10.2	33.0	26.9	3.3	NA	NA	13.9	4.0	C	205	0.7	p	g
10	91.7	5.02	-10.1	38.1	NA	NA	NA	NA	15.8[3]	4.2	C	NA	NA	f	g

Notes:

NA - Not Available
[1] Relative density is best estimate
[2] Temperature based on bottom thermistor
[3] Maximum reliable deviator stress, but higher stresses may have been possible (see Fig. 5.58).
[4] S = Stability Qualifiers
[5] A = ACDT Qualifiers

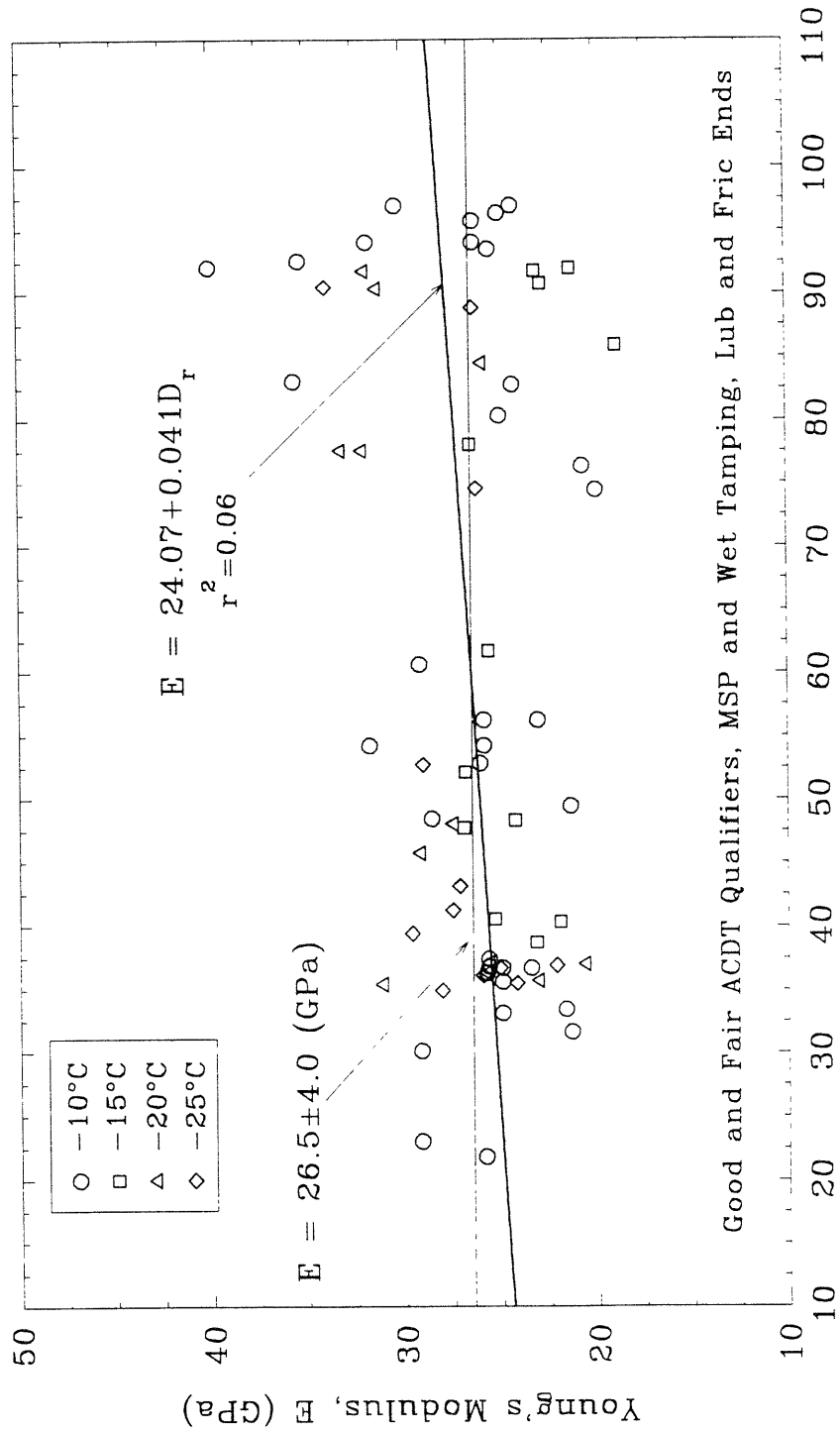

Figure 5.1 Young's Modulus versus Relative Density for Conventional Frozen MFS Tests at Different Temperatures (Includes All Confining Pressures and Strain Rates)

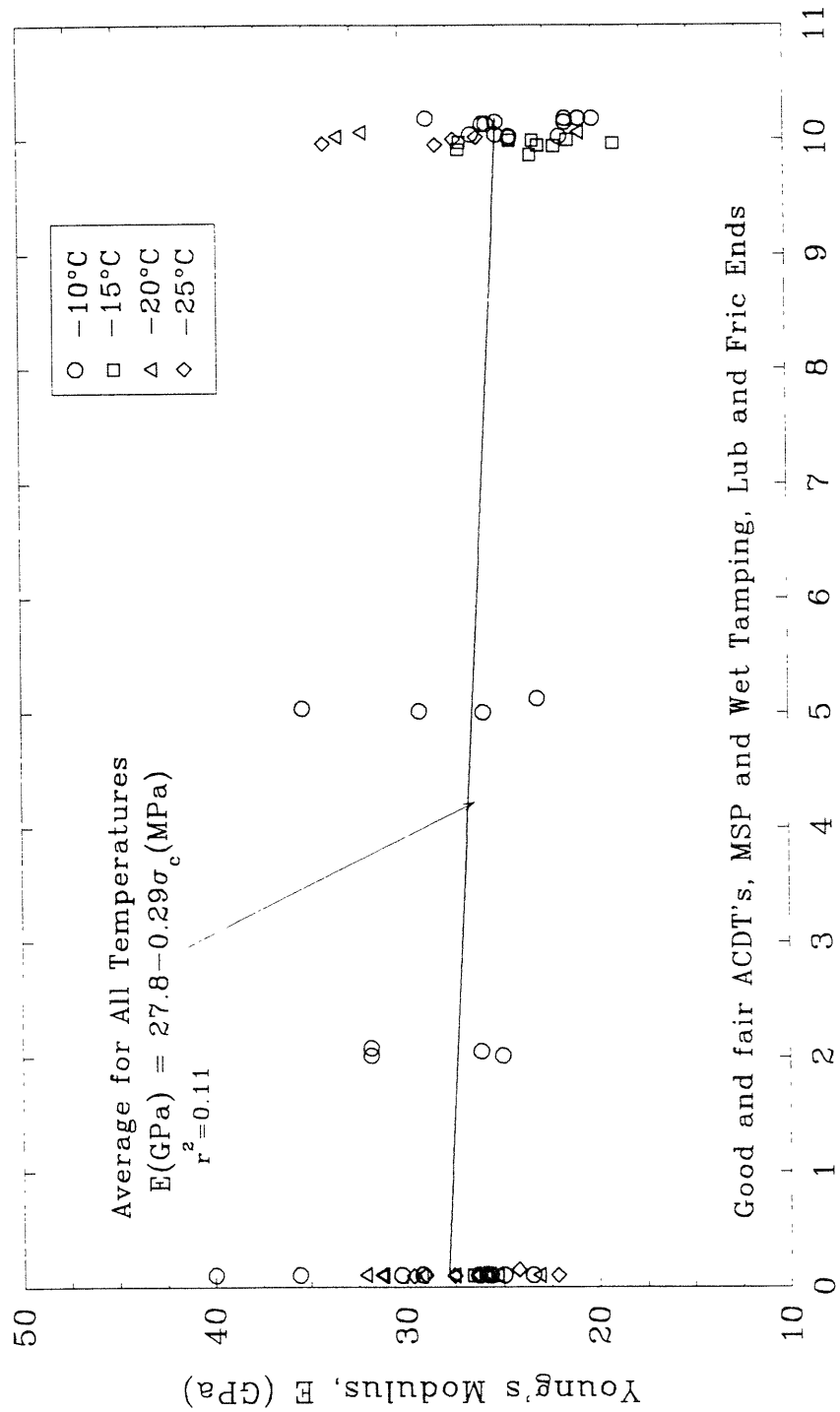

Figure 5.2 Young's Modulus versus Confining Pressure for Conventional Frozen MFS Tests at Different Temperatures

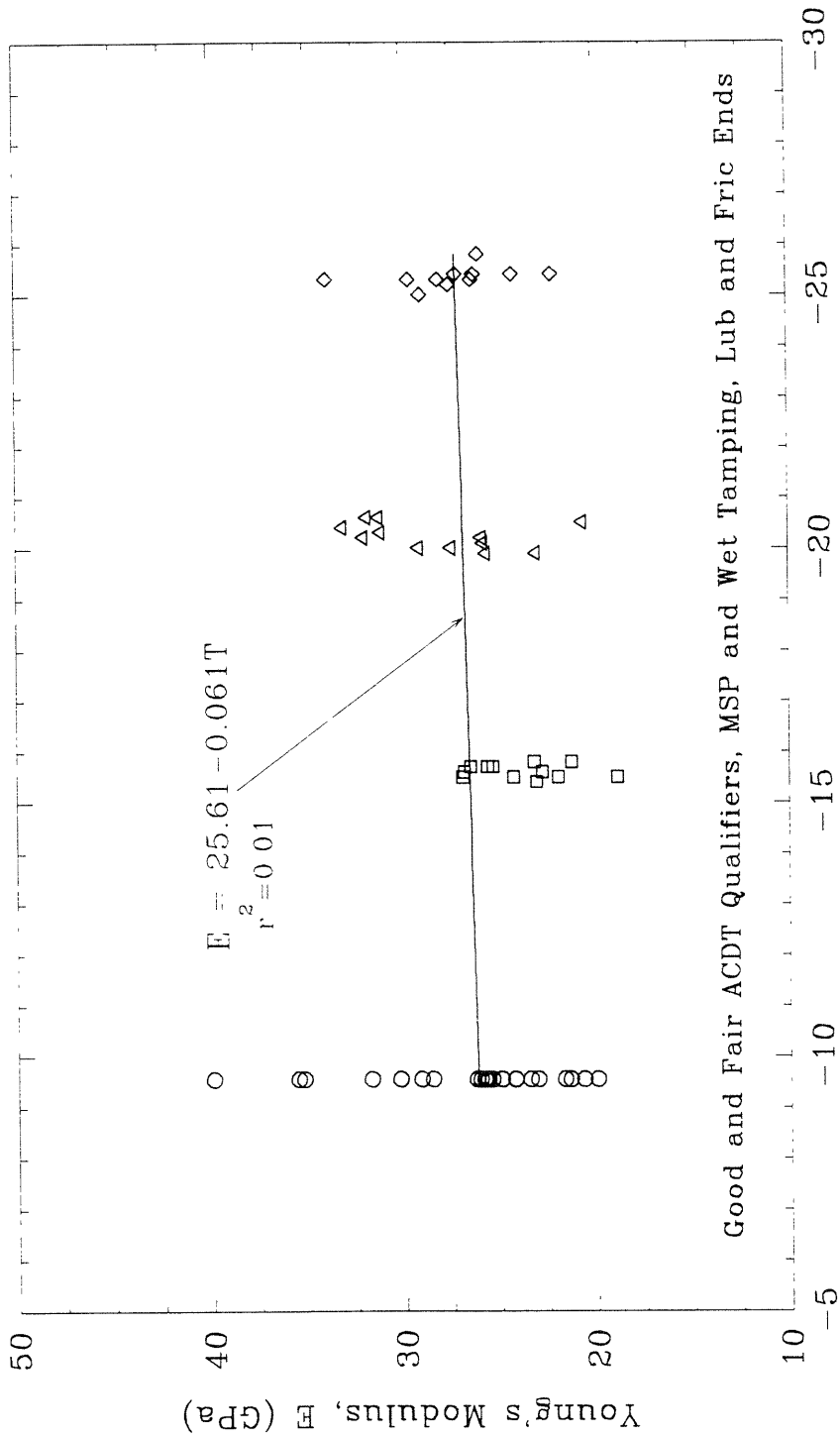

Figure 5.3 Young's Modulus versus Temperature for Conventional Frozen MFS Tests

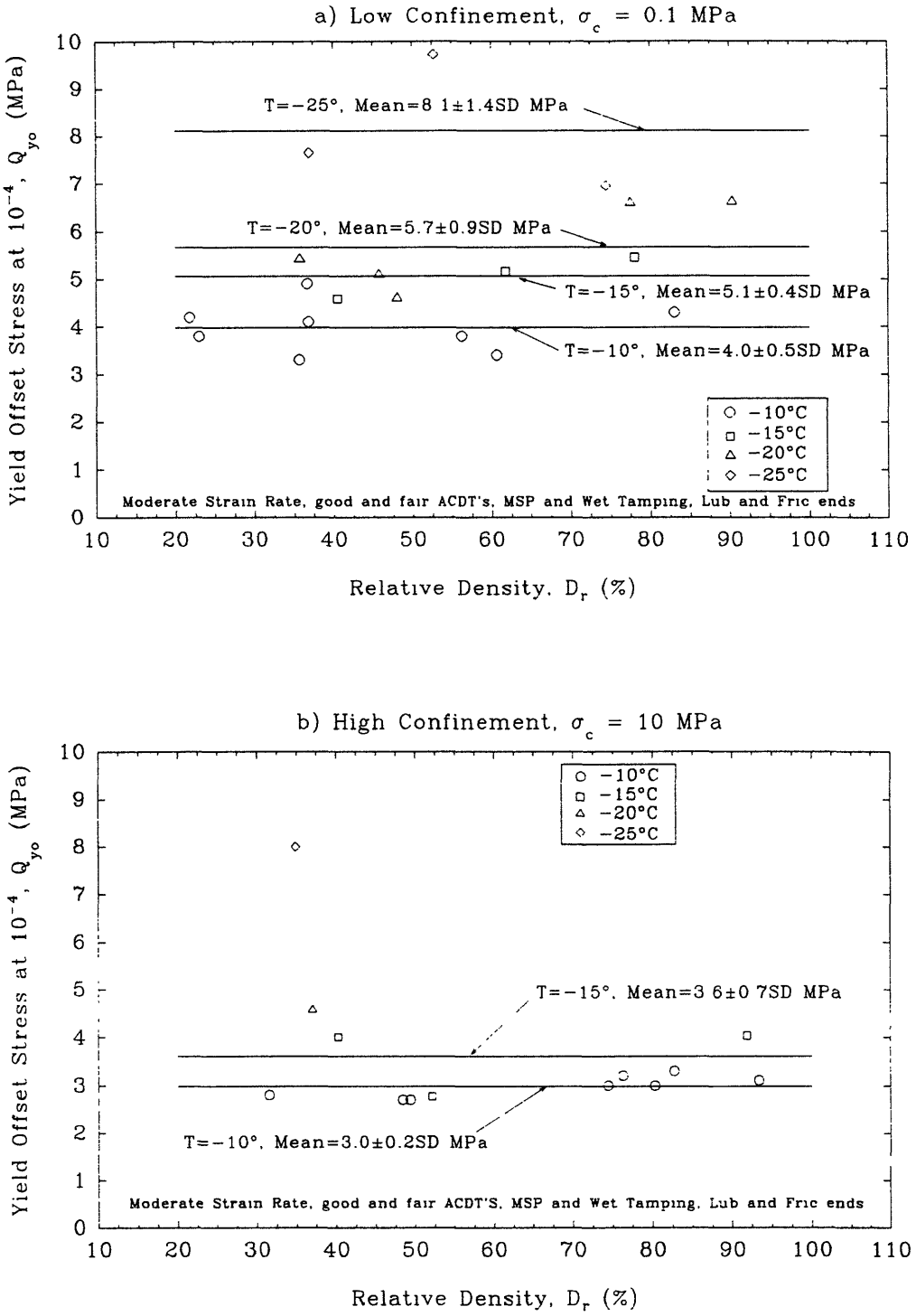

Figure 5.4 Yield Offset Stress at 10^{-4} Strain versus Relative Density for Conventional Frozen MFS Tests at Low and High Confinement, Moderate Strain Rate and Different Temperatures

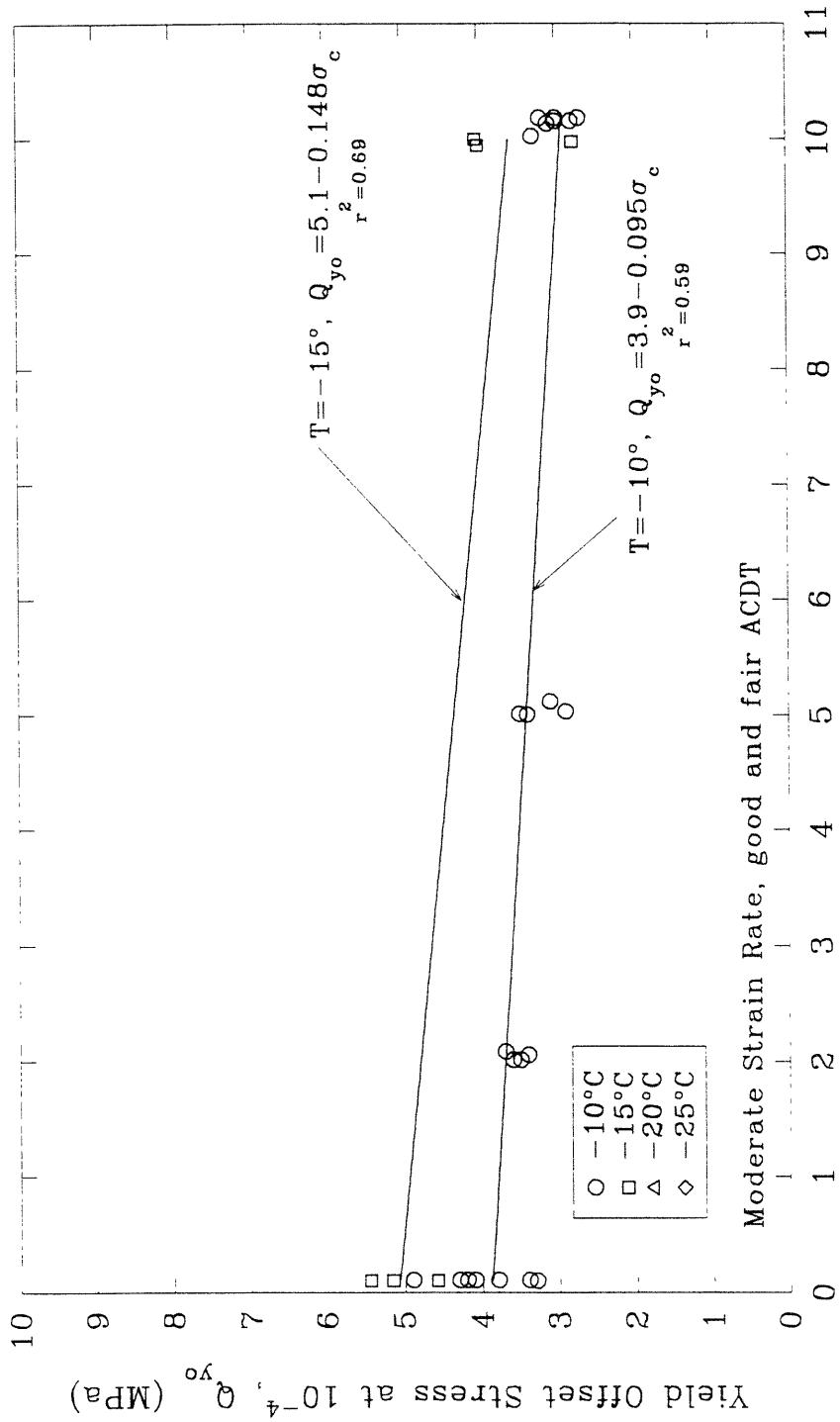

Figure 5.5 Yield Offset Stress at 10^{-4} Strain versus Confining Pressure for Conventional Frozen MFS Tests at Moderate Strain Rate and Different Temperatures

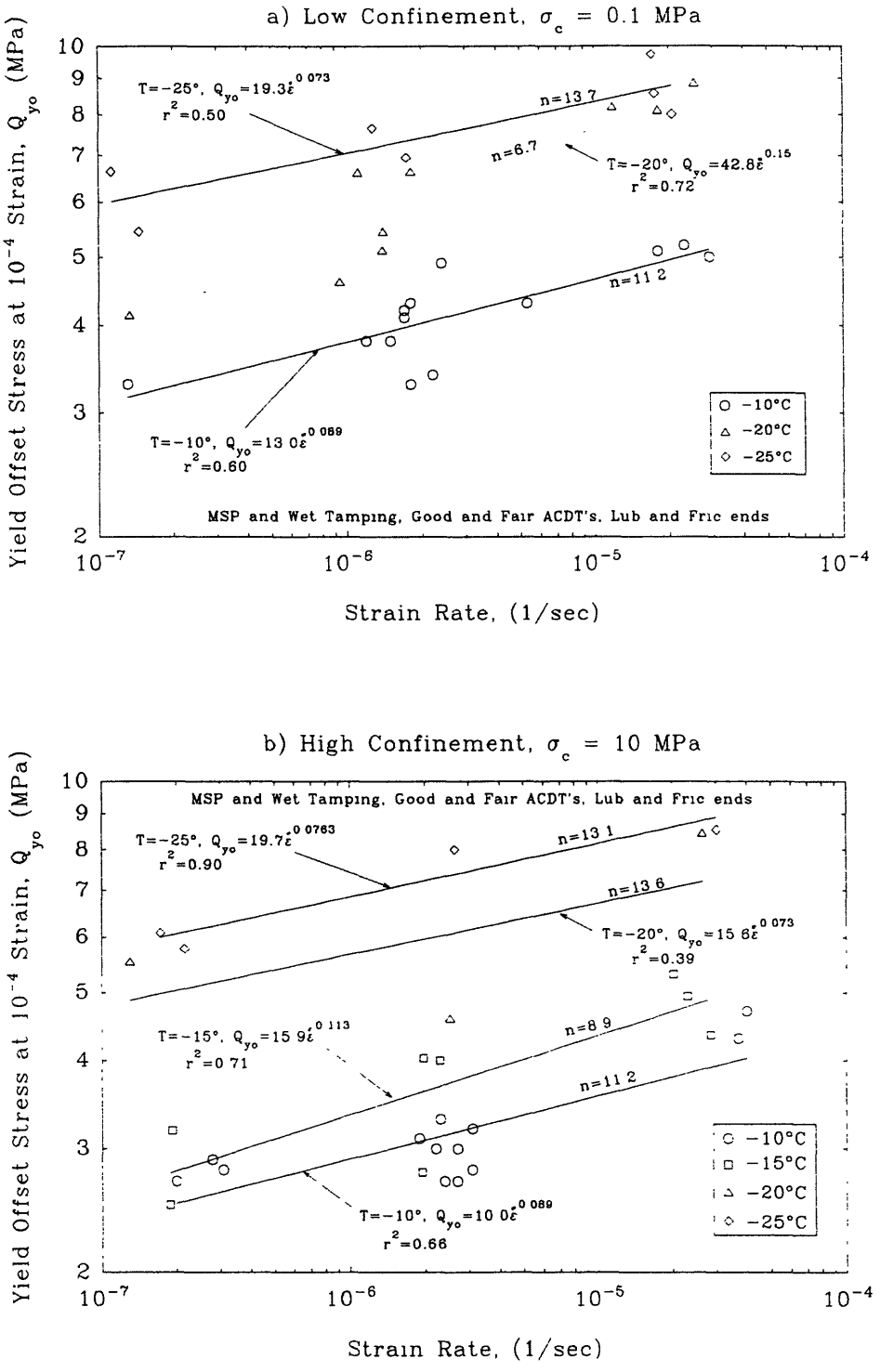

Figure 5.6 Yield Offset Stress at 10^{-4} Strain versus Strain Rate for Conventional Frozen MFS Tests at Low and High Confinement

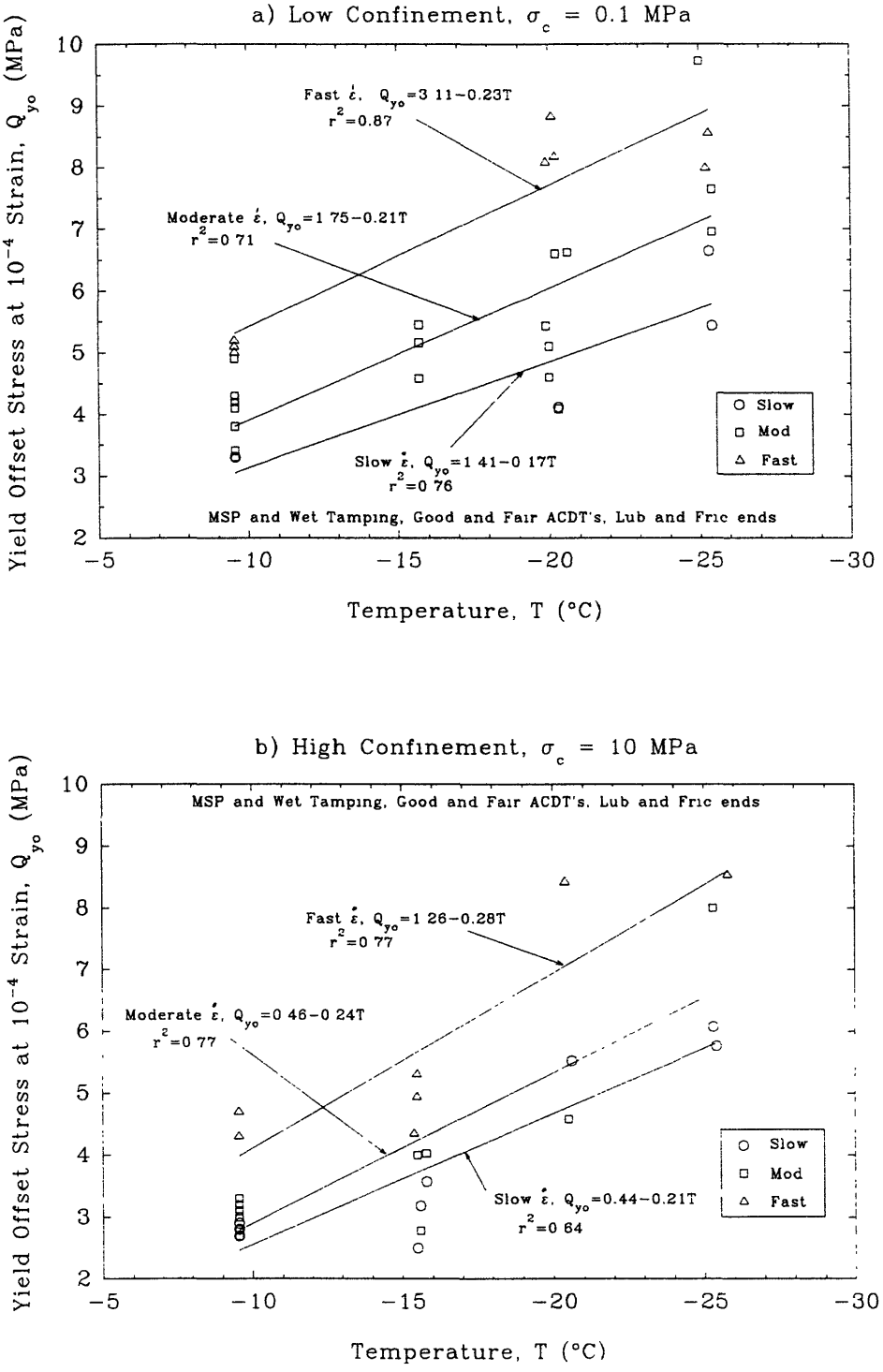

Figure 5.7 Yield Offset Stress at 10^{-4} Strain versus Temperature for Conventional Frozen MFS Tests at Low and High Confinement

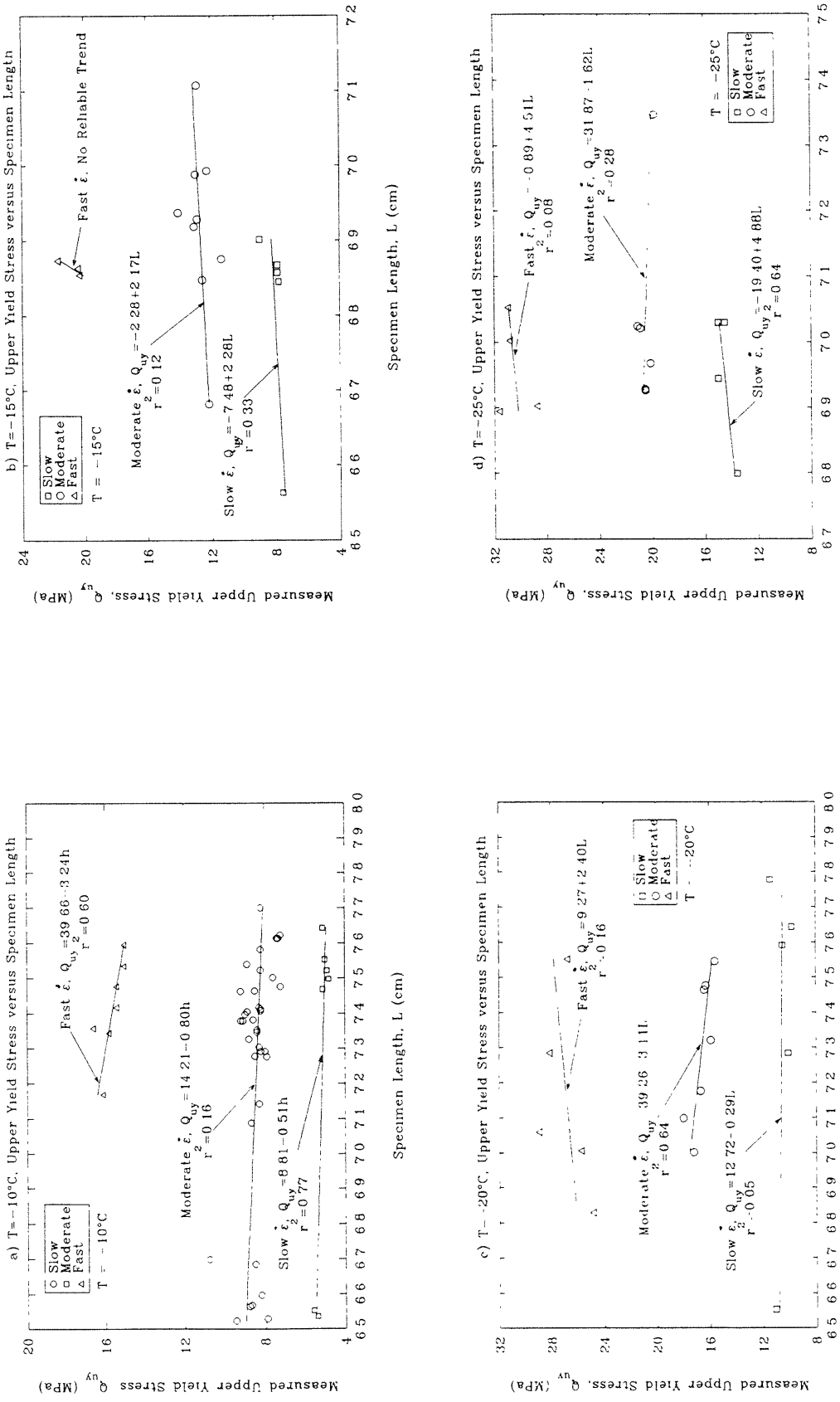

Figure 5 8 Upper Yield Stress versus Specimen Length for Conventional Frozen MFS Tests at Different Temperatures

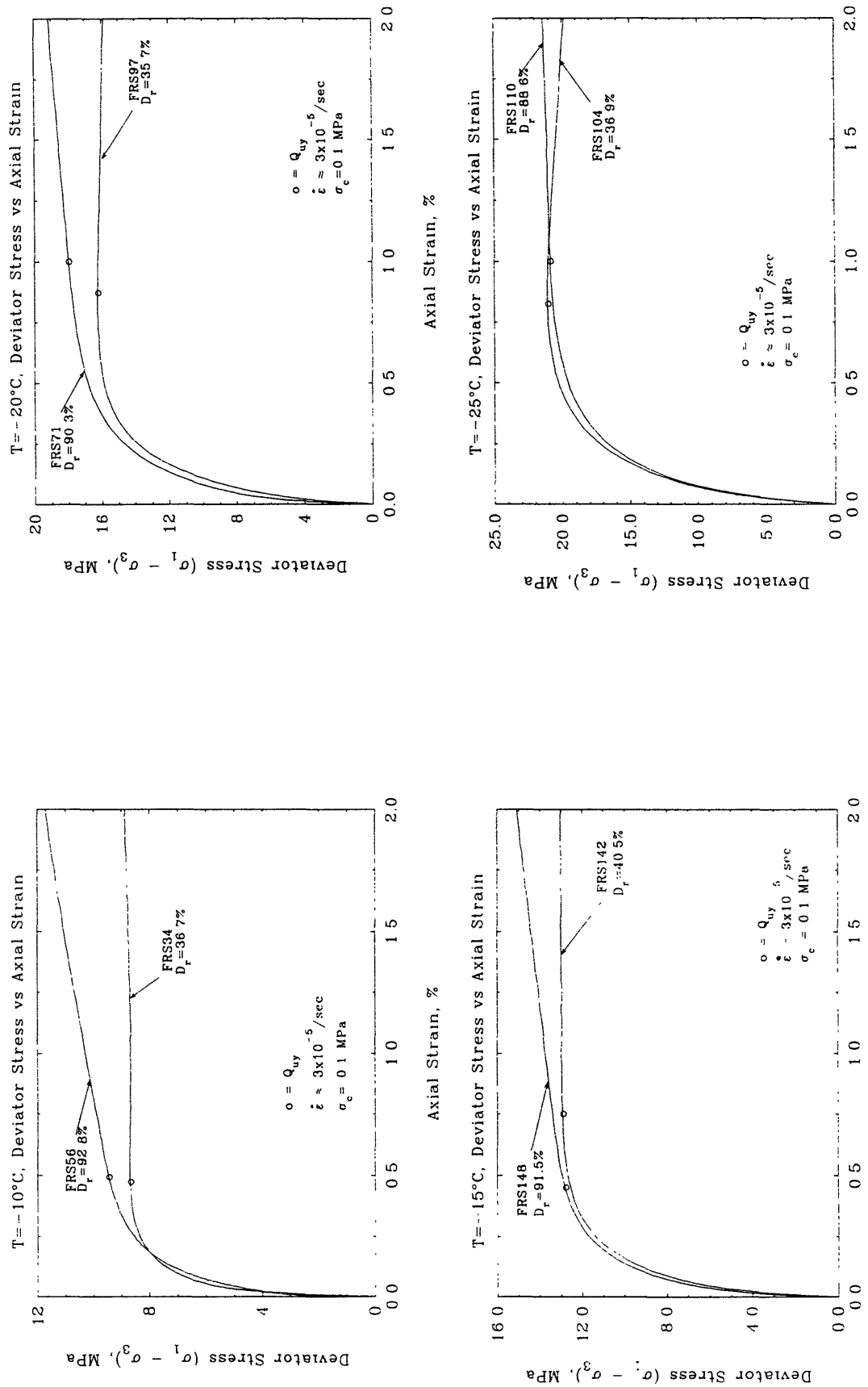

Figure 5 9 Initial Stress–Strain Curves Showing the Effect of Relative Density on Upper Yield Stress for Conventional Frozen MFS Tests at Moderate Strain Rate and Low Confinement

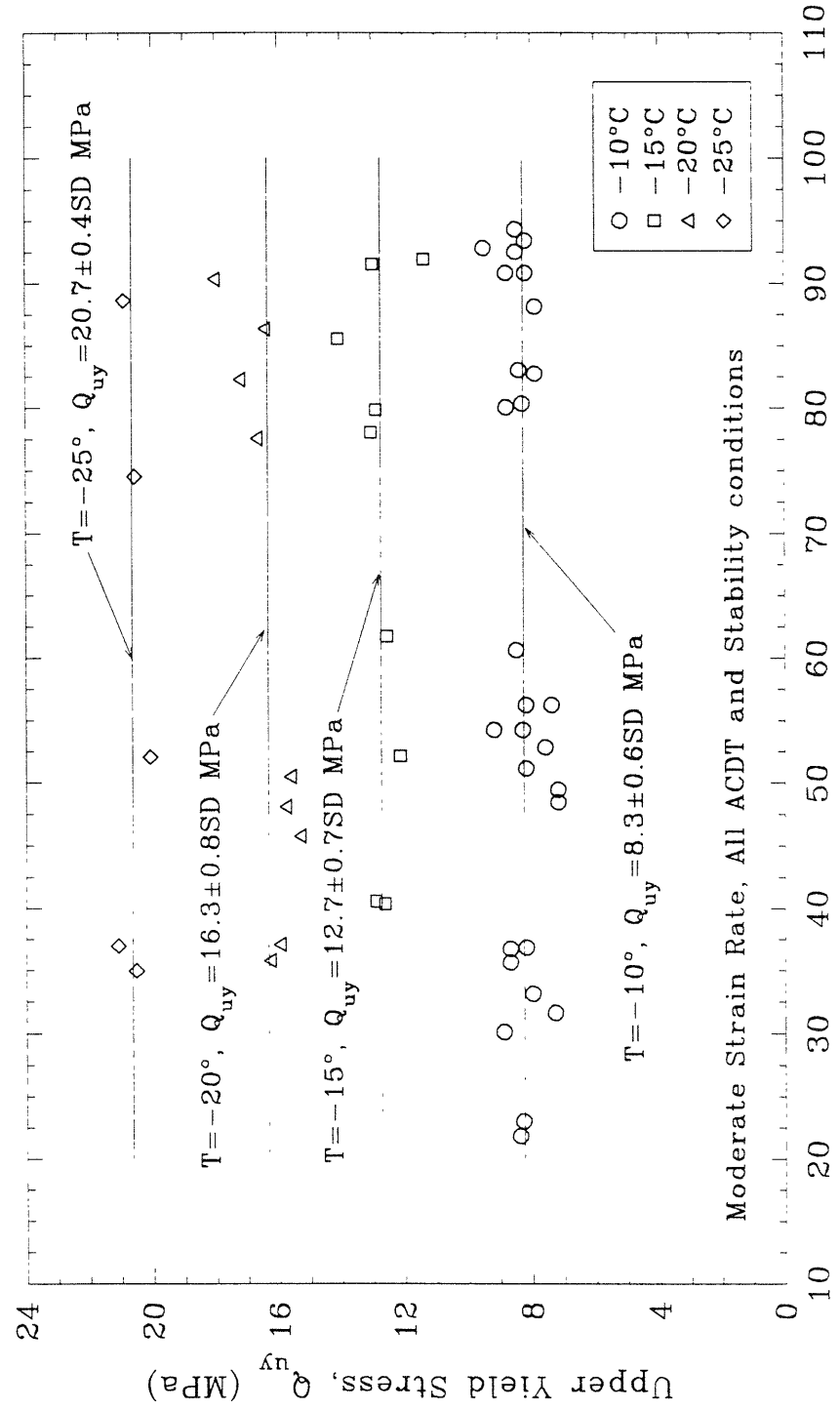

Figure 5.10a Upper Yield Stress versus Relative Density for Conventional Frozen MFS Tests at Moderate Strain Rate and Different Temperatures and Confining Pressures

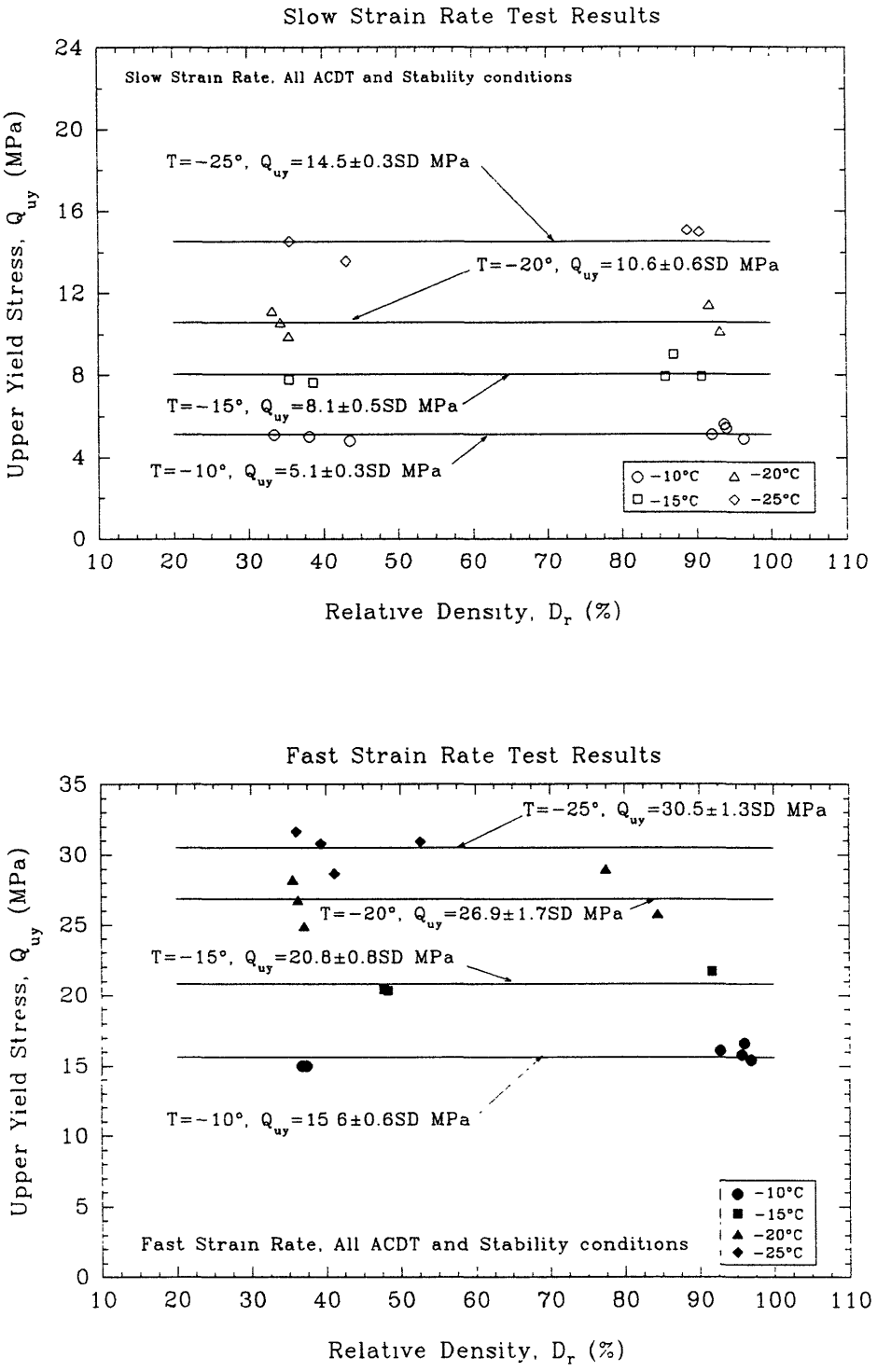

Figure 5.10b Upper Yield Stress versus Relative Density for Conventional Frozen MFS Tests at Slow and Fast Strain Rates and Different Temperatures and Confining Pressures

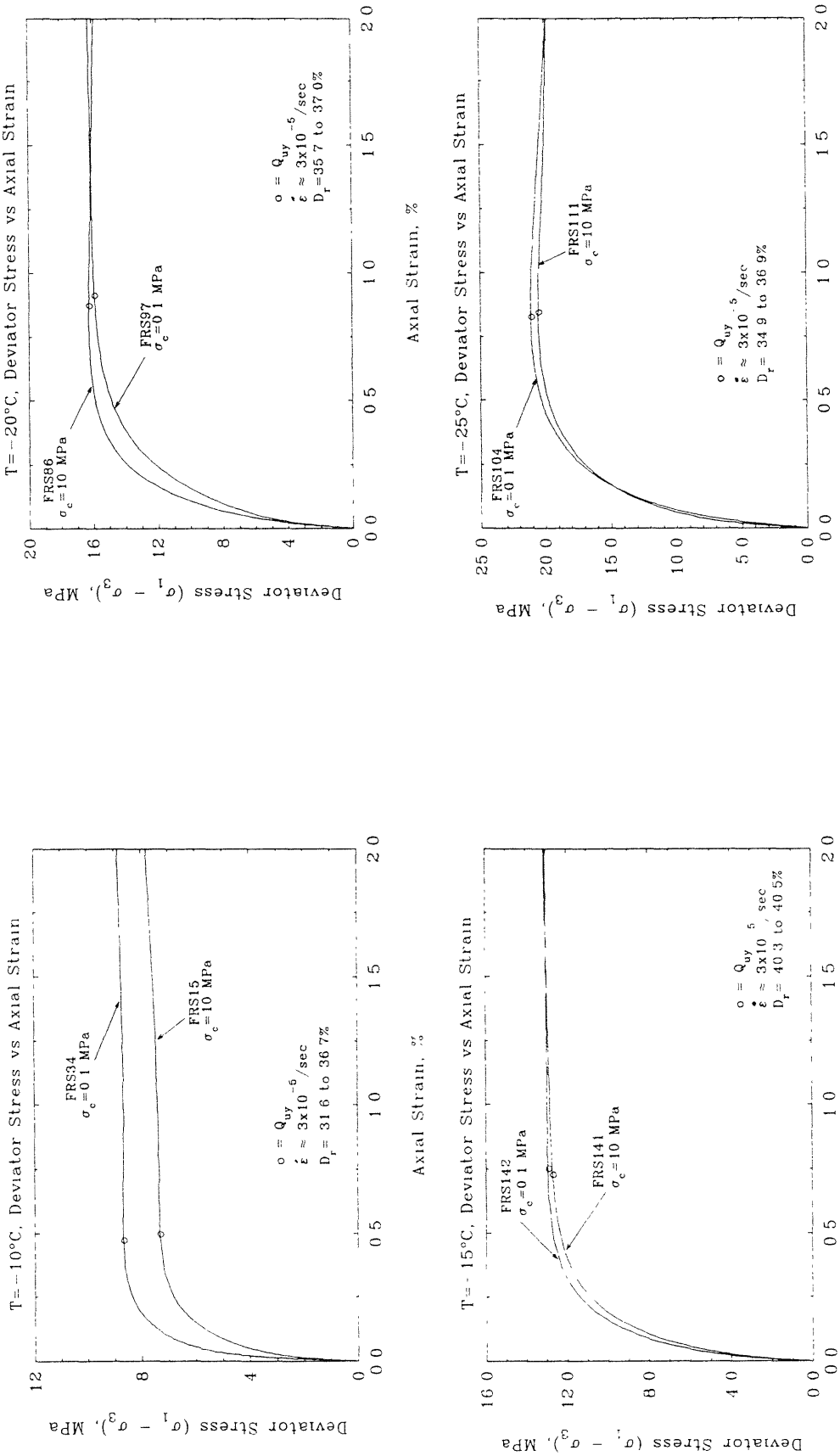

Figure 5 11 Initial Stress–Strain Curves Showing the Effect of Confinement on the Upper Yield Stress for Conventional Frozen MFS Tests on Loose Specimens at Moderate Strain Rate

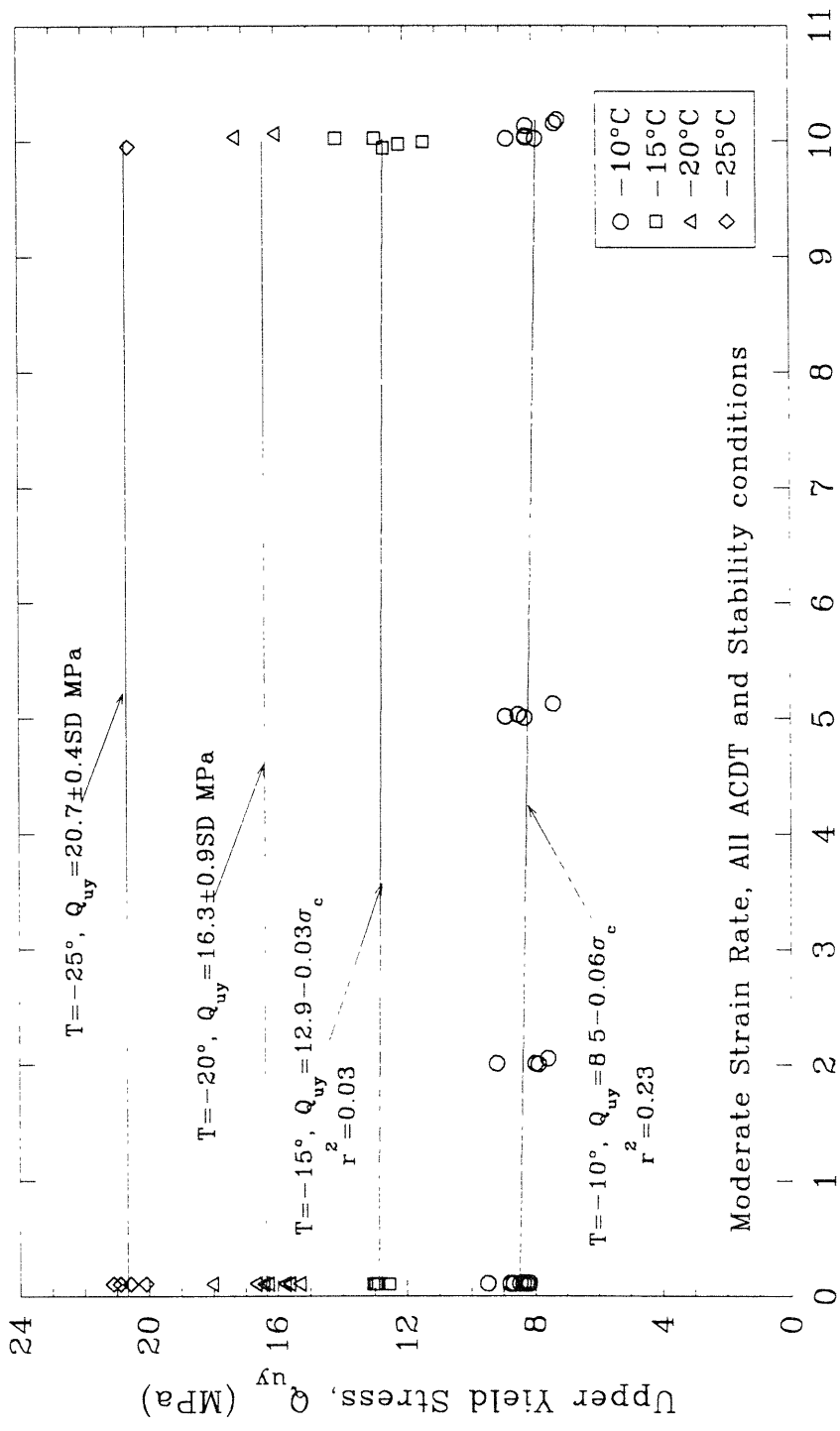

Figure 5.12a Upper Yield Stress versus Confining Pressure for Conventional Frozen MFS Tests at Moderate Strain Rate and Different Temperatures

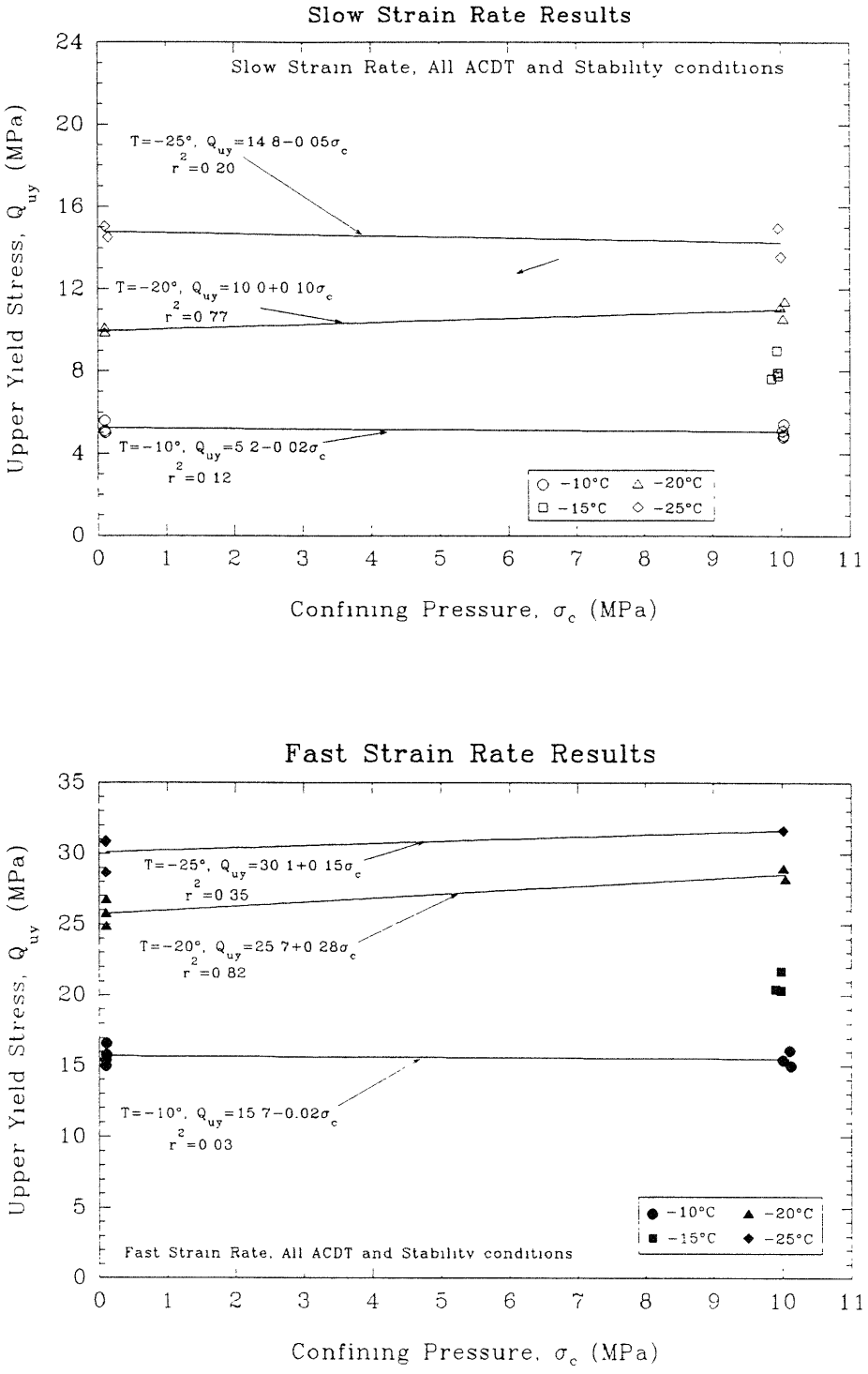

Figure 5.12b Upper Yield Stress versus Confining Pressure for Conventional Frozen MFS Tests at Various Strain Rates and Different Temperatures

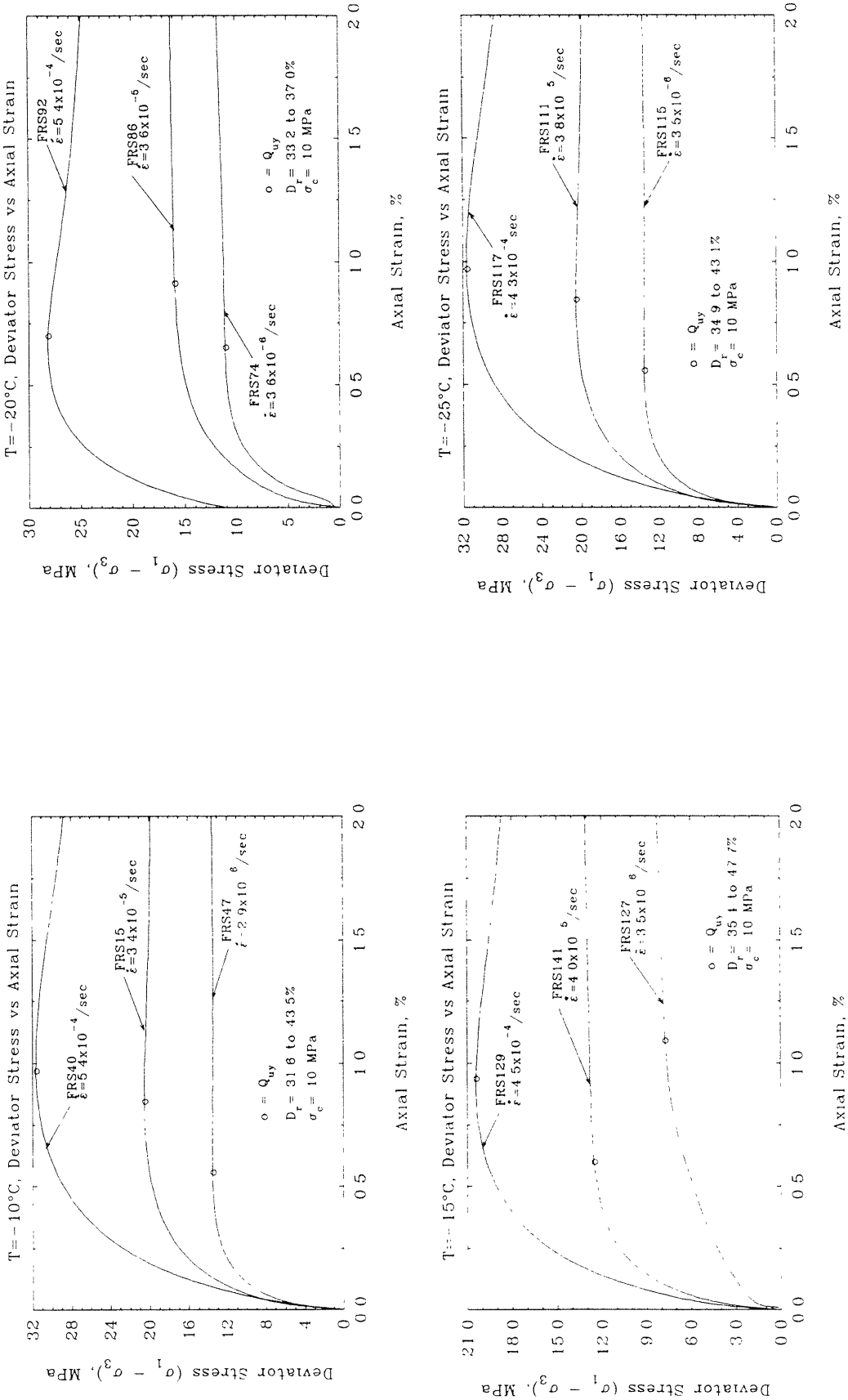

Figure 5 13 Initial Stress–Strain Curves Showing the Effect of Strain Rate on Upper Yield Stress for Conventional Frozen MFS Tests on Loose Specimens at High Confinement

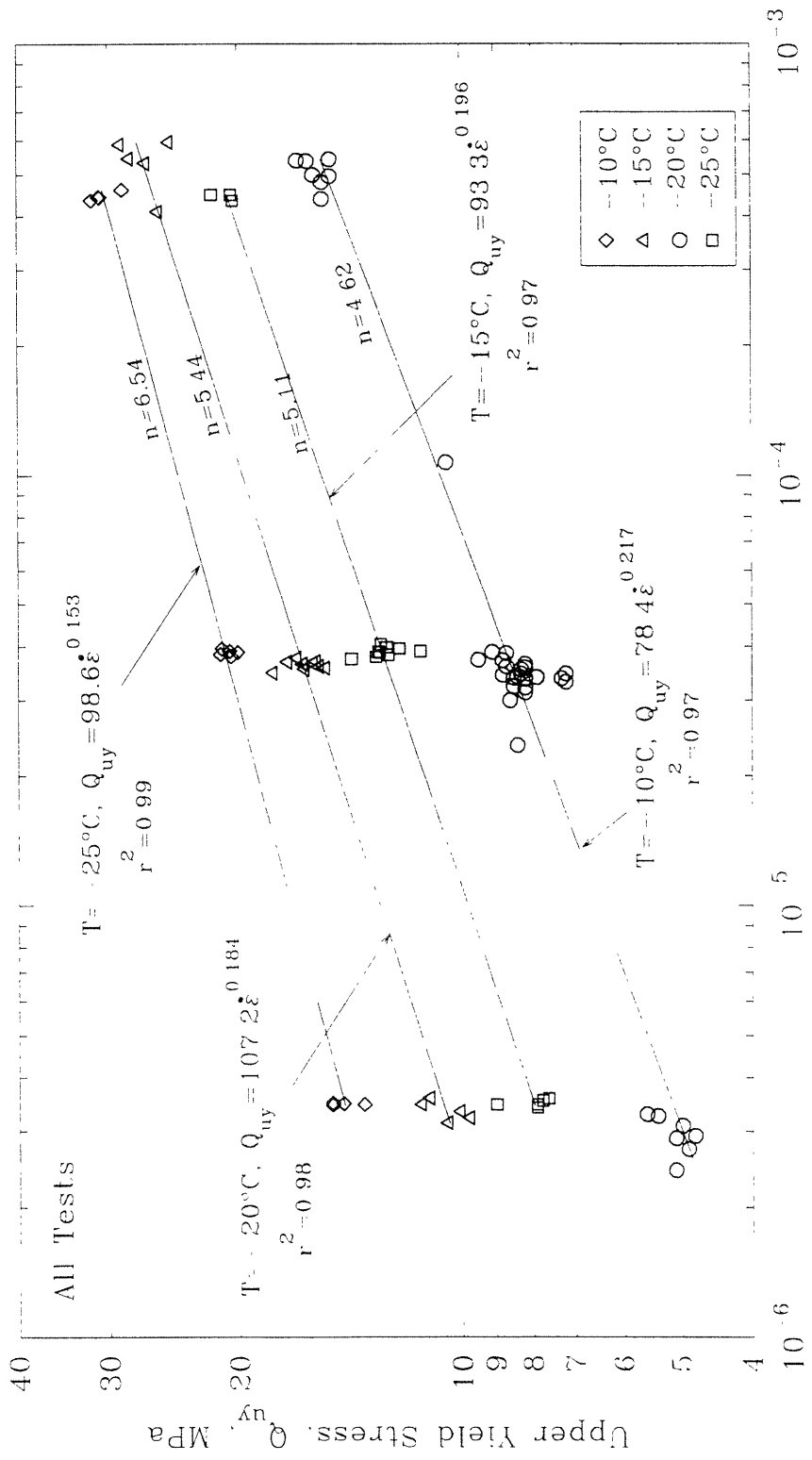

Figure 5.14 Upper Yield Stress versus Strain Rate for Conventional Frozen MFS Tests at Different Temperatures

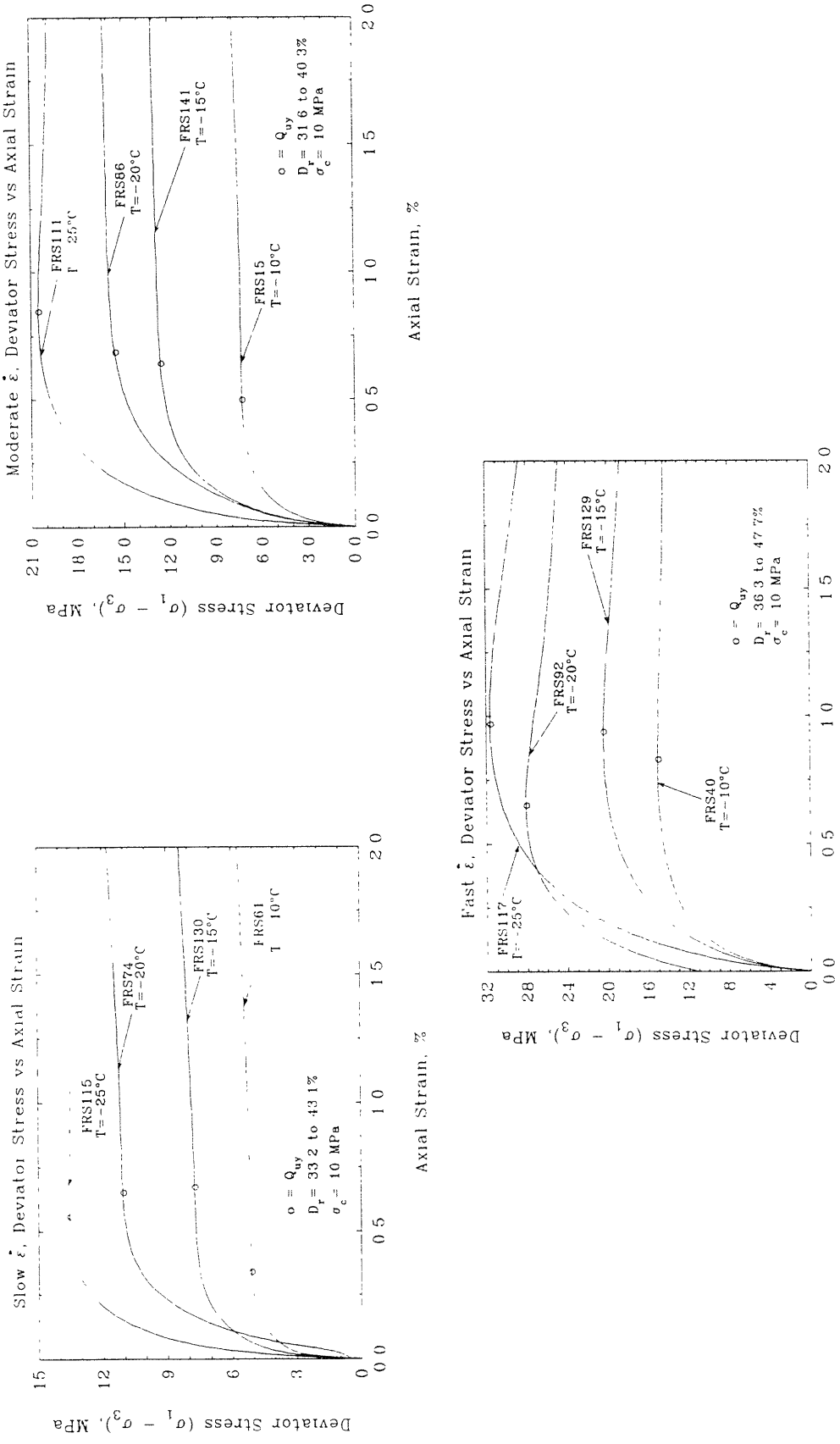

Figure 5 15 Initial Stress-Strain Curves Showing the Effect of Temperature on Upper Yield Stress on Conventional Frozen MFS Tests on Loose Specimens at High Confinement

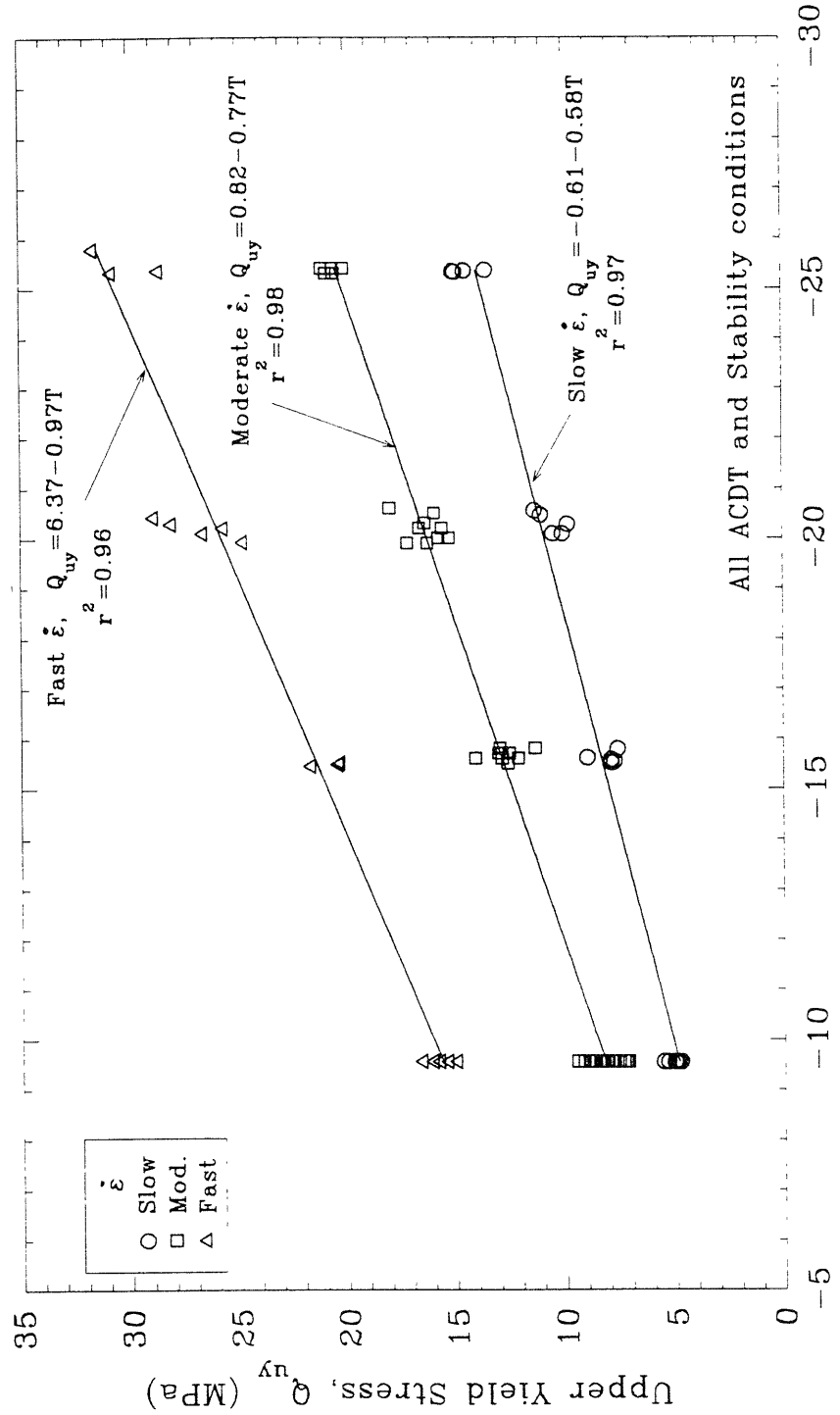

Figure 5.16 Upper Yield Stress versus Temperature for Conventional Frozen MFS Tests at Different Strain Rates

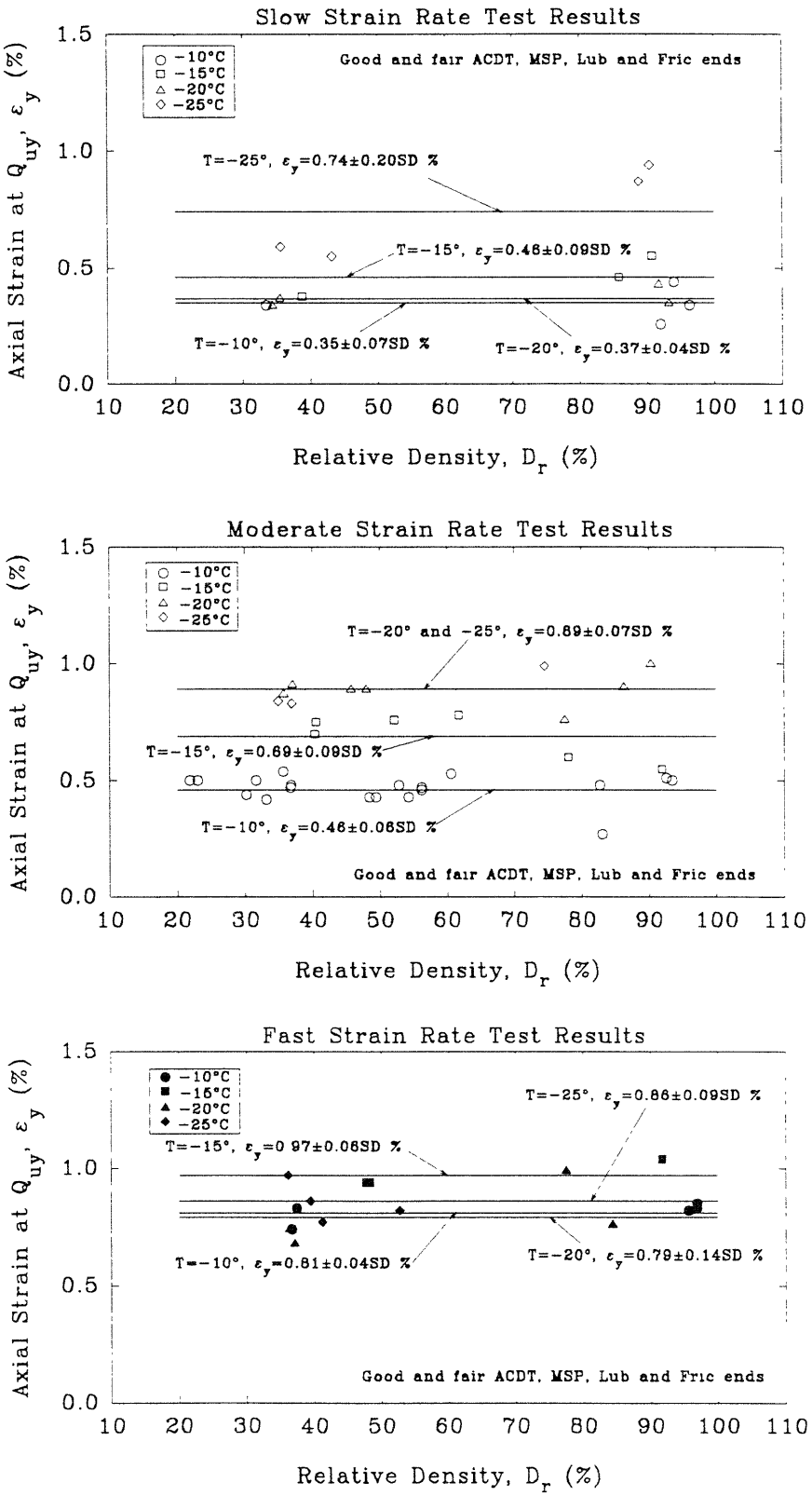

Figure 5.17 Axial Strain at Q_{uy} versus Relative Density for Conventional Frozen MFS Tests at Different Strain Rates and Different Temperatures

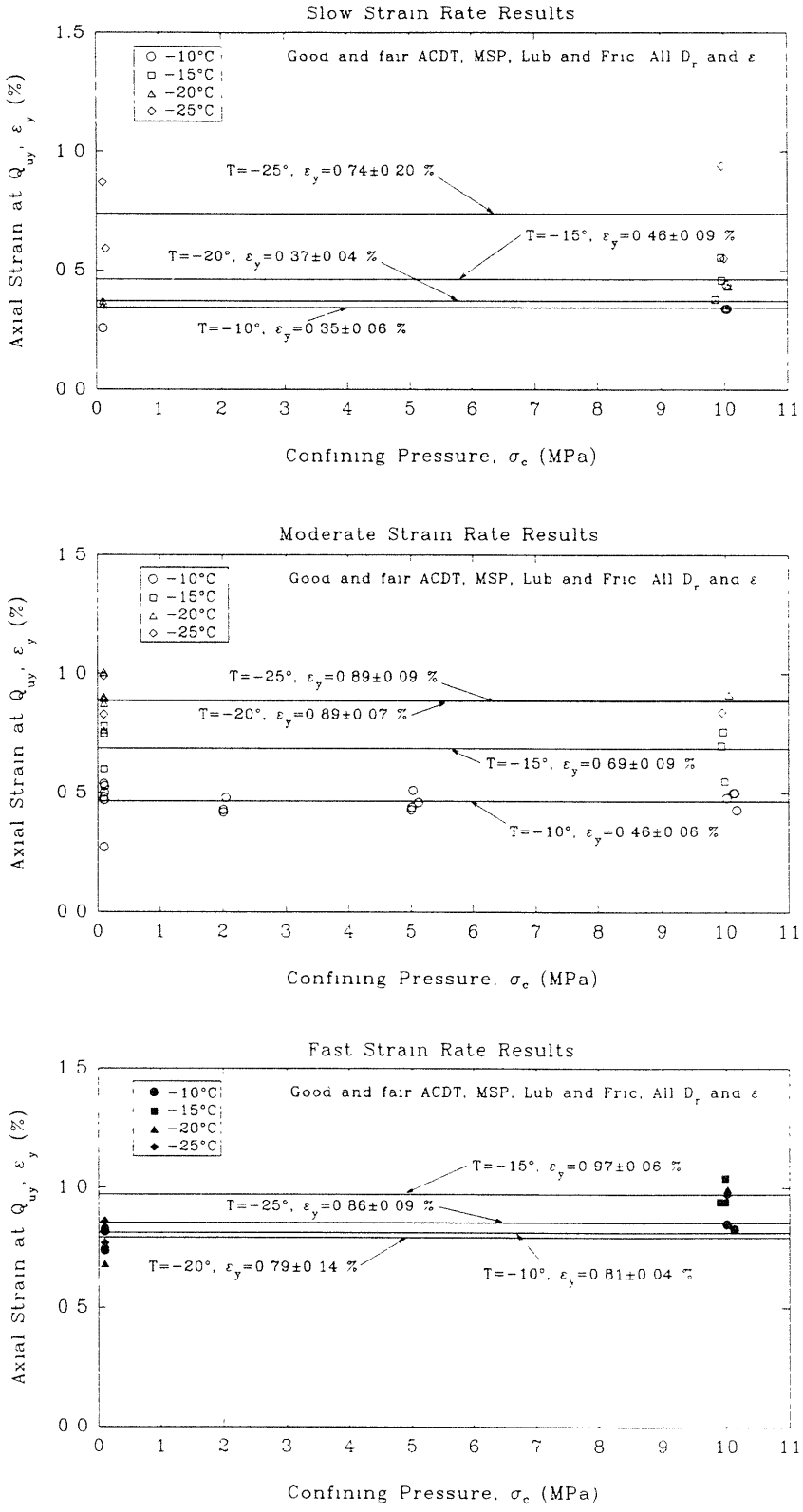

Figure 5.18 Axial Strain at Q_{uv} versus Confining Pressure for Conventional Frozen MFS Tests at Different Temperatures

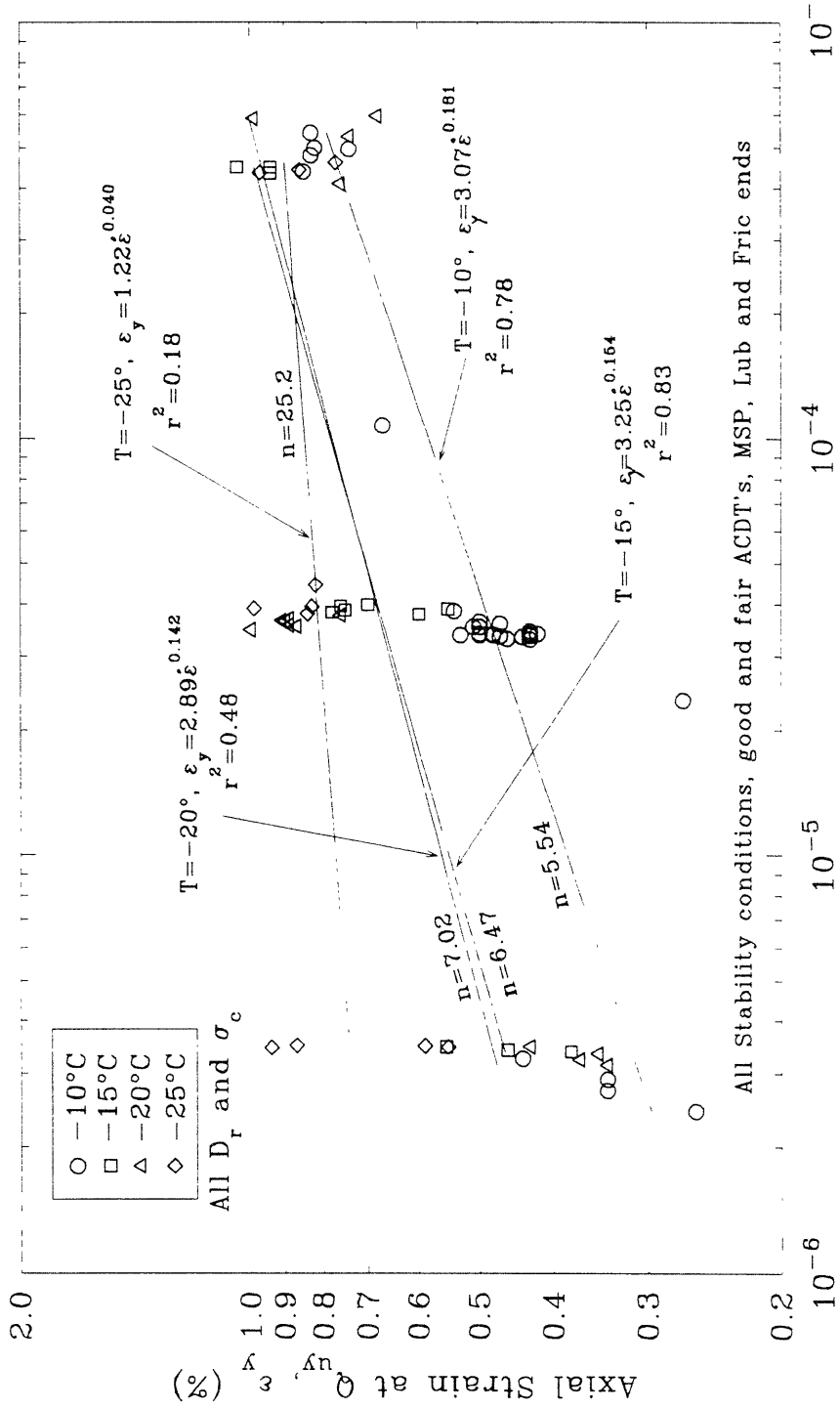

Figure 5.19 Axial Strain at Q_{uy} versus Strain Rate for Conventional Frozen MFS Tests at Different Temperatures

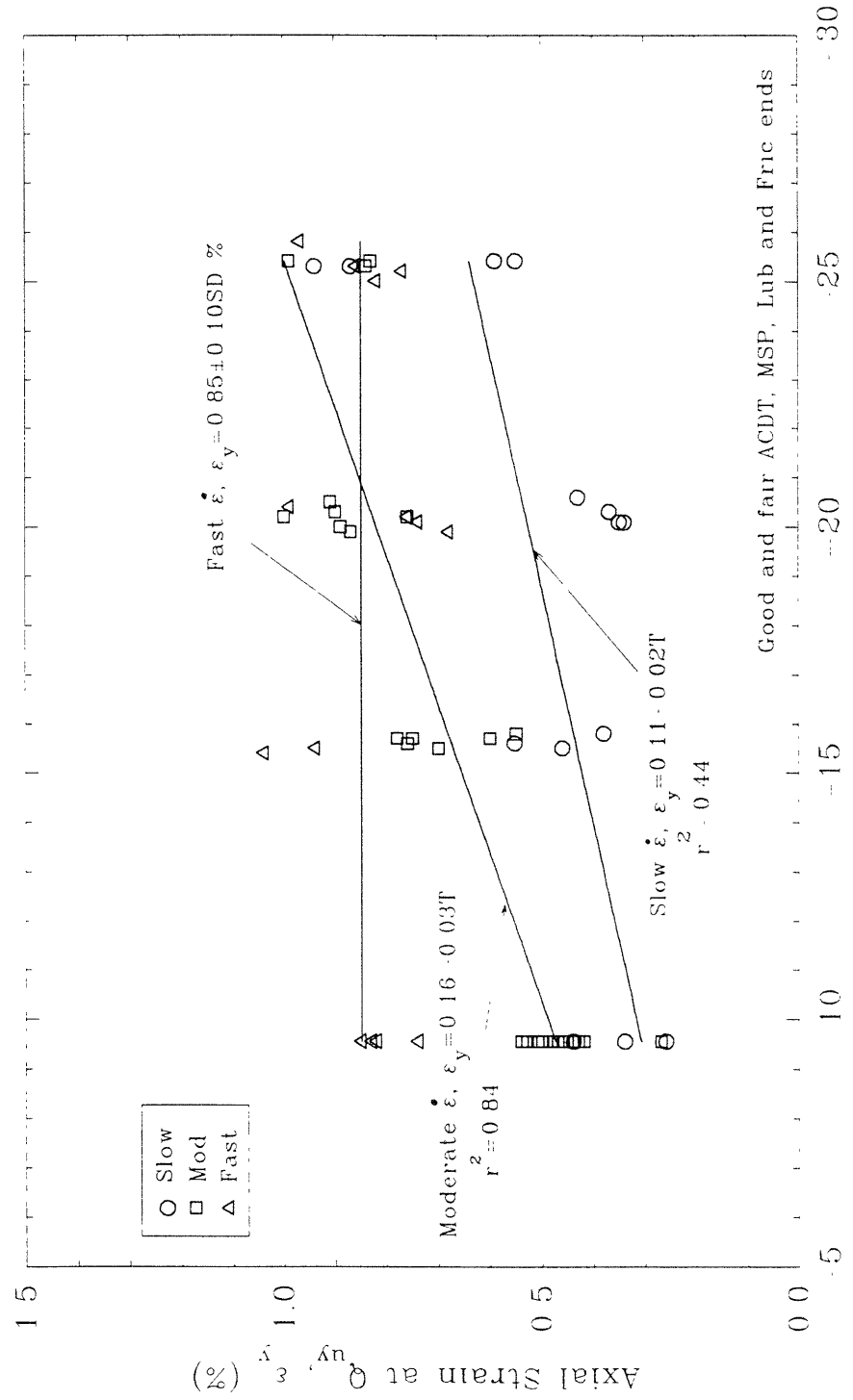

Figure 5.20 Axial Strain at Q_{uy} versus Temperature for Conventional Frozen MFS Tests

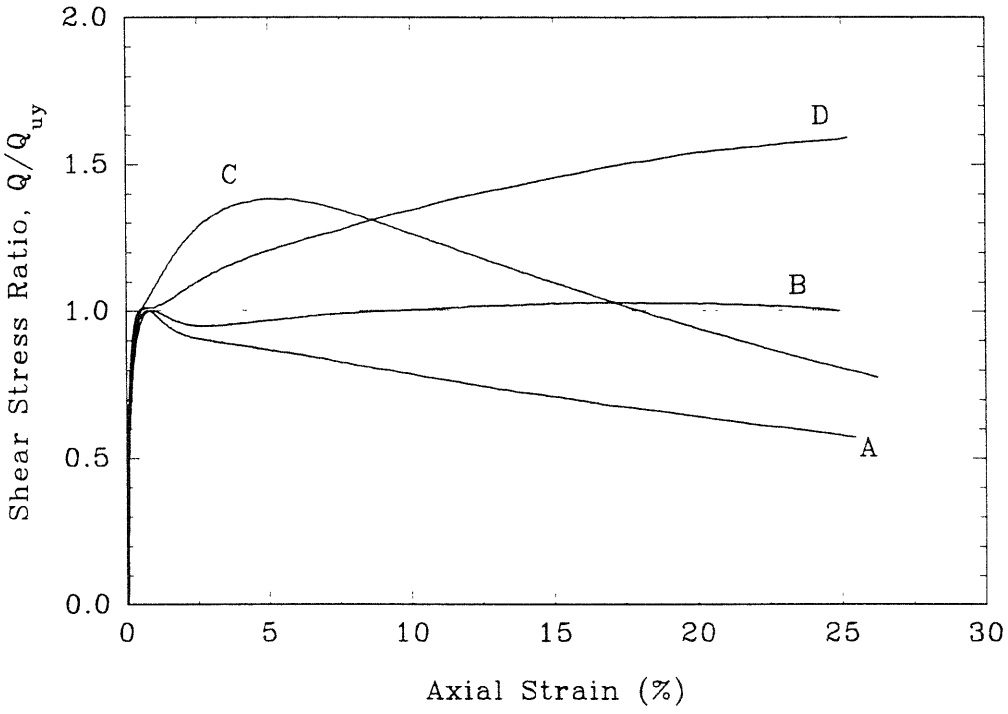

Description of Curve Types

A: Peak occurs at upper yield and is followed by significant strain softening

B: Slight to moderate strain softening after upper yield, then zero to slight strain hardening so that Q_p is approximately equal to Q_{uy}; little or no softening at large strains

C: Significant strain hardening after upper yield, with Q_p occurring at moderate axial strain and then followed by significant strain softening

D: Significant strain hardening after upper yield, with Q_p occurring at large axial strain and no post peak strain softening

Figure. 5.21 Basic Types of Stress–Strain Curves for Conventional Triaxial Compression Tests on Frozen MFS

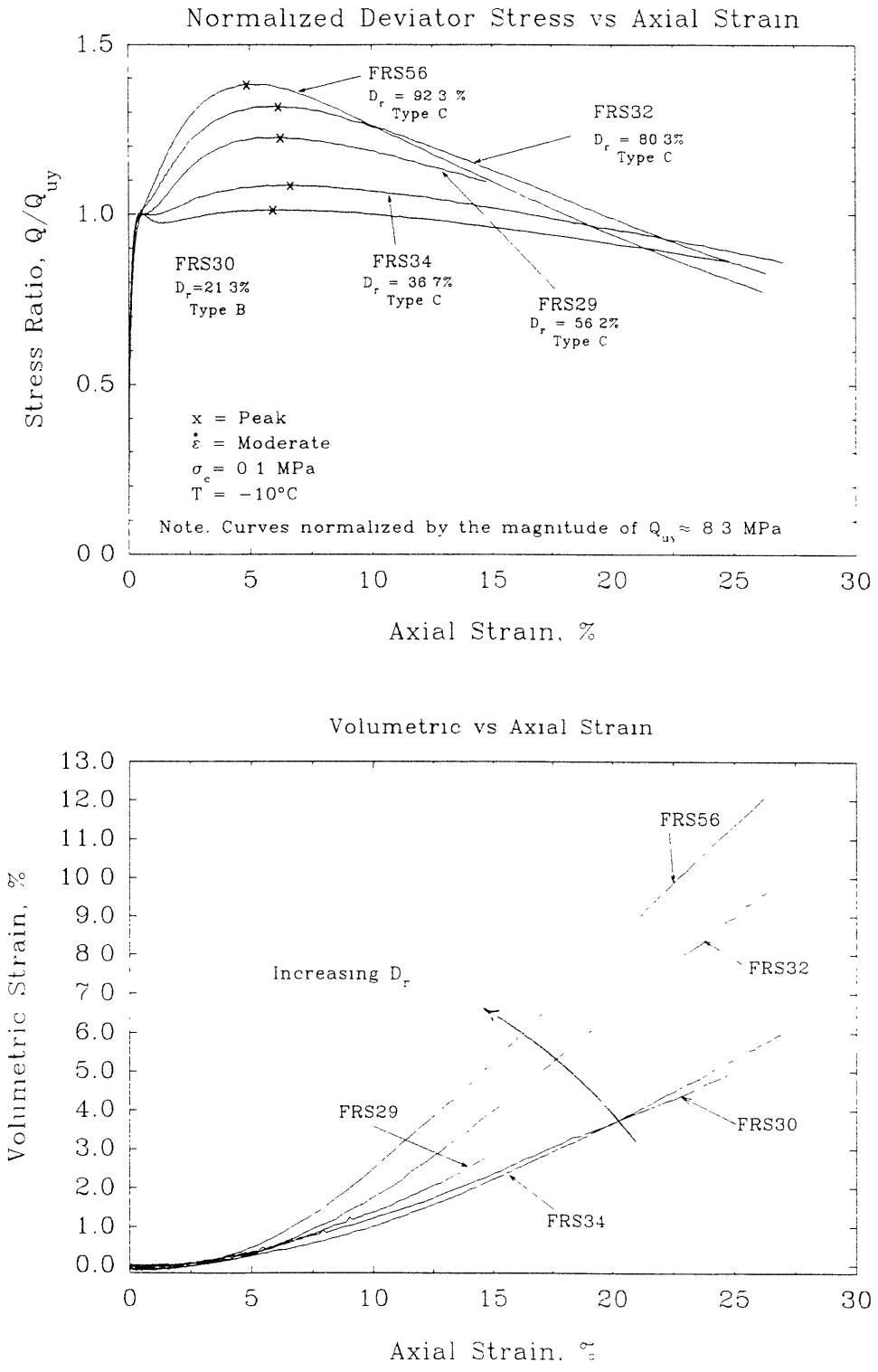

Figure 5.22a Normalized Stress–Strain Curves Showing the Effect of Relative Density for Conventional Frozen MFS Tests at Moderate Strain Rate, Low Confinement and T = −10°C

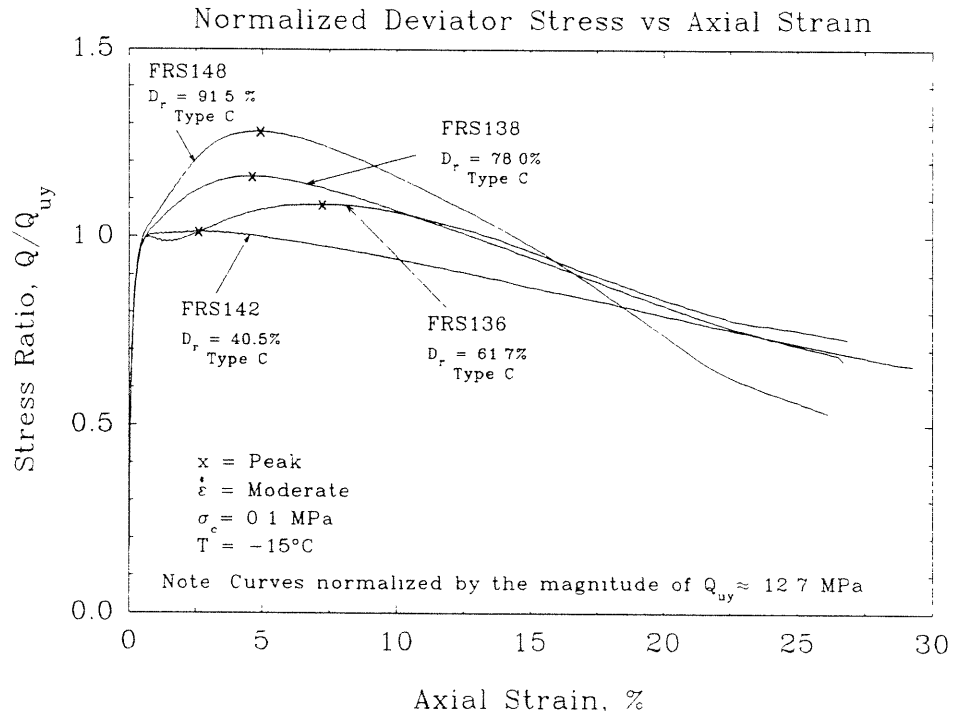

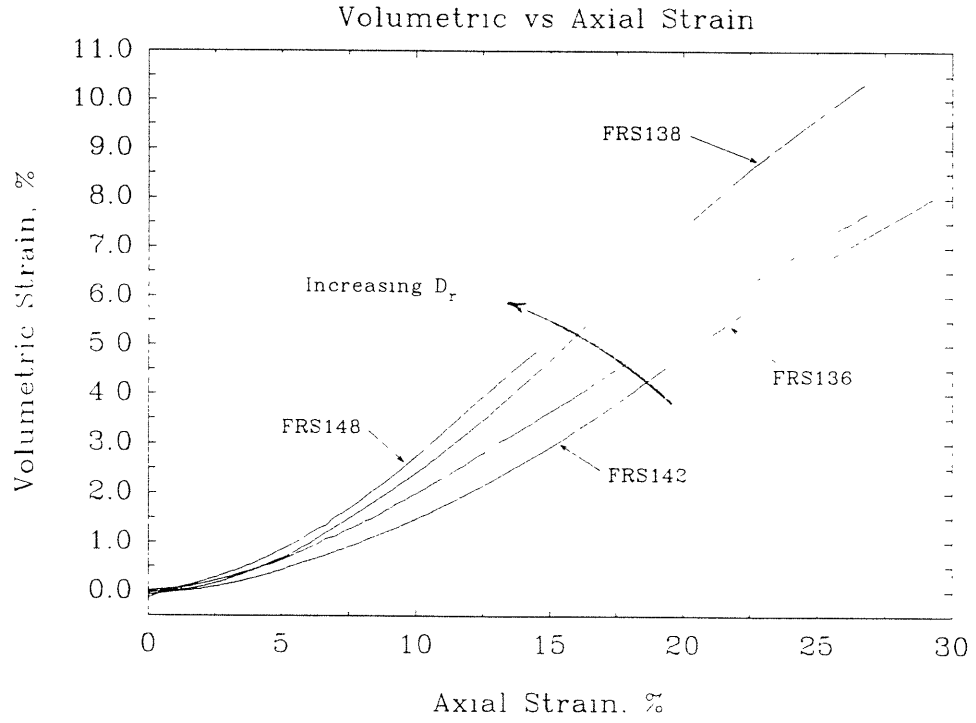

Figure 5.22b Normalized Stress–Strain Curves Showing the Effect of Relative Density for Conventional Frozen MFS Tests at Moderate Strain Rate, Low Confinement and T = −15°C

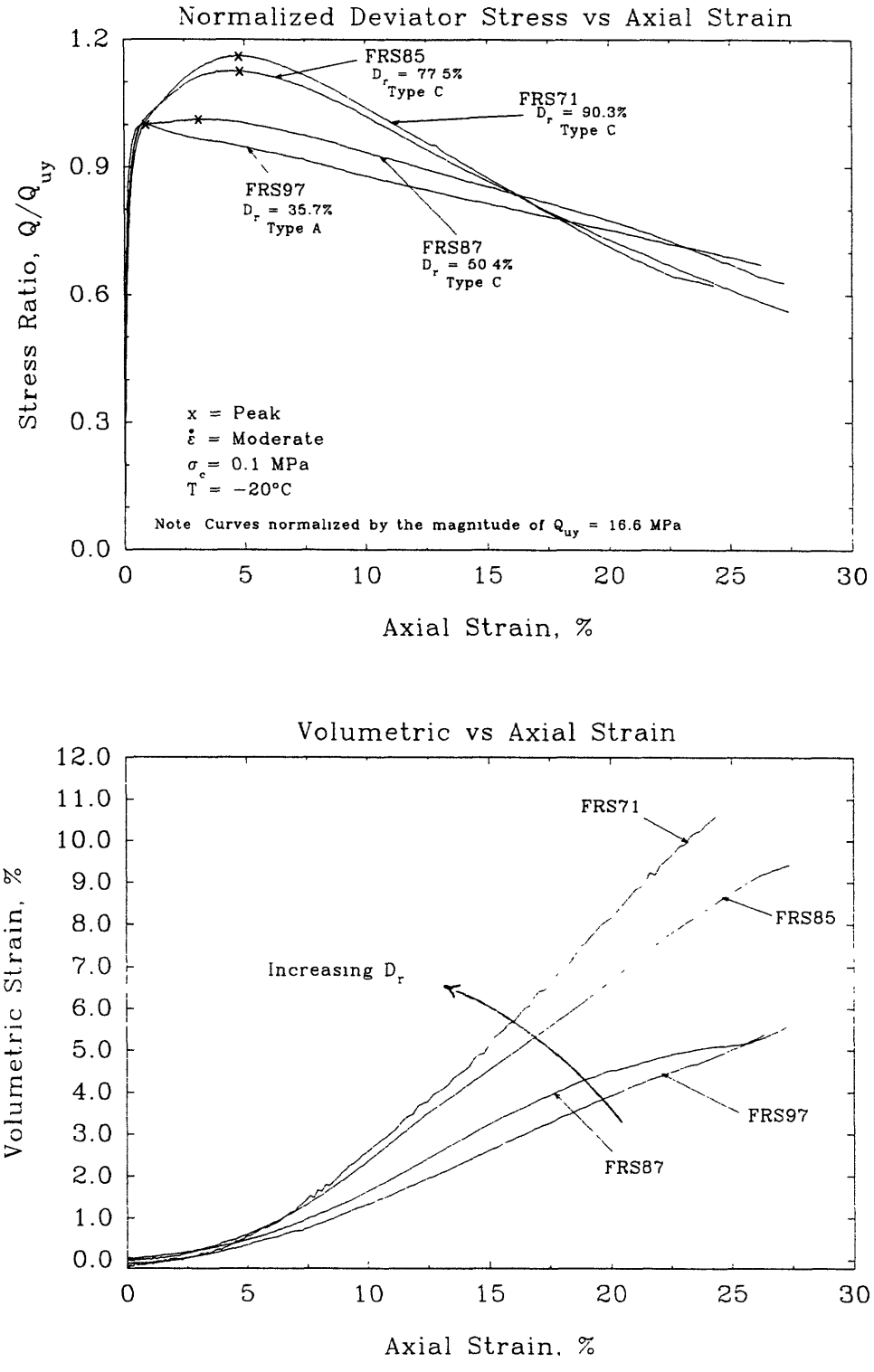

Figure 5.22c Normalized Stress–Strain Curves Showing the Effect of Relative Density for Conventional Frozen MFS Tests at Moderate Strain Rate, Low Confinement and T=−20°C

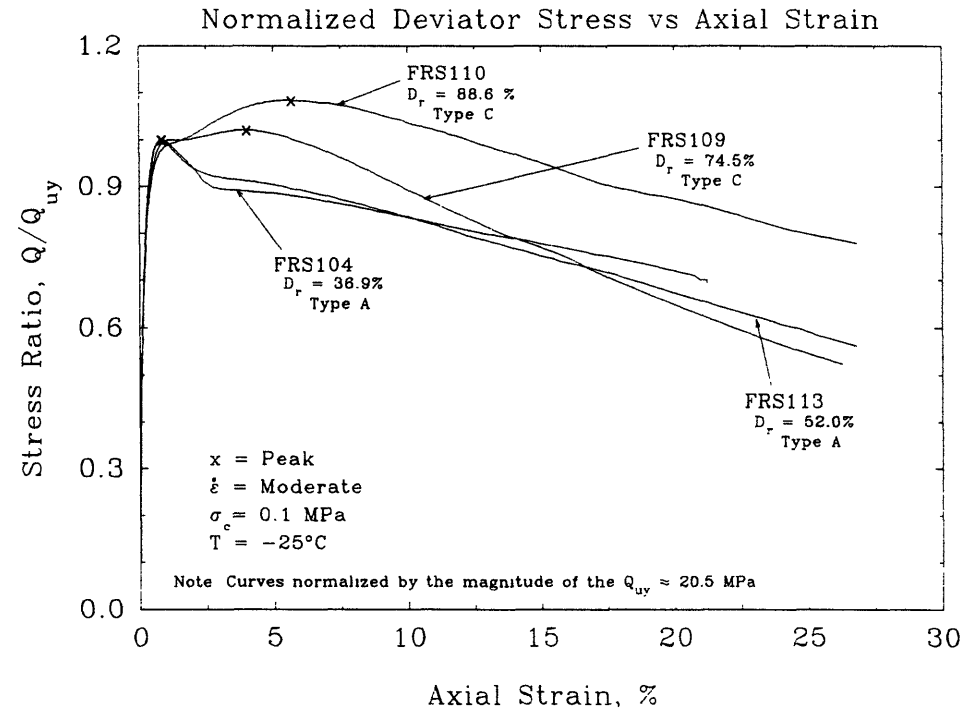

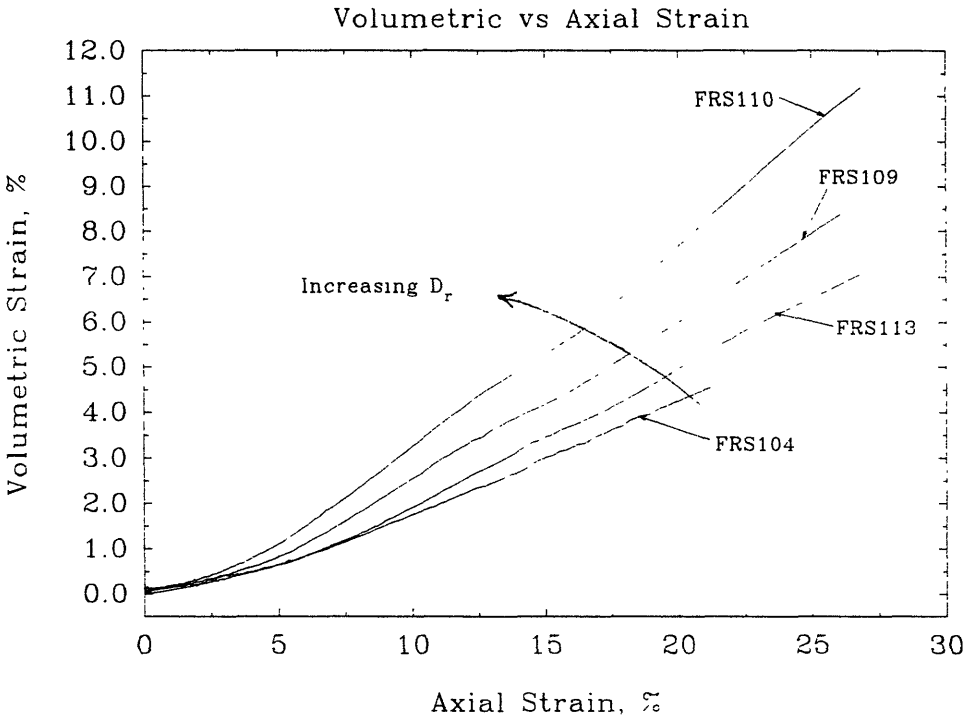

Figure 5.22d Normalized Stress–Strain Curves Showing the Effect of Relative Density for Conventional Frozen MFS Tests at Moderate Strain Rate, Low Confinement and T=−25°C

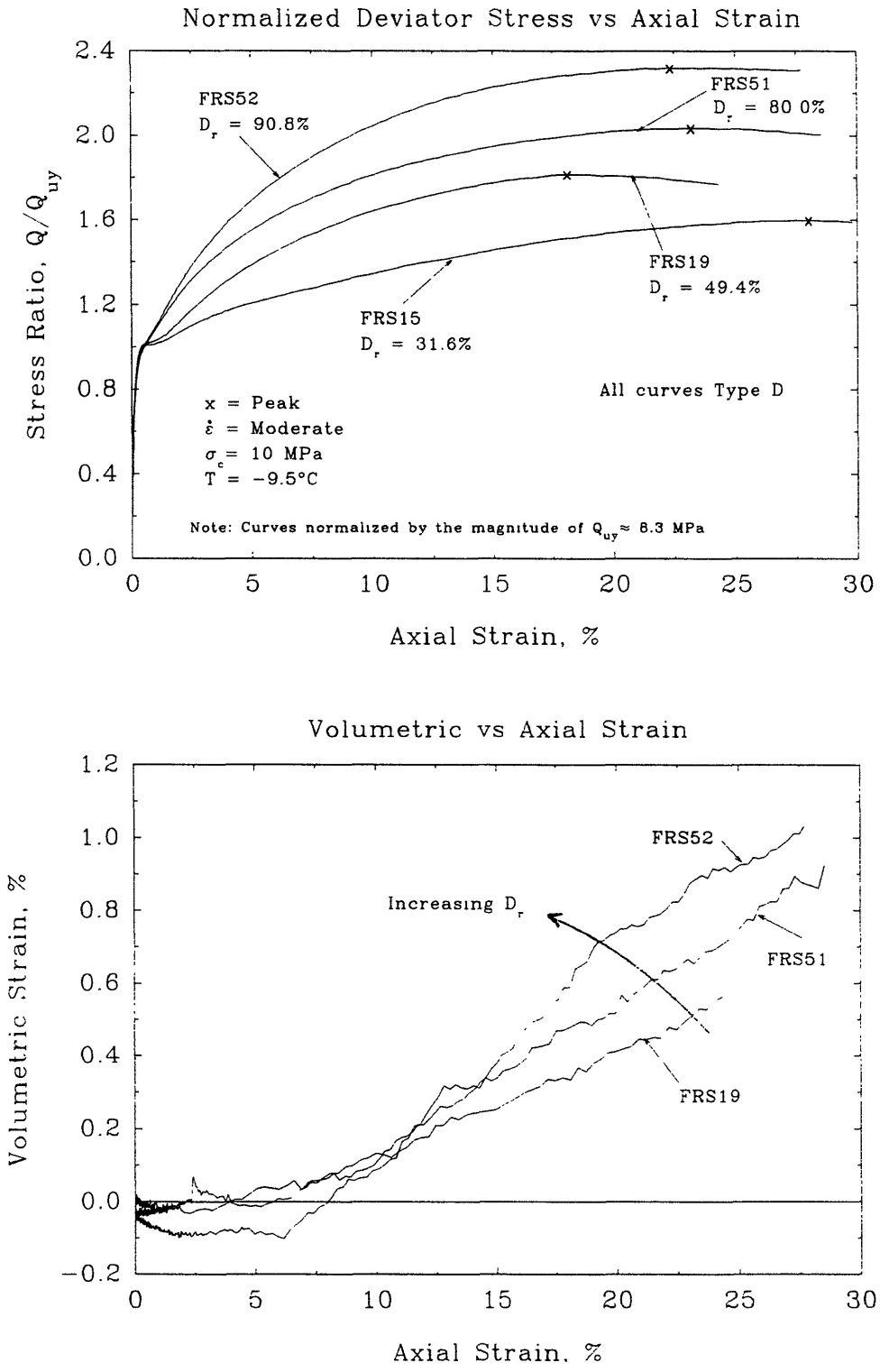

Figure 5.23 Normalized Stress–Strain Curves Showing the Effect of Relative Density for Conventional Frozen MFS Tests at Moderate Strain Rate, High Confinement and T = −10°C

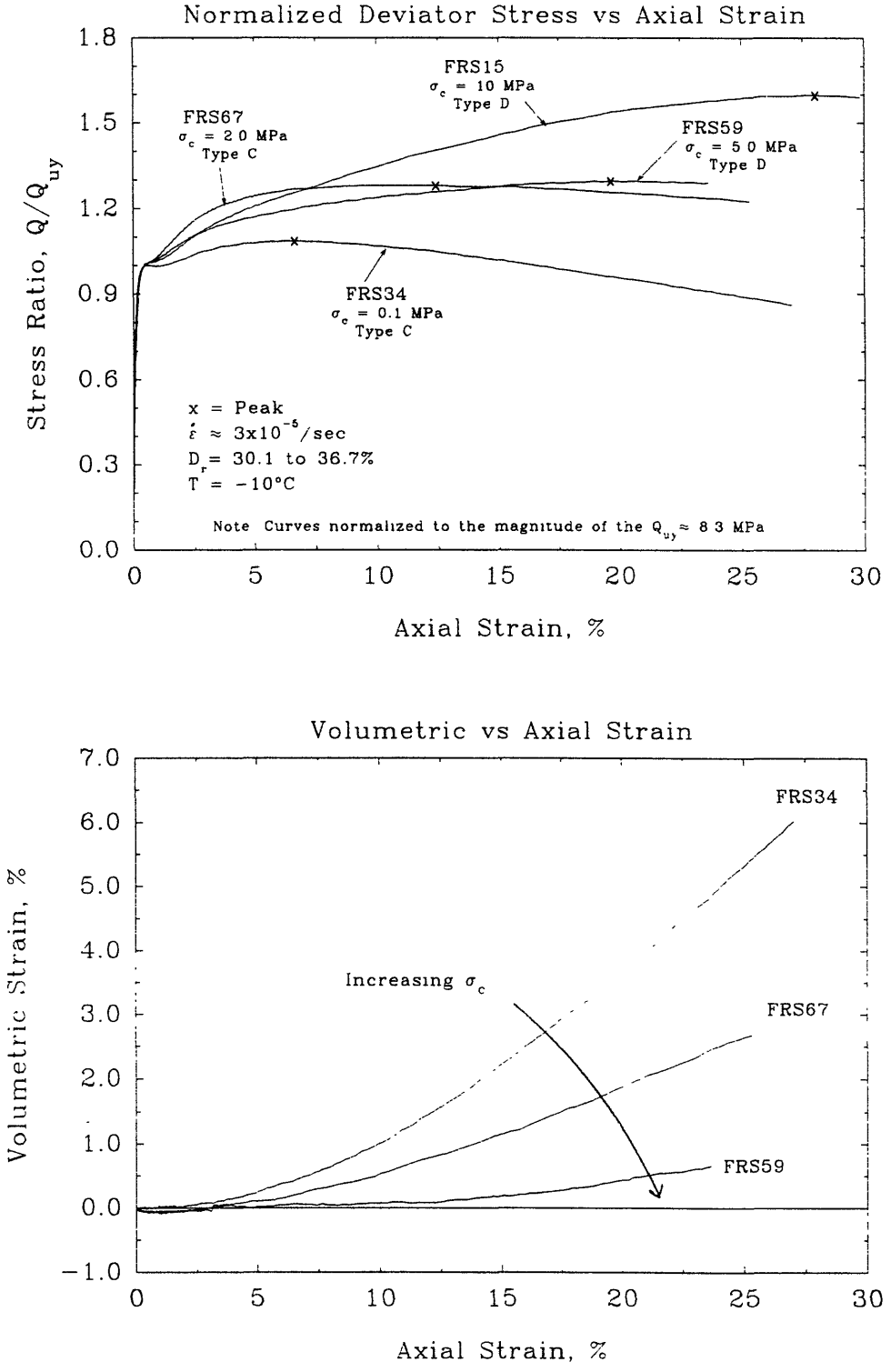

Figure 5.24a Normalized Stress–Strain Curves Showing the Effect of Confinement for Conventional Frozen MFS Tests on Loose Specimens at Moderate Strain Rate and T=−10°C

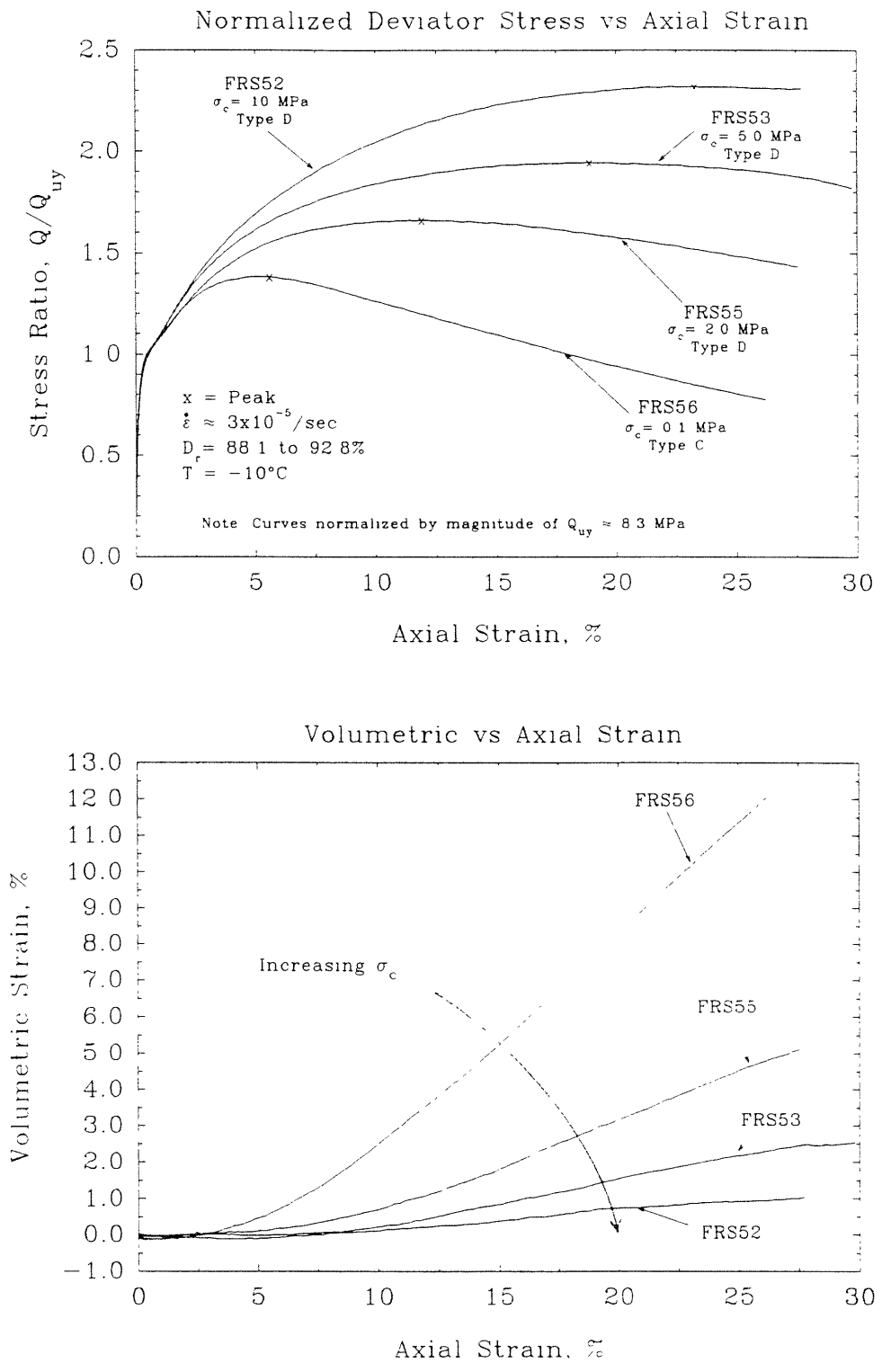

Figure 5.24b Normalized Stress–Strain Curves Showing the Effect of Confinement for Conventional Frozen MFS Tests on Dense Specimens at Moderate Strain Rate and T=−10°C

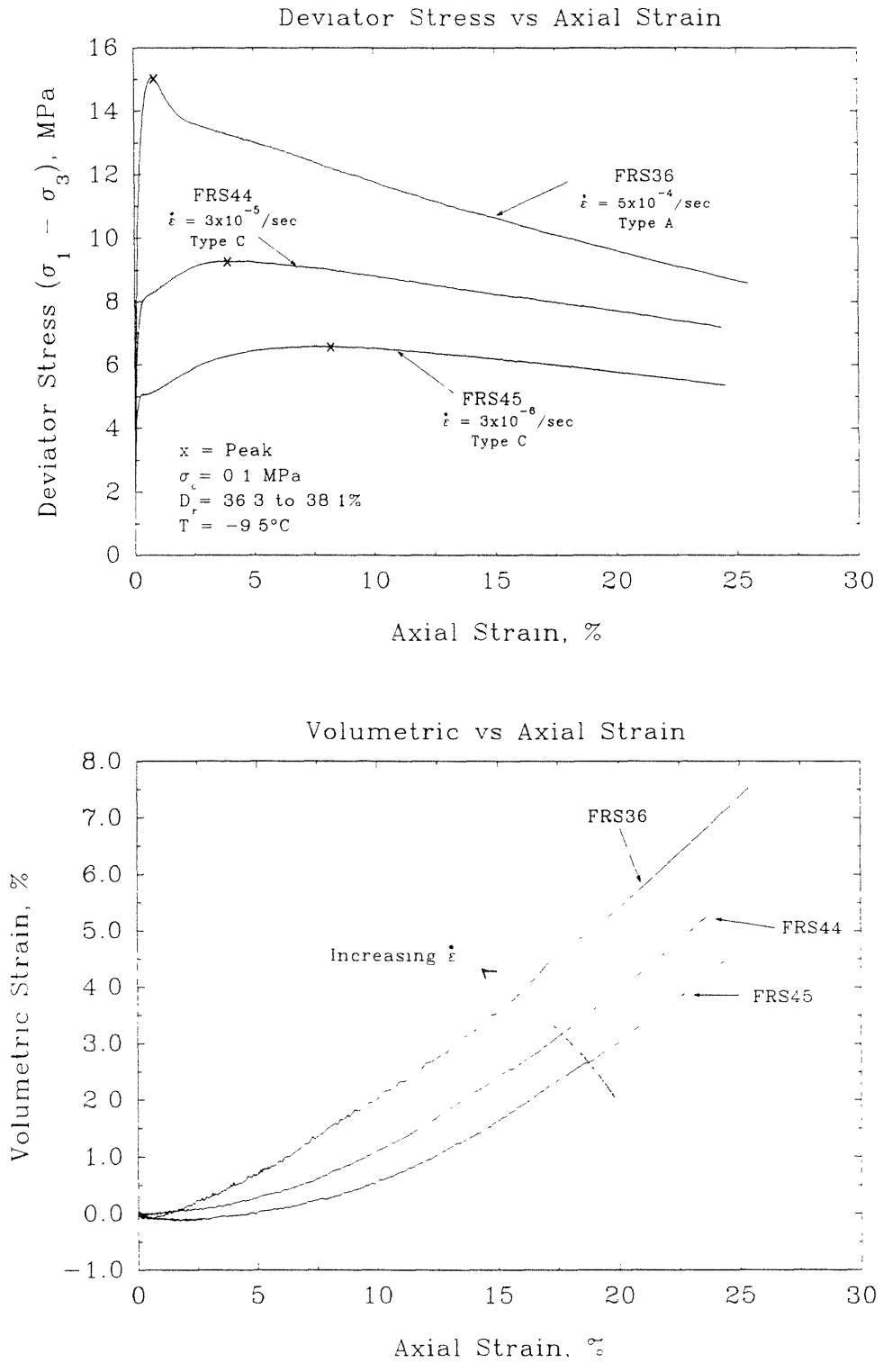

Figure 5.25a Stress–Strain Curves Showing the Effect of Strain Rate for Conventional Frozen MFS Tests on Loose Specimens at Low Confinement and T=−10°C

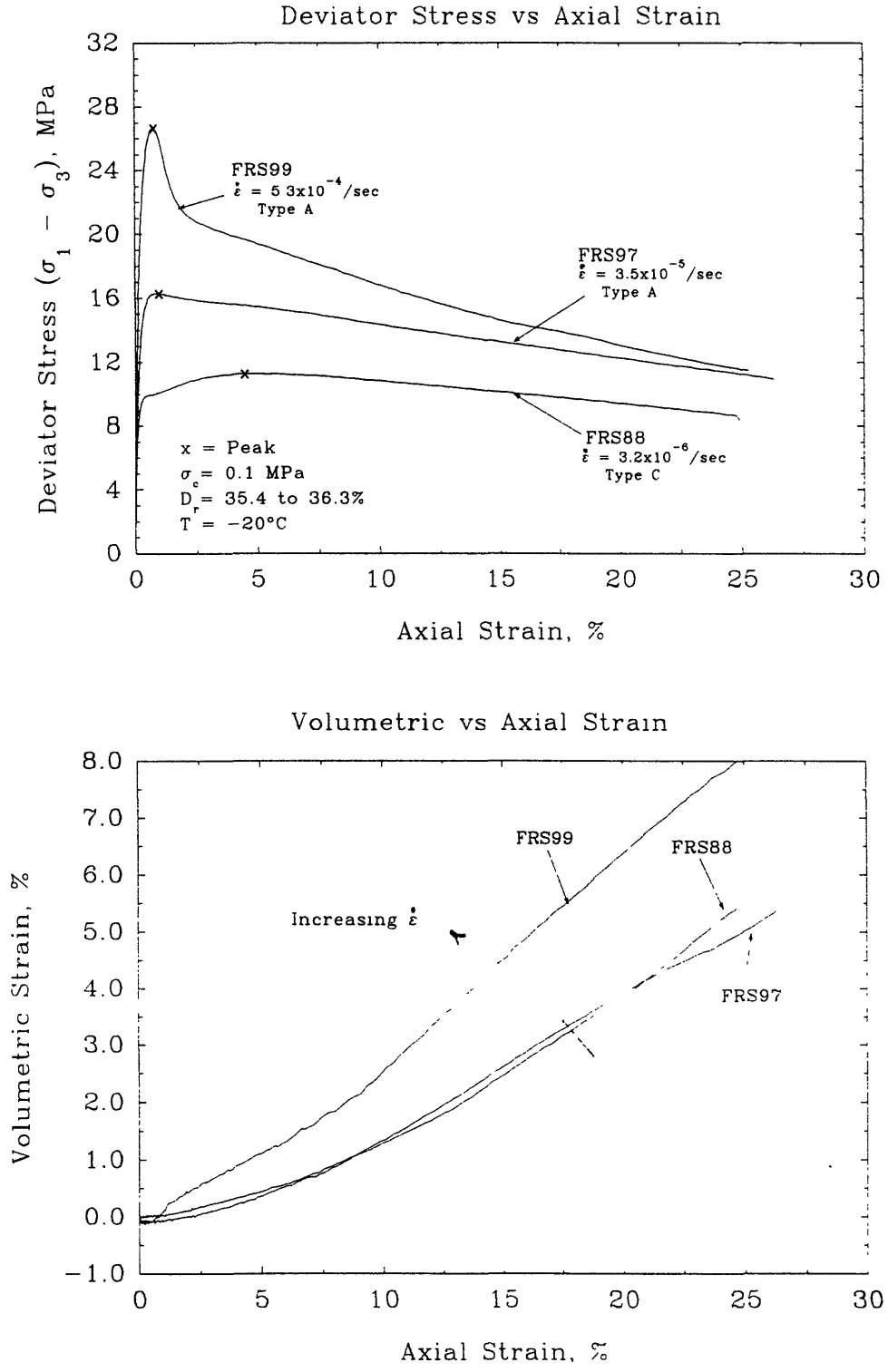

Figure 5.25b Stress–Strain Curves Showing the Effect of Strain Rate for Conventional Frozen MFS Tests on Loose Specimens at Low Confinement and T=−20°C

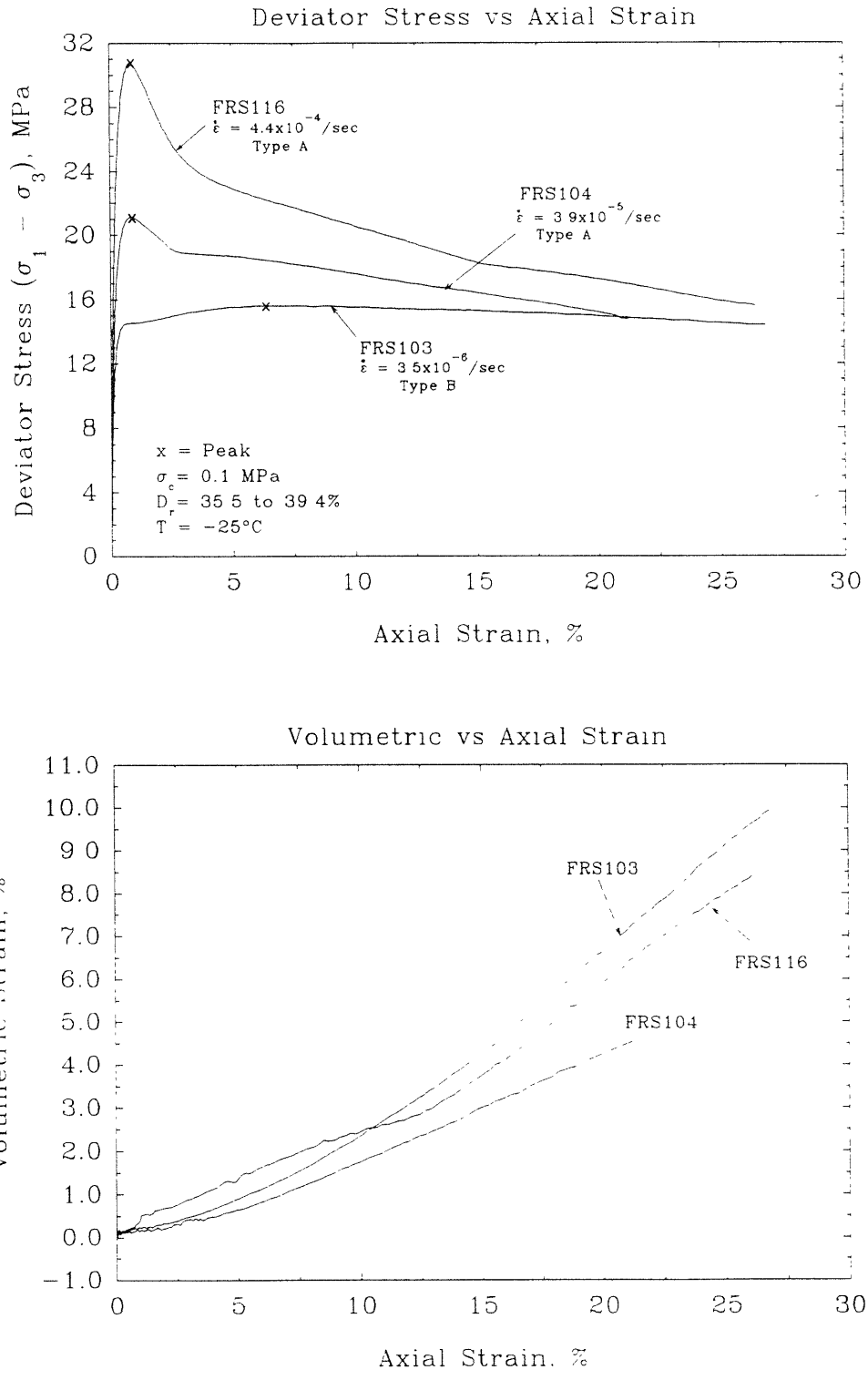

Figure 5.25c Stress–Strain Curves Showing the Effect of Strain Rate for Conventional Frozen MFS Tests on Loose Specimens at Low Confinement and T=–25°C

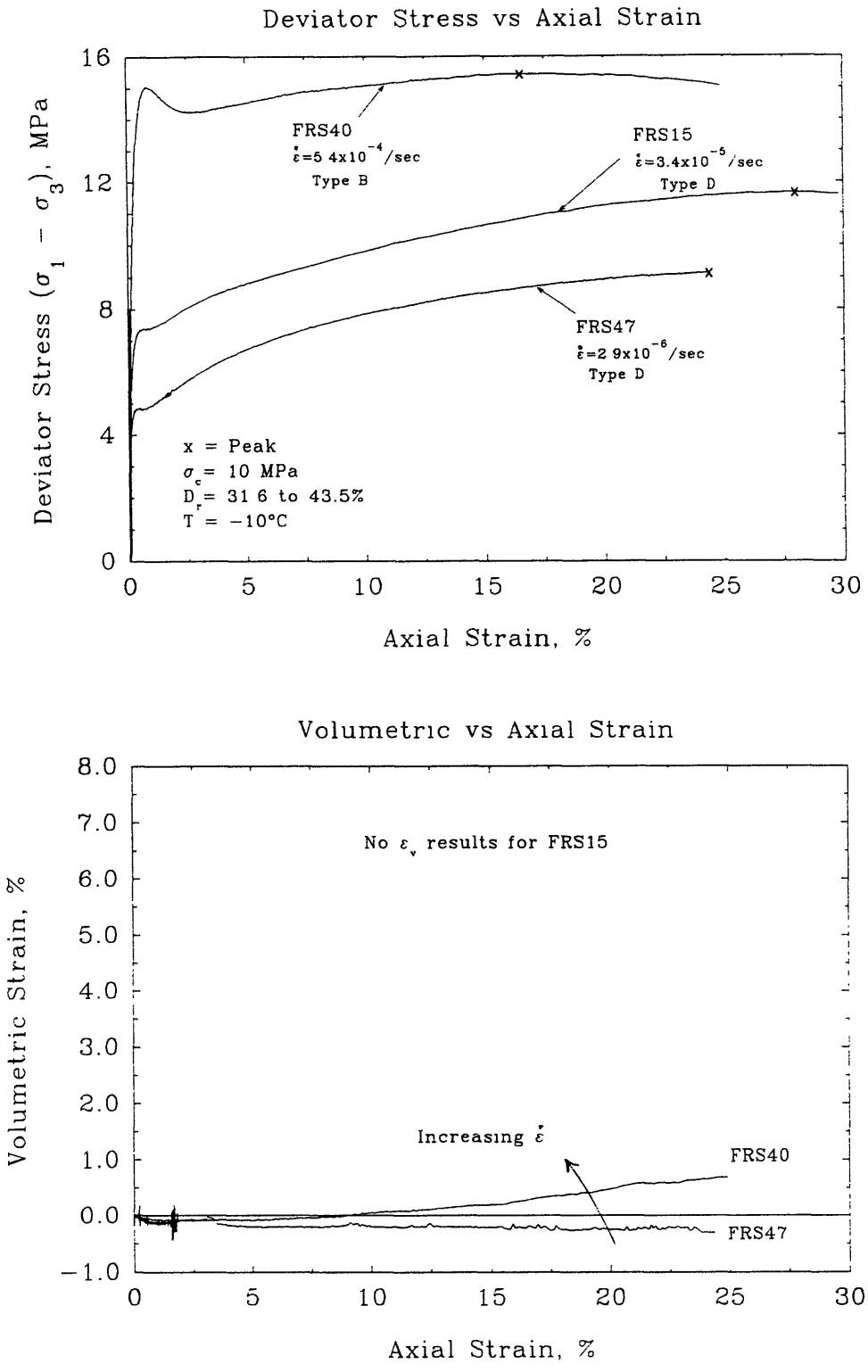

Figure 5.26a Stress–Strain Curves Showing the Effect of Strain Rate for Conventional Frozen MFS Tests on Loose Specimens at High Confinement and T=−10°C

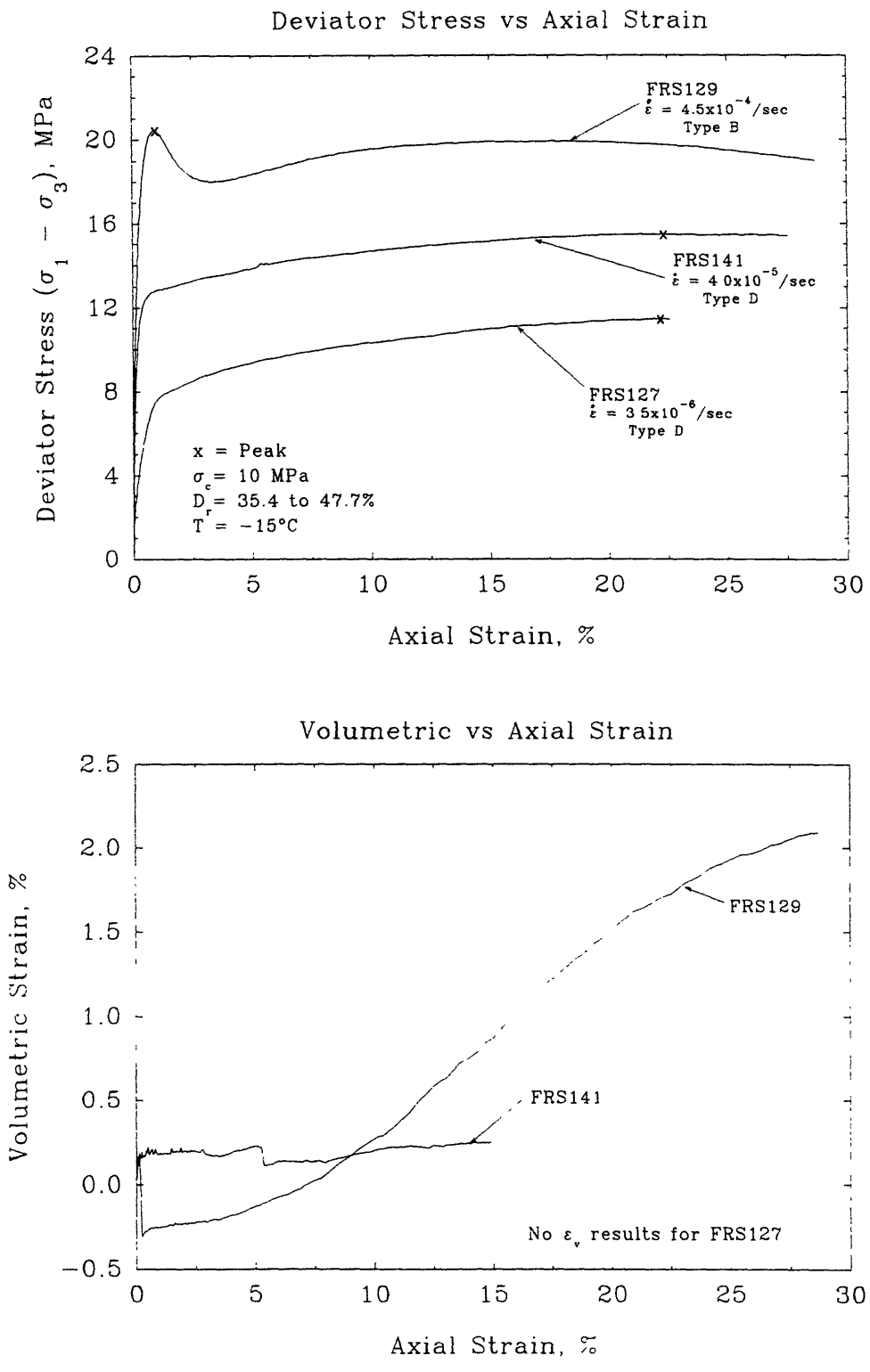

Figure 5.26b Stress–Strain Curves Showing the Effect of Strain Rate on Conventional Frozen MFS Tests on Loose Specimens at High Confinement and T=−15°C

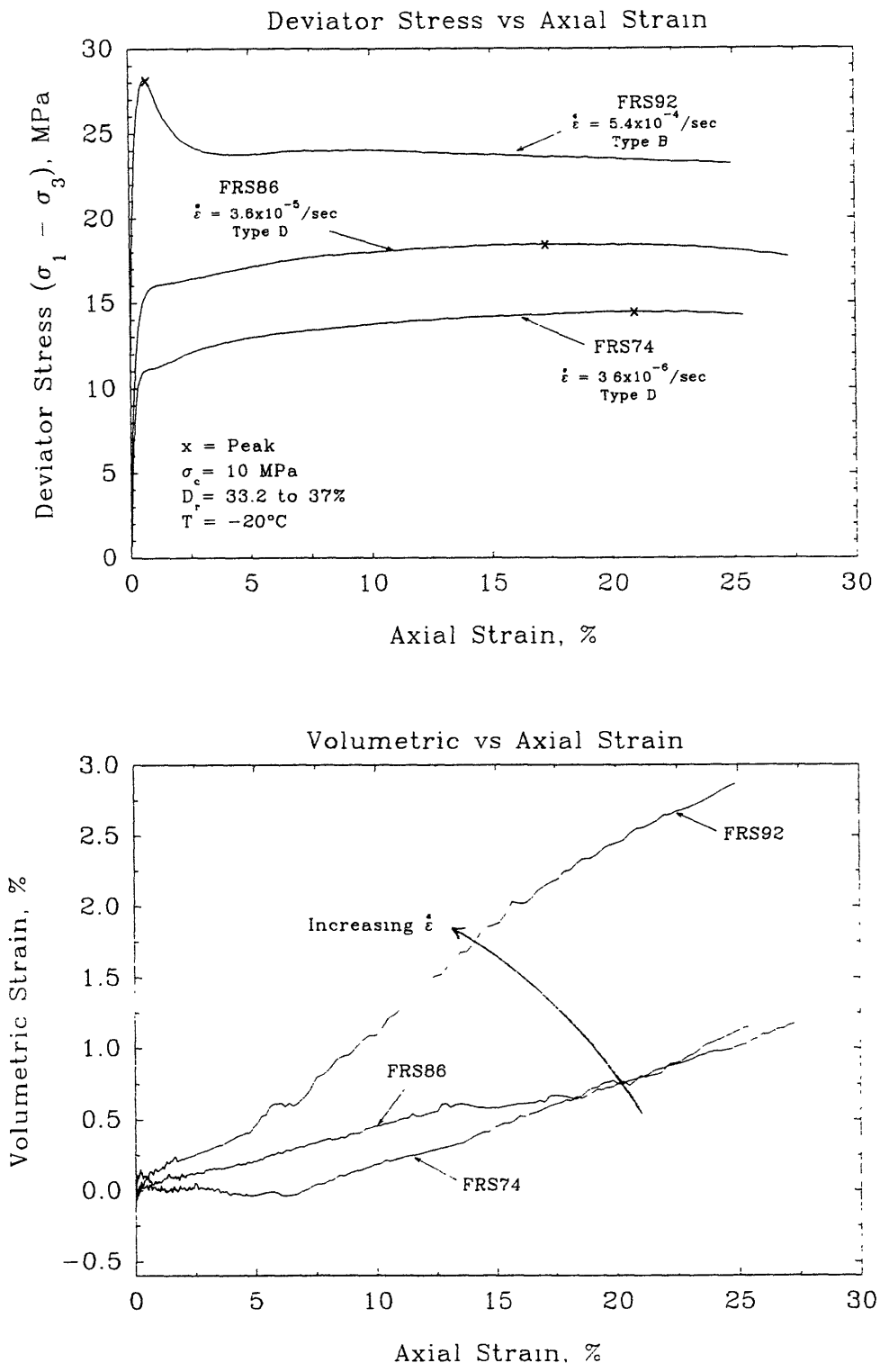

Figure 5.26c Stress–Strain Curves Showing the Effect of Strain Rate for Conventional Frozen MFS Tests on Loose Specimens at High Confinement and T=−20°C

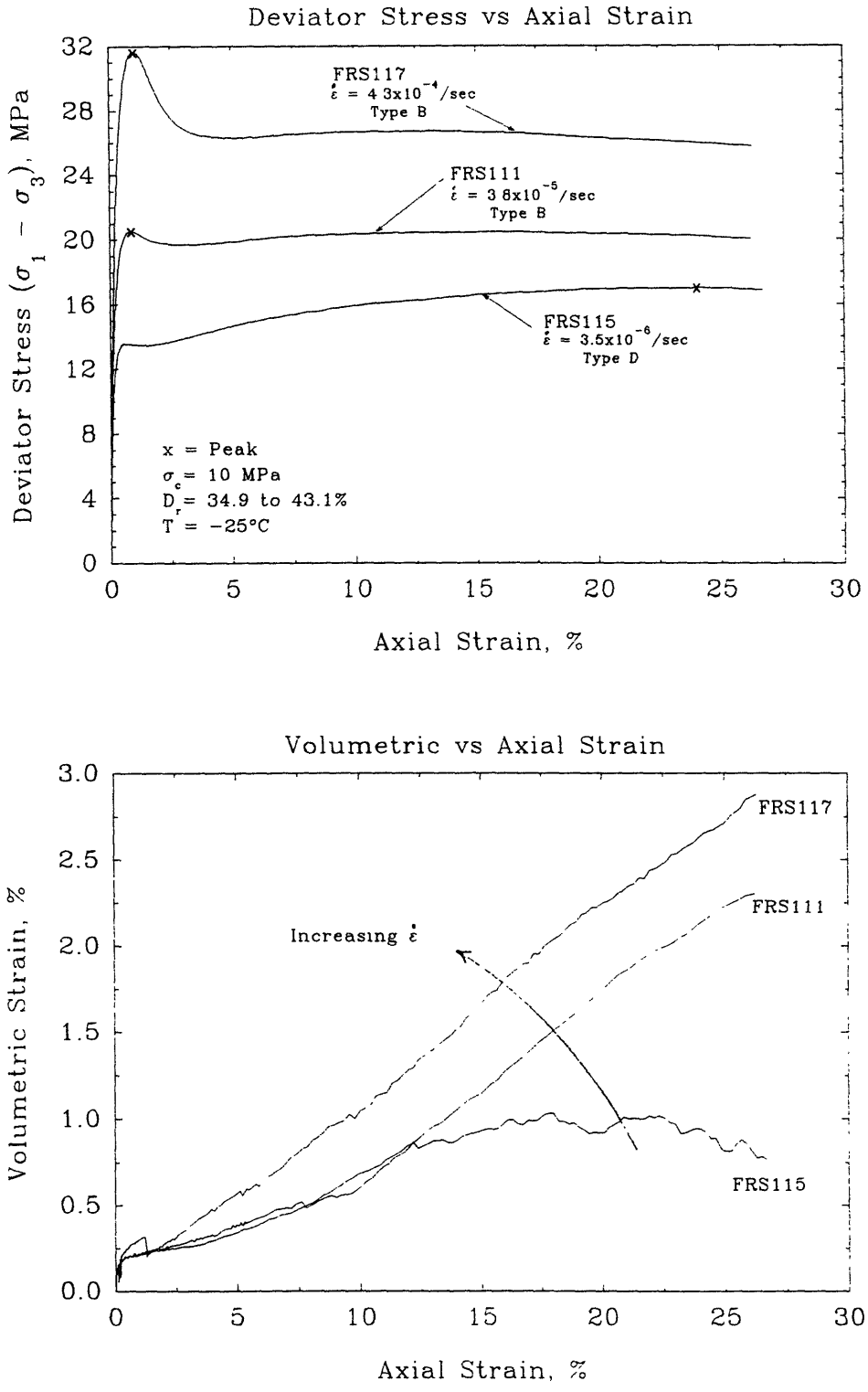

Figure 5.26d Stress–Strain Curves Showing the Effect of Strain Rate for Conventional Frozen MFS Tests on Loose Specimens at High Confinement and T=−25°C

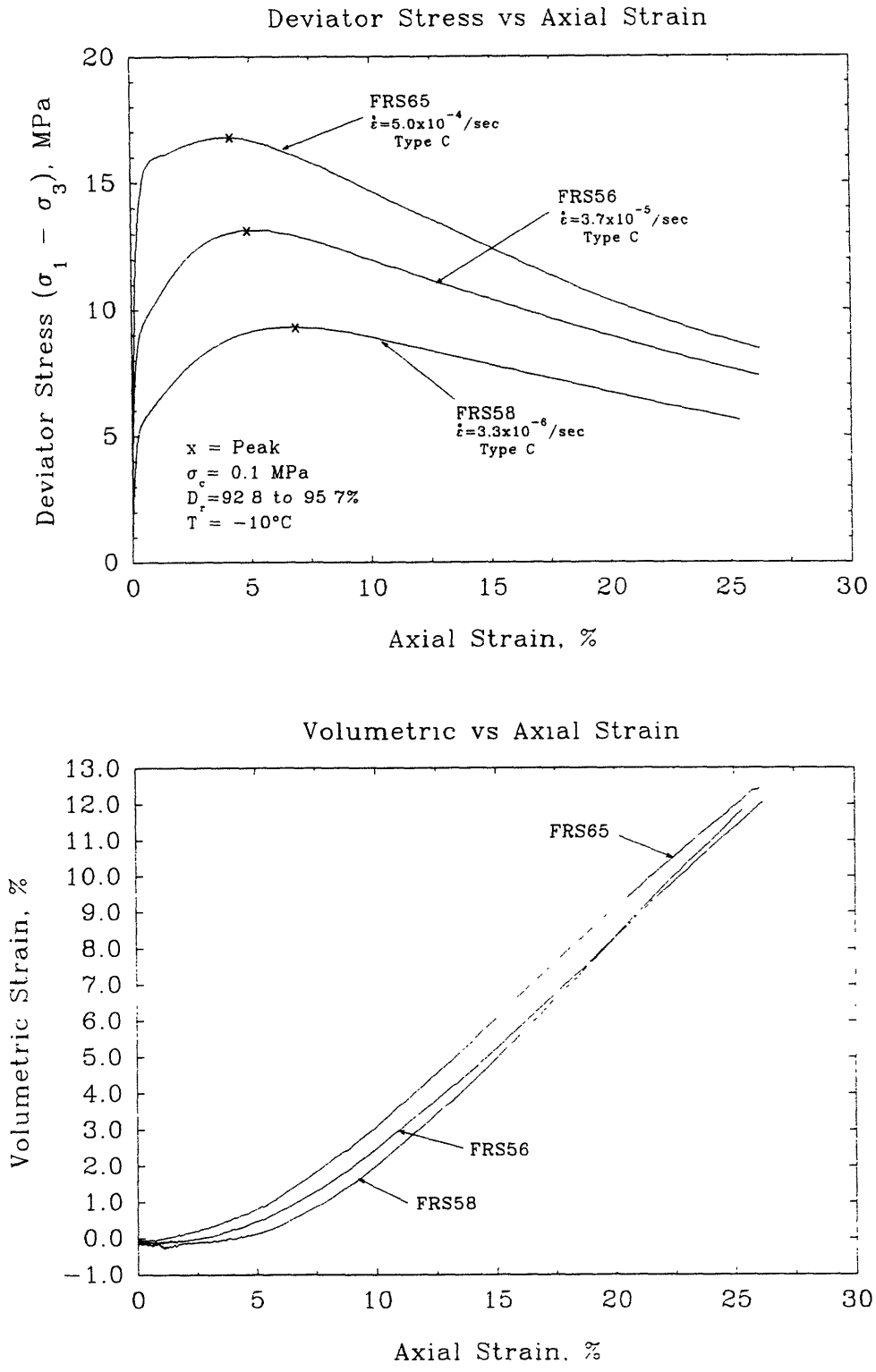

Figure 5.27a Stress–Strain Curves Showing the Effect of Strain Rate for Conventional Frozen MFS Tests on Dense Specimens at Low Confinement and T=−10°C

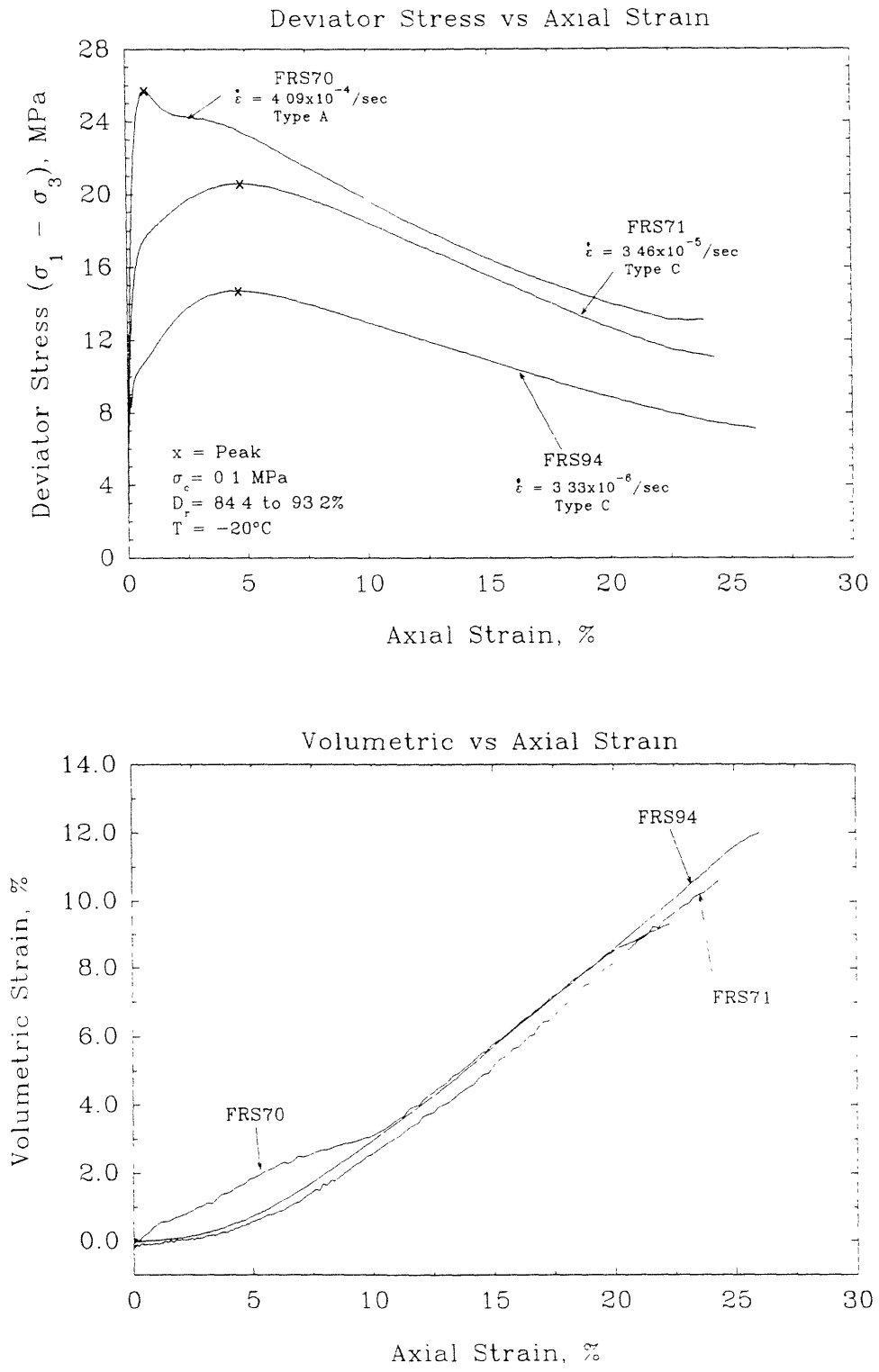

Figure 5.27b Stress-Strain Curves Showing the Effect of Strain Rate for Conventional Frozen MFS Tests on Dense Specimens at Low Confinement and T=-20°C

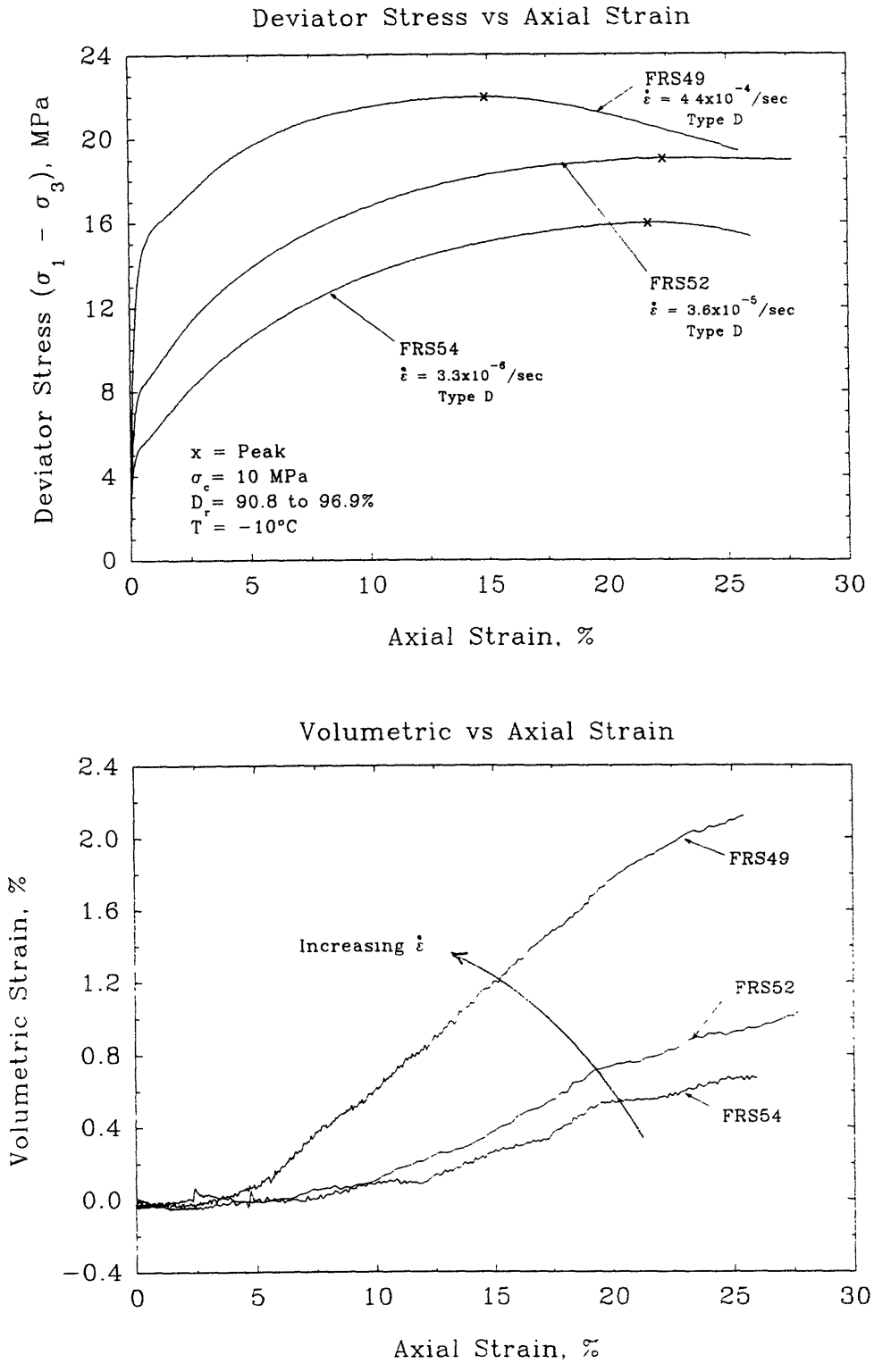

Figure 5.28a Stress–Strain Curves Showing the Effect of Strain Rate on Conventional Frozen MFS Tests on Dense Specimens at High Confinement and T=−10°C

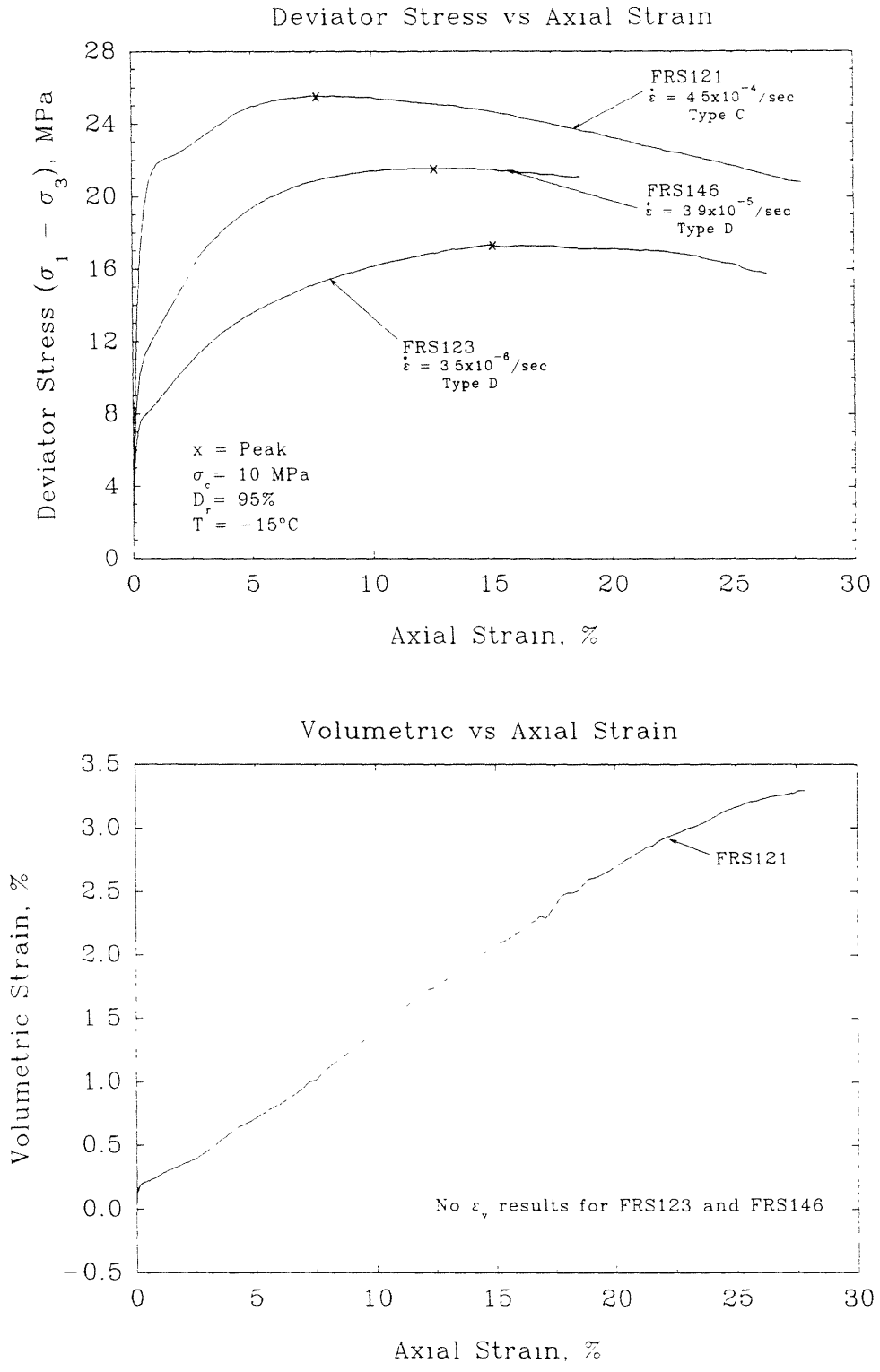

Figure 5.28b Stress–Strain Curves Showing the Effect of Strain Rate on Conventional Frozen MFS Tests on Dense Specimens at High Confinement and T=-15°C

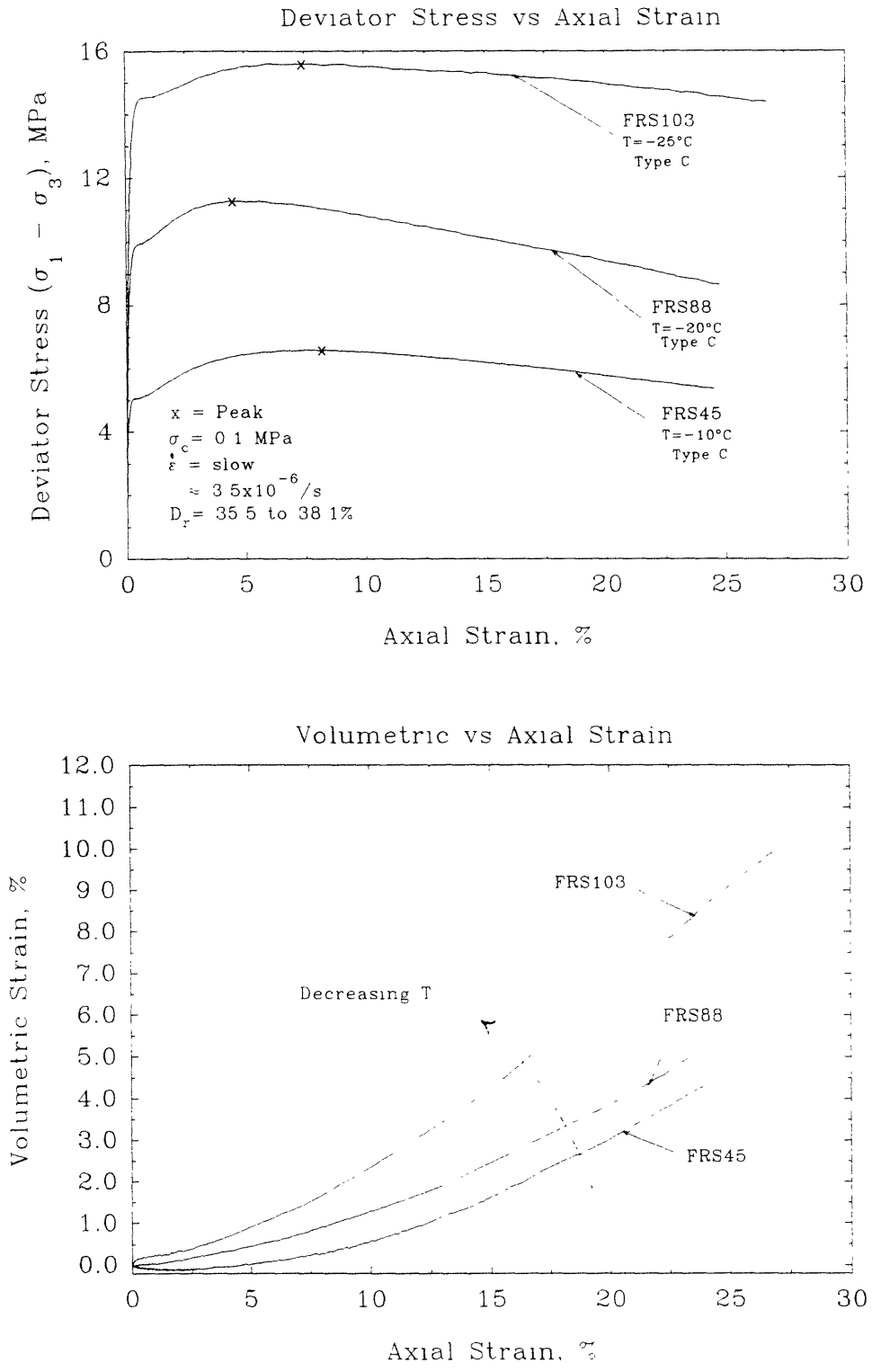

Figure 5.29a Stress-Strain Curves Showing the Effect of Temperature on Conventional Frozen MFS Tests on Loose Specimens at Low Confinement and Slow Strain Rate

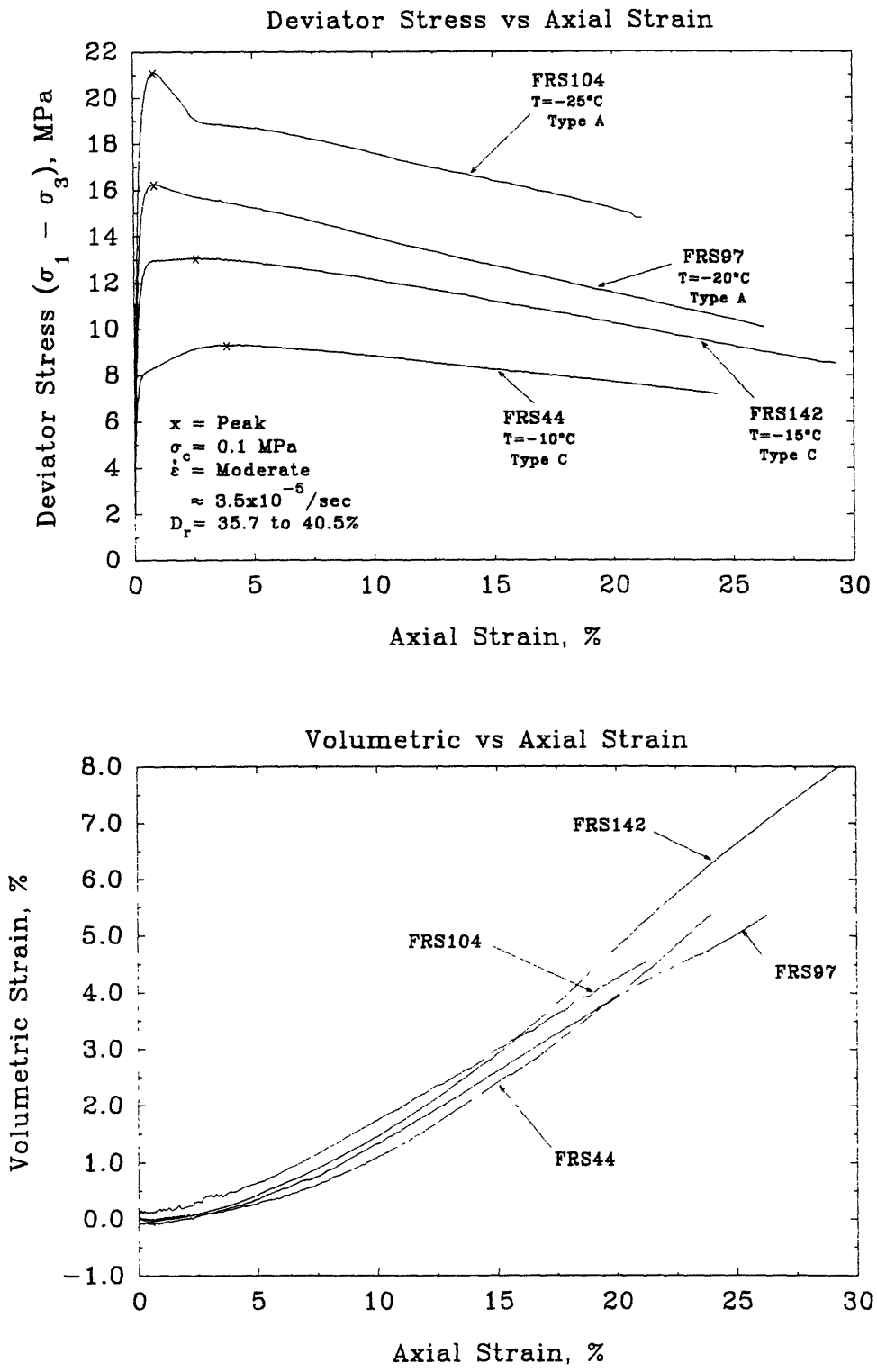

Figure 5.29b Stress–Strain Curves Showing the Effect of Temperature on Conventional Frozen MFS Tests on Loose Specimens at Low Confinement and Moderate Strain Rate

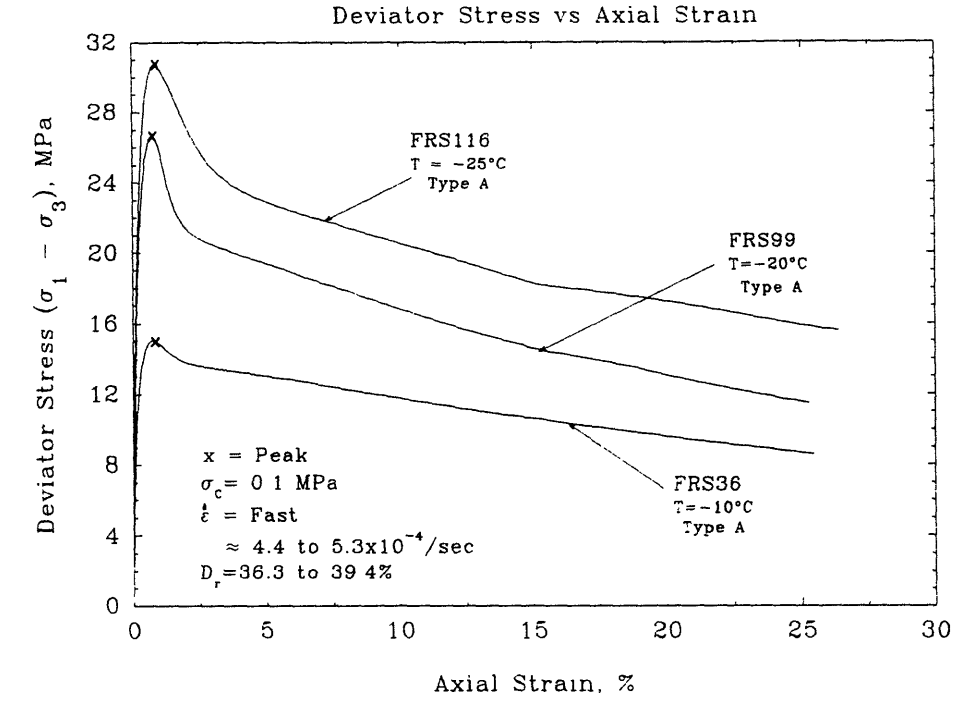

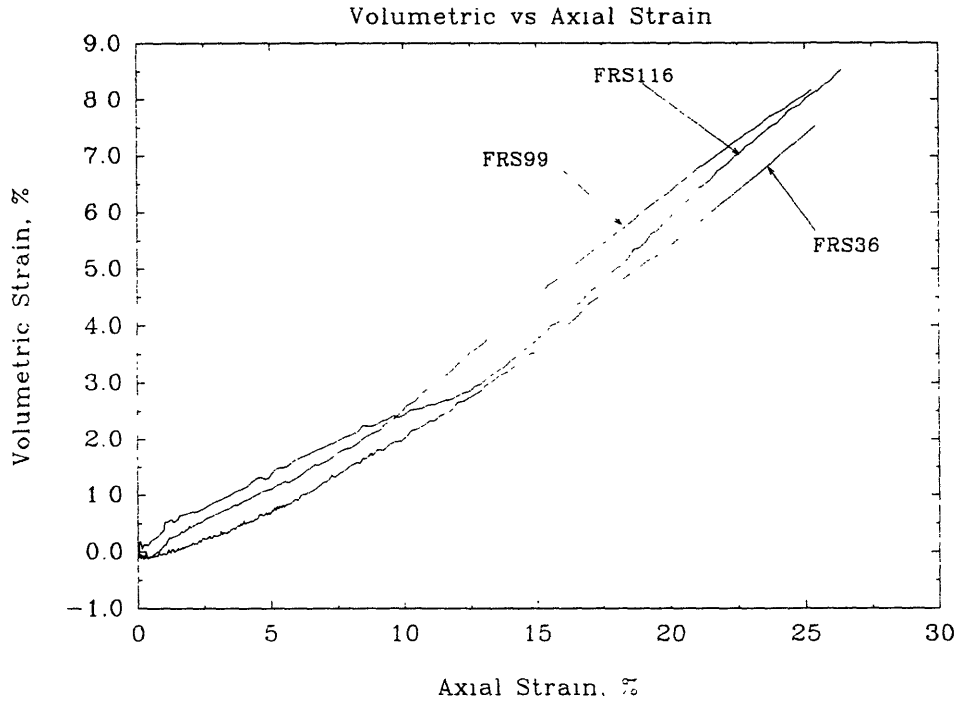

Figure 5.29c Stress–Strain Curves Showing the Effects of Temperature on Conventional Frozen MFS Tests on Loose Specimens at Low Confinement and Fast Strain Rate

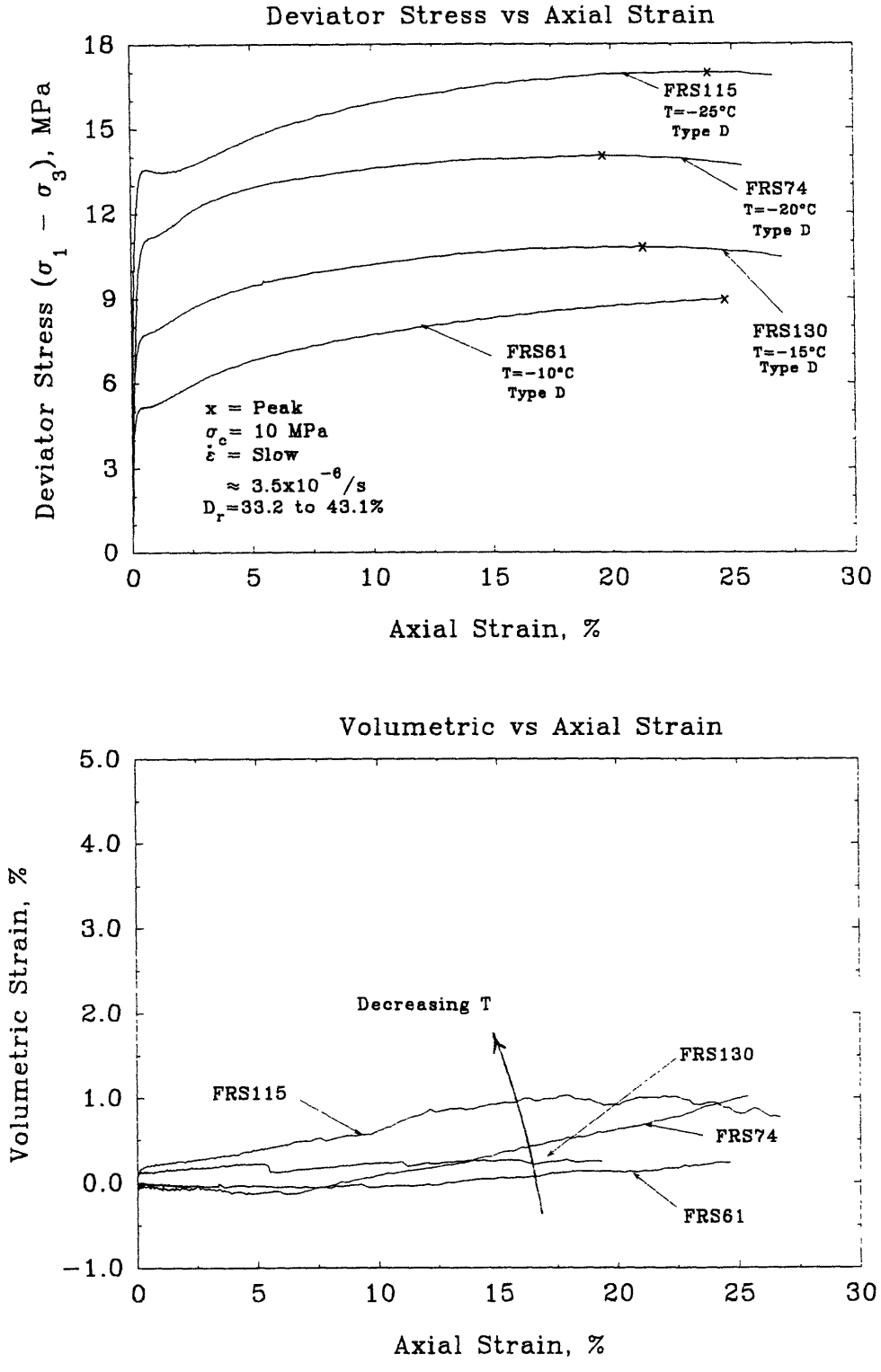

Figure 5.30a Stress–Strain Curves Showing the Effect of Temperature on Conventional Frozen MFS Tests on Loose Specimens at High Confinement and Slow Strain Rate

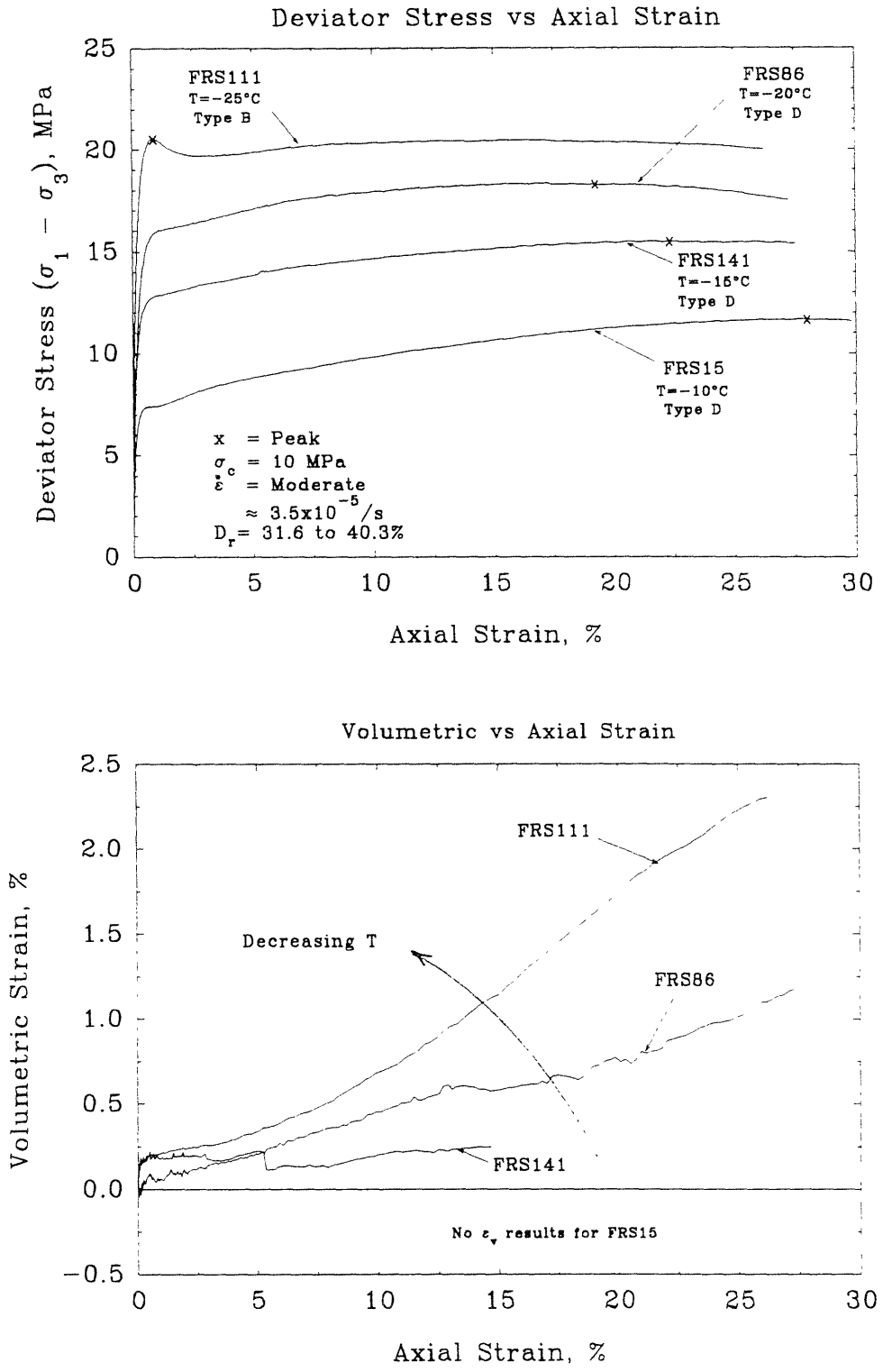

Figure 5.30b Stress–Strain Curves Showing the Effect of Temperature on Conventional Frozen MFS Tests on Loose Specimens at High Confinement and Moderate Strain Rate

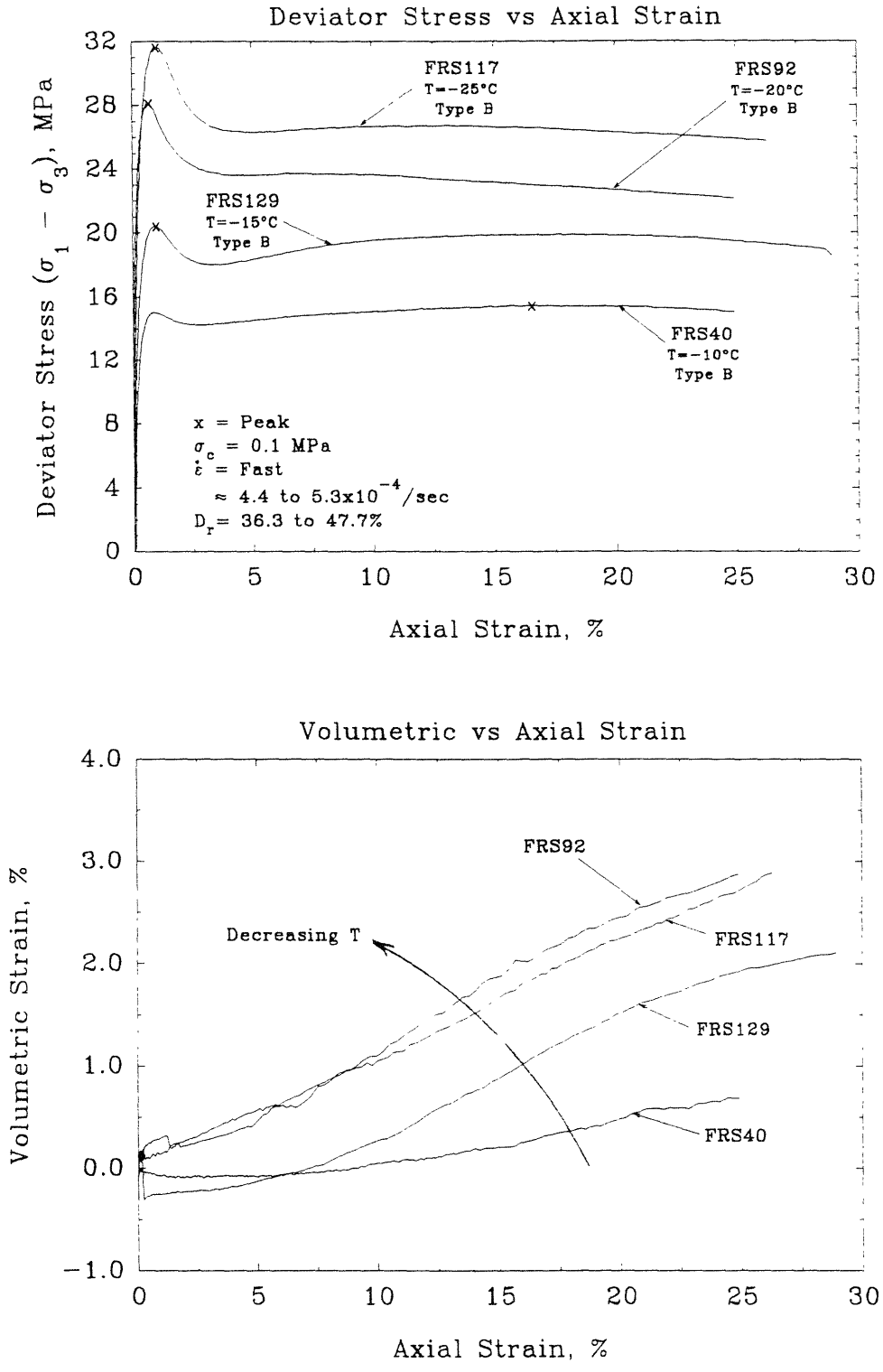

Figure 5.30c Stress–Strain Curves Showing the Effect of Temperature on Conventional Frozen MFS Tests on Loose Specimens at High Confinement and Fast Strain Rate

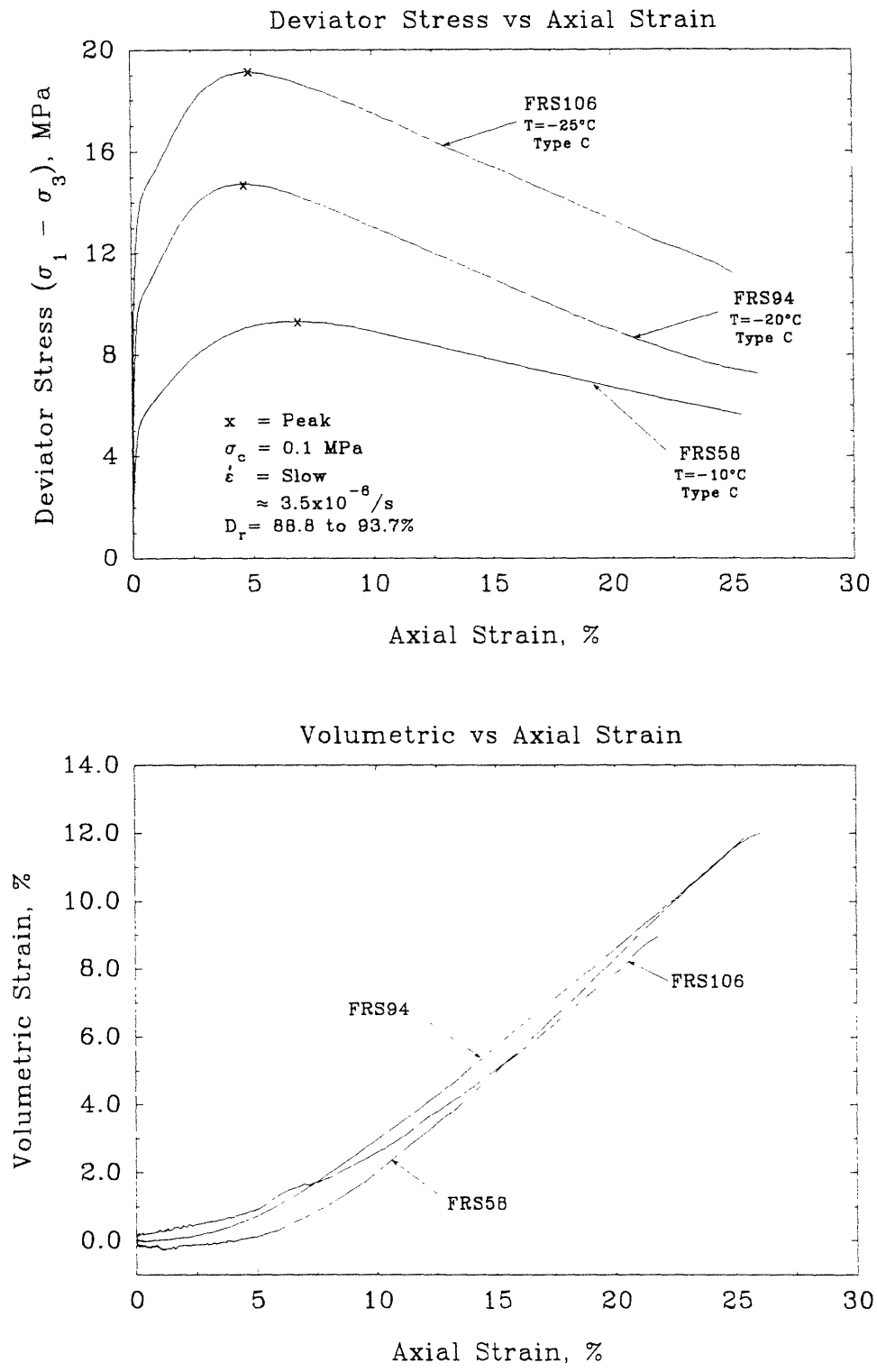

Figure 5.31a Stress–Strain Curves Showing the Effects of Temperature on Conventional Frozen MFS Tests on Dense Specimens at Low Confinement and Slow Strain Rate

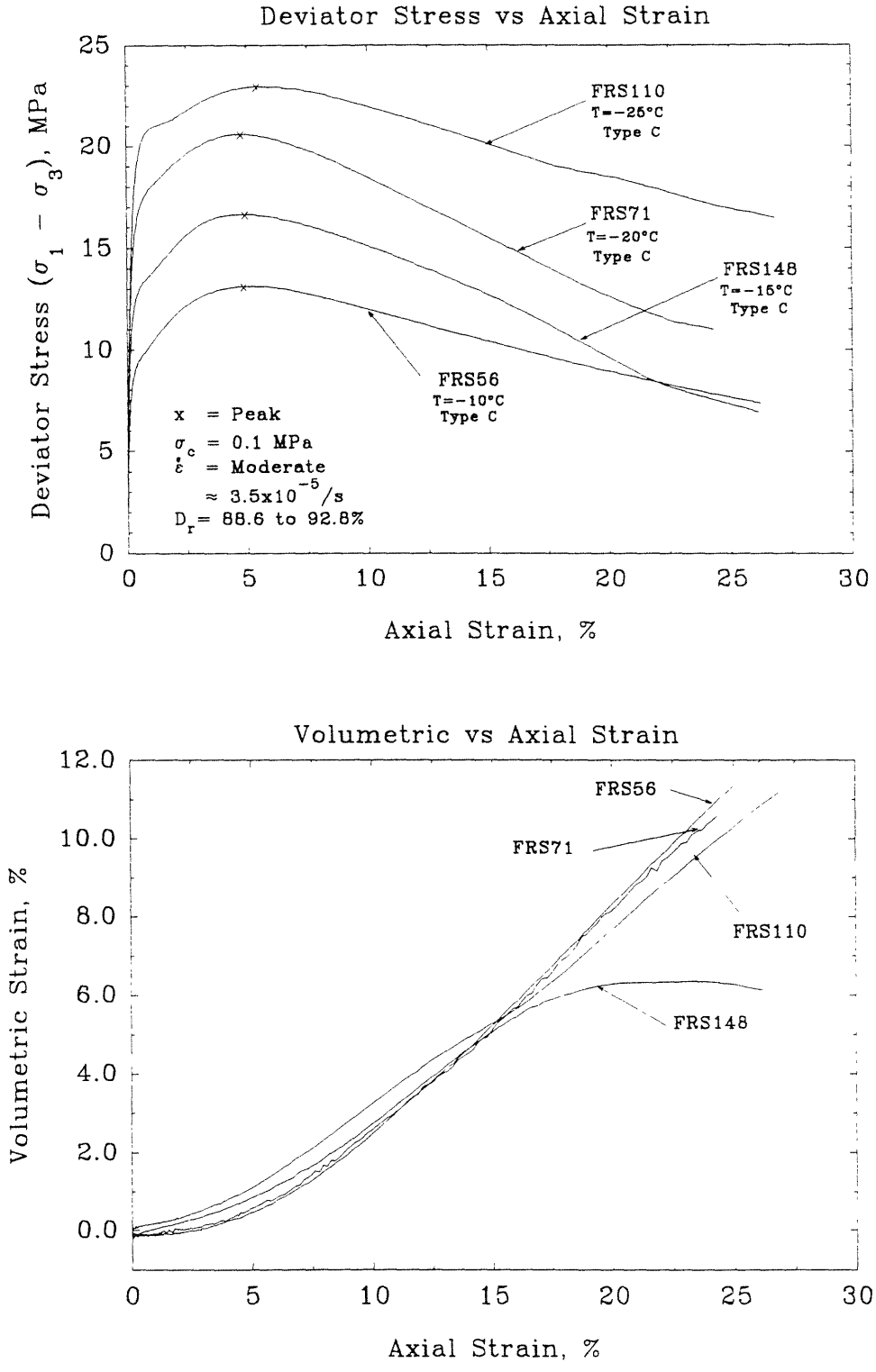

Figure 5.31b Stress–Strain Curves Showing the Effect of Temperature on Conventional Frozen MFS Tests on Dense Specimens at Low Confinement and Moderate Strain Rate

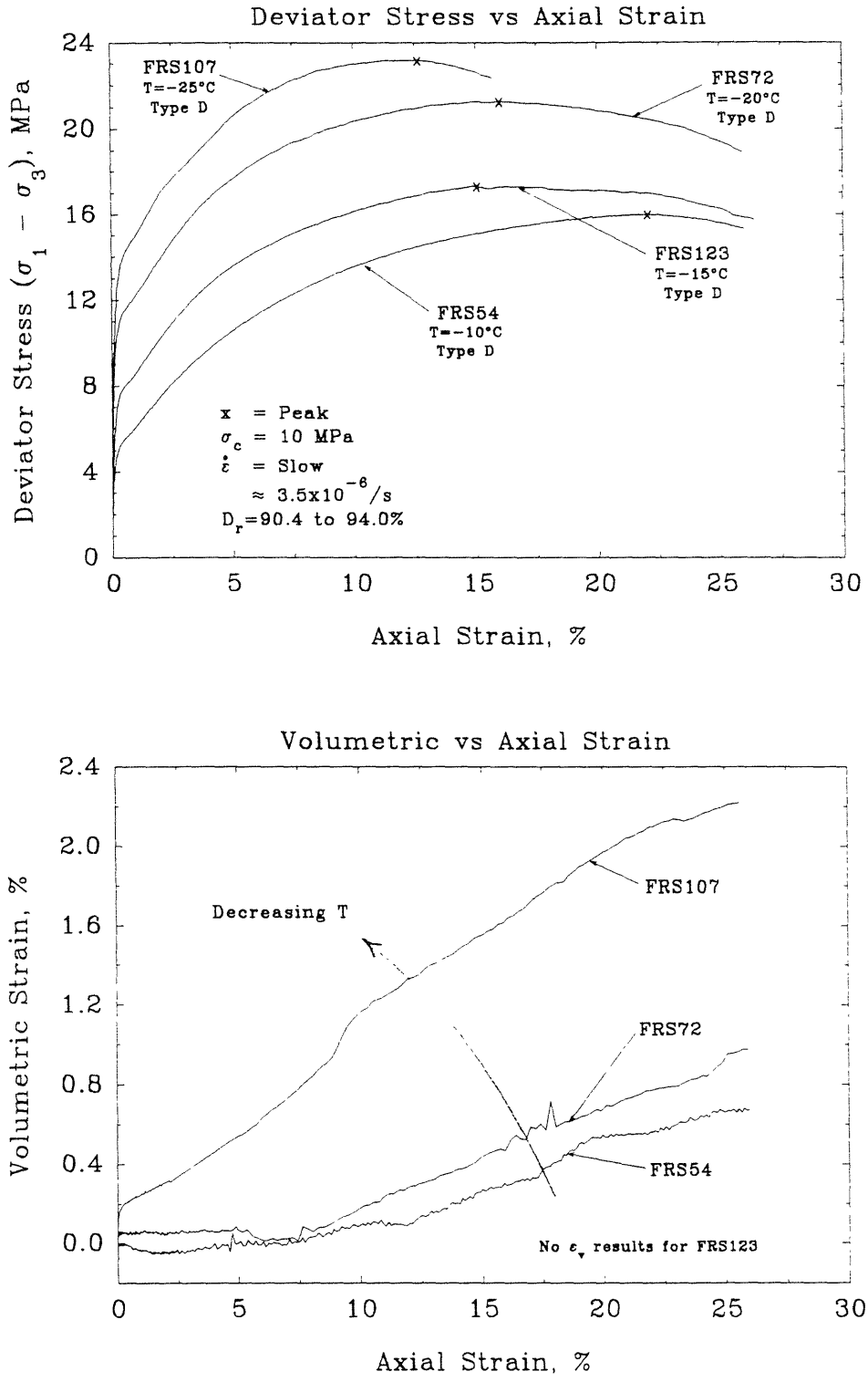

Figure 5.32 Stress–Strain Curves Showing the Effect of Temperature on Conventional Frozen MFS Tests on Dense Specimens at High Confinement and Slow Strain Rate

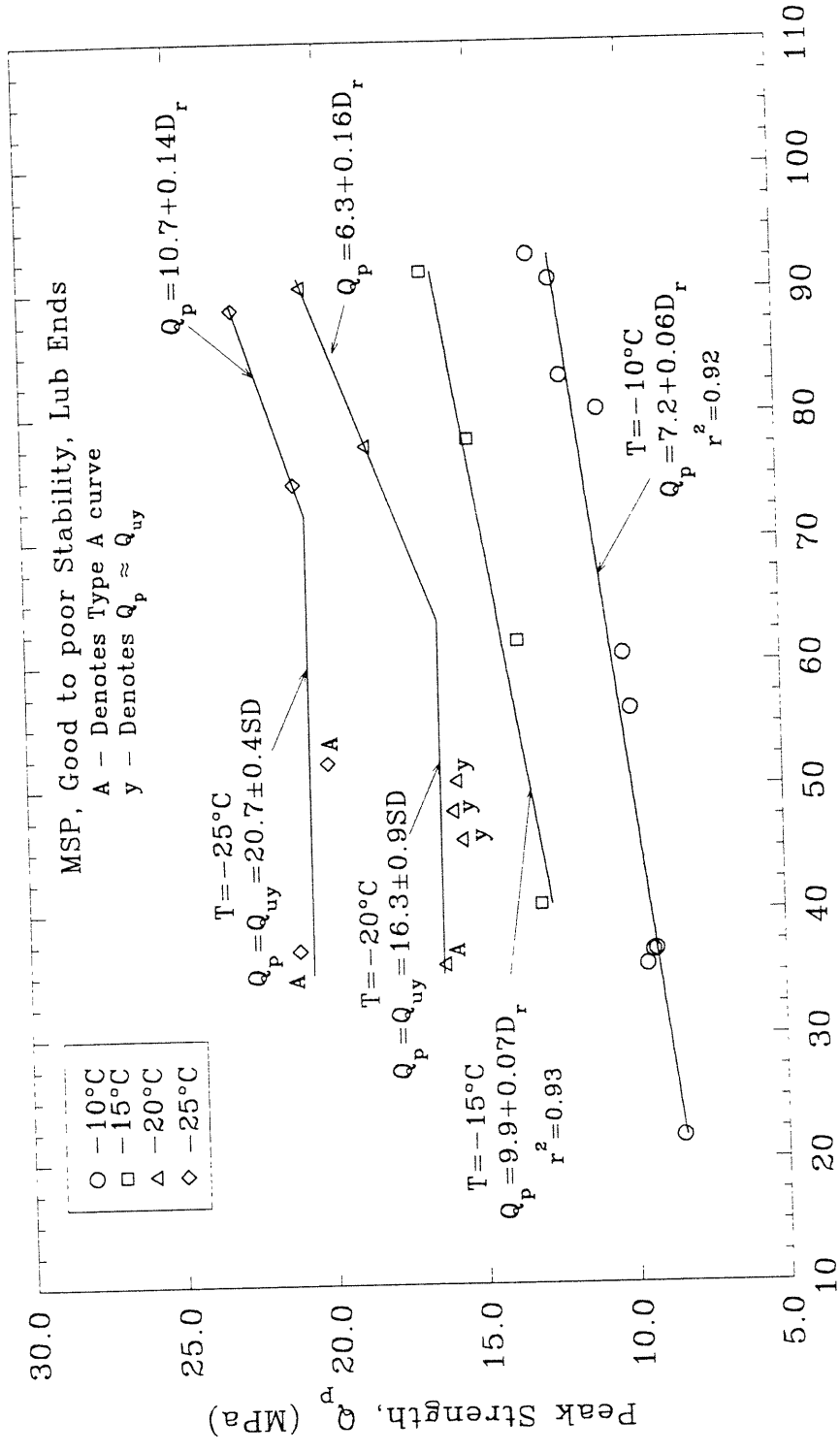

Figure 5.33 Peak Strength versus Relative Density for Conventional Frozen MFS Tests at Moderate Strain Rate, Low Confinement and Different Temperatures

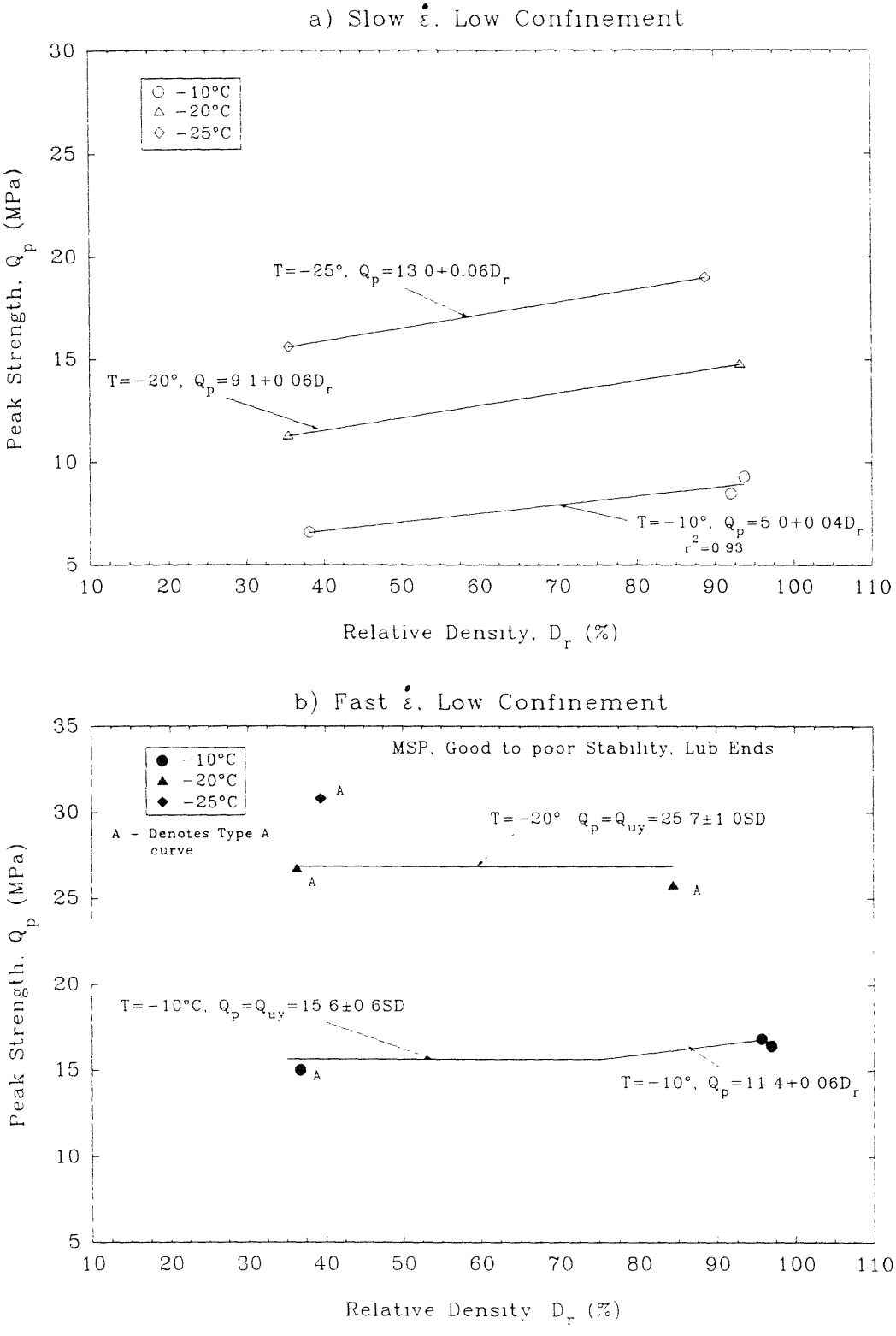

Figure 5.34 Peak Strength versus Relative Density for Conventional Frozen MFS Tests at Slow and Fast Strain Rates, Low Confinement and Different Temperatures

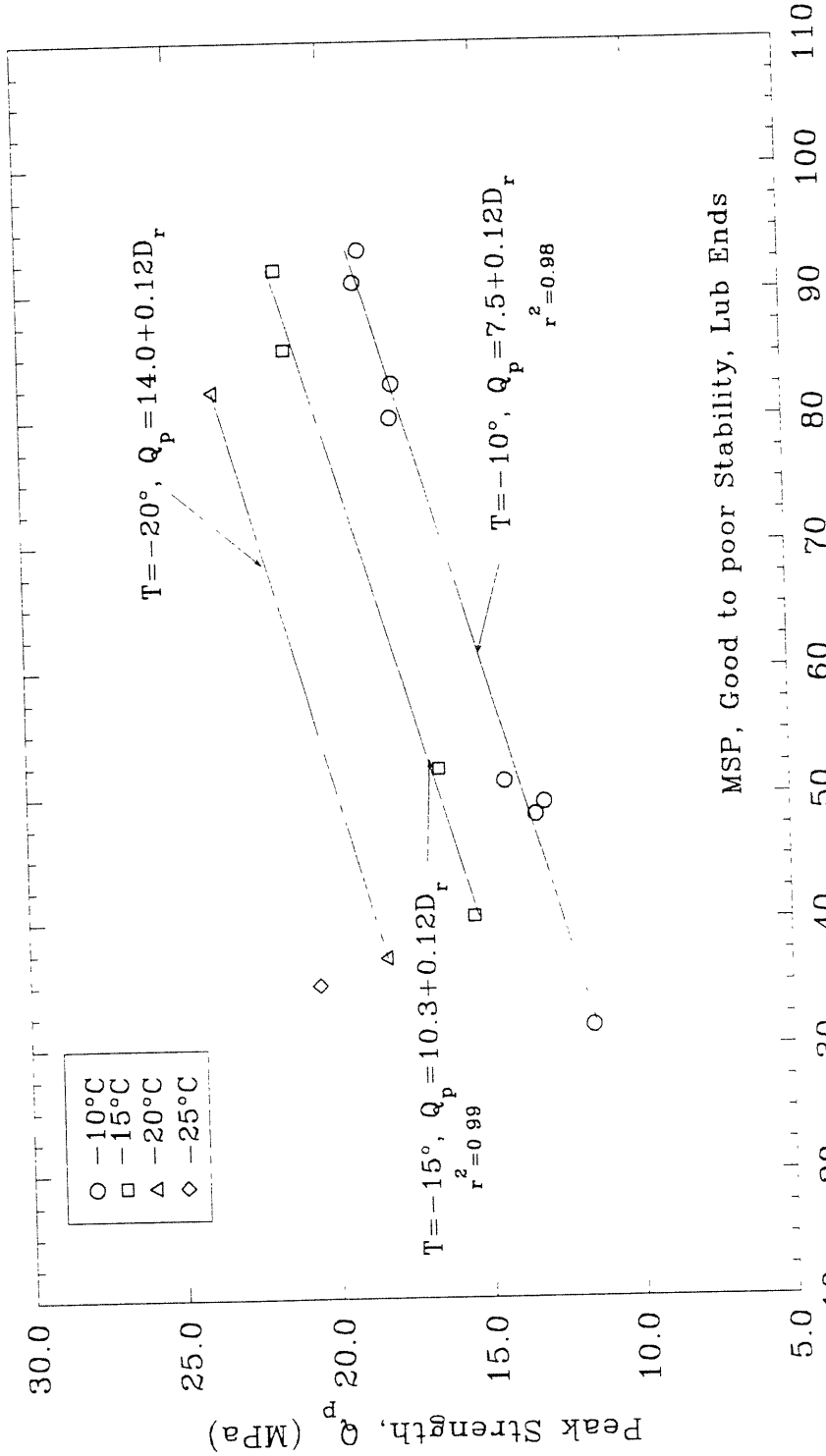

Figure 5.35 Peak Strength versus Relative Density for Conventional Frozen MFS Tests at Moderate Strain Rate, High Confinement and Different Temperatures

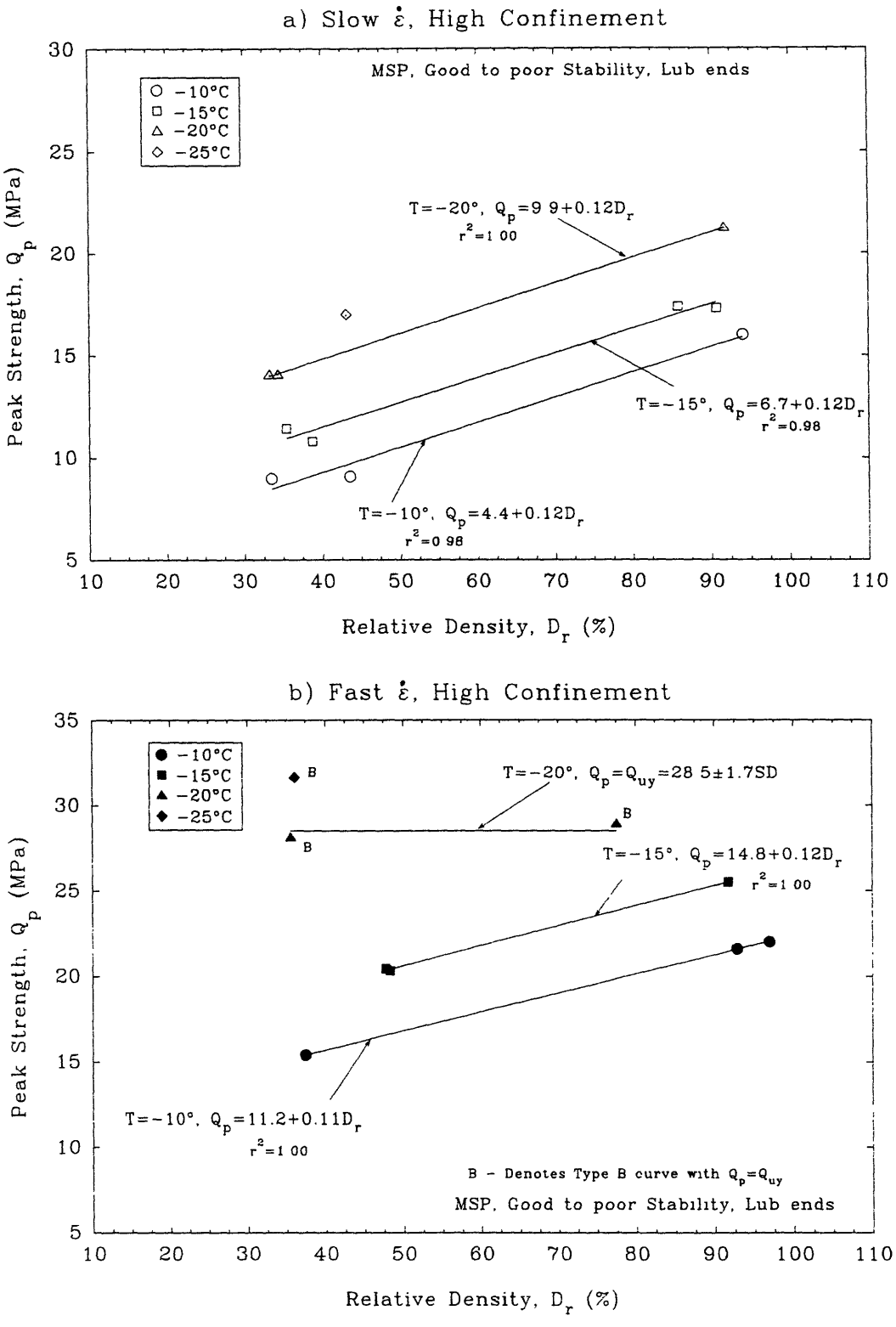

Figure 5.36 Peak Strength versus Relative Density for Conventional Frozen MFS Tests at Slow and Fast Strain Rates, High Confinement and Different Temperatures

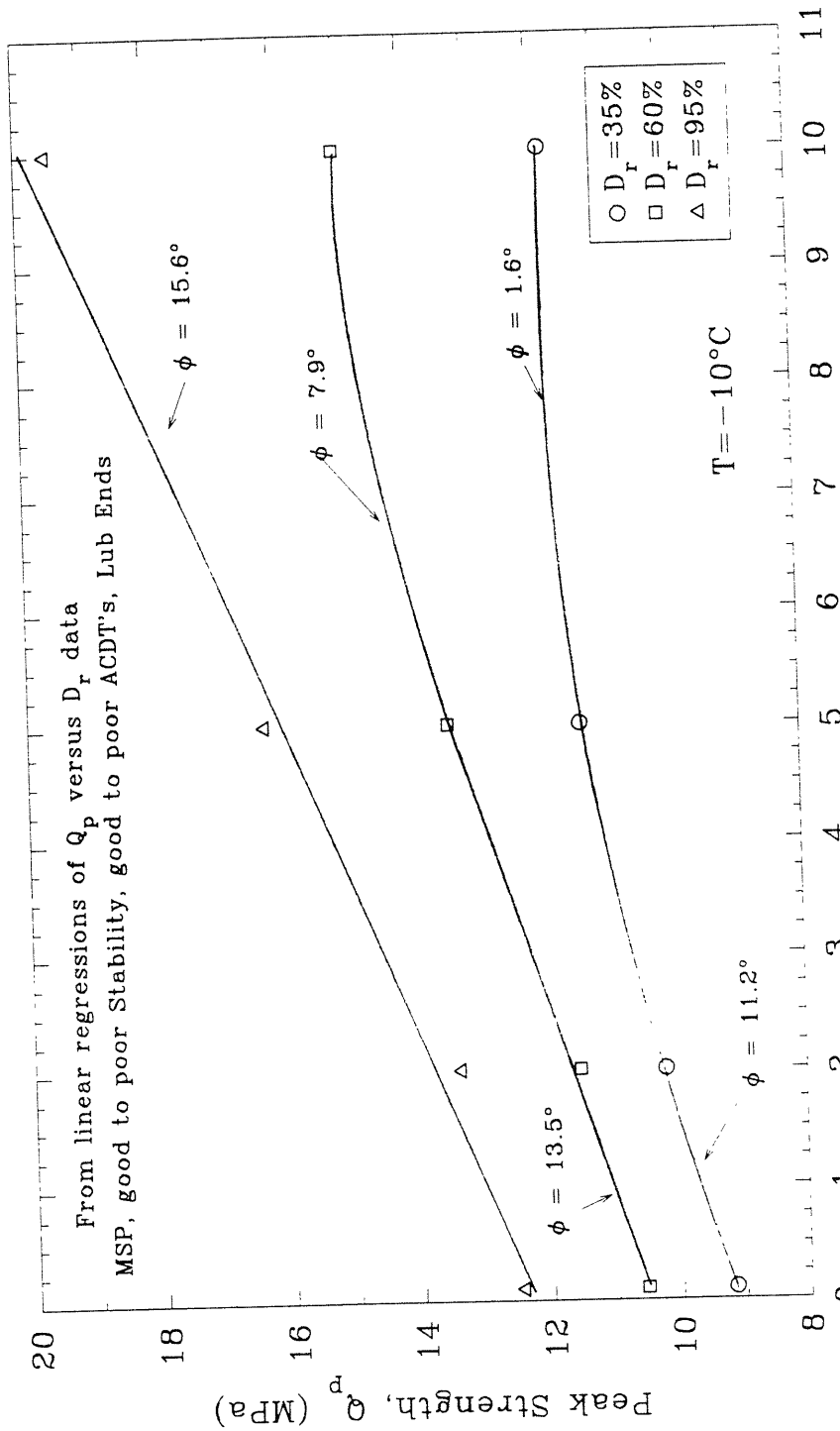

Figure 5.37 Peak Strength versus Confining Pressure for Conventional Frozen MFS Tests at Moderate Strain Rate, Low Confinement and T = −10°C (from Andersen 1991)

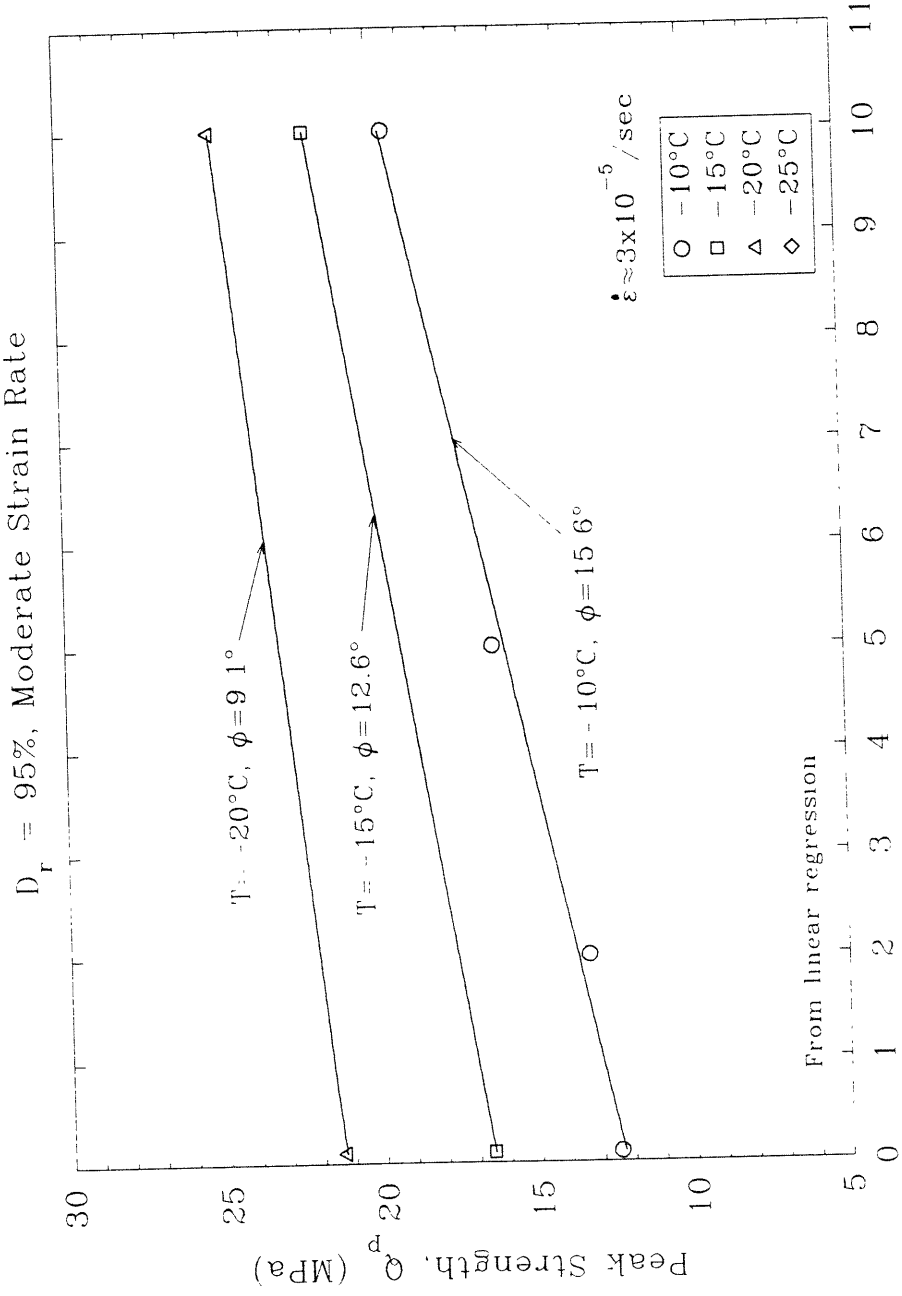

Figure 5.38 Peak Strength versus Confining Pressure for Conventional Frozen MFS Tests on Dense Specimens at Moderate Strain Rate and Different Temperatures

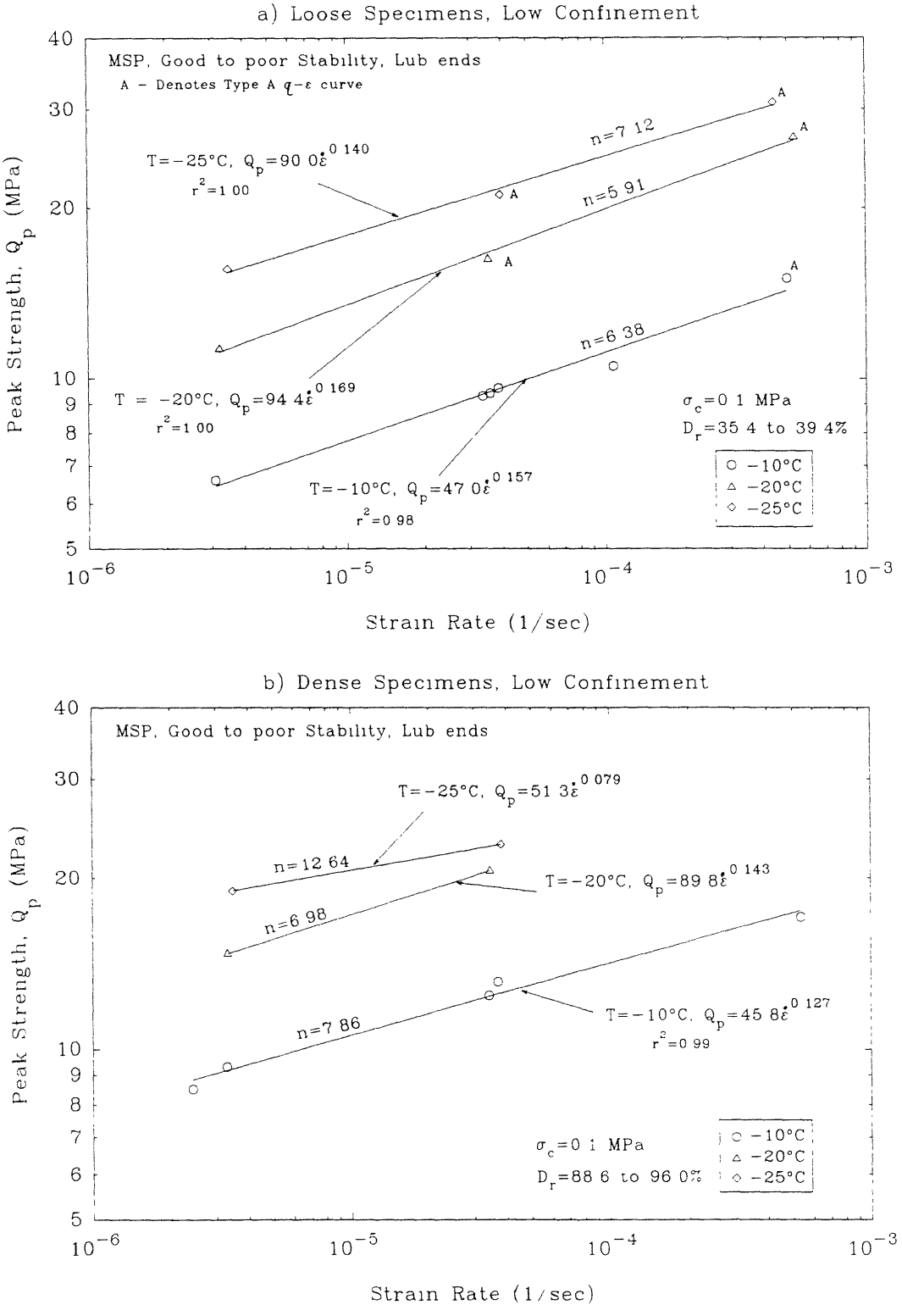

Figure 5.39 Peak Strength versus Strain Rate for Conventional Frozen MFS Tests on Loose and Dense Specimens at Low Confinement and Different Temperatures

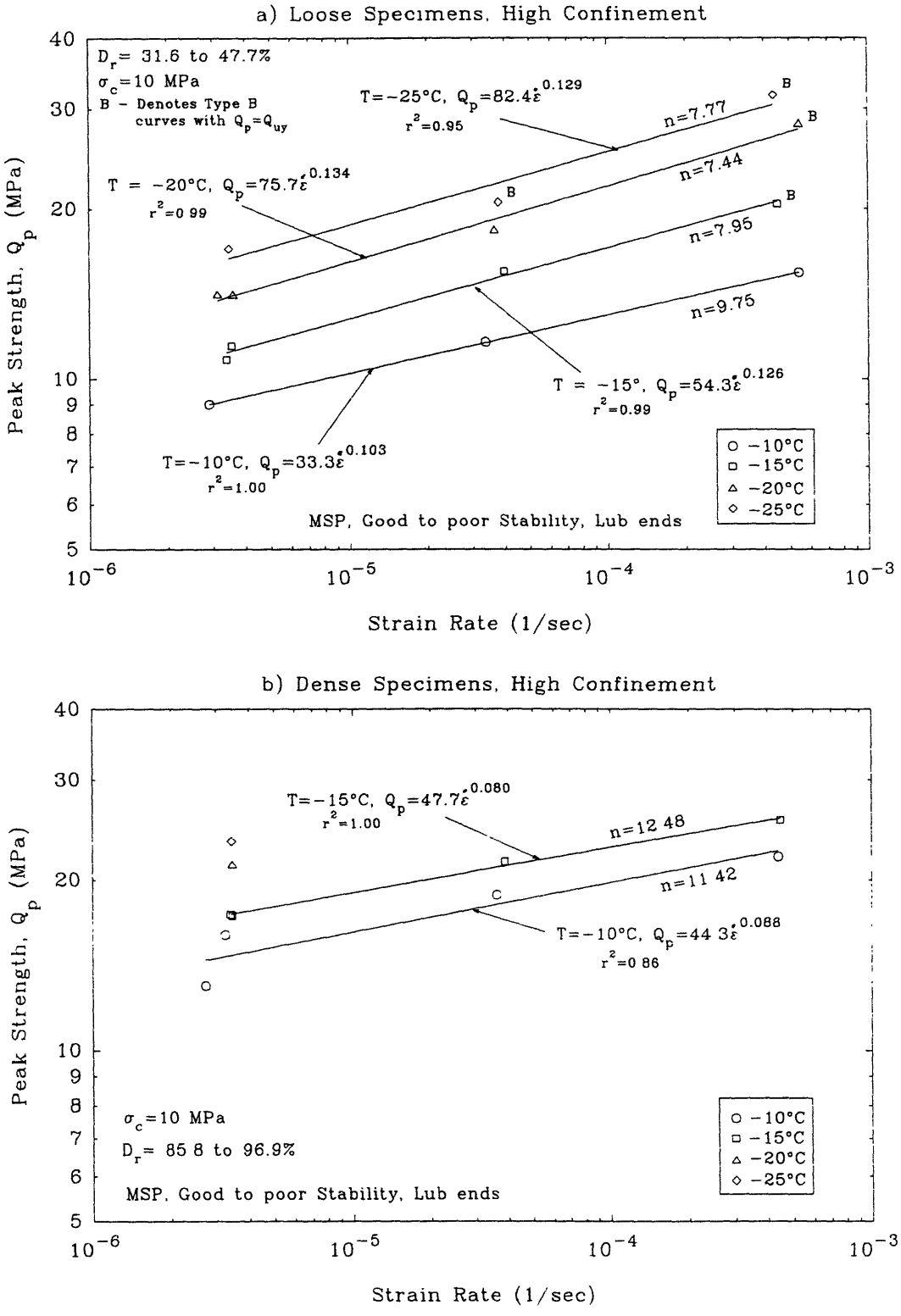

Figure 5.40 Peak Strength versus Strain Rate for Conventional Frozen MFS Tests on Loose and Dense Specimens at High Confinement and Different Temperatures

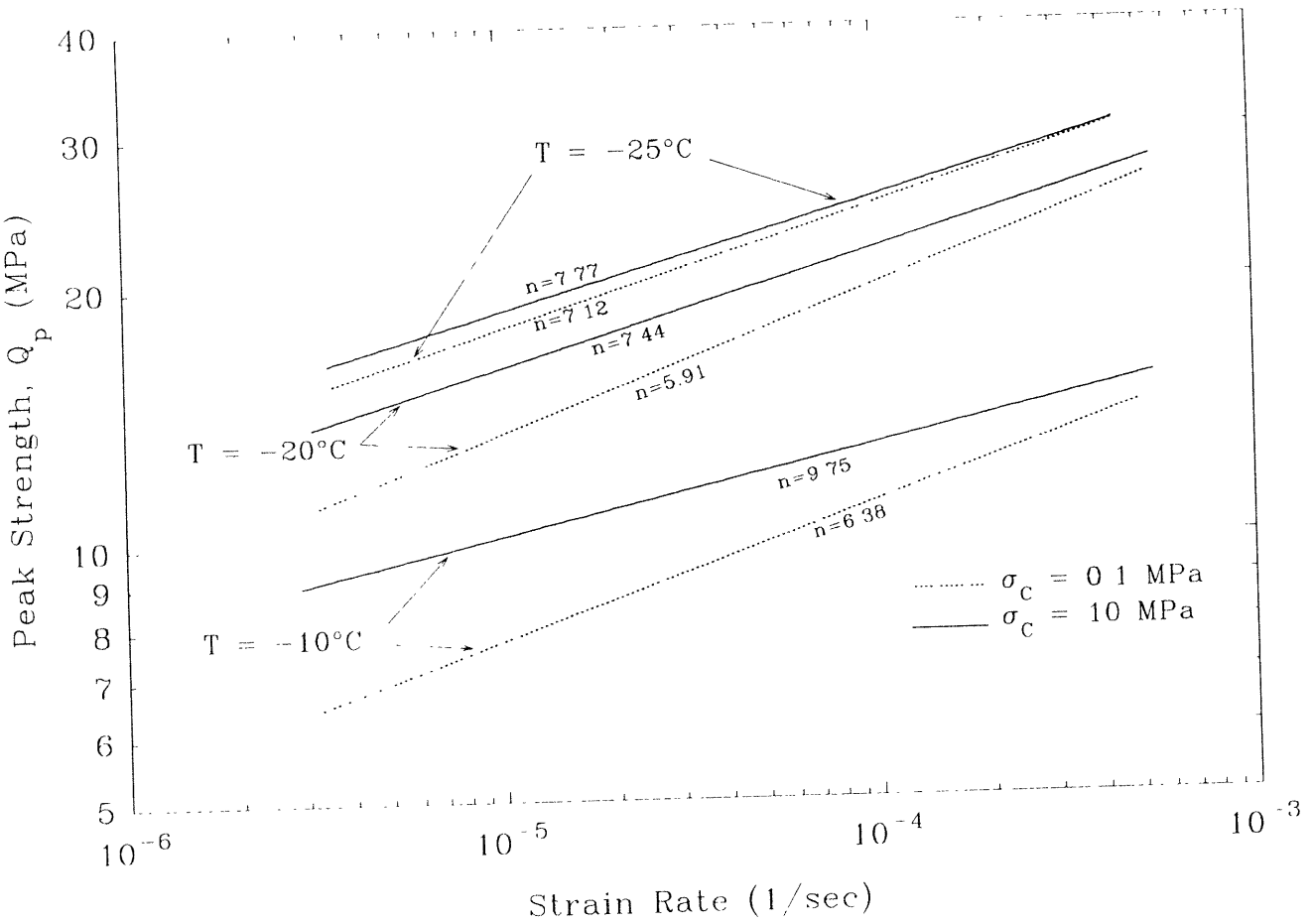

Figure 5.41 Comparison of Peak Strength versus Strain Rate Results of Loose Specimens at Low and High Confinement

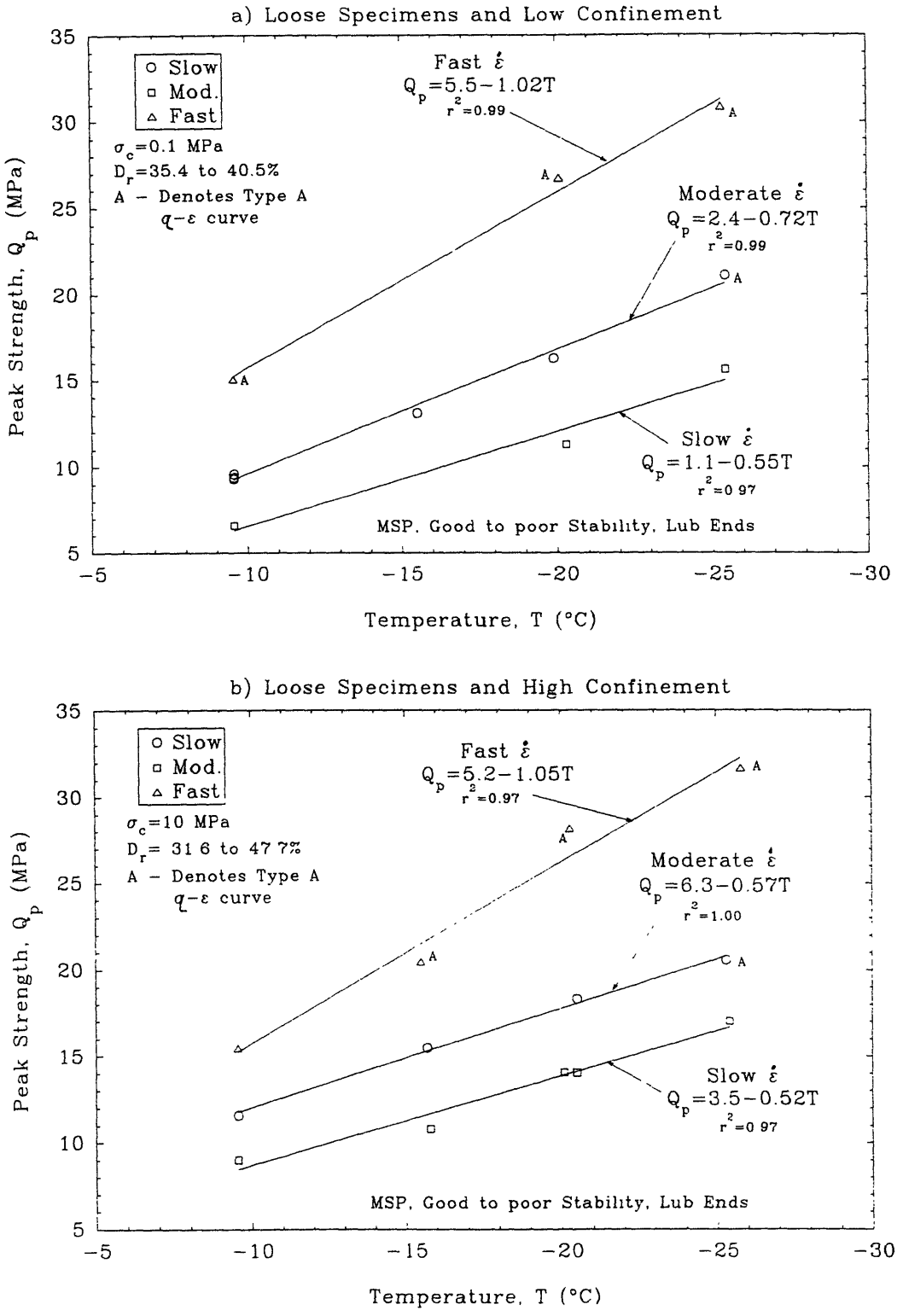

Figure 5.42 Peak Strength versus Temperature for Conventional Frozen MFS Tests on Loose Specimens at Low and High Confinement

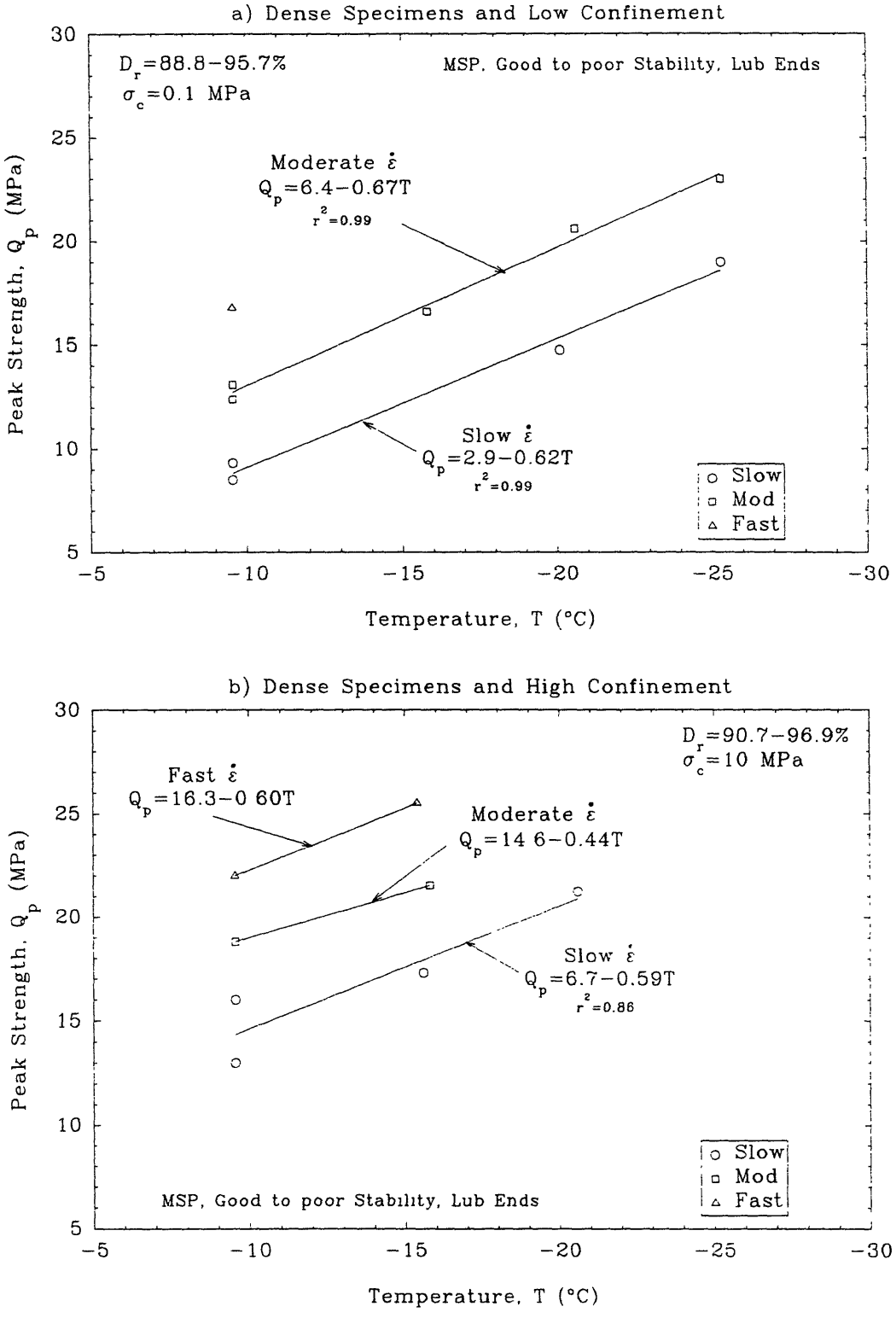

Figure 5.43 Peak Strength versus Temperature for Conventional Frozen MFS Tests on Dense Specimens at Low and High Confinement

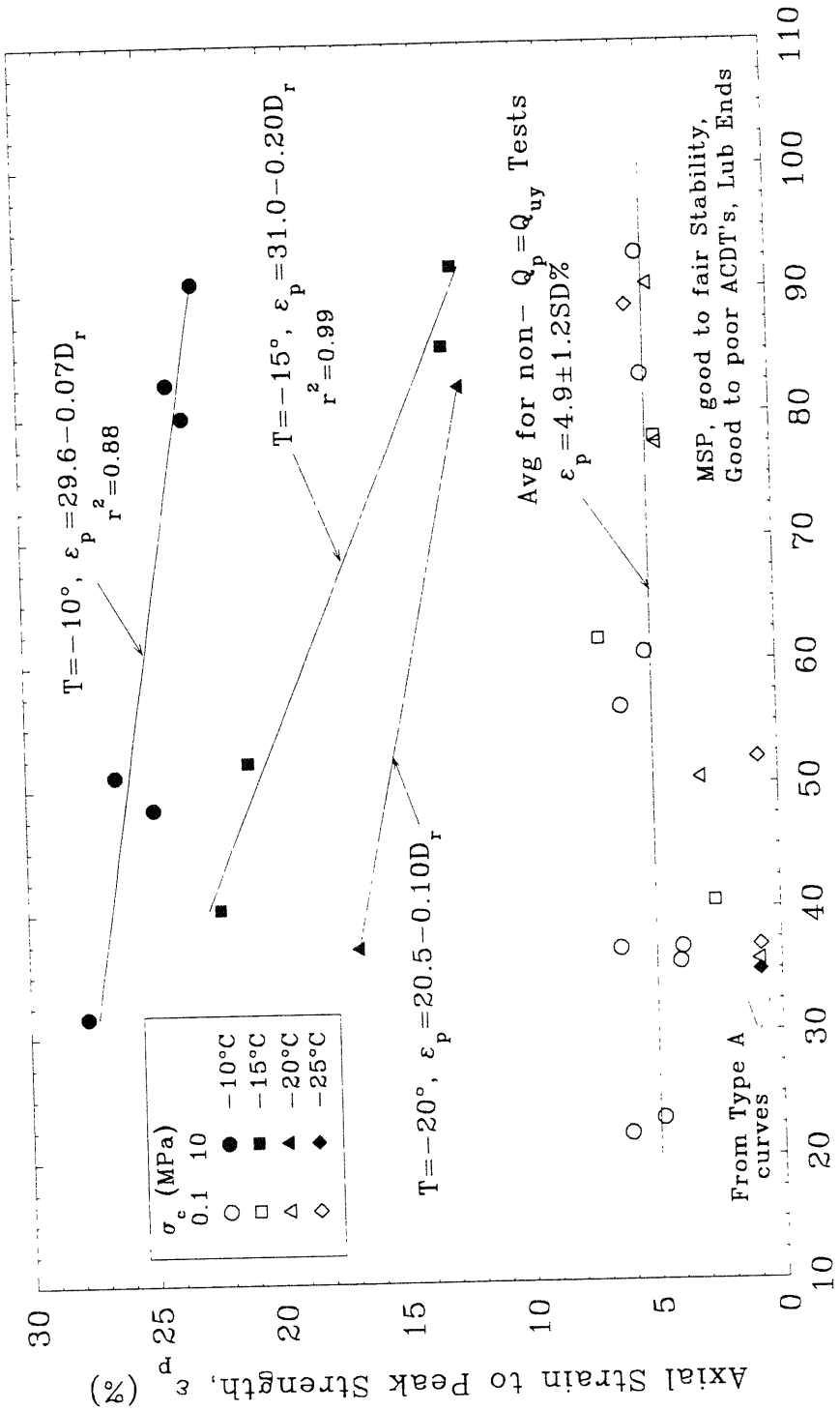

Figure 5.44a Axial Strain to Peak Strength versus Relative Density for Conventional Frozen MFS Tests at Moderate Strain Rate and Different Temperatures

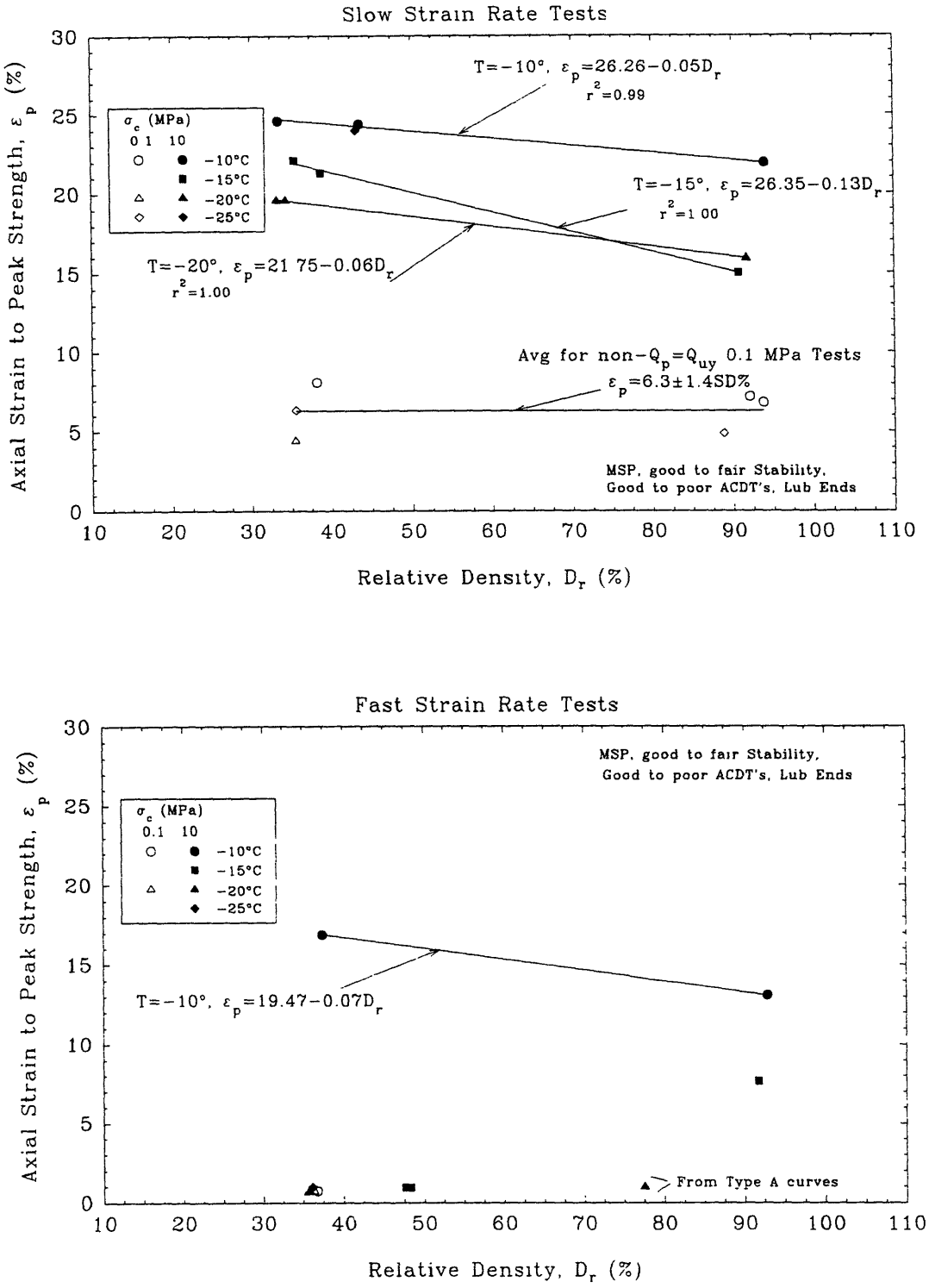

Figure 5.44b Axial Strain to Peak Strength versus Relative Density for Conventional Frozen MFS Tests at Slow and Fast Strain Rates and Different Temperatures

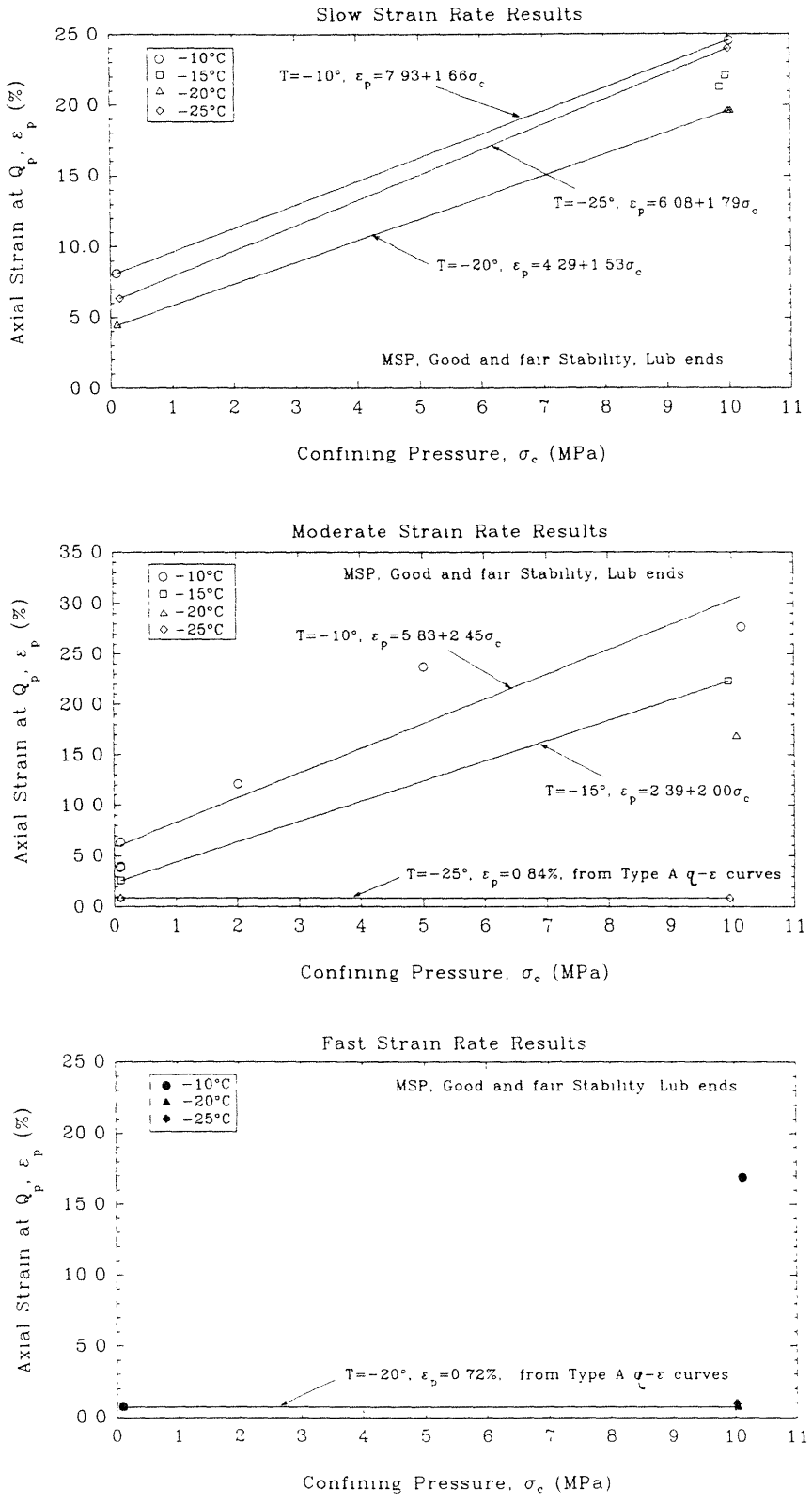

Figure 5.45a Axial Strain at Q_p versus Confining Pressure for Conventional Frozen MFS Tests on Loose Specimens at Different Temperatures

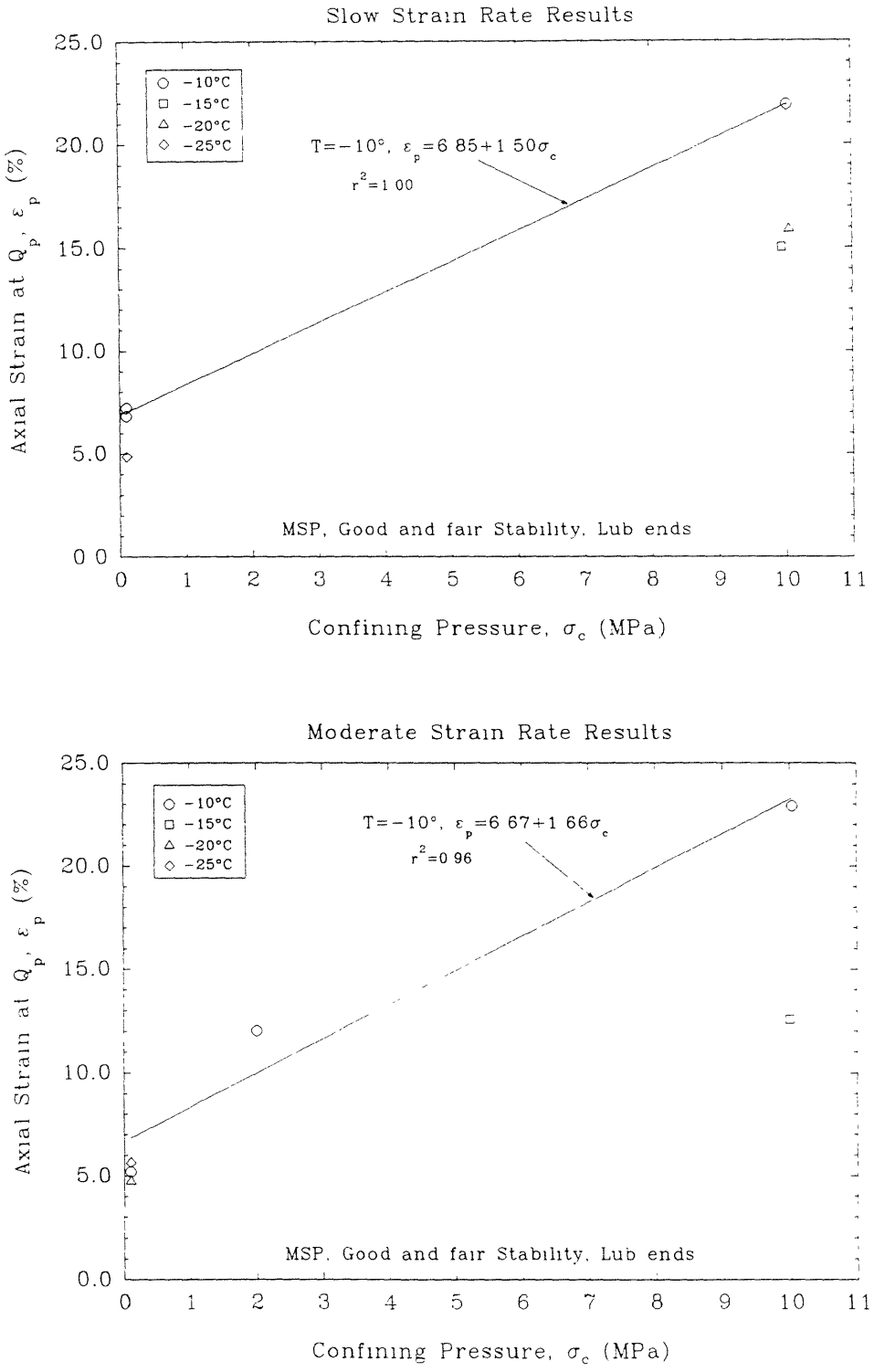

Figure 5.45b Axial Strain at Q_p versus Confining Pressure for Conventional Frozen MFS Tests on Dense Specimens at Different Temperatures

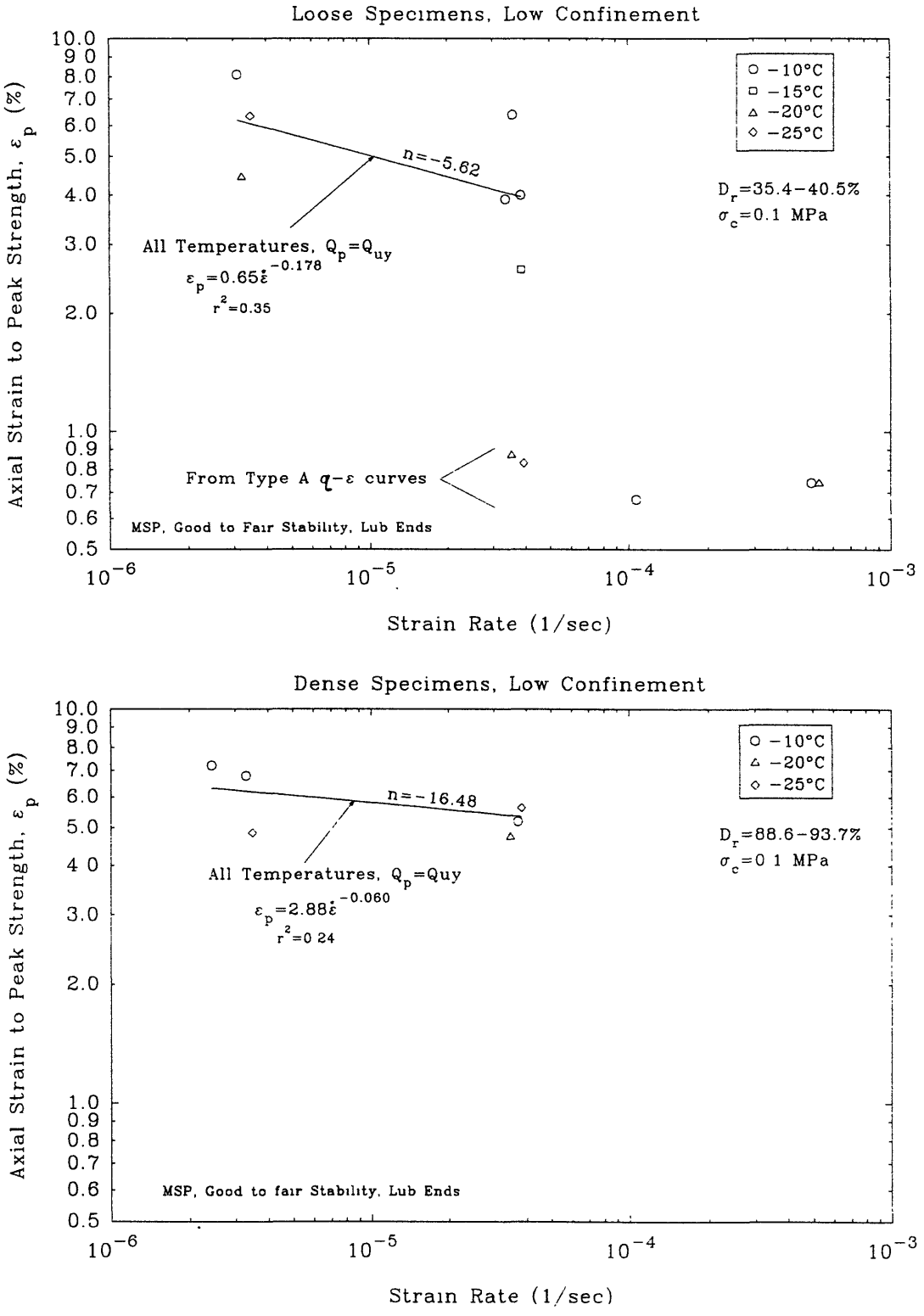

Figure 5.46a Axial Strain to Peak Strength versus Strain Rate for Conventional Frozen MFS Tests on Loose and Dense Specimens at Low Confinement and Different Temperatures

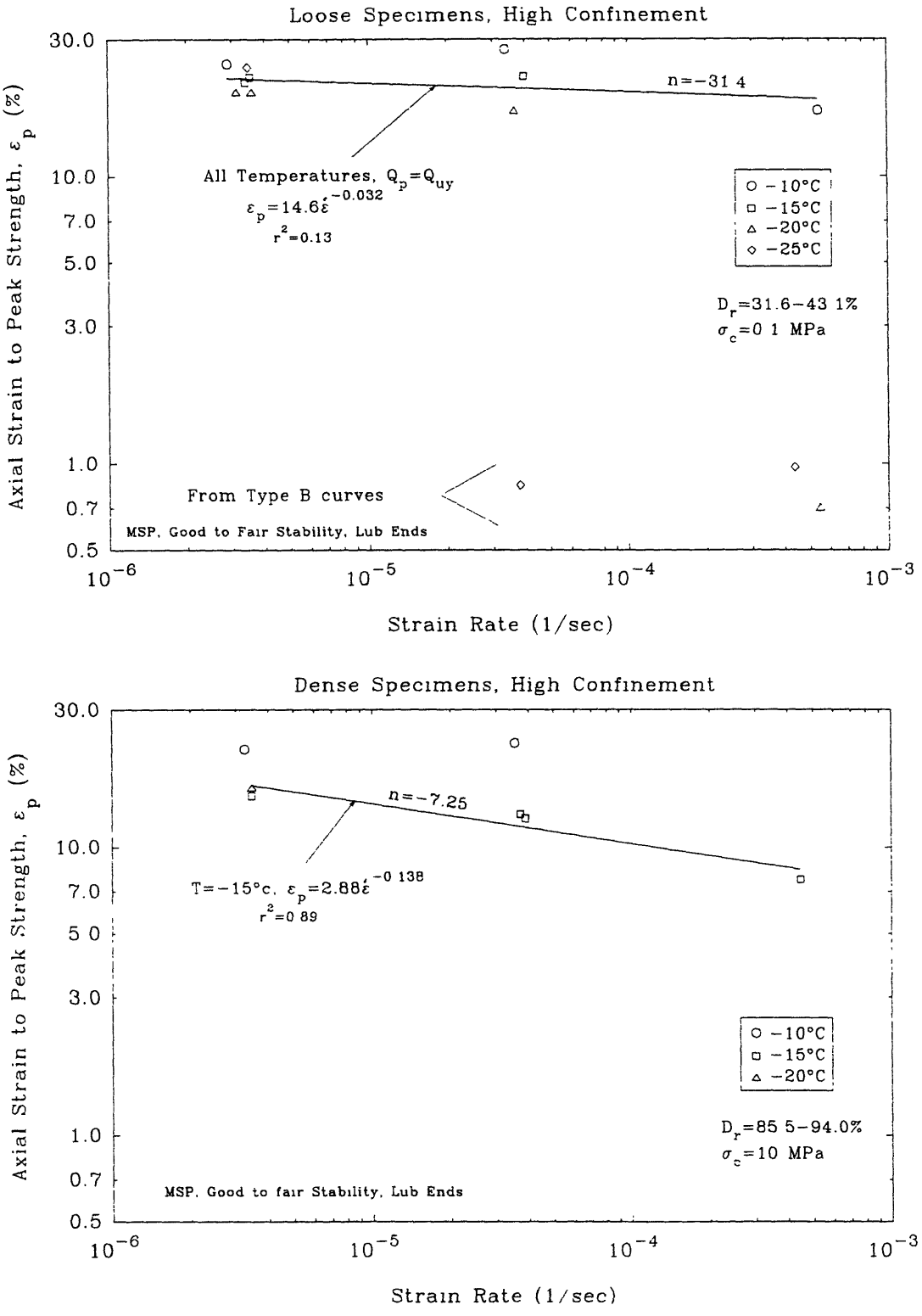

Figure 5.46b Axial Strain to Peak Strength versus Strain Rate for Conventional Frozen MFS Tests on Loose and Dense Specimens at HIgh Confinement and Different Temperatures

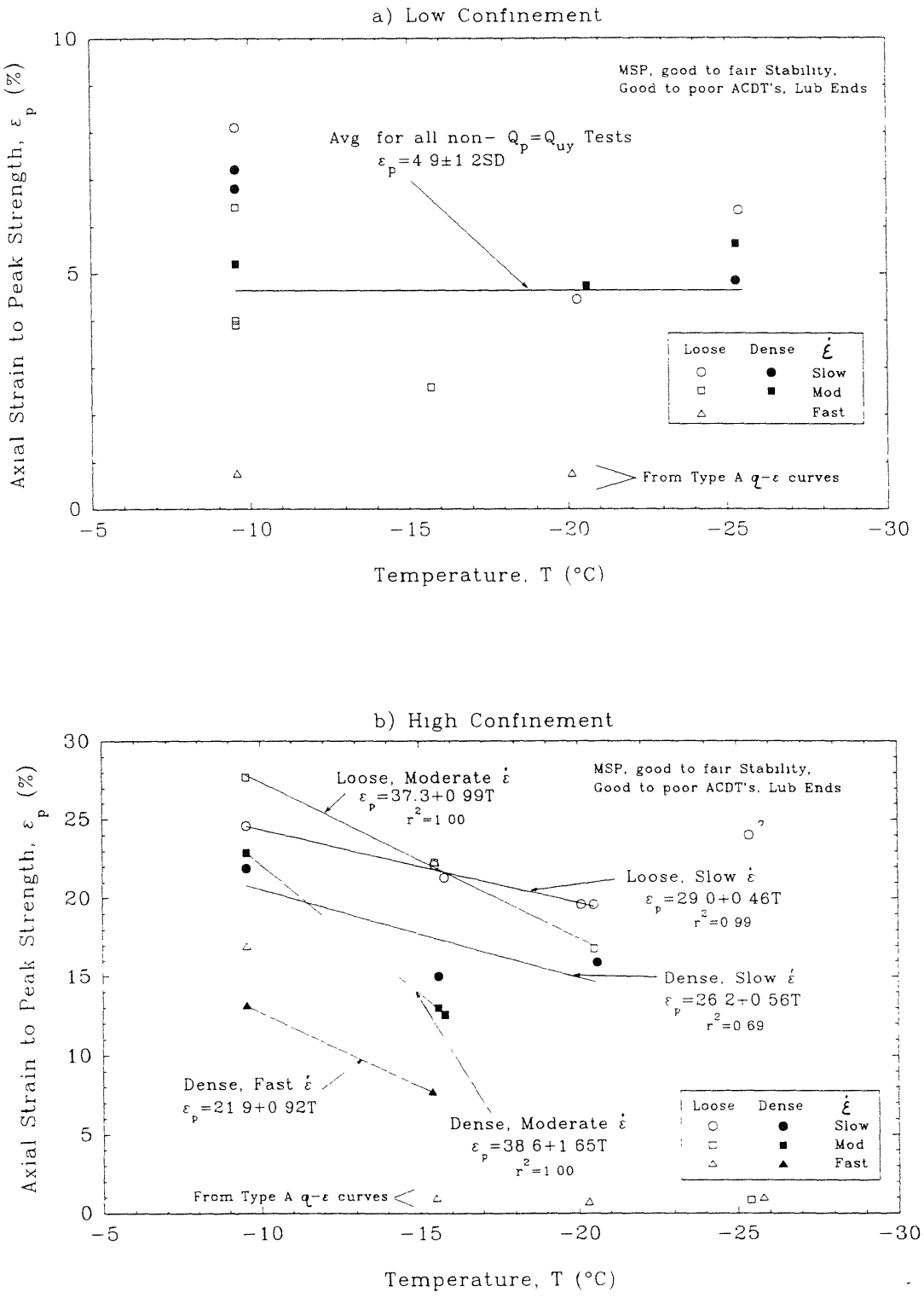

Figure 5.47 Axial Strain to Peak Strength versus Temperature for Conventional Frozen MFS Tests at Low and High Confinement

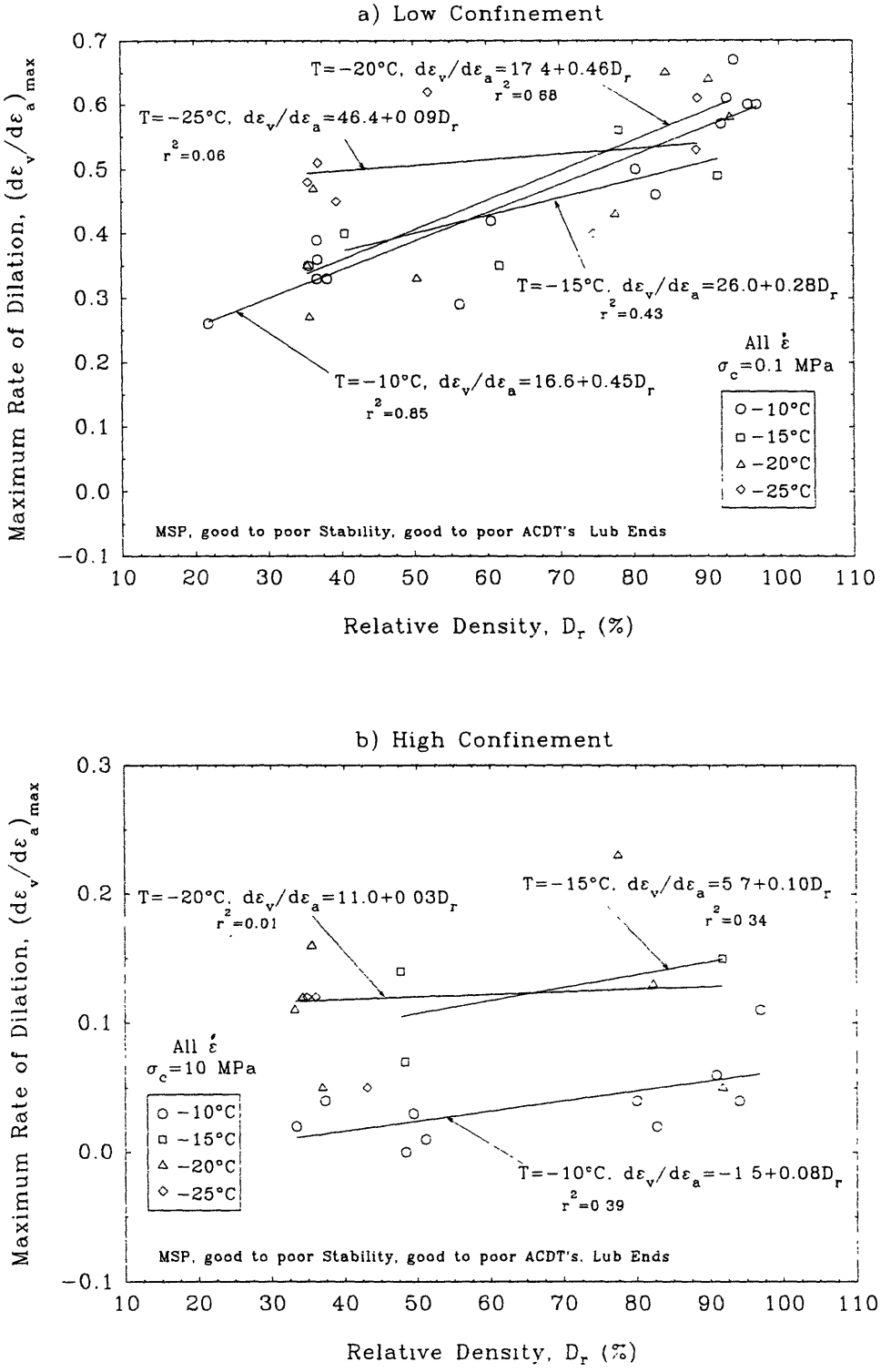

Figure 5.48 Maximum Rate of Dilation versus Relative Density for Conventional Frozen MFS Tests at Low and High Confinement, Various Strain Rates and Different Temperatures

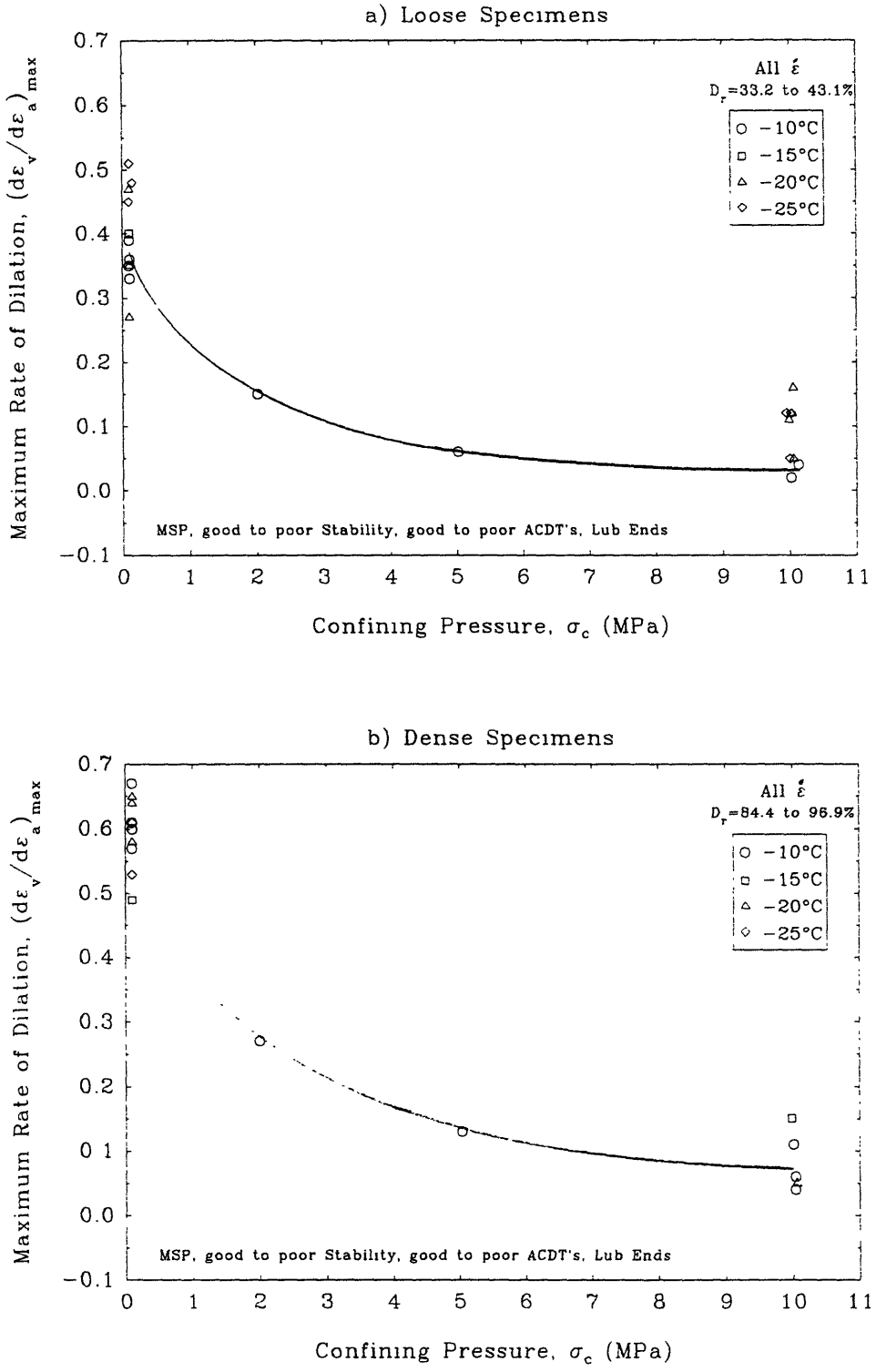

Figure 5.49 Maximum Rate of Dilation versus Confining Pressure for Conventional Frozen MFS Tests on Loose and Dense Specimens at Various Strain Rates and Different Temperatures

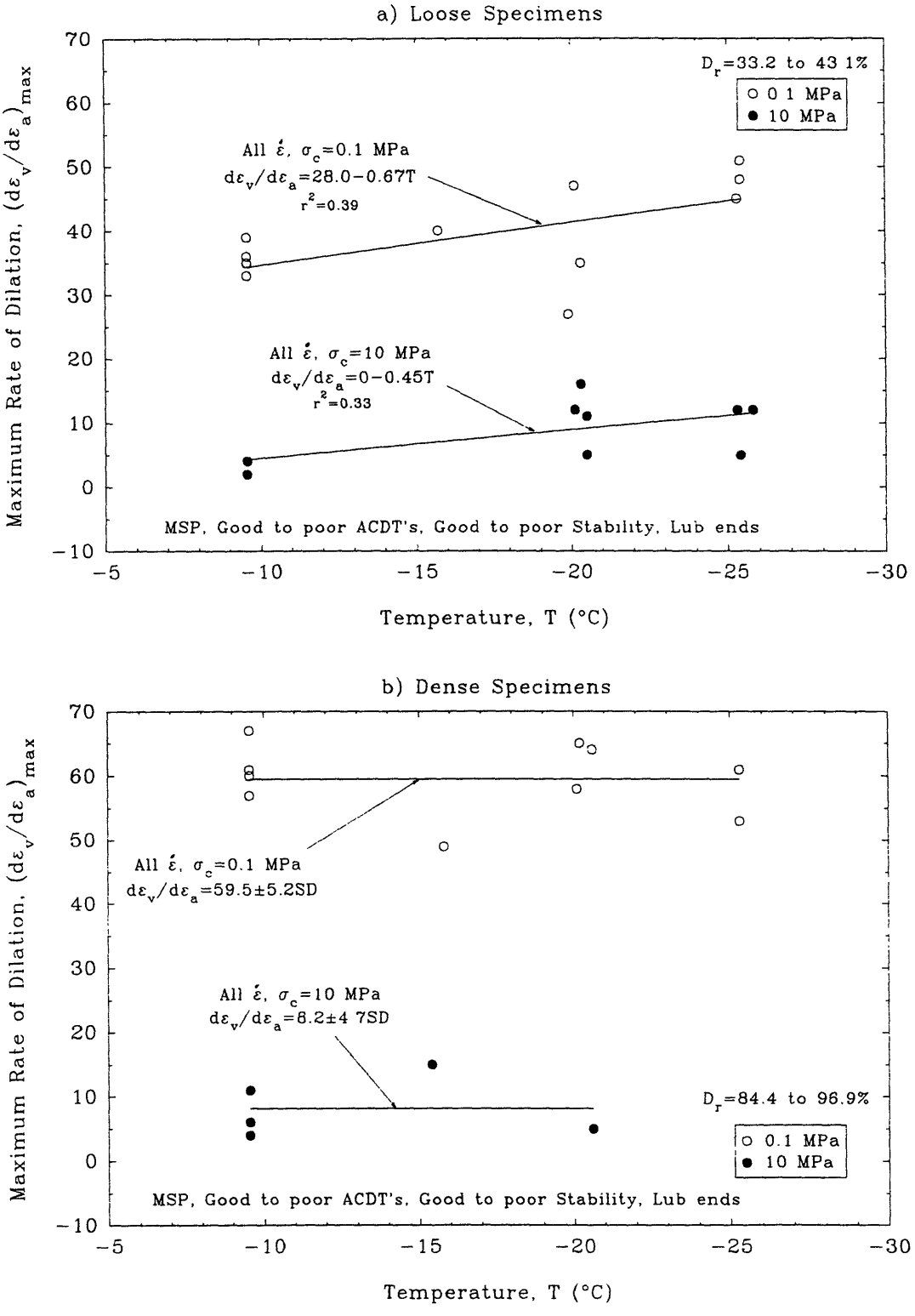

Figure 5.50 Maximum Rate of Dilation versus Temperature for Conventional Frozen MFS Tests on Loose and Dense Specimens at Various Strain Rates

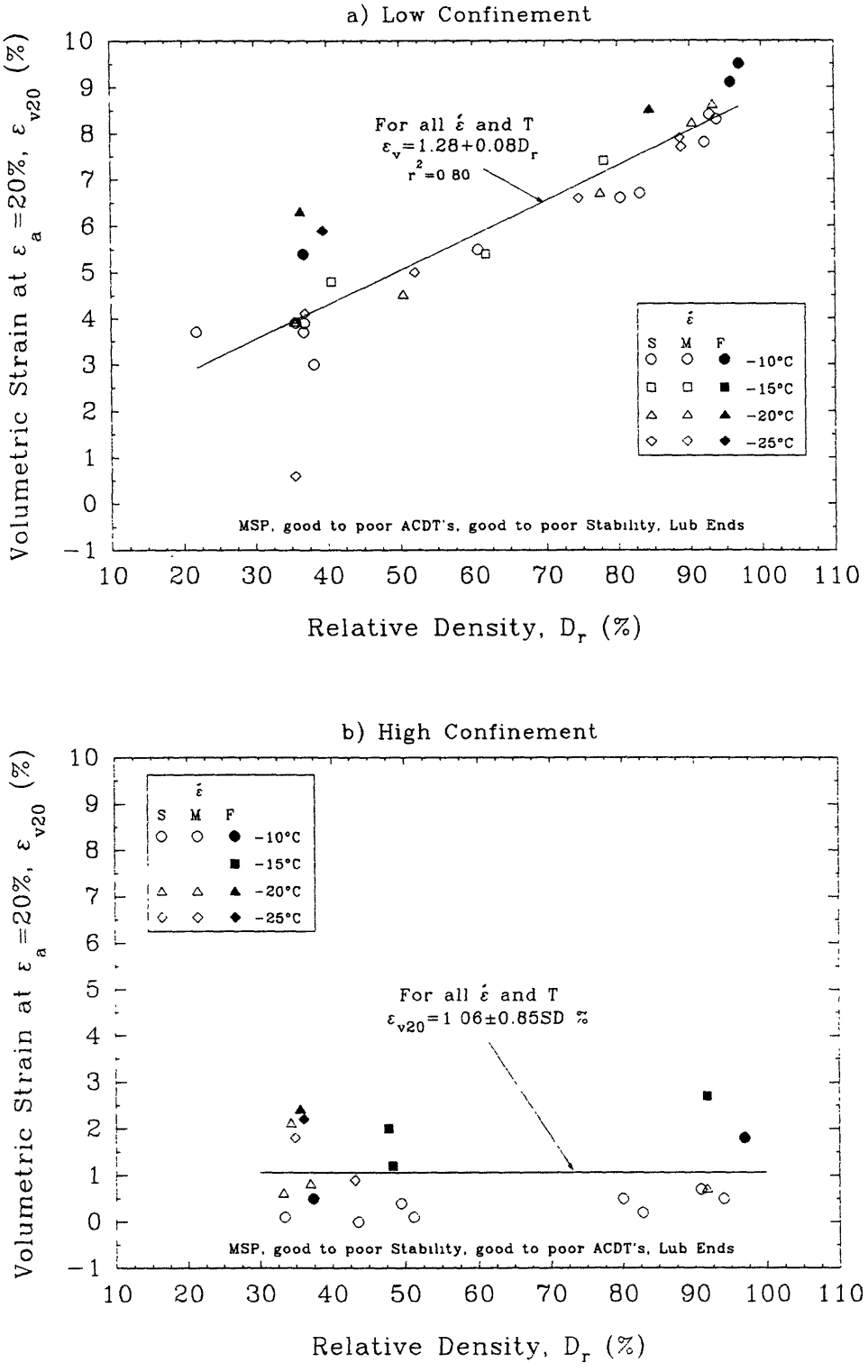

Figure 5.51 Volumetric Strain at ε_a=20% versus Relative Density for Conventional Frozen MFS Tests at Low and High Confinement, Various Strain Rates and Different Temperatures

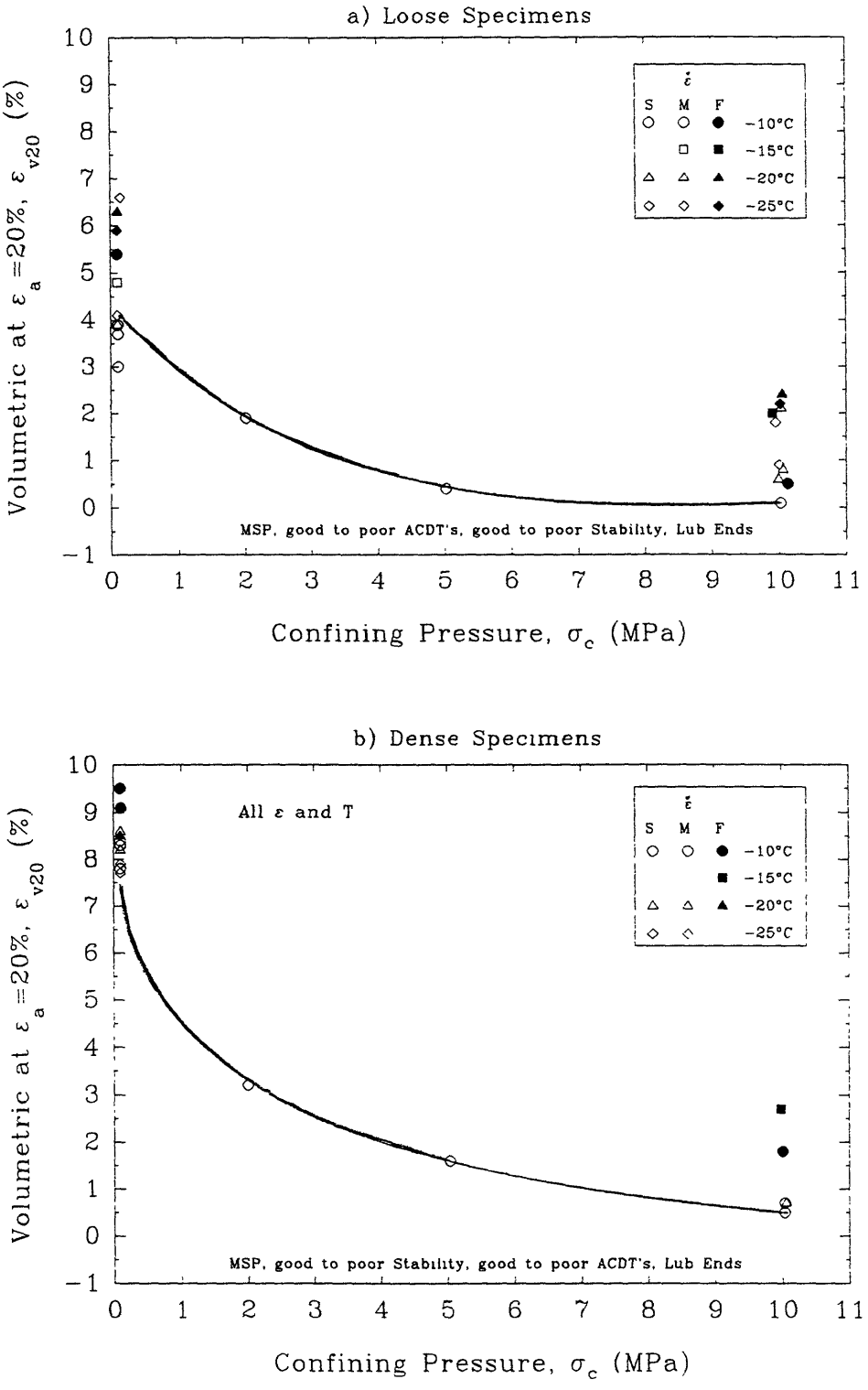

Figure 5.52 Volumetric Strain at ε_a = 20% versus Confining Pressure for Conventional Frozen MFS Tests on Loose and Dense Specimens at Various Strain Rates and Different Temperatures

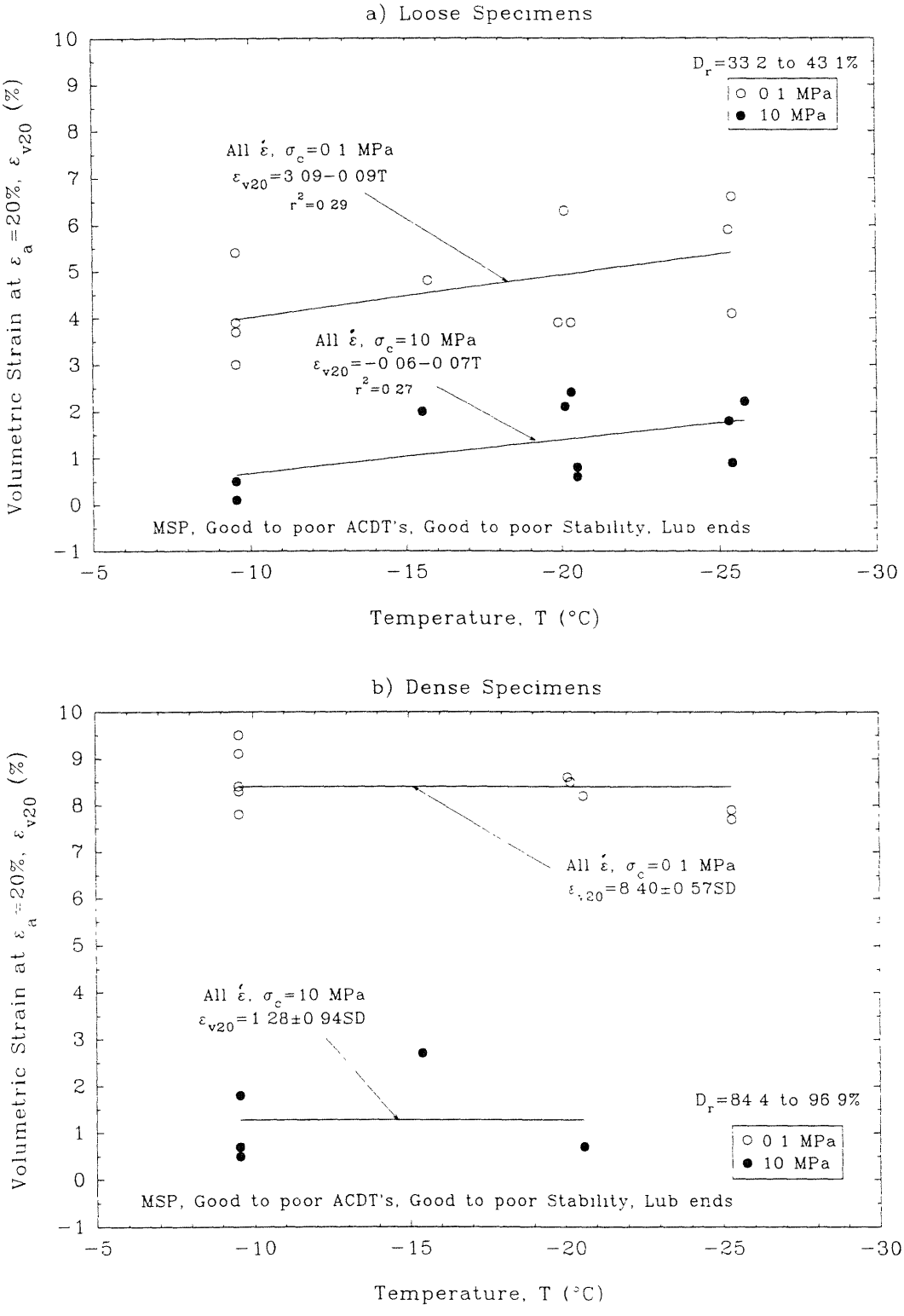

Figure 5.53 Volumetric Strain at ε_a=20% versus Temperature for Conventional Frozen MFS Tests on Loose and Dense Specimens at Various Strain Rates

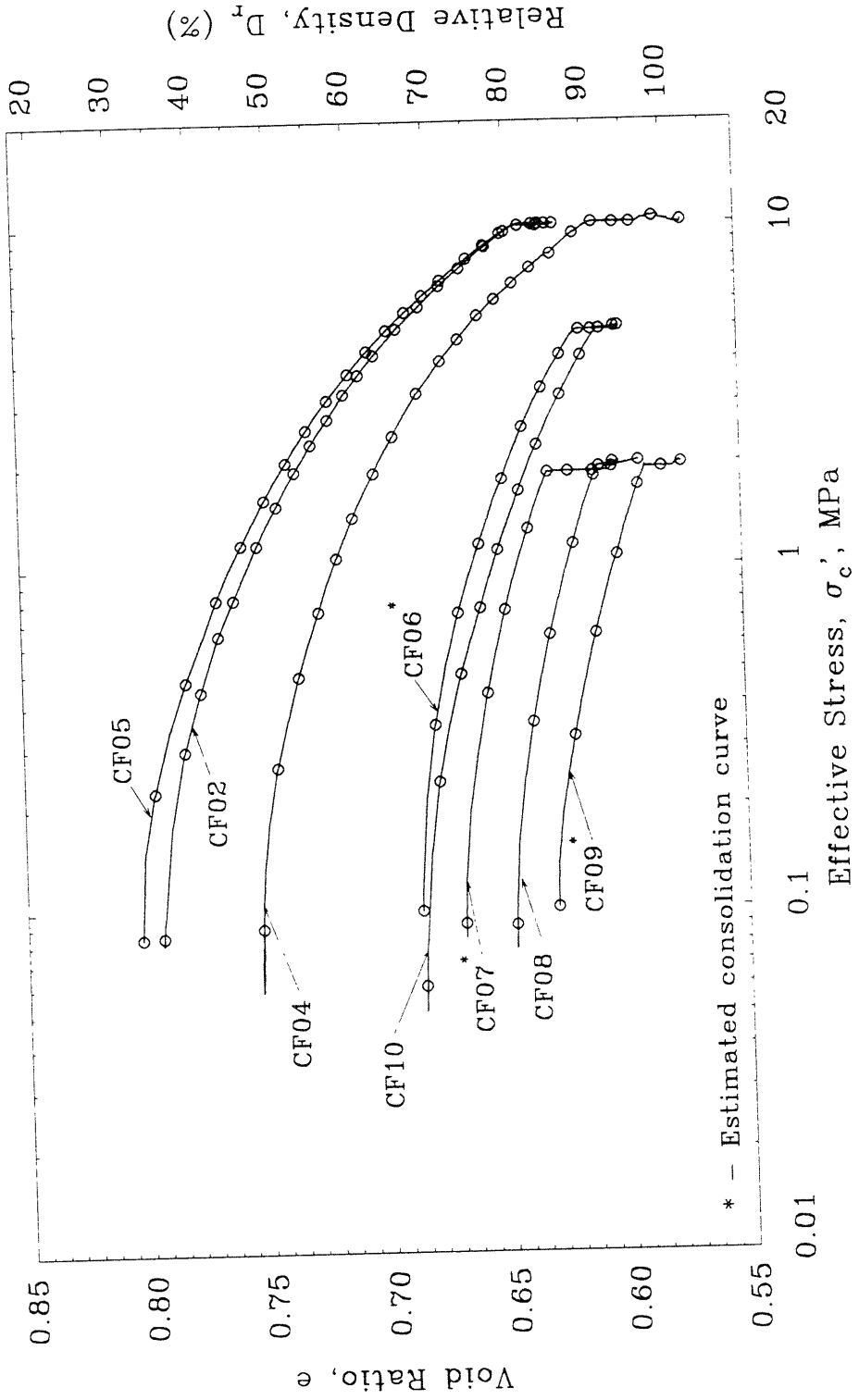

Figure 5.54 Void Ratio and Relative Density versus Effective Stress for Isotropically Consolidated Consolidate–Freeze Tests

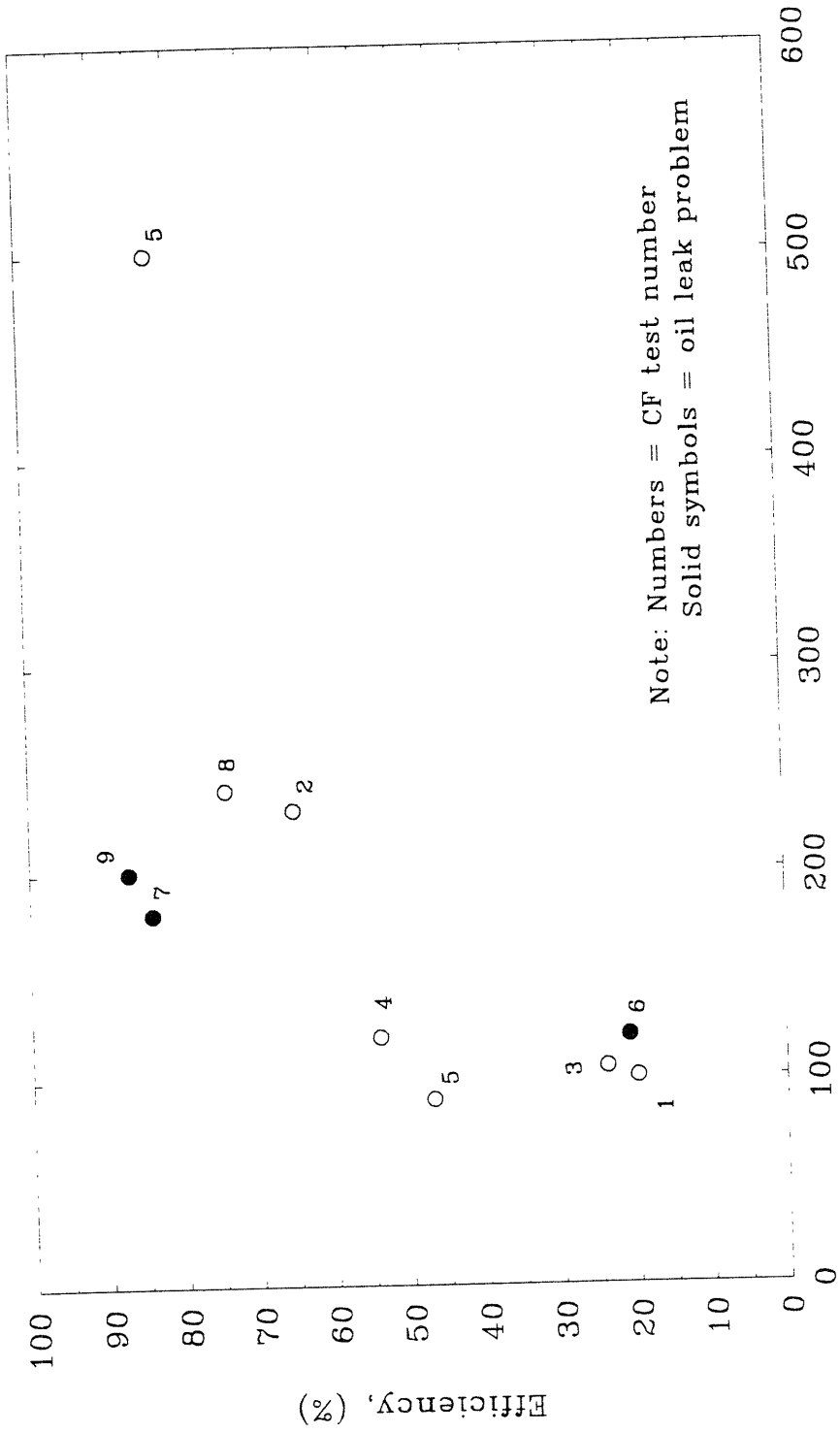

Figure 5.55 Efficiency of Specimen Freezing versus Elapsed Freezing Time for Consolidate–Freeze Tests on Dense Specimens

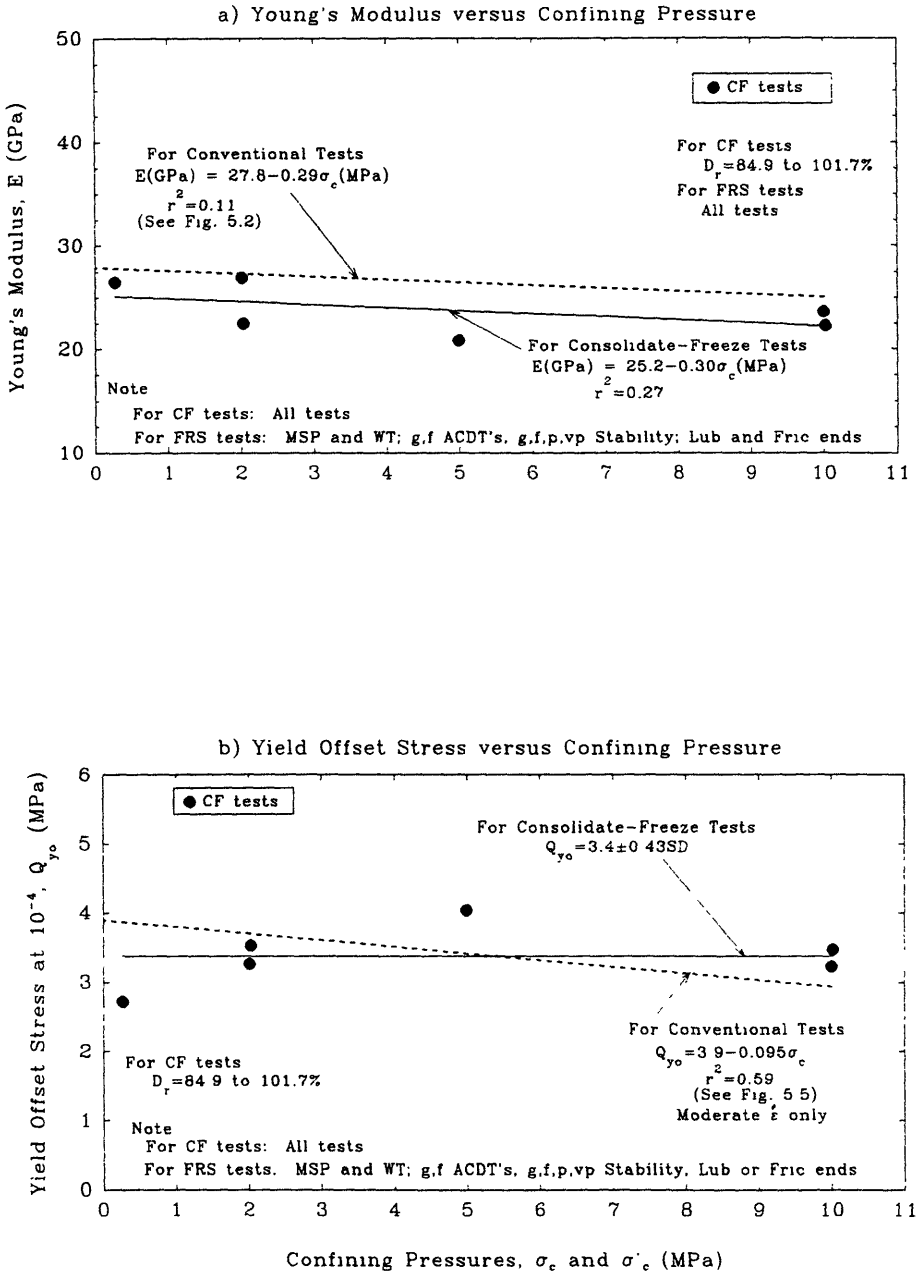

Figure 5.56 Small Strain Parameters versus Confining Pressure for Consolidate–Freeze and Conventional Frozen Tests on Dense Specimens at T = −10°C

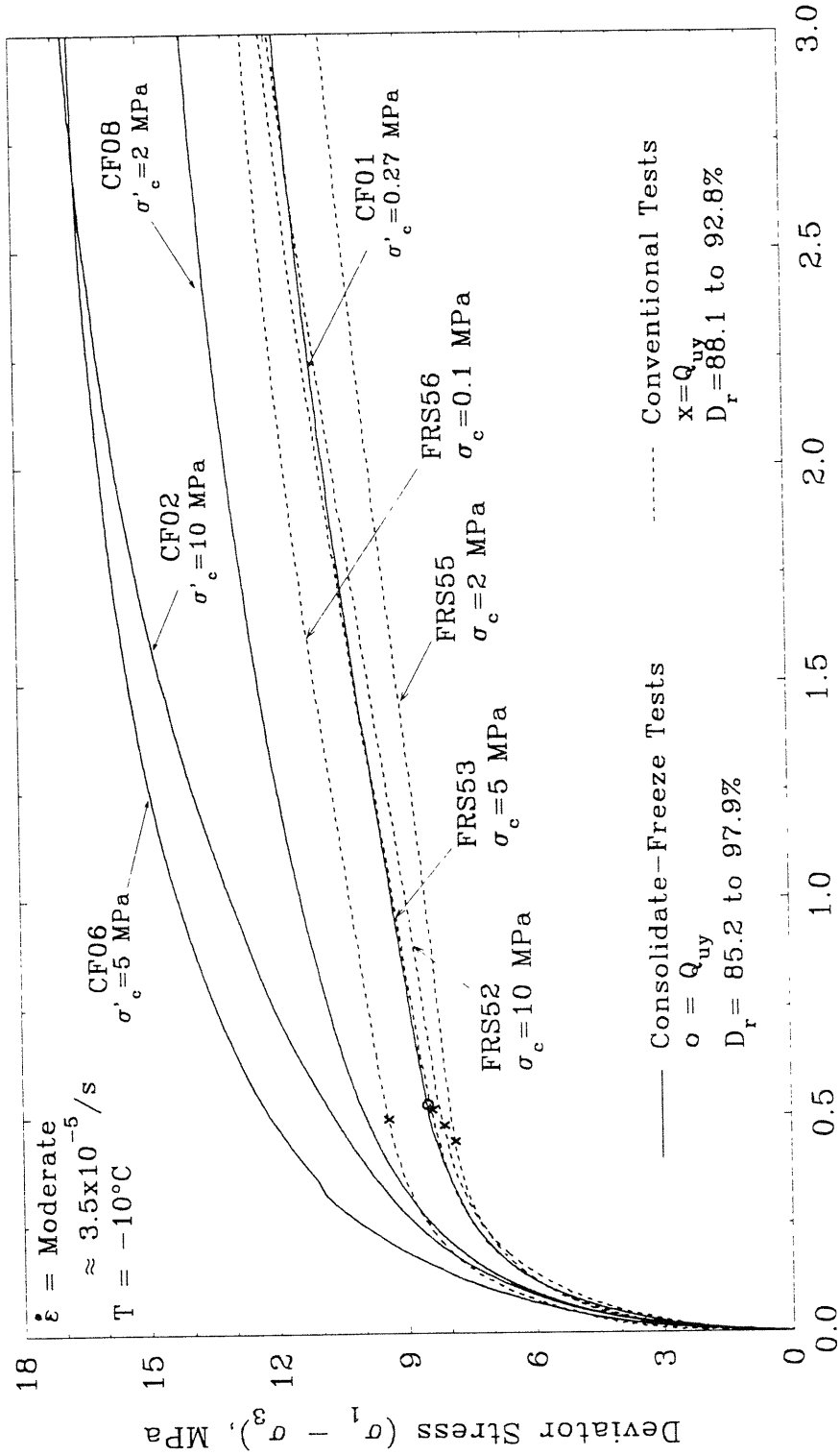

Figure 5.57 Initial Stress−Strain Curves Showing the Upper Yield Region for Consolidate−Freeze and Conventional Tests on Dense Specimens at Moderate Strain Rate and T = −10°C

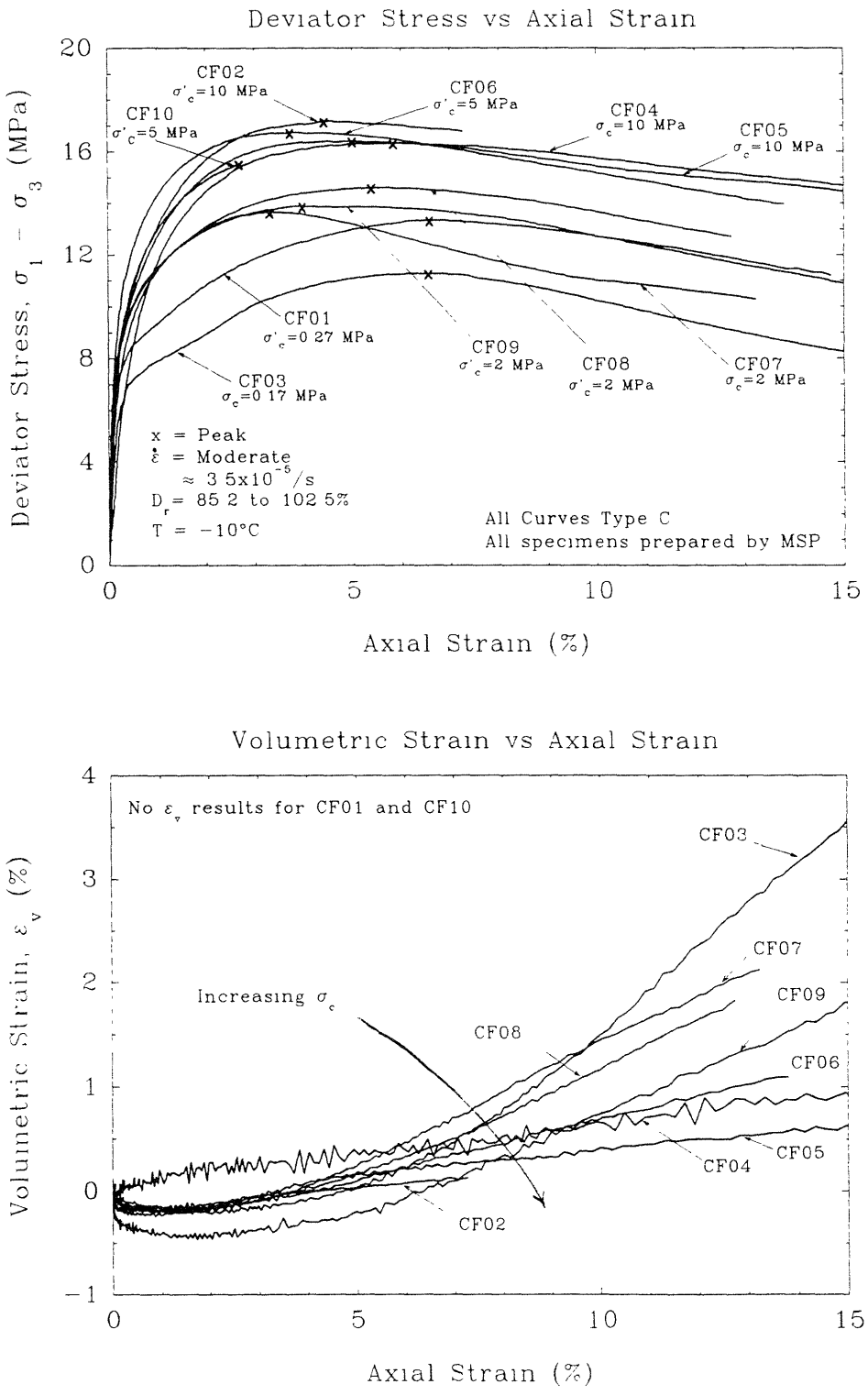

Figure 5.58 Comparison of Stress-Strain Curves for Consolidate-Freeze Tests on Dense Specimens at Moderate Strain Rate and T = −10°C

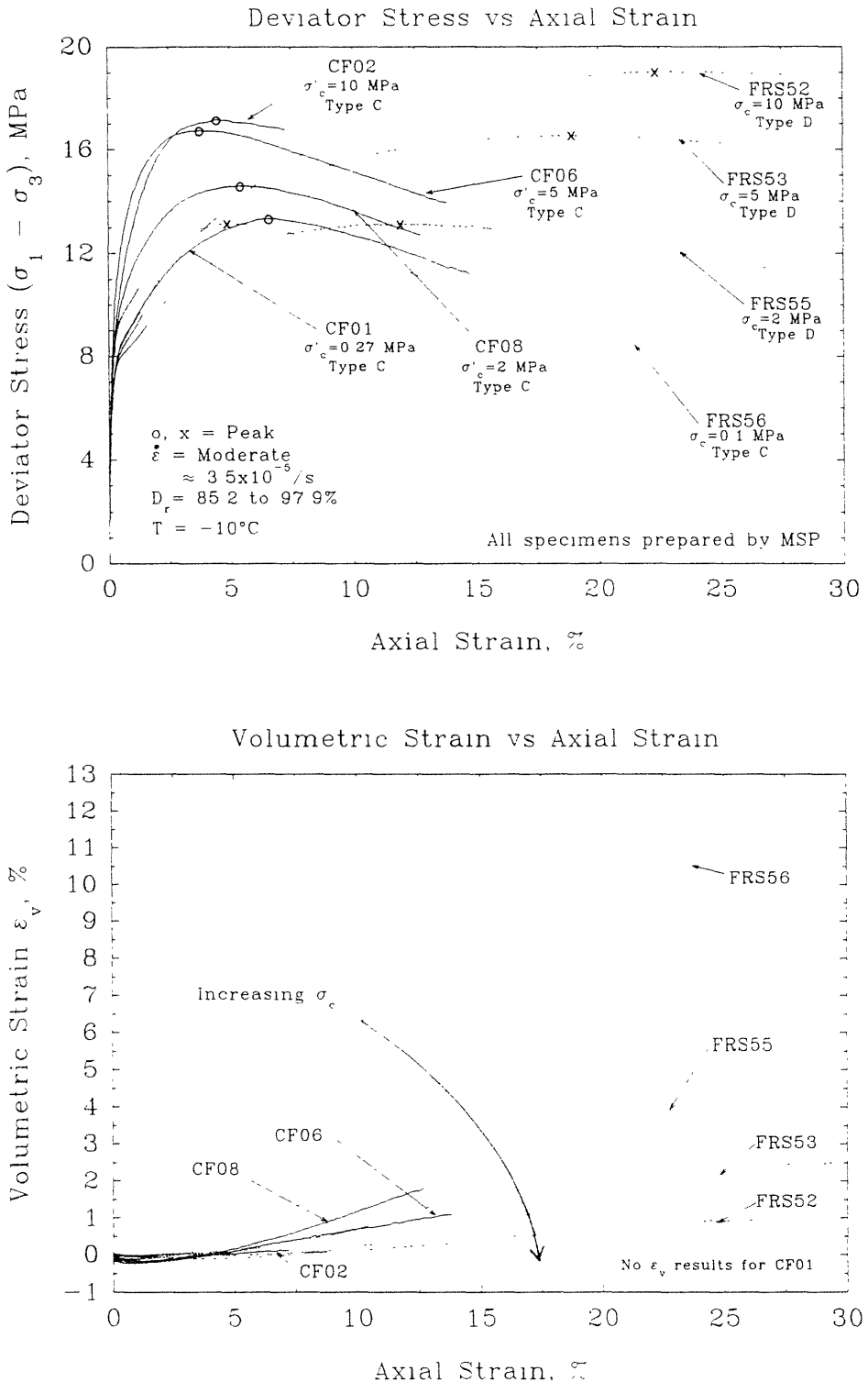

Figure 5.59 Comparison of Stress–Strain Curves for Consolidate–Freeze and Conventional Frozen Tests on Dense Specimens at Moderate Strain Rate and T = −10°C

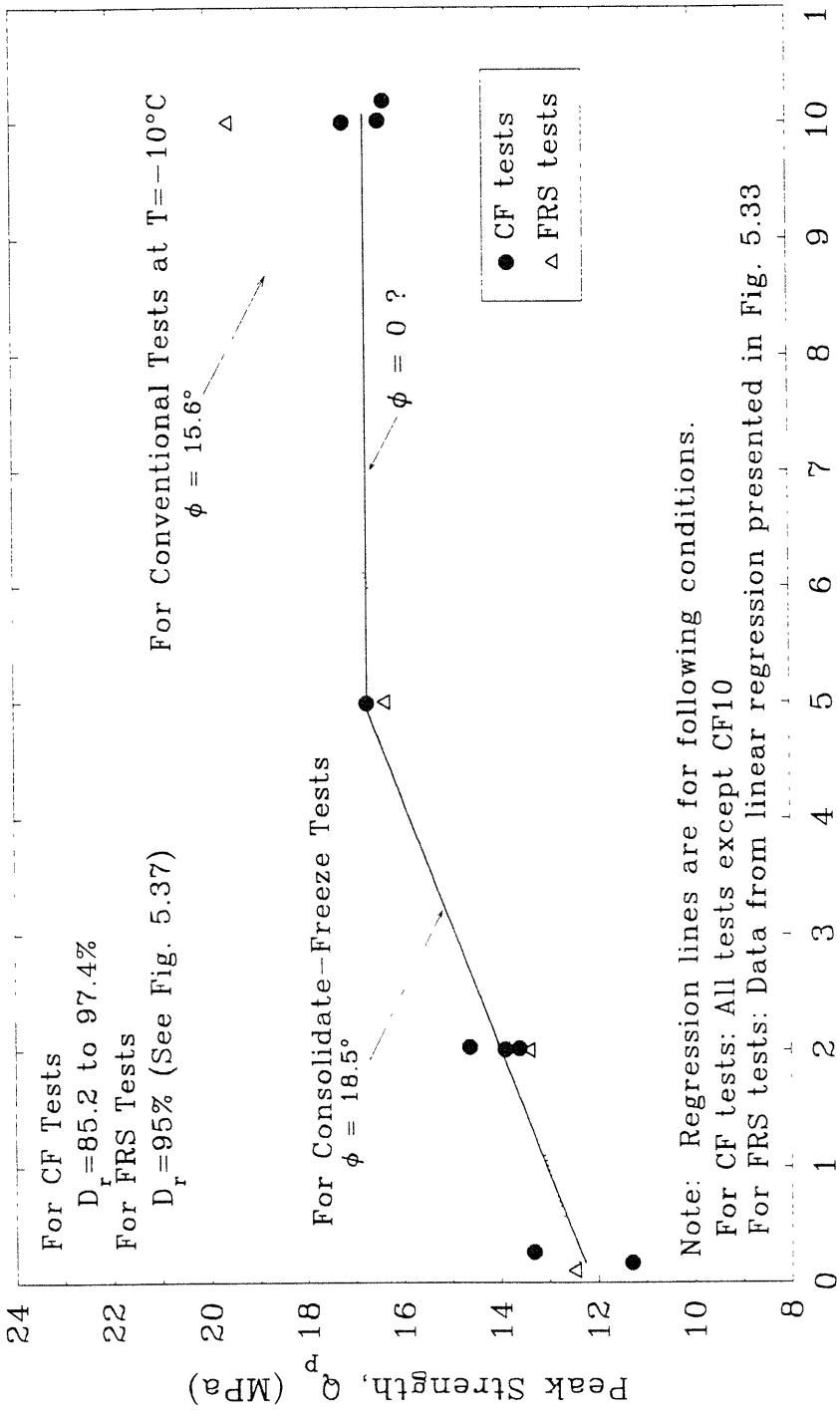

Figure 5.60 Peak Strength versus Confining Pressure for Consolidate–Freeze and Conventional Tests on Dense Specimens at Moderate Strain Rate and T = –10°C

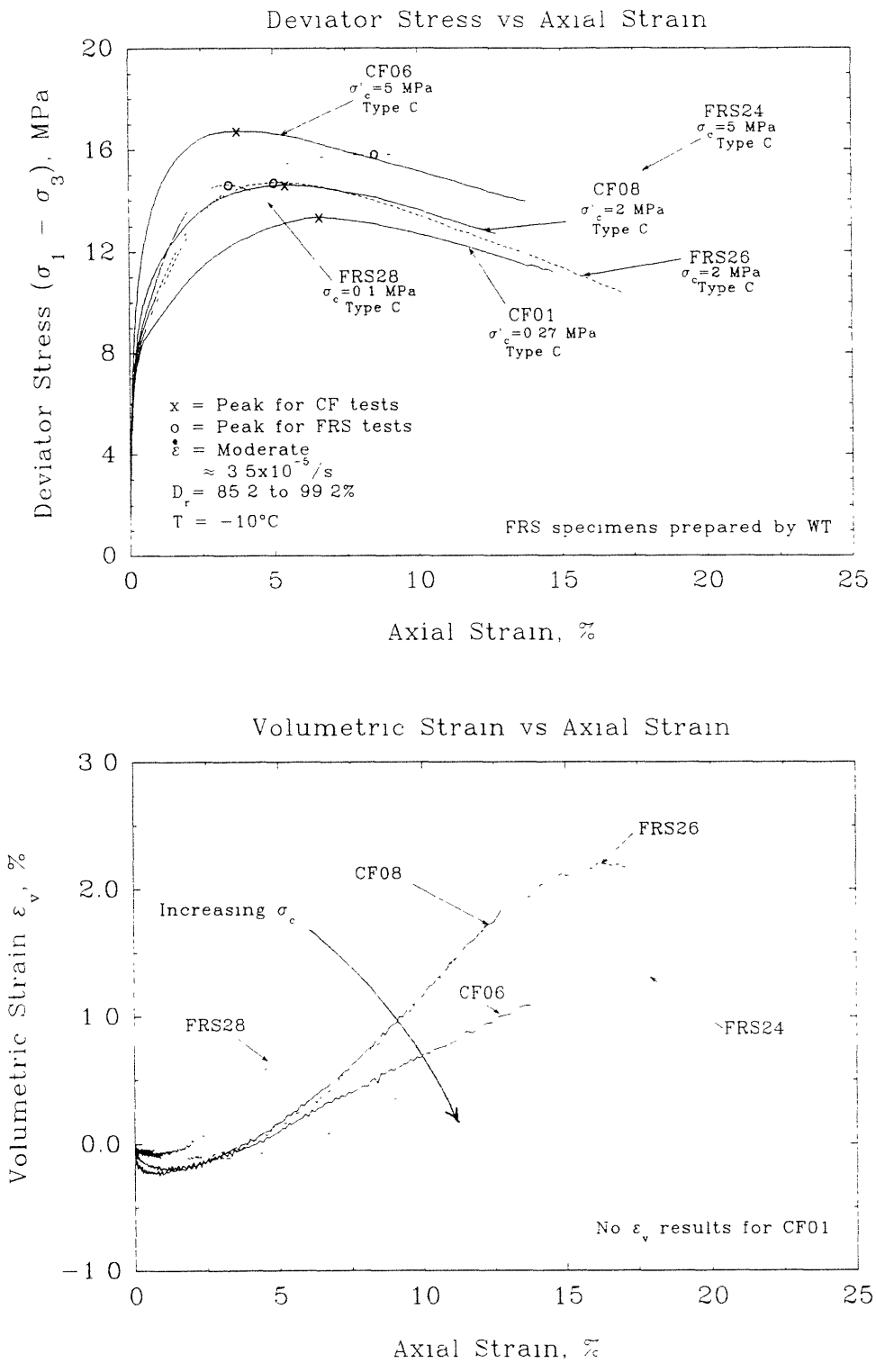

Figure 5.61 Comparison of Stress–Strain Curves for Consolidate–Freeze Tests and Conventional Frozen Tests on Wet Tamped Specimens at Moderate Strain Rate and T = −10°C

CHAPTER 6
ANALYSIS OF FROZEN MFS RESULTS

This chapter consists of four sections. The first section compares the results of the conventional frozen MFS tests with tests results on other frozen sands. The effect of sand density, confining pressure, strain rate and temperature on frozen MFS presented in Chapter 5 will be compared with testing programs which examined similar testing variables. The writer notes that comparisons between the previous test results from others and those presented in Chapter 5 are made in so far as possible since the majority of previous testing programs cited in the literature considered only one or two testing variables.

The second section of this chapter presents an analysis of the frozen sand results using the isostrain and dilatancy–hardening models previously discussed in Section 2.4. Results from the isostrain model will be compared to the Young's modulus measured in the frozen MFS tests. Results from the dilatancy–hardening model will be compared to the upper yield stress (Q_{uy}) and peak strength (Q_p) measured in the frozen MFS tests. The unfrozen MFS test results will be used in the dilatancy–hardening model to determine the effective critical confining stress and the effective friction angle.

The third section presents a discussion of the possible mechanisms involved in the deformation–strength behavior of frozen sands considering previously proposed mechanisms and their applicability to frozen MFS. The final section presents a proposed conceptual description of frozen MFS as a composite material based on the results from the conventional frozen MFS testing program. This conceptual description of the frozen MFS behavior serves as a starting point for

future analysis of frozen sand behavior as a composite. The description covers the entire stress–strain and volumetric behavior of frozen MFS and uses deformation and strength mechanisms "established" for unfrozen sands and polycrystalline ice in developing its concepts.

6.1 COMPARISON OF FROZEN MFS WITH PREVIOUS FROZEN SAND STUDIES

The work by Andersen et al. (1992) and the current research effort for frozen MFS presents a unique set of results for a frozen sand with testing performed under various combinations of relative density, confining pressure, strain rate and temperature. No study has been presented in the literature for any other frozen sand which was tested under similar ranges in conditions. In addition, some of the test results presented in Chapter 5, e.g., the yield offset stress (Q_{yo}), have not been reported in the currently available literature; therefore, no comparison can be made.

6.1.1 Small Strain Behavior

Comparison of small strain results ($\epsilon_a < 1\%$)is limited to the modulus and upper yield stress. Each of these parameters are discussed below. Much of the following discussion on the small strain behavior of conventional frozen MFS results can also be found in Andersen et al. (1994)

6.1.1.1 Young's Modulus

Young's modulus results for other frozen granular soils are available from studies by Kaplar (1963), Vinson (1978), Parameswaran (1980) and Baker and Kurfurst (1985). Each of these programs were previously described in Section 2.3. Table 6.1 summarizes the results from these programs and the effects of the different testing variables on the modulus as measured in these programs and in

the frozen MFS testing program. As described in Section 2.3, Kaplar measured the modulus of Peabody gravelly sand ranging from 34.5 to 47.1 GPa for a variety of temperatures using resonant beam techniques. Baker and Kurfurst measured the modulus of Ottawa 16–100 sand ranging from 24 to 45 GPa for different densities and two temperatures (–3.2 and –10° C) using acoustic wave propagation and on–specimen axial strain measurement techniques.

Vinson measured the modulus of Ottawa 20–30 sand ranging from 5 to 13.5 GPa for different densities and confining pressures using cyclic triaxial tests. However, these results are questionable due to the level of plastic straining which occurred during testing. Parameswaran measured the modulus of frozen Ottawa sand (ASTM C–109) ranging from 0.5 to 4.8 GPa using external displacement as measured by the loading device. These low values indicate significant seating and compliance problems associated with external strain measurements.

Effect of Relative Density on Young's Modulus

For frozen MFS, the Young's modulus shows a slight increase with increasing D_r (approximately 15% over a D_r range from 20 to 100%). Andersen et al. (1992) noted that for frozen MFS tests at –10° C, there was essentially no change in modulus with D_r; however, upon further review and after inclusion of tests at –15°, –20° and –25° C, a slight increase in modulus with increasing D_r was apparent (see Fig. 5.1) The modulus results from both the Vinson study and Baker and Kurfurst study also show an increase in modulus with increasing density. The results of Baker and Kurfurst show a similar level of increase as that of the current study (20% increase over a D_r range from 20 to 100%). The Vinson data show a larger increase for a wider range in of sand content (60% increase from sand–ice mixture to dense frozen sand) but these data are suspect given the large plastic deformations which occurred in the cyclic triaxial testing.

Effect of Confining Pressure on Young's Modulus

For all frozen MFS tests, the Young's modulus exhibited a slight decrease with confining pressure (approximately 11% over the entire pressure range, see Fig. 5.2). This behavior contradicts that measured by Vinson which showed a 69% increase in modulus for dense frozen specimens for a change in confining pressure from zero (unconfined) to 1.3 MPa. Vinson suggests that the increase in modulus was due to a possible increase in stresses at the contact points between sand grains, the closing of microfissures in the frozen sand due to higher confining pressures leading to a densification of the pore ice and higher modulus.

Andersen (1991) suggested that pressure melting at sand–ice contacts and an increase in unfrozen water content lead to the decrease in Young's modulus for frozen MFS tests at –10° C. The writer questions these mechanisms based on the additional results at –25° C, which also follow this trend, yet pressure melting can not occur at this temperature based on the phase diagram of ice (Fig. 2.68).

Effect of Temperature on Young's Modulus

Kaplar, in his study on Peabody gravelly sand, showed a 37% increase in modulus with decreasing temperature for a temperature range of –1 to –28° C (Fig. 2.78). Baker and Kurfurst show essentially no change in modulus for frozen Ottawa sand tested between –4 and –10° C. The frozen MFS Young's modulus results exhibit essentially no change with temperature (Fig. 5.3).

6.1.1.2 Upper Yield Stress

The measurement and presentation of the upper yield stress is a unique aspect of the frozen MFS testing program. As noted in Section 5.2, the upper yield stress, Q_{uy}, was strongly influenced by the strain rate and temperature, but was essentially not affected by relative density and confining pressure. Few other programs presented in the literature note the existence of an upper yield region.

However, Chamberlain et al. (1972), Parameswaran and Jones (1981), Baker and Kurfurst (1985) and Bourbonnais and Ladanyi (1985) note distinctive upper yield stresses in their tests on medium dense to dense frozen sands (see Section 2.3). For the frozen MFS tests, the use of on–specimen strain measurement and careful specimen preparation techniques allow the first complete exploration of this region.

Effect of Relative Density on Upper Yield Stress

The test results from Baker and Kurfurst indicate two distinct yield stresses, which they term the "lower yield stress" (i.e., Q_{uy}) and an "upper yield stress" (i.e., Q_p). They do not show the results for the Q_{uy} except in the case where the $Q_{uy} = Q_p$. Similar to the trends shown in Fig. 5.33, their results show that the Q_{uy} and Q_p are coincident (Type A curves) for lower density tests ($\gamma_d \leq$ 1.63 g/cm^3 in their tests) while at higher densities the peak strength was higher than the Q_{uy}. They note that in cases where the $Q_{uy} = Q_p$, the strengths were approximately the same for all tests at the applied strain rate of 1.67×10^{-4}/sec; thus, indicating that the Q_{uy} was not significantly affected by specimen density; a conclusion found for the frozen MFS tests.

Effect of Confining Pressure on Upper Yield Stress

Both the testing by Chamberlain et al. and Parameswaran and Jones indicate the yield stress increases with increases in confinement (Fig. 2.3.5). Their programs were conducted to higher levels of confinement than the frozen MFS program (280 MPa and 70 MPa, respectively, compared to 10 MPa in the frozen MFS program). Their trends within the confinement range of the current research are complexing and questionable. Parameswaran and Jones results show a similar trend with confinement as those of the frozen MFS program performed at fast strain rate (Fig. 5.12b). The results by Chamberlain et al. exhibit enormous confining pressure sensitivity but few tests exist within the confinement range of

the current study (2 tests). The writer has no explanation for this behavior.

Comparison of Q_{uy} with Polycrystalline Ice Behavior

Andersen et al. (1992) noted that the rate sensitivity exhibited by the upper yield stress for frozen MFS tests at –10° C is similar to that for the peak strength of polycrystalline ice tested at –7° C (Hawkes and Mellor, 1972, see Fig. 2.49). Both the frozen MFS at –10° C and the polycrystalline ice have identical power law coefficients (n = 4.6) for tests at similar strain rates. Andersen et al. also noted that the Q_{uy} for frozen MFS was approximately twice the peak strength of polycrystalline ice. Therefore, they suggested that the physical mechanisms controlling the yield behavior of frozen MFS might be similar to those controlling the strength of polycrystalline ice.

The frozen MFS tests at lower temperatures show that the rate sensitivity of the Q_{uy} decreases (power law coefficient increases) as the temperature decreases. It is possible that this trend in Q_{uy} behavior follows that of polycrystalline ice, where at lower temperatures for tests over the same range in strain rate, the rate sensitivity will decrease (flattening out of the flow curve). This trend in ice behavior can be estimated using the sinh–form of the combined creep law equation developed by Barnes et al. (1971) and presented in Section 2.2 (Eq. 2.21 and Figs. 2.55 and 2.60). Figure 6.1 compares the measured Q_{uy} behavior for frozen MFS with the peak strength of polycrystalline ice calculated from the sinh–form of the combined creep law equation. The peak strength of ice at –7° C, as measured by Hawkes and Mellor (1972), is also presented in the figure. It is clear in this figure that the flow curve for polycrystalline ice, as described by Barnes et al. equation, leads to increased power law coefficients (indicated by the leveling out of flow curves) as the strain rate increases or as the temperature decreases. This behavior is similar to that of Q_{uy} for frozen MFS as the temperature decreases; however, n

did not increase with increasing strain rate. Further research with regards to ice behavior in the range of strain rates studied in the frozen MFS program is required before more substantive conclusion can be drawn.

6.1.2 Large Strain Behavior

Significantly more effort has been placed on the measurement of large strain behavior of frozen sands, especially the behavior in the peak strength region.

6.1.2.1 Peak Strength

The peak strength behavior of frozen MFS was discussed in Chapter 5 and presented in Figs. 5.33 to 5.43. From these results, it is clearly evident that the peak strength of frozen MFS is influenced by all four testing variables. Trends in peak strength behavior found by other researchers are presented and compared below.

Effect of Relative Density on Peak Strength

The effect of relative density on the peak strength of frozen MFS is shown in Figs. 5.33 to 5.36. Test results show that for moderate strain rate tests at low confinement and low temperatures, the peak strength exhibited a bi–linear relationship with respect to increasing D_r, with looser specimens having Type A stress–strain curves ($Q_{uy} = Q_p$) and denser specimens showing a linear increase in Q_p with increasing density. This bi–linear trend also occurs for fast strain rate tests at –10° C, whereas fast strain rate tests at lower temperatures exhibit Type A responses for the full range of D_r. A similar bi–linear trend was noted by Baker and Kurfurst (1985) in their tests on frozen Ottawa sand (Fig 2.73).

Effect of Confining Pressure on Peak Strength

Figures 5.37 and 5.38 show the effect of confining pressure on frozen MFS tests. These figures highlight moderate strain rate results at –10° C since they are the only set of results to include tests at the intermediate confining pressures of 2

and 5 MPa. These trends for the –10° C tests were previously discussed in Andersen (1991) and Andersen et al. (1992). As shown in Fig. 5.37, the effect of increasing confinement leads to a decrease in the total stress friction angle for loose to medium dense MFS specimens. For dense specimens, a linear increase in strength with increasing confinement is found. The total stress friction angle at high confinement ranges from 1.6 to 15.6°, and it ranges from 11.2° to 15.6° at low confinement. These latter friction angles fall within the range of values found in the work by Sayles (1973), Andersland and Alkire (1973) and Shibata et al. (1985) as discussed in Section 2.3 (Fig. 2.74). As shown in Fig. 5.38, decreasing temperature tends to lead to a lower friction angle for tests on dense specimens. This result, though preliminary, is similar to that found by Shibata et al. in their tests on dense Toyoura sand.

Effect of Strain Rate on Peak Strength

The effect of strain rate on frozen MFS is shown in Figs. 5.39 through 5.41. In general, the power law coefficient tends to increase with increasing D_r and confinement. Andersen et al. (1992) note that the increase in the power law coefficient is probably due to the increased frictional resistance provided by the sand skeleton. This resistance is rate insensitive, within the range of strain rates studied, and increased strength due to the increased frictional resistance would lead to lower rate sensitivity (i.e., higher power law coefficients) of the frozen sand.

No other program in the literature provides information regarding the effects of relative density on the rate sensitivity of the peak strength. However, prior studies have examined the rate sensitive of dense sands. These programs were summarized in Section 2.3 and in Fig. 2.75. Figure 6.2 compares the strain rate sensitivity of dense MFS specimens at $\sigma_c = 0.1$ MPa at different temperatures and the rate sensitivity of dense sands at low or no confinement from other testing

programs. The figure clearly shows that the power law coefficients for frozen MFS fall within those from other programs. However, the rate insensitivity for $\dot{\epsilon} \geq 10^{-5}$/sec observed by Bragg and Andersland was not observed for the frozen MFS. Figure 6.3 shows the rate sensitivity of dense frozen MFS at $\sigma_c = 10$ MPa and the rate sensitivity exhibited in frozen tests by Shibata et al. at a similar level of confinement. The rate sensitivities of the frozen MFS are slightly lower than those by Shibata et al., but are in a similar range.

Effect of Temperature on Peak Strength

The effect of temperature on the peak strength of frozen MFS is shown in Figs. 5.42 and 5.43. In general, the peak strength increases linearly with decreasing temperature for the three strain rate conditions tested regardless of the relative density or confining pressure. Similar trends were noted in results compiled by Bourbonnais and Ladanyi (1985) for unconfined compressive strengths (Fig. 2.81).

6.1.2.2 Axial Strain to Peak Strength

The axial strain at peak strength is summarized in Figs. 5.44 through 5.47. The ϵ_p is relatively constant (4.9±1.2%) with respect to D_r for low confinement tests at all strain rates and temperatures (i.e., Type C curves), except for Type A curves which have $\epsilon_p = \epsilon_y \approx 0.5$ to 1%. The ϵ_p increased significantly with increases in confinement but also showed a decrease with decreasing temperature. There is an abrupt decrease in ϵ_p with strain rate for loose specimens when the stress–strain curve changes from Type C or D to Type A or B as the strain rate increases.

This data set represents the most complete evaluation of the axial strain to failure; however, other programs have presented failure strain results. Baker and Kurfurst (1985) show that the strain at failure is essentially constant for tests at

low densities (Type A responses), but increases as specimen density increases (Fig. 2.76a). Bragg and Andersland (1980) noted that an abrupt decrease in ϵ_p occurred at relatively fast strain rates ($\epsilon \geq 2x10^{-4}$/sec), where ϵ_p changes from 5 to 7% to less than 1% (Fig. 2.76c). The writer believes this transition strain rate corresponds to the change from a Type C to Type A curve.

6.1.3 Volumetric Strain Behavior

The volumetric strain responses are shown in Figs. 5.22 through 5.32 and the volumetric strain behavior is summarized, using the maximum rate of dilation and ϵ_v at 20% axial strain, in Figs. 5.48 through 5.53. The level of detail in describing the volumetric strain response has no parallel in the literature. In fact, few programs measure the volumetric response of the frozen sand. Ladanyi and Morel (1990) measured volumetric strain for a set of frozen tests on dense frozen Ottawa sand. They do not present any stress–strain or volumetric strain curves but do note that the rate of dilation at failure for the frozen sand decreased with increasing confining pressures; an observation similar to the reduction of the maximum rate of dilation with increasing confining pressure found for the frozen MFS tests. Their range in confining pressures was relatively small (zero to 0.3 MPa) compared to that for frozen MFS tests. Chamberlain et al. (1972), Baker et al. (1982) and Shibata et al. (1985) also measured volumetric responses in their testing programs. However, the responses were not evaluated beyond noting that the volumetric response decreased with increases in confining pressure; again an observation noted in the present frozen MFS program.

6.2 ANALYSIS OF FROZEN MFS USING COMPOSITE/PARTICULATE MODELS

This section compares the measured frozen MFS results with two models:

an isostrain composite model to estimate the Young's modulus and a dilatancy–hardening particulate model to estimate the peak strength.

6.2.1 Isostrain Model

The isostrain model developed by Counto (1964) has been previously described in Section 2.4. To review, the model considers the frozen sand to act as a composite material with a "stiff" sand aggregate placed in a "soft" pore ice matrix. The model assumes a "cube–in–a–cube" geometry and sums the strains of the three sections of the composite (two pure ice ends and a central section of ice and sand particle) caused by an applied axial stress to determine a composite modulus, E_c. The model assumes perfect bonding between the ice and the sand particle.

Andersen et al. (1992) performed an analysis for the frozen sand using a modulus for the sand particles (E_s) equal to 90 GPa (the average modulus for quartzite as quoted in Table 26.1 in Lambe and Whitman, 1969) and a modulus for ice (E_i) equal to 7.5 GPa based on one ice test at –10° C performed by Andersen (1991) during his work on frozen MFS. Considering both forms of the equation and using a volume fraction of solids (V_s) equal to 0.56 (D_r = 35%), the estimated E_c was 25 ± 2.5 GPa. For a V_s = 0.63 (D_r = 95%), the estimated E_c equaled 29 ± 3 GPa. These estimates agreed well with the average modulus of 26.6 ± 4.5 GPa found for the frozen MFS at –10° C; however, the increasing trend in modulus with increasing D_r, as suggested by the model, was not initially noted for the test results.

This prior analysis has been revised using the additional modulus results from tests at –15° C, –20° C and –25° C. The new analysis assumes that the modulus for the pore ice is equal to 9 GPa as determined by Sinha (1989). As shown in Fig. 5.1, there is a slight increase in Young's modulus with increasing D_r

(approximately 15% over the full scale of densities used). Figure 6.4 shows the results of the new isostrain model analysis using the revised pore ice modulus. The trend of the measured results shown in Fig. 5.1 is also shown. It can be clearly seen that there is a very good agreement between the measured and estimated moduli for the case of assuming the area–to–length ratio of the sand particle is unity. A higher estimated moduli is calculated if the sand particle is considered a perfect cube. This revised analysis and interpretation of the measured modulus results are also presented in Andersen et al. (1994).

6.2.2 Dilatancy–Hardening Model

The dilatancy–hardening model developed by Ladanyi (1985) and Ladanyi and Morel (1990) was previously discussed in Section 2.4. The model attempts to estimate the peak strength of the frozen sand by accounting for the increase in the frictional strength of the sand skeleton due to the increased level of negative pore pressure provided by the pore ice, as well as adding the shear strength of the pore ice matrix to the overall strength produced by the composite material.

Andersen et al. (1992) presented the results of an analysis using the dilatancy–hardening model for dense frozen MFS tests at –10° C. This previous analysis used the available results from the unfrozen MFS testing program to develop the unfrozen sand parameters used in analysis. The effect of confinement was also analyzed using the prior available unfrozen sand and ice data. The following analysis uses more complete results from the unfrozen MFS testing program to develop more refined unfrozen sand parameters and analyzes the effect of confinement. The prior analysis also has been expanded to include the entire range of D_r, the effect of temperature and applicability to the limited consolidate–freeze results.

6.2.2.1 Unfrozen Sand Parameters

In order to use the model, unfrozen sand parameters are required, namely the maximum effective stress friction angle (ϕ'_{max}) and the critical effective confining pressure (σ'_{3crit}) for the sand (see Section 2.4). For ϕ'_{max}, the results from the unfrozen MFS testing program, presented in Section 4.3, will be used. The friction angles at maximum obliquity for all undrained tests were plotted in Fig. 4.30 with an average value of 34.9° found for undrained tests having effective stress at failure (p'_f) > 1 MPa. The effective friction angle decreased at high mean effective failure stresses ($p'_f \geq 10$ MPa), but this occurred only in the CIDC tests. For dense specimens at low confinement ($\sigma'_c \leq 0.1$ MPa), ϕ' values from drained or undrained tests averaged 36.2° with a $c' = 0.017$ MPa, but these values occurred at low p' levels before dilatancy–hardening of the sand had occurred. Once the undrained effective stress path started to climb up the failure envelope (Fig. 4.44), the ϕ' reduced to the lower 34.9° level; therefore, a $\phi'_{max} = 34.9°$ is an appropriate value for analysis.

The σ'_{3crit} can be estimated using the results of the steady state analysis presented in Section 4.4. For the unfrozen sand, σ'_{3crit} occurs when the pore pressure change at failure (or volume change at failure) is zero. Based on the correlation between the pore pressure parameter at failure, A_f, and the Ψ–value (Fig. 4.54), the Ψ corresponding to the condition of an $A_f = 0$ was calculated as –0.061. This Ψ–value can be used to determine a line in void ratio – log mean effective stress space (e – log I′) which defines values of σ'_{3crit}. This line is presented in Fig. 6.5. The σ'_{3crit} (or I'_{crit}) can now be determined for any void ratio (or D_r) by using this line.

6.2.2.2 Pore Ice Parameters

The pore ice supplies tensile stresses to the sand skeleton which allow

dilatancy–hardening to occur and supplies shear stresses to the overall composite material. Based on test results by Hawkes and Mellor (1972) (Fig. 2.46) and Haynes (1978) (Fig. 2.59), the tensile strength of ice exhibits little change with strain rate or temperature over the range of conditions used for the frozen MFS tests. An average tensile strength of 2.15 MPa, based on the results from Hawkes and Mellor (1972), was used for all analyses.

Little data are available on the compressive strength of polycrystalline ice under the conditions used in the frozen MFS testing programs, i.e. constant rate of strain tests at various strain rates, confining pressures and temperatures. Jones (1982) presents results of constant rate of strain tests on polycrystalline ice specimens (grain diameter of 1 mm) at an average temperature of $-11.6 \pm 0.8^{\circ}$C. These tests consisted of unconfined and confined triaxial tests with levels of confinement up to 85 MPa (see Section 2.2 for more details). Results for unconfined tests and tests at a nominal 10 MPa confinement at different strain rates are shown in Fig. 6.6. Power law coefficients of 5.43 and 4.26 were determined for the unconfined and 10 MPa confinement tests, respectively. Using these results as a baseline condition, the combined creep law (Section 2.2) was used to generate ice strengths for temperatures of -10°C, -15°C, -20°C and -25°C. The variables used in calculating ice strengths for both low and high confinement cases are summarized in Table 6.2. The computed ice strengths are plotted in Fig. 6.7. Also shown in the figure are six test results from Murrell et al. (1989) on polycrystalline ice of 1 mm grain size. Comparison of these strengths show that at low confinement the measured strength is lower than that calculated at -10°C, but approximately the same at -20°C. At high confinement, the measured strength at -20°C is slightly higher than that calculated. Although this comparison is certainly not conclusive, it can be seen that the calculated strengths are reasonable

compared to other measured data.

6.2.2.3 Results of Analysis

With the unfrozen sand and ice parameters, the analysis proceeded as follows.

1) The σ'_{3crit} was determined for each frozen MFS test based on the specimens D_r (void ratio).

20 The σ'_{3crit}, the confining pressure and the tensile strength of 2.15 MPa was used to determine if the specimen followed the cavitation or non–cavitation formulae (see Section 2.4). In general, low confinement tests (σ_c = 0.1 MPa) would cavitate while high confinement tests (σ_c = 10 MPa) would not cavitate.

3) The appropriate calculation for the enhanced frictional strength of the sand was then performed and the ice strength, corresponding the actual strain rate and temperature of the test, was added to obtain the peak strength of the specimen.

Figure 6.8 through 6.11 show plots of measured and predicted peak strengths versus strain rate for loose ($D_r \approx 35\%$) and dense ($D_r \approx 95\%$) specimens under low and high confinement. As shown in the figures, the predicted Q_p from the dilatancy–hardening model is consistently lower than its measured counterpart for all conditions. The difference between the measured and predicted values of Q_p increased as the temperature decreases. The best correlation between the measured and predicted Q_p occurred for dense specimens at low confinement and –10° C (Fig. 6.9) where the predicted Q_p was 75 to 92% of the measured peak strength. In terms of rate sensitivity, the trends are not consistent. The model predicts a similar rate sensitivity to that measured for loose specimens at low confinement (Fig. 6.8) and dense specimens at high confinement (Fig. 6.11).

However, the predicted power law coefficients are significantly lower for loose specimens at high confinement (Fig. 6.10) and slightly higher for dense specimens at low confinement (Fig. 6.9).

The difference between the predicted and measured peak strength was evident for other relative densities as illustrated in Fig. 6.12, which shows the measured and predicted Q_p results for moderate strain rate tests at low confinement (the test condition with the most varied range in D_r). This figure shows that the predicted increases in Q_p with increasing D_r are fairly reasonable, but the model fails to capture the bi–linear behavior exhibited by tests at the lower temperatures (i.e., where $Q_{uy} = Q_p$ for Type A curves).

Use of the dilatancy–hardening model for estimating the strength of the consolidate–freeze tests lead to similar results as found for the conventional frozen MFS tests. The five consolidate–freeze tests performed at low or high confinement at –10° C along with the predicted strengths are shown in Figs. 6.9 and 6.11. As seen in the figures, the predicted peak strengths are lower than those measured, even for the tests at high confinement which have measured strengths lower than those measured in the conventional frozen MFS tests.

6.2.2.4 Discussion of Dilatancy–Hardening Model Results

The results of the analysis with the dilatancy–hardening model clearly show that the model is deficient in estimating the strength of frozen MFS regardless of the density, confining pressure, strain rate and temperature. The model is most deficient in estimating the peak strength with decreases in temperature where, as shown in Fig. 6.13, the ratio between predicted and measured peak strengths decreases with decreasing temperature [perhaps due to errors in extrapolating Jones (1982) ice data to lower temperatures]. The highest predicted–to–measured peak strength ratio, $Q_{fs}/Q_p \approx 1$, occurs for dense frozen tests at low confinement,

slow strain rate and –10° C.

Problems in applying the model to frozen MFS have been discussed in Section 2.4. To review, there is a strain incompatibility associated with the peak strength in ice, which occurs at ≈ 1% ϵ_a, and the peak undrained strength of a dilative sand, which for unfrozen MFS can occurs at 15 to 25% ϵ_a. For example, dense unfrozen MFS at low confinement in undrained shear develops its peak strength at 20% (Test C–34 Fig. 4.41), while a similar specimen under high confinement approaches its peak strength at strains of only 2% (Fig. 4.41).

There is also a difference in "effective" stress systems between unfrozen sand (no ice–sand contact forces) and frozen sands (ice–sand contact forces present) (Fig. 2.104). The use of polycrystalline ice strengths for tests with grain sizes at 1 mm is also a questionable assumption given that the ice in the frozen sand's pore space may have a grain size one to two orders of magnitude lower than the minimum grain size for which tests results are currently available in the literature (Section 2.2). The model also assumes that the frozen sand is "unconsolidated" and therefore does not account for effective stresses on the sand prior to freezing. However, comparison with the consolidate–freeze tests suggest that this is not a major variable.

If the components of the predicted frozen sand strength are examined individually, it is found that the enhanced frictional strengths of the sand approximate those measured in CIUC tests in the unfrozen MFS testing program (which used a high back pressure to prevent cavitation). Dense specimens under low confinement lead to the largest amount of dilatancy–hardening in the unfrozen MFS tests and, as predicted by the model, lead to some of the larger predicted sand strengths in the analysis. For example, the predicted enhanced sand strength, Q_{ss} ($= 2 \cdot q_{ss}$) is 6.0 MPa for dense ($D_r = 95\%$) frozen specimens at $\sigma_c = 0.1$ MPa,

while the measured Q_p for undrained test C–34 (D_r = 94.9%) was 5.5 MPa. For D_r = 95% at high confinement, the model predicts non–cavitation conditions and the critical confining stress is 2.52 MPa (Fig. 6.9), leading to a predicted sand strength which also approximates the measured undrained peak strength from dense undrained tests at high confinement [e.g. Q_{ss} = 6.8 MPa for a D_r = 95% frozen specimen at σ_c = 10 MPa ($\sigma_c > \sigma'_{crit}$), while Q_p for unfrozen test C–22 was 6.5 MPa).

The pore ice compressive strength is not as well defined and may be the most questionable variable in the analysis. The compressive ice strengths used in the analysis were an extension of existing ice data at one temperature, and, although these extrapolated strengths appear reasonable, their extension to the possible strength of the pore ice is suspect (e.g., due the smaller grain size of the pore ice). Moreover, the interaction of the pore ice with the sand skeleton may lead to a "strengthening" of the pore ice. The behavior of the pore ice deserves additional study.

6.3 DISCUSSION OF FROZEN SAND BEHAVIOR

This section discusses possible mechanisms involved in the deformation and strength of frozen sands, in particular frozen MFS. The discussion will focus on the similarities and differences between frozen MFS behavior and that of its principal components, sand and ice. The writer notes that the deformation and strength mechanisms discussed are inferred from the preceding analyses and the measured unfrozen and frozen MFS behavior presented in Chapters 4 and 5, respectively.

6.3.1 Small Strain Behavior

6.3.1.1 Young's Modulus

The small strain behavior, most notably the modulus, of the unfrozen and frozen MFS exhibit very different behaviors. For unfrozen MFS, Figs. 4.35 and 4.36 show that Young's modulus is almost independent of relative density and increases with effective confining stress from 0.2 to 4 GPa. In contrast, the Young's modulus of frozen MFS varied only slightly with all testing variables with an average value of 26.5 ± 4.0 GPa for all tests. That is, the frozen modulus was found to increase slightly with increasing relative density, and to decrease slightly with increasing confining pressure for all temperatures. For ice, the modulus has been found to increase with decreasing temperature (see Section 2.2, Sinha 1989), but the modulus variation is minor over the current research's temperature range of 15° C (≈ 9.1 ± 0.1 GPa).

The measured moduli for the unfrozen and frozen MFS reflect their strong differences in initial behavior. The unfrozen results reflect the modulus of the sand skeleton since the increasing effective confining (consolidation) pressure causes an increase in contact stresses between sand particles and hence a stiffer response when a deviator stress is applied. For frozen MFS, the measured modulus reflects that of the composite sand and ice. In this case, the elastic deformation of the individual sand particles, along with the elastic deformation of the ice matrix, act in concert to create the composite modulus. Since the sand particles are stiffer than pore ice, more sand in the composite should lead to an increase in the composite modulus. Moreover, increased confinement on the sand skeleton prior to freezing (i.e. consolidate–freeze testing) should have no effect on the composite modulus since additional confinement only affects the condition of the sand skeleton and not the individual sand particles.

The isostrain model by Counto provides valuable insight into the Young's modulus behavior as a function of sand content. However, it must be noted that sand–to–sand contacts do exist in the frozen sand, although only over a very small area of each sand particle. Contrary to the assumption that the sand is completely surrounded by ice (the isostrain model's depiction), in the writer's opinion, it would be more precise to consider the entire sand skeleton as imbedded in a matrix of pore ice. This latter composite structure is schematically illustrated in Fig. 6.14. This proposed structure is only a slight variation of the one proposed by Andersen (1991) in that it shows that sand–to–sand contacts do exist occasionally on any given plane through the frozen sand.

6.3.1.2 Upper Yield Region

Examination of the upper yield region represents one of the unique attributes of the unfrozen and frozen MFS programs. For unfrozen MFS, the upper yield stress increased linearly with increases in relative density (the rate of increase was greater with higher confinement) and with increases in effective confining pressure (see Figs. 4.37 and 4.38). In contrast, Q_{uy} for the frozen MFS was relatively independent of D_r and σ_c, but highly influenced by the strain rate and temperature. This analysis of the behavior in the upper yield region has no parallel in the literature.

Parameswaran (1980) noted a yield stress at small strains in some tests on dense frozen Ottawa sand (Type C curves shown in Fig. 2.80). This yield occurred prior to the development of higher deviator stresses (i.e., the specimens peak strength). He attributed this stress drop to the yielding or "rupture" of the pore ice matrix. Orth (1985) also recognized a distinct low strain yielding of frozen Karlsrude sand followed by a drop in stress (Type A or B curve) which he attributed to the initiation of pressure melting followed by dynamic

recrystallization of the pore water once stresses reduced. The writer much prefers Parameswaran's hypothesis that the pore ice yields or "ruptures" prior to the strain hardening (or softening) of the frozen sand. This rupture may correspond to internal fracturing of the pore ice which occurs as the ice reaches failure. For the consolidate–freeze tests, the "loss" of this distinct upper yield behavior was surprising and unexpected. No explanation currently exists to explain this observation. Further testing at lower applied confining stresses and faster strain rates may shed some light on this phenomenon.

6.3.1.3 Volumetric Behavior in Small Strain Region

For virtually all frozen MFS tests there was no volumetric strain up to the Q_{uy}. For unfrozen MFS tests, the volumetric response was immediate compression leading to pore pressure increase in undrained tests or volumetric contraction in drained tests.

6.3.2 Large Strain Behavior

6.3.2.1 Peak Strength Region

The post–upper yield behavior of frozen MFS take numerous forms (Section 5.2.2.1, Fig. 5.21). For Type A curves, the specimen continuously strain softens ($dQ/d\epsilon_a < 0$) with continued shear. In this case the peak strength is also the upper yield point. Type B curves may first slightly strain soften or slightly strain hardening, but the deviator stress at large strains are essentially constant with the peak strength is only slightly higher than Q_{uy} (or may coincide with the Q_{uy}). Type C and D curves exhibit significant strain hardening after reaching the upper yield point. Type C curves reach peak strength at moderate strain levels (typically 3 to 7 % ϵ_a) then exhibit significant strain softening with continued straining. Type D curves exhibit continuous strain hardening to high strain levels after reaching the upper yield stress, but the maximum rate of strain hardening can be

less than that of a Type C curve for frozen sand specimens with similar densities.

Numerous researchers (e.g., Orth 1985) have noted similar changes in stress–strain response for other frozen sands, although their curves were not quantified by the declaration of a curve type. The majority of previous testing programs consisted of unconfined tests which exhibit Type A or Type C curves. The mechanism most cited as reasons for Type C curves is that the frictional resistance of the sand increases the frozen sand strength after the "initial" yield has occurred in the pore ice, which is estimated to occur at approximately 1 to 2% axial strain.

6.3.2.2 Volumetric Strain Behavior at Large Strains

Andersen (1991) and Andersen et al. (1992) note that the volumetric behavior of frozen sand at large strains does not coincide with that for drained shear of unfrozen sands . The results presented in Chapters 4 (Figs. 4.18 and 4.20) and 5 (Figs. 5.22 through 5.32) clearly substantiate this statement. Unfrozen MFS in drained shear showed significant dilation at low levels of confinement, but this dilation is suppressed with increased confinement to where ultimately the specimens always exhibit contraction during shear. This was illustrated for constant p' CIDC tests (Fig. 4.47) but a similar phenomenon occurs for undrained tests (via pore pressure response) where the dilative response is suppressed with higher confining pressure (Fig. 4.41). In contrast, frozen MFS tests exhibit dilation at all confining pressures and relative densities (but approach zero at high confinement levels). Andersen et al. (1992) state that the dilative response is due not only to the sand skeleton but also involved expansion of the pore ice matrix. For example, the volumetric response for loose specimens at low confinement and fast strain rates leads to final D_r values $< 0\%$.

6.3.3 Frozen Sand Mechanisms as Presented by Ting et al. (1983)

The mechanisms of strength as proposed by Ting et al. (1983) were summarized in Table 2.3 and were derived from three components: the pore ice, the sand skeleton and the ice–sand interaction. The writer believes that these components are appropriate; however, some of the concepts proposed by Ting et al. are debatable. For example, the structure of the pore ice in the sand skeleton may be ultra–fine grained granular ice (diameters << 1 mm) which may exhibit significantly different stress–strain behavior than that of granular ice normally found in nature or tested in the laboratory (diameter ≈ 1 mm). However, from a conceptual point of view, the methodology used to describe the behavior of frozen sands (i.e., the three components) appears reasonable.

Andersen (1991) presents a discussion of the frozen sand mechanisms as presented in Ting et al. (1983) and compares the proposed structure and deformation–strength mechanisms with the observed behavior of frozen MFS at –10° C. Andersen's arguments are summarized below.

1) Proposed Structure. Andersen notes that the structure proposed by Ting et al. overemphasizes the number of sand contacts. He proposed an different structure where the sand particles are suspended in a pore ice matrix. This structure was illustrated in Section 2.3 (Fig. 2.67). Andersen based his proposed structure on the previously described isostrain model where the sand particles are surrounded by the ice matrix. (A slight variation of this structure is presented as Fig. 6.14).

2) Ice Strength. Ting et al. suggest that the ice strength does increases with the addition of sand particles, but they believed that this increase was relatively small over the full range of specimen densities compared to the other components which contribute to frozen sand strength. Andersen notes that the data which Ting et al. relied upon were developed from two different specimen preparation techniques (snow and sand mixture versus uniaxial freezing of the pore water) which may inherently create different pore ice grain sizes and behaviors (see above). Andersen hypothesis that the smaller pore ice grain size (from uniaxial freezing) may lead to a lower pore ice strength compared to the strength for pore ice with larger grain sizes (from snow–sand mixing).

3) Sand Strength. Ting et al. and Andersen agree that the strength of the sand is difficult to determine without knowledge of the effective stresses acting on it. Andersen suggests that it may be more advantageous to consider the frozen sand as a composite where the properties of the sand particles are more important than the properties of the sand skeleton.

4) Ice–Sand Interaction. Andersen argues that hypotheses based on whether the presence of the pore ice effects the sand skeleton or vice versa are not well suited to frozen sand behavior. For example, Andersen notes that the concept of enhanced sand strength due to higher tensile stresses in the pore ice (as used in development of the dilatancy–hardening model) is not fully accounted for by considering the dilation to be only attributable to the sand skeleton. He suggests that the interaction between the ice and sand should be considered in terms of composite behavior.

In the writer opinion, the difference in describing frozen sand behavior between Ting et al. and Andersen is more a question of the level of observation. The concepts proposed by Ting et al. attempt to describe the mechanisms of frozen sand strength in terms of the macro–level behaviors of its two principal components, i.e., the sand skeleton and pore ice matrix. Andersen's proposed use of composite behavior methodology implies a similar direction; description of the frozen material in terms of its micro–level behavior, i.e., sand particles and pore ice grains. The writer believes that future consideration of frozen soils must consider the behaviors associated with the "micro–level" of the individual components (i.e., grains) and the behavior on the "macro–level" of the frozen sand (i.e., sand–ice interaction).

6.4 CONCEPTUAL BEHAVIOR OF FROZEN SAND AS A COMPOSITE

The concept that frozen soils may be more appropriately characterized as a composite has been proposed by others; for example, Ladanyi (1981). However, analysis of frozen soils as a composite requires experimental results, both at the micro– and macro–levels of observation, for different density frozen soils under

various confining pressures, strain rates and temperatures. This analysis also requires information on the behavior of the various components which make–up the composite (i.e., the soil and pore ice). The following discussion presents simple concepts for the modeling of frozen MFS as a composite material. These concepts were principally derived from the observed stress–strain and volumetric behaviors for frozen and unfrozen MFS in the current research. The behavior of polycrystalline ice as described in the literature was also used in forming these concepts.

The writer stresses that the following discussion does not lead to a quantitative model complete with constitutive relationships. Rather, these concepts should be considered as simple "building blocks" which can form the basis of a model. The writer also realizes that some of these concepts are speculative. Little or no experimental evidence, especially on the micro–level of observation, exists on the behavior of frozen sands over a large range of strains. Knowledge is limited of the behavior of the sand particle–to–sand particle, sand–to–ice or ice–to–ice contacts and the effects of unfrozen pore water on overall frozen sand behavior. Evaluation of these important behaviors are needed for a more complete understanding of frozen soil behavior. Given these limitation, the following discussion uses the measured macro–behavior of frozen sands, in particular MFS. In fact, the measured behaviors described in Chapters 4 and 5 were used as extensively as possible to develop these concepts.

To simplify the conceptual description, the influence of unfrozen pore water, air inclusion or other impurities is ignored. The concepts are presented in a format following the presentation of the frozen MFS test results in Chapter 5. The small strain behavior is first described followed by the large strain behavior.

6.4.1 Small Strain Behavior

6.4.1.1 Initial Stress–Strain Response (Fig. 6.15a)

As discussed earlier, the isostrain model provides valuable insight into the behavior of frozen sands from the perspective of a composite material. The initial straining of the composite involves the deformation of the "rigid" sand particles and "soft" pore matrix ice in concert, as suggested by the "perfect bonding" assumption in the isostrain model. Continued deformation of the frozen sand leads to initial yielding, but this yielding is not necessarily only due to the pore ice matrix as suggested by the extension of the isostrain model (see Section 2.4.1). Initial straining of the frozen sand will incur both the initial yielding of the sand–ice bonds as well as the yielding of the pore ice matrix. Conceptually, these combined yielding behaviors dictate the yielding behavior of the composite. Pore ice yielding could possibly involve the mobility of dislocations (pile–up and glide) which may begin to occur soon after elastic deformation of the ice grains begins. At slower strain rates, pore ice yielding may also include diffusional flow along ice grain boundaries. [In this case, the presence of unfrozen water may also contribute to the yielding process.] Fig. 6.15a shows the initial stress–strain response for test FRS109 (–25° C, D_r = 74.5%, σ_c = 0.1 MPa, moderate $\dot{\epsilon}$) illustrating this initial strain behavior.

In terms of sand–ice interaction, composite yielding incurs the loss of the "perfect bonds" between the pore ice and sand grains. However, though the "perfect bond" is broken, the composite is still intact. Therefore, the sand does not reach a point where it behaves as an unfrozen sand but continues to interacts with the pore ice matrix.

6.4.1.2 Upper Yield Region (Fig. 6.15b)

After the initial yielding of the composite, as described above for the initial

straining, the composite continues to strain with the pore ice yielding but still intact. This yielding is analogous to the creep or ductile deformation of ice described in Section 2.2 (Fig. 2.47). However, with continued deformation the pore ice matrix begins to fracture and crack. Unless failure occurs by brittle fracture, internal fracturing does not necessary mean the pore ice is crumbling or becoming unstable but that the pore ice is developing microcracks. This internal fracturing phenomenon has been observed in pure polycrystalline ice using acoustic emission as well as visible measurement techniques (e.g., see Cole 1986, and Murrell et al. 1989). Cole and St. Lawrence (1981) observed that the highest intensity of the cracking activity in polycrystalline ice occurred slightly before or at the peak strength ($\approx$ 1% axial strain). In addition, the initiation of extensive internal fracturing may occur instantaneous in the pore ice and continue to occur for a wide range of strain and stress levels (Murrell et al. 1989). However, the internal fracturing may also be influenced by the rigid sand particles since they may "interfere" with the normal yielding process (stress concentrations at sand–ice contacts). In fact, presence of the sand particles may enhance the fracturing process to where fracturing of the pore ice may occur where in ice alone fracturing may not occur, or the intensity of the fracturing would be less.

Conceptually, the initiation of fracturing behavior can be seen as the mechanism causing the upper yield point. As a frozen MFS specimen reaches its upper yield stress, the rate of yielding in the pore ice (i.e., cracking activity) rapidly increases. Since a composite follows the behavior of its components, the rate and temperature sensitivities associated with polycrystalline ice behavior are more dominant at this point. However, the strength (Q_{uy}) of the composite is based on the interaction of the sand particles and the "intact" pore ice matrix as discussed previously for the case of initial strains. This simultaneously explains

why measured Q_{uy} values are essentially independent of relative density or confining pressure (which affect sand skeleton behavior), but are strongly influenced by the strain rate and temperature, and why Q_{uy} for frozen MFS exceeds the peak strength of polycrystalline ice tested at a similar strain rate and temperature.

As straining continues, the rapid cracking causes the structure of the pore ice matrix to evolve, weaken and become less "intact". The "damage" caused by pore ice fracturing causes many of the contacts points between ice grains to be separated (microcracks) as well as many sand–to–ice contacts (loss in ice tensional strength). However, this does not mean that the pore ice matrix has "failed" but rather that it is evolving from an "intact" (stronger) matrix material to a more "granular" (weaker) matrix material. The transition in the pore ice matrix from "intact" to "damaged" represents the upper yield stress. Fig. 6.15b shows the upper yield region for test FRS109 illustrating the continuous yielding behavior up to Q_{uy}.

6.4.2 Large Strain Behavior

The large strain behavior of frozen sands involves a number of complex processes making its description in terms of composite behavior difficult and speculative. However, the deformation and strength mechanisms involved include those used to describe the composite behavior at smaller strains and extend upon those involved in the Q_{uy} region. Post–upper yield behavior of the composite is dictated by the granular nature of both the sand and fracturing pore ice. Therefore, confining pressure and sand density become more important in the composite's stress–strain behavior, but strain rate and temperature still play a role in this behavior. Large strain behavior is presented for low confinement and high confinement cases and the presentation also illustrates the importance of san

density.

6.4.2.1 Low Confinement (Figs. 6.16 a and b)

For tests at low confinement, the composite expands with continued deformation as the pore ice fractures. The fracturing also allows greater mobility of the individual granular components. Whether post–Q_{uy} strengthening or weakening occurs depends on whether strain hardening mechanisms, such as the interaction of the sand particles with each other and the sand's interaction with the "damaged" pore ice [i.e., frictional resistance and dilatancy as suggested by Rowe (1962)], exceeds the strain softening mechanisms which are predominantly related to the continued fracturing of the pore ice. First, the strain hardening or Type C–curve–producing process is presented then the strain softening or Type A–curve–producing process.

For tests which undergo post–Q_{uy} strengthening (i.e., $Q_p > Q_{uy}$), the rate and extent of pore ice fracturing (softening process) is relatively low allowing strengthening due to frictional resistance to occur. Conceptually, the rigid sand particles, now more free to interact in the "damaged" ice matrix, behave in a similar manner as unfrozen sands (i.e., dilatancy and particle interference). However, unlike unfrozen sand, the sand particles are interacting with the pore ice grains as well as with each other; thus, providing higher composite strengths. Therefore, as shown in Fig. 6.16a, denser specimens (FRS56) want to dilate more than looser specimens (FRS36) and will exhibit a stronger rate of strain hardening.

Both the frozen sand's frictional resistance (dilatancy) and pore ice fracturing combine to accelerate the rate of volumetric expansion of the composite. However, the accelerating rate of dilation also reduces the effects of sand–ice interaction since the combined expansion reduces the available frictional resistance (lowers density of the composite as sand particles mover further apart). With

continued deformation, the expansion due to pore ice fracturing and frozen sand dilation reduce the ability of the composite to strengthen; thus leading to the peak strength. The peak strength occurs at relatively moderate axial strain levels (3 to 7% in the frozen MFS tests have σ_c = 0.1 MPa). Post–peak strength behavior consists of a further decrease in the strengthening process (frictional resistance), but a continuation of the weakening process (pore ice fracturing), with continued deformation. However, both the strengthening and weakening processes continue to combine to create even faster rates of volumetric dilation while the strength of the composite begins to decrease.

Finally, the extensive fracturing of the pore ice matrix allows no further strengthening to occur. In fact, the fracturing leads to a continuous, near–constant rate of weakening or strain softening. In other words, any attempt by the composite to strengthen (via frictional resistance) is constantly countered by the expansion caused by pore ice fracturing. This leads to a condition where the rate of volumetric dilation and the amount of strain softening become constant with continued strain. Figure 6.16b shows the above described behavior. This entire strain hardening behavior is also evident in the frozen MFS shown in Fig. 5.22, which shows the effect of D_r for low confinement, moderate strain rate tests for all tested temperatures. Note that the majority of curves are Type C curves and that faster strain hardening (strengthening) occurs for the densest specimen (more sand–to–sand contacts) and that the volumetric strain increases more rapidly as specimen density increases. A similar strain hardening behavior is shown for 1) tests on dense specimens at –10° C and various strain rates (Fig. 5.27a) and 2) moderate strain rate tests on dense specimens at various temperatures (Fig. 5.31a).

Description of post–Q_{uy} strain softening (or Type A curve) involves a number of speculative assumptions, especially with respect to pore ice fracturing.

However, Type A curves typically occur at faster strain rates or lower temperatures where the pore ice exhibits a more brittle (fracture) behavior. Conceptually, this brittle behavior not only leads to a higher initial pore ice matrix strength (exhibited by higher Q_{uy}) but faster and more extensive pore ice fracturing at the Q_{uy} point. If a significant portion of the pore ice matrix becomes fractured, the ability to generate additional strength beyond Q_{uy} (via frictional resistance) is lost and the composite softens. That is, the pore ice fracturing may be so extensive, the 'instantaneous' volumetric expansion does not allow for any composite strengthening to occur.

Immediately after this initial pore ice "rupture" at Q_{uy}, there is still little to no frictional resistance associated with sand–to–sand or sand–to–ice interaction. Therefore, the synergistic combination of frictional resistance and pore ice fracturing that led to an accelerating rate of volumetric strain for the case of strain hardening does not occur. However, the composite does dilate, due primarily to the continued pore ice fracturing, and this dilation occurs at a near constant rate (see Fig. 6.16a). With continual deformation, sand–to–sand contacts are established and the composite attempts to strengthen; however, similar to the post–Q_p strain softening for Type C curves, the frictional resistance and the pore ice fracturing mechanisms combine to accelerate the rate of volumetric dilation, thus weakening the composite. After sufficient deformation, a steady state condition develops between the frictional resistance and pore ice fracturing leading to a constant rate of strain softening and constant rate of dilation.

The Type A curve composite behavior is illustrated in Figs. 6.16a and b. This behavior, with respect to increasing strain rate, is evident in Figs. 5.25 b and c for loose specimens at low confinement (note the initially linear $d\epsilon_v/d\epsilon_a$ response for the fast strain rate tests). In terms of decreasing temperature, this behavior is

evident in Fig. 5.29c for loose specimens under low confinement and fast strain rate (again note the initially linear post–Q_{uy} $d\epsilon_v/d\epsilon_a$ response).

In summary, for both the strain hardening and strain softening cases, competing mechanisms are simultaneously occurring: composite strengthening due to frictional resistance, and composite weakening due to pore ice fracturing. The pore ice fracturing mechanism may be strain rate and temperature sensitive but the frictional resistance mechanism is less (or not) sensitive since it involves the sand skeleton, which is rate and temperature insensitive, and sand–ice grain interaction.

6.4.2.2 High Confinement (Figs. 6.17 a and b)

For high confinement, the same mechanisms (frictional resistance and pore ice fracturing) are occurring. However, strengthening due to the dilation and weakening due to pore ice fracturing are suppressed by increased confinement which also leads to less volumetric expansion of the composite. As for low confinement tests, post–Q_{uy} behavior for high confinement tests can range from strain hardening, leading to Type D curve, or initial strain softening, leading to Type B curve.

To strain harden, strengthening due to dilatancy and frictional resistance strength mechanisms must occur, but with dilation suppressed, strengthening occurs through "particle" interference. However, this interference includes not only that between the sand particles but also that between sand particles and ice grains. In fact, it may be more appropriate to consider the post–Q_{uy} strength behavior at high confinement in terms of the interference of sand particles in a "damage" pore ice matrix. With continued deformation, strengthening due to particle interference can lead to a significant strength gain above Q_{uy} stress levels. It also follows that denser specimens, which have more sand–to–sand contacts, will

exhibit higher tendency to strain harden with continued deformation than looser specimens, all other variables constant. This behavior is illustrated by FRS52 (D_r = 90.8%) in Figs. 6.17a and b.

For strain softening to occur, the pore ice must fracture. Even at high confinement, pore ice fracturing still occurs during deformation with the level of fracturing still a function of the "brittleness" of the pore ice matrix, i.e., faster strain rates or lower temperatures lead to more extensive fracturing. Therefore, at faster strain rates or lower temperatures, the composite cannot initially strengthen after Q_{uy} due to the weakening caused by pore ice fracturing. However, due to the high confinement, strengthening due to "particle" interference still occurs such that denser specimens can develop a significant strength above Q_{uy} with continued deformation (Type D curves). For looser specimens, the weakening and strengthening processes may balance out leading to constant composite strength with continued deformation. This behavior is illustrated for FRS40 (D_r = 37.4%) in Fig. 6.17a and b. These post–Q_{uy} composite behaviors are also evident in other conventional frozen MFS results. The effect of increasing strain rate (leading from Type D to Type B curves) is shown in Fig. 5.26d which shows the results of high confinement tests on loose specimens at –25° C. These tests show that as the strain rate increases the amount of post–Q_{uy} strain softening increases to where at the moderate and fast strain rates Q_{uy} represents the peak strength, yet for all cases the resistance remains constant at large strains. The effect of decreasing temperature (also leading from Type D to Type B curves) is shown in Fig. 5.30b which shows high confinement, moderate strain rate tests on loose specimens. It is clear to see in the figure that post–Q_{uy} strain hardening becomes more difficult as temperature is decreased, until at –25° C there is post–Q_{uy} strain softening followed by essentially constant deviator stress.

6.4.2.3 Influence of Volumetric Behavior on Strain Softening

Based on the preceding discussion, the stress–strain behavior of the frozen sand is highly dependent on its volumetric strain. If dilation occurs, the frozen sand will exhibit strain softening; if dilation is suppressed, so is the softening. As an evaluation of this correlation, Fig. 6.18 shows a plot of the rate of strain hardening at the maximum rate of dilation versus the maximum rate of dilation. The results are presented in terms of curve type. This figure includes all tests prepared by multiple sieve pluviation, good to poor stability and lubricated ends. As clearly illustrated in the figure, there is trend of increasing strain softening (or decreasing strain hardening) with increasing maximum rate of dilation. It should be noted strain softening/hardening occurs at the maximum rate of dilation for all curve types, which is contrary to unfrozen drained sand behavior where the maximum rate of dilation corresponds to the peak strength. It should also be noted that the the maximum rate of dilation for Type A and B curves does not occur at the maximum rate of strain softening, which generally occurs just after the Q_{uy}.

One possible explanation as to why the rate of strain softening increases at the maximum rate of dilation increases is that the specimens cannot dilate unless the ice fractures; the maximum rates of dilation reflects higher levels of ice cracking; and higher levels of ice cracking produce both a decrease in the strength of the ice matrix and a reduction in the frictional resistance of the sand skeleton (less dilatancy–hardening due to loss of ice tensile strength).

6.4.3 Concluding Remarks

As noted at the beginning of this section, this conceptual description poses hypotheses about the possible processes involved in describing frozen sand behavior. This description is based the measured results for one frozen sand.

Although the hypotheses should apply to other frozen sands, they can not be extended to other types of frozen soil, such as silt or clay, since their stress–strain behaviors have not been documented. The description also assumes possible mechanisms involved in the stress–strain response concerning sand–ice and sand–sand interactions which have not been substantiated.

One of the most speculative processes is the level and rate of pore ice fracturing. It is assumed that 1) the initial pore ice fracturing is what leads to the Q_{uy}, and 2) pore ice fracturing occurs in frozen sand even at "slow" strain rates ($3x10^{-6}$/sec) and high confinement (σ_c = 10 MPa). Experimental evidence to confirm these assumptions are lacking; therefore, the behavior of the pore ice in frozen soils during deformation requires addition research.

TABLE 6.1
COMPARISON OF MEASURED FROZEN INITIAL MODULUS RESULTS
WITH PRIOR TESTING PROGRAMS ON FROZEN SANDS

REFERENCE	MATERIAL PROPERTIES	MEASUREMENT TECHNIQUE	TEMP (°C)	YOUNG'S MODULUS (GPa)	OBSERVED TRENDS WITH		
					INCREASING DENSITY	CONFINING PRESSURE	TEMPERATURE
Kaplar (1963)	Peabody Gravelly Sand (SP) D_{50} = 3.8 mm C_u = 16 C_c = 0.6	Resonant Beam (Longitudinal Vibration)	-1.1 to -27.8	34.5 to 47.1	Not Applicable	Not Applicable	Increases 37% over temperature range Fig. 2.78
Vinson* (1978)	Ottawa 20 - 30 Sand D_{50} = 0.7 mm C_u = 1.1	Cyclic Triaxial	-4	5 to 13.5	Increases by 60% from sand-ice mix to dense sand in unconfined compression	Increases by 69% for dense sand with σ_c from 0 to 1.3 MPa	
Baker and Kurfurst (1985)	Ottawa 16-100 Sand D_{50} = 0.4 mm C_u = 2	Acoustic Wave Propagation On-specimen Strain	-3.2 to -10	24 to 30 26 to 45	Increases 20% for D_r from 20 to 100% Increases 61% for same D_r range	Unconfined	Unaffected Fig. 2.79 Tests only at -10°C
Parameswaran (1980)	Ottawa 30-100 Sand D_{50} = 0.3 mm C_u = 1.5	External Displacement	-2 to -15	0.5 to 4.8	Not applicable	Unconfined	No apparent trend
Current Program	Manchester Fine Sand D_{50} = 0.18 mm C_u = 2.4	On-specimen axial strain in triaxial compression	-9.5 to -25	26.5 ±4.0 Tbl.5.3	Slight increase 15% over D_r range Fig. 5.1	Slight decrease σ_c = 0.1-10 MPa 12% decrease Fig. 5.2	No apparent trend Fig. 5.3

* significant amounts of plastic deformation

TABLE 6.2
VARIABLES USED IN DILATANCY-HARDENING ANALYSIS

VARIABLE	RANGE OF USE	VALUES	SOURCE
Effective Friction Angle, ϕ'	All tests	34.9°	Fig. 4.30
Critical Confining Pressure, σ'_{crit}	All D_r	Varies with D_r but ranges from 0.29 to 2.86 MPa	Fig. 6.4
Ice Tensile Strength	All tests	2.15 MPa	Hawkes and Mellor (1972) Fig. 2.49
Ice Compressive Strength	0.1 MPa tests	$\sigma_{ice} = 0.09 \cdot \exp(1507/T) \cdot \dot{\epsilon}^{0.184}$ = 2.54 to 6.88 MPa, -10°C = 4.83 to 4.87 MPa, -15°C = 3.41 to 8.85 MPa, -20°C = 3.91 to 9.62 MPa, -25°C	Extension of Jones (1982) Figs. 6.6 and 6.7
	10 MPa tests	$\sigma_{ice} = 0.04 \cdot \exp(1921/T) \cdot \dot{\epsilon}^{0.235}$ = 3.02 to 10.5 MPa, -10°C = 3.78 to 13.5 MPa, -15°C = 4.24 to 14.6 MPa, -20°C = 5.09 to 16.1 MPa, -25°C	Same as above

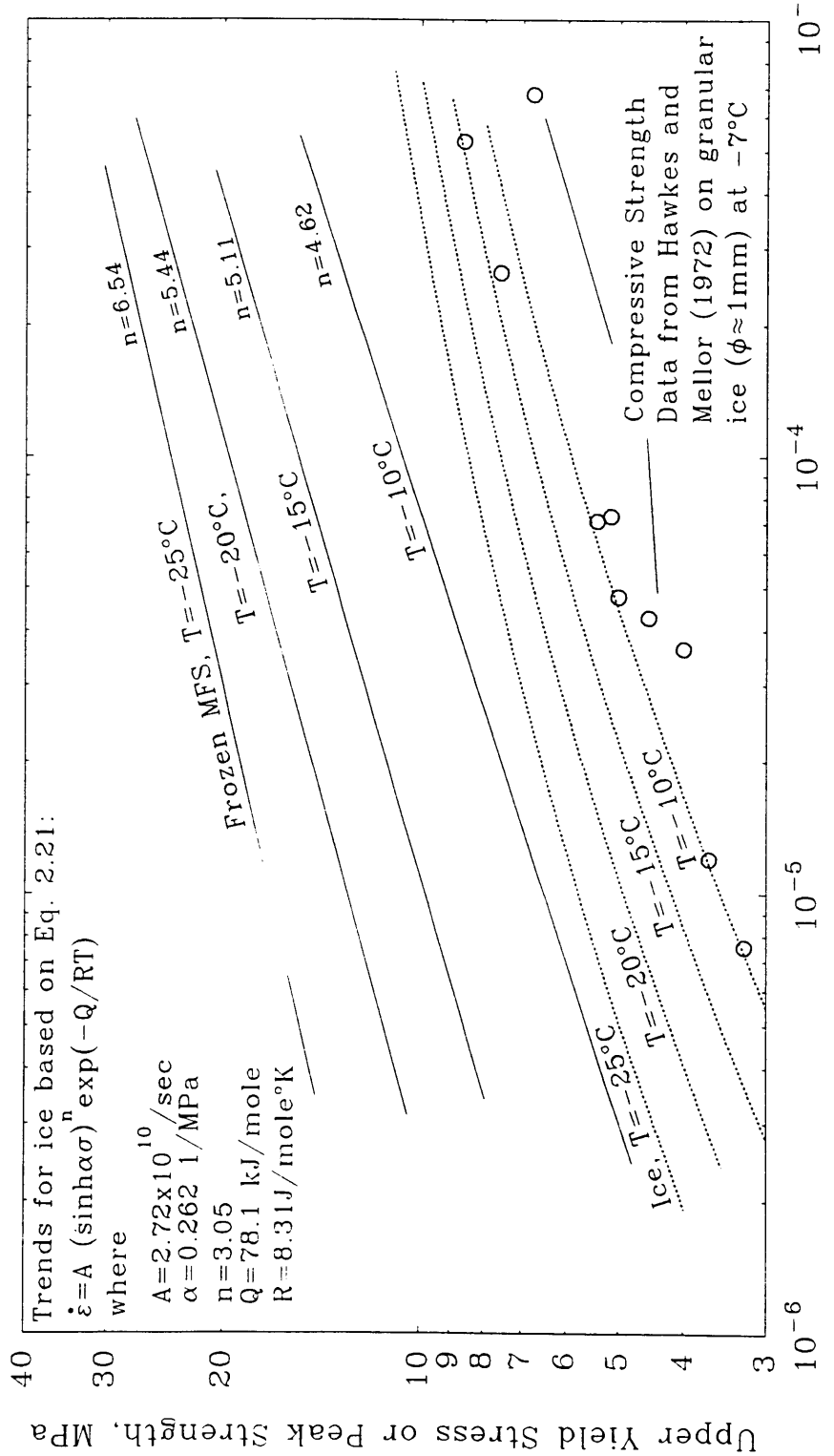

Figure 6.1 Comparison of Magnitude and Rate Sensitivity of Q_{uy} for Conventional Frozen MFS and Calculated Peak Strength of Polycrystalline Ice

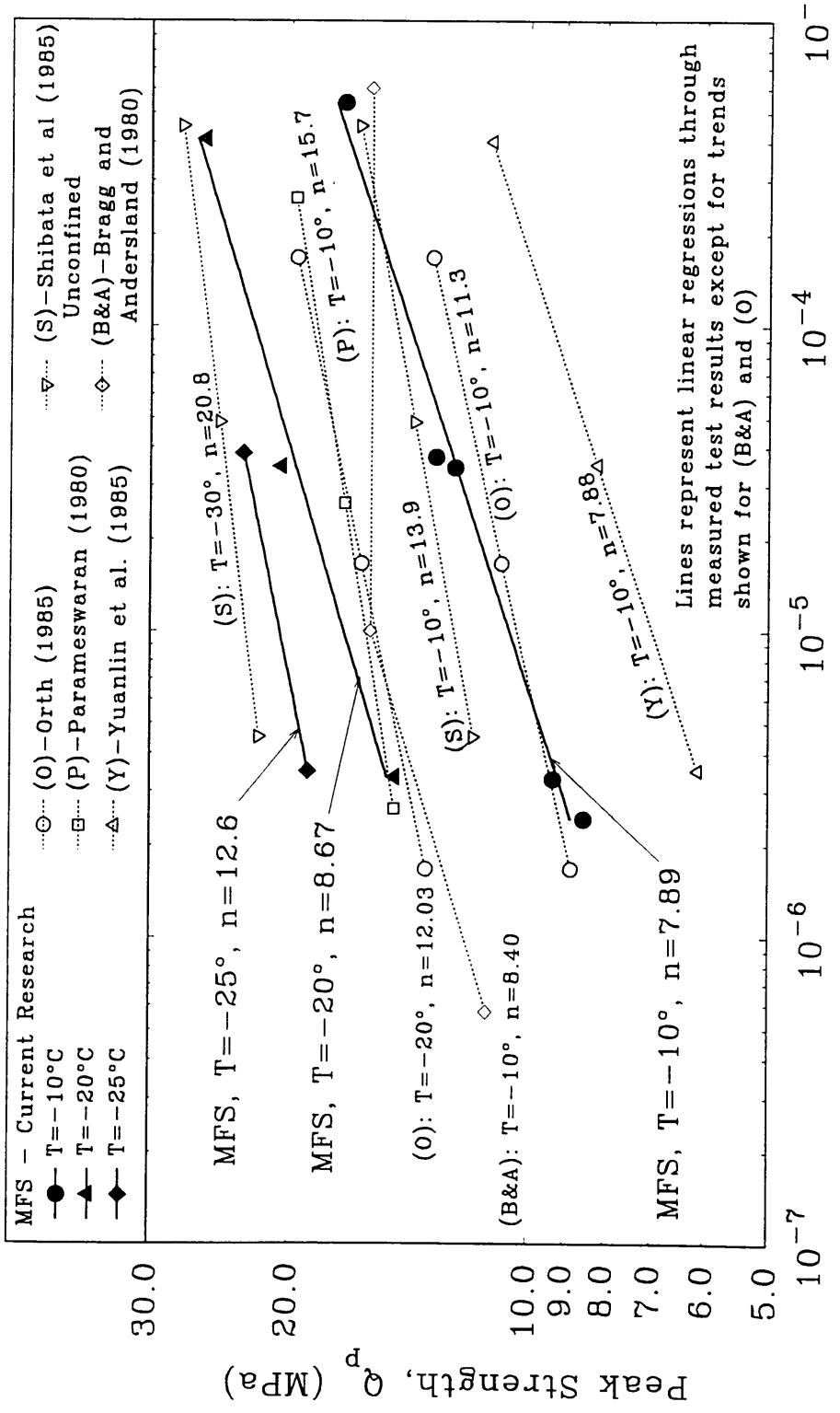

Figure 6.2 Comparison of Peak Strength versus Applied Strain Rate for Various Sands and Frozen MFS on Dense Specimens at at No or Low Confinement

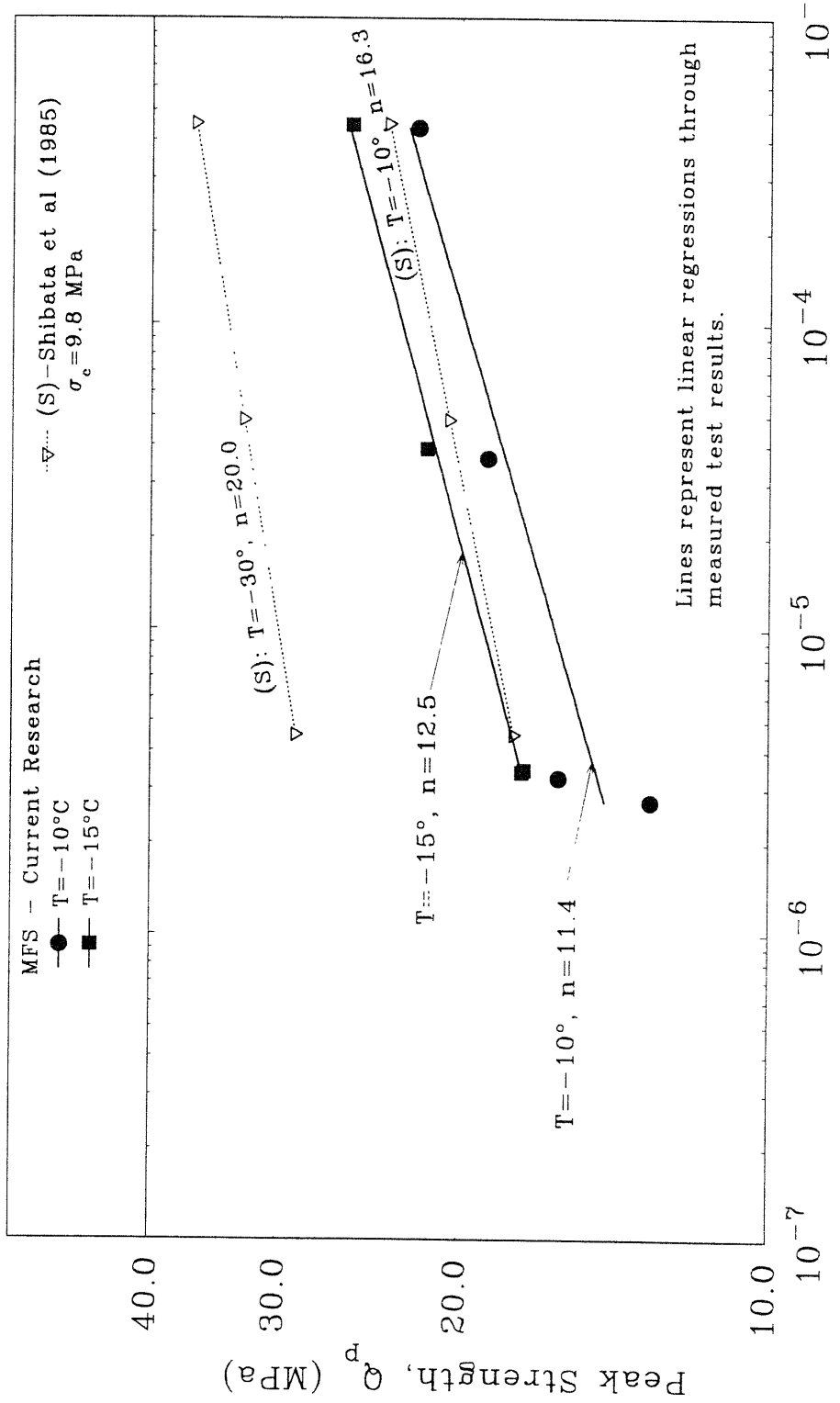

Figure 6.3 Comparison of Peak Strength versus Applied Strain Rate for Various Sands and Frozen MFS on Dense Specimens at High Confinement

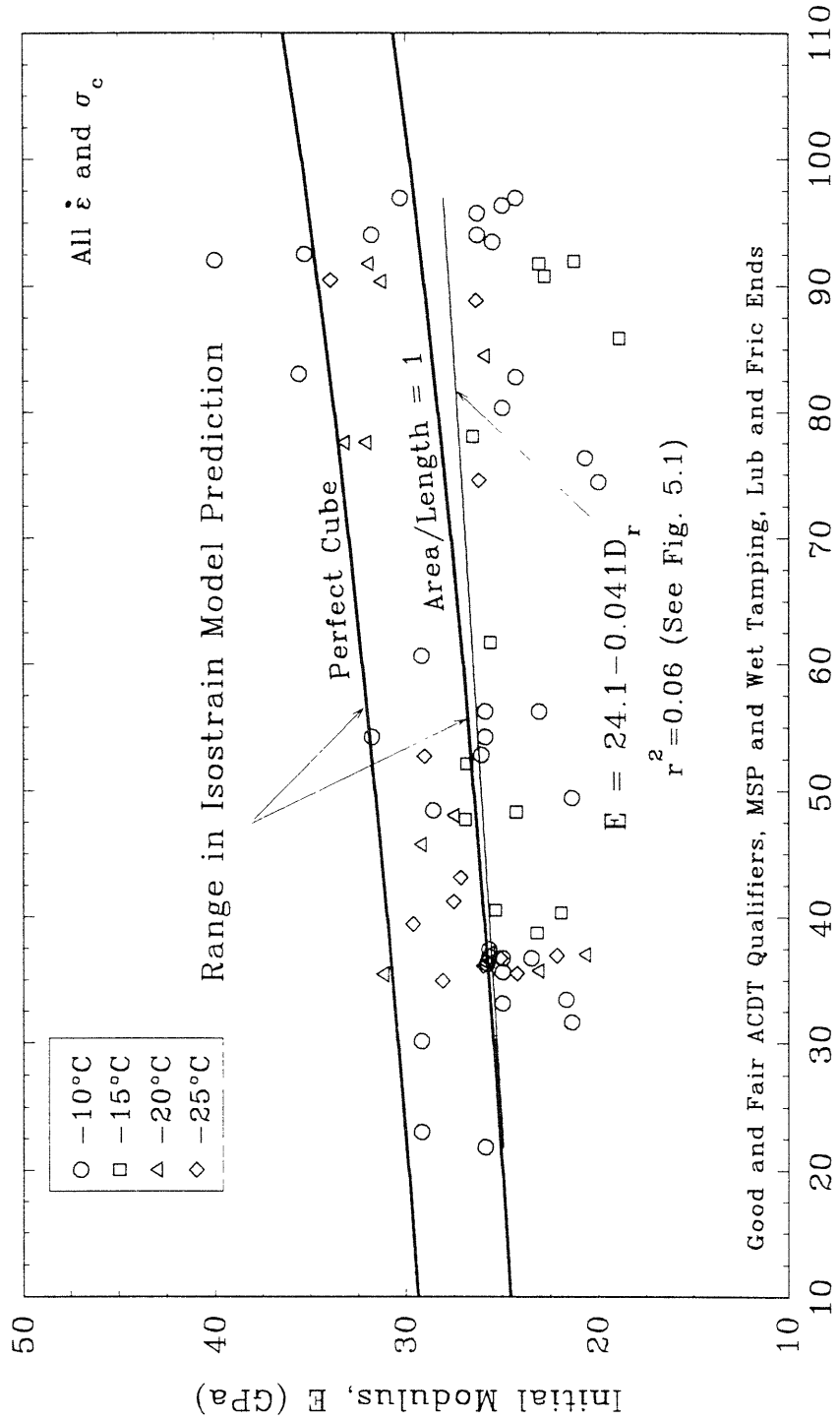

Figure 6.4 Comparison of Predicted Initial Modulus from Isostrain Model and Measured Initial Modulus from Conventional Frozen MFS Tests

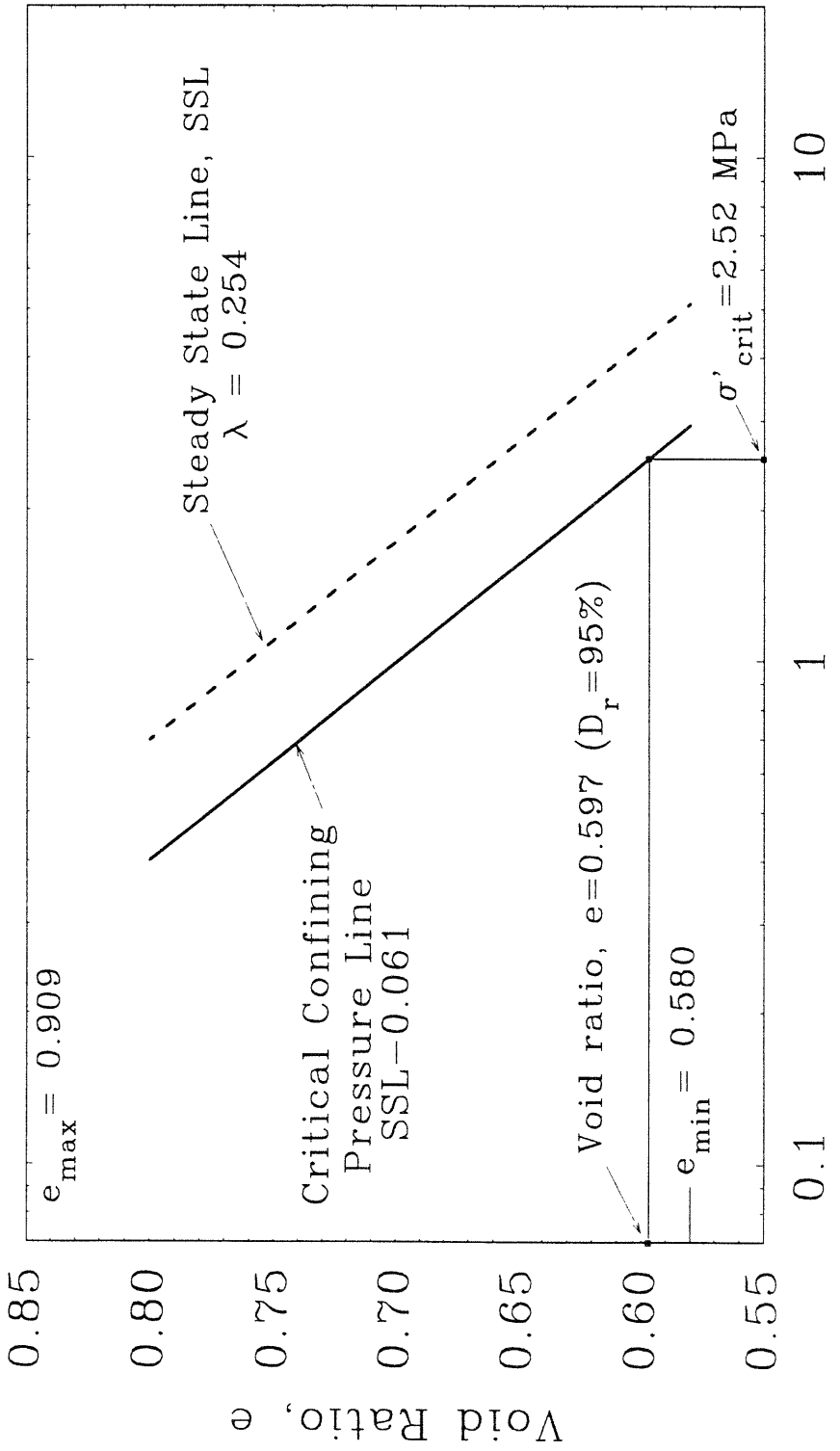

Figure 6.5 Critical Confining Pressure Line of Unfrozen MFS Based on Steady State Analysis of CIUC Tests

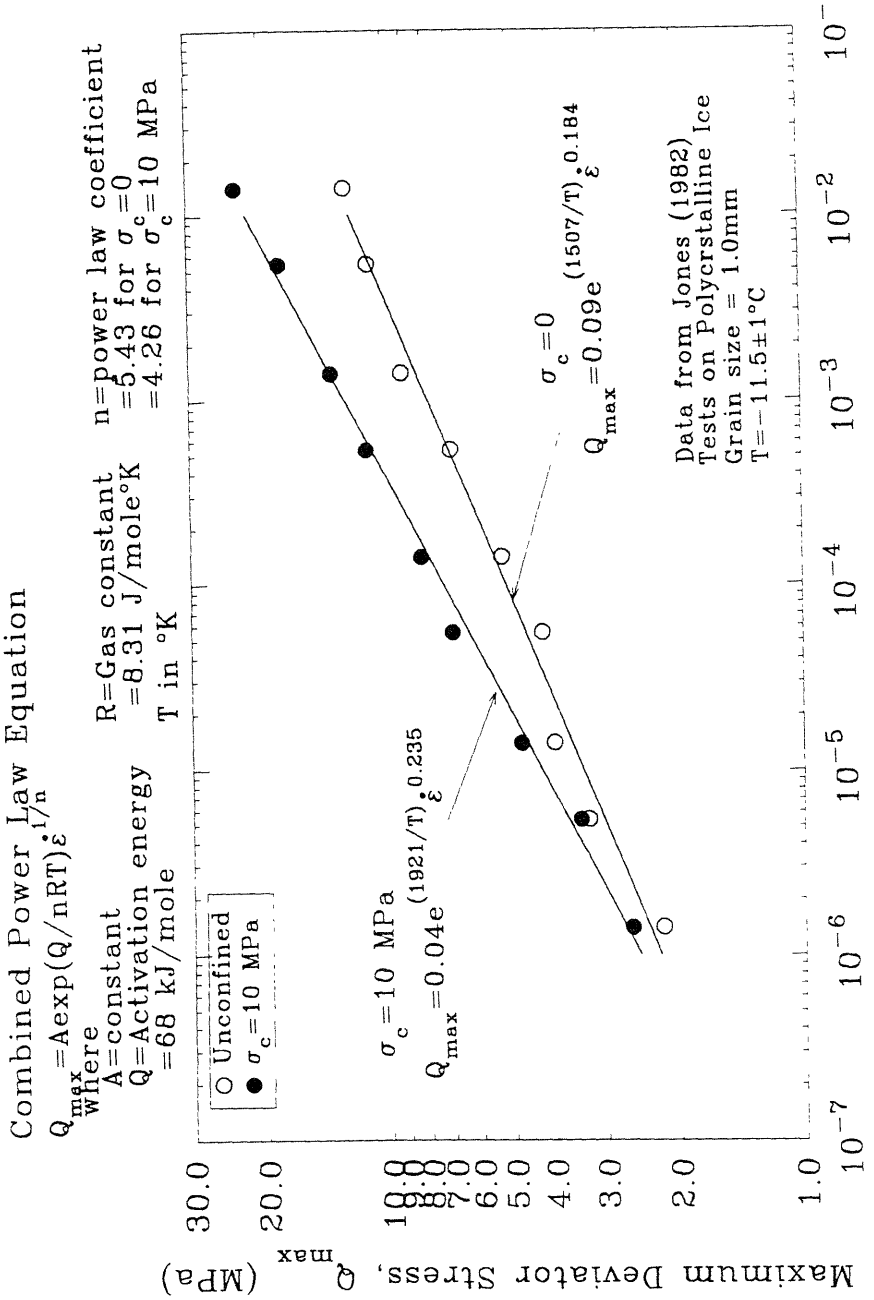

Figure 6.6 Peak Strength versus Strain Rate Equations for Polycrystalline Ice Developed from Results by Jones (1982)

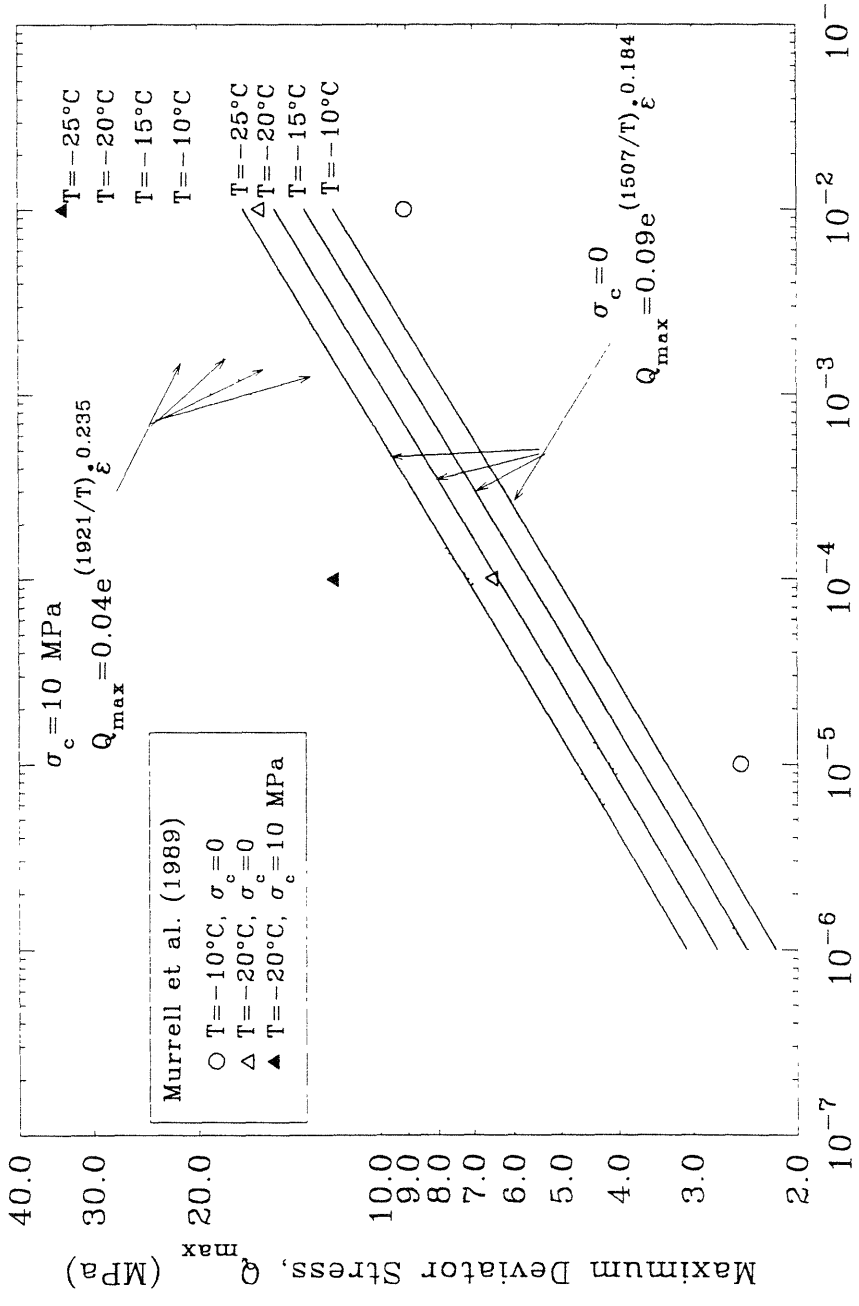

Figure 6.7 Calculated Peak Strengths of Polycrystalline Ice Used in the Dilatancy–Hardening Model Compared with Results by Murrell et al. (1989)

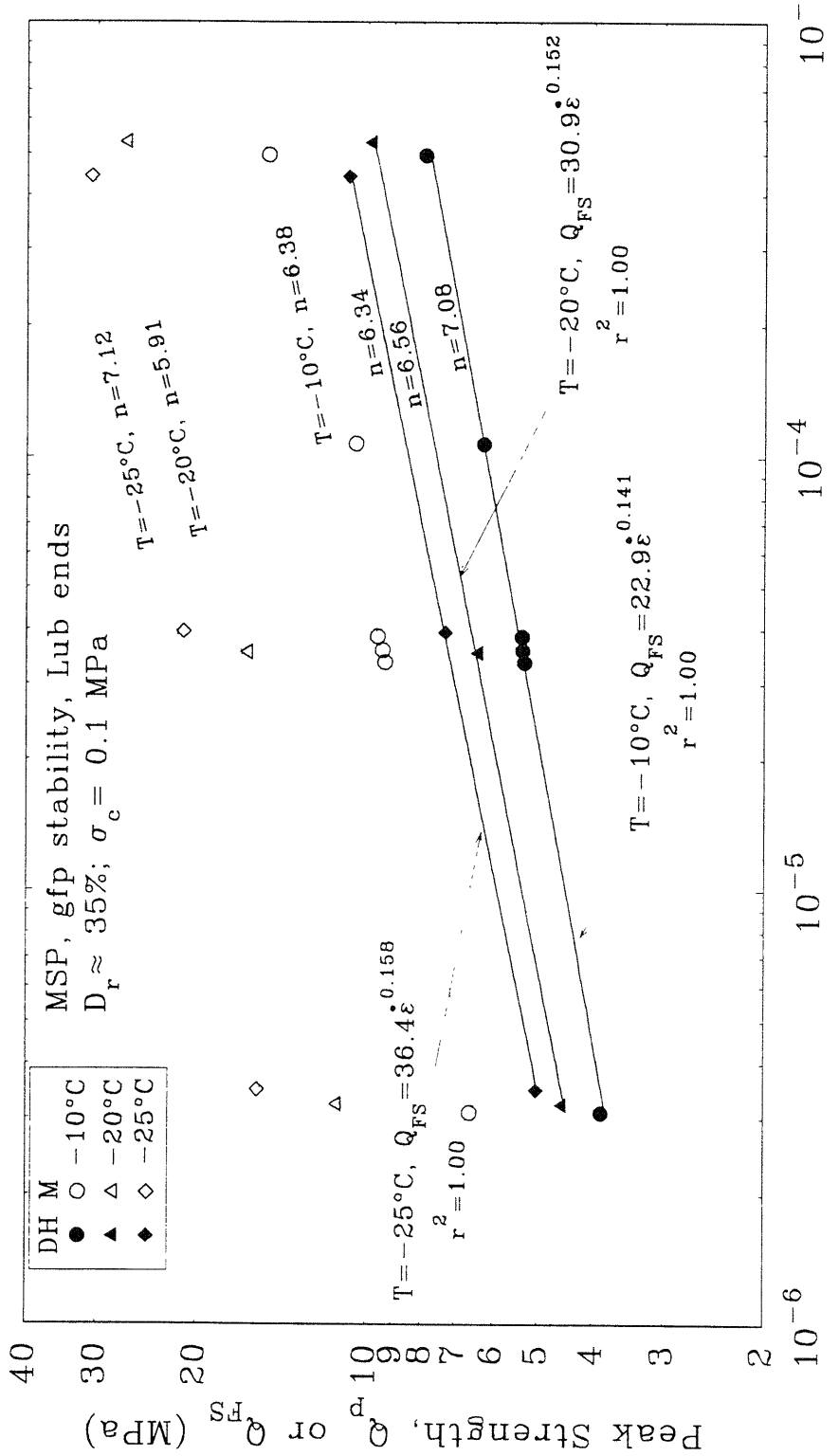

Figure 6 8 Peak Strength versus Strain Rate Comparing Measured Results from Conventional Frozen Tests on Loose Specimens at Low Confinement with Predicted Results from Dilatancy-Hardening Model

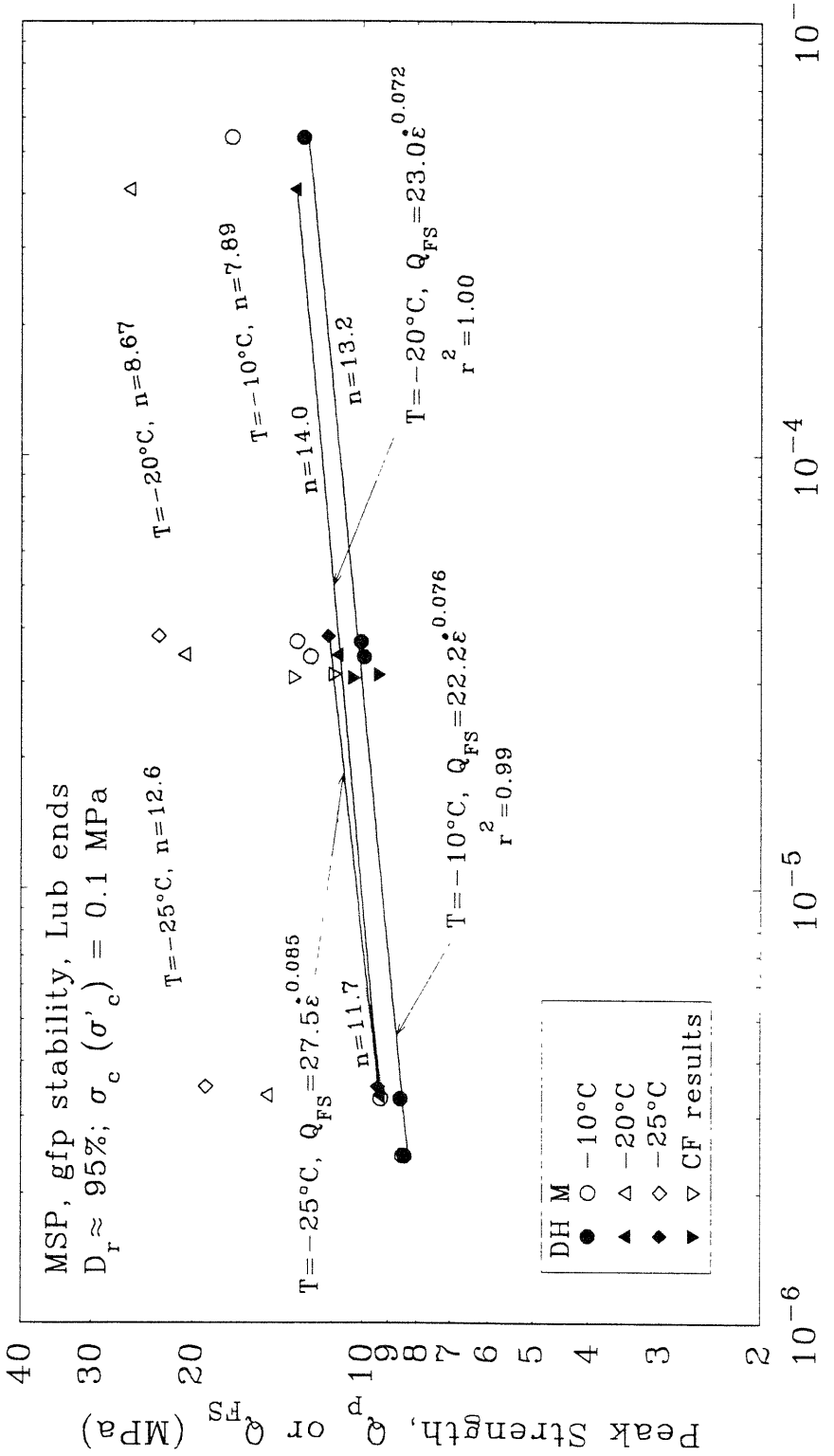

Figure 6.9 Peak Strength versus Strain Rate Comparing Measured Results from Conventional and Consolidate-Freeze Tests on Dense Specimens at Low Confinement with Predicted Results from Dilatancy-Hardening Model

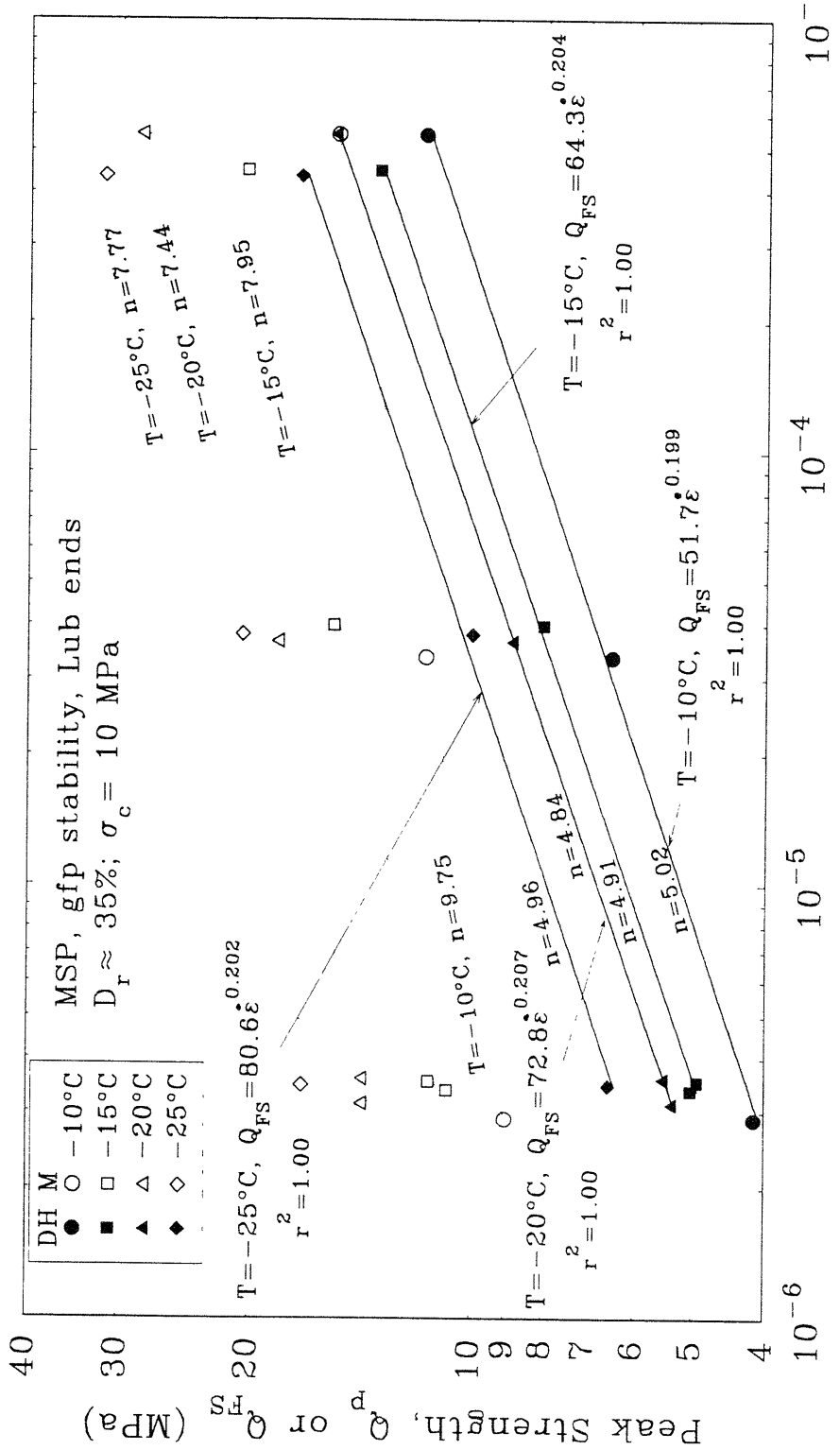

Figure 6.10 Peak Strength versus Strain Rate Comparing Measured Results from Conventional Frozen Tests on Loose Specimens at High Confinement with Predicted Results from Dilatancy-Hardening Model

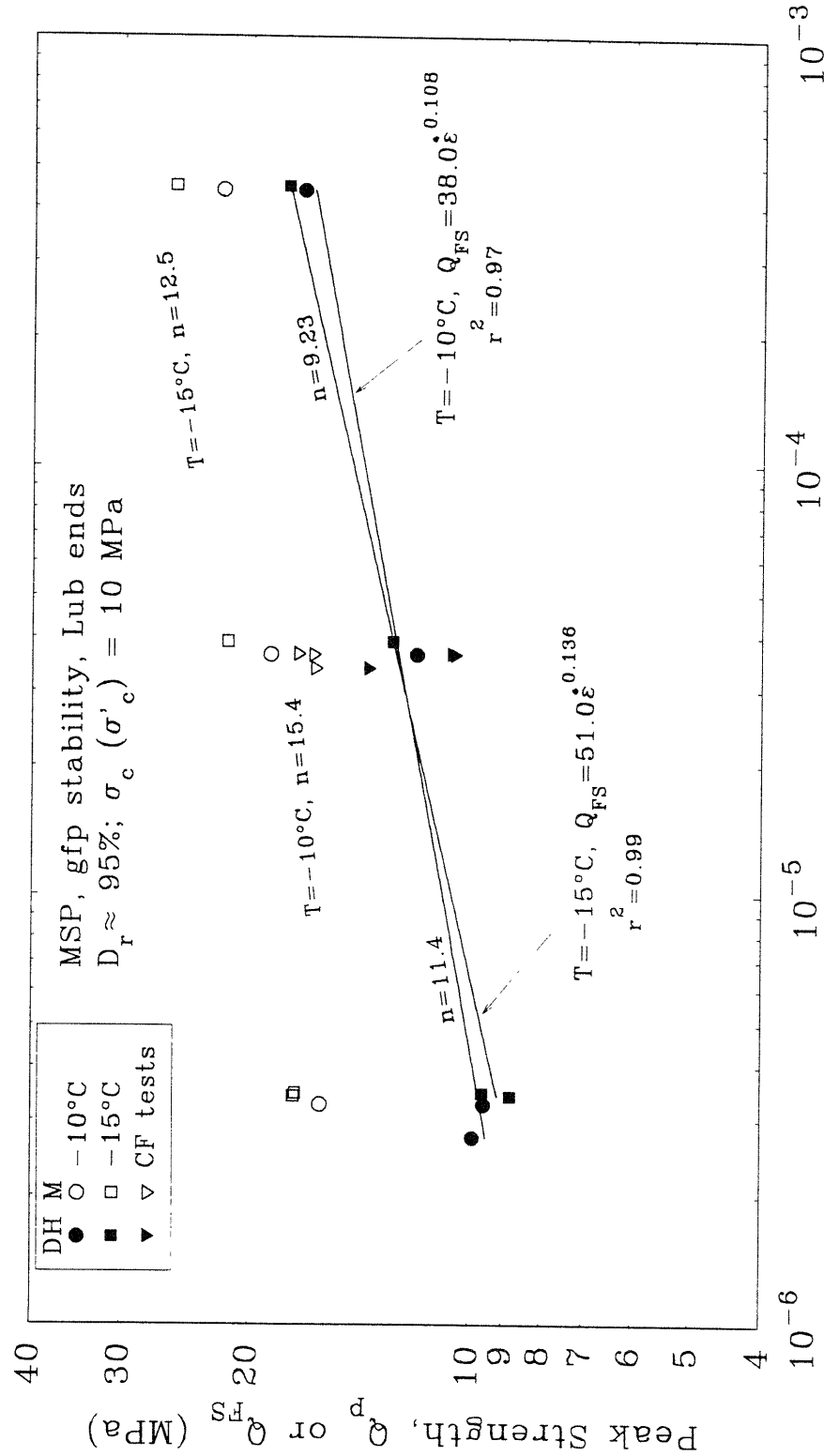

Figure 6.11 Peak Strength versus Strain Rate Comparing Measured Results from Conventional and Consolidate–Freeze Tests on Dense Specimens at High Confinement with Predicted Results from Dilatancy–Hardening Model

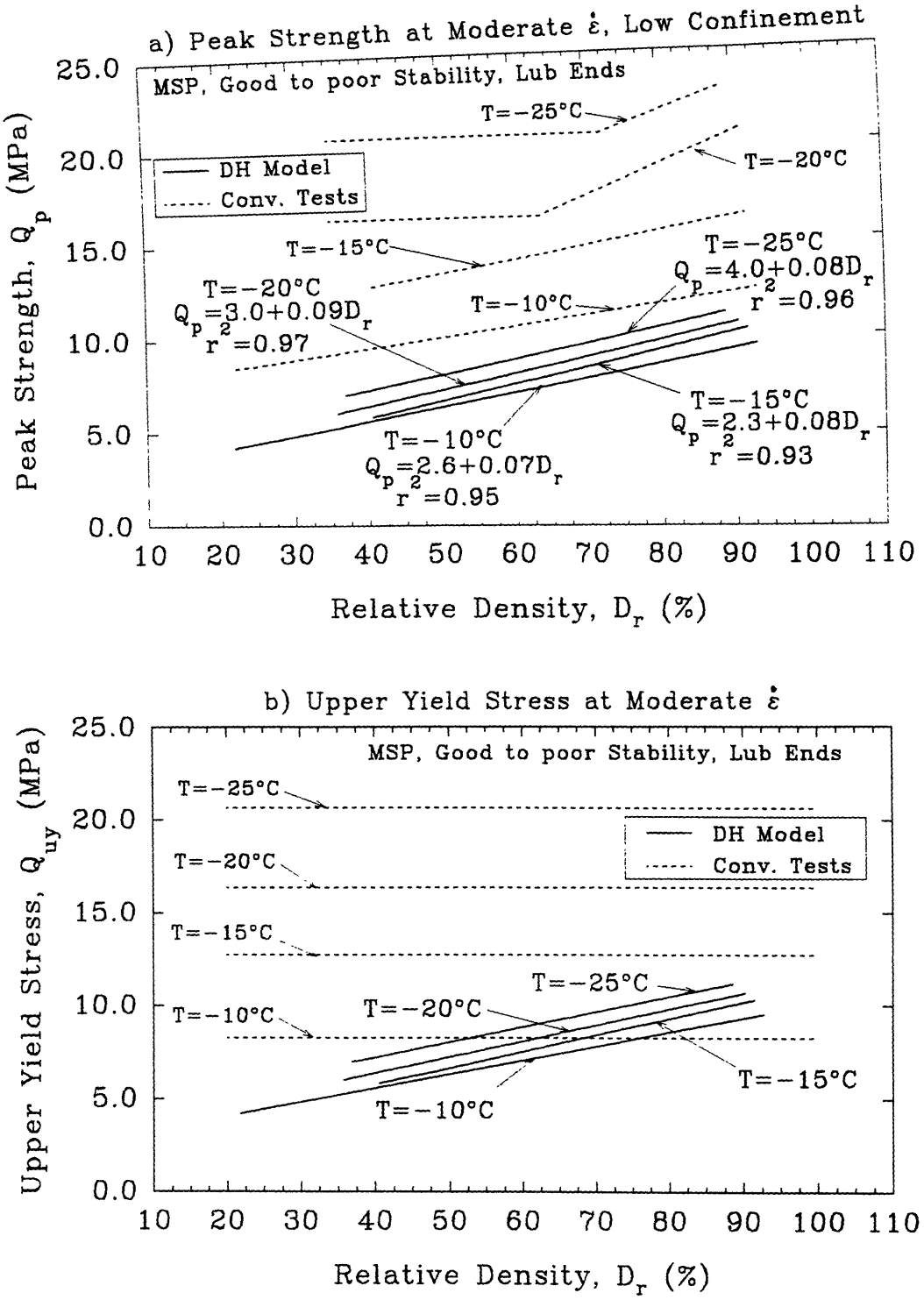

Figure 6.12 Comparison of Peak Strength versus Relative Density from Dilatancy–Hardening Model and and Peak Strength and Upper Yield Stress from Conventional MFS Tests at Moderate Strain Rate and Different Temperatures

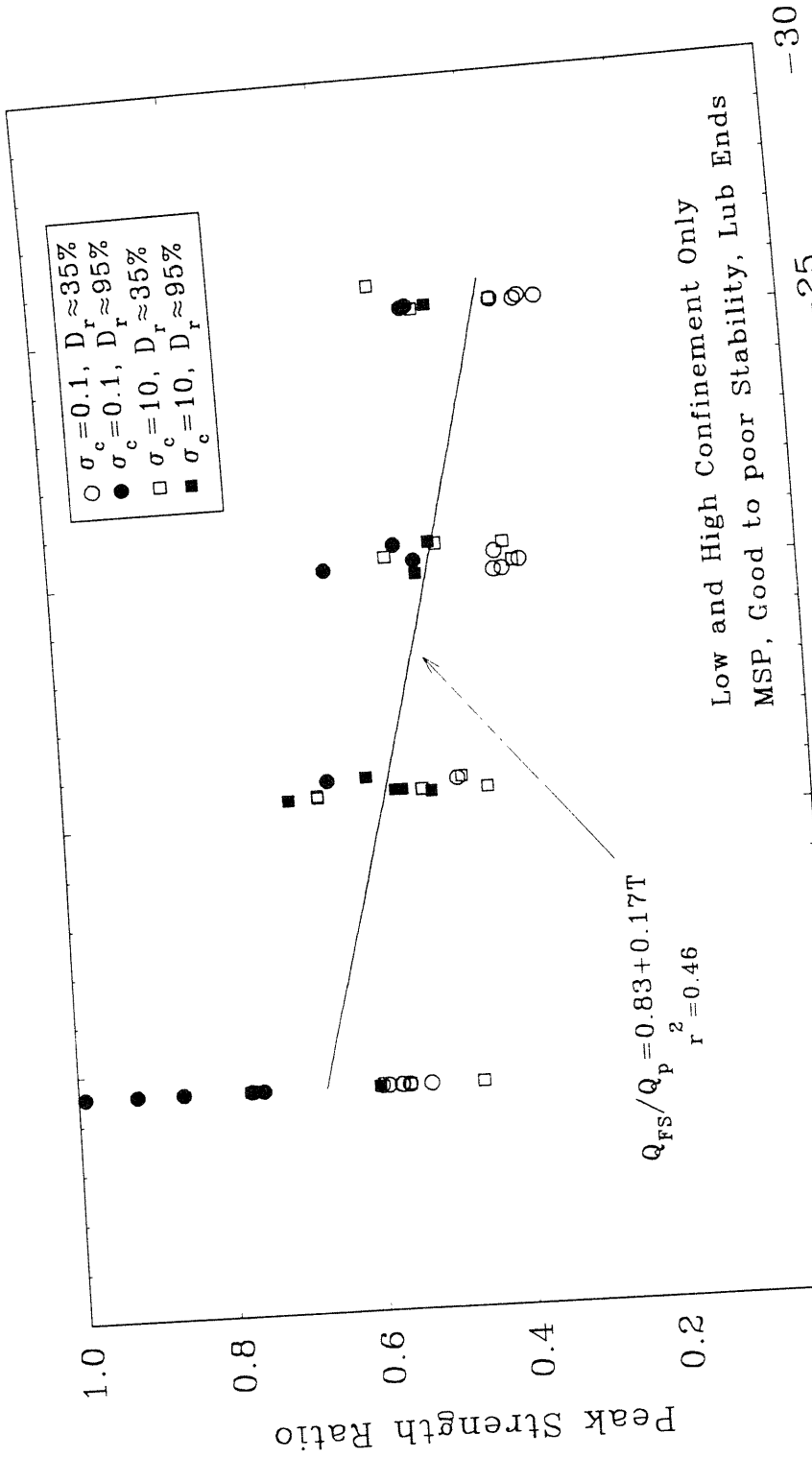

Figure 6.13 Ratio of PredictedPeak Strength from Dilatancy Hardening Model to Measured Peak Strength versus Temperature for Conventional Frozen MFS Tests

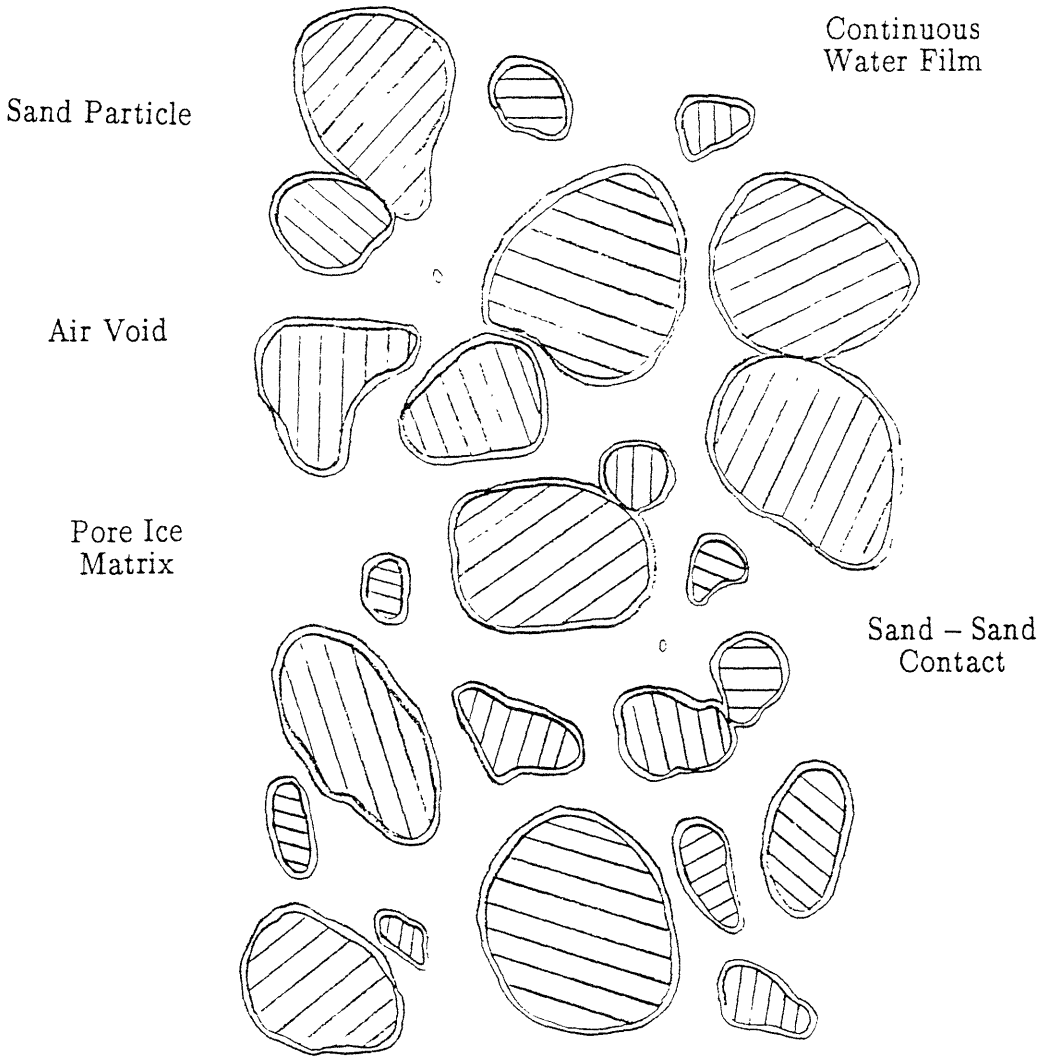

Figure 6.14 Schematic Representation of Frozen Manchester Fine Sand

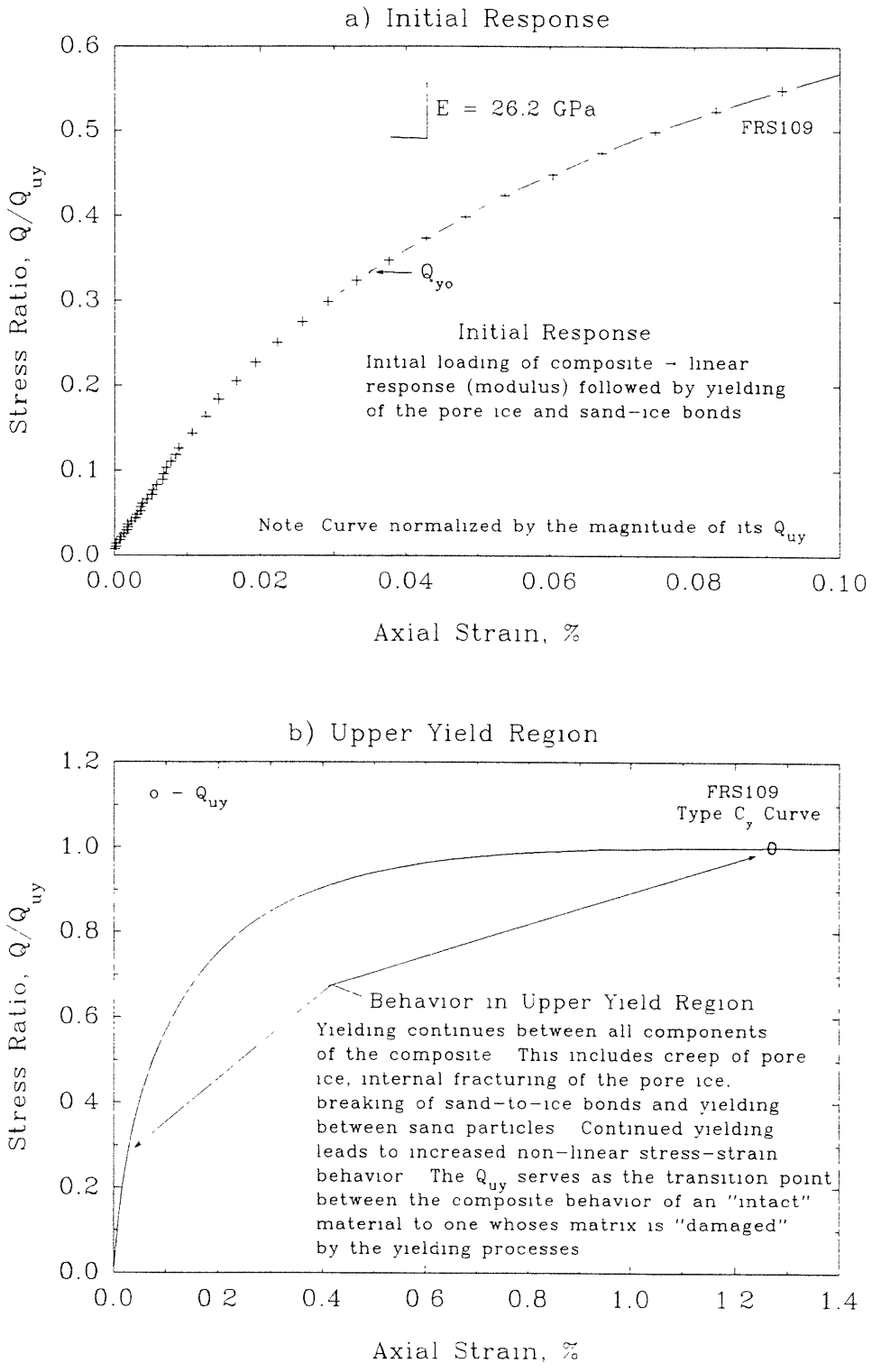

Figure 6.15 Conceptual Composite Behavior of Conventional Frozen MFS - Initial Response and Upper Yield Region

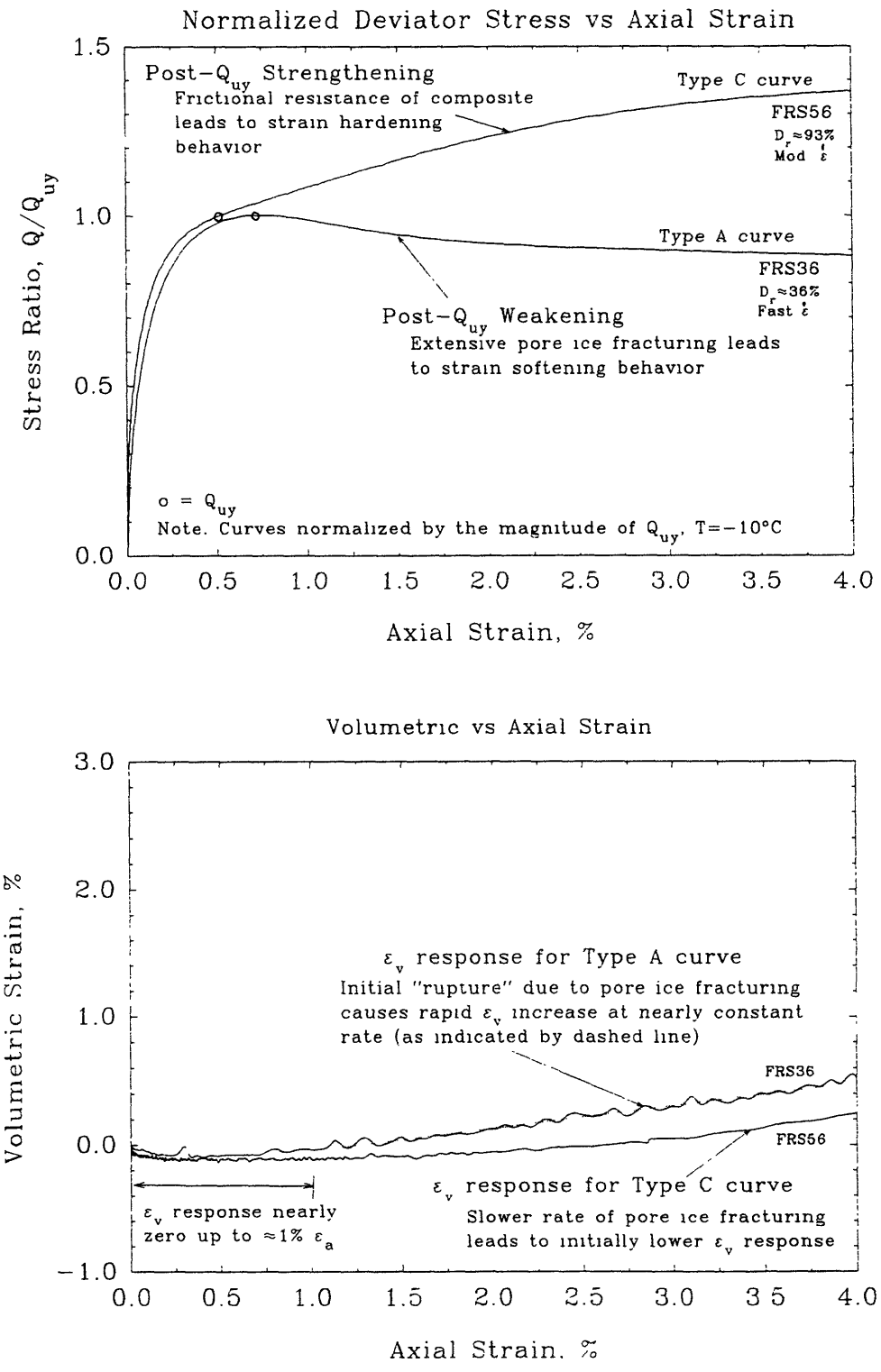

Figure 6.16a Conceptual Composite Behavior of Frozen MFS at Low Confinement – Post-Upper Yield Behavior

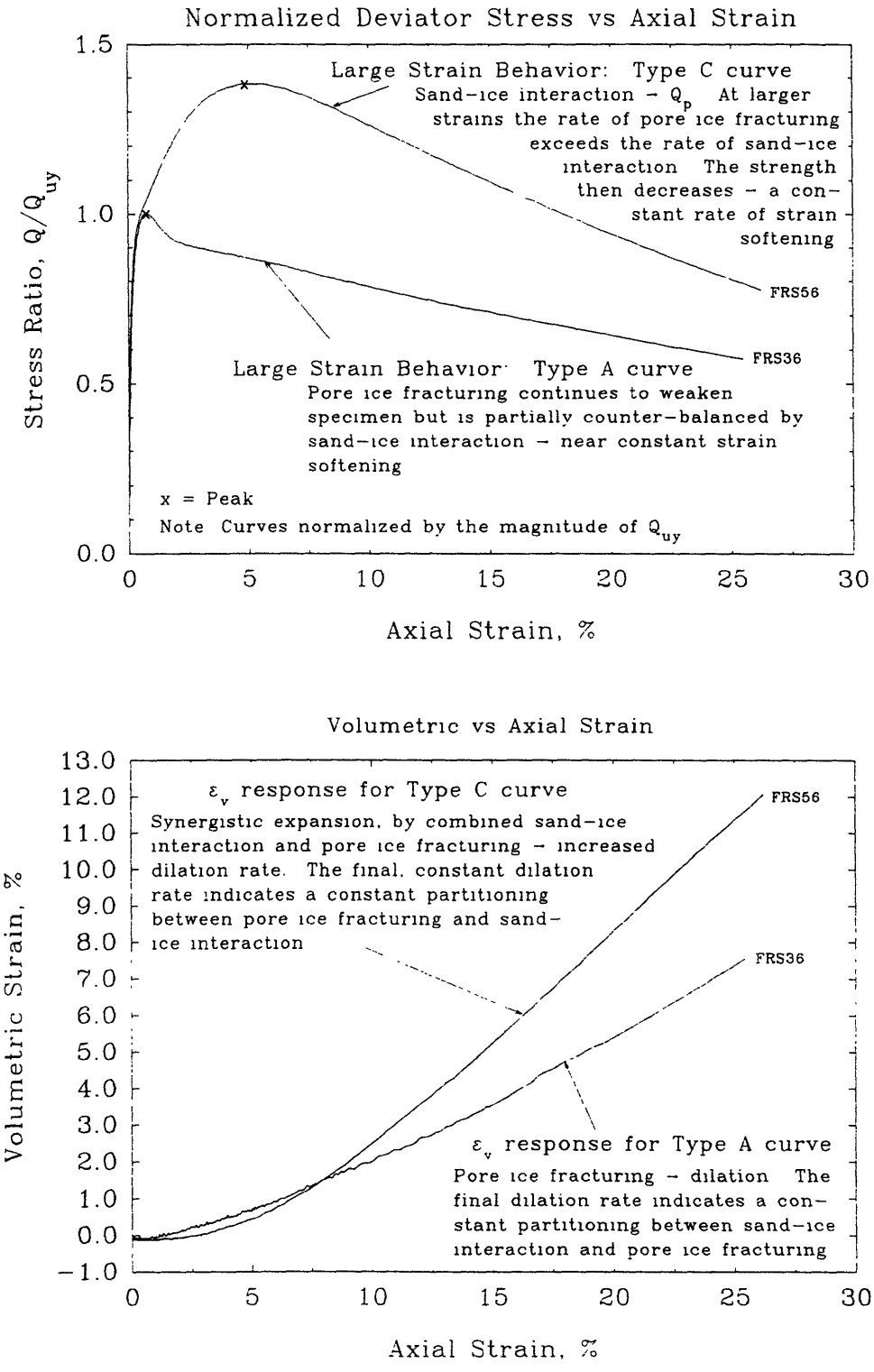

Figure 6.16b Conceptual Composite Behavior of Frozen MFS at Low Confinement - Large Strain Behavior

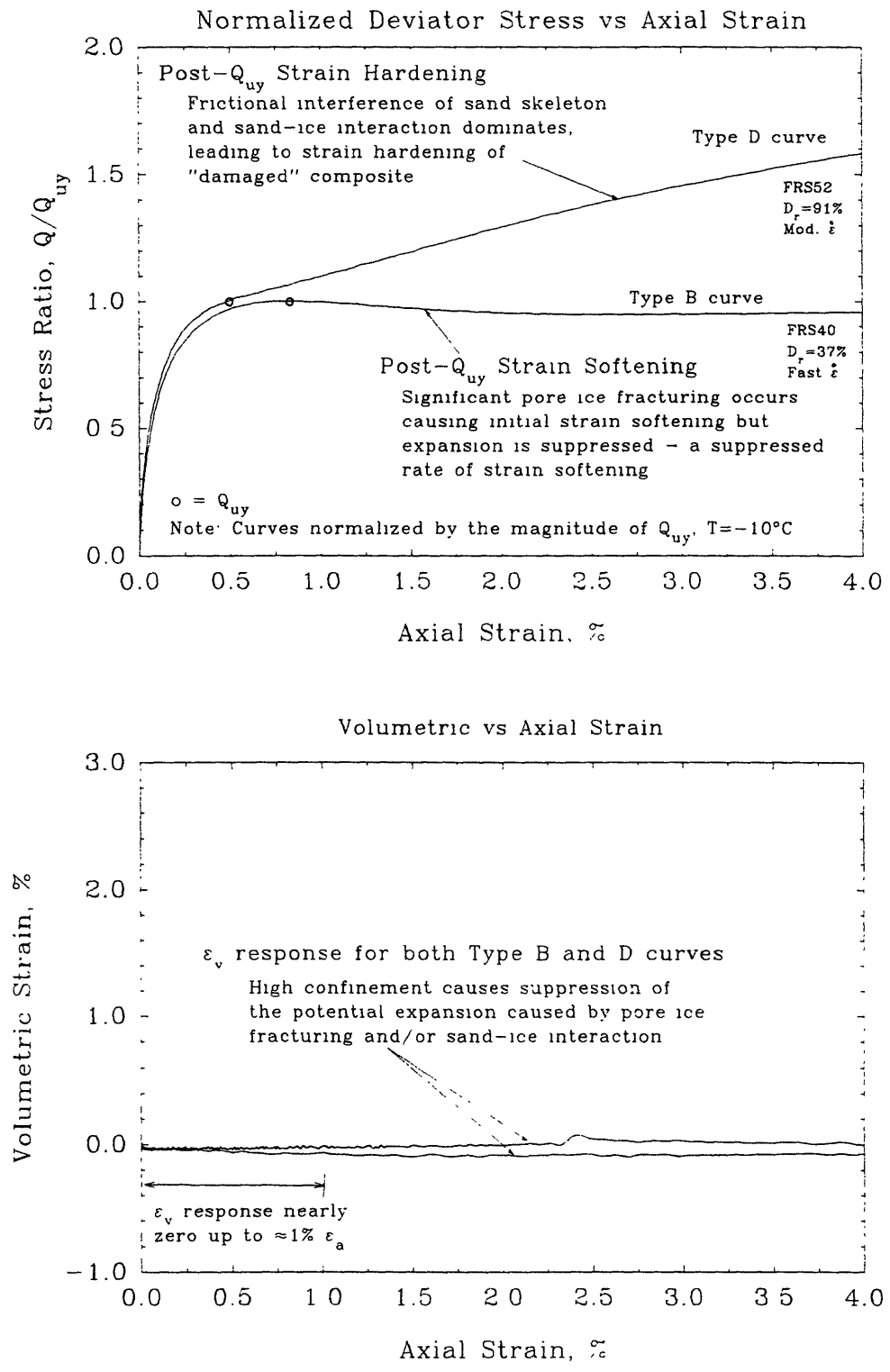

Figure 6.17a Conceptual Composite Behavior of Frozen MFS at High Confinement − Post−Upper Yield Behavior

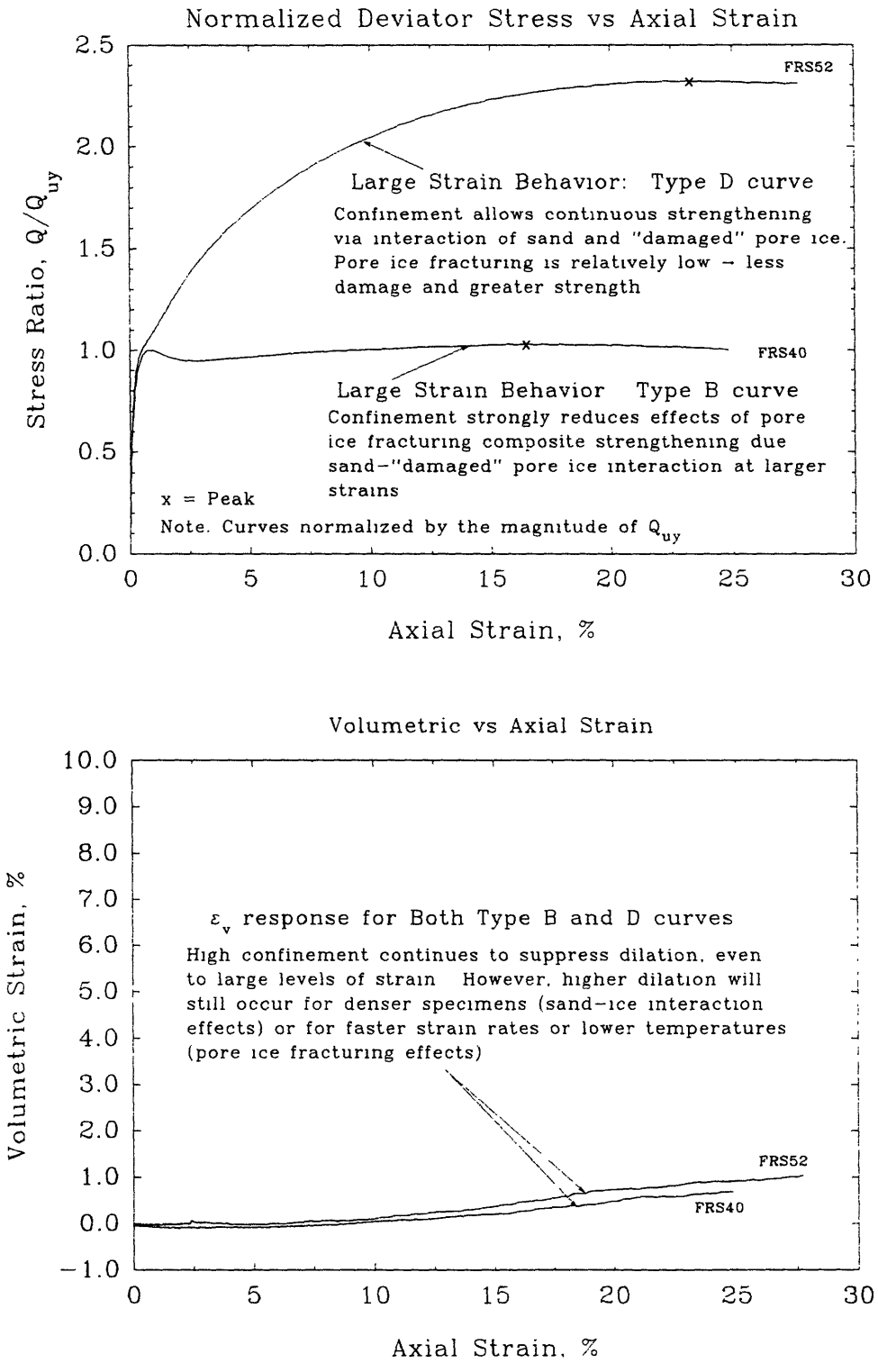

Figure 6.17b Conceptual Composite Behavior of Frozen MFS at High Confinement – Large Strain Behavior

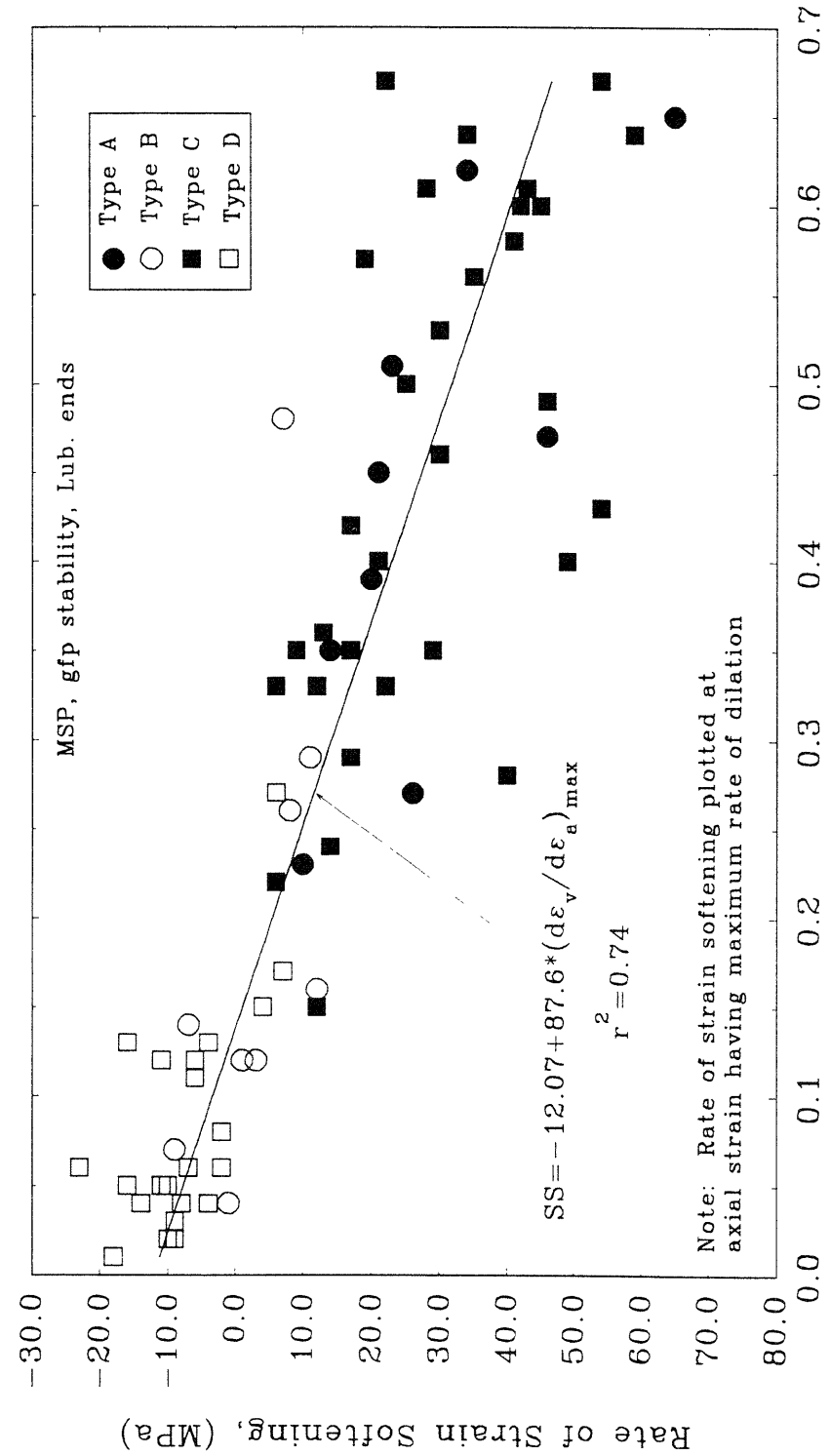

Figure 6.18 Rate of Strain Softening versus Maximum Rate of Dilation for all Testing Conditions

CHAPTER 7
SUMMARY, CONCLUSIONS AND RECOMMENDATIONS

Present engineering practice generally relies on empirically–based methods for the design of construction that involves frozen soils, which are perhaps the most difficult of all geomaterials to understand and model. These designs often incorporate large factors of safety to mitigate against the potential risks arising from the significant uncertainties in predicted performances. More reliable prediction methods should lead to more efficient designs and lower construction costs.

Development of rational design methods requires a better understanding of the physical mechanisms that control the strength and deformation behavior of frozen soils. This research represents a first step in this process by conducting the first comprehensive triaxial compression shear results to show how four principal variables (soil density, confining pressure, strain rate and temperature) affect the strength–deformation properties of a frozen soil. This experimental program selected a natural soil, Manchester Fine Sand (MFS), as the testing material and also included tests to quantify the stress–strain behavior of this sand in an *unfrozen* state. Based on a careful evaluation of these data and results from the literature for other frozen sands and for polycrystalline ice, progress has been made in identifying several physical mechanisms that are thought to control the stress–strain–time behavior of frozen sands.

7.1 SUMMARY

7.1.1 Literature Review

Chapter 2 presents a review of the available literature which describes the behavior of unfrozen sand, polycrystalline ice and frozen sand. Chapter 2 also describes two models which were used to predict the initial modulus and peak strength of frozen MFS. The following summarizes this review.

7.1.1.1 Unfrozen Sand

Sands are always classified by their particle size distribution (gradation) and may be classified according to the roundness and shape of the sand particles. The void ratio (e) and relative density (D_r) are measures of the packing of the sand particles. Particle size and shape affect the types of packing arrangements that are possible. The structure of a sand is described by two components: the fabric, which refers to both the distribution and orientation of the particles; and the magnitude and direction of the contact forces.

Stresses on sand masses are considered to act over a representative area. Through the principle of effective stress, total normal stresses (σ) are partitioned between the sand skeleton (σ') and the pore water (u), so that $\sigma = \sigma' + u$.

The stress–strain–strength behavior of a sand depends primarily on its D_r, preshear confining stress (σ'_c) and the drainage conditions. Rowe (1962) proposed that the drained strength of a sand can be divided into three components: sliding friction (ϕ_u), particle interference (ϕ_i), and dilation of the sand skeleton (ϕ_d) (Fig. 2.1). Drained triaxial compression tests on sands show that an increase in σ'_c or a decrease in D_r leads to lower peak friction angles, larger failure strains and the suppression of dilation (or enhancement of contraction). Dense sands at high σ'_c respond similarly to loose sands at low σ'_c (Fig. 2.3). Undrained triaxial compression tests show similar $\sigma'_c - D_r$ trends (Fig. 2.5). However, the change in

volume during drained shear translates to a change in pore pressure in undrained shear, i.e., the tendency to dilate leads to the development of negative pore pressures. As with drained tests, the undrained shearing of dense sands at high σ'_c will exhibit similar stress–strain behavior as the shearing of loose sands at low σ'_c.

Steady State Behavior

Since the pioneering studies by Casagrande, the steady state (critical state or residual state) of sands has been a topic of much research and debate. The major cause of controversy lies in the fact that different testing methods have been used to arrive at a "steady state" condition. The differences include the specimen preparation technique, the initial state relative to the steady state condition and the method of shearing. These major differences in testing procedures, in turn, have led to different definitions of the "steady state" condition. For example, Sladen et al. (1985) and Been et al. (1991) consider the steady state and critical state terms interchangeable and essentially equivalent. However, Poulos (1981) insists that the various terms may describe different sand states.

Poulos (1981) defines the steady state of deformation as a continuous, unique condition for a given soil that is a function only of the soil's in–situ void ratio. It is independent of the method or rate of loading and the soil's initial structure. The steady state condition can be represented in e – log σ'_{3f} space by the steady state line (Figure 2.12). The steady state of deformation is characterized by four conditions:

1) constant void ratio,
2) constant shear stress,
3) constant normal effective stress,
4) constant velocity.

He further states that the condition of critical state can be considered as

co–existing at the steady state condition; however, not all critical state conditions may be considered as steady state. Steady state conditions are best achieved for contractive (loose) sand states.

Been and Jefferies (1985) introduce the state parameter Ψ to account for the combined effects of σ'_c and D_r on stress–strain behavior (Fig. 2.18). By referencing the initial state (initial void ratio and mean effective stress) to the steady state line (SSL), they propose that the general nature of the stress–strain behavior and certain other parameters (e.g., normalized undrained shear strength and drained peak friction angle) can be related to the magnitude of the state parameter Ψ. For consolidated–undrained tests, a negative state parameter predicts a dilative (strain hardening) type behavior and a positive state parameter predicts a contractive (strain softening) type behavior. Been et al. (1991) expanded on the universality of the state parameter and found that the steady state line was unique and independent of various loading methods, specimen preparation techniques, stress paths and drainage conditions, and they found that the SSL becomes bi–linear at stresses sufficiently high to cause particle crushing.

However, the universality of the state parameter approach has not been clearly demonstrated in the literature. The steady state condition, and hence the location of the steady state line, may be influenced by numerous factors. These factors include sand grain characteristics, strain rate, initial fabric, initial Ψ and stress path (see Table 2.1).

7.1.1.2 Polycrystalline Ice

A summary of polycrystalline ice behavior was described in Section 2.2 with the presentation focusing on the structure of polycrystalline ice, the possible deformation mechanisms, the mechanical behavior of single ice crystals, and the mechanical behavior of polycrystalline ice.

Ice Structure

Ice Ih is the most predominant form of ice encountered in most engineering applications. It's basic building structure consists of a tetrahedron formed by the five oxygen atoms of five water molecules (Fig. 2.37). A hexagonal ring of oxygen atoms which lie in a slightly distorted plane form the basal plane. The axis normal to the basal plane is referred to as the c–axis. Slip along the basal plane is referred to as easy glide and slip in other directions is referred to as hard glide.

Many researchers [e.g., Ladanyi (1981); and Ting et al. (1983)] assume that the pore ice in frozen soils is granular in nature, although at smaller grain sizes than that commonly tested in the laboratory. Sayles (1989) suggests that the pore ice may be columnar in nature following a tortuous path through the pore space.

Mechanisms of Deformation

Numerous possible mechanisms exist to explain the deformation behavior of polycrystalline ice. These mechanisms fall into one of five groups: elastic processes; anelastic processes, plastic deformation processes, evolving microstructure processes and internal fracturing processes (Table 2.2 and Fig. 2.39).

Mechanical Behavior of Single Ice Crystals

The orientation of the c–axis of single ice crystals affects their strength–deformation behavior (Fig. 2.41), such that single ice crystals strained in hard glide may exhibit strengths 60 times that of crystals strained in easy glide. Various ionic impurities incorporated into the ice lattice (e.g., hydrogen fluoride, HF, and hydrochloric acid, HCl) can lead to an increased mobility of dislocations and thus lower strengths. In contrast, other ionic impurities such as ammonia (NH_3), may increase the strength of an ice crystal.

Mechanical Behavior of Granular Ice

The mechanical behavior of polycrystalline ice ranges from ductile (creep) to brittle (fracture). In general, unconfined compression and tension creep (constant load) or strength (constant strain rate) tests are used to study ice behavior (Fig. 2.44). Mellor and Cole (1982) report on a correspondence established experimentally between the results of creep tests and strength tests. The stress/strain–rate correspondence is a relationship between the applied stress and minimum strain rate ($\sigma_a/\dot{\epsilon}_{min}$) in a creep test and the peak strength and applied strain rate ($Q_p/\dot{\epsilon}_a$) in a strength test, and is valid as long as the mechanical properties of the ice do not change under these two loading conditions.

The "flow curve" of ice describes the stress–strain rate relationship from the ductile to brittle regime (Fig. 2.47). In the ductile region, the linear portion of the flow curve is commonly called the region of power law creep. At faster strain rates ($> 10^{-2}$/sec) the ice behaves in a brittle manner. This region is also known as power law breakdown. A transition zone exists between the ductile and brittle regimes which involves attributes from both regions.

The stress–strain rate correspondence in the ductile region can be described by a simple power law equation (Eq. 2.17). The power law coefficient (inverse slope of the flow curve) typically ranges from 3 to 4.5 for strain rates between 10^{-7}/sec to 10^{-4}/sec. A summary of compression tests on polycrystalline ice by Hawkes and Mellor (1972) illustrates this ductile behavior (Fig. 2.49) where a power law coefficient of 4.6 can be calculated for compression test results at strain rates between 10^{-7}/sec and 10^{-4}/sec. Polycrystalline ice exhibits a different behavior in uniaxial tension than in compression (Fig. 2.46). Murrell et al. (1989) note that a ductile failure in tension can be obtained for tests at strain rates below 10^{-7}/sec.

Glen (1955) used the Arrhenius equation to describe the temperature–dependent behavior of polycrystalline ice in the ductile region (Eq. 2.18). Mellor and Testa (1969b) investigated the effect of temperature on the behavior of granular ice and they observed a decrease in the minimum strain rate with a decrease in temperature, with this trend being linear for temperatures below –10° C but non–linear for higher temperatures (Fig. 2.52). Their results lead to a constant activation energy of 69 kJ/mole for temperatures from –10° C to –60° C. Review of results from other studies (Barnes et al. 1971 and Weertman 1983) find activation energies range from 120 to 200 kJ/mole for temperatures above –10° C, but range from 55 to 85 kJ/mole for temperatures less than –10° C.

The combined power law equation (Eqs. 2.19 and 2.20) can be used to estimate the combined effects of temperature, stress and strain rate. While not a complete constitutive relationship, the equation does quantify the relationship between temperature and strain rate as long as the deformation regime is not changing.

The ductile–to–brittle transition region represents one of the most complex areas in ice behavior given that mechanisms from both the ductile and brittle regions occur. Within this region, the power law coefficient increases to infinity (rate insensitivity) and may become negative (Fig. 2.49). Extension of the combined power law equation (Eqs. 2.19 and 2.20) is commonly used in describing the behavior in the transition region. Barnes et al. (1971) suggest the use of a variation of the combined power law equation (Eq.2.21) which they found provided a better fit of their data (Fig. 2.55). Results from a number of testing programs on granular ice suggest a consistent, overall behavior of granular ice from the ductile to brittle regions (Fig. 2.60). These test results followed similar trends of increasing power law coefficients with increasing strain rate and/or decreasing

temperature, even in the ductile region of deformation (data from Jacka 1984).

Other factors which affect the behavior of polycrystalline ice include the level of confinement (Figs. 2.61 through 2.63), grain size (Fig. 2.64) and initial fabric.

7.1.1.3 Frozen Sand

Frozen sands exhibit extremely complex behavior. The review for frozen sands considered the description and structure of frozen sand, an overview of it's mechanical behavior, and a review of possible effects of a pre–freezing effective stress.

Description and Structure

Frozen soil be classified according to the Unified Soil Classification System (Sayles 1989). The ice in a frozen soil is classified on whether it is visible to the naked eye, if it is well–bonded with the soil, and if there is "excess" ice (i.e., increased pore space in the soil due to the freezing process). Frozen soils are also described in terms of the unfrozen water content and the degree of saturation.

Ting et al. (1983) present a possible, idealized structure for frozen sand (Fig. 2.66) for which they suggest: 1) solid contacts exist between most of the sand particles; 2) a continuous unfrozen water film surrounds the silicate particles and is present to very low temperatures; 3) the unfrozen water in this film is mobile parallel to the surface of the particles, but strong tensile and moderate shear adhesional forces can be transmitted between the pore ice and the silicate particles; 4) there are no direct ice to soil contacts; and 5) the macroscopic structure of the ice in the pores is polycrystalline (granular) and the maximum grain size is limited to the size of the individual pores.

Ting et al. (1983) also proposed mechanisms of strength for frozen sand (Table 2.3 and Fig. 2.69). They describe these mechanisms as being derived from three components: the pore ice, the sand skeleton and the ice–sand interaction.

The ice–sand interaction component includes: 1) ice strengthening due to changes in structure, state of stress, deformation constraints and/or strain rate; and 2) soil strengthening due to dilation and structural hindrance.

Overview of the Mechanical Behavior of Frozen Sand

Uniaxial compression or tension tests at constant strain rate (strength test) or constant stress (creep test) are commonly used to study the behavior of frozen sands. Based on these studies, the strength and deformation behavior of frozen sands have been found to depend on numerous variables such as relative density, confining pressure, strain rate and temperature. The behavior may be divided into two regions; small strain behavior and large strain behavior. Idealized stress–strain curves from triaxial compression testing on frozen Manchester Fine Sand show the major features in each of these regions (Fig. 2.70).

The small strain "elastic" properties of Young's modulus and Poisson's ratio have been measured in a number of testing programs (e.g., Baker and Kurfurst 1985; Kaplar 1963; Vinson 1978; and Parameswaran 1980). In summary, a review of these programs indicate the Young's modulus increases moderately with increasing dry density, and perhaps increases with increasing confining pressure. With respect to temperature, Kaplar (1963) found the Young's modulus increases with decreasing temperature ($0 > T > -27^{\circ}C$) for frozen Peabody gravelly sand. In contrast, Baker and Kurfurst (1985) found virtually no change in Young's modulus with decreasing temperature for frozen Ottawa sand (Fig. 2.79).

Limited data exists on the upper yield stress behavior; however, these limited results show an increase in upper yield stress with increasing confinement (Fig. 2.71).

Programs reviewed for large strain behavior are summarized in Table 2.4. In general, these prior programs present only peak strength results, but various

conditions have been studied, i.e., confining pressure, strain rate and temperature. Some general trends include:

1) An increase in sand content or relative density leads to an increase in peak strength (Figs. 2.72 and 2.73).

2) An increase in confining pressure (σ_c) from 0 to 10 MPa generally leads to an increase in peak strength (Fig. 2.74) with total stress friction angle from 0° to 28° reported in this range of σ_c.

3) Strain rate effects (for tests at –10° C) can be described by a simple power law relationship, i.e., $Q_p = k \cdot \dot{\epsilon}^{1/n}$ with power law coefficients generally range from 7 to 16 (Fig. 2.75). Test results from Bragg and Andersland (1980) and Yuanlin et al. (1989) exhibit rate insensitive at higher strain rates.

4) The peak strength was found to consistently increased with decreasing temperature (e.g., Figs. 2.83, 2.84, 2.88, 2.89, 2.90 and 2.92).

5) In general, power law coefficients ranged from 8.5 to 28 for tests at temperatures below –5° C. Tests conducted at –2° C (e.g., Parameswaran 1980, Fig. 2.83; Braggs and Andersland 1980, Fig. 2.84; Orth 1985, Fig. 2.85; and Yuanlin et al. 1988, Fig. 2.91) measured power law coefficients between 3 and 5.6 which are within the range of pure polycrystalline ice.

Limited information on the measured volumetric strain response of frozen sands indicate a net dilation ($+\epsilon_v$) at the end of tests (Figs. 2.77 and 2.86). The total amount of dilation decreases with increased confinement.

Effect of Pre–Freezing Confinement on Frozen Sand Behavior

A review of the available literature found no published testing programs which have compared the effects of confinement on the behavior of frozen sands

using both conventional and consolidate–freeze testing methods. However, a few researchers have frozen sands after applying a confining pressure. Singh et al. (1982) evaluated the effect of freezing on the undisturbed sampling of sands by unidirectionally freezing sand specimens under a hydrostatic effective confining stress of 0.56 ksc. Sego et al. (1982) present test results on a concrete mortar sand which was first consolidated and then frozen and sheared. However, the process was not continuous since the confining pressure was removed prior to shear.

7.1.1.4 Composite/Particulate Modeling of Frozen Sand

This section describes two models which can be used to analyze frozen sand.

Isostrain Model

The isostrain model, adapted from work by Counto (1964) for evaluating the initial modulus of concrete, considers the sand particles to be embedded in a pore ice matrix (Fig. 2.100). This model was previously used by Andersen (1991) and Andersen et al. (1992) to model the initial modulus of frozen MFS. The major assumptions are:

1) The composite material consists of two phases, the aggregate (sand particles) and matrix (pore ice).

2) The sand particles and ice matrix exhibit only elastic deformations; no time dependent behavior can occur.

3) A "perfect bond" exists between the aggregate and matrix. Thus, strain compatibility between the silicate prism and the ice matrix is assured.

Dilatancy–Hardening Model

Ladanyi, in a series of papers (Ladanyi 1981a and b; Ladanyi 1985; and Ladanyi and Morel 1990), developed this particulate model to estimate the strength of a dense frozen sand. The model is based on the dilatancy and soil strengthening mechanisms proposed by Ting et al. (1983). The soil strengthening

is derived from the increased dilative strength of the soil skeleton due to higher effective stresses provided by the tensile strength of the pore ice. In addition, the pore ice matrix can also provide shear strength. In essence, the model predicts the frozen sand strength as the sum of the increased sand strength (due to dilatancy) and the pore ice strength.

7.1.2 Material, Equipment and Experimental Procedures

Chapter 3 describes the materials, equipment, and testing procedures used in the unfrozen and frozen testing programs as well as the data reduction methods and possible errors associated with the test results.

7.1.2.1 Material and Equipment

Manchester Fine Sand (MFS), used in all testing programs, consists primarily of sub–angular quartz and feldspar with some mica flakes. Field samples of the sand were collected from Hooksett, New Hampshire; processed to remove excess fines and re–mixed to form a relatively uniform sand. Figure 3.1 presents the average gradation curve from nine sieve analyses on the processed material. The processed MFS had a median grain size (d_{50}) of 0.18 mm with approximately 7% fines (i.e., < 0.074 mm).

The majority of reported test results were prepared using multiple sieve pluviation (Fig. 3.2). Specimens for unfrozen and consolidate–freeze tests were prepared directly on the base pedestal of the triaxial cell. *Conventional* frozen test specimens were prepared in molds, saturated and frozen prior to set–up in the triaxial cell.

Many of the test components used in the various testing programs can be considered universal since they were identical (i.e., the same design) and could be interchanged between testing programs. Five such components were: 1) modified, high pressure triaxial cells which incorporate lubricated end platens and internal

axial force measurements (Figs. 3.3 and 3.4); 2) pressure/volume control systems (Fig. 3.5); 3) either a screw–driven loading frame (10,000 lb capacity) or a hydraulically–controlled loading frame (8,000 lb capacity); and 4) electronic measuring devices for measuring load, pressure and displacement (with special emphasis on the on–specimen axial strain device, Fig. 3.7). All measurements were recorded using M.I.T. Geotechnical Laboratory's Central Control Acquisition System. Other testing components such as temperature control and measurement techniques and the use of Flexible Automated Technologies for Computer Assisted Testing (FATCAT) systems are also described

7.1.3.2 Experimental Procedures

Chapter 3 briefly described the procedures for the unfrozen, conventional frozen and consolidate–freeze testing programs. Reported unfrozen MFS tests were conducted at a range in relative densities (43.8 to 115.0%) and effective confining stresses (0.1 to 12.5 MPa plus 3 anisotropically consolidated tests). A typical unfrozen MFS test consists of four stages; 1) cell and specimen preparation, 2) specimen saturation, 3) consolidation and 4) shear of the specimen. Sieve analyses of the specimens were performed after shearing. Table 3.2 lists the specimen histories for the unfrozen MFS testing program. Modifications to unfrozen testing procedures are discussed in detail.

The conventional frozen test procedures closely follow those developed by Andersen (1991). Table 3.3 summarizes the histories for the conventional frozen MFS specimens. Forty–nine new tests are reported; 17 at T = –15° C; 19 at T = –20° C and 13 at T = –25° C. Tests were prepared in molds to preshear relative densities between 33 to 93% with the majority of specimens at two D_r, ≈ 35% and ≈ 90%. Nominal confining pressures of either 0.1 and 10 MPa and the three strain rates; slow ($3x10^{-6}$/sec), moderate ($3.5x10^{-5}$/sec) and fast ($5x10^{-4}$/sec), were used

for all tests.

Tests procedures are divided into three stages; specimen preparation and freezing, specimen trimming and set–up, and shearing.

The consolidate–freeze tests represent a unique testing condition where specimens are first consolidated and then frozen while under the desired effective confining stress. Ten consolidate–freeze tests were performed at –10° C on dense specimens under four confining pressures, 0.1, 2, 5 and 10 MPa. All tests were performed at moderate strain rate (3.5×10^{-5}/sec). Test procedures essentially combine the procedures of the unfrozen and conventional frozen MFS testing programs with a specimen freezing phase of testing. Consolidate–freeze testing procedures underwent numerous modifications, especially with respect to specimen freezing procedures.

7.1.2.3 Data Reduction Procedures and Errors

For all test programs, raw data were collected on the Central Control Acquisition System, converted to engineering units using conversion factors, and then used to calculate various testing parameters associated with the different phases of testing. Unfrozen data collection was performed for overnight back–pressure saturation, B–value evaluation, consolidation, and shear. A leakage rate correction was included in calculating the changes in specimen volume during consolidation and drained shear tests. Axial strains measured during shear were corrected for compliance of the loading piston and cell base. Area corrections for sheared specimens consisted of a combination of both parabolic and right–circular cylinder formulations.

Data reduction for conventional frozen tests consisted of determining the preshear leakage rate and cell fluid compressibility for subsequent correction to volumetric strain calculations. Two specimen area correction methods were also

described. Procedures for reducing raw temperature data are presented with additional details presented in Appendix A.

As for the case for the consolidate–freeze testing procedures, consolidate–freeze reduction procedures combine those from the unfrozen and conventional frozen MFS programs.

Test parameters developed for consolidation and shear results are presented as prelude to discussion of the possible errors in the testing programs. Figure 3.14 presents schematic stress–strain (Q–ϵ_a) and volumetric strain (ϵ_v–ϵ_a) responses which illustrate these parameters. Parameters derived from the stress–strain curves were the Young's modulus (E), the yield offset stress at 10^{-4} strain (Q_{yo}), the upper yield stress and corresponding axial strain (Q_{uy} and ϵ_y, respectively) and the peak strength and corresponding axial strain (Q_p and ϵ_p, respectively). The volumetric behavior is described by the maximum rate of dilation, $(d\epsilon_v/d\epsilon_a)_{max}$, and volumetric strain at 20% axial strain, ϵ_{v20}. Additional parameters are used to describe the shear behavior of unfrozen MFS tests include the maximum obliquity, $R_{max} = (\sigma'_1/\sigma'_3)_{max}$; excess pore pressure, u_e; and effective friction angle, ϕ'.

Errors associated with the testing programs include computational sources (i.e., measurement of initial specimen dimensions, volumetric strain corrections and specimen area corrections) and mechanical sources (i.e. membrane rupture and o–ring seal failures).

A repeatability analysis, similar to the one performed by Andersen (1991), was performed for the unfrozen and conventional frozen results. This analysis lead to conclusions as to which tests to include in subsequent presentations.

7.1.3 Unfrozen MFS Behavior

Chapter 4 presents the behavior of unfrozen MFS for various relative densities, effective confining stresses and drainage conditions. State Parameter

concepts, as proposed by Been and Jefferies (1985), were also used to analyze both the undrained and drained test results. The observed consolidation and shear results as well as the steady state analysis are summarized below.

7.1.3.1 Scope of Unfrozen MFS Testing Program

The scope of the unfrozen MFS testing program includes a total of 49 "useful" test: 35 CIUC, 11 CIDC and three CAUC tests. The term "useful" signifies that the tests provide reliable shear results for analysis. Preshear D_r ranged from 30 to 115% with the majority of tests sheared at a nominal strain rate between 8 and 10%/hour. Isotropic consolidation stresses (σ'_c) ranged from nominal 0.1 to 12.5 MPa. Three tests were anisotropically consolidated with final K_c values (σ'_3/σ'_1) ranging from 0.51 to 0.59.

7.1.3.2 Consolidation of Unfrozen MFS

Specimen void ratios decreased with increases in effective confining pressure (Figs. 4.1 through 4.5). Primary consolidation was essentially instantaneous with secondary compression noted for all final consolidation stresses. The rate of secondary compression increased with increased final consolidation stress; however, the rate also decreased with time for all tests.

7.1.3.3 Shear Results

For CIUC tests, the initial stress–strain response is relatively stiff to $\epsilon_a \leq$ 2%. This initially stiff $Q - \epsilon_a$ response is followed by an upper yield point, after which a transition in behavior occurs where the specimens can exhibit strain hardening (low σ'_c, e.g., Fig. 4.) or strain softening followed by little or no strain hardening (high σ'_c, e.g., Fig. 4.12) with continued straining. For CAUC tests, the initial response is also relatively stiff but to less of an extent given the existing high deviator stresses (Fig. 4.16). Continued deformation leads to strain softening after the peak to a nearly constant stress level.

Effective stress paths varied from strong dilative responses for low confinement tests (Fig. 4.7) to strong contractive responses for high confinement tests (Figs. 4.13 and 4.15). The stress paths exhibited a consist trend to loop back beneath themselves. This behavior is indicative of the post–Q_p strain softening.

Constant p′ stress paths were used for all drained tests. For CIDC tests, the initial stress–strain response is also relatively stiff but a distinctive upper yield stress does not exist (Figs. 4.18 and 4.20). Confining pressure has a significant influence on the strength and volumetric behavior of drained tests (Fig. 4.20), with the strength increasing and the volumetric response changing from dilation to compression as confinement increased.

Review of the post–shear sieve analyses (performed on all tests) indicated that undrained tests at high confinement (σ'_c or $\sigma'_{1c} \geq 10$ MPa) exhibited an increase in fines content (3% or greater) from the average gradation curve of non–tested MFS (e.g., Figs. 4.25 and 4.26). A similar condition was found for the drained tests, but at a wider range of confinement levels (Fig. 4.29).

The effective friction angle at maximum obliquity (ϕ'_{max}) varied with applied stress level. For CIUC tests (except those performed at $\sigma'_c = 0.1$ MPa), the average $\phi' = 34.9 \pm 1.4°$ (Fig. 4.30). For low confinement ($\sigma'_c = 0.1$ MPa) CIUC and CIDC tests, a similar friction angle (36.2°) exists with a small effective cohesion ($c' = 0.017$ MPa) (Fig. 4.32). Drained tests at high confinement (10 MPa) exhibited a lower ϕ' (Fig. 4.31).

The initial modulus increases with effective confining stress from 0.2 GPa at $\sigma'_c = 0.1$ MPa to approximately 4 GPa at $\sigma'_c \geq 5$ MPa (Fig. 4.36). The upper yield stress (Q_{uy}), distinct for only the undrained tests, increases with increases in D_r (Fig. 4.37) and σ'_c (Fig. 4.38). The peak strength (Q_p) also increased with increases in D_r and σ'_c (Figs. 4.39 and 4.40, respectively).

Figure 4.41 compared the stress–strain and pore pressure responses of undrained tests at similar D_r ($\approx$ 95%) but different σ'_c. The initial stress–strain response increased significantly with confinement, but all tests exhibited similar strengths at large strains. The pore pressures varied from negative responses for low confinement tests to very high positive responses for high confinement tests. The effective stress paths for these same tests either follow along or fall back to the failure envelope, and all tend to reach a similar point in the q–p′ space (Fig. 4.42). A similar comparison was presented for undrained tests with similar σ'_c ($\approx$ 2 MPa) and different D_r (Figs. 4.43 through 4.46). Increases in D_r translate to increased strength and decreased pore pressure response. Changes in D_r also lead to changes in effective stress paths with looser specimens exhibiting a more contractive response (Fig. 4.45). These tests also exhibited marked "elbows" in their stress paths, i.e., phase transformations.

Comparisons of stress–strain and volumetric strain responses for drained tests were also presented for similar conditions. For the condition of constant D_r ($\approx$ 90%) with varying σ'_c, there is a significant increase in strength with increased σ'_c (Fig. 4.47). In addition, the volumetric responses change from being strongly dilative to strongly contractive. For the condition of varying D_r with constant σ'_c ($\approx$ 0.1 MPa), other is an increase in strength and in dilative volumetric response with increasing D_r (Fig. 4.49).

7.1.3.4 Steady State Analysis Via the State Parameter, Ψ

The steady state analysis of the unfrozen MFS results first required the assessment of appropriate steady state conditions (Fig. 4 51). Chosen steady state points (SSPs) were found to form a linear relationship in e – log I'_1 space (Fig. 4.53) for tests which exhibited small changes in fines content (< 10% total fines). Tests with higher final fines contents indicated a curved SSL would be more

appropriate at high stresses and the results from drained tests (Fig. 4.56) lend more credence to a curved steady state line at low stresses. The linear line was chosen for computational convenience. The slope (λ_{ss}) of the SSL was 0.254 with an $r^2 = 0.95$. Correlations with the state parameter Ψ were presented for the A–parameter at failure (Fig. 4.54) and normalized strength, q/I'_1 (Fig. 4.55).

7.1.4 Behavior of Frozen MFS in Triaxial Compression

Chapter 5 presents the results of the conventional and consolidate–freeze triaxial compression tests performed on frozen Manchester Fine Sand. Discussion focused on the effects of relative density (D_r), confining pressure (σ_c), strain rate ($\dot{\epsilon}$) and temperature (T) on the conventional frozen tests performed at –10° C (by Andersen 1991), –15° C, –20° C and –25° C. A limited discussion was presented on the consolidate–freeze tests performed at T = –10° C.

7.1.4.1 Scope of Testing Program

Presentation of the conventional frozen tests included the work of Andersen at –10° C (50 tests at D_r ranging from 20 to 100% and σ_c of 0.1, 2, 5 and 10 MPa) and tests at –15, –20 and –25° C (49 tests at D_r ranging from 33 to 93% and σ_c of 0.1 and 10 MPa). Tests were conducted at one of three nominal strain rates ($\dot{\epsilon}$): $3x10^{-6}$/sec (termed "slow"), $3.5x10^{-5}$/sec ("moderate") and $5x10^{-4}$/sec ("fast"). Table 5.1 presents the total number of tests from each temperature.

Ten consolidate freeze tests have been performed on relatively dense specimens (D_r = 85 to 103%) and are also summarized in Table 5.1. Nominal σ'_c of 0.1, 2, 5 and 10 MPa were used with all tests sheared at moderate strain rate and T = –10° C.

7.1.4.2 Results of Conventional Frozen Triaxial Compression Tests

Test parameter are summarized in Table 5.3. Discussion is divided into small strain results (E, Q_{yo}, Q_{uy} and ϵ_y) and large strain results (Q_p and ϵ_p).

Volumetric strain results ($(d\epsilon_v/d\epsilon_a)_{max}$ and ϵ_{v20}) are also presented.

Small Strain Behavior

Small strain behavior is summarized in Table 5.4. An average Young's modulus of 26.5 ±4.0 SD GPa is measured for all tests. The Young's modulus for frozen MFS was found to slightly increase with increasing D_r (Fig. 5.1), but slightly decrease with increasing σ_c (Fig. 5.2). The yield offset stress results ranged from 2.7 to 9.7 MPa. The yield offset stress is essentially independent of D_r (Fig. 5.3); decreases slightly with increasing σ_c (Fig. 5.4); and is strongly influence by strain rate (Fig. 5.5) and temperature (Fig. 5.6).

The consistent occurrence of an Q_{uy} represents a significant characteristic of the conventional frozen MFS tests. The Q_{uy} is essentially independent of D_r (Figs. 5.9 and 5.10) and σ_c (Figs. 5.11 and 5.12), but may a slight increase or decrease with increasing σ_c. In contrast, strain rate (Figs. 5.13 and 5.14) and temperature (Figs. 5.15 and 5.16) strongly influence Q_{uy} behavior. For example, power law coefficients, which range from 4.6 to 6.5, increase with decreasing temperature. In addition, the rate of change in Q_{uy} with temperature (dQ_{uy}/dT) increases with increasing strain rate. Similar to the behavior of Q_{uy}, the axial strain at upper yield stress, ϵ_y, is independent of D_r (Fig. 5.17) and σ_c (Fig. 5.18), but is influenced by strain rate and temperature (Figs. 5.19 and 5.20, respectively).

Large Strain Behavior

The effect of D_r, σ_c, $\dot{\epsilon}$ and T on large strain results are summarized in Table 5.5. Figure 5.21 presents a classification system for the stress–strain responses of frozen MFS. Stress–strain curves may be classified as Type A (yield followed by strain softening), Type B (yield followed by approximately constant shear stress), Type C (post–yield strain hardening to peak followed by strain softening) and Type D (post–yield strain hardening to large strains). Figures 5.22 to 5.32

presents comprehensive stress–strain and volumetric strain responses highlighting the effects of D_r, σ_c, $\dot{\epsilon}$, and T on behavior. Based on the σ–ϵ curves in Figs. 5.22 to 5.32 it is clear that all testing variables potentially affect the behavior at peak strength. Figures 5.33 to 5.36 show plots of Q_p versus D_r for a variety of test conditions. In general, increases in D_r lead to increases in Q_p except at lower temperatures and faster strain rates where Q_p coincides with Q_{uy} (i.e., Type A or B curves as shown in Fig. 5.33).

Figures 5.37 and 5.38 presented the Q_p results of tests at different confining pressures. In general, Q_p was found to increase with increasing confinement except at lower densities and faster strain rates/lower temperatures where $Q_p \approx Q_{uy}$.

Figures 5.39 through 5.41 show plots of Q_p versus strain rate for a variety of conditions. The Q_p increased with increasing strain rate with power law coefficients decreasing towards those for Q_{uy} (Fig. 5.14) as the D_r and temperature decreased (Fig. 5.41).

The effects of temperature on Q_p are illustrated in Figs. 5.42 and 5.43. Peak strength tended to linearly increase with decreasing temperature.

The strain at peak strength (ϵ_p) was found to exhibit a complex behavior with D_r and σ_c where low confinement, non–Type A tests exhibited an essentially constant $\epsilon_p = 4.9 \pm 1.2\%$ SD for all D_r and all temperatures (Fig. 5.44). At higher confinement, the ϵ_p for $Q_p \neq Q_{uy}$ stress–strain responses could range from 7 to 20% depending on D_r. The ϵ_p tended to decrease with increasing strain rate or decreasing temperature (Figs. 5.46 and 5.47).

The volumetric behavior is strongly influenced by the D_r and σ_c. For tests at low confinement, an increase in D_r, from loose to dense, leads to a two–fold increase in ϵ_v. Tests on loose and dense specimens at high confinement also suggest a two–fold increase in ϵ_v (Fig. 5.22). Confinement has a significant effect

on ϵ_v where for both loose and dense specimens, there is an approximately twelve–fold decrease in ϵ_v from low to high confinement (Figs. 5.23 and 5.24). The effect of $\dot{\epsilon}$ on ϵ_v is relatively small and complex compared to the effects of D_r and σ_c (Figs. 5.25 through 5.28). A similar behavior is noted for the effects of temperature (Figs. 5.29 through 5.32).

There is a general trend of increasing $(d\epsilon_v/d\epsilon_a)_{max}$ with increasing D_r (Fig. 5.48); a significant reduction in $(d\epsilon_v/d\epsilon_a)_{max}$ with increasing σ_c (Fig. 5.49); and $(d\epsilon_v/d\epsilon_a)_{max}$ may increase or decrease with decreasing temperature (Fig. 5.50). The ϵ_{v20} increases with increasing D_r for tests at low confinement (Fig. 5.51a), but ϵ_{v20} is essentially constant for tests at high confinement (Fig. 5.51b). Increases in σ_c led to a decrease in ϵ_{v20} (Fig. 5.52). The ϵ_{v20} may decrease or increase with decreasing temperature (Fig. 5.53)

7.1.4.3 Results of Consolidate–Freeze Triaxial Tests

Results of consolidate–freeze tests were presented in terms of the unfrozen consolidation, specimen freezing and subsequent shearing. These results are preliminary and should be treated as such.

Freezing of the specimens proved to be the most difficult task, with expelled volumes of pore water lower than theoretically predicted (Table 5.7 and Fig. 5.55).

Shear parameters of consolidate–freeze tests are presented in Table 5.8. In terms of small strain results, Young's moduli for consolidate–freeze tests are slightly lower than comparable conventional frozen tests but are within the range of all conventional frozen results (Fig. 5.56a). A similar condition exist for Q_{yo} versus σ_c (Fig. 5.56b). But, consolidate–freeze tests exhibited no distinguishable upper yield stress at $\sigma'_c \geq 2$ MPa (Fig. 5.57).

The stress–strain responses for consolidate–freeze tests differ substantially from those of comparable conventional frozen tests (Figs. 5.58 an 5.59). However,

the peak strength of consolidate–freeze tests are similar to those for conventional frozen tests, except at σ_c = 10 MPa where the consolidate–freeze tests were somewhat weaker (Figs. 5.59 and 5.60). The volumetric strain responses for the consolidate–freeze are slightly more dilatant than those of conventional frozen tests at similar confinement levels (Fig. 5.59). These preliminary results suggest additional consolidate–freeze testing is warranted.

7.1.5 Analysis of Frozen MFS Results

7.1.5.1 Small Strain Behavior

The extensive evaluation of the Young's modulus, yield offset stress and upper yield region in M.I.T.'s current frozen soil research has no parallel in the current literature. The Young's modulus measured in the conventional frozen and consolidate–freeze tests (26±4.0 GPa) was found to be affected only slightly by relative density and confining pressures and virtually independent of strain rate and temperature. The measured modulus for frozen MFS falls within the range of moduli for other frozen sands measured in programs by other researchers (Table 6.1), with the trend of increasing modulus with density noted in both the current frozen MFS results and in tests on frozen Ottawa sand by Baker and Kurfurst (1985).

The analysis of the frozen results using the isostrain composite model predicted an initial modulus which agreed well with that measured for frozen MFS (Fig. 6.4). The model, adapted from work by Counto (1964) on modeling concrete, also predicts an increase in composite modulus with increasing sand content (specimen density). Based on the excellent agreement between the measured and predicted frozen MFS moduli, it may be more appropriate to consider the frozen sand as a composite material where the mechanisms involved with the interactions between sand skeleton and pore ice matrix describe the strength and deformation

behavior. The assumptions and methodology behind the isostrain model formed the starting point of the conceptual description of frozen MFS as a composite, presented in Section 6.4. For the initial straining of the frozen sand, the sand skeleton and pore ice matrix behave in concert (deform with identical strains). Further straining incurs yielding of the pore ice matrix and the bonds between the sand grains and pore ice (Fig. 6.15).

Analysis of the upper yield region (Q_{uy} and ϵ_y) represents a unique component of the current research since few programs consistently measured or analyzed this region of the stress–strain curve (unless $Q_{uy} = Q_p$). However, the behavior in upper yield region, especially with respect to rate and temperature sensitivities, compares well to that found for the peak strength behavior of ice. However, although exhibiting similar sensitivities, the peak strength of ice is significantly lower than Q_{uy}, probably due to the presence of the sand skeleton. The physical mechanisms involved with "ice strengthening", as proposed by Ting et al. (1983), may apply to this measured small strain behavior, specifically the mechanism of constrained pore ice deformations (caused by the sand skeleton) which may lead to increased ice strength. However, the magnitude of this increased strength is larger than Ting et al. hypothesized.

The Q_{uy} behavior can be conceptually described as a transition of pore ice matrix from an "intact" state, where fracturing is minimal, to a "damaged" state where significant fracturing occurs (Fig. 5.15b). This fracturing does not necessarily lead to a brittle fracture of the frozen sand but does lead to a change in composite structure to a more "granular" state where sand density and confining pressure become more important. This concept of pore ice fracturing mirrors that of pore ice "rupture" at the upper yield stress suggested by Parameswaran (1980).

7.1.5.2 Large Strain Behavior

The large strain behavior, as principally described by the peak strength (Q_p), agrees well with existing data. For frozen MFS tests at higher temperatures where $Q_p \neq Q_{uy}$, the linear increase in Q_p for frozen MFS with increasing D_r (Fig. 5.33) is similar to that of prior programs (Fig. 2.72). For lower temperatures where Q_p may coincide with Q_{uy}, the noted bi–linear trend (Fig. 5.33) is similar to that found by Baker and Kurfurst (Fig. 2.73). The effects of strain rate and temperature on dense frozen MFS behavior compare well with prior data in the sense that similar power law coefficients exist for frozen MFS and other frozen sands tested under similar conditions (Figs. 6.2 and 6.3). The analyses for the axial strain at peak strength and the volumetric strain, presented in Chapter 5, also have no equal in the literature.

Section 6.2 2 details the results of analysis using Ladanyi's (1985) dilatancy–hardening model, which predicts the peak strength of dense frozen sands. The results clearly show that the model consistently under–predicts the measured frozen MFS strength (Figs. 6.8 through 6.13). Review of the model's assumptions indicates that for frozen MFS the model suffers from severe problems of strain incompatibility between the Q_p of frozen and unfrozen MFS and may possibly underestimate the pore ice strength.

The mechanisms involved in the strength of frozen MFS, specifically, those described by Ting et al. (1983) (Section 2.3, Fig. 2.69), were evaluated for their applicability to the measured results. Their mechanisms described in "soil strengthening" (dilatancy and structural hindrance) should lead to a bi–linear $Q_p - D_r$ relationship for non–Type A ($Q_p \neq Q_{uy}$) curves, but linear relationships for the frozen MFS tests in this research was noted (Figs. 5.33 and 5.34). In addition, the results of the aforementioned dilatancy–hardening analysis also

suggest uncertainty in the dilatancy component of soil strengthening.

The conceptual description of frozen MFS behavior (Section 6.4) is extended to large strain behavior using the measured stress–strain behavior (i.e. curve types) as the basis of development (Figs. 6.16 and 6.17). The description considers possible strain softening and strain hardening mechanisms associated with the individual components; i.e., the frictional resistance developed from sand–sand, sand–ice and ice–ice contacts/interactions and the dilatancy (volumetric expansion) caused by sand–ice interactions and pore ice fracturing. The testing variables of relative density, confining pressure, strain rate and temperature combine to form complex variations in post–Q_{uy} behavior to where post–Q_{uy} strengthening or weakening (or both) may occur. Comparison of the rate of strain softening (at the maximum rate of dilation) to the maximum rate of dilation shows that a strong correspondence between stress–strain behavior and dilation exists (Fig. 6.18).

7.2 CONCLUSIONS

A number of conclusions on the behavior of MFS can be drawn from the results of the unfrozen and frozen testing programs. The following presents the conclusions developed from the test results.

1) The unfrozen MFS results follow behavioral patterns which are well–established in soil mechanics. Changes in effective confining stress and relative densities lead to significant changes in stress–strain and pore pressure/volumetric strain responses. An upper yield stress is determined for undrained tests that is mainly dependent on the effective confining stress. Steady state analysis using the state parameter (Ψ) provides a useful method to combine the effects of

density (void ratio) and effective confining stress (σ'_c) on the undrained behavior of MFS. Particle breakage occurs at higher σ'_c levels, which affects the steady state analysis. Representation of the steady state line by a linear segment is appropriate for a range of mean normal effective stress, as long as changes in fines content are taken into account.

2) The stress–strain results from the conventional frozen MFS tests represent the most comprehensive data set on a frozen sand found in the literature. Careful preparation and set–up procedures; along with sophisticated testing techniques such as on–specimen strain measurement, volumetric strain measurements, and lubricated end platens, has lead to robust and high–caliber test results. The current conventional frozen test results, along with the previous results by Andersen (1991) and Andersen et al. (1992) provides the first complete set of data for one frozen soil from very small ($< 0.01\%$) to large ($> 20\%$) strains for a variety of relative densities, confining pressures, strain rates and temperature (Table 5.3).

3) The behavior of frozen MFS at small strains ($\epsilon_a < 1\%$) exhibits similar rate and temperature sensitivities found for polycrystalline ice. The volumetric strain at small strains is essentially zero. The Young's modulus is only slightly dependent on relative density, as predicted by Counto's (1964) isostrain model, and is independent of all other variables. The upper yield stress (Q_{uy}) is essentially independent of relative density and confining pressure, but strongly dependent on strain rate and temperature. For all temperatures and strain rates, the strain at the upper yield stress (ϵ_y) ranged from approximately 0.3 to

1%, which is a similar range found for the failure strain of granular ice. The Q_{uy} also exhibits similar rate and temperature sensitivities found for the peak strength of ice. These aspect of behavior suggest that the same physical mechanisms that control the strength of granular ice also control the of frozen MFS in the Q_{uy} region. It is hypothesized that Q_{uy} represents the onset of significant cracking and fracturing of the pore ice matrix. The yield offset stress illustrates the first effect of yielding of the pore ice matrix, being slightly sensitive to strain rate and temperature.

4) The large strain behavior of frozen MFS is a function of relative density, confining pressure, strain rate and temperature. The affects of these variables can lead to post–upper yield strain hardening or strain softening behavior. It may be best to describe the stress–strain and volumetric behavior of conventional frozen MFS as that of a composite material with the sand skeleton and pore ice matrix continually changing and interacting during deformation. Strain hardening behavior is indicative of a strong frictional resistance (due to the interaction of the sand skeleton in the "damaged" pore ice matrix) caused by increases in relative density or confining pressure. Strain softening behavior is indicative of large volumetric expansion (due to extensive pore ice fracturing). The possible mechanism involved with these interactions, especially those at and beyond the upper yield stress, deserve further research.

These mechanisms combine, in various and, at times, complex manners, to form four basic curve types (Fig. 5.21). Type A curves, where Q_{uy} and Q_p are coincident, generally occur for looser specimens

at low confinement and faster strain rates and/or lower temperatures. Type A curves exhibit significant post–Q_{uy} strain softening and volumetric expansion. In contrast, Type D curves, where $Q_p > Q_{uy}$, generally occur for denser specimens at high confinement and slower strain rates and/or higher temperatures. Type D curves exhibit significant post–Q_{uy} strain hardening and little volumetric expansion.

5) Preliminary results of consolidate–freeze tests show that the effect of a pre–freezing effective stress on the sand skeleton can be fairly significant. Increases in pre–freezing σ'_c led to disappearance of Q_{uy} and a decrease in ϵ_p, while Q_p changed very little. Additional studies are required before definitive conclusions can be made.

6) The isostrain model (Counto 1964) predicts a modulus in excellent agreement with the that measured in the frozen MFS tests. This model provides excellent insight into the initial response of the frozen MFS, suggesting that the material may be better represented as a composite. In contrast, the dilatancy–hardening model (Ladanyi 1985; Ladanyi and Morel 1990) proves deficient in estimating the upper yield or peak strength behavior of frozen MFS. The assumption that similar effective stress systems exist in frozen and unfrozen sands, on which the model is based, is questionable for the following reasons:

    1) Large strain incompatibility between the predicted peak resistance of the sand skeleton in an unfrozen system and the sand skeleton in pore ice matrix;

    2) Presence of pore ice alters the strain pattern of the sand skeleton from that in an unfrozen system.

However, more information on the strength of the pore ice is needed

before a definitive conclusion is reached as to the applicability of this model.

7.3 RECOMMENDATIONS

The writer makes the following recommendations for further research. Recommendations are presented in two areas: improvements in the equipment and testing procedures and suggestions for future research topics.

7.3.1 Equipment and Procedures Development

1) Increase load cell and loading frame capacity to test frozen soils at higher strain rates and possibly lower temperatures
2) For frozen tests, develop a cell fluid circulator which is housed inside the triaxial cell. Fluid circulation should decrease the temperature gradient from the specimen's top to the bottom so that higher temperature tests can be performed. Also, use more accurate thermistors to measure temperatures.
3) Construct an additional triaxial cell to expedite frozen soil testing.
4) For future frozen testing, develop a system to measure very small volumetric strains to the same order as the on–specimen axial strain device ($\approx 0.001\%$).
5) For testing frozen soils, acoustic emission techniques should be used to capture the pore ice cracking activity. Additional tests should also employ careful sectioning techniques on specimens deformed to different strain levels to measure cracking behavior and determine pore ice matrix characteristics (e.g., grain size).
6) Improve the lubricated end cap design for the frozen and unfrozen testing programs to create more consistently stable specimens.

7) Improve the specimen freezing procedures in consolidate–freeze tests to prevent pre–mature freezing of the port for exiting specimen pore fluid as well as enhance specimen freezing efficiency.

8) Develop procedures for forming sand–ice mixtures with $D_r << 0\%$. This should lead to procedures to form pure granular ice specimens.

7.3.2 Future Research Topics

1) Perform further analyses with the existing frozen and unfrozen MFS results. Existing behavioral models, beyond those presented in this thesis, should be evaluated with respect to describing the stress–strain and volumetric behavior of conventional frozen MFS. Satisfactory models, if developed, can be used as a basis for future design procedures.

2) Perform additional conventional frozen tests at –5° C as well as some additional tests at the temperatures of –15°, –20° and –25° C to "fill–in the gaps" of the presently available data set, e.g., tests at $\sigma_c = 2$ and 5 MPa. Additional conventional frozen tests should also be performed at faster strain rates ($\approx 10^{-2}$/sec) to study more brittle behavior of frozen MFS.

3) Continue the consolidate–freeze testing program to evaluate other testing variables, i.e., strain rates and temperatures.

4) Perform tests sand–ice mixtures at $D_r << 0\%$ at similar confining pressures, strain rates and temperatures used in the conventional frozen MFS program. Such data should shed light on the behavior of both "dirty" ice and frozen sand up to the upper yield stress.

5) Perform unload/reload cycles from different strain levels to better define the elastic and anelastic properties of frozen MFS.

CHAPTER 8
BIBLIOGRAPHY

CRREL= U.S. Army Cold Regions Research and Engineering Laboratory
IAHR = International Association for Hydraulics Research
JGE = Journal of Geotechnical Engineering
JGED = Journal of the Geotechnical Engineering Division
JSMFD= Journal of the Soil Mechanics and Foundations Division
SPE–AIME= American Institute of Mining, Metallurgical, and Petroleum Engineers

Adachi, T., F. Oka and H.B. Poorooshap (1990), "A Constitutive Model for Frozen Sand", Journal of Energy Resources Technology, ASME, Vol. 112, Sept. 1990, pp. 208–212

Alarcon–Guzman, A., G.A. Leonards and J.L. Chameau (1988), "Undrained Monotonic and Cyclic Strength of Sands", JGE – ASCE, Vol. 114, No. 10, pp. 1089–1109

Alkire, B.D. and O.B. Andersland (1973), "The Effect of Confining Pressure on the Mechanical Properties of Sand–Ice Materials", Journal of Glaciology, Vol. 12, No. 66, pp. 469–481

Andersen, G.R. (1991), "Physical Mechanisms Controlling the Strength and Deformation Behavior of Frozen Sand", Thesis submitted in partial fulfillment for Doctor of Science degree, Massachusetts Institute of Technology, 560p.

Andersen, G.R., J.T. Germaine, C.C. Ladd and C.W. Swan (1992) "Physical Mechanisms Controlling the Strength and Deformation Behavior of Frozen Sand: I", Final Report to U.S. Army Research Office Contract Number DAAL03–89–K0023, April 1992, 166p.

Andersen, G.R., C.W. Swan, C.C. Ladd, J.T. Germaine (1994), "Small Strain Behavior of Frozen Sand in Triaxial Compression", Submitted to Canadian Geotechnical Journal.

Andersen, O.B. and I. AlNouri (1970), "Time–Dependent Strength Behavior of Frozen Soils", JSMFE – ASCE, Vol. 96, No. SM4, pp. 1249–1265

Andersland, O.B. and D.M. Anderson (1978), Geotechnical Engineering for Cold Regions, McGraw–Hill Book Co. Inc., New York, N.Y.

Andersland, O.B. (1989), "General Report on the Mechanical Properties of Frozen Soil", 5th International Symposium on Ground Freezing, Jones and Holden editors, pp. 433–441

Anderson, D.M. and P. Hoekstra (1965), "Crystallization of Clay–Adsorbed Water", Science, Vol. 149, No. 3681, pp. 318–319

Anderson, D.M. and N.R. Morgenstern (1973), "Physics, Chemistry, and Mechanics of Frozen Ground: A Review", Proceedings of the 2nd International Conference on Permafrost, Yakutsk, U.S.S.R., North American Contribution, pp. 257–288

Anderson, D.M. and A.R. Tice (1980), "Low Temperature Phase Changes in Montmorillonite and Nontronite at High Water Contents and High Salt Contents", Cold Regions Science and Technology, Vol. 3, pp. 139–144

Ang, A. H–S. and W.H. Tang (1975), Probability Concepts in Engineering Planning and Design Volume I Basic Principles. John Wiley and Sons New York, 409p.

Armstrong, R.W. (1970), "The Influence of Polycrystal Grain Size on Several Mechanical Properties of Materials", Metallurgical Transactions, Vol. 1, pp. 1169–1176

Arthur, J.R.F., B.K. Menzies (1972), "Inherent Anisotrophy in a Sand," Geotechnique, Vol. 22, No. 1, pp. 115–128.

Ashby, M.F., and P. Duval (1983), "The Creep of Polycrystalline Ice", Cold Regions Science and Technology, Vol. 11, pp. 285–300

Ashby, M.F., C. Gandhi and D.M.R. Taplin (1979), "Fracture–Mechanism Map and Their Construction for F.C.C. Metals and Alloys, Acta Metallurgica, Vol. 27, pp. 699–729

Athanasiou–Grivas, D. and M.E. Harr (1980), "Particle Contacts in Discrete Materials", JGED, Vol. 106, No. GT5, pp. 559–564

Baker, T.H.W., S.J. Jones, and V.P. Parameswaran (1980), "Confined and Unconfined Compression Tests on Frozen Sands", Proceedings of 4th Canadian Permafrost Conference, pp. 387–393

Baker, T.H.W. and P.J. Kurfurst (1985), "Acoustic and Mechanical Properties of Frozen Sand", 4th International Symposium on Ground Freezing, Sapporo, pp. 227–234

Barnes, P., D. Tabor and J.G.F. Walker (1971), "The Friction and Creep of Polycrystalline Ice", Proceedings of the Royal Society of London, Series A, No. 324, pp. 127–155

Been, K. and M.G. Jefferies (1985), "A State Parameter for Sands", Géotechnique, Vol. 35, No. 2, pp. 99–112

Been, K. and M.G. Jefferies (1986), Discussion, "A State Parameters for Sands", Geotechnique, Vol. 36, No. 1, pp. 123–132

Been, K. and M.G. Jefferies (1986), "Reply: A State Parameters for Sands", Geotechnique, Vol. 36, No. 2, pp. 127–132

Been, K., M.G. Jefferies and J. Hachey (1991), "The Critical State of Sands", Géotechnique, Vol. 41, No. 3, pp. 365–381

Been, K., M.G. Jefferies and J. Hachey (1992), "Reply–The Critical State of Sands", Geotechnique, Vol. 42, No. 4, pp. 660–663

Bishop, A.W. (1954), "The Use of Pore–Pressure Coefficients in Practice", Géotechnique, Vol. 6, pp. 148–152

Bishop, A.W. (1966), Sixth Rankine Lecture "The Strength of Soils as Engineering Materials", Géotechnique, Vol. 16, No. 2, pp. 91–128

Bishop, A.W. (1973), "The Influence of an Undrained Change in Stress on the Pore Pressure in Porous Media of Low Compressibility", Géotechnique, Vol. 23, pp. 435–442

Bishop, A.W. and G. Edlin (1950), "Undrained Triaxial Tests on Saturated Sands and Their Significance in General Theory of Shear Strength", Geotechnique, Vol. 2, pp. 13–32

Black, D.K. and K.L. Lee (1973), "Saturating Laboratory Samples by Back Pressure", JSMFE – ASFE, Vol. 99, SM 1, pp. 75–93

Bourbonnais, J. and B. Ladanyi (1985), "The Mechanical Behavior of Frozen Sand Down to Cryogenic Temperatures", 4th International Symposium on Ground Freezing, Sapporo, pp. 235–244

Bragg, R.A. and O.B. Andersland (1980), "Strain Rate, Temperature, and Sample Size Effects on Compression and Tensile Properties of Frozen Sand", 2nd International Symposium on Ground Freezing, Trondheim, pp. 34–47

Bragg, R.A. and O.B. Andersland (1982), "Strain Rate, Temperature, and Sample Size Effects on Compression and Tensile Properties of Frozen Sand", 2nd International Symposium on Ground Freezing Ground Freezing 80, Frivik, Jambu, Sactersdal and Finbornd eds, [Engineering Geology Vol. 18, Nos. 1–4] pp. 35–46

Brewer, R. (1964), Fabric and Mineral Analysis of Soils, John Wiley and Sons, Inc. pp. 129–158.

Casagrande, A. (1936), "Characteristics of Cohesionless Soils Affecting the Stability of Slopes and Earth Fills", originally published in Journal of the Boston Society of Civil Engineers, Jan. 1936, reprinted in Contributions to Soil Mechanics 1925–1940, BSCE, Boston, pp. 257–276

Casagrande, A. (1975), "Liquefaction and Cyclic Deformation and Sands – A Critical Review", Proceedings of 5th Pan–American Conference Soil Mechanics, Buenios Aires, Vol. 5, pp. 80–133

Castro, G. (1969), "Liquefaction of Sands", Harvard Soil Mechanics Series No. 81, Pierce Hall, Cambridge Ma, 111p

Castro, G. and S.J. Poulos (1977), "Factors Affecting Liquefaction and Cyclic Mobility", JGE – ASCE, Vol. 103, No. GT6, pp. 501–516

Chamberlain, E, C. Groves and R. Perham (1972), "The Mechanical Behavior of Frozen Earth Materials Under High Pressure Triaxial Test Conditions", Géotechnique, Vol. 22, No. 3, pp. 469–483

Chamberlain, E. (1973), "Mechanical Properties of Frozen Ground Under High Pressure", Proceedings of the 2nd International Conference on Permafrost, Yakutsk U.S.S.R., North American Contribution, pp. 295–305

Chu, J. and S–C.R. Lo (1992), "Discussion – Critical State of Sands", Geotechnique, Vol. 42, No. 4, p. 65s.

Coble, R.L. (1963), "A Model for Boundary Diffusion Controlled Creep in Polycrystalline Materials", Journal of Applied Physics, Vol. 34, No. 6, pp. 1679–1682

Colbeck, S.C. (1982), "Configuration of Ice in Frozen Media", Soil Science, Vol. 133, No. 2, pp. 116–123

Colbeck, S.C. (1985), "A Technique for Observing Freezing Fronts", Soil Science, Vol. 139, No. 1, pp. 13–20

Cole, D.M. (1979), "Preparation of Polycrystalline Ice Specimens for Laboratory Experiments", Cold Regions Science and Technology, Vol. 1, pp. 153–159

Cole, D.M. (1983), "The Relationship Between Creep and Strength Behavior of Ice at Failure", Cold Regions Science and Technology, Vol. 8, pp. 189–197

Cole, D.M. (1985), "Grain Size and the Compressive Stength of Ice", Journal of Energy Resources Technology – ASME, Vol. 107, Sept. 1985, pp. 369–374

Cole, D.M. (1986), "Effect of Grain Size on the Internal Fracturing of Polycrystalline Ice", CRREL Report 86–5, 79p

Cole, D.M. (1987), "Strain–Rate and Grain–Size Effects in Ice", Journal of Glaciology, Vol. 33, No. 115, pp. 274–280

Cole, D.M. (1988), "Crack Nucleation in Polycrystalline Ice", Cold Regions Science and Technology, Vol. 15, pp. 79–87

Cole, D.M. (1990), "Reversed Direct–Stress Testing of Ice: Initial Experimental Results and Analysis", Cold Regions Science and Technology, Vol. 18, pp. 303–321

Cole, D.M. and W. F. St. Lawrence (1981), "Acoustic Emissions from Ice", Acoustic Emission/Microseismic Activity in Geologic Structures and Materials, Trans Tech Publications, Germany, pp. 19–35

Corte, A.E. (1962), "Vertical Migration of Particles in Front on a Moving Freezing Plane", Journal of Geophysical Research, Vol. 67, No. 3, pp. 1085–1090

Cottrell, A.H. (1953), Dislocations and Plastic Flow in Crystals, Oxford at the Clarendon Press

Counto, U.J. (1964), "The Effect of the Elastic Modulus of the Aggregate on the Elastic Modulus, Creep and Creep Recovery of Concrete", Magazine of Concrete Research, Vol. 16, No. 48, pp. 129–138

Cundall, P.A., A. Drescher and O.D.L. Strack (1982), "Numerical Experiments on Granular Assemblies; Measurements and Observations", IUTAM Conference on Deformation and Failure of Granular Materials, Delft, pp. 355–370

Dantl, G. (1969), "Elastic Moduli of Ice", Physics of Ice, N. Riehl,, B. Bullemer and H. Engelhardt editors, Plenum Press, New York, pp. 223–230

Duval, P. (1978), "Anelastic Behavior of Polycrystalline Ice", Journal of Glaciology, Vol. 21, No. 85, pp. 621–628

Duval, P., M.F. Ashby and I. Anderman (1983), "Rate–Controlling Processes in the Creep of Polycrystalline Ice", Journal of Physical Chemistry, Vol. 87, No. 21, 1983, pp. 4066–4074

Frydman, S., J.G. Zeitlan and I. Alpan (1973), "The Membrane Effect in Triaxial Testing of Granular Soils", Journal of Testing and Evaluation JTEVA, Vol. 1, No. 1, pp. 37–41

Fukuda, A., T. Hondoh and A. Higashi (1987), "Dislocation Mechanisms of Plastic Deformation of Ice", Journal de Physique, colloque C1, supplément au n° 3, Tome 48, pp. 163–173

Germaine, J.T. and C.C. Ladd (1988), "State of the Art: Triaxial Testing of Saturated Cohesive Soils", ASTM Symposium on Advanced Triaxial Testing of Soil and Rock, Louisville, KY, June 1986

Glen, J.W. (1955), "The Creep of Polycrystalline Ice", Proceedings of the Royal Society of London, Series A, Vol. 228, pp. 519–538

Glen, J.W. (1958), "The Mechanical Properties of Ice I. The Plastic Properties of Ice", Advances in Physics, Vol. 17, pp. 254–265

Glen, J.W. (1963), "The Rheology of Ice", Ice and Snow, The M.I.T. Press, Cambridge, pp. 3–7

Glen, J.W. (1968), "The Effect of Hydrogen Disorder on Dislocation Movement and Plastic Deformation of Ice", Phys. kondens. Materie, Vol. 7, pp. 43–51

Gold, L.W. (1963), "Deformation Mechanisms in Ice", Ice and Snow, W.D. Kingery editor, The M.I.T. Press, Cambridge, pp. 8–27

Gold, L.W. (1972), "The Process of Failure in Columnar–Grained Ice", Philosophical Magazine, Vol. XXVI, series 8, pp. 311–328

Gold, L.W. (1977), "Engineering Properties of Fresh–Water Ice", Journal of Glaciology, Vol. 19, No. 81, pp. 197–212

Goodman, D.J., H.J. Frost and M.F. Ashby (1981), "The Plasticity of Polycrystalline Ice", Philosophical Magazine, Vol. 43, No. 3, pp. 665–695

Goughnour, R.R. and O.B. Andersland (1968), "Mechanical Properties of a Sand–Ice System", JSMFD, Vol. 94, No. SM4, pp. 923–950

Gow, A.J. (1975), "Application of Thin Section Techniques to Studies of Internal Structure of Frozen Silt", Technical Note, U.S. Army CRREL

Hawkes, I. and M. Mellor (1972), "Deformation and Fracture of Ice Under Uniaxial Stress", Journal of Glaciology, Vol. 11, No. 61, pp. 103–131

Haynes, F.D. (1978), "Temperature Effect On the Uniaxial Strength of Ice", 5th International Conference Port and Ocean Engineering Under Arctic Conditions, Norwegian Institute of Technology, pp. 667–681

Herring, C. (1950), "Diffusional Viscosity of a Polycrystalline Solid", Journal of Applied Physics, Vol. 21, pp. 437–445

Hertzberg, R.W. (1989), Deformation and Fracture Mechanics of Engineering Materials 3rd edition, John Wiley and Sons, New York

Higashi, A. (1967), "Mechanisms of Plastic Deformation in Ice Single Crystals", Physics of Snow and Ice, H. Oura editor, pp. 277–289

Higashi, A. (1969), "Mechanical Properties of Ice Single Crystals", Physics of Ice, N. Riehl, B. Bullemer and H. Engelhardt editors, Plenum Press, Hird, C.C. and F. Hassona (1986), "Discussion: A State Parameter for Sands", Geotechnique, Vol. 36, No. 2, pp. 124–127

Hird, C.C. and F.A.K. Hassona (1990), "Some Factors Affecting the Liquefaction and Flow of Saturated Sands in Laboratory Tests", Engineering Geology, Vol. 28, pp. 149–170

Hobbs, P.V. (1974), Ice Physics, Clarendon Press, Oxford

Hoekstra, P. and E. Chamberlain (1964), "Soil Science, Electro–Osmosis in Frozen Soil", Nature, Vol. 203, No. 4952, pp. 1406–1407

Hoekstra, P. (1965), "Conductance of Frozen Bentonite Suspension", Soil Science Society of America Proceedings, Vol. 29, pp. 519–522

Horne, M.R. (1965), "The Behavior of an Assembly of Rotund, Rigid, Cohesionless Particles", Proceedings of the Royal Society of London, Series A, Vol. 286, pp. 62–78

Hvorslev, M.J. (1937), "On the Physical Properties of Disturbed Cohesive Soils", Ingeniorvidenskabelige Skrifter, A., No. 45, 159p.

Ishihara, K., F. Tatsuoka and S. Yasuda (1975), "Undrained Deformation and Liquefaction of Sand Under Cyclic Stresses", Soils and Foundations, Vol. 15, No. 1, pp. 29–40

Ignat, M. and H.J. Frost (1987), "Grain Boundary Sliding in Ice", Journal de Physique, Colloque C1, supplément au n° 3, Tome 48, pp. C1–189 to C1–195

Jellinek, H.H.G. (1962), "Ice Adhesion", Canadian Journal of Physics, Vol. 40, pp. 1294–1309

Jones, S.J. (1978), "Triaxial Testing of Polycrystalline Ice", Proceedings of the Third International Conference on Permafrost, Vol. 1, pp. 670–674

Jones, S.J. (1982), "The Confined Compressive Strength of Polycrystalline Ice", Journal of Glaciology, Vol. 28, No. 98, pp. 171–177

Jones, S.J. and J.W. Glen (1969a), "The Mechanical Properties of Single Crystals of Pure Ice", Journal of Glaciology, Vol. 8, No. 54, pp. 463–473

Jones, S.J. and J.W. Glen (1969b), "Impurity Effects on the Plasticity of Ice and Their Explanation in Terms of Hydrogen Reorientation", Physics of Ice, N. Riehl, B. Bullemer and H. Engelhardt editors, Plenum Press, New York, pp. 217–222

Jones, S.J. and N.K. Gilra (1975), "Dislocations in Ice Observed by X–ray Topography", Physics and Chemistry of Ice, E. Whalley, S.J. Jones and L.W.Gold editors, pp. 344–349

Jones, S.J. and V.R. Parameswaran (1983), "Deformation Behavior of Frozen Sand–Ice Materials Under Triaxial Compression", 4th International Conference on Permafrost, Fairbanks, pp. 560–565

Jacka, T. H. (1984), "The Time and Strain Required for Development of Minimum Strain Rates in Ice", Cold Regions Science and Technology, Vol. 8, pp. 261–268

Kaplar, C.W. (1963), "Laboratory Determination on the Dynamic Moduli of Frozen Soils and of Ice", Proceedings Permafrost International Conference, Lafayette Indiana, pp. 293–301

Koerner, R.M. (1970), "Effect of Particle Characteristics on Soil Strength", JSMFE – ASCE, Vol. 96, SM 4, July 1970, pp. 1221–1234

Konrad, J.M. (1990a), "Minimum Undrained Strength of Two Sands", JGE, Vol. 116, No. 6, pp. 932–947

Konrad, J.M. (1990b), "Minimum Undrained Strength Versus Steady–State Strength of Sands", JGE, Vol. 116, No. 6, pp. 948–963

Kramer, S.L., N. Sivaneswaran and R.O. Davis (1990), "Analysis of Membrane Penetration in Triaxial Tests", Journal of Engineering Mechanics – ASCE, Vol. 116, No. 4, April 1990, pp. 773–789

Ladanyi, B. (1981a), "Mechanical Behavior of Frozen Soils", Mechanics of Structured Media Proceedings of the International Symposium on Mechanical Behavior of Structured Media, Part B, Ottawa, pp. 205–245

Ladanyi, B. (1981b), "Shear–induced Stresses in the Pore Ice in Frozen Particulate Materials", Proceedings of the Symposium on Free Boundary Problems, A. Fasano and M. Primicerio eds., Montecatini, Vol. II, pp. 549–560

Ladanyi, B. (1985), "Stress Transfer Mechanism in Frozen Soils", Proceedings of the Tenth Canadian Congress of Applied Mechanics, University of Western Ontario, London

Ladanyi, B. and J. Morel (1990), "Effect of Internal Confinement on Compression Strength of Frozen Sand", Canadian Geotechnical Journal, Vol. 27, pp. 8–18

Ladd, C.C., R. Foott, K. Ishihara, F. Schlosser and H.G. Poulos (1977), "Stress–Deformation and Strength Characteristics", Ninth International Conference on Soil Mechanics and Foundation Engineering, Tokyo, pp. 421–494

Lambe, T.W. and R.V. Whitman (1969), Soil Mechanics, John Wiley and Sons, New York

Langdon, T.G. (1973), "Creep Mechanisms in Ice", Physics and Chemistry of Ice, E. Whalley, S.J. Jones and L.W. Gold editors, pp. 356–361

Lee, K.L. (1977), "Adhesion Bonds in Sands at High Pressures", JGED, Vol. 103, No. GT8, pp. 908–913

Lee, K.L. and H.B. Seed (1967), "Drained Strength Characteristics of Sands", JSMFD, Vol. 93, No. SM6, pp. 117–141

Martin, R.T., J.M. Ting and C.C. Ladd (1981), "Creep Behavior of Frozen Sand Final Report Part 1", M.I.T. Department of Civil Engineering, Research Report No. R81–19, 237p

Mellor, M. (1980), "Mechanical Properties of Polycrystalline Ice", Physics and Mechanics of Ice, Symposium Copenhagen 1979 IUTAM, pp. 217–245

Mellor, M. and D.M. Cole (1982), "Deformation and Failure of ice Under Constant Stress of Constant Strain–Rate", Cold Regions Science and Technology, Vol. 5, pp. 201–219

Mellor, M. and R. Testa, (1969a) "Effect of Temperature on the Creep of Ice", Journal of Glaciology, Vol. 8, No. 52, pp. 131–145

Mellor, M. and R. Testa, (1969b), "Creep of Ice Under Low Stress", Journal of Glaciology, Vol. 8, No. 52, pp. 147–152

Mitchell, J.K. (1976), Fundamentals of Soil Behavior, John Wiley and Sons, New York

Mohamad, R. and R. Dobry (1986), "Undrained Monotonic and Cyclic Triaxial Strength of Sand", JGE, Vol. 112, No. 10, pp. 941–958

Murrell, S.A.F., P.R. Sammonds and M.A. Rist (1989), "Strength and Failure Modes of Pure Ice and Multi–Year Sea Ice Under Triaxial Loading" Ice–Structure Interaction, IUTAM–IAHR Symposium, 1989, St. John's Newfoundland, Canada, pp. 339–361.

Nabarro, F.R.N. (1947), "Dislocations in a Simple Cubic Lattice", The Proceedings of the Physical Society, Vol. 59, pp. 256–272

Nadreau, J.P. and B. Michel (1986), "Yield Envelope for Confined Ice", Ice Technology, Proceedings of 1st International Conference, Murthy, Connor, and Breffia eds., Cambridge, MA, pp. 25–36

Neguesey, D., W.K.D. Wijewickreme and V.P. Vaid (1988), "Constant–Volume Friction Angle of Granular Materials", Canadian Geotechnical Journal, Vol. 25, pp. 50–55

Nicholoson, P.G., H.A. Ammer and R.B. Seed (1992), "An Injection–Correction System to Mitigate Membrane Compliance", Geotechnical Testing Journal, Vol. 15, No. 2, pp. 190–197

Ochiai, H. and P.V. Lade (1983), "Three–Dimensional Behavior of Sand with Anisotropic Fabric", JGE, Vol. 109, No. 10, pp. 1313–1328

Oda, M. (1972), "Initial Fabrics and Their Relations to Mechanical Properties of Granular Material", Soils and Foundations, Vol. 12, No. 1, pp. 17–36

Oda, M. and J. Konishi (1974), "Microscopic Deformation Mechanism of Granular Material in Simple Shear", Soils and Foundations, Vol. 14, No. 4, pp. 25–38

Oda, M. (1981), "Anisotropic Strength of Cohesionless Sands", JGED, Vol. 107, No. GT9, pp. 1219–1231

Orth, W. (1985), "Deformation Behavior of Frozen Sand and Its Physical Interpretation", 4th International Symposium on Ground Freezing, Sapporo, pp. 245–253

Parameswaran, V.R. (1980), "Deformation Behavior and Strength of Frozen Sand", Canadian Geotechnical Journal, Vol. 17, pp. 74–88

Parameswaran, V.R., and S.J. Jones (1981), "Triaxial Testing of Frozen Sand", Journal of Glaciology, Vol. 27, No. 95, pp. 147–155

Parameswaran, V.R. and M. Roy (1982), "Strength and Deformation of Frozen Saturated Sand at –30° C", Canadian Geotechnical Journal, Vol. 19, pp. 104–107

Perkins, T.K. and R.A. Reudrich (1973), "The Mechanical Behavior of Synthetic Permafrost", Society of Petroleum Engineers Journal, Transactions SPE–AIME, Vol. 255, pp. 211–220

Pettijohn, F.J. (1975), Sedimentary Rocks 3rd ed., Harper and Row, New York

Poulos, S.J. (1981), "The Steady State of Deformation", JGED, Vol. 107, No. GT5, pp. 553–562

Poulos, S.J., G. Castro and J.W. France (1985), "Liquefaction Evaluation Procedure", JGE, Vol. 111, No. 6, pp. 772–792

Poulos, S.J., G. Castro and J.W. France (1988), closure to "Liquefaction Evaluation Procedure", JGE, Vol. 114, No. 2, pp. 251–259

Raj, R. and M.F. Ashby (1971), "On Grain Boundary Sliding and Diffusional Creep", Metallurgical Transactions, Vol. 2, pp. 1113–1127

Roscoe, K.H., A.N. Schofield and C.P. Wroth (1958), "On the Yielding of Soils", Géotechnique, Vol. 8, pp. 22–53

Rowe, P.W. (1962), "The stress–Dilatancy Relation for Static Equilibrium of an Assembly of Particles in Contact", Proceedings of the Royal Society of London, Series A, Vol. 269, pp. 500–527

Rowe, P.W. (1971), "Theoretical Meaning and Observed Values of Deformation Parameters for Soil", Stress–Strain Behavior of Soils, R.H.G. Parry editor, G.T. Foulis & Co., Henley–on–Thames, Oxfordshire, pp. 143–194

Sayles, F.H. and N.V. Epanchin (1966), "Rate of Strain Compression Tests on Frozen Ottawa Sand and Ice", Technical Note for Internal Distribution at U.S. Army CRREL

Sayles, F.H. (1973), "Triaxial and Creep Tests on Frozen Ottawa Sand", 2nd International Permafrost Conference, North American Contribution, pp. 384–391

Sayles, F.H., T.H.W. Baker, F. Gallavres, H.L. Jessberger, S. Kinosita, A.V. Sadovskiy, D. Sego and S.S. Vyalov (1987), "Classification and Laboratory Testing of Artificially Frozen Ground", Journal of Cold Regions Engineering, Vol. 1, No. 1, pp. 22–48

Sayles, F.H. (1989), "State–of–the–Art: Mechanical Properties of Frozen Soil", 5th International Symposium on Ground Freezing",

Schulson, E.M. and N.P. Cannon (1984), "The Effect of Grain Size on the Compressive Strength of Ice", IAHR Ice Symposium 1984, Hamburg, pp. 29–38

Schulson, E.M. (1987), "The Fracture of Ice Ih", Journal De Physique, Colloque C1, supplément au n° 3, Tome 48, pp. 207–220

Seed, H.B. and R. Lundgren (1954), "Investigation of the Effect of Transient Loading on the Strength and Deformation Characteristics of Saturated Sands", Proceedings ASTM, Vol. 54, pp. 1288–1306

Seed, H.B. and I.K. Lee (1967), "Undrained Strength Characteristics of Cohesionaless Soils", JSMFD, Vol. 93, No. SM6, pp. 333–360

Sego, D.C., T. Schultz and R. Banasch (1982), "Strength and Deformation Behavior of Frozen Saline Sand", 3rd International Symposium on Ground Freezing, Hanover, pp.11–17

Sheahan, T.C. (1991), "An Experimental Study of the Time–Dependent Undrained Shear Behavior of Resedimented Boston Blue Clay Using Automated Stress Path Triaxial Equipment", Thesis submitted in partial fulfillment for Doctor of Science degree, Massachusetts Institute of Technology, 970p.

Shibata, T., T. Adachi, A. Yashima, T. Takahashi and I. Yoshioka, (1985), "Time–Dependence and Volumetric Change Characteristic of Frozen Sand Under Triaxial Stress Condition", 4th International Symposium on Ground Freezing, Sapporo, pp. 173–179

Shyam Sunder, S. (1993) "Statement of Research in Ice Mechanics", M.I.T. Department of Civil and Environmental Engineering, 74 p.

Shyam Sunder, S. and M.S. Wu (1989), "A Differential Flow Model for Polycrystalline Ice", Cold Regions Science and Technology, Vol. 16, pp. 45–62

Shyam Sunder, S. and M.S. Wu (1990), "Crack Nucleation Due to Elastic Anisotropy in Polycrystalline Ice", Cold Regions Science and Technology, Vol. 18, pp. 29–47

Singh, S., H.B. Seed and C.K.Chan (1982), "Undisturbed Sampling of Saturated Sands by Freezing", JGED, Vol. 108, No. GT2, pp. 247–264

Sinha, N.K. (1978), "Observation of Basal Dislocations in Ice by Etching and Replicating", Journal of Glaciology, Vol. 21, No. 85, pp. 385–395

Sinha, N.K. (1989), "Elasticity of Natural Types of Polycrystalline Ice", Cold Regions Science and Technology, Vol. 17, pp. 127–135

Skempton, A.W. (1954), "The Pore–Pressure Coefficients A and B", Géotechnique, Vol. 4, pp. 143–147

Sladen, J.A., R.D. O'Hollander and J. Krahn (1985), "The Liquefaction of Sand, A Collapse Surface Approach", Canadian Geotechnical Journal, Vol. 22, pp.564–578

Steinfink, H. J.E. Gebhart (1962), "Compression Apparatus for Powder X–Ray Difffractometry", The Review of Scientific Instruments, Vol. 33, No. 5, pp. 542–544

Sayles, F. (1989), "State of the Art: Mechanical Properties of Frozen Soil", 5th International Symposium on Ground Freezing Ground Freezing 88, Jones and Holden eds., Vol. 1, pp. 143–165

Schulson, E.M. (1990), "The Brittle Compressive Fracture of Ice", Acta Metal, Material, Vol. 38, No. 10, pp. 1863–1976

Terzaghi, K. (1925), Erdbaumechanik, Franz Deuticke, Vienna, portions reproduced in From Theory to Practice in Soil Mechanics, John Wiley and Sons, New York, 1960

Ting, J.M., R.T. Martin and C.C. Ladd (1983), "Mechanisms of Strength for Frozen Sand", JGE, Vol. 109, No. 10, pp. 1286–1302

Vinson, T.S. (1978), "Parameter Effects on Dynamic Properties of Frozen Soils", JGED, Vol. 104, GT10, pp. 1289–1306

Vaid, Y.P. and J.C. Chern (1985), "Cyclic and Monotonic Undrained Response of Saturated Sands", Advances in the Art of Testing Soils Under Cyclic Conditions, ASCE Annual Convention, Detroit, pp. 120–147

Vaid, Y.P., E.K.F. Chung and R.H. Kuerbis (1990), "Stress Path and Steady State", Canadian Geotechnical Journal, Vol. 27, pp. 107

Vaid, Y.P. and V. S. Pillai (1992), "Discussion – Critical States of Sands", Geotechnique, Vol. 42, pp. 658–660

Verdugo, R. (1992), "Discussion – Critical States of Sand", Geotechnique, Vol. 42, No. 4, pp. 655–658

Vesic, A.S. and G.W. Clough (1968), "Behavior of Granular Materials Under High Stresses", JSMFE – ASCE, Vol. 94, No. SM3, pp. 661–688

Weertman, J. (1983), "Creep Deformation of Ice", Annuals of Review of Earth and Planetary Science, Vol. 11, pp 215–240

Wilson, C.J.L. and D.S. Russell–Head (1982), "Steady–State Preferred Orientation of Ice Deformed in Plane Strain at –1° C", Journal of Glaciology, Vol. 28, No. 98, pp. 145–160

Wong, R.K.S. and J.R.F. Arthur (1985), "Induced and Inherent Anistrophy in Sand", Geotechnique, Vol. 35, No. 4, pp. 471–481

Yuanlin, Z., Z. Jiayi and S. Zhongyan (1988), "Uniaxial Compressive Strength of Frozen Medium Sand Under Constant Deformation Rates", 5th International Symposium on Ground Freezing", pp. 225–232

Zener (1948), see Cole (1988) or Cole (1986)

Zheleznyi, B.V. (1969) "The Density of Supercooled Water", Russian Journal of Physical Chemistry, Vol. 43, No. 9, p. 1311

ADDITIONAL REFERENCES

The following references were not used in preparation of this thesis, primarily due to the writer's self–imposed limits in thesis length (and time). However, these references may prove useful to readers who wishes to further explore certain aspects of the research. The below references pertain to laboratory testing procedures and techniques as well as additional material on the behaviors of unfrozen sand, ice and frozen soils. The writer notes that the following reference list is not complete for any of these of subjects but is included merely to provide additional information from which to base future research efforts.

Alarcon–Guzman, A. and G.A. Leonards (1988), "Discussion: Liquefaction Evaluation Procedure", JGL – ASCE, Vol. 114, No. 2, pp. 232–236

Armstrong, R.W. (1969), "Strength Properties of Ultrafine–Grain Metals", Ultrafine–Grain Metals, J.J.Burke and V. Weiss editors, Syracuse University Press, pp. 1–28

Arthur, J.R.F., S. Bekenstein, J.T. Germaine and C.C. Ladd (1981), "Stress Path Tests with Controlled Rotation of Principal Stress Directions", ASTM special technical publication 740, pp.516–540

Ashby, M.F. (1972), "A First Report on Deformation–Mechanism Maps", Acta Metallurgica, Vol. 20, pp. 887–897

Baker, R.W. (1978), "The Influence of Ice–Crystal Size on Creep", Journal of Glaciology, Vol. 21, No. 85, pp. 485–500

Bao, G.W., J.W. Hutchinson and R.M. McMeeking (1991) "The Flow Stress of Dual–Phase, Non–Hardening Solids", Mechanics of Materials, Vol. 12, pp. 85–94

Bao, G., J.W. Hutchinson and R.M. McMeeking (1991) "Particle Reinforcement of Ductile Matrices Against Plastic Flow and Creep", Acta Metall. mater, Vol. 39, No. 8, pp. 1871–1882

Billam, J. (1971), "Some Aspects of the Behavior of Granular Materials at High Pressures", Stress–Strain Behavior of Soils, R.H.G. Parry editor, G.T. Foulis & Co., Henley–on–Thames, Oxfordshire

Bishop, A.W. (1971), "Shear Strength Parameter for Undisturbed and Remolded Soil Specimens", Proceedings Roscoe Memorial Symposium on Stress–Strain Behavior of Soils, Cambridge, U.K., pp. 3–58

Bishop, A.W. and G. Edlin (1953), "The Effort of Stress History on the Relation Between Ø and Porosity in Sand", Proceedings of 3rd International Conference of SMFE, Vol. 1, pp. 100–105

Bishop, A.W. and G.E. Greene (1964), "The Influence of End Restraint on the Compression Strength of a Cohesionless Soil", Geotechnique, Vol. 15, No. 3, pp. 243–265

Bishop, A.W., D.L. Webb and A.E. Skinner (1965), "Triaxial Tests on Soil at Elevated Cell Pressures", 6th International Conference of SMFE, Montreal, pp. 120–174

Bolton, M.D. (1986), "The Strength and Dilatancy of Sands", Geotechnique, Vol. 36, No. 1, pp. 65–78

Bora, P.K. (1984), "Shear Failure in Granular Media", JGE, Vol. 110, No. 5, pp. 582–598

Bosscher, P.J. and D.L. Nelson (1987), "Resonant Column Testing of Frozen Ottawa Sand", Geotechnical Testing Journal, ASTM, Vol. 10, No. 3, pp. 123–134

Bowden, F.P. and D. Tabor (1964), The Friction and Lubrication of Solids Part II, Oxford, Clarendon Press

Bowles, J.E. (1978), Engineering Properties of Soils and Their Measurement 2nd ed., McGraw–Hill, New York

Brace, W.F. (1963), "Behavior of Quartz During Indentation", Journal of Geology, Vol. 71, pp. 581–595

Bromwell, L.G. (1996), "The Friction of Quartz in High Vacuum", Research in Earth Physics Phase Report No. 7, MIT Department of Civil Engineering, 119p

Cannon, N.P., E.M. Schulson, T.R. Smith and H.J. Frost, (1990), "Wing Cracks and Brittle Compressive Fracture", Artic metall. Materials, Vol. 38, No. 10, pp. 1955–1962

Chu, J. and S–C.R. Lo (1993), "On the Measurement of Critical State Parameters of Dense Granular Soils", Geotechnical Testing Journal, GTJODJ, Vol. 16, No. 1, pp 27–35

Colliat–Dangus, J.L., J. Desrues and P. Forny (1988), "Triaxial Testing of Granular Soil Under Elevated Cell Pressure", Advanced Triaxial Testing of Soil and Rock, ASTM STP 977, pp. 290–310

Dillon, H.B. and O.B. Andersland (1966), "Deformation Rates of Polycrystalline Ice", Physics of Snow and Ice, International Conference on Low Temperature Science, Aug. 1966, Sapparo, Japan, Vol. I, Part I, pp. 313–327

Duncan, J.M. and H.B. Seed (1962), "Corrections for Strength Test Data", JSMFE – ASCE, Vol. 93, SM5, pp. 121–137

Epifanov, V.P. (1982), "On the Mechanical Properties of Ice", Mechanics of Solids (USSR), Vol. 17, No. 1, pp. 182–192

Faruque, M.D. and M.M. Zaman (1991), "On the Concept of Characteristic States of Cohesionless Soil and Constitutive Modeling", Soils and Foundations, Vol. 31, No. 2, pp. 164–174

Fish, A. M. (1982), "Deformation and Failure of Frozen Soils and Ice at Constant and Steadily Increasing Stresses", Proceedings of 4th Canadian Permafrost Conference, pp. 419–428

Frank, F.C. (1965), "On Dilatancy in Relation to Seismic Sources", Reviews of Geophysics, Vol. 3, No. 4, pp. 485–503

Friedel, J. (1963), "On the Elastic Limit of Crystals", Electron Microscopy and Strength of Crystals, G. Thomas and J. Washburn editors, John Wiley and Sons, New York, pp. 605–649

Fukumoto, T. (1992), "Particle Breakage Characteristics of Granular Soils", Soils and Foundations, Vol. 32, No. 1, pp. 26–40

Fukuda, A. and A. Higashi (1973), "Dynamical Behavior of Dislocations in Ice Crystals", Crystal Lattice Defects, Vol. 4, pp. 203–210

Gilbert, P.A. and W.F. Marcuson III (1988), "Density Variation in Specimens Subjected to Cyclic and Monotonic Loads", JGE, Vol. 114, No. 1, pp. 1–20

Gittus, J. (1975), Creep, Viscoelasticity and Creep Fracture in Solids, John Wiley and Sons, New York

Glen, J.W. and S.J. Jones (1967), "The Deformation of Ice Single Crystals at Low Temperatures", Physics of Snow and Ice, H. Oura editor, pp. 267–275

Goodman, D.J., H.J. Frost and M.F. Ashby (1981), "The Plasticity of Polycrystalline Ice", Philosophical Magazine, A, Vol. 43, No. 3, pp. 665–695

Goodman, M.A, (1975), "Mechanical Properties of Simulated Deep Permafrost", ASME, Journal of Engineering for Industry, Series B, Vol. 97, No. 5, pp. 417–425.

Gourves, R. (1981), discussion of "Particle Contacts in Discrete Materials", JGED, Vol. 107, No. GT10, pp. 1437–1439

Hall, E.O. (1951), "The Deformation and Ageing of Mild Steel: III Discussion of Results", Proceedings of the Physical Society of London, Series B, Vol. 64, pp. 747–753

Hardin, B.O. (1985), "Crushing of Soil Particles", JGE, Vol. 111, No. 10, pp. 1177–1192

Hardin, B.O. (1989), "Low–Stress Dilation Test", JGE, Vol. 115, No. 6, pp. 769–787

Hanzana, H. (1980), "Undrained Strength and Stability Analysis for a Quick Sand", Soils and Foundations, Vol. 20, No. 2, pp. 17–29

Healy, K.A. (1963), "The Dependence of Dilation in Sand on Rate of Shear Strain", Thesis submitted in partial fulfillment of the requirements for the degree of Doctor of Science at MIT

Hoekstra, P. (1969), "The Physics and Chemistry of Frozen Soils", Special Report #103, Highway Research Board, pp. 78–90

Homer, D.R. and J.W. Glen (1978), "The Creep Activation Energies of Ice", Journal of Glaciology, Vol. 21, No. 85, pp. 429–444

Hooke, R. Leb., B.B. Dahlin, and M.T. Kauper (1972), "Creep of Ice Containing Dispersed Fine Sand" Journal of Glaciology, Vol. 11, No. 63, pp. 327–336

Horne, M.R. (1968), "The Behavior of an Assembly of Rotund, Rigid, Cohesionless Particles, Part III", Proceedings of Royal Society of London, Series A, Vol. 310, pp. 21–34

Jacka, T.H. and M. Maccagnan (1984), "Ice Crystallographic and Strain Rate Changes with Strain in Compression and Extension", Cold Regions Science and Technology, Vol. 8, pp. 269–286

Jardine, R.J., M.J. Symes and J.B. Burland (1984), "The Measurement of Soil Stiffness in the Triaxial Apparatus", Géotechnique, Vol. 34, pp. 323–340

Jefferies, M.G. (1993), "Nor–Sand: A Simple Critical State Model for a Sand", Geotechnique, Vol. 43, No. 1, pp. 91–103

Johnston, T.L. and C.E. Feltner (1970), "Grain Size Effects in the Strain Hardening of Polycrystals", Metallurgical Transactions, Vol. 1, pp.1161–1167

Karr, D.G. (1985) "A Damage Mechanics Model for Uniaxial Deformation of Ice", 4th Intl. Symp. on Offshore Mechanics and Antic Engineering, Feb. 1985, ASME and Journal of Energy Resources Technology, Vol. 107, Sept. 1985, pp. 363–368

Keh, A.S. and S. Weissmann (1963), "Deformation Substructure in Body–Centered Cubic Metals", Electron Microscopy and Strength of Crystals, G. Thomas and J. Washburn editors, John Wiley and Sons, New York, pp. 231–300

Kim, Y.R. and D.N. Little (1990), "One–Dimensional Constitutive Modeling of Asphalt Concrete", Journal of Engineering Mechanics – ASCE, Vol. 116, No. 4, April 1990, pp. 751–772

Konrad, J.M. (1993), "Undrained Response of Loosely Compacted Sands During Monotonic and Cyclic Compression Tests", Geotechnique, Vol. 43, No. 1, pp. 69–89

Kuribayashi, E., M. Kawamura and Y. Yui (1985), "Stress–Strain Characteristics of and Artificially Frozen Sand in Uniaxially Compressive Tests", 4th International Symposium on Ground Freezing, Sapporo, pp. 177–182

Ladd, R.S. (1974), "Specimen Preparation and Liquefaction of Sand", JGED – ASCE, Vol 100, No. SM10, pp. 1180–1184

Lade, P.V and J.M. Duncan (1973), "Cubical Triaxial Tests on Cohesionless Soil", JSMFD, Vol. 99, No. SM10, pp. 793–812

Lade, P.V. and J.M. Duncan (1976), "Stress–Path Dependent Behavior of Cohesionless Soil", JGED – ASCE, Vol. 102, No. GT1, pp. 51–68

Lade, P.V. and S.B. Herrandez (1977), "Membrane Penetration Effects in Undrained Tests", JGED – ASCE, Vol. 103, No. GT2, pp. 109–125

Lambe, T.W. (1951), Soil Testing for Engineers, John Wiley and Sons, New York

Lee, K.L. and I. Farhoomand (1967), "Compressibility and Crushing of Granular Soil in Anisotropic Triaxial Compression", Canadian Geotechnical Journal, Vol. 4, No. 1, pp. 68–86

Li, J.C.M. (1963), "Petch Relation and Grain Boundary Sources", Transactions of the Metallurgical Society of AIME, Vol. 227, pp. 239–247

Li, J.C.M. and Y.T. Chou (1970), "The Role of Dislocations in the Flow Stress Grain Size Relationships", Metallurgical Transactions, Vol. 1, pp. 1145–1159

Linell, K.A. and C.W. Kaplar (1966), "Description and Classification of Frozen Soil", Technical Report 150, U.S. Army CRREL

Maishman, D., J.P. Powers and V.J. Lunardini (1988), "Freezing a Temporary Roadway for Transport of a 3000 ton Dragline", 5th International Symposium on Ground Freezing, Nottingham, pp. 357–366

Mellor, M. and D.M. Cole (1983), "Stress/Strain/Time Relations for Ice Under Uniaxial Compression", Cold Regions Science and Technology, Vol. 6, pp. 207–230

Mellor, M. and J.H. Smith (1967), "Creep of Snow and Ice", Physics of Snow and Ice, Vol. 1, Part 2, Oura, H. ed., pp. 843–855

Michel, B. (1978), "The Strength of Polycrystalline Ice", Canadian Journal of Civil Engineering, Vol. 5, No. 3, Sept. 1978, pp. 285–300

Miller, R.D. (1973), "Soil Freezing in Relation to Pore Water Pressure and Temperature [1]", Proceedings of the 2nd International Conference on Permafrost, Yakutsk, U.S.S.R., North American Contribution, pp. 344–352

Mitchell, J.K. and Z.V. Solymar (1984), "Time–Dependent Strength Gain in Freshly Deposited of Densified Sand", JGE, Vol. 110, No. 11, pp. 1559–1576

Miura, N., H. Murata and N. Yasufuku (1984), "Stress–Strain Characteristics of Sand in a Particle – Crushing Region", Soils and Foundations, Vol. 24, No. 1, pp. 77–89

Miura, S. and S. Toki (1982), " A Sample Preparation Method and Its Effect on Static and Cyclic Deformation – Strength Properties of Sand", Soils and Foundations, Vol. 22, No. 1, pp. 61–77

Murrmann, R.P., P. Hoekstra and R.C. Bialkowski, (1968), "Self–Diffusion of Ions in Frozen Wyoming Bentonite–Water Paste", Soil Science Society of America Proceedings, Vol. 32, pp. 501–506

Nakamura, T. and S.J. Jones (1973), "Mechanical Properties of Impure Ice Crystals", Physics and Chemistry of Ice, E. Whalley, S.J. Jones and L.W. Gold editors, pp. 365–369

Nicholson, P.G., R.B. Seed and H. Anwar (1989), "Measurement and Elimination of Membrane Compliance Effects in Undrained Triaxial Testing", Earthquake Engineering Research Center, Report No. UCB/EERC–89/10, 267p

Nadreau, J.P. and B. Michel (1984), "Ice Properties in Relation to Ice Forces" IAHR Ice Symposium 1984, Hamburg, Vol. 4, pp. 63–115

Nash, K.L. (1953), "The Shearing Resistance of a Fine Closely Graded Sand", Proceedings of 3rd International Conference SMFE, Vol. 1, pp. 110–164

Newland, P.L. and B.H. Allely (1957), "Volume Changes in Drained Triaxial Tests on Granular Materials", Geotechnique, Vol. 7, pp. 17–34

Newland, P.I. and B.H. Allely (1959), "Volume Changes During Undrained Triaxial Tests on Saturated Dilatant Granular Materials", Geotechnique, Vol. 9, No. 4, pp. 174–182

Peierls, R. (1940), "The Size of a Dislocation", The Proceedings of the Physical Society, Vol. 52, pp. 34–37

Perez, J., C. Mai and Vassoille, R. (1978), "Cooperative Movements of H_2O Molecules and Dynamic Behavior of Dislocations in Ice Ih", Journal of Glaciology, Vol. 21, pp.361–374

Petch, N.J. (1953), "The Cleavage Strength of Polycrystals", Journal of the Iron and Steel Institute, Vol. 174, pp. 25–28

Pihlainen, J.A. and G.H. Johnston (1963), "Guide to a Field Description of Permafrost", Tech. Mem. 79, NRC of Canada Assn. Comm. Soil Snow Mech.

Popov, E.P. (1968), Introduction to Mechanics of Solids, Prentice–Hall Inc., Englewood Cliffs, New Jersey, 571p

Penman, A.D.M. (1953), "Shear Characteristics of A Saturated Silt Measured in Triaxial Compression", Geotechnique, Vol. 3, No. 8, pp. 312–328

Perrone, V.J. (1978), "Strength–Deformation Characteristics of Manchester Fine Sand", Thesis submitted in partial fulfillment of the requirements for the degree of Master of Science at MIT, 133p.

Presti, D.G.F.L., S. Pedroni and V. Crippa (1992), "Maximum Dry Density of Cohesionless Soils by Pluviation and ASTM D 4253–83: A Comparative Study", Geotechnical Testing Journal, Vol. 15, No. 2, pp. 180–189

Rad, H..S. and M.T. Tumay (1987), "Factors Affecting Sand Specimen Preparation by Raining", Geotechnical Testing Journal, Vol. 10, No. 1, pp. 31–37

Ramana, K.V. and V.S. Raju (1981), "Constant–Volume Triaxial Tests to Study the Effects of Membrane Penetration", Geotechnical Testing Journal, Vol. 4, pp. 117–122

Raraty, L.E. and D. Tabor (1958), "The Adhesion and Strength Properties of Ice", Proceedings of the Royal Society of London, Series A, No. 245, pp. 184–201

Read, W.T. Jr. (1953), Dislocations in Crystals, McGraw–Hill, New York

Restelli, A.B., G. Tonoli and A.Volpe (1988), "Ground Freezing Solves a Tunneling Problem at Agri Sauro, Pontenza, Italy", 5th International Symposium on Ground Freezing, Nottingham, pp. 395–402

Reynolds, O. (1886), Nature, Vol. 33, pp. 429– ,see Frank (1965)

Riemer, M.F., R.B. Seed, P.G. Nicholson and H.L. Jong (1990), "Steady State Testing of Loose Sands: Limiting Minimum Density", JGE, Vol. 116, No. 2, pp. 332–337

St. Lawrence, W.F. and D.M. Cole (1982), "Acoustic Emissions from Polycrystalline Ice", Cold Regions Science and Technology, Vol. 5, pp. 183–199

Scott, R. (1969), "The Freezing Process and Mechanics of Frozen Ground", CRREL Report, Oct. 1969

Seed, H.B., S. Singh and C.K. Chan (1982), "Considerations in Undisturbed Sampling of Sands", JGED – ASCE, Vol. 108, No. GT2, Feb. 1982, pp. 265–283

Shen, L., S. Zhao, X. Lu and Y. Shi (1986), "Effects of Temperative and Strain Rate on Uniaxial Compressive Stength of Naturally Formed Fresh–Water Ice", 7th International Conference on Offshore Mechanics and Artic Engineering, Houston, TX, Vol. 4, pp. 19–23

Shoji, H. and A. Higashi (1978), "A Deformation Mechanism Map of Ice", Journal of Glaciology, Vol. 21, No. 85, pp. 419–427

Sinha, N.K. (1978), "Rheology of Columnar–Grained Ice", Experimental Mechanics, Vol. 18, No. 12, Dec. 1978, pp. 464–470

Sinha, N.K. (1979), "Grain Boundary Sliding in Polycrystalline Materials", Philosophical Magazine A, Vol. 40, No. 6, pp. 825–842

Sinha, H.K. (1981), "Rate Sensitivity of Compressive Strength of Columnar – Grained Ice", Experimental Mechanics, Vol. 21, No. 6, Jan 1981, pp. 209–218

Skempton, A.W. (1961), "Effective Stress in Soils, Concrete and Rocks", in Pore Pressure and Suction in Soils, Butterworths, London, pp. 4–16

Skinner, A.E. (1969), "A Note on the Influence of Interparticle Friction on the Shearing Strength of a Random Assembly of Spherical Particles", Géotechnique, Vol. 69, No. 1, pp. 150–157

Sladen, J.A., J. Krahn and R.D. Hollander (1986), "Discussion: A State Parameter for Sands" Geotechnique, Vol. 36, No. 2, pp. 123–124

Spangler, M.G. and R.L. Handy (1982), Soil Engineering 4th ed., Harper and Row, New York

Spencer, P.A., D.M. Masterson and J.F. Dorris (1991), "The Measurement of Volumetric Strain in the Triaxial Testing of Ice Samples", Proceedings of 10th International Conference on Offshore Mechanics and Artic Engineering, Vol. IV, ASME, pp. 237–243

Symes, M.J.P.R., A. Gens and D.W. Hight (1984), "Undrained Anisotropy and Principal Stress Rotation in Saturated Sand", Géotechnique, Vol. 34, No. 1, pp. 11–27

Tatsuoka, F. (1987), "Discussion: The Strength and Dilatancy of Sands by Bolton", Geotechnique, Vol. 37, No. 2, pp. 219–226 (reply by author)

Thurairajah, A. and B. LeLievre (1971), "Undrained Shear Strength Characteristics of Sand", Geotechnical Engineering, Vol. 2, pp. 101–117

Ting, J.M. (1981), "The Creep of Frozen Sands: Qualitative and Quantitative Models", Research Report R81–5, MIT Department of Civil Engineering

Tzou–Shin, U., Y.N. Tzou and C.S. Lee (1988), "The Effect of End Restraint on Volume Change and Particle Breakage of Sands in Triaxial Tests", Advanced Triaxial Testing of Soil and Rock, ASTM STP 977, pp. 679–691

Vaid, Y.P. and D. Negusey (1984), "A Critical Assessment of Membrane Penetration in the Triaxial Test", Geotechnical Testing Journal, Vol. 7, No. 2, pp. 70–76

Vaid, Y.P. and D. Negusey (1988), "Preparation of Reconstituted Sand Specimens", Advanced Triaxial Testing of Soil and Rock ASTM STP 977, pp. 405–417

Vaid, Y.P., E.K.F. Chung and R.H. Kuerbis (1989), "Preshearing and Undrained Response of Sand", Soils and Foundations, Vol. 29, No. 4, pp. 49–61

Wakahama, G. (1967), "On the Plastic Deformation of Single Crystal of Ice", Physics of Snow and Ice, H. Oura editor, Vol. 1, pp. 291–311

Weertman, J. (1973), "Creep of Ice", Physics and Chemistry of Ice, E. Whalley, S.J. Jones and L.W. Gold editors, pp. 320–337

Whitman, R.V. and K.A. Healy (1962), "Shear Strength of Sands During Rapid Loadings", JSMFD, Vol. 88, No. SM2, pp. 99–132

Wijewcera, H. and R.C. Joshi (1990), "Compressive Strength Behavior of Fine–Grained Frozen Soil", Canadian Geotechnical Journal, Vol. 27, pp. 472–483

Wissa, A.E.Z. (1969), "Pore Pressure Measurements in Saturated Stiff Soils", JSMFD, Vol. 35, No. SM4, pp. 1063–1073

Wong, C.L.Y. (1990), "A Normalizing Relation for Granular Materials", Canadian Geotechnical Journal, Vol. 27, pp. 68–78

Wong, R.K.S. and J.R.F. Arthur (1985), "Induced and Inherent Anisotropy in Sand", Géotechnique, Vol. 35, No. 4, pp. 471–481

Yasufuku, N., H. Marata, M. Hyodo, and A.F.L. Hyde (1991), "A Stress–Strain Relationship for Anistropically Consolidated Sand Over a Wide Stress Region", Soils and Foundations, Vol. 31, No. 4, pp. 75–92

Yasufuku, H., H. Murata and M. Hyodo (1991), "Yield Characteristics of Anistropically Consolidated Sand Under Low and High Stresses", Soils and Foundation, Vol. 31, No. 1, pp. 95–109

Yin, J.H., L. Domaschuk and J. Graham (1990) "Elastic Visco–Plastic Modeling of a Frozen Sand Using Equivalent Time", Offshore and Arctic Operations Symposium, ASME, pp. 133–139

Youssef, H. and A. Hanna (1990), "Behavior of Frozen and Unfrozen Sands in Triaxial Testing", Transportation Research Record 1190 Artificial Ground Freezing and Soil Stabilization, pp. 57–64

Yuanlin, Z., Z. Jiayi, P. Wanwei, S. Zhongyan and M. Lina (1991), "Constitutive Relations of Frozen Soil in Uniaxial Compression", Ground Freezing 91, Yu and Weng eds., pp. 21

APPENDIX A

EXPERIMENTAL PROCEDURES

EXPERIMENTAL PROCEDURES

Temperature Measurement and Calculation

This appendix describes the components used in measuring temperatures in conventional frozen and consolidate–freeze testing programs. As described in Section 3.2, temperature measurements were performed using epoxy–coated thermistors incorporated into a Wheatstone bridge configuration. Figure 3.10, which has been reproduced as Fig. A.1, shows the various components.

For calculations, each thermistor follows a characteristic curve (temperature versus resistance calibration) from which temperatures can be determined once the thermistor's resistance is known. Given the known resistance (R_1, R_2, R_3 and R_4) and the measured input and output voltages, the following equation is used to solve for the thermistor resistance, R_t

$$R_t = \frac{\Delta V \cdot (R_1+R_2) + \frac{\Delta V \cdot R_1 \cdot R_2 - V_{in} \cdot R_2 \cdot R_3}{R_3 + R_4} + V_{in} \cdot R_2}{\frac{V_{in} \cdot R_3 - \Delta V \cdot R_1}{R_3 + R_4} - \Delta V} \qquad \text{A.1}$$

where V_{in} and ΔV are the input and output voltages, respectively. Note that if $\Delta V = 0$, the equation reduces to that of a balanced Wheatstone bridge, namely $R_t = (\frac{R_2}{R_3}) \times R_4$.

Beta (β) Values

The relationship between temperature and thermistor resistance can be characterized by a factor β;

$$\beta = \frac{\ln(R_{T_1}/R_{T_2})}{1/T_1 - 1/T_2} \qquad \text{A.2}$$

where R_{T_1} and R_{T_2} are the resistances of the thermistor at the temperatures

T_1 and T_2, respectively, with temperatures T_1 and T_2 in °K. The β also has units of °K. To compute the temperature (T) for each thermistor, the known thermistor resistance (R_{ref}) at a known temperature (T_{ref}) is compared to the resistance R_t. Using β, which is calculated from the known characteristic curve, the temperature for any R_t can be determined by the following:

$$T = \frac{1}{\frac{\ln (R_t/R_{ref})}{\beta} + 1/T_{ref}} \qquad \text{A.3}$$

This method of temperature calculation differs from Andersen (1991) in that he used an interpolation scheme between points of the manufacturer–supplied characteristic curve for temperature calculation. The use of β's allows for a simpler calculation of temperature using a continuous curve defined by an equation. However, while using β's is simpler, the β–value will vary slightly over a large range in temperatures for each thermistor. For example, for one calibrated thermistor β = 3830°K around T = –5°C but β = 3680°K around T = –30°C. [However, β's from various thermistors do not vary significantly within the same temperature range (e.g. at T = –5 °C, β = 3829 ± 5°K for all thermistors), hence the thermistors can be interchanged without introducing significant error.]

To reduce the error in temperature calculations using β's, two procedures are used. One is to develop a series of β's and R_{ref}'s for temperatures between –5°C and –30°C, at five degree increments, for each thermistor. A two degree temperature range is used to determine β's. Therefore, for a test at a nominal temperature of –20°C, calculated temperatures for each thermistor are based on the β associated with a temperature range of –19 to –21°C. The thermistor resistance at –19°C is

chosen as the R_{ref} for this case.

The second procedure consists of an actual calibration of the thermistors. The calibration consisted of placing the four thermistors to be used in the tests (electronically connected as they would be during the test) in an oil bath placed inside the thermo–regulated environmental chamber. Bath temperatures are independently measured using two thermometers. At best, readings from the thermometers can be recorded to the nearest 0.1 °C. Thus thermistor accuracies are increased to ±0.1 °C. Using the thermometers as the "true" temperature, the thermistor–calculated temperature is then corrected to the "true" temperature via correction factors (ratio of the measured temperature during calibration and the temperature calculated using Eq. A.3). In Andersen's work, the thermistors were not calibrated at MIT; the stated temperature values in Andersen (1991) are based solely on the manufacturer's calibration (characteristic) curve. Therefore, the current method of temperature measurement goes an additional step beyond the previous work. However, correction factors varied from 1.008 to 1.042; suggesting that past temperature calculations using supplied characteristic curves are very close to thermometer–measured values.

To summarize the complete temperature calculation procedure, thermistor resistances (R_t) are calculated based on input and output voltages and known circuit resistances. These R_t values are then converted to temperatures using β's and reference resistances. These calculated temperatures are then corrected using the correction factors determined from oil bath calibrations.

APPENDIX B

TEST RESULTS FOR UNFROZEN MFS TESTING PROGRAM

SECTION B.1

Consolidation Results

This section of presents consolidation summary plots for the unfrozen MFS testing program. Only consolidation results from Series B and Series C are presented. Plots of volumetric strain (ϵ_v) versus $\log_{10}$ effective stress and void ratio versus $\log_{10}$ effective stress are presented for each test.

Volumetric Strain vs Log Effective Stress

SERIES B : TEST #01
Volumetric Strain vs Effective Stress

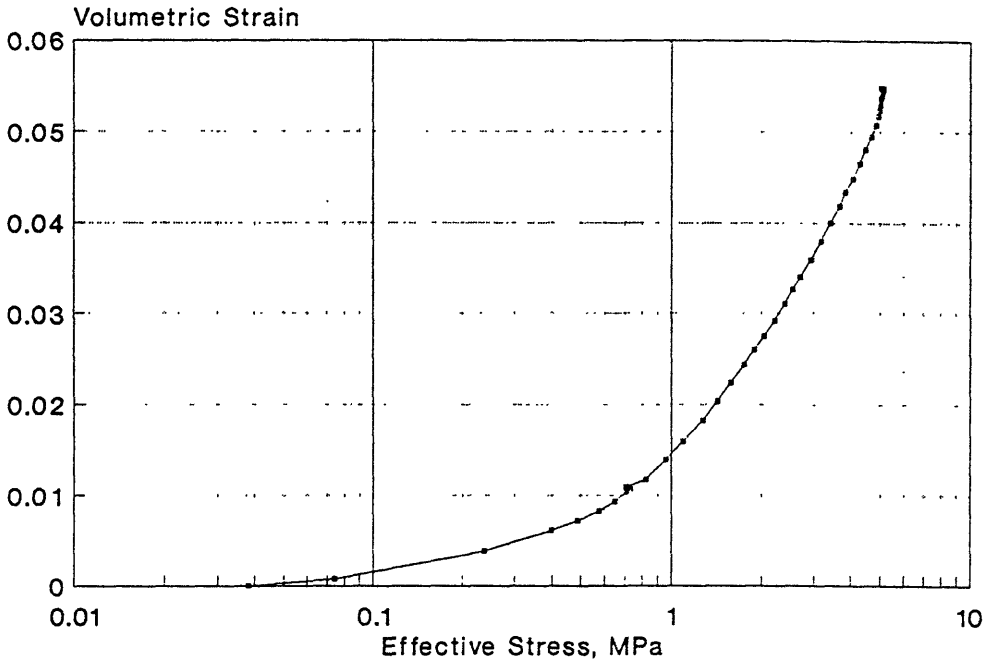

SERIES B : TEST #02
Volumetric Strain vs Effective Stress

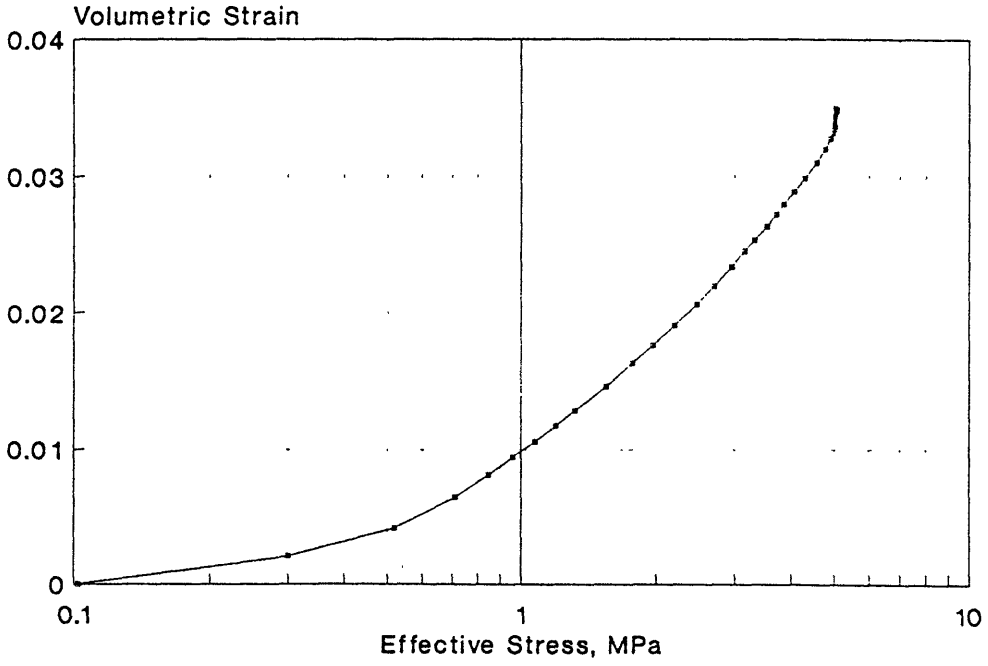

SERIES B : TEST #03
Volumetric Strain vs Effective Stress

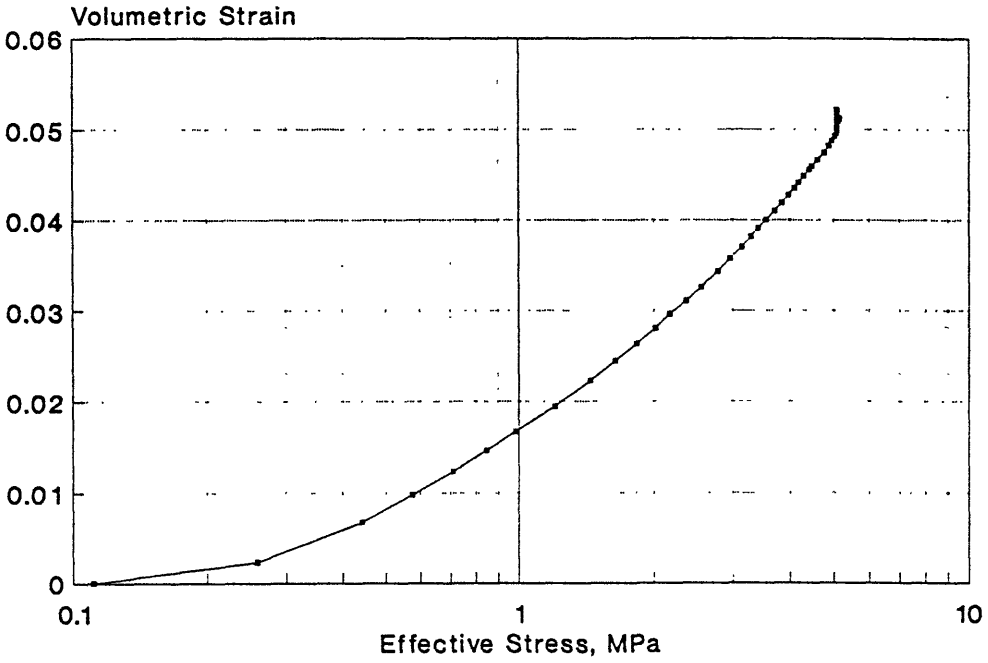

SERIES B : TEST #04
Volumetric Strain vs Effective Stress

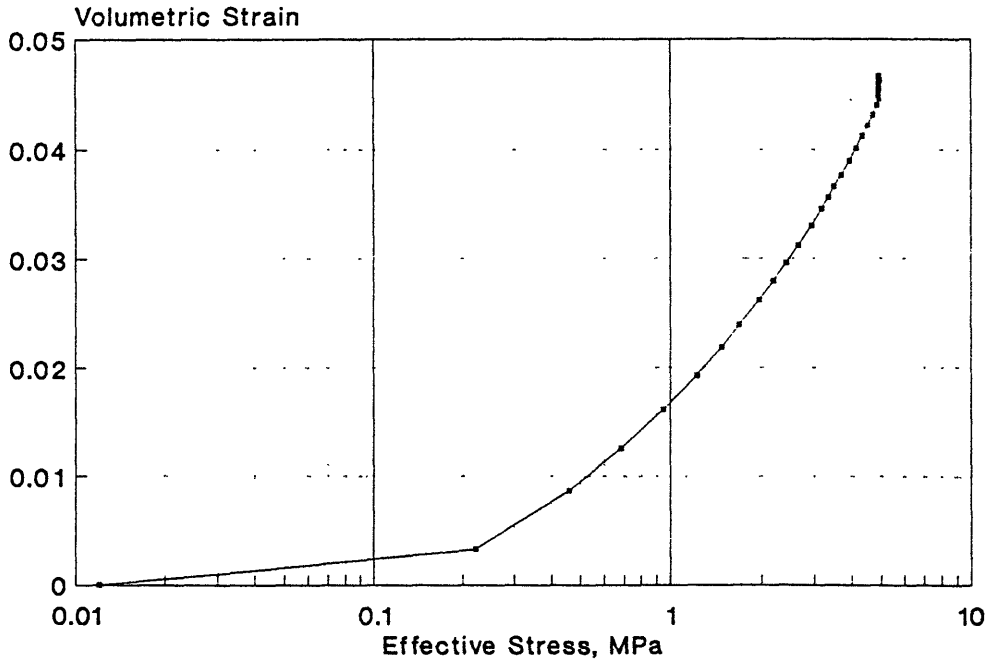

SERIES B : TEST #05
Volumetric Strain vs Effective Stress

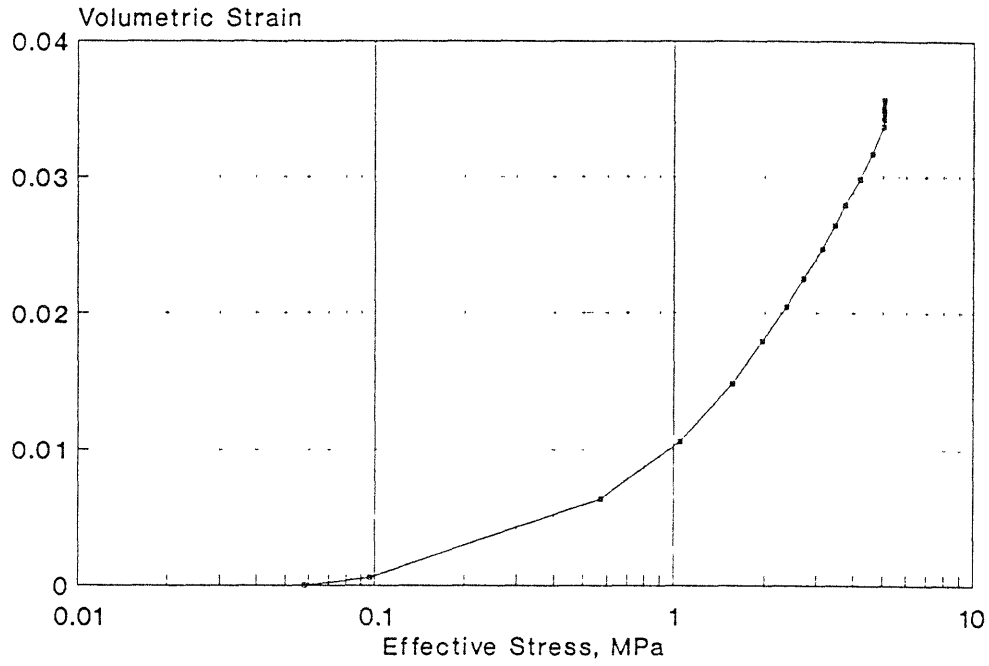

SERIES B : TEST #06
Volumetric Strain vs Effective Stress

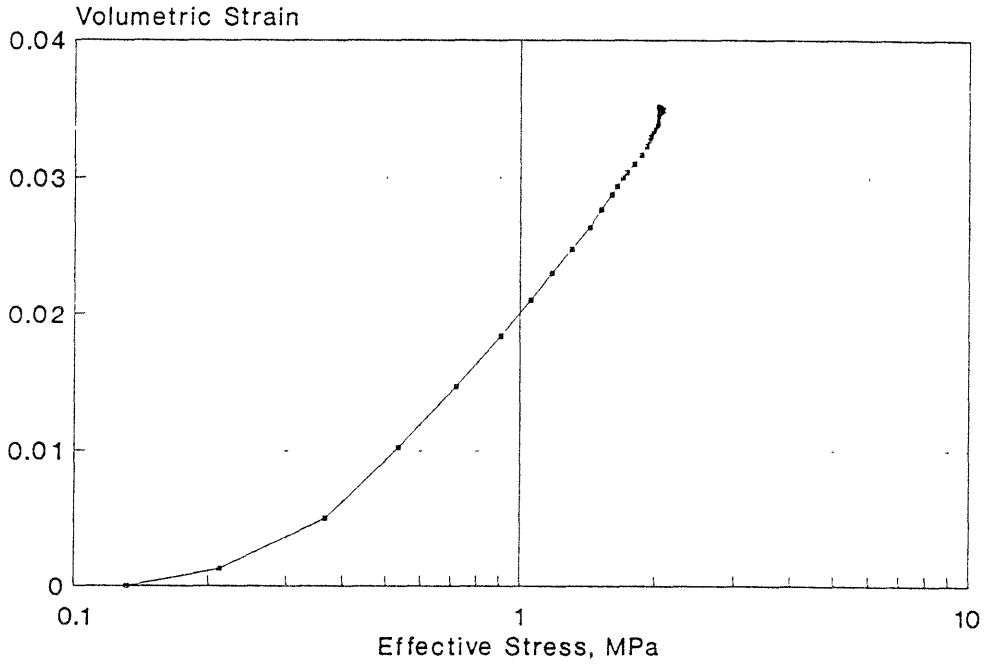

SERIES B : TEST #07
Volumetric Strain vs Effective Stress

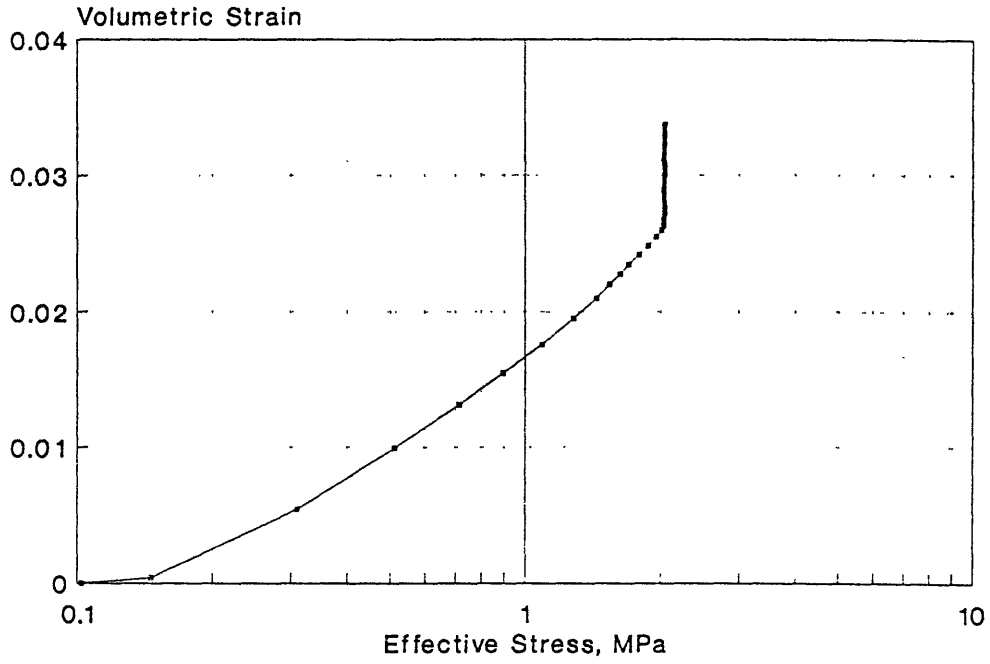

SERIES B : TEST #11
Volumetric Strain vs Effective Stress

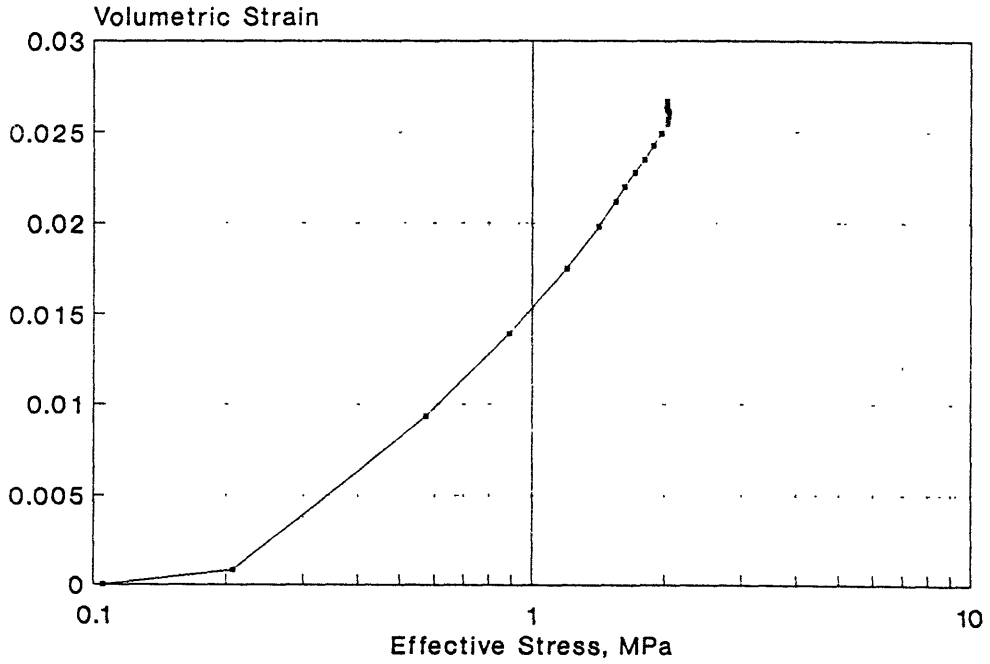

SERIES B : TEST #13
Volumetric Strain vs Effective Stress

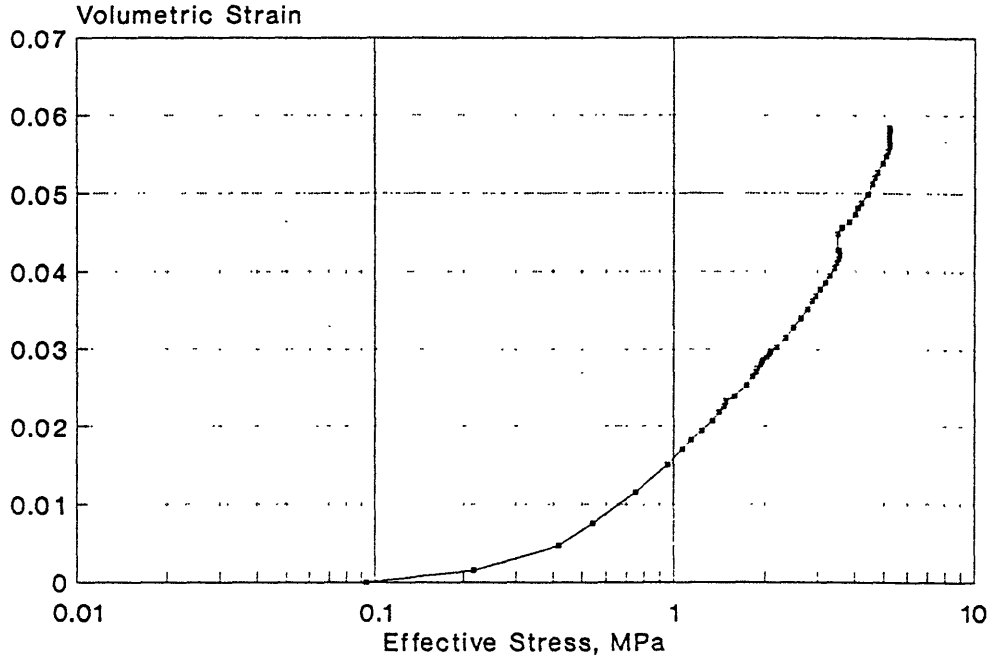

SERIES B : TEST #14
Volumetric Strain vs Effective Stress

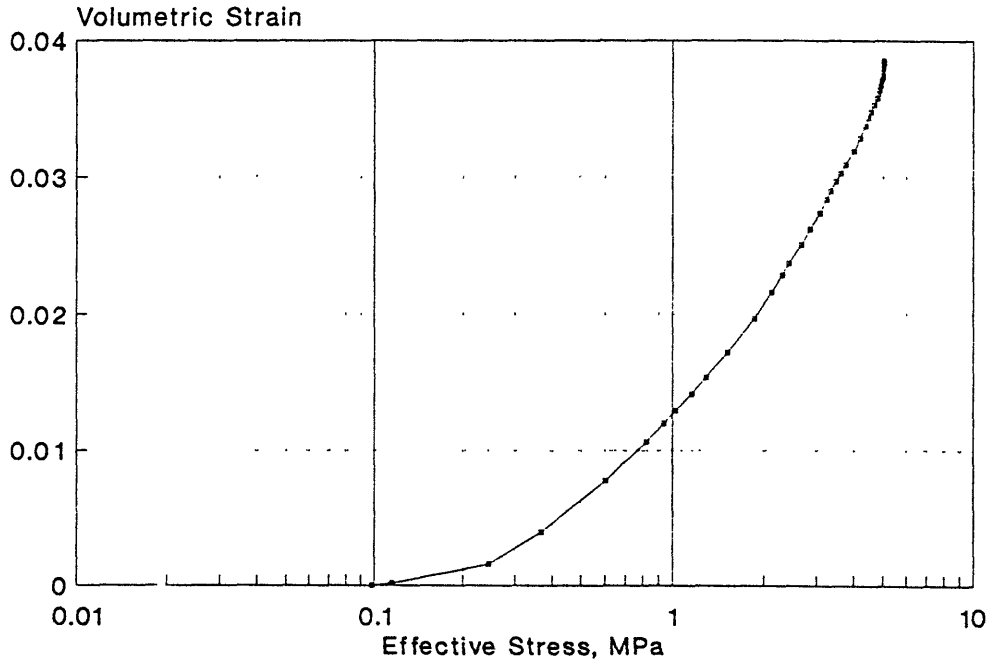

SERIES B : TEST #15
Volumetric Strain vs Effective Stress

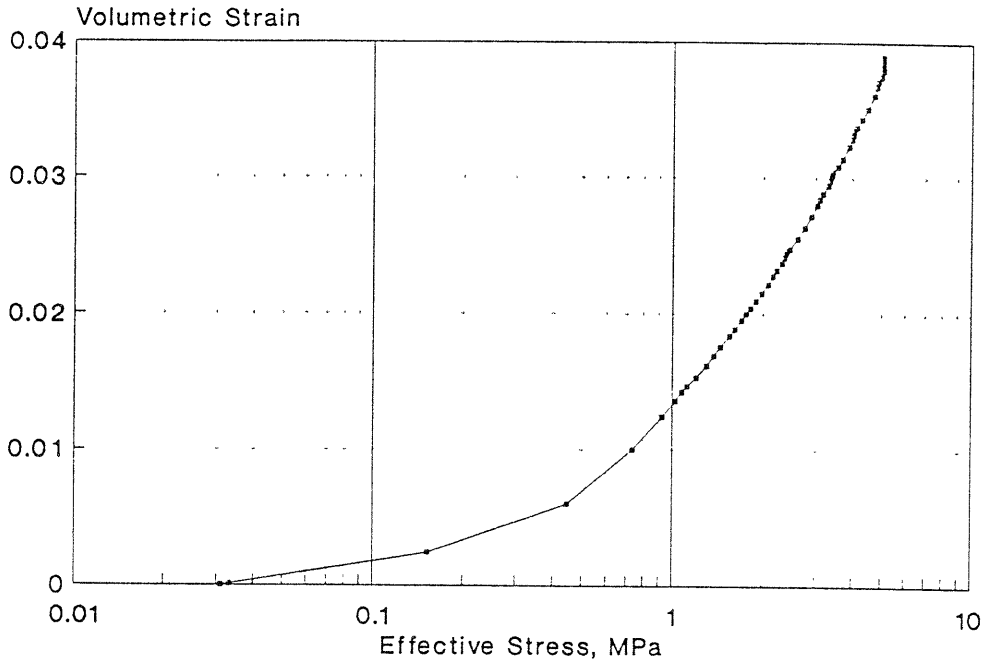

SERIES B : TEST #16
Volumetric Strain vs Effective Stress

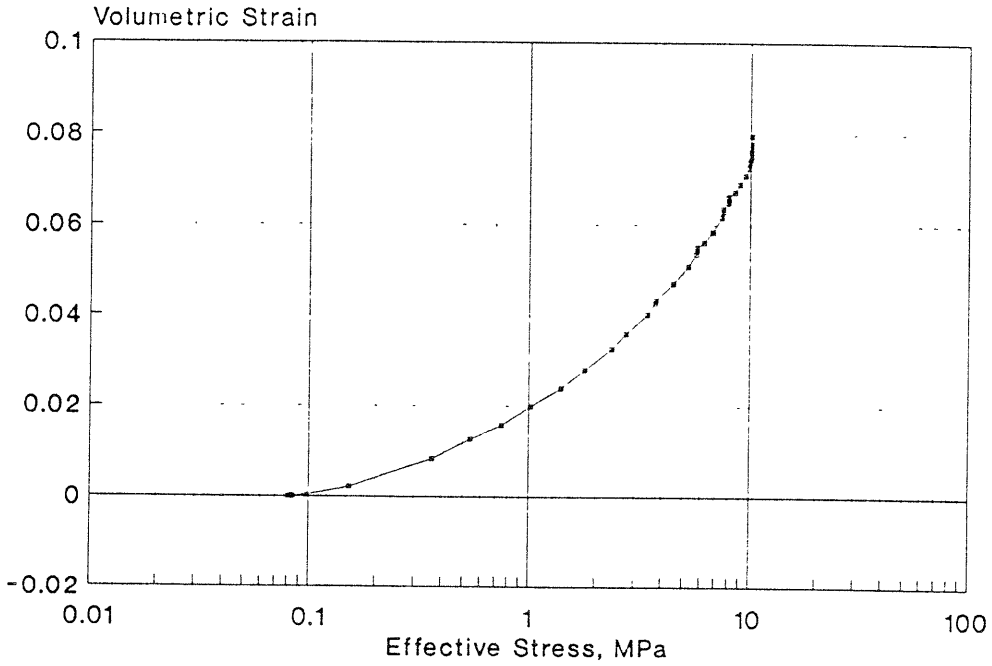

SERIES B : TEST #17
Volumetric Strain vs Effective Stress

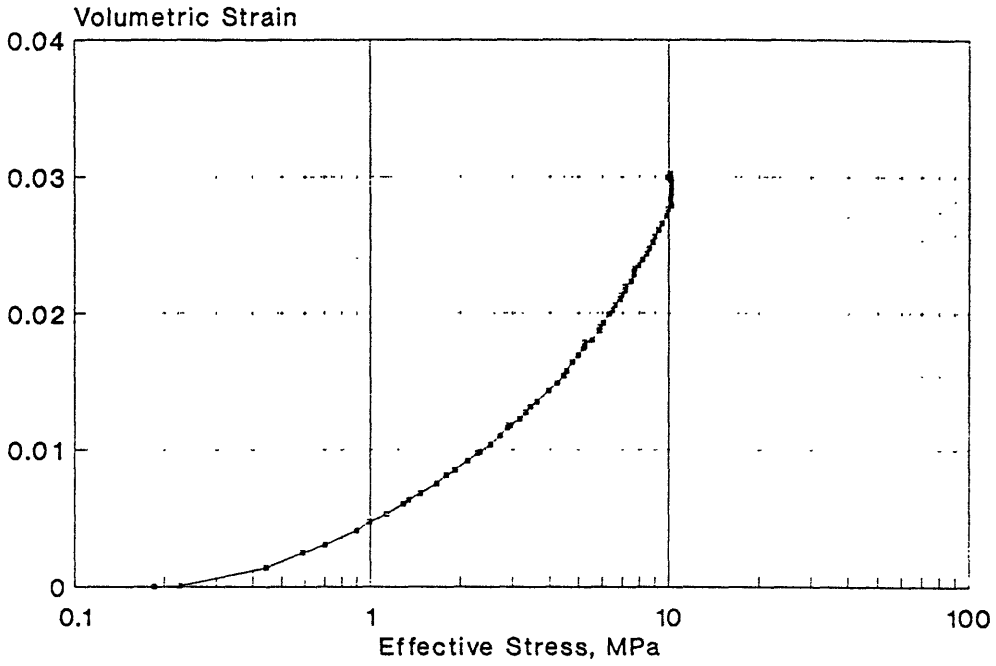

SERIES B : TEST #18
Volumetric Strain vs Effective Stress

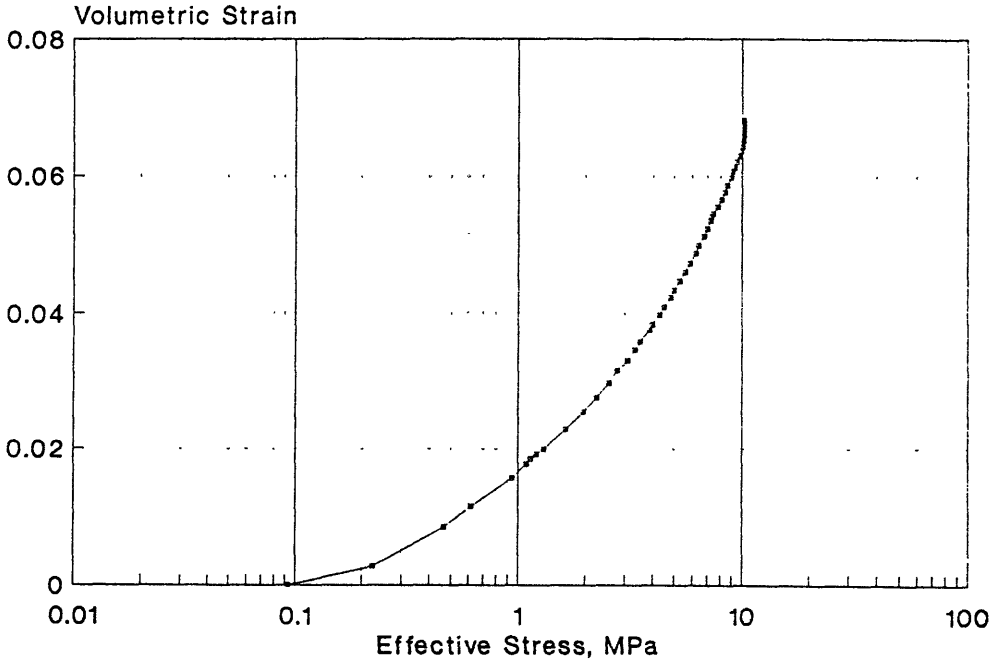

SERIES B : TEST #19
Volumetric Strain vs Effective Stress

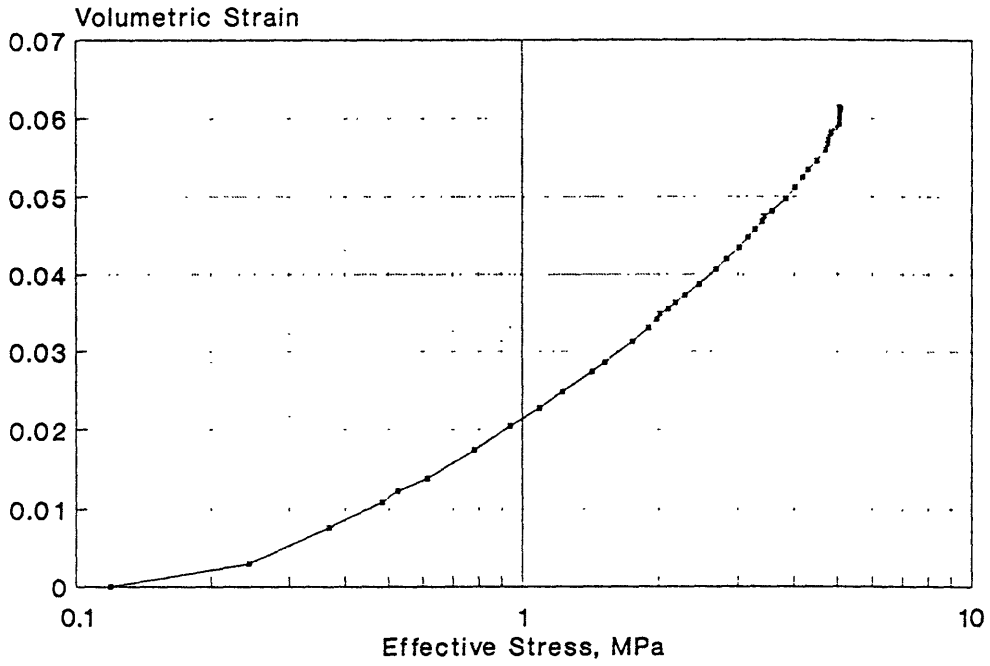

SERIES B : TEST #20
Volumetric Strain vs Effective Stress

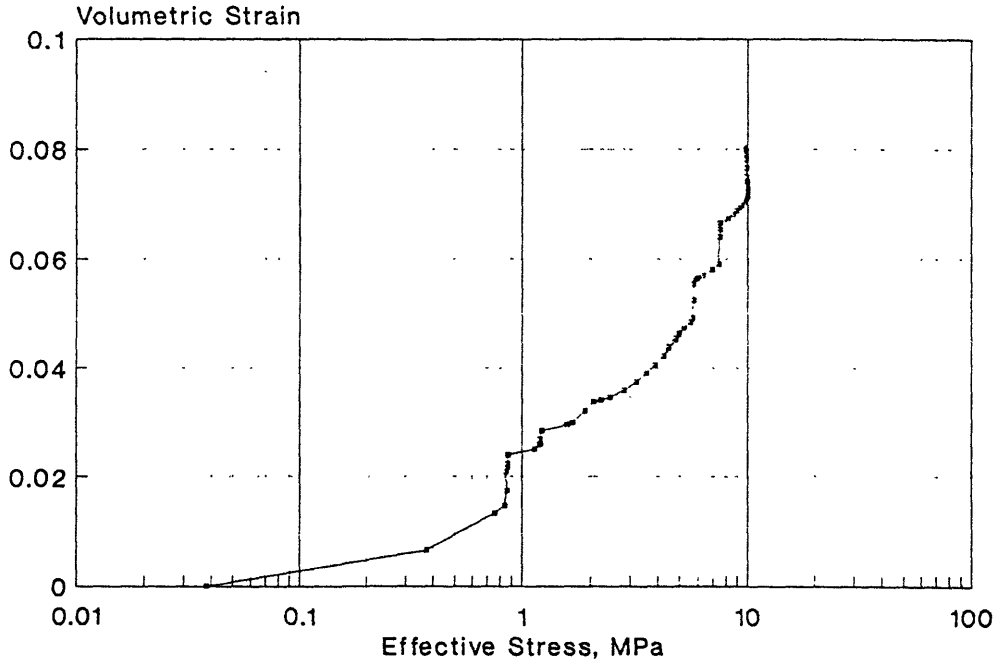

SERIES B : TEST #21
Volumetric Strain vs Effective Stress

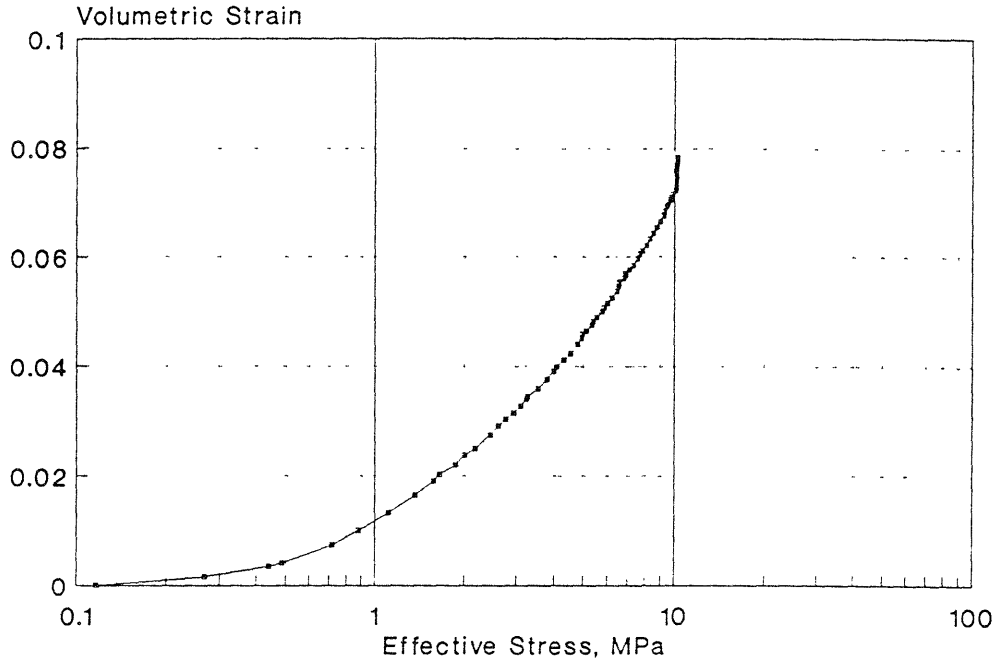

SERIES B : TEST #23
Volumetric Strain vs Effective Stress

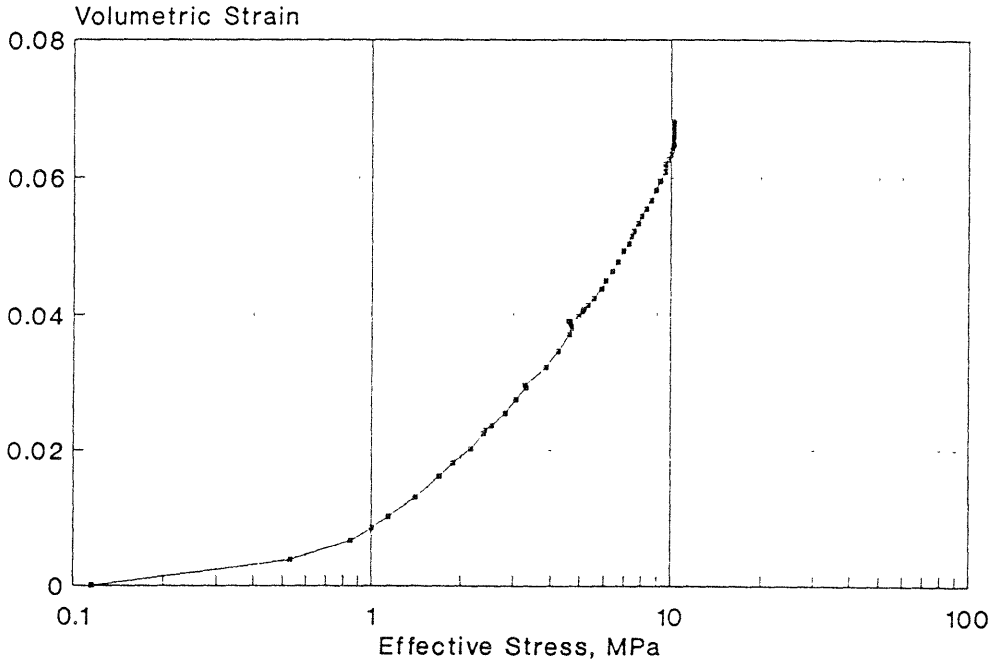

SERIES B : TEST #24

Volumetric Strain vs Effective Stress

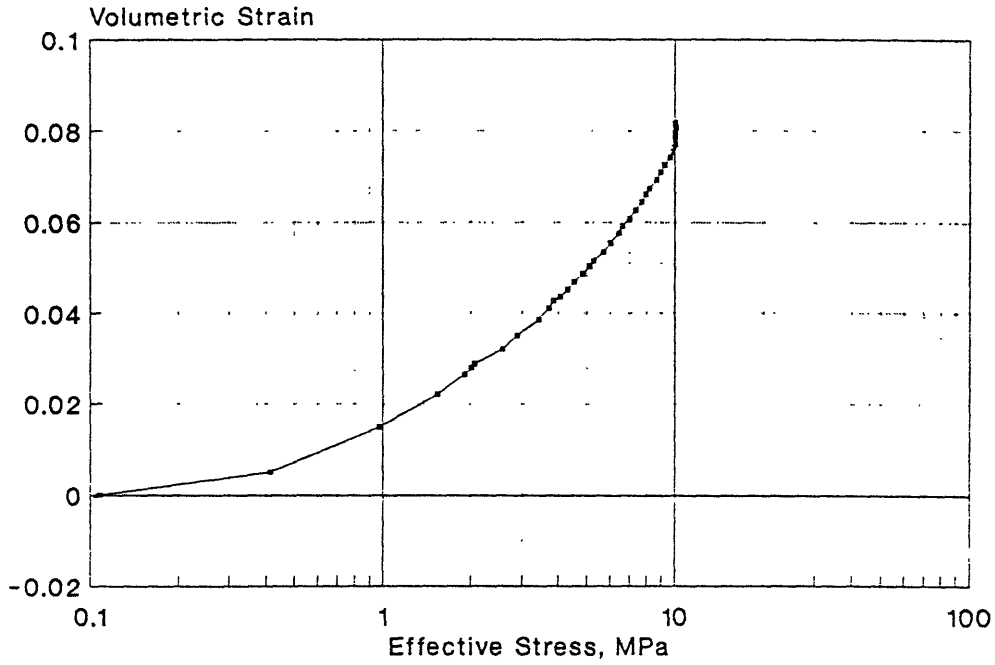

SERIES C : TEST #01
Volumetric Strain vs Effective Stress

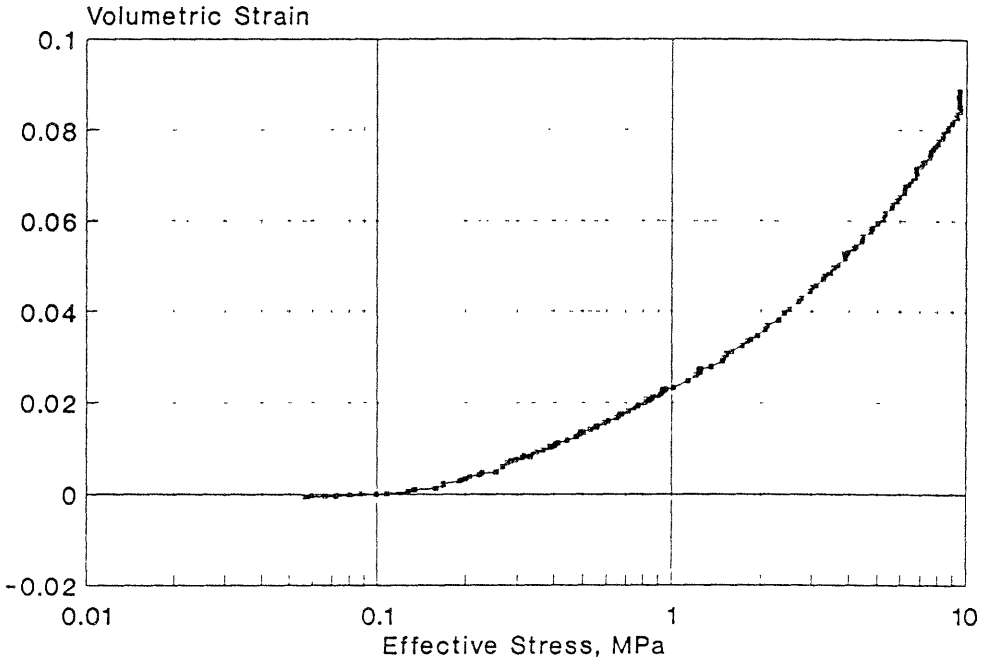

SERIES C : TEST #02
Volumetric Strain vs Effective Stress

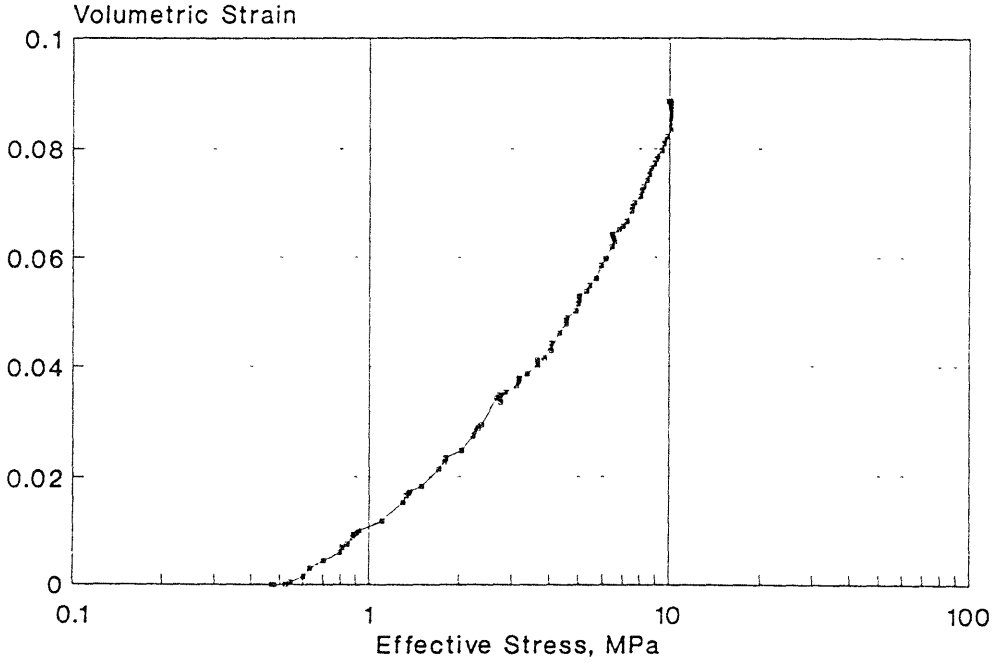

SERIES C : TEST #03
Volumetric Strain vs Effective Stress

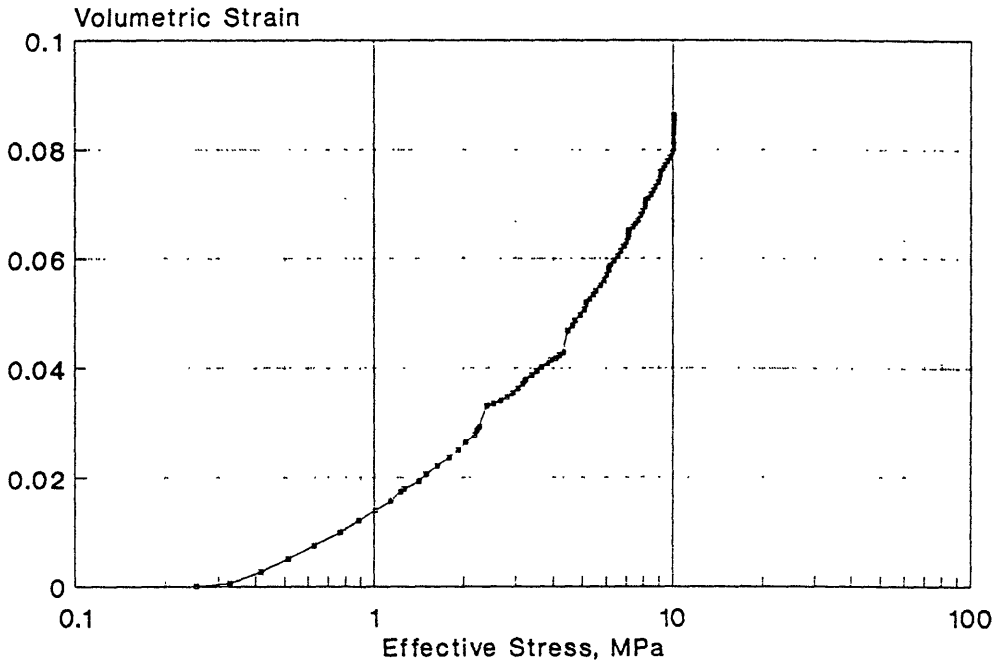

SERIES C : TEST #04
Volumetric Strain vs Effective Stress

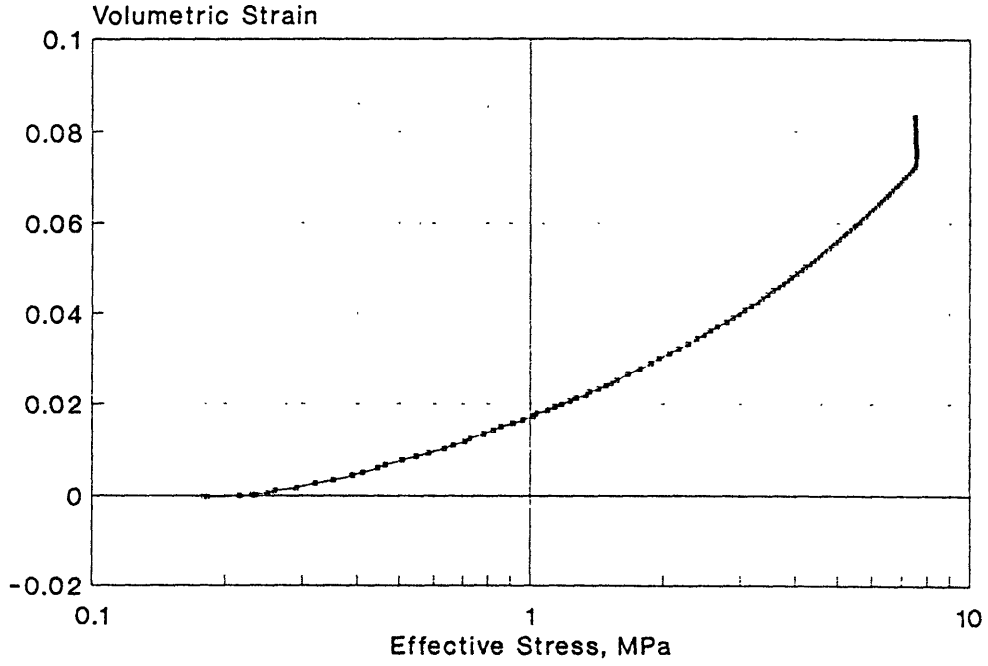

SERIES C : TEST #08
Volumetric Strain vs Effective Stress

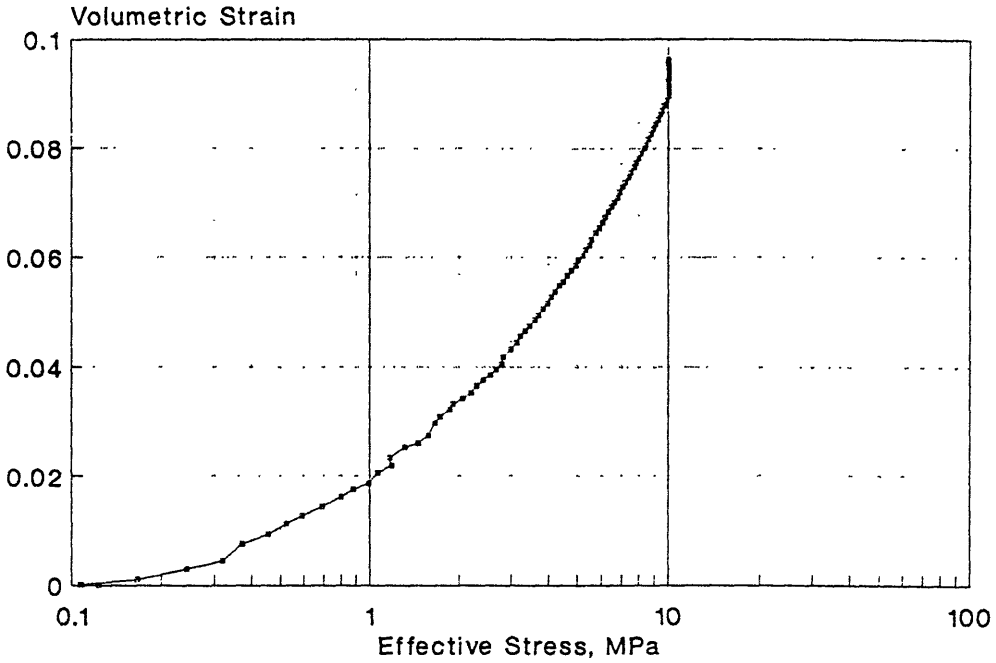

SERIES C : TEST #09
Volumetric Strain vs Effective Stress

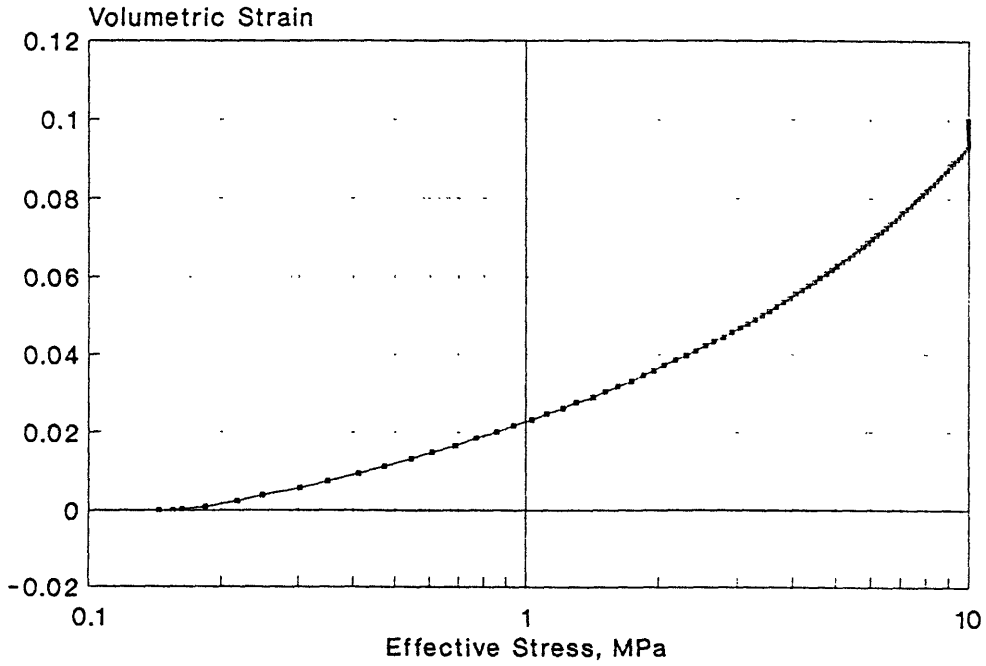

SERIES C : TEST #10
Volumetric Strain vs Effective Stress

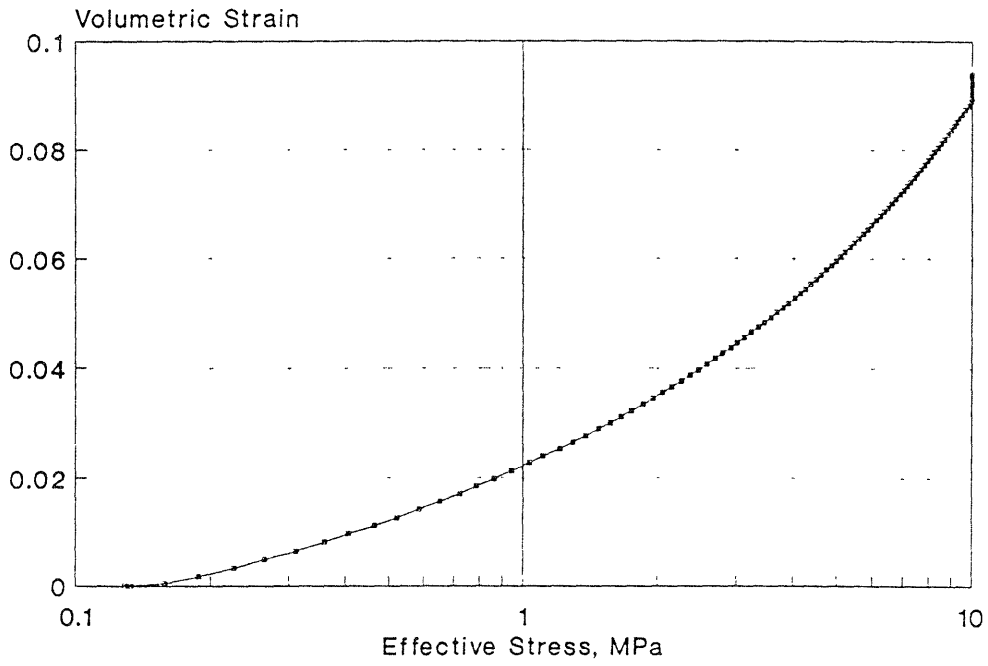

SERIES C : TEST #11
Volumetric Strain vs Effective Stress

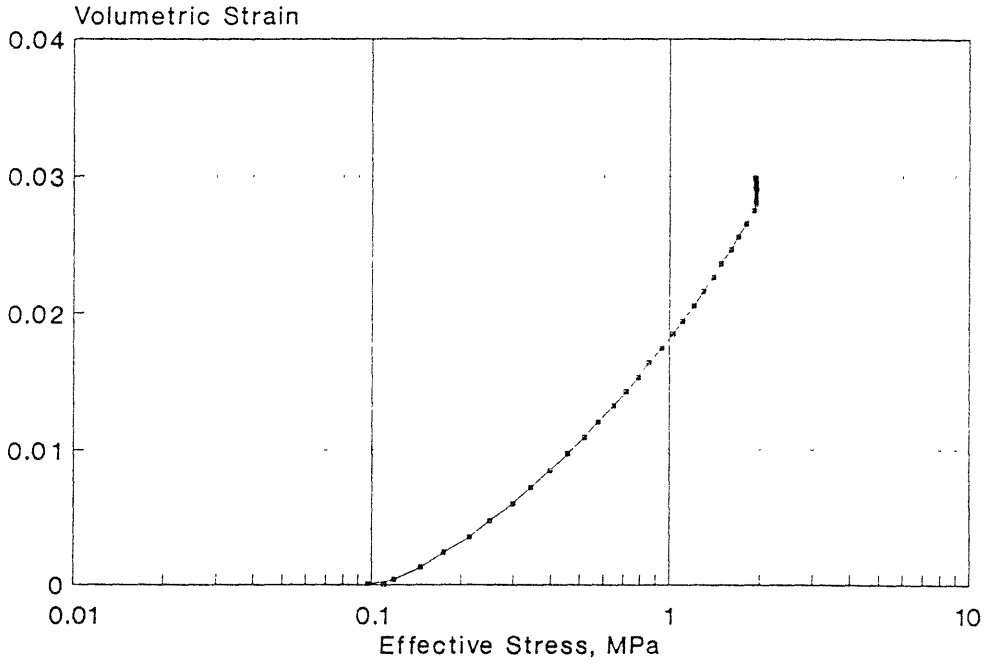

SERIES C : TEST #12
Volumetric Strain vs Effective Stress

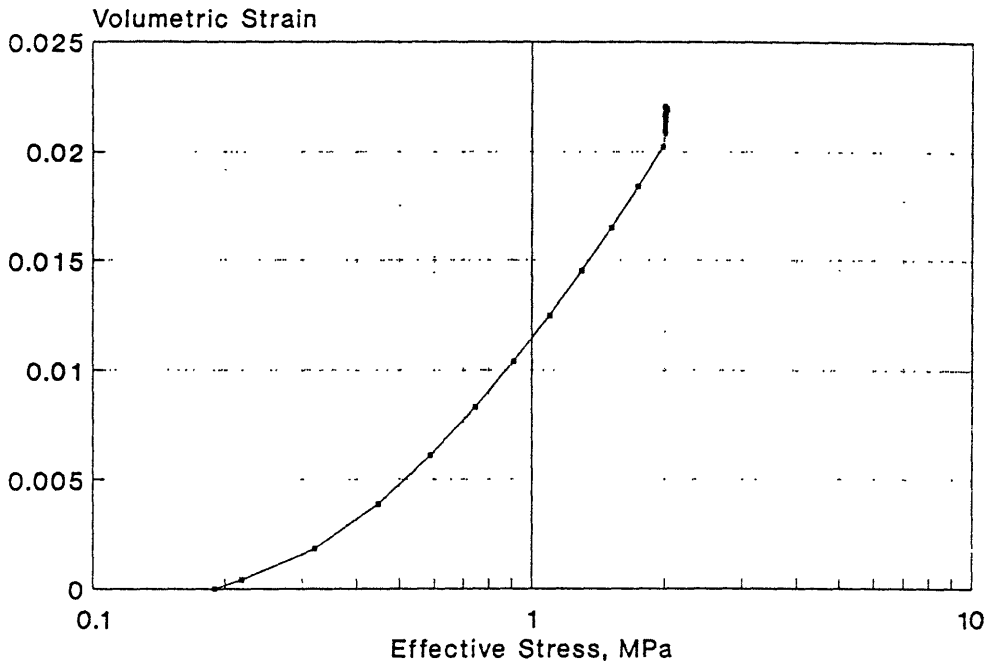

SERIES C : TEST #13
Volumetric Strain vs Effective Stress

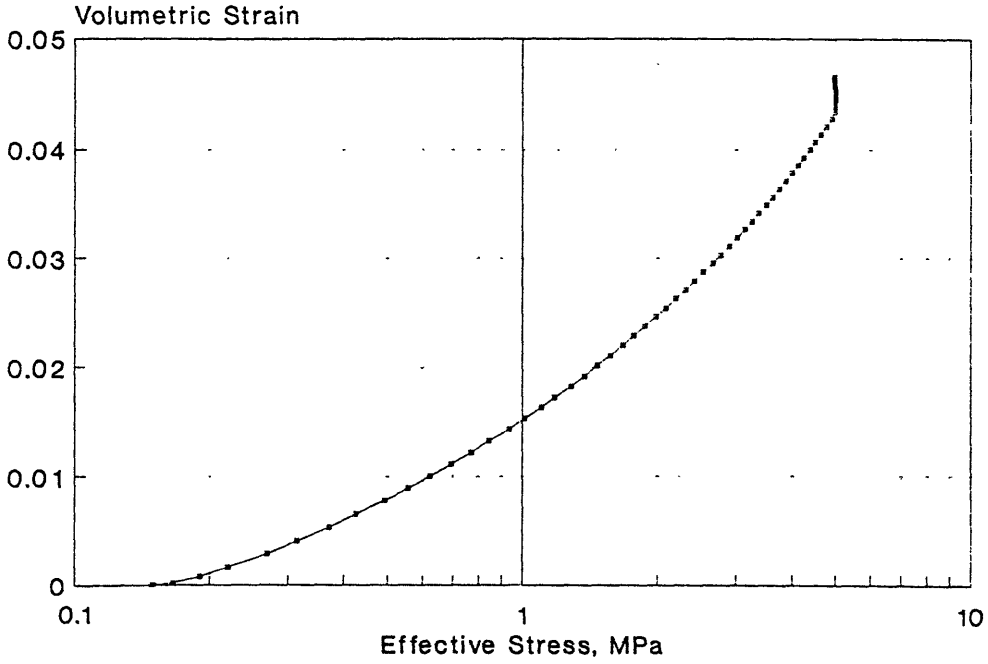

SERIES C : TEST #15
Volumetric Strain vs Effective Stress

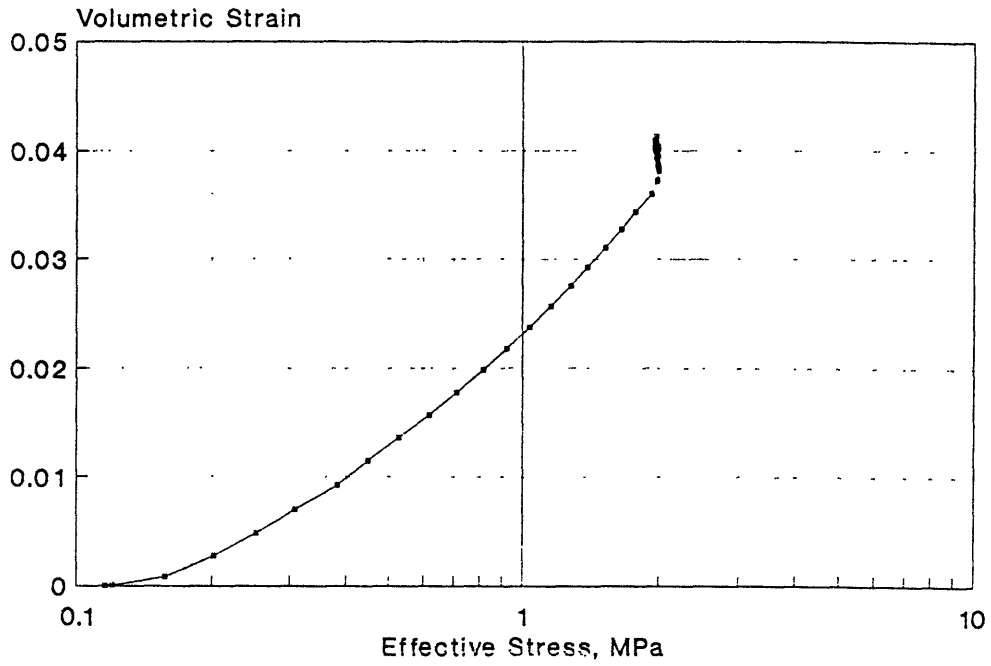

SERIES C : TEST #16
Volumetric Strain vs Effective Stress

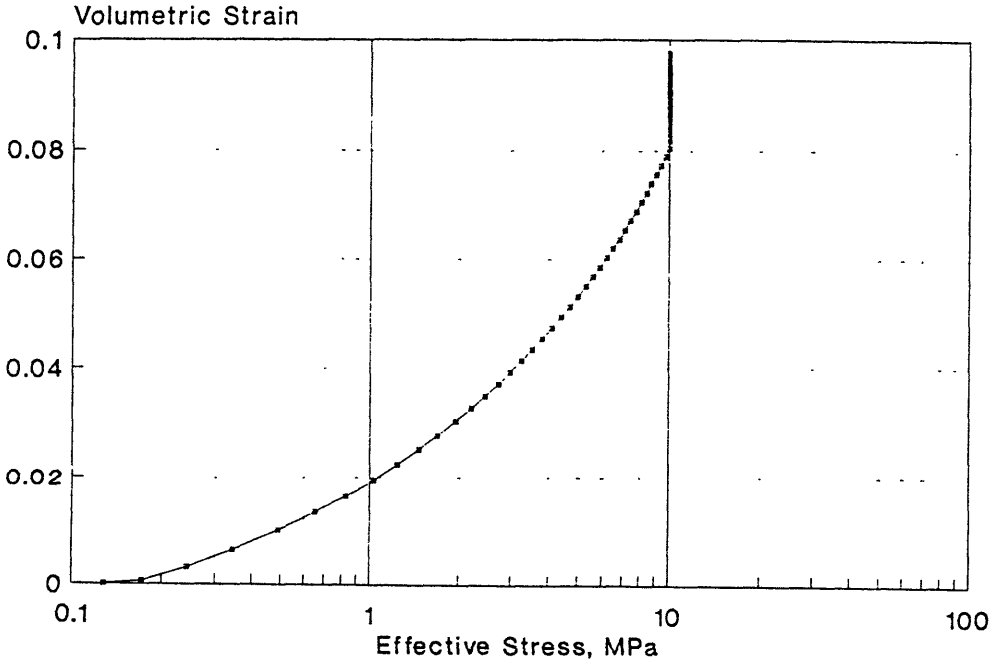

SERIES C : TEST # 22
Volumetric Strain versus Eff. Stress

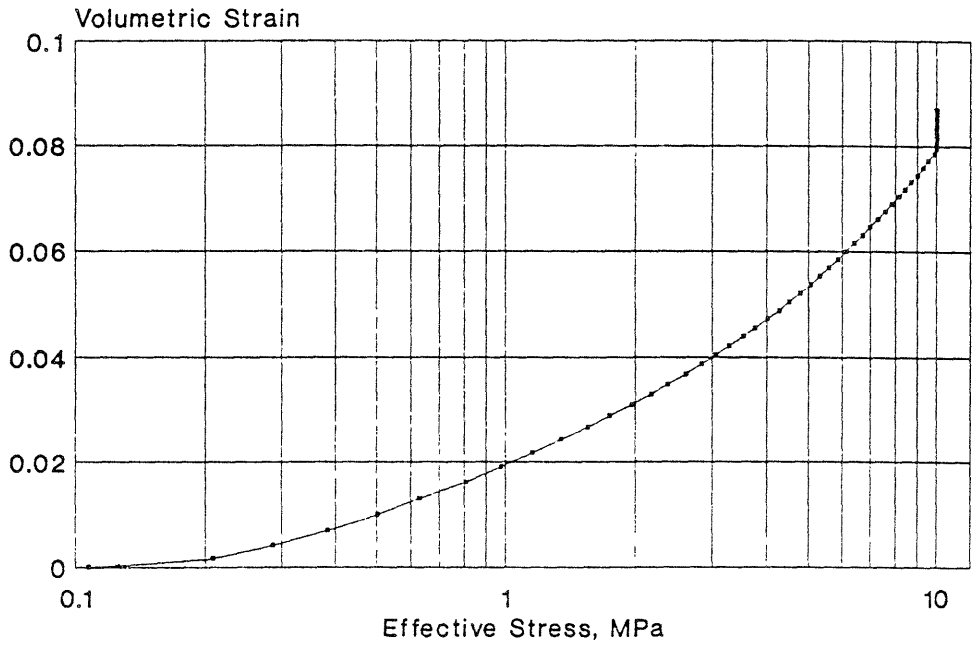

SERIES C : TEST #23
Volumetric Strain versus Eff. Stress

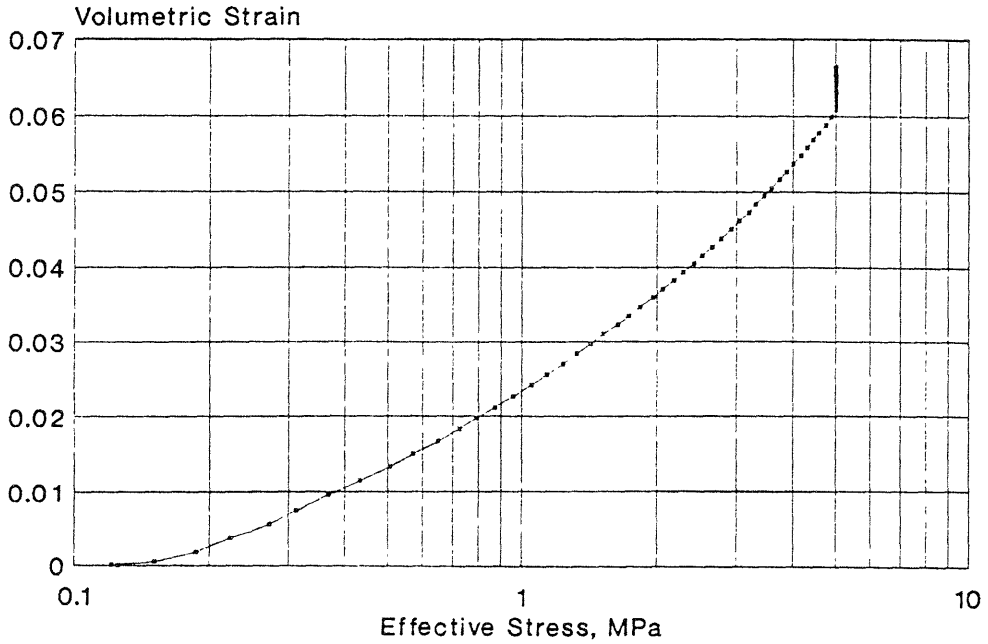

SERIES C : TEST #24
Volumetric Strain versus Eff. Stress

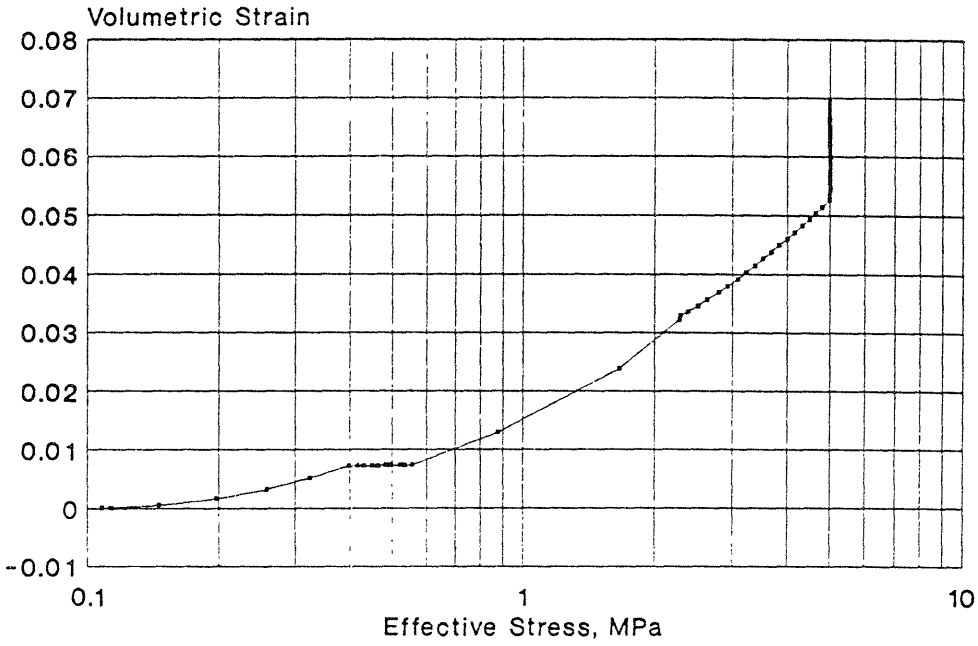

SERIES C : TEST # 25
Volumetric Strain versus Eff. Stress

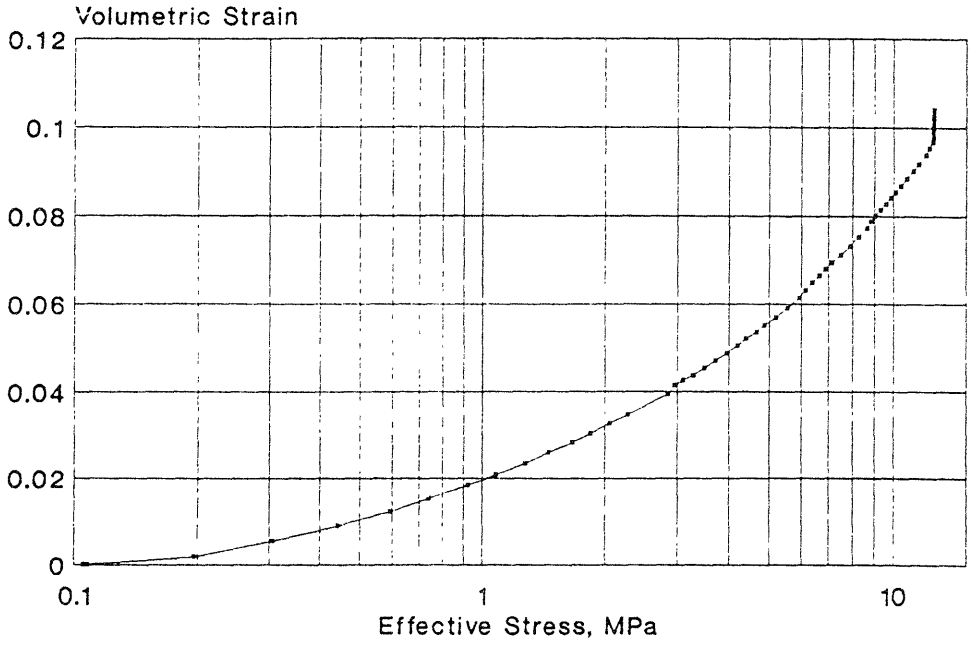

SERIES C : TEST # 27
Volumetric Strain versus Eff. Stress

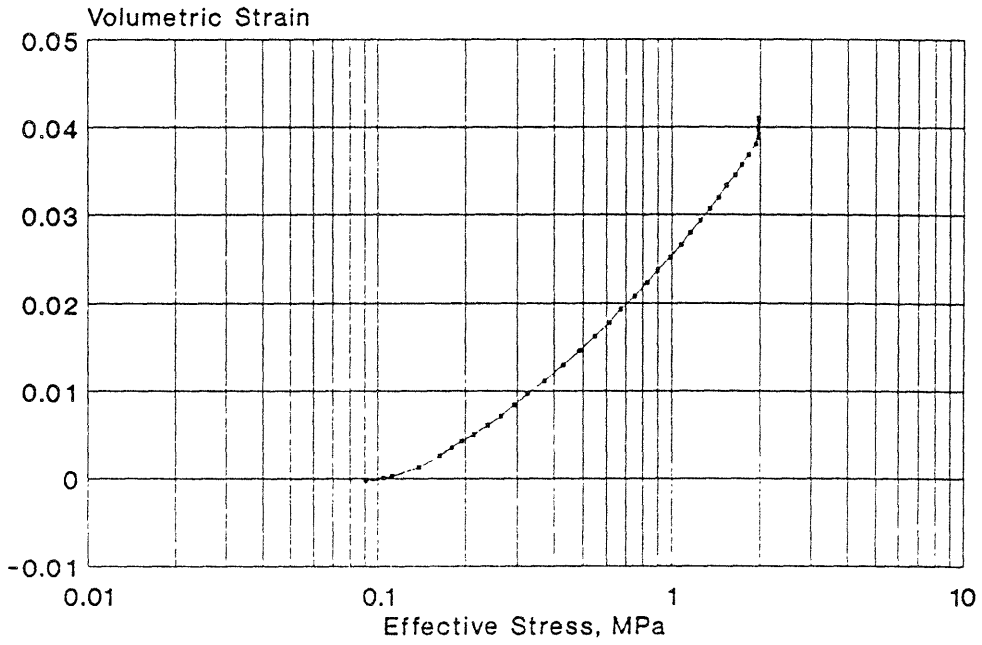

SERIES C : TEST #28
Volumetric Strain vs Vert. Eff. Stress

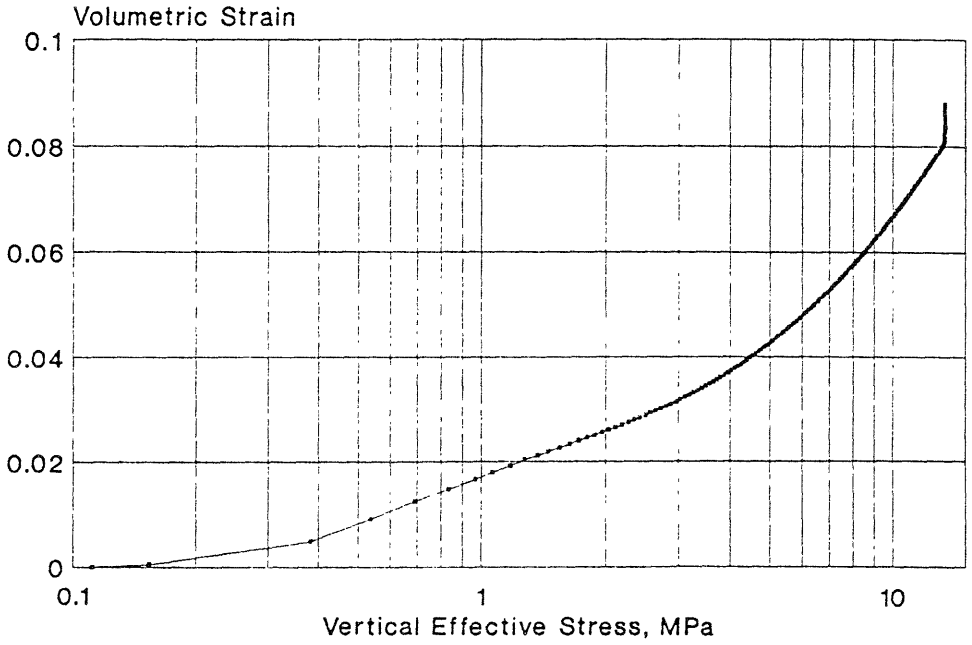

SERIES C : TEST #29
Volumetric Strain vs Vert. Eff. Stress

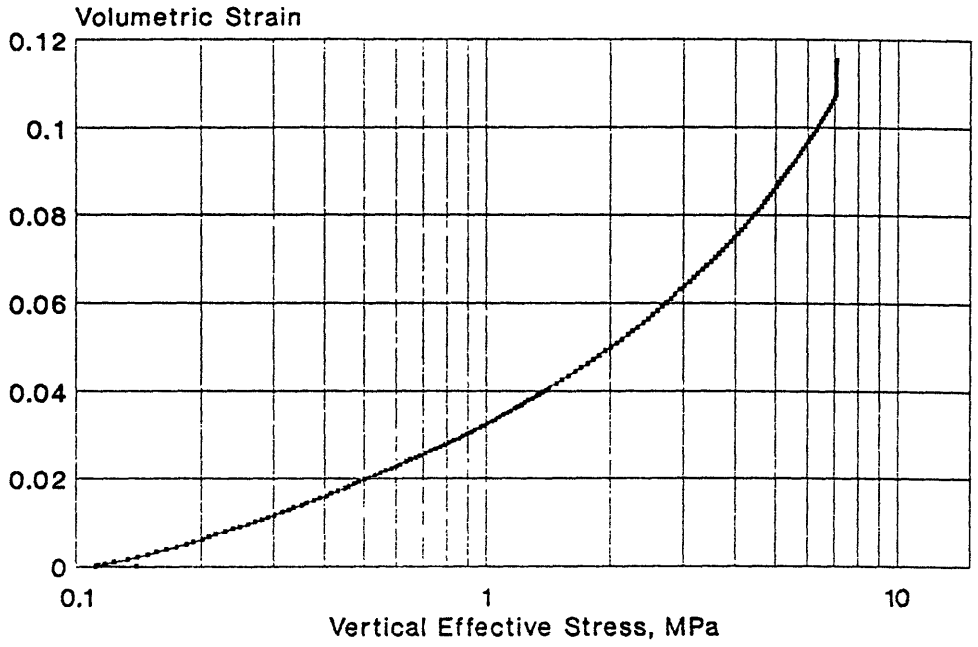

SERIES C : TEST #30
Volumetric Strain versus Eff. Stress

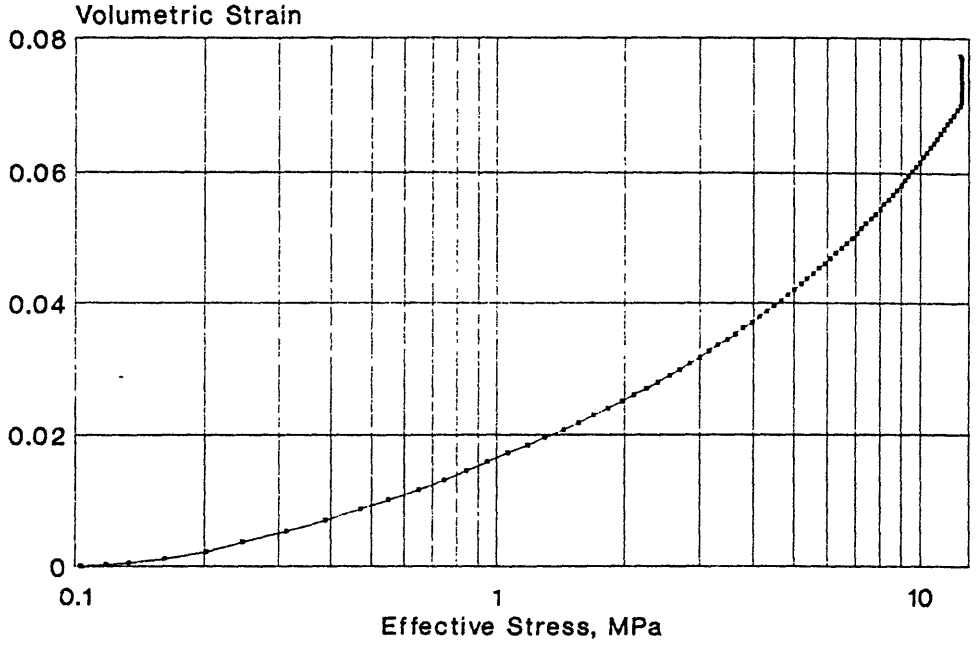

SERIES C : TEST #32
Volumetric Strain vs Vert. Eff. Stress

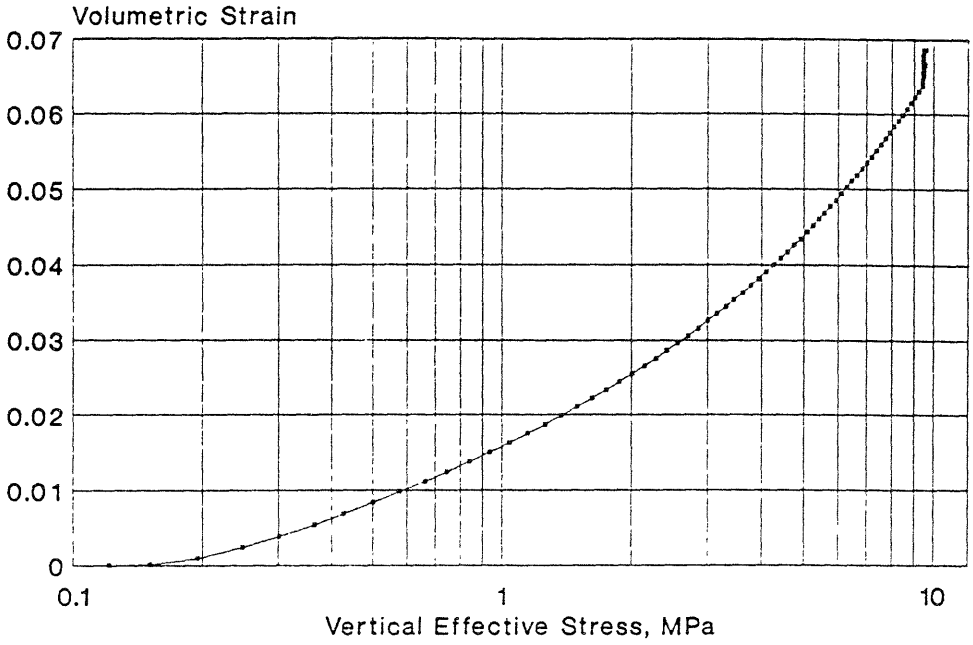

SERIES C : TEST #33
Volumetric Strain versus Eff. Stress

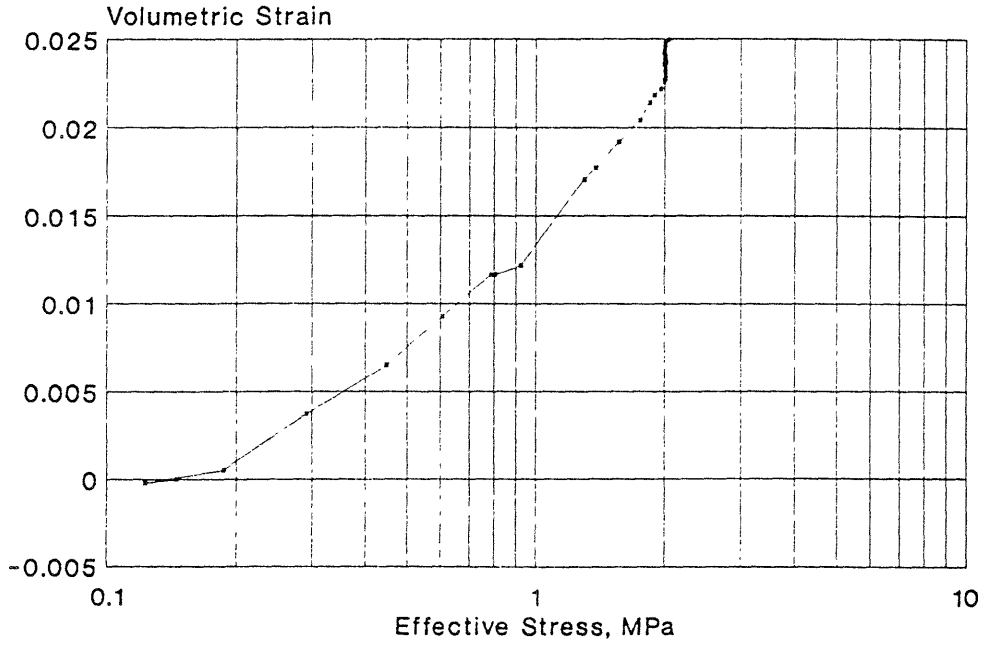

SERIES C : TEST #35

Volumetric Strain versus Eff. Stress

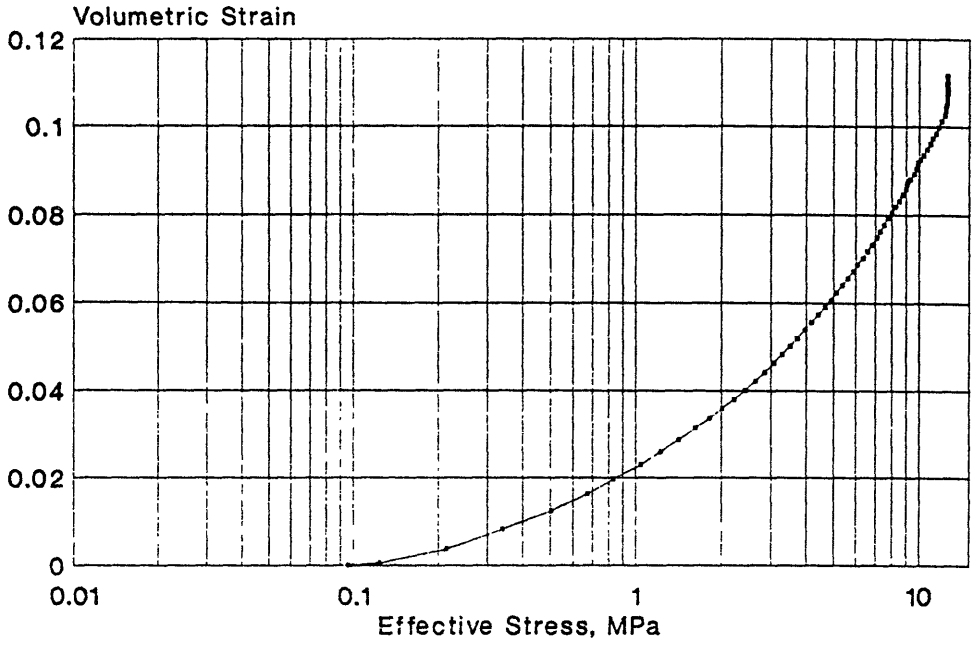

Void Ratio vs Log Effective Stress

SERIES B : TEST #01
Void Ratio versus Effective Stress

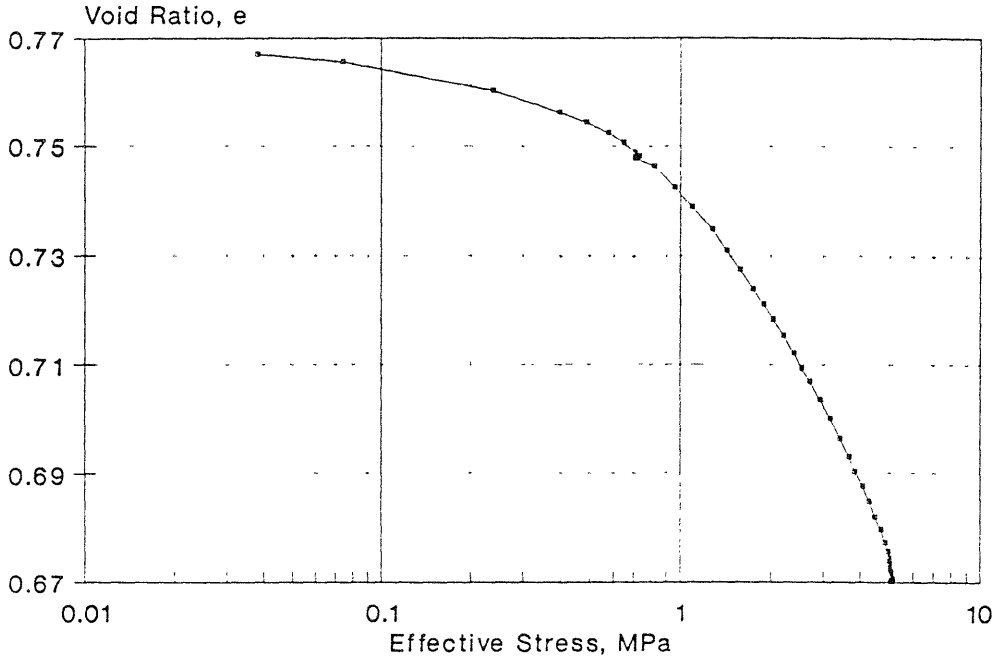

SERIES B : TEST #02
Void Ratio versus Effective Stress

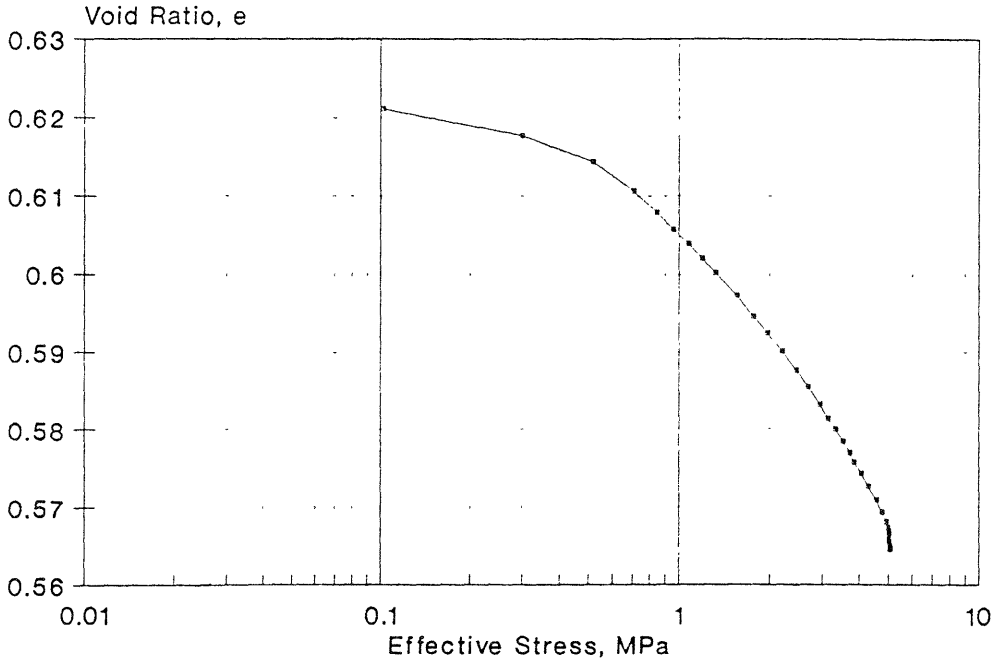

SERIES B : TEST #03
Void Ratio versus Effective Stress

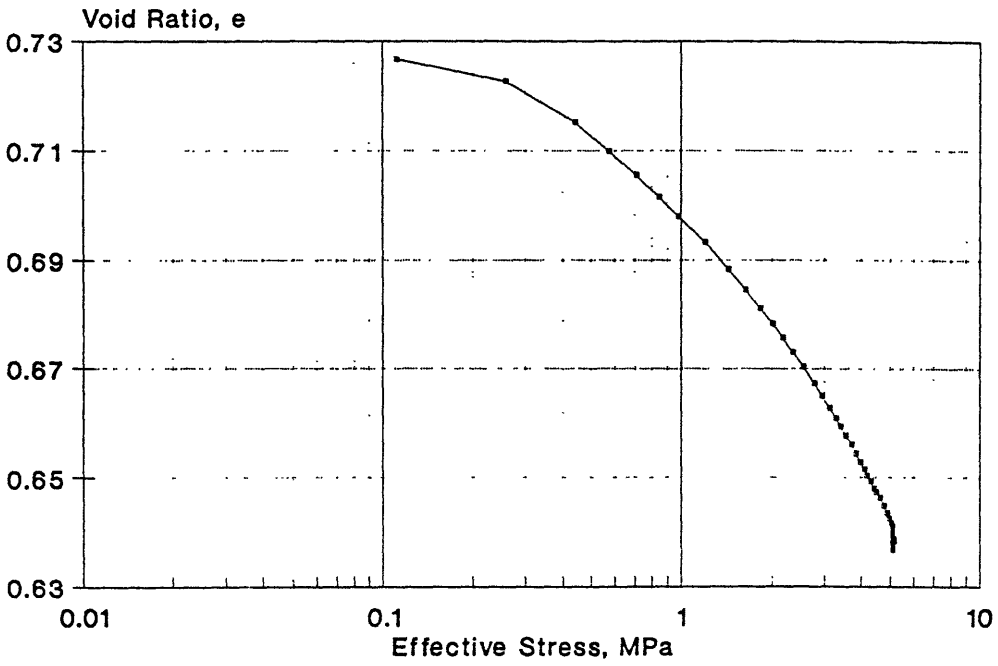

SERIES B : TEST #04
Void Ratio versus Effective Stress

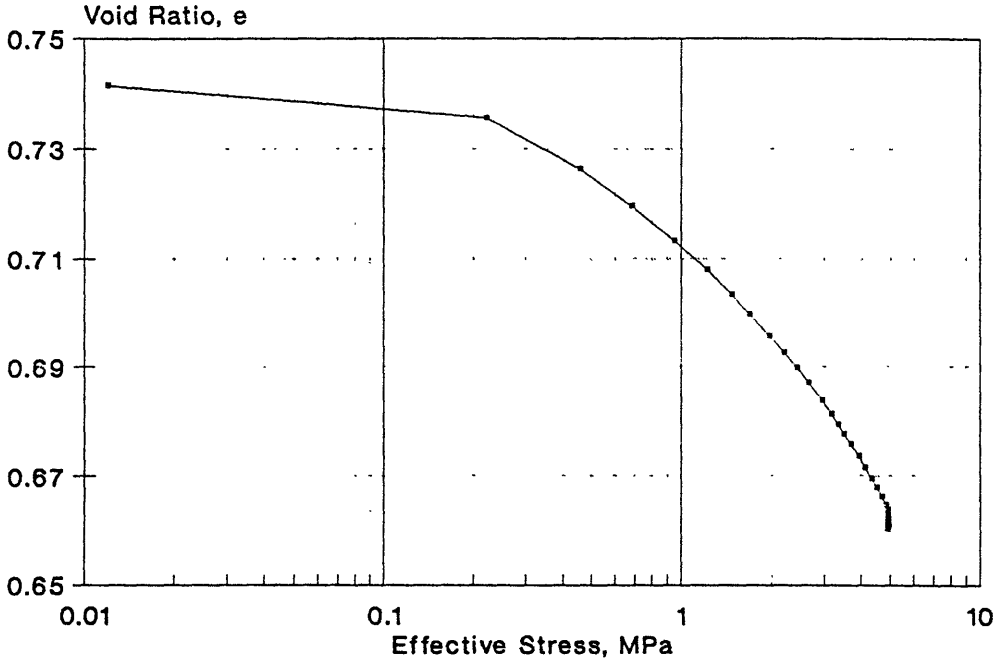

SERIES B : TEST #05
Void Ratio versus Effective Stress

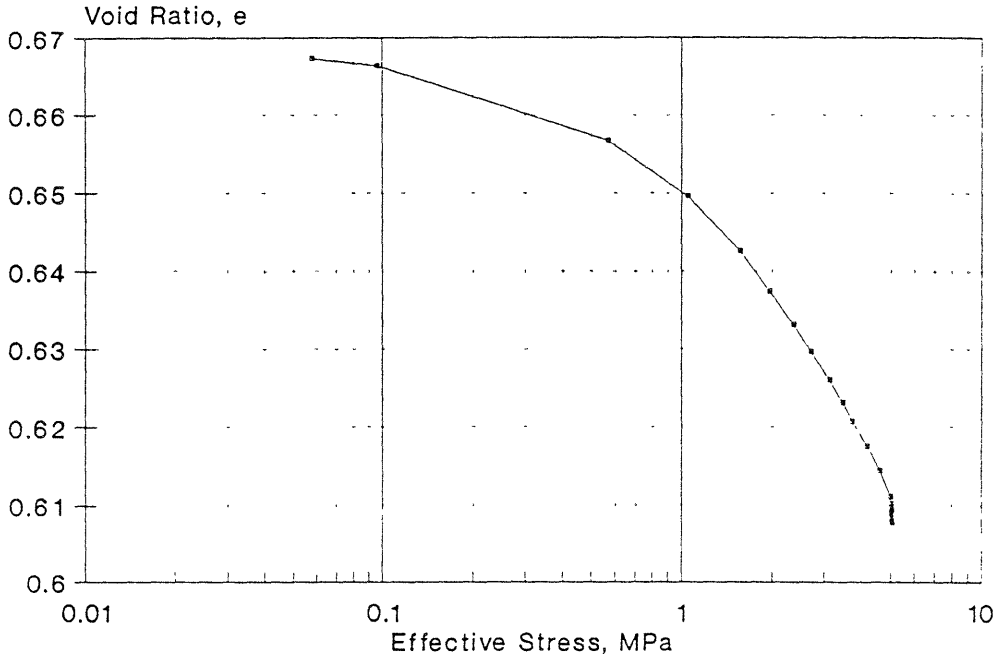

SERIES B : TEST #06
Void Ratio versus Effective Stress

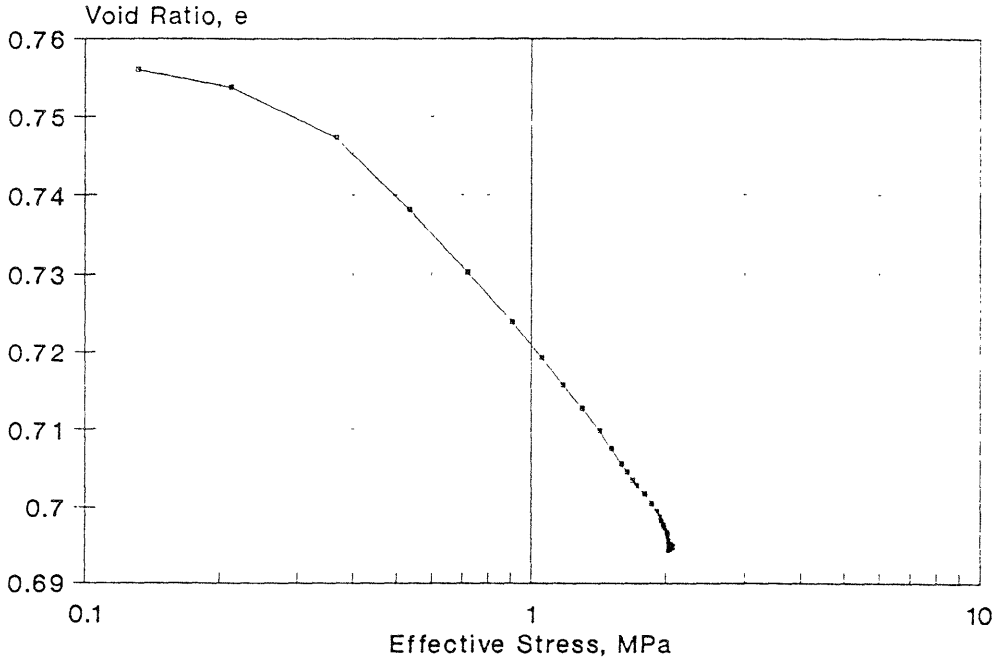

SERIES B : TEST #07
Void Ratio versus Effective Stress

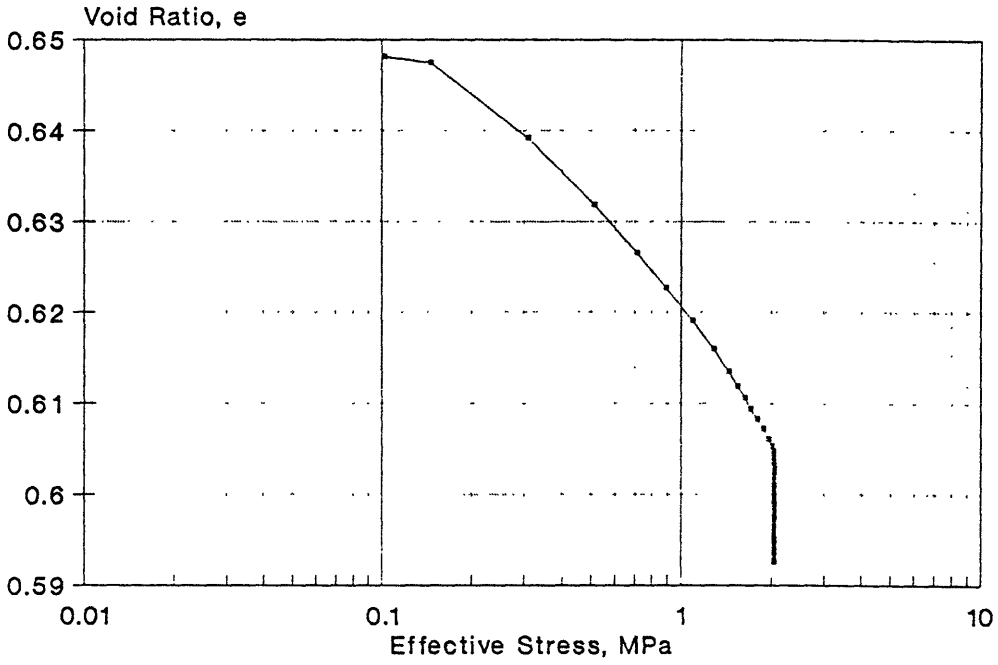

SERIES B : TEST #11
Void Ratio versus Effective Stress

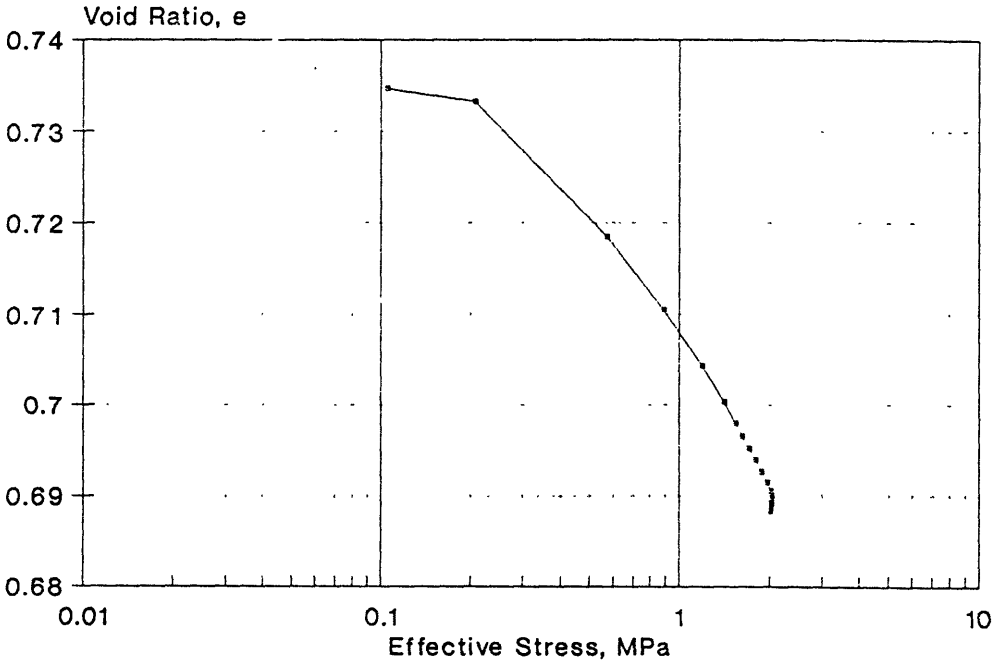

SERIES B : TEST #13
Void Ratio versus Effective Stress

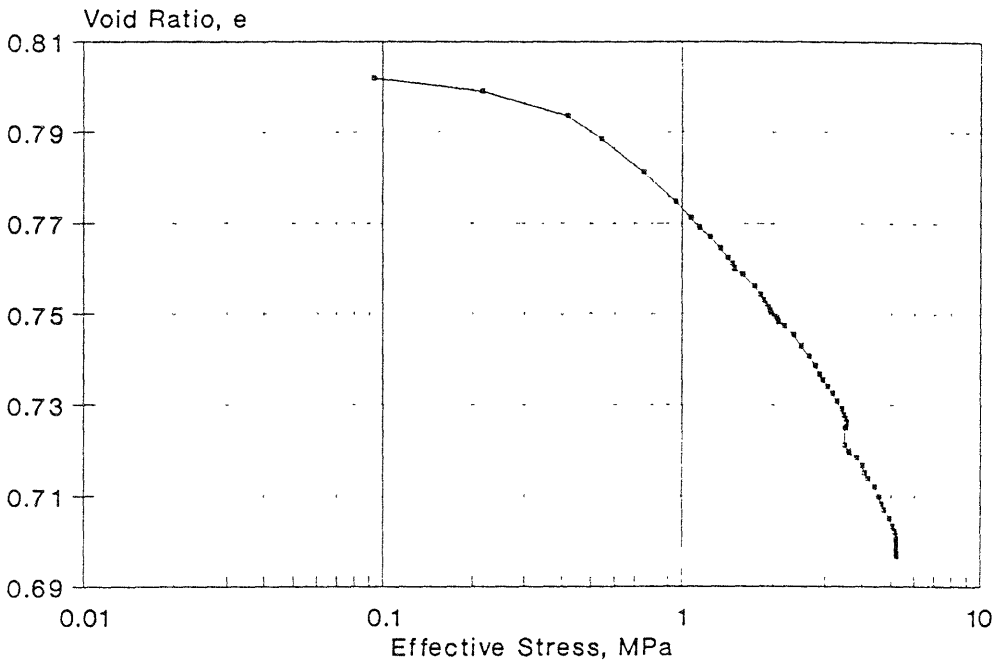

SERIES B : TEST #14
Void Ratio versus Effective Stress

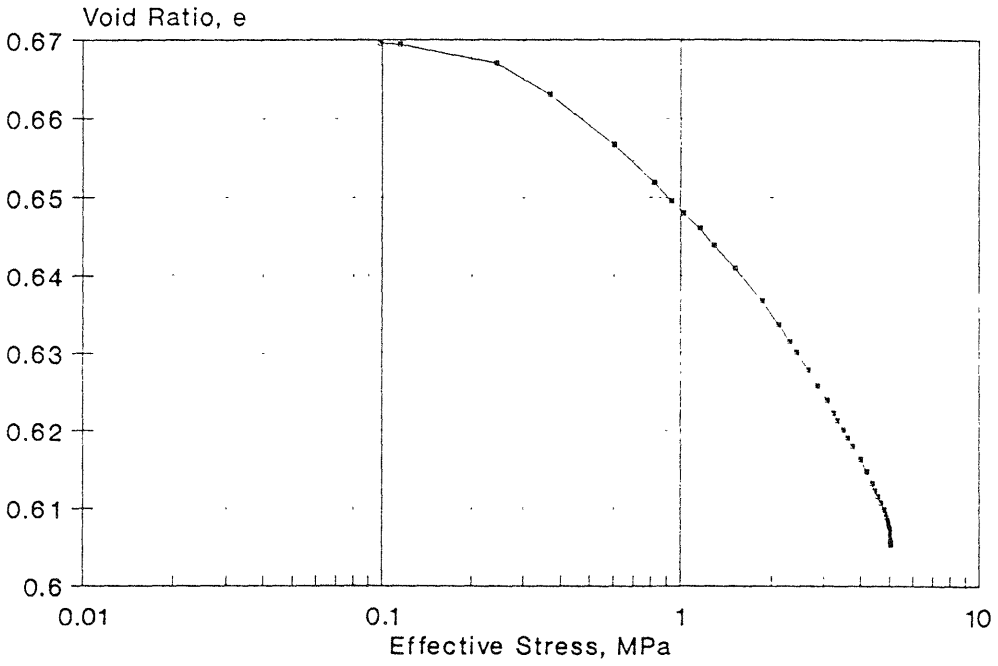

SERIES B : TEST #15
Void Ratio versus Effective Stress

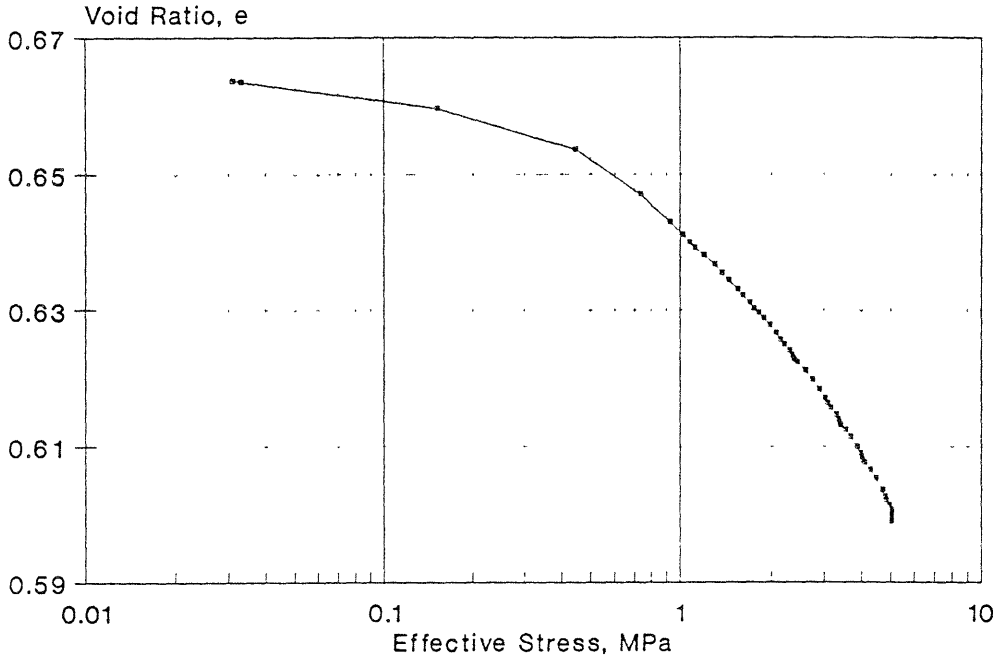

SERIES B : TEST #16
Void Ratio versus Effective Stress

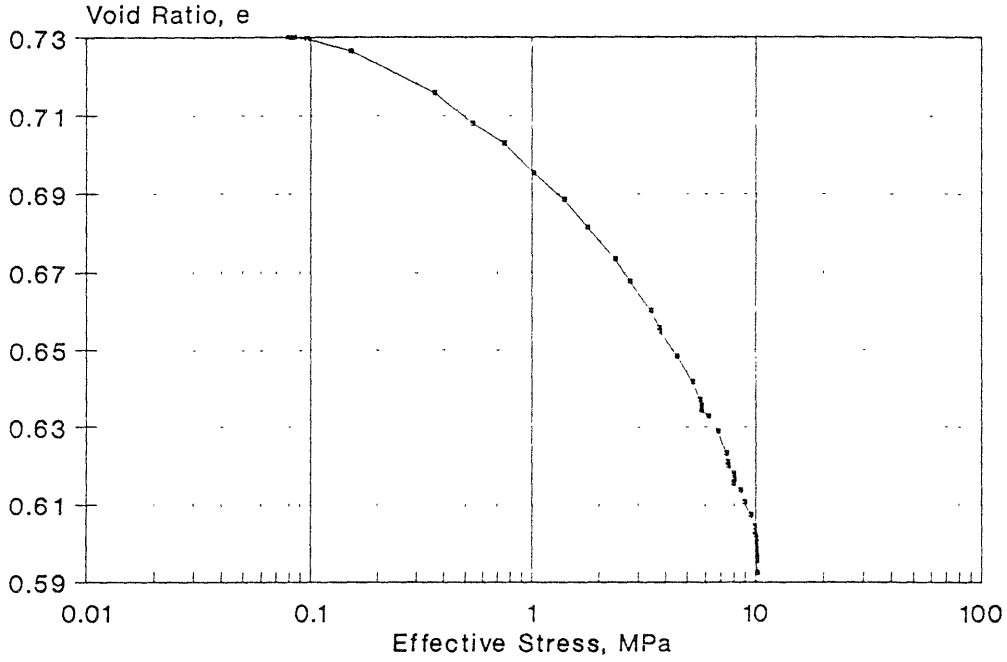

SERIES B : TEST #17
Void Ratio versus Effective Stress

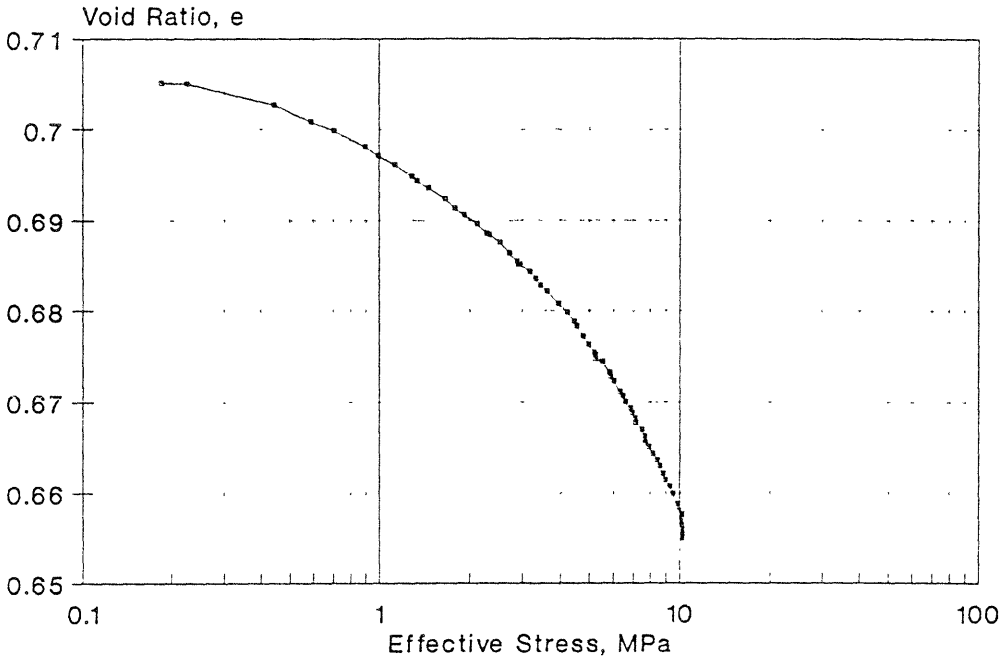

SERIES B : TEST #18
Void Ratio versus Effective Stress

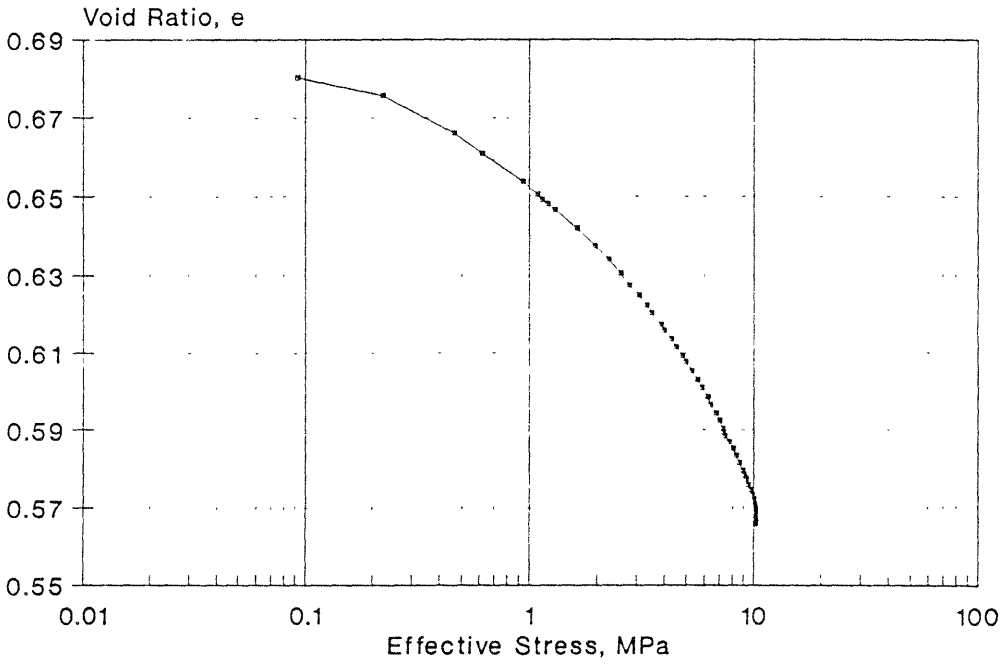

SERIES B : TEST #19
Void Ratio versus Effective Stress

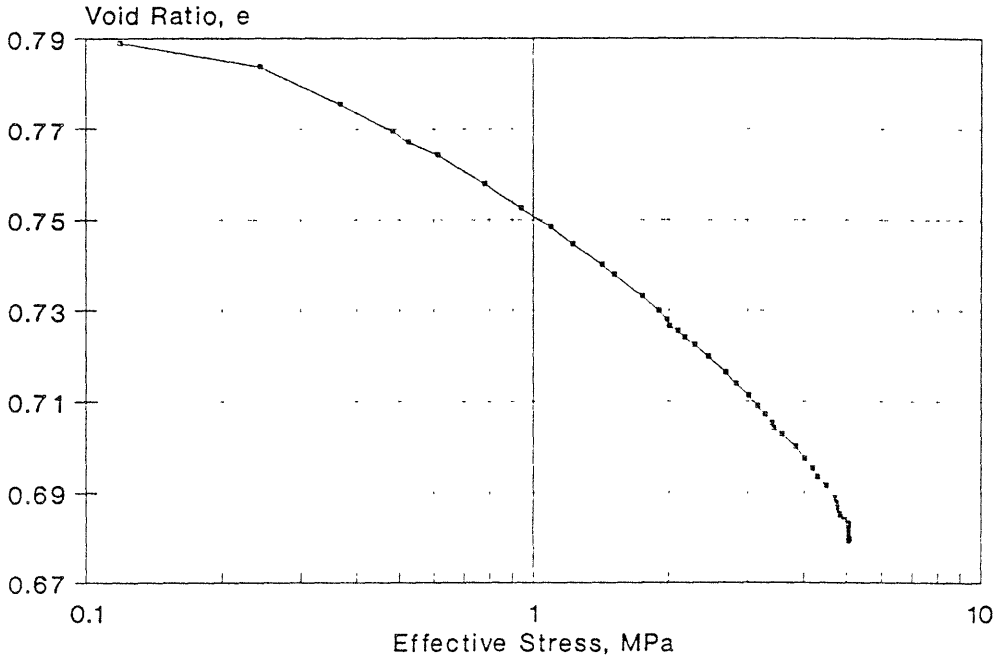

SERIES B : TEST #20
Void Ratio versus Effective Stress

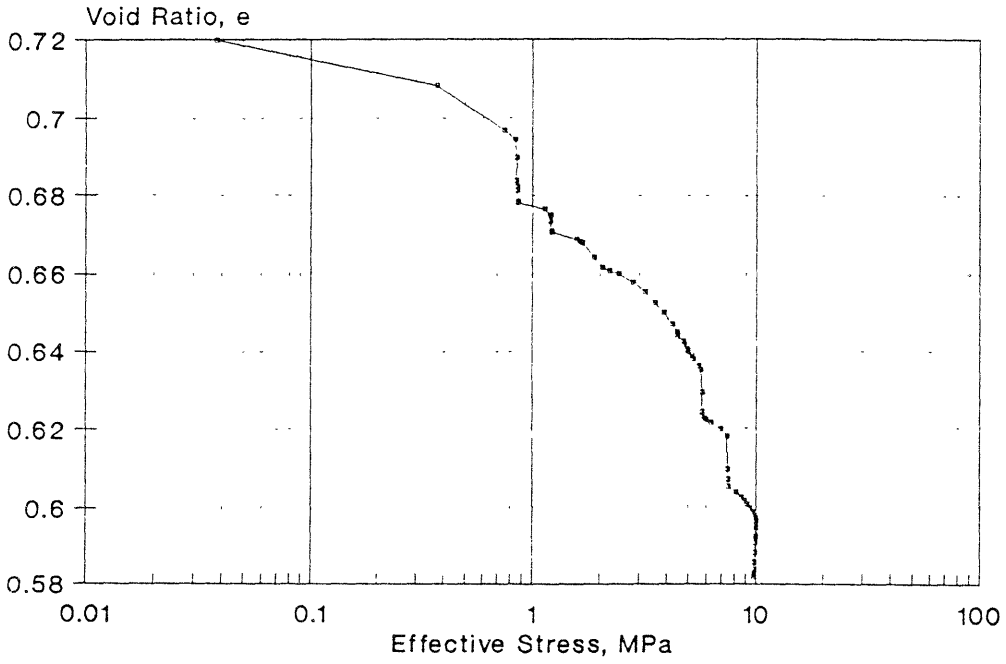

SERIES B : TEST #21
Void Ratio versus Effective Stress

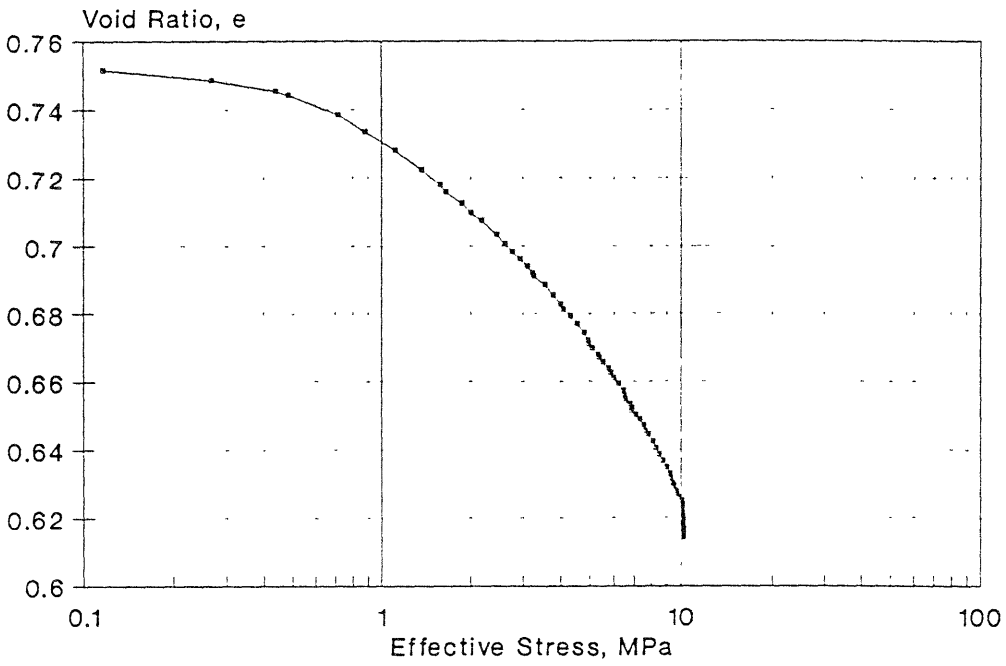

SERIES B : TEST #23
Void Ratio versus Effective Stress

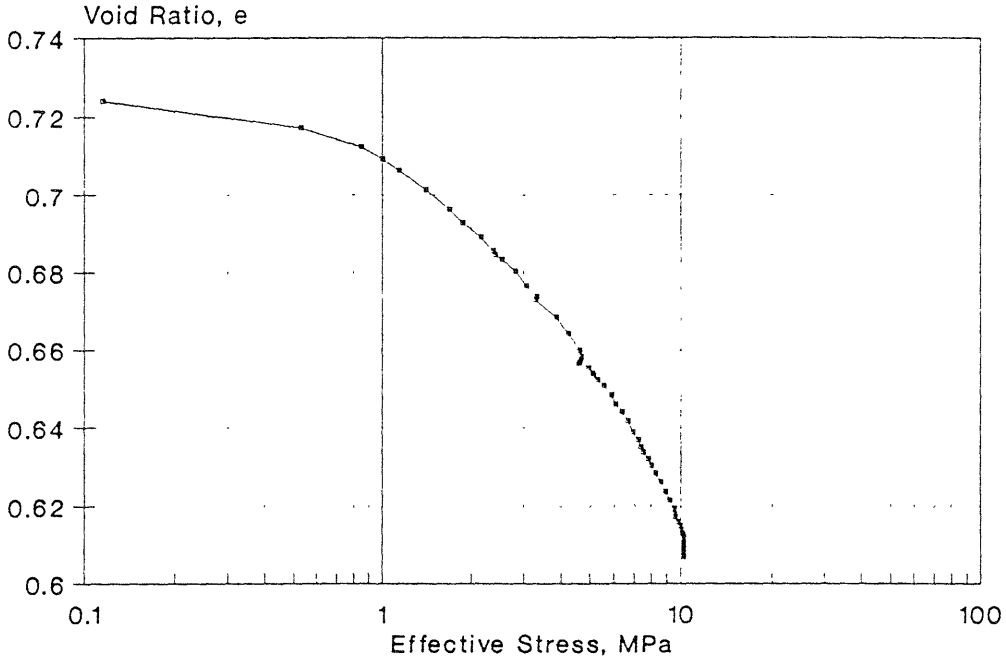

SERIES B : TEST #24
Void Ratio versus Effective Stress

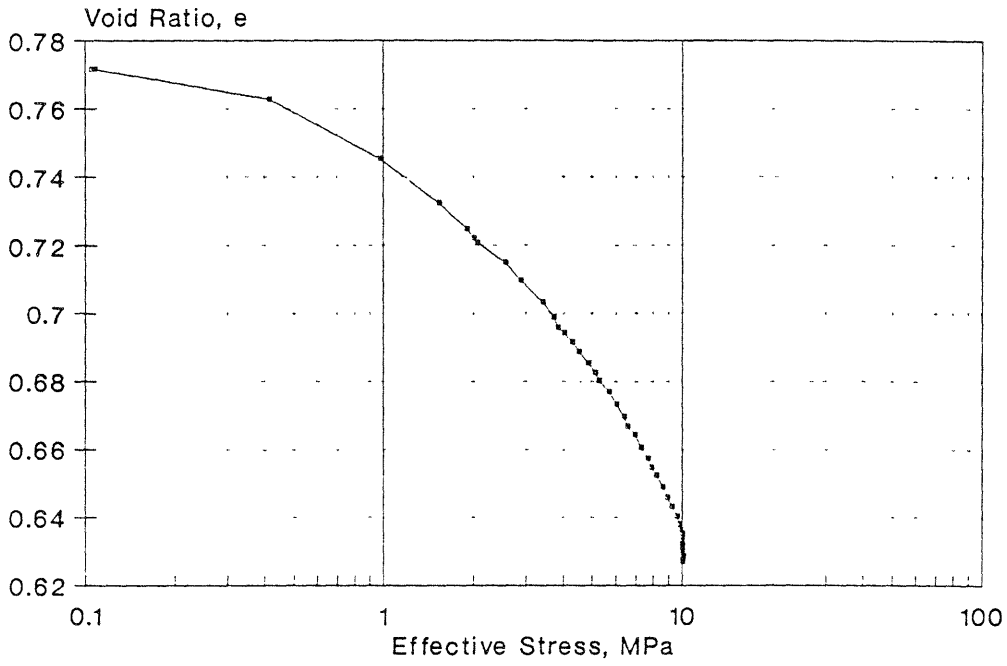

SERIES C : TEST #01
Void Ratio versus Effective Stress

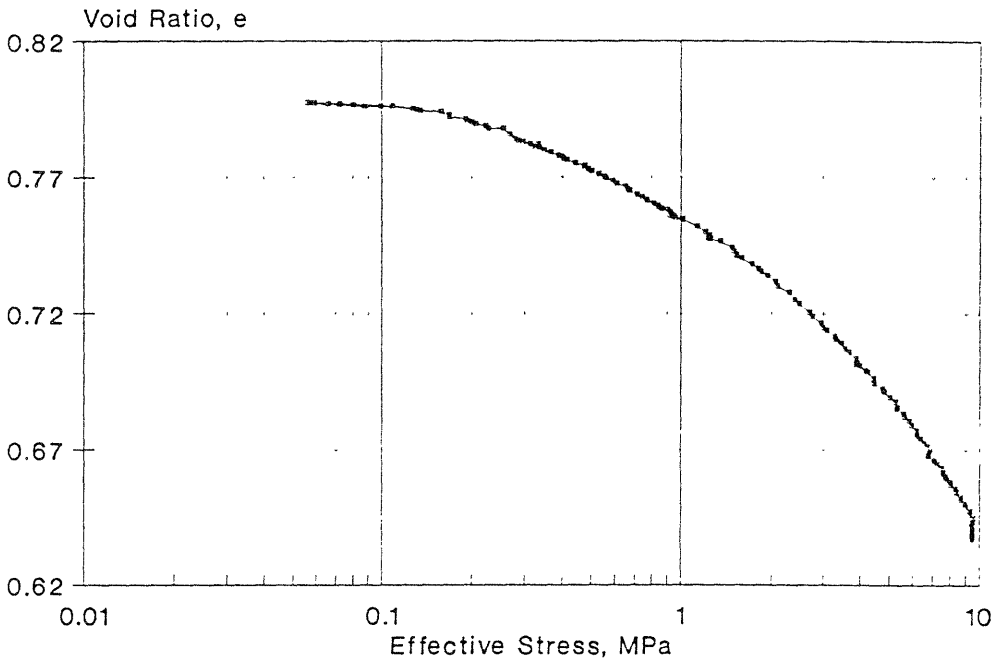

SERIES C : TEST #02
Void Ratio versus Effective Stress

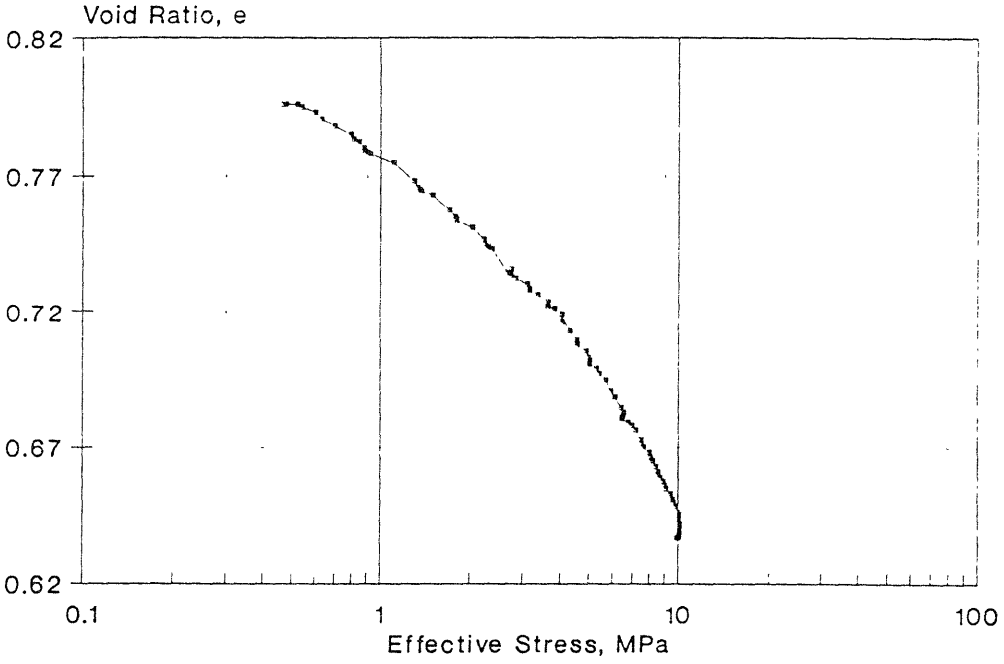

SERIES C : TEST #03
Void Ratio versus Effective Stress

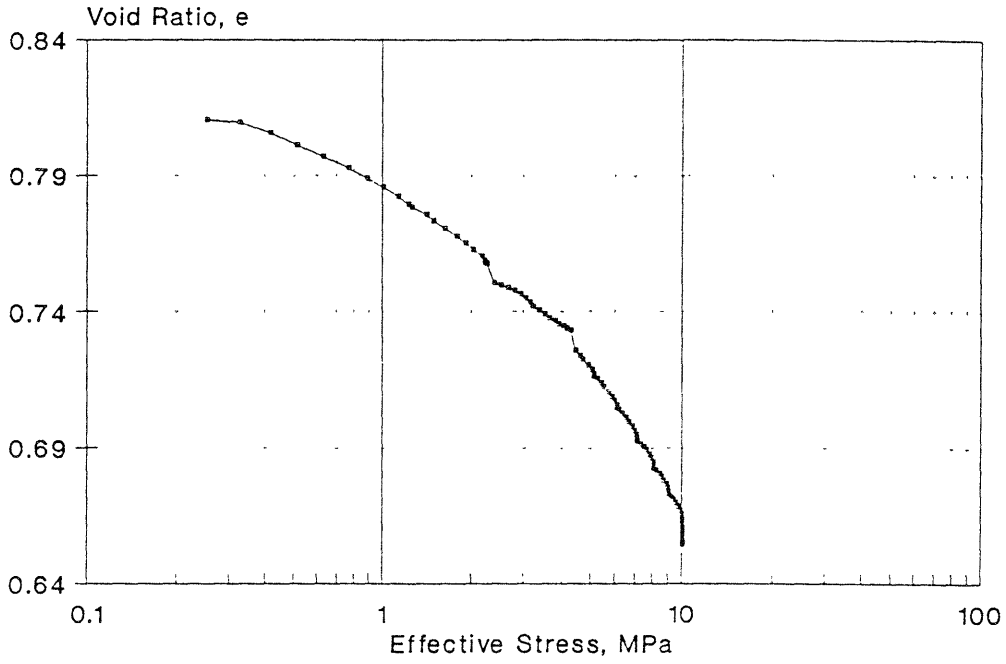

SERIES C : TEST #04
Void Ratio versus Effective Stress

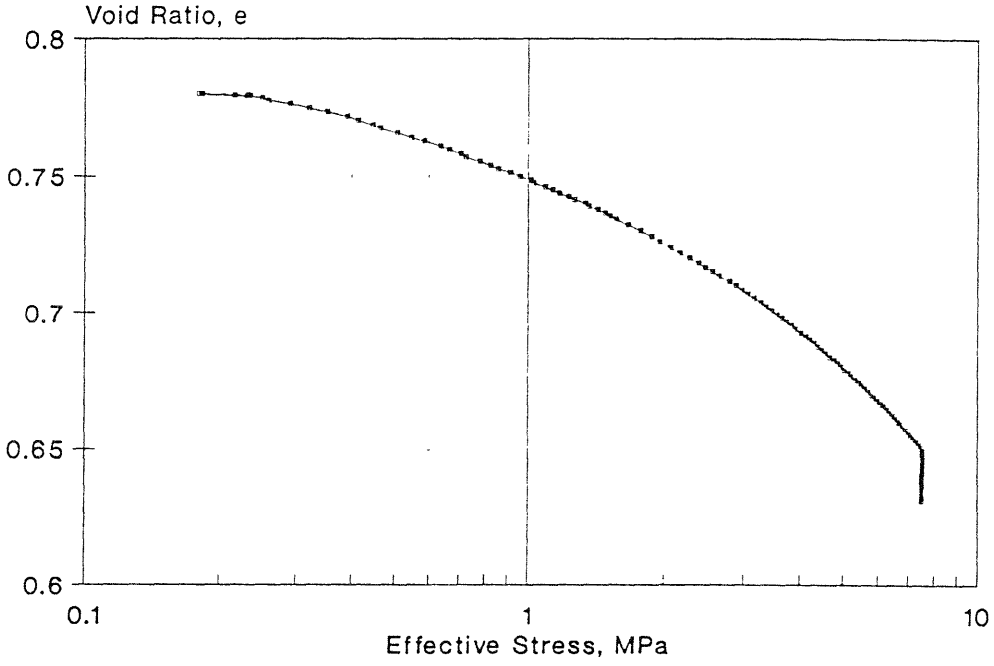

SERIES C : TEST #08
Void Ratio versus Effective Stress

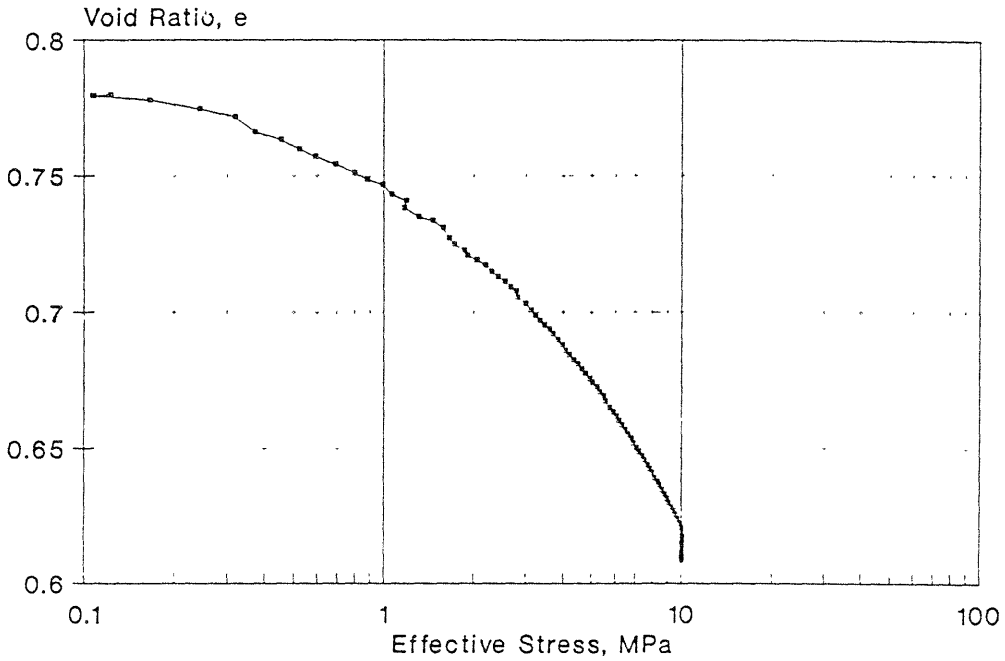

SERIES C : TEST #09
Void Ratio versus Effective Stress

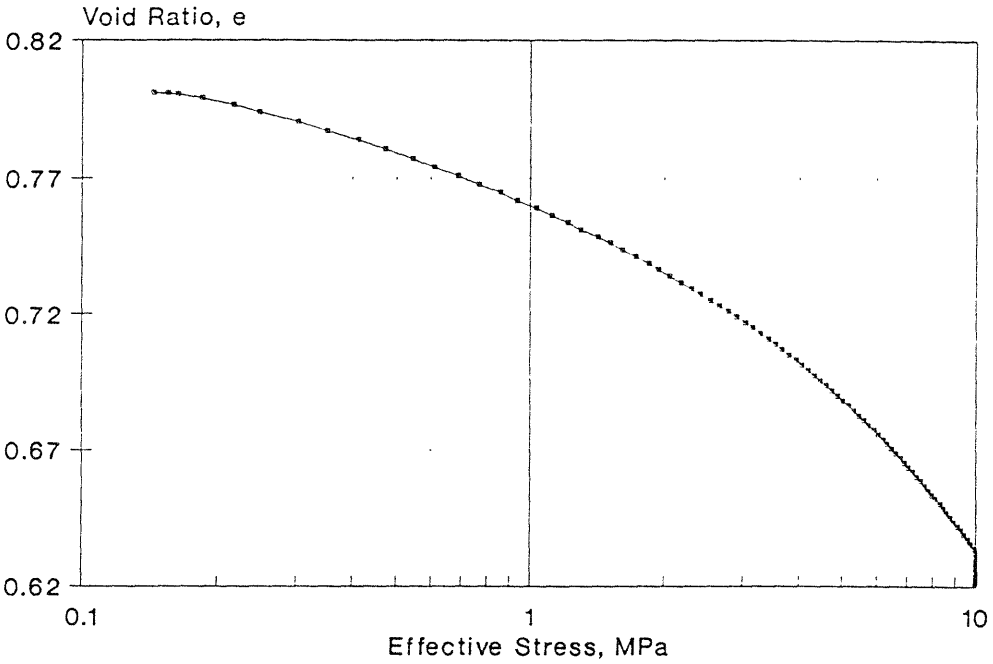

SERIES C : TEST #10
Void Ratio versus Effective Stress

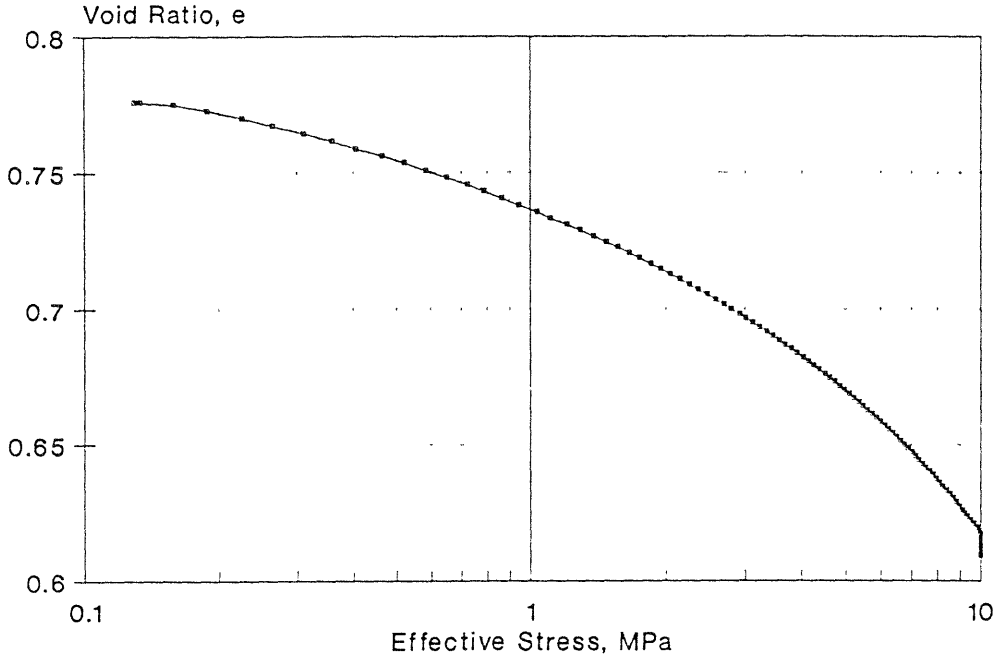

SERIES C : TEST #11
Void Ratio versus Effective Stress

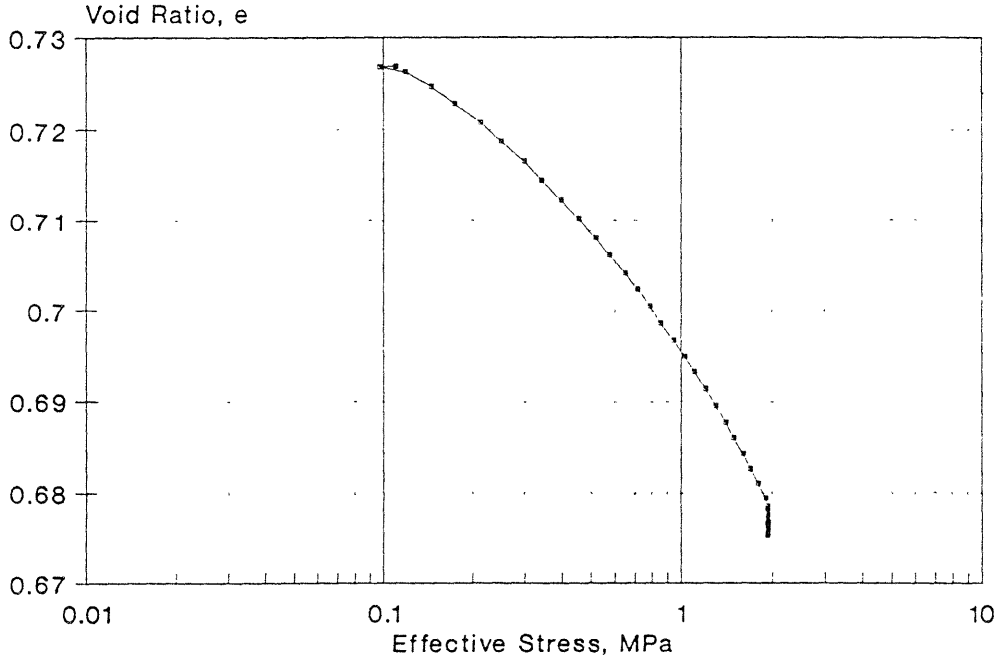

SERIES C : TEST #12
Void Ratio versus Effective Stress

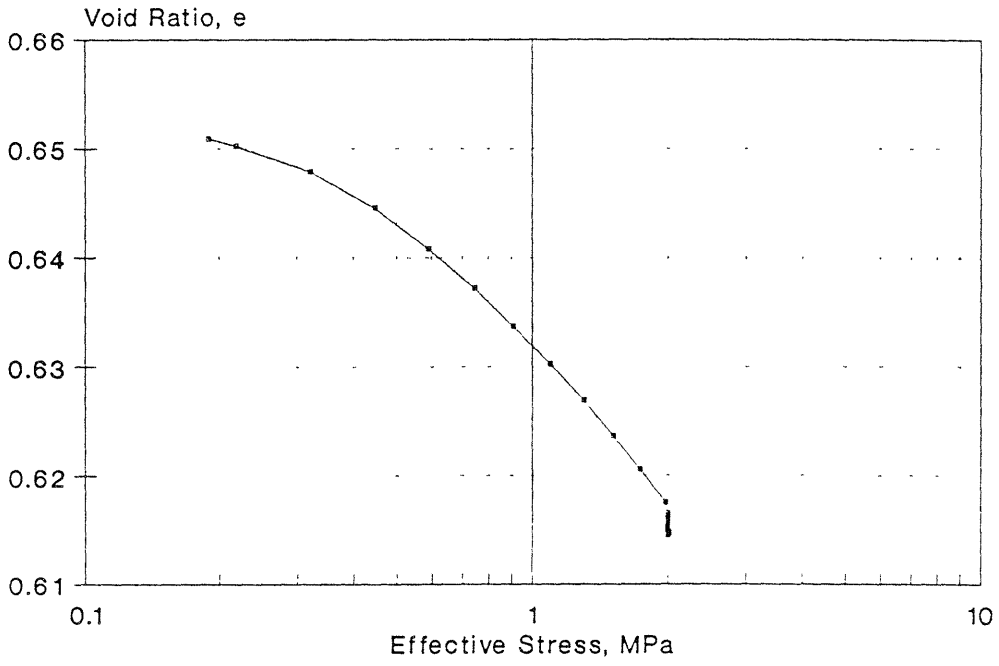

SERIES C : TEST #13
Void Ratio versus Effective Stress

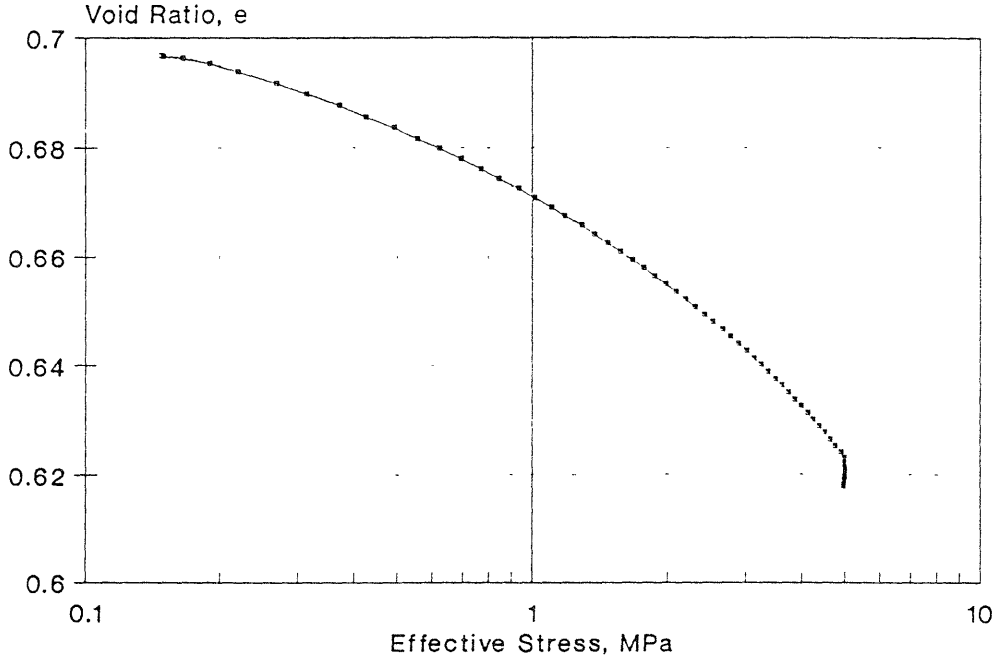

SERIES C : TEST #15
Void Ratio versus Effective Stress

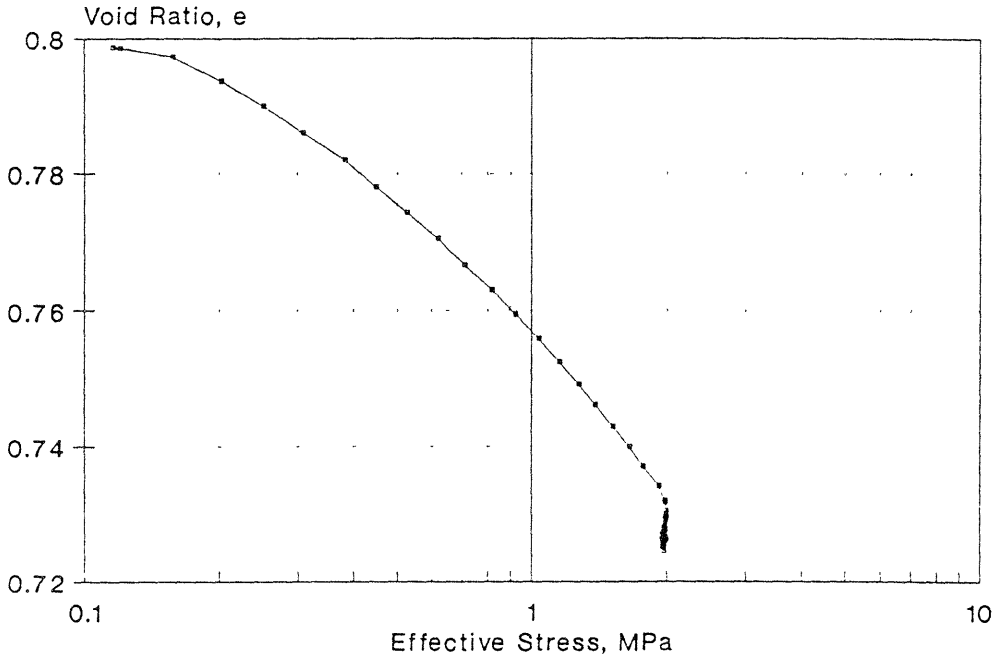

SERIES C : TEST #16
Void Ratio versus Effective Stress

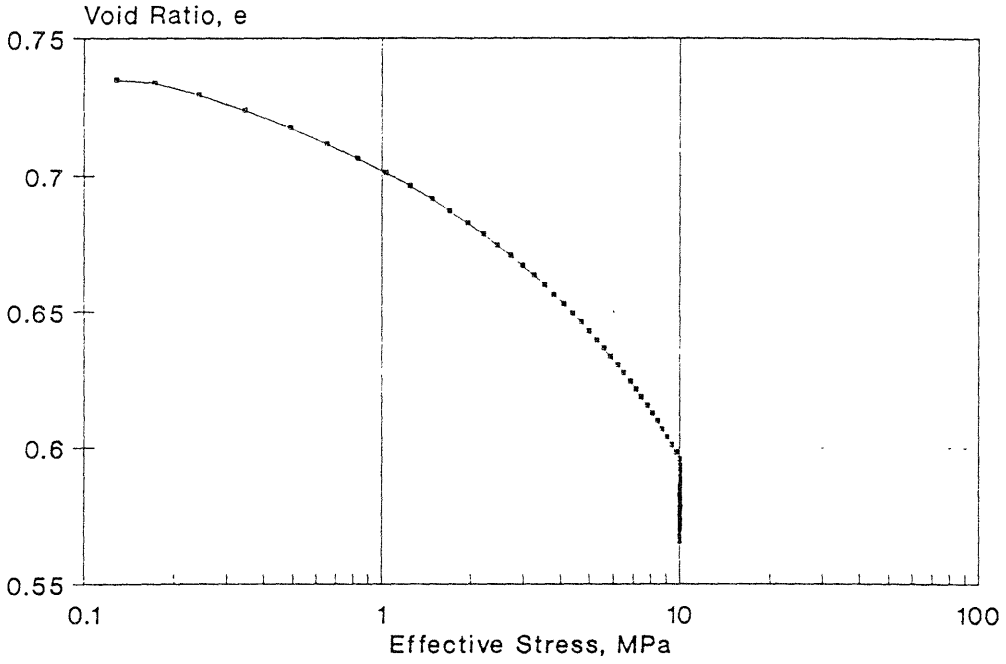

SERIES C : TEST #22
Void Ratio versus Effective Stress

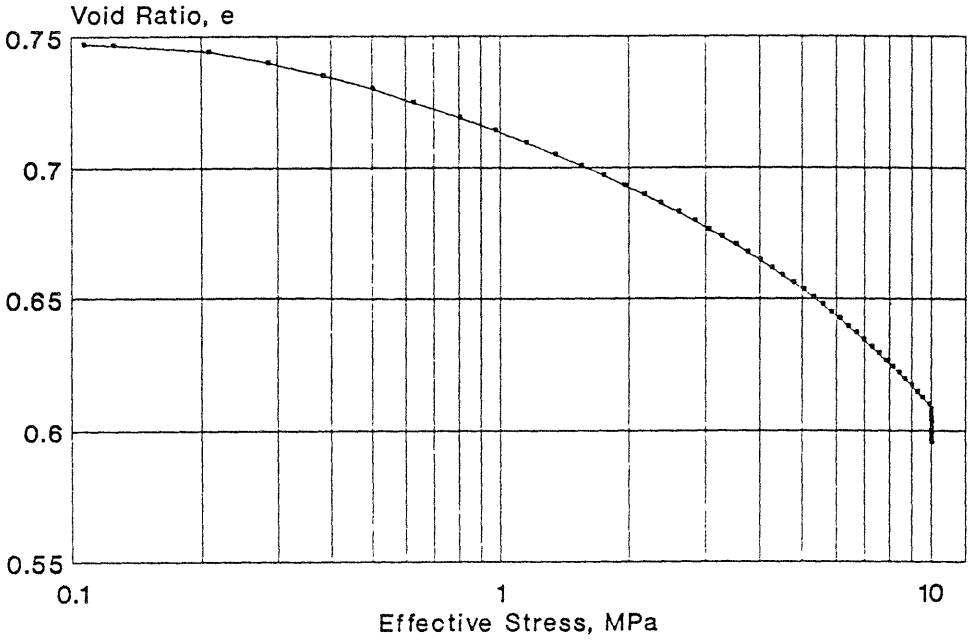

SERIES C : TEST #23
Void Ratio versus Effective Stress

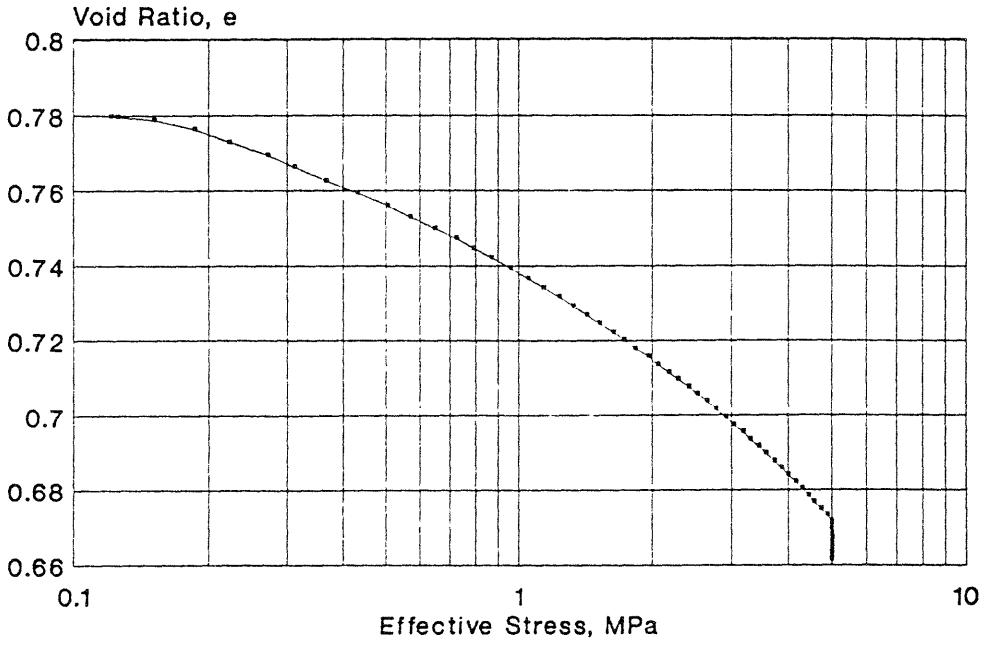

SERIES C : TEST #24
Void Ratio versus Effective Stress

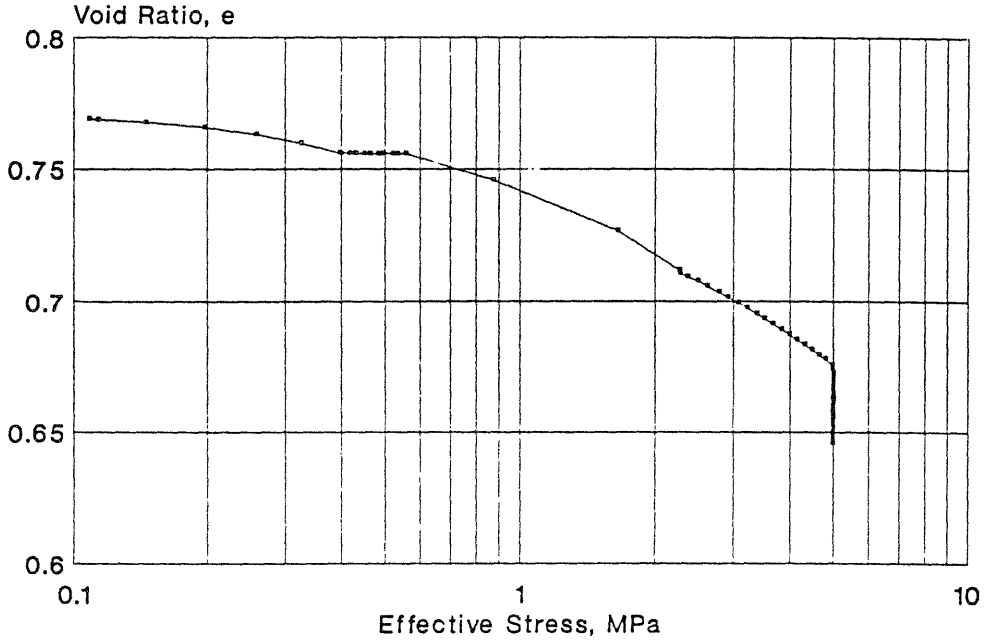

SERIES C : TEST #25
Void Ratio versus Effective Stress

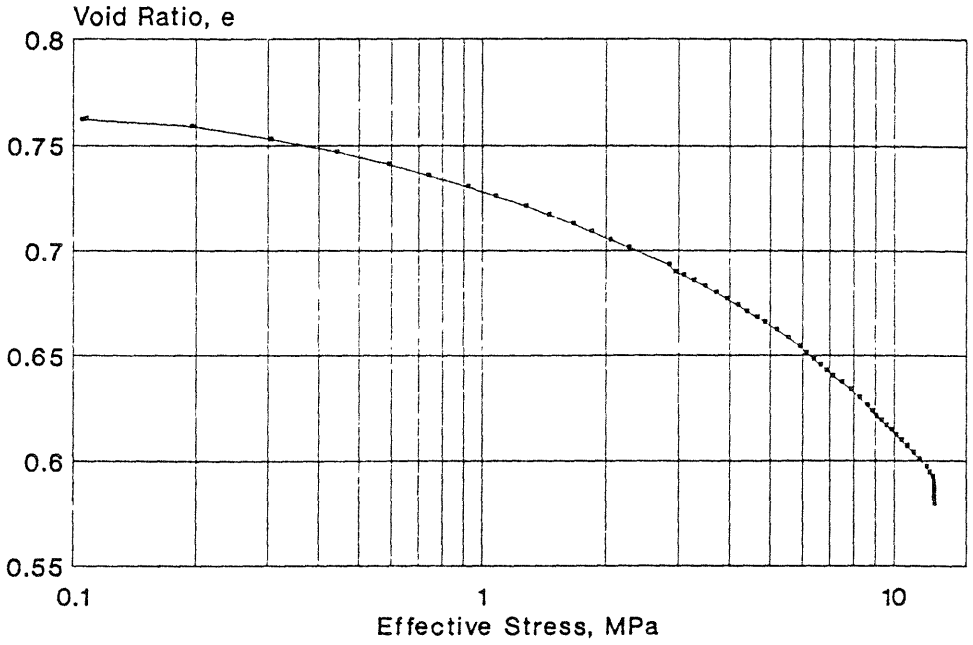

SERIES C : TEST #27
Void Ratio versus Effective Stress

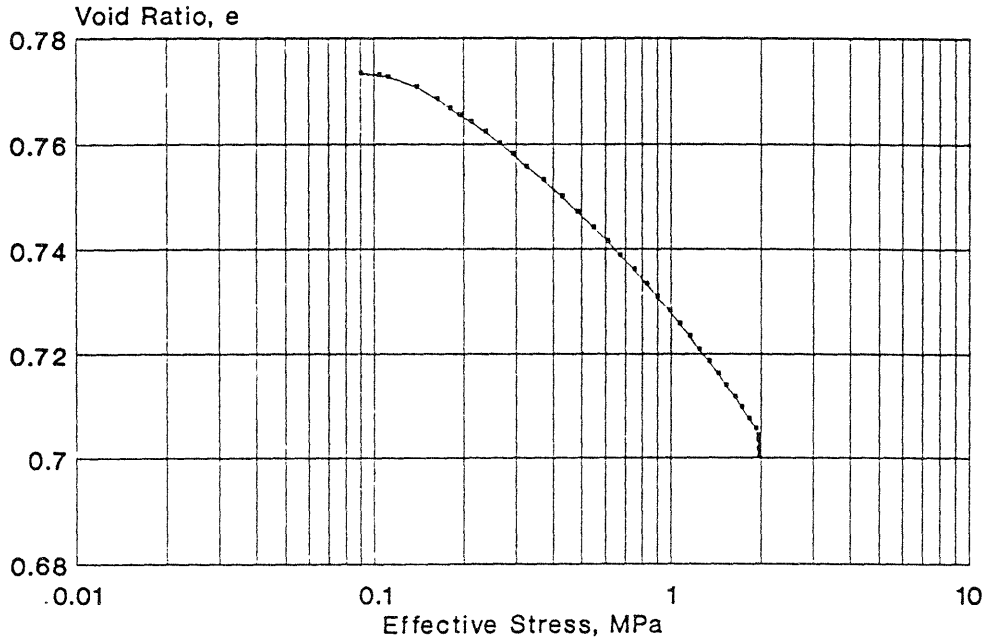

SERIES C : TEST #28
Void Ratio vs Vertical Effective Stress

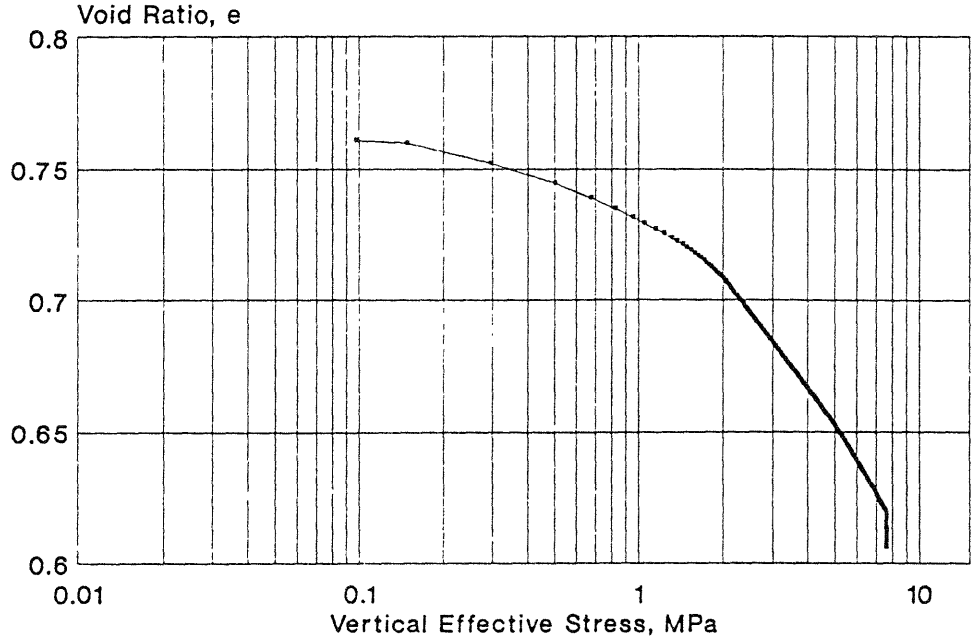

SERIES C : TEST #29
Void Ratio vs Vertical Effective Stress

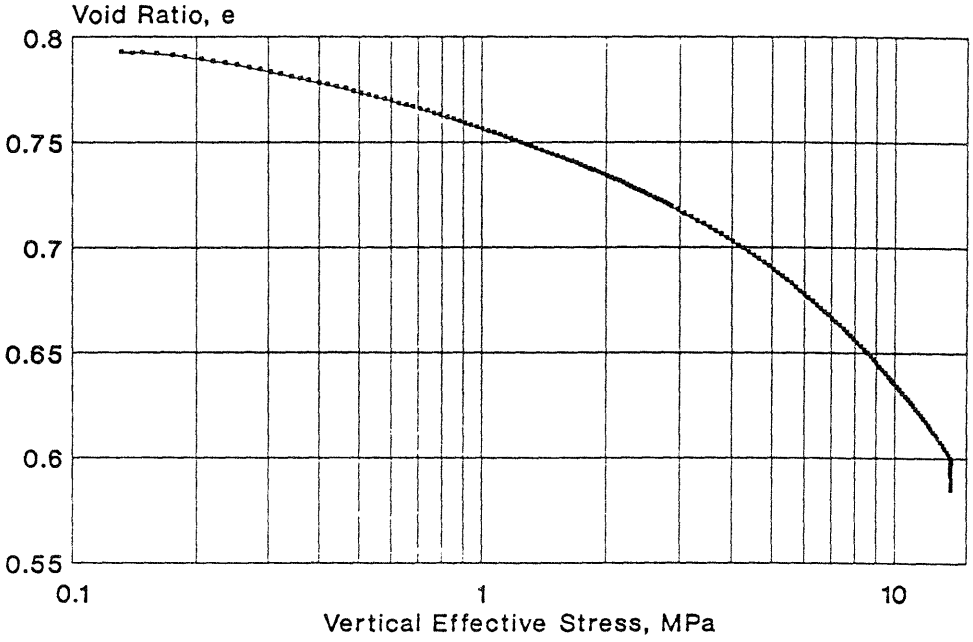

SERIES C : TEST #29
Void Ratio vs Vertical Effective Stress

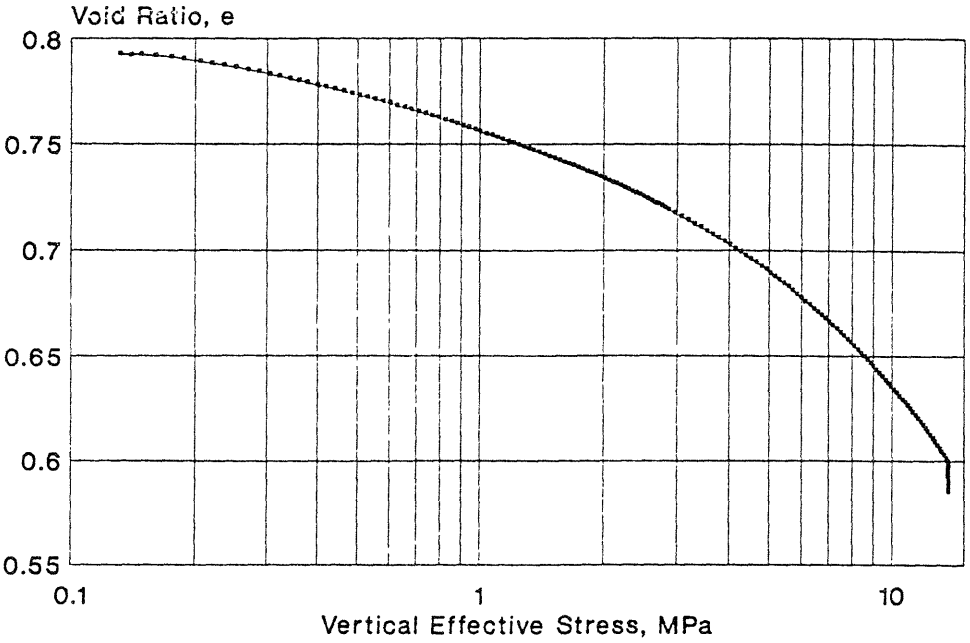

SERIES C : TEST #32
Void Ratio vs Vertical Effective Stress

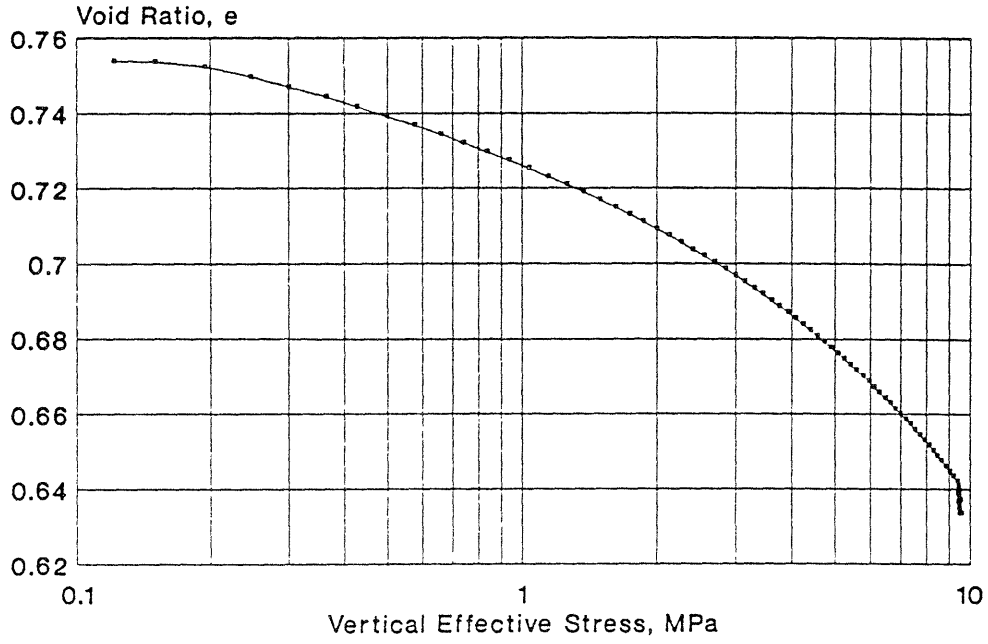

SERIES C : TEST #33
Void Ratio versus Effective Stress

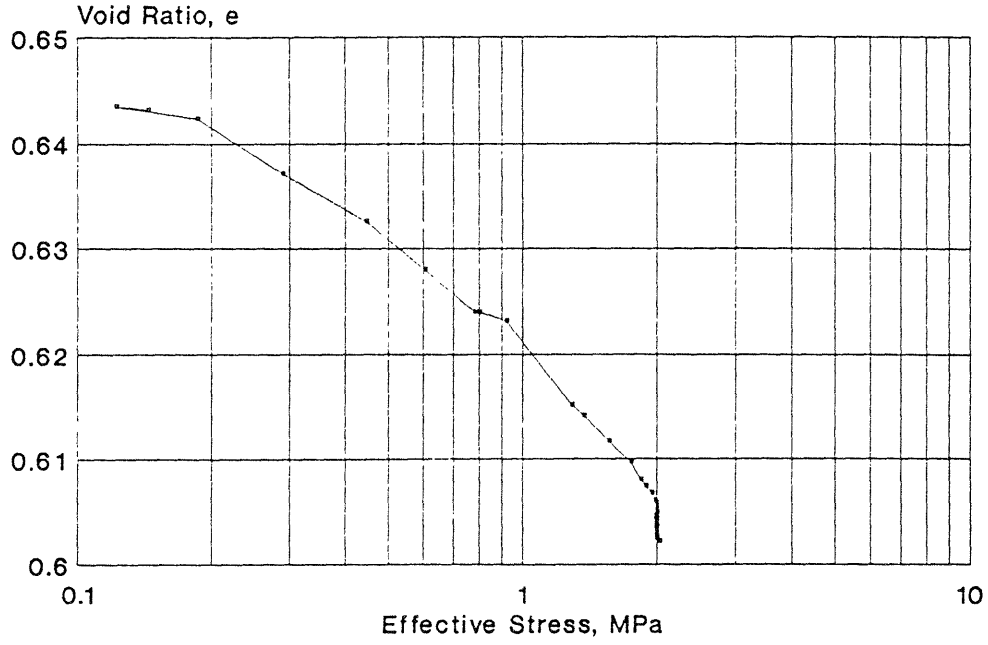

SERIES C : TEST # 35

Void Ratio versus Effective Stress

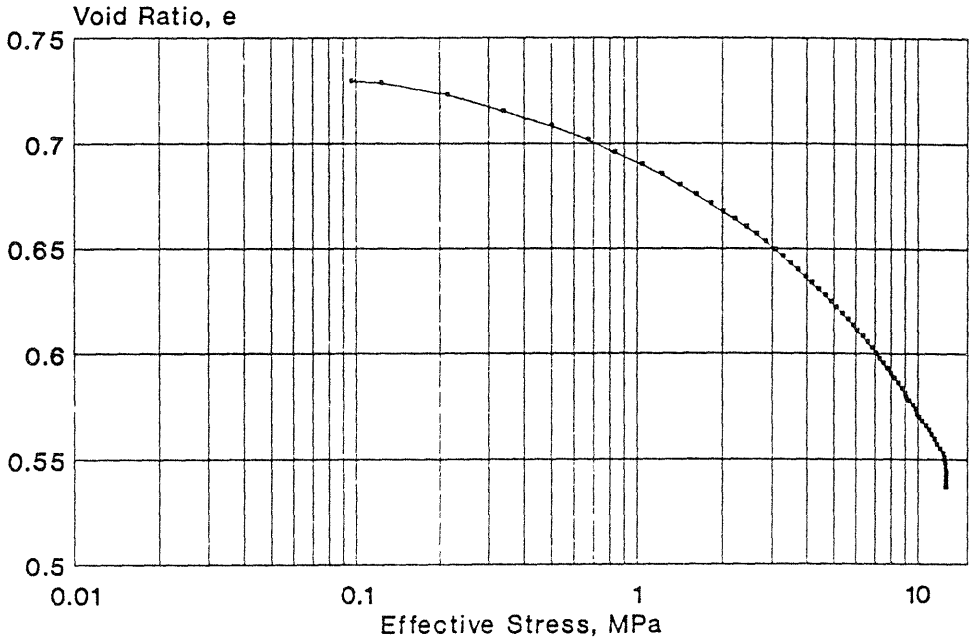

SECTION B.2

Shear Results

This section presents the shear results for Series B and Series C tests from the unfrozen MFS testing program. For each test, four plots are presented to summarized the shear characteristics. For undrained tests, the four plots are:

1) Deviator stress ($2q = \sigma_1 - \sigma_3$) and excess pore pressure (u_e) versus axial strain (ϵ_a)
2) A–parameter (A) versus axial strain
3) Effective stress path ($p' - q$)
4) Obliquity (R) versus axial strain

For CAUC tests, the plot of A vs ϵ_a is omitted. For drained tests, the four plots are:

1) Deviator stress versus axial strain
2) Volumetric strain (ϵ_v) versus axial strain
3) Effective stress path
4) Obliquity versus axial strain

Series B – Test #01

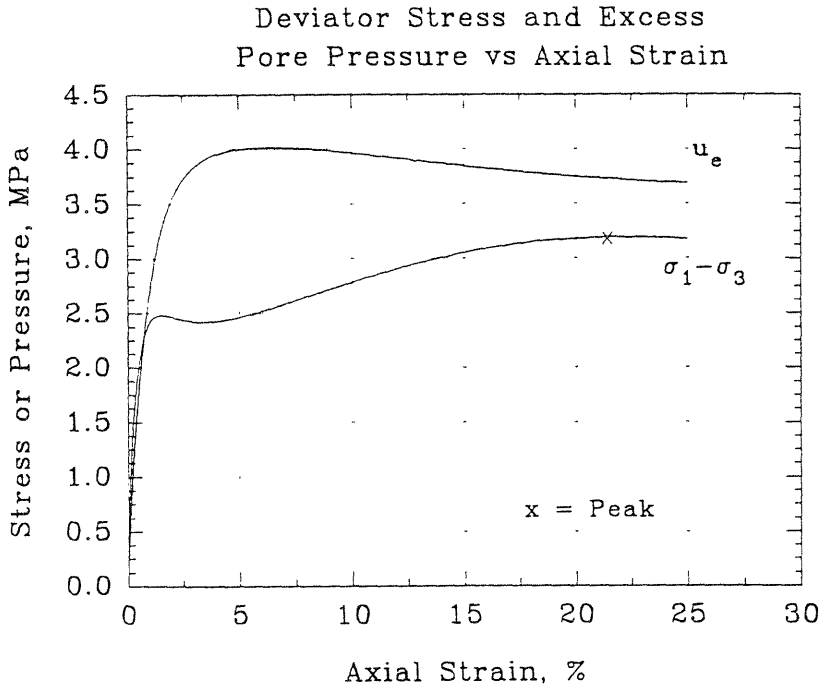

σ'_c = 5 MPa
e = 0.670
D_r = 72.7%

Q_p = 3.19 MPa
ε_p = 21.38 %

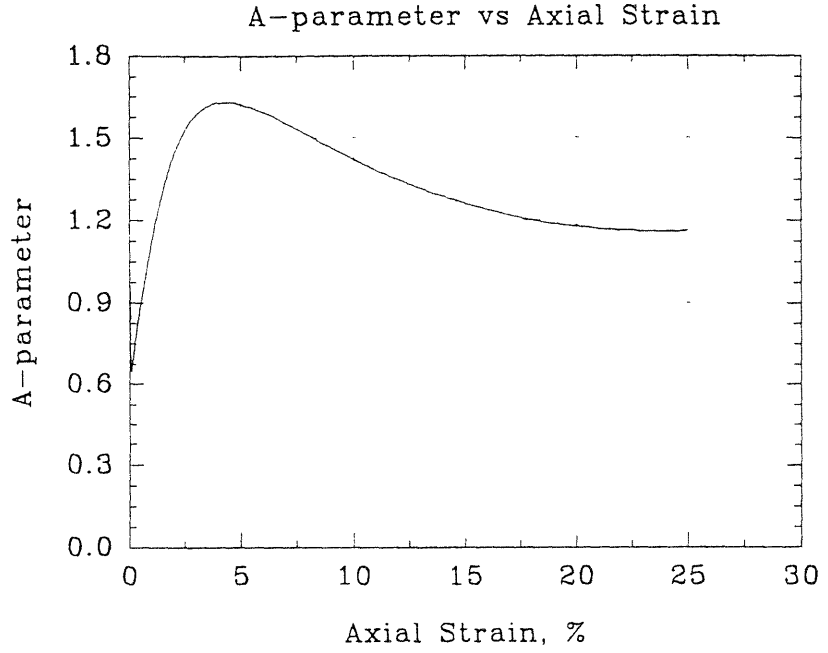

A_f = 1.167

Series B – Test #01

Effective Stress Path

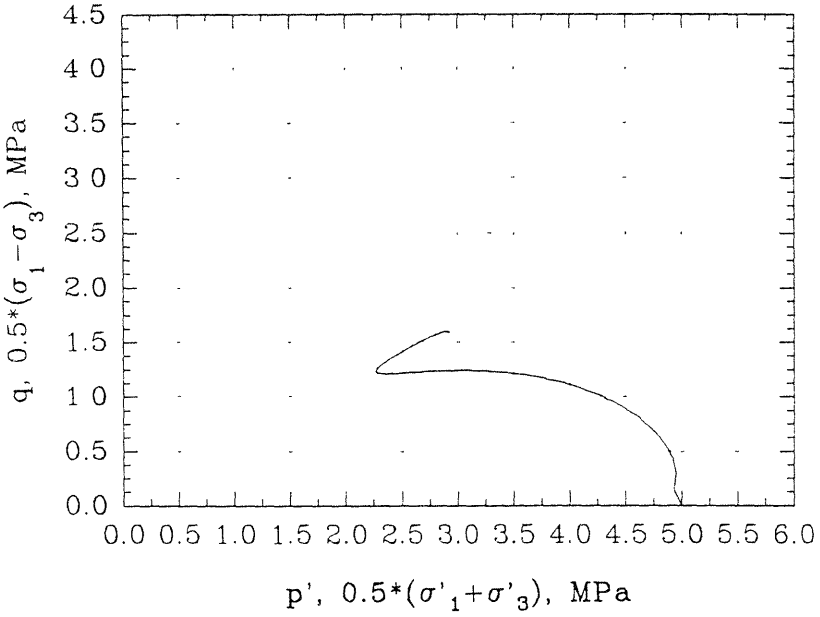

α' = 29.5 °
ϕ' = 34.4 °

Obliquity vs Axial Strain

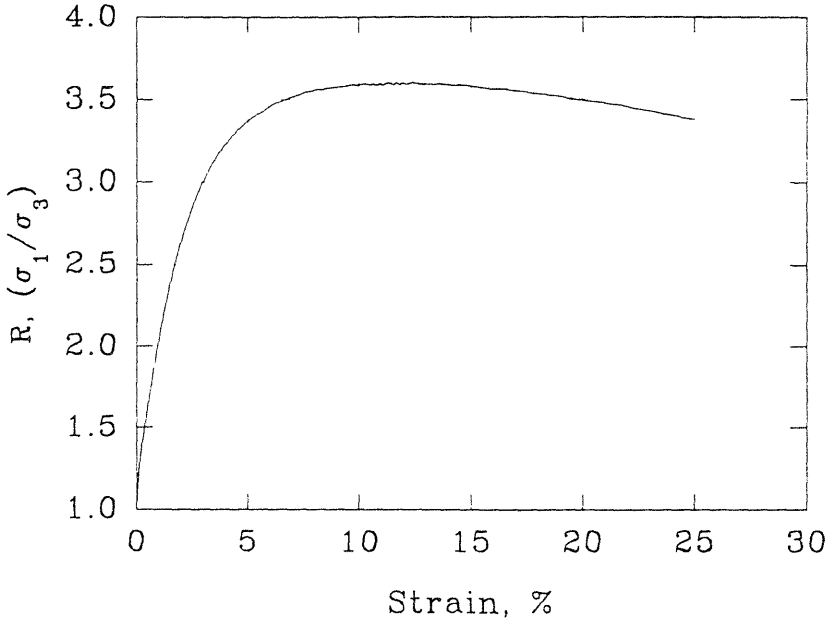

R_{max} = 3.60

Series B – Test #02

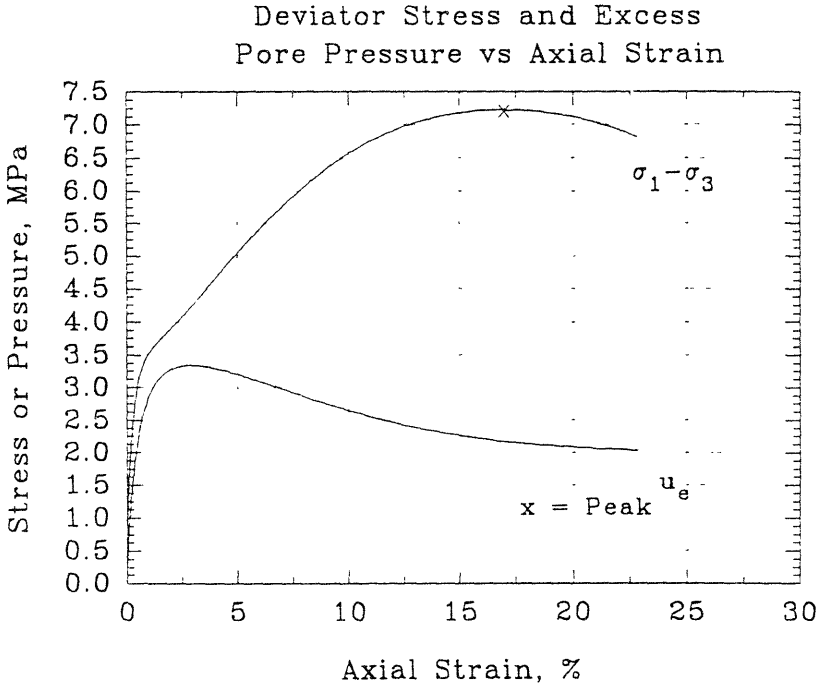

σ'_c = 5 MPa
e = 0.564
D_r = 104.9%

Q_p = 7.23 MPa
ε_p = 16.95 %

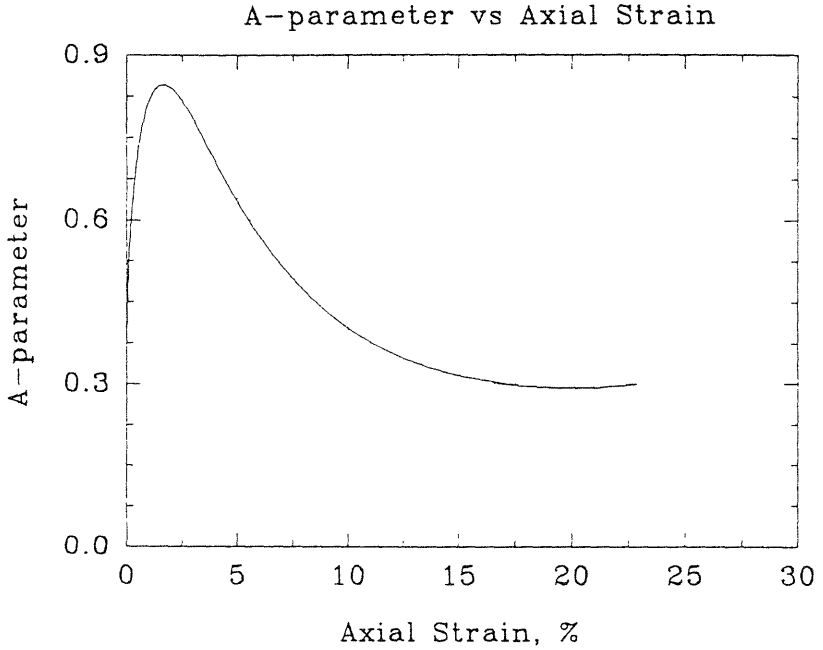

A_f = 0.301

Series B – Test #02

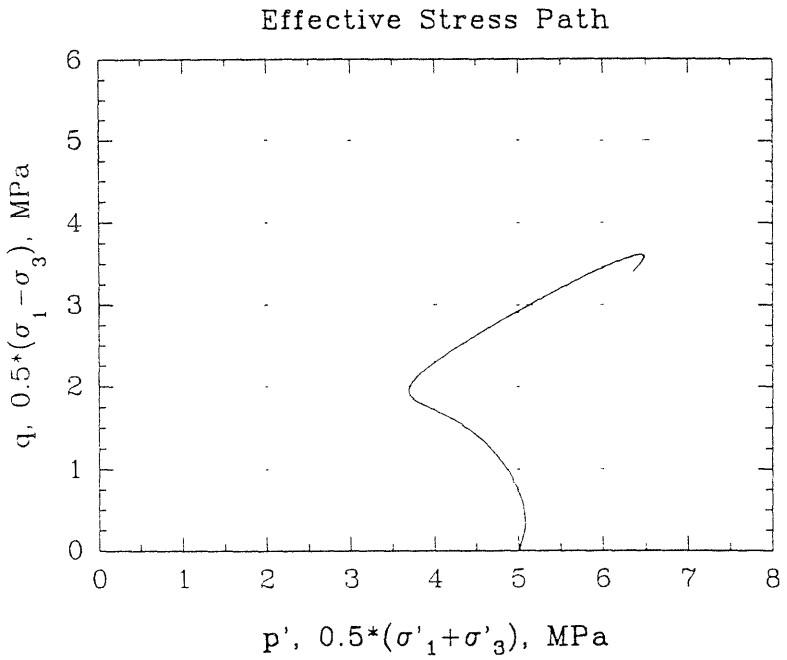

α' = 30.2 °
φ' = 35.8 °

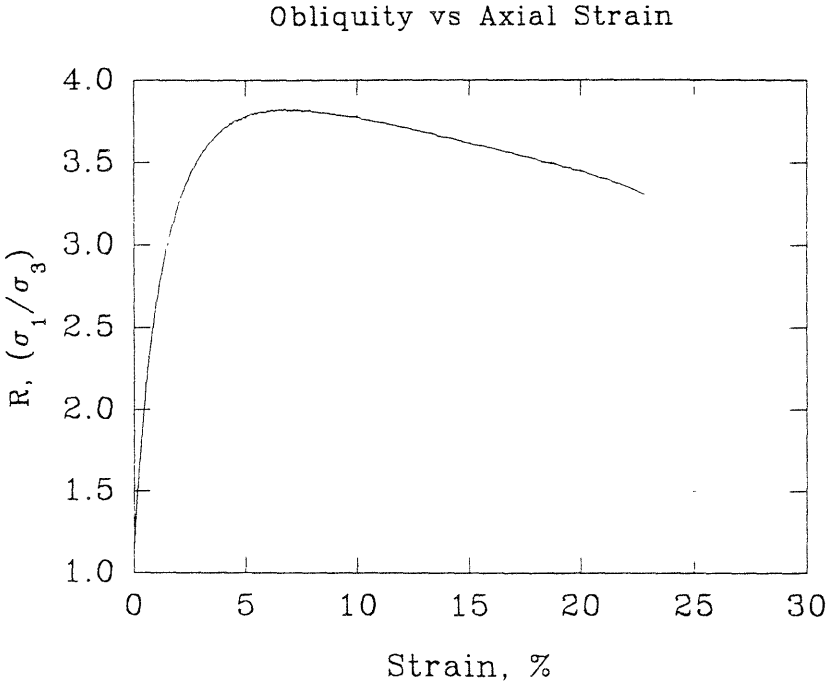

R_{max} = 3.82

Series B – Test #04

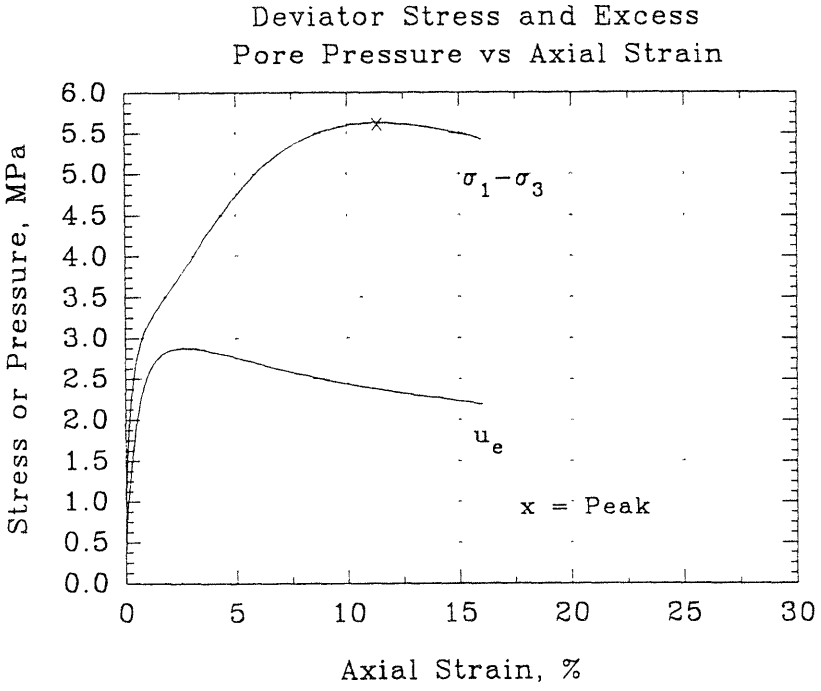

σ'_c = 5 MPa
e = 0.660
D_r = 75.7%

Q_p = 5.63 MPa
ε_p = 11.31 %

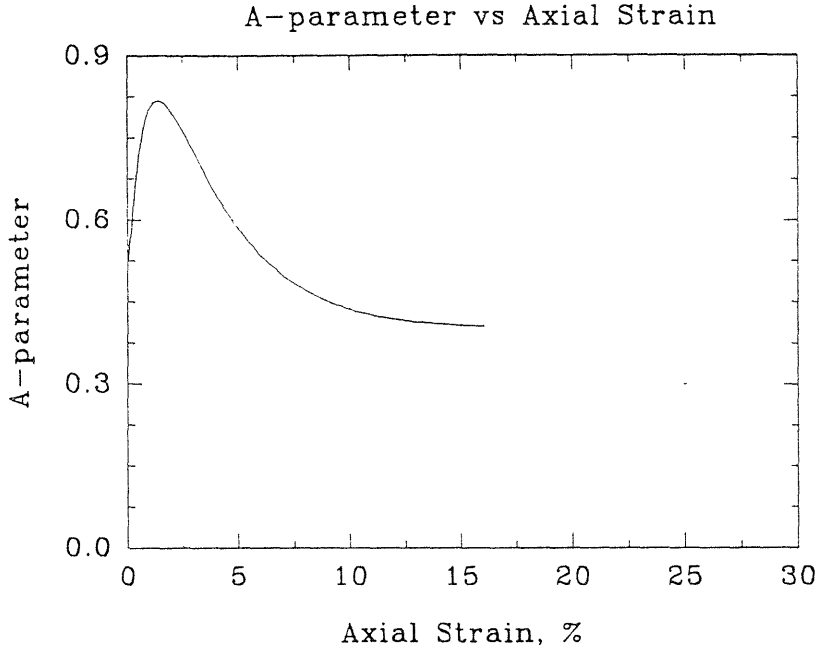

A_f = 0.421

Series B – Test #04

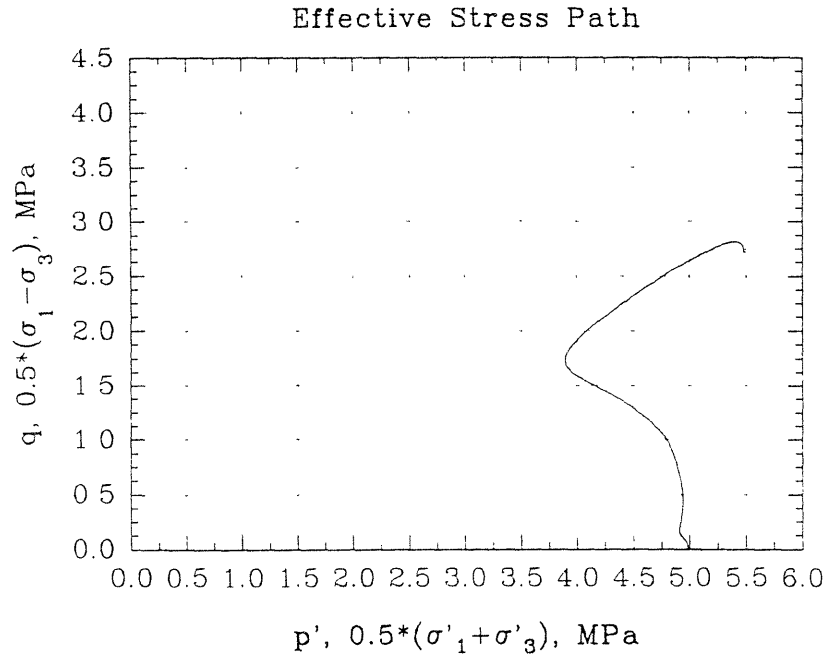

α' = 27.9 °
φ' = 31.9 °

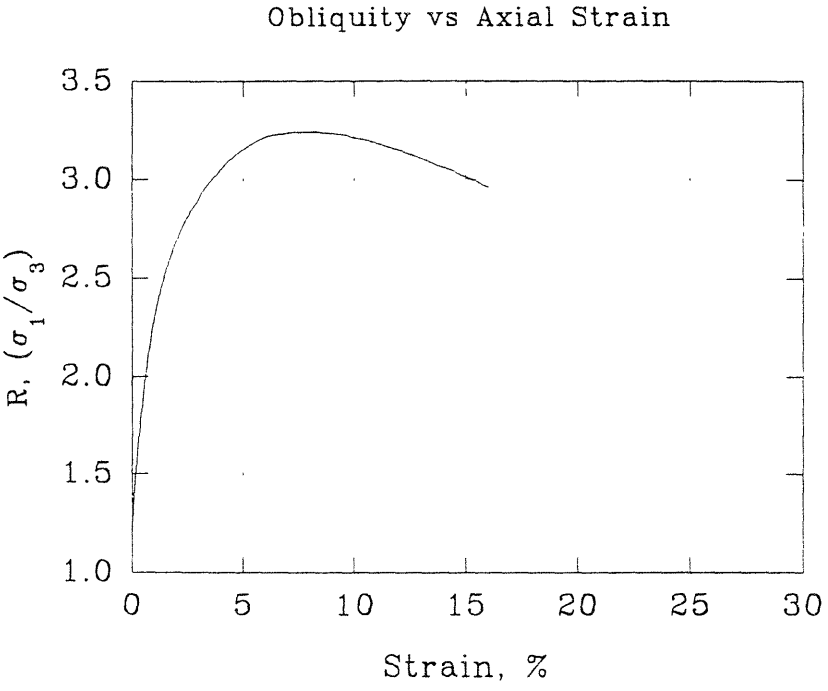

R_{max} = 3.24

Series B – Test #05

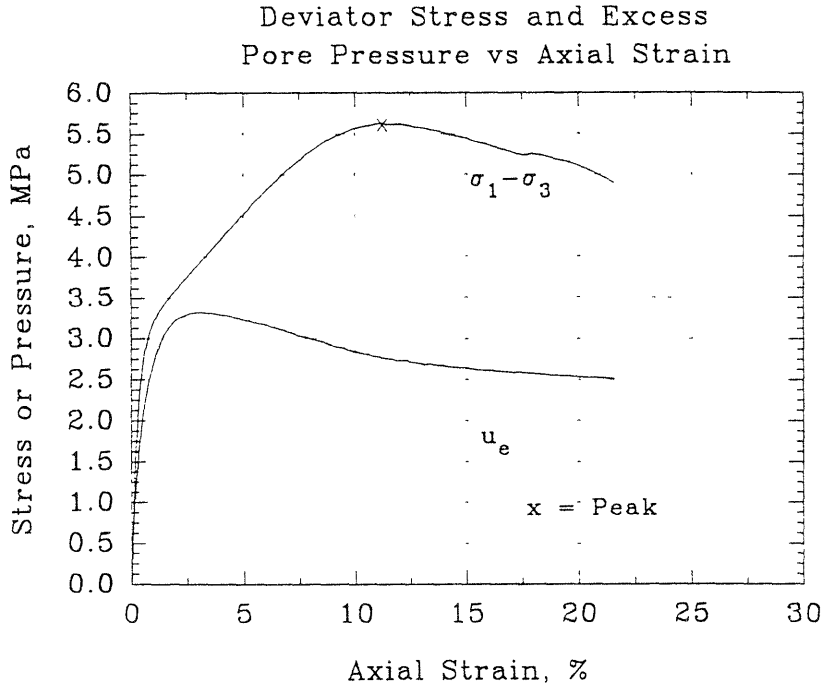

σ'_c = 5 MPa
e = 0.608
D_r = 91.5%

Q_p = 5.63 MPa
ε_p = 11.21 %

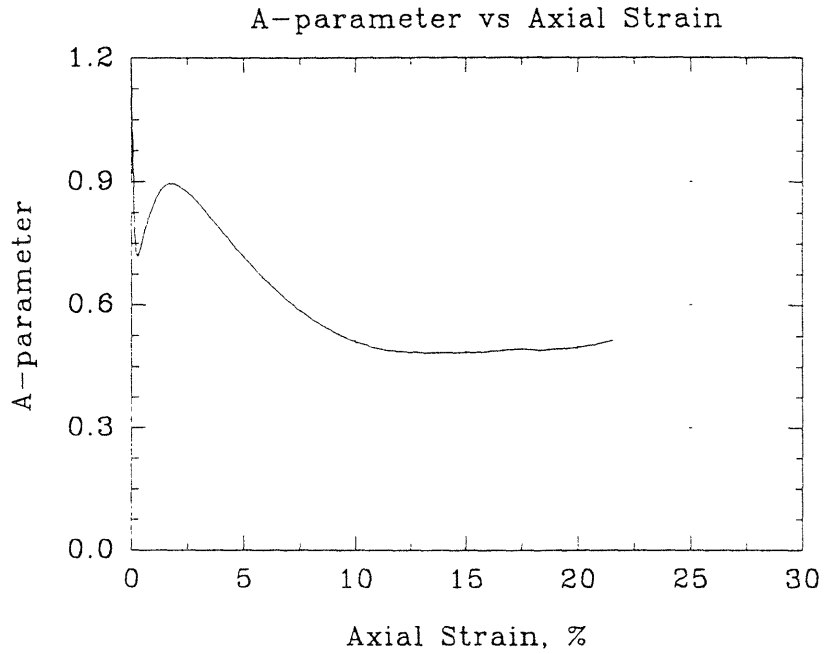

A_f = 0.491

Series B – Test #05

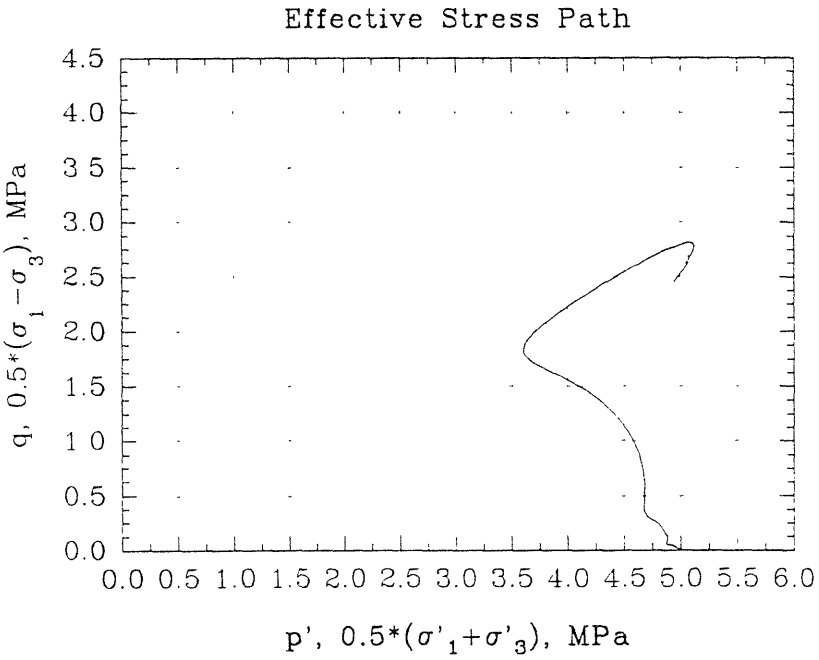

α' = 29.5 °
φ' = 34.5 °

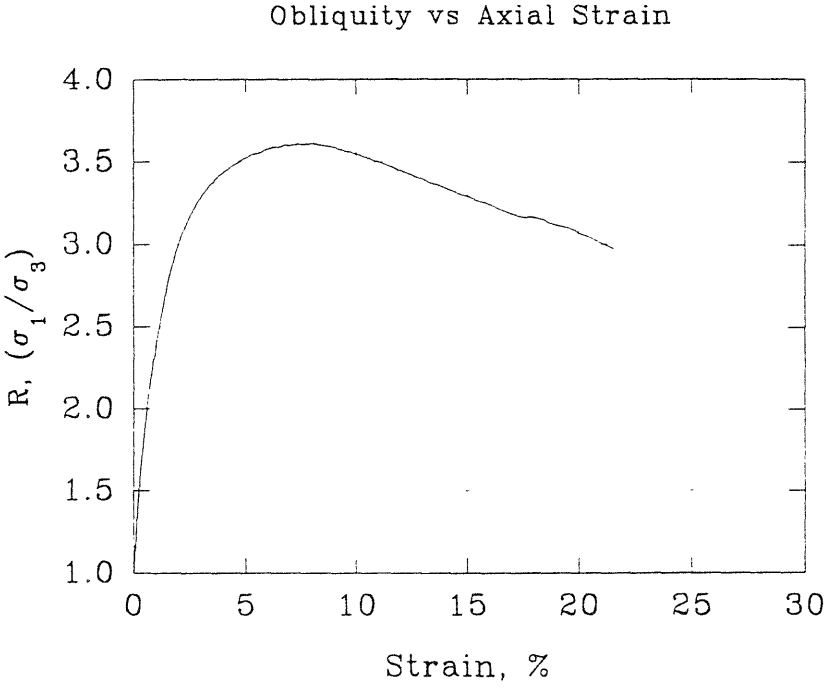

R_{max} = 3.61

Series B – Test #06

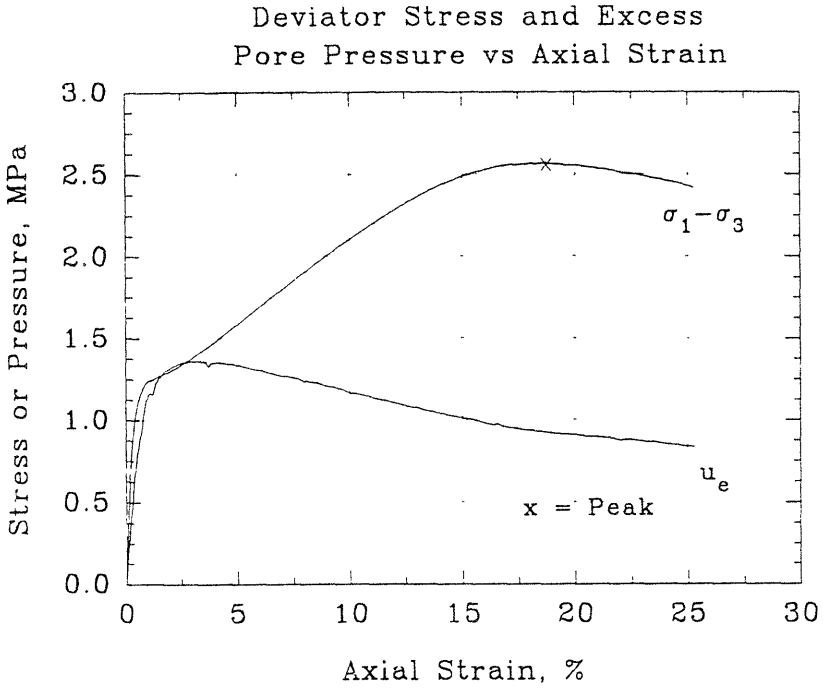

σ'_c = 2 MPa
e = 0.694
D_r = 65.4%

Q_p = 2.57 MPa
ε_p = 18.74 %

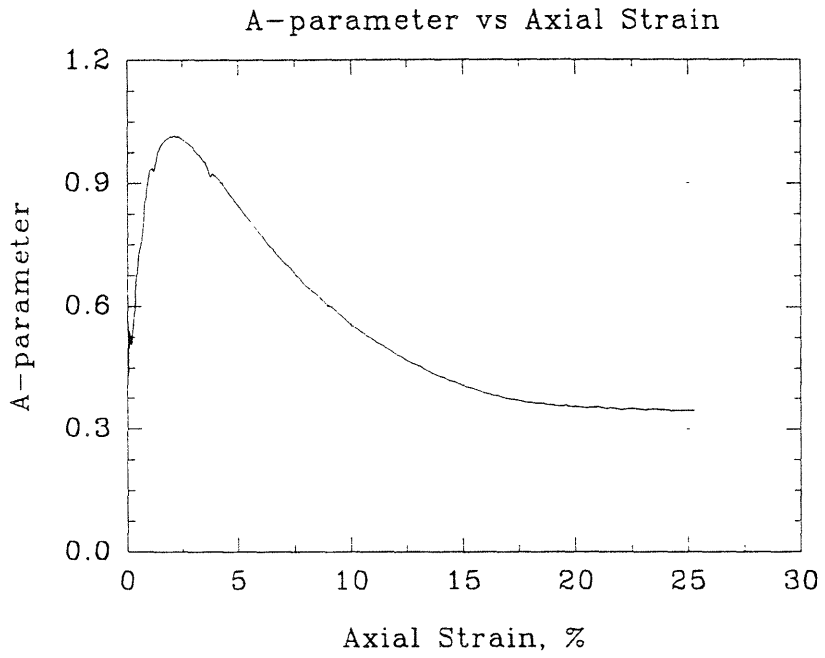

A_f = 0.361

Series B – Test #06

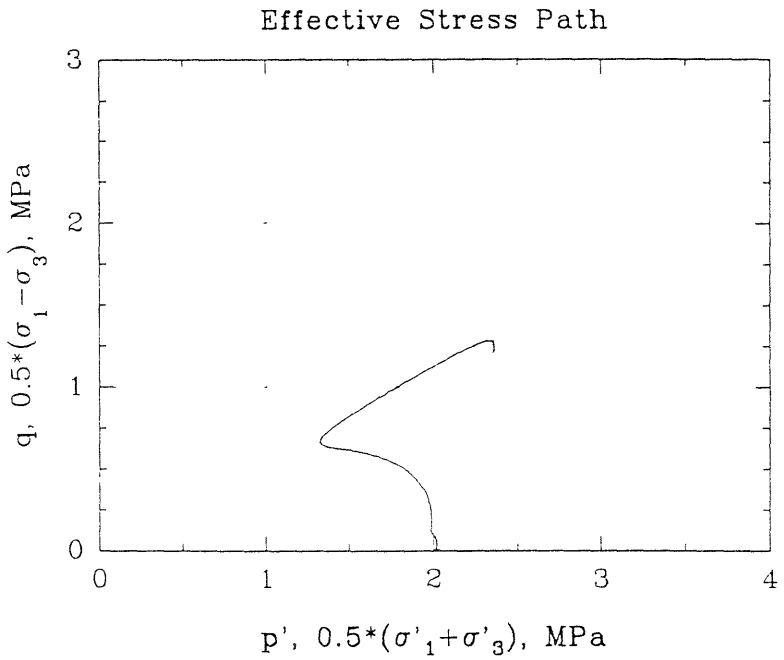

$\alpha' = 29.3\ °$
$\phi' = 34.2\ °$

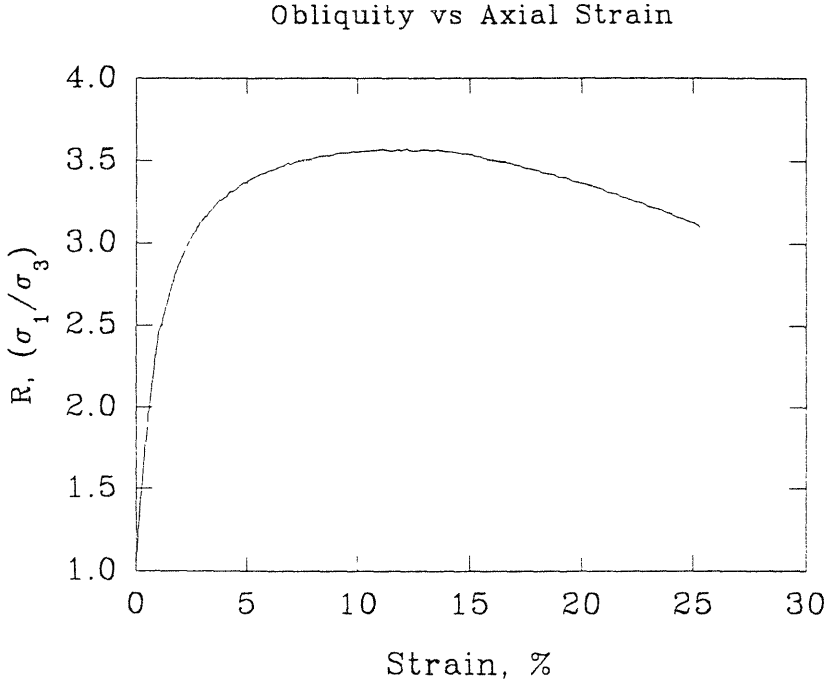

$R_{max} = 3.57$

Series B – Test #07

Deviator Stress and Excess
Pore Pressure vs Axial Strain

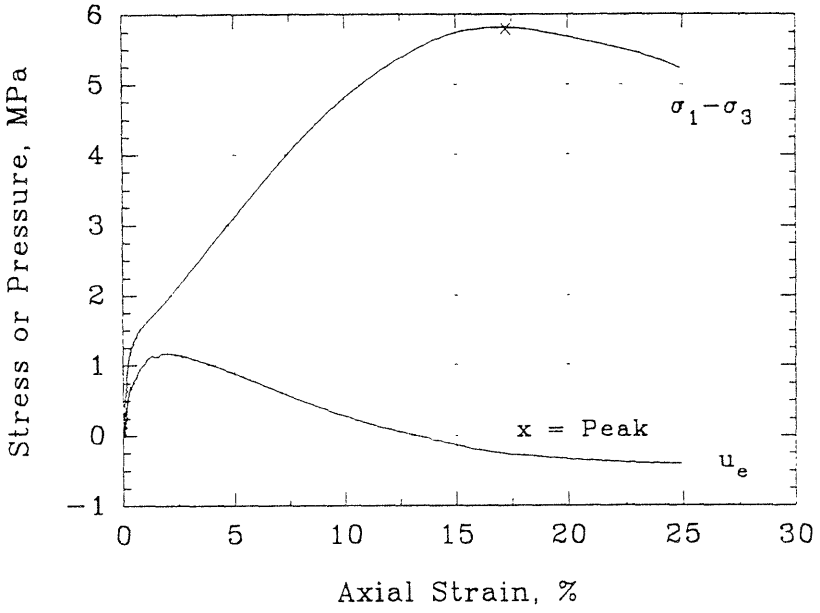

σ'_c = 2 MPa
e = 0.593
D_r = 96.1%

Q_p = 5.82 MPa
ε_p = 17.24 %

A–parameter vs Axial Strain

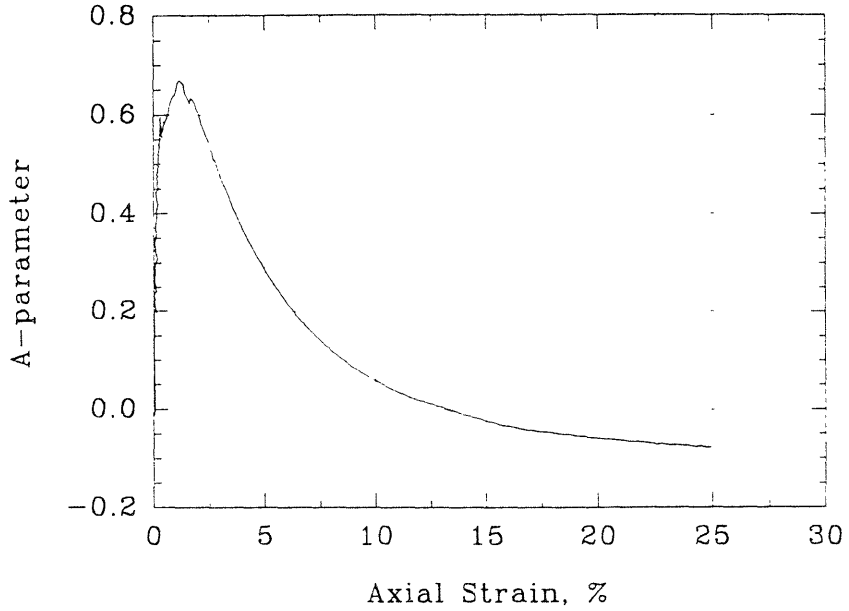

A_f = −0.041

Series B – Test #07

Effective Stress Path

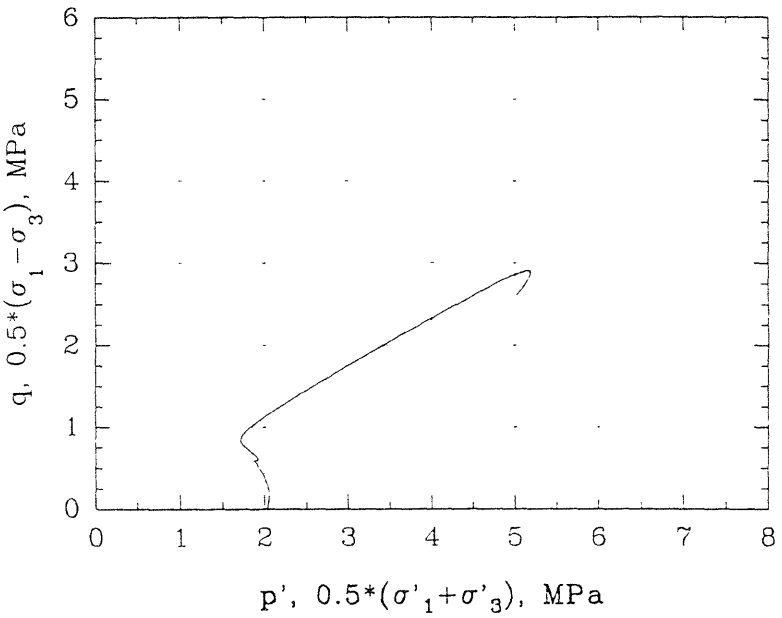

α' = 30.3 °
φ' = 35.8 °

Obliquity vs Axial Strain

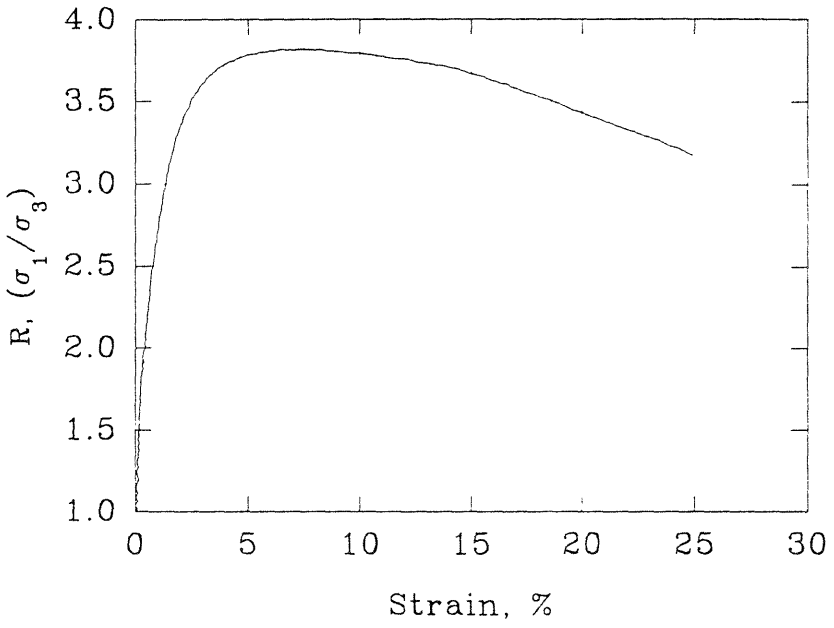

R_{max} = 3.82

Series B – Test #08

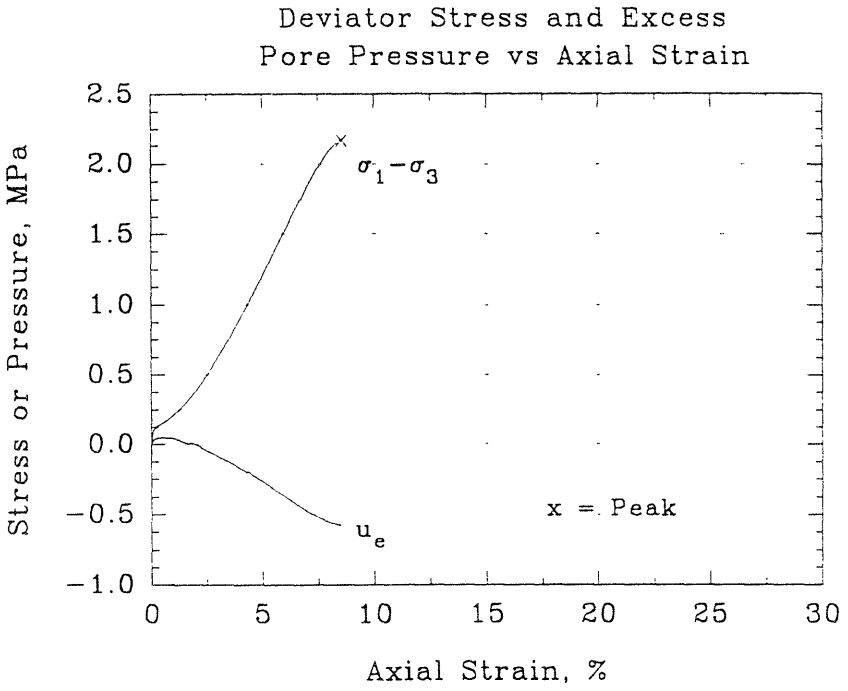

σ'_c = 0.1 MPa
e = 0.636
D_r = 83.0%

Q_p = 2.18 MPa
ε_p = 8.54 %

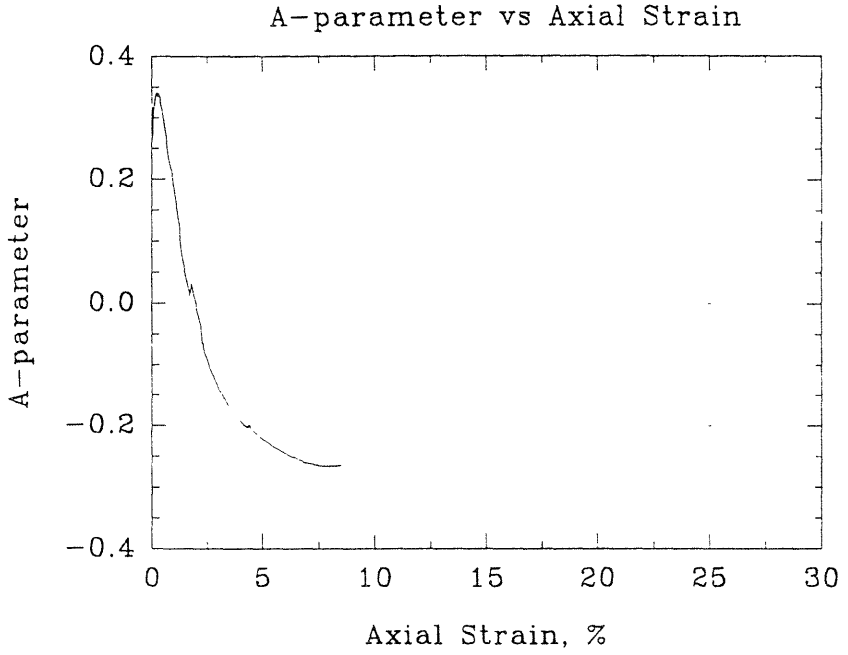

A_f = −0.264

Series B – Test #08

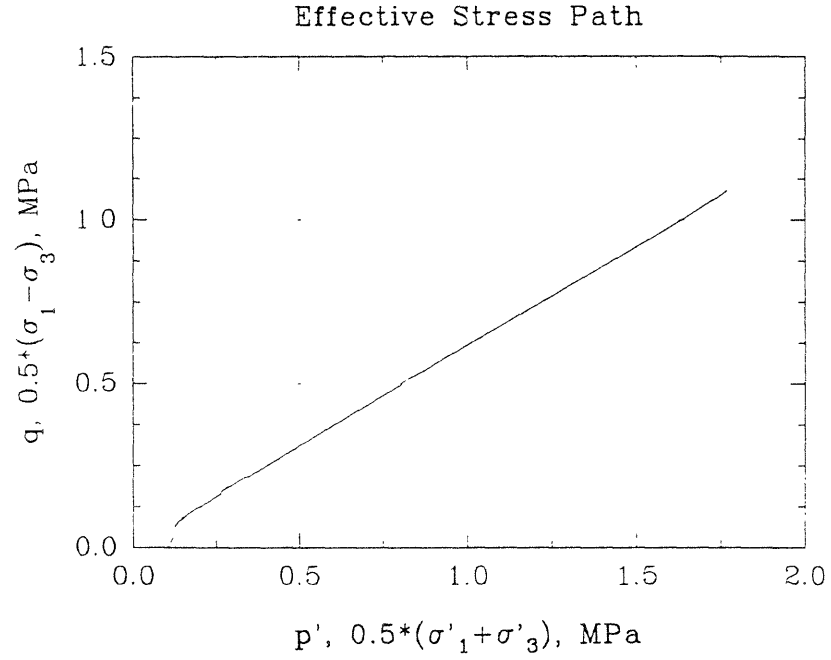

α' = 32.8 °
ϕ' = 40.1 °

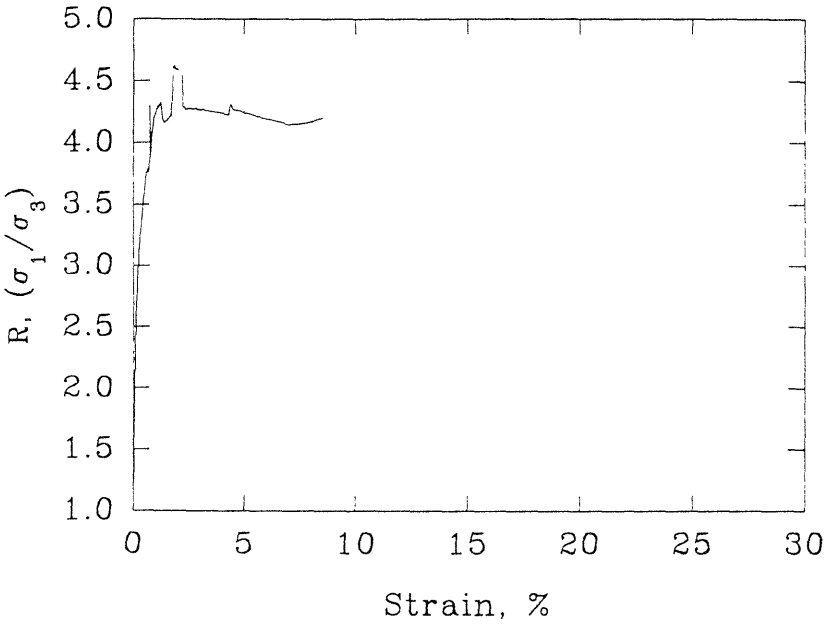

R_{max} = 4.63

Series B – Test #09

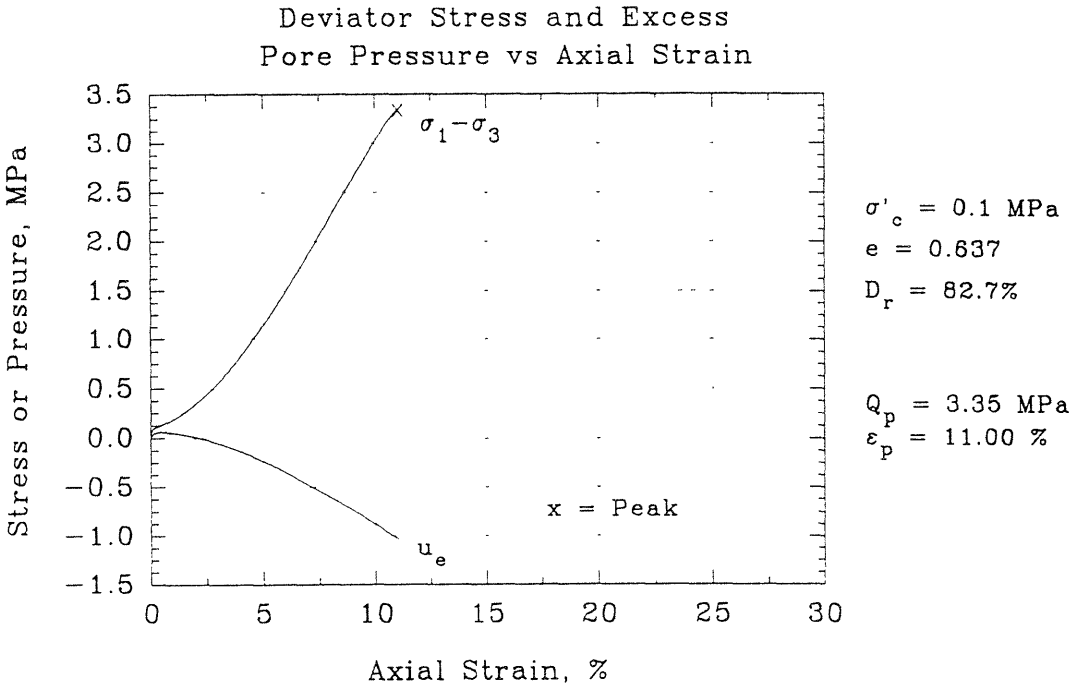

σ'_c = 0.1 MPa
e = 0.637
D_r = 82.7%

Q_p = 3.35 MPa
ε_p = 11.00 %

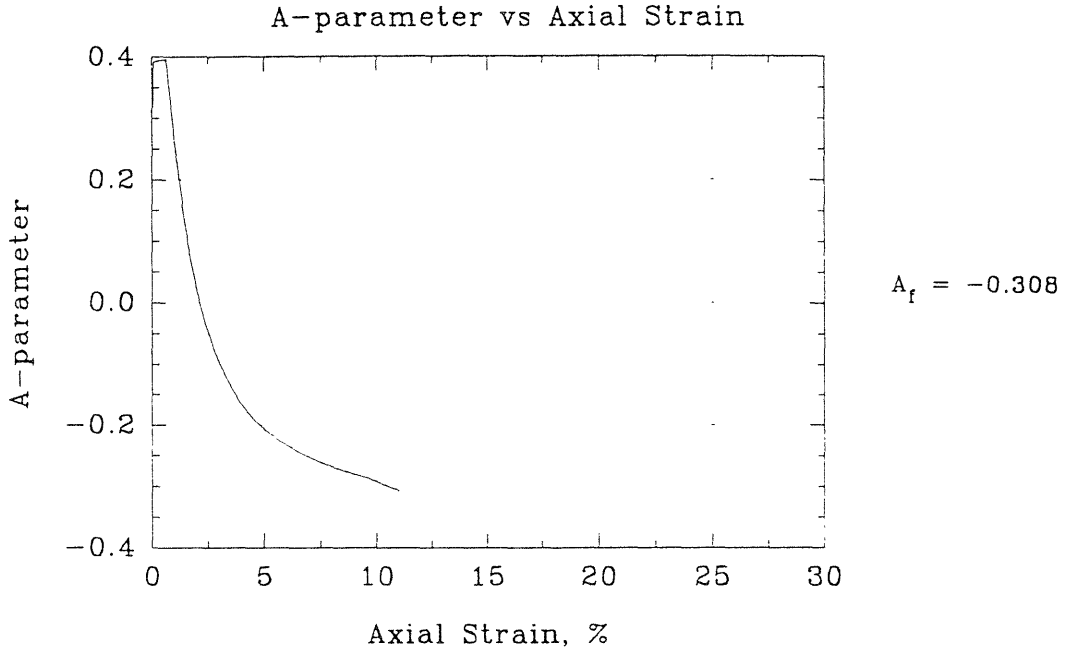

A_f = −0.308

Series B – Test #09

Effective Stress Path

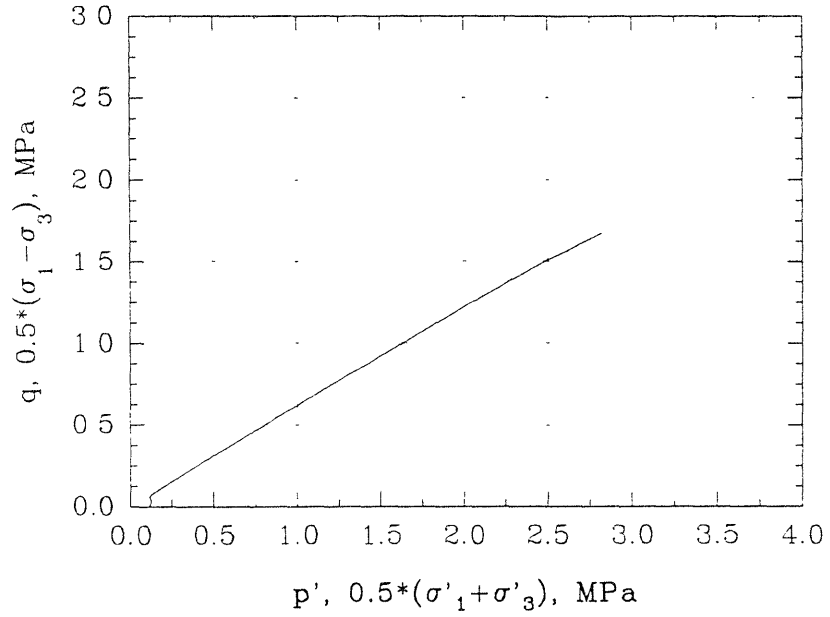

$\alpha' = 31.9\ °$
$\phi' = 38.5\ °$

Obliquity vs Axial Strain

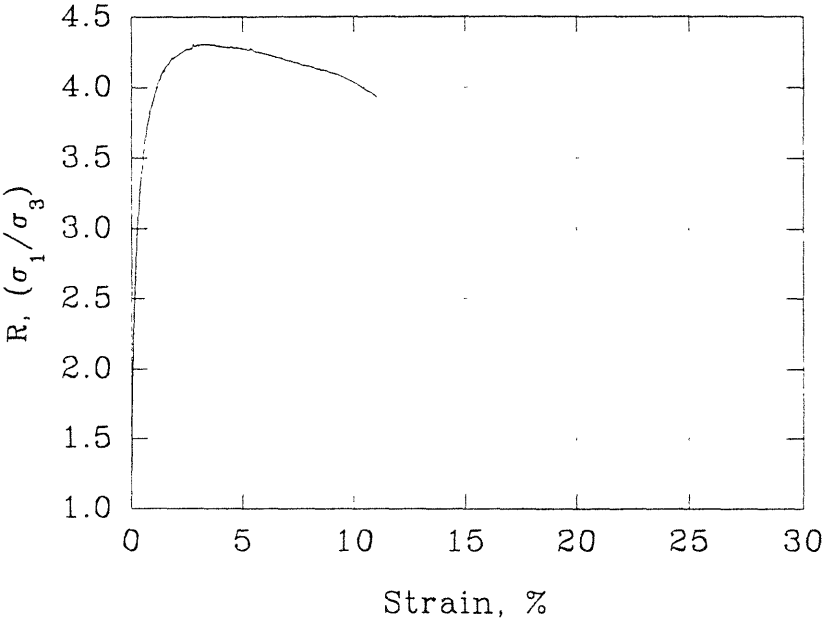

$R_{max} = 4.31$

Series B – Test #10

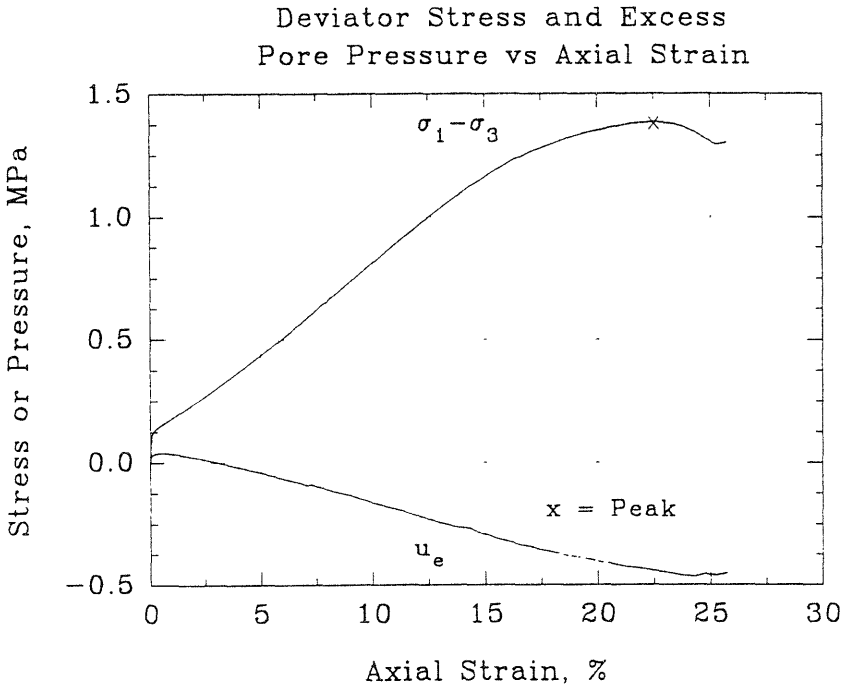

σ'_c = 0.1 MPa
e = 0.765
D_r = 43.8%

Q_p = 1.39 MPa
ε_p = 22.50 %

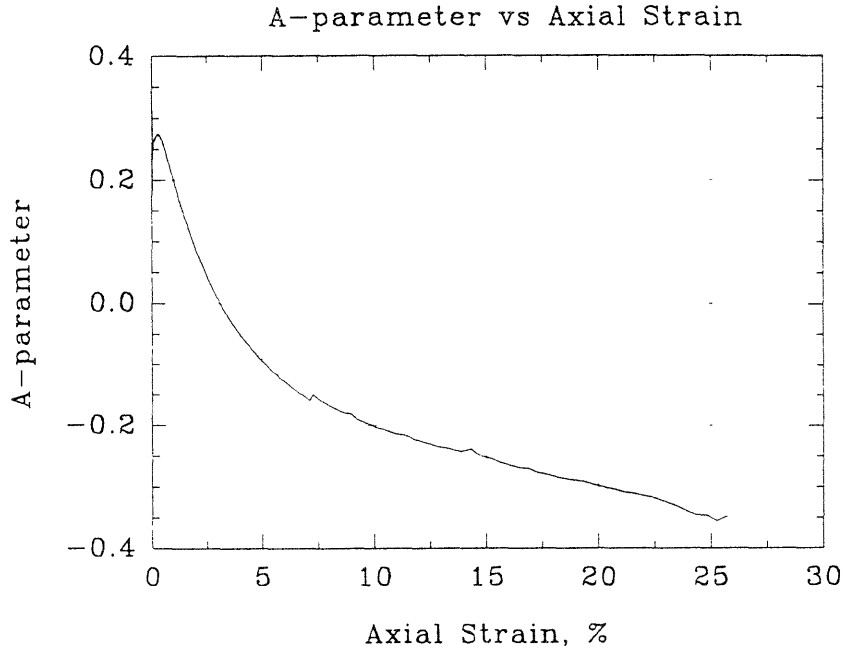

A_f = −0.318

Series B – Test #10

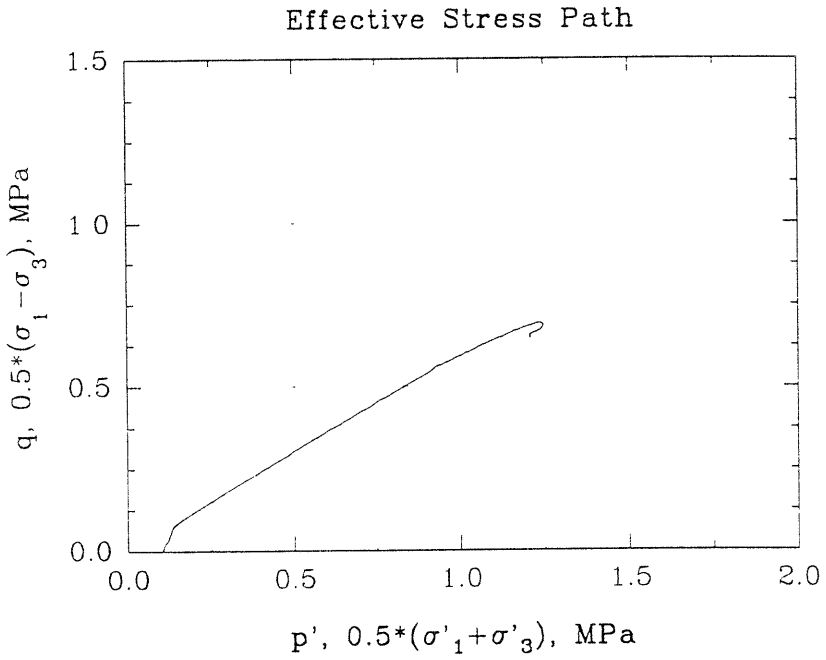

$\alpha' = 31.3\ °$
$\phi' = 37.5\ °$

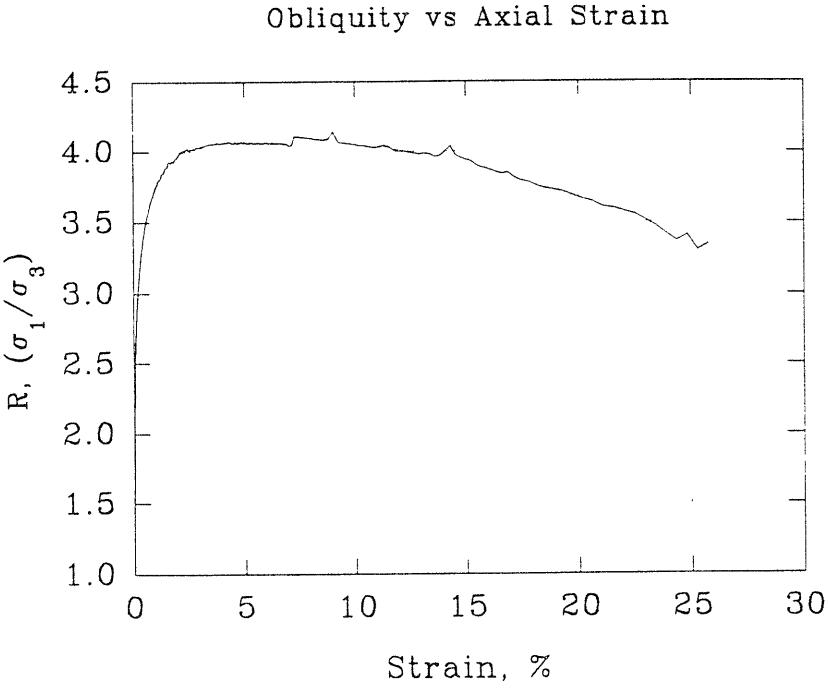

$R_{max} = 4.12$

Series B – Test #11

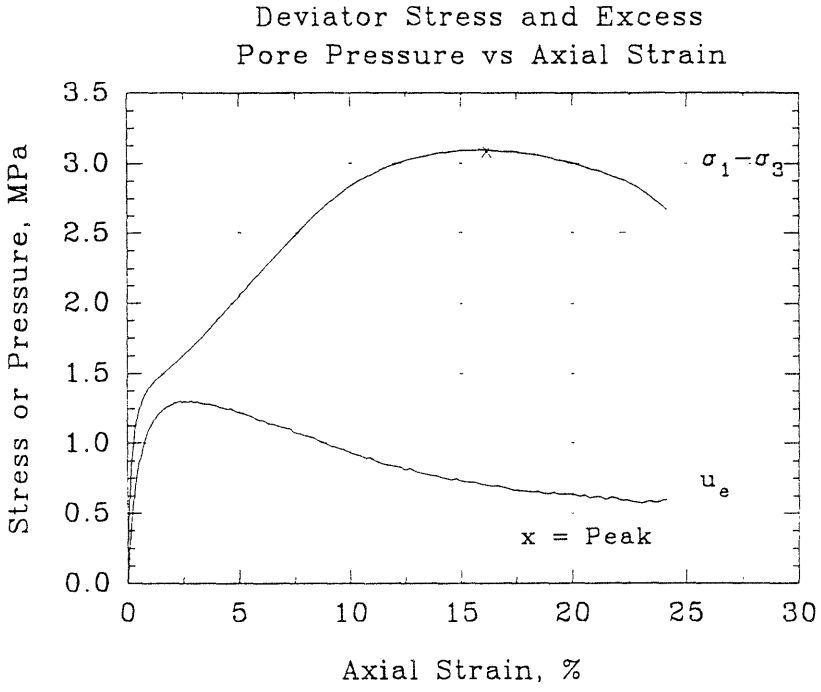

σ'_c = 2 MPa
e = 0.688
D_r = 67.2%

Q_p = 3.09 MPa
ε_p = 16.17 %

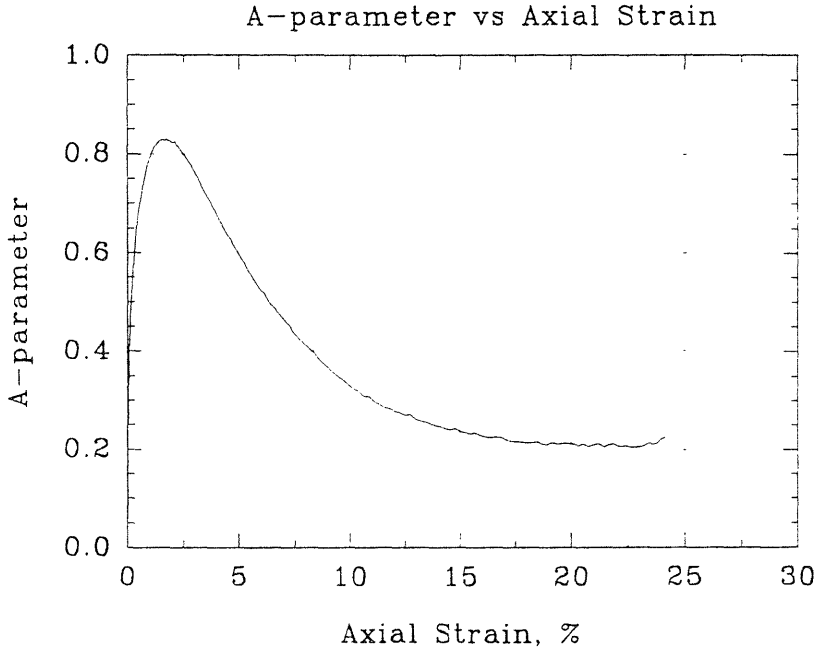

A_f = 0.226

Series B – Test #11

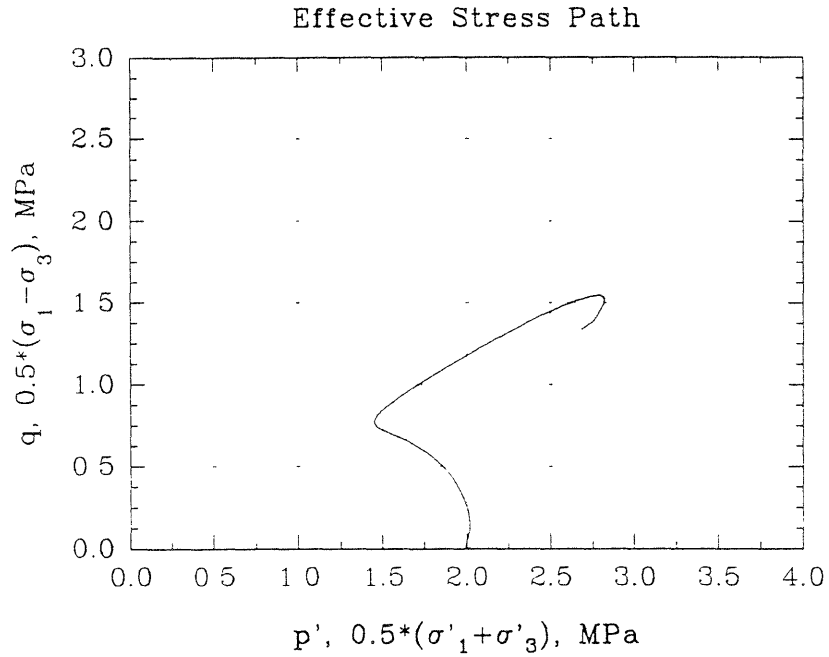

$\alpha' = 30.4\ °$
$\phi' = 36.0\ °$

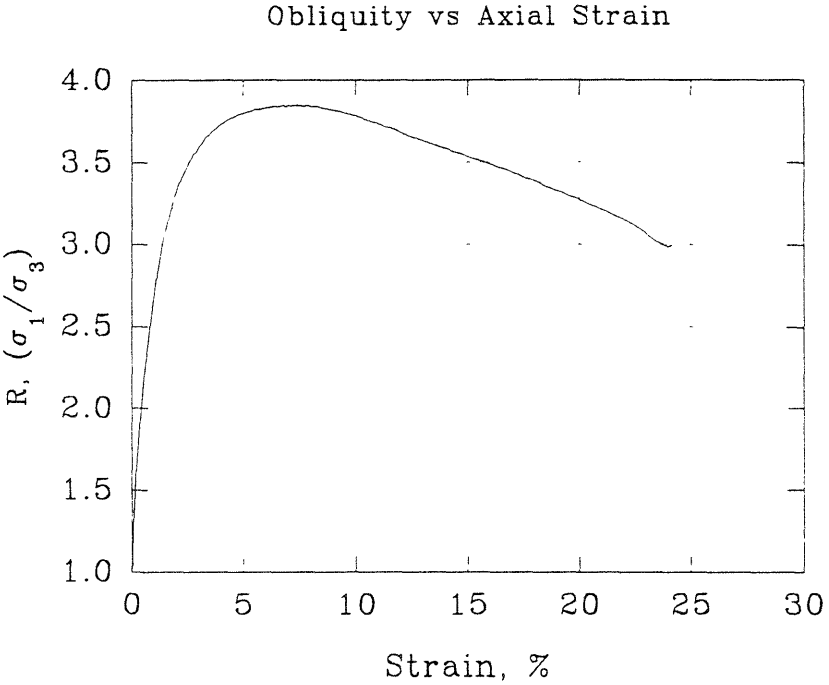

$R_{max} = 3.85$

Series B – Test #12

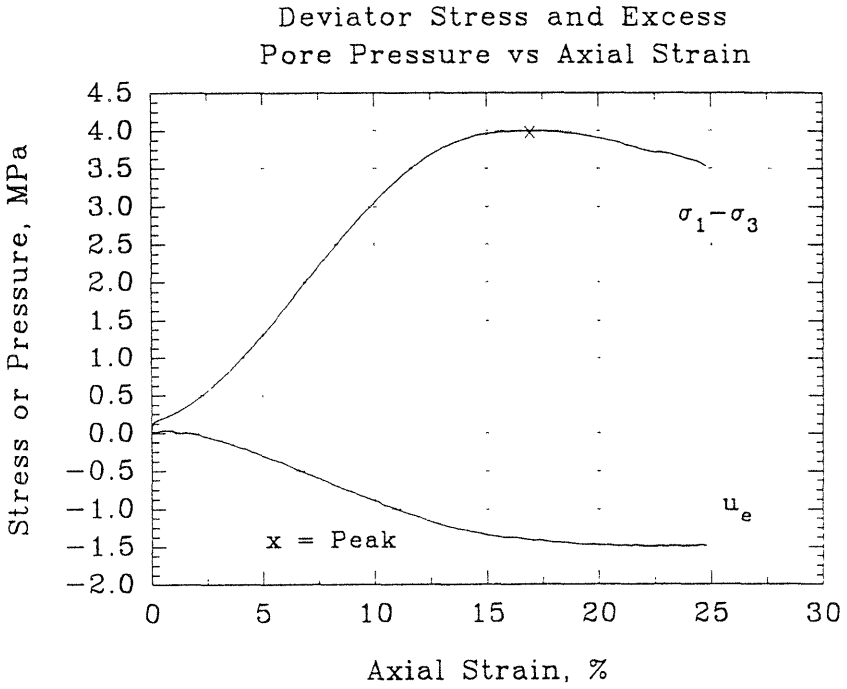

σ'_c = 0.1 MPa
e = 0.626
D_r = 86.1%

Q_p = 4.01 MPa
ε_p = 16.90 %

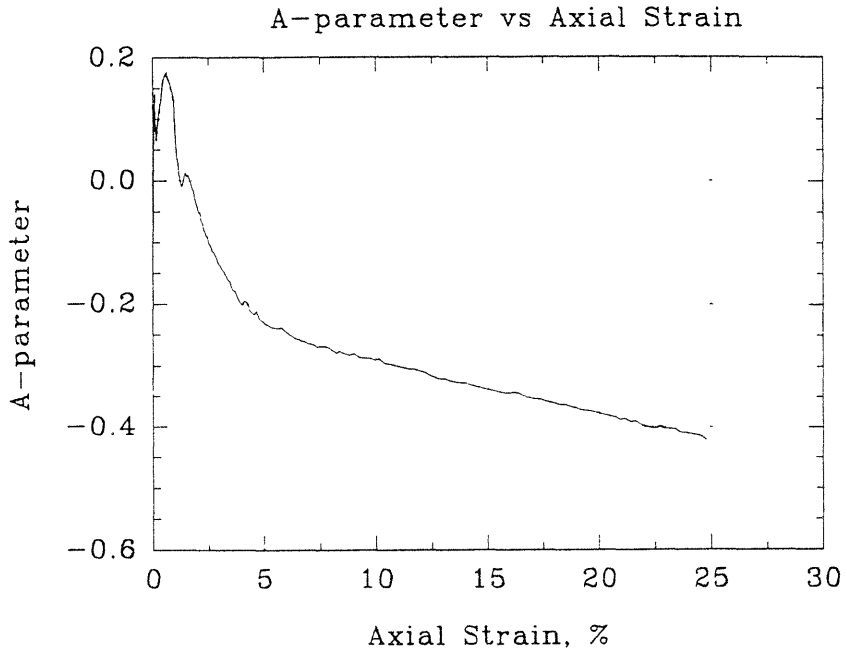

A_f = 0.226

Series B – Test #12

Effective Stress Path

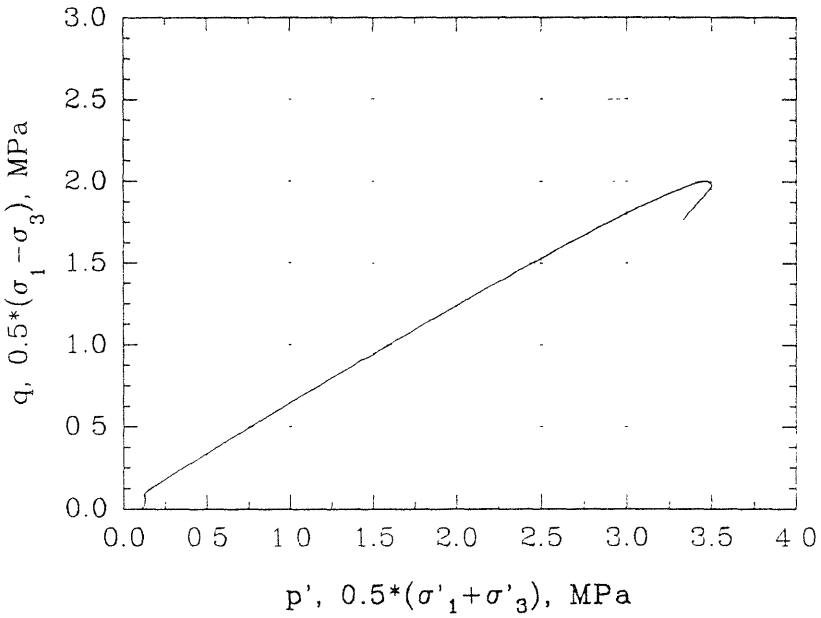

α' = 37.2 °
ϕ' = 49.4 °

Obliquity vs Axial Strain

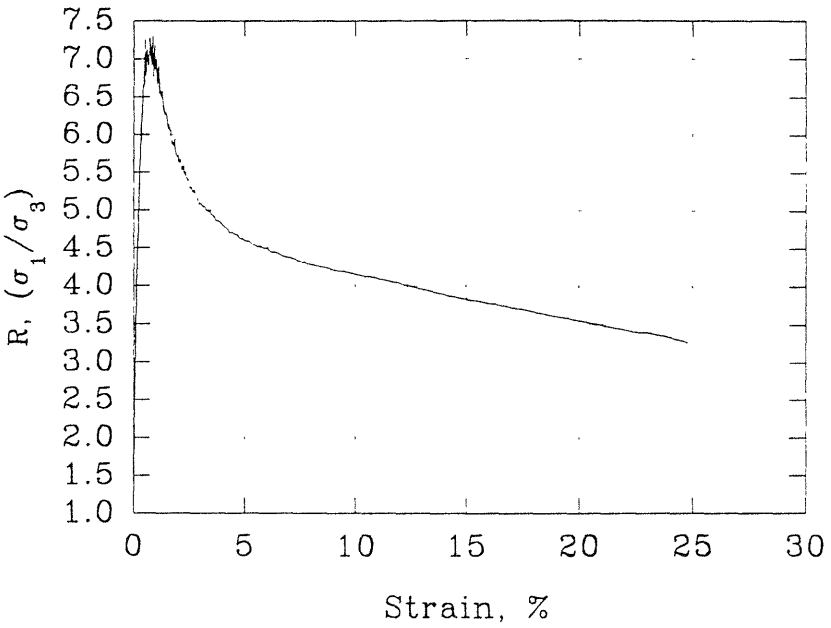

R_{max} = 7.29

Series B – Test #13

Deviator Stress and Excess
Pore Pressure vs Axial Strain

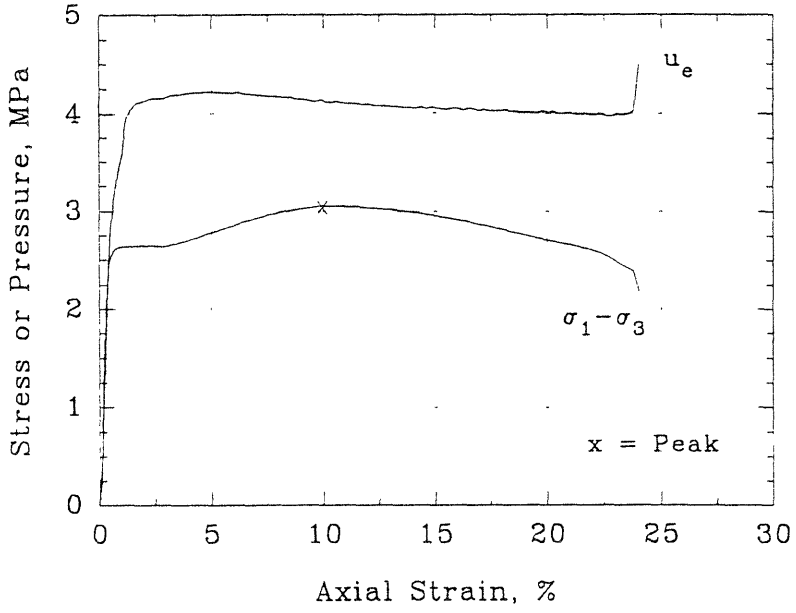

σ'_c = 5 MPa
e = 0.697
D_r = 64.5%

Q_p = 3.05 MPa
ε_p = 9.92 %

A–parameter vs Axial Strain

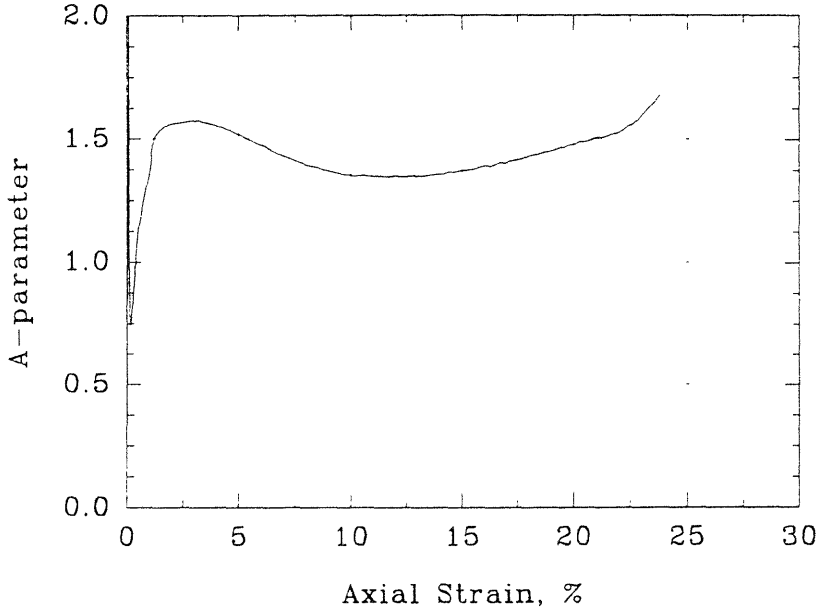

A_f = 1.354

Series B – Test #13

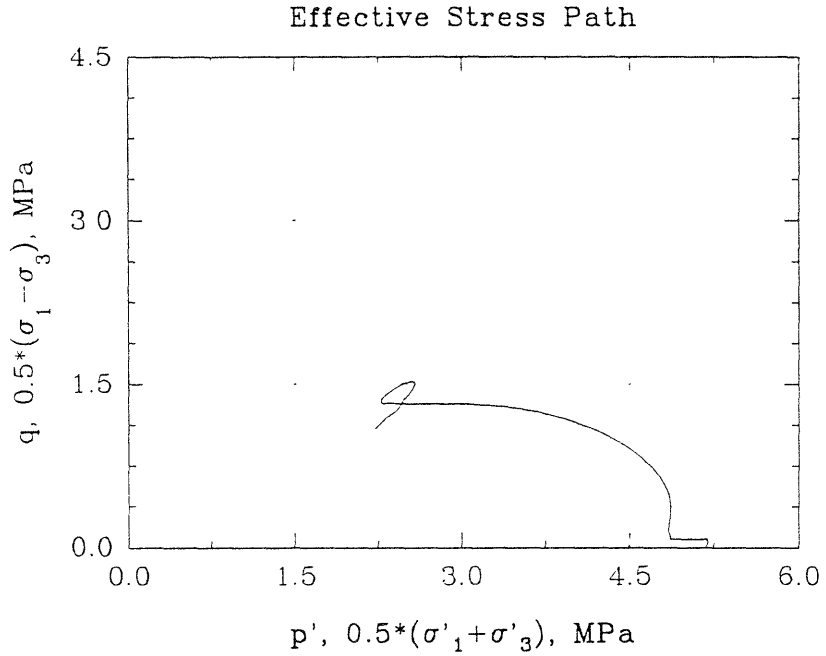

α' = 37.5 °
φ' = 31.3 °

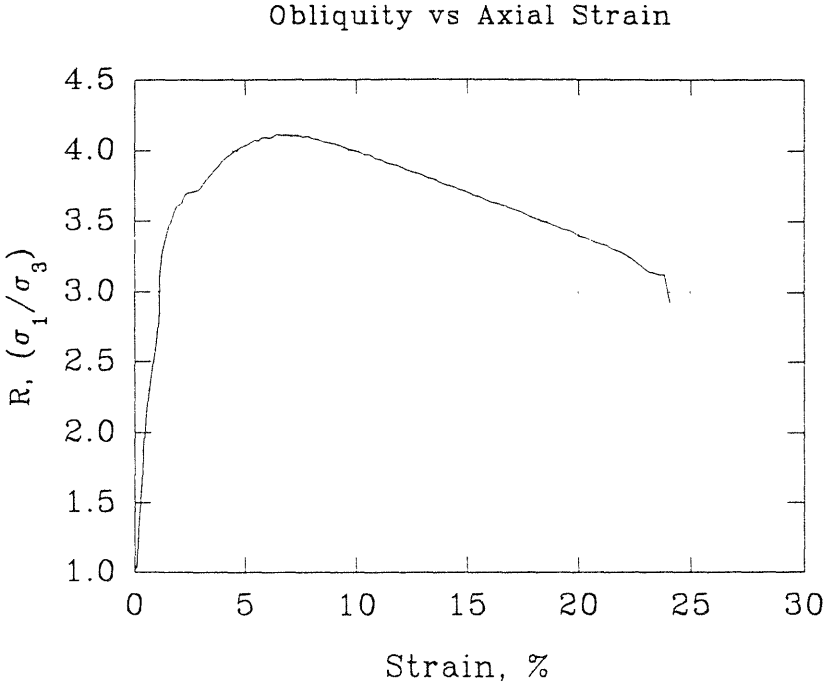

R_{max} = 4.11

Series B – Test #14

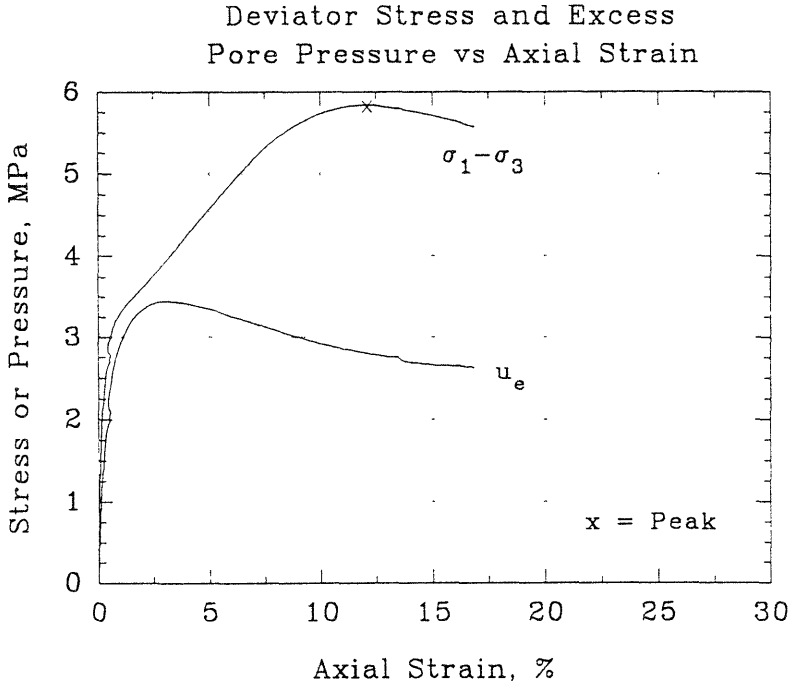

σ'_c = 5 MPa
e = 0.605
D_r = 92.5%

Q_p = 5.84 MPa
ε_p = 12.07 %

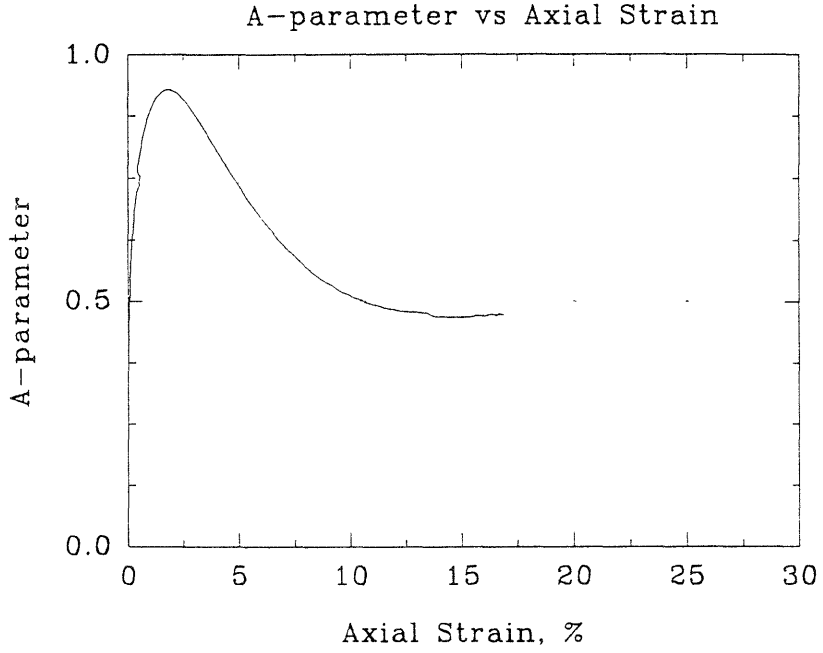

A_f = 0.481

Series B – Test #14

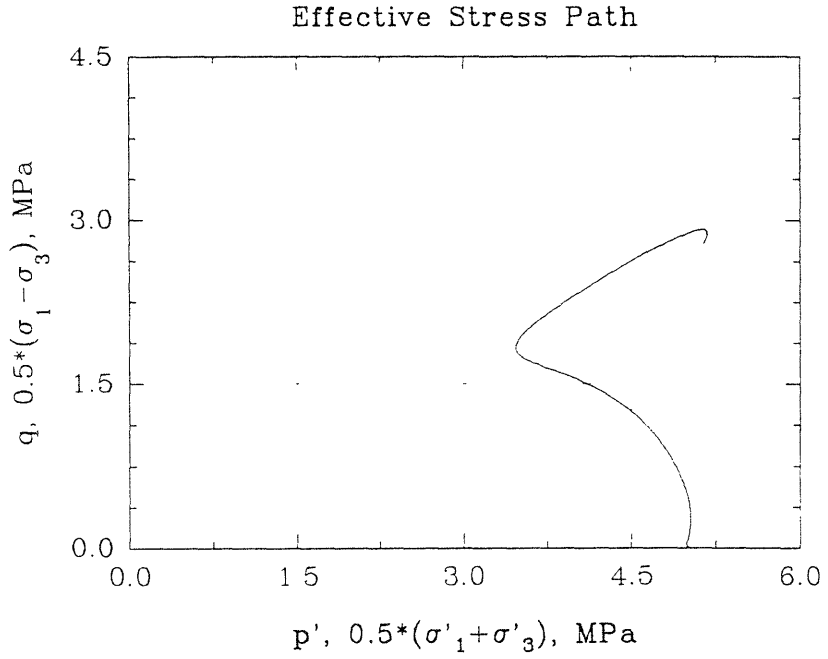

$\alpha' = 31.3\ °$
$\phi' = 37.5\ °$

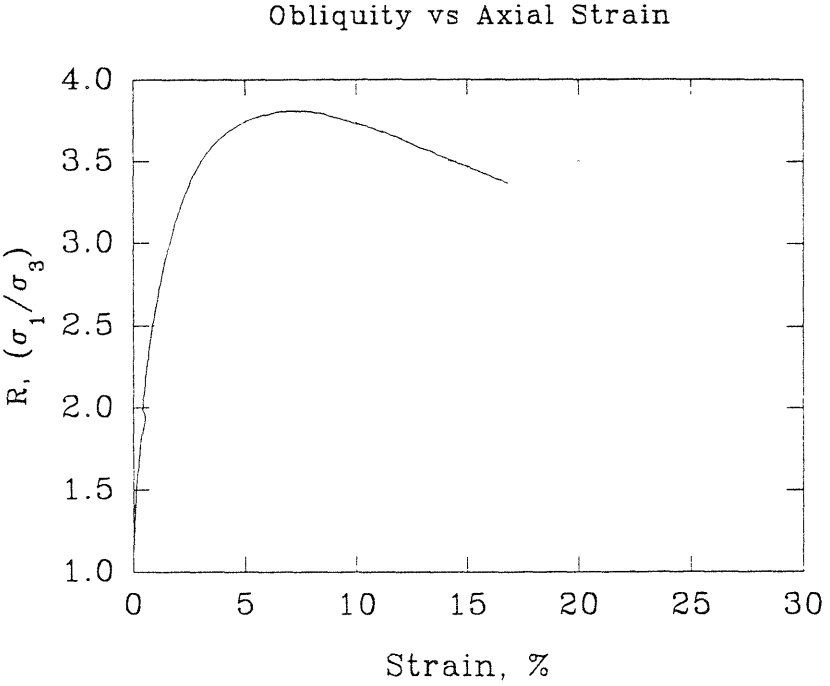

$R_{max} = 3.81$

Series B – Test #15

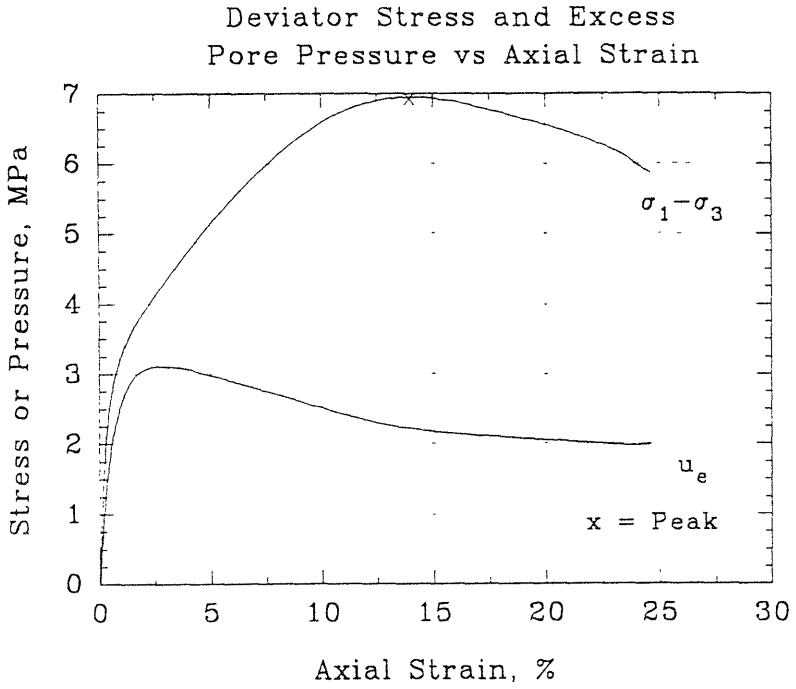

σ'_c = 5 MPa
e = 0.599
D_r = 94.3%

Q_p = 6.95 MPa
ε_p = 13.93 %

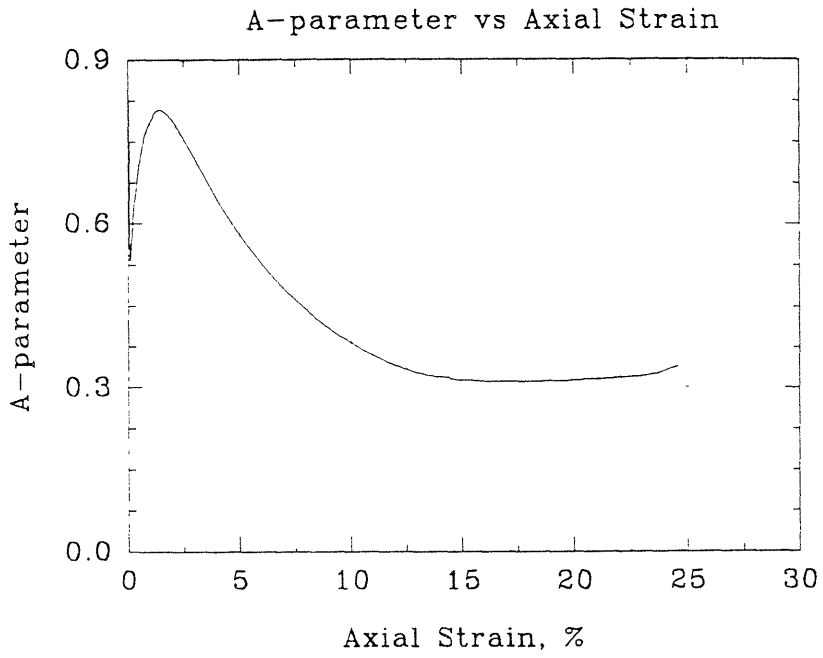

A_f = 0.320

Series B – Test #15

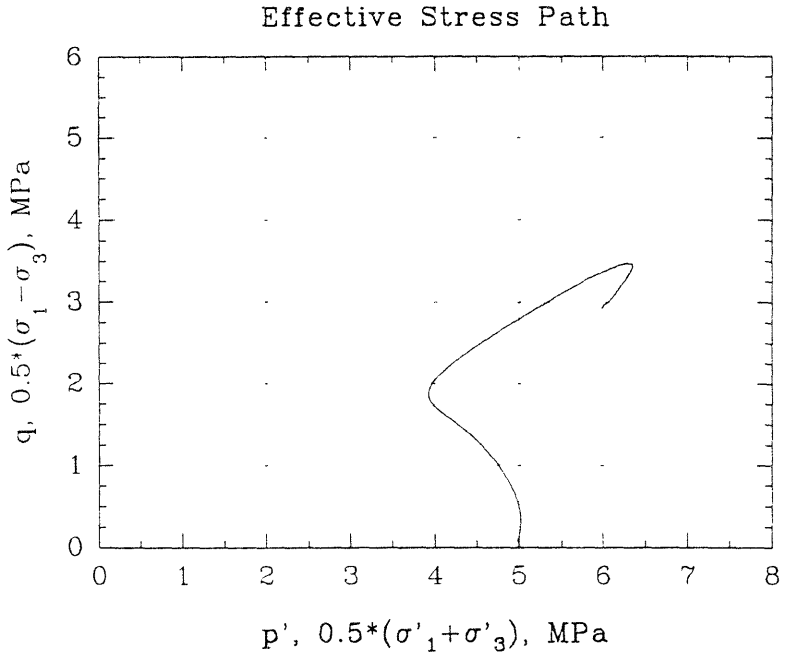

α' = 29.5 °
φ' = 34.5 °

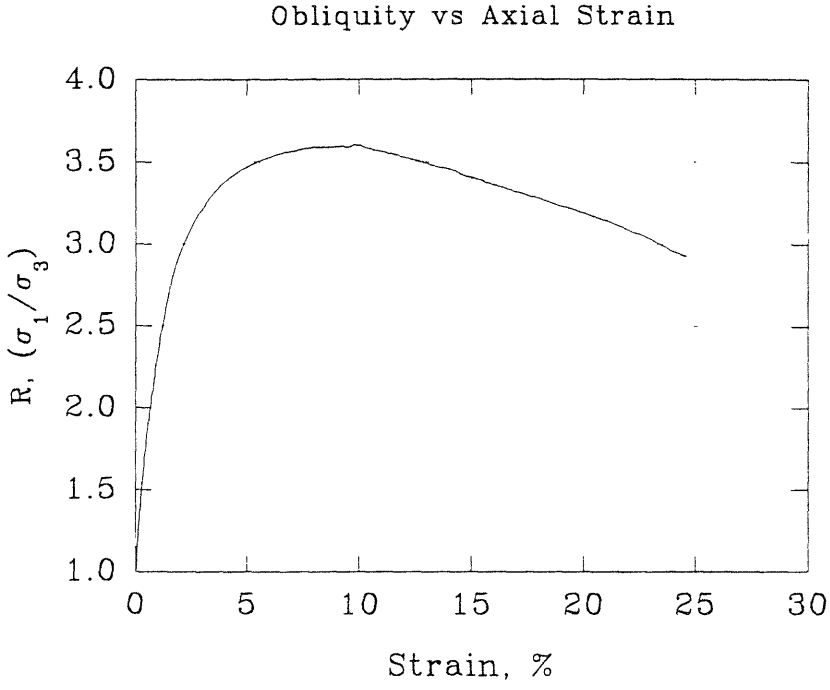

R_{max} = 3.61

Series B – Test #19

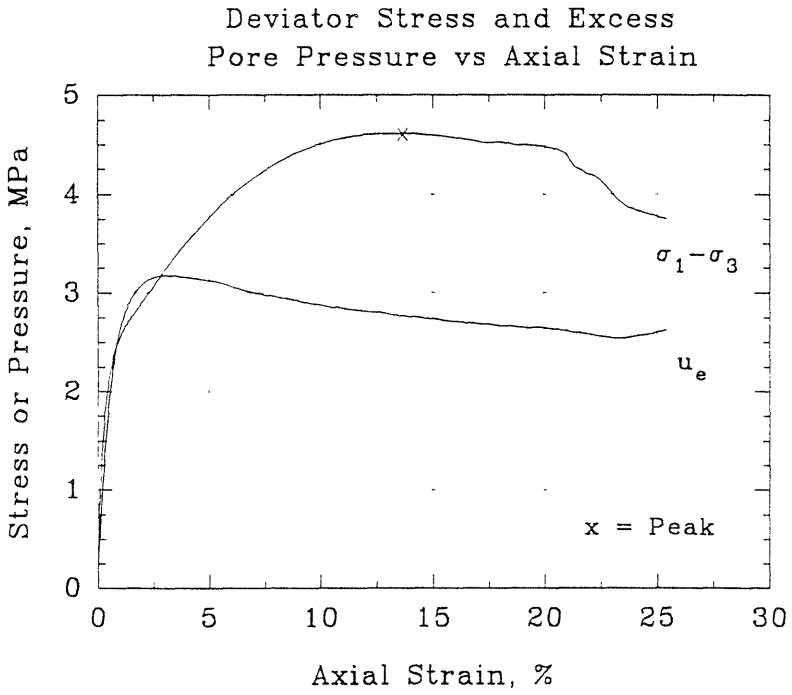

σ'_c = 5 MPa
e = 0.679
D_r = 70.0%

Q_p = 4.62 MPa
ε_p = 13.64 %

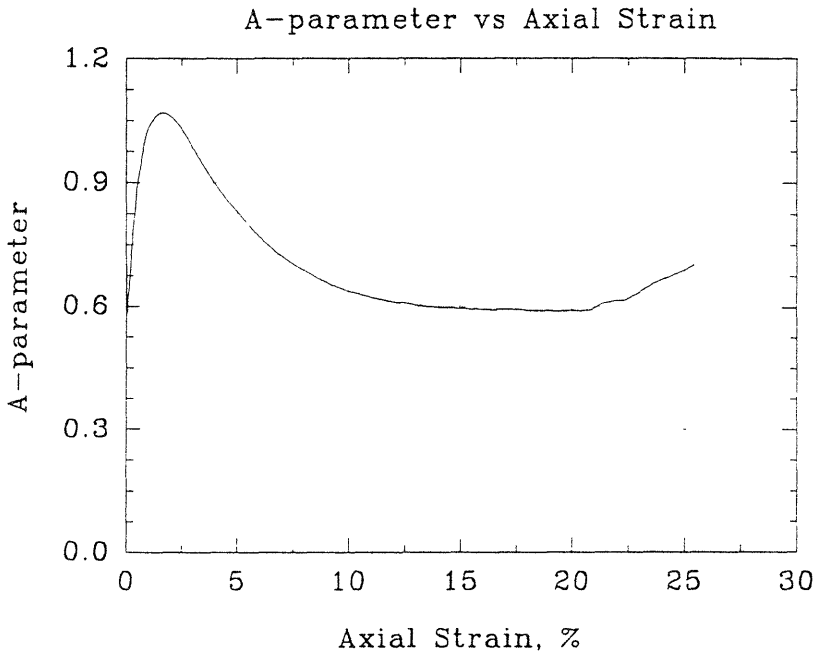

A_f = 0.600

Series B – Test #19

Effective Stress Path

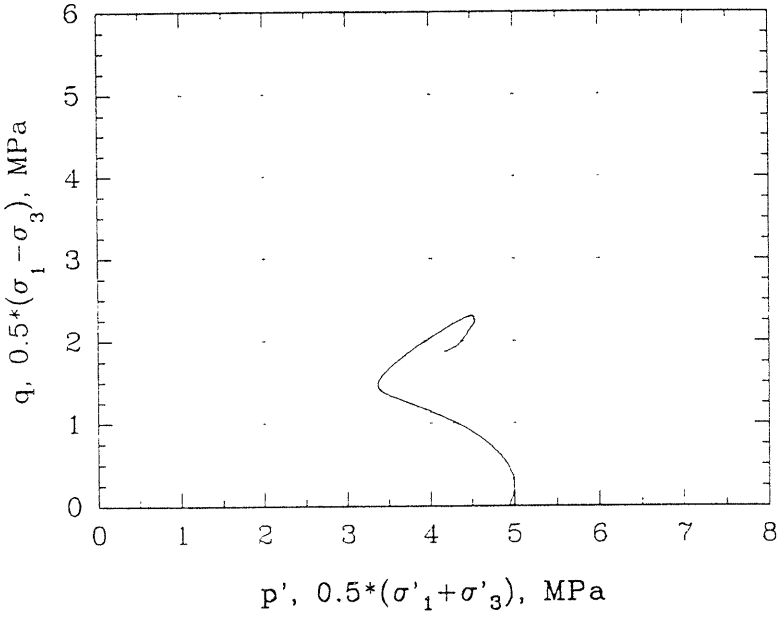

$\alpha' = 27.3\ °$

$\phi' = 31.1\ °$

Obliquity vs Axial Strain

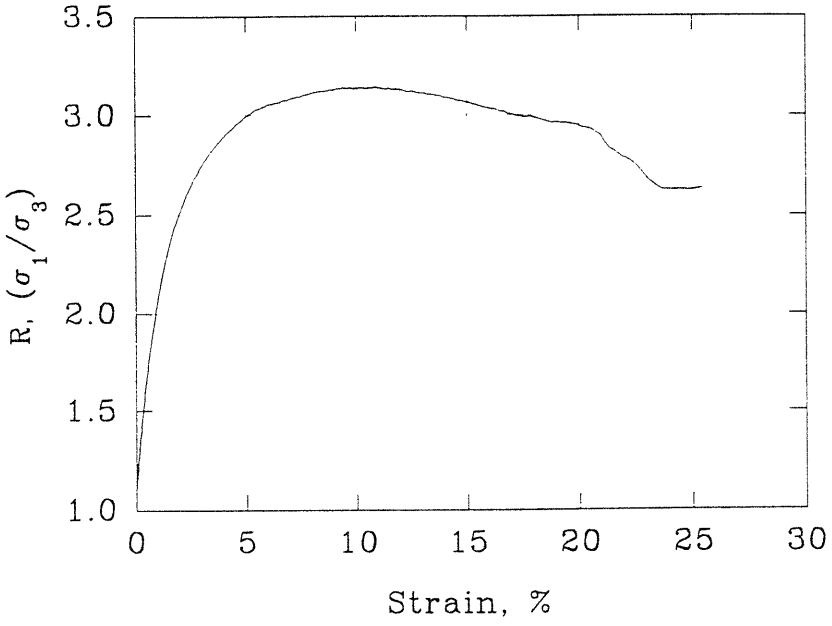

$R_{max} = 3.14$

Series B – Test #22

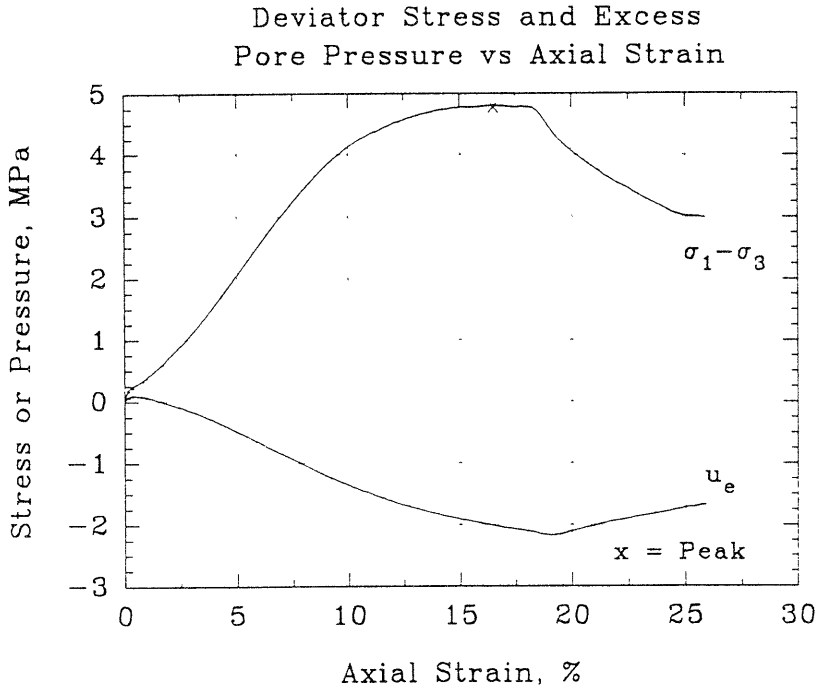

σ'_c = 0.1 MPa
e = 0.600
D_r = 94.0%

Q_p = 4.81 MPa
ε_p = 16.50 %

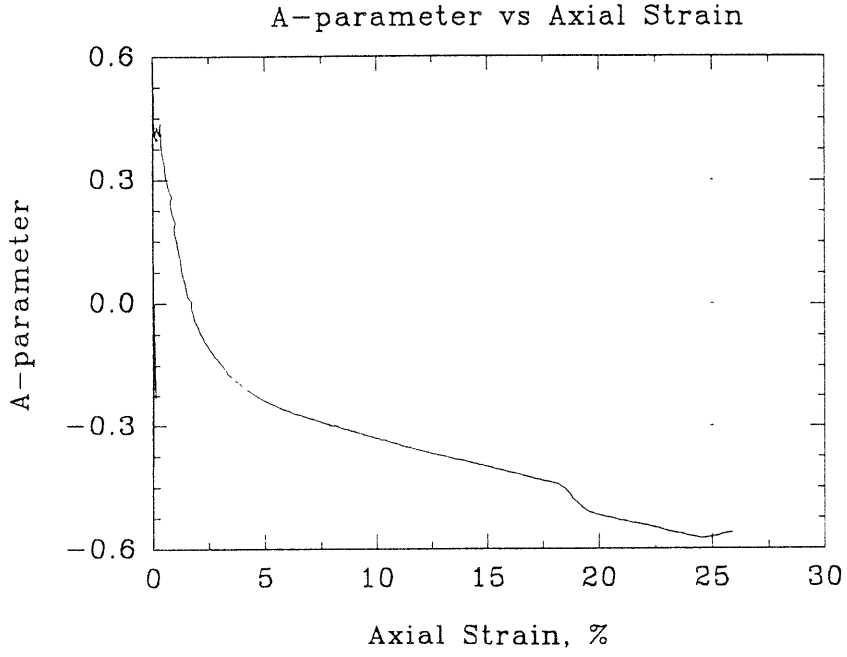

A_f = −0.419

Series B – Test #22

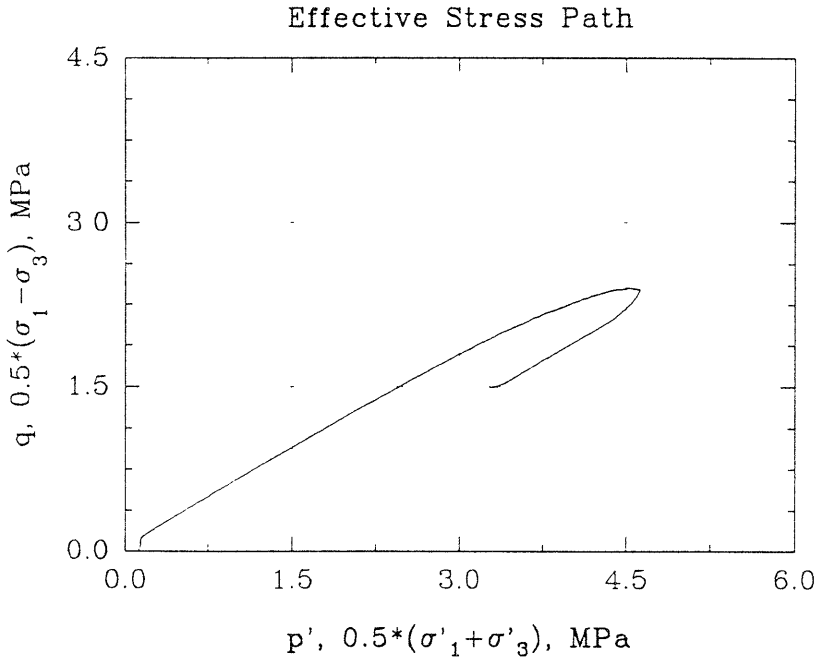

$\alpha' = 39.8°$
$\phi' = 56.4°$

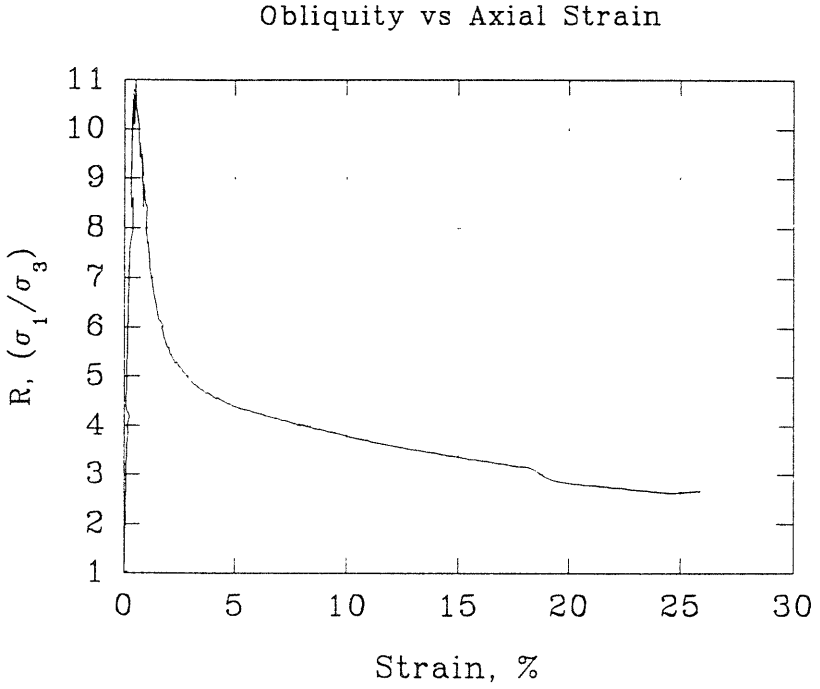

$R_{max} = 10.99$

Series B – Test #23

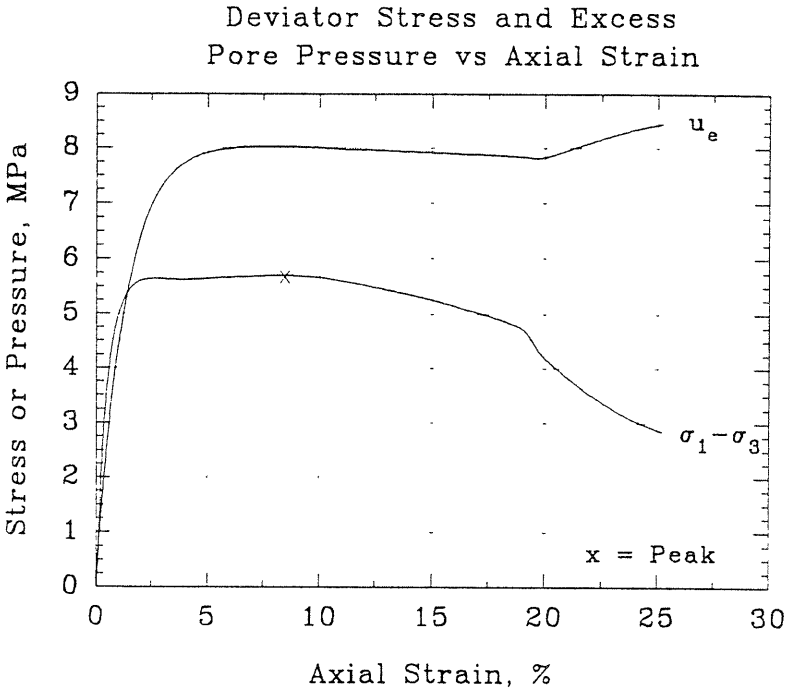

σ'_c = 10 MPa
e = 0.616
D_r = 89.1%

Q_p = 5.70 MPa
ε_p = 8.44 %

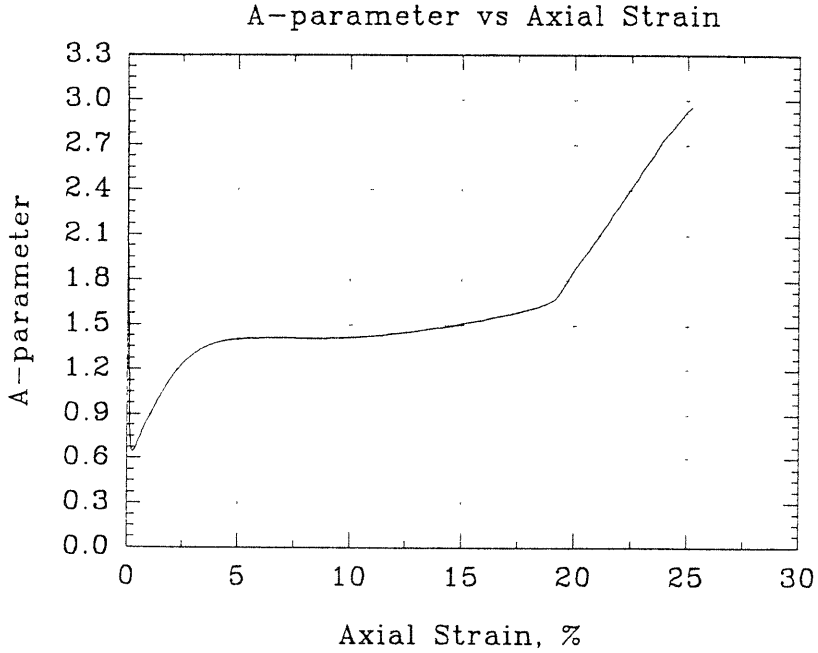

A_f = 1.408

Series B – Test #23

Effective Stress Path

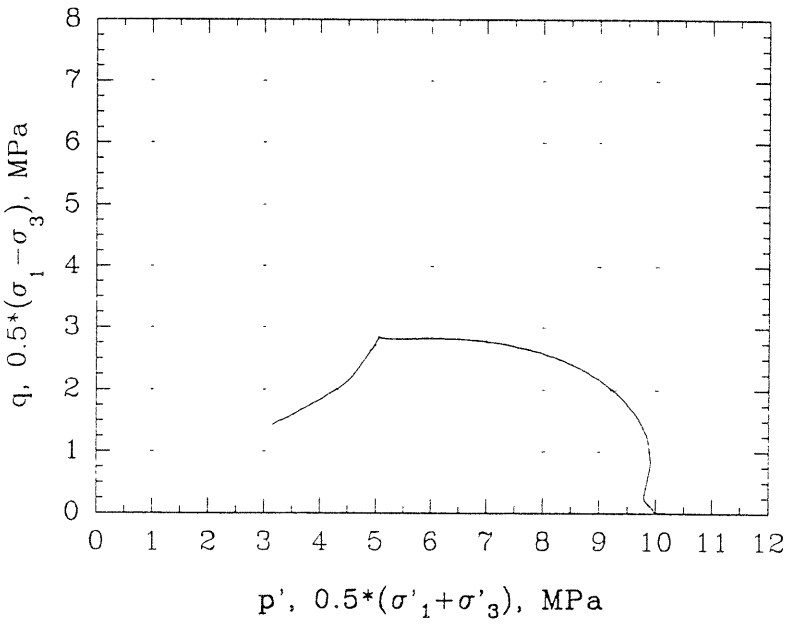

$\alpha' = 29.5°$
$\phi' = 34.4°$

Obliquity vs Axial Strain

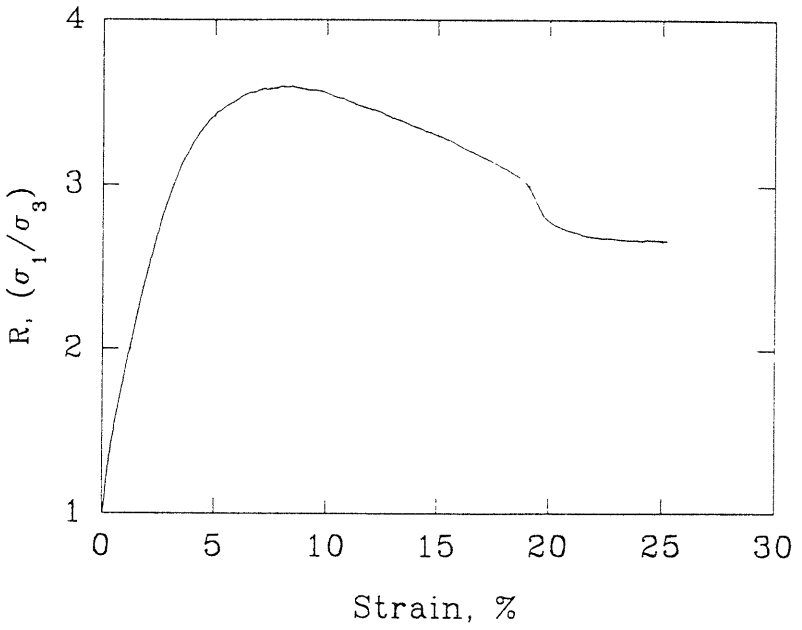

$R_{max} = 3.59$

Series B – Test #24

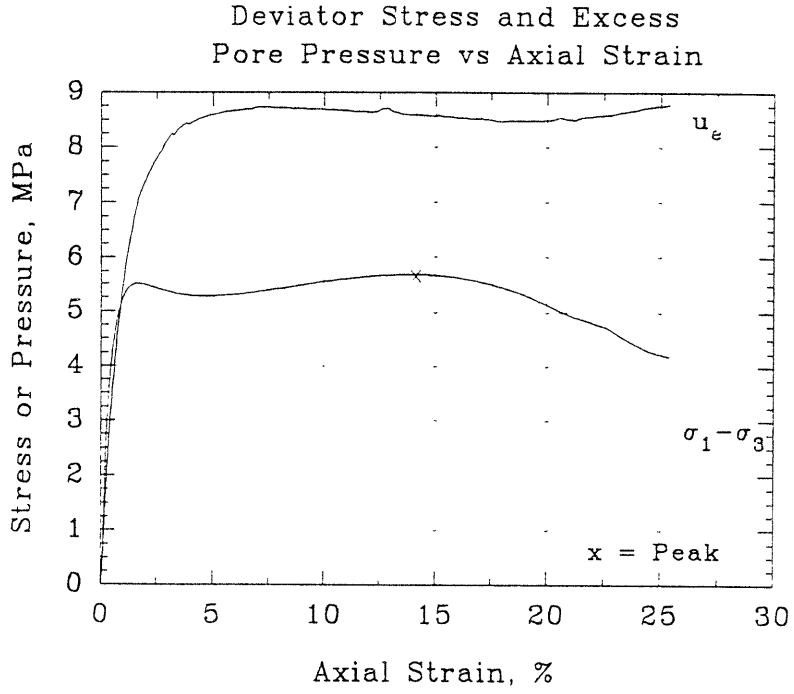

σ'_c = 10 MPa
e = 0.627
D_r = 85.8%

Q_p = 5.69 MPa
ε_p = 14.11 %

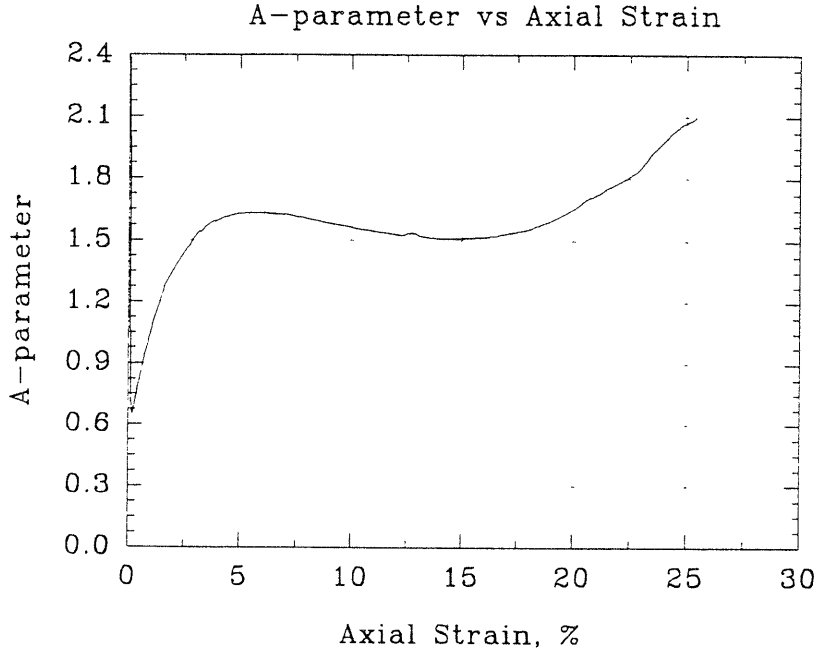

A_f = 1.509

Series B – Test #24

Effective Stress Path

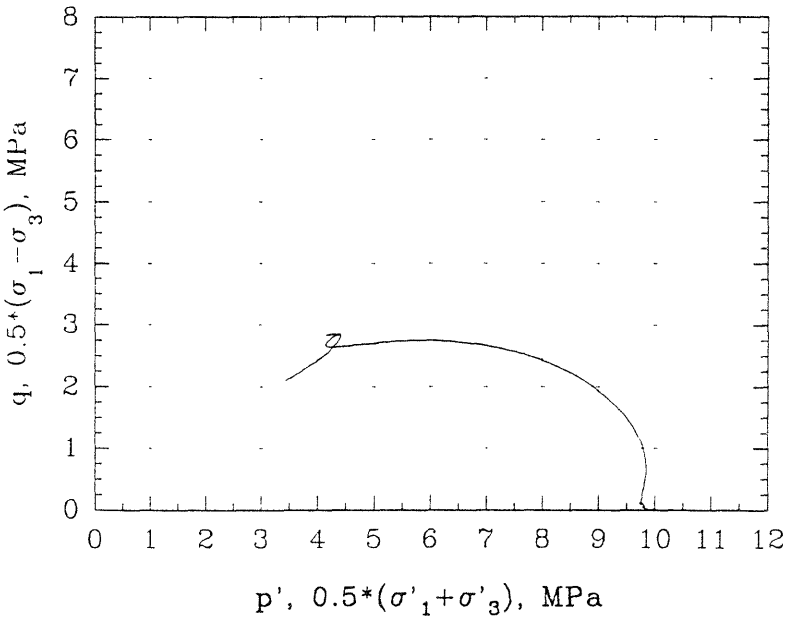

$\alpha' = 33.3°$
$\phi' = 41.0°$

Obliquity vs Axial Strain

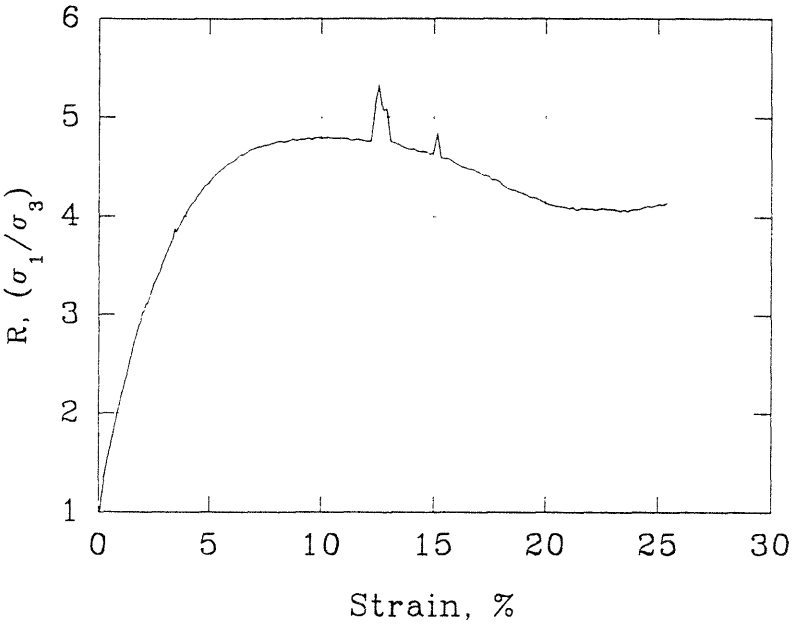

$R_{max} = 4.80$

Series C – Test #01

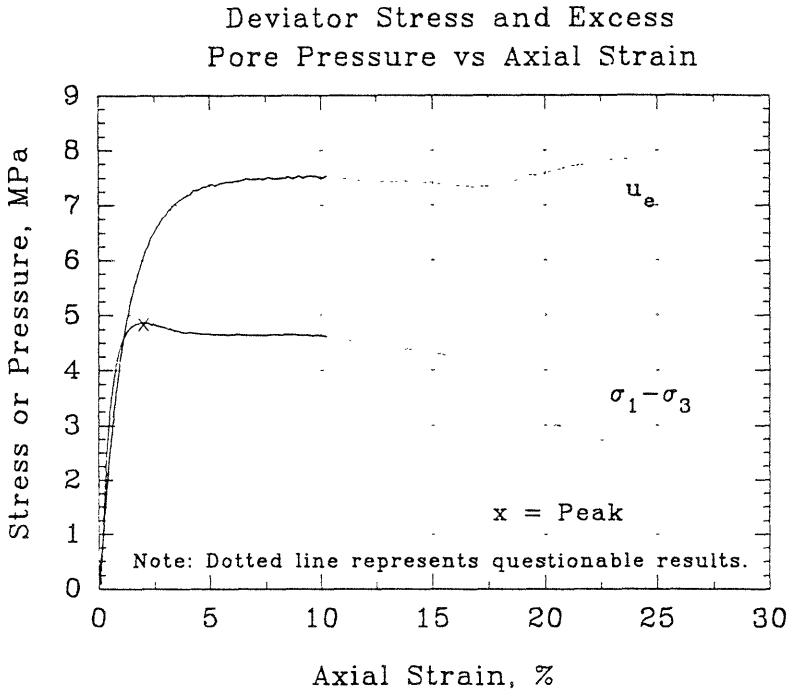

σ'_c = 10 MPa
e = 0.637
D_r = 82.7%

Q_p = 4.87 MPa
ε_p = 1.97 %

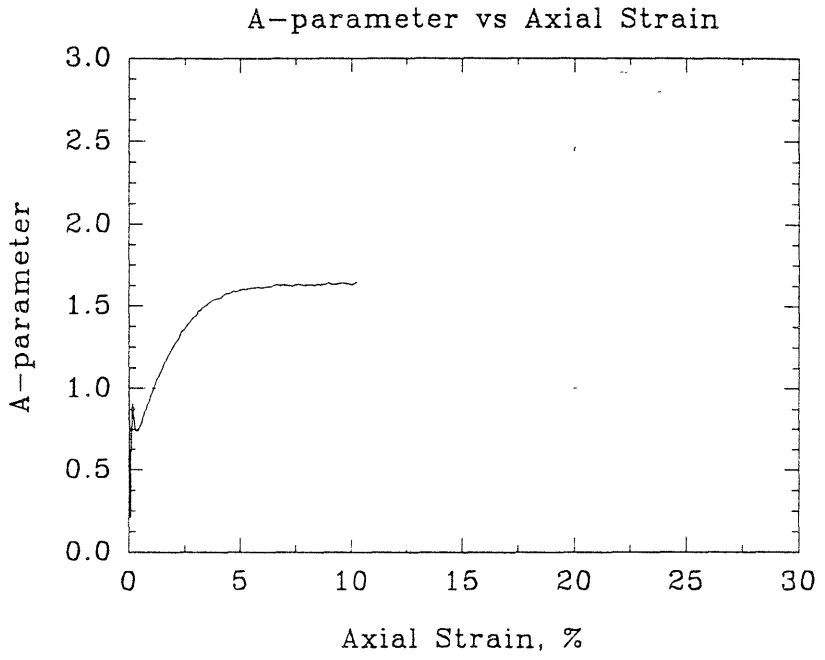

A_f = 1.251

Series C – Test #01

Effective Stress Path

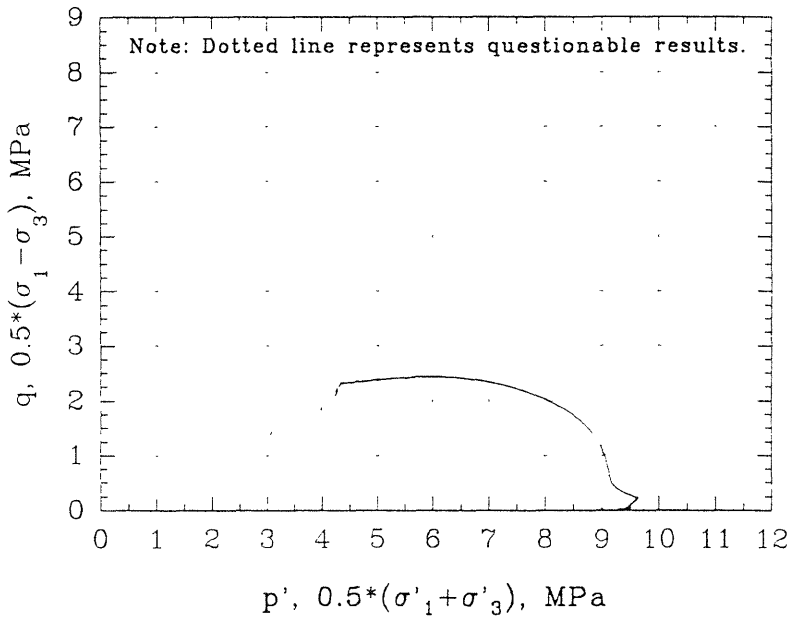

α' = 28.2 °
φ' = 32.5 °

Obliquity vs Axial Strain

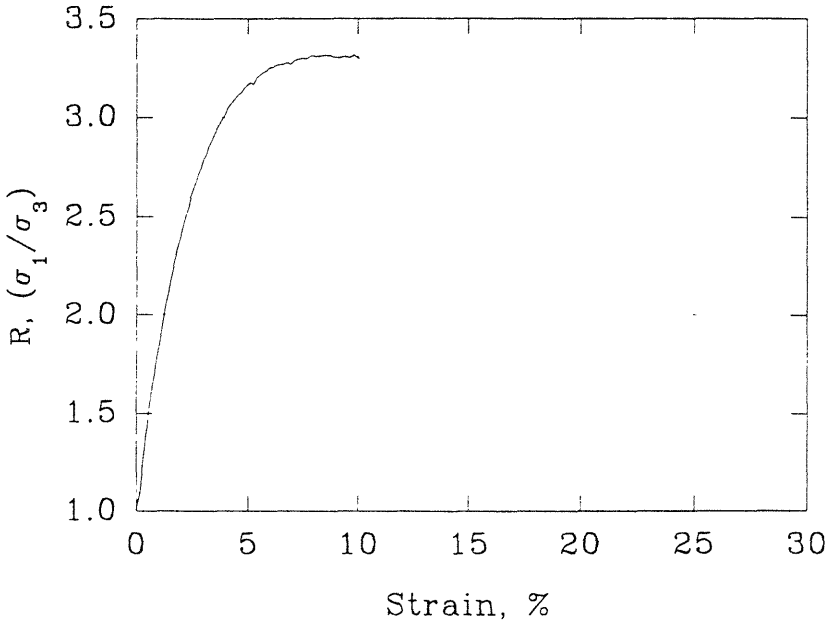

R_{max} = 3.32

Series C – Test #02

Deviator Stress and Excess
Pore Pressure vs Axial Strain

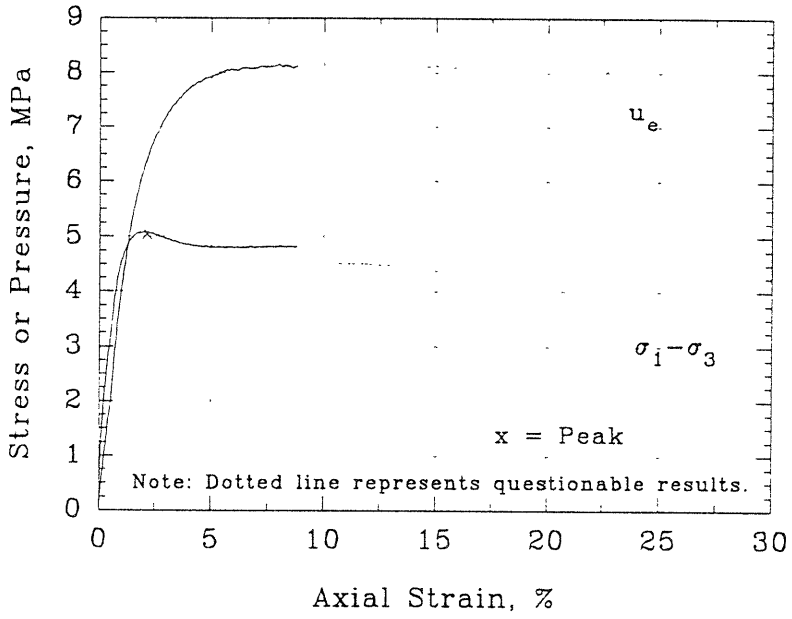

σ'_c = 10 MPa
e = 0.637
D_r = 82.7%

Q_p = 5.081 MPa
ε_p = 2.12 %

A–parameter vs Axial Strain

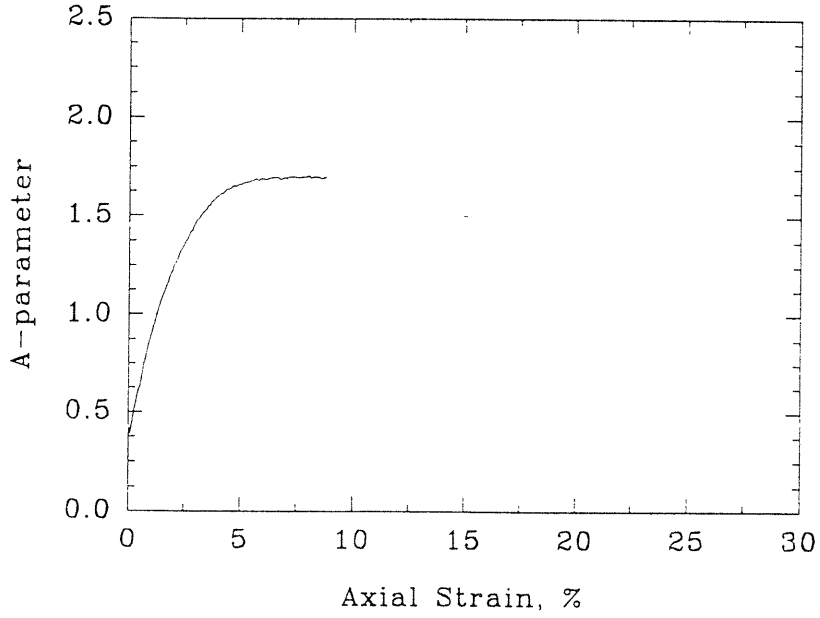

A_f = 1.263

Series C – Test #02

Effective Stress Path

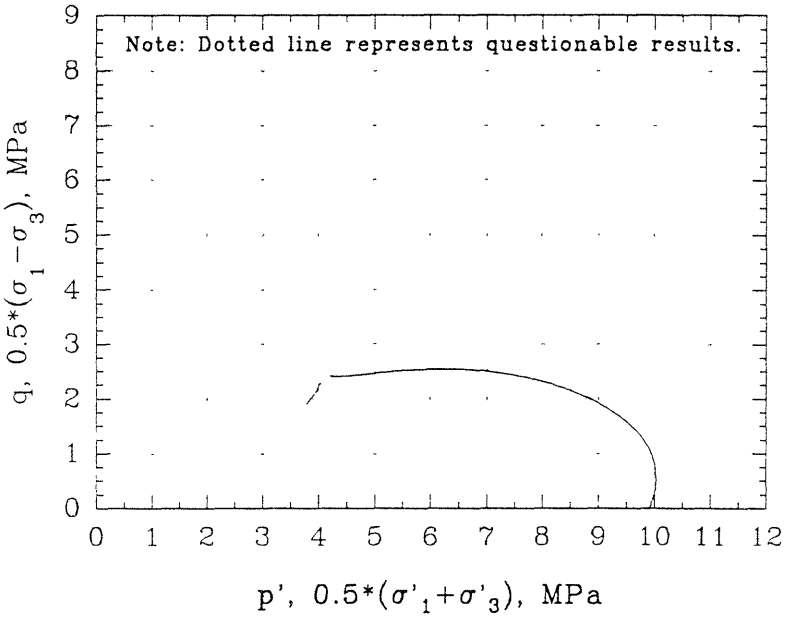

α' = 29.8 °
ϕ' = 35.0 °

Obliquity vs Axial Strain

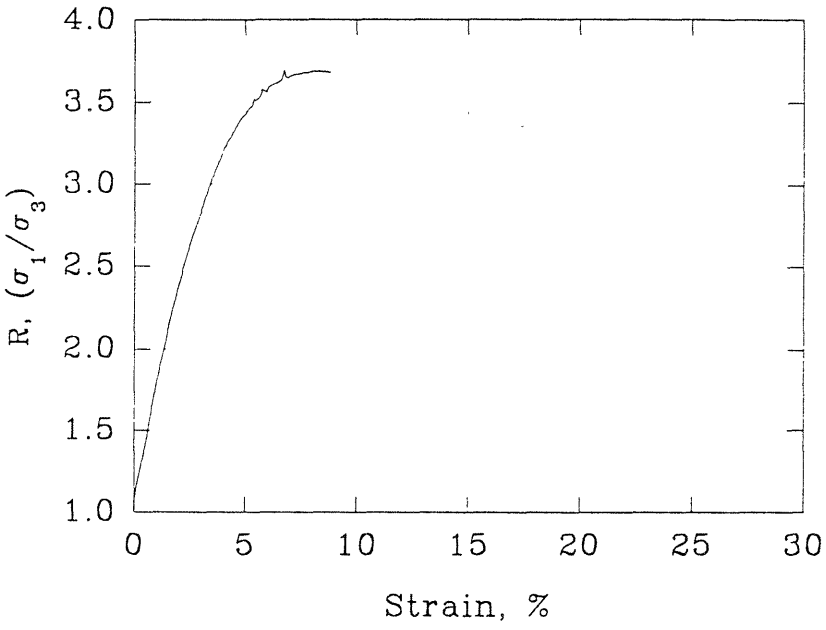

R_{max} = 3.69

Series C – Test #03

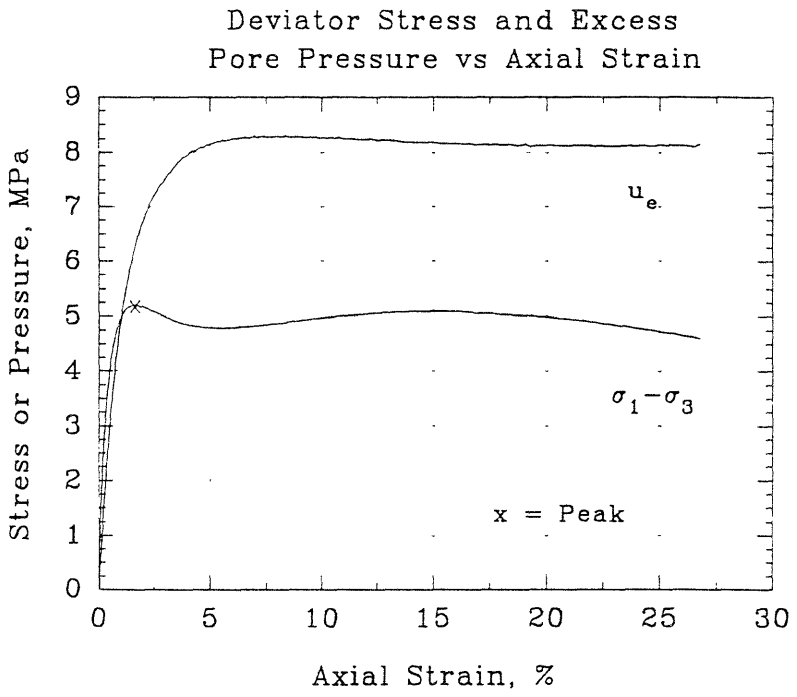

σ'_c = 10 MPa
e = 0.655
D_r = 77.3%

Q_p = 5.20 MPa
ε_p = 1.63 %

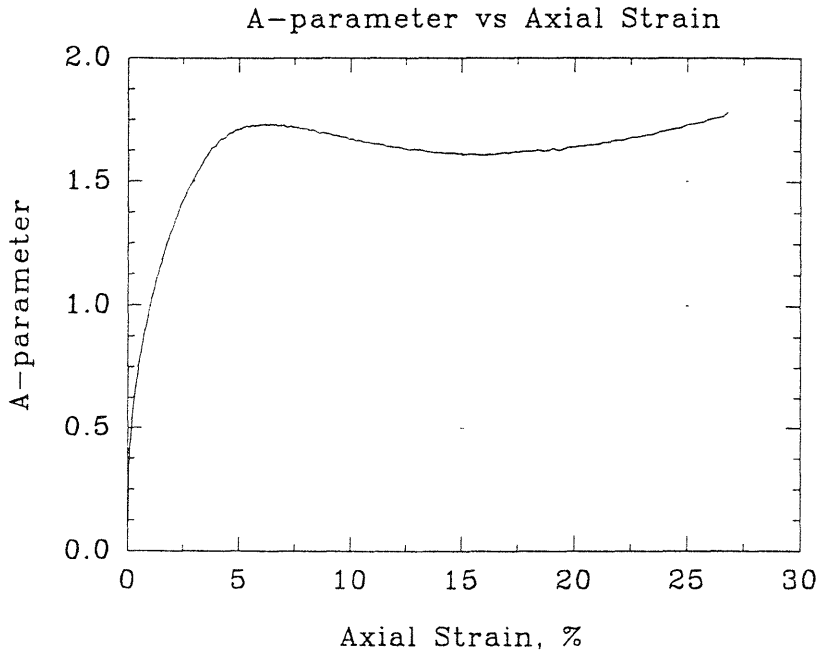

A_f = 1.205

Series C – Test #03

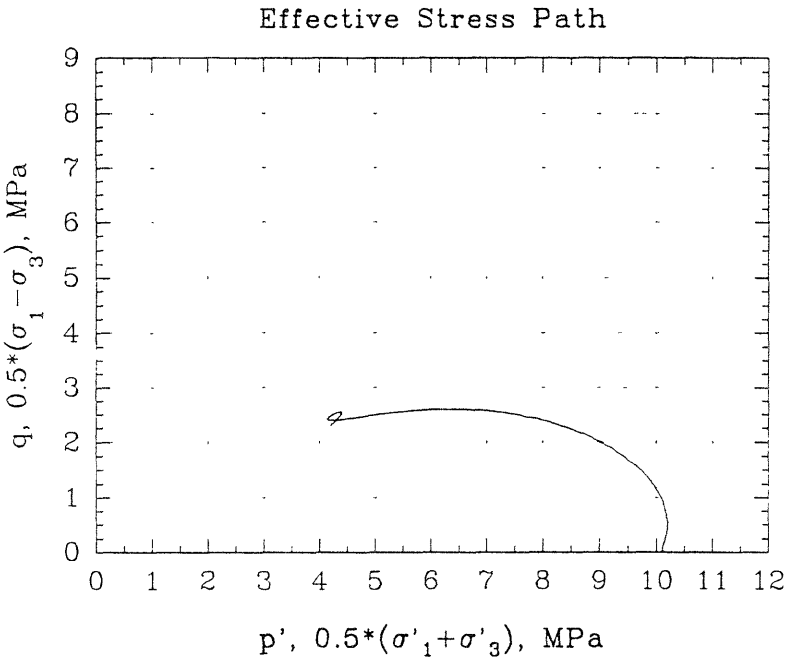

$\alpha' = 30.5°$
$\phi' = 36.1°$

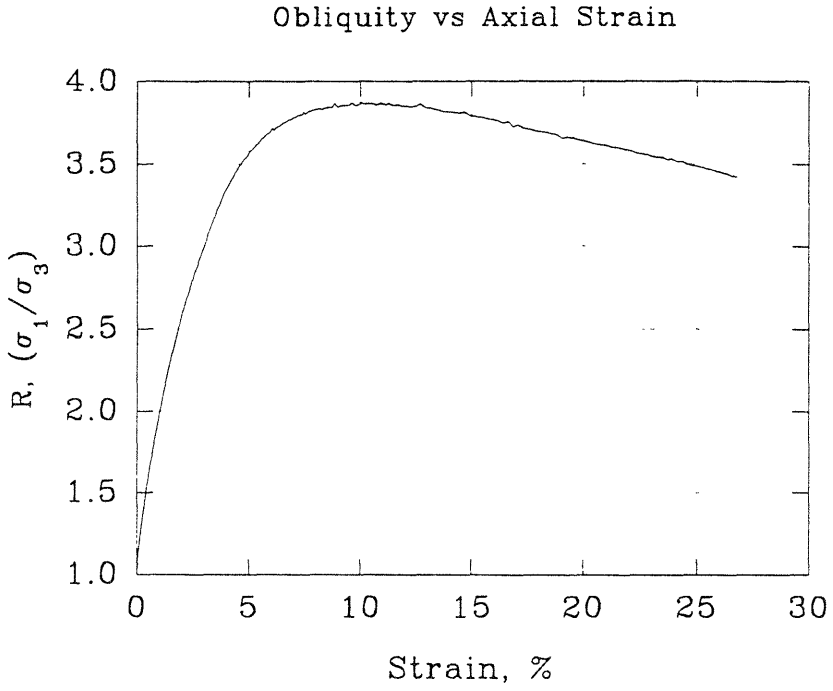

$R_{max} = 3.87$

Series C – Test #04

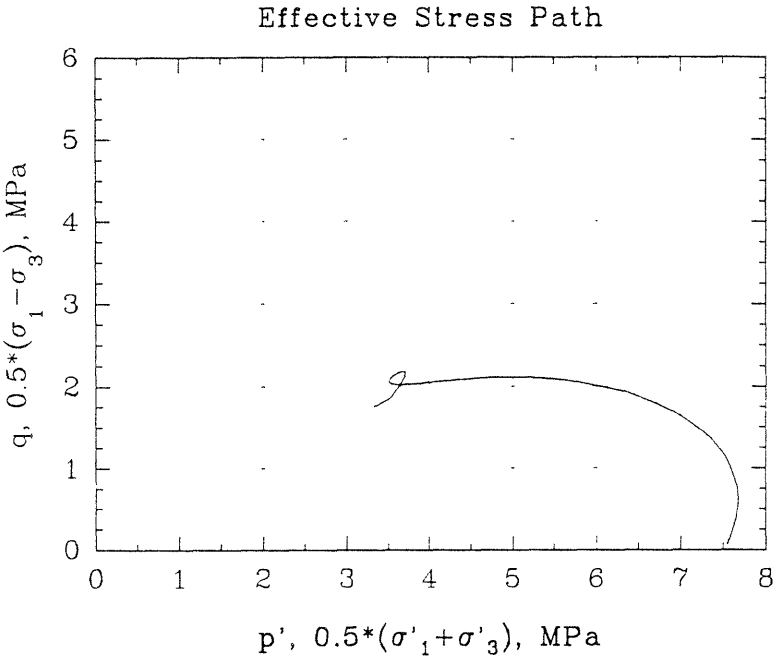

α' = 30.8 °
φ' = 36.6 °

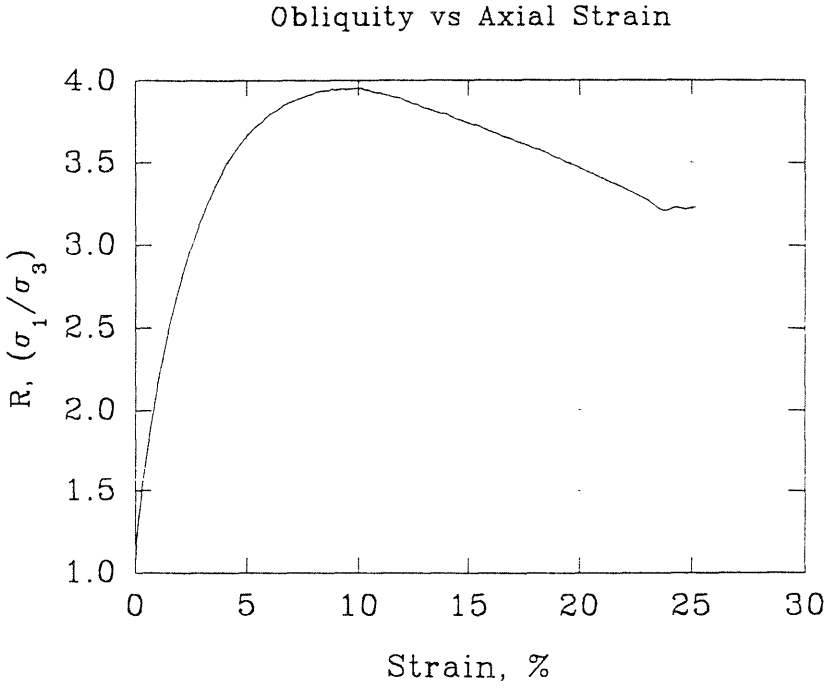

R_{max} = 3.96

Series C – Test #04

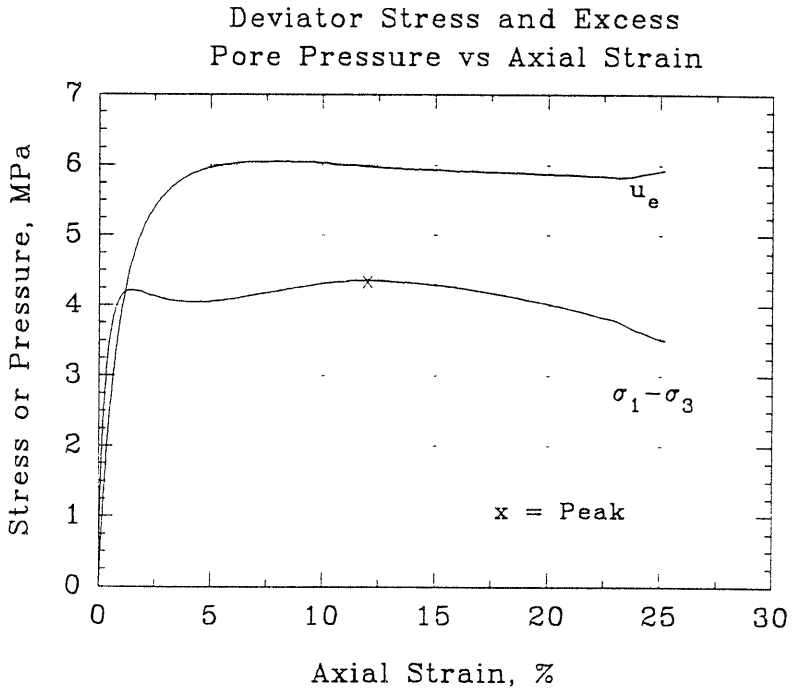

σ'_c = 7.5 MPa
e = 0.631
D_r = 84.6 %

Q_p = 4.36 MPa
ε_p = 11.98 %

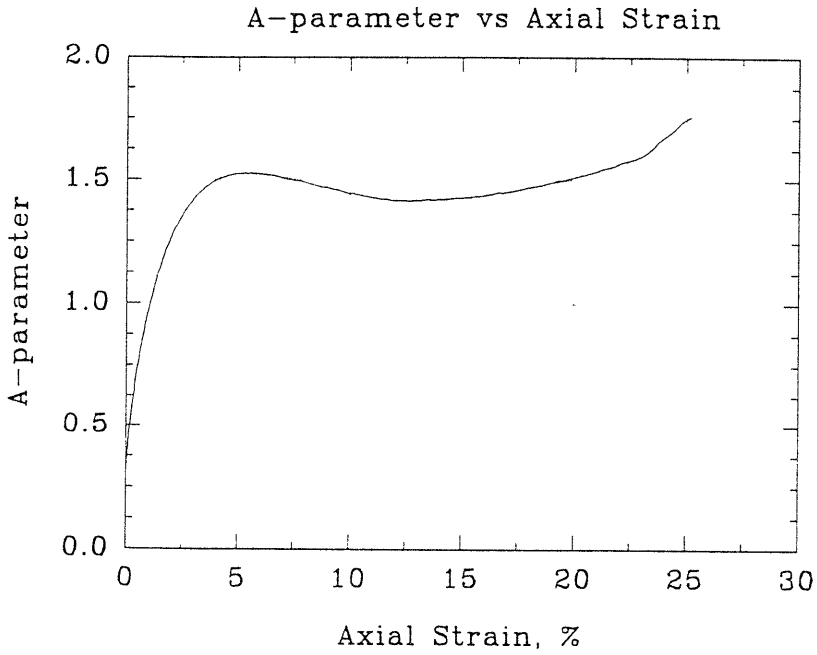

A_f = 1.417

Series C – Test #09

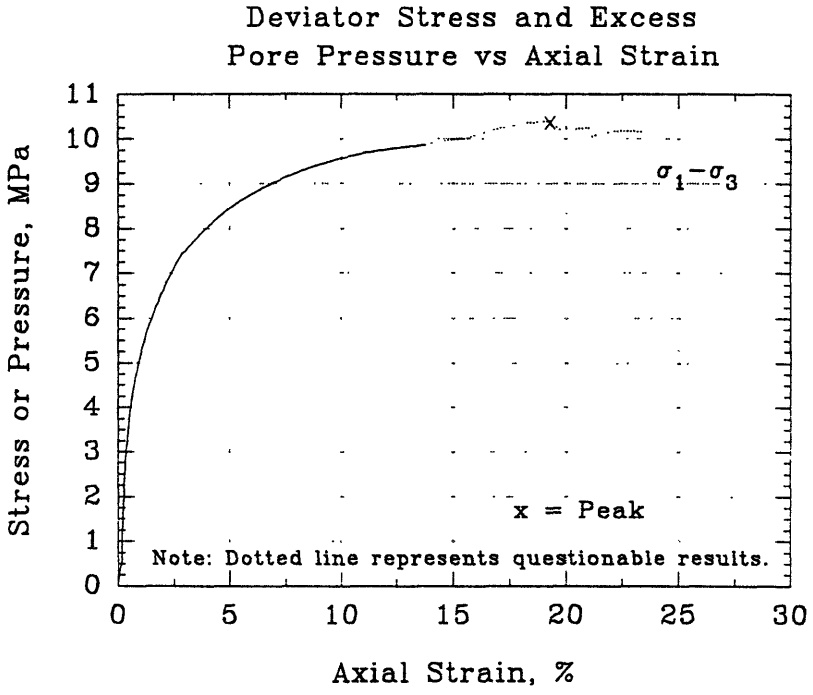

σ'_c = 10 MPa
e = 0.621
D_r = 87.6%

Q_p = 10.40 MPa
ε_p = 13.77 %

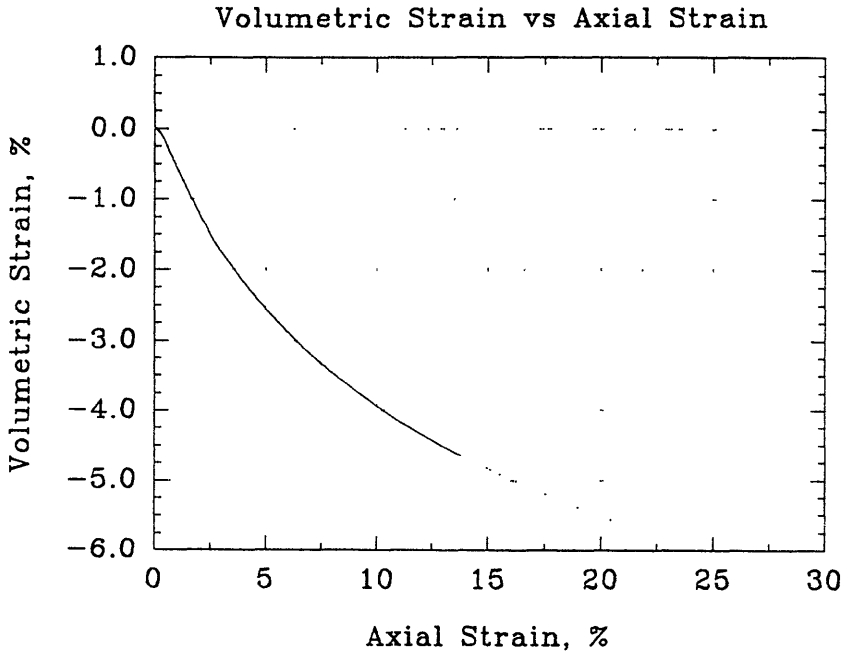

$\frac{d\varepsilon_v}{d\varepsilon_a}$ = −0.161

Series C – Test #09

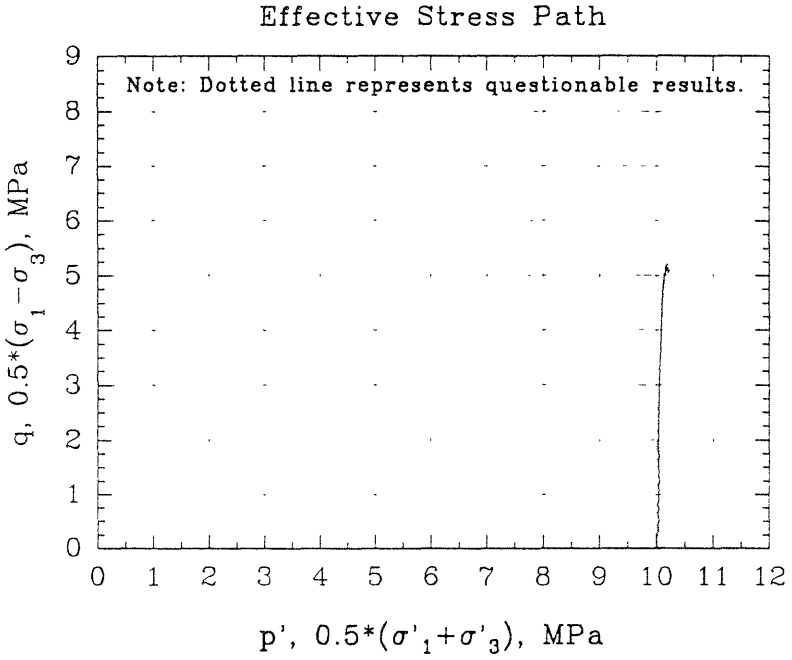

$\alpha' = 25.9°$
$\phi' = 29.1°$

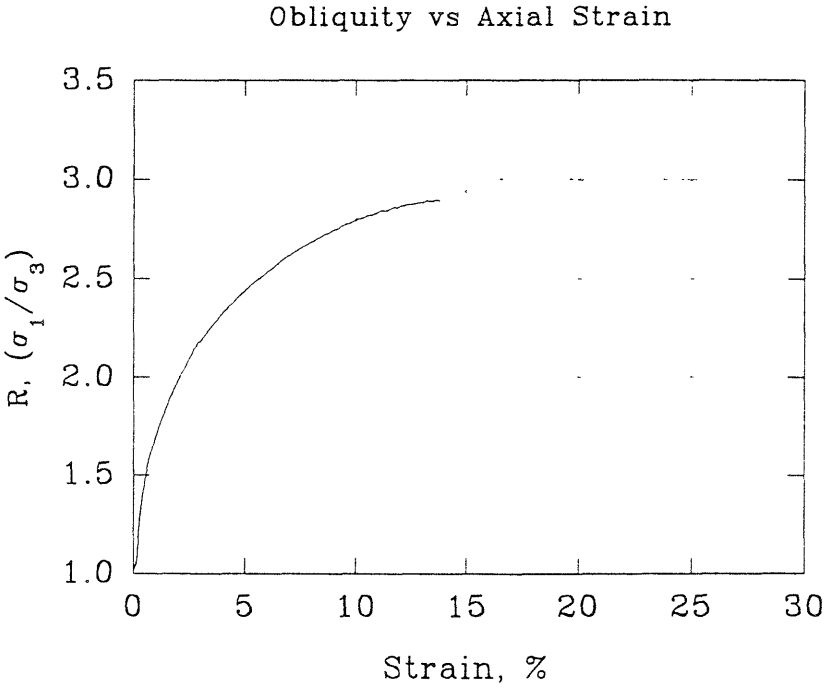

$R_{max} = 2.89$

Series C – Test #10

Deviator Stress and Excess
Pore Pressure vs Axial Strain

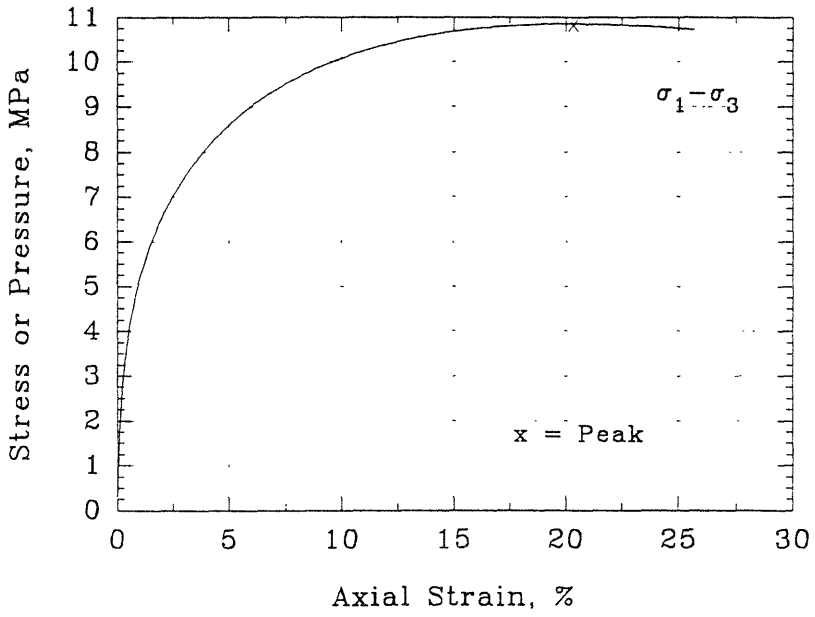

σ'_c = 10 MPa
e = 0.609
D_r = 91.2%

Q_p = 10.86 MPa
ε_p = 19.56 %

Volumetric Strain vs Axial Strain

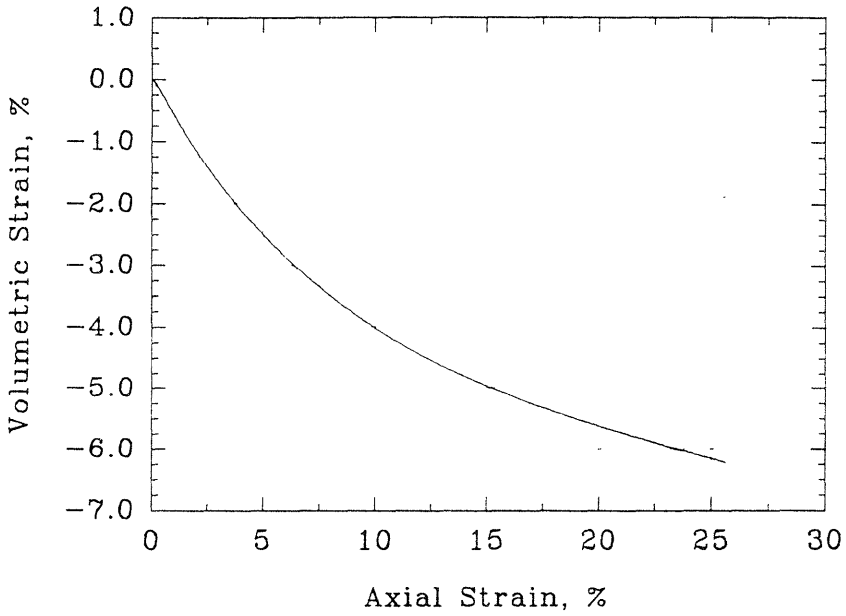

$\frac{d\varepsilon_v}{d\varepsilon_a}$ = −0.119

Series C – Test #10

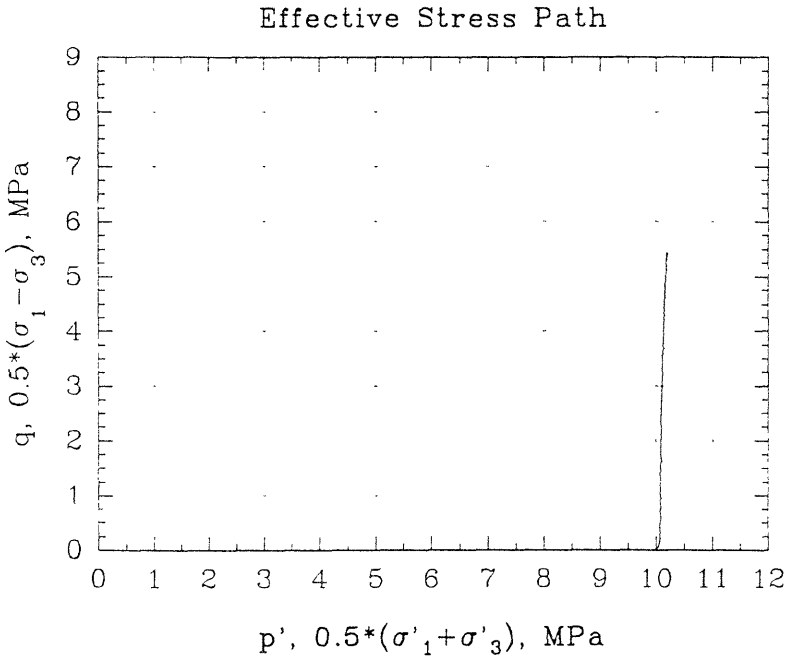

α' = 28.0 °
φ' = 32.2 °

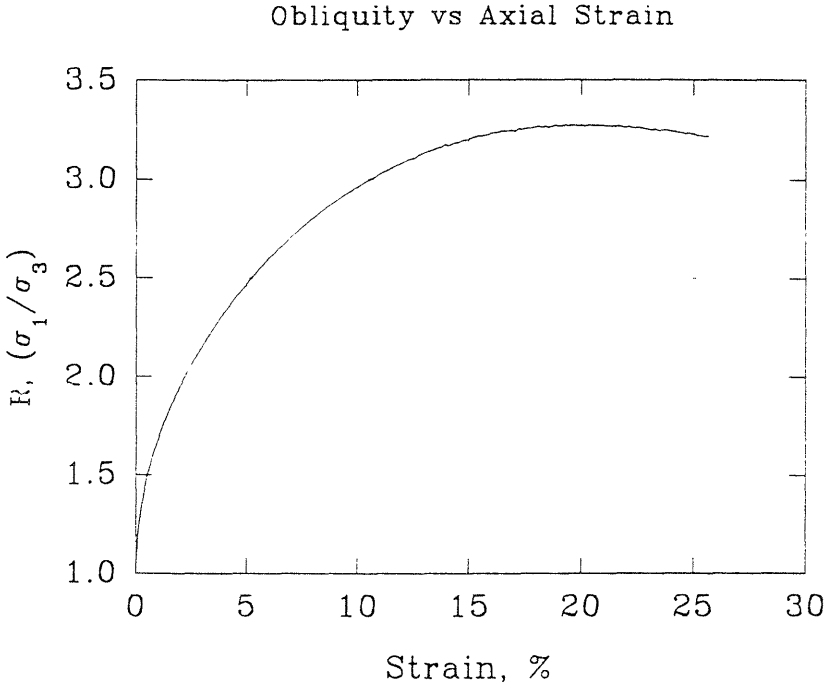

R_{max} = 3.27

Series C – Test #11

Deviator Stress and Excess
Pore Pressure vs Axial Strain

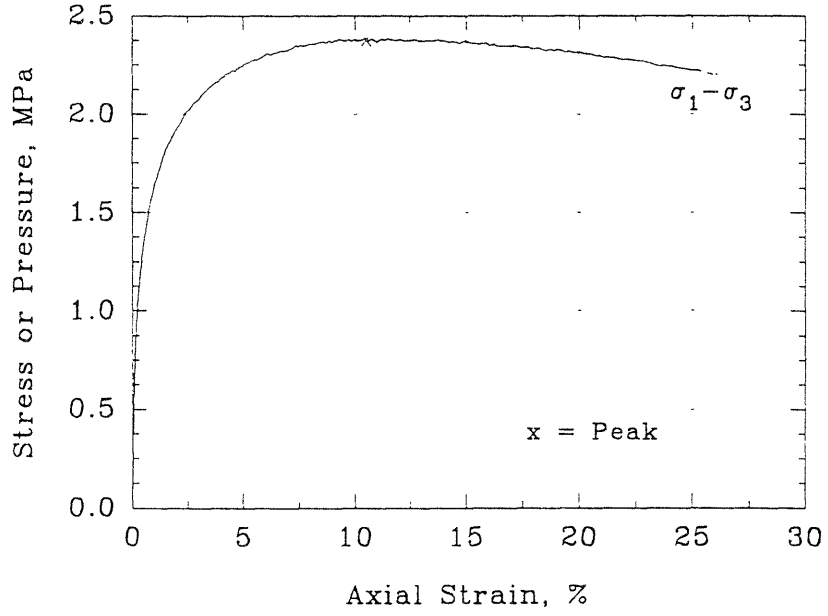

σ'_c = 2 MPa
e = 0.675
D_r = 71.2%

Q_p = 2.39 MPa
ε_p = 12.90 %

Volumetric Strain vs Axial Strain

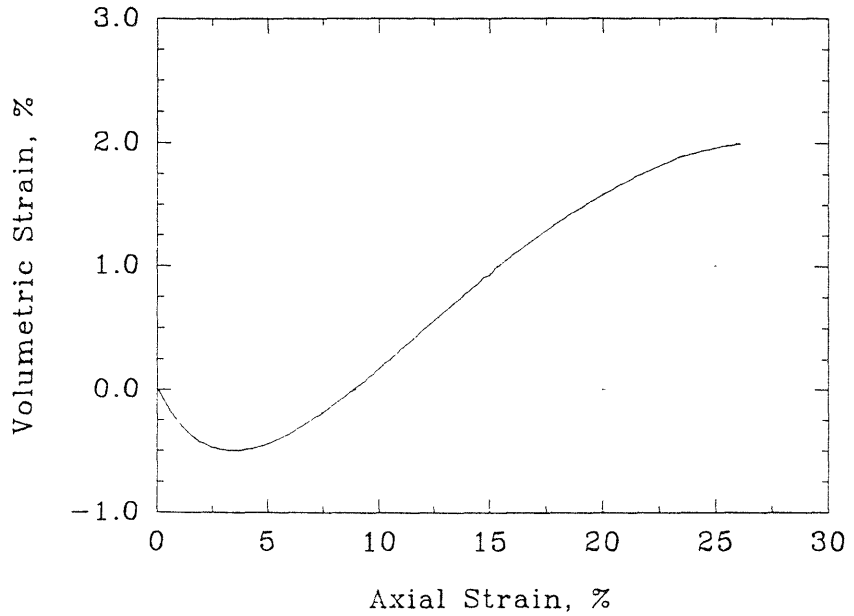

$\frac{d\varepsilon_v}{d\varepsilon_a}$ = 0.151

Series C – Test #11

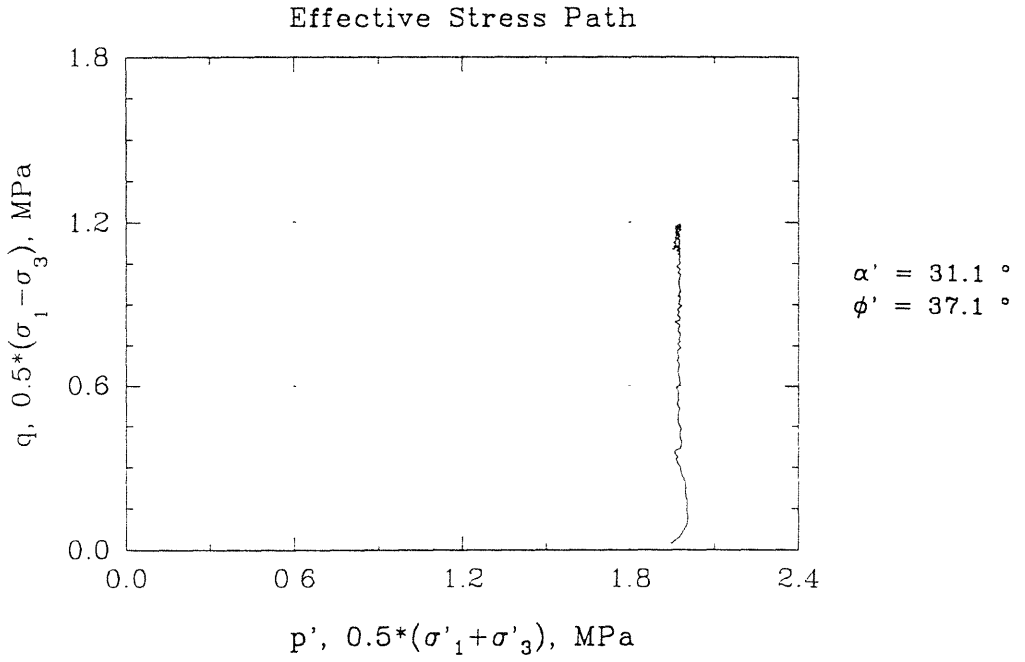

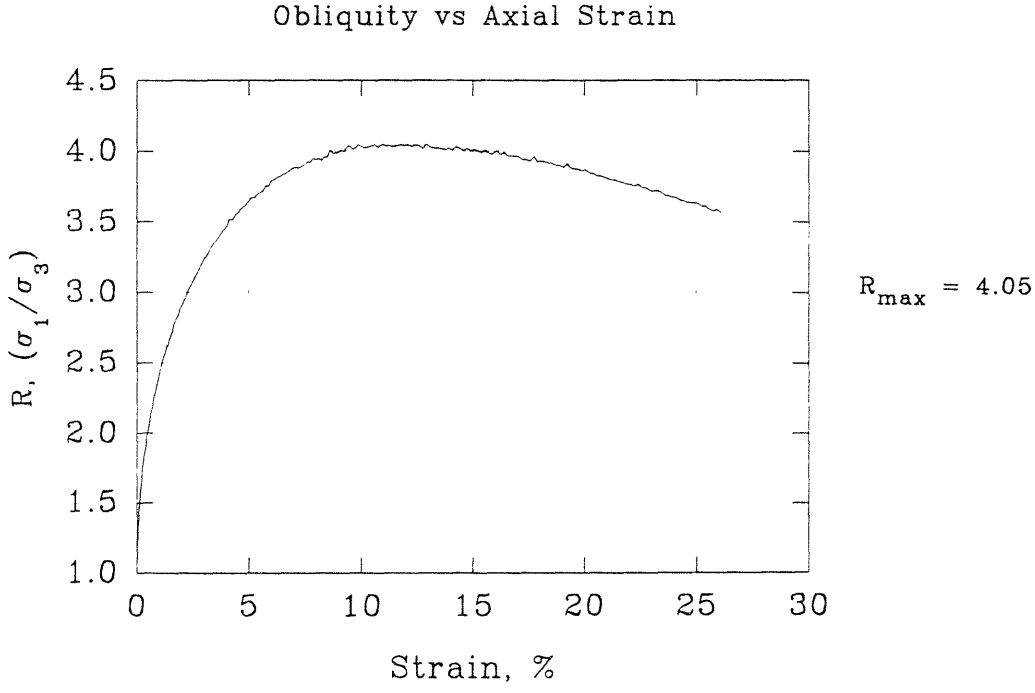

Series C – Test #12

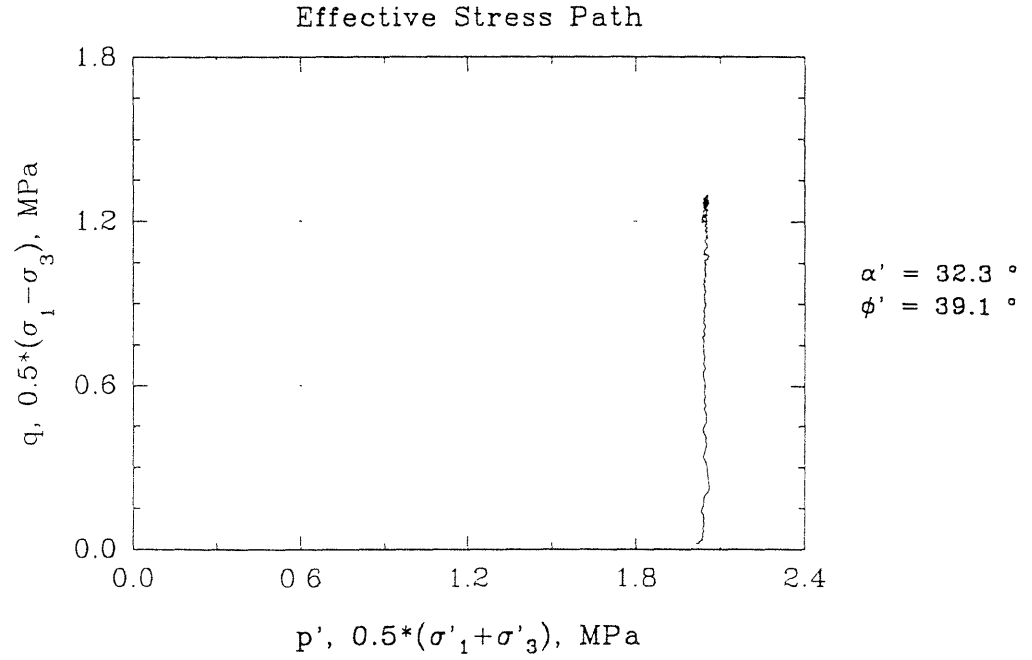

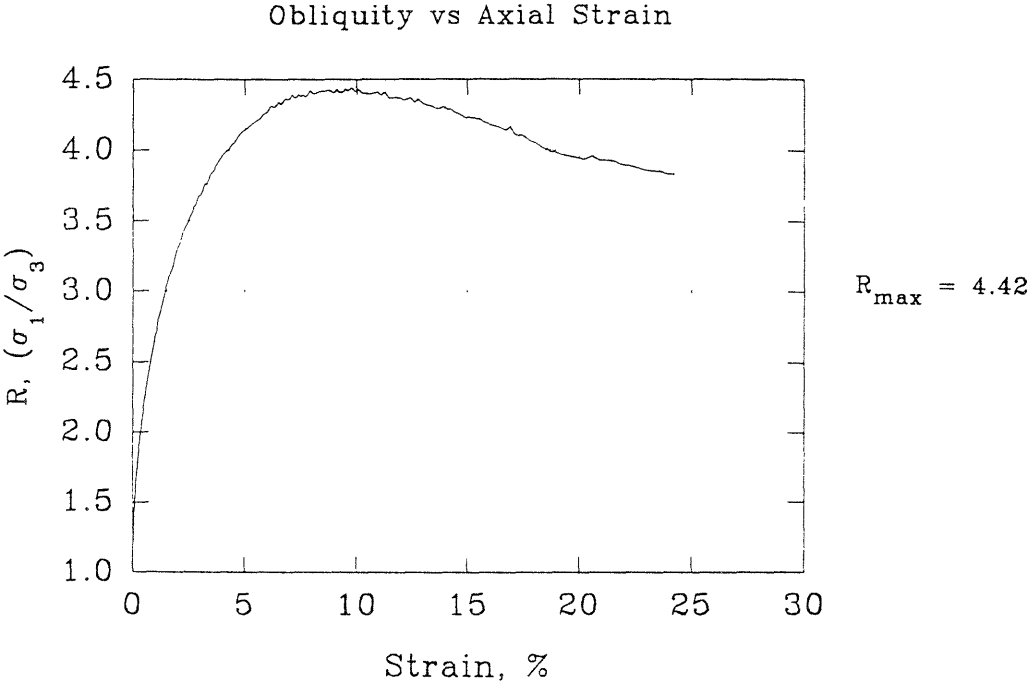

Series C – Test #12

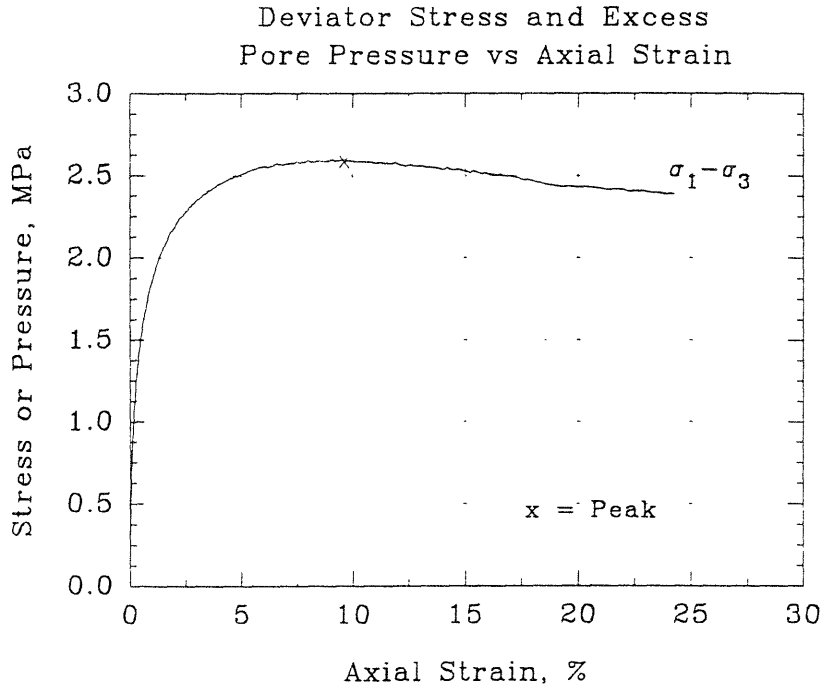

σ'_c = 2 MPa
e = 0.614
D_r = 89.7%

Q_p = 2.59 MPa
ε_p = 8.79 %

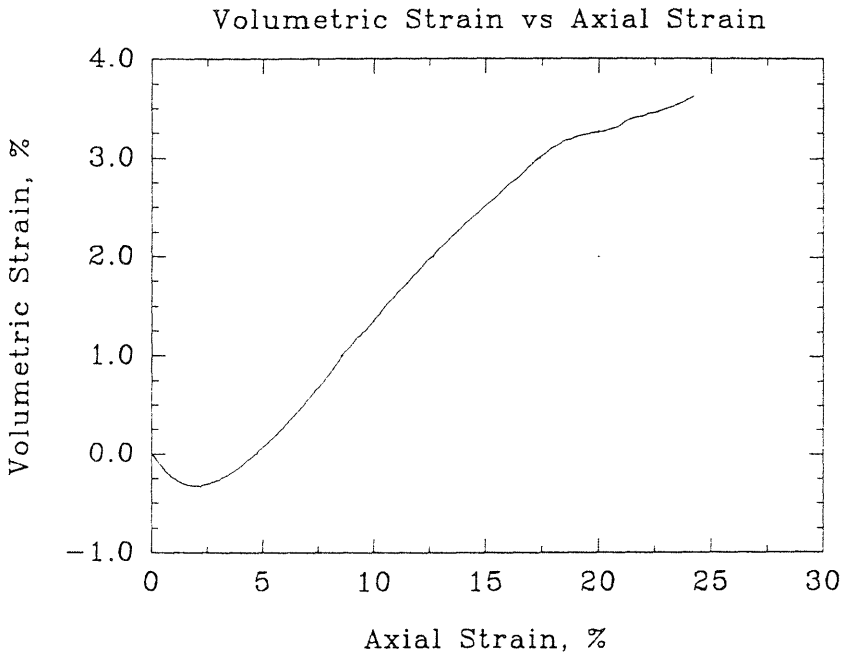

$\frac{d\varepsilon_v}{d\varepsilon_a}$ = 0.289

Series C – Test #13

Deviator Stress and Excess
Pore Pressure vs Axial Strain

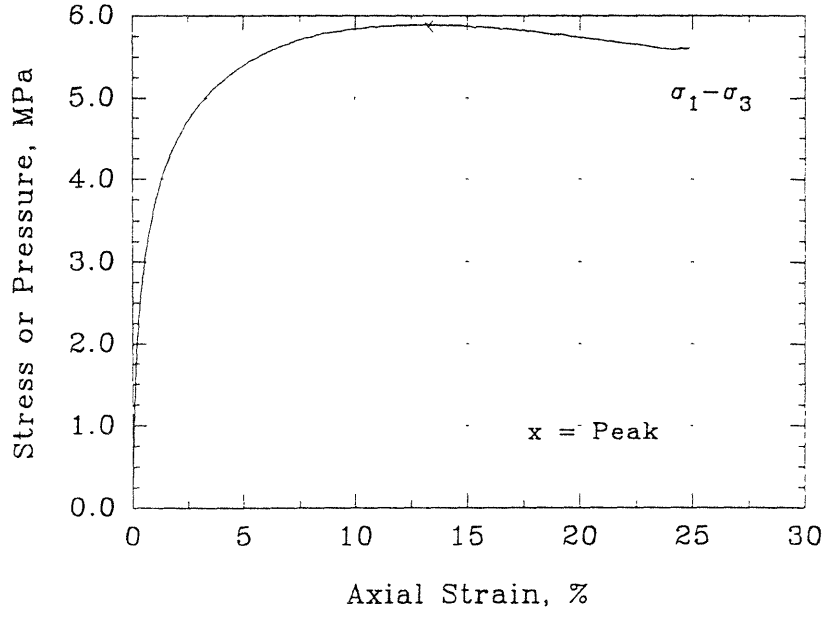

σ'_c = 5 MPa
e = 0.618
D_r = 88.5%

Q_p = 5.89 MPa
ε_p = 13.24 %

Volumetric Strain vs Axial Strain

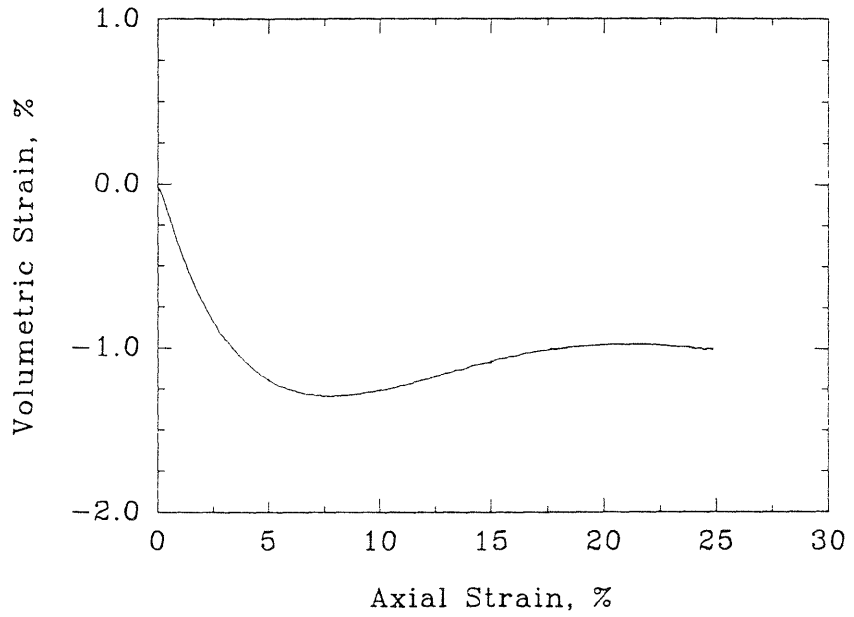

$\frac{d\varepsilon_v}{d\varepsilon_a}$ = 0.036

Series C – Test #13

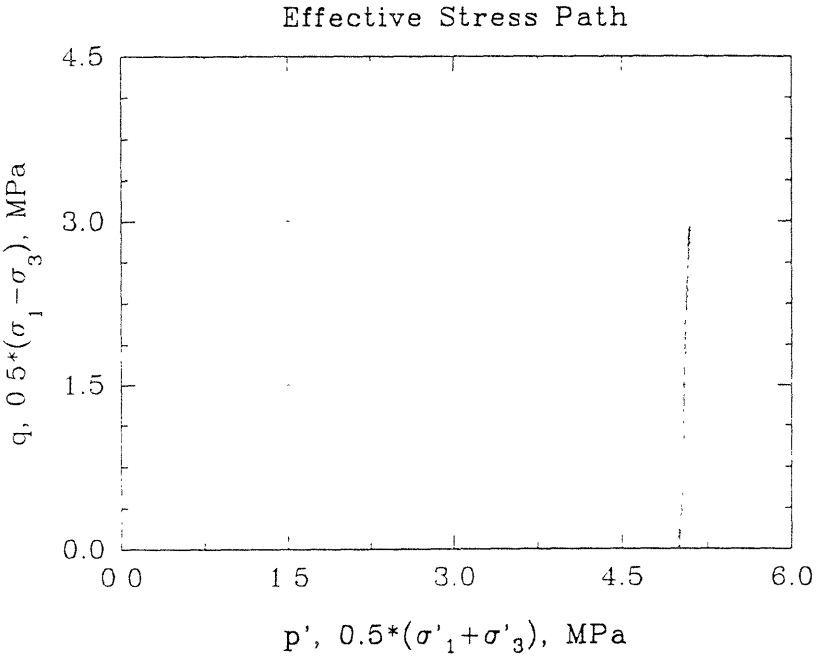

α' = 30.0 °
ϕ' = 35.3 °

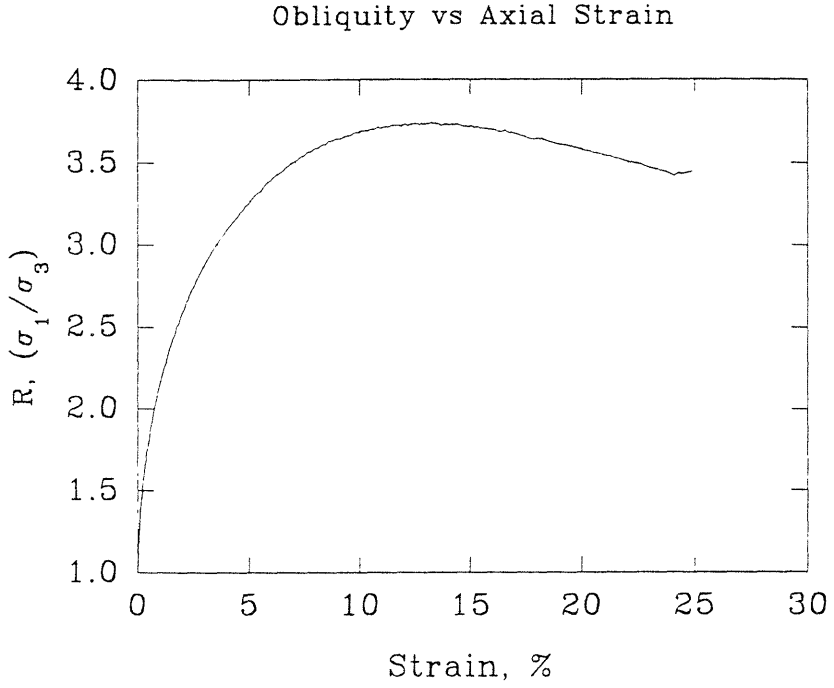

R_{max} = 3.74

Series C – Test #14

Deviator Stress and Excess
Pore Pressure vs Axial Strain

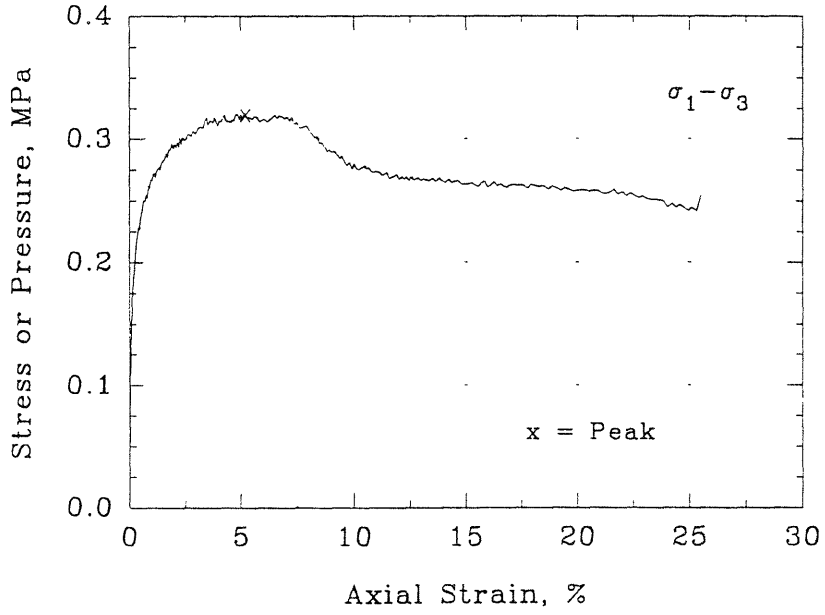

σ'_c = 0.1 MPa
e = 0.626
D_r = 86.1%

Q_p = 0.32 MPa
ε_p = 5.72 %

Volumetric Strain vs Axial Strain

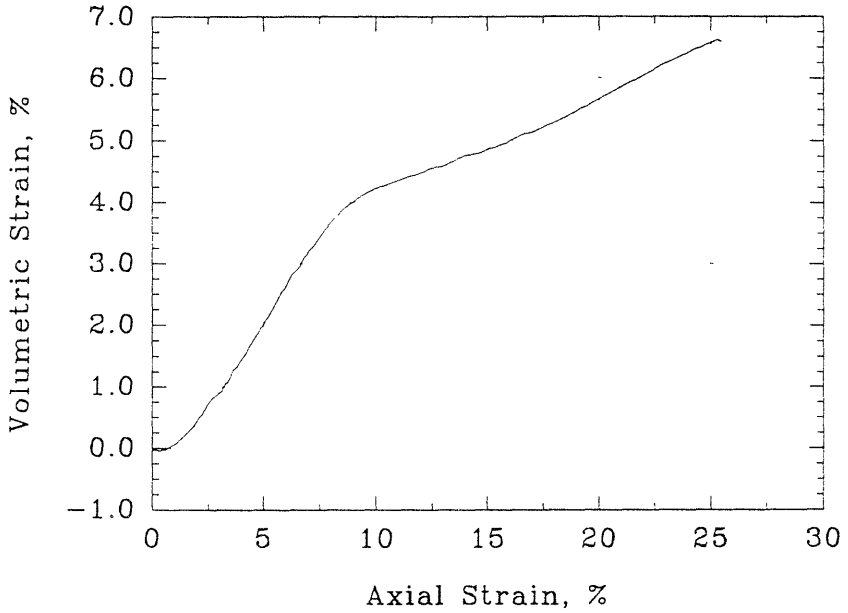

$\frac{d\varepsilon_v}{d\varepsilon_a}$ = 0.649

Series C – Test #14

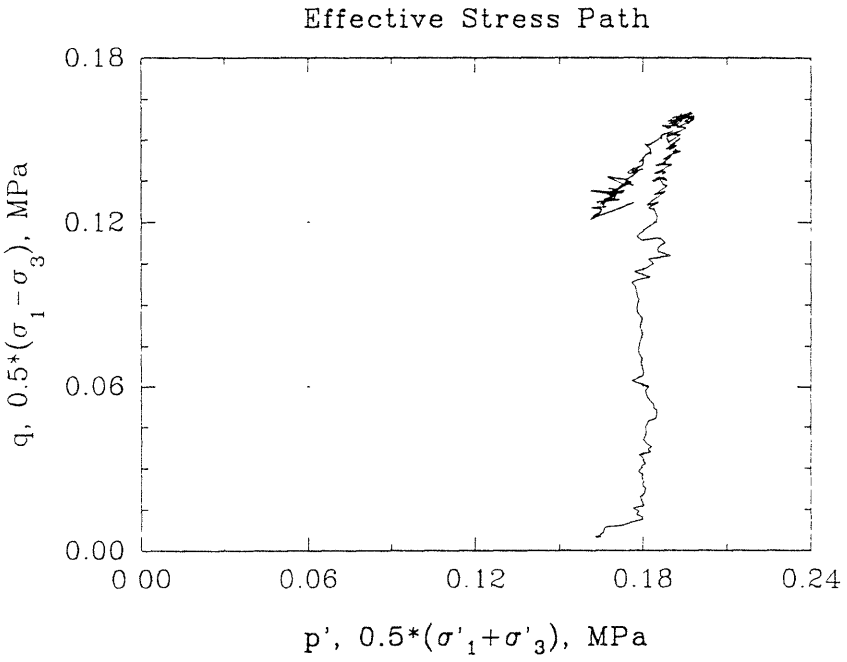

$\alpha' = 39.6\ °$
$\phi' = 56.0\ °$

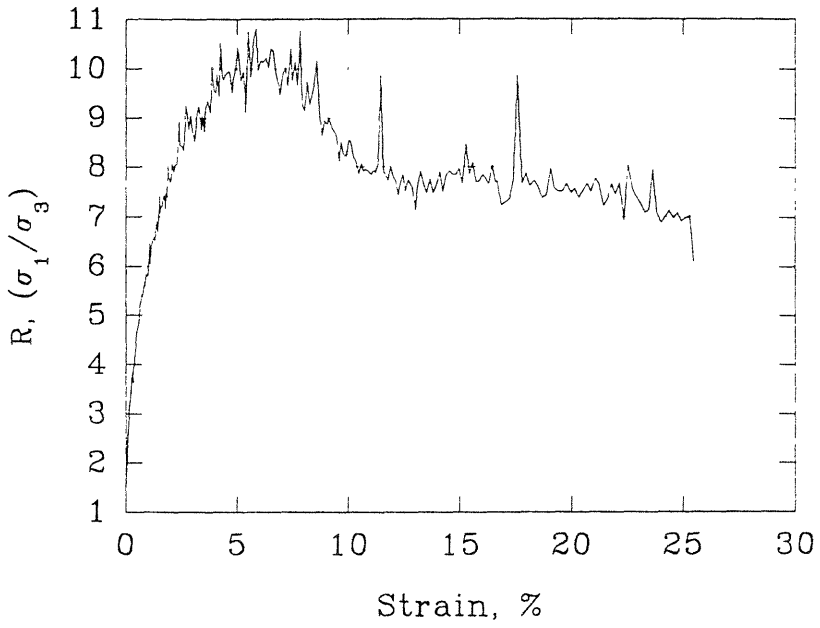

$R_{max} = 10.55$

Series C – Test #15

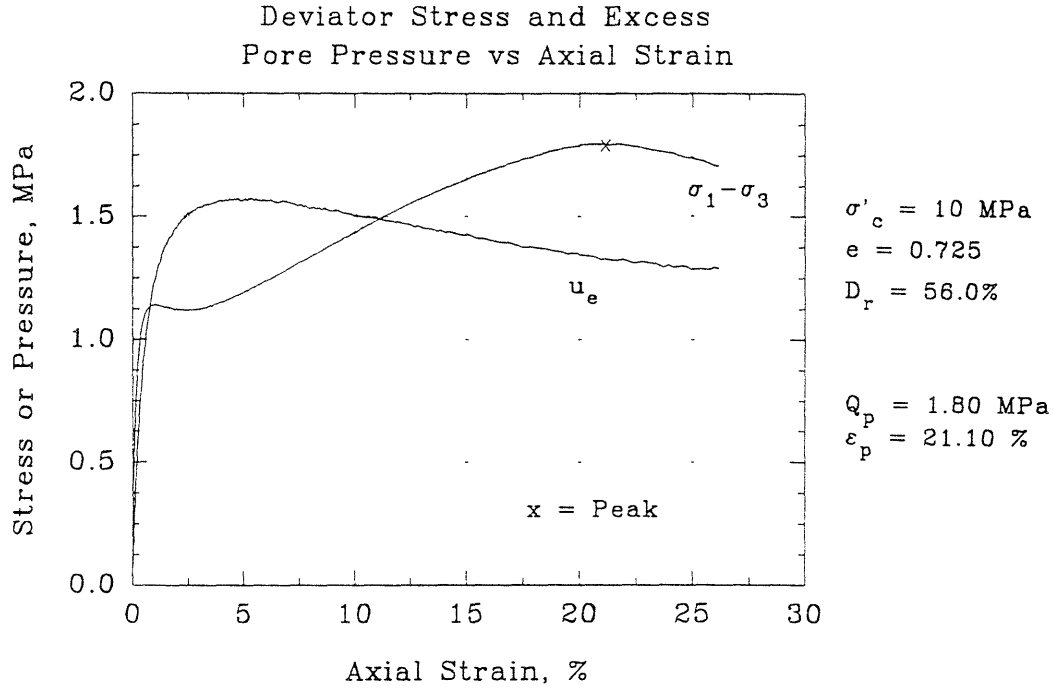

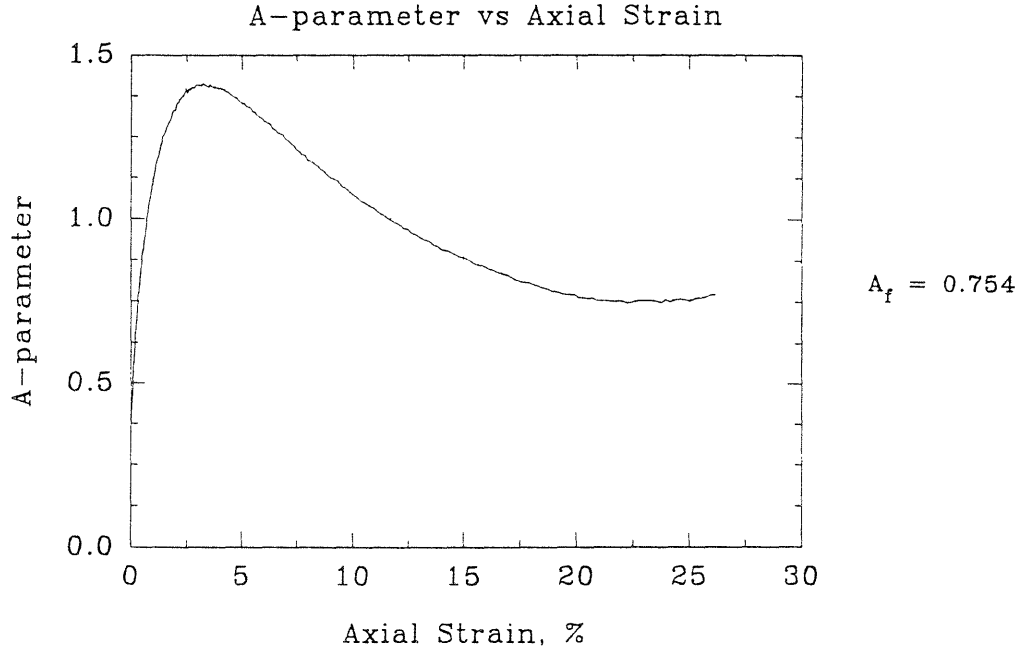

Series C – Test #15

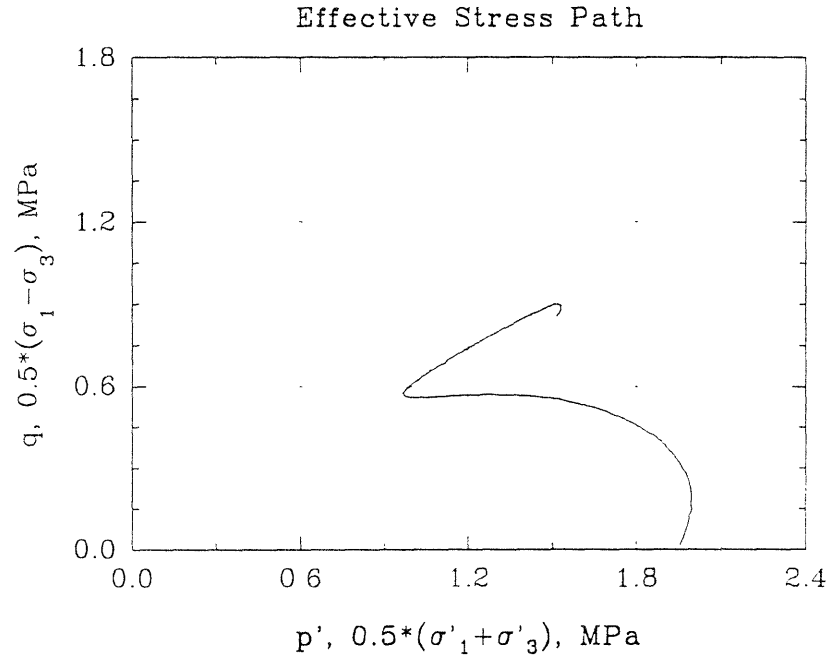

α' = 31.8 °
ϕ' = 38.2 °

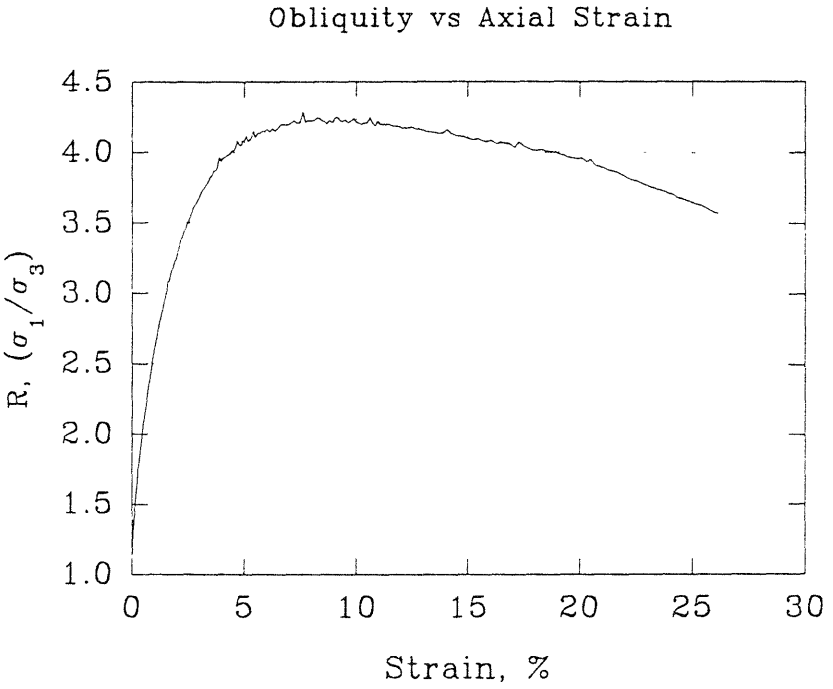

R_{max} = 3.96

Series C – Test #16

Deviator Stress and Excess
Pore Pressure vs Axial Strain

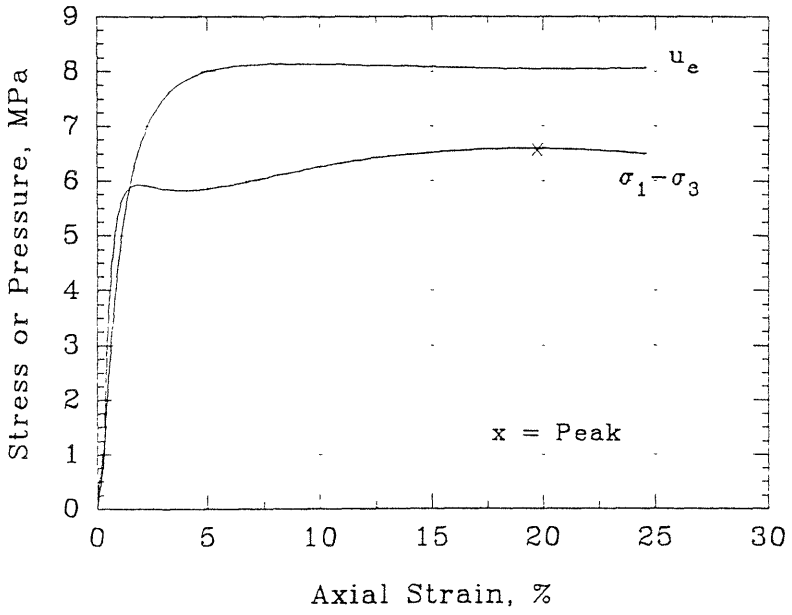

σ'_c = 10 MPa
e = 0.566
D_r = 104.3%

Q_p = 6.60 MPa
ε_p = 19.71 %

A–parameter vs Axial Strain

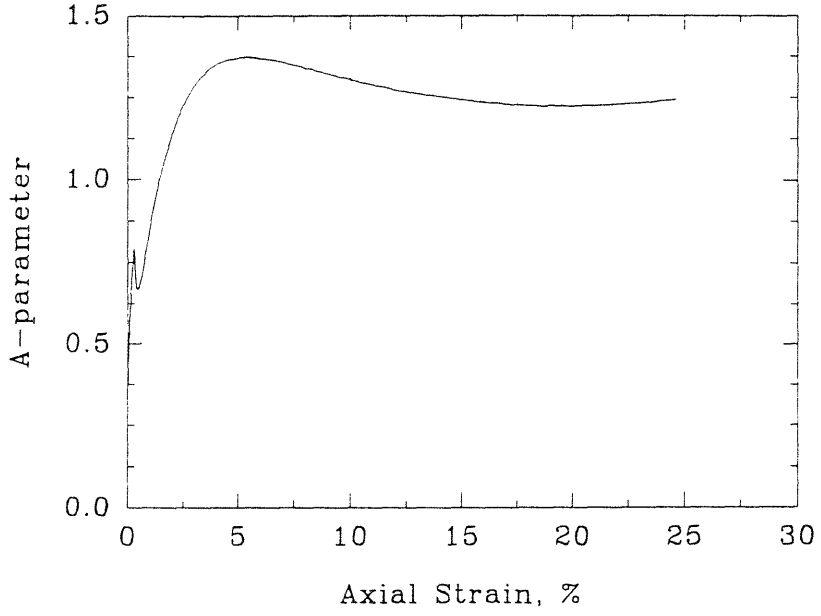

A_f = 1.223

Series C – Test #16

Effective Stress Path

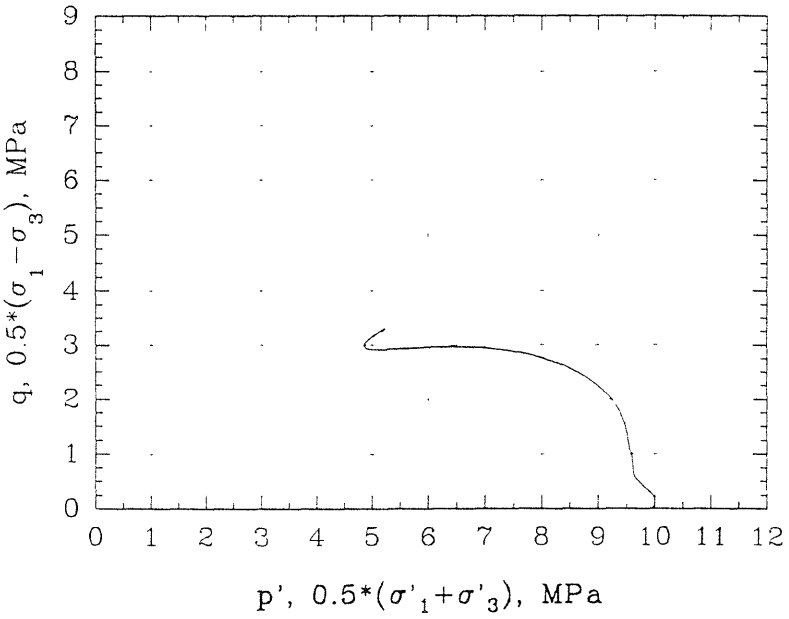

α' = 32.3 °
φ' = 39.2 °

Obliquity vs Axial Strain

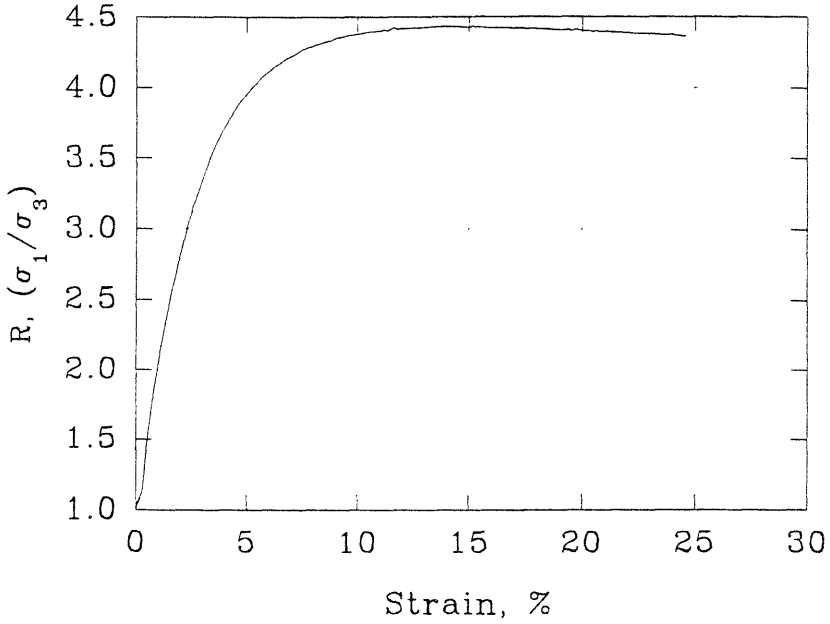

R_{max} = 4.43

Series C – Test #17

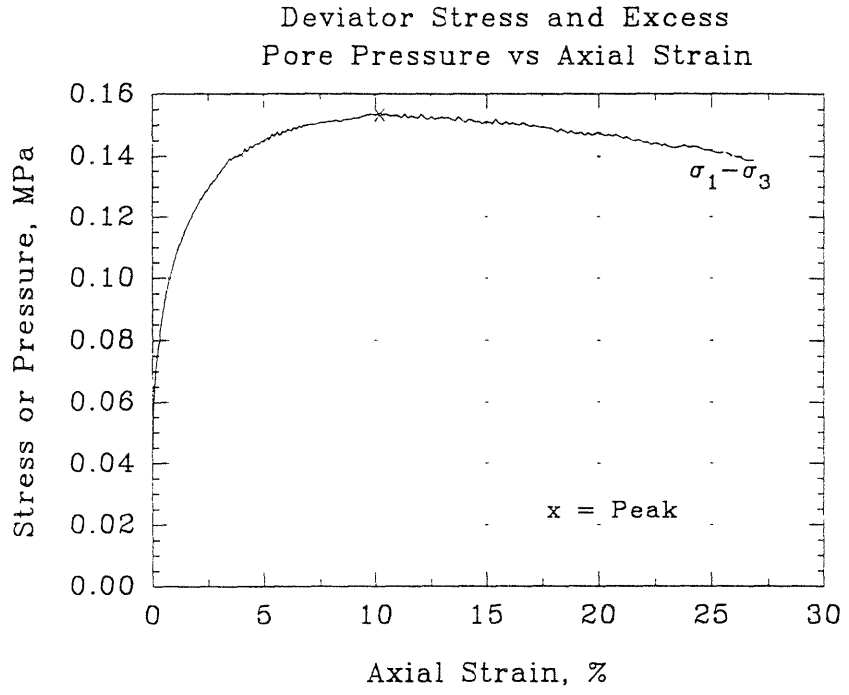

σ'_c = 0.1 MPa
e = 0.807
D_r = 31.0 %

Q_p = 0.15 MPa
ε_p = 10.18 %

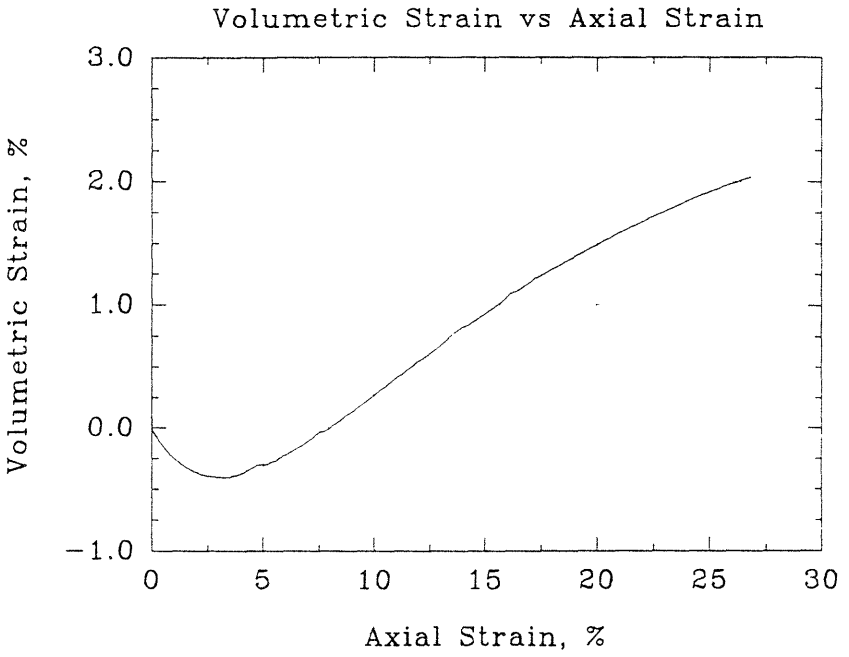

$\frac{d\varepsilon_v}{d\varepsilon_a}$ = 0.140

Series C – Test #17

Effective Stress Path

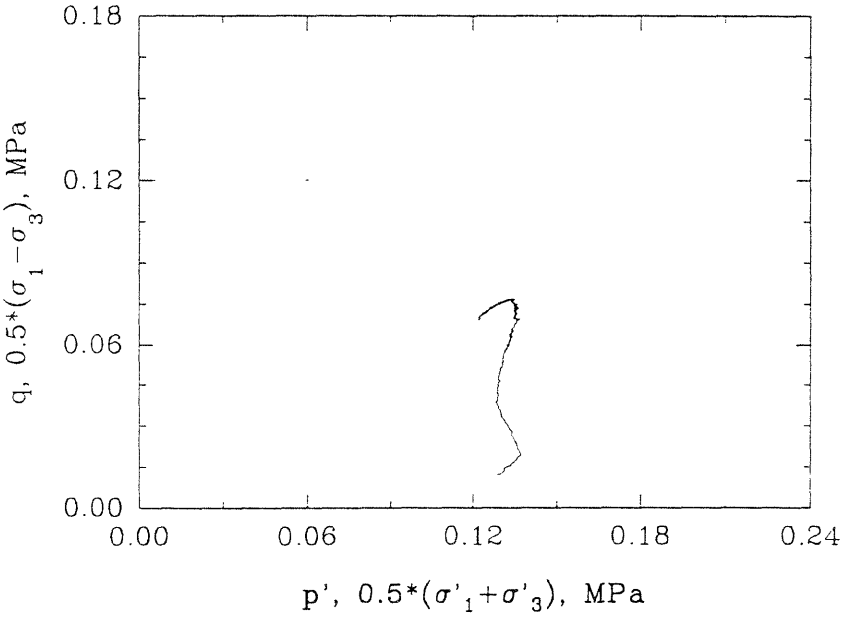

α' = 29.9 °
φ' = 35.0 °

Obliquity vs Axial Strain

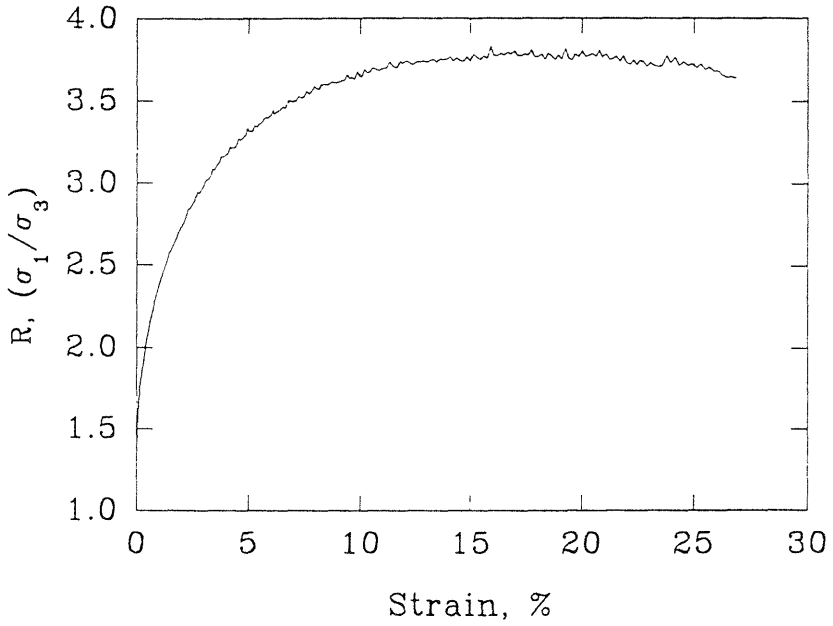

R_{max} = 3.69

Series C – Test #18

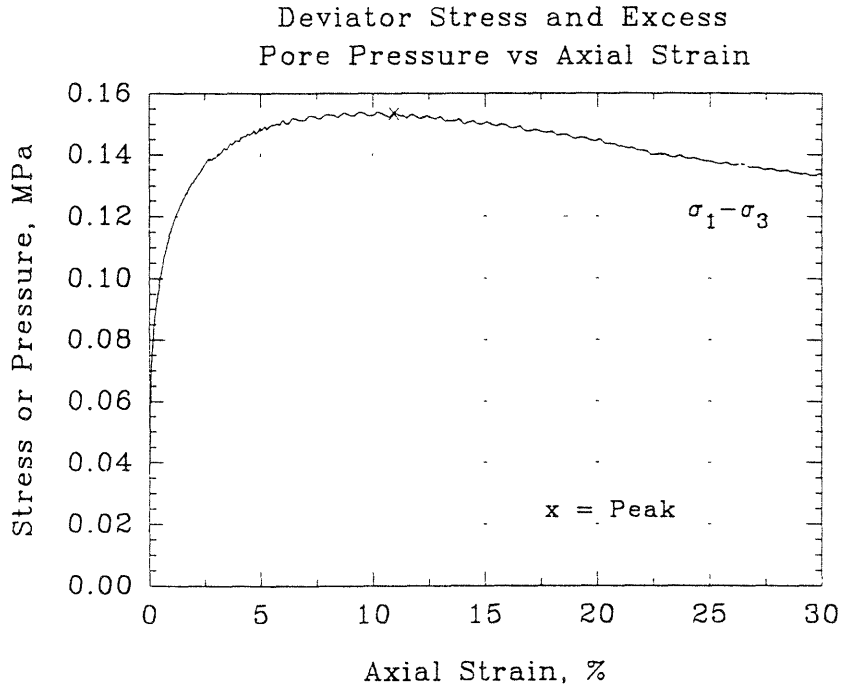

σ'_c = 0.1 MPa
e = 0.811
D_r = 29.8 %

Q_p = 0.15 MPa
ε_p = 10.20 %

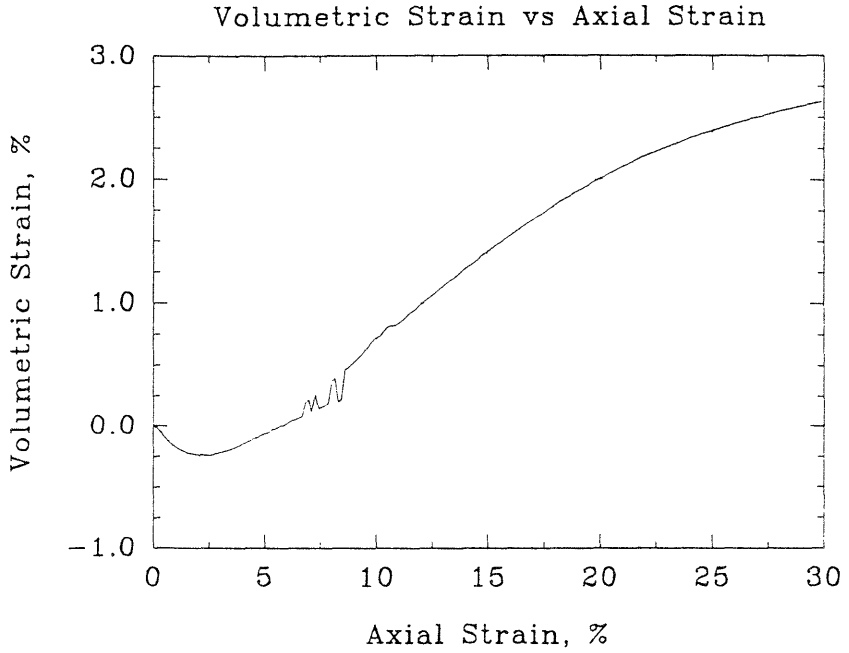

$\frac{d\varepsilon_v}{d\varepsilon_a}$ = 0.142

Series C – Test #18

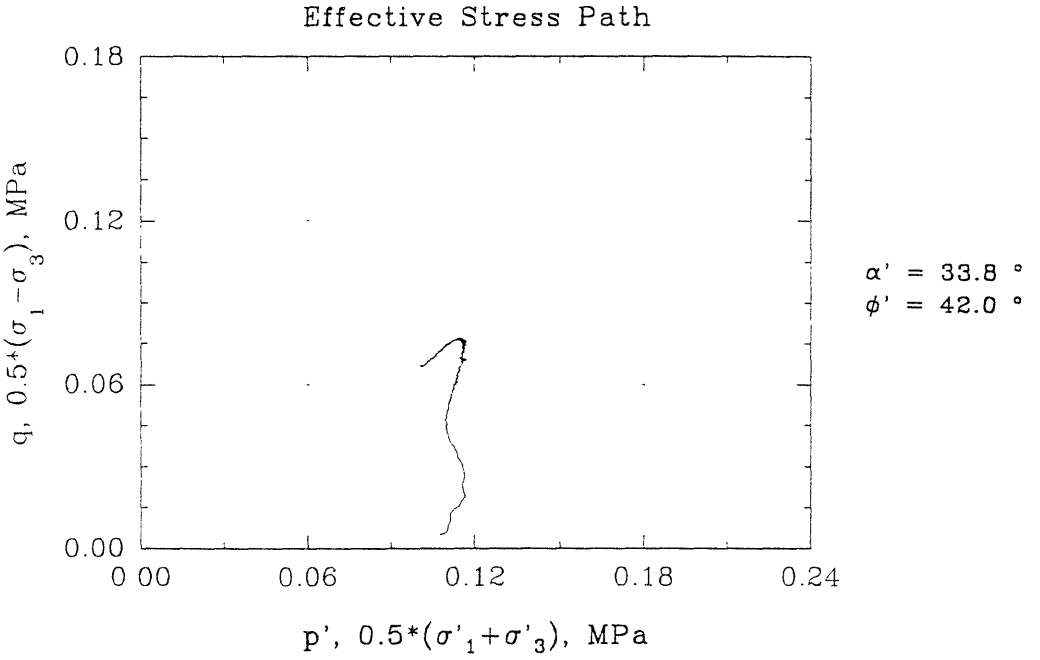

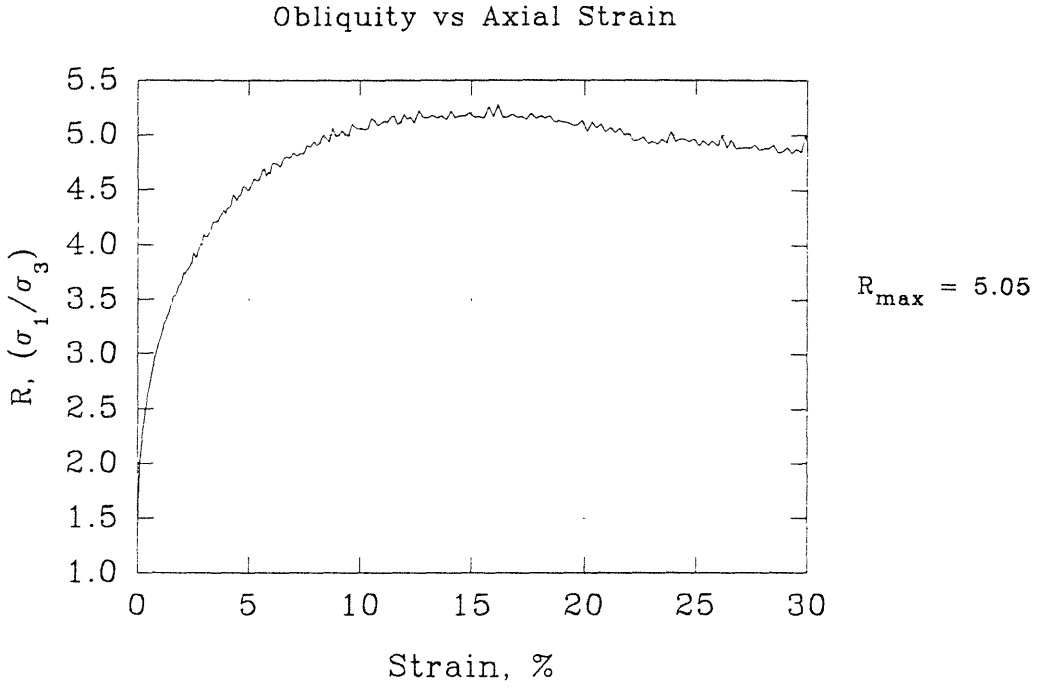

Series C – Test #19

Deviator Stress and Excess
Pore Pressure vs Axial Strain

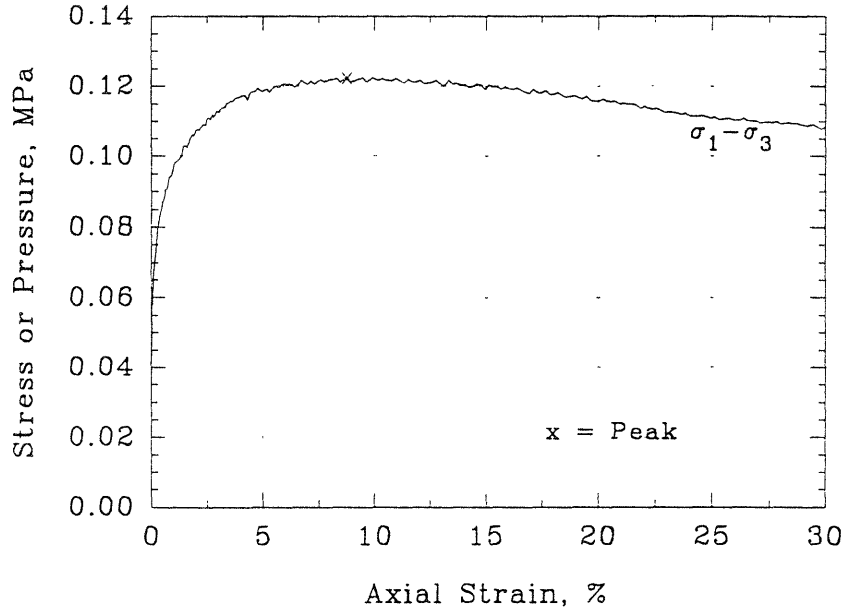

σ'_c = 0.1 MPa
e = 0.805
D_r = 31.7 %

Q_p = 0.12 MPa
ε_p = 8.77 %

Volumetric Strain vs Axial Strain

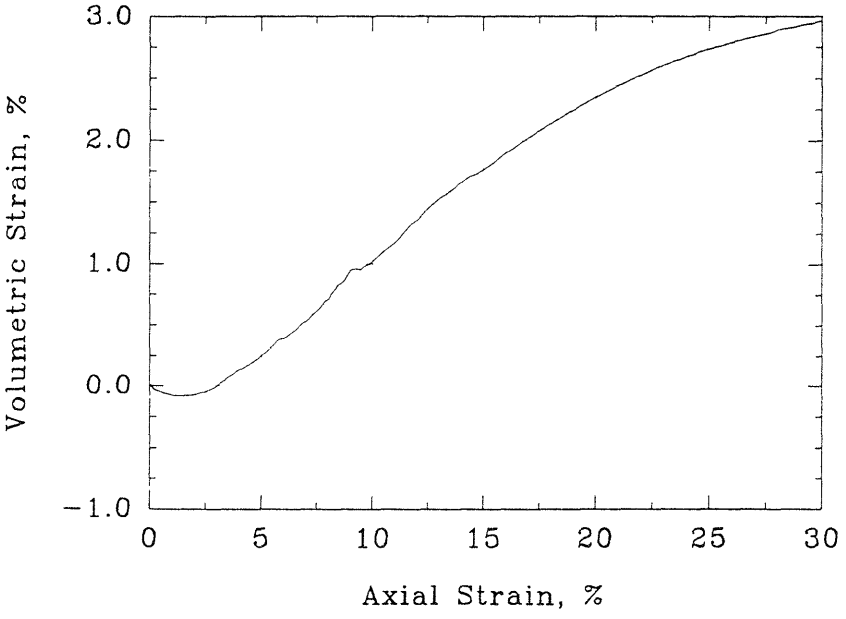

$\frac{d\varepsilon_v}{d\varepsilon_a}$ = 0.166

Series C – Test #19

Effective Stress Path

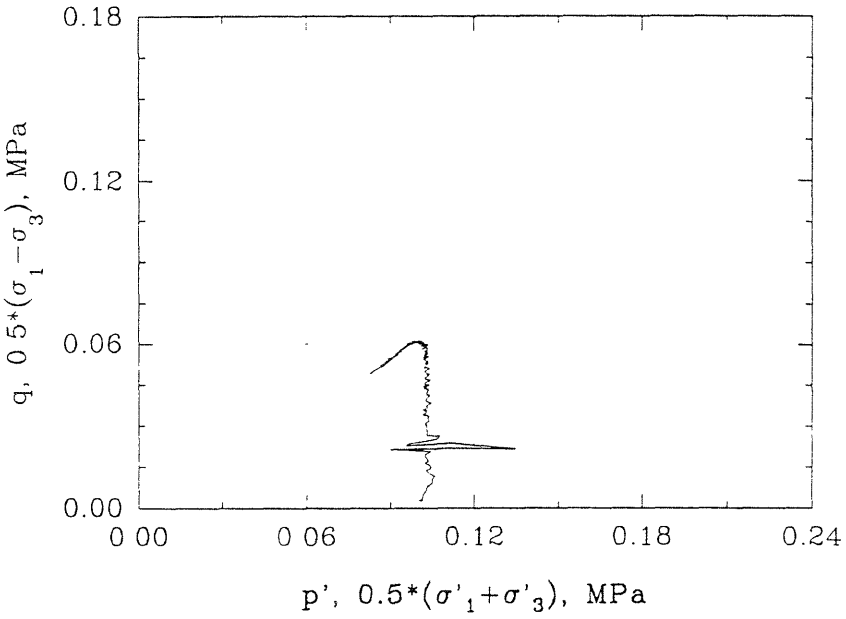

α' = 31.1 °
ϕ' = 37.5 °

Obliquity vs Axial Strain

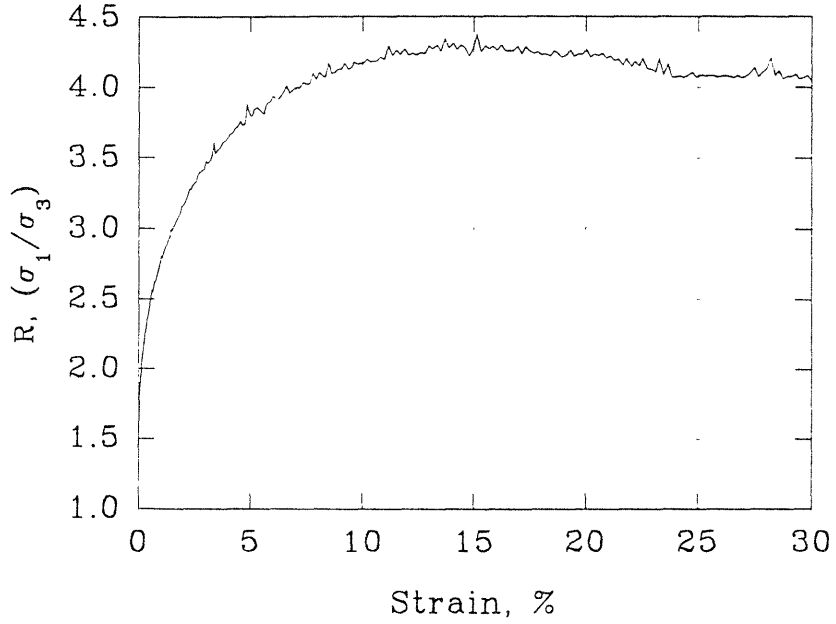

R_{max} = 4.11

Series C – Test #20

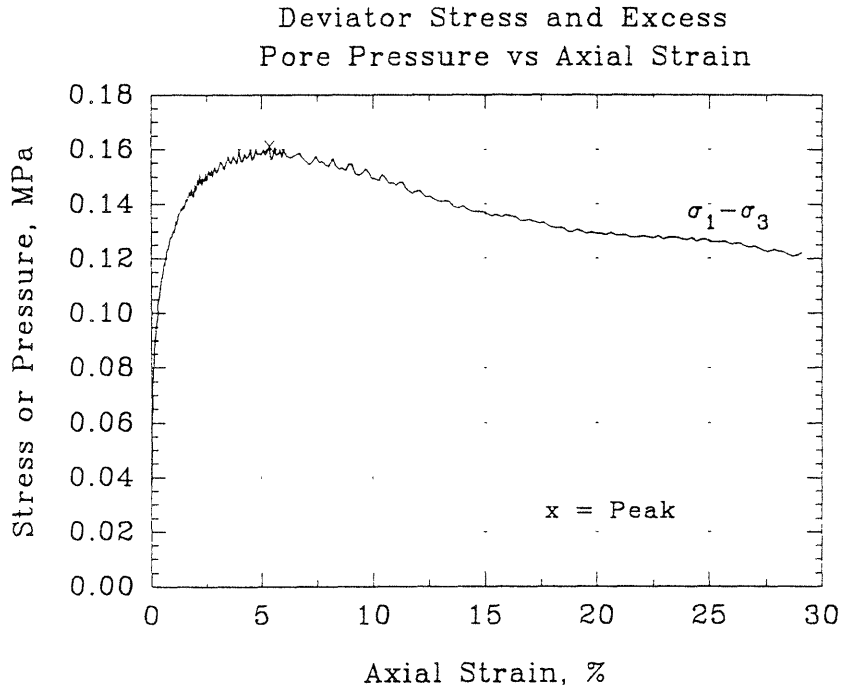

σ'_c = 0.1 MPa
e = 0.852
D_r = 78.2 %

Q_p = 0.16 MPa
ε_p = 8.77 %

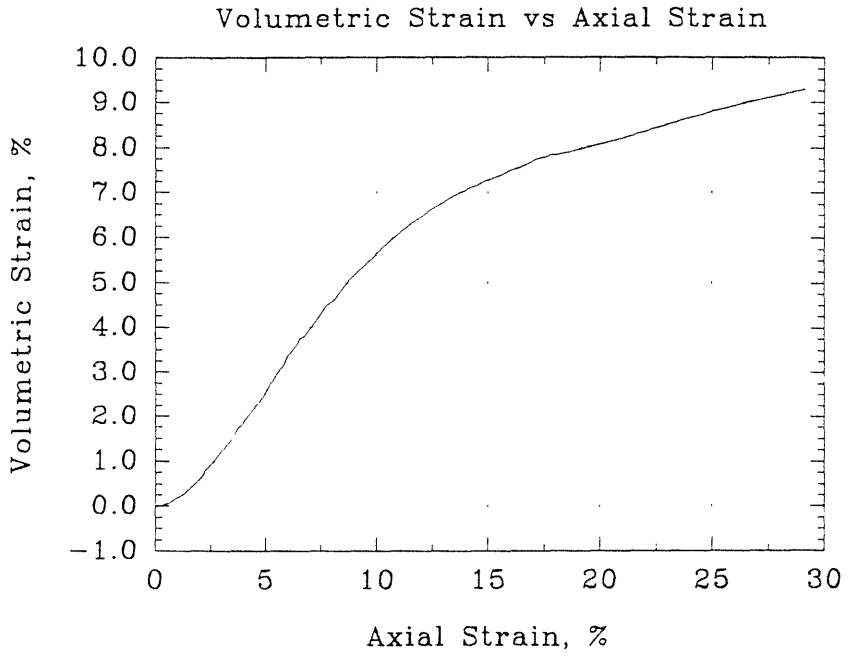

$\frac{d\varepsilon_v}{d\varepsilon_a}$ = 0.755

Series C – Test #20

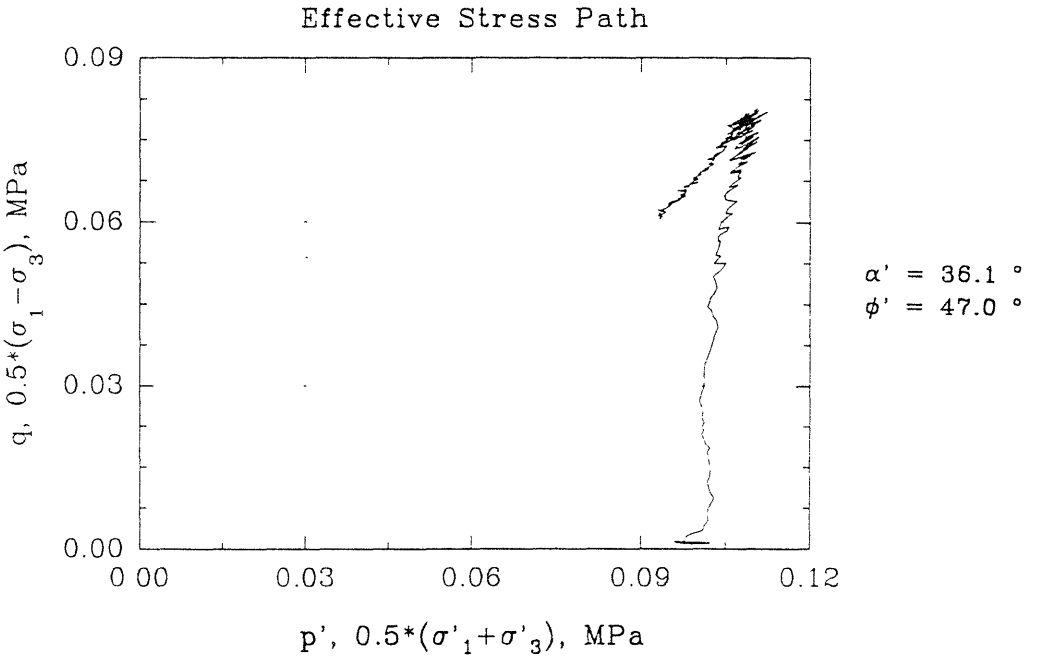

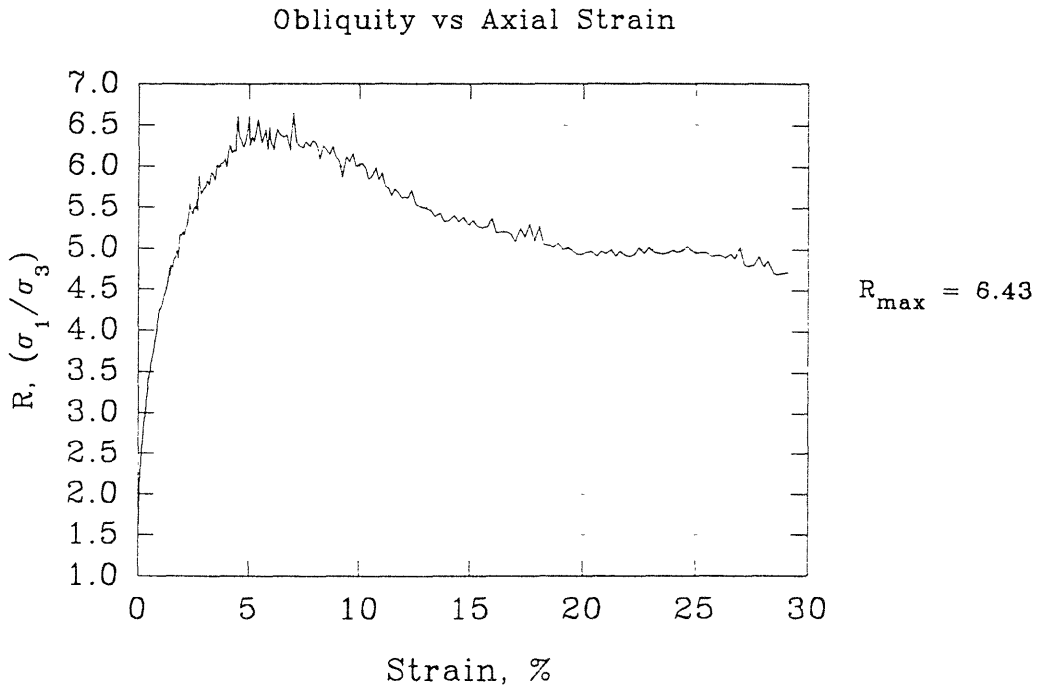

Series C – Test #21

Deviator Stress and Excess
Pore Pressure vs Axial Strain

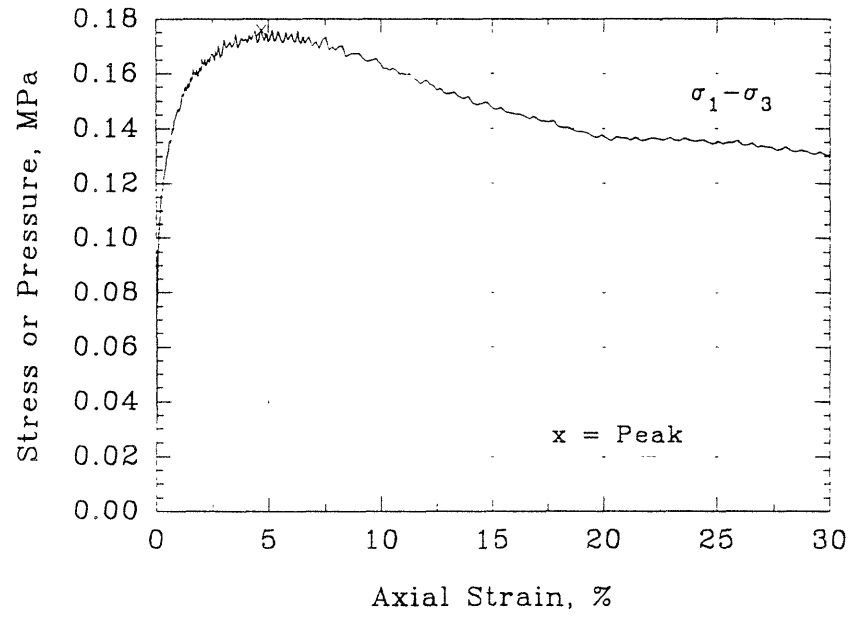

σ'_c = 0.1 MPa
e = 0.632
D_r = 84.3 %

Q_p = 0.17 MPa
ε_p = 4.74 %

Volumetric Strain vs Axial Strain

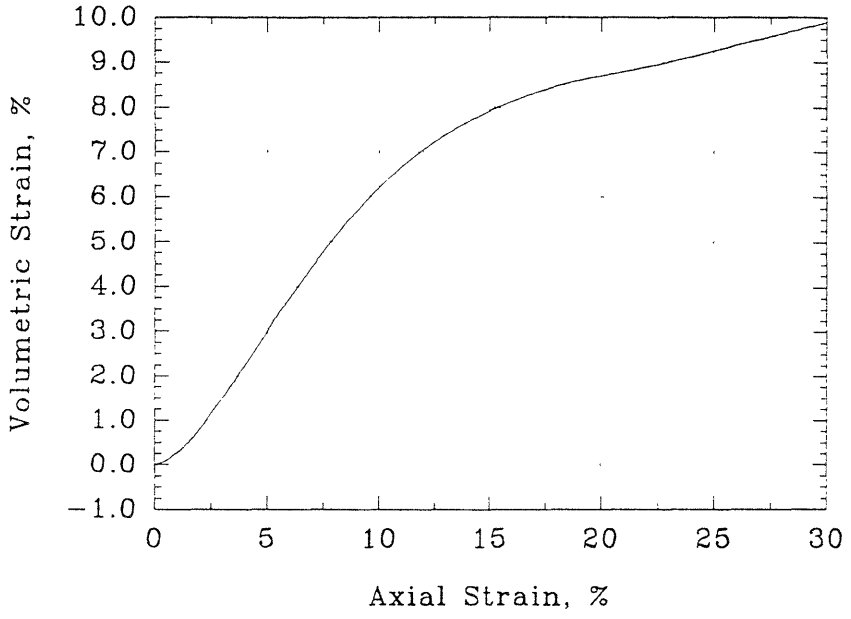

$\frac{d\varepsilon_v}{d\varepsilon_a}$ = 0.789

Series C – Test #21

Effective Stress Path

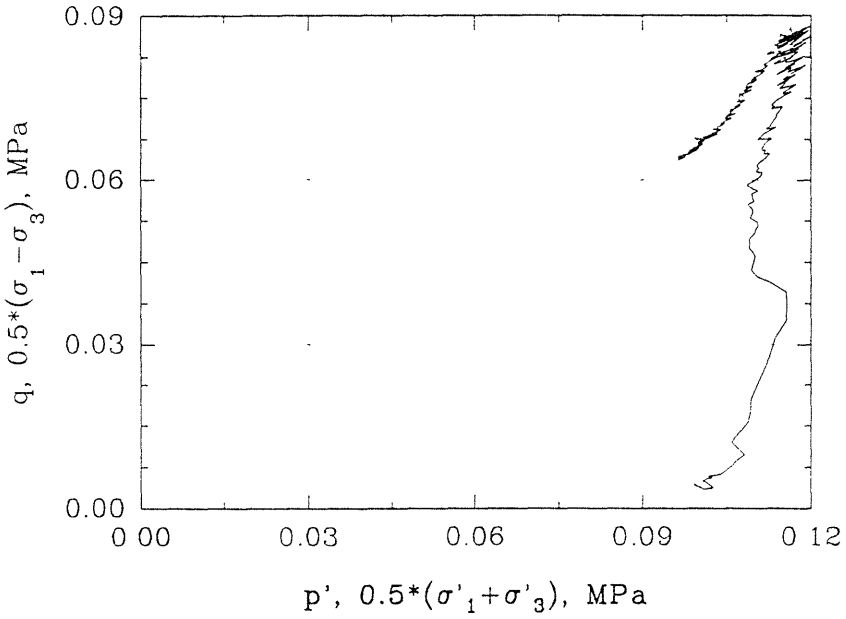

α' = 36.6 °
φ' = 48.0 °

Obliquity vs Axial Strain

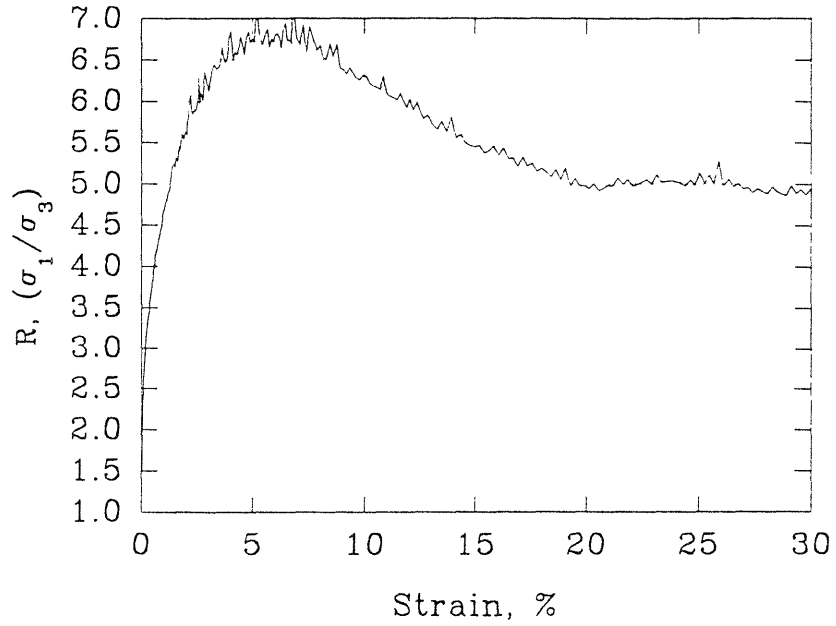

R_{max} = 6.78

Series C – Test #22

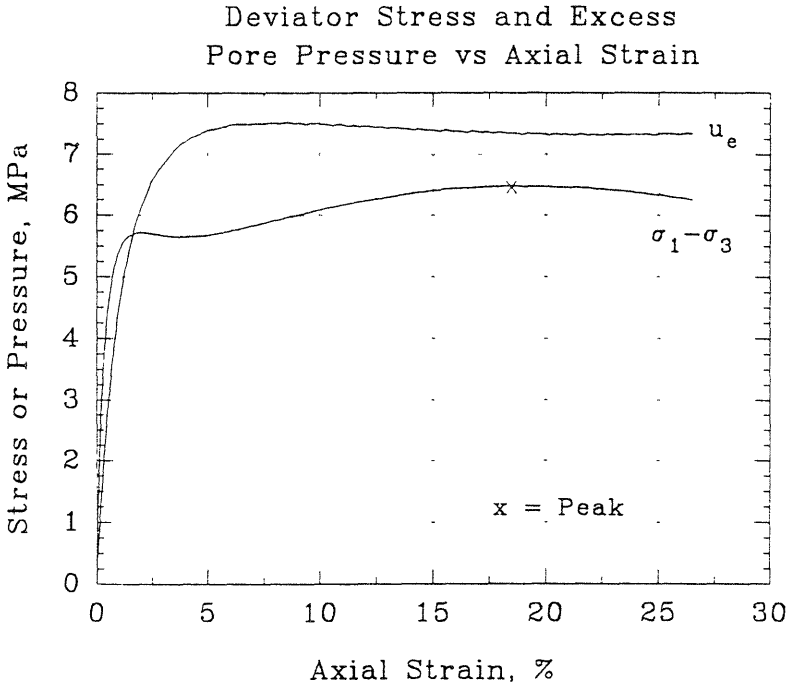

σ'_c = 10 MPa
e = 0.596
D_r = 95.2%

Q_p = 6.49 MPa
ε_p = 18.46 %

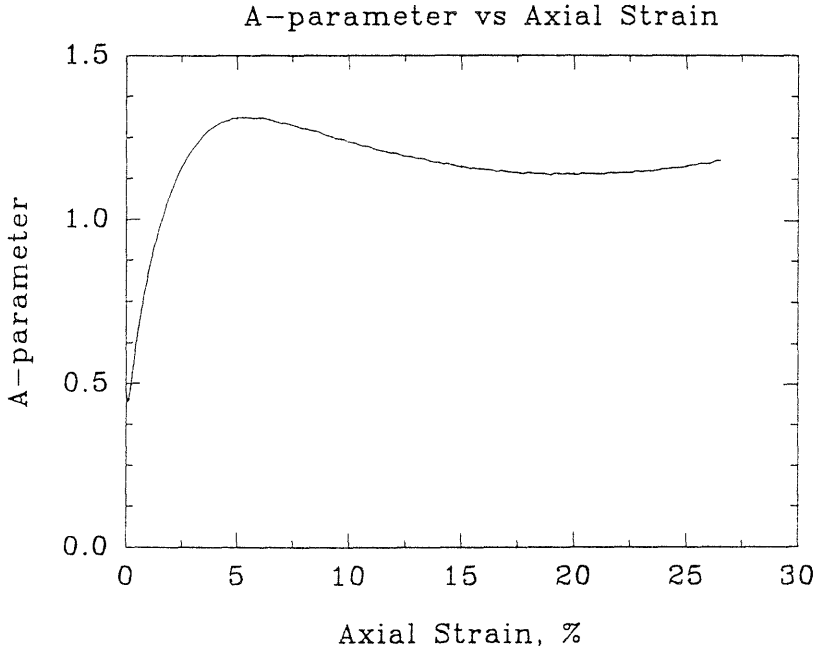

A_f = 1.140

Series C – Test #22

Effective Stress Path

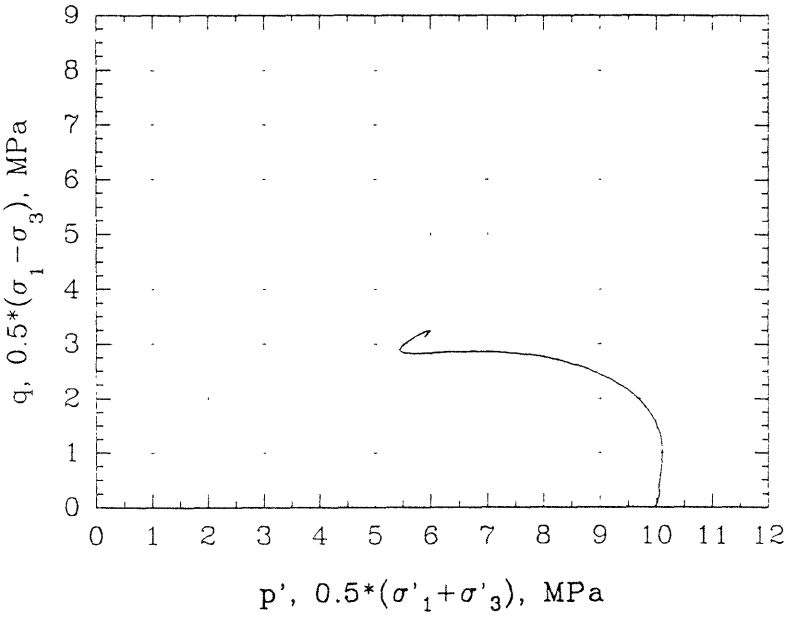

α' = 28.7 °
ϕ' = 33.3 °

Obliquity vs Axial Strain

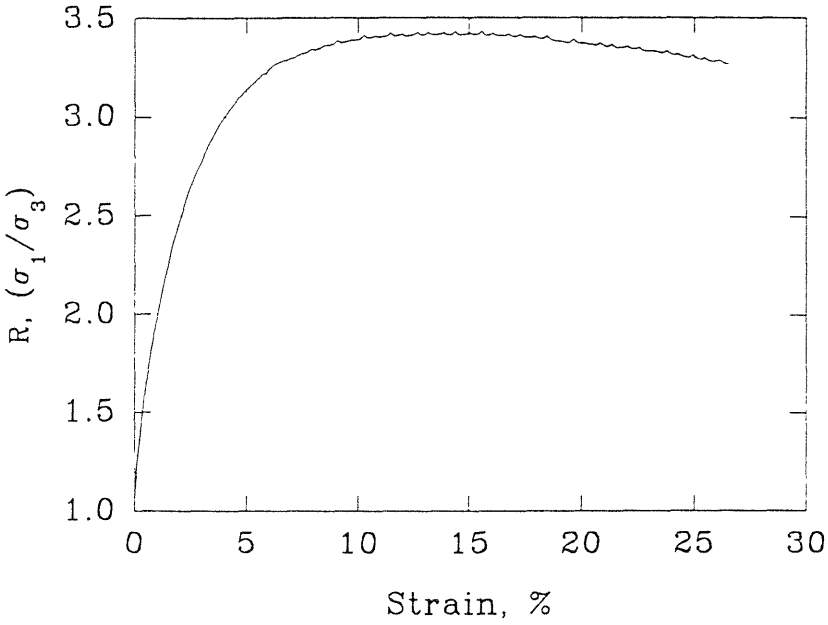

R_{max} = 3.43

Series C – Test #23

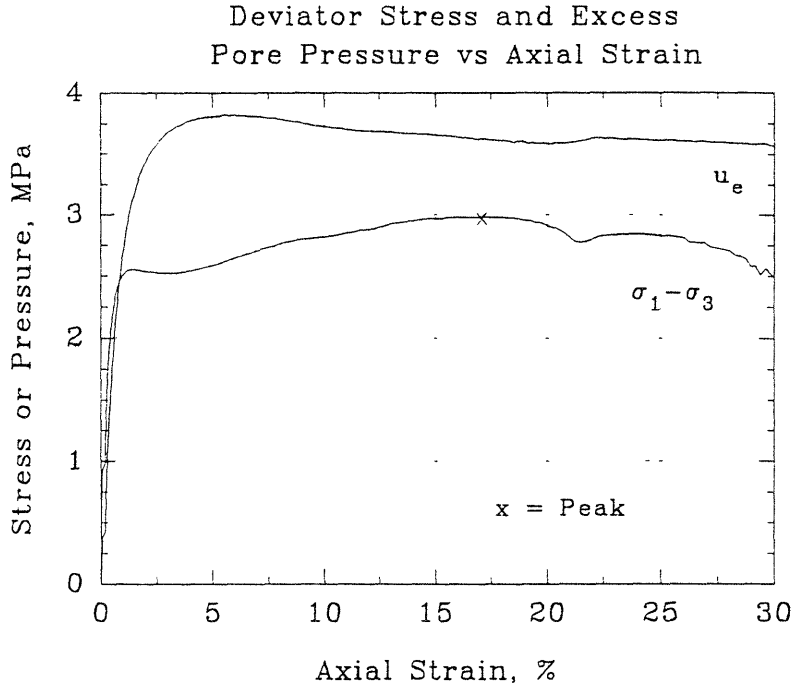

σ'_c = 5 MPa
e = 0.661
D_r = 75.4%

Q_p = 2.98 MPa
ε_p = 17.06 %

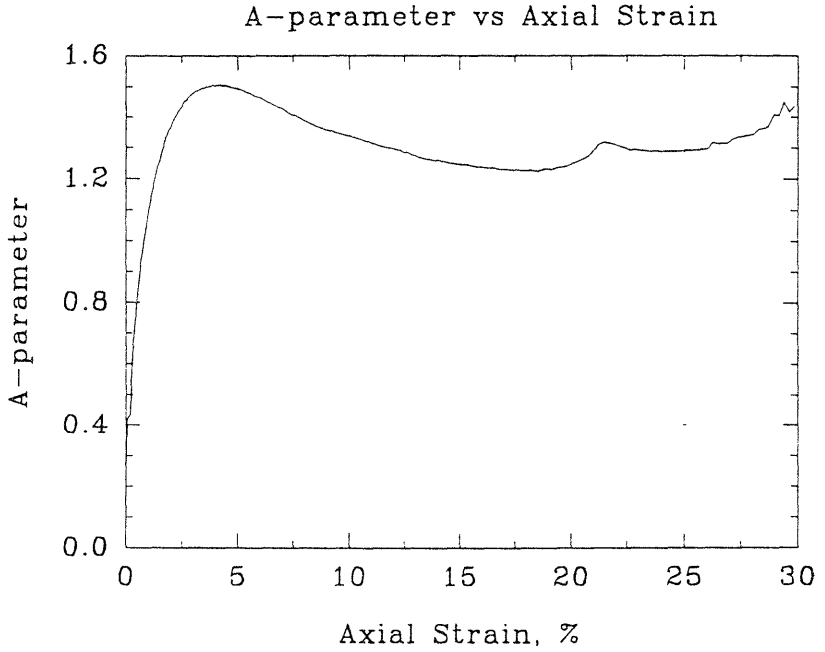

A_f = 1.228

Series C – Test #23

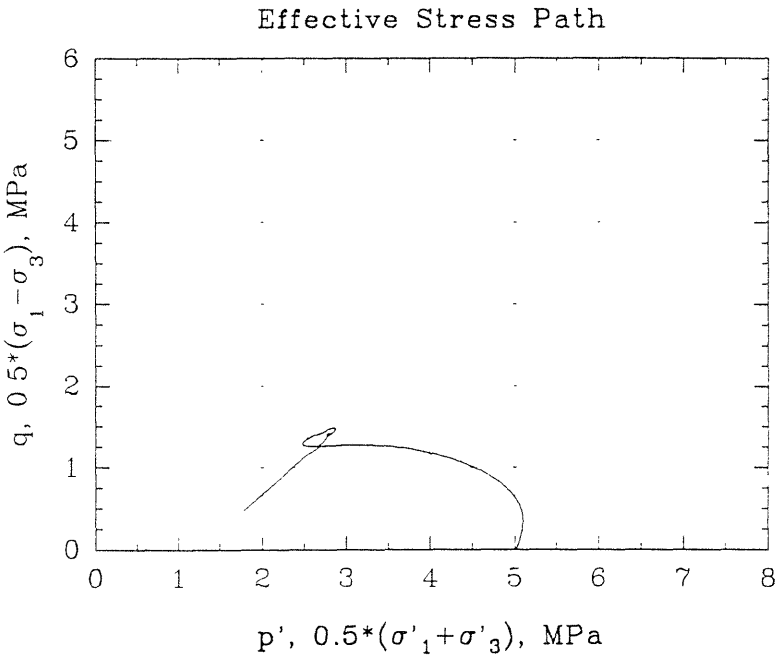

α' = 28.1 °
φ' = 32.3 °

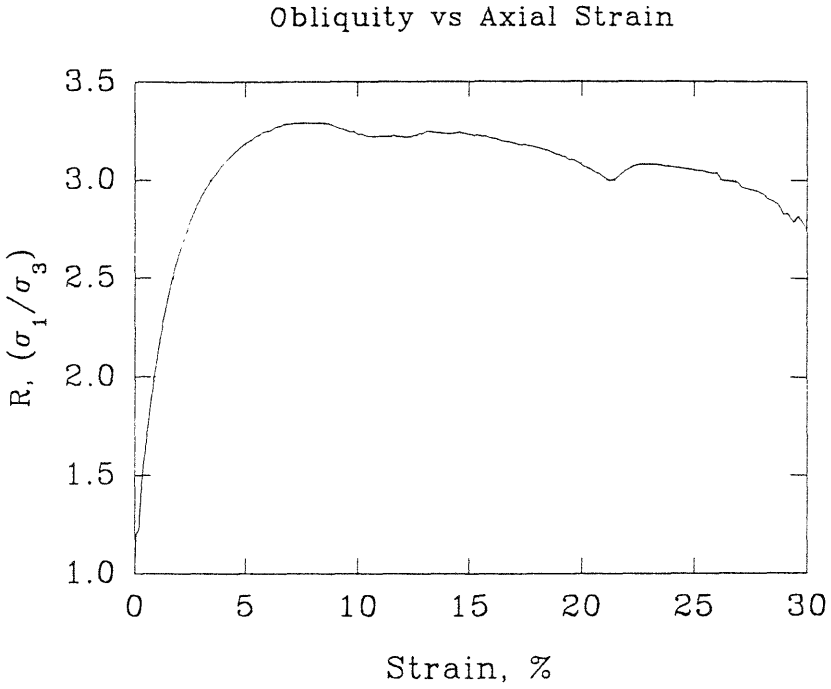

R_{max} = 3.29

Series C – Test #24

Deviator Stress and Excess
Pore Pressure vs Axial Strain

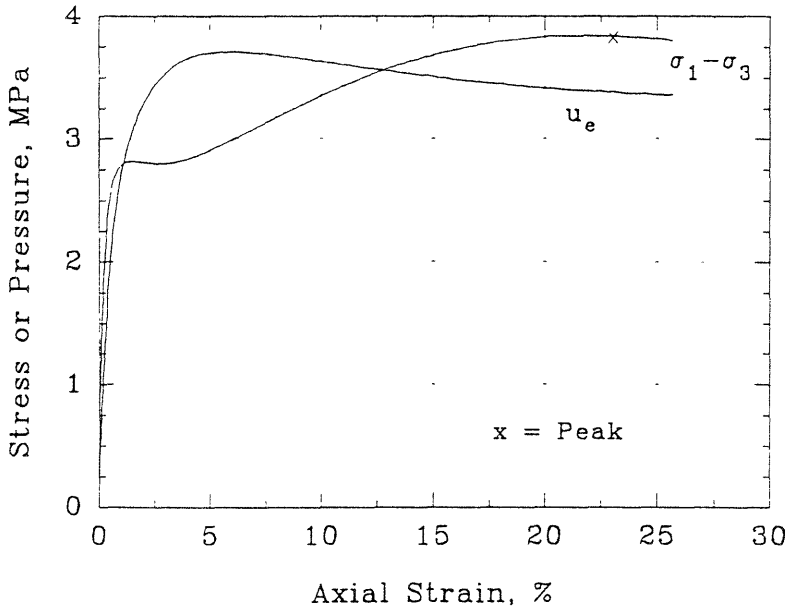

σ'_c = 5 MPa
e = 0.642
D_r = 81.2%

Q_p = 3.84 MPa
ε_p = 21.80 %

A-parameter vs Axial Strain

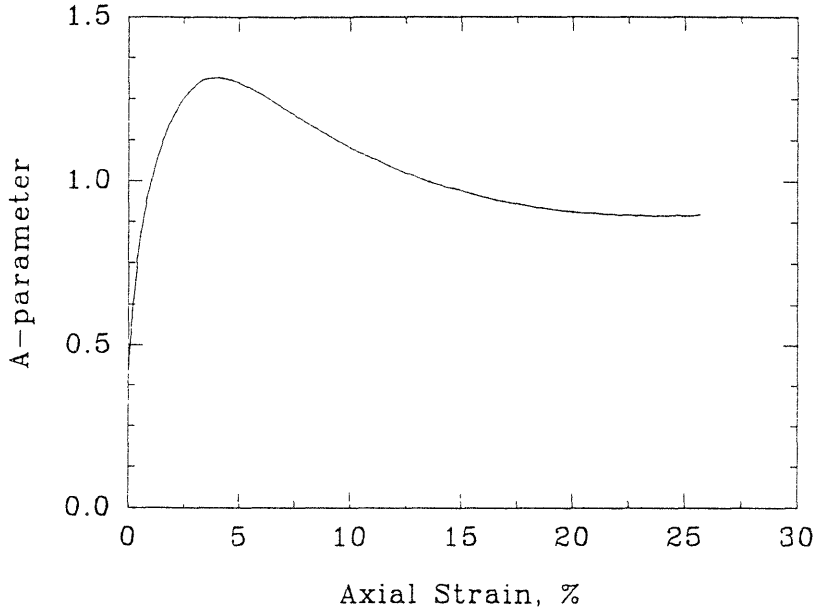

A_f = 0.897

Series C – Test #24

Effective Stress Path

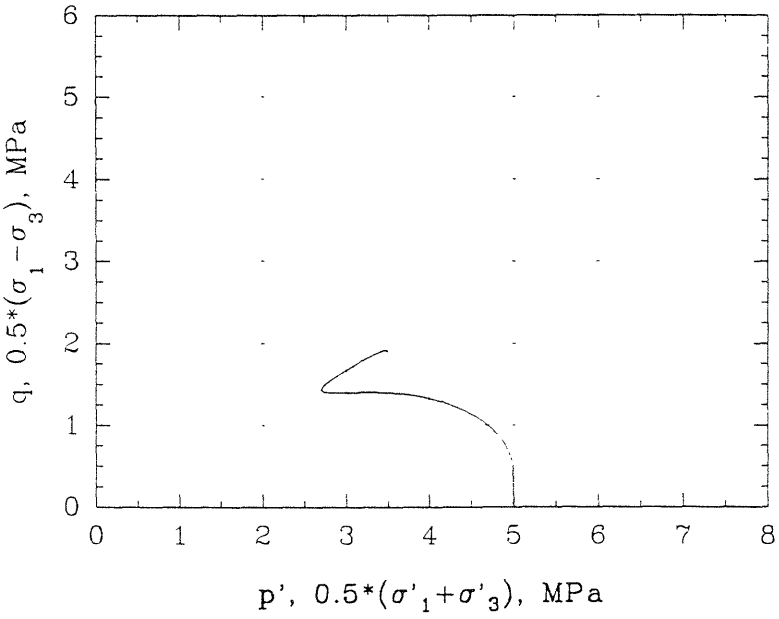

α' = 29.3 °
ϕ' = 34.1 °

Obliquity vs Axial Strain

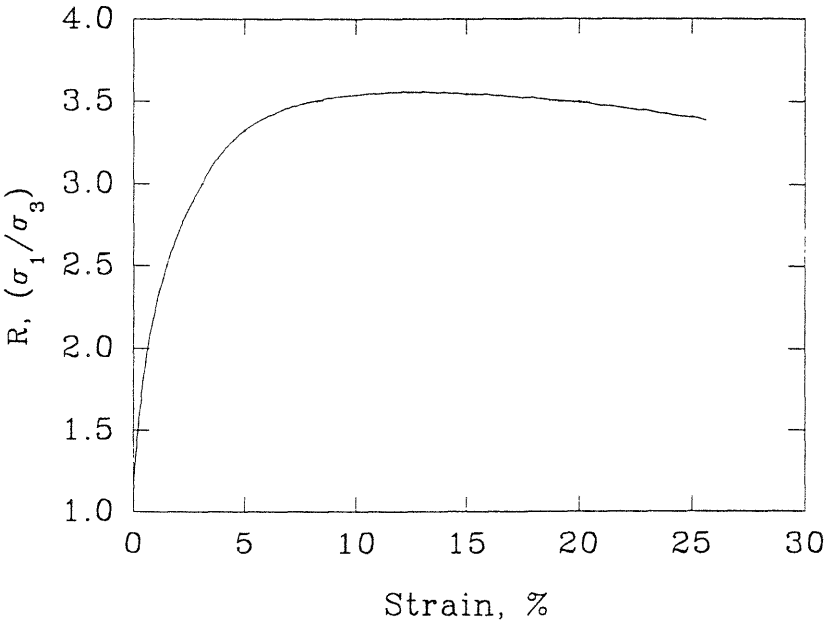

R_{max} = 3.56

Series C – Test #25

Effective Stress Path

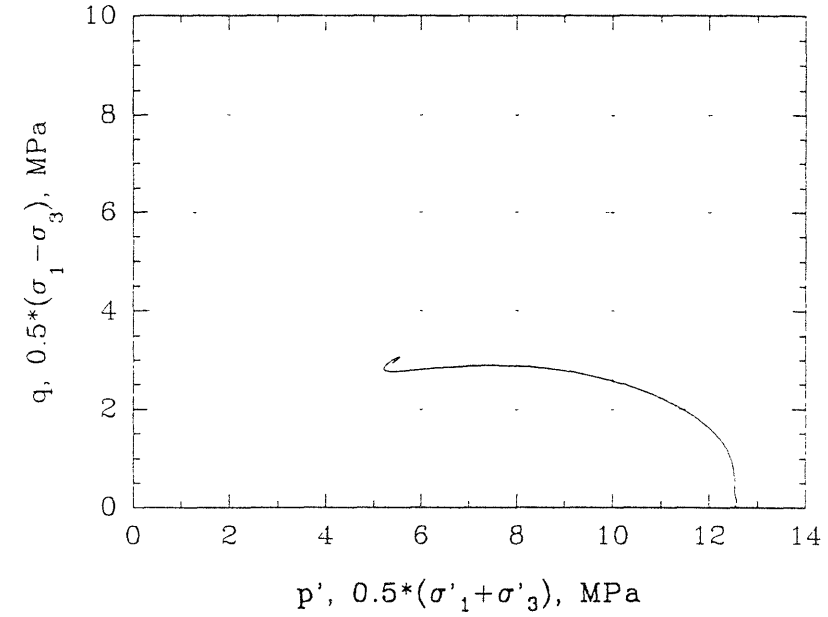

α' = 29.2 °
φ' = 33.9 °

Obliquity vs Axial Strain

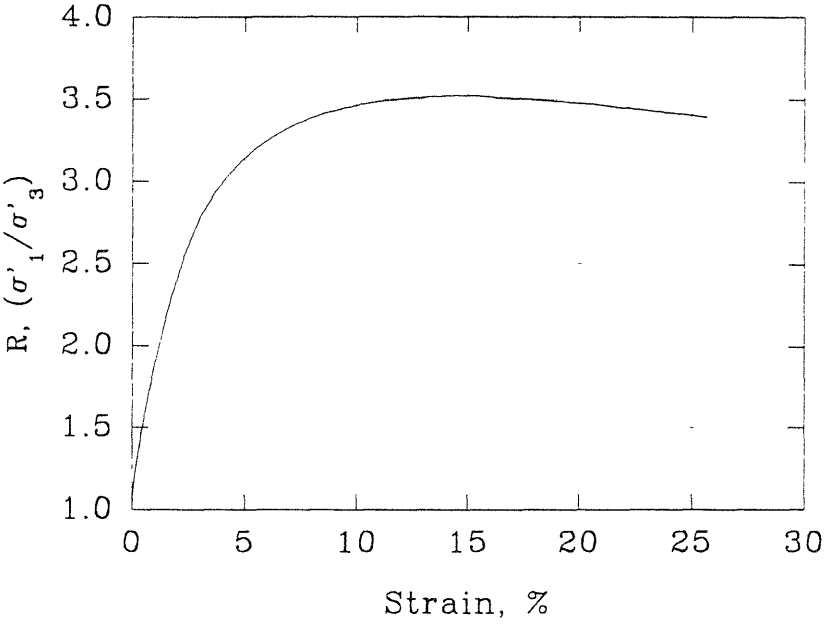

R_{max} = 3.52

Series C – Test #25

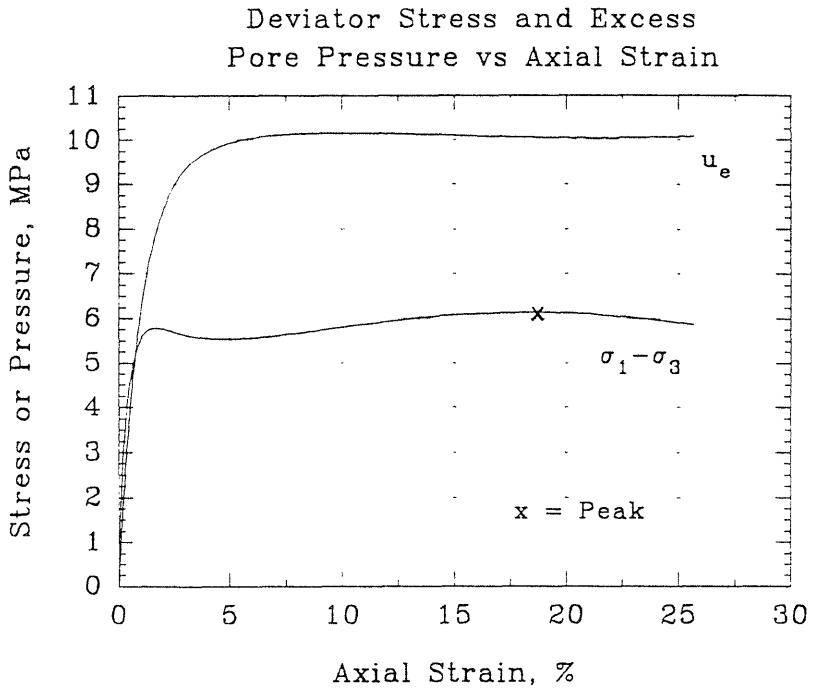

σ'_c = 12.5 MPa
e = 0.579
D_r = 100.4%

Q_p = 6.14 MPa
ε_p = 18.69 %

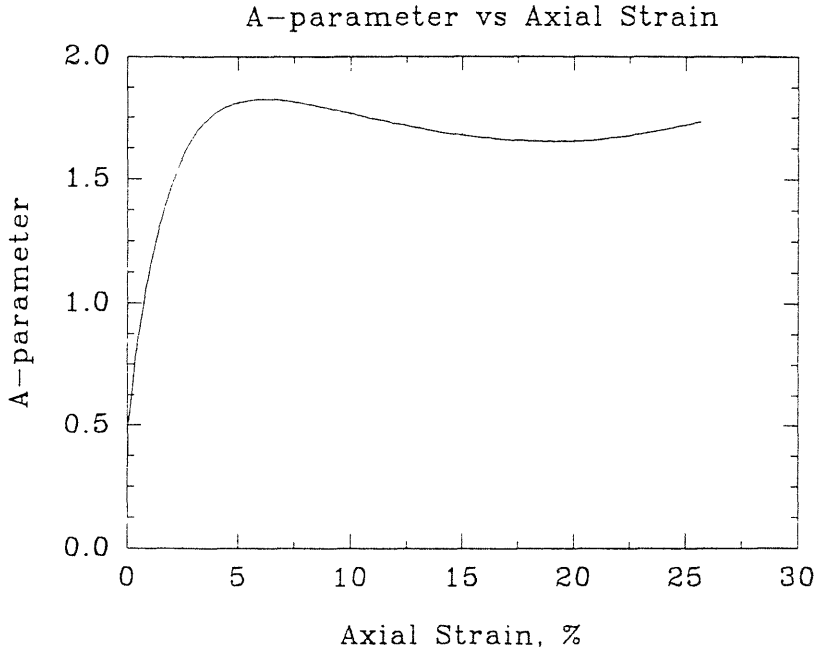

A_f = 1.652

Series C – Test #26

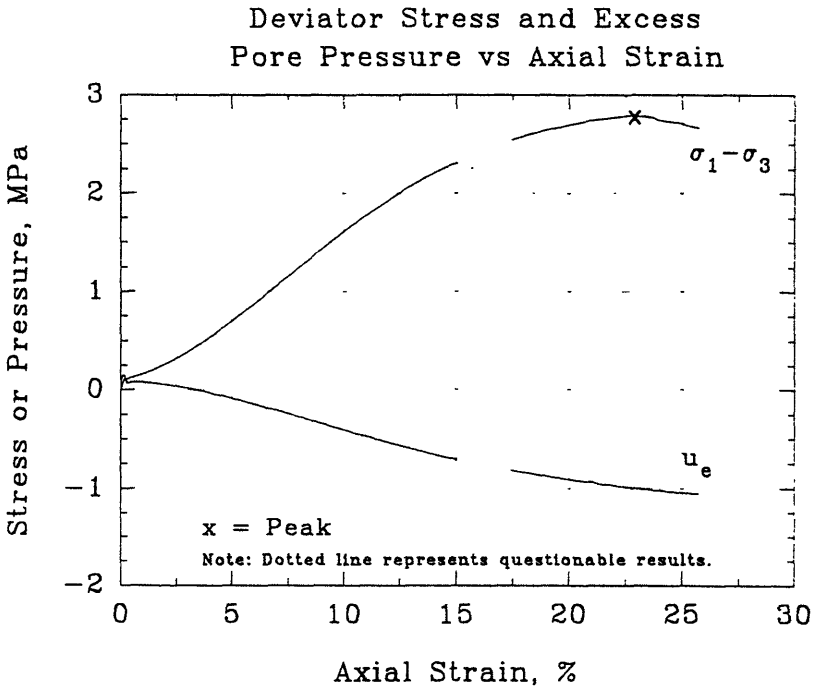

σ'_c = 0.1 MPa
e = 0.683
D_r = 68.7 %

Q_p = 2.79 MPa
ε_p = 22.83 %

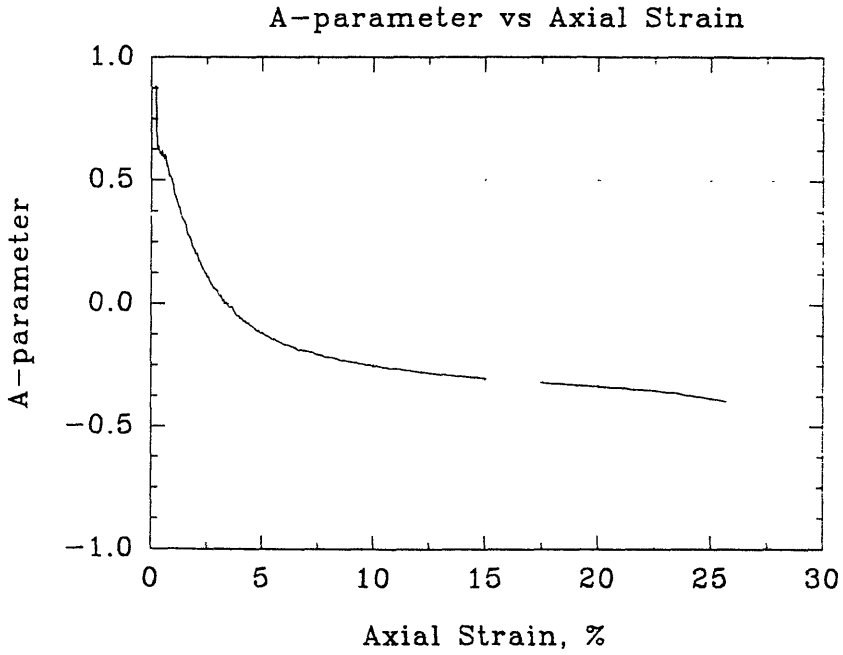

A_f = −0.357

Series C – Test #26

Effective Stress Path

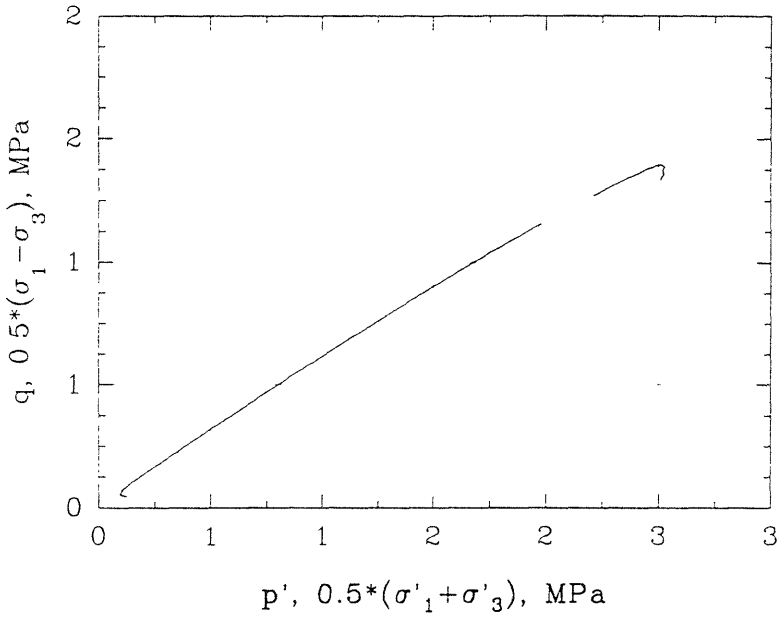

α' = 34.7 °
φ' = 44.1 °

Obliquity vs Axial Strain

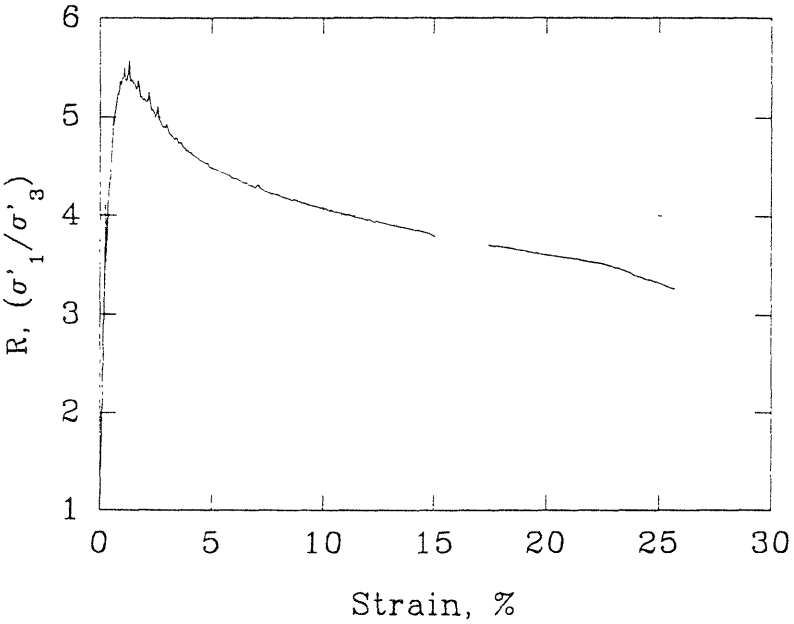

R_{max} = 5.57

Series C – Test #27

Deviator Stress and Excess
Pore Pressure vs Axial Strain

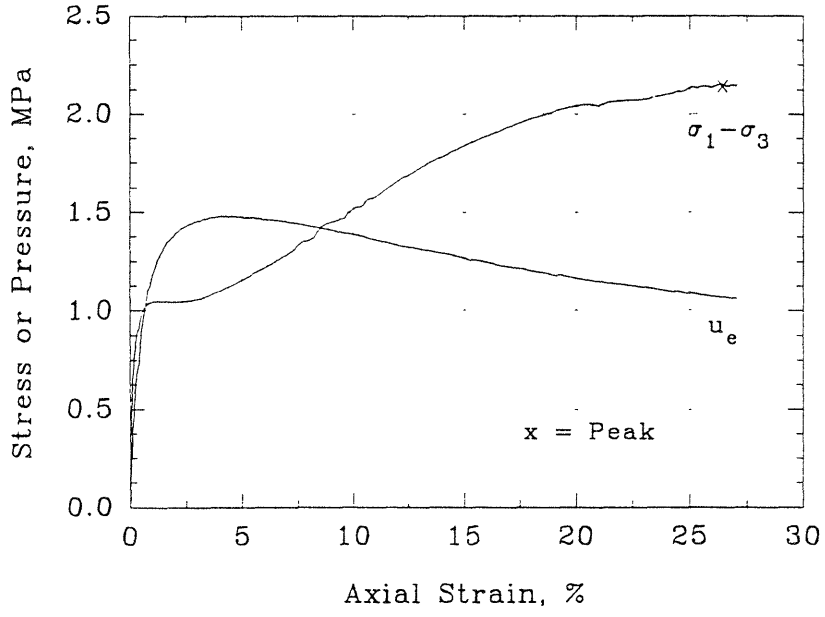

σ'_c = 2 MPa
e = 0.700
D_r = 63.7%

Q_p = 2.15 MPa
ε_p = 26.40 %

A–parameter vs Axial Strain

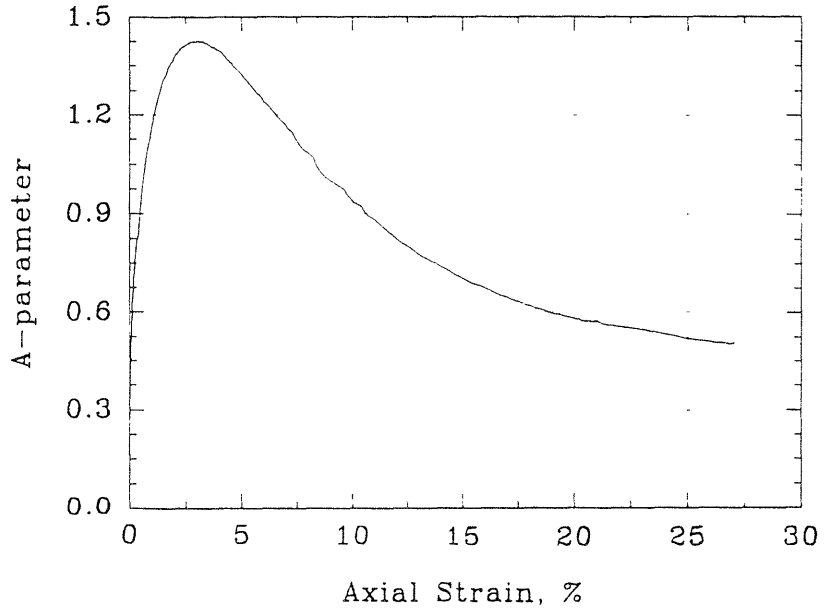

A_f = 0.506

Series C – Test #27

Effective Stress Path

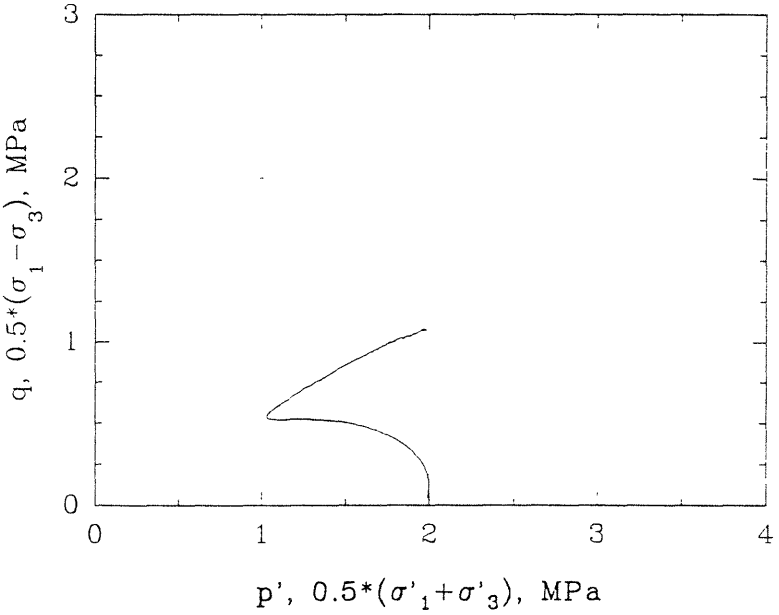

α' = 29.7 °
φ' = 34.8 °

Obliquity vs Axial Strain

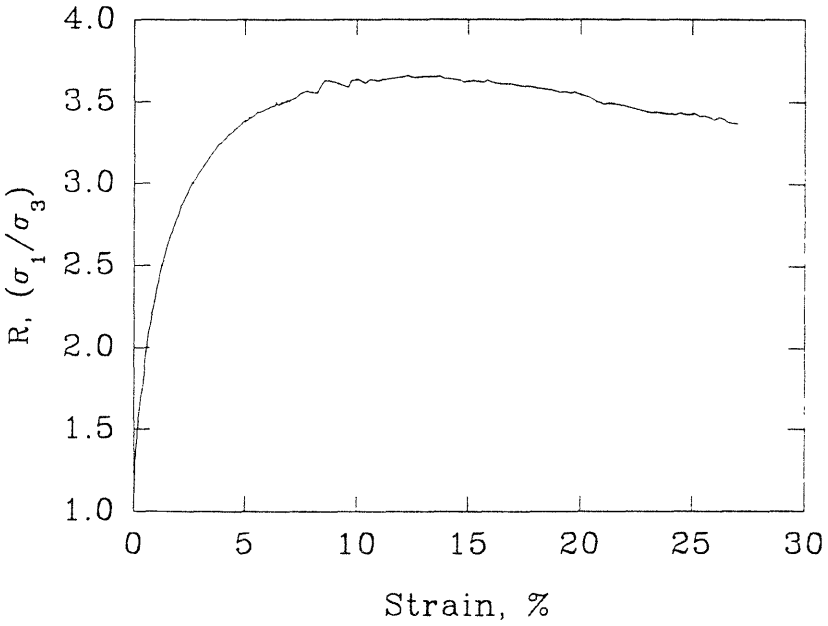

R_{max} = 3.66

Series C – Test #28

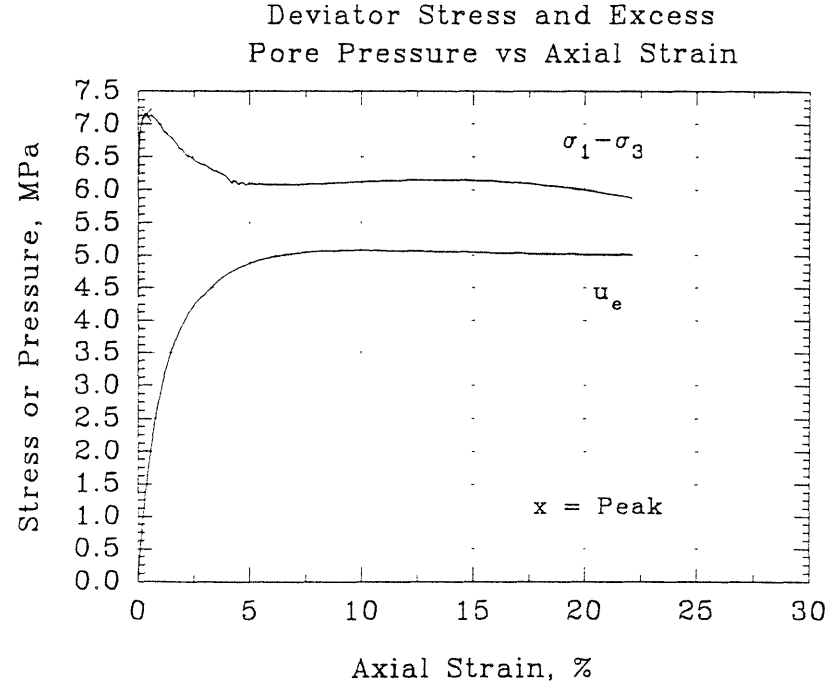

σ'_c = 7.5 MPa
e = 0.606
D_r = 92.2%

Q_p = 7.16 MPa
ε_p = 0.34 %

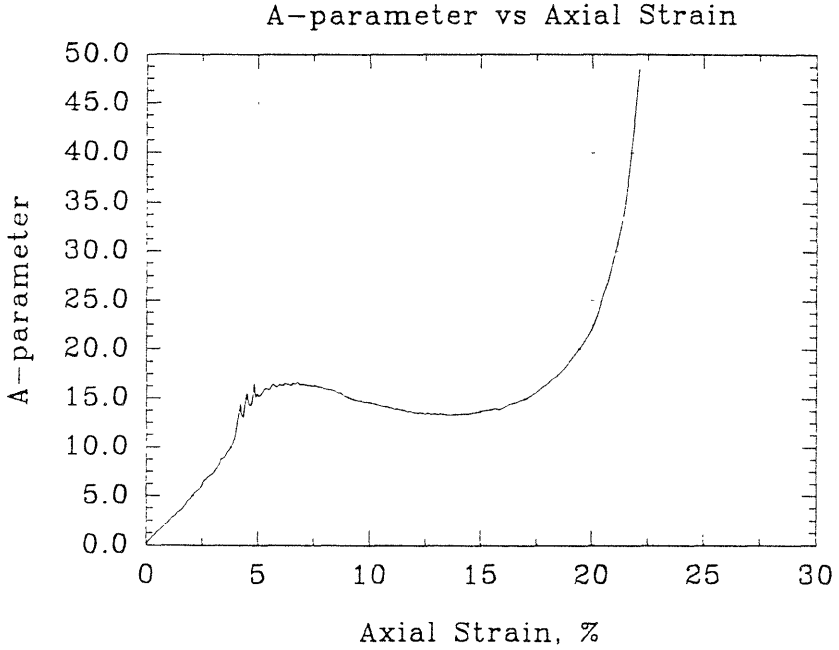

A_f = 0.981

Series C – Test #28

Effective Stress Path

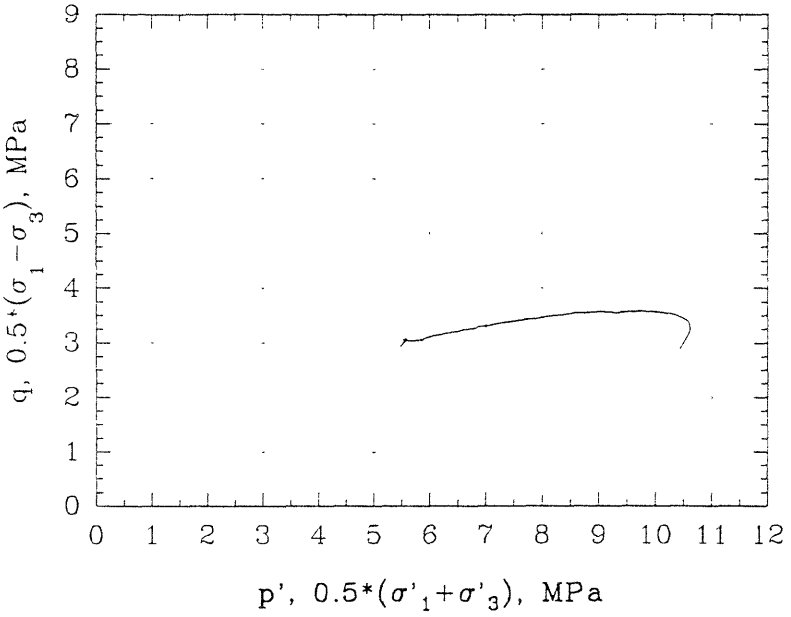

α' = 29.0 °
φ' = 33.6 °

Obliquity vs Axial Strain

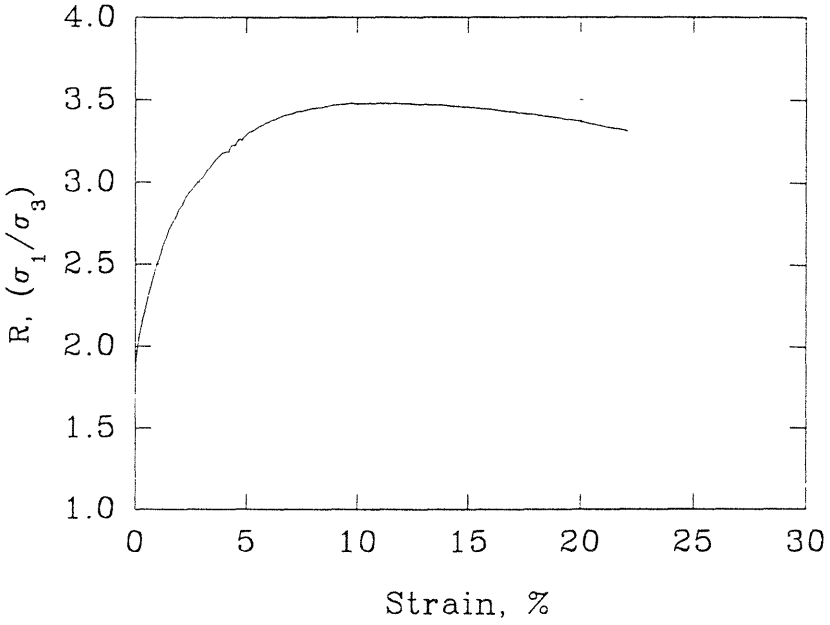

R_{max} = 3.48

Series C – Test #29

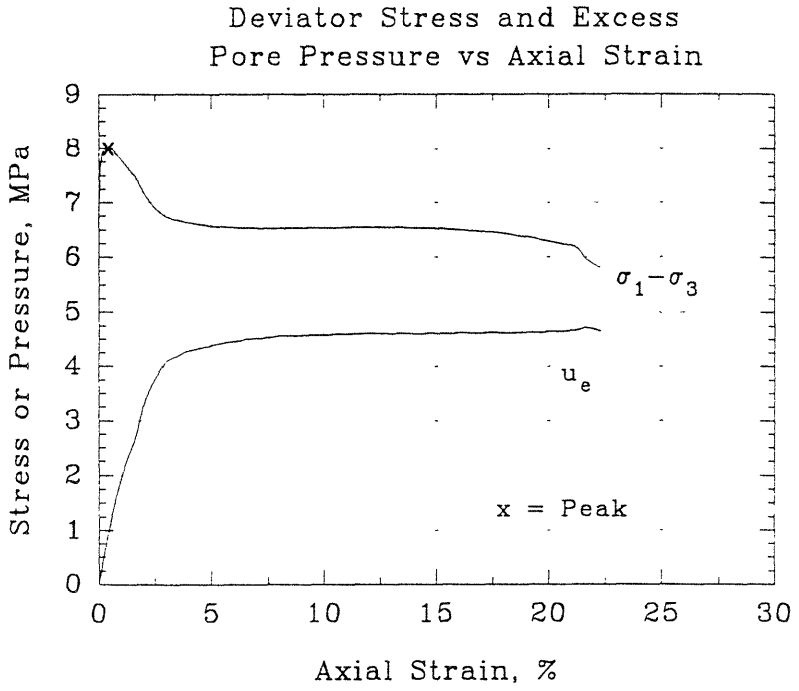

σ'_c = 7 MPa
e = 0.585
D_r = 98.5%

Q_p = 8.03 MPa
ε_p = 0.39 %

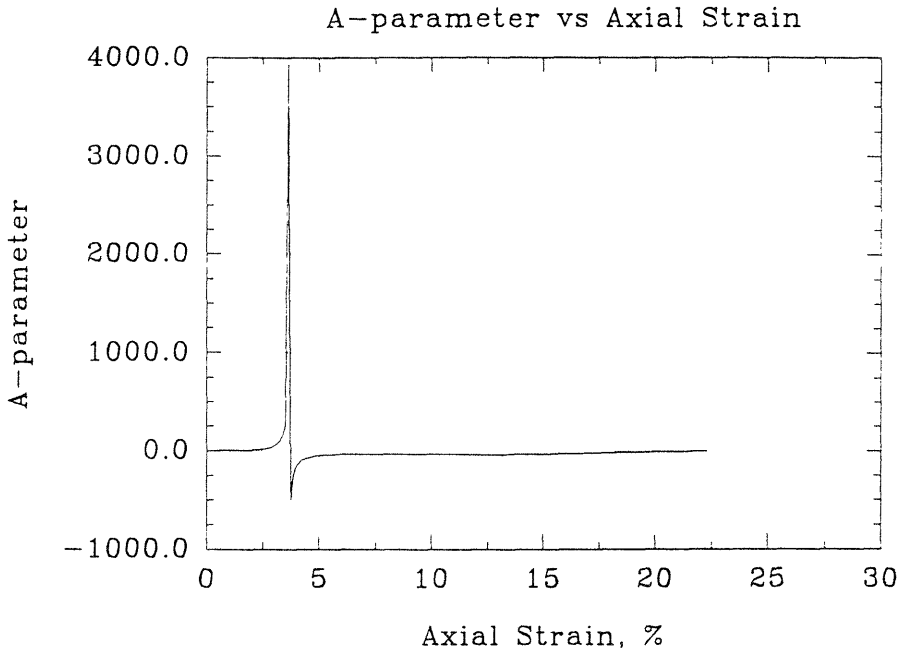

A_f = 0.650

Series C – Test #29

Effective Stress Path

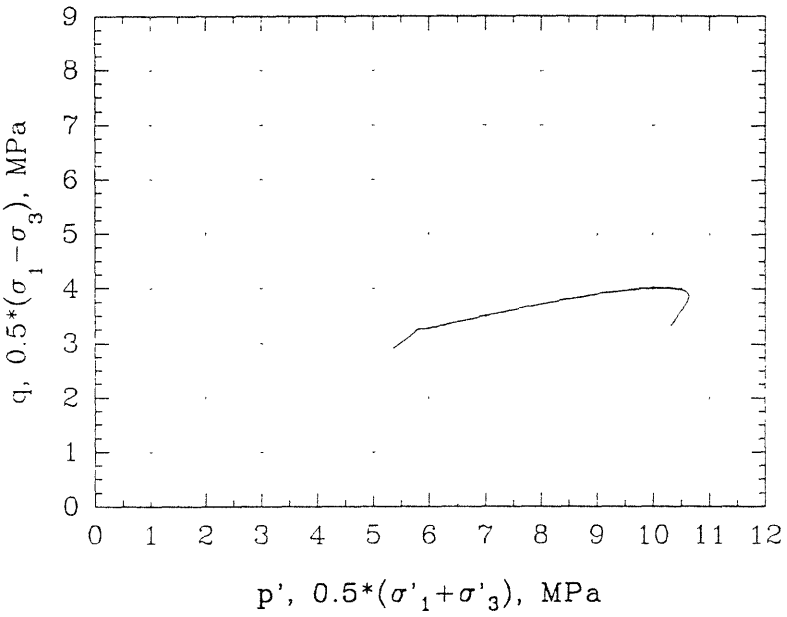

α' = 29.4 °
φ' = 34.3 °

Obliquity vs Axial Strain

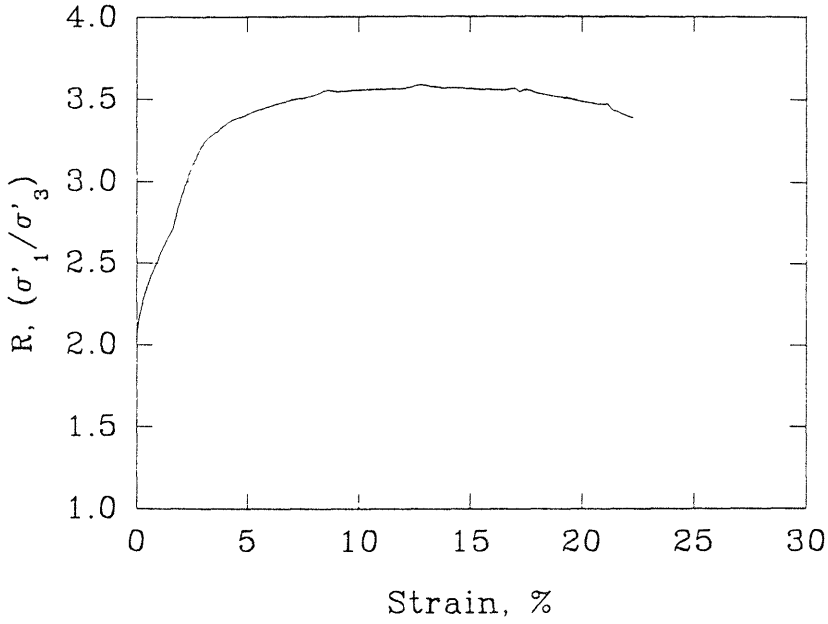

R_{max} = 3.59

Series C – Test #30

Deviator Stress and Excess
Pore Pressure vs Axial Strain

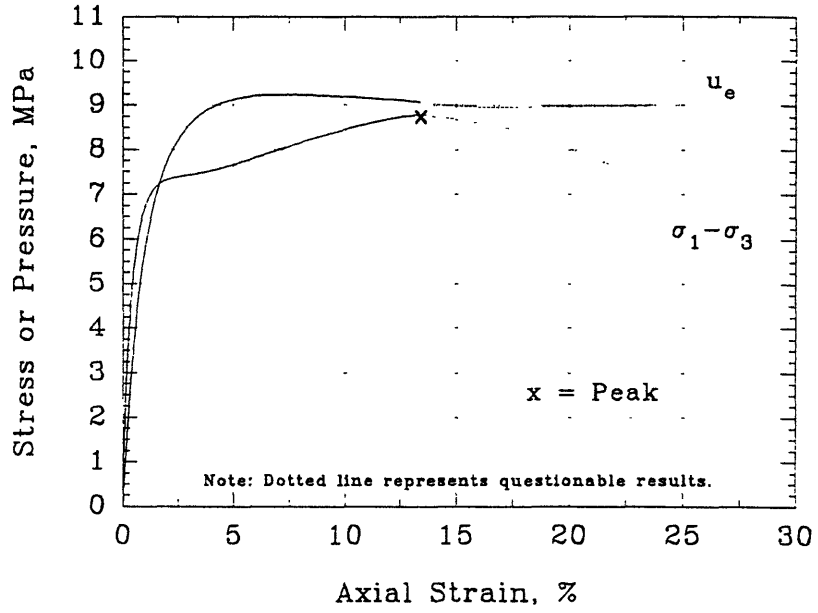

σ'_c = 12.5 MPa
e = 0.531
D_r = 115.0%

Q_p = 8.78 MPa
ε_p = 13.43 %

A–parameter vs Axial Strain

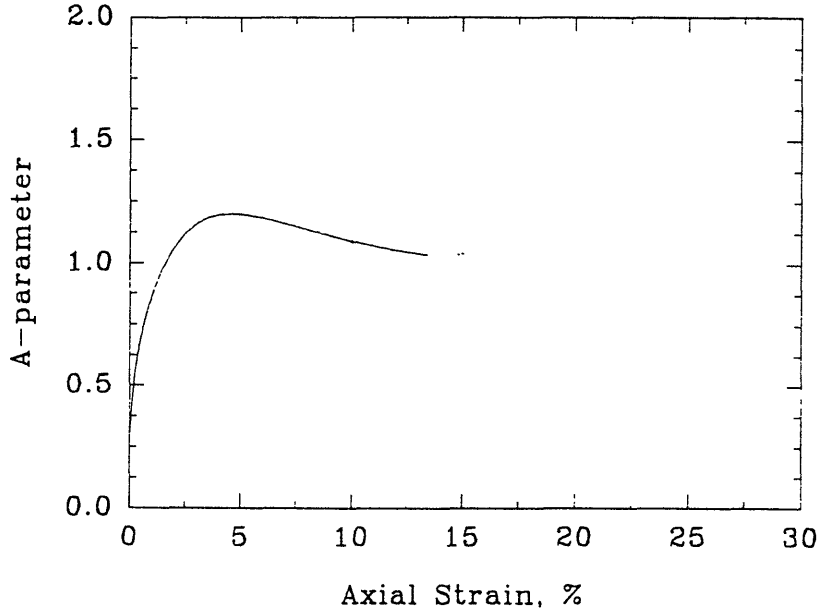

A_f = 1.037

Series C – Test #30

Effective Stress Path

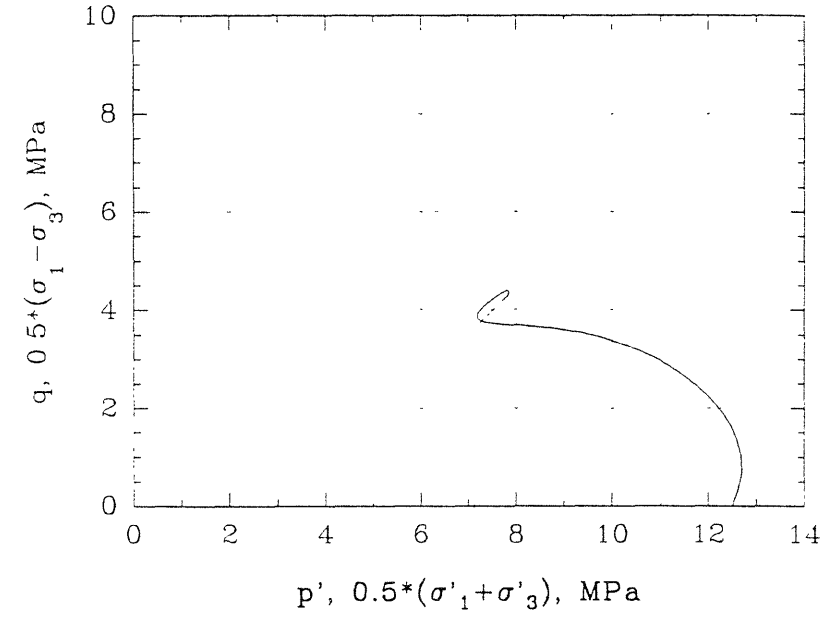

α' = 29.4 °
φ' = 34.4 °

Obliquity vs Axial Strain

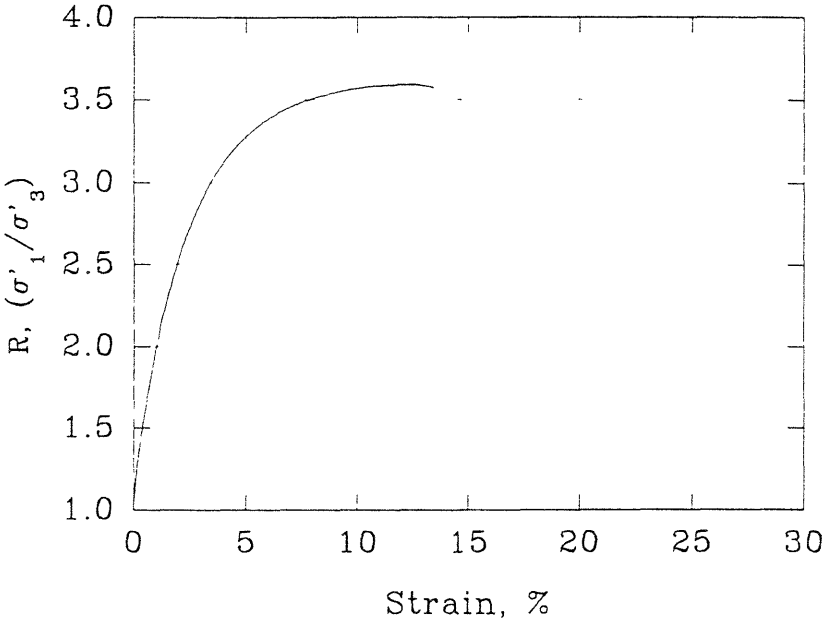

R_{max} = 3.59

Series C – Test #31

Effective Stress Path

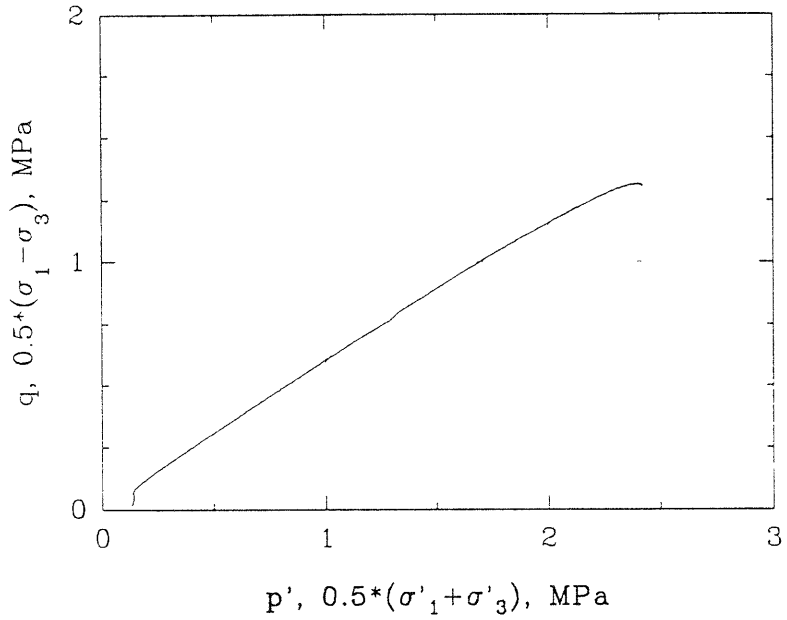

α' = 31.9 °
ϕ' = 38.6 °

Obliquity vs Axial Strain

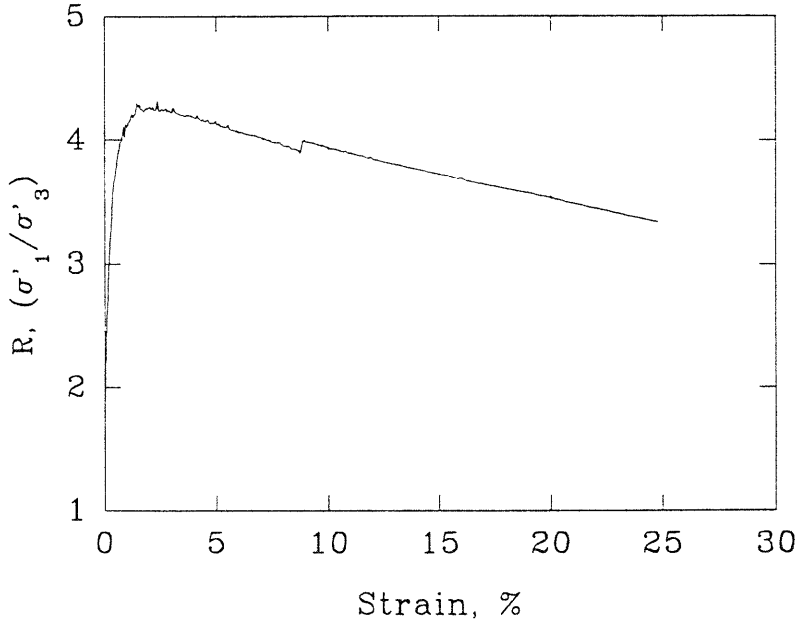

R_{max} = 4.31

Series C – Test #31

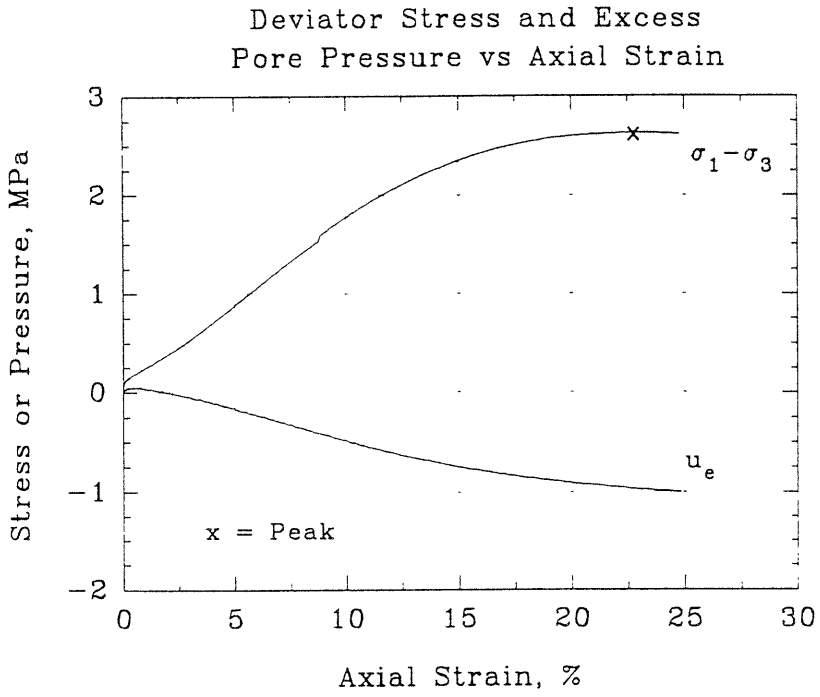

σ'_c = 0.1 MPa
e = 0.688
D_r = 67.8 %

Q_p = 2.62 MPa
ε_p = 22.75 %

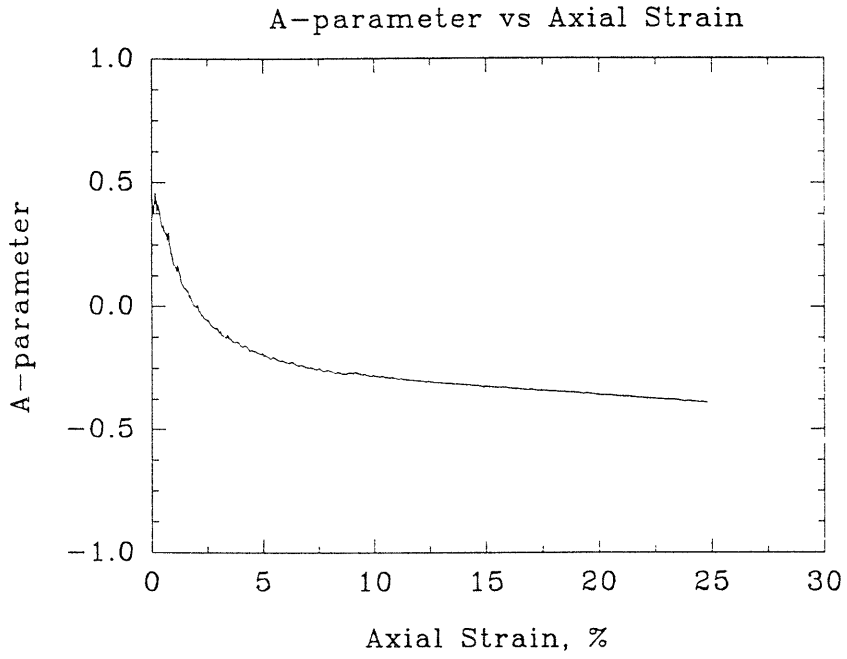

A_f = −0.374

Series C – Test #32

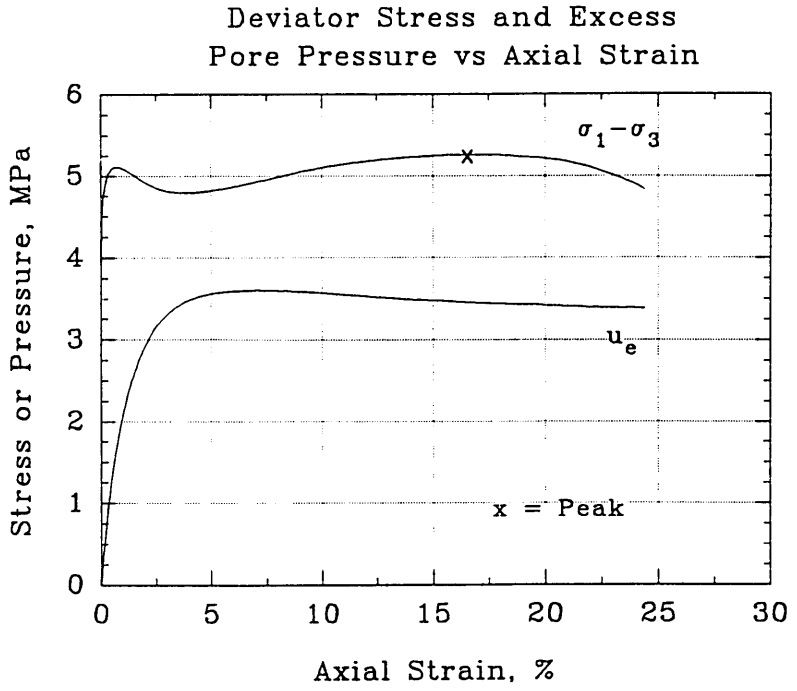

σ'_{1c} = 9.45 MPa
σ'_{3c} = 5.57 MPa
e = 0.633
D_r = 83.8 %

Q_p = 5.26 MPa
ε_p = 16.53 %

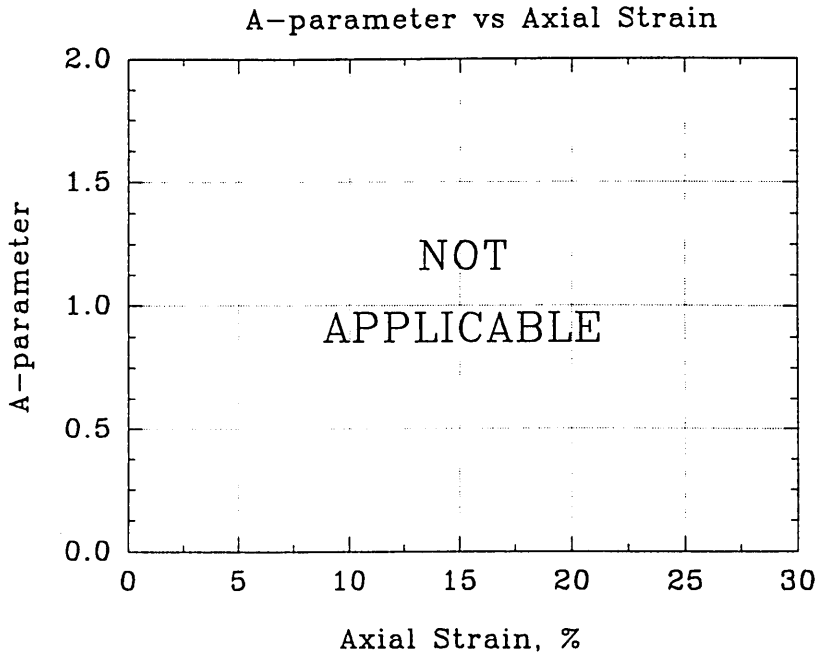

Series C – Test #32

Effective Stress Path

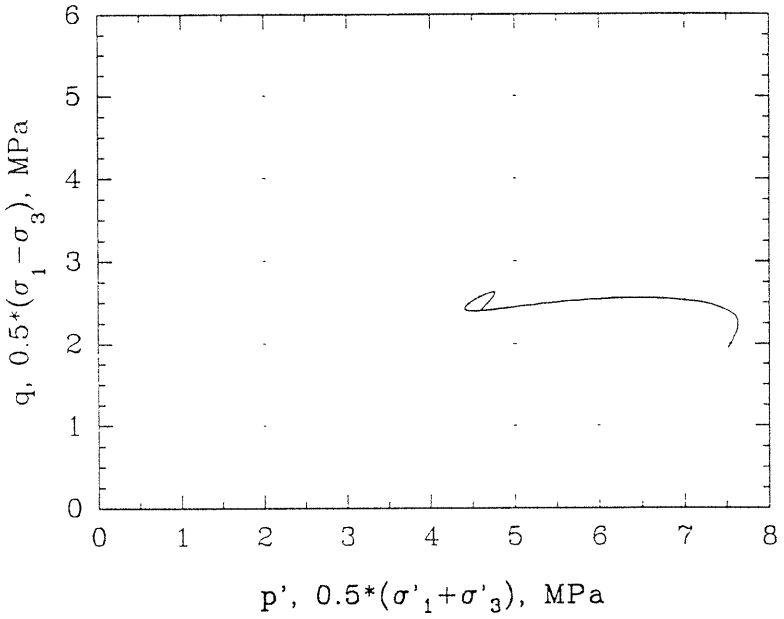

α' = 29.3 °
ϕ' = 34.1 °

Obliquity vs Axial Strain

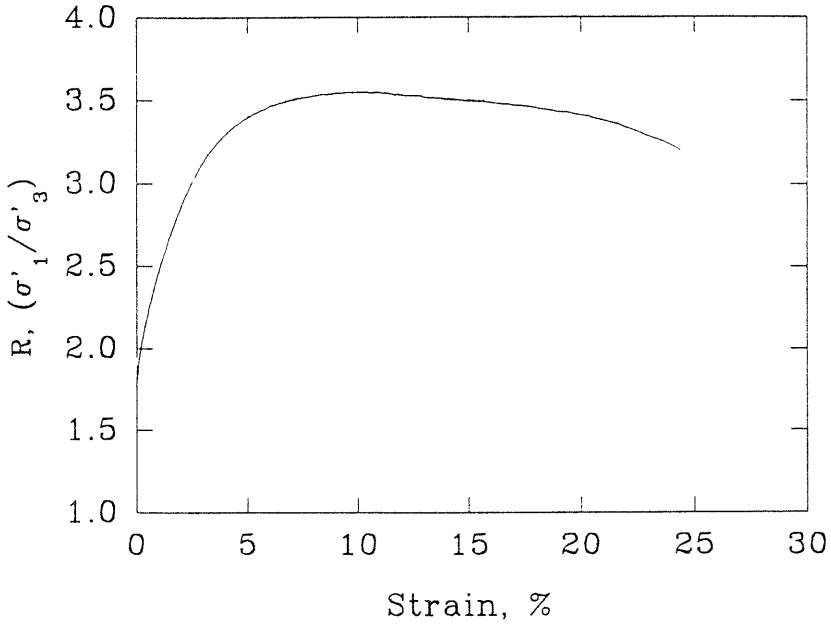

R_{max} = 3.55

Series C – Test #33

Deviator Stress and Excess
Pore Pressure vs Axial Strain

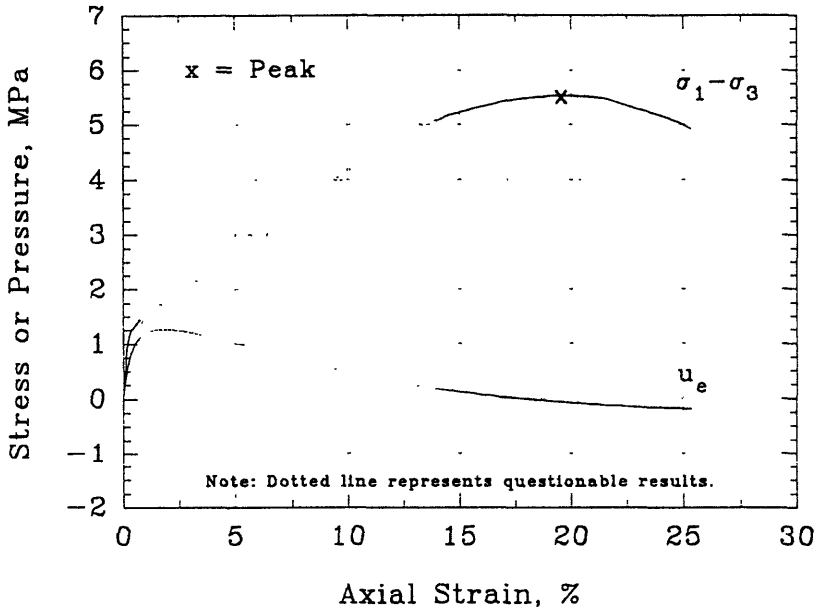

σ'_c = 2 MPa
e = 0.602
D_r = 93.3 %

Q_p = 5.63 MPa
ε_p = 19.54 %

A–parameter vs Axial Strain

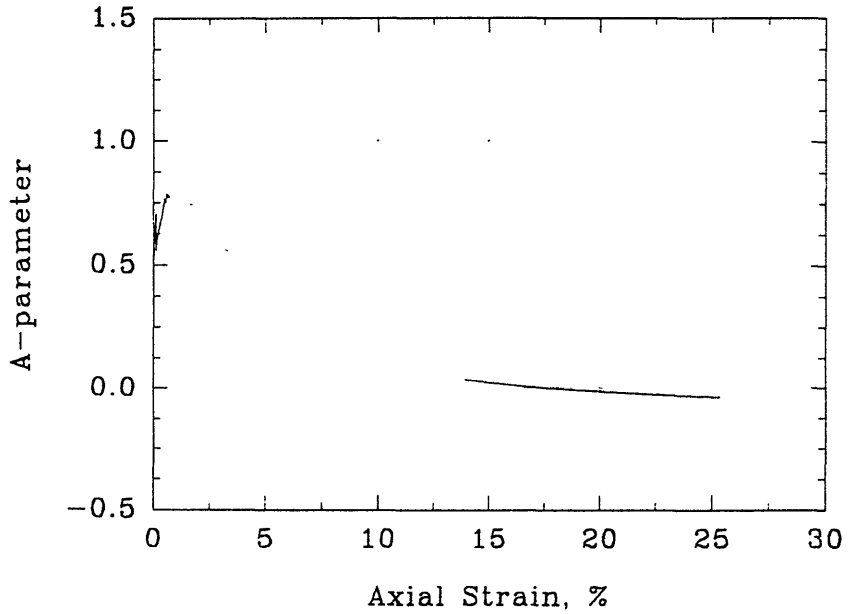

A_f = −0.012

Series C – Test #33

Effective Stress Path

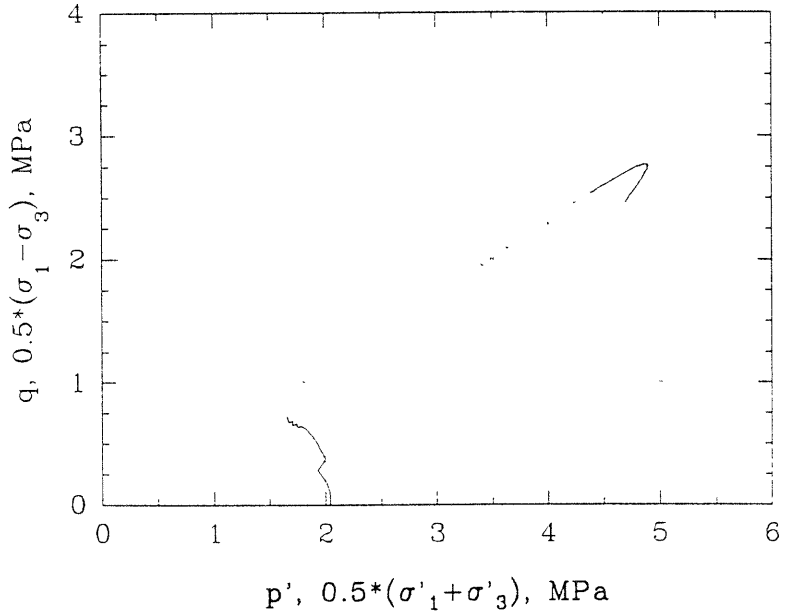

$\alpha' = 30.4°$
$\phi' = 35.6°$

Obliquity vs Axial Strain

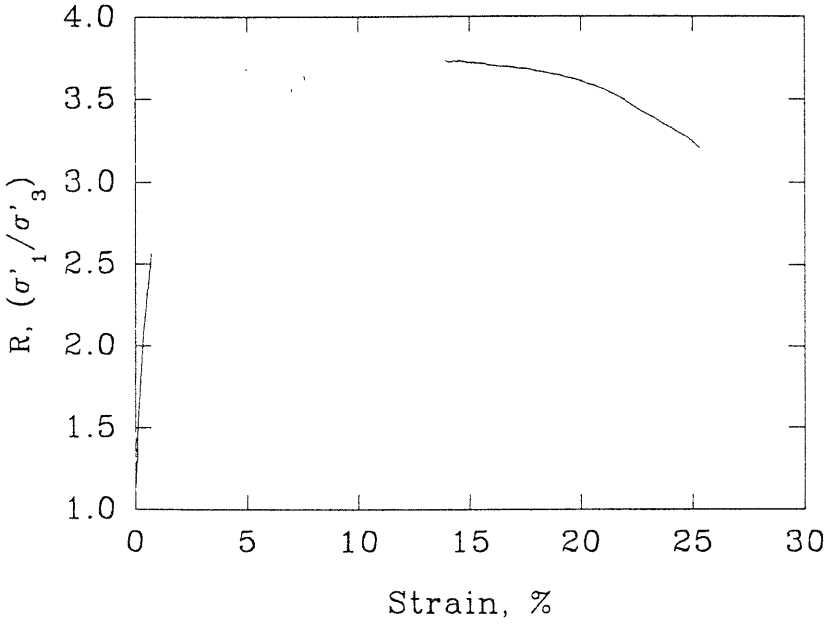

$R_{max} = 3.84$

Series C – Test #34

Effective Stress Path

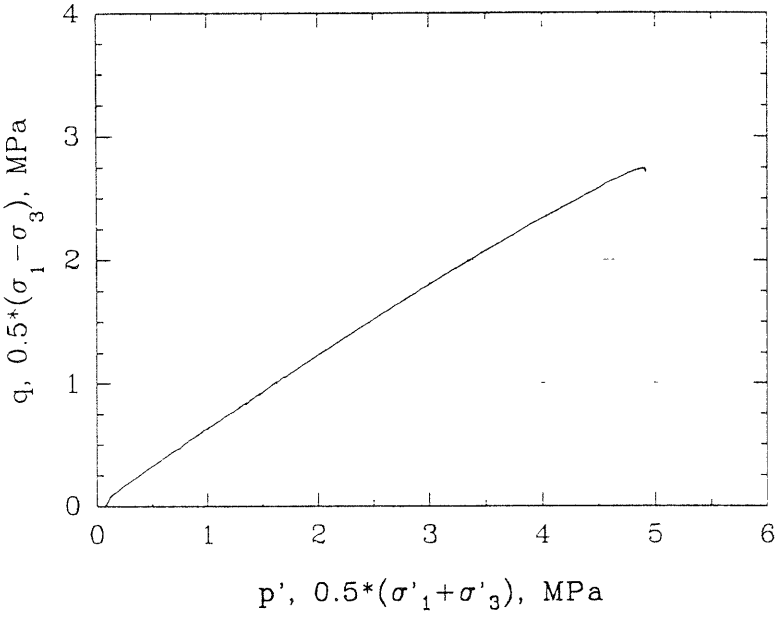

α' = 33.9 °
φ' = 42.5 °

Obliquity vs Axial Strain

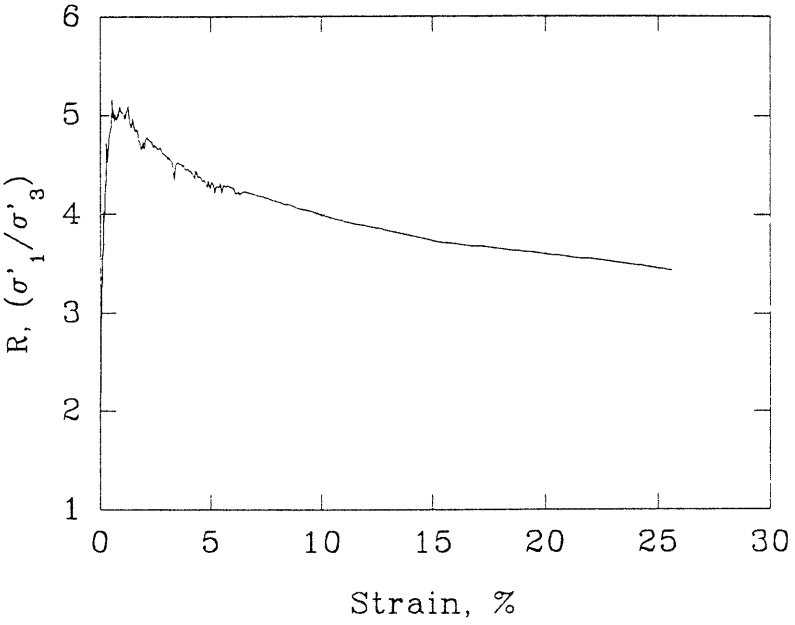

R_{max} = 5.16

Series C – Test #34

Deviator Stress and Excess
Pore Pressure vs Axial Strain

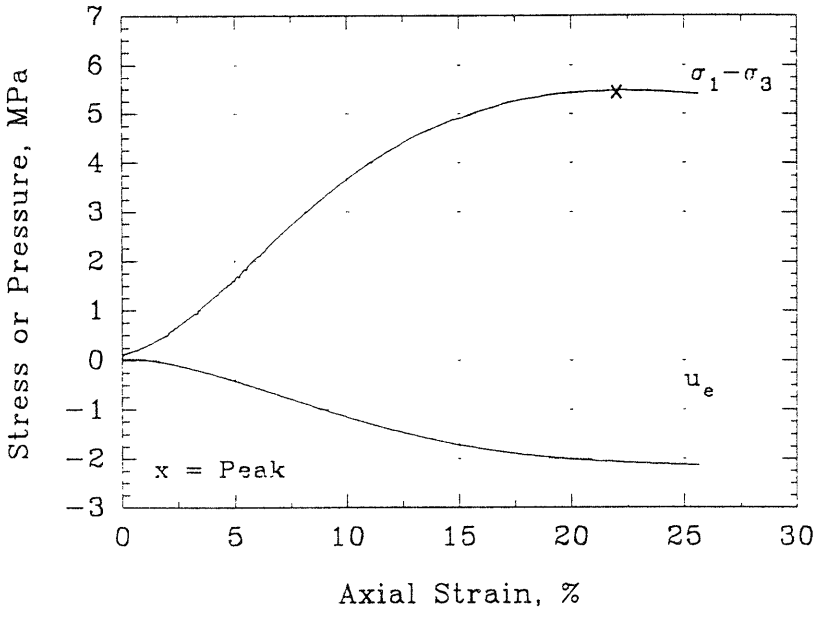

σ'_c = 0.1 MPa
e = 0.597
D_r = 94.9 %

Q_p = 5.48 MPa
ε_p = 21.99 %

A–parameter vs Axial Strain

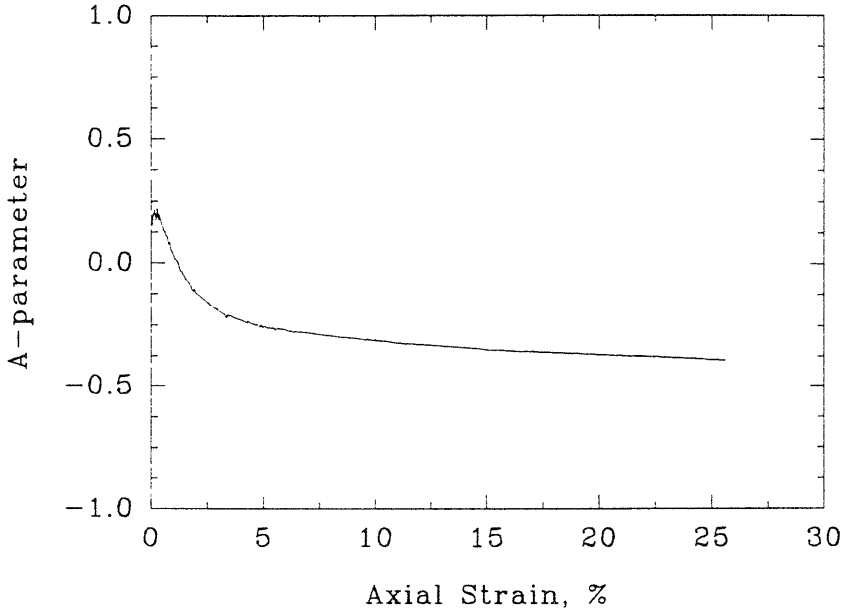

A_f = −0.377

Series C – Test #35

Deviator Stress and Excess
Pore Pressure vs Axial Strain

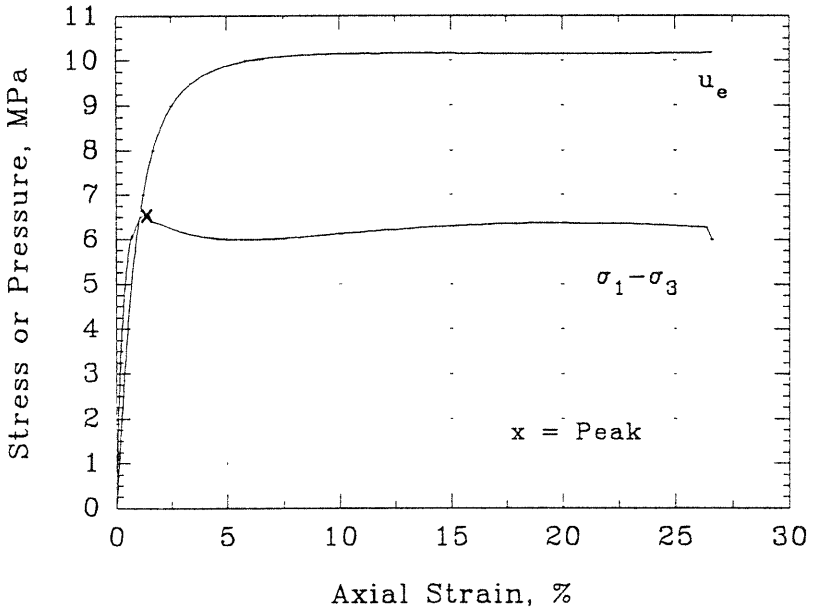

σ'_c = 12.5 MPa
e = 0.540
D_r = 112.2 %

Q_p = 6.57 MPa
ε_p = 1.36 %

A–parameter vs Axial Strain

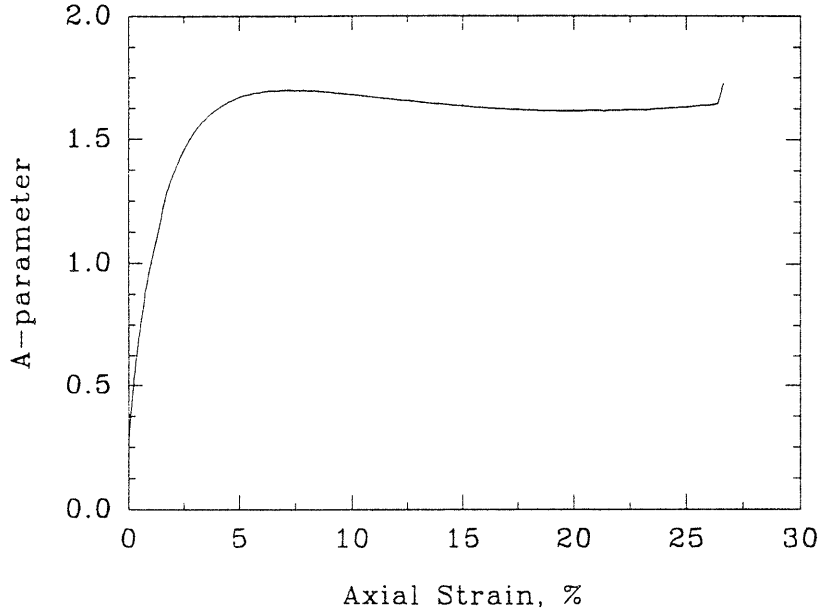

A_f = 1.135

Series C – Test #35

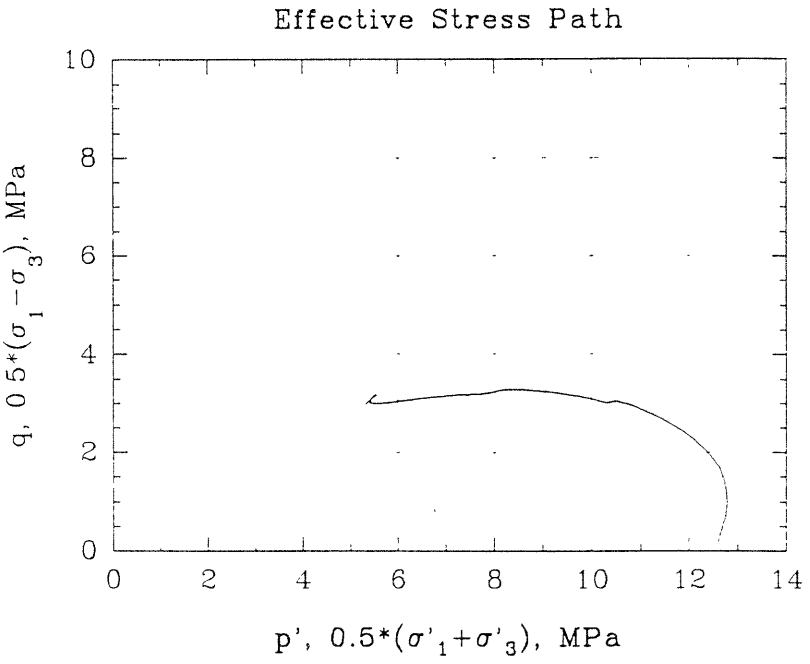

$\alpha' = 29.9\ °$
$\phi' = 35.2\ °$

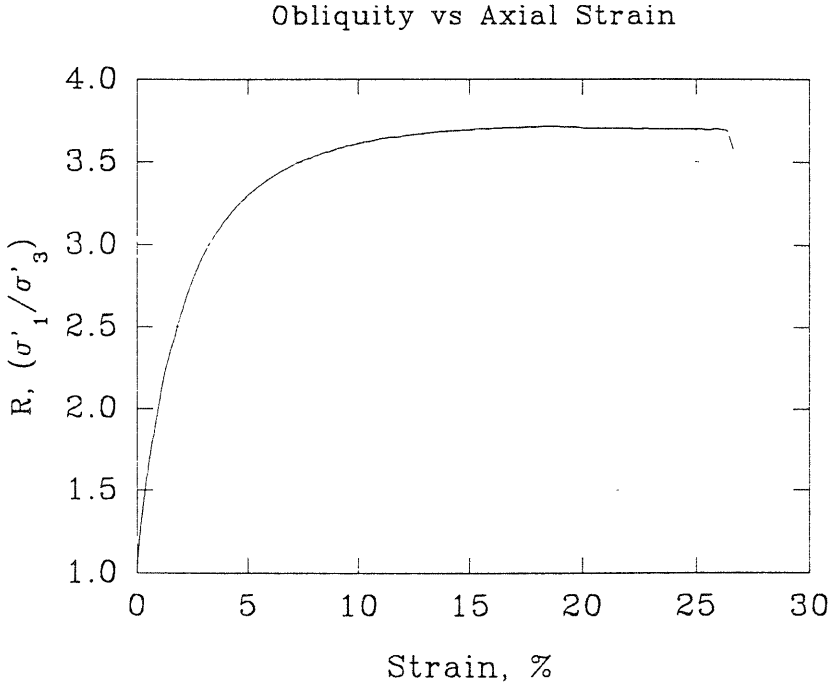

$R_{max} = 3.72$

SECTION B.3

Steady State Analysis

This section presents a record of the steady state points chosen for steady state analysis of unfrozen MFS. In all, 32 undrained tests were evaluated for use in the steady state analysis. For each test, a summary of the test conditions and post–shear specimen descriptions are presented followed by a summary of the steady state point determination.

Evaluation of the steady state points was based on the applicability of the three criteria used to determine the steady state of deformation (Poulos 1981), i.e., constant shear stress, constant excess pore pressure and constant effective mean normal stress. For a "true" steady state condition, these criteria must be meet simultaneously and under conditions of continued straining. However, in the evaluation of the unfrozen MFS results, a true steady state condition was obtained for only a few of the tests. For the remaining tests, the point closest to meeting these criteria was chosen as the steady state point. In the evaluation of steady state points, the responses of the three criteria were plotted against axial strain and reviewed for correspondence. This plot is presented for each test. At the chosen steady state point, each criteria was judged as to whether a constant state was reached (yes); a constant state was not reached or was not being maintained (no); or the response was nearing a constant state (approaching). Also included in the following presentation are the steady state characteristics, namely, the effective mean normal stress at steady state (both measured and calculated from the steady state line presented in Section 4.4, Fig. 4.53) and the state parameter Ψ.

Series B – Test #01

Test type: CIUC
Lubricated Ends: Membrane and teflon lubrication
Post-Shear Conditions:
Specimen shape?: Slight bulging
Rupture Surface?: No
End behavior?: No sliding but some lateral expansion
Steady State Conditions Satisfied:
Constant shear stress?: Yes
Constant pore pressure?: Yes
Constant mean normal stress?: Yes

Pre-shear			Steady State Characteristics			
D_r (%)	e	I_c (MPa)	Strain (%)	I_{ss} (MPa) Measured	Calculated	ψ
72.7	0.670	4.982	22.40	2.371	2.263	0.087

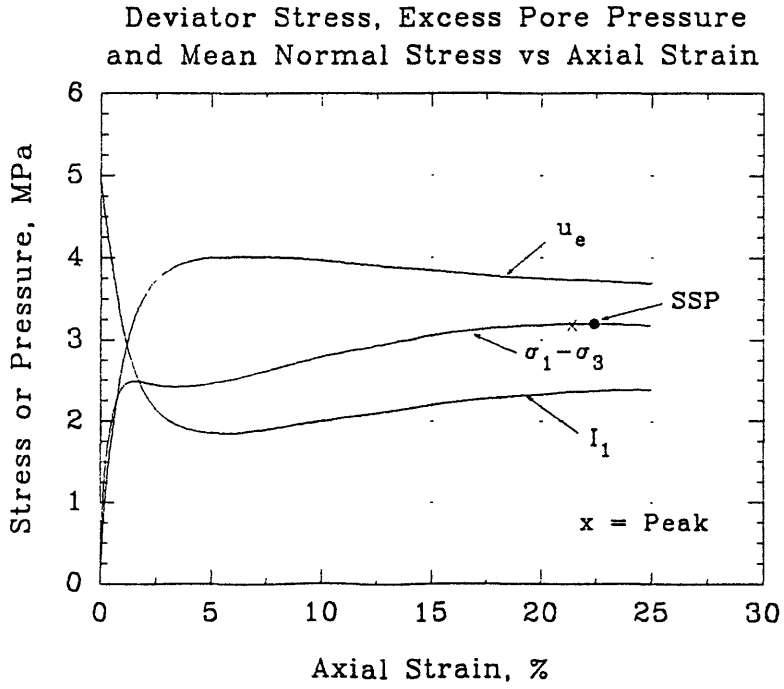

Series B – Test #02

Test type: CIUC
Lubricated Ends: Teflon lubrication
Post-Shear Conditions:
Specimen shape?: Significant bulging
Rupture Surface?: No
End behavior?: No sliding or lateral expansion
Steady State Conditions Satisfied:
Constant shear stress?: No
Constant pore pressure?: Approaching
Constant mean normal stress?: Yes

Pre-shear			Steady State Characteristics			
D_r (%)	e	I_c (MPa)	Strain (%)	I_{ss} (MPa) Measured	Calculated	ψ
104.9	0.564	5.017	22.82	5.221	5.110	-0.003

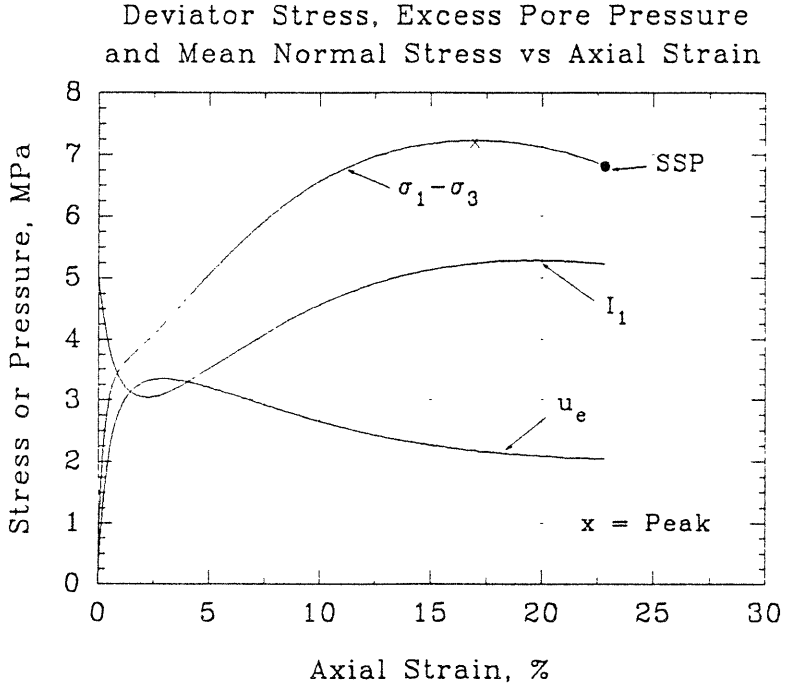

Series B – Test #05

Test type: CIUC
Lubricated Ends: Membrane and vacuum grease
Post-Shear Conditions:
Specimen shape?: RCC with some bulging, S-shaped
Rupture Surface?: No
End behavior?: Sliding at top cap, moderate to large lateral expansion
Steady State Conditions Satisfied:
Constant shear stress?: No
Constant pore pressure?: Approaching
Constant mean normal stress?: Yes

Pre-shear			Steady State Characteristics			
D_r (%)	e	I_c (MPa)	Strain (%)	I_{ss} (MPa) Measured	Calculated	ψ
91.5	0.608	5.009	17.58	4.174	3.973	0.026

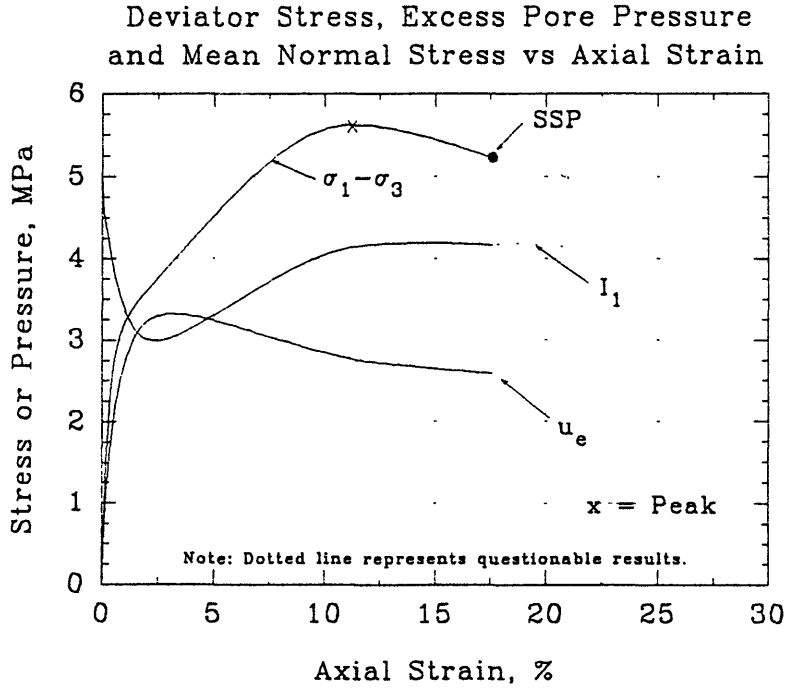

Series B – Test #06

Test type: CIUC
Lubricated Ends: Membrane and vacuum grease
Post-Shear Conditions:
Specimen shape?: RCC with little bulging, S-shaped
Rupture Surface?: No
End behavior?: Sliding at top cap, moderate to large lateral expansion
Steady State Conditions Satisfied:
Constant shear stress?: No
Constant pore pressure?: Approaching
Constant mean normal stress?: Yes

Pre-shear			Steady State Characteristics			
D_r (%)	e	I_c (MPa)	Strain (%)	I_{ss} (MPa) Measured	Calculated	ψ
65.4	0.694	2.035	25.28	1.960	1.820	0.020

Deviator Stress, Excess Pore Pressure and Mean Normal Stress vs Axial Strain

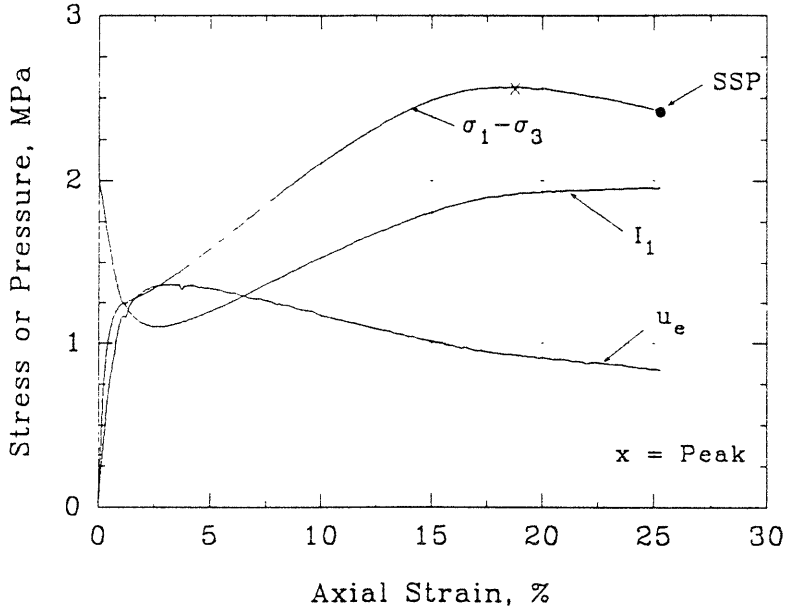

Series B – Test #07

Test type: CIUC
Lubricated Ends: Membrane and vacuum grease
Post-Shear Conditions:
Specimen shape?: RCC with slight bulging, S-shaped
Rupture Surface?: No
End behavior?: Sliding at top cap, large lateral expansion
Steady State Conditions Satisfied:
Constant shear stress?: No
Constant pore pressure?: Yes
Constant mean normal stress?: Yes

Pre-shear			Steady State Characteristics			
D_r (%)	e	I_c (MPa)	Strain (%)	I_{ss} (MPa) Measured	Calculated	ψ
96.1	0.593	2.030	24.92	4.147	4.553	-0.089

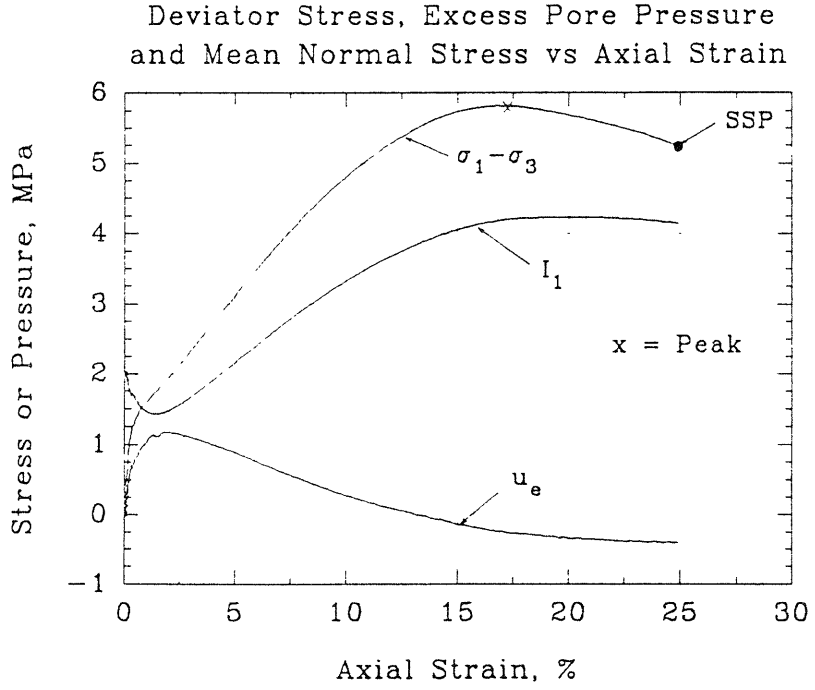

Series B – Test #10

Test type: CIUC
Lubricated Ends: Membrane and vacuum grease
Post-Shear Conditions:
Specimen shape?: RCC with some bulging
Rupture Surface?: Yes
End behavior?: Sliding at top cap, low to moderate lateral expansion
Steady State Conditions Satisfied:
Constant shear stress?: No
Constant pore pressure?: Yes
Constant mean normal stress?: Yes

Pre-shear			Steady State Characteristics			
D_r (%)	e	I_c (MPa)	Strain (%)	I_{ss} (MPa) Measured	I_{ss} (MPa) Calculated	ψ
43.8	0.765	0.102	25.27	0.993	0.956	-0.246

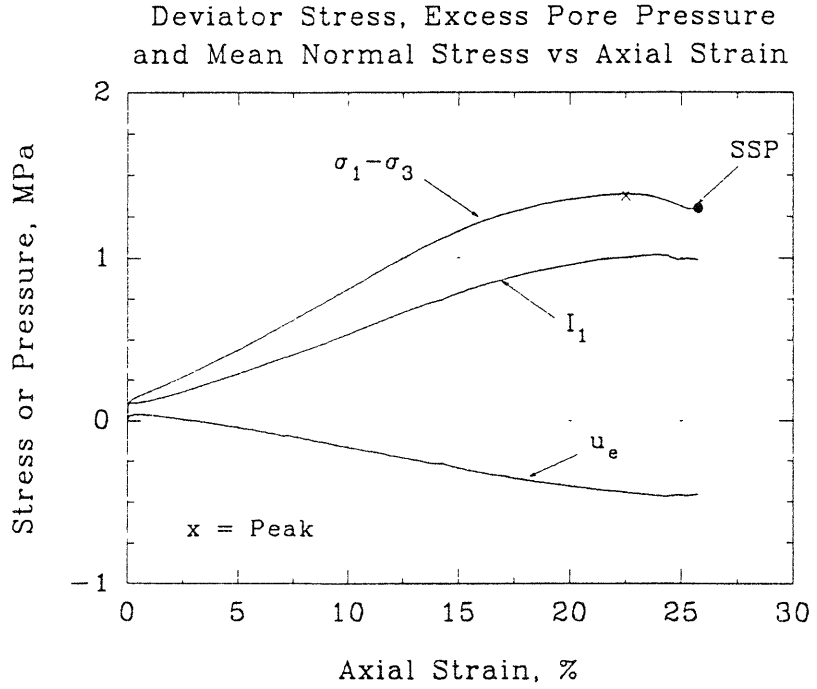

Series B – Test #11

Test type: CIUC
Lubricated Ends: Membrane and vacuum grease
Post-Shear Conditions:
Specimen shape?: RCC with little bulging, S-shaped
Rupture Surface?: No
End behavior?: Sliding at top cap, moderate to large lateral expansion
Steady State Conditions Satisfied:
Constant shear stress?: No
Constant pore pressure?: Approaching
Constant mean normal stress?: Yes

Pre-shear			Steady State Characteristics			
D_r (%)	e	I_c (MPa)	Strain (%)	I_{ss} (MPa) Measured	Calculated	ψ
67.2	0.688	2.013	22.58	2.308	1.920	0.005

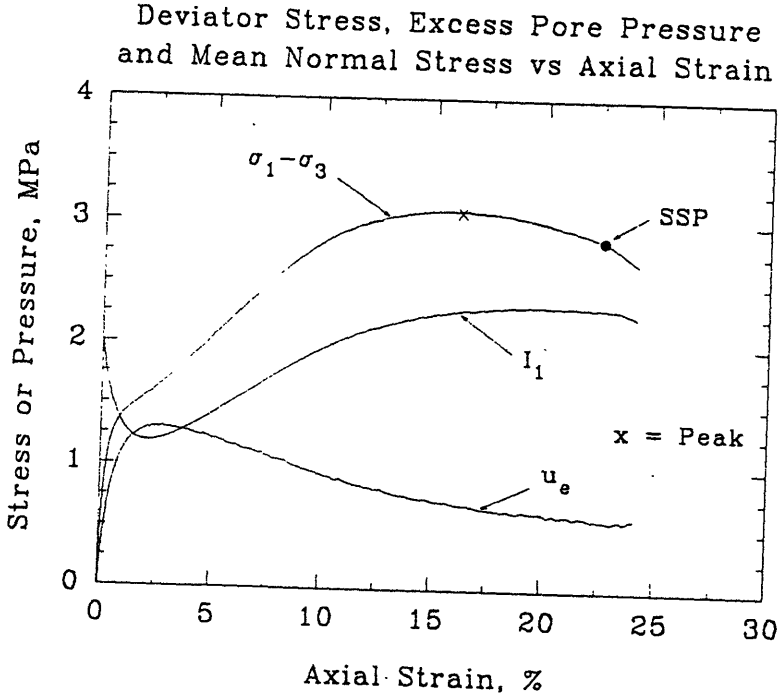

Series B – Test #12

Test type: CIUC
Lubricated Ends: Membrane and vacuum grease
Post-Shear Conditions:
Specimen shape?: RCC with slight bulging, S-shaped
Rupture Surface?: No
End behavior?: Sliding at top cap, large lateral expansion
Steady State Conditions Satisfied:
Constant shear stress?: No
Constant pore pressure?: Yes
Constant mean normal stress?: Yes

Pre-shear			Steady State Characteristics			
D_r (%)	e	I_c (MPa)	Strain (%)	I_{ss} (MPa) Measured	Calculated	ψ
86.1	0.626	0.110	22.53	2.788	3.574	-0.377

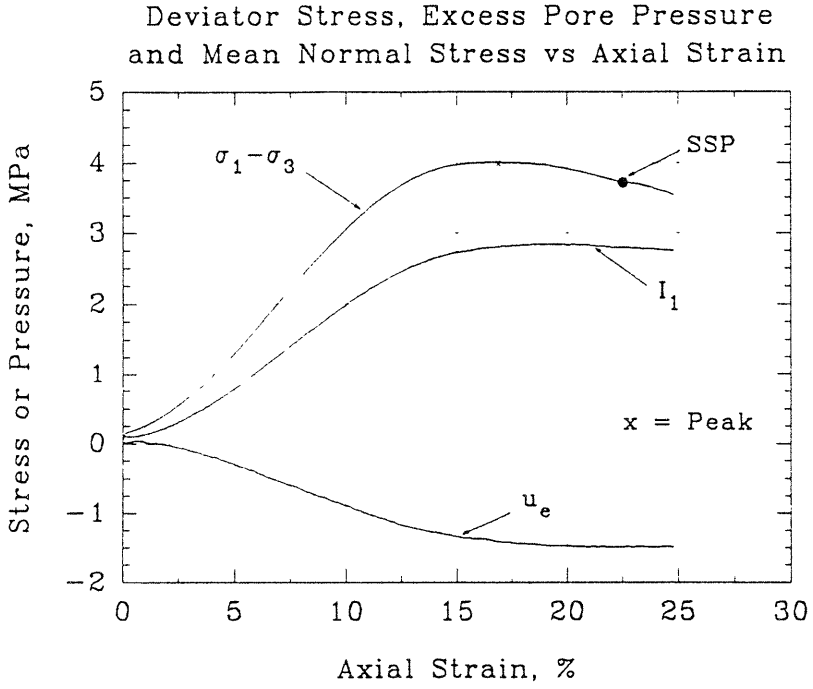

Series B – Test #13

Test type: CIUC
Lubricated Ends: Membrane and vacuum grease
Post-Shear Conditions:
Specimen shape?: RCC with some bulging, S-shaped
Rupture Surface?: Yes
End behavior?: Sliding at top cap and pedestal, large lateral expansion
Steady State Conditions Satisfied:
Constant shear stress?: No
Constant pore pressure?: Yes
Constant mean normal stress?: Yes

Pre-shear			Steady State Characteristics			
D_r (%)	e	I_c (MPa)	Strain (%)	I_{ss} (MPa) Measured	Calculated	ψ
64.5	0.697	5.184	23.09	1.986	1.771	0.118

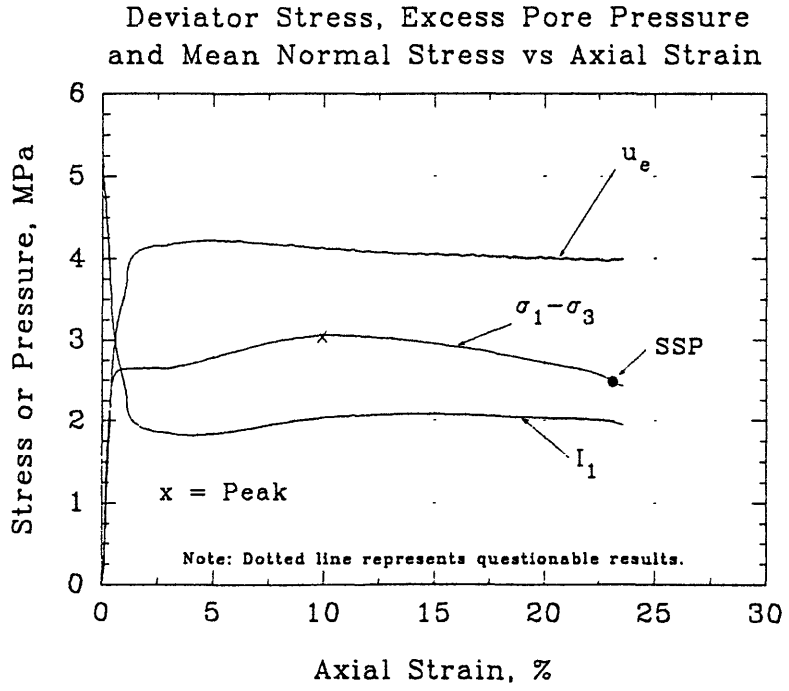

Series B – Test #14

Test type: CIUC
Lubricated Ends: Membrane and vacuum grease
Post-Shear Conditions:
Specimen shape?: RCC with little bulging, S-shaped
Rupture Surface?: No
End behavior?: Sliding at top cap, moderate lateral expansion
Steady State Conditions Satisfied:
Constant shear stress?: No
Constant pore pressure?: Approaching
Constant mean normal stress?: Yes

Pre-shear			Steady State Characteristics			
D_r (%)	e	I_c (MPa)	Strain (%)	I_{ss} (MPa) Measured	Calculated	ψ
92.5	0.605	5.003	16.18	4.216	4.083	0.022

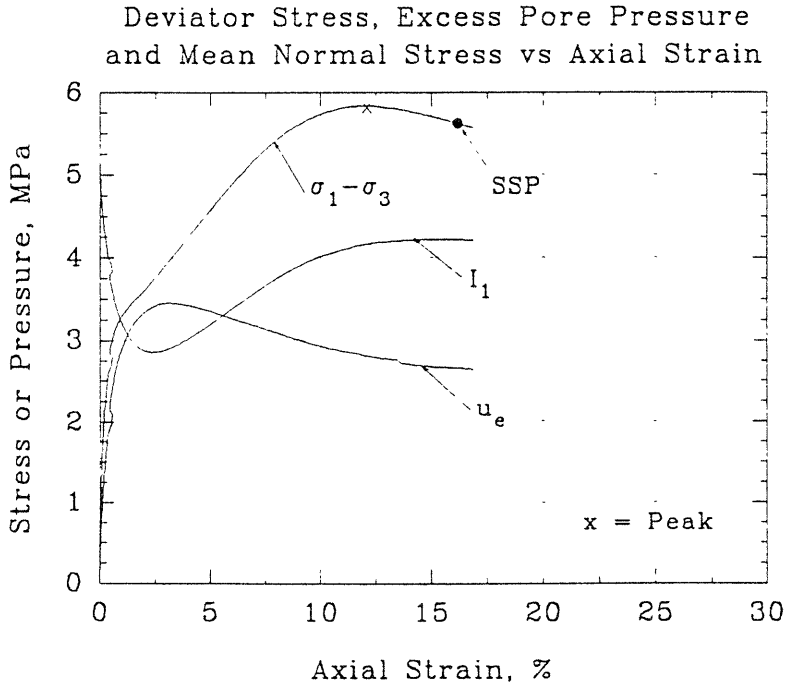

Series B – Test #15

Test type: CIUC
Lubricated Ends: Membrane and vacuum grease
Post-Shear Conditions:
Specimen shape?: RCC with little bulging, S-shaped
Rupture Surface?: Yes
End behavior?: Sliding at top cap, large lateral expansion
Steady State Conditions Satisfied:
Constant shear stress?: No
Constant pore pressure?: Approaching
Constant mean normal stress?: Yes

Pre-shear			Steady State Characteristics			
D_r (%)	e	I_c (MPa)	Strain (%)	I_{ss} (MPa) Measured	Calculated	ψ
94.3	0.599	5.033	23.74	5.077	4.311	0.017

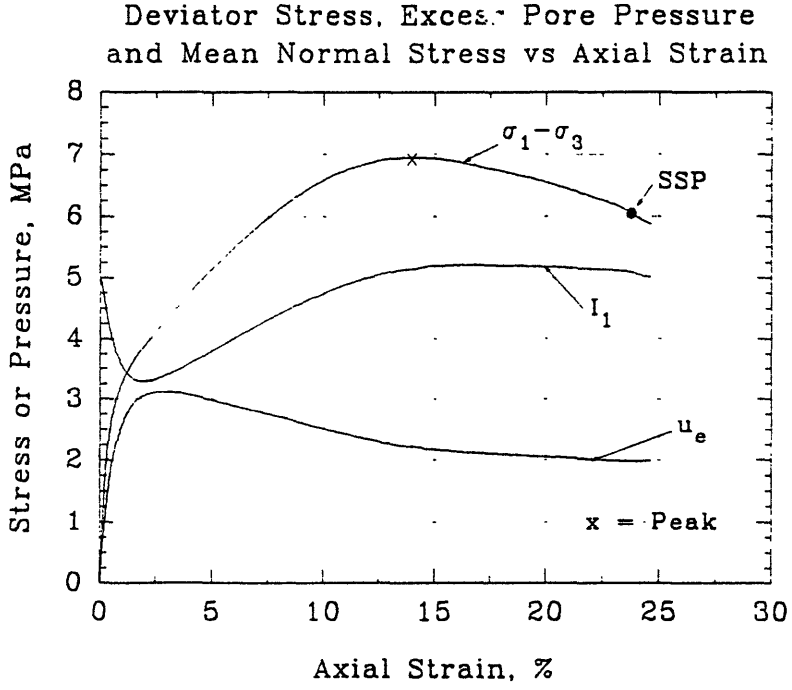

Series B – Test #23

Test type: CIUC
Lubricated Ends: Membrane and vacuum grease
Post-Shear Conditions:
Specimen shape?: RCC with some bulging, S-shaped
Rupture Surface?: Yes
End behavior?: Sliding at top cap and pedestal, moderate to large lateral expansion
Steady State Conditions Satisfied:
Constant shear stress?: Yes
Constant pore pressure?: Yes
Constant mean normal stress?: Yes

Pre-shear			Steady State Characteristics			
D_r (%)	e	I_c (MPa)	Strain (%)	I_{ss} (MPa) Measured	Calculated	ψ
89.1	0.616	10.174	8.44	4.100	3.864	0.180

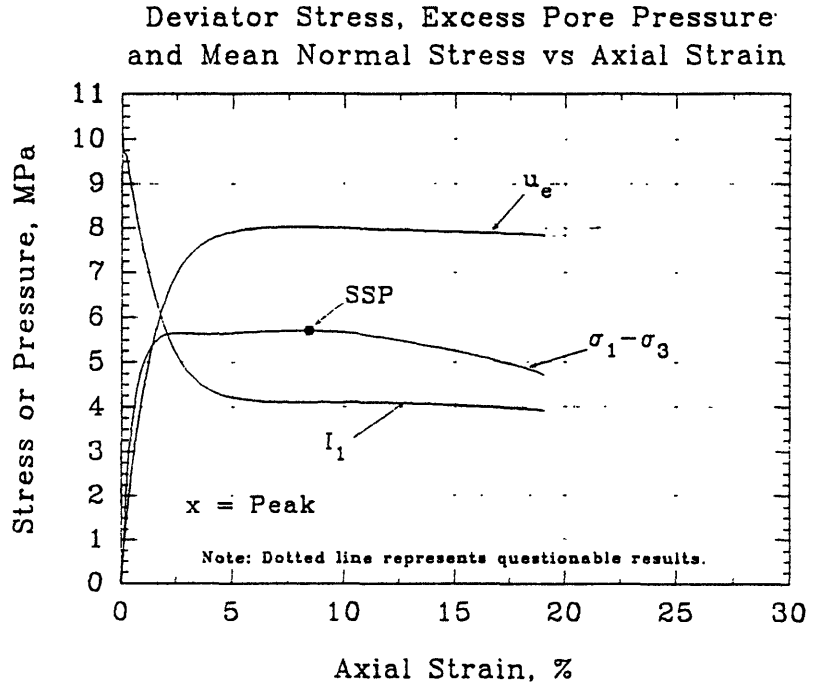

Series B – Test #24

Test type: CIUC
Lubricated Ends: Teflon lubrication
Post-Shear Conditions:
Specimen shape?: Some bulging
Rupture Surface?: Yes
End behavior?: No sliding with only slight lateral expansion
Steady State Conditions Satisfied:
Constant shear stress?: No
Constant pore pressure?: No
Constant mean normal stress?: No

Pre-shear			Steady State Characteristics			
D_r (%)	e	I_c (MPa)	Strain (%)	I_{ss} (MPa) Measured	Calculated	ψ
85.8	0.627	10.027	18.79	3.425	3.642	0.188

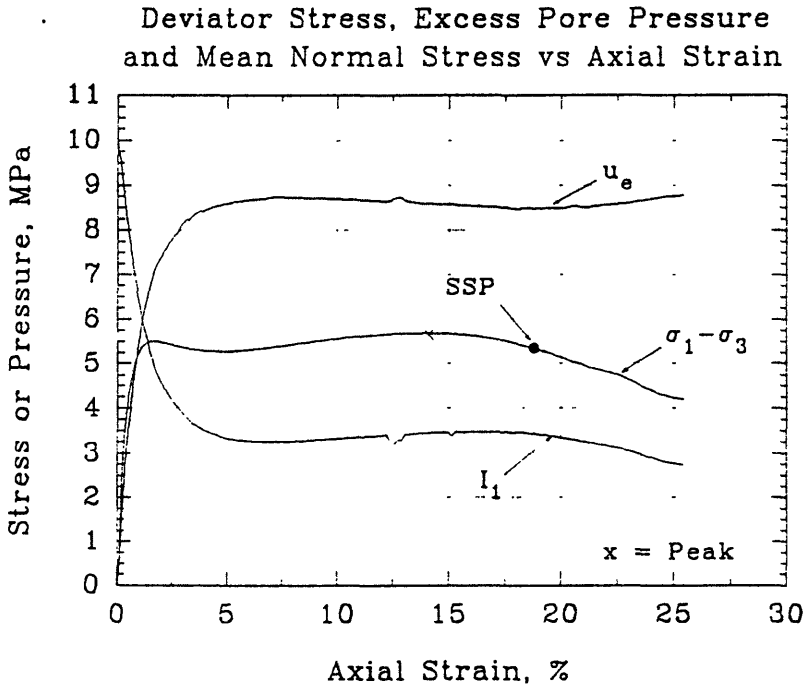

Series C – Test #01

Test type: CIUC
Lubricated Ends: Membrane and vacuum grease
Post-Shear Conditions:
Specimen shape?: RCC with some bulging, S-shaped
Rupture Surface?: Yes
End behavior?: Sliding at top cap and pedestal, large lateral expansion
Steady State Conditions Satisfied:
Constant shear stress?: Yes
Constant pore pressure?: Yes
Constant mean normal stress?: Yes

Pre-shear			Steady State Characteristics			
D_r (%)	e	I_c (MPa)	Strain (%)	I_{ss} (MPa) Measured	Calculated	ψ
82.7	0.637	9.375	10.04	3.559	3.452	0.186

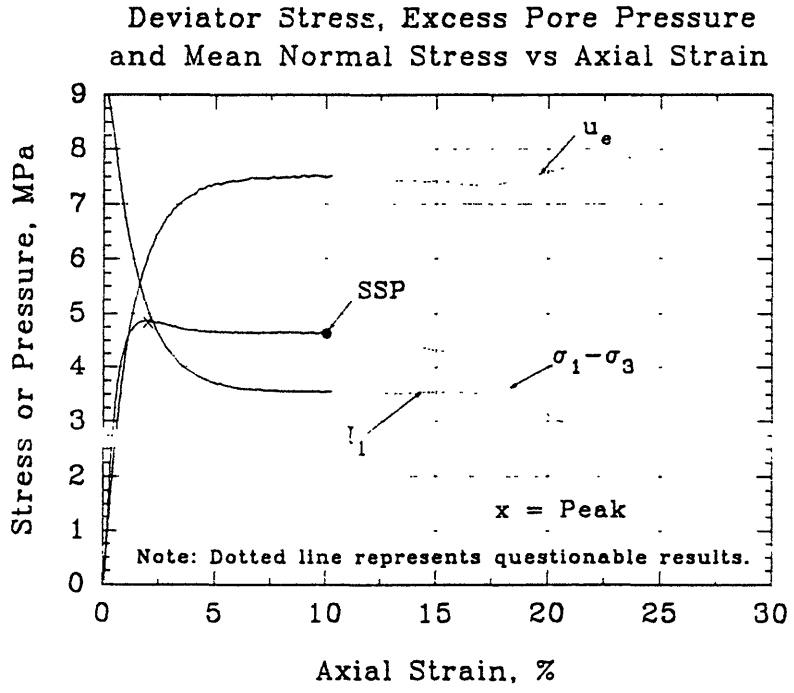

Series C – Test #02

Test type: CIUC
Lubricated Ends: Membrane and vacuum grease
Post-Shear Conditions:
Specimen shape?: RCC with some bulging, S-shaped
Rupture Surface?: Yes
End behavior?: Sliding at top cap and pedestal, moderate to large lateral expansion
Steady State Conditions Satisfied:
Constant shear stress?: Yes
Constant pore pressure?: Yes
Constant mean normal stress?: Yes

Pre-shear			Steady State Characteristics			
D_r (%)	e	I_c (MPa)	Strain (%)	I_{ss} (MPa) Measured	I_{ss} (MPa) Calculated	ψ
82.7	0.637	9.921	8.50	3.404	3.452	0.196

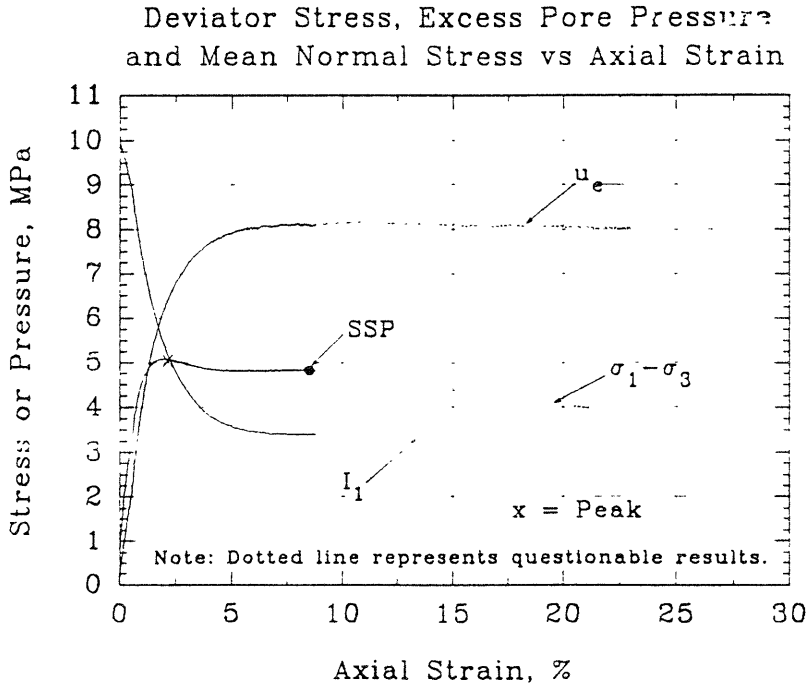

Series C – Test #03

Test type: CIUC
Lubricated Ends: Teflon lubrication
Post-Shear Conditions:
Specimen shape?: Significant bulging
Rupture Surface?: Yes
End behavior?: No sliding with only slight lateral expansion
Steady State Conditions Satisfied:
Constant shear stress?: No
Constant pore pressure?: Yes
Constant mean normal stress?: Yes

Pre-shear			Steady State Characteristics			
D_r (%)	e	I_c (MPa)	Strain (%)	I_{ss} (MPa) Measured	I_{ss} (MPa) Calculated	ψ
77.3	0.655	10.108	19.08	3.557	3.133	0.218

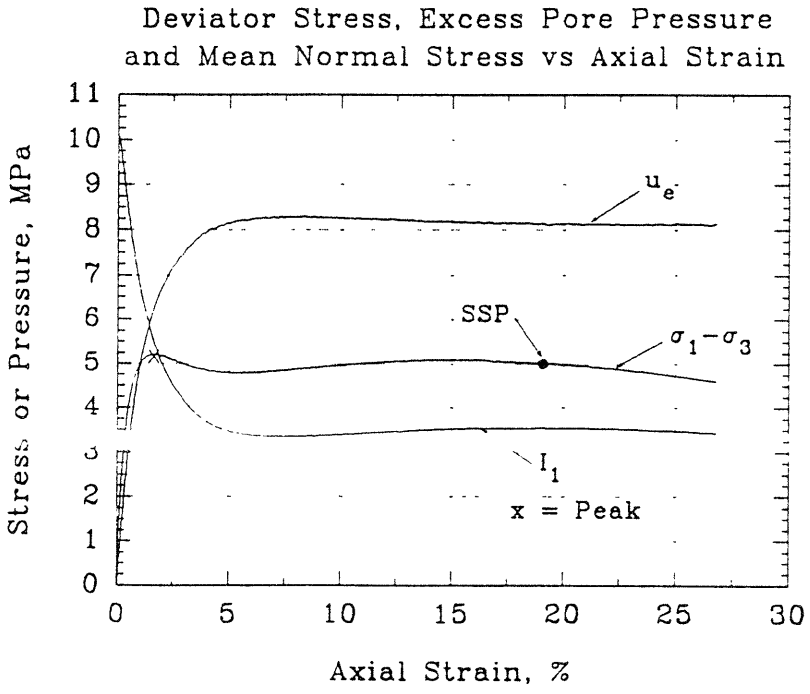

Series C – Test #04

Test type: CIUC
Lubricated Ends: Membrane only
Post-Shear Conditions:
Specimen shape?: RCC with some bulging, S-shaped
Rupture Surface?: Yes
End behavior?: Sliding at top cap and pedestal, moderate lateral expansion
Steady State Conditions Satisfied:
Constant shear stress?: No
Constant pore pressure?: Approaching
Constant mean normal stress?: Yes

Pre-shear			Steady State Characteristics			
D_r (%)	e	I_c (MPa)	Strain (%)	I_{ss} (MPa) Measured	Calculated	ψ
84.6	0.631	7.529	23.08	2.924	3.225	0.093

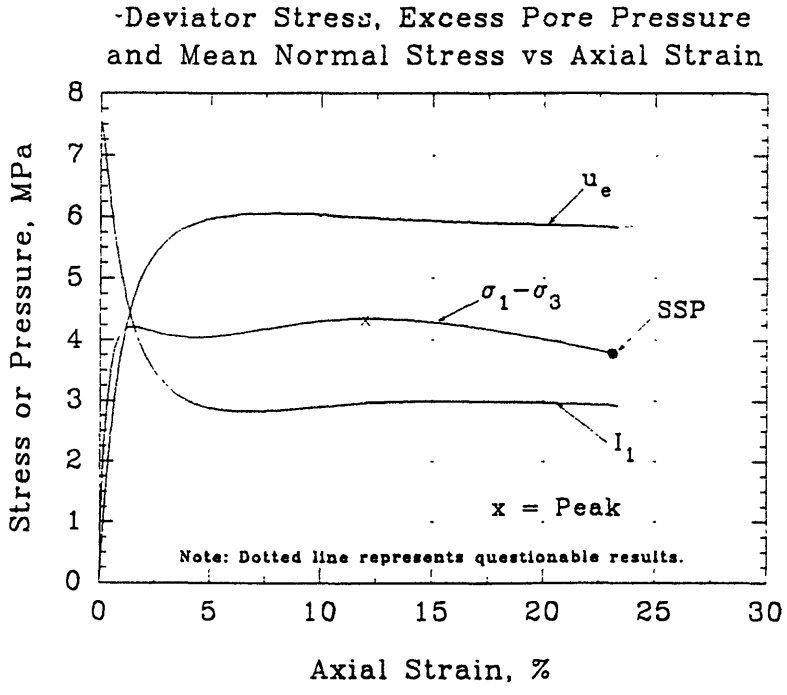

Series C – Test #15

Test type: CIUC
Lubricated Ends: Membrane only
Post-Shear Conditions:
Specimen shape?: RCC with slight bulging
Rupture Surface?: No
End behavior?: Sliding at top cap, large lateral expansion
Steady State Conditions Satisfied:
Constant shear stress?: No
Constant pore pressure?: Yes
Constant mean normal stress?: Yes

Pre-shear			Steady State Characteristics			
D_r (%)	e	I_c (MPa)	Strain (%)	I_{ss} (MPa) Measured	Calculated	ψ
56.0	0.725	1.948	26.14	1.233	1.374	0.038

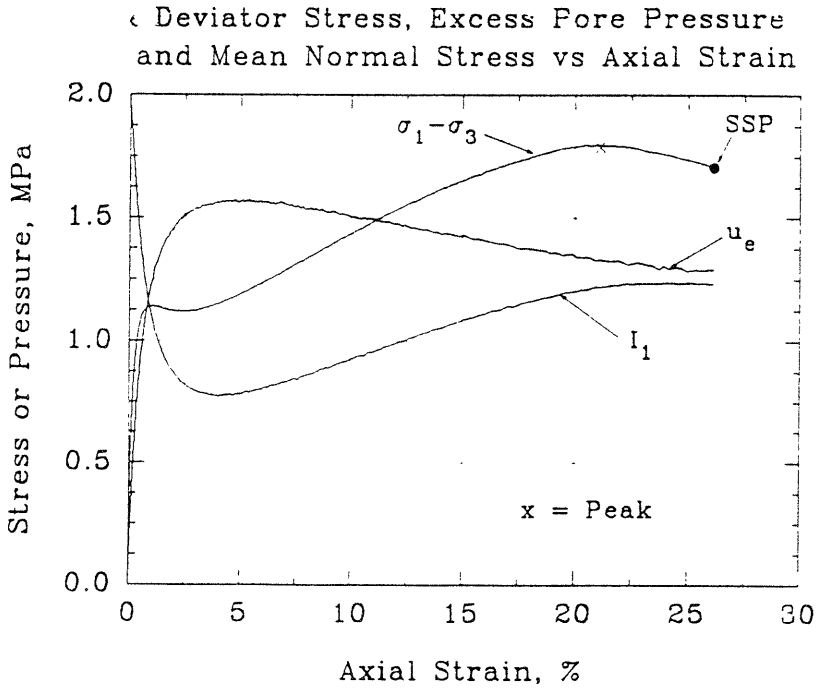

Series C – Test #16

Test type: CIUC
Lubricated Ends: Membrane only
Post-Shear Conditions:
Specimen shape?: RCC with little bulging
Rupture Surface?: No
End behavior?: No sliding, large lateral expansion
Steady State Conditions Satisfied:
Constant shear stress?: No
Constant pore pressure?: Yes
Constant mean normal stress?: Yes

Pre-shear			Steady State Characteristics			
D_r (%)	e	I_c (MPa)	Strain (%)	I_{ss} (MPa) Measured	Calculated	ψ
104.3	0.566	9.968	19.71	4.133	5.055	0.126

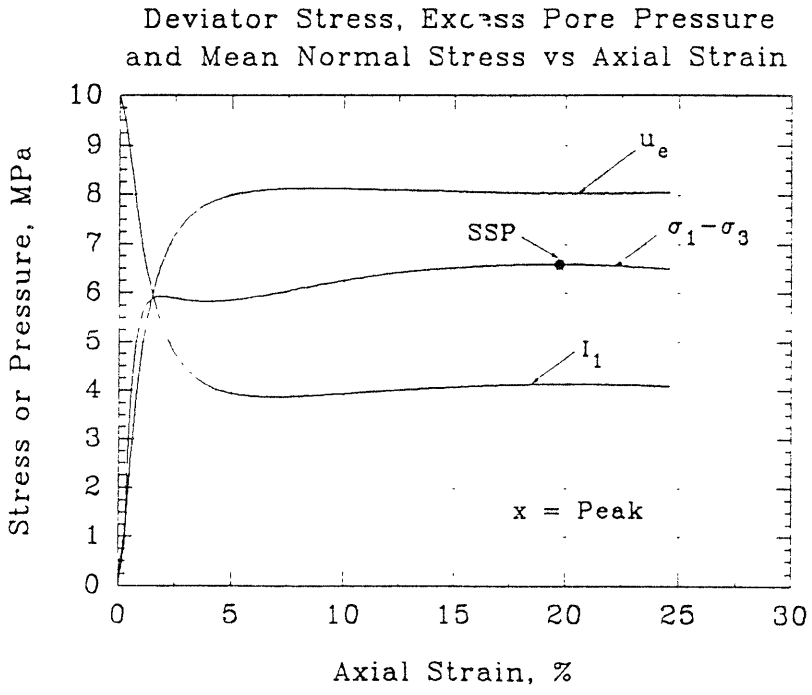

Series C – Test #22

Test type: CIUC
Lubricated Ends: Membrane and vacuum grease
Post-Shear Conditions:
Specimen shape?: Bulging with some RCC
Rupture Surface?: No
End behavior?: Some constraint at top cap and padestal, moderate expansion
Steady State Conditions Satisfied:
Constant shear stress?: No
Constant pore pressure?: Yes
Constant mean normal stress?: Yes

Pre-shear			Steady State Characteristics			
D_r (%)	e	I_c (MPa)	Strain (%)	I_{ss} (MPa) Measured	Calculated	ψ
95.3	0.596	9.991	24.10	4.881	4.302	0.157

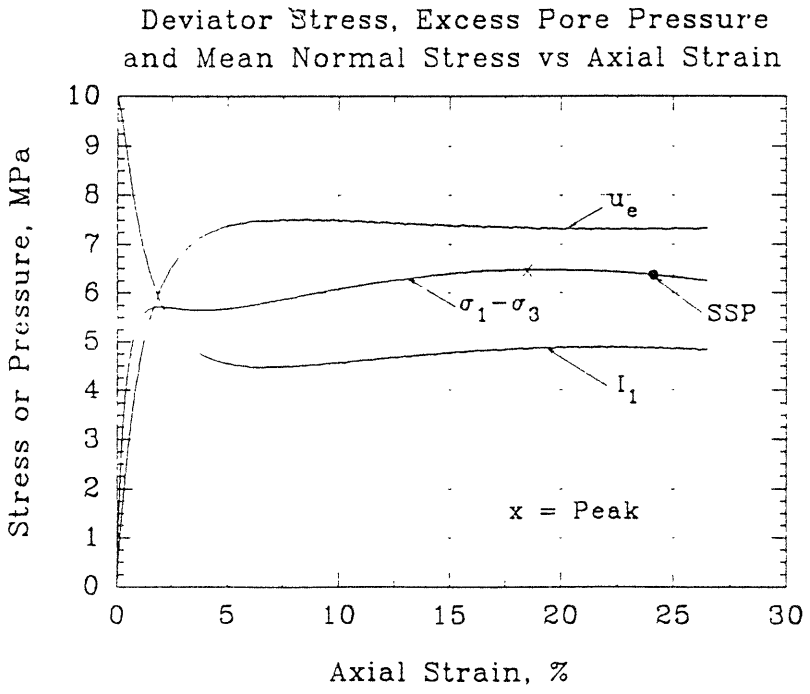

Series C – Test #23

Test type: CIUC
Lubricated Ends: Membrane and vacuum grease
Post-Shear Conditions:
Specimen shape?: RCC with some bulging, S-shaped
Rupture Surface?: Yes
End behavior?: Sliding at top cap and pedestal, moderate expansion
Steady State Conditions Satisfied:
Constant shear stress?: Yes
Constant pore pressure?: No
Constant mean normal stress?: No

Pre-shear			Steady State Characteristics			
D_r (%)	e	I_c (MPa)	Strain (%)	I_{ss} (MPa) Measured	Calculated	ψ
75.5	0.661	5.010	18.08	2.371	2.456	0.079

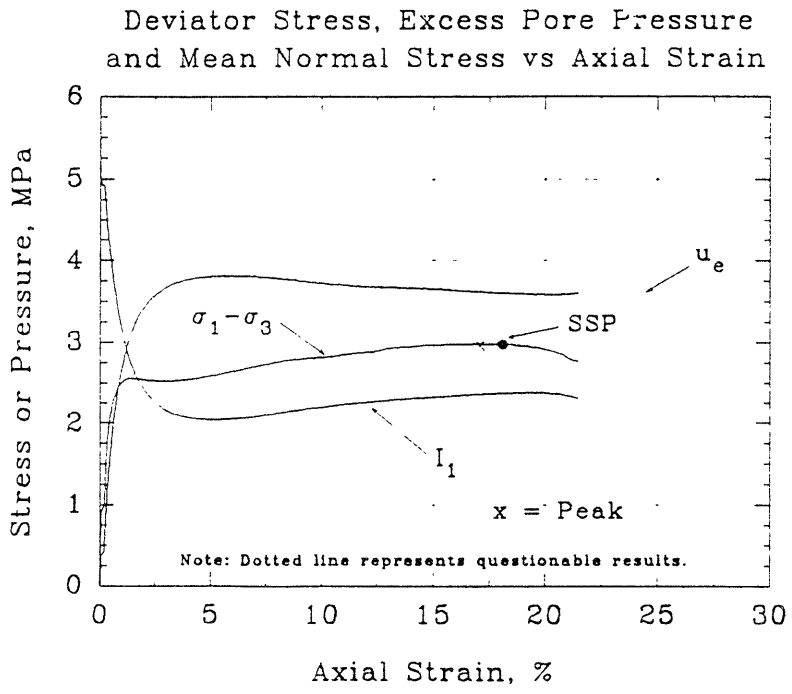

Series C – Test #24

Test type: CIUC
Lubricated Ends: Membrane and vacuum grease
Post-Shear Conditions:
Specimen shape?: Bulging with some RCC
Rupture Surface?: No
End behavior?: Some constraint at top cap and pedestal, moderate expansion
Steady State Conditions Satisfied:
Constant shear stress?: Yes
Constant pore pressure?: Yes
Constant mean normal stress?: Yes

Pre-shear			Steady State Characteristics			
D_r (%)	e	I_c (MPa)	Strain (%)	I_{ss} (MPa) Measured	Calculated	ψ
81.2	0.642	4.979	25.04	2.859	2.918	0.059

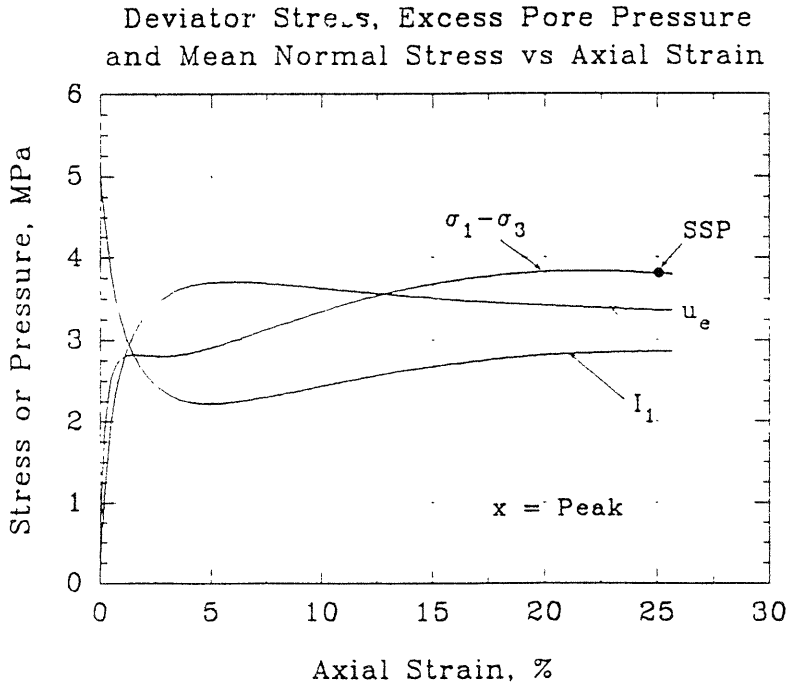

Series C – Test #25

Test type: CIUC
Lubricated Ends: Membrane and vacuum grease
Post-Shear Conditions:
Specimen shape?: RCC with little bulging
Rupture Surface?: No
End behavior?: Slight constraint at top cap and pedestal, moderate to large lateral expansion
Steady State Conditions Satisfied:
Constant shear stress?: No
Constant pore pressure?: Yes
Constant mean normal stress?: Yes

Pre-shear			Steady State Characteristics			
D_r (%)	e	I_c (MPa)	Strain (%)	I_{ss} (MPa) Measured	Calculated	ψ
100.4	0.579	12.534	25.67	4.406	4.714	0.182

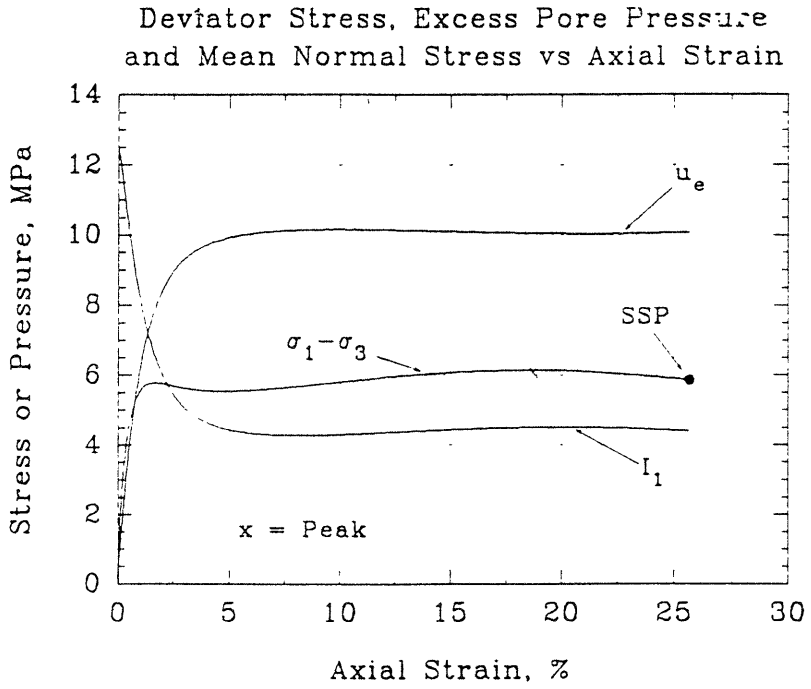

Series C – Test #26

Test type: CIUC
Lubricated Ends: Membrane and vacuum grease
Post-Shear Conditions:
Specimen shape?: Bulging with some RCC
Rupture Surface?: Yes
End behavior?: Sliding at top cap, slight expansion
Steady State Conditions Satisfied:
Constant shear stress?: Approaching
Constant pore pressure?: Approaching
Constant mean normal stress?: Approaching

Pre-shear			Steady State Characteristics			
D_r (%)	e	I_c (MPa)	Strain (%)	I_{ss} (MPa) Measured	Calculated	ψ
68.7	0.683	0.106	22.83	2.046	2.011	-0.324

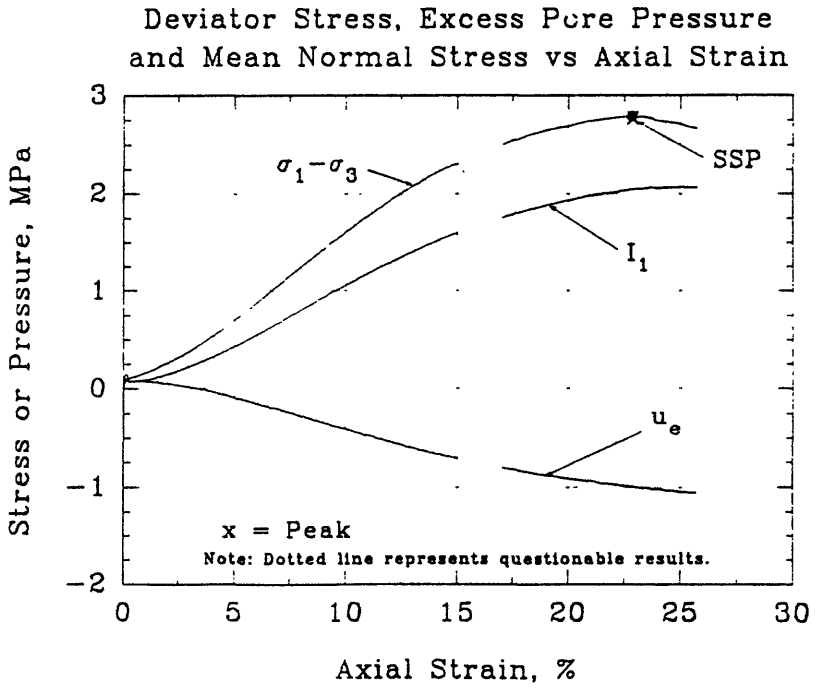

Series C – Test #27

Test type: CIUC
Lubricated Ends: Membrane and vacuum grease
Post-Shear Conditions:
Specimen shape?: Bulging with some lateral spreading
Rupture Surface?: Yes
End behavior?: Some constraint at top cap and pedestal, slight lateral expansion
Steady State Conditions Satisfied:
Constant shear stress?: No
Constant pore pressure?: No
Constant mean normal stress?: No

Pre-shear			Steady State Characteristics			
D_r (%)	e	I_c (MPa)	Strain (%)	I_{ss} (MPa) Measured	Calculated	ψ
63.5	0.700	1.972	27.04	1.622	1.724	0.015

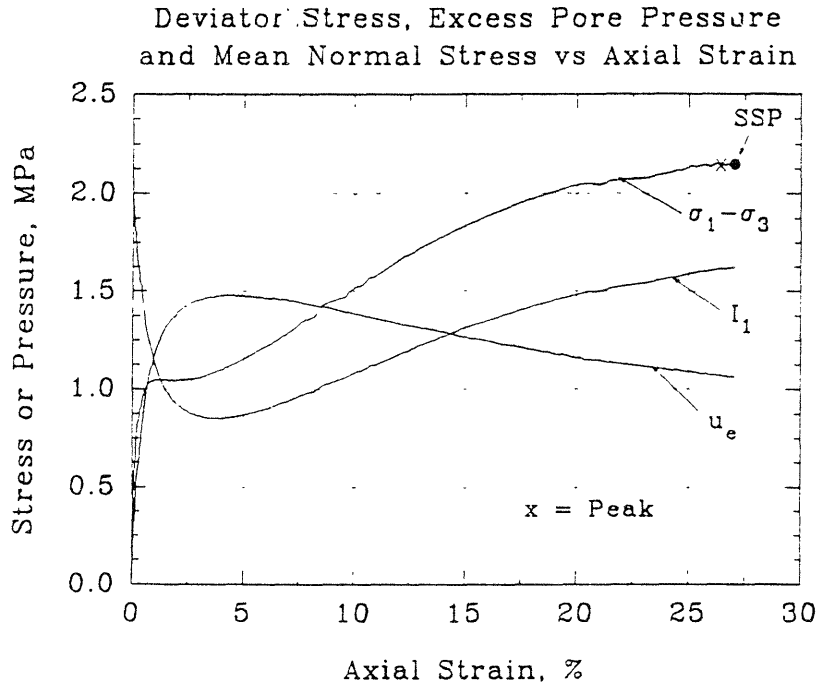

Series C – Test #28

Test type: CAUC
Lubricated Ends: Membrane and vacuum grease
Post-Shear Conditions:
Specimen shape?: RCC with little bulging
Rupture Surface?: No
End behavior?: Sliding at top cap and pedestal, moderate to large lateral expansion
Steady State Conditions Satisfied:
Constant shear stress?: Yes
Constant pore pressure?: Yes
Constant mean normal stress?: Yes

Pre-shear			Steady State Characteristics			
D_r (%)	e	I_c (MPa)	Strain (%)	I_{ss} (MPa) Measured	Calculated	ψ
92.1	0.606	9.480	14.95	4.549	4.077	0.157

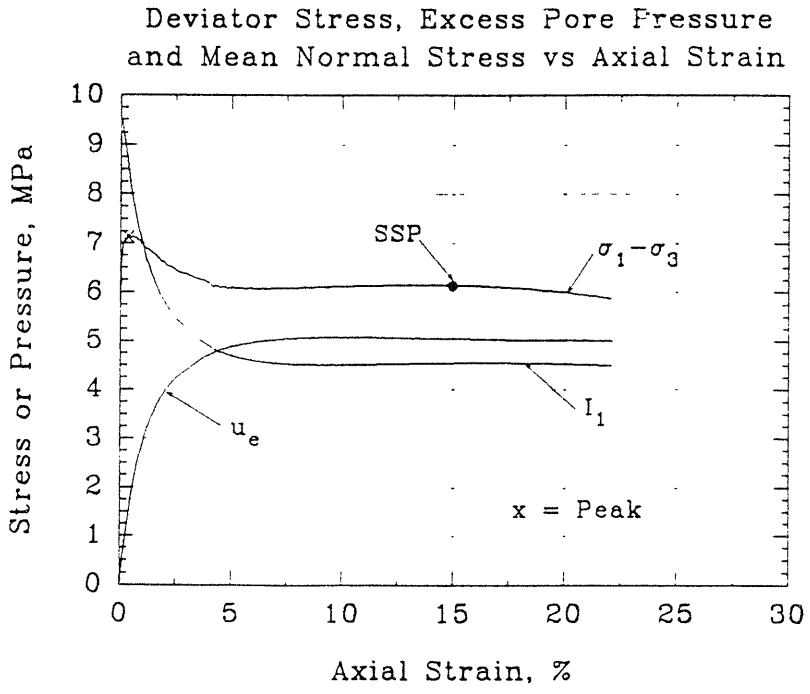

Series C – Test #29

Test type: CAUC
Lubricated Ends: Membrane and vacuum grease
Post-Shear Conditions:
Specimen shape?: RCC throughout
Rupture Surface?: No
End behavior?: No sliding at top cap or pedestal, large lateral expansion
Steady State Conditions Satisfied:
Constant shear stress?: Yes
Constant pore pressure?: Yes
Constant mean normal stress?: Yes

Pre-shear			Steady State Characteristics			
D_r (%)	e	I_c (MPa)	Strain (%)	I_{ss} (MPa) Measured	Calculated	ψ
98.5	0.585	9.204	15.10	4.716	4.564	0.130

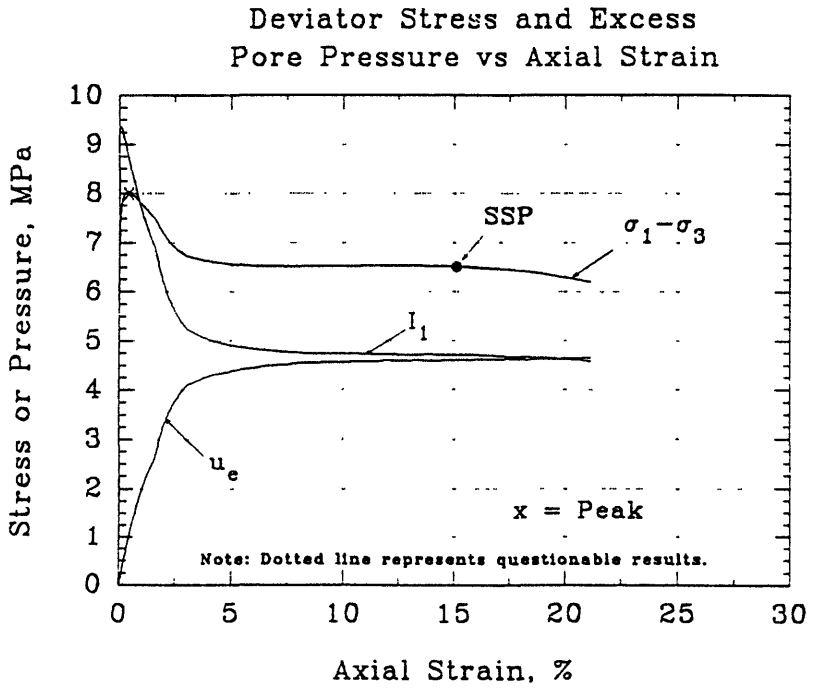

Series C – Test #31

Test type: CIUC
Lubricated Ends: Membrane and vacuum grease
Post-Shear Conditions:
Specimen shape?: Bulging throughout
Rupture Surface?: No
End behavior?: Very constrained at ends, no lateral expansion
Steady State Conditions Satisfied:
Constant shear stress?: Yes
Constant pore pressure?: Yes
Constant mean normal stress?: Approaching

Pre-shear			Steady State Characteristics			
D_r (%)	e	I_c (MPa)	Strain (%)	I_{ss} (MPa) Measured	I_{ss} (MPa) Calculated	ψ
67.2	0.688	0.115	24.79	1.988	1.922	-0.310

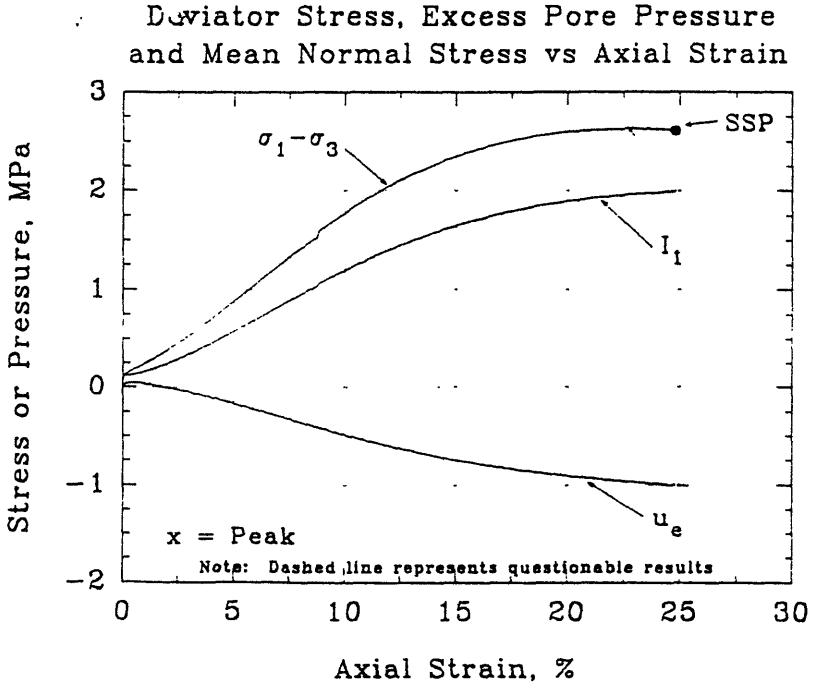

Series C – Test #32

Test type: CAUC
Lubricated Ends: Membrane and vacuum grease
Post-Shear Conditions:
Specimen shape?: RCC with slight bulging
Rupture Surface?: No
End behavior?: Some sliding at top cap, moderate lateral expansion
Steady State Conditions Satisfied:
Constant shear stress?: No
Constant pore pressure?: Yes
Constant mean normal stress?: Yes

Pre-shear			Steady State Characteristics			
D_r (%)	e	I_c (MPa)	Strain (%)	I_{ss} (MPa) Measured	Calculated	ψ
83.9	0.633	7.529	20.10	3.896	3.527	0.141

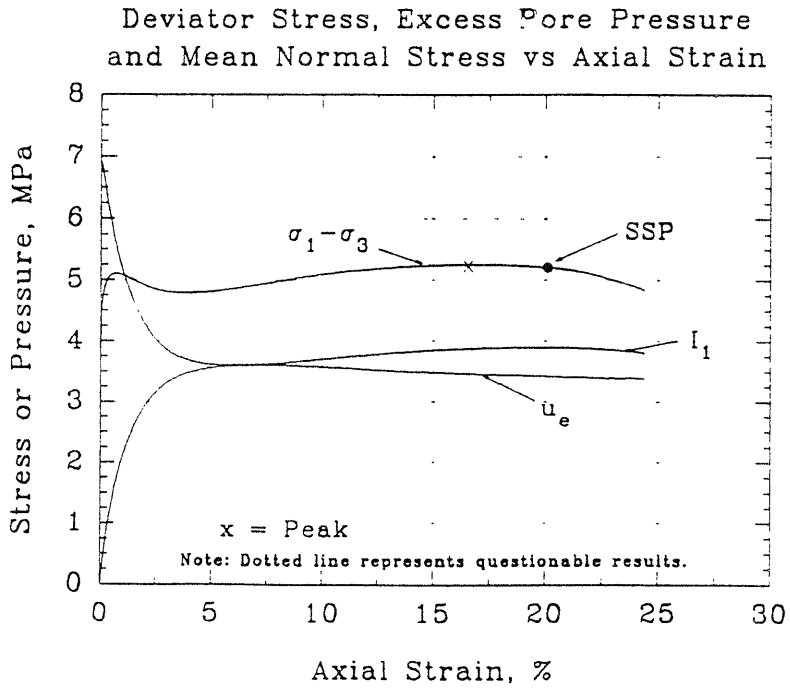

Series C – Test #33

Test type: CIUC
Lubricated Ends: Membrane and vacuum grease
Post-Shear Conditions:
Specimen shape?: RCC with some bulging, S-shaped
Rupture Surface?: No
End behavior?: Sliding at top cap, moderate lateral expansion
Steady State Conditions Satisfied:
Constant shear stress?: No
Constant pore pressure?: Approaching
Constant mean normal stress?: No

Pre-shear			Steady State Characteristics			
D_r (%)	e	I_c (MPa)	Strain (%)	I_{ss} (MPa) Measured	Calculated	ψ
93.4	0.602	2.031	22.43	3.970	4.195	-0.080

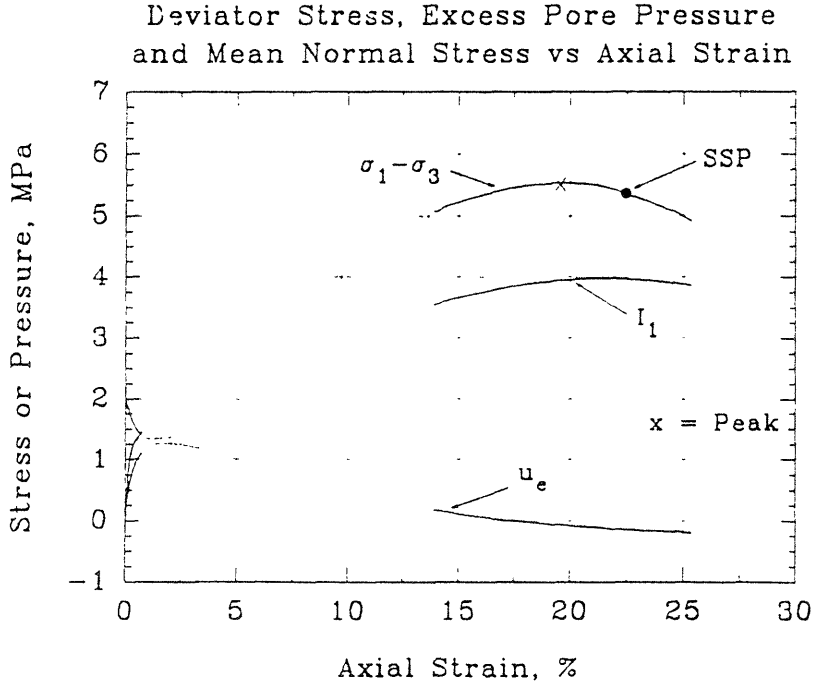

Series C – Test #34

Test type: CIUC
Lubricated Ends: Membrane and vacuum grease
Post-Shear Conditions:
Specimen shape?: Bulging with some RCC
Rupture Surface?: Yes
End behavior?: No sliding at top cap and pedestal, moderate lateral expansion
Steady State Conditions Satisfied:
Constant shear stress?: Yes
Constant pore pressure?: Yes
Constant mean normal stress?: Yes

Pre-shear			Steady State Characteristics			
D_r (%)	e	I_c (MPa)	Strain (%)	I_{ss} (MPa) Measured	Calculated	ψ
94.9	0.597	0.077	25.63	4.011	4.390	-0.445

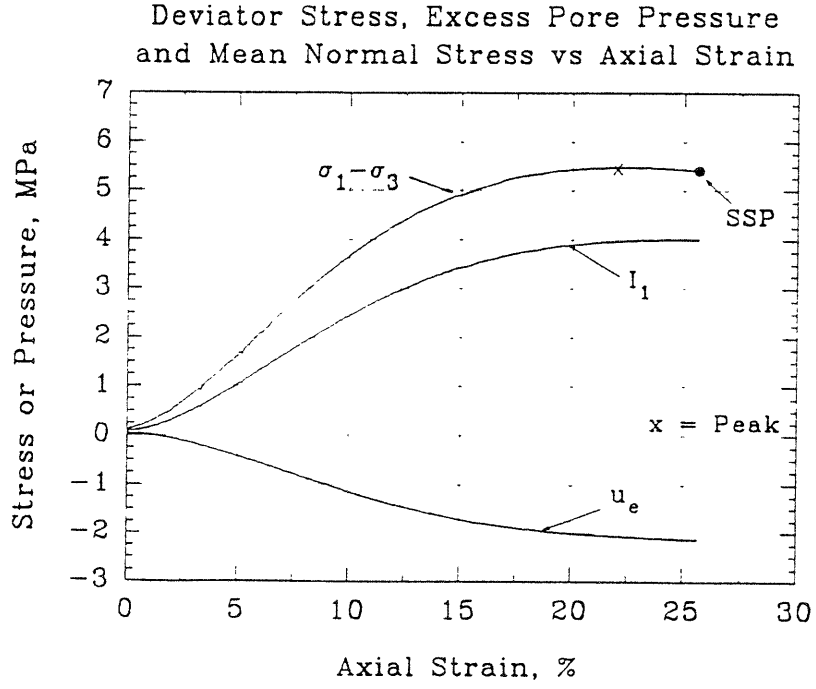

Series C – Test #35

Test type: CIUC
Lubricated Ends: Membrane and vacuum grease
Post-Shear Conditions:
Specimen shape?: RCC throughout
Rupture Surface?: No
End behavior?: No sliding at top cap and pedestal, large lateral expansion
Steady State Conditions Satisfied:
Constant shear stress?: Yes
Constant pore pressure?: Yes
Constant mean normal stress?: Yes

Pre-shear			Steady State Characteristics			
D_r (%)	e	I_c (MPa)	Strain (%)	I_{ss} (MPa) Measured	Calculated	ψ
112.2	0.540	12.527	20.64	4.474	5.813	0.143

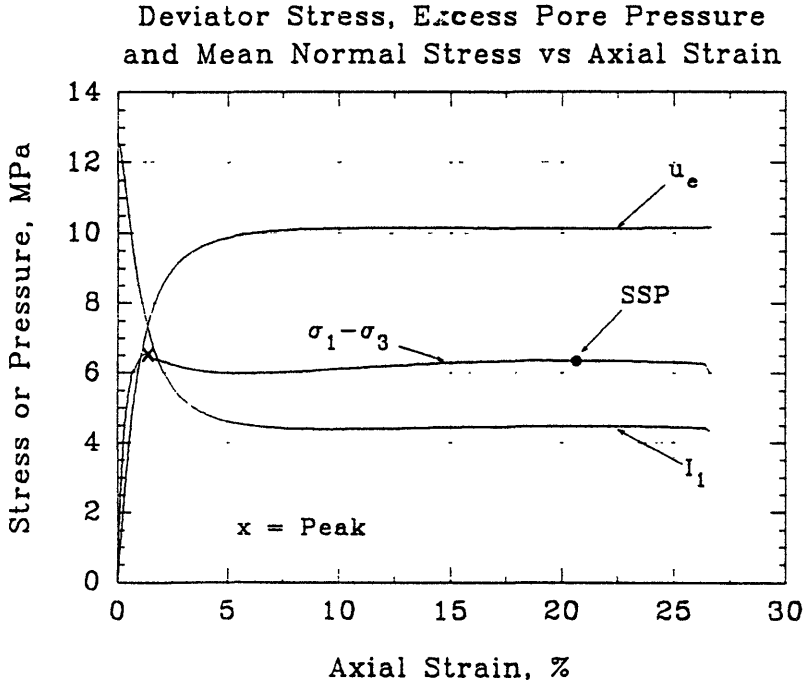

APPENDIX C

TEST RESULTS FOR CONVENTIONAL FROZEN MFS TESTING PROGRAM

APPENDIX C

TEST RESULTS FOR CONVENTIONAL FROZEN MFS TESTING PROGRAM

This appendix presents the measured stress–strain and volumetric strain responses for the conventional frozen MFS tests. Tests are presented in four sections with respect to testing temperature.

Section C.1 Tests at T = –10° C

Section C.2 Tests at T = –15° C

Section C.3 Tests at T = –20° C

Section C.4 Tests at T = –25° C

SECTION C.1

Tests at T = –10° C

(As Performed by Andersen 1991)

FRS15

Deviator Stress vs Axial Strain

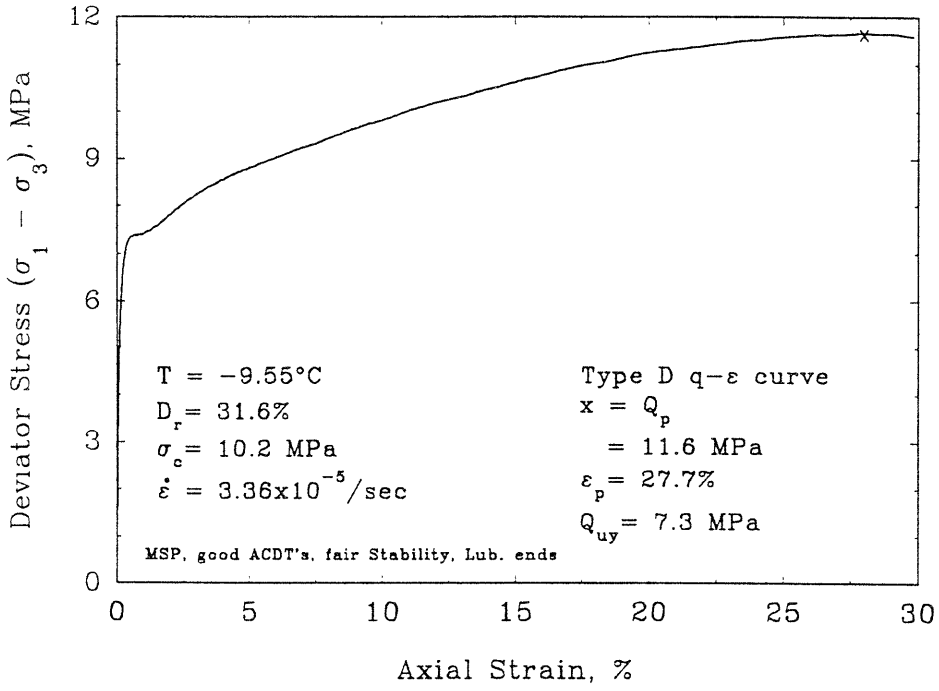

Volumetric vs Axial Strain

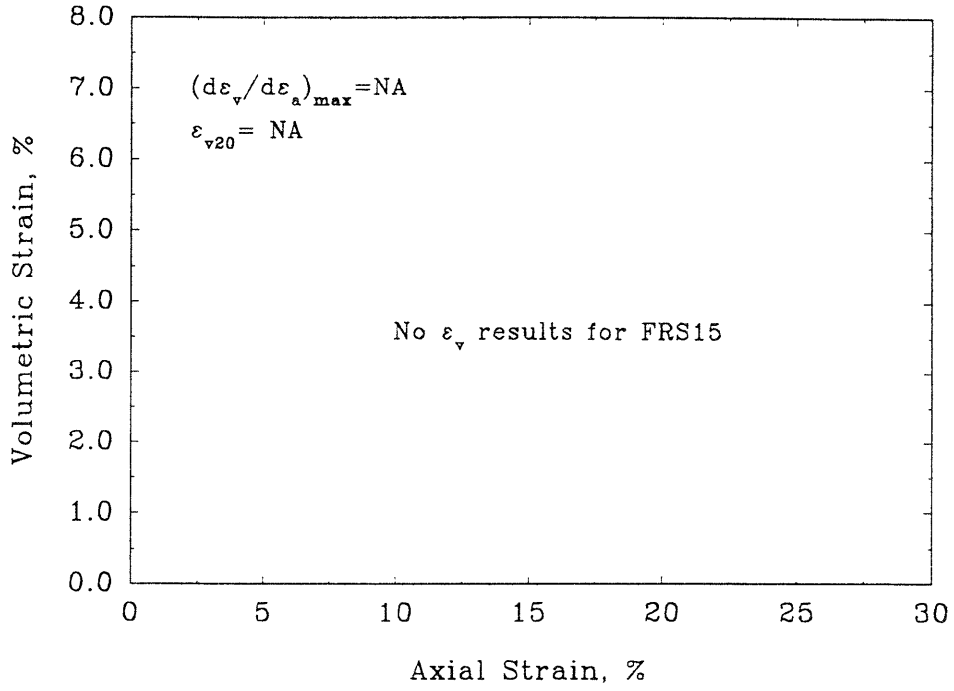

FRS18

Deviator Stress vs Axial Strain

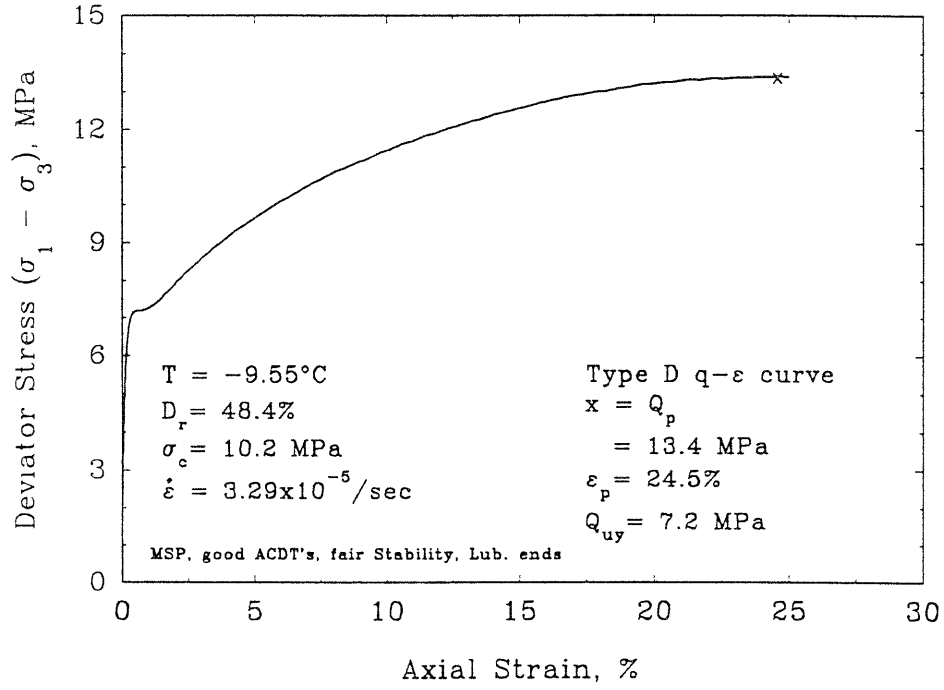

Volumetric vs Axial Strain

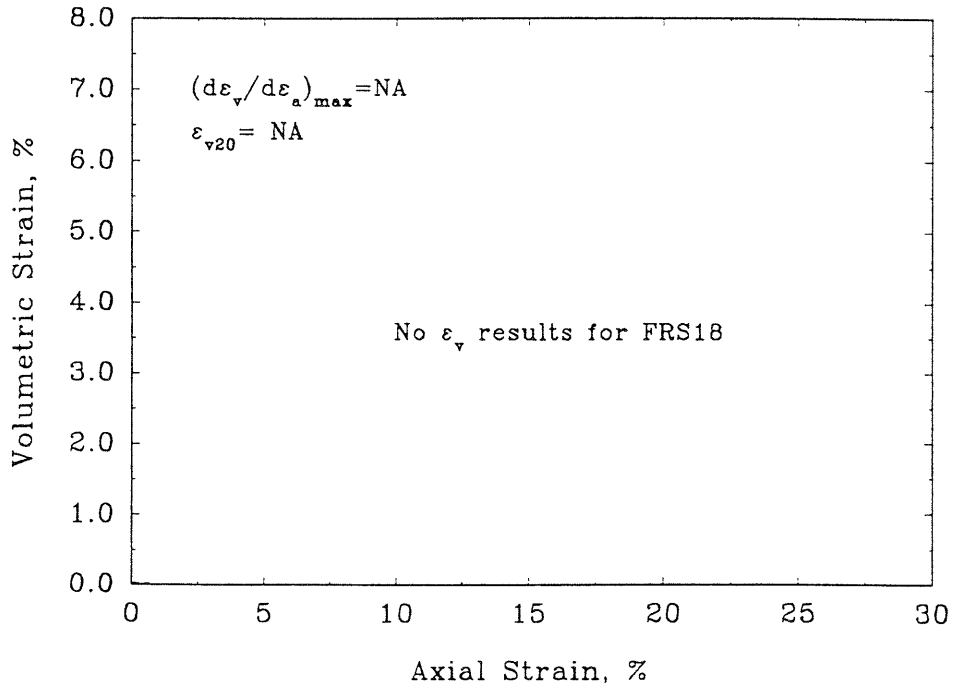

FRS19

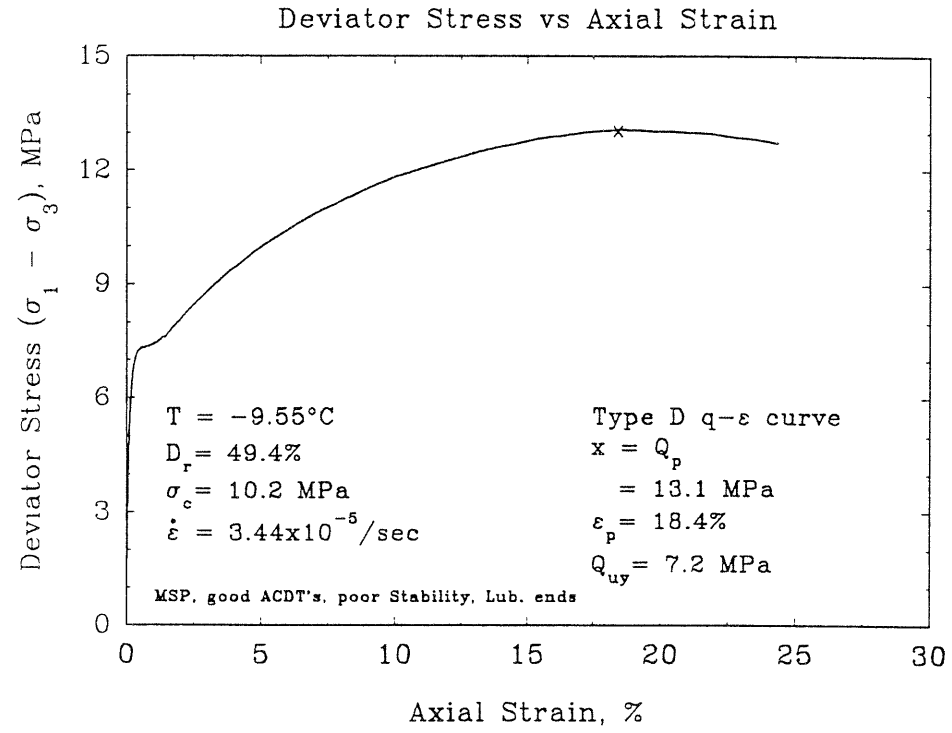
Deviator Stress vs Axial Strain
Deviator Stress ($\sigma_1 - \sigma_3$), MPa
Axial Strain, %
T = -9.55°C
D_r = 49.4%
σ_c = 10.2 MPa
$\dot{\varepsilon}$ = 3.44x10^{-5}/sec
Type D q-ε curve
x = Q_p
= 13.1 MPa
ε_p = 18.4%
Q_{uy} = 7.2 MPa
MSP, good ACDT's, poor Stability, Lub. ends

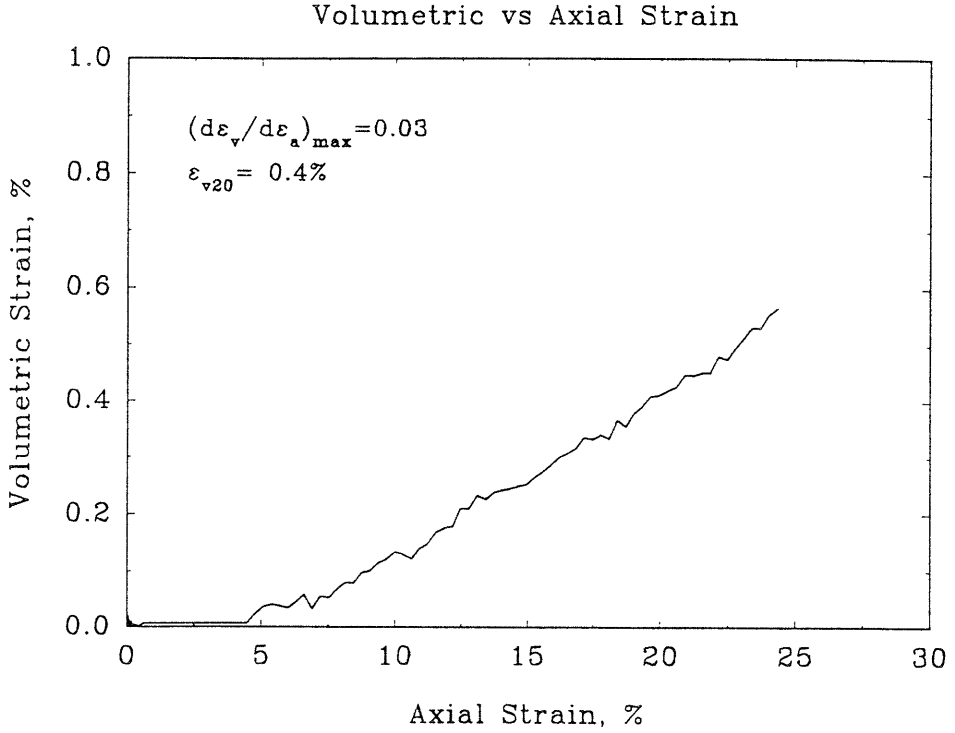
Volumetric vs Axial Strain
Volumetric Strain, %
Axial Strain, %
$(d\varepsilon_v/d\varepsilon_a)_{max}$=0.03
ε_{v20}= 0.4%

FRS20

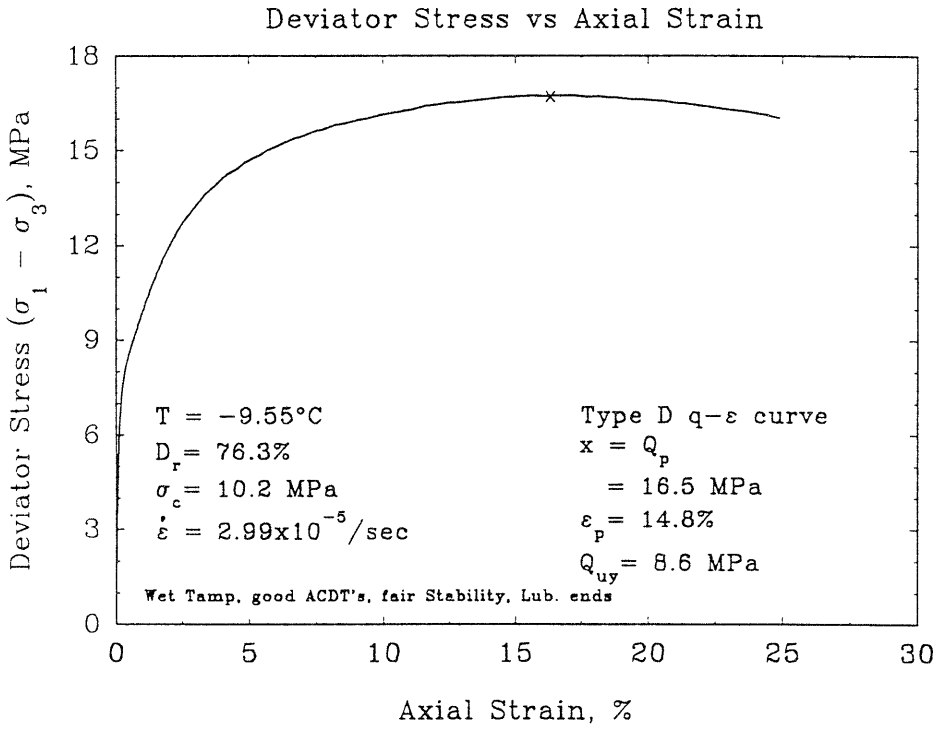
Deviator Stress vs Axial Strain
Deviator Stress ($\sigma_1 - \sigma_3$), MPa
Axial Strain, %
T = −9.55°C
D_r= 76.3%
σ_c= 10.2 MPa
$\dot{\varepsilon}$ = 2.99x10^{-5}/sec
Type D q−ε curve
x = Q_p
= 16.5 MPa
ε_p= 14.8%
Q_{uy}= 8.6 MPa
Wet Tamp, good ACDT's, fair Stability, Lub. ends

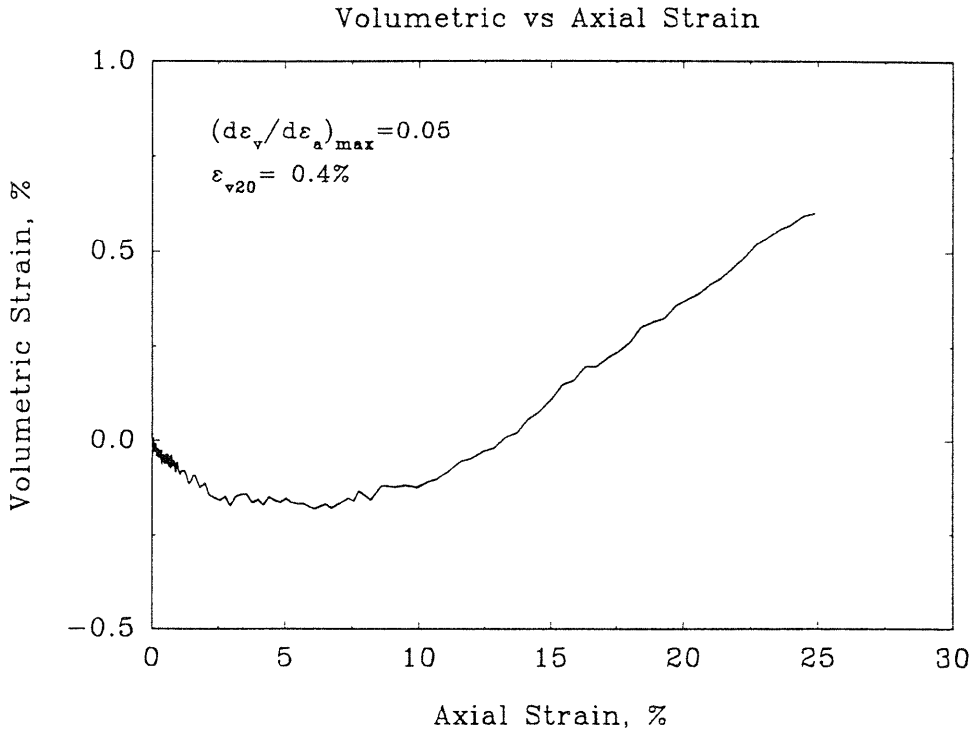
Volumetric vs Axial Strain
Volumetric Strain, %
Axial Strain, %
$(d\varepsilon_v/d\varepsilon_a)_{max}$=0.05
ε_{v20}= 0.4%

FRS21

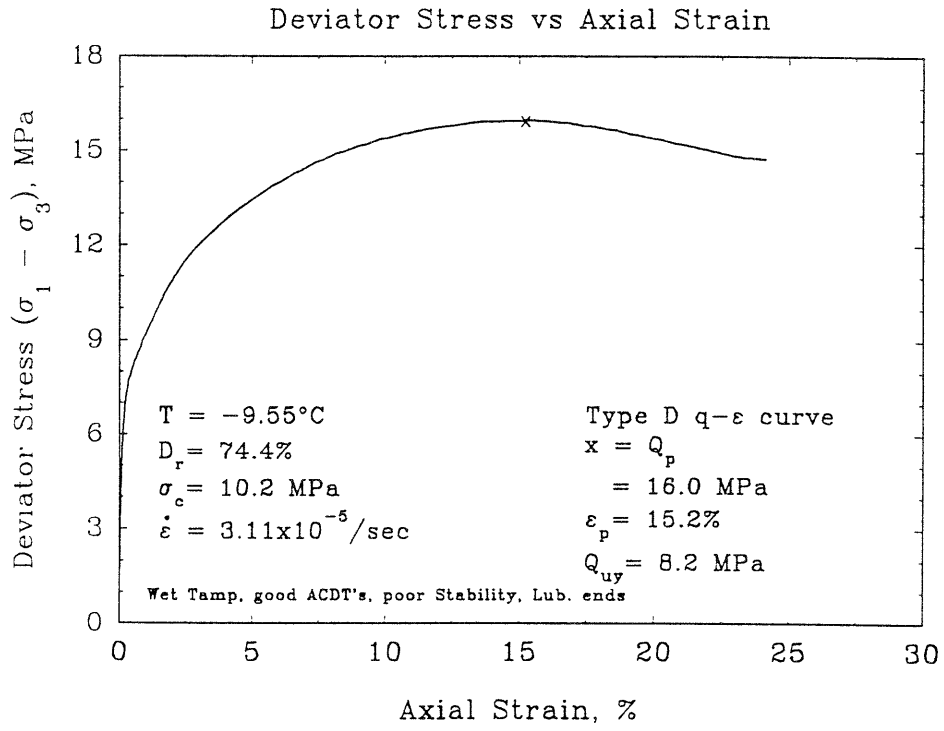
Deviator Stress vs Axial Strain
Deviator Stress ($\sigma_1 - \sigma_3$), MPa
Axial Strain, %
T = −9.55°C
D_r = 74.4%
σ_c = 10.2 MPa
$\dot{\varepsilon}$ = 3.11x10^{-5}/sec
Type D q−ε curve
x = Q_p
= 16.0 MPa
ε_p = 15.2%
Q_{uy} = 8.2 MPa
Wet Tamp, good ACDT's, poor Stability, Lub. ends

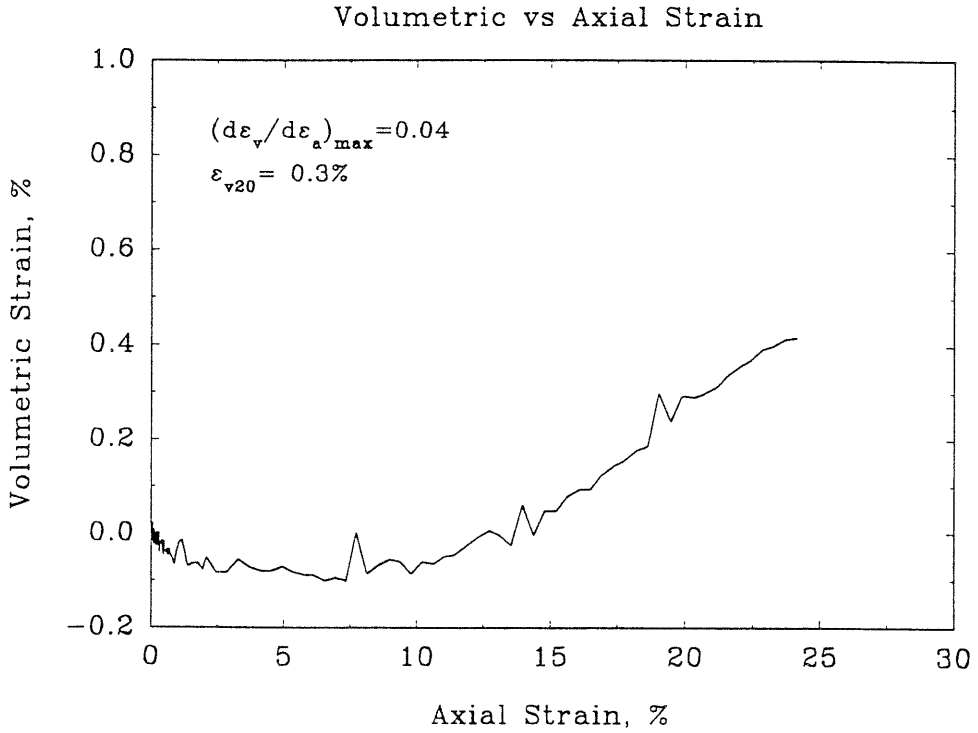
Volumetric vs Axial Strain
Volumetric Strain, %
Axial Strain, %
$(d\varepsilon_v/d\varepsilon_a)_{max}$=0.04
ε_{v20}= 0.3%

FRS22

Deviator Stress vs Axial Strain

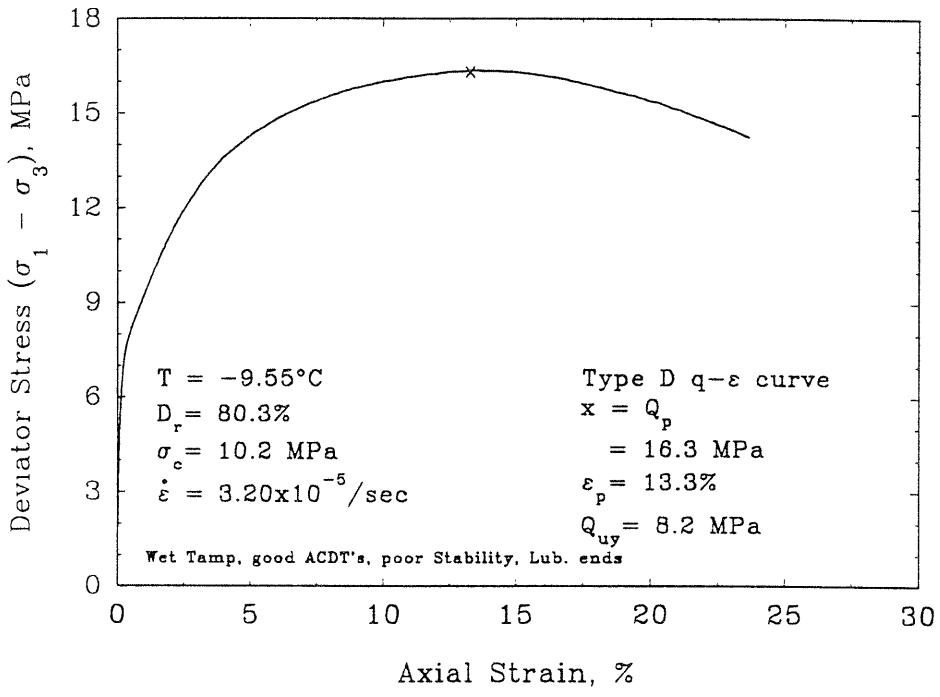

Volumetric vs Axial Strain

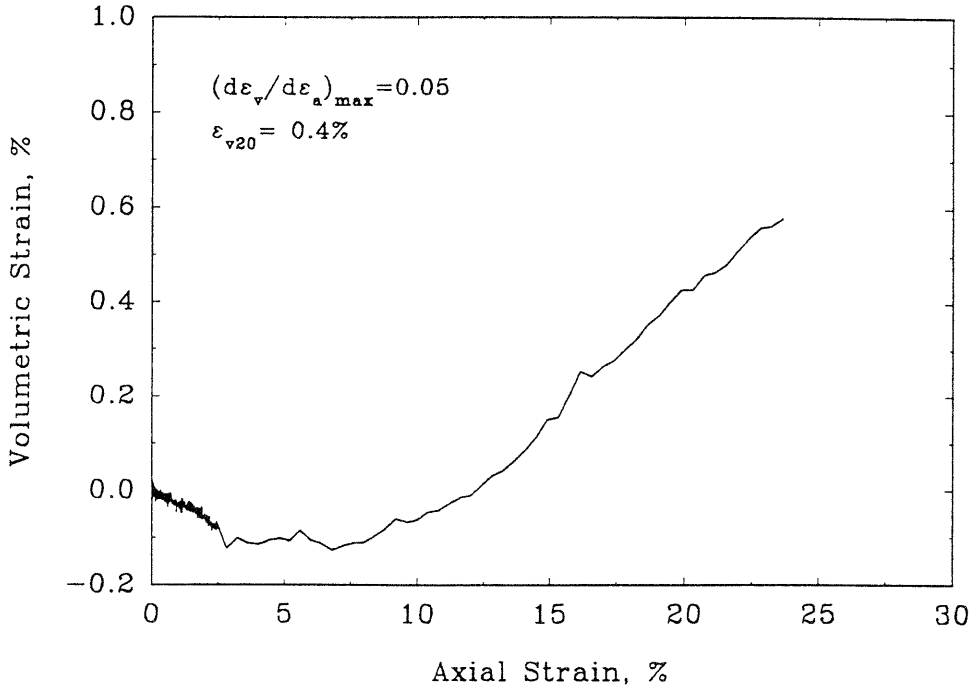

FRS23

Deviator Stress vs Axial Strain

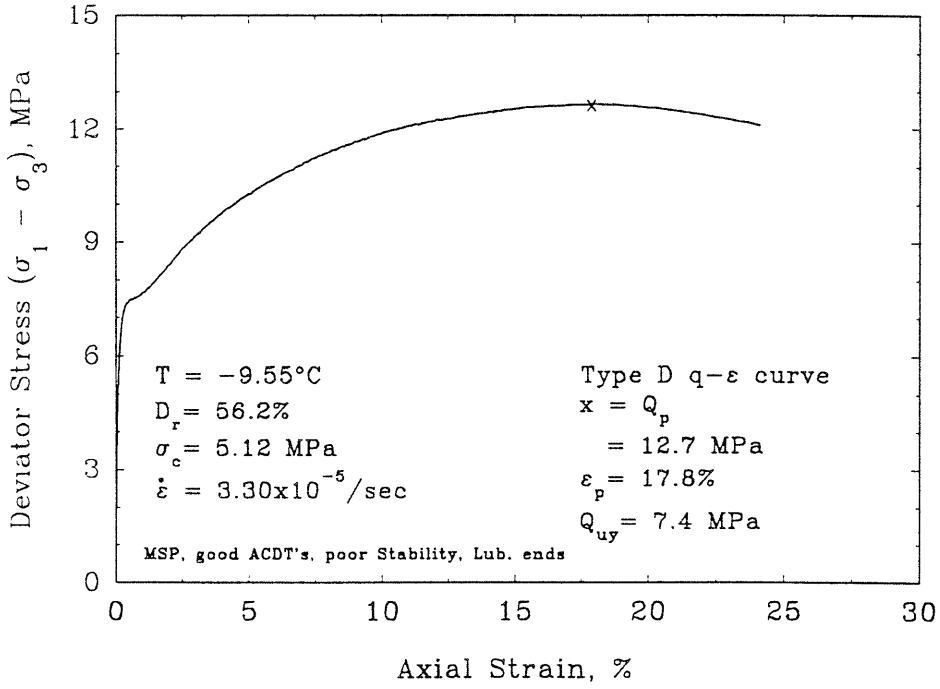

Volumetric vs Axial Strain

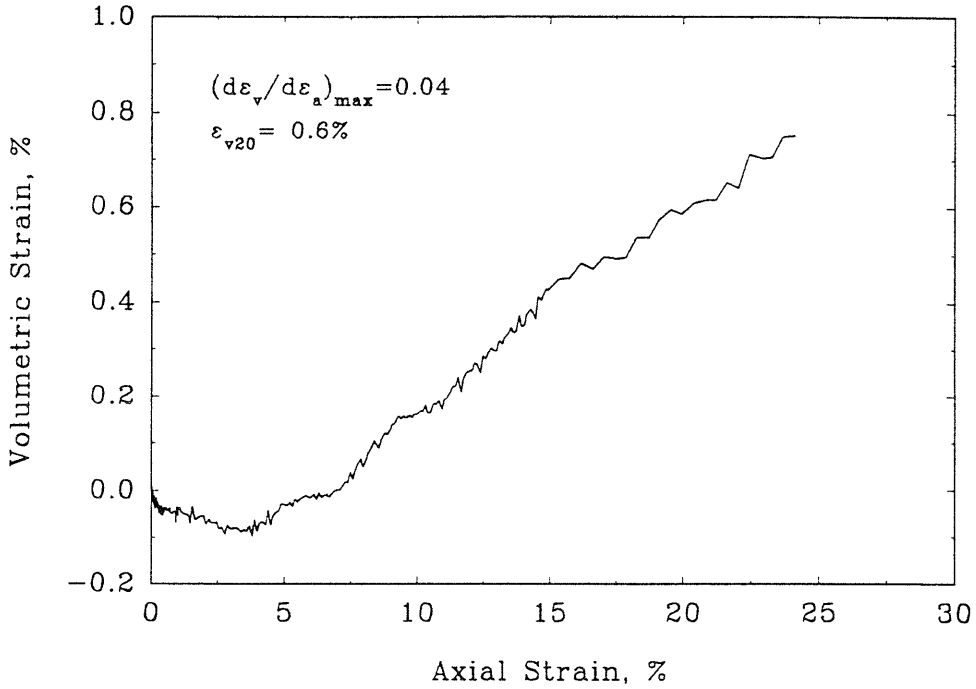

FRS24

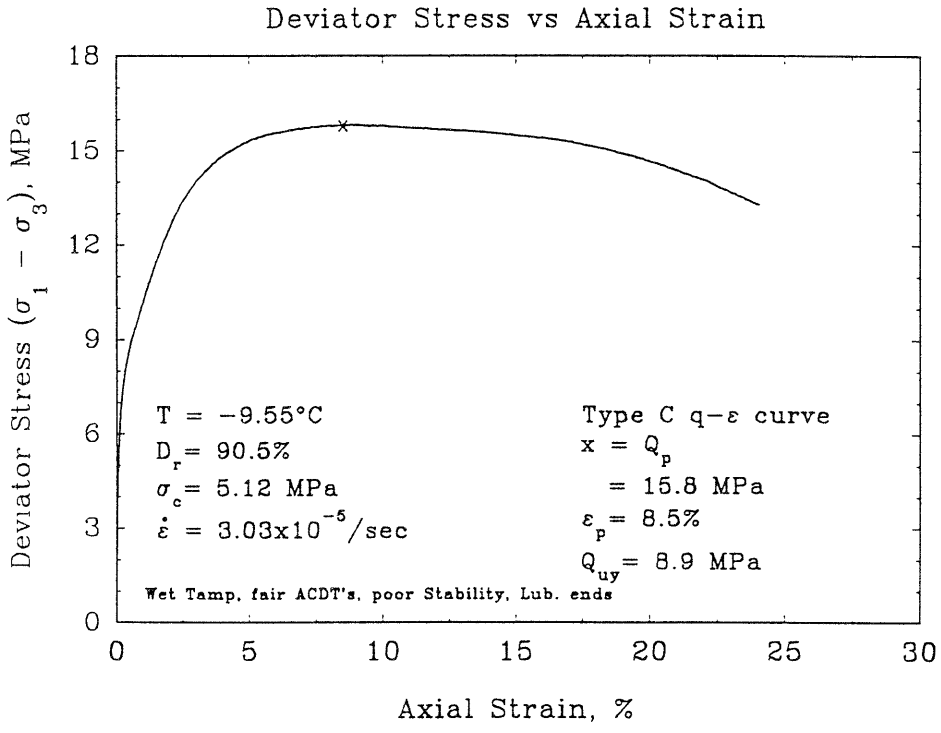
Deviator Stress vs Axial Strain
Deviator Stress ($\sigma_1 - \sigma_3$), MPa
Axial Strain, %
T = −9.55°C
D_r= 90.5%
σ_c= 5.12 MPa
$\dot{\varepsilon}$ = 3.03x10^{-5}/sec
Type C q−ε curve
x = Q_p
= 15.8 MPa
ε_p= 8.5%
Q_{uy}= 8.9 MPa
Wet Tamp, fair ACDT's, poor Stability, Lub. ends

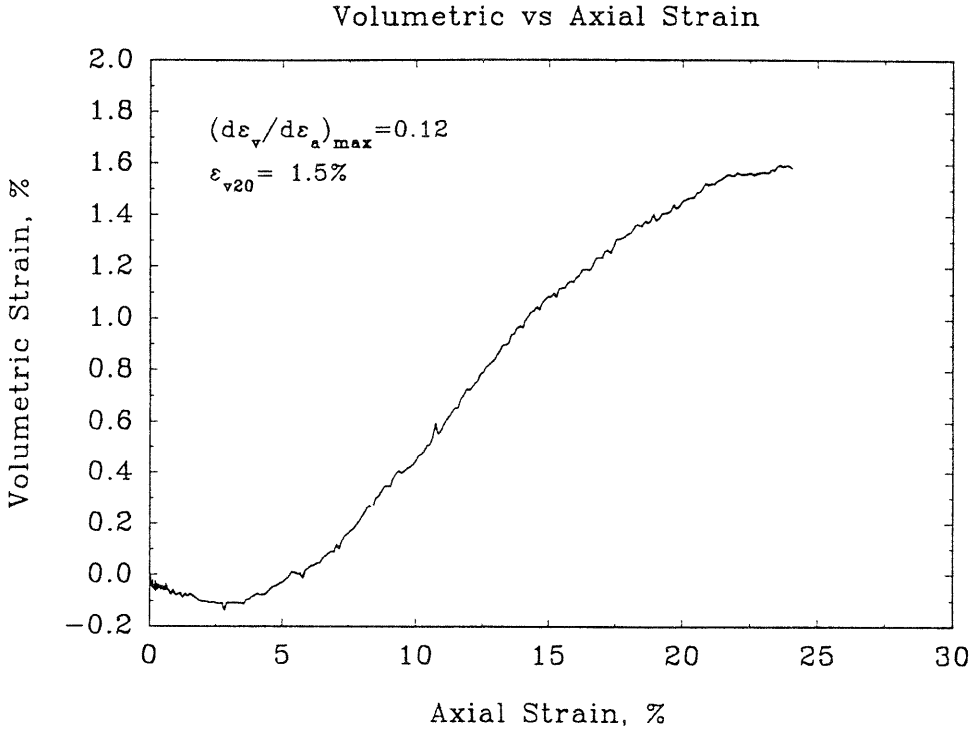
Volumetric vs Axial Strain
Volumetric Strain, %
Axial Strain, %
$(d\varepsilon_v/d\varepsilon_a)_{max}$=0.12
ε_{v20}= 1.5%

FRS25

Deviator Stress vs Axial Strain

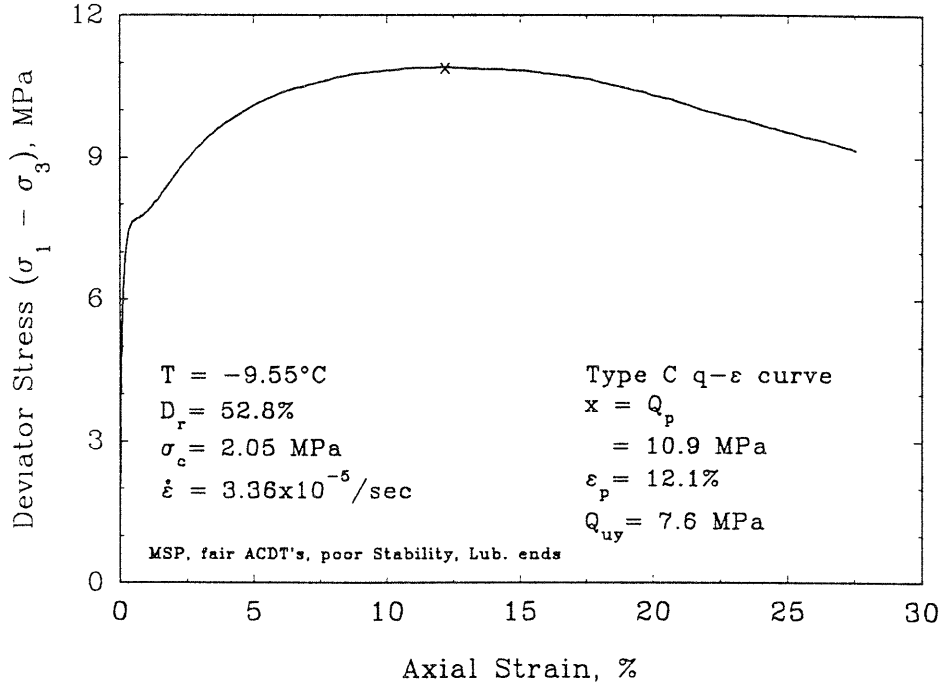

Volumetric vs Axial Strain

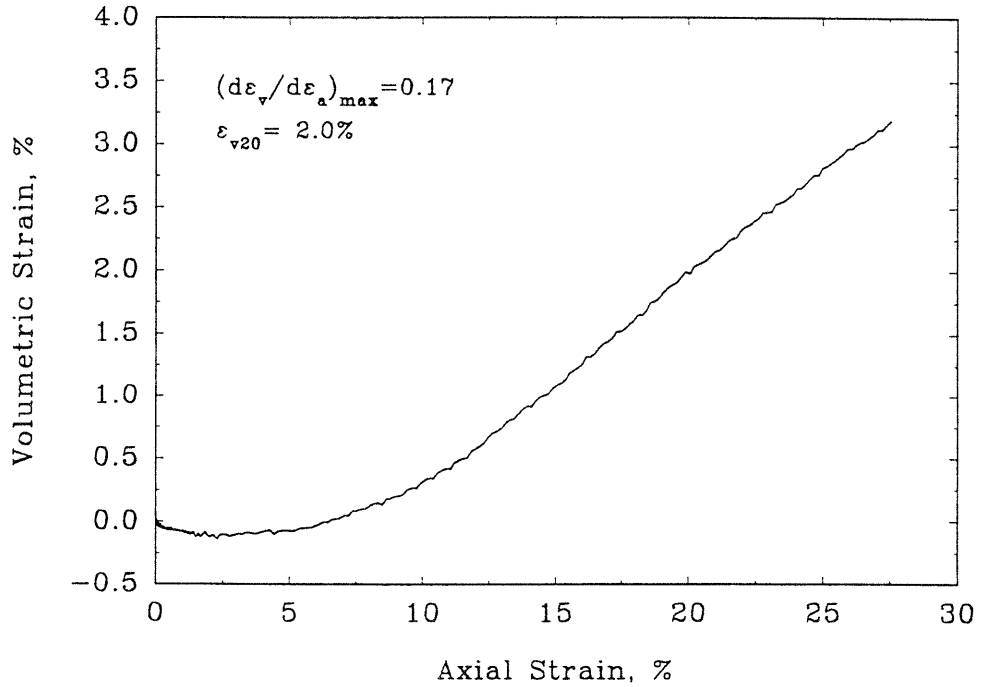

FRS26

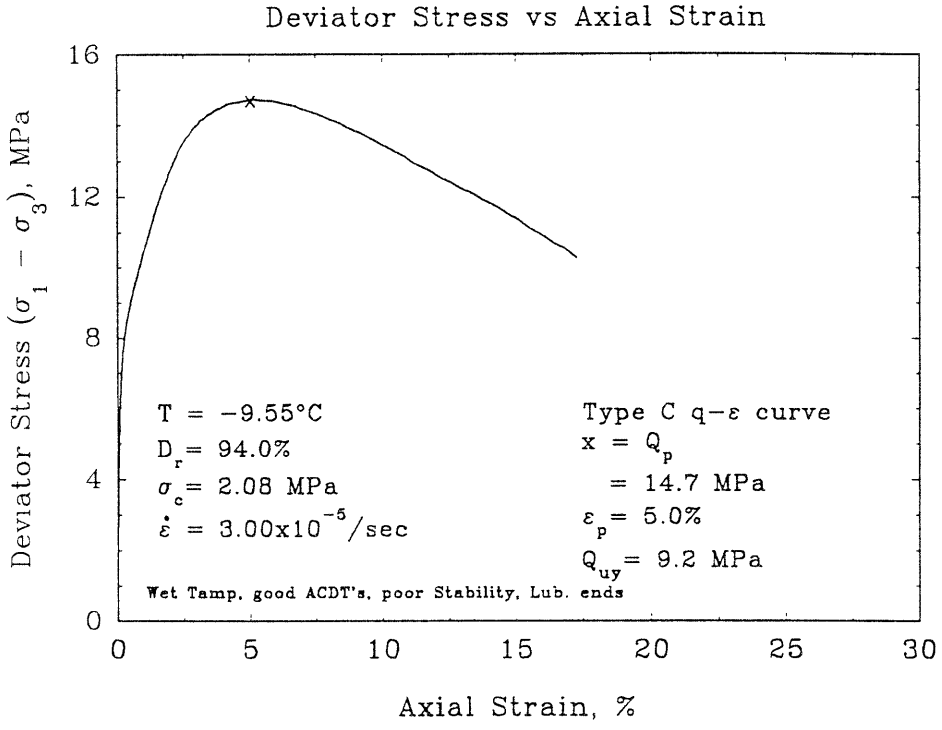
Deviator Stress vs Axial Strain
Deviator Stress ($\sigma_1 - \sigma_3$), MPa
Axial Strain, %
T = -9.55°C
D_r = 94.0%
σ_c = 2.08 MPa
$\dot{\varepsilon}$ = 3.00x10^{-5}/sec
Type C q-ε curve
x = Q_p
= 14.7 MPa
ε_p = 5.0%
Q_{uy} = 9.2 MPa
Wet Tamp, good ACDT's, poor Stability, Lub. ends

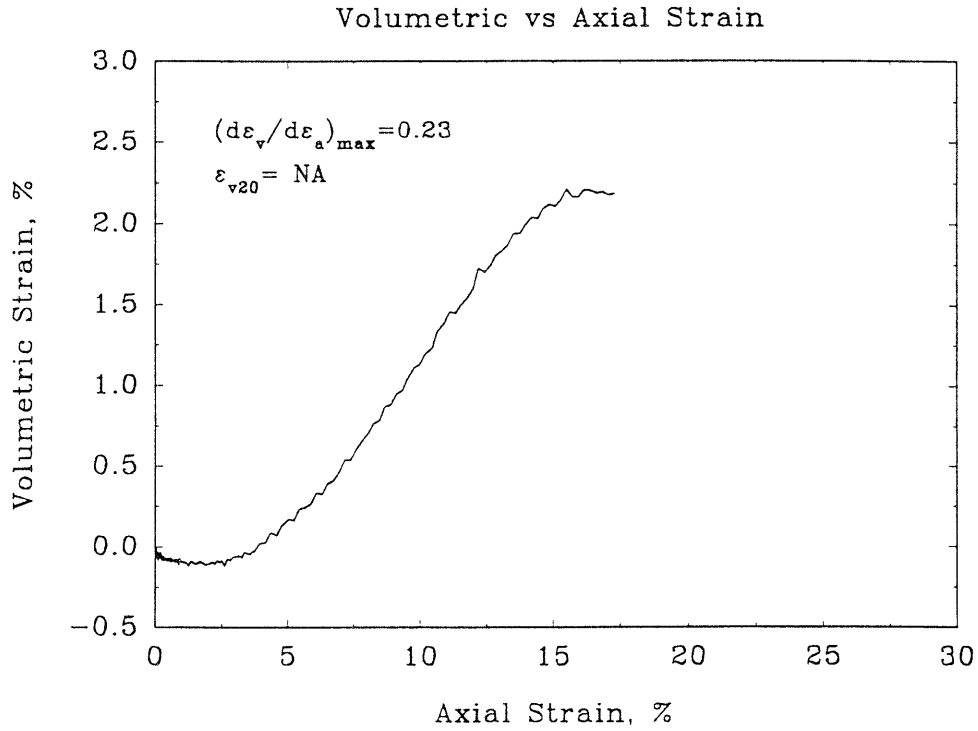
Volumetric vs Axial Strain
Volumetric Strain, %
Axial Strain, %
$(d\varepsilon_v/d\varepsilon_a)_{max}$=0.23
ε_{v20}= NA

FRS27

Deviator Stress vs Axial Strain

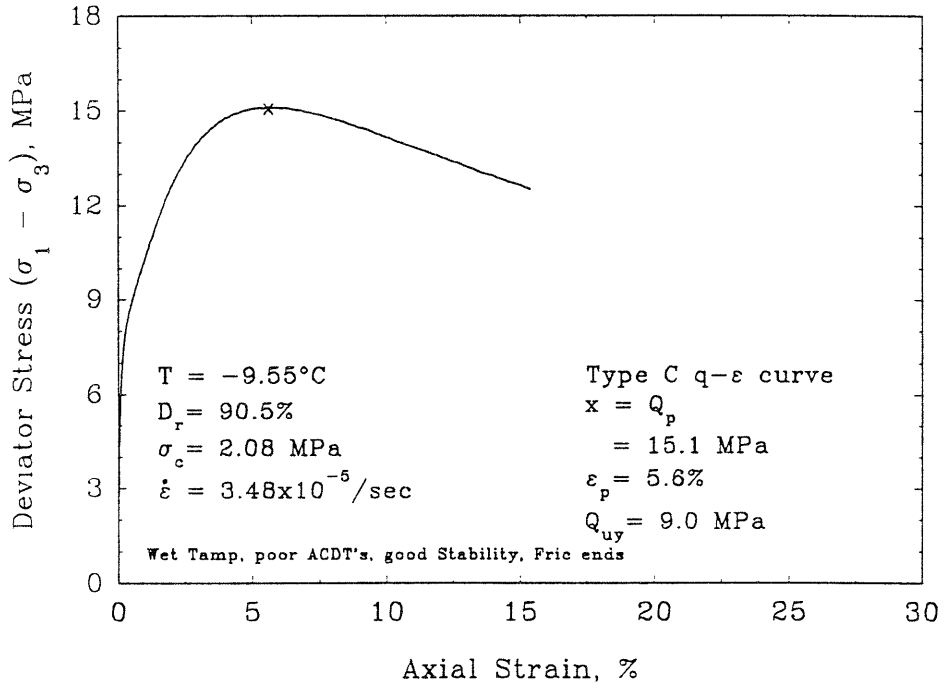

Volumetric vs Axial Strain

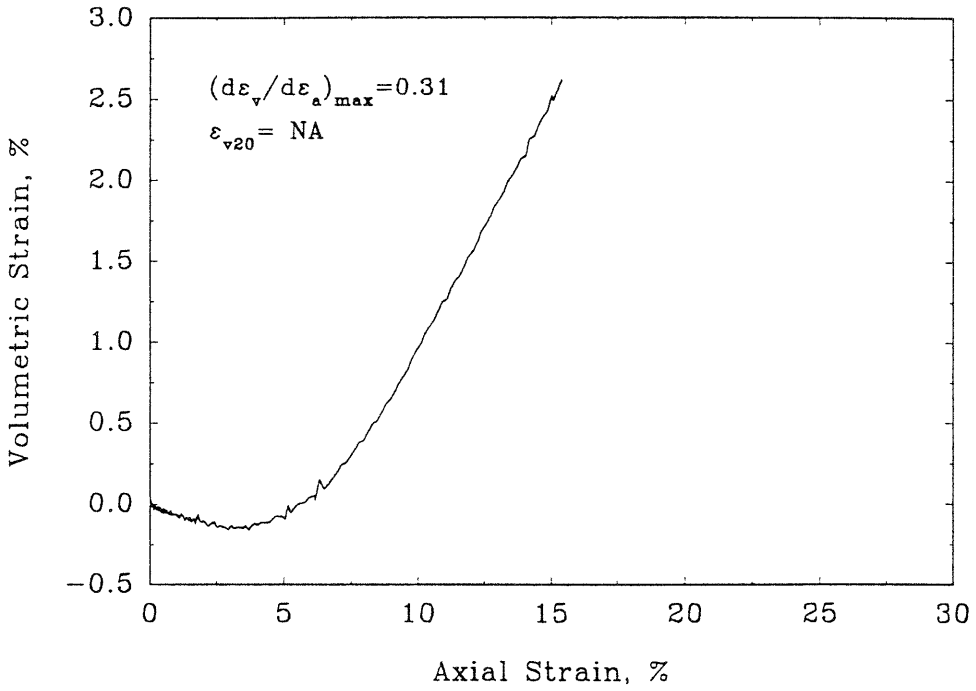

FRS28

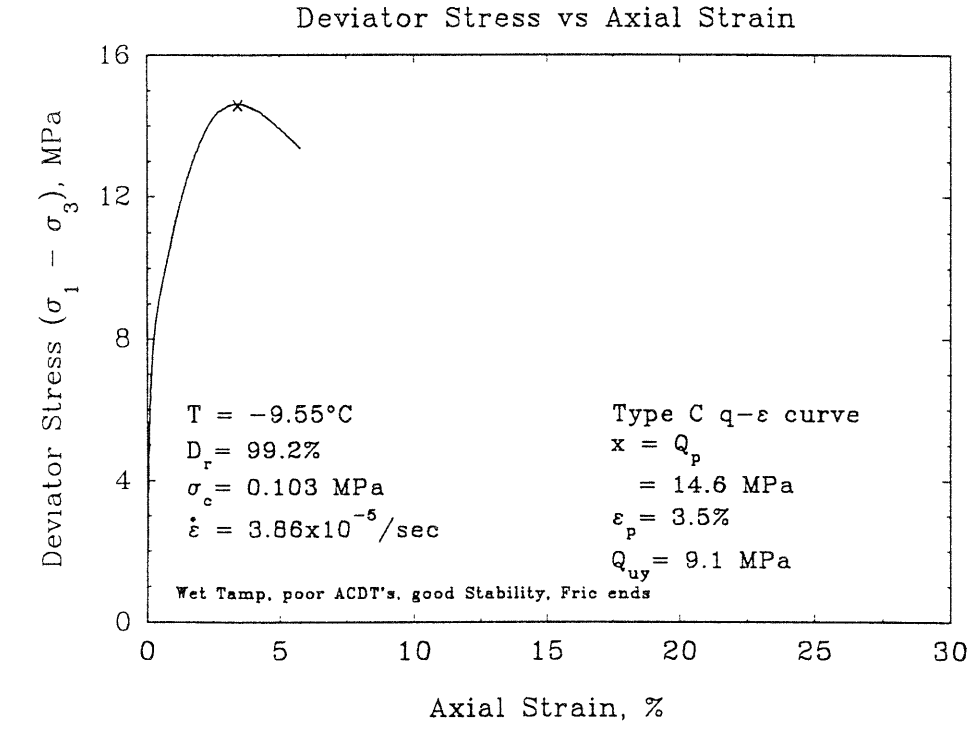
Deviator Stress vs Axial Strain
Deviator Stress ($\sigma_1 - \sigma_3$), MPa
16
12
8
4
0
0
5
10
15
20
25
30
Axial Strain, %
T = −9.55°C
D_r= 99.2%
σ_c= 0.103 MPa
$\dot{\varepsilon}$ = 3.86x10^{-5}/sec
Type C q−ε curve
x = Q_p
= 14.6 MPa
ε_p= 3.5%
Q_{uy}= 9.1 MPa
Wet Tamp, poor ACDT's, good Stability, Fric ends

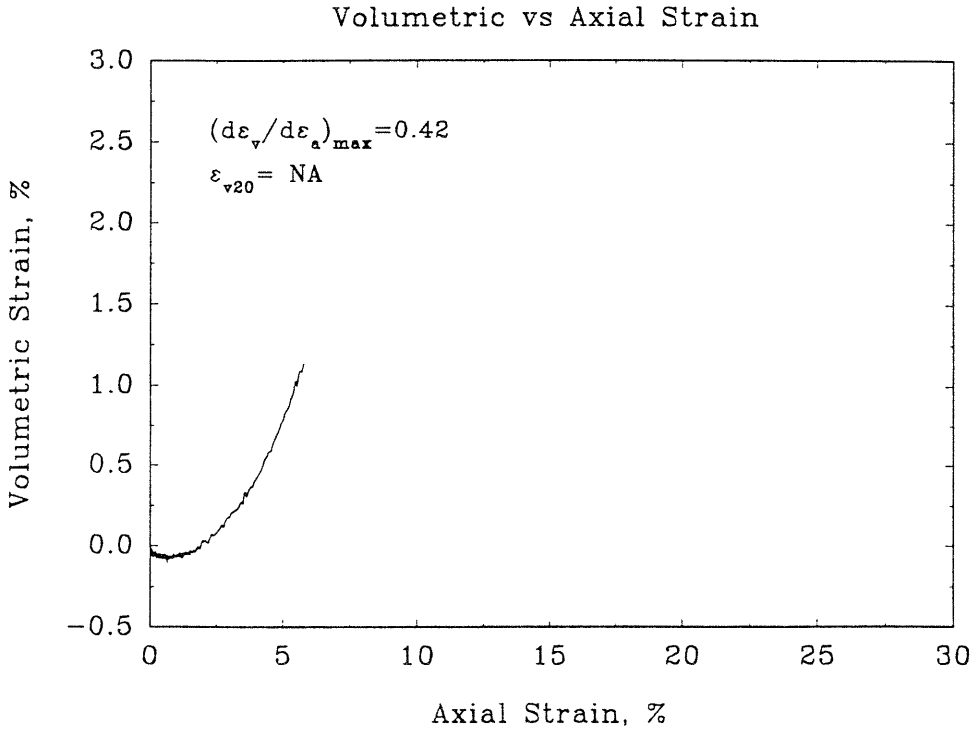
Volumetric vs Axial Strain
Volumetric Strain, %
3.0
2.5
2.0
1.5
1.0
0.5
0.0
−0.5
0
5
10
15
20
25
30
Axial Strain, %
$(d\varepsilon_v/d\varepsilon_a)_{max}$=0.42
ε_{v20}= NA

FRS29

Deviator Stress vs Axial Strain

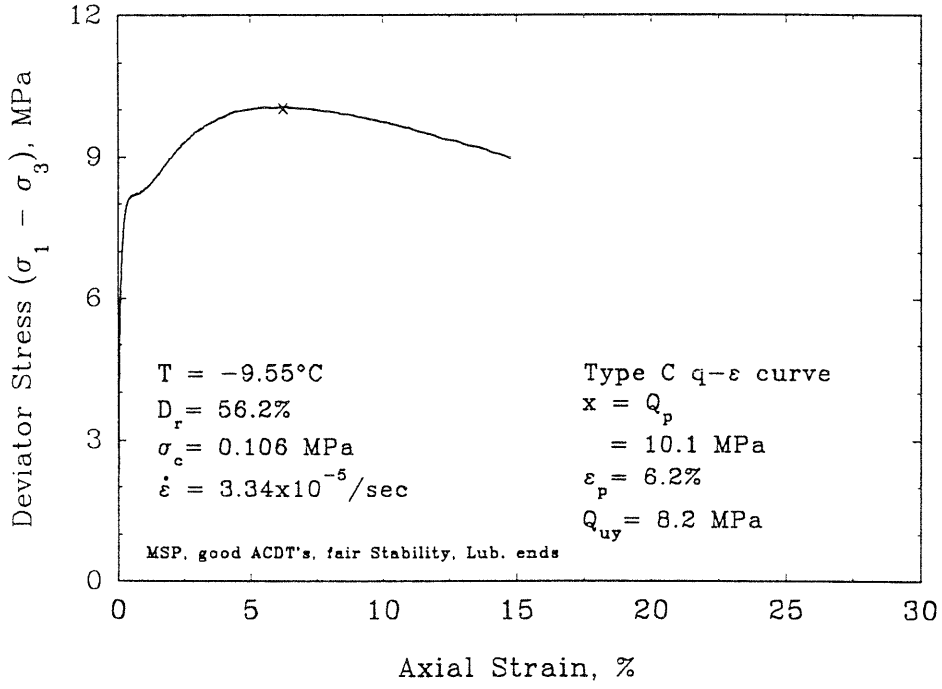

Volumetric vs Axial Strain

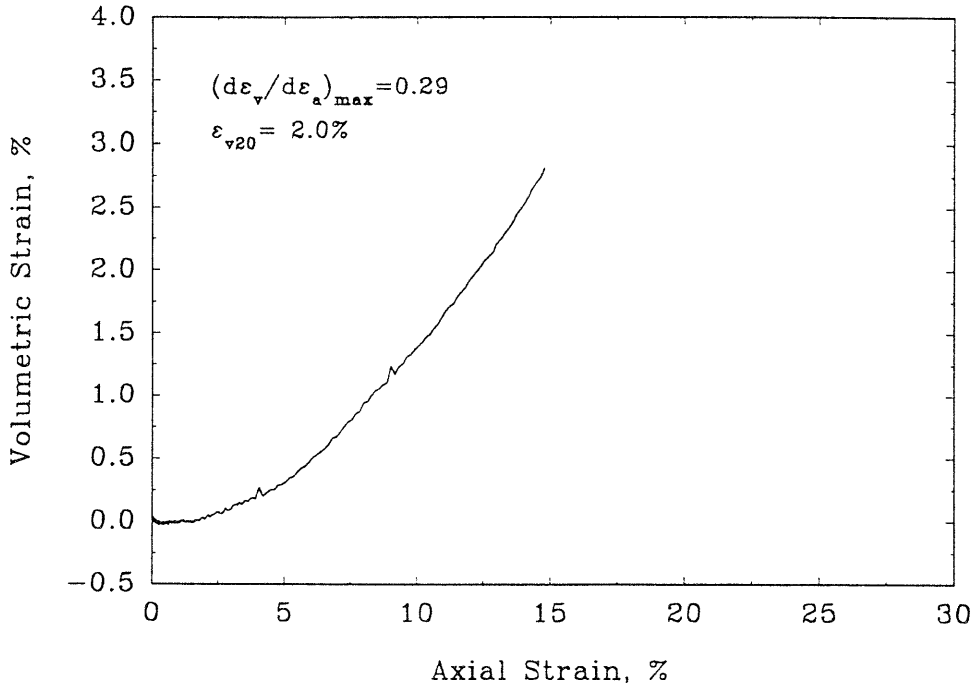

FRS30

Deviator Stress vs Axial Strain

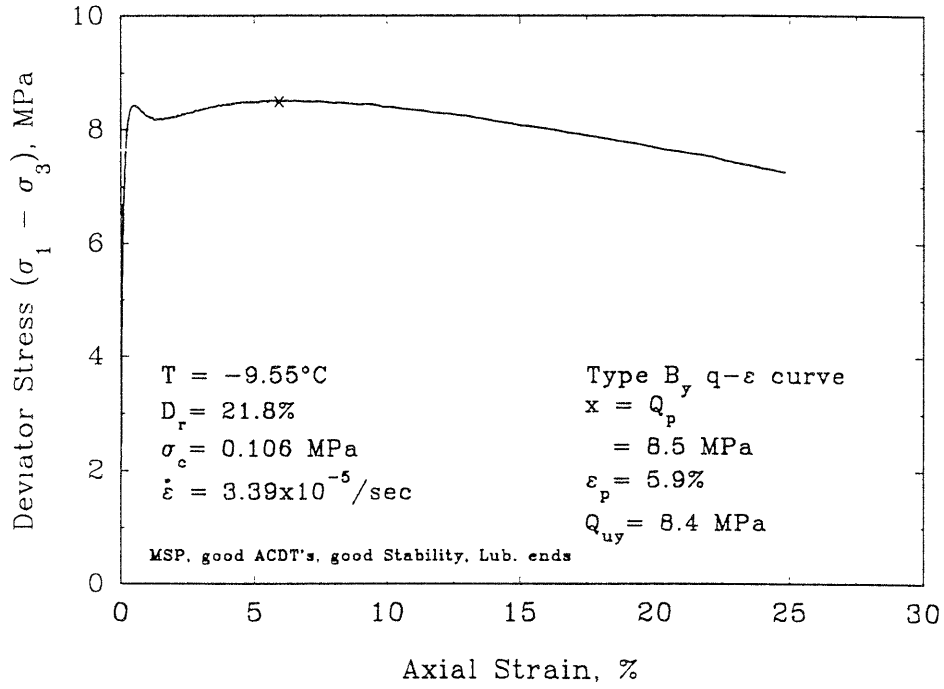

Volumetric vs Axial Strain

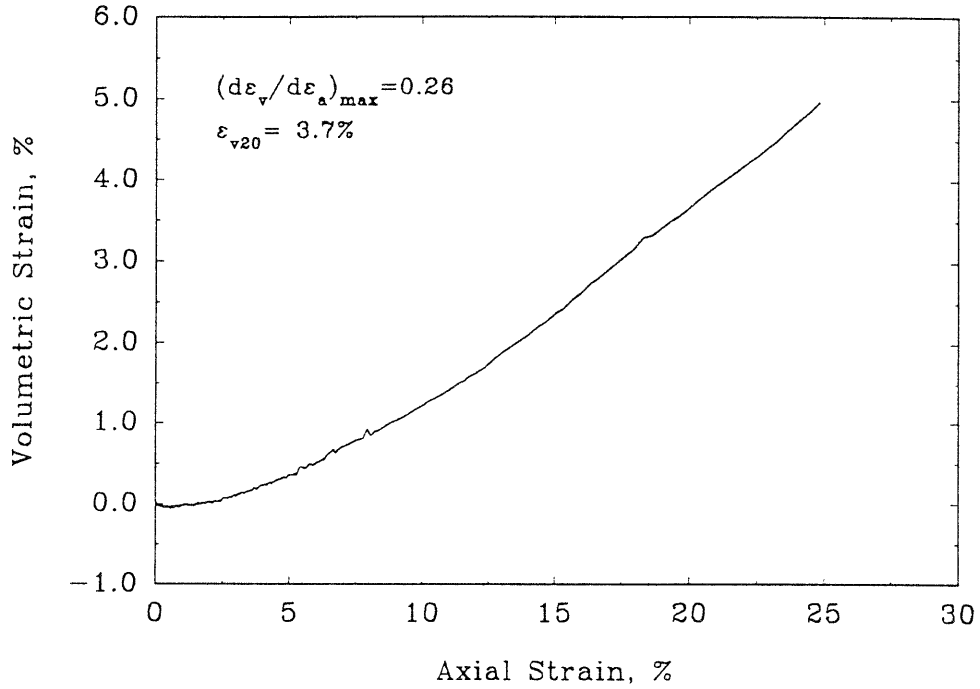

FRS31

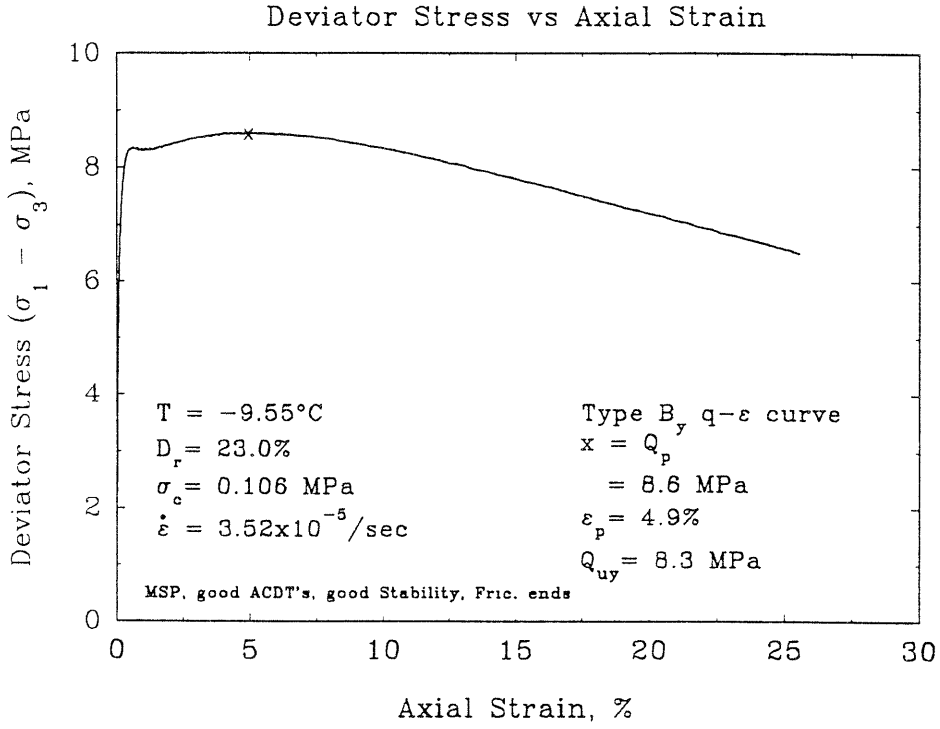
Deviator Stress vs Axial Strain
Deviator Stress ($\sigma_1 - \sigma_3$), MPa
Axial Strain, %
T = −9.55°C
D_r= 23.0%
σ_c= 0.106 MPa
$\dot{\varepsilon}$ = 3.52x10^{-5}/sec
Type B_y q−ε curve
x = Q_p
= 8.6 MPa
ε_p= 4.9%
Q_{uy}= 8.3 MPa
MSP, good ACDT's, good Stability, Fric. ends

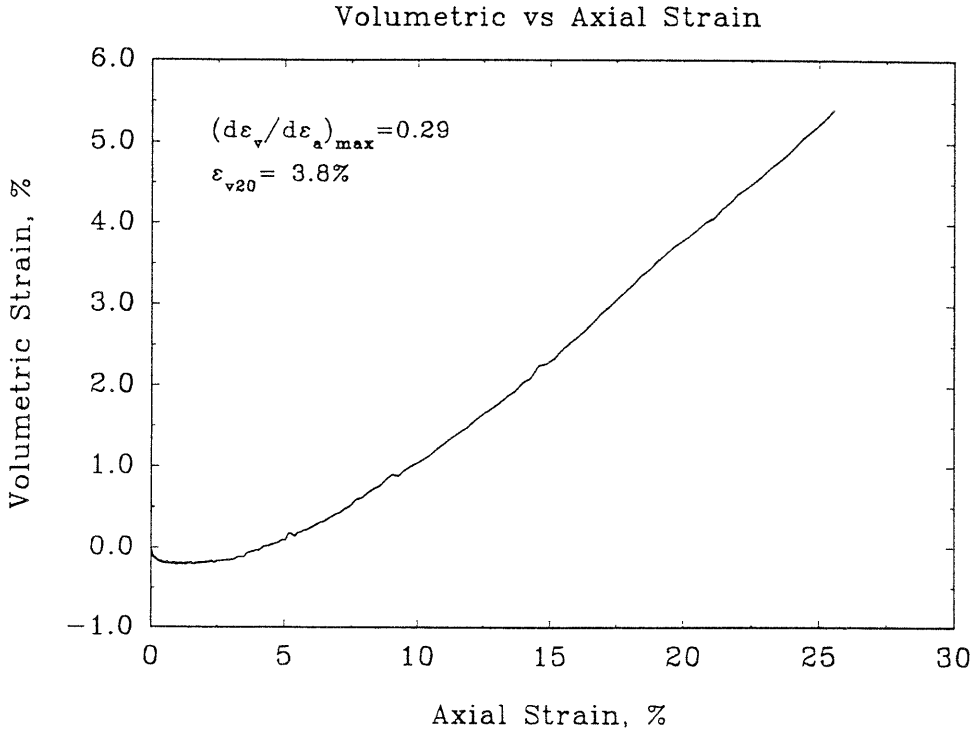
Volumetric vs Axial Strain
Volumetric Strain, %
Axial Strain, %
$(d\varepsilon_v/d\varepsilon_a)_{max}$=0.29
ε_{v20}= 3.8%

FRS32

Deviator Stress vs Axial Strain

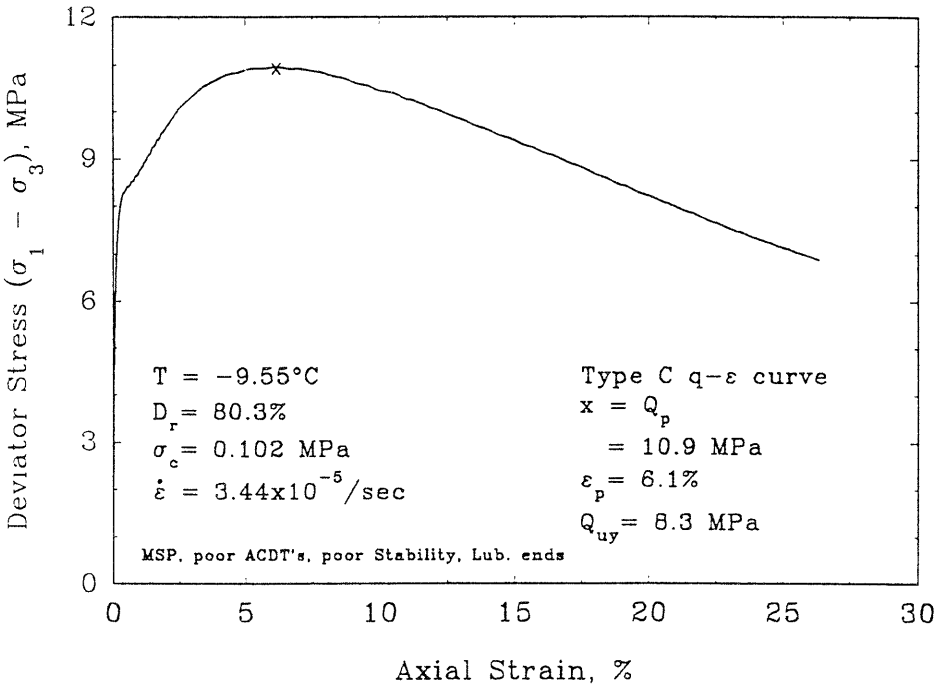

Volumetric vs Axial Strain

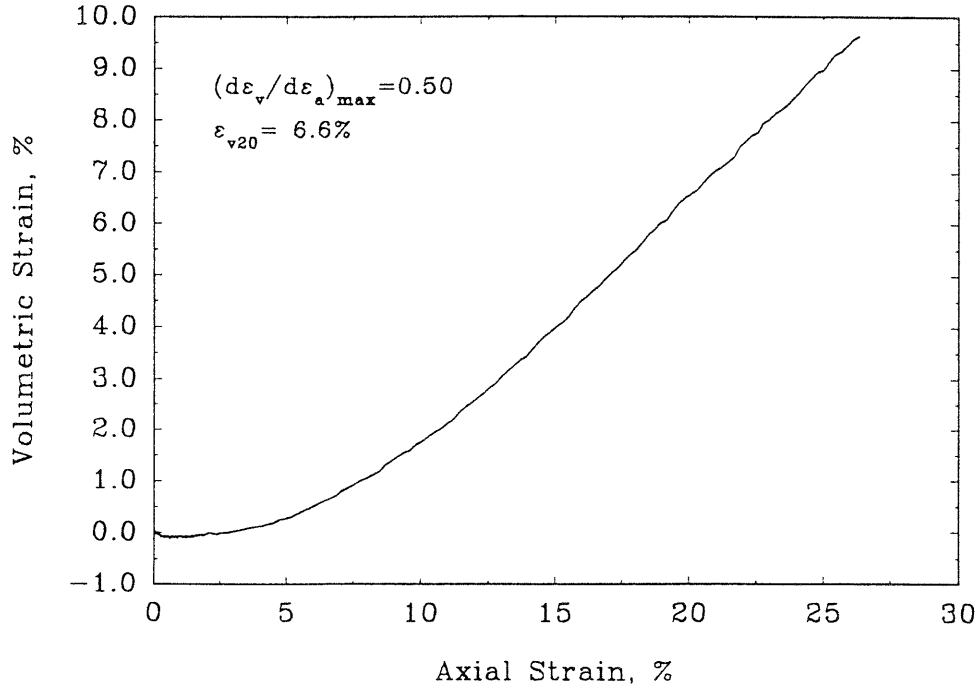

FRS33

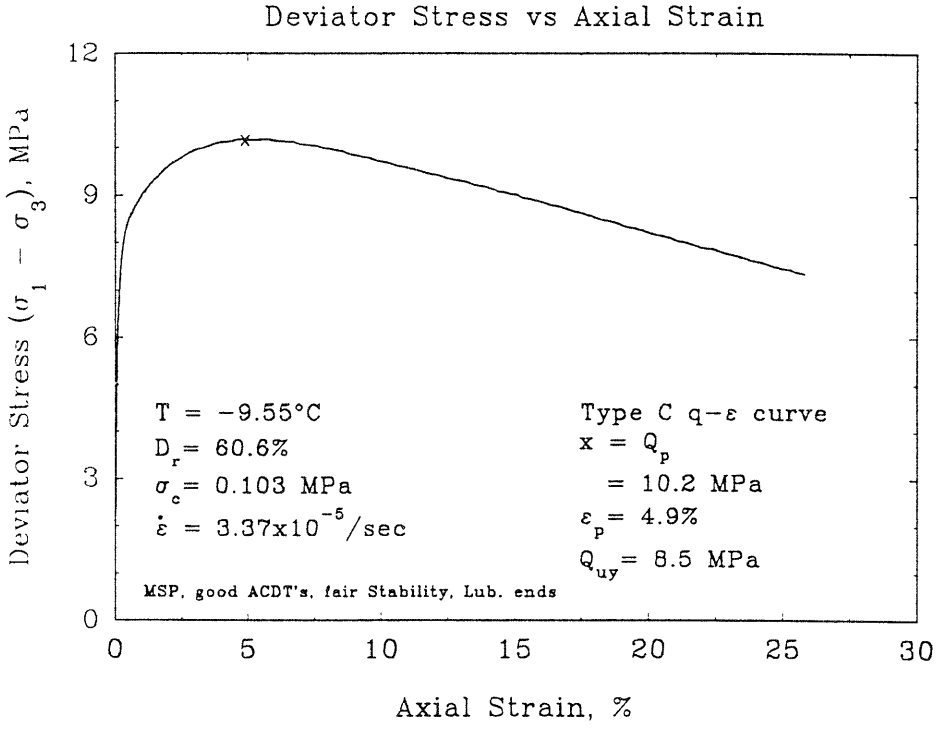
Deviator Stress vs Axial Strain
Deviator Stress ($\sigma_1 - \sigma_3$), MPa
Axial Strain, %
T = −9.55°C
D_r= 60.6%
σ_c= 0.103 MPa
$\dot{\varepsilon}$ = 3.37x10^{-5}/sec
Type C q−ε curve
x = Q_p
= 10.2 MPa
ε_p= 4.9%
Q_{uy}= 8.5 MPa
MSP, good ACDT's, fair Stability, Lub. ends

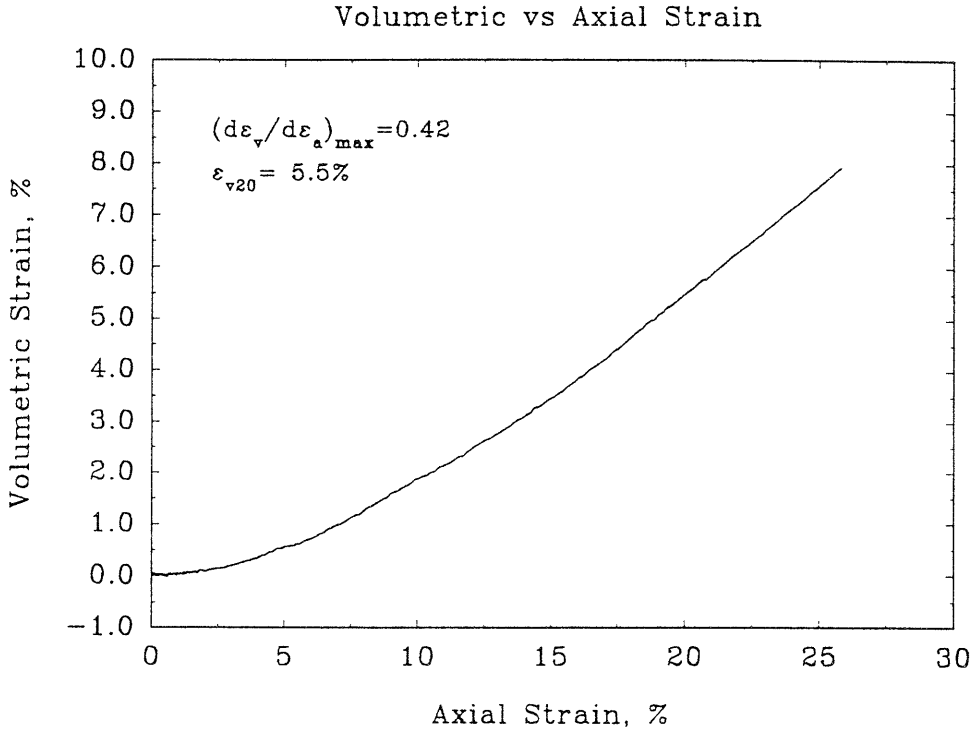
Volumetric vs Axial Strain
Volumetric Strain, %
Axial Strain, %
$(d\varepsilon_v/d\varepsilon_a)_{max}$=0.42
ε_{v20}= 5.5%

FRS34

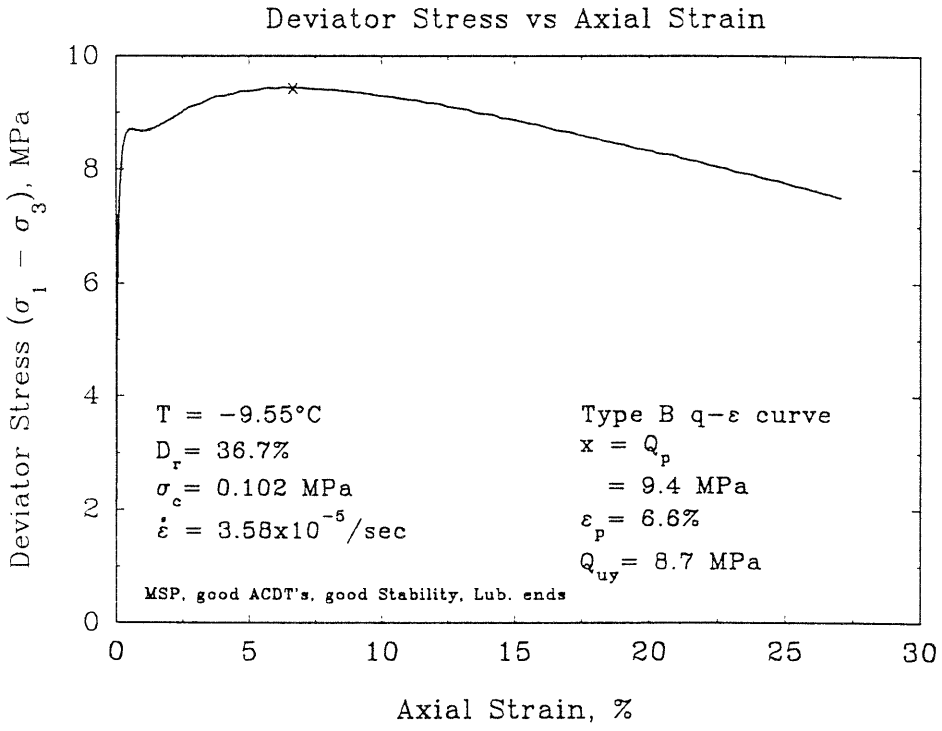
Deviator Stress vs Axial Strain
Deviator Stress ($\sigma_1 - \sigma_3$), MPa
Axial Strain, %
T = −9.55°C
D_r = 36.7%
σ_c = 0.102 MPa
$\dot{\varepsilon}$ = 3.58x10^{-5}/sec
Type B q−ε curve
x = Q_p
= 9.4 MPa
ε_p = 6.6%
Q_{uy} = 8.7 MPa
MSP, good ACDT's, good Stability, Lub. ends

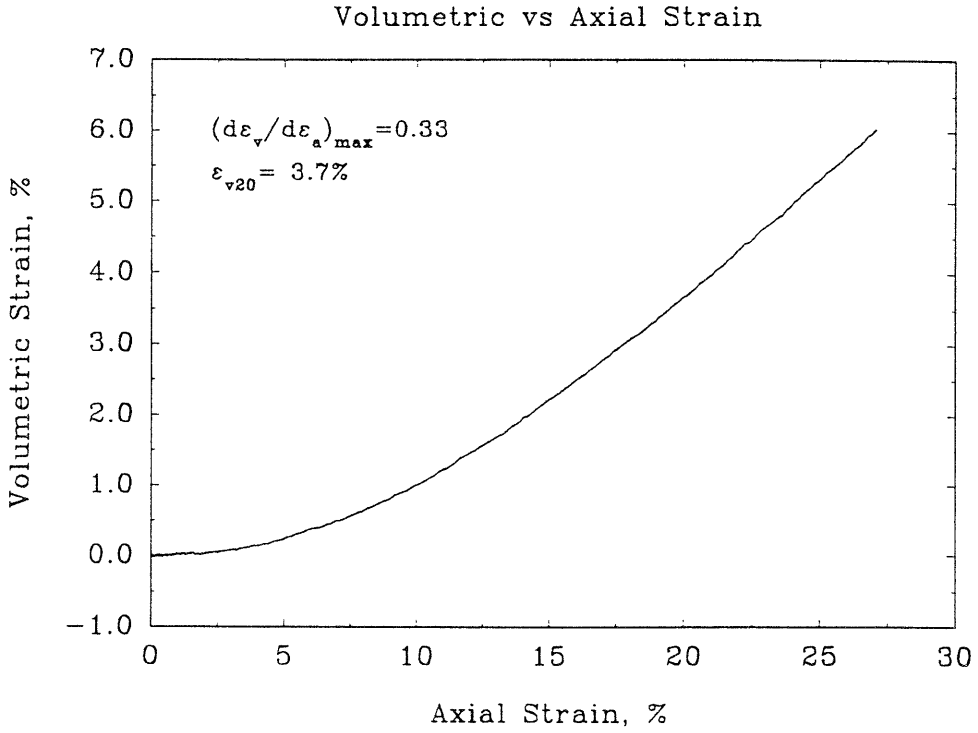
Volumetric vs Axial Strain
Volumetric Strain, %
Axial Strain, %
$(d\varepsilon_v/d\varepsilon_a)_{max}$=0.33
ε_{v20}= 3.7%

FRS35

Deviator Stress vs Axial Strain

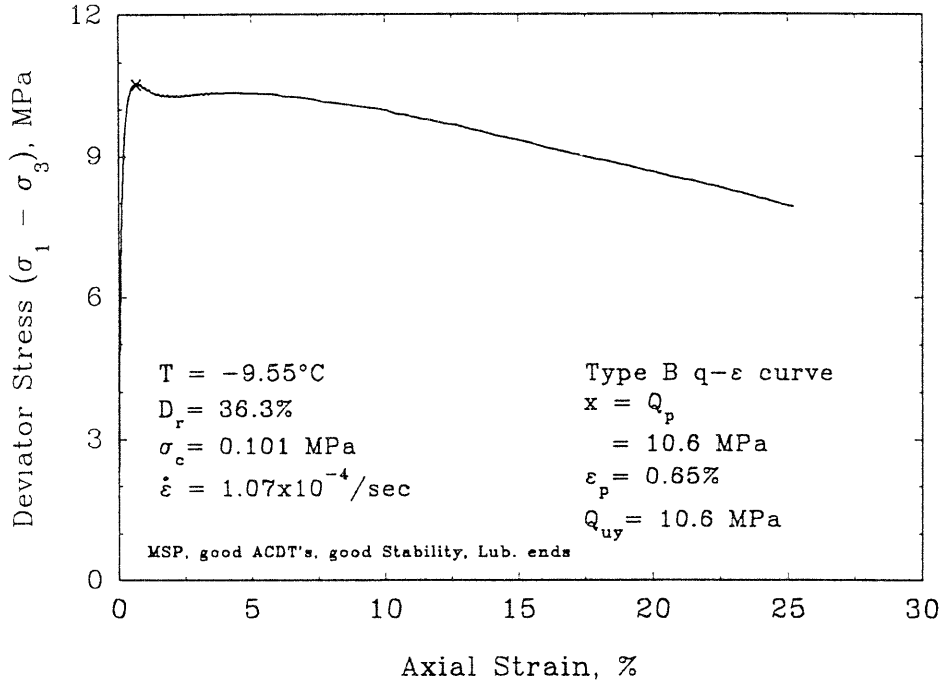

Volumetric vs Axial Strain

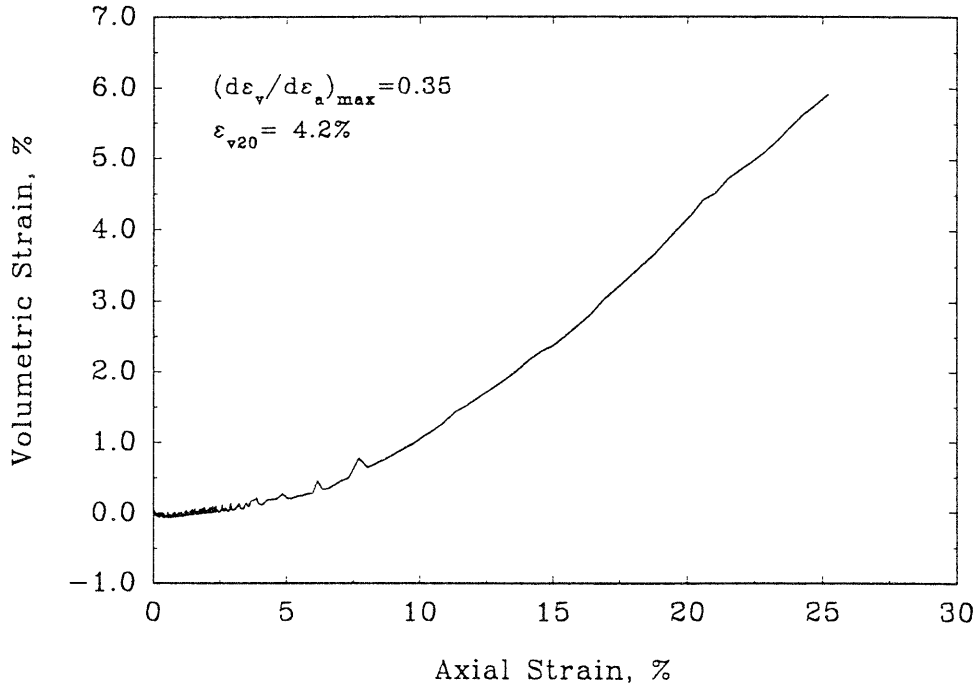

FRS36

Deviator Stress vs Axial Strain

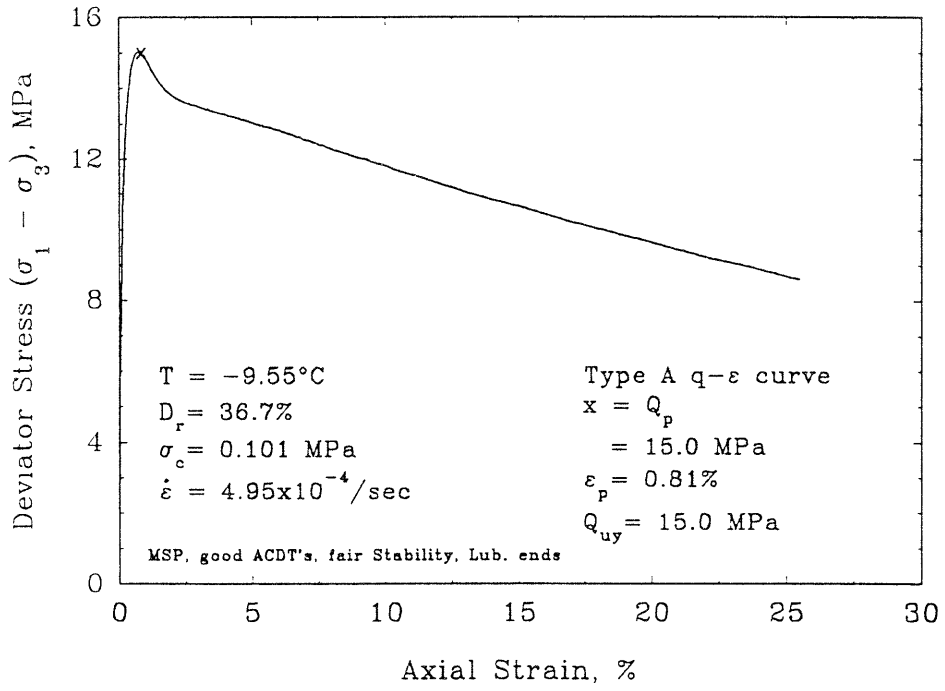

Volumetric vs Axial Strain

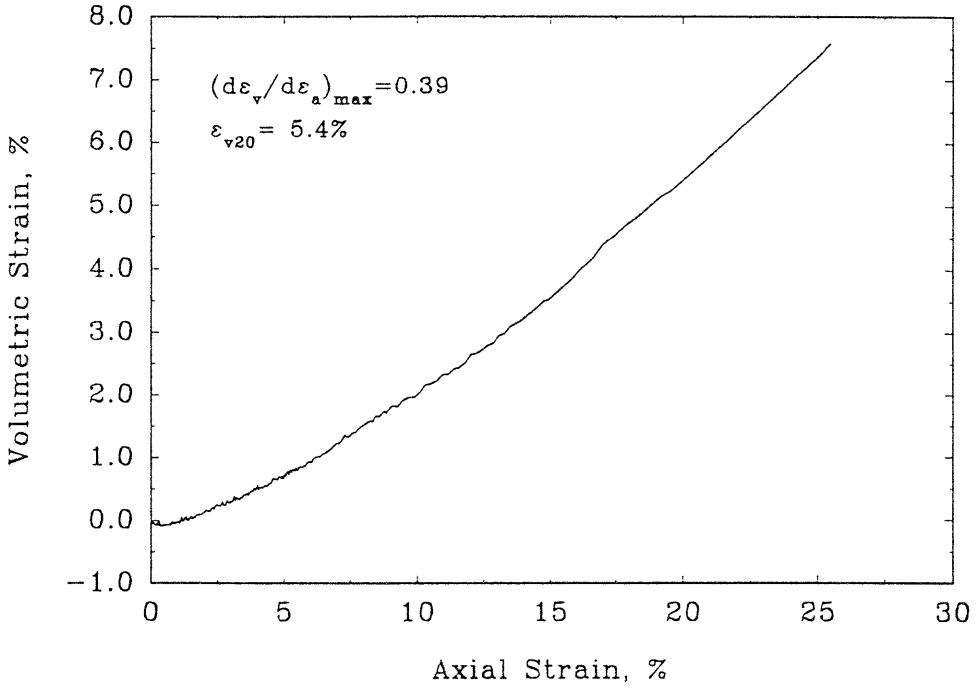

FRS37

Deviator Stress vs Axial Strain

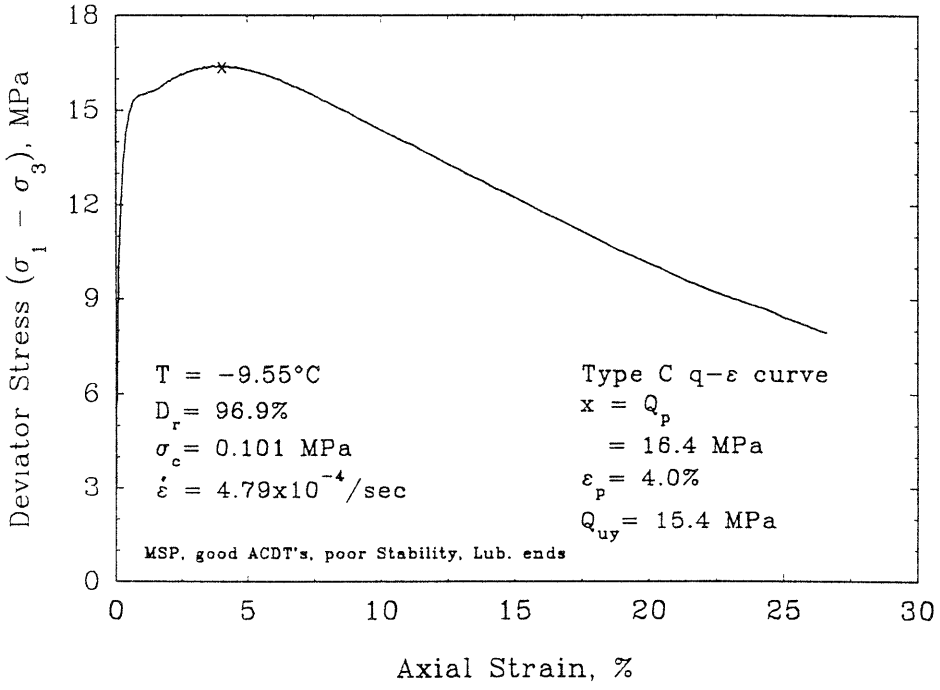

Volumetric vs Axial Strain

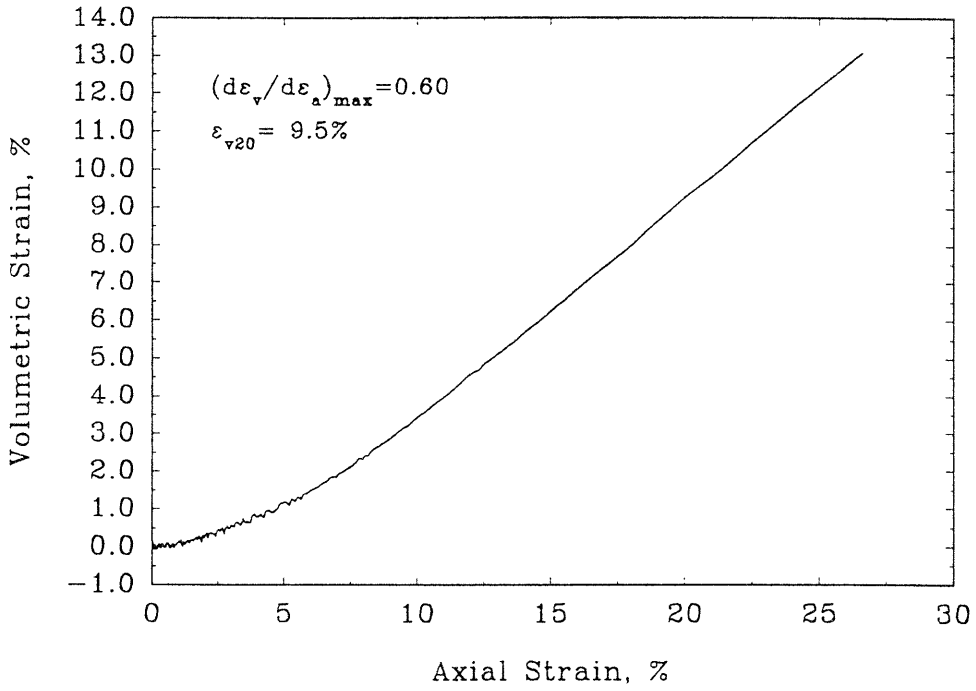

FRS38

Deviator Stress vs Axial Strain

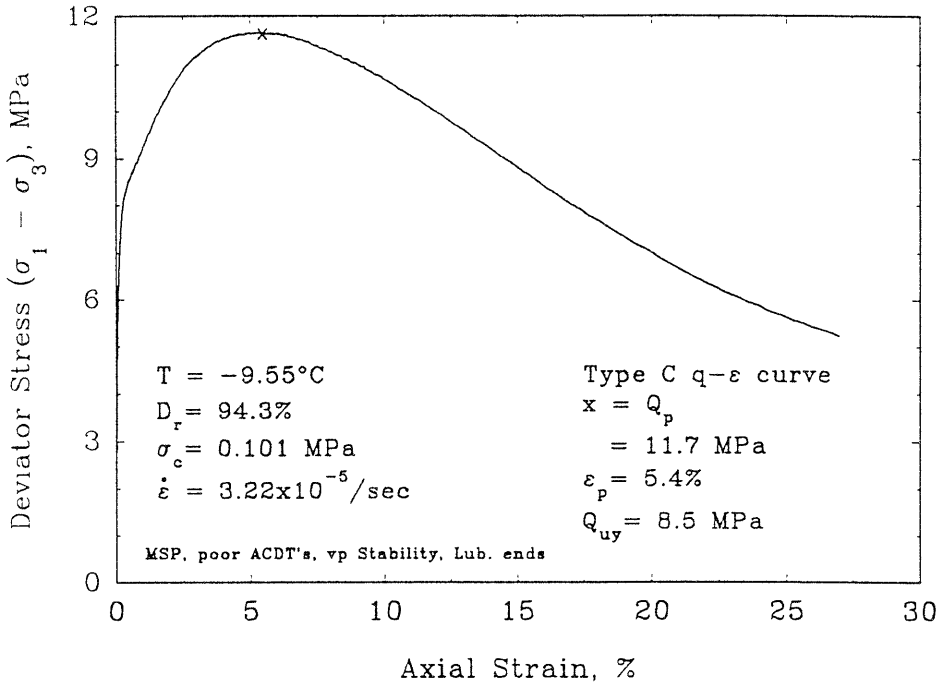

Volumetric vs Axial Strain

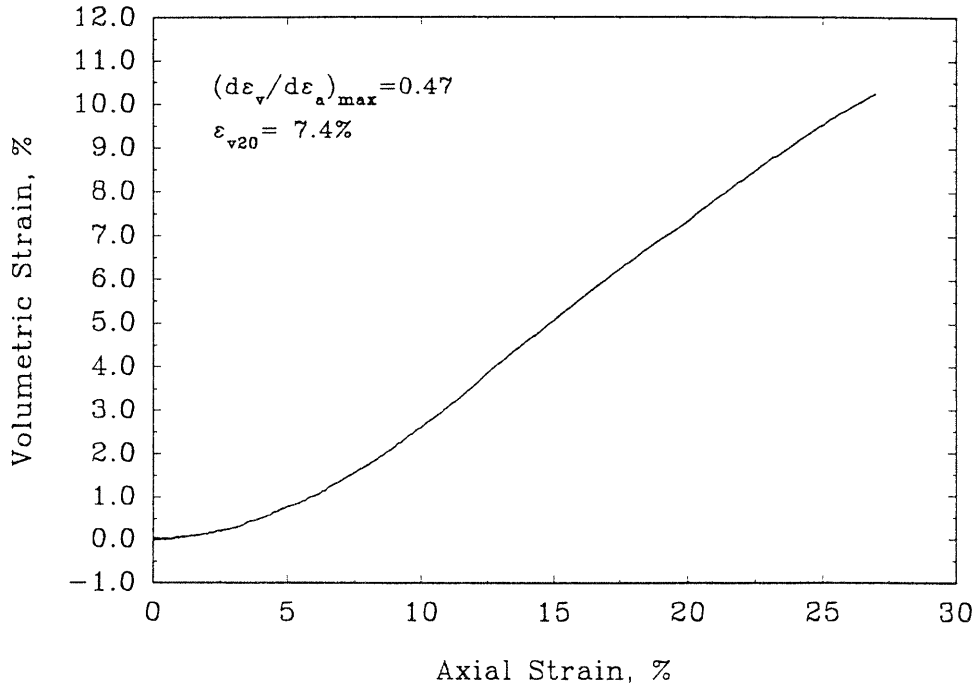

FRS39

Deviator Stress vs Axial Strain

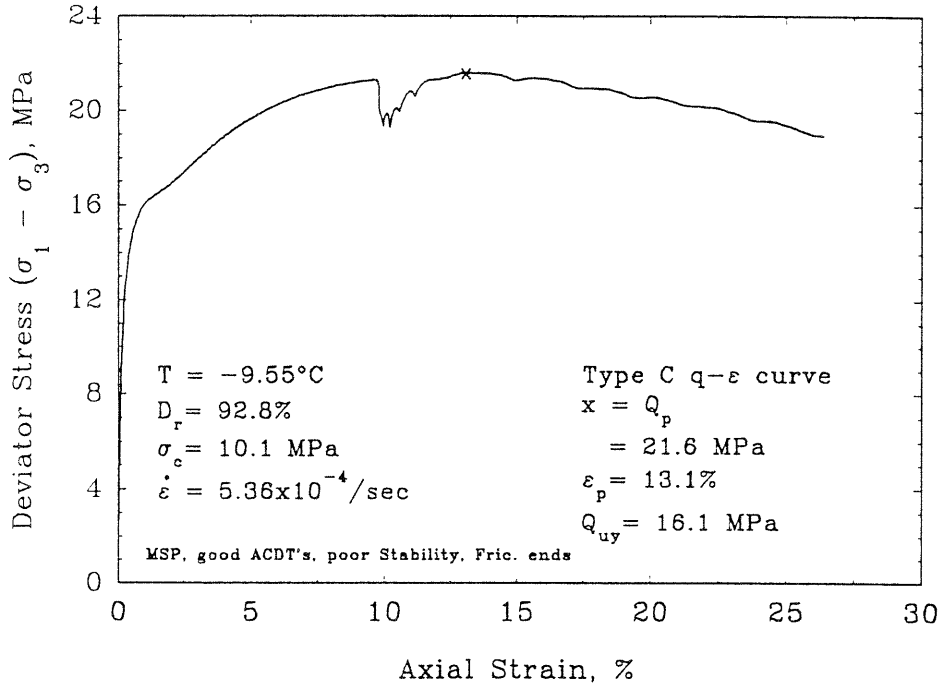

Volumetric vs Axial Strain

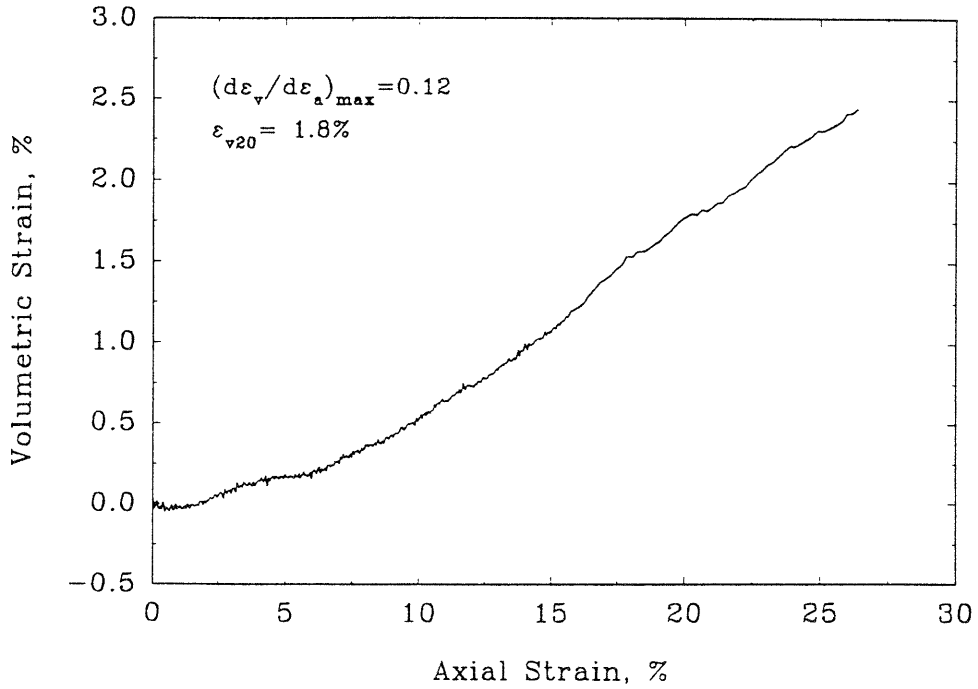

FRS40

Deviator Stress vs Axial Strain

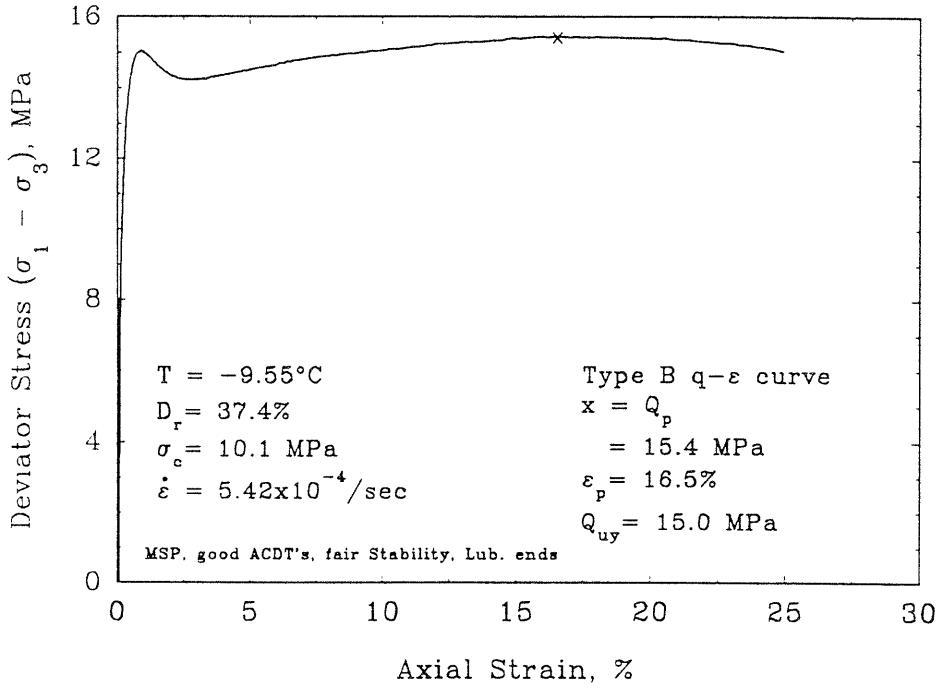

Volumetric vs Axial Strain

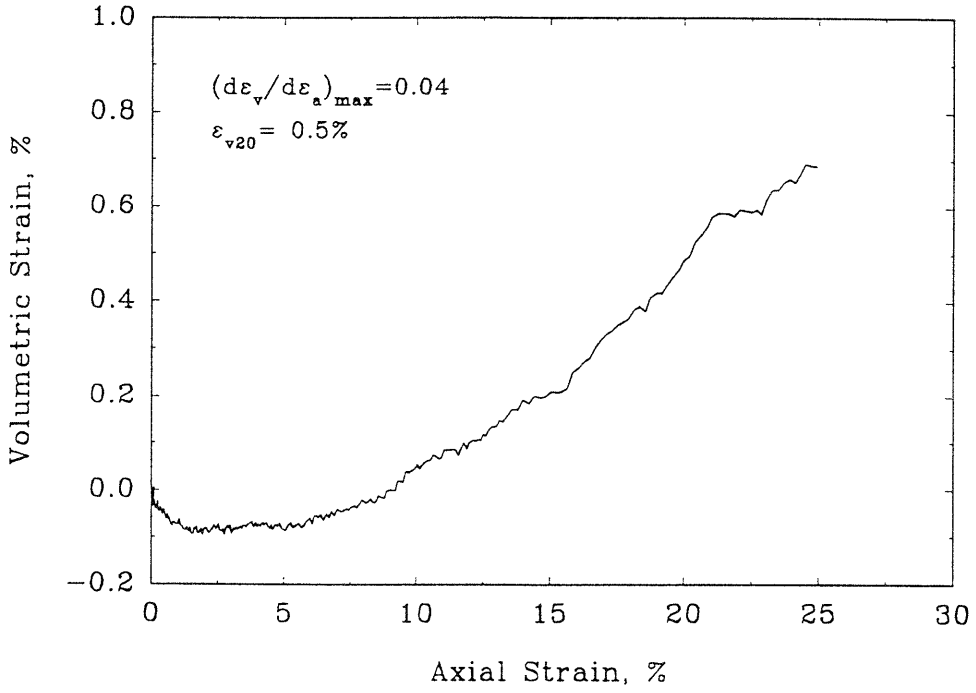

FRS41

Deviator Stress vs Axial Strain

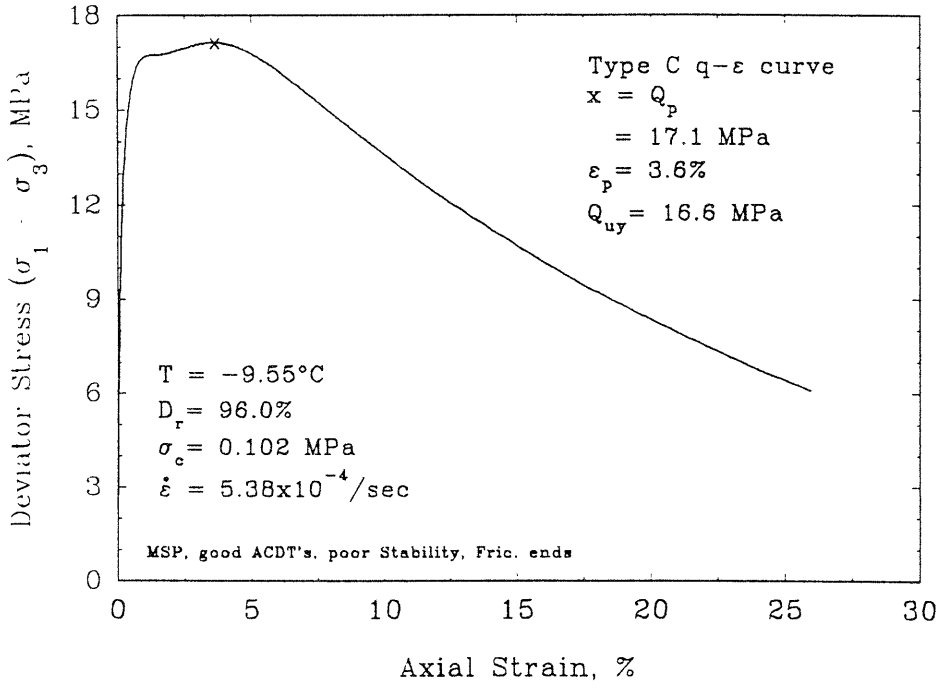

Volumetric vs Axial Strain

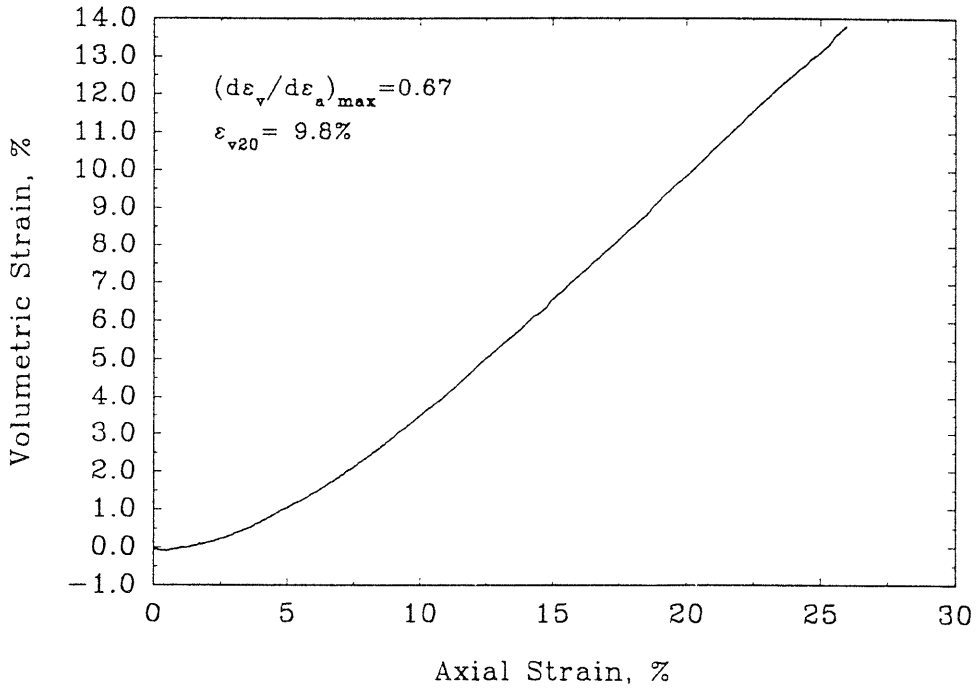

FRS42

Deviator Stress vs Axial Strain

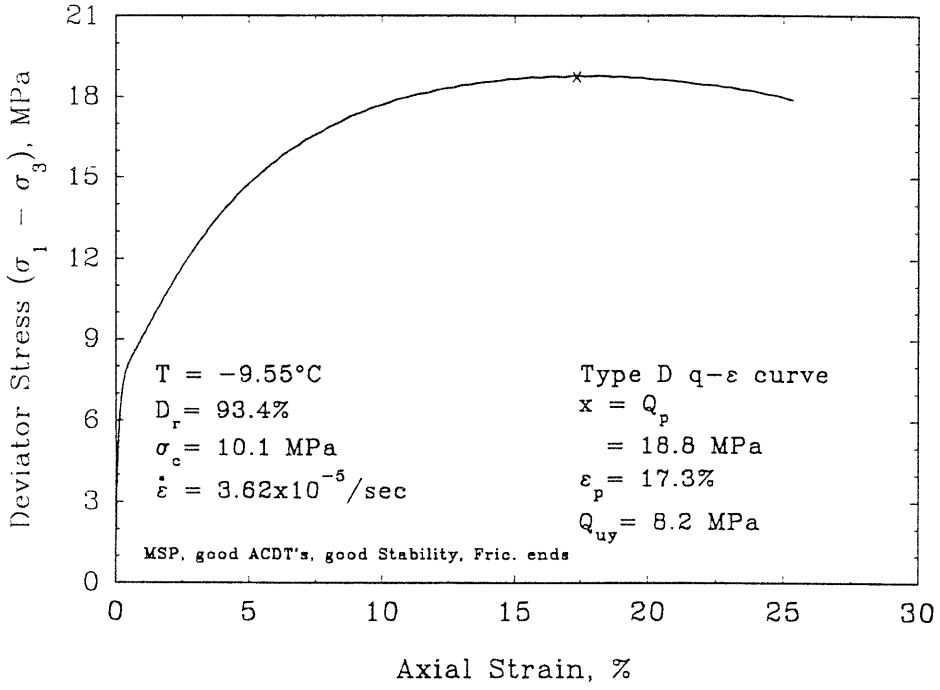

Volumetric vs Axial Strain

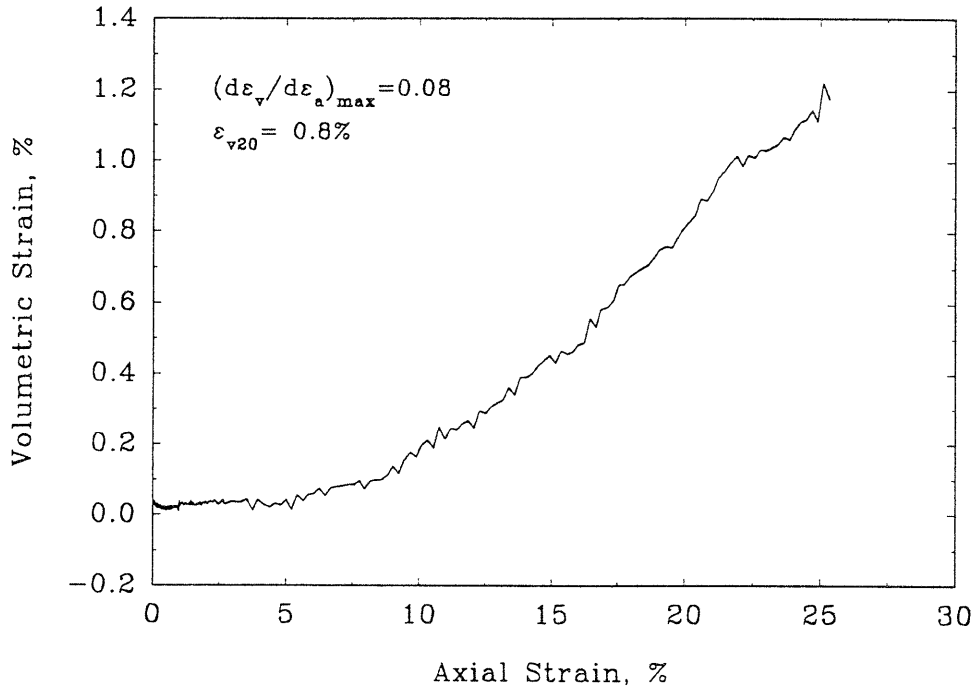

FRS43

Deviator Stress vs Axial Strain

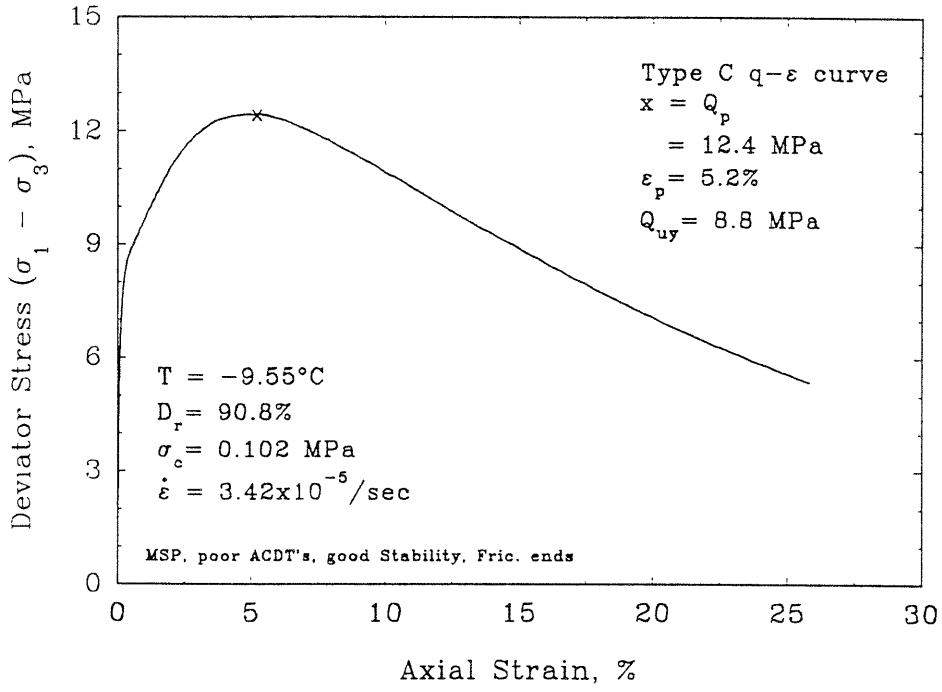

Volumetric vs Axial Strain

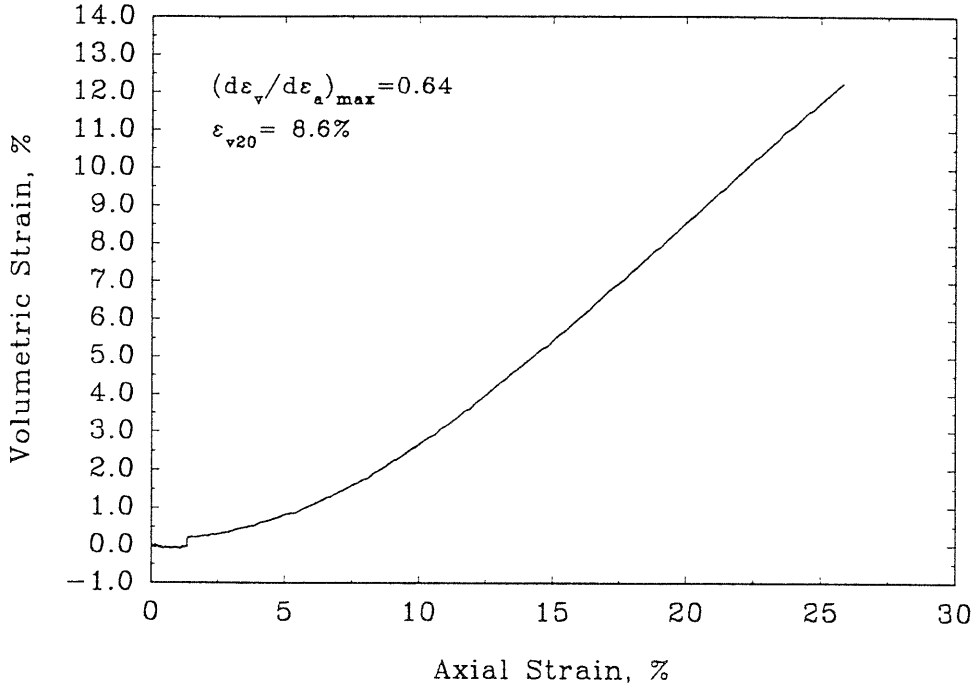

FRS44

Deviator Stress vs Axial Strain

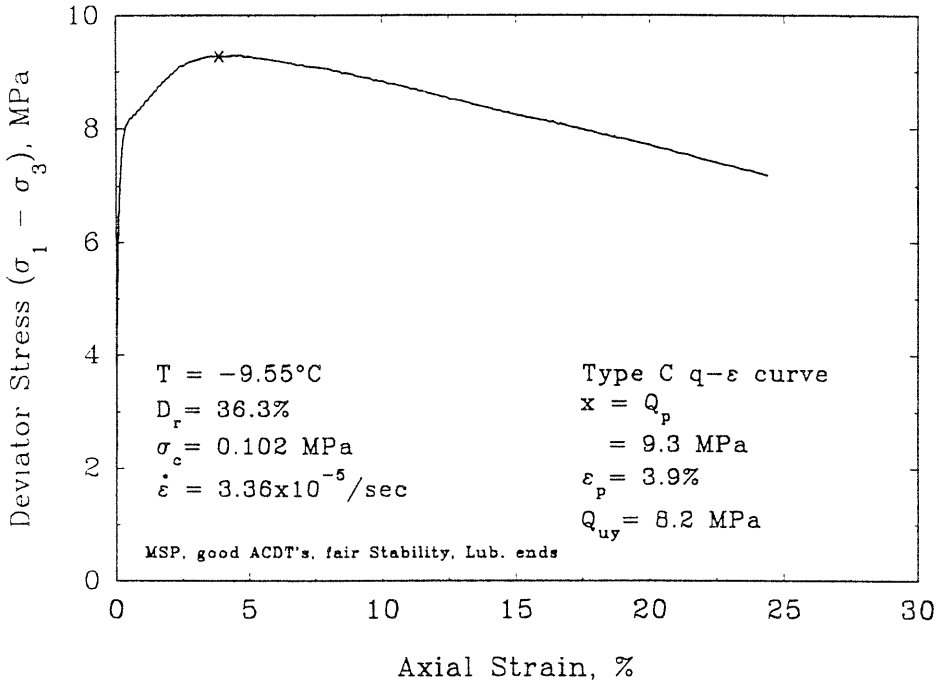

Volumetric vs Axial Strain

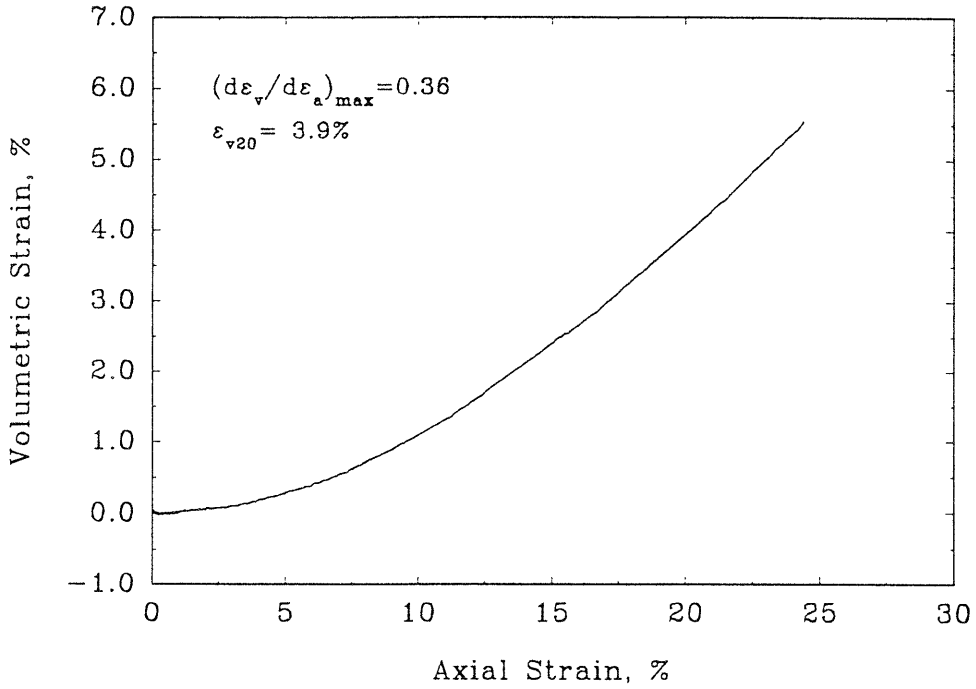

FRS45

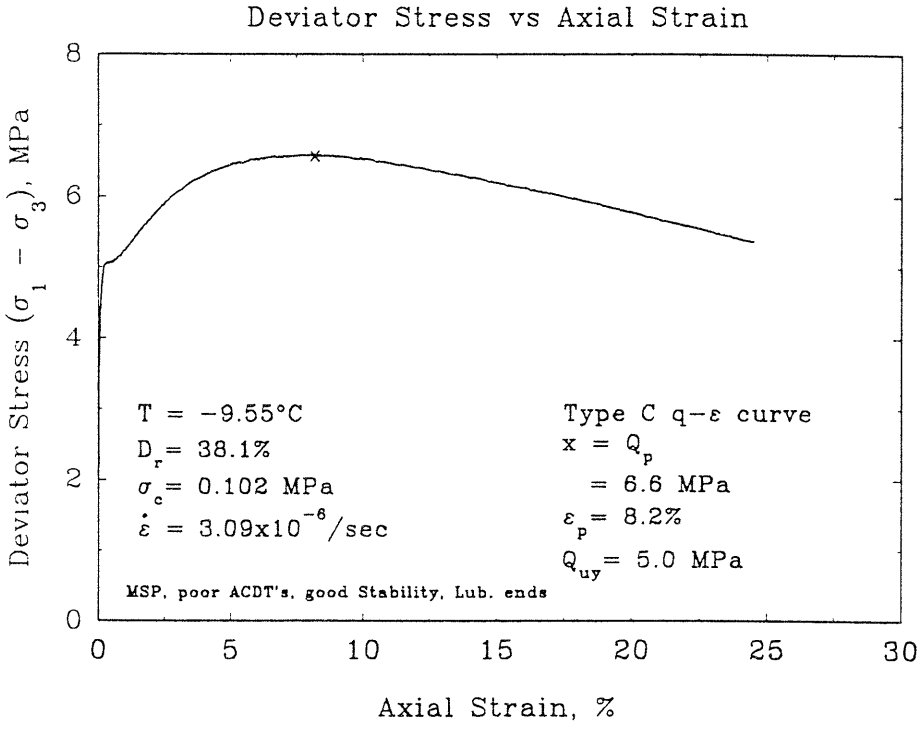
Deviator Stress vs Axial Strain
Deviator Stress ($\sigma_1 - \sigma_3$), MPa
Axial Strain, %
T = −9.55°C
D_r = 38.1%
σ_c = 0.102 MPa
$\dot{\varepsilon}$ = 3.09x10^{-6}/sec
Type C q−ε curve
x = Q_p
= 6.6 MPa
ε_p = 8.2%
Q_{uy} = 5.0 MPa
MSP, poor ACDT's, good Stability, Lub. ends

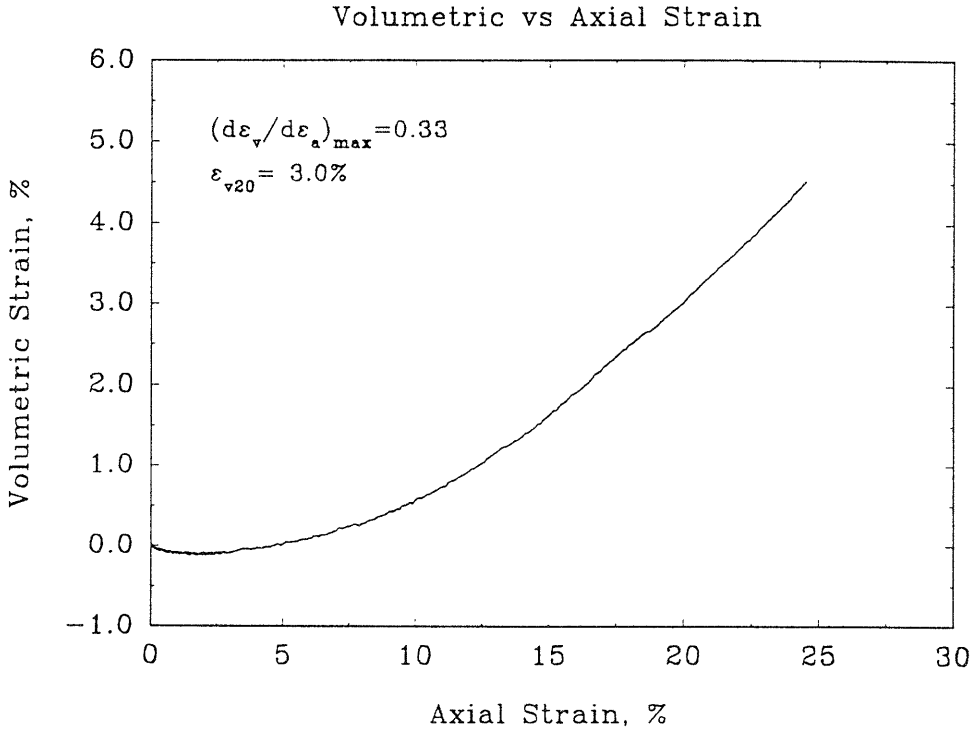
Volumetric vs Axial Strain
Volumetric Strain, %
Axial Strain, %
$(d\varepsilon_v/d\varepsilon_a)_{max}$=0.33
ε_{v20}= 3.0%

FRS46

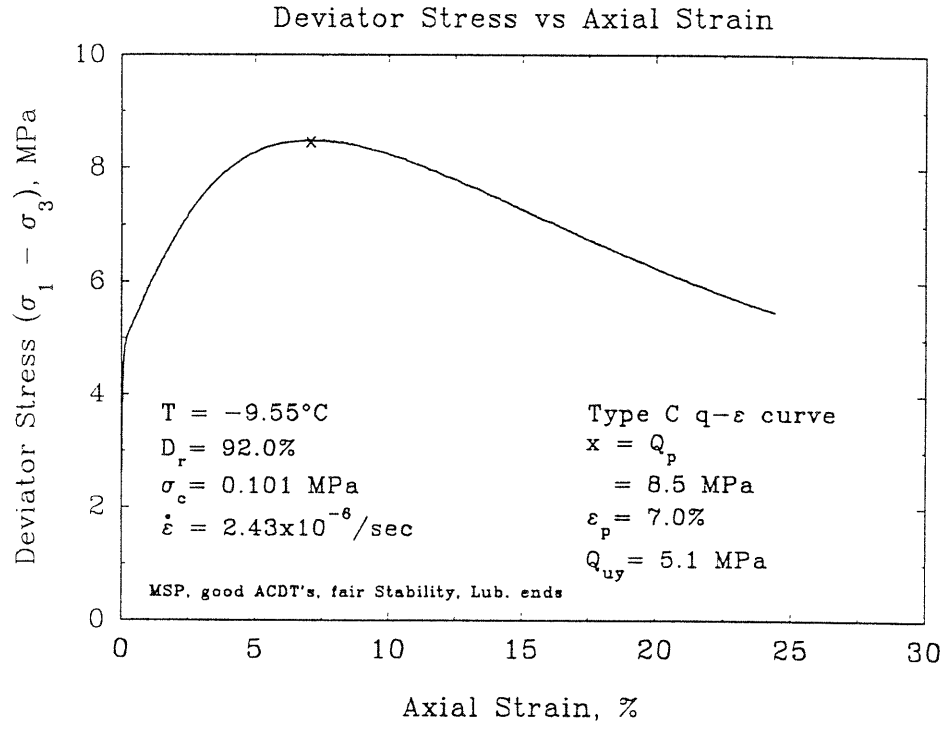
Deviator Stress vs Axial Strain
Deviator Stress ($\sigma_1 - \sigma_3$), MPa
Axial Strain, %
T = −9.55°C
D_r= 92.0%
σ_c= 0.101 MPa
$\dot{\varepsilon}$ = 2.43x10^{-6}/sec
Type C q−ε curve
x = Q_p
= 8.5 MPa
ε_p= 7.0%
Q_{uy}= 5.1 MPa
MSP, good ACDT's, fair Stability, Lub. ends

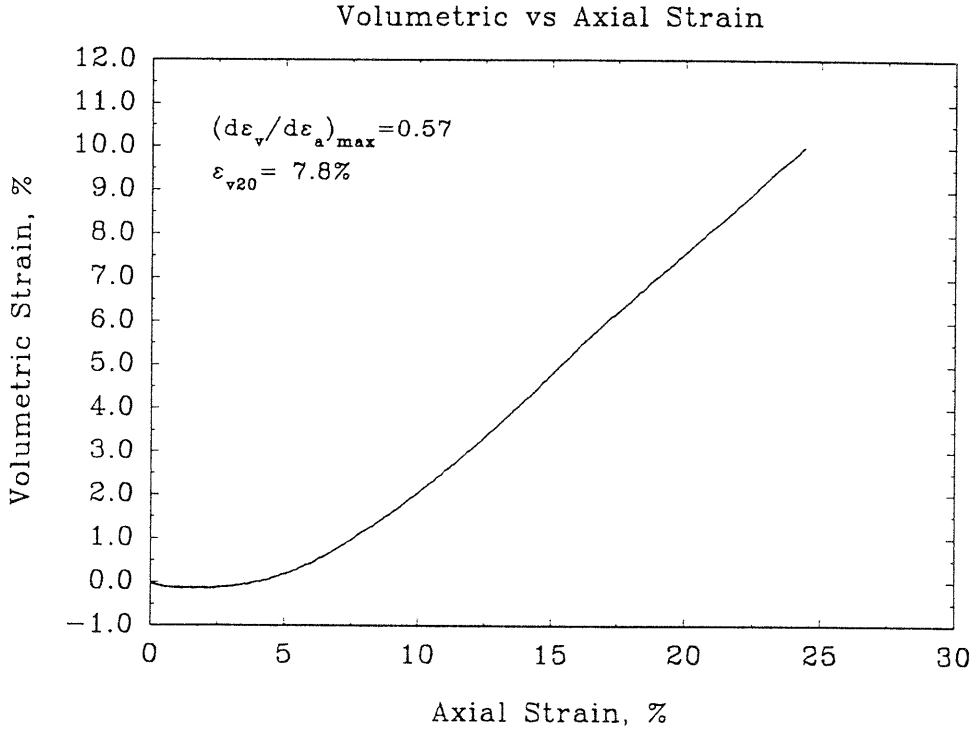
Volumetric vs Axial Strain
Volumetric Strain, %
Axial Strain, %
$(d\varepsilon_v/d\varepsilon_a)_{max}$=0.57
ε_{v20}= 7.8%

FRS47

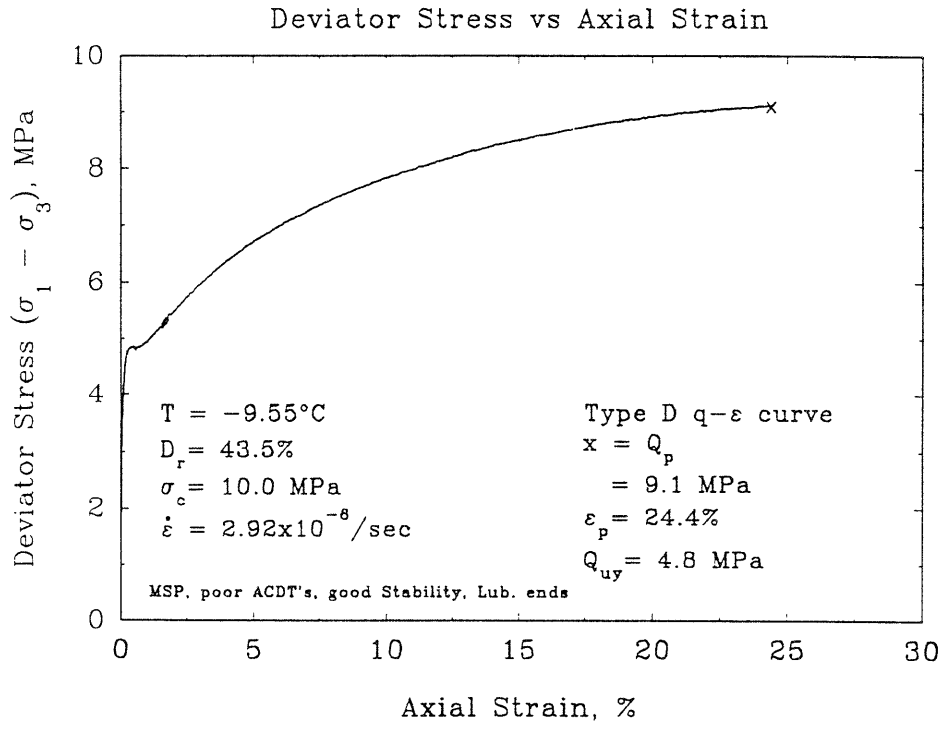
Deviator Stress vs Axial Strain
Deviator Stress ($\sigma_1 - \sigma_3$), MPa
Axial Strain, %
T = −9.55°C
D_r = 43.5%
σ_c = 10.0 MPa
$\dot{\varepsilon}$ = 2.92x10^{-6}/sec
Type D q−ε curve
x = Q_p
= 9.1 MPa
ε_p = 24.4%
Q_{uy} = 4.8 MPa
MSP, poor ACDT's, good Stability, Lub. ends

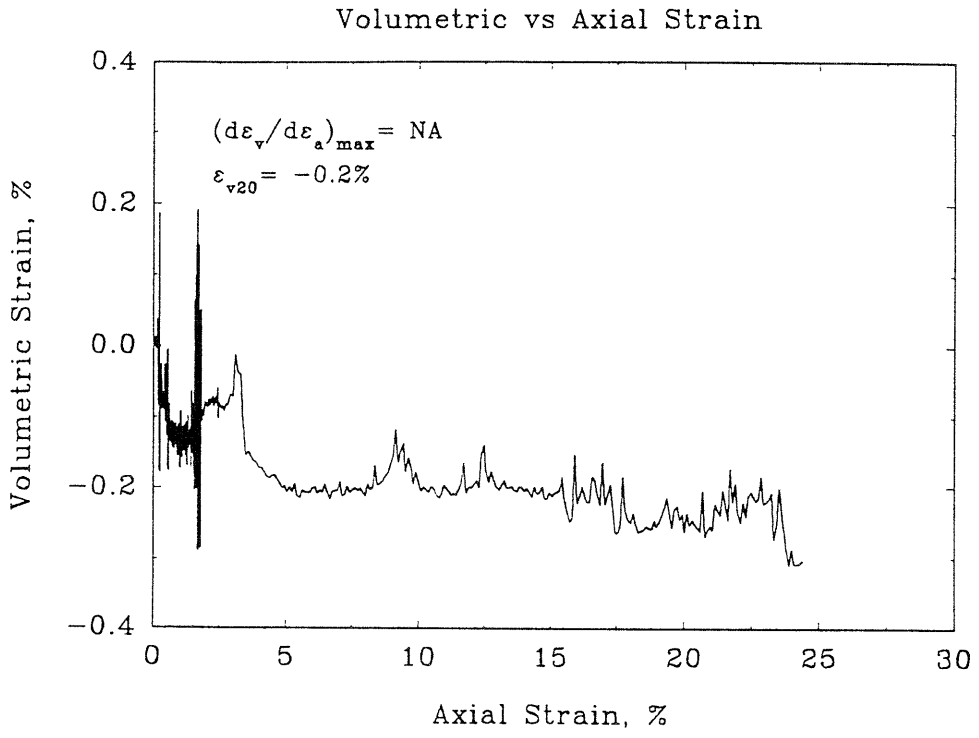
Volumetric vs Axial Strain
Volumetric Strain, %
Axial Strain, %
$(d\varepsilon_v/d\varepsilon_a)_{max}$ = NA
ε_{v20} = −0.2%

FRS48

Deviator Stress vs Axial Strain

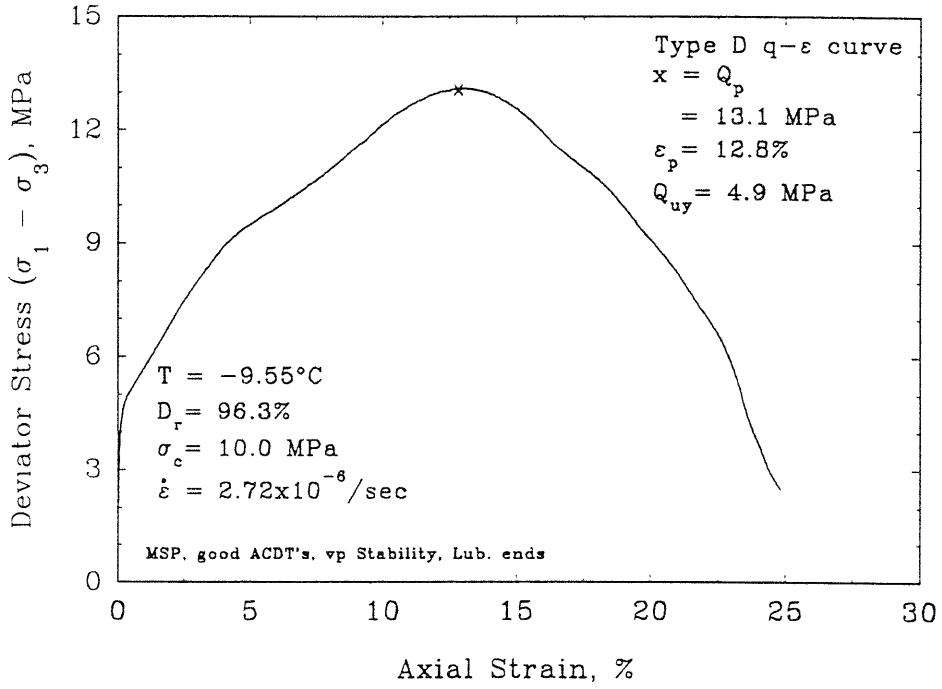

Volumetric vs Axial Strain

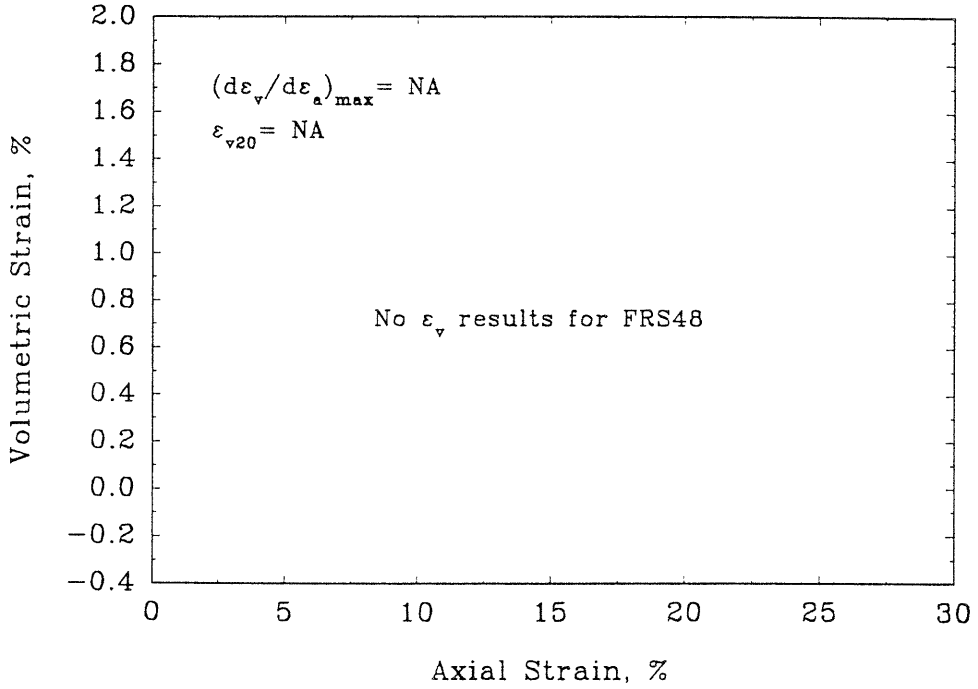

FRS49

Deviator Stress vs Axial Strain

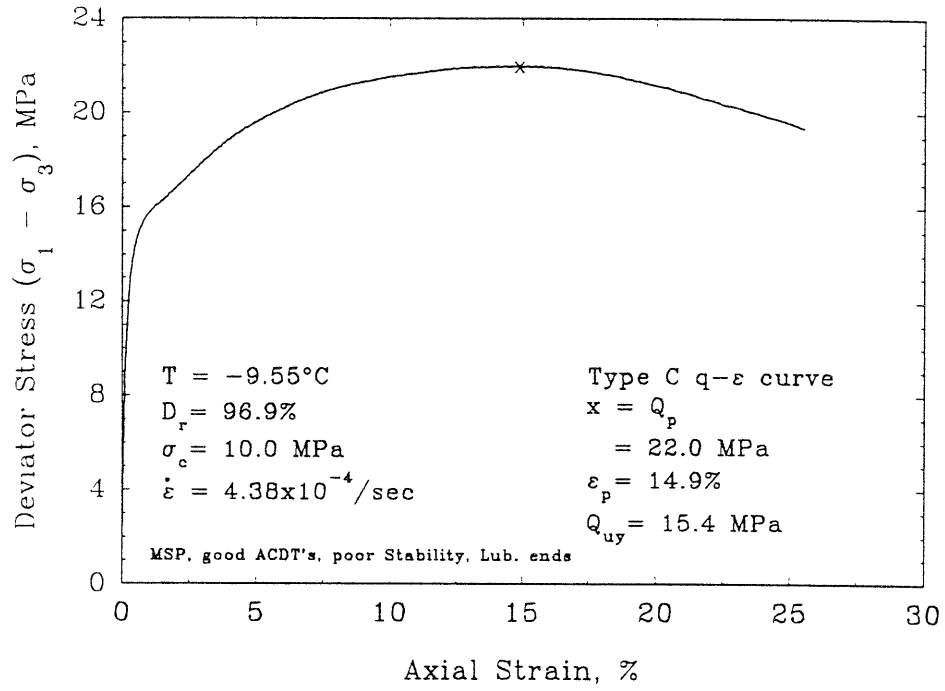

Volumetric vs Axial Strain

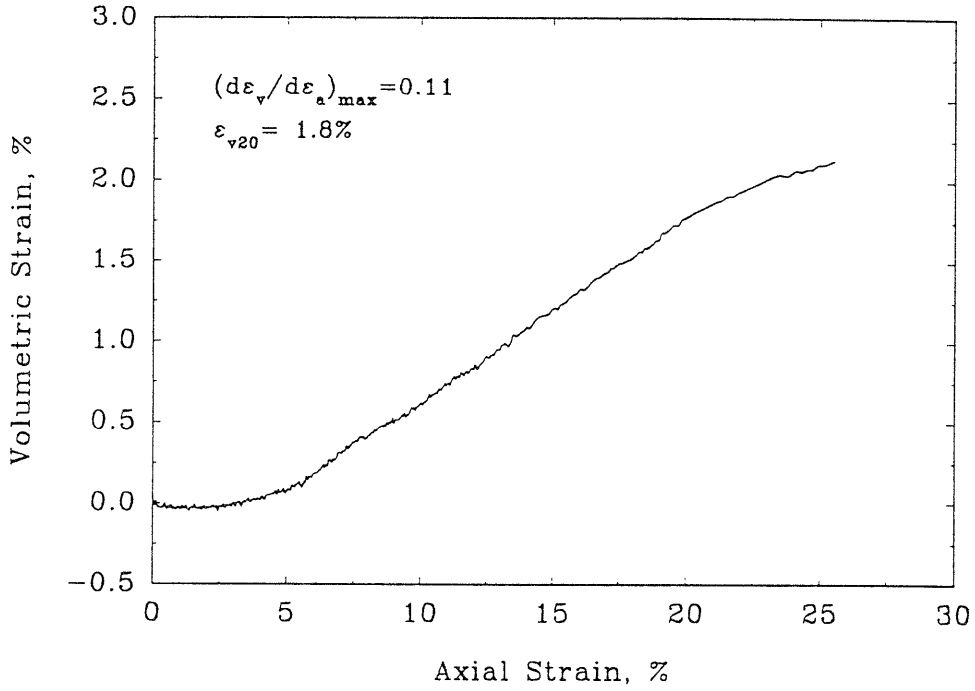

FRS51

Deviator Stress vs Axial Strain

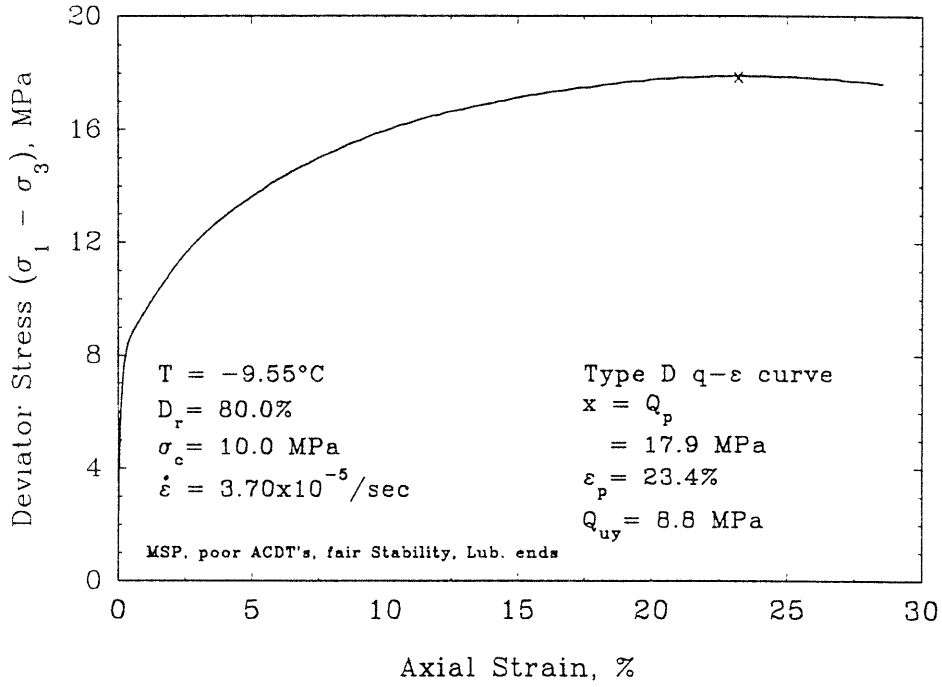

Volumetric vs Axial Strain

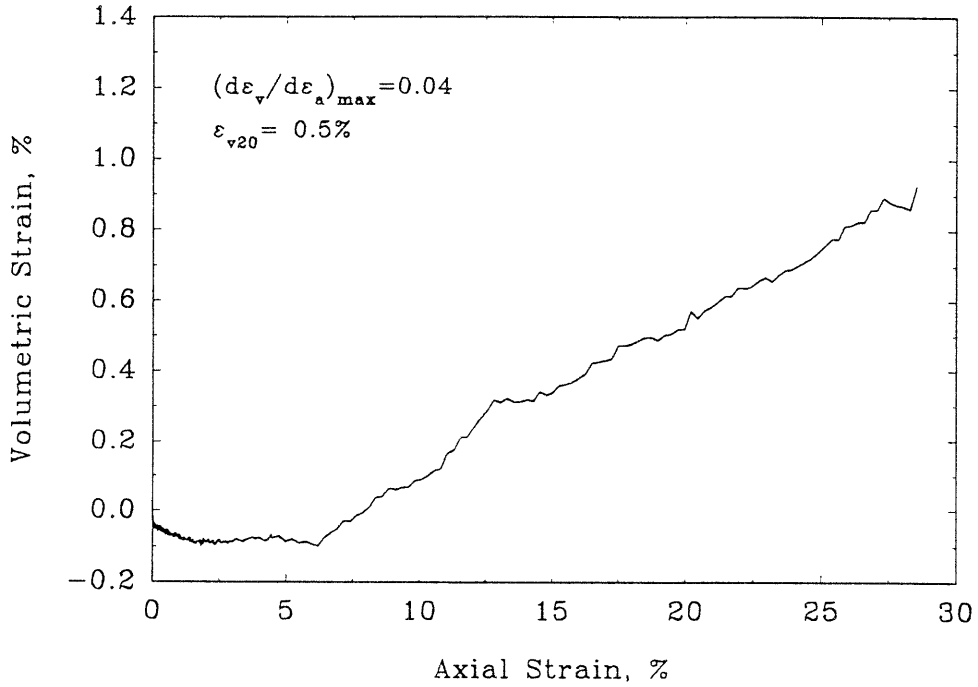

FRS52

Deviator Stress vs Axial Strain

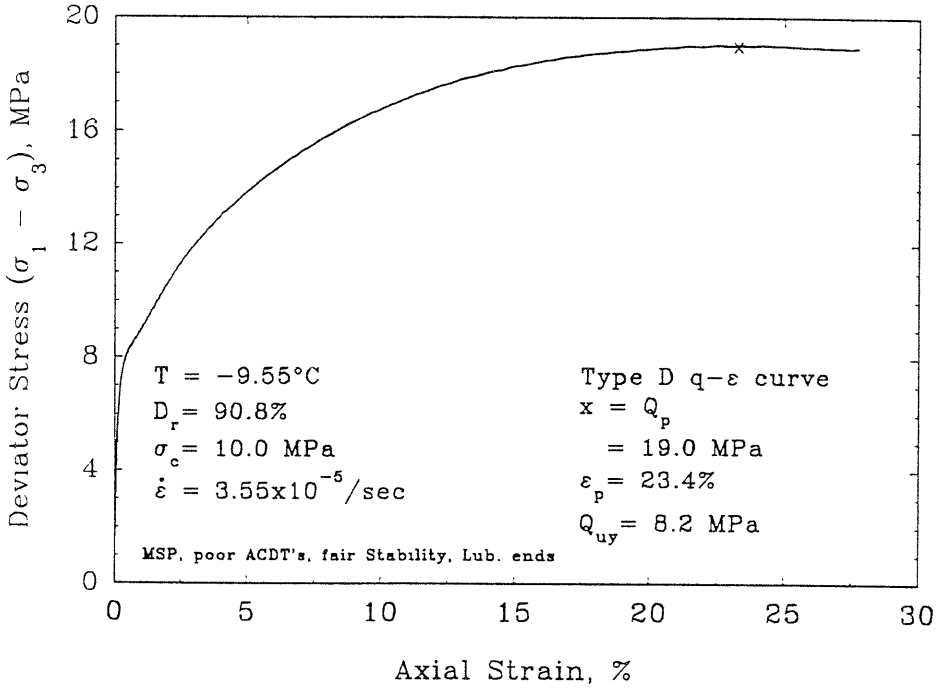

Volumetric vs Axial Strain

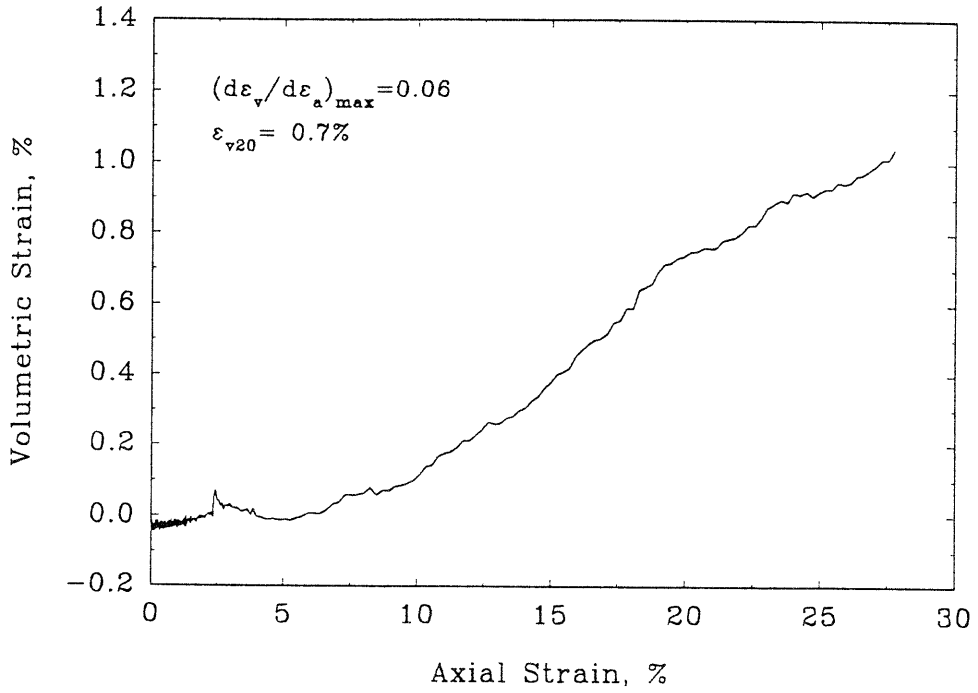

FRS53

Deviator Stress vs Axial Strain

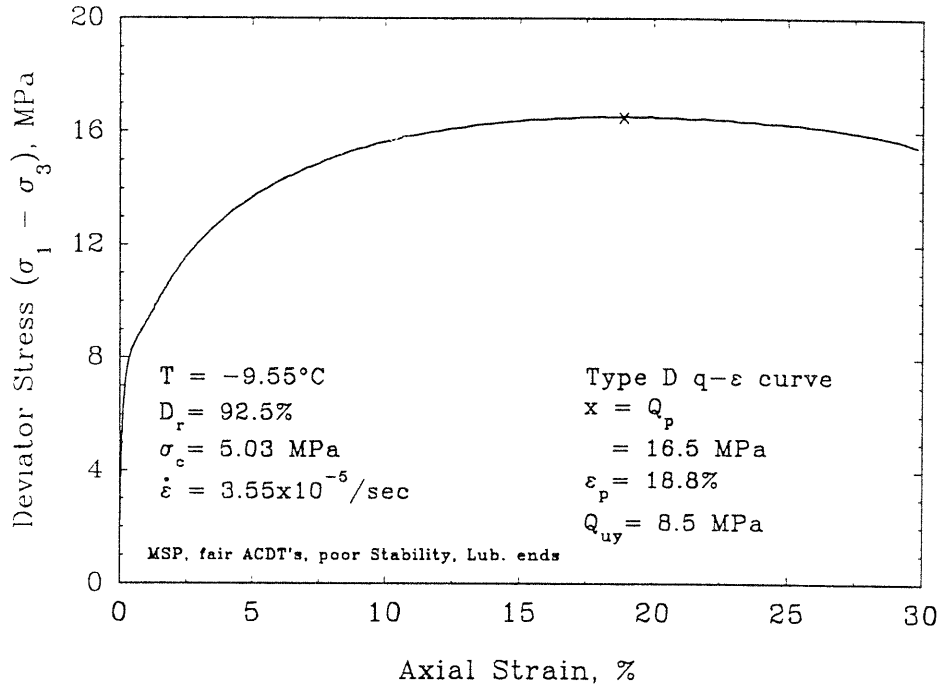

Volumetric vs Axial Strain

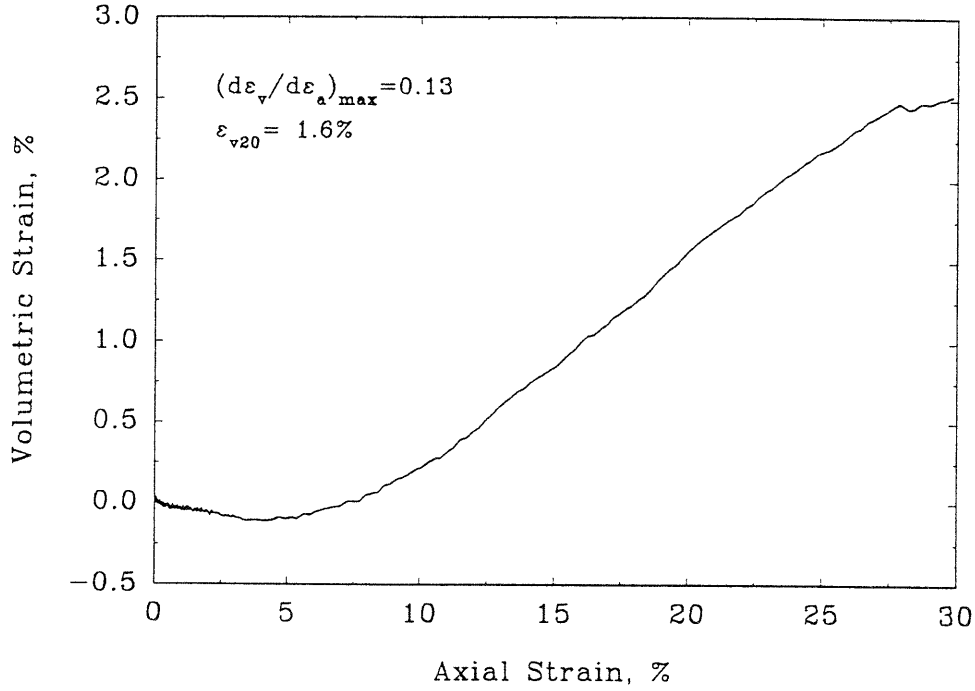

FRS54

Deviator Stress vs Axial Strain

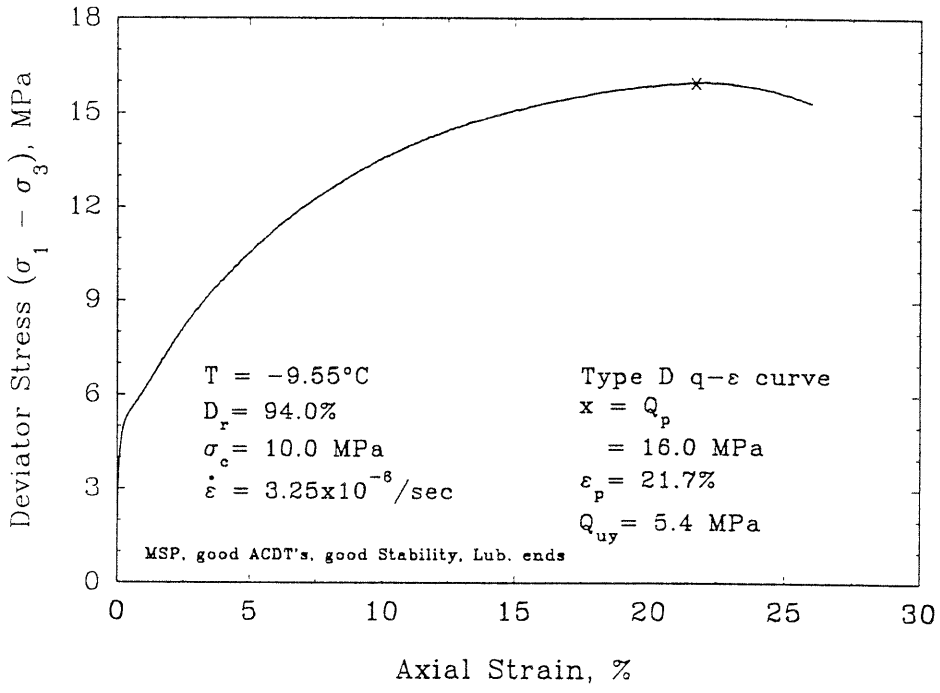

Volumetric vs Axial Strain

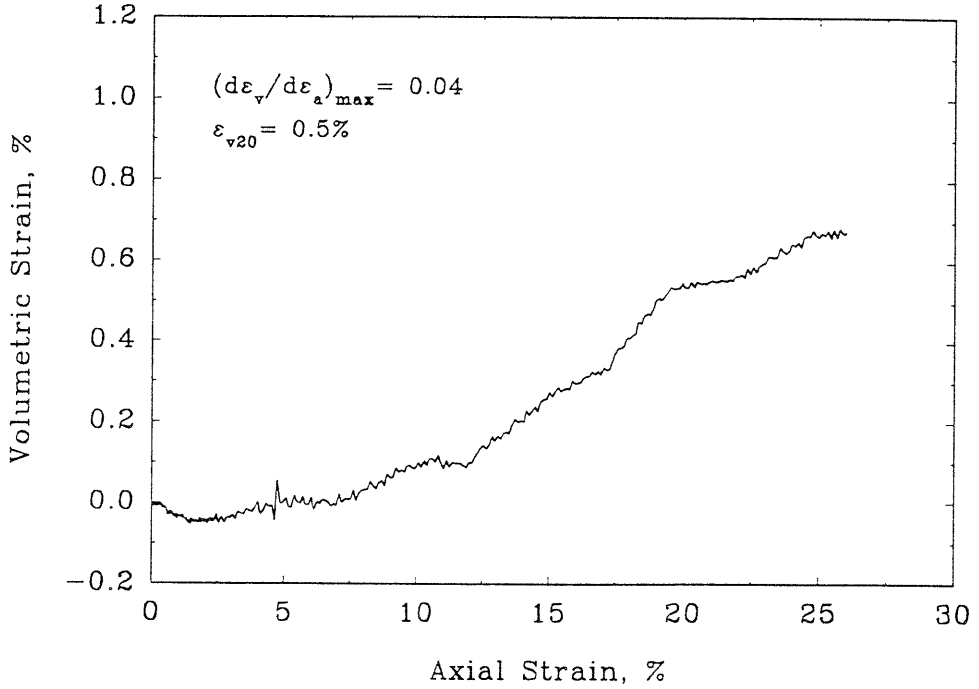

FRS55

Deviator Stress vs Axial Strain

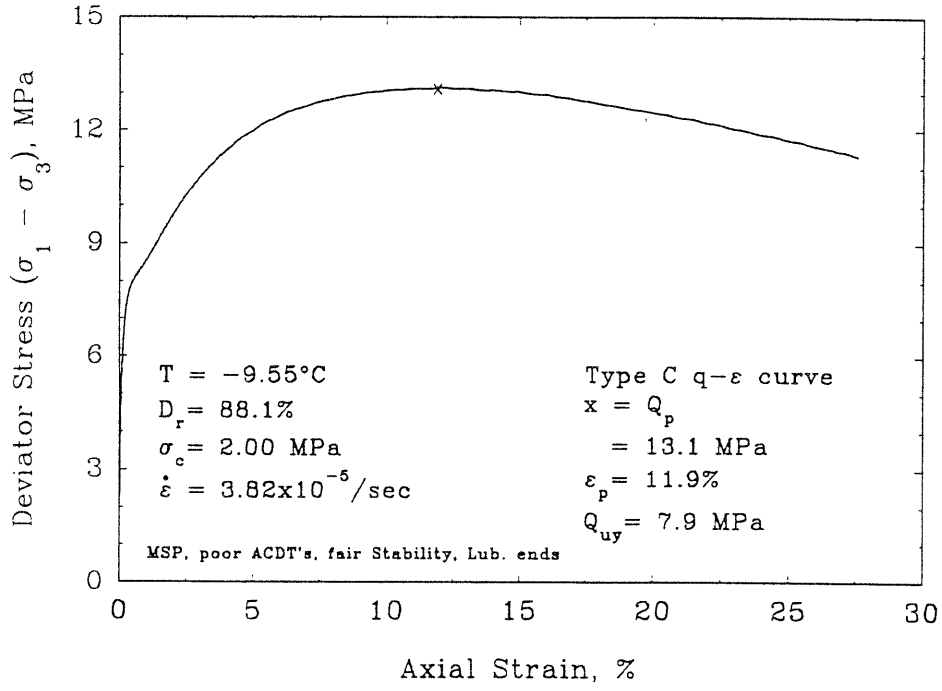

Volumetric vs Axial Strain

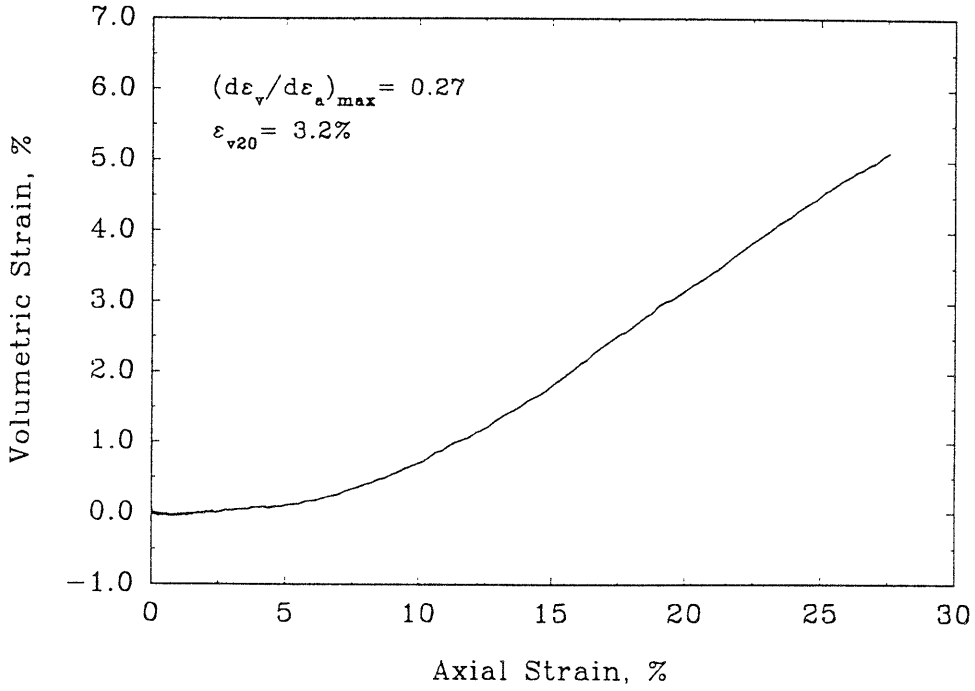

FRS56

Deviator Stress vs Axial Strain

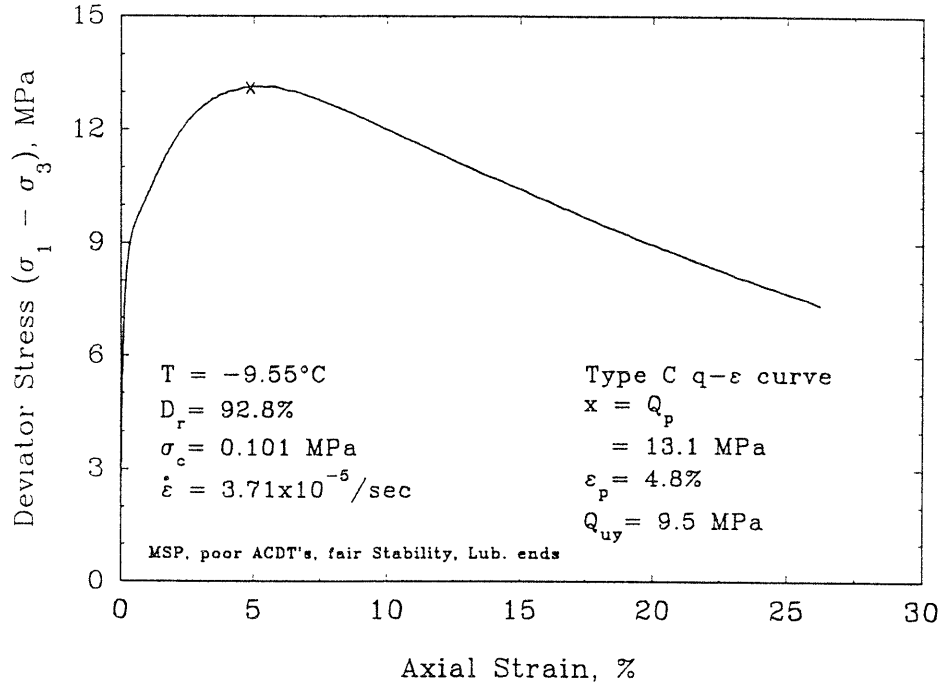

Volumetric vs Axial Strain

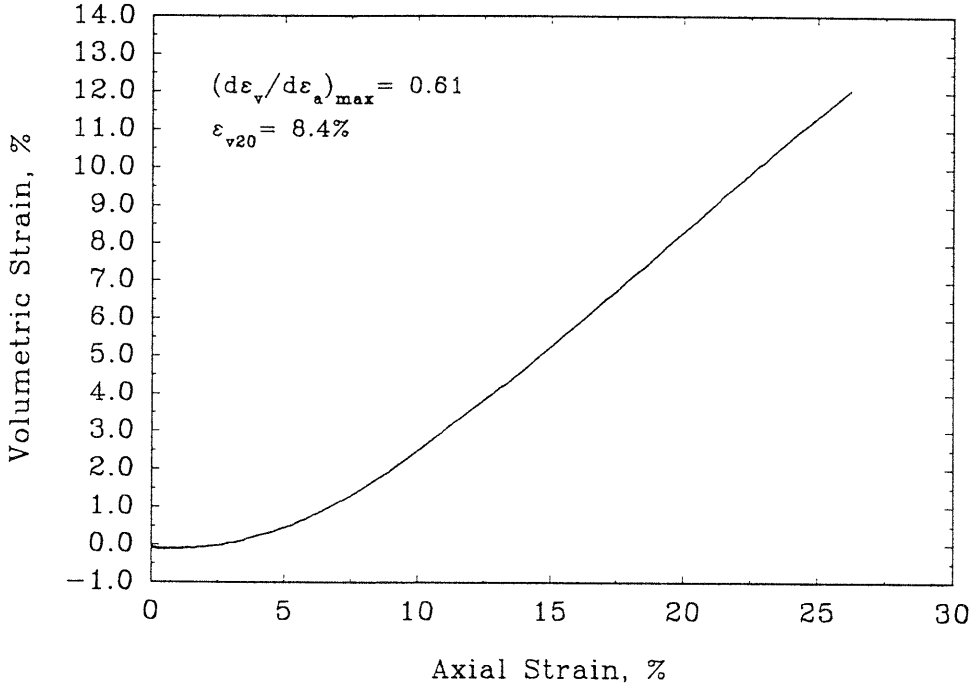

FRS57

Deviator Stress vs Axial Strain

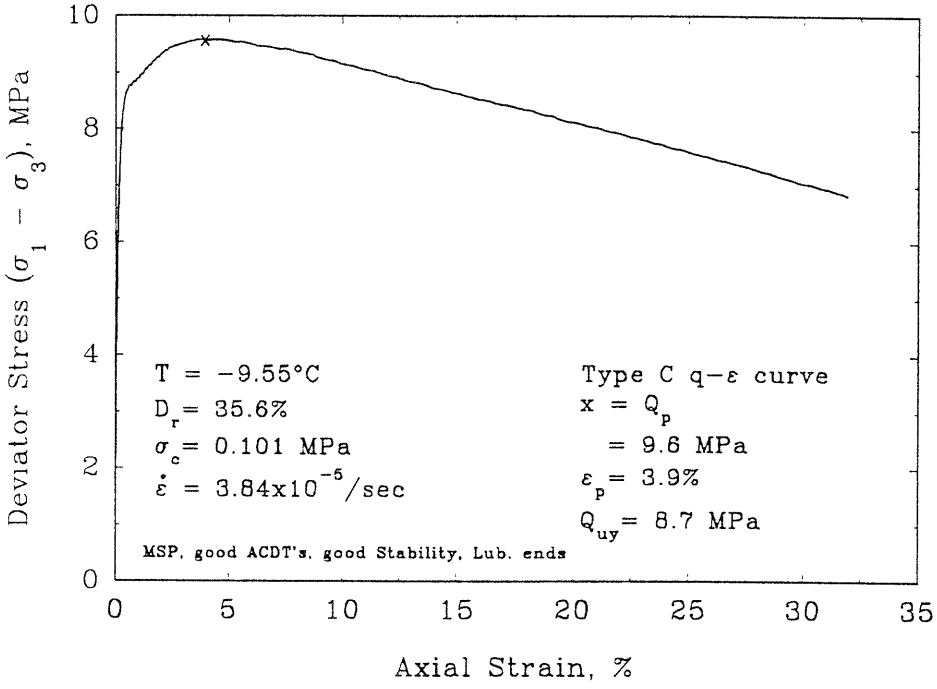

Volumetric vs Axial Strain

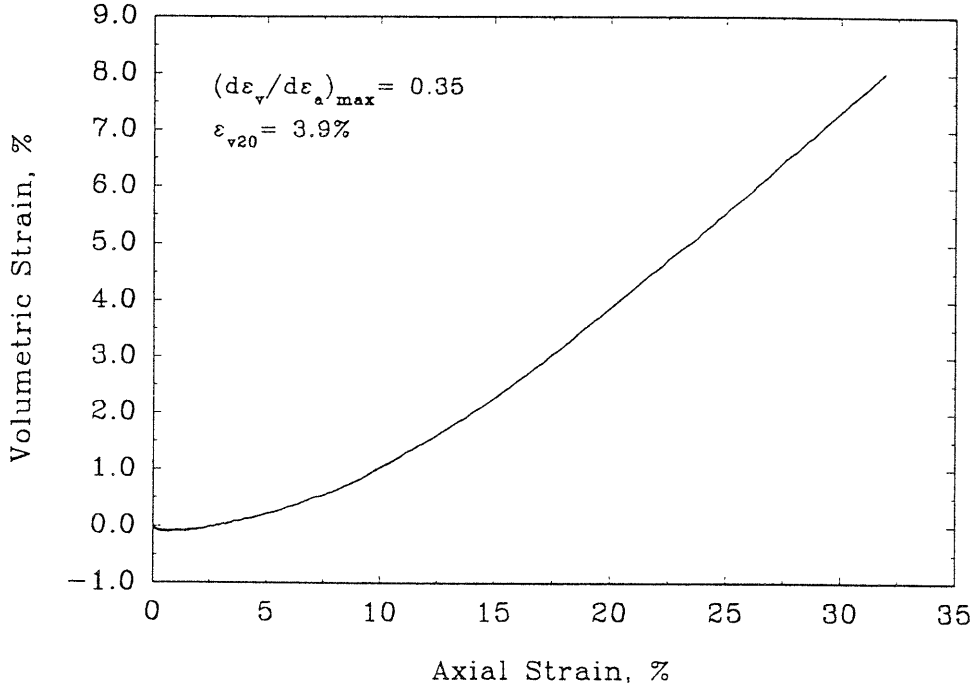

FRS58

Deviator Stress vs Axial Strain

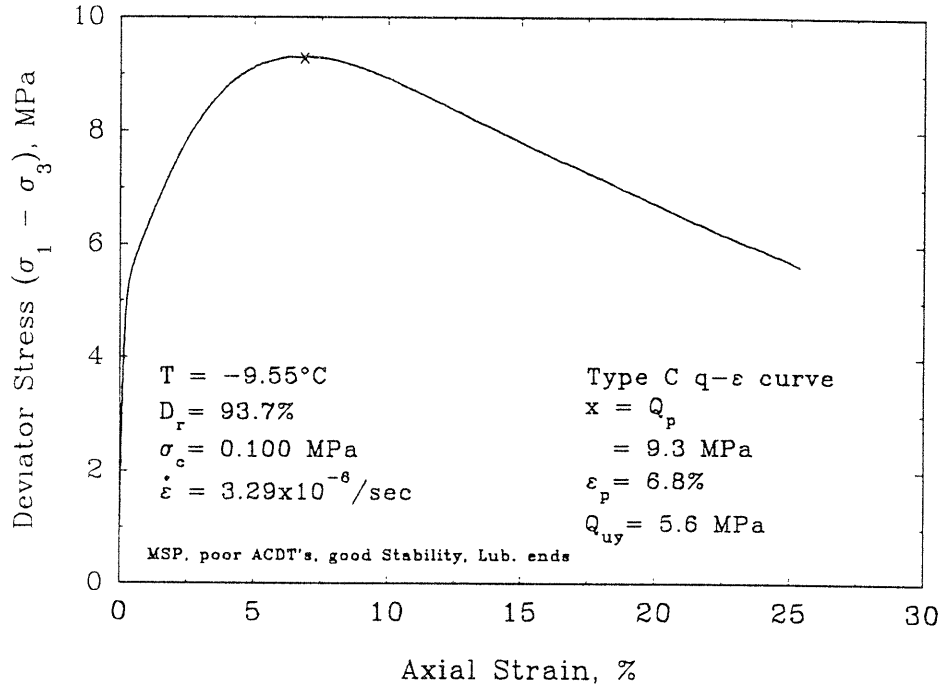

Volumetric vs Axial Strain

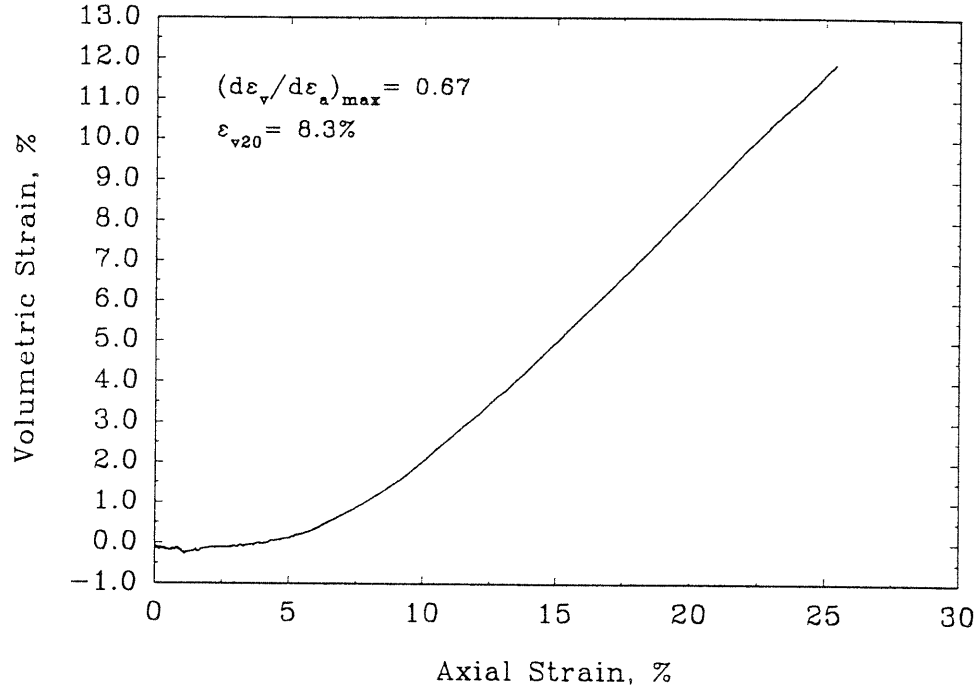

FRS59

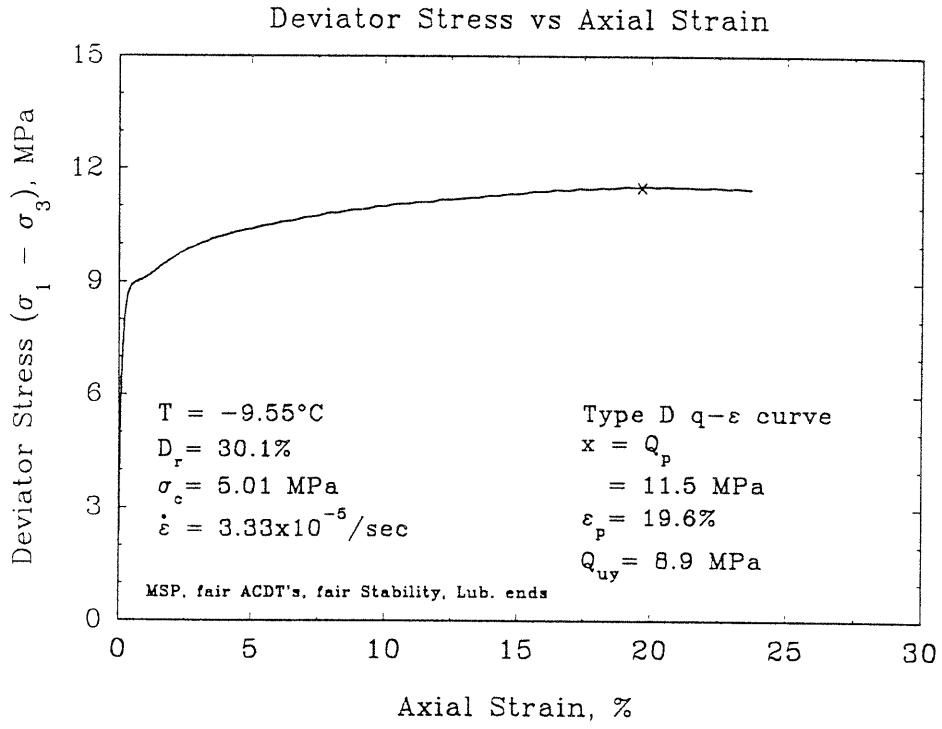
Deviator Stress vs Axial Strain
Deviator Stress ($\sigma_1 - \sigma_3$), MPa
Axial Strain, %
T = −9.55°C
D_r= 30.1%
σ_c= 5.01 MPa
$\dot{\varepsilon}$ = 3.33x10^{-5}/sec
MSP, fair ACDT's, fair Stability, Lub. ends
Type D q−ε curve
x = Q_p
= 11.5 MPa
ε_p= 19.6%
Q_{uy}= 8.9 MPa

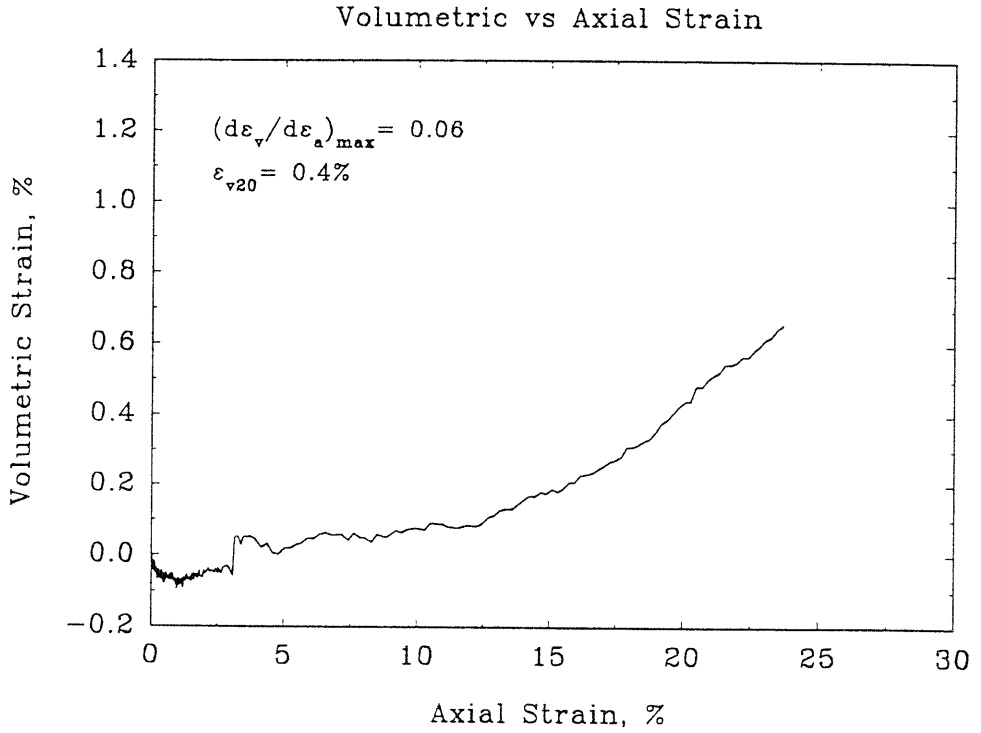
Volumetric vs Axial Strain
Volumetric Strain, %
Axial Strain, %
$(d\varepsilon_v/d\varepsilon_a)_{max}$= 0.06
ε_{v20}= 0.4%

FRS60

Deviator Stress vs Axial Strain

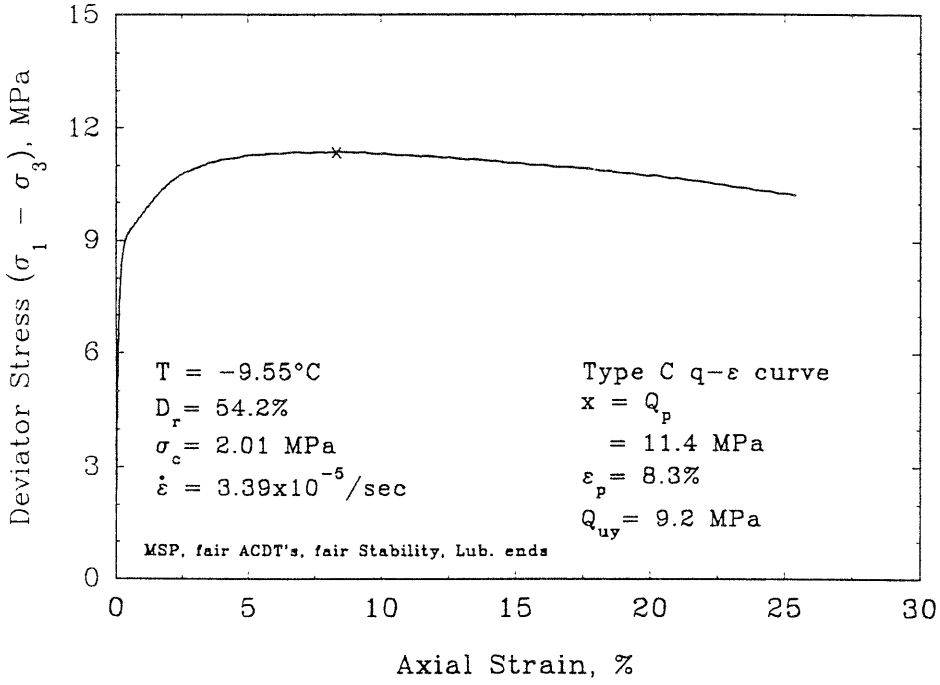

Volumetric vs Axial Strain

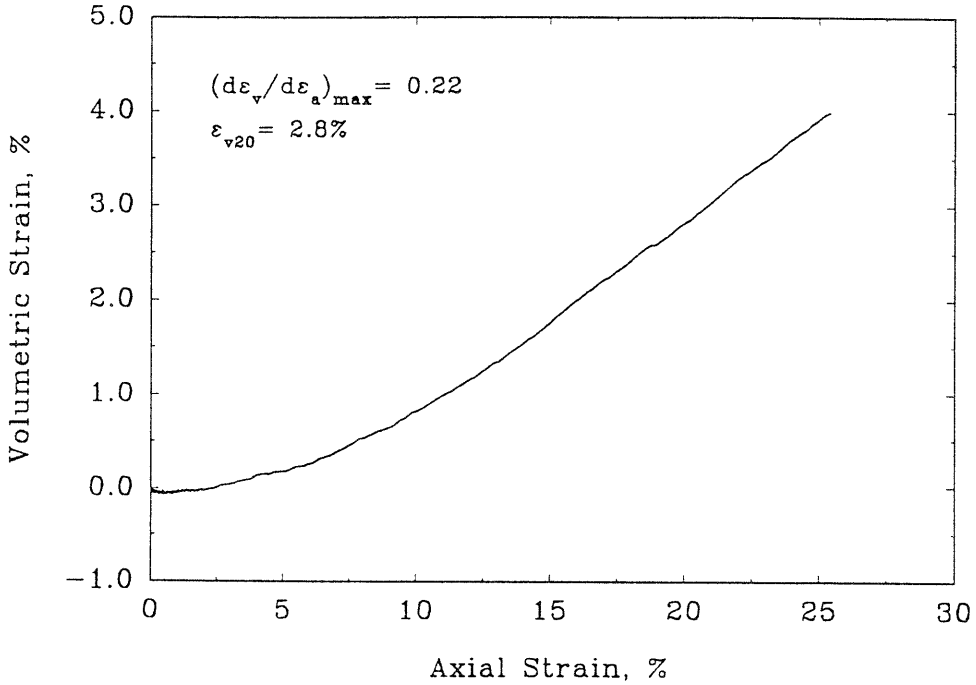

FRS61

Deviator Stress vs Axial Strain

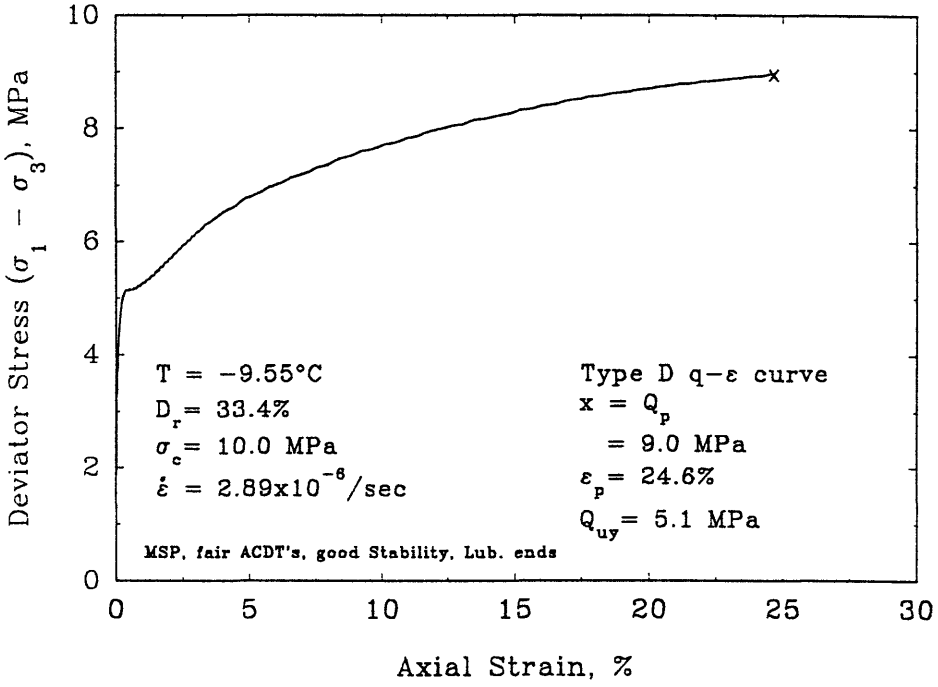

Volumetric vs Axial Strain

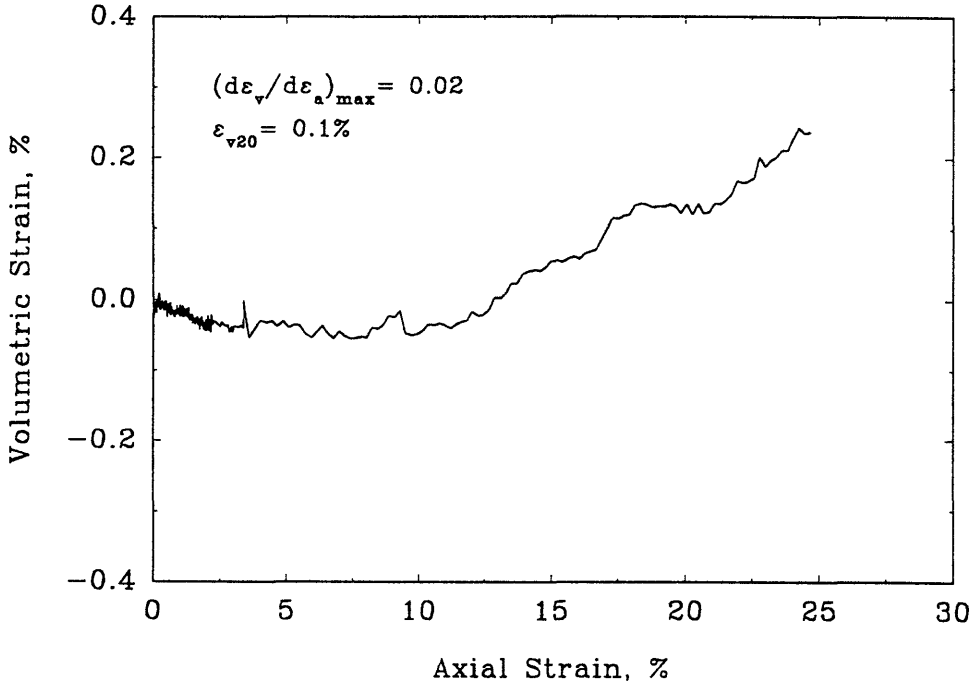

FRS62

Deviator Stress vs Axial Strain

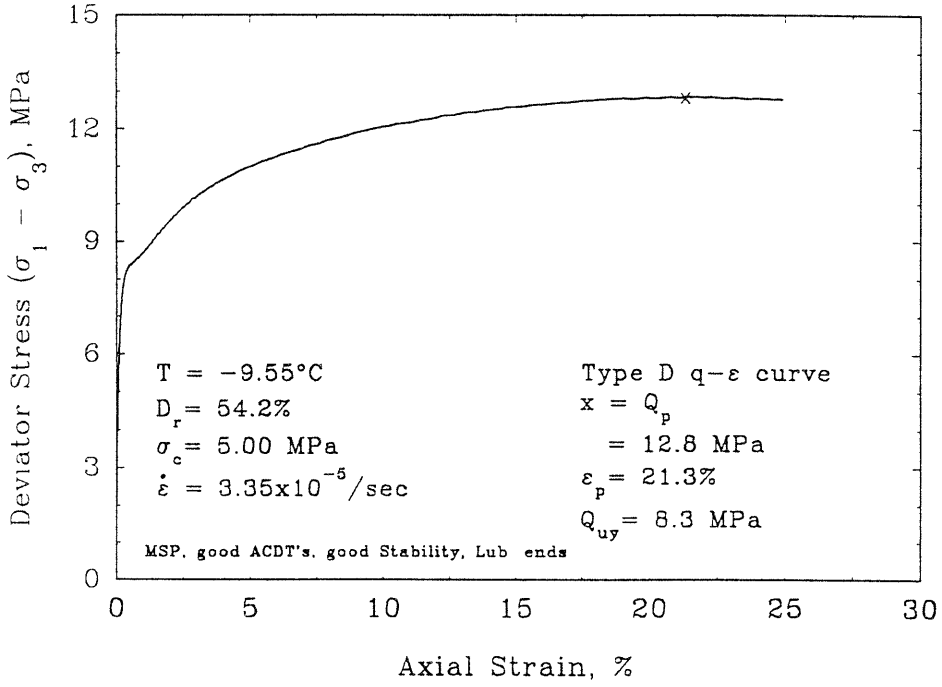

Volumetric vs Axial Strain

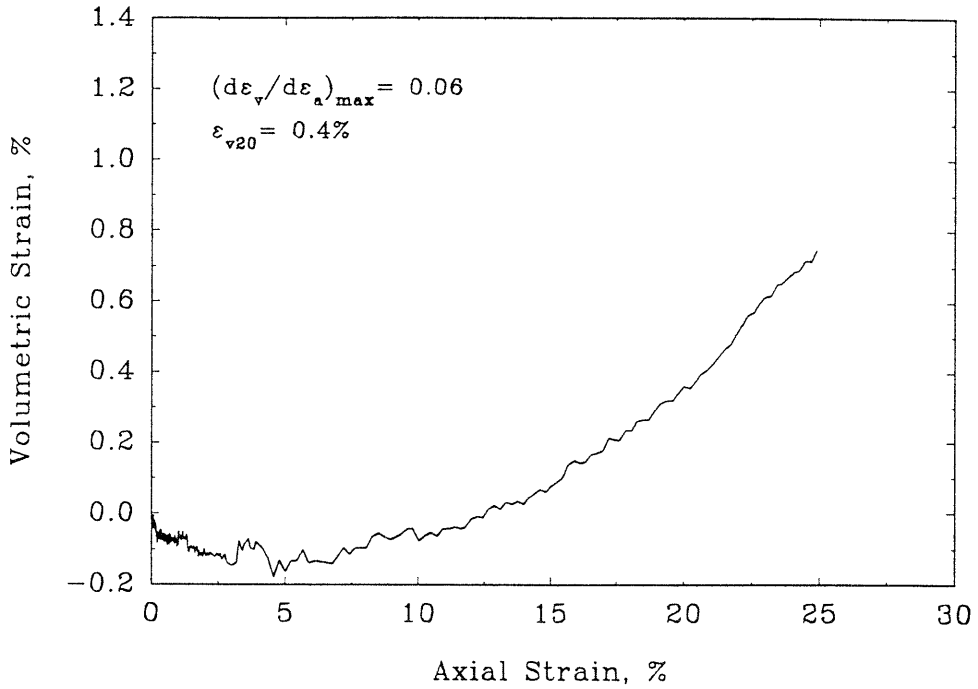

FRS63

Deviator Stress vs Axial Strain

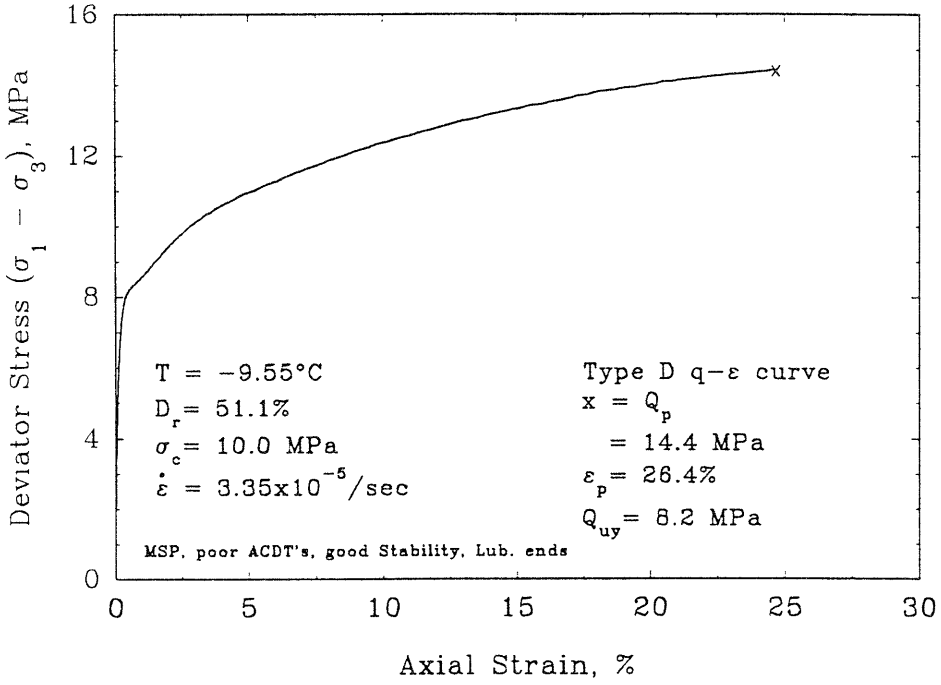

Volumetric vs Axial Strain

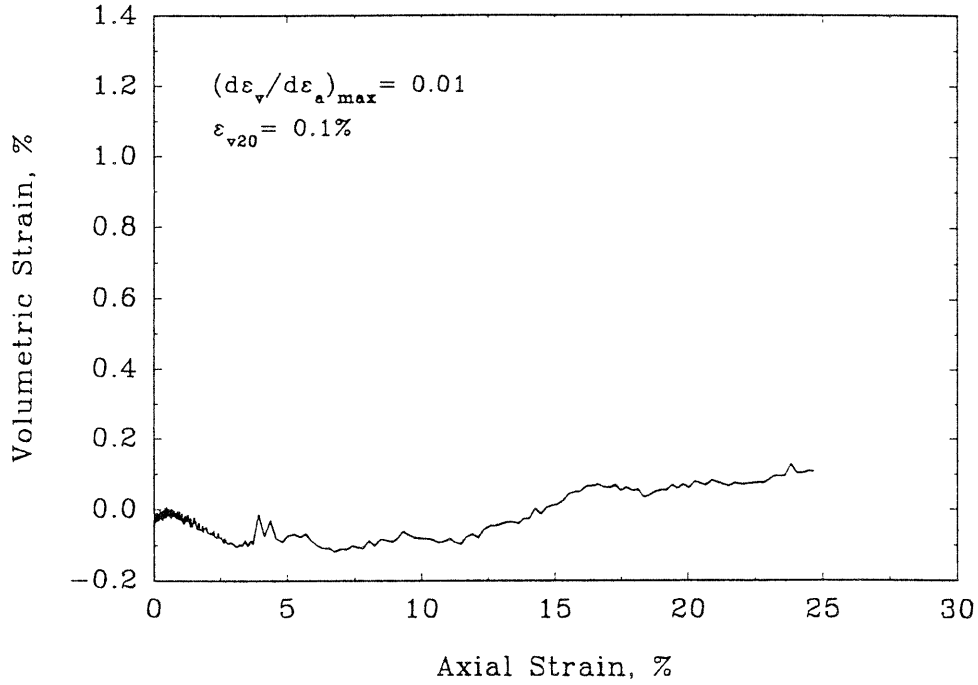

FRS64

Deviator Stress vs Axial Strain

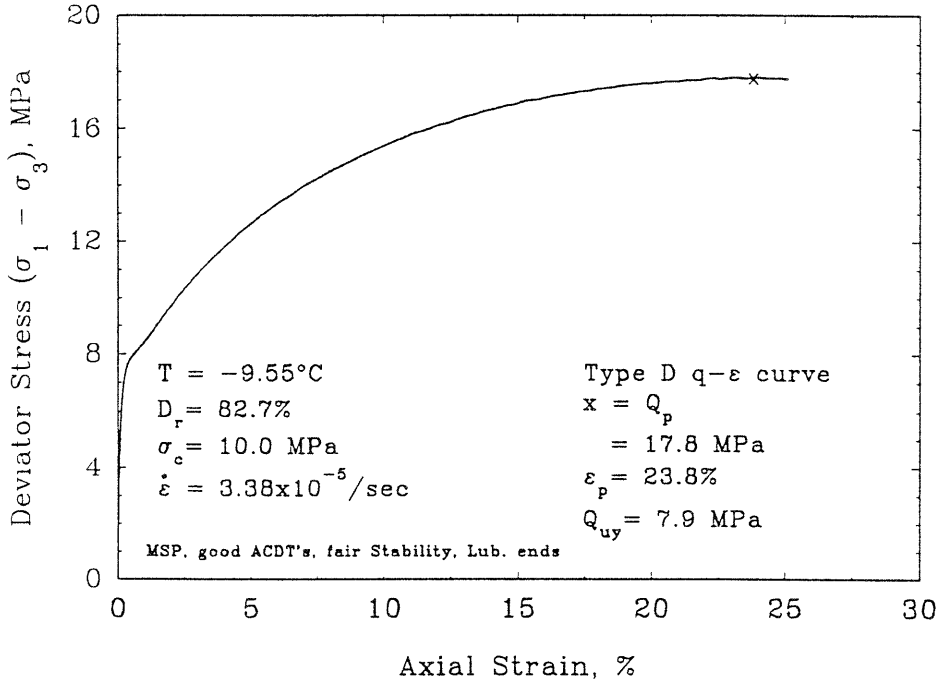

Volumetric vs Axial Strain

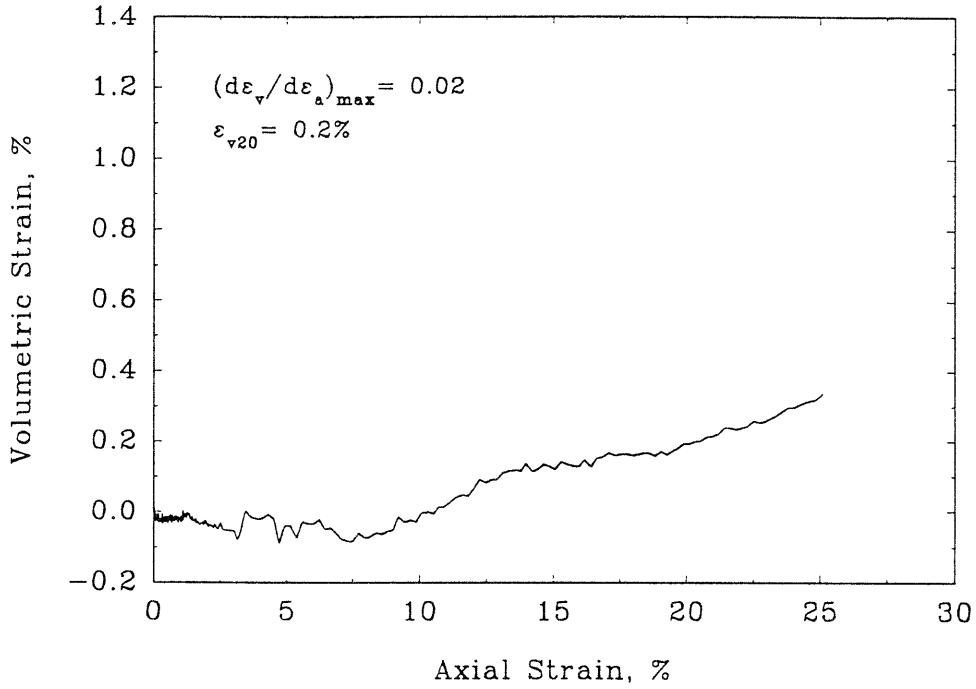

FRS65

Deviator Stress vs Axial Strain

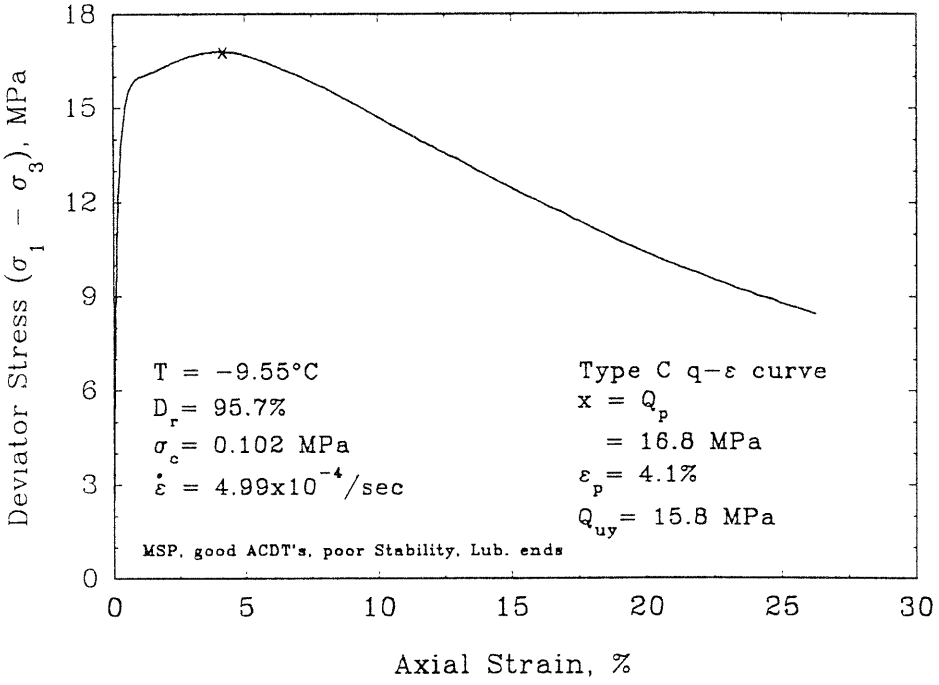

Volumetric vs Axial Strain

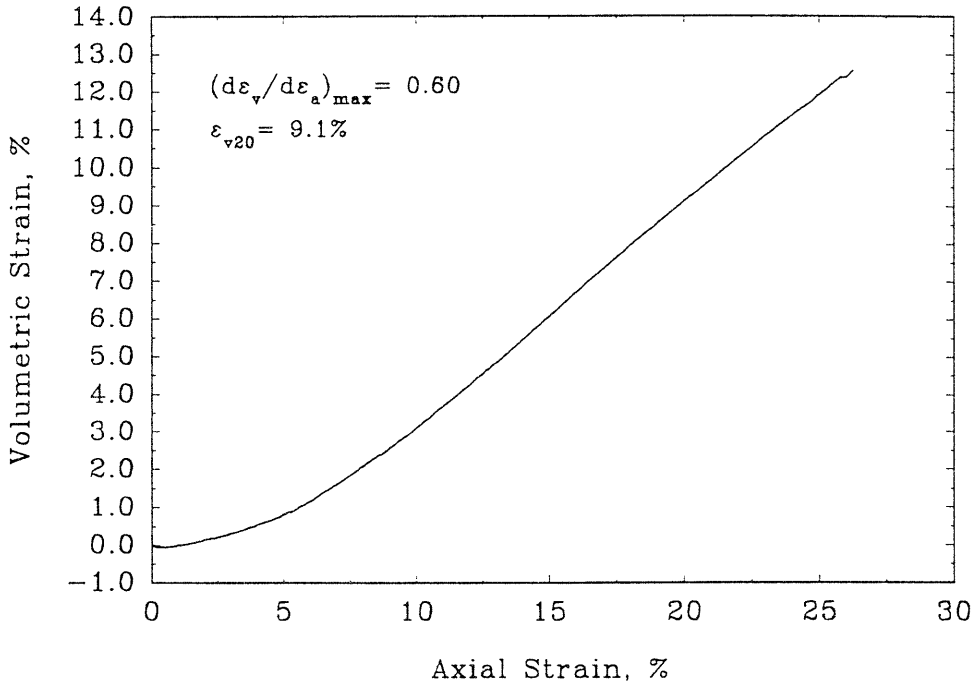

FRS66

Deviator Stress vs Axial Strain

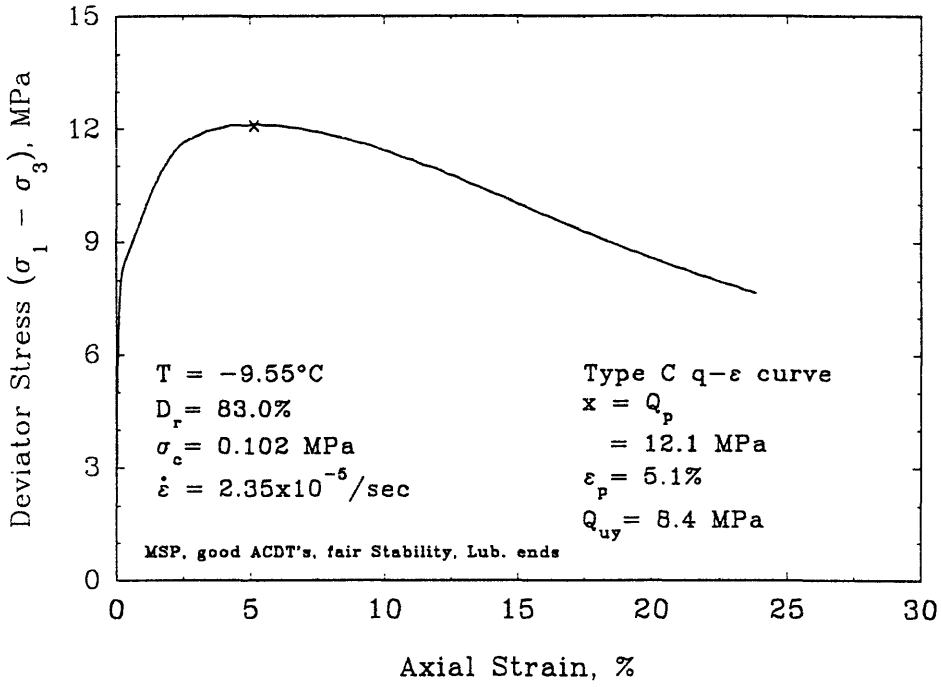

Volumetric vs Axial Strain

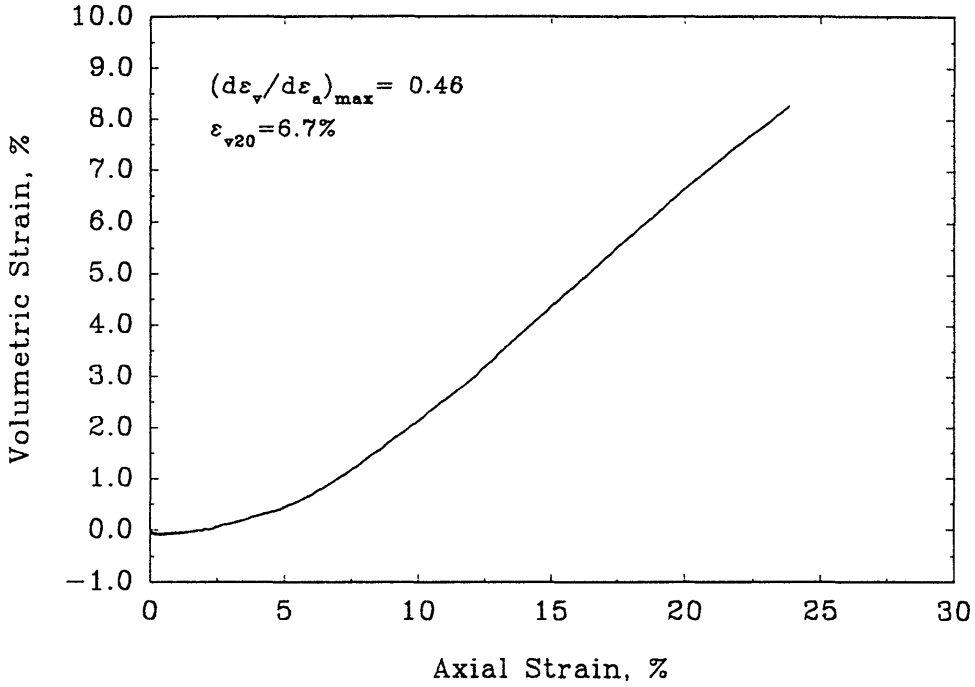

FRS67

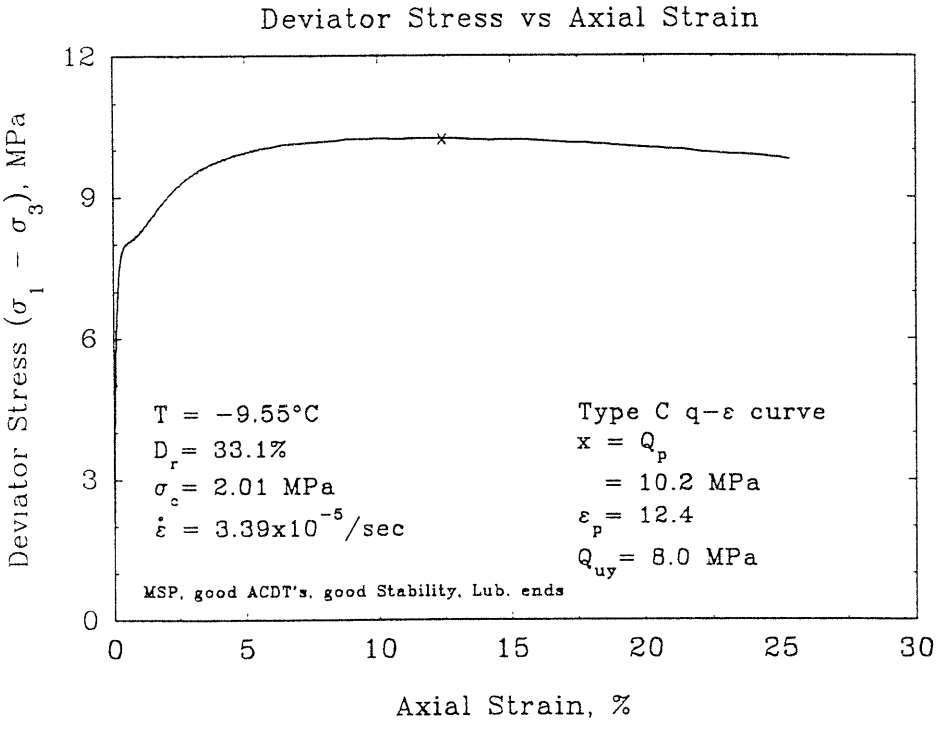
Deviator Stress vs Axial Strain
Deviator Stress ($\sigma_1 - \sigma_3$), MPa
Axial Strain, %
T = −9.55°C
D_r = 33.1%
σ_c = 2.01 MPa
$\dot{\varepsilon}$ = 3.39x10^{-5}/sec
Type C q−ε curve
x = Q_p
= 10.2 MPa
ε_p = 12.4
Q_{uy} = 8.0 MPa
MSP, good ACDT's, good Stability, Lub. ends

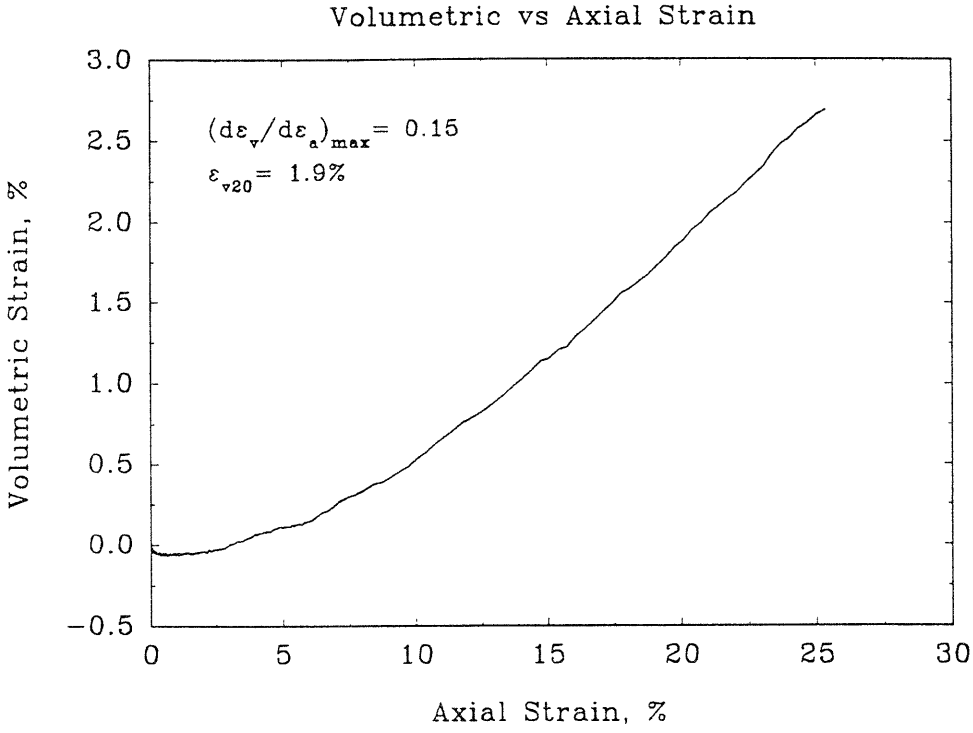
Volumetric vs Axial Strain
Volumetric Strain, %
Axial Strain, %
$(d\varepsilon_v/d\varepsilon_a)_{max}$ = 0.15
ε_{v20} = 1.9%

SECTION C.2

Tests at T = –15° C

FRS121

Deviator Stress vs Axial Strain

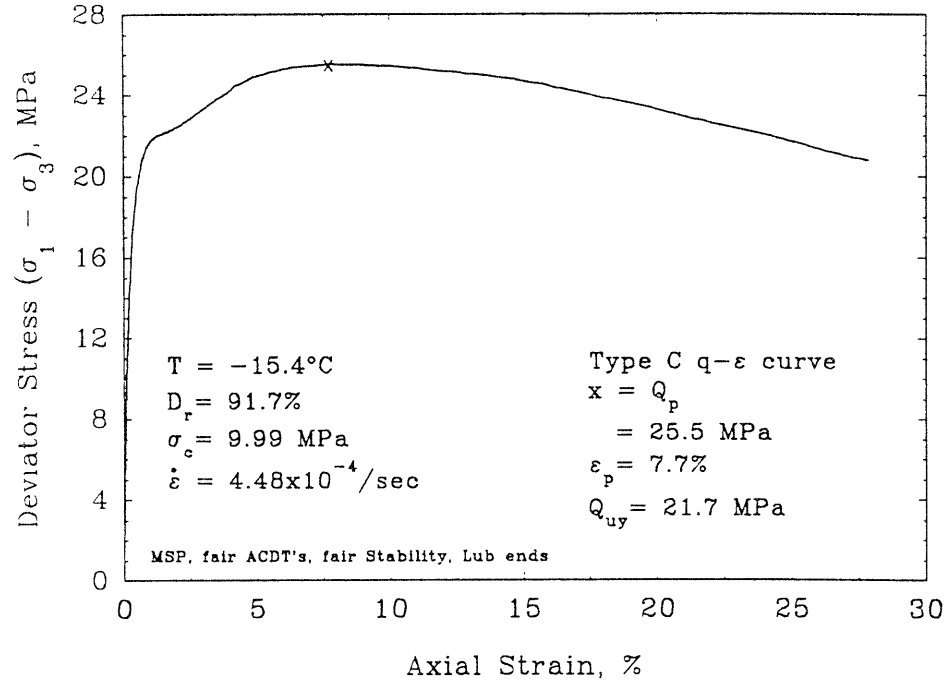

Volumetric vs Axial Strain

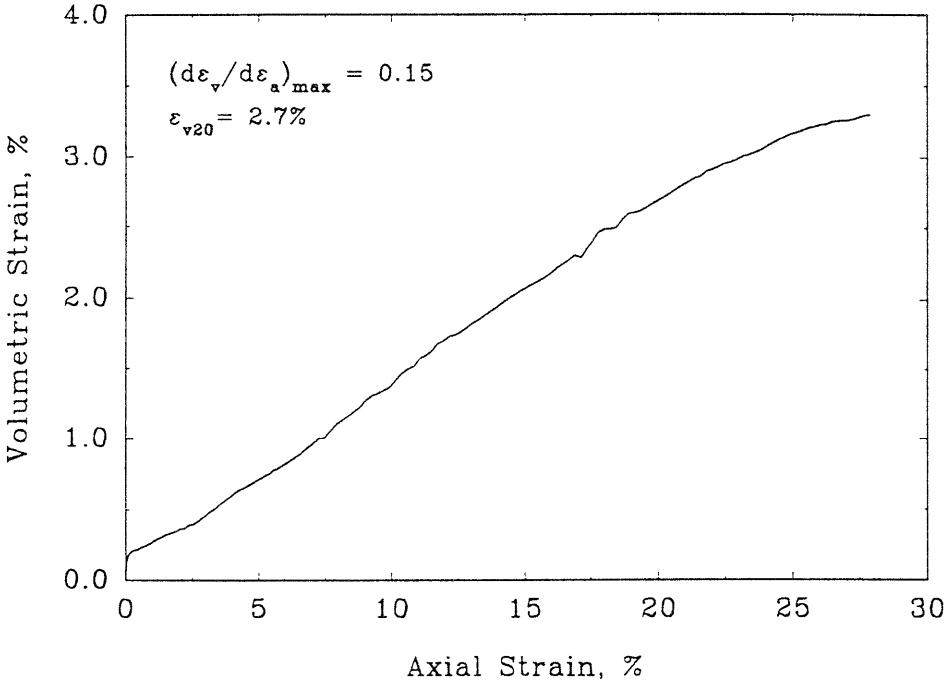

FRS123

Deviator Stress vs Axial Strain

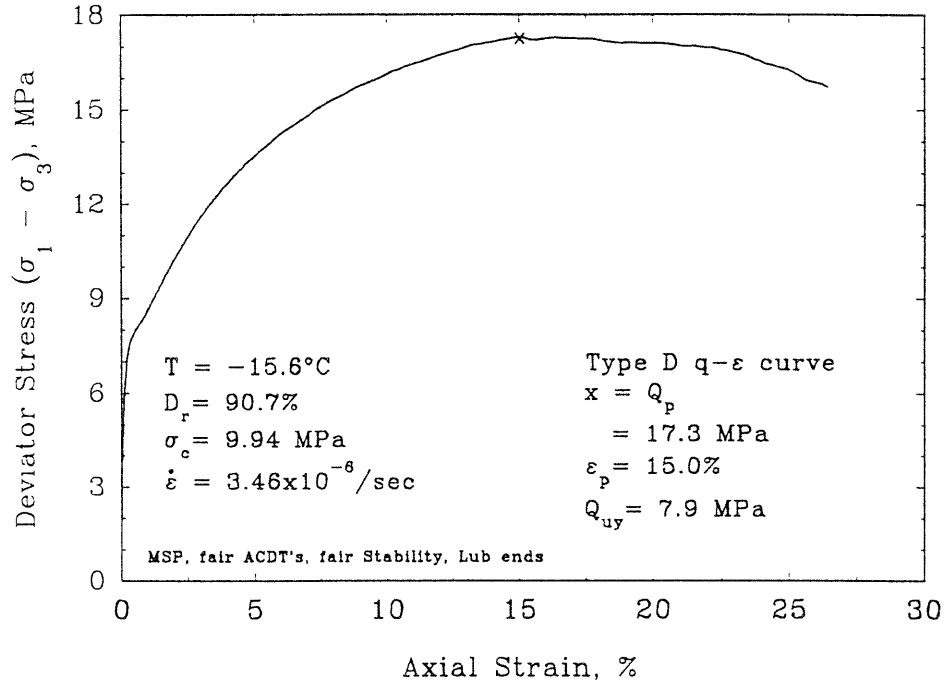

Volumetric vs Axial Strain

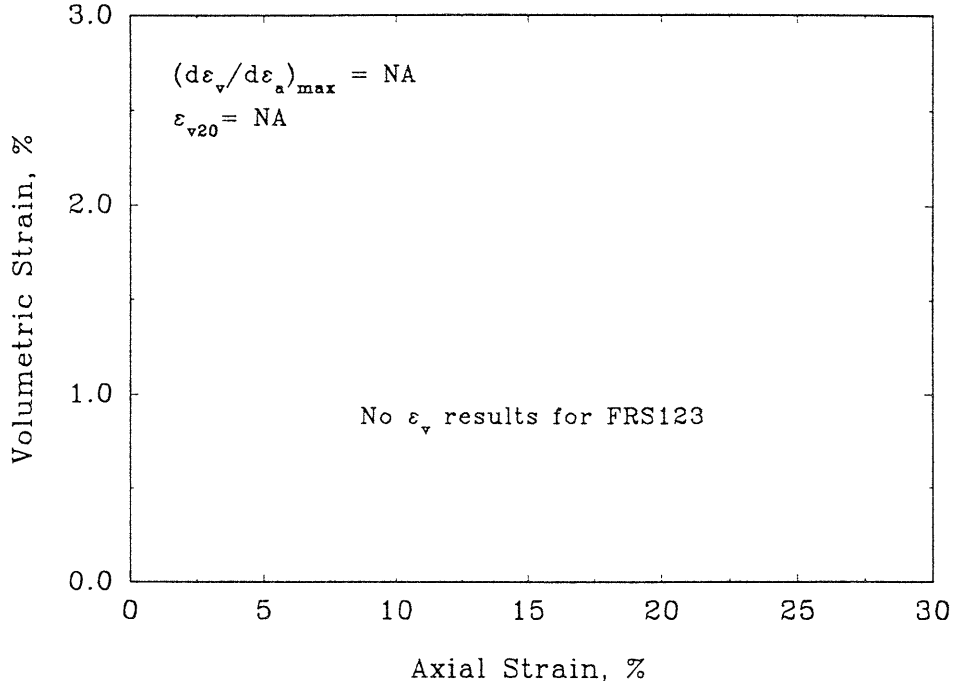

FRS126

Deviator Stress vs Axial Strain

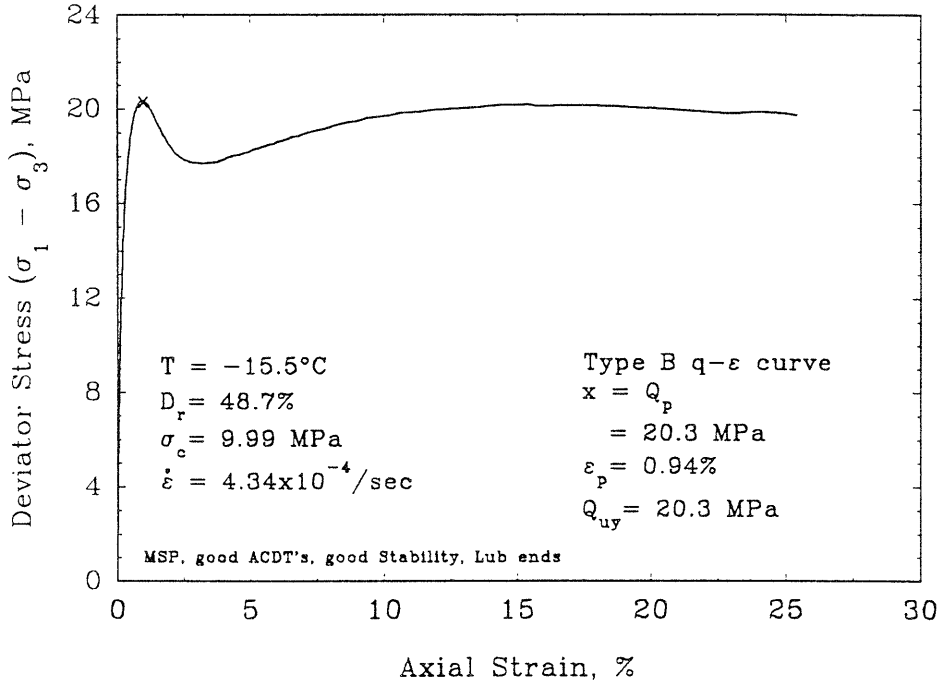

Volumetric vs Axial Strain

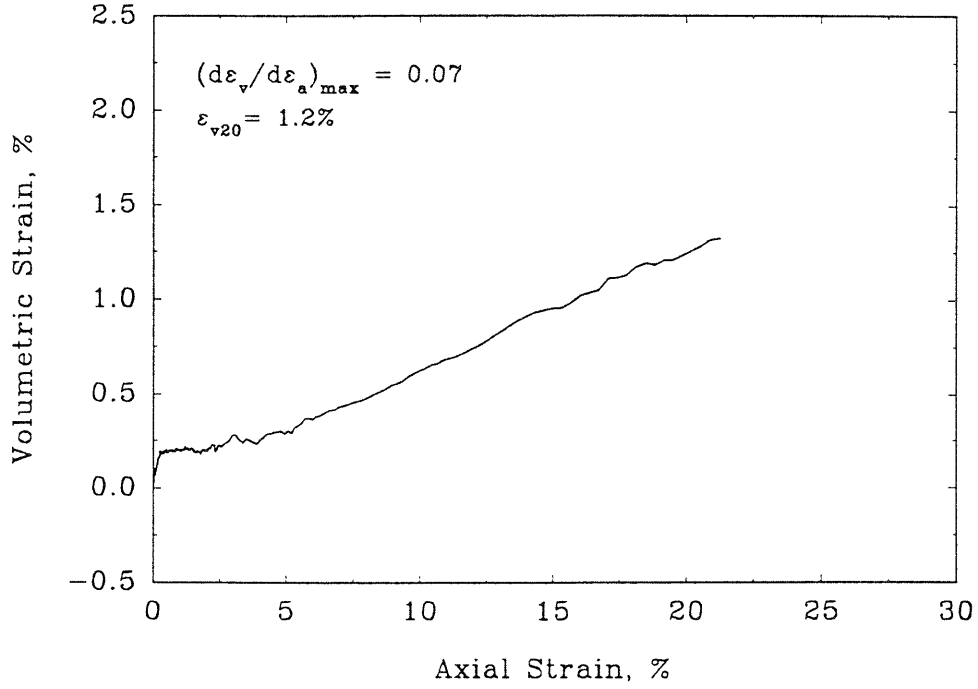

FRS127

Deviator Stress vs Axial Strain

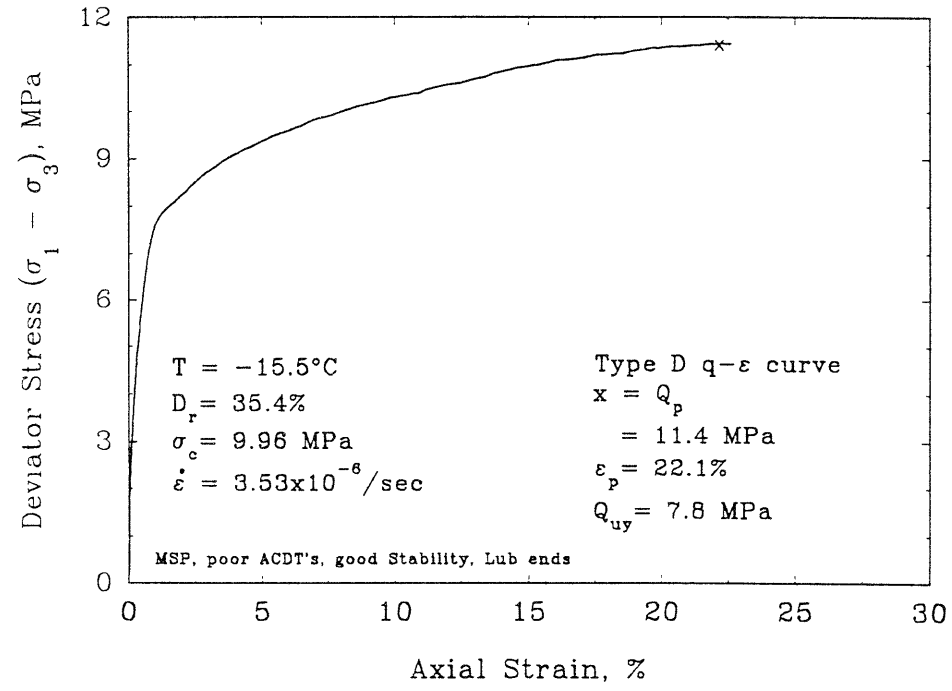

Volumetric vs Axial Strain

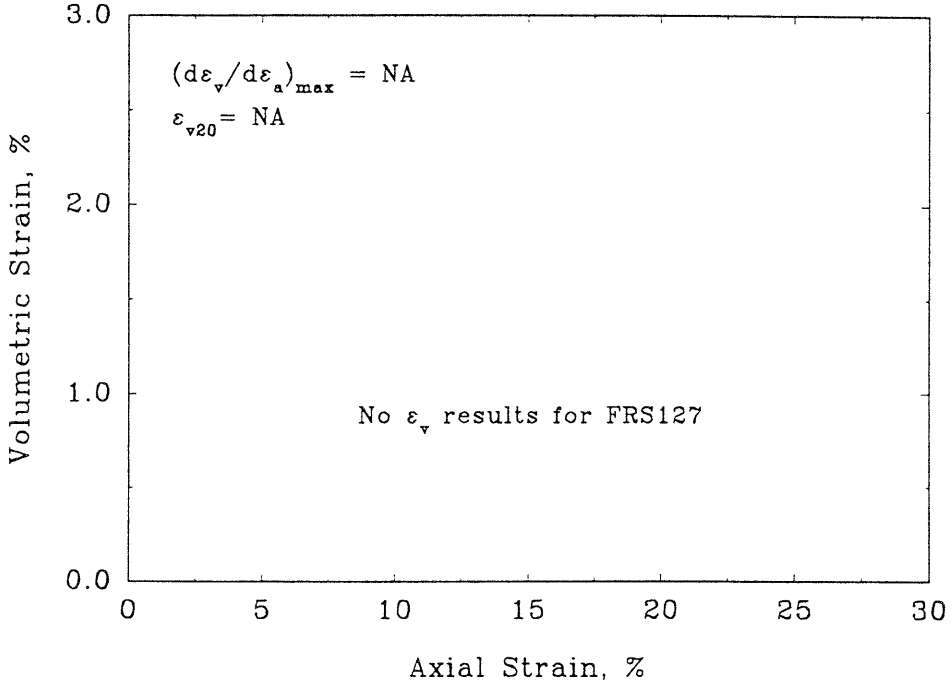

FRS128

Deviator Stress vs Axial Strain

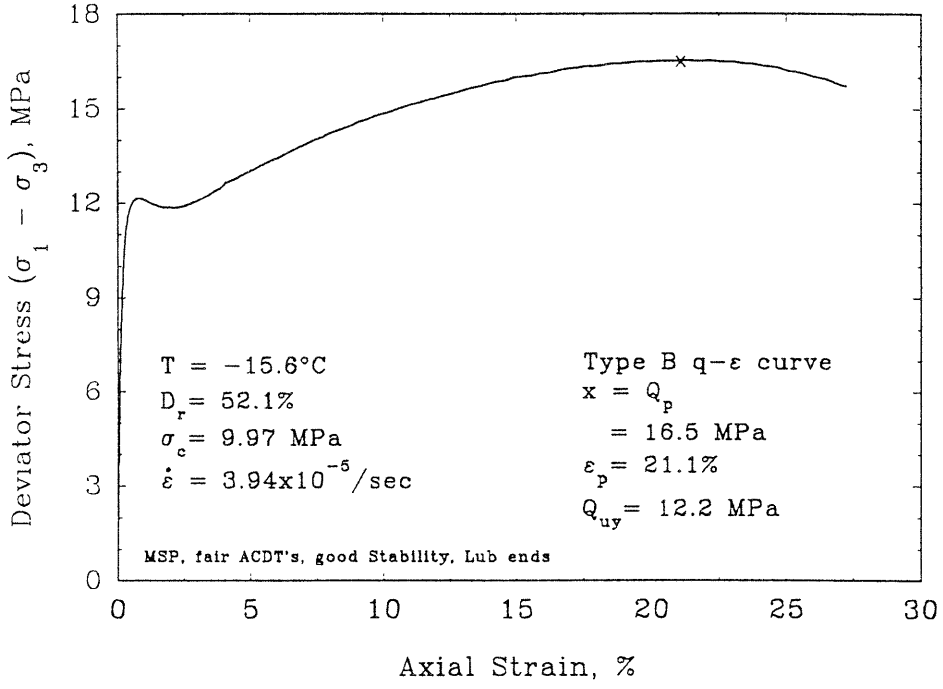

Volumetric vs Axial Strain

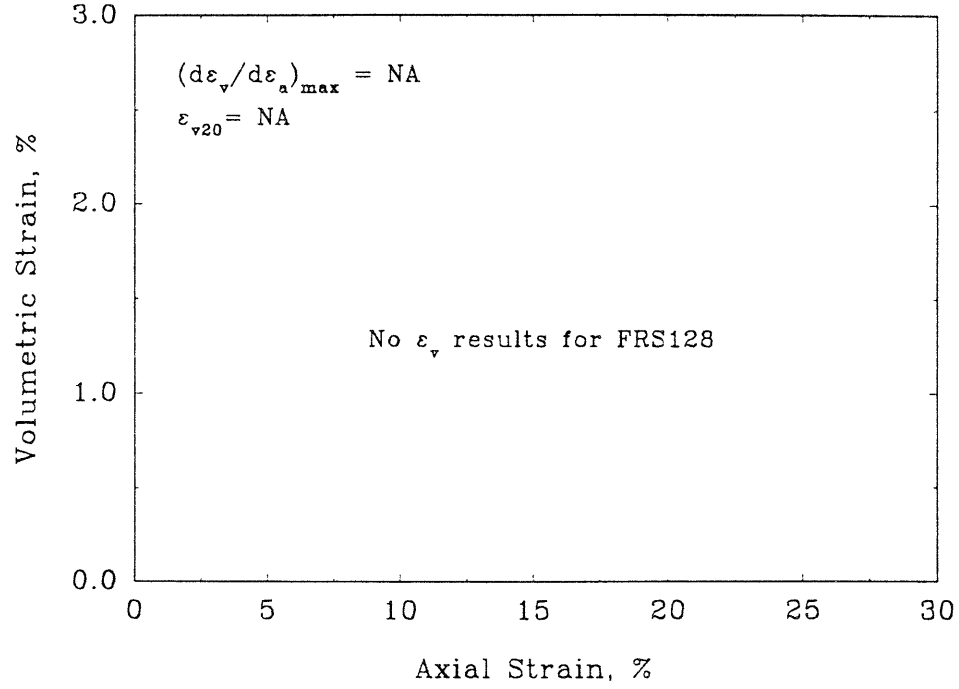

FRS129

Deviator Stress vs Axial Strain

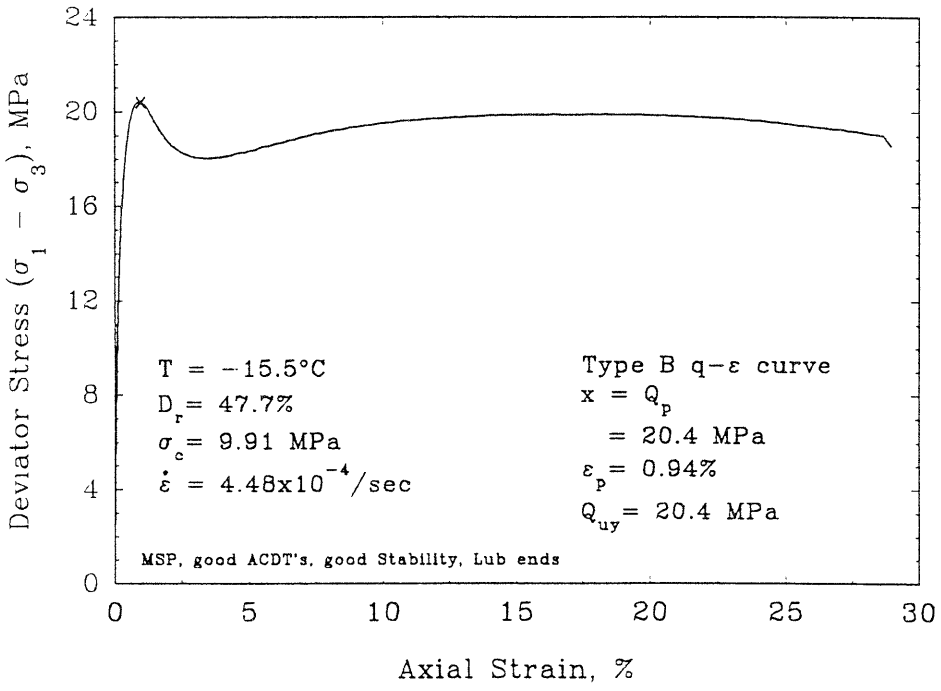

Volumetric vs Axial Strain

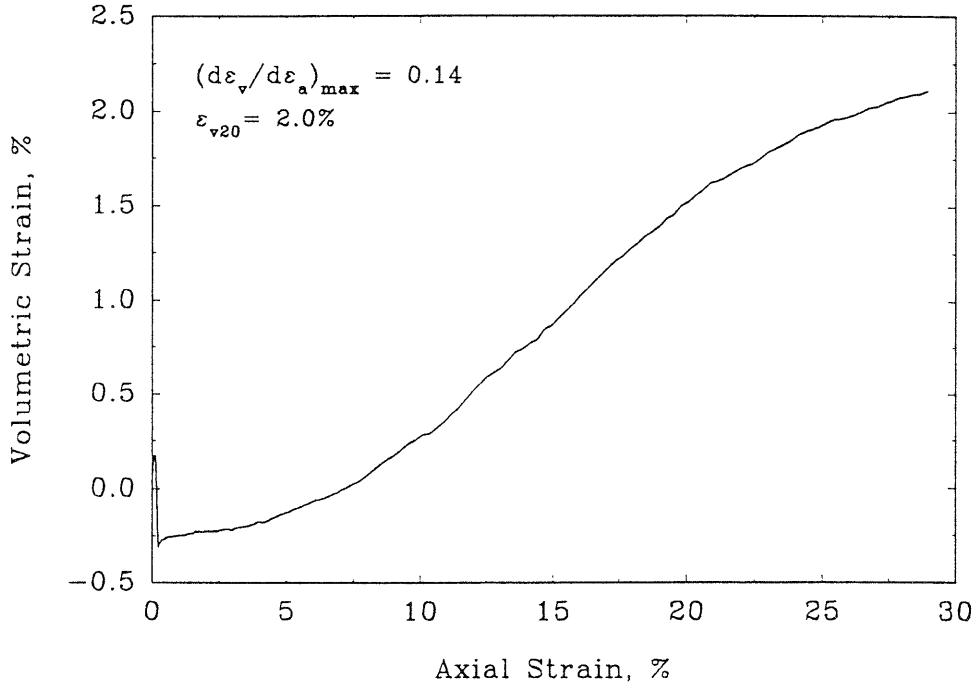

FRS130

Deviator Stress vs Axial Strain

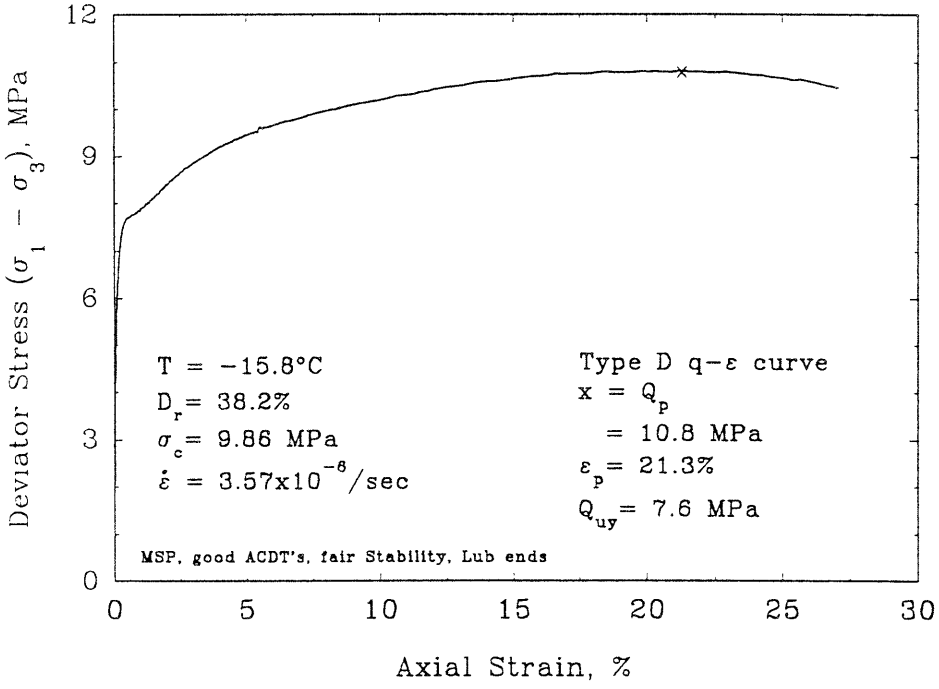

Volumetric vs Axial Strain

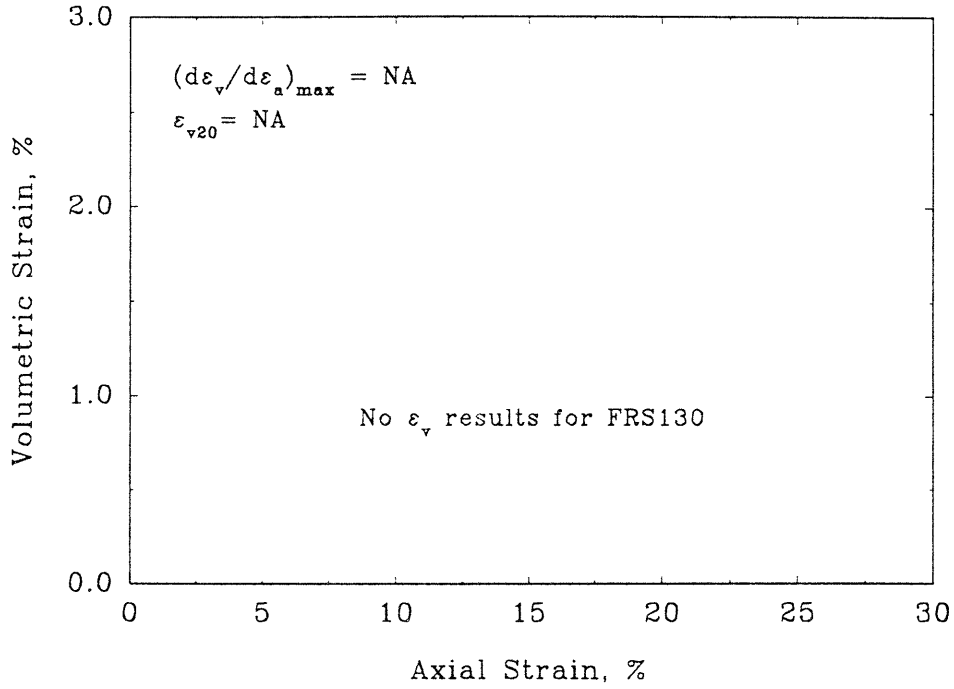

FRS131

Deviator Stress vs Axial Strain

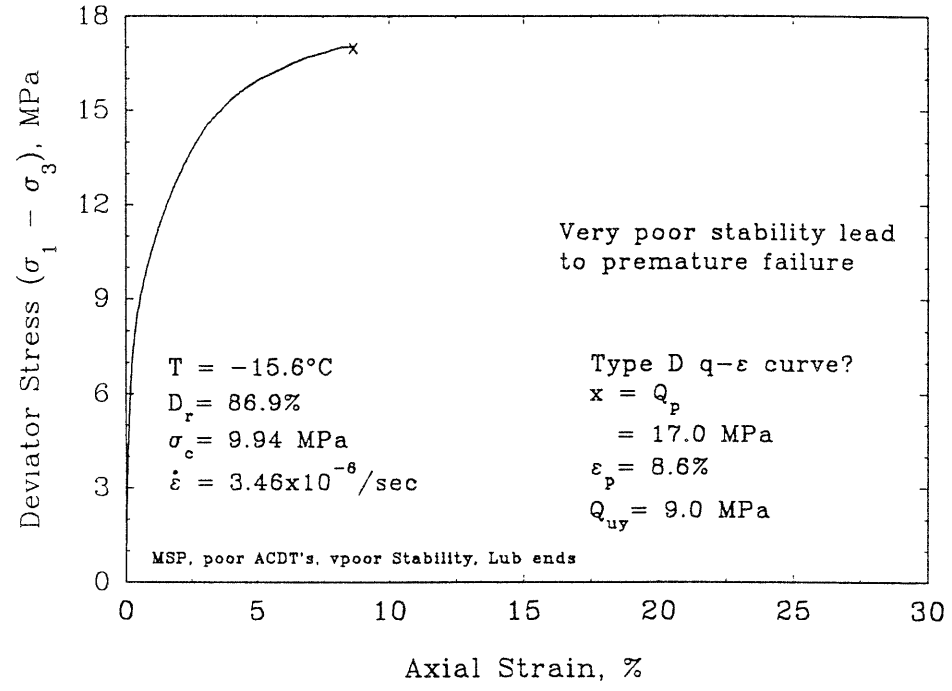

Volumetric vs Axial Strain

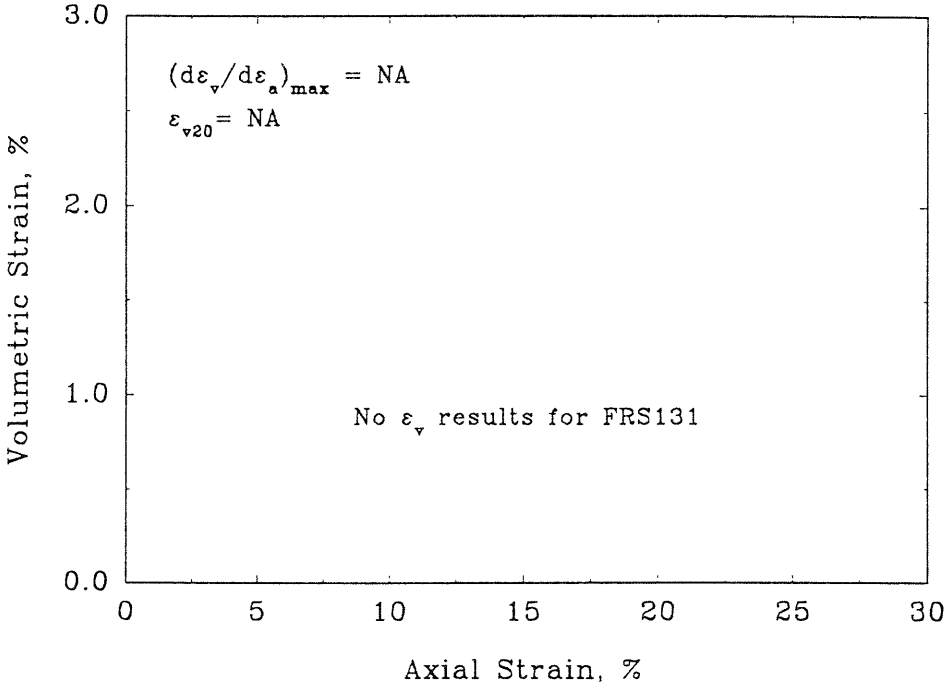

FRS133

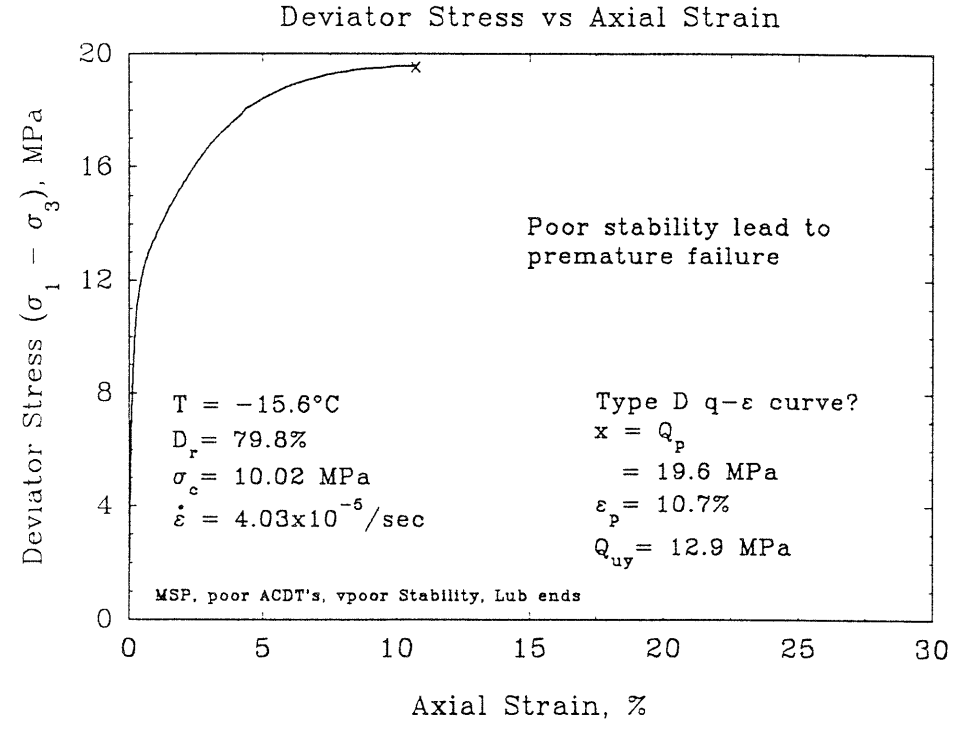
Deviator Stress vs Axial Strain
Deviator Stress ($\sigma_1 - \sigma_3$), MPa
Axial Strain, %
Poor stability lead to premature failure
T = −15.6°C
D_r= 79.8%
σ_c= 10.02 MPa
$\dot{\varepsilon}$ = 4.03x10^{-5}/sec
Type D q−ε curve?
x = Q_p
= 19.6 MPa
ε_p= 10.7%
Q_{uy}= 12.9 MPa
MSP, poor ACDT's, vpoor Stability, Lub ends

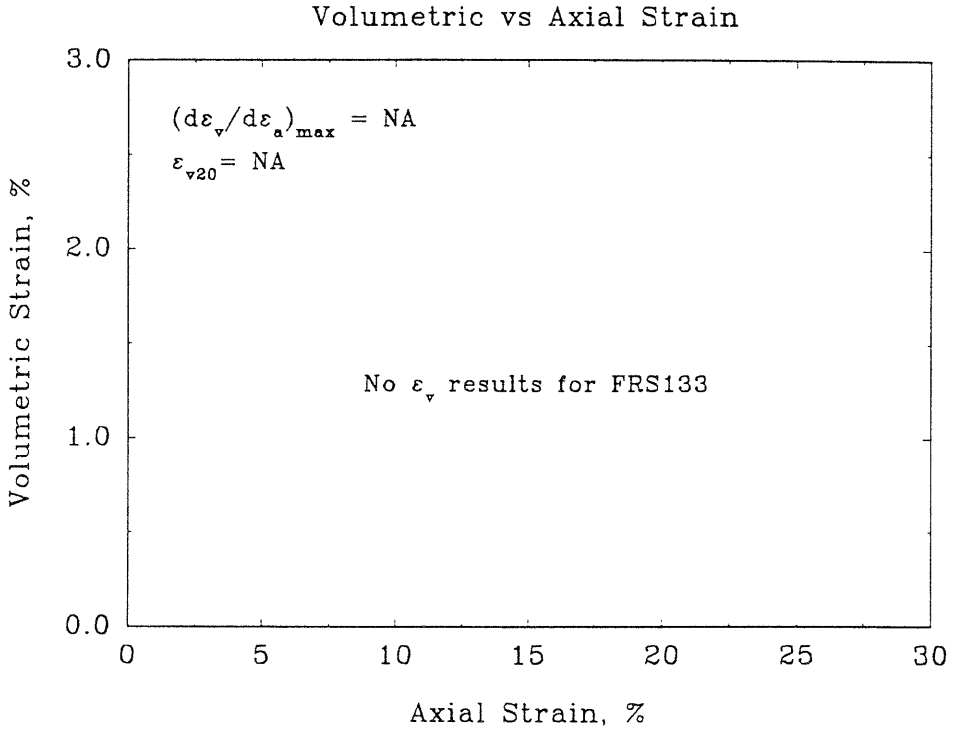
Volumetric vs Axial Strain
Volumetric Strain, %
Axial Strain, %
$(d\varepsilon_v/d\varepsilon_a)_{max}$ = NA
ε_{v20}= NA
No ε_v results for FRS133

FRS134

Deviator Stress vs Axial Strain

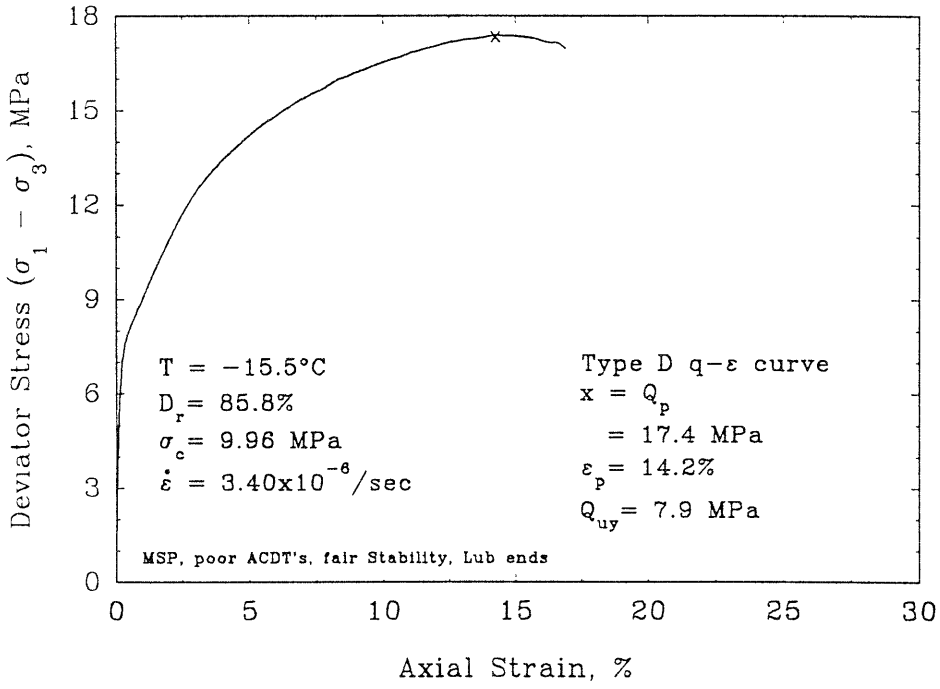

Volumetric vs Axial Strain

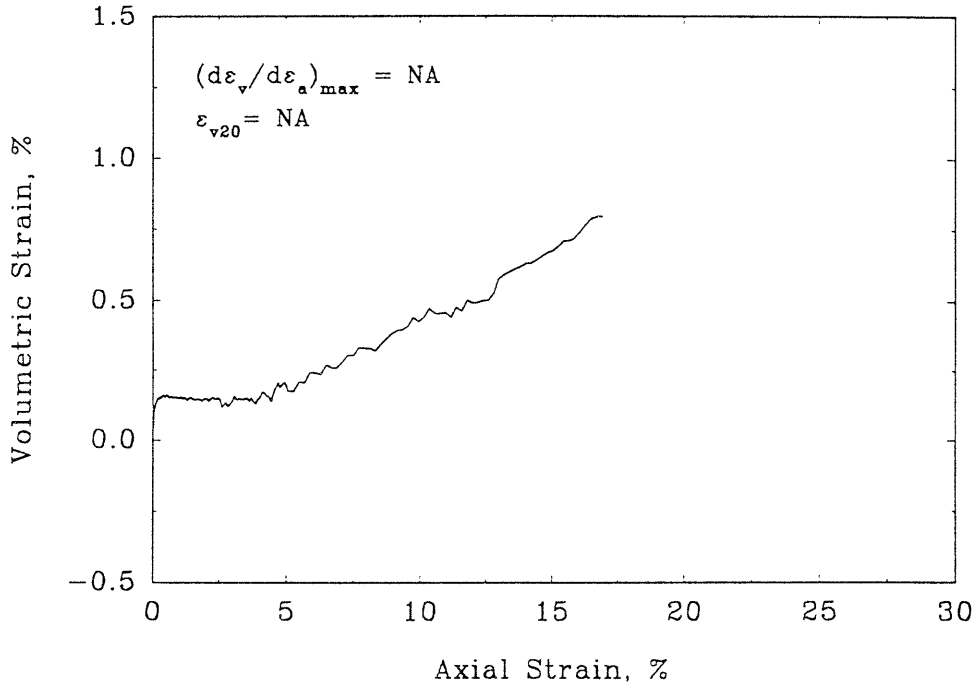

FRS135

Deviator Stress vs Axial Strain

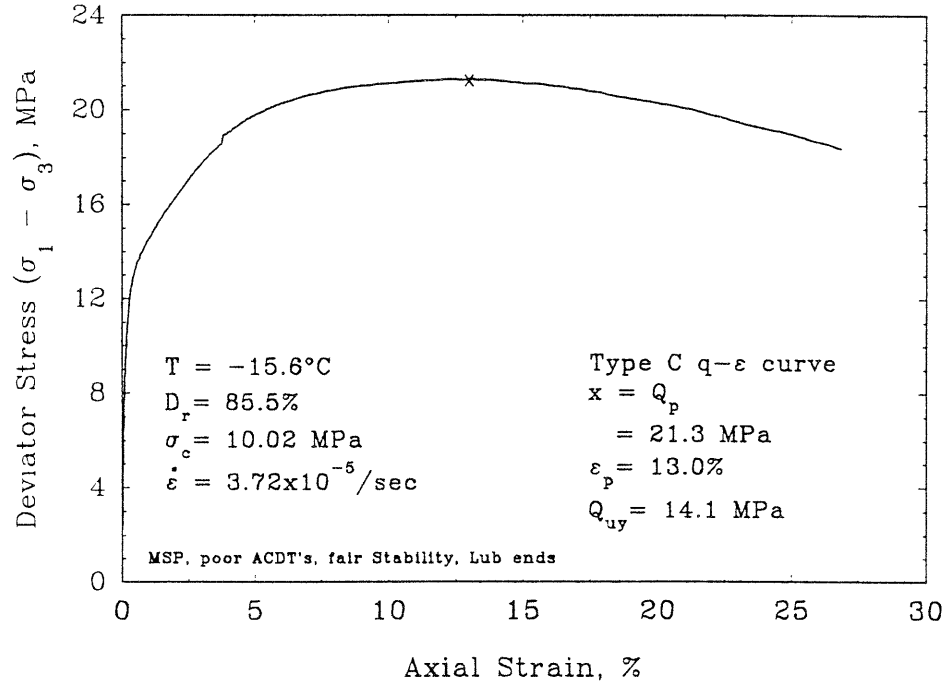

Volumetric vs Axial Strain

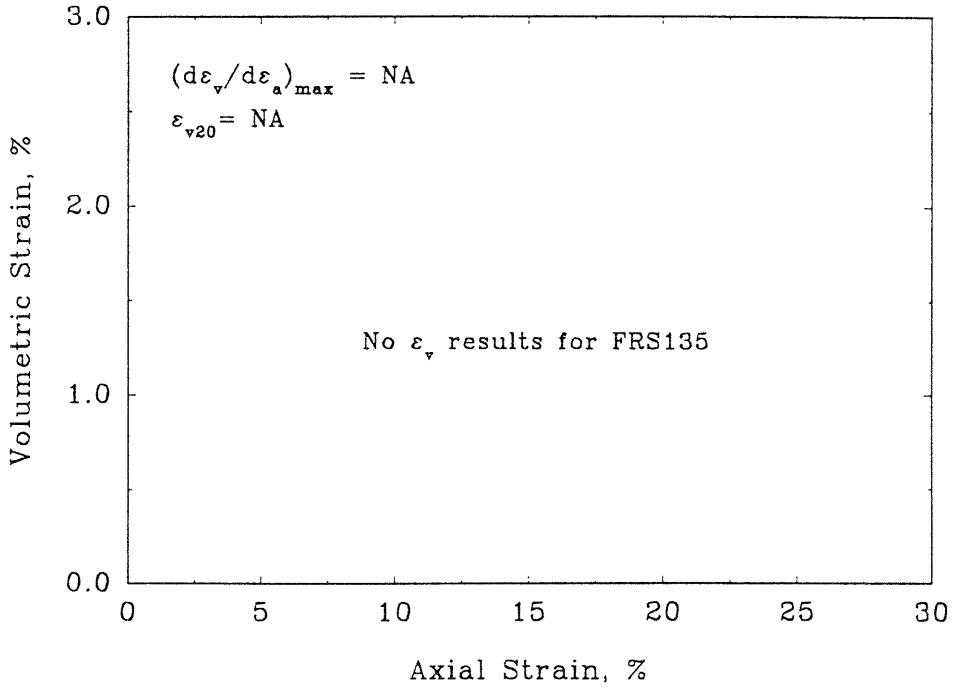

FRS136

Deviator Stress vs Axial Strain

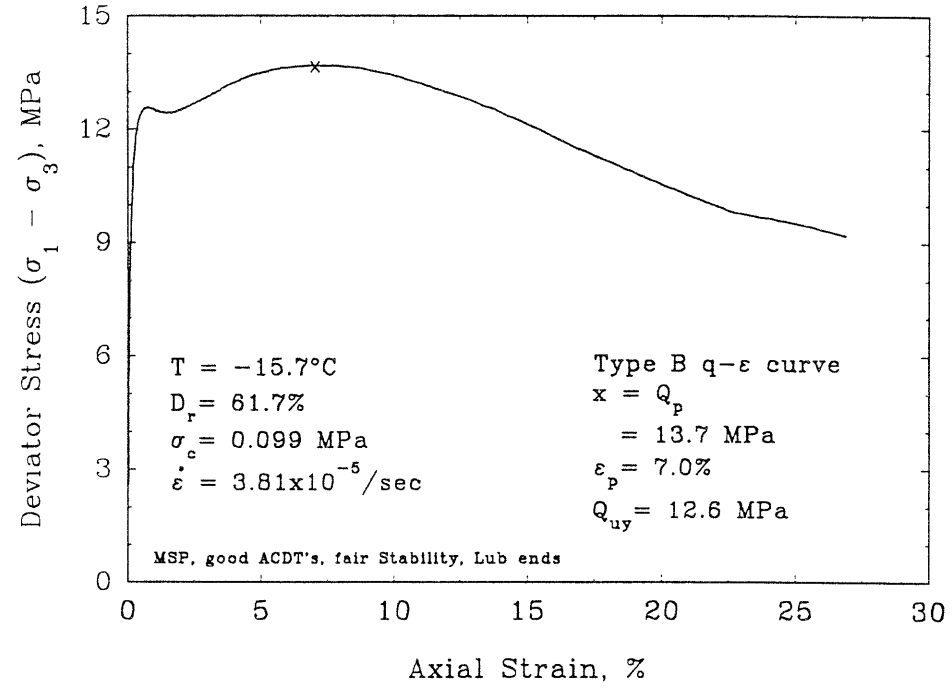

Volumetric vs Axial Strain

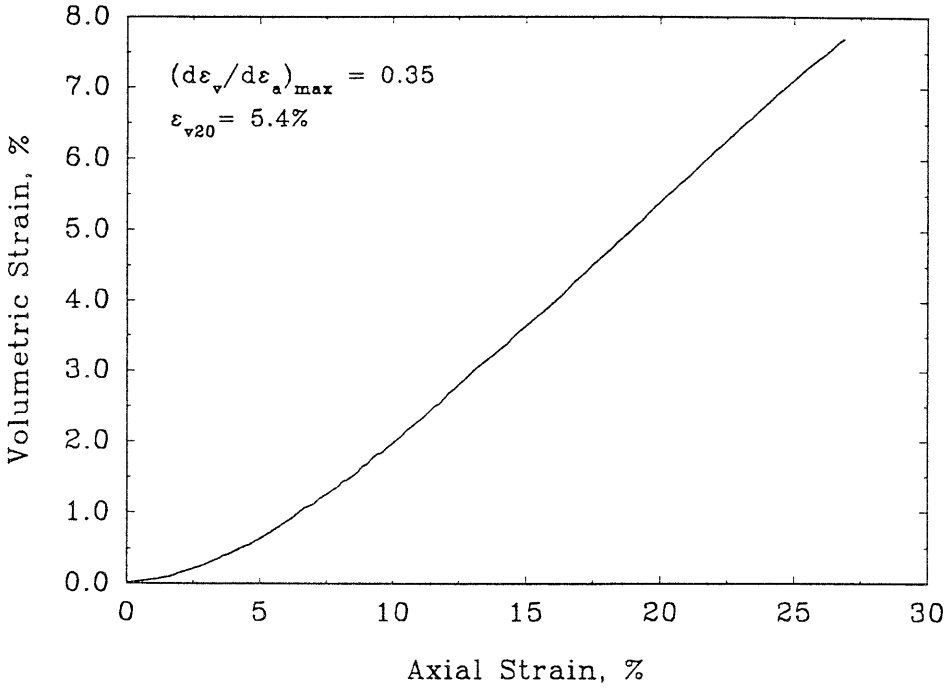

FRS138

Deviator Stress vs Axial Strain

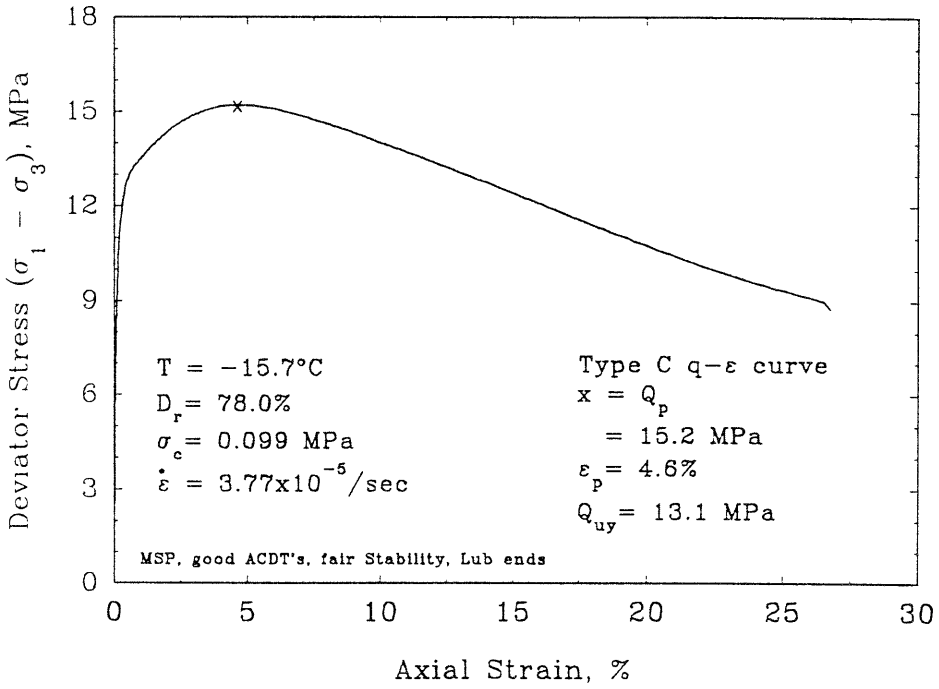

Volumetric vs Axial Strain

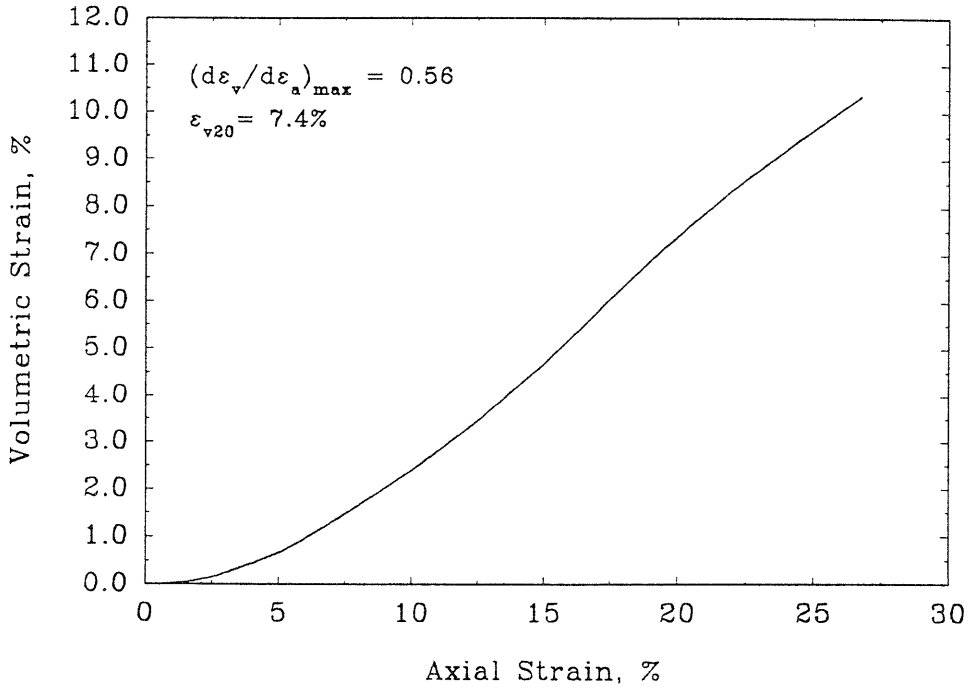

FRS141

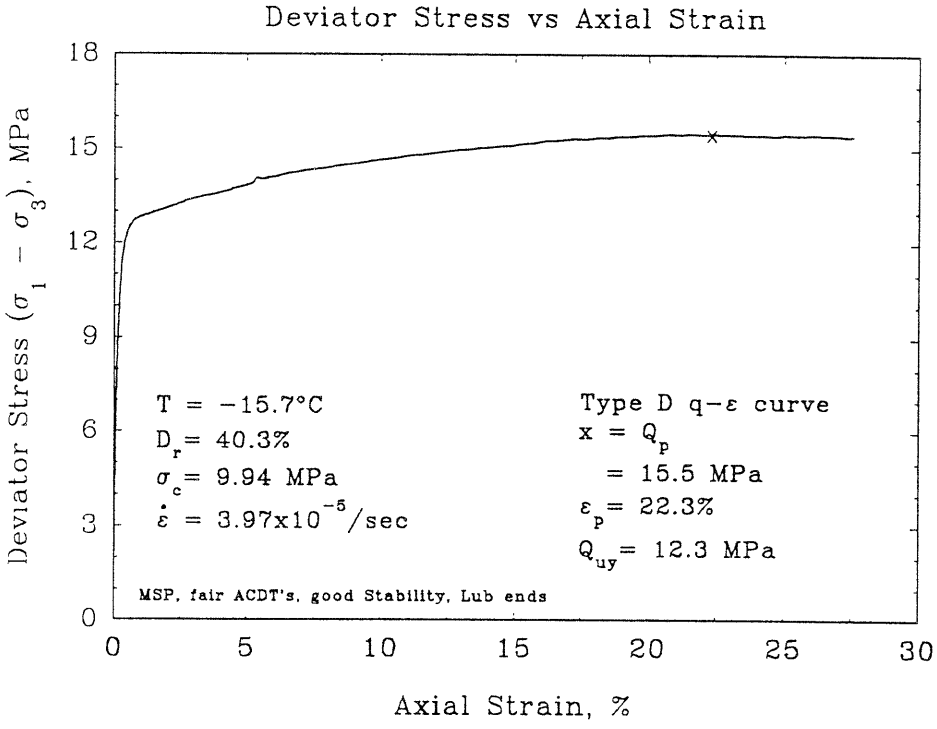
Deviator Stress vs Axial Strain
Deviator Stress ($\sigma_1 - \sigma_3$), MPa
Axial Strain, %
T = −15.7°C
D_r= 40.3%
σ_c= 9.94 MPa
$\dot{\varepsilon}$ = 3.97x10^{-5}/sec
Type D q−ε curve
x = Q_p
= 15.5 MPa
ε_p= 22.3%
Q_{uy}= 12.3 MPa
MSP, fair ACDT's, good Stability, Lub ends

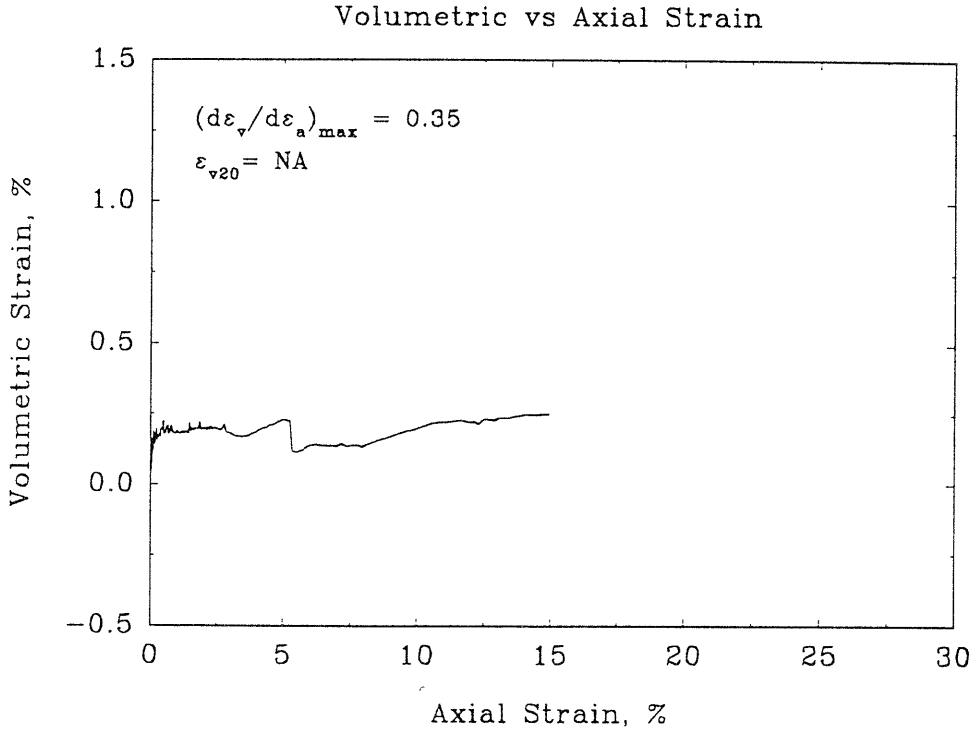
Volumetric vs Axial Strain
Volumetric Strain, %
Axial Strain, %
$(d\varepsilon_v/d\varepsilon_a)_{max}$ = 0.35
ε_{v20}= NA

FRS142

Deviator Stress vs Axial Strain

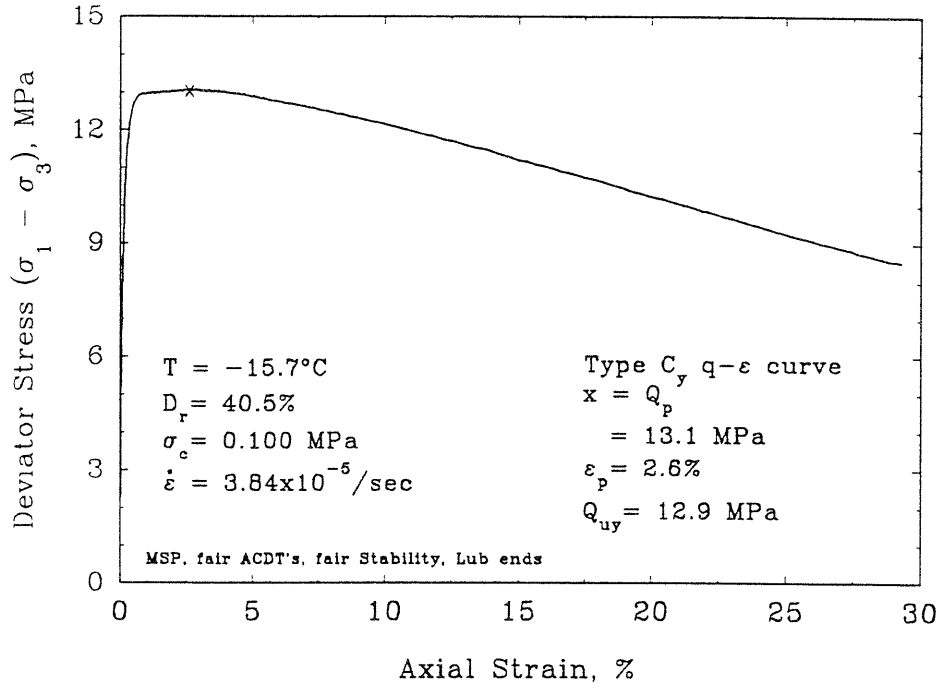

Volumetric vs Axial Strain

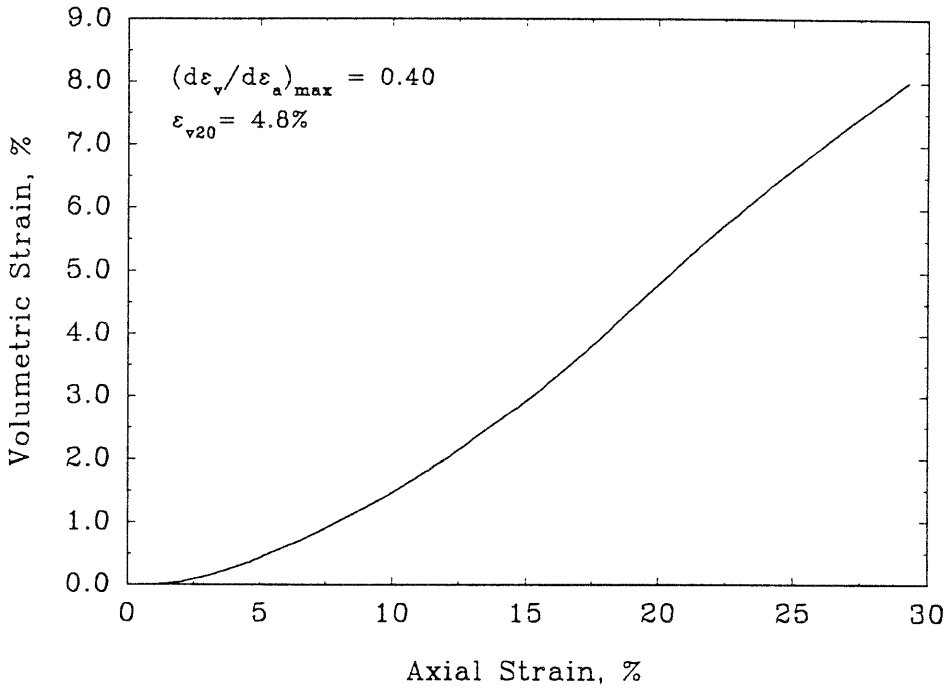

FRS146

Deviator Stress vs Axial Strain

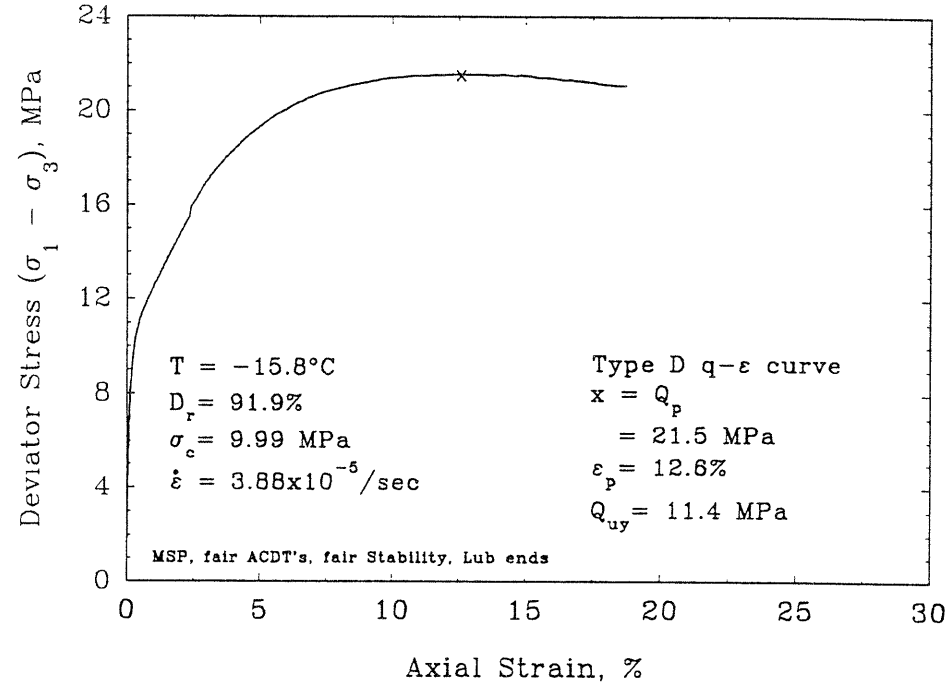

Volumetric vs Axial Strain

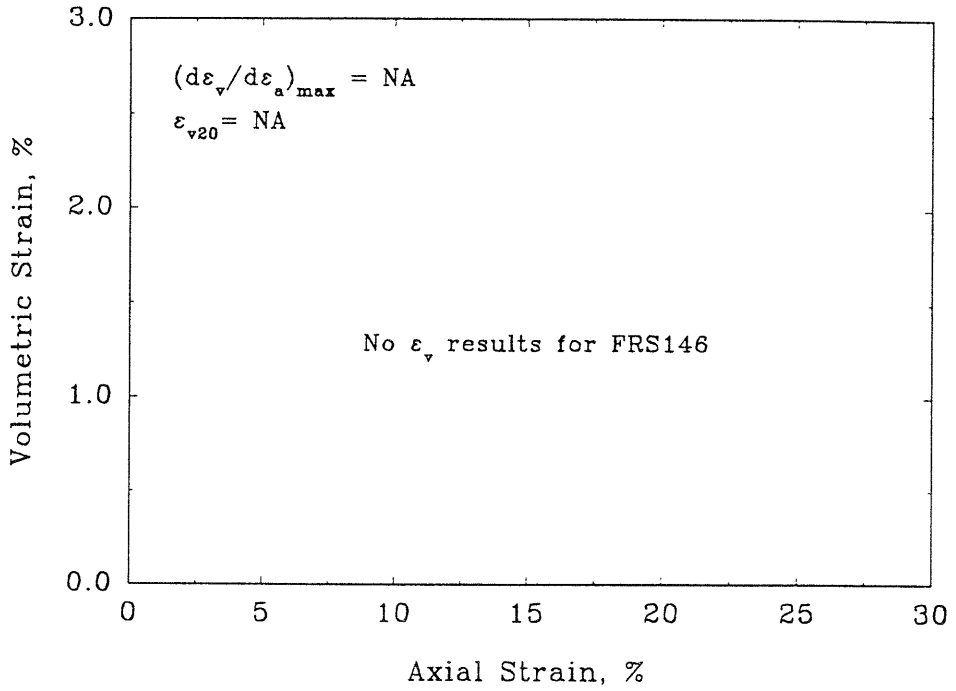

FRS148

Deviator Stress vs Axial Strain

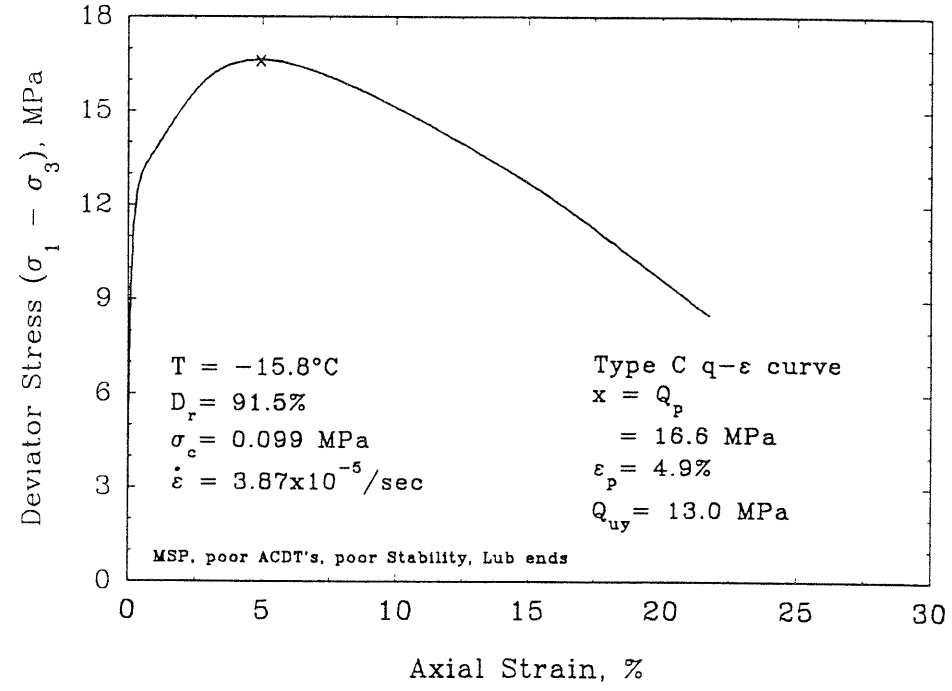

Volumetric vs Axial Strain

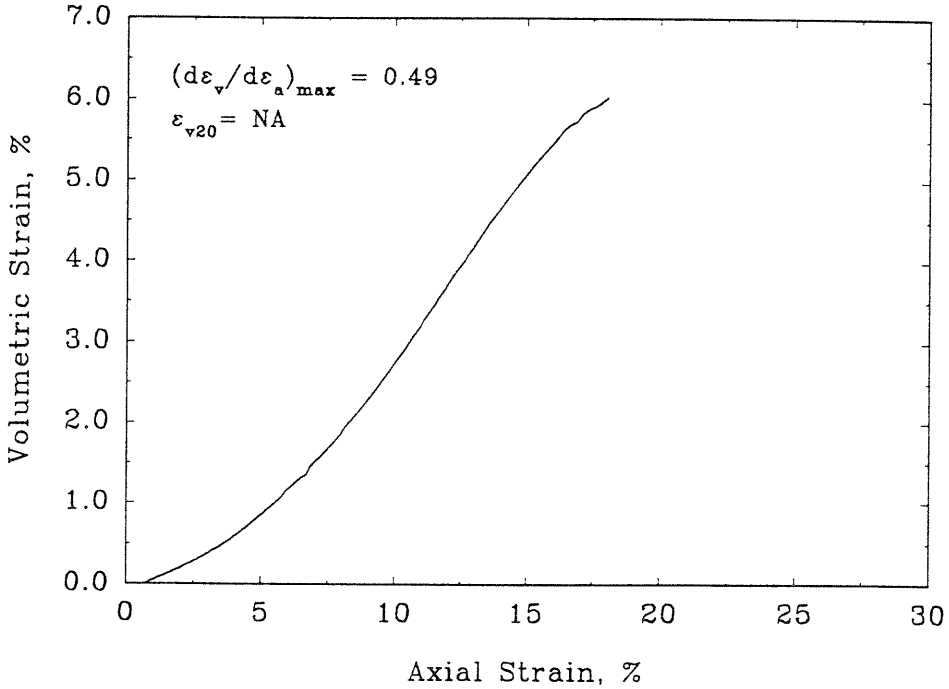

SECTION C.3

Tests at T = –20° C

FRS70

Deviator Stress vs Axial Strain

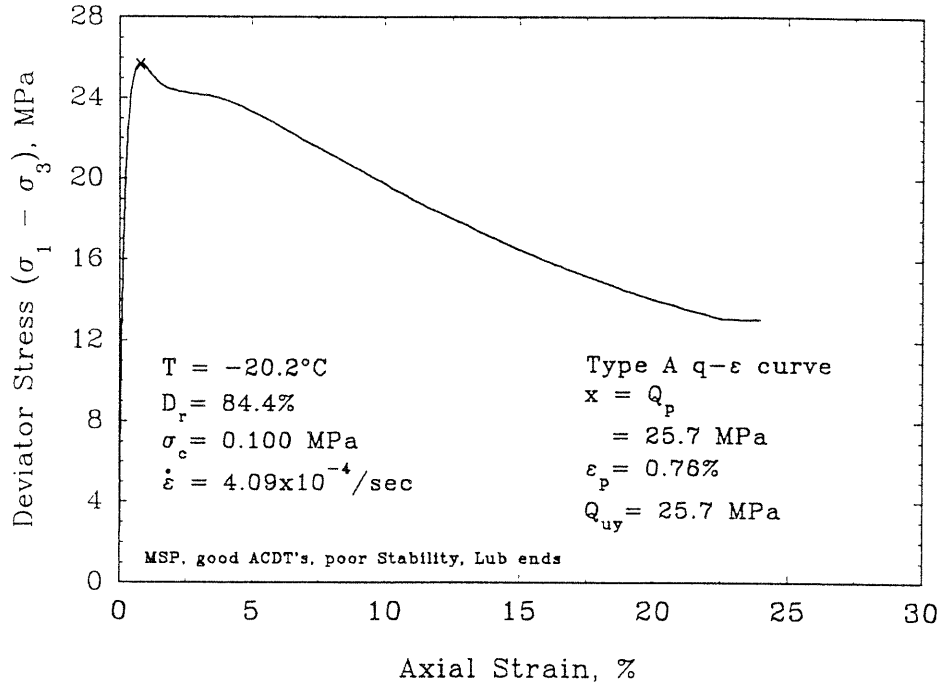

Volumetric vs Axial Strain

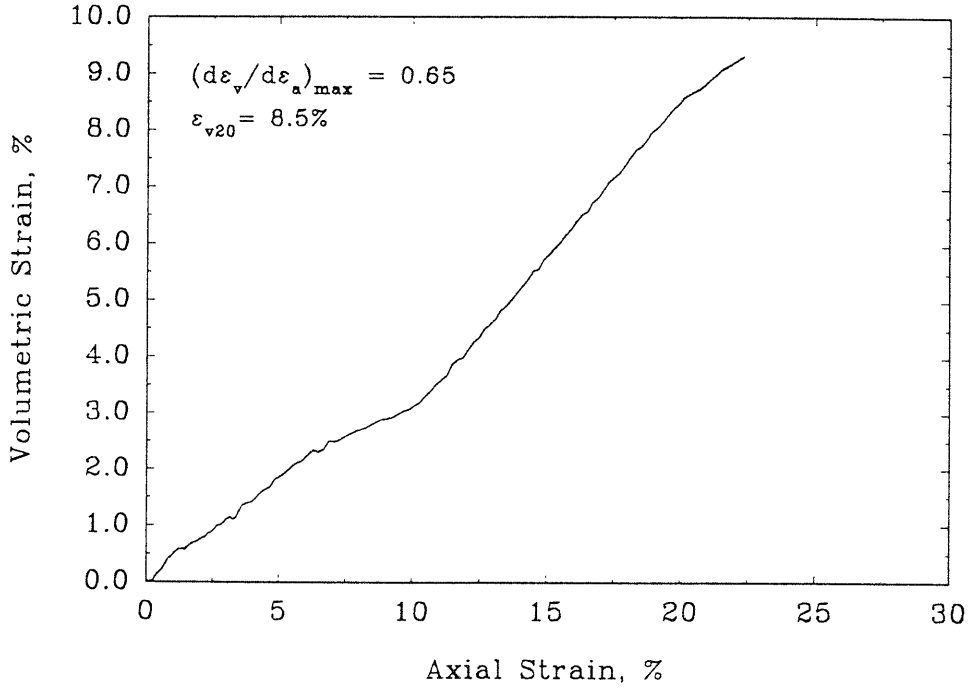

FRS71

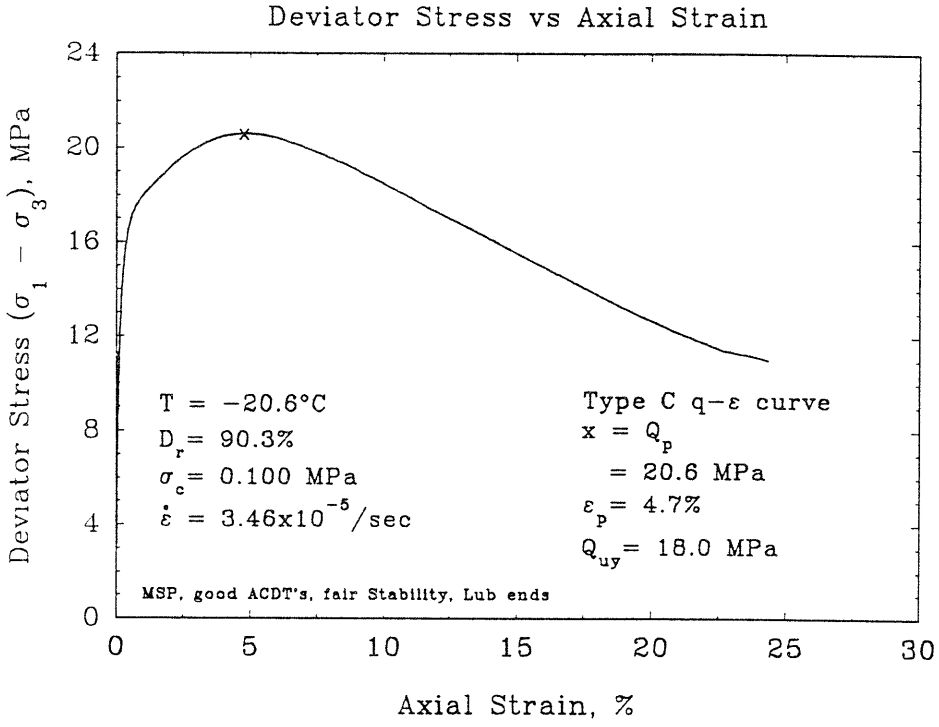
Deviator Stress vs Axial Strain
Deviator Stress ($\sigma_1 - \sigma_3$), MPa
Axial Strain, %
T = −20.6°C
D_r= 90.3%
σ_c= 0.100 MPa
$\dot{\varepsilon}$ = 3.46x10^{-5}/sec
Type C q−ε curve
x = Q_p
= 20.6 MPa
ε_p= 4.7%
Q_{uy}= 18.0 MPa
MSP, good ACDT's, fair Stability, Lub ends

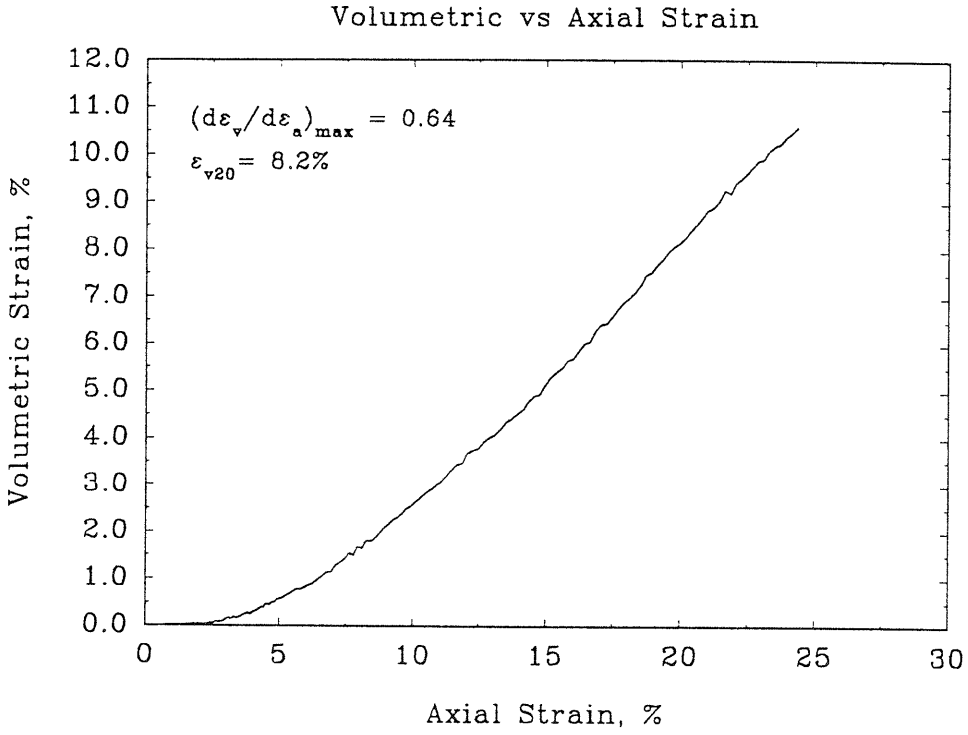
Volumetric vs Axial Strain
Volumetric Strain, %
Axial Strain, %
$(d\varepsilon_v/d\varepsilon_a)_{max}$ = 0.64
ε_{v20}= 8.2%

FRS72

Deviator Stress vs Axial Strain

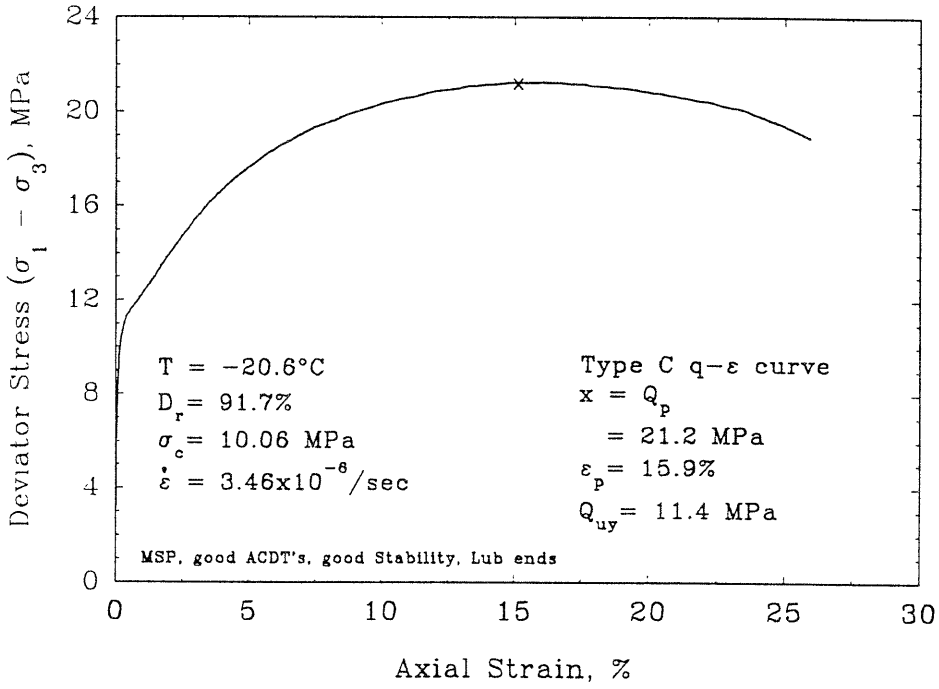

Volumetric vs Axial Strain

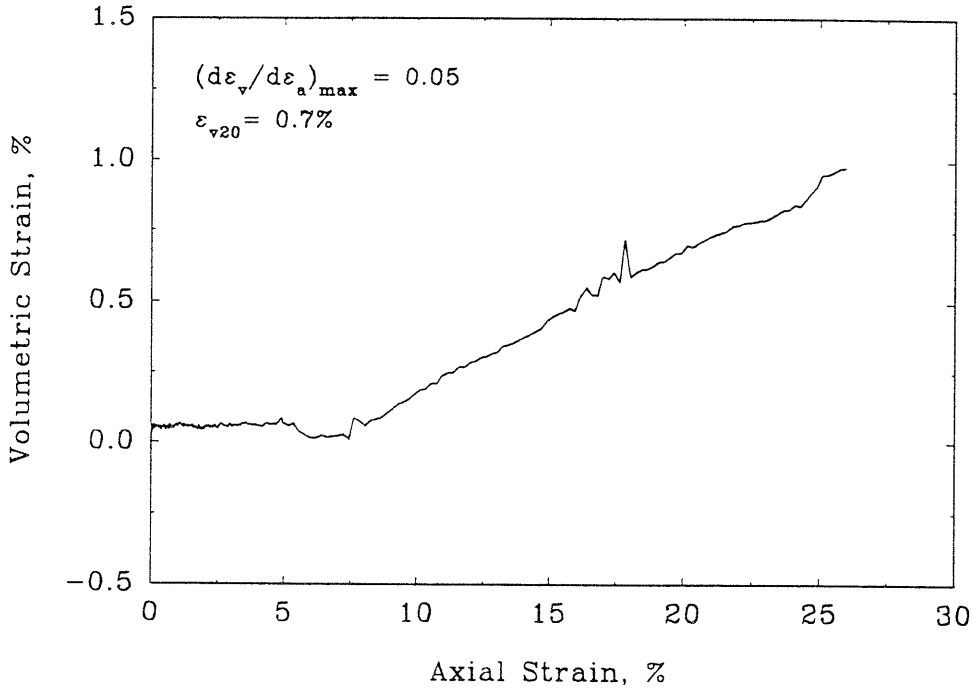

FRS74

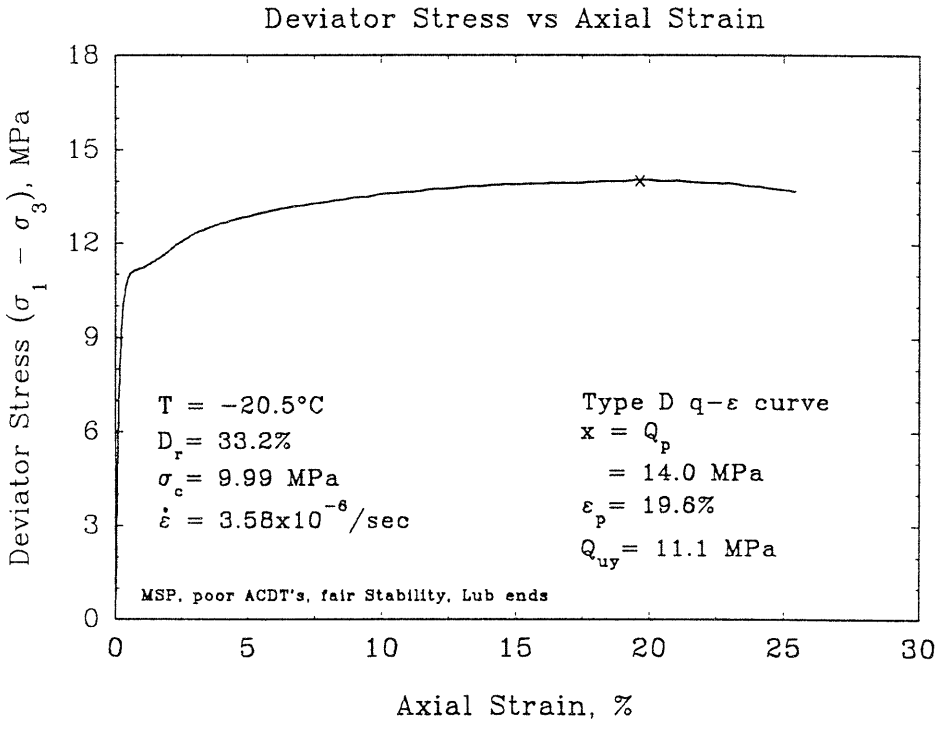
Deviator Stress vs Axial Strain
Deviator Stress ($\sigma_1 - \sigma_3$), MPa
Axial Strain, %
T = -20.5°C
D_r= 33.2%
σ_c= 9.99 MPa
$\dot{\varepsilon}$ = 3.58x10^{-6}/sec
Type D q-ε curve
x = Q_p
= 14.0 MPa
ε_p= 19.6%
Q_{uy}= 11.1 MPa
MSP, poor ACDT's, fair Stability, Lub ends

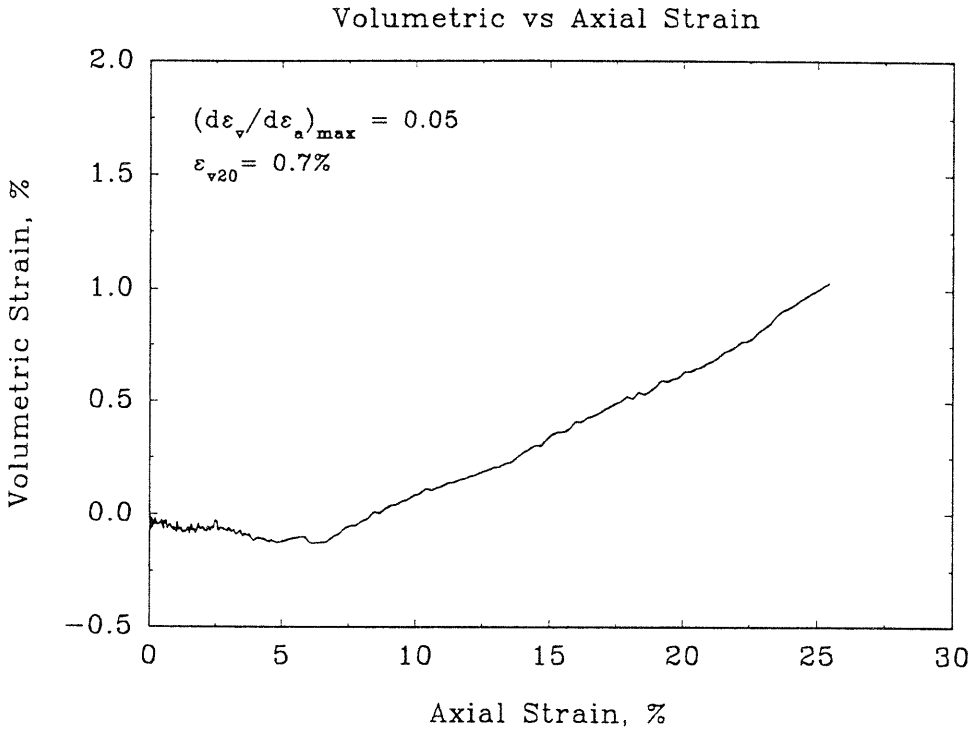
Volumetric vs Axial Strain
Volumetric Strain, %
Axial Strain, %
$(d\varepsilon_v/d\varepsilon_a)_{max}$ = 0.05
ε_{v20}= 0.7%

FRS75

Deviator Stress vs Axial Strain

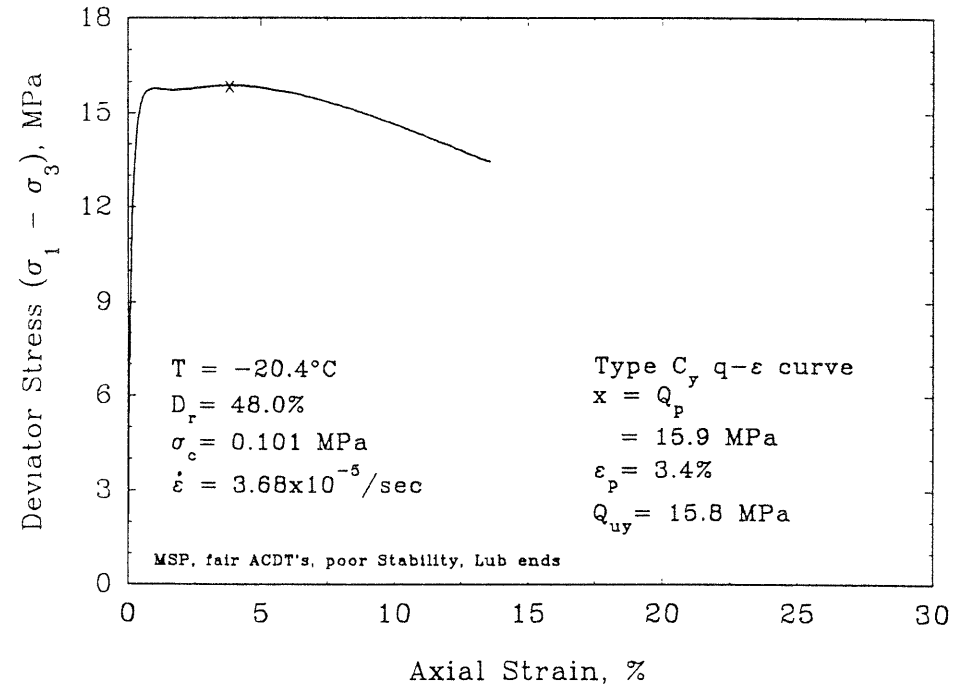

Volumetric vs Axial Strain

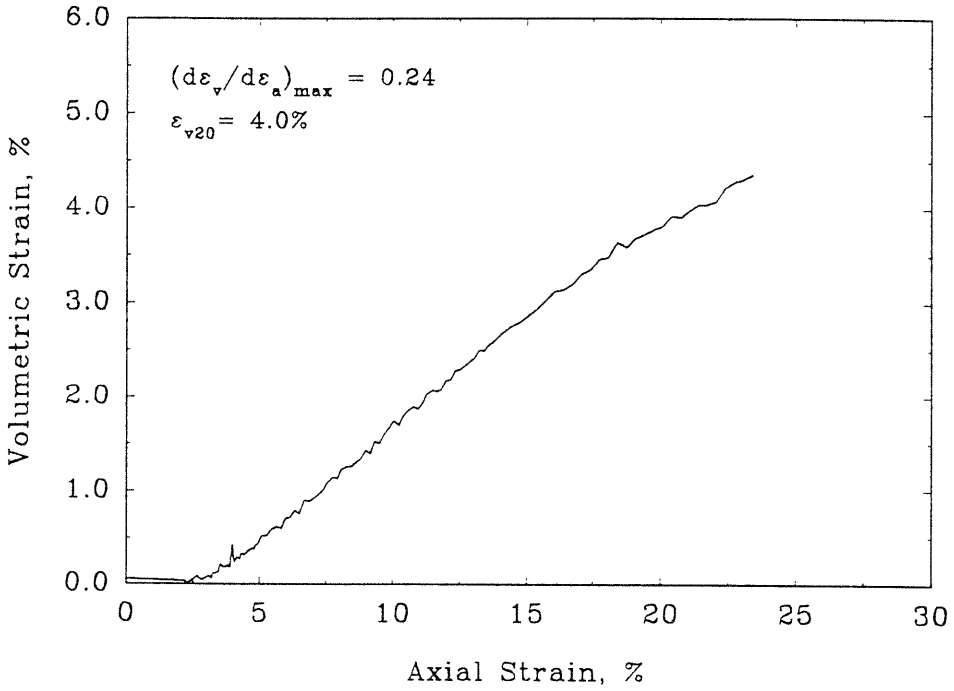

FRS76

Deviator Stress vs Axial Strain

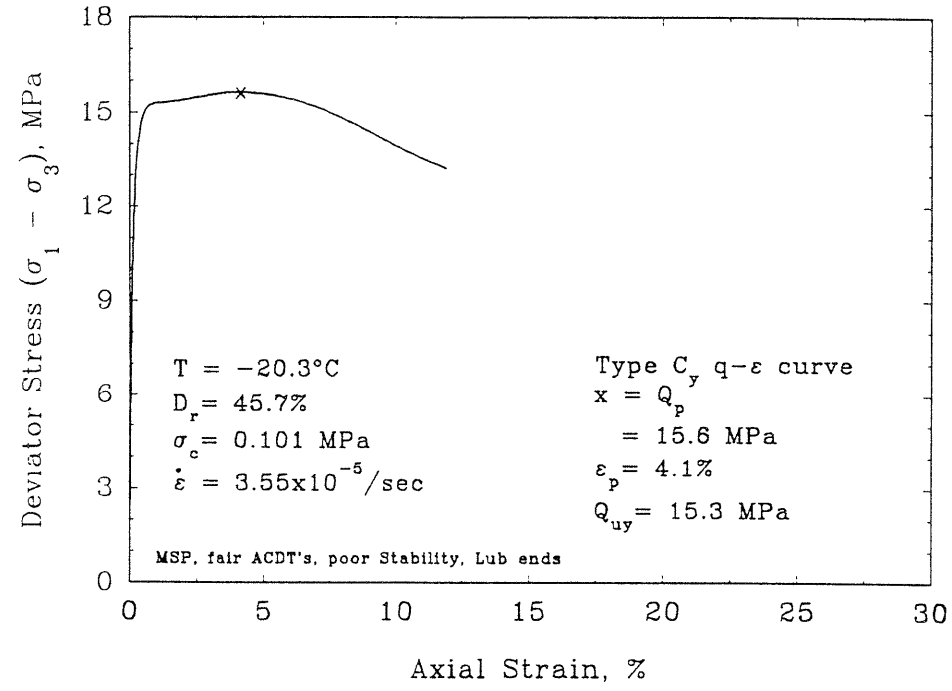

Volumetric vs Axial Strain

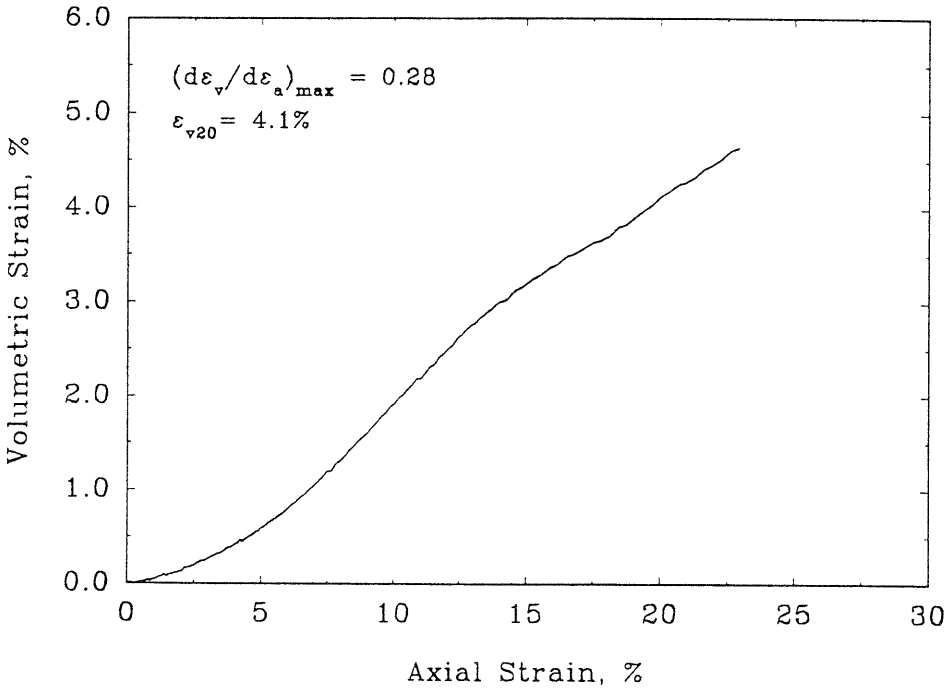

FRS85

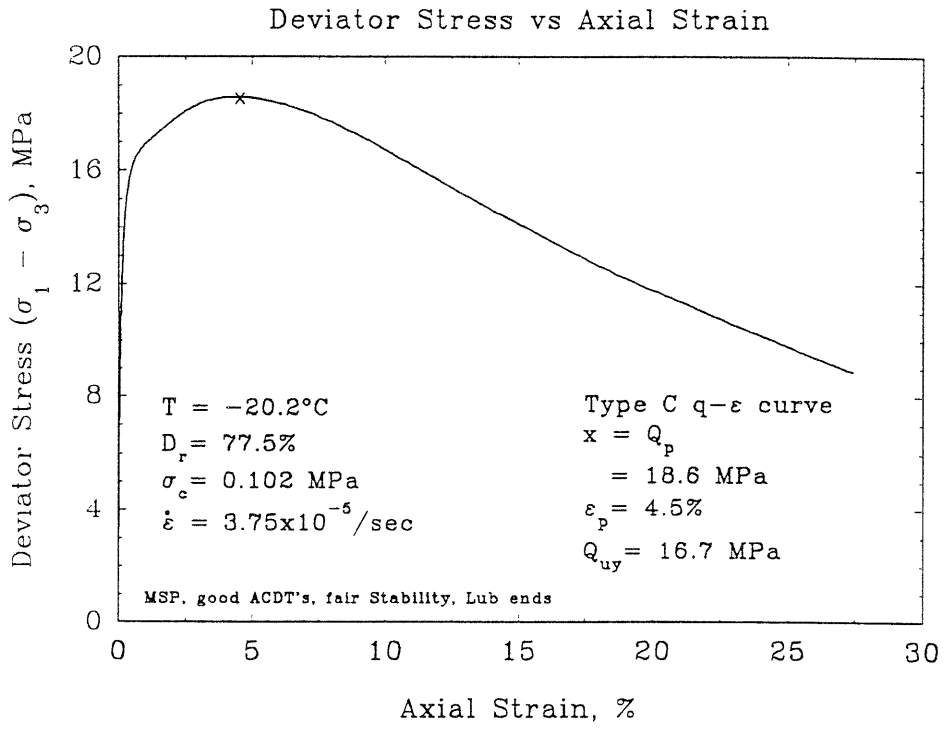
Deviator Stress vs Axial Strain
Deviator Stress ($\sigma_1 - \sigma_3$), MPa
Axial Strain, %
T = −20.2°C
D_r = 77.5%
σ_c = 0.102 MPa
$\dot{\varepsilon}$ = 3.75x10^{-5}/sec
Type C q−ε curve
x = Q_p
= 18.6 MPa
ε_p = 4.5%
Q_{uy} = 16.7 MPa
MSP, good ACDT's, fair Stability, Lub ends

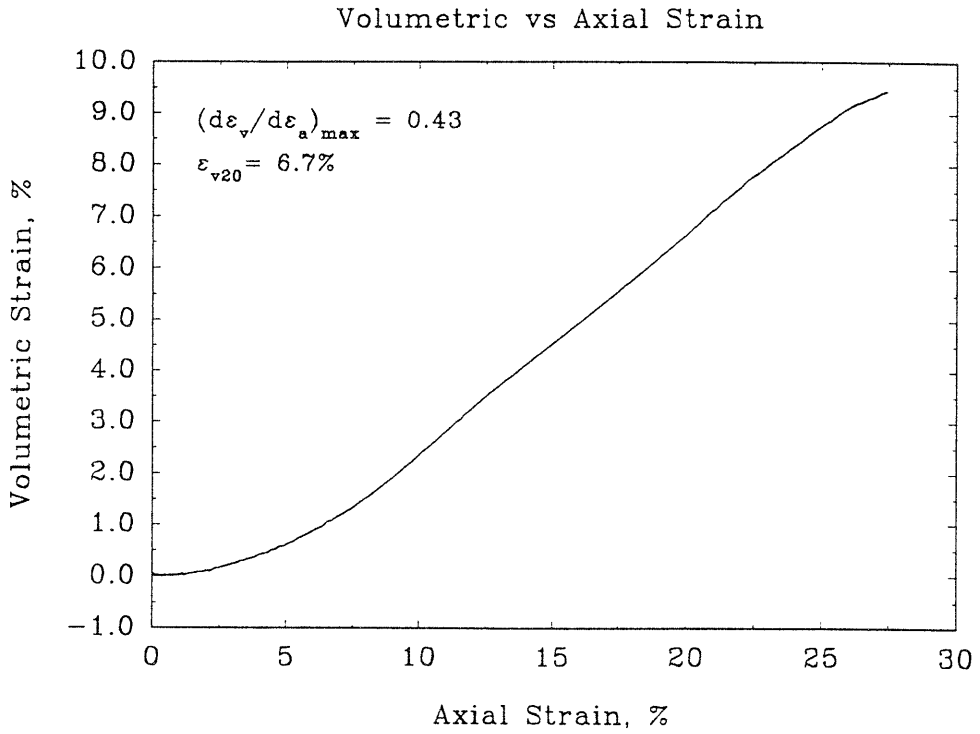
Volumetric vs Axial Strain
Volumetric Strain, %
Axial Strain, %
$(d\varepsilon_v/d\varepsilon_a)_{max}$ = 0.43
ε_{v20} = 6.7%

FRS86

Deviator Stress vs Axial Strain

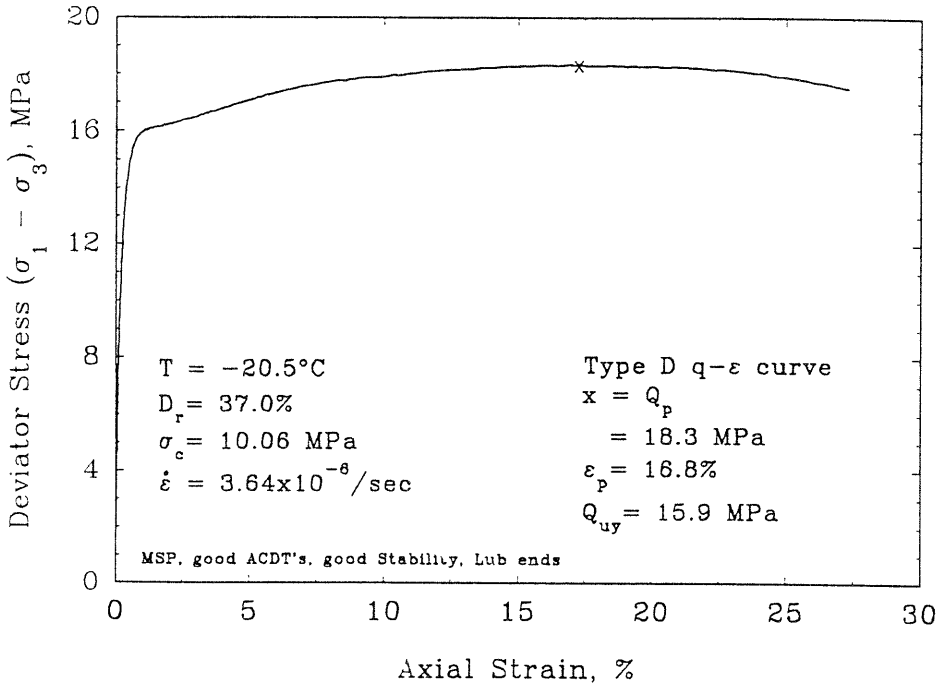

Volumetric vs Axial Strain

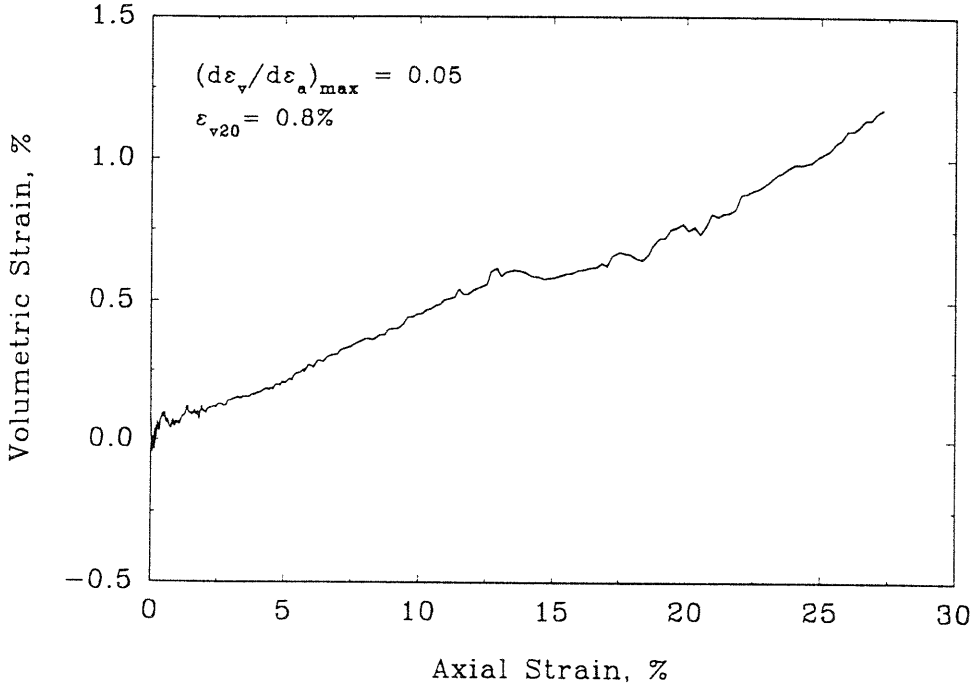

FRS87

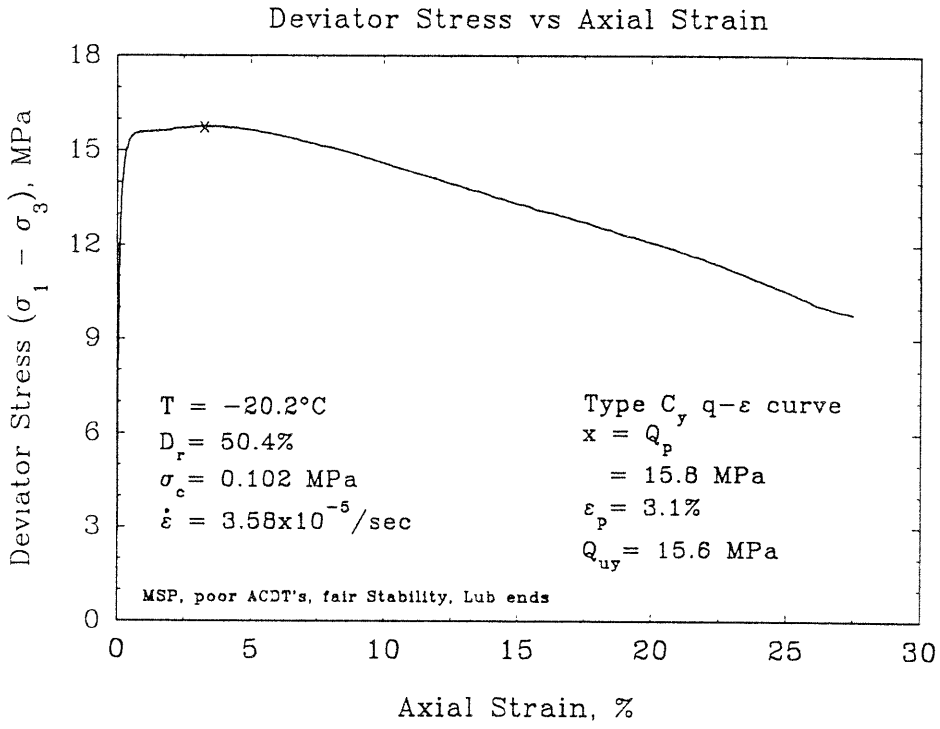
Deviator Stress vs Axial Strain
Deviator Stress ($\sigma_1 - \sigma_3$), MPa
Axial Strain, %
T = −20.2°C
D_r = 50.4%
σ_c = 0.102 MPa
$\dot{\varepsilon}$ = 3.58x10^{-5}/sec
Type C_y q−ε curve
x = Q_p
= 15.8 MPa
ε_p = 3.1%
Q_{uy} = 15.6 MPa
MSP, poor ACDT's, fair Stability, Lub ends

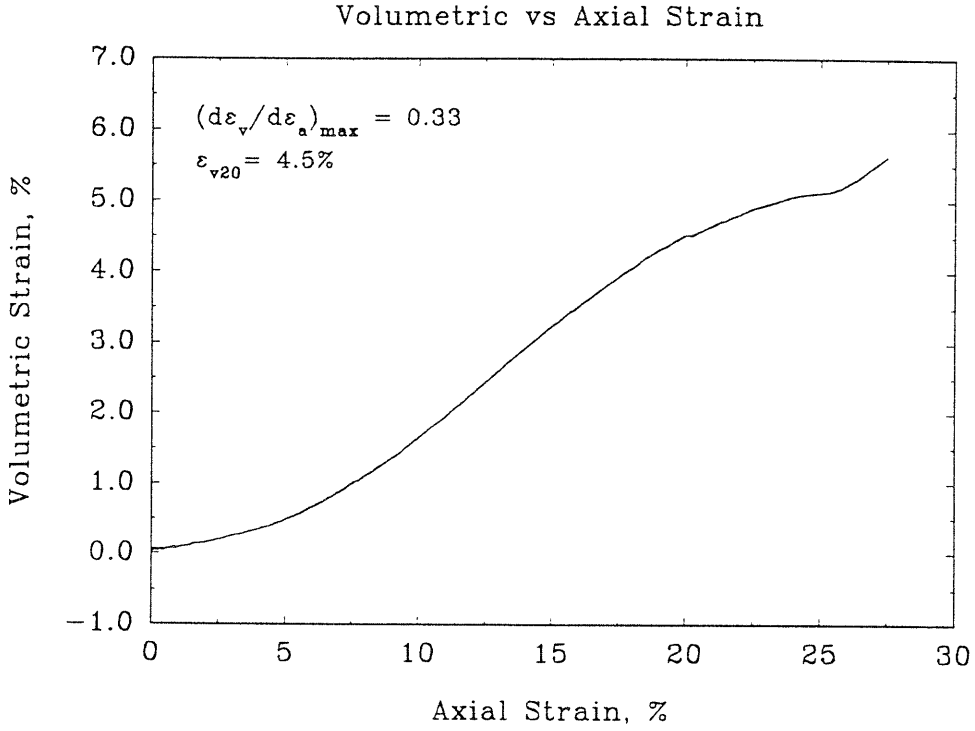
Volumetric vs Axial Strain
Volumetric Strain, %
Axial Strain, %
$(d\varepsilon_v/d\varepsilon_a)_{max}$ = 0.33
ε_{v20} = 4.5%

FRS88

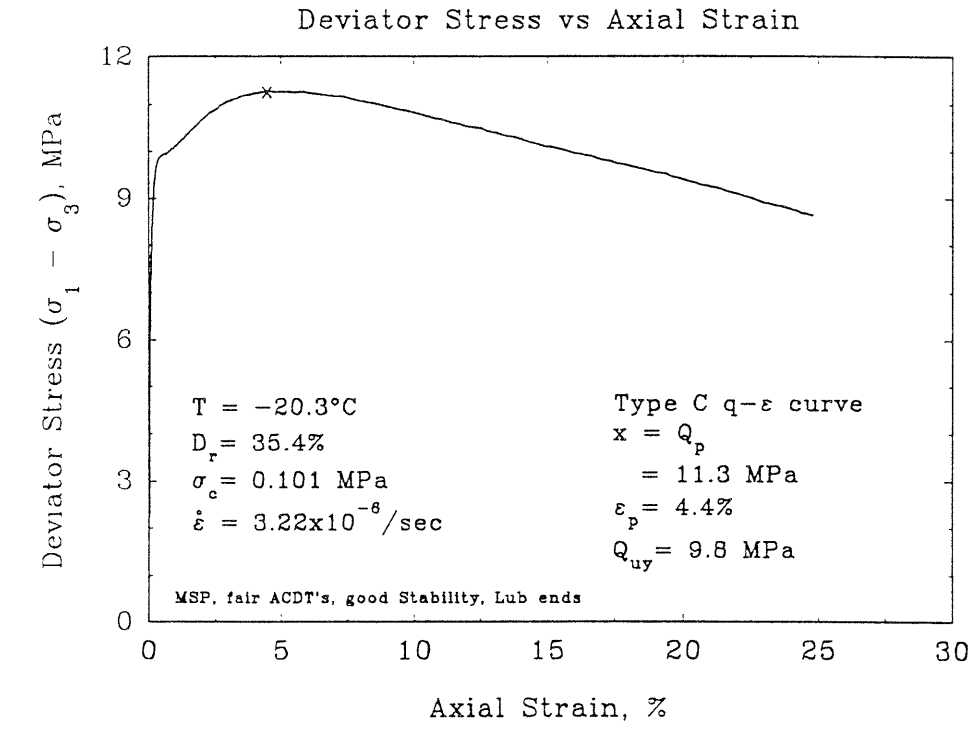
Deviator Stress vs Axial Strain
Deviator Stress ($\sigma_1 - \sigma_3$), MPa
12
9
6
3
0
0
5
10
15
20
25
30
Axial Strain, %
T = −20.3°C
D_r= 35.4%
σ_c= 0.101 MPa
$\dot{\varepsilon}$ = 3.22x10^{-6}/sec
Type C q−ε curve
x = Q_p
= 11.3 MPa
ε_p= 4.4%
Q_{uy}= 9.8 MPa
MSP, fair ACDT's, good Stability, Lub ends

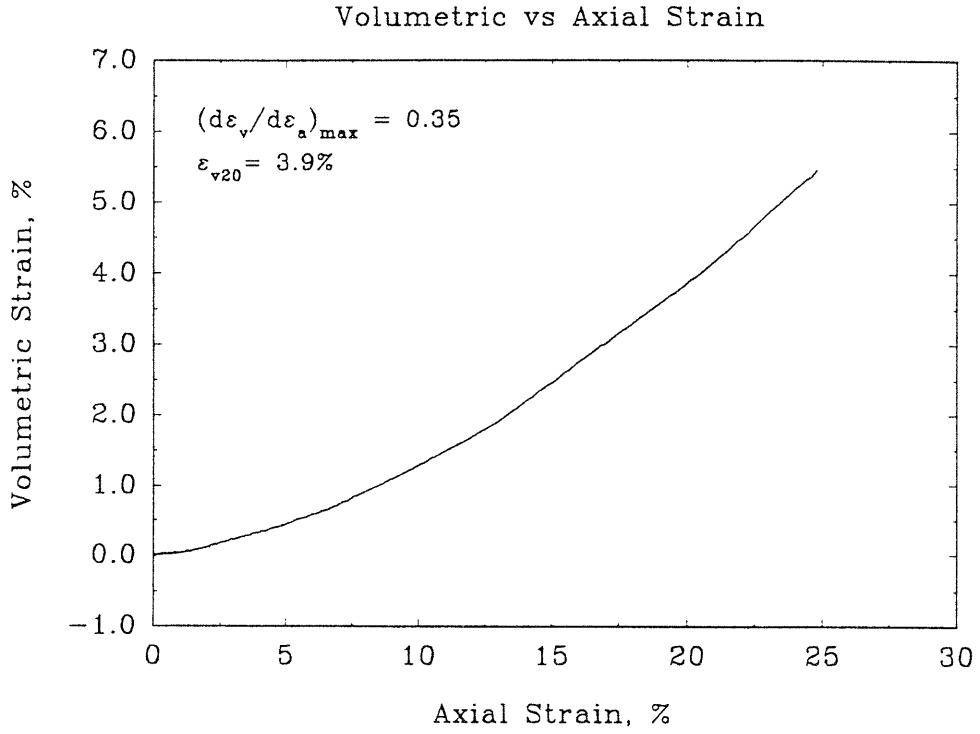
Volumetric vs Axial Strain
Volumetric Strain, %
7.0
6.0
5.0
4.0
3.0
2.0
1.0
0.0
−1.0
0
5
10
15
20
25
30
Axial Strain, %
$(d\varepsilon_v/d\varepsilon_a)_{max}$ = 0.35
ε_{v20}= 3.9%

FRS89

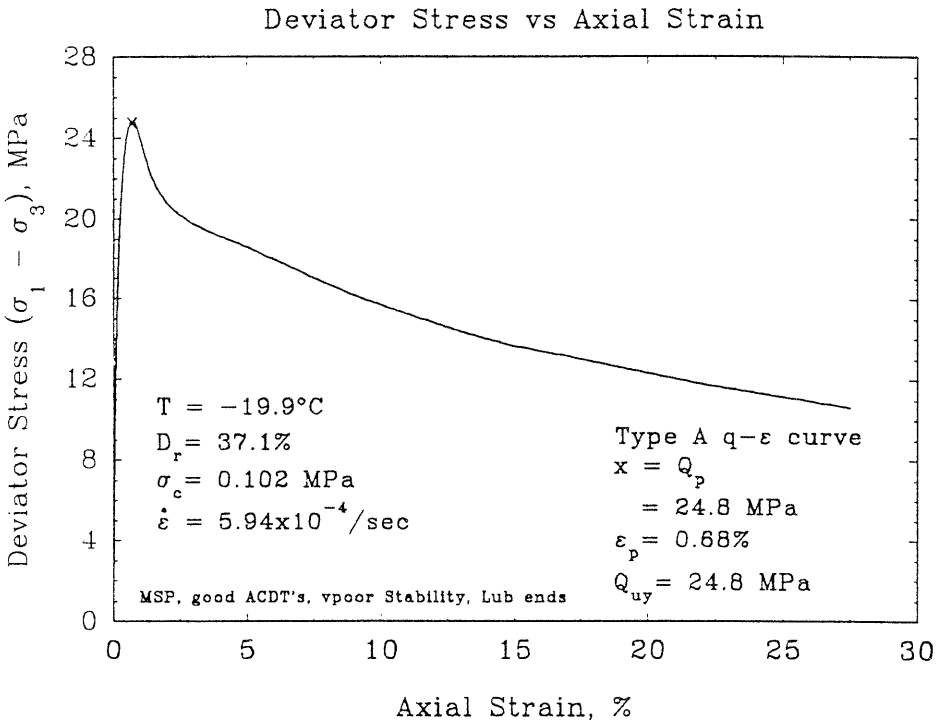
Deviator Stress vs Axial Strain
Deviator Stress ($\sigma_1 - \sigma_3$), MPa
Axial Strain, %
T = −19.9°C
D_r = 37.1%
σ_c = 0.102 MPa
$\dot{\varepsilon}$ = 5.94x10^{-4}/sec
MSP, good ACDT's, vpoor Stability, Lub ends
Type A q−ε curve
x = Q_p
= 24.8 MPa
ε_p = 0.68%
Q_{uy} = 24.8 MPa

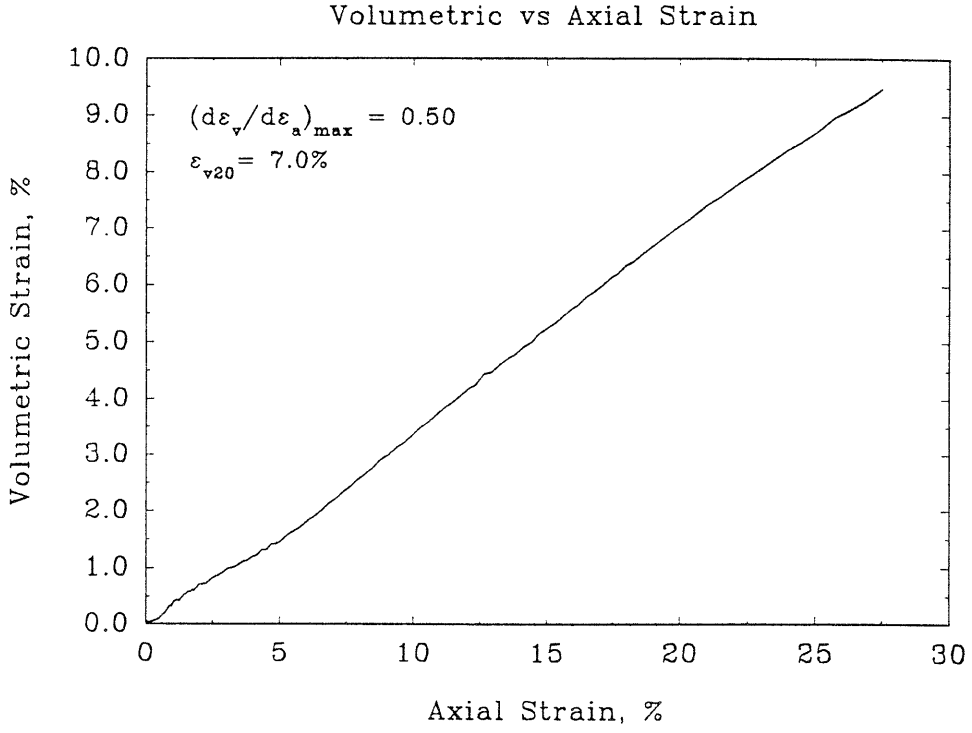
Volumetric vs Axial Strain
Volumetric Strain, %
Axial Strain, %
$(d\varepsilon_v/d\varepsilon_a)_{max}$ = 0.50
ε_{v20} = 7.0%

FRS92

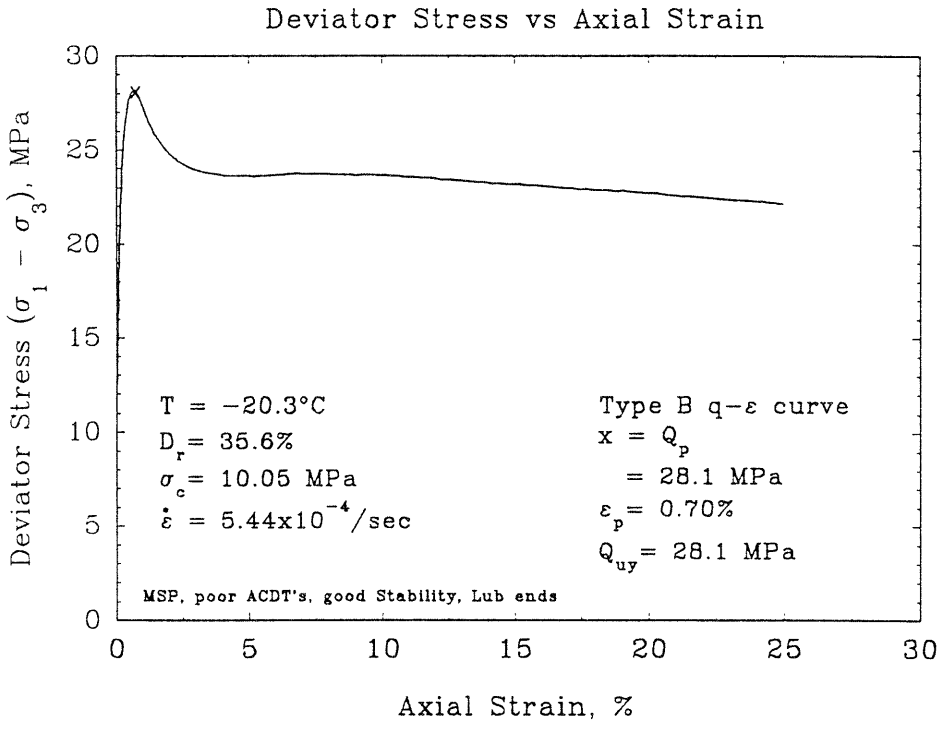
Deviator Stress vs Axial Strain
Deviator Stress ($\sigma_1 - \sigma_3$), MPa
Axial Strain, %
T = −20.3°C
D_r= 35.6%
σ_c= 10.05 MPa
$\dot{\varepsilon}$ = 5.44x10^{-4}/sec
Type B q−ε curve
x = Q_p
= 28.1 MPa
ε_p= 0.70%
Q_{uy}= 28.1 MPa
MSP, poor ACDT's, good Stability, Lub ends

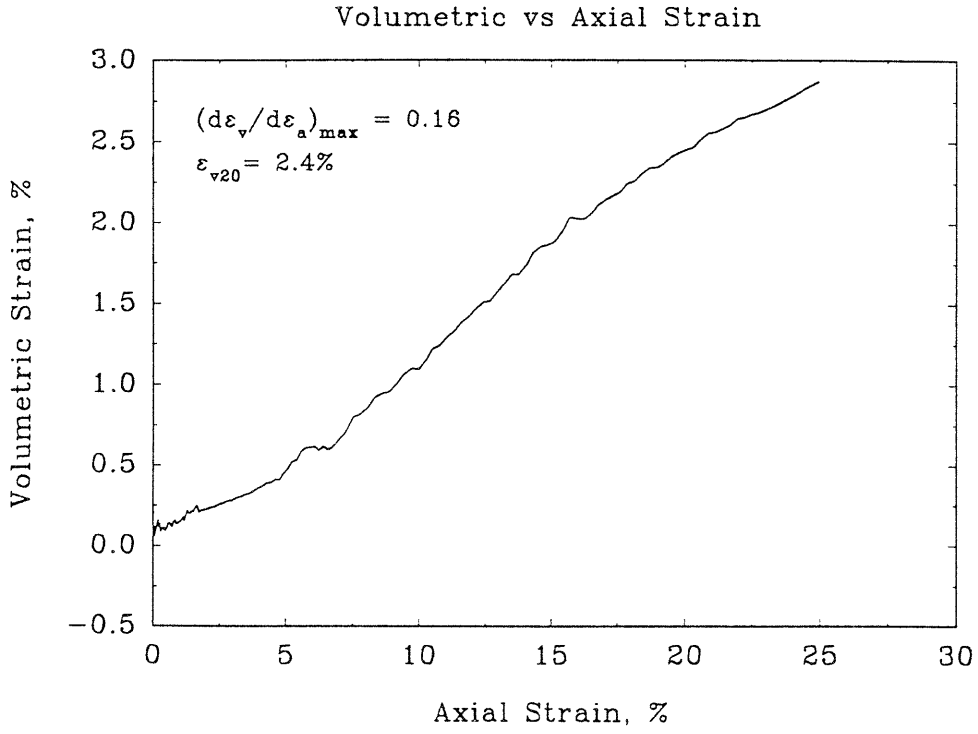
Volumetric vs Axial Strain
Volumetric Strain, %
Axial Strain, %
$(d\varepsilon_v/d\varepsilon_a)_{max}$ = 0.16
ε_{v20}= 2.4%

FRS93

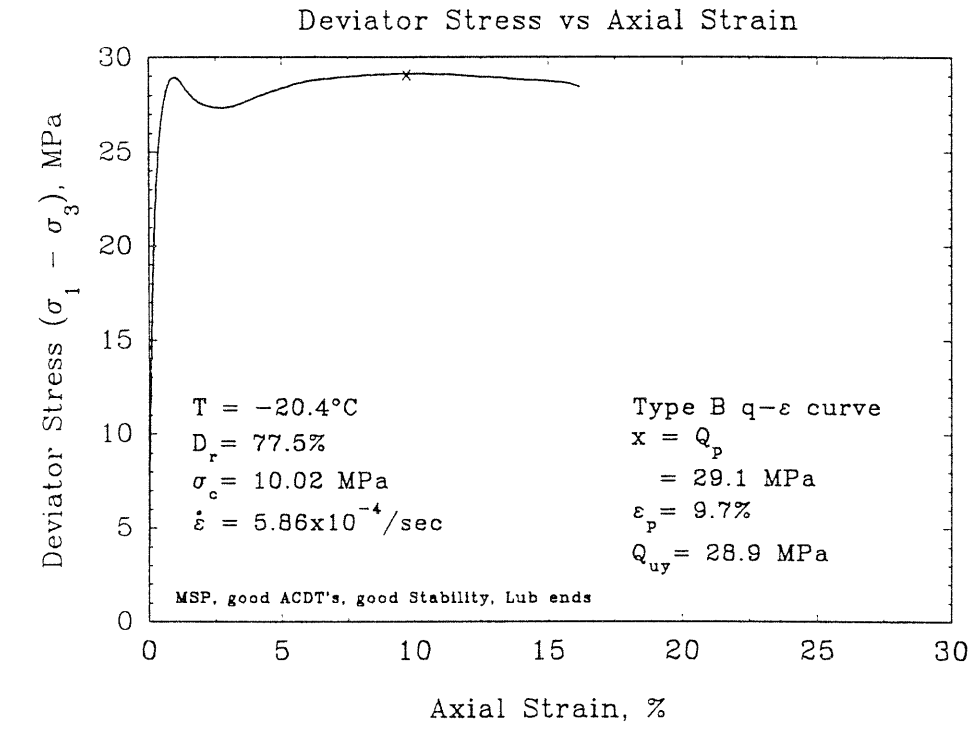
Deviator Stress vs Axial Strain
Deviator Stress ($\sigma_1 - \sigma_3$), MPa
Axial Strain, %
T = −20.4°C
D_r = 77.5%
σ_c = 10.02 MPa
$\dot{\varepsilon}$ = 5.86x10^{-4}/sec
Type B q−ε curve
x = Q_p
= 29.1 MPa
ε_p = 9.7%
Q_{uy} = 28.9 MPa
MSP, good ACDT's, good Stability, Lub ends

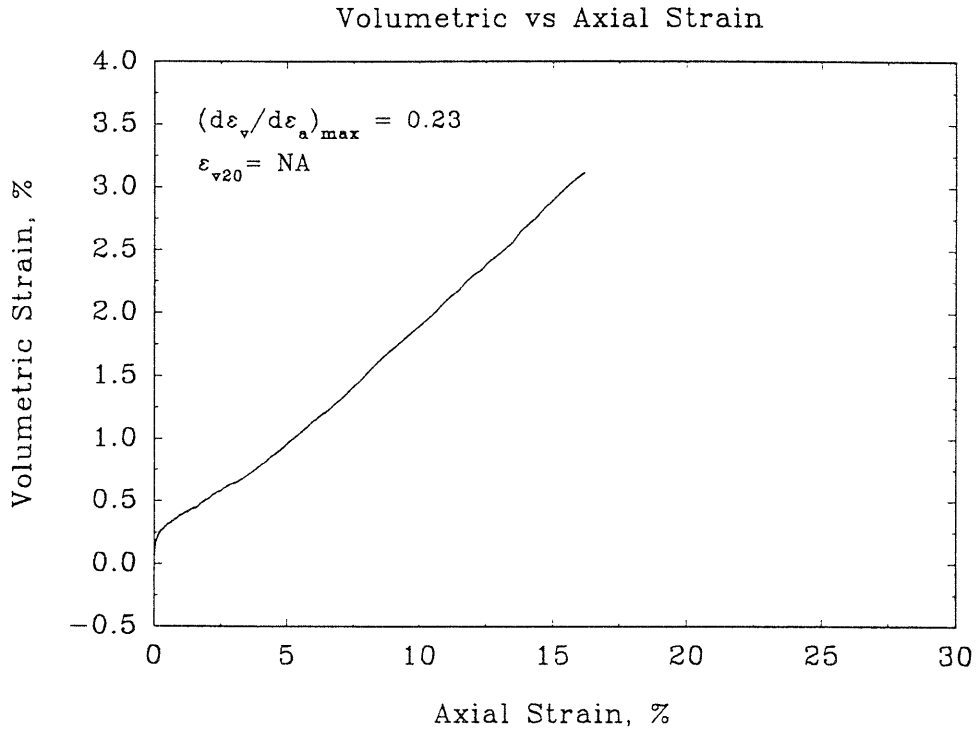
Volumetric vs Axial Strain
Volumetric Strain, %
Axial Strain, %
$(d\varepsilon_v/d\varepsilon_a)_{max}$ = 0.23
ε_{v20} = NA

FRS94

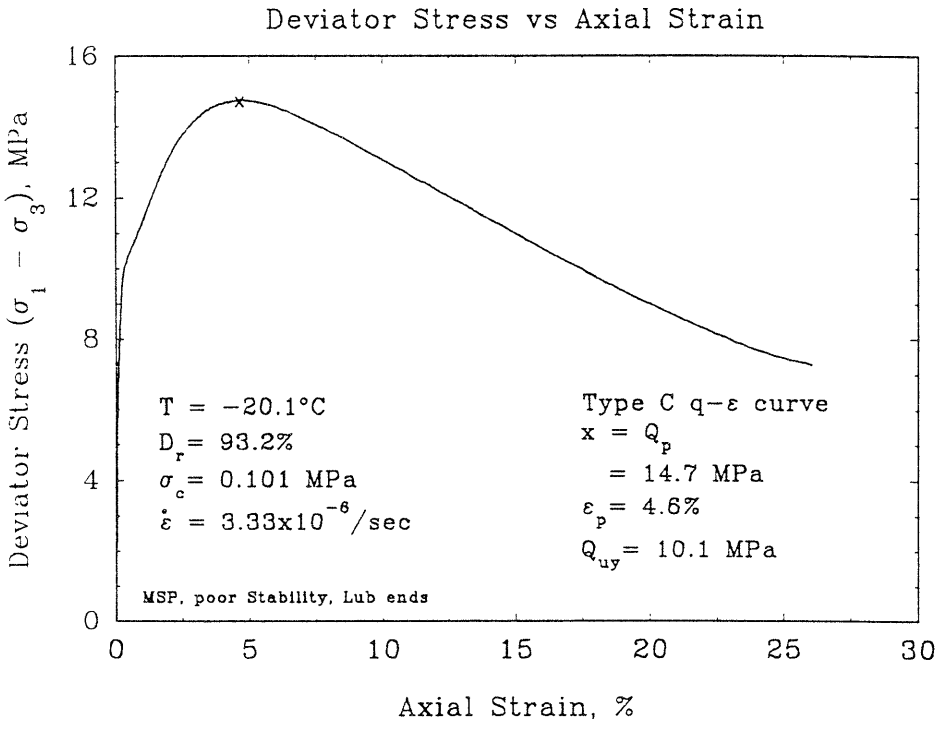
Deviator Stress vs Axial Strain
Deviator Stress ($\sigma_1 - \sigma_3$), MPa
16
12
8
4
0
0
5
10
15
20
25
30
Axial Strain, %
T = −20.1°C
D_r= 93.2%
σ_c= 0.101 MPa
$\dot{\varepsilon}$ = 3.33x10^{-6}/sec
MSP, poor Stability, Lub ends
Type C q−ε curve
x = Q_p
= 14.7 MPa
ε_p= 4.6%
Q_{uy}= 10.1 MPa

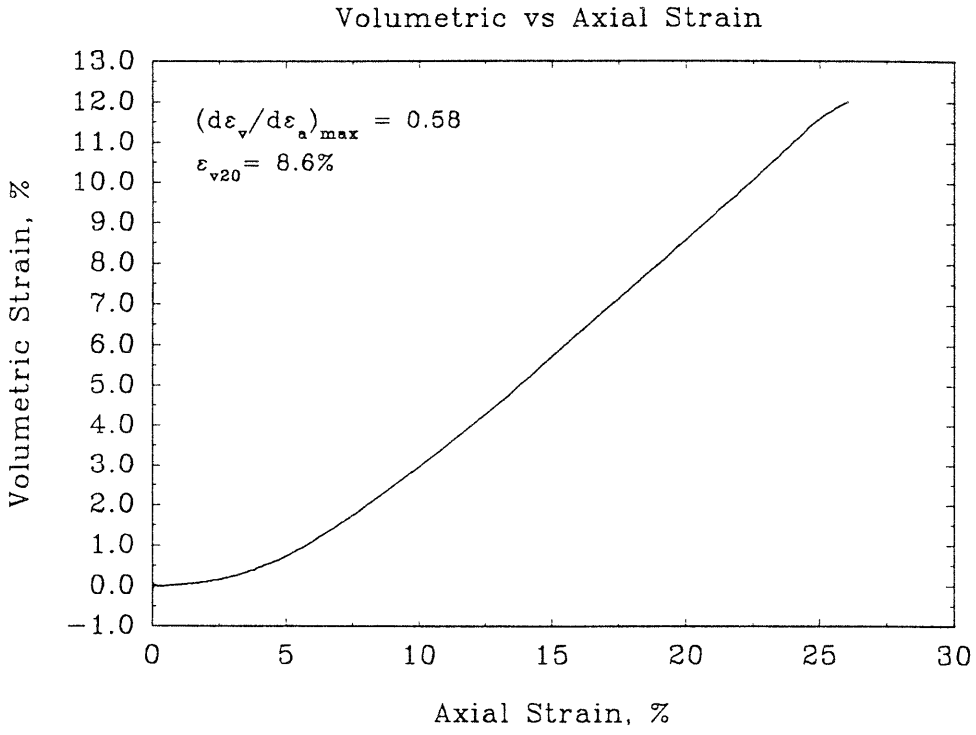
Volumetric vs Axial Strain
Volumetric Strain, %
13.0
12.0
11.0
10.0
9.0
8.0
7.0
6.0
5.0
4.0
3.0
2.0
1.0
0.0
−1.0
0
5
10
15
20
25
30
Axial Strain, %
$(d\varepsilon_v/d\varepsilon_a)_{max}$ = 0.58
ε_{v20}= 8.6%

FRS95

Deviator Stress vs Axial Strain

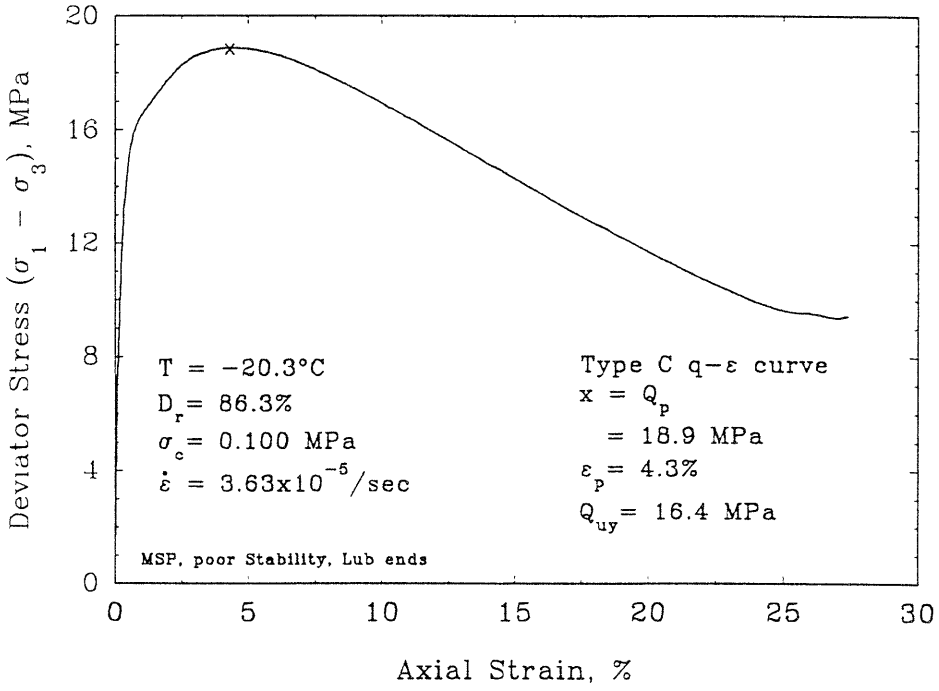

Volumetric vs Axial Strain

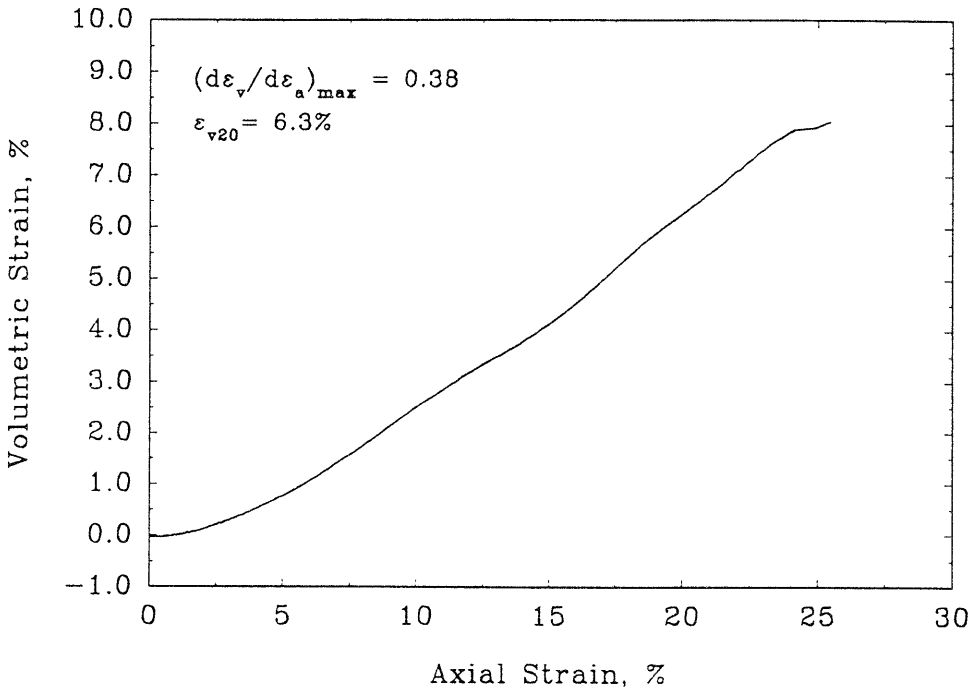

FRS97

Deviator Stress vs Axial Strain

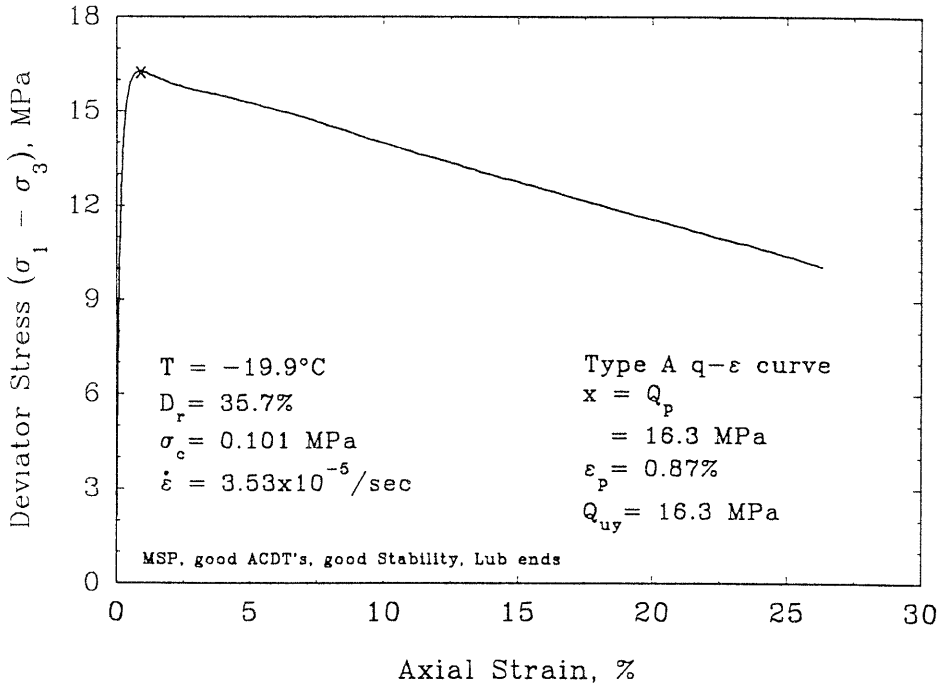

Volumetric vs Axial Strain

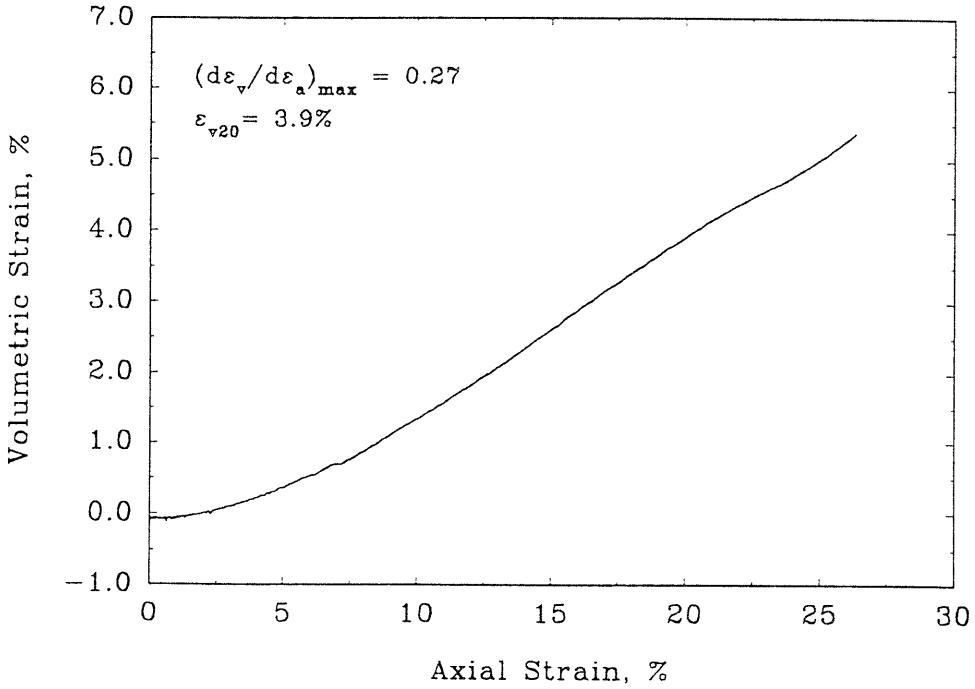

FRS98

Deviator Stress vs Axial Strain

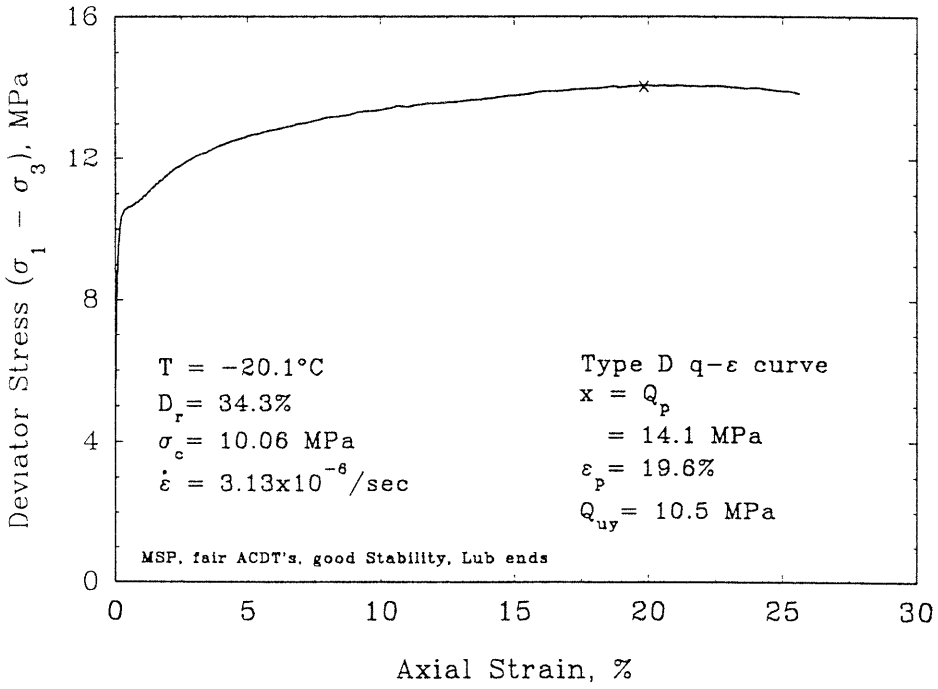

Volumetric vs Axial Strain

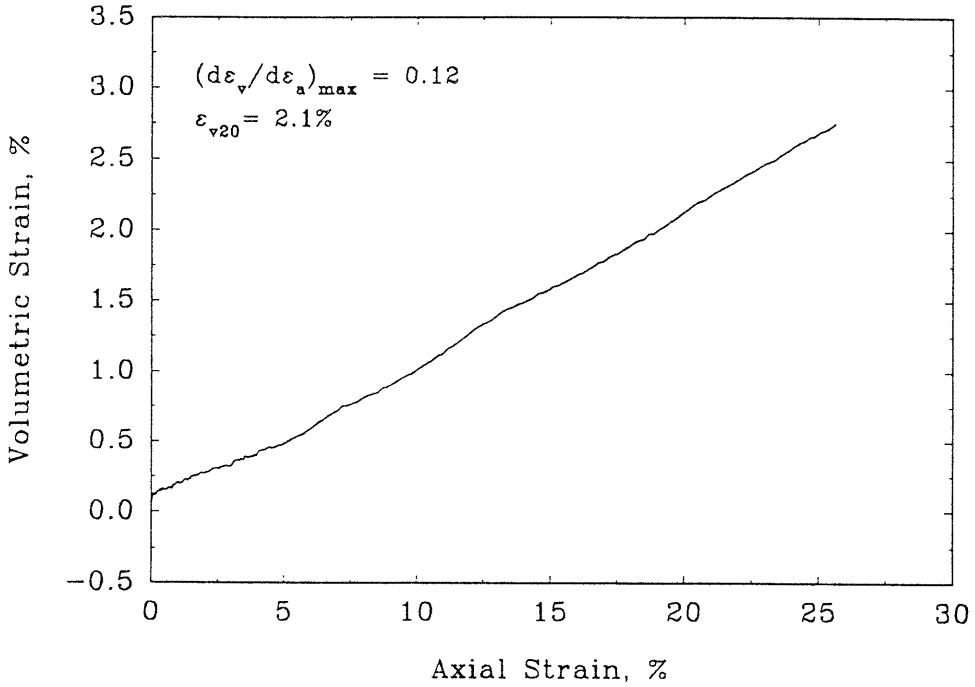

FRS99

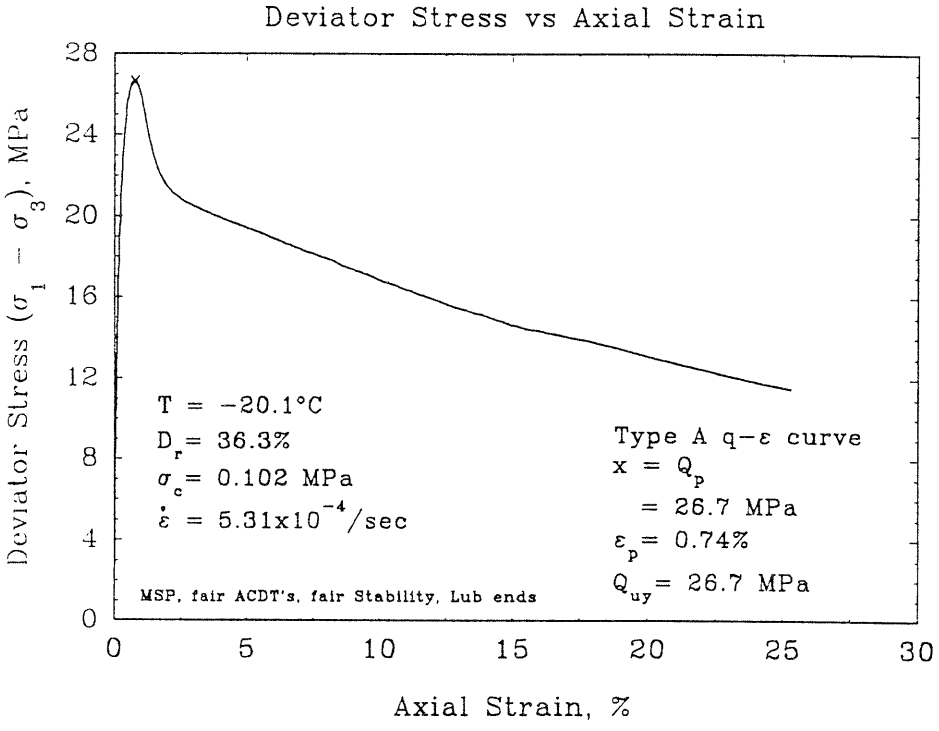
Deviator Stress vs Axial Strain
Deviator Stress ($\sigma_1 - \sigma_3$), MPa
Axial Strain, %
T = -20.1°C
D_r= 36.3%
σ_c= 0.102 MPa
$\dot{\varepsilon}$ = 5.31x10^{-4}/sec
MSP, fair ACDT's, fair Stability, Lub ends
Type A q-ε curve
x = Q_p
= 26.7 MPa
ε_p= 0.74%
Q_{uy}= 26.7 MPa

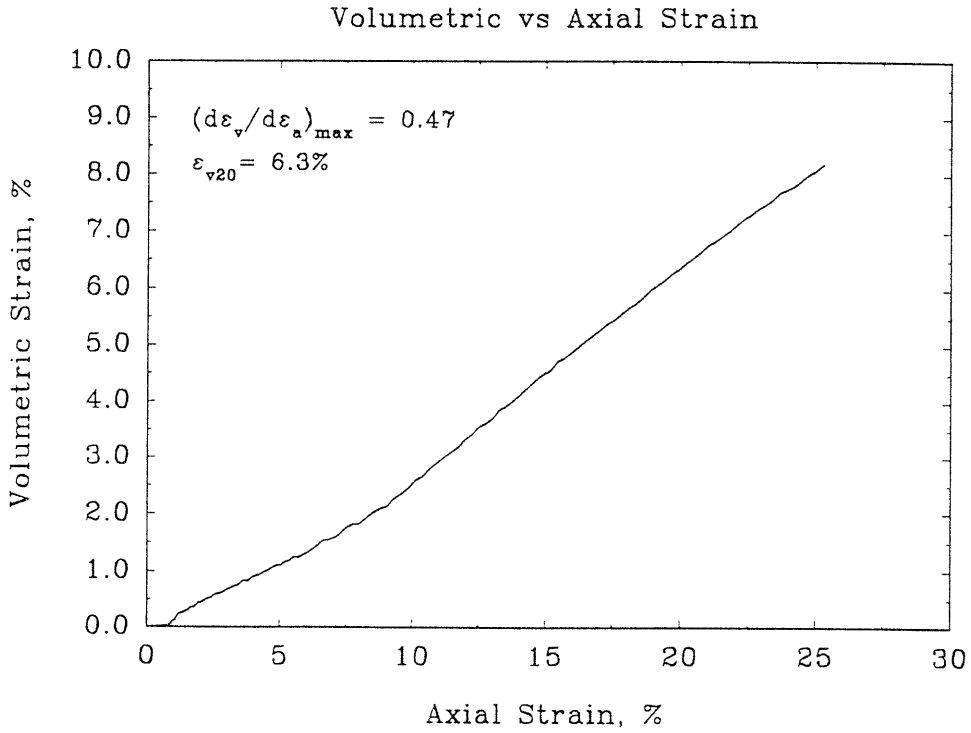
Volumetric vs Axial Strain
Volumetric Strain, %
Axial Strain, %
$(d\varepsilon_v/d\varepsilon_a)_{max}$ = 0.47
ε_{v20}= 6.3%

FRS100

Deviator Stress vs Axial Strain

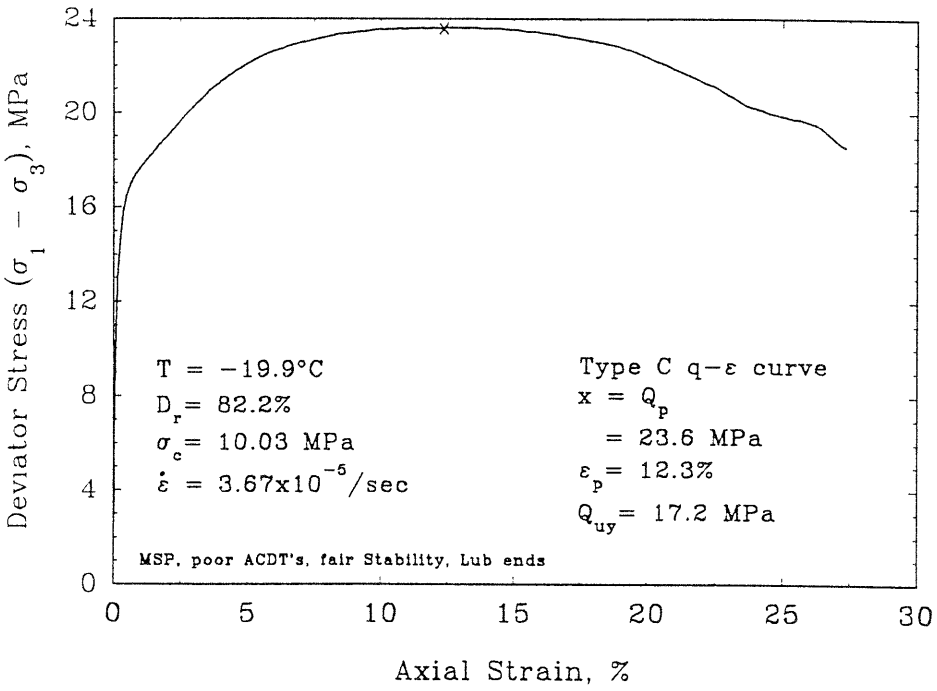

Volumetric vs Axial Strain

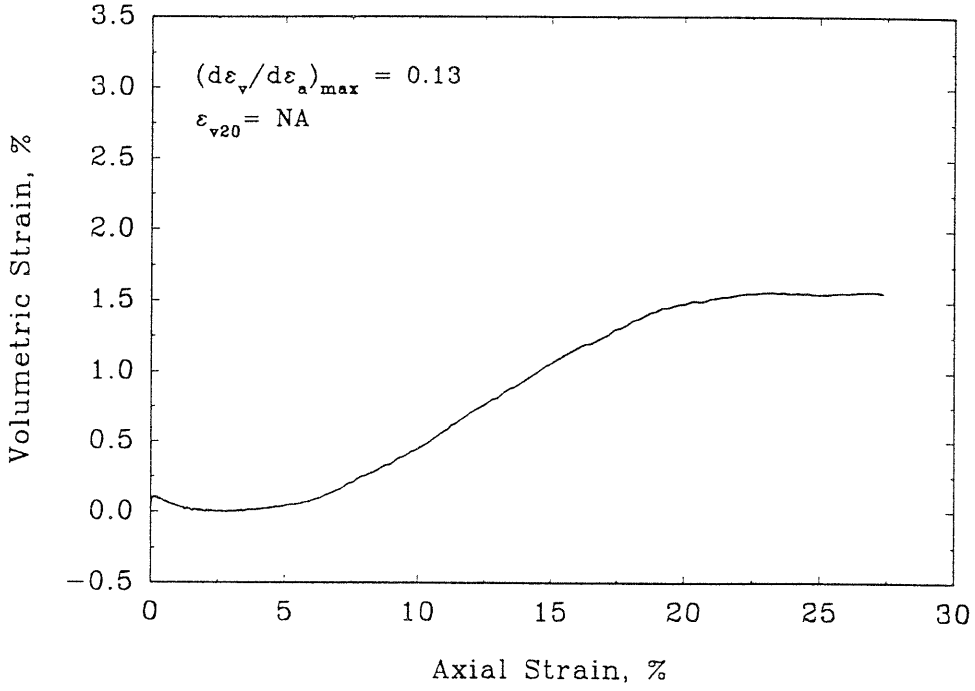

SECTION C.4

Tests at T = –25° C

FRS103

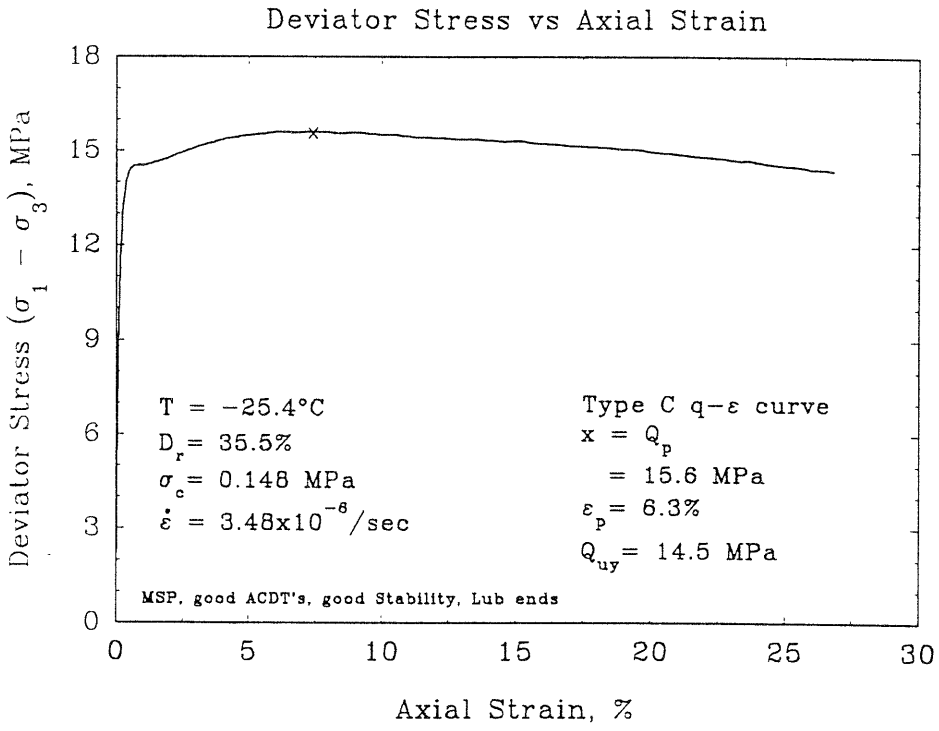
Deviator Stress vs Axial Strain
Deviator Stress ($\sigma_1 - \sigma_3$), MPa
Axial Strain, %
T = −25.4°C
D_r = 35.5%
σ_c = 0.148 MPa
$\dot{\varepsilon}$ = 3.48x10^{-6}/sec
Type C q−ε curve
x = Q_p
= 15.6 MPa
ε_p = 6.3%
Q_{uy} = 14.5 MPa
MSP, good ACDT's, good Stability, Lub ends

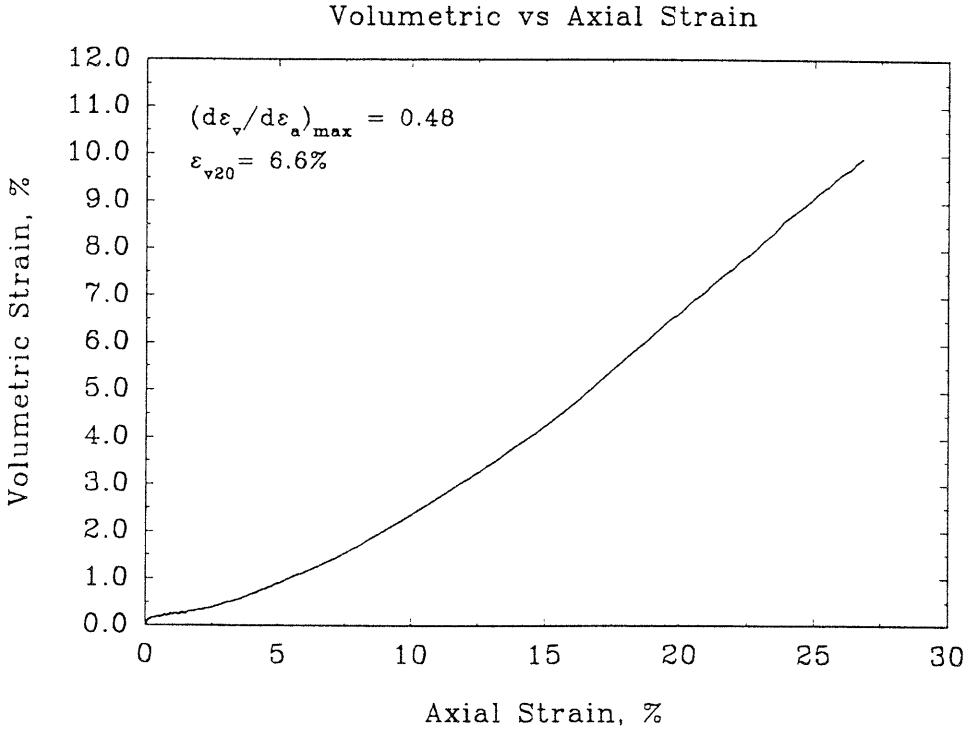
Volumetric vs Axial Strain
Volumetric Strain, %
Axial Strain, %
$(d\varepsilon_v/d\varepsilon_a)_{max}$ = 0.48
ε_{v20} = 6.6%

FRS104

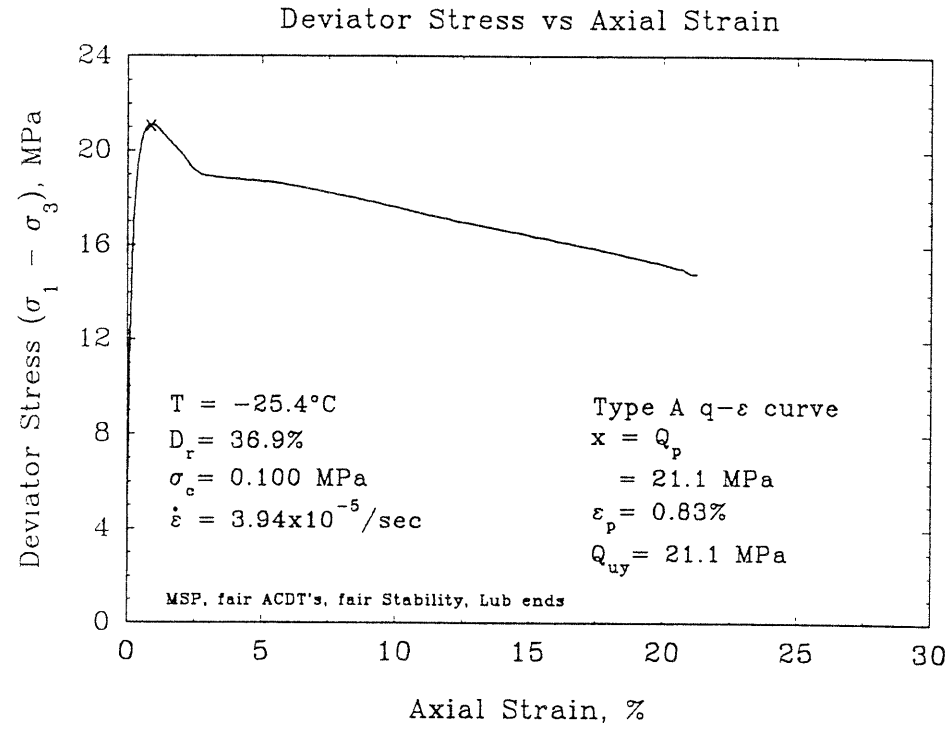
Deviator Stress vs Axial Strain
Deviator Stress ($\sigma_1 - \sigma_3$), MPa
Axial Strain, %
T = -25.4°C
D_r = 36.9%
σ_c = 0.100 MPa
$\dot{\varepsilon}$ = 3.94x10^{-5}/sec
Type A q−ε curve
x = Q_p
= 21.1 MPa
ε_p = 0.83%
Q_{uy} = 21.1 MPa
MSP, fair ACDT's, fair Stability, Lub ends

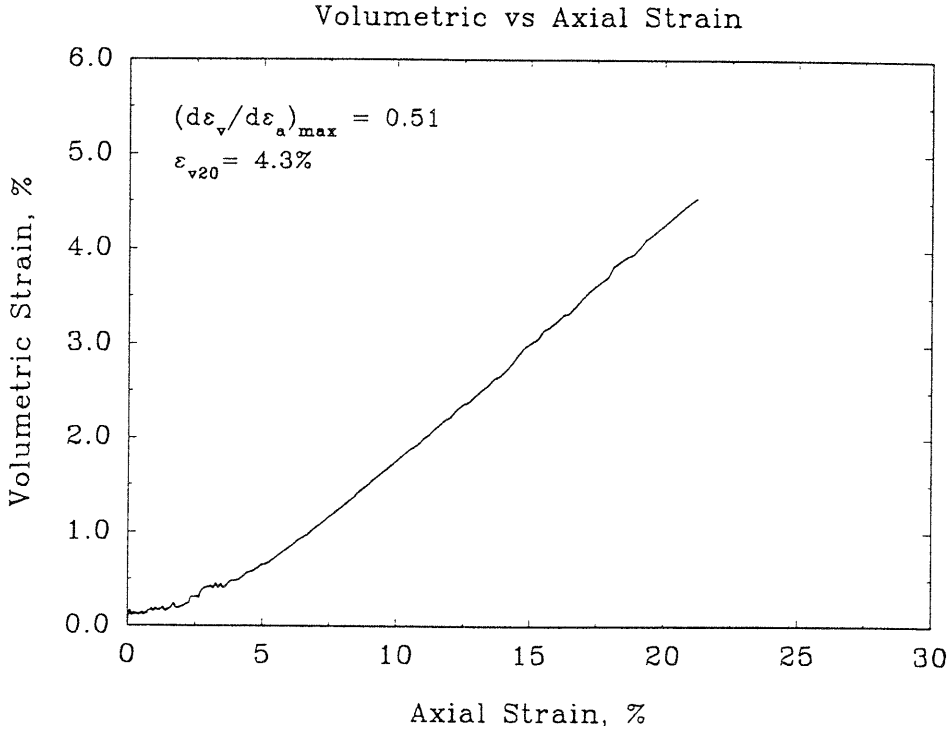
Volumetric vs Axial Strain
Volumetric Strain, %
Axial Strain, %
$(d\varepsilon_v/d\varepsilon_a)_{max}$ = 0.51
ε_{v20} = 4.3%

FRS106

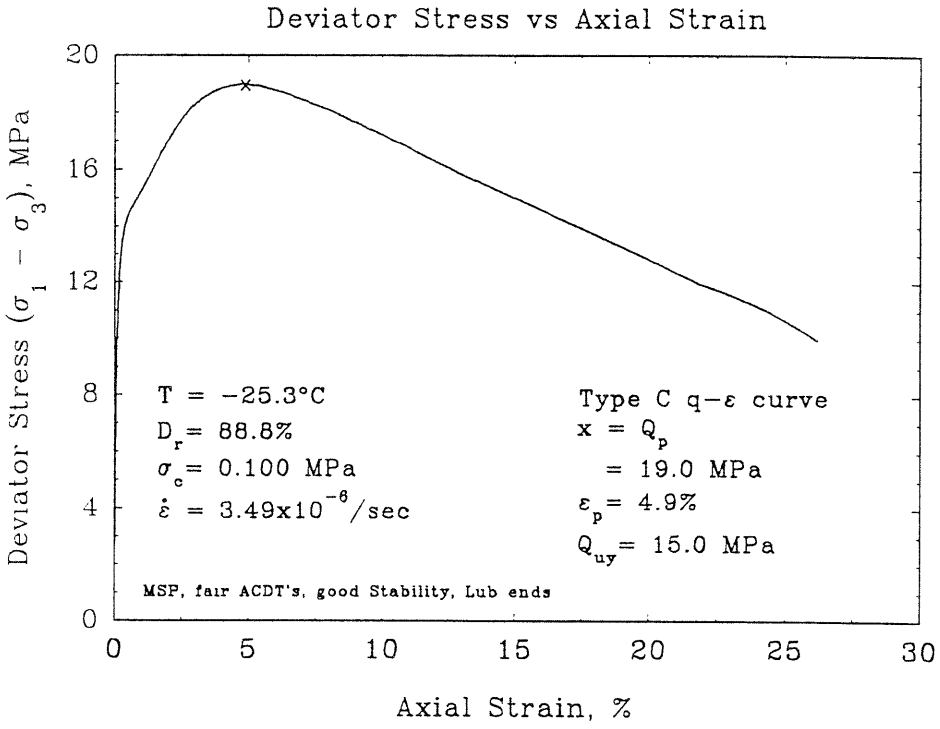
Deviator Stress vs Axial Strain
Deviator Stress ($\sigma_1 - \sigma_3$), MPa
Axial Strain, %
T = −25.3°C
D_r = 88.8%
σ_c = 0.100 MPa
$\dot{\varepsilon}$ = 3.49x10^{-6}/sec
Type C q−ε curve
x = Q_p
= 19.0 MPa
ε_p = 4.9%
Q_{uy} = 15.0 MPa
MSP, fair ACDT's, good Stability, Lub ends

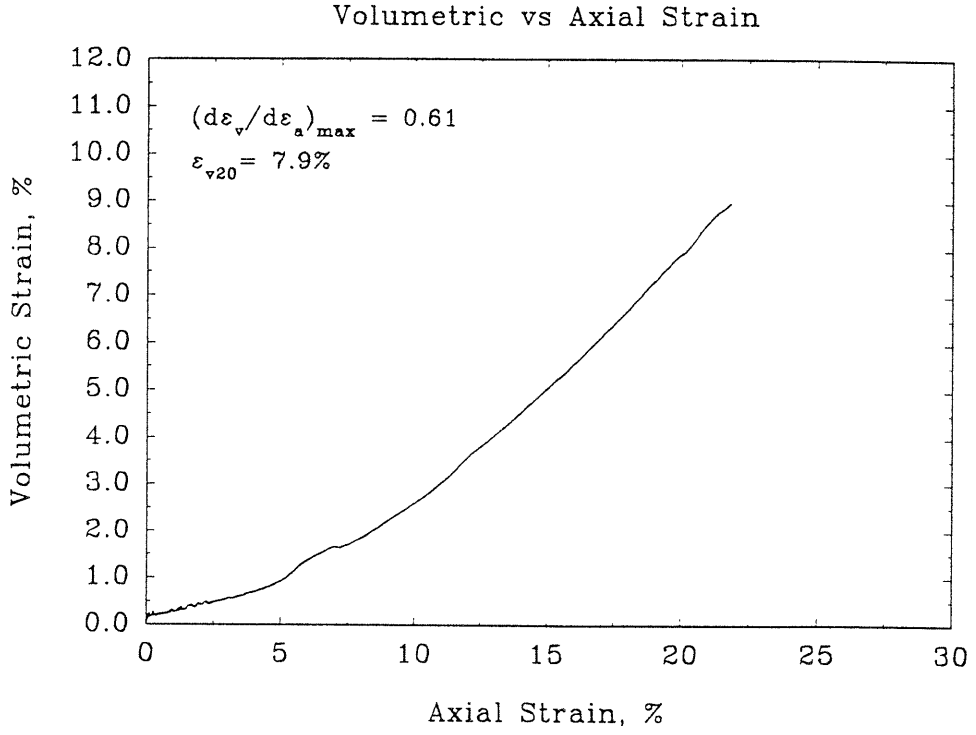
Volumetric vs Axial Strain
Volumetric Strain, %
Axial Strain, %
$(d\varepsilon_v/d\varepsilon_a)_{max}$ = 0.61
ε_{v20} = 7.9%

FRS107

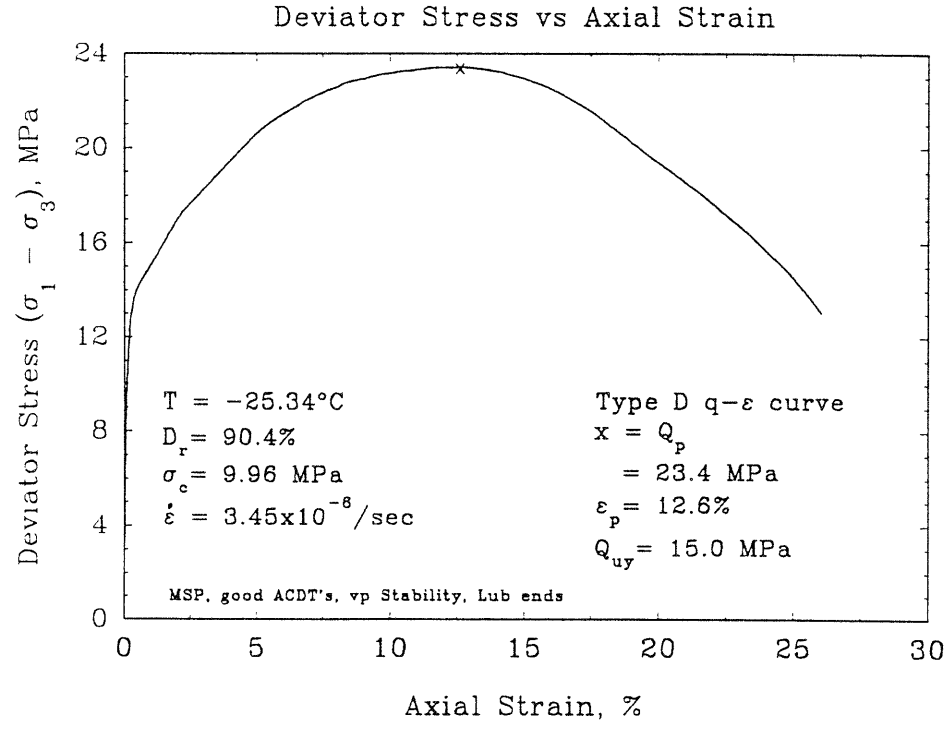
Deviator Stress vs Axial Strain
Deviator Stress ($\sigma_1 - \sigma_3$), MPa
Axial Strain, %
T = -25.34°C
D_r = 90.4%
σ_c = 9.96 MPa
$\dot{\varepsilon}$ = 3.45x10^{-8}/sec
Type D q−ε curve
x = Q_p
= 23.4 MPa
ε_p = 12.6%
Q_{uy} = 15.0 MPa
MSP, good ACDT's, vp Stability, Lub ends

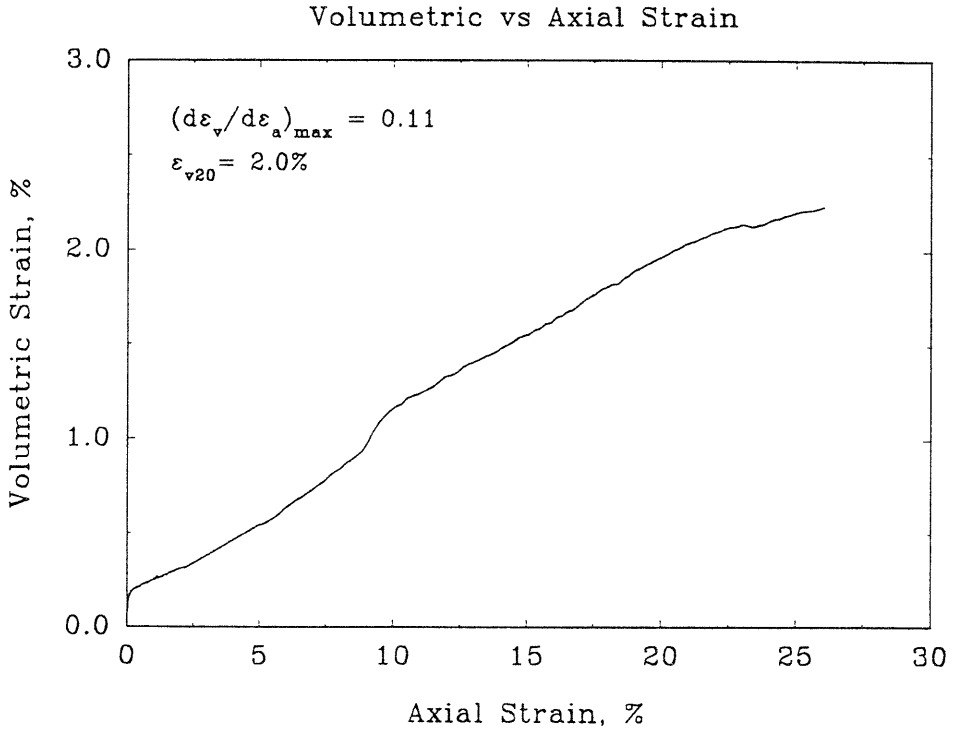
Volumetric vs Axial Strain
Volumetric Strain, %
Axial Strain, %
$(d\varepsilon_v/d\varepsilon_a)_{max}$ = 0.11
ε_{v20} = 2.0%

FRS109

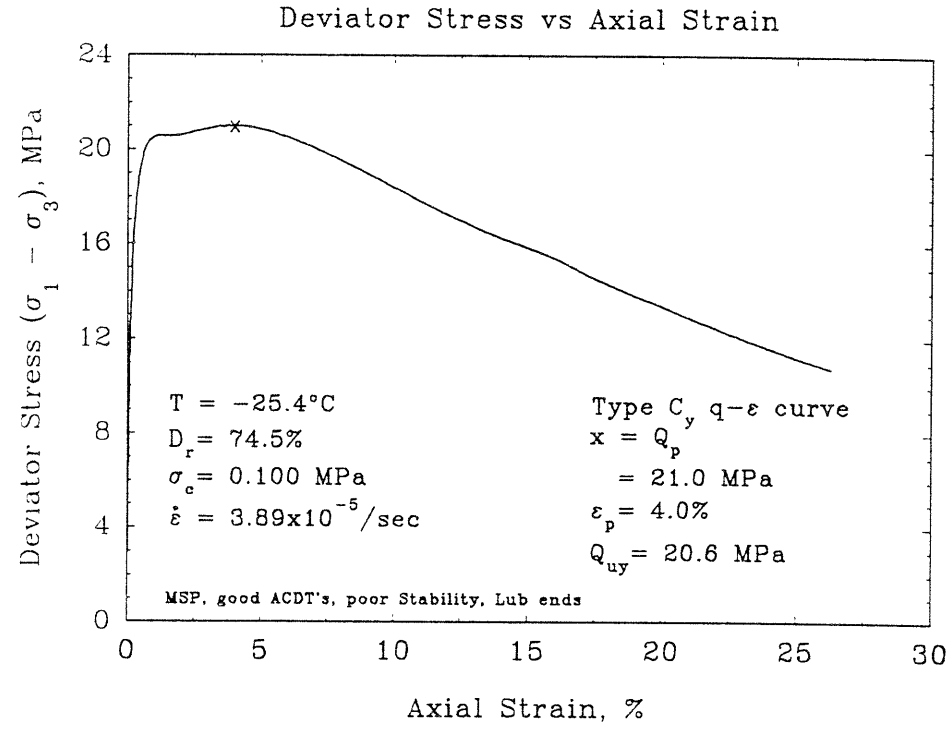
Deviator Stress vs Axial Strain
Deviator Stress ($\sigma_1 - \sigma_3$), MPa
Axial Strain, %
T = -25.4°C
D_r= 74.5%
σ_c= 0.100 MPa
$\dot{\varepsilon}$ = 3.89x10^{-5}/sec
Type C_y q-ε curve
x = Q_p
= 21.0 MPa
ε_p= 4.0%
Q_{uy}= 20.6 MPa
MSP, good ACDT's, poor Stability, Lub ends

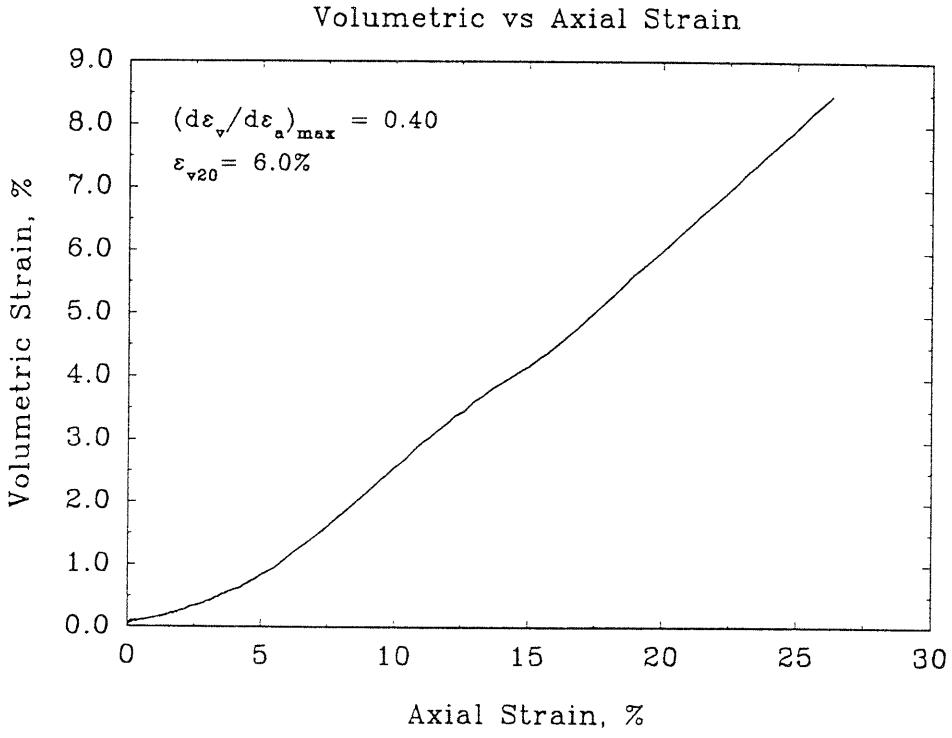
Volumetric vs Axial Strain
Volumetric Strain, %
Axial Strain, %
$(d\varepsilon_v/d\varepsilon_a)_{max}$ = 0.40
ε_{v20}= 6.0%

FRS110

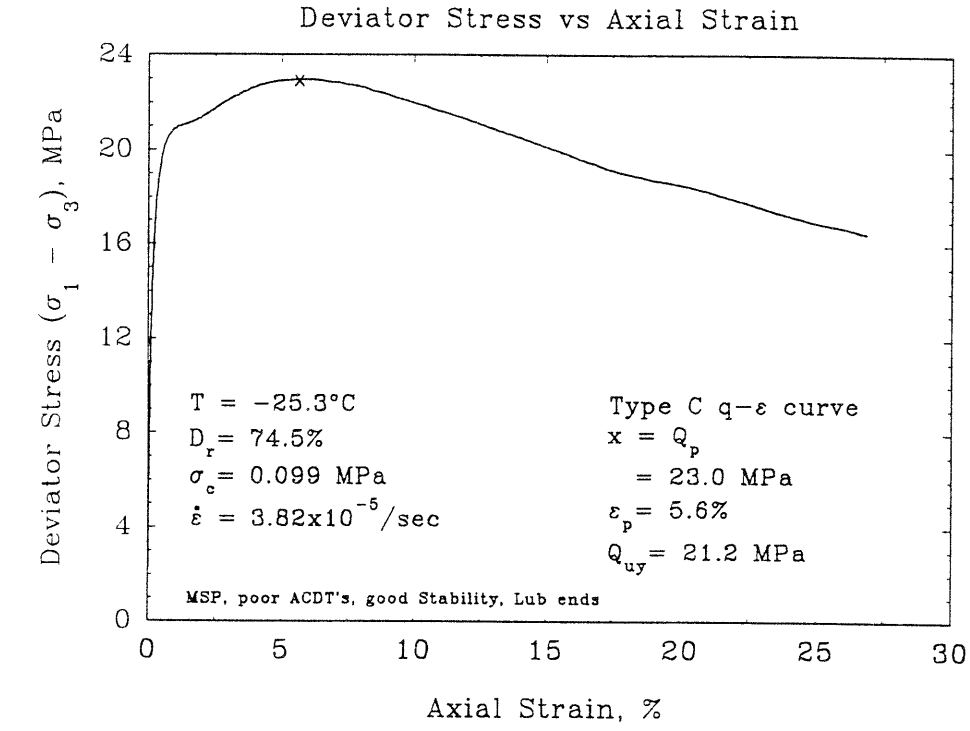
Deviator Stress vs Axial Strain
Deviator Stress ($\sigma_1 - \sigma_3$), MPa
Axial Strain, %
T = -25.3°C
D_r= 74.5%
σ_c= 0.099 MPa
$\dot{\varepsilon}$ = 3.82x10^{-5}/sec
Type C q−ε curve
x = Q_p
= 23.0 MPa
ε_p= 5.6%
Q_{uy}= 21.2 MPa
MSP, poor ACDT's, good Stability, Lub ends

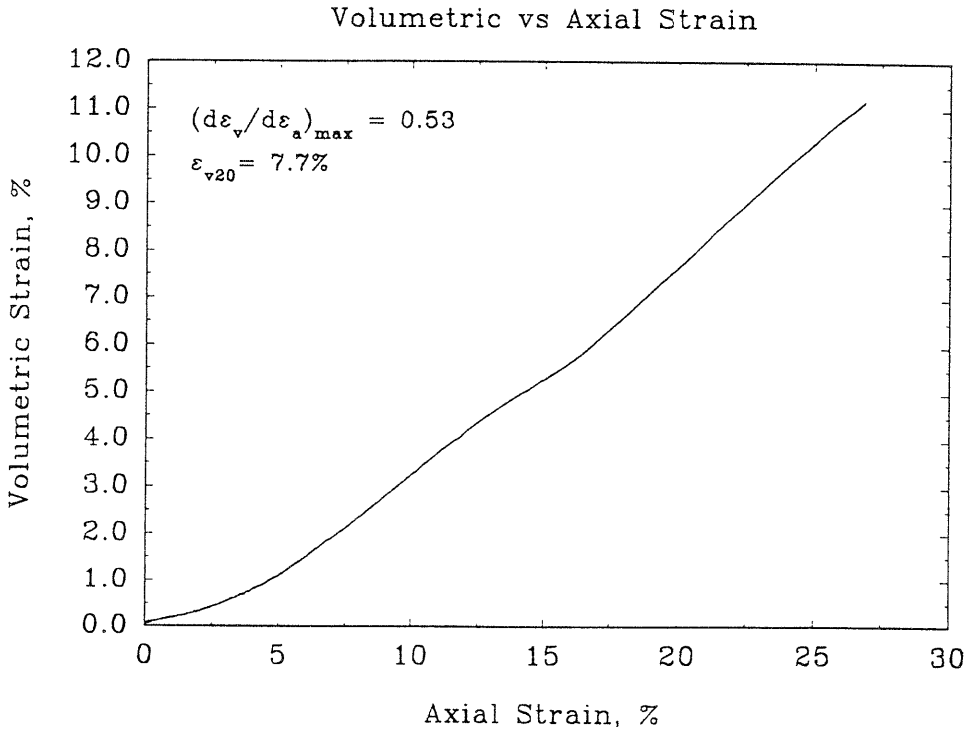
Volumetric vs Axial Strain
Volumetric Strain, %
Axial Strain, %
$(d\varepsilon_v/d\varepsilon_a)_{max}$ = 0.53
ε_{v20}= 7.7%

FRS111

Deviator Stress vs Axial Strain

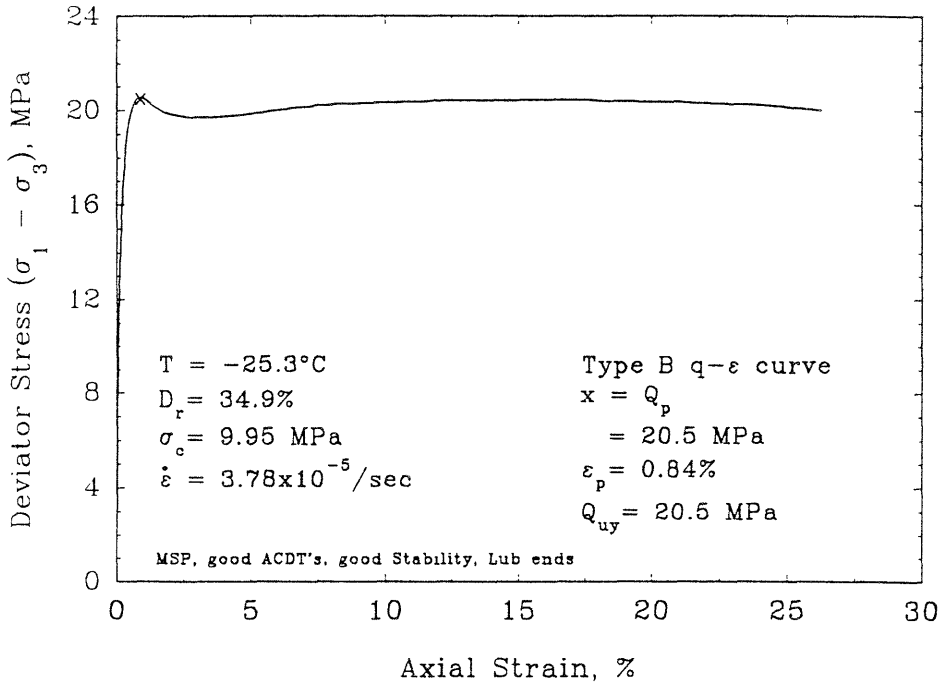

Volumetric vs Axial Strain

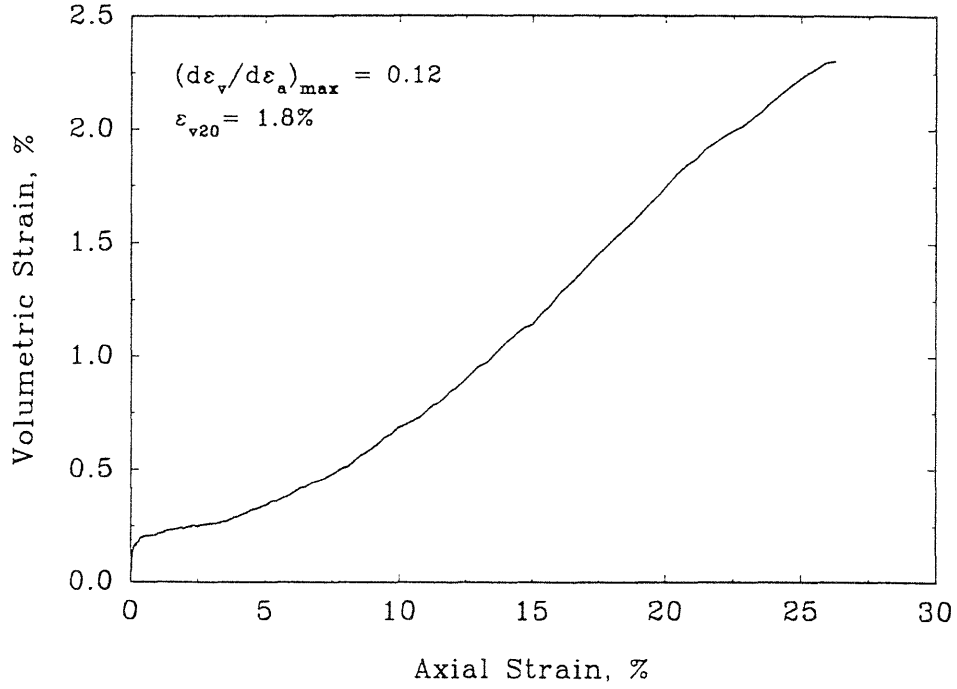

FRS113

Deviator Stress vs Axial Strain

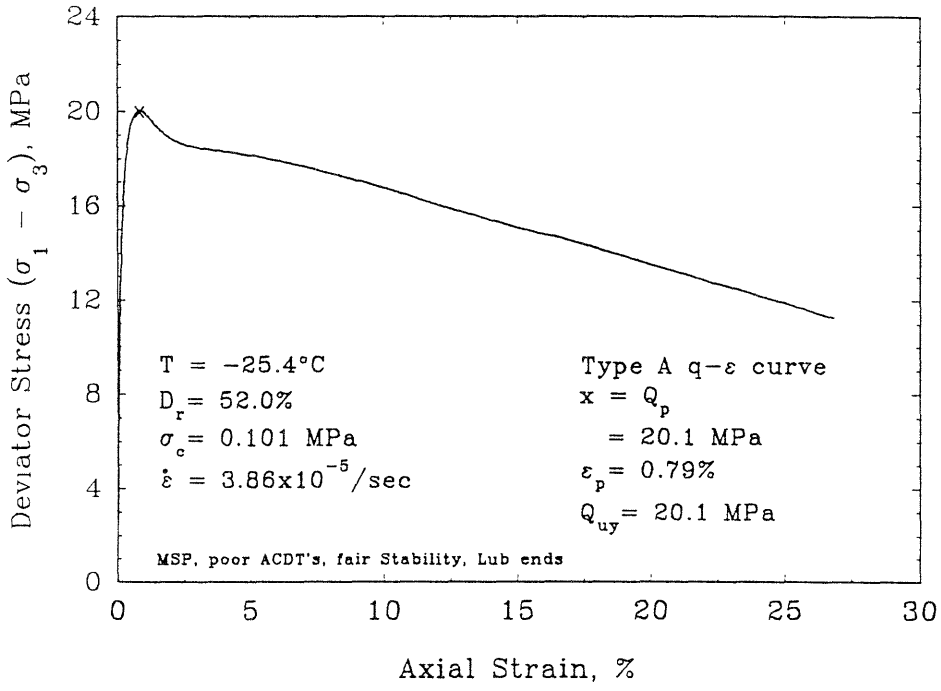

Volumetric vs Axial Strain

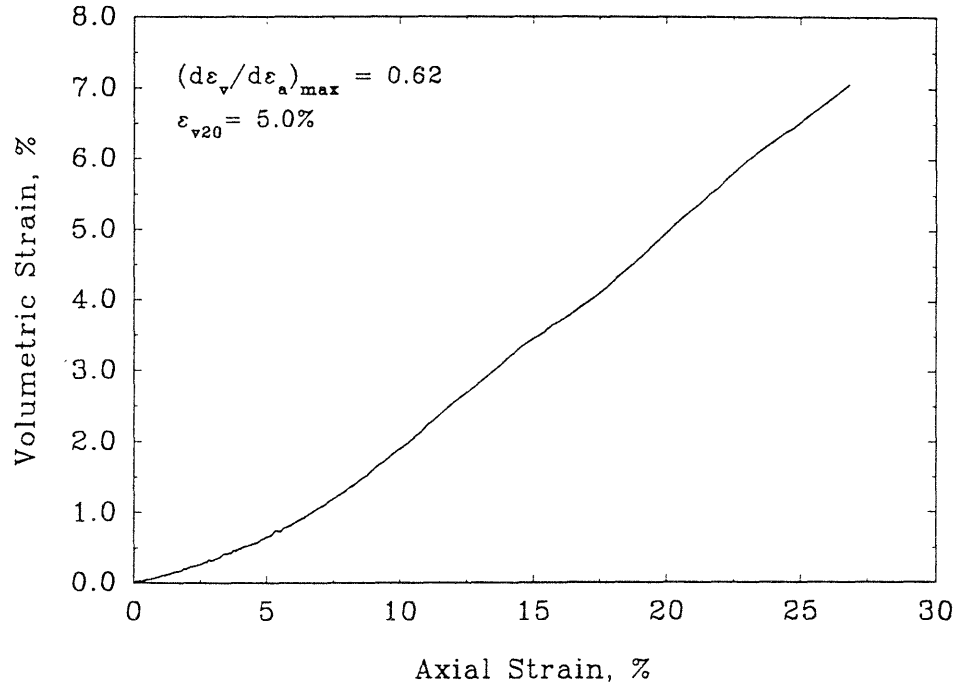

FRS114

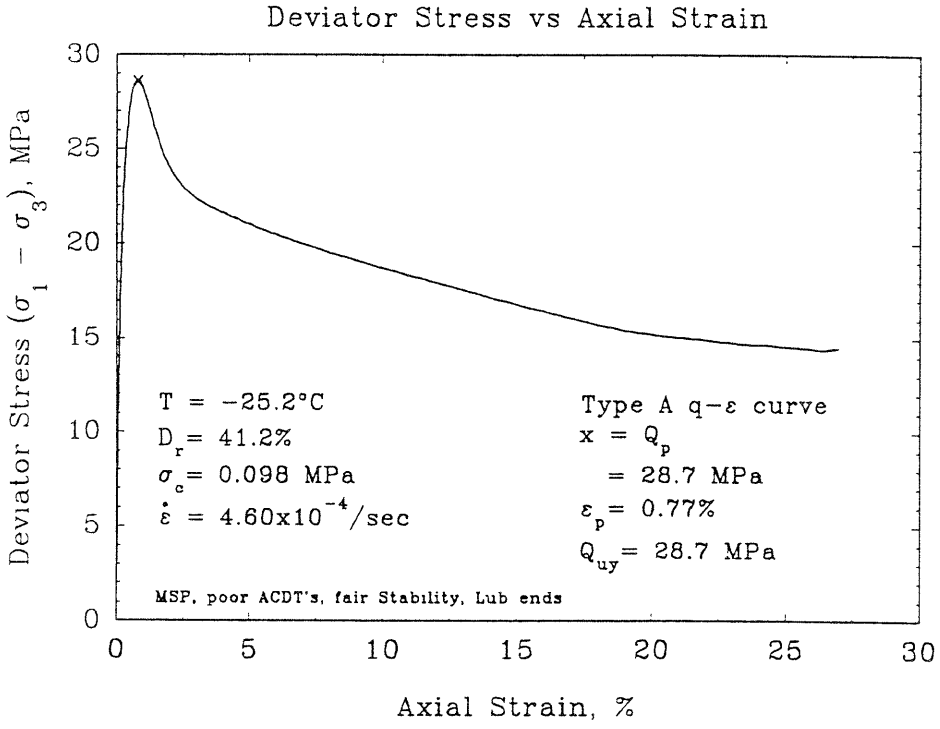
Deviator Stress vs Axial Strain
Deviator Stress ($\sigma_1 - \sigma_3$), MPa
Axial Strain, %
T = -25.2°C
D_r = 41.2%
σ_c = 0.098 MPa
$\dot{\varepsilon}$ = 4.60x10^{-4}/sec
Type A q-ε curve
x = Q_p
= 28.7 MPa
ε_p = 0.77%
Q_{uy} = 28.7 MPa
MSP, poor ACDT's, fair Stability, Lub ends

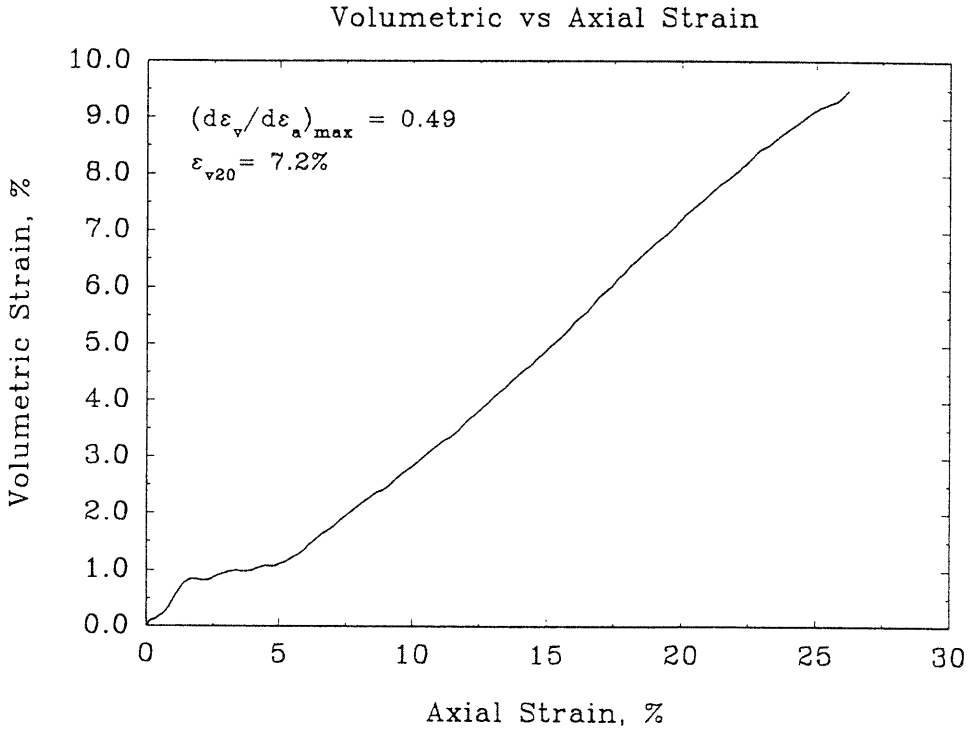
Volumetric vs Axial Strain
Volumetric Strain, %
Axial Strain, %
$(d\varepsilon_v/d\varepsilon_a)_{max}$ = 0.49
ε_{v20} = 7.2%

FRS115

Deviator Stress vs Axial Strain

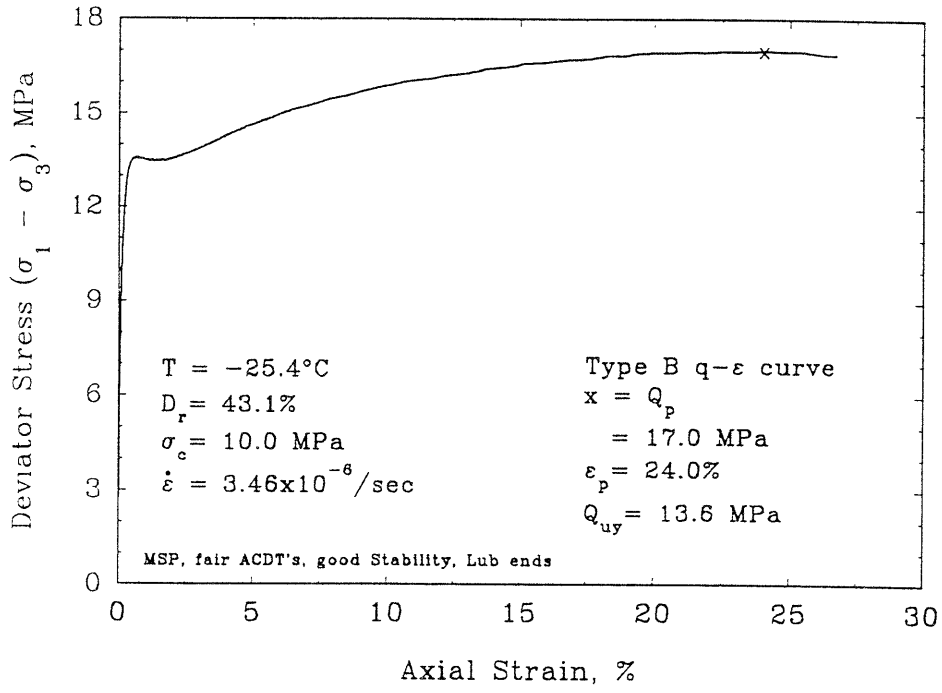

Volumetric vs Axial Strain

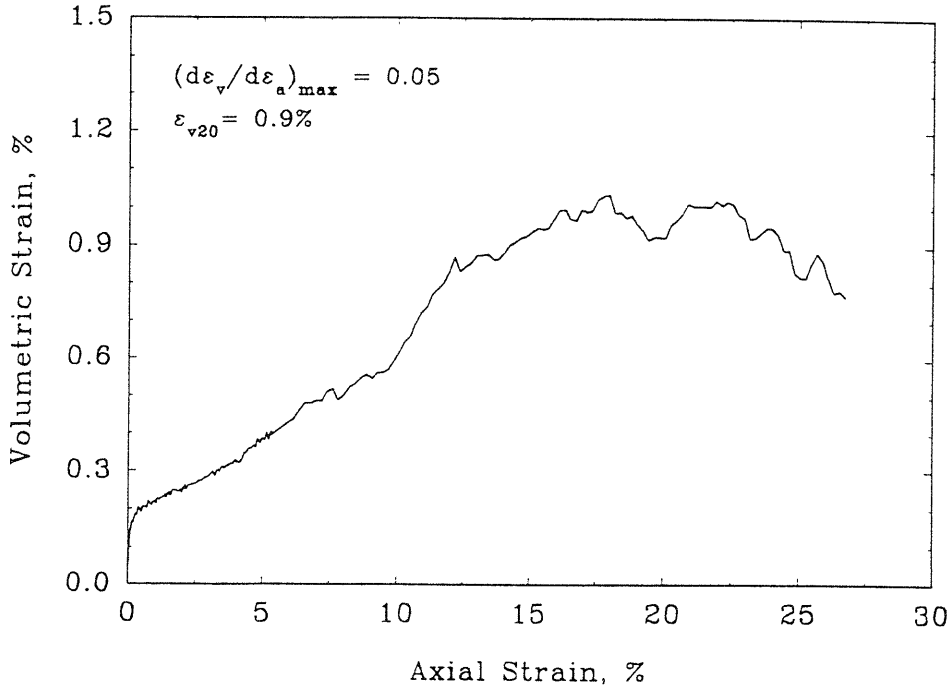

FRS116

Deviator Stress vs Axial Strain

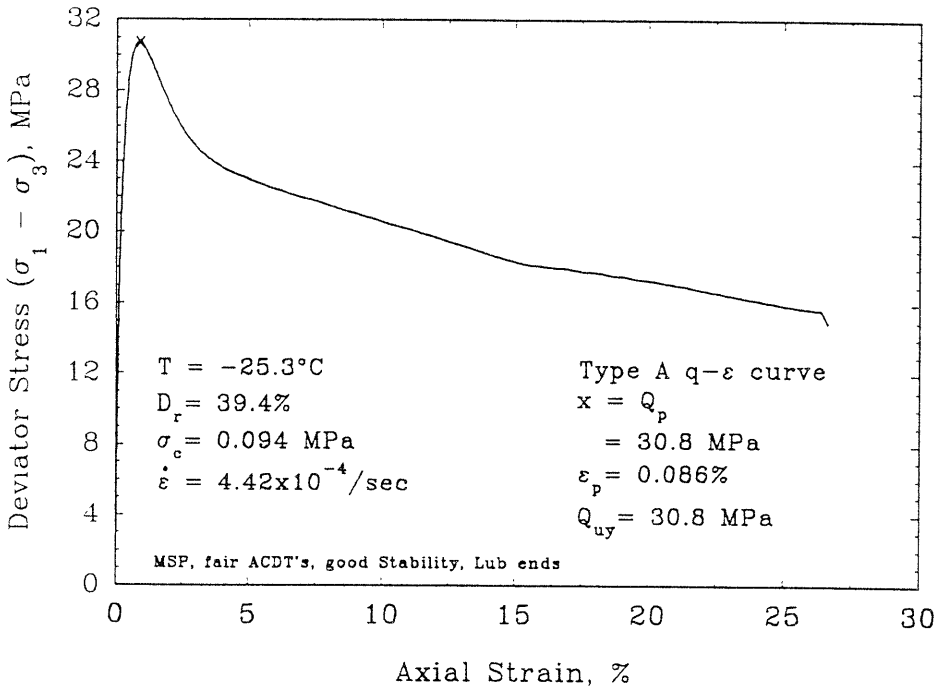

Volumetric vs Axial Strain

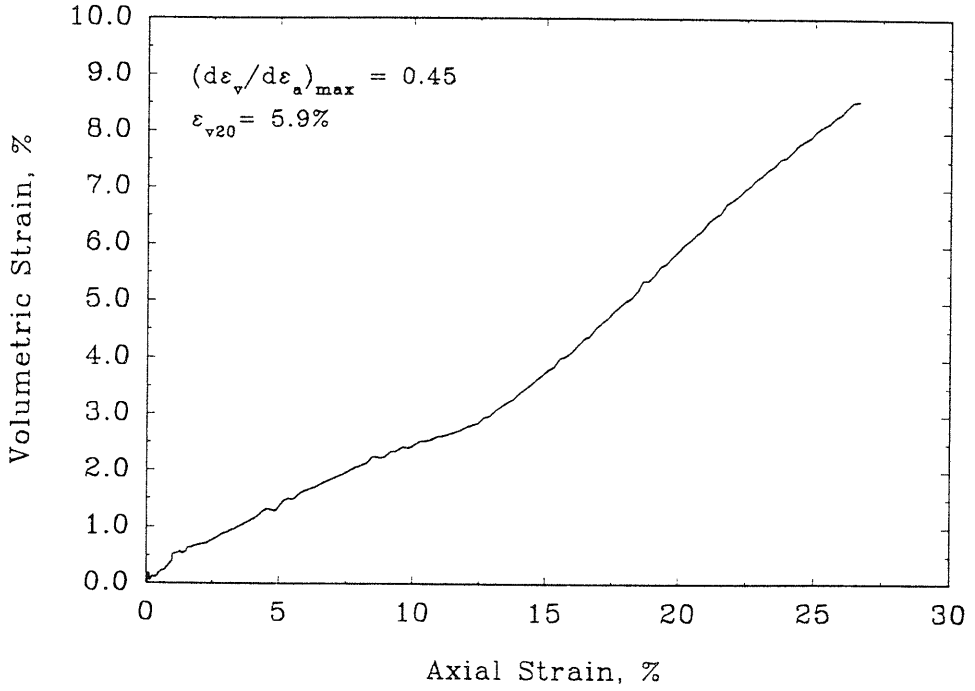

FRS117

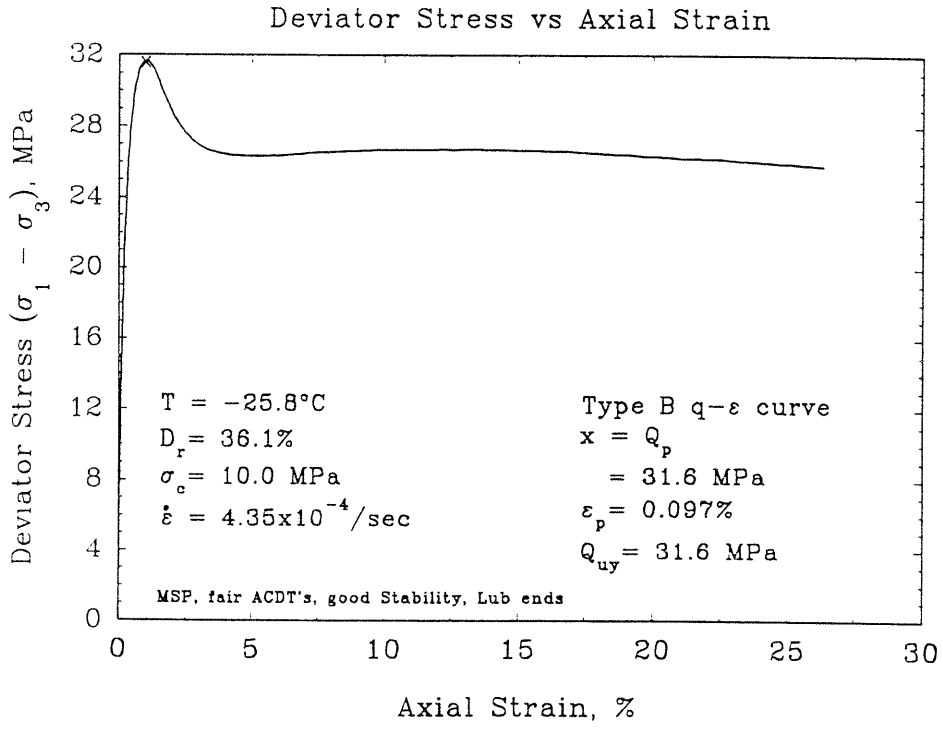
Deviator Stress vs Axial Strain
Deviator Stress ($\sigma_1 - \sigma_3$), MPa
Axial Strain, %
T = -25.8°C
D_r= 36.1%
σ_c= 10.0 MPa
$\dot{\varepsilon}$ = 4.35x10^{-4}/sec
Type B q-ε curve
x = Q_p
= 31.6 MPa
ε_p= 0.097%
Q_{uy}= 31.6 MPa
MSP, fair ACDT's, good Stability, Lub ends

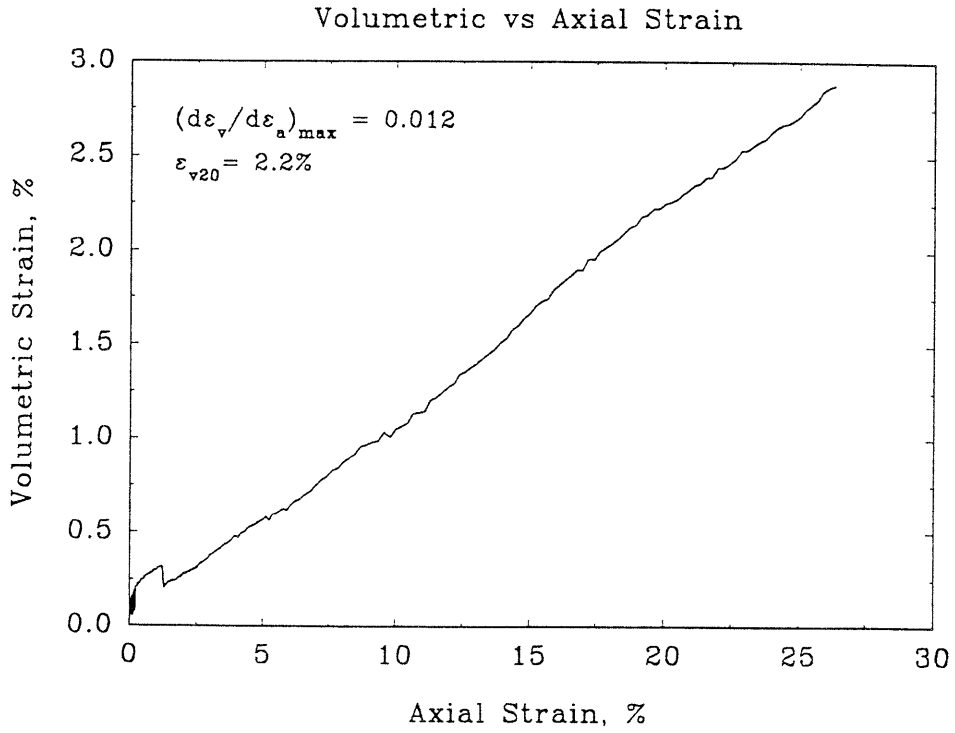
Volumetric vs Axial Strain
Volumetric Strain, %
Axial Strain, %
$(d\varepsilon_v/d\varepsilon_a)_{max}$ = 0.012
ε_{v20}= 2.2%

APPENDIX D

TEST RESULTS FOR CONSOLIDATE-FREEZE TESTING PROGRAM

APPENDIX D

TEST RESULTS FOR COSOLIDATE–FREEZE TESTING PROGRAM

This appendix presents the measured stress–strain and volumetric strain responses for the 10 consolidate–freeze tests.

CF01

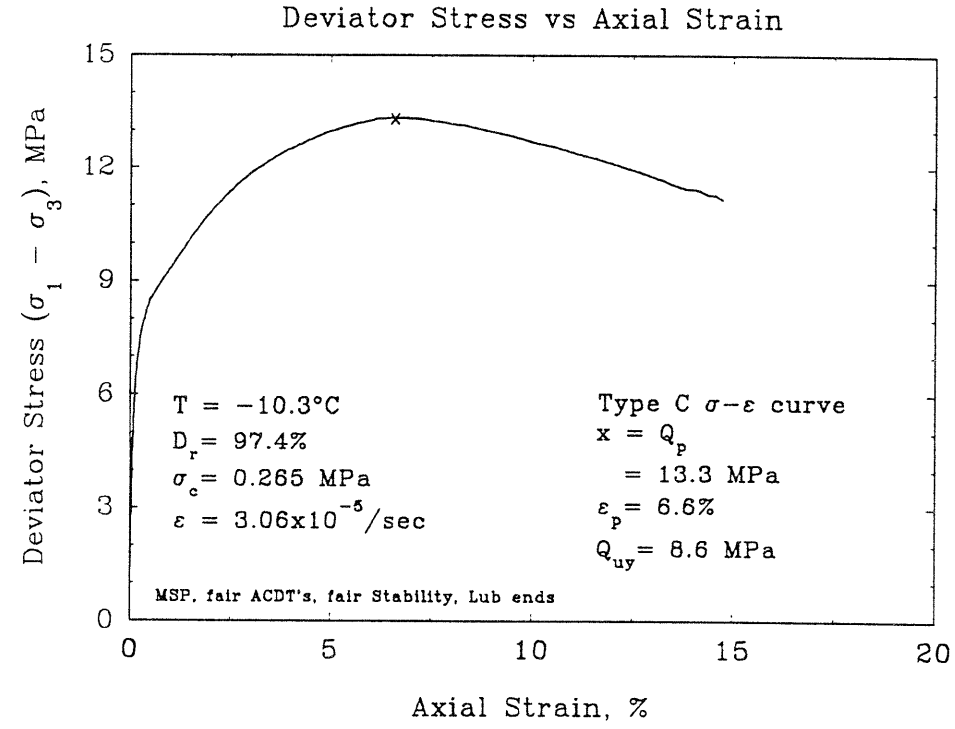
Deviator Stress vs Axial Strain
Deviator Stress ($\sigma_1 - \sigma_3$), MPa
Axial Strain, %
T = −10.3°C
D_r= 97.4%
σ_c= 0.265 MPa
$\dot{\varepsilon}$ = 3.06x10^{-5}/sec
Type C σ−ε curve
x = Q_p
= 13.3 MPa
ε_p= 6.6%
Q_{uy}= 8.6 MPa
MSP, fair ACDT's, fair Stability, Lub ends

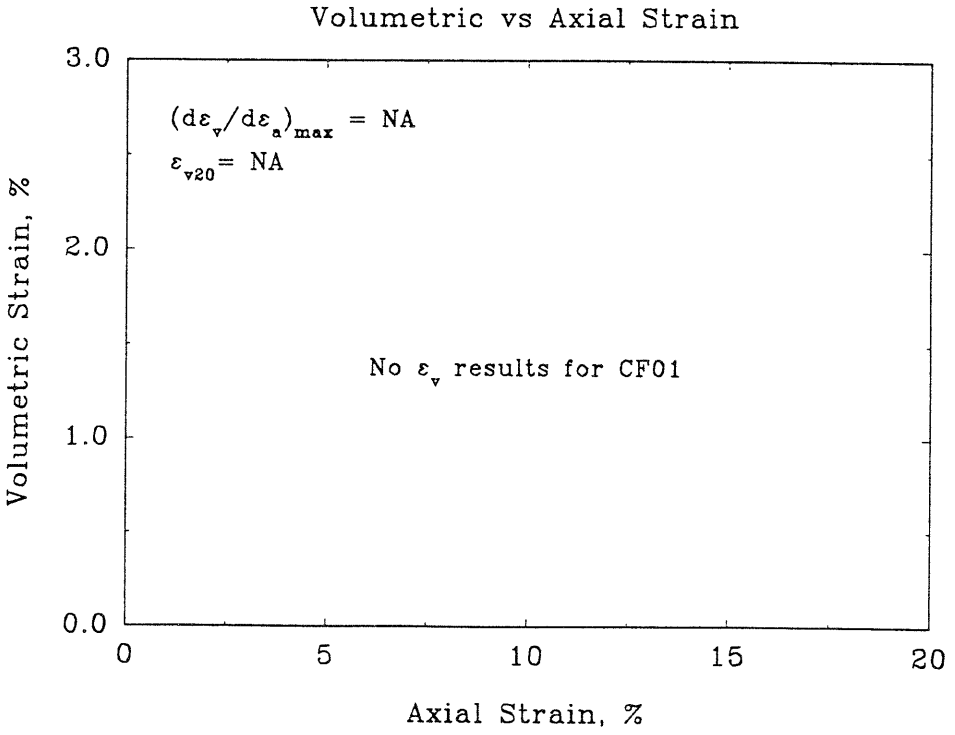
Volumetric vs Axial Strain
Volumetric Strain, %
Axial Strain, %
$(d\varepsilon_v/d\varepsilon_a)_{max}$ = NA
ε_{v20}= NA
No ε_v results for CF01

CF02

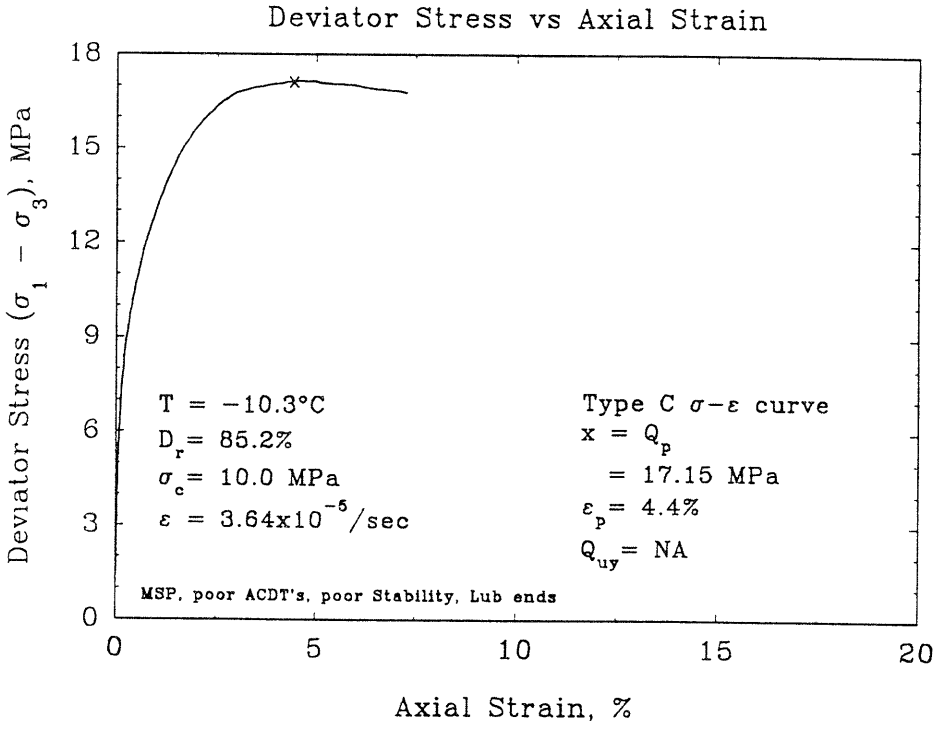
Deviator Stress vs Axial Strain
Deviator Stress ($\sigma_1 - \sigma_3$), MPa
Axial Strain, %
T = −10.3°C
D_r= 85.2%
σ_c= 10.0 MPa
ε = 3.64x10^{-5}/sec
Type C $\sigma-\varepsilon$ curve
x = Q_p
= 17.15 MPa
ε_p= 4.4%
Q_{uy}= NA
MSP, poor ACDT's, poor Stability, Lub ends

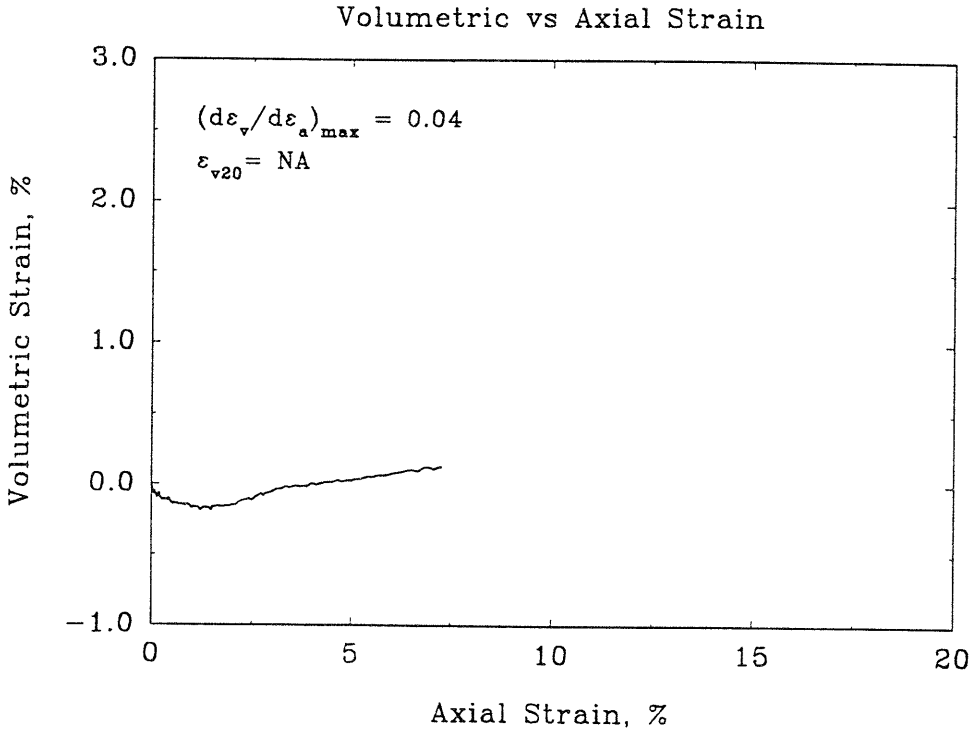
Volumetric vs Axial Strain
Volumetric Strain, %
Axial Strain, %
$(d\varepsilon_v/d\varepsilon_a)_{max}$ = 0.04
ε_{v20}= NA

CF03

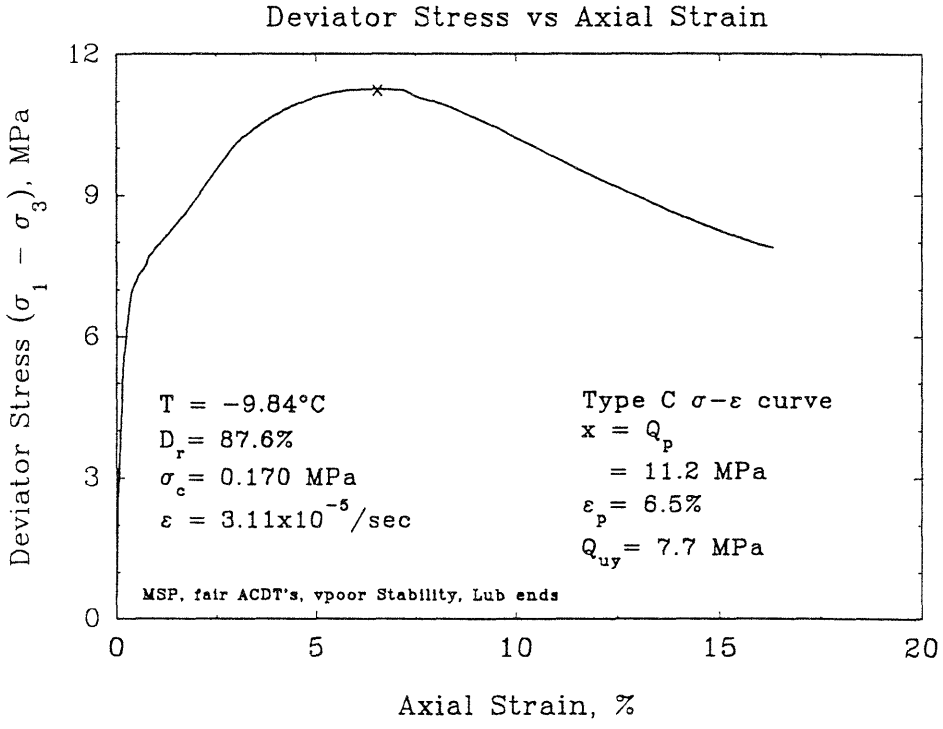
Deviator Stress vs Axial Strain
Deviator Stress ($\sigma_1 - \sigma_3$), MPa
Axial Strain, %
T = -9.84°C
D_r= 87.6%
σ_c= 0.170 MPa
$\dot{\varepsilon}$ = 3.11x10^{-5}/sec
Type C $\sigma-\varepsilon$ curve
x = Q_p
= 11.2 MPa
ε_p= 6.5%
Q_{uy}= 7.7 MPa
MSP, fair ACDT's, vpoor Stability, Lub ends

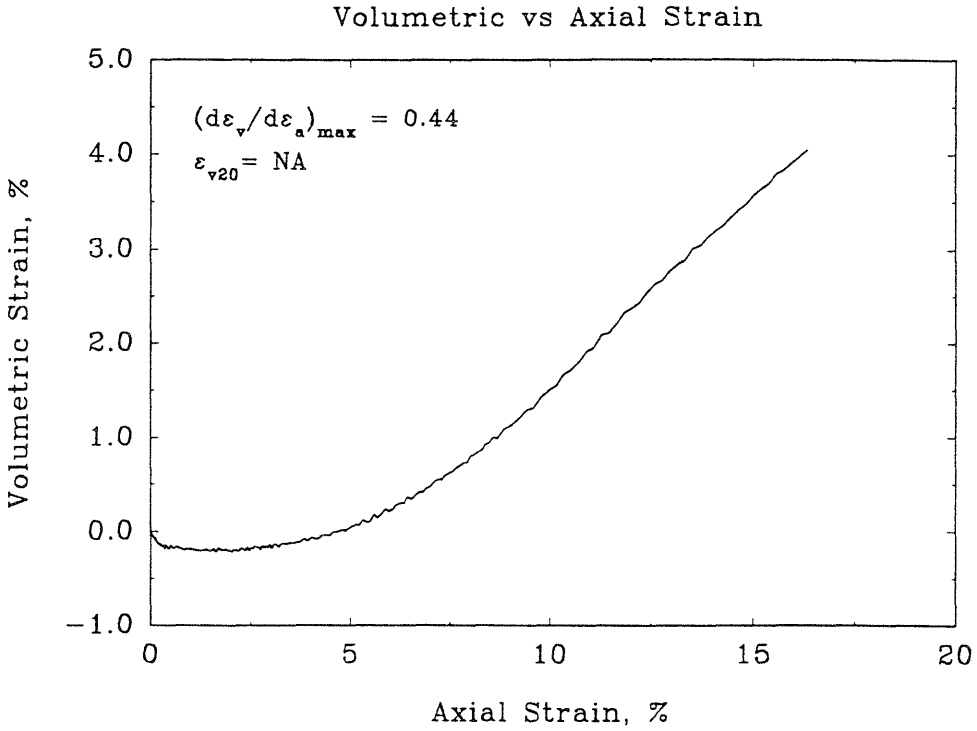
Volumetric vs Axial Strain
Volumetric Strain, %
Axial Strain, %
$(d\varepsilon_v/d\varepsilon_a)_{max}$ = 0.44
ε_{v20}= NA

CF04

Deviator Stress vs Axial Strain

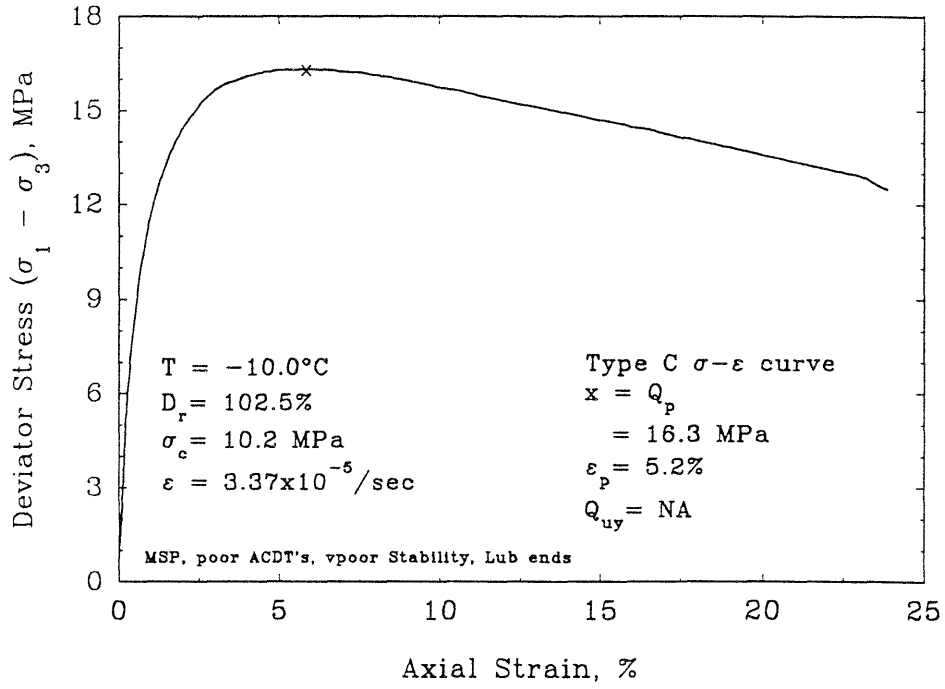

Volumetric vs Axial Strain

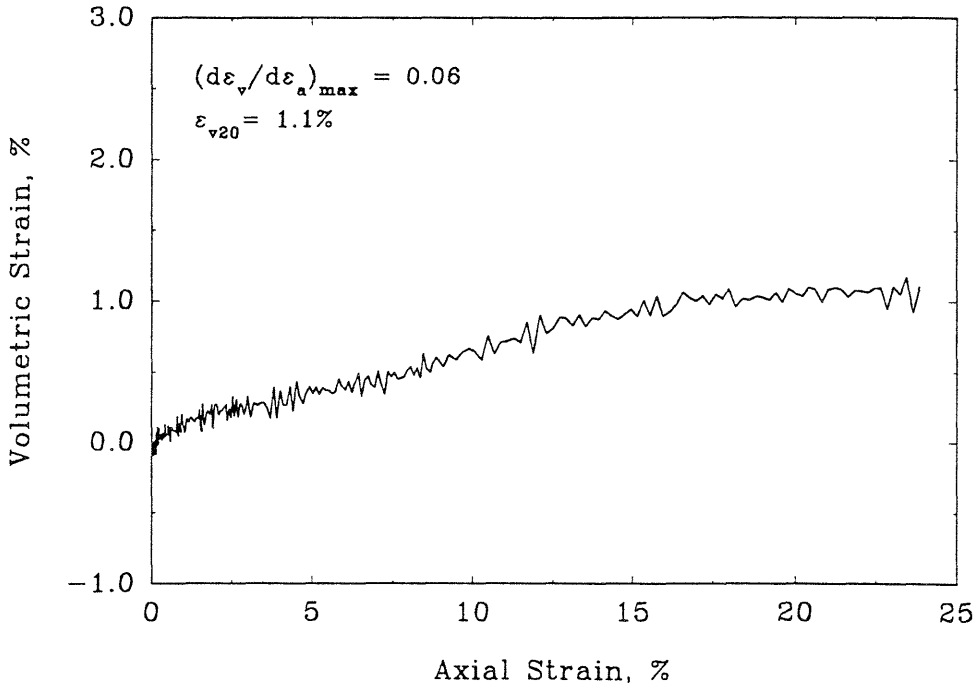

CF05

Deviator Stress vs Axial Strain

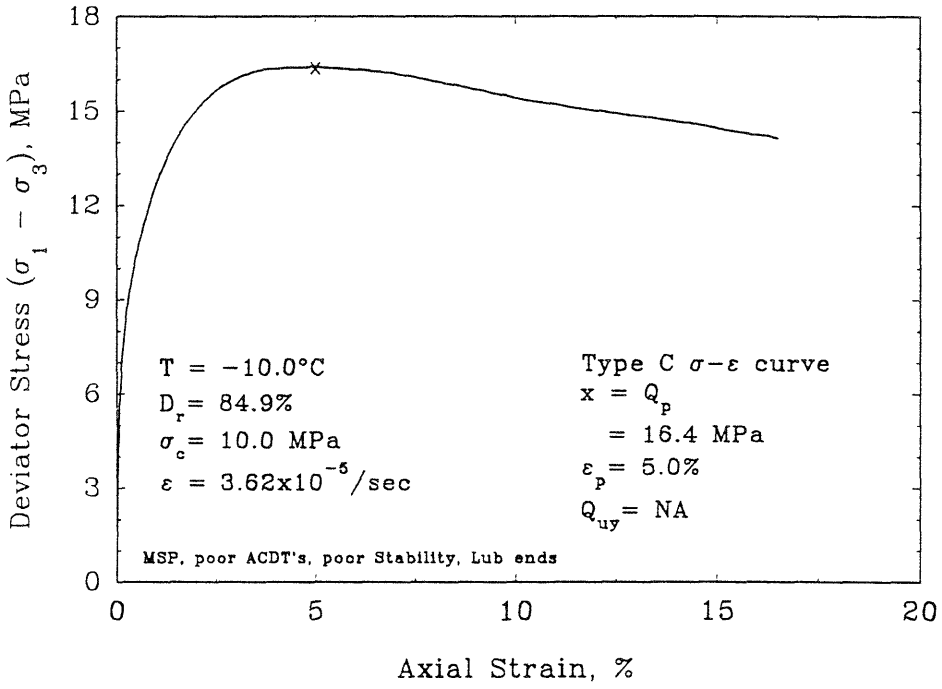

Volumetric vs Axial Strain

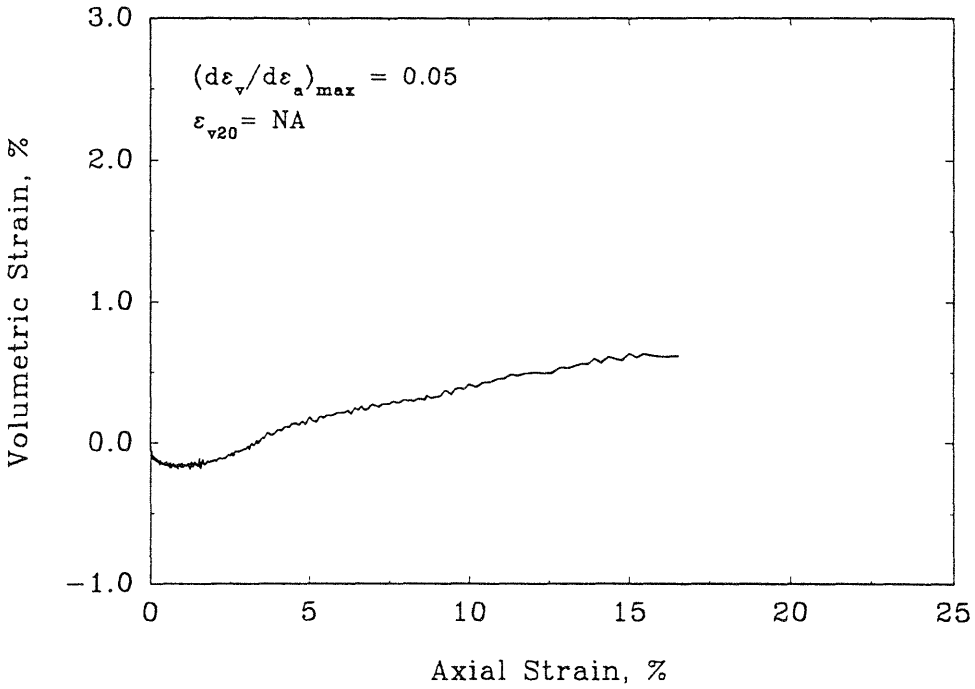

CF06

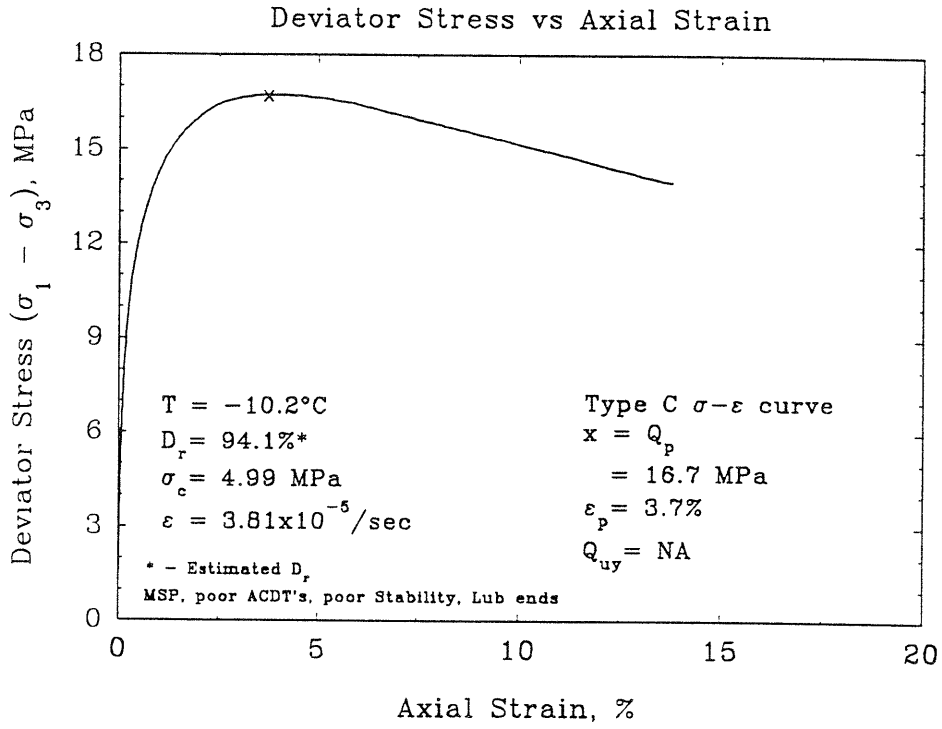
Deviator Stress vs Axial Strain
Deviator Stress ($\sigma_1 - \sigma_3$), MPa
Axial Strain, %
T = −10.2°C
D_r = 94.1%*
σ_c = 4.99 MPa
ε = 3.81x10^{-5}/sec
* - Estimated D_r
MSP, poor ACDT's, poor Stability, Lub ends
Type C $\sigma-\varepsilon$ curve
x = Q_p
= 16.7 MPa
ε_p = 3.7%
Q_{uy} = NA

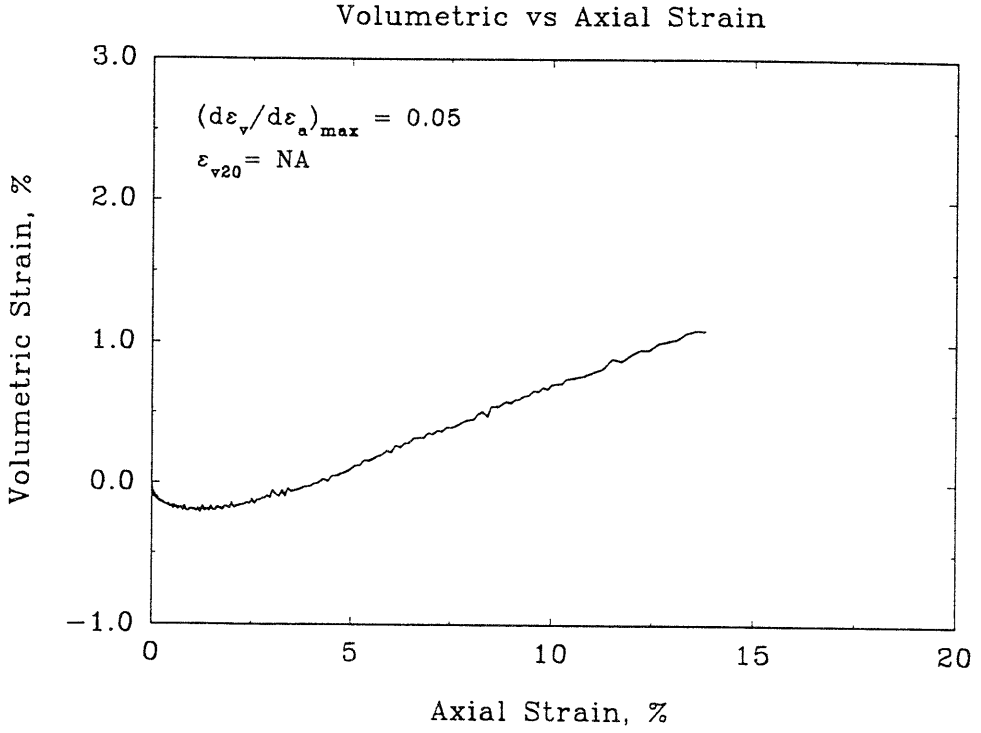
Volumetric vs Axial Strain
Volumetric Strain, %
Axial Strain, %
$(d\varepsilon_v/d\varepsilon_a)_{max}$ = 0.05
ε_{v20} = NA

CF07

Deviator Stress vs Axial Strain

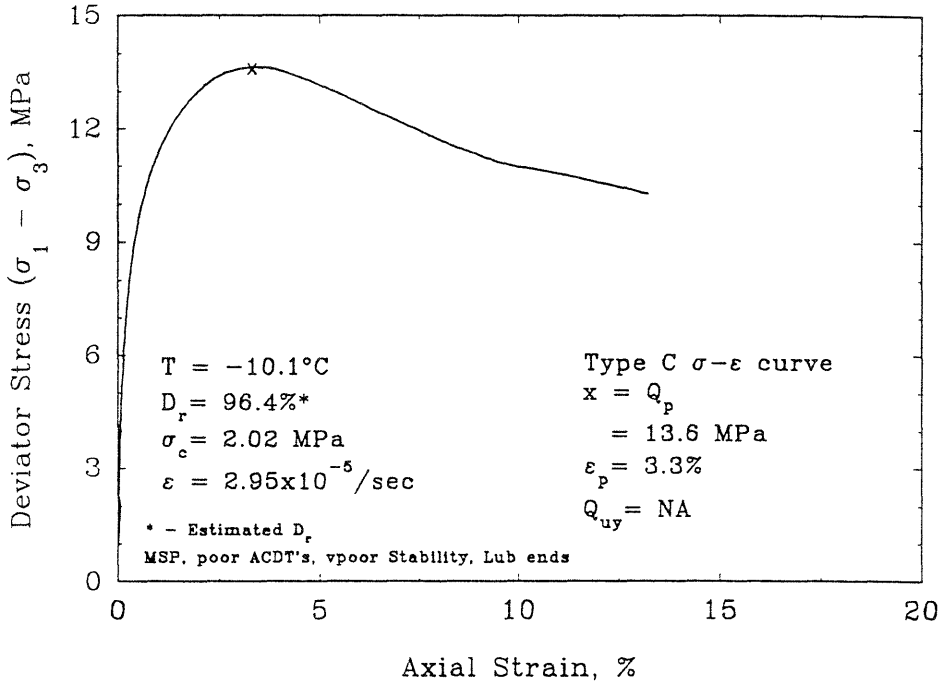

Volumetric vs Axial Strain

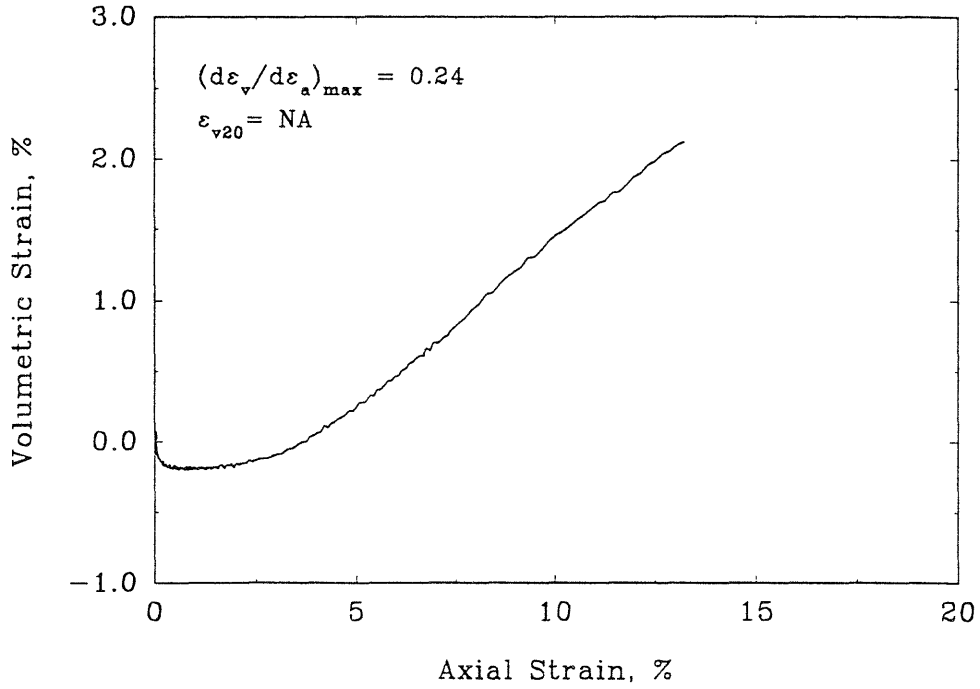

CF08

Deviator Stress vs Axial Strain

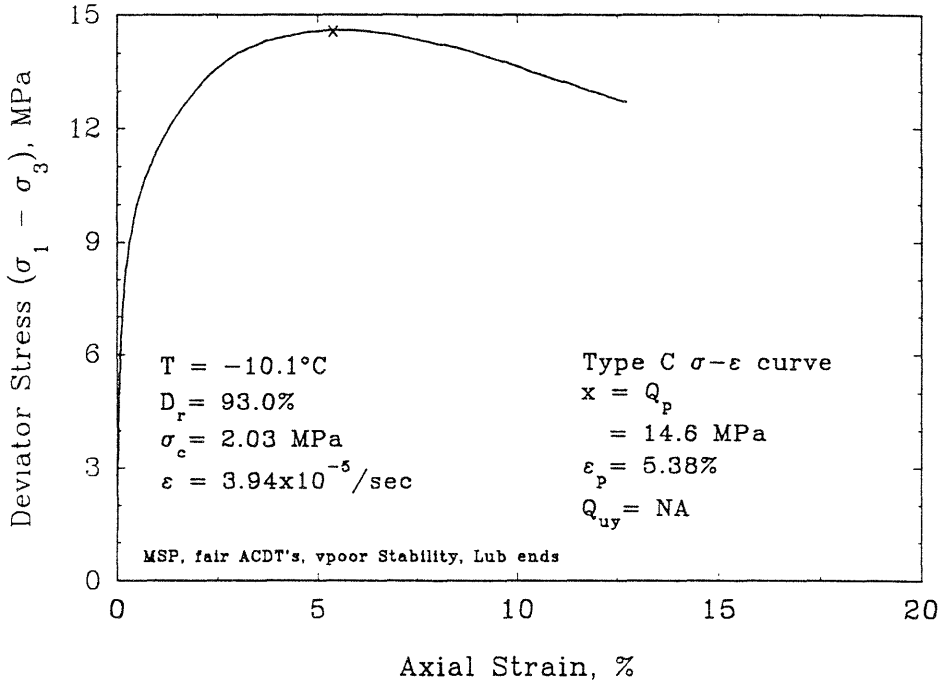

Volumetric vs Axial Strain

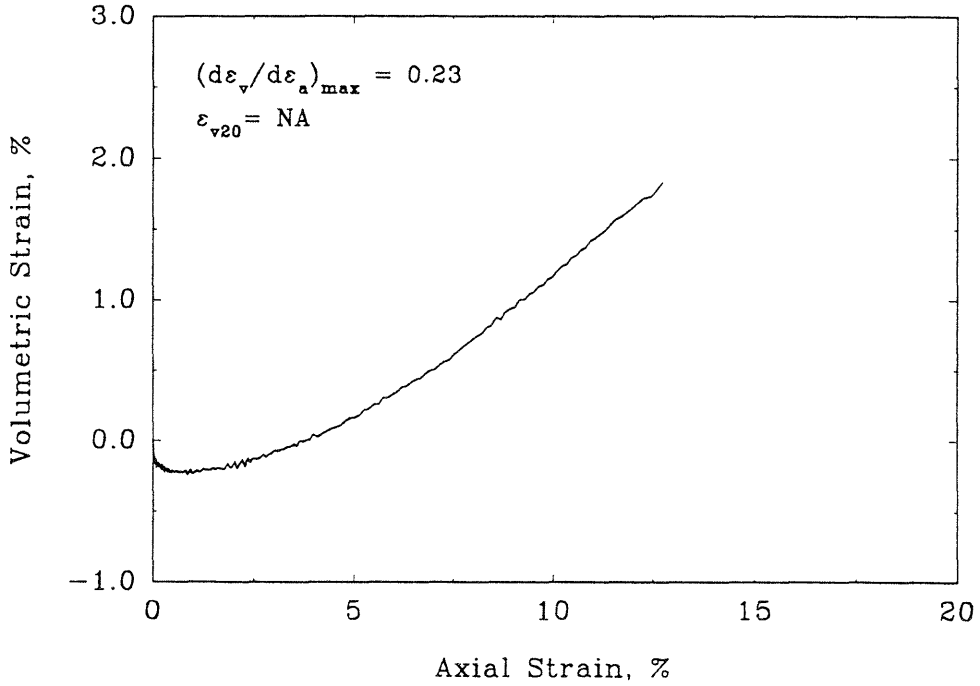

CF09

Deviator Stress vs Axial Strain

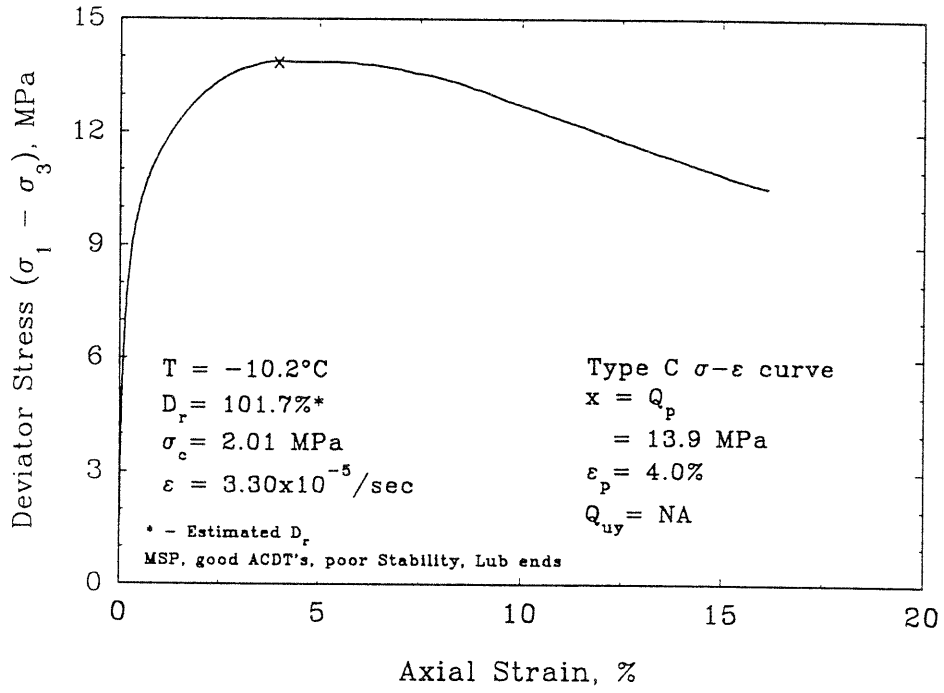

Volumetric vs Axial Strain

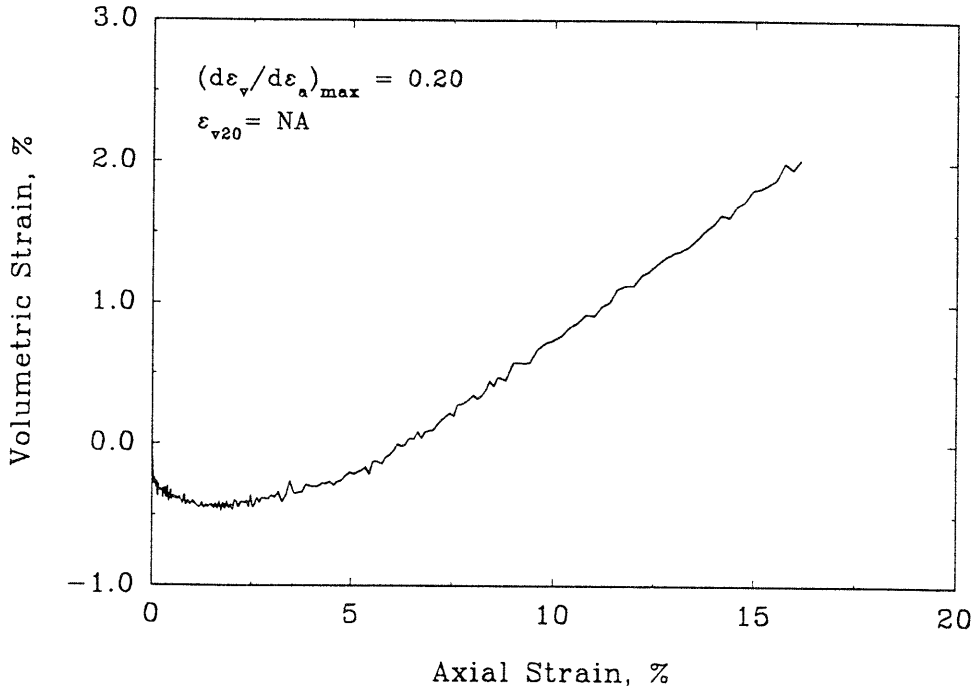

CF10

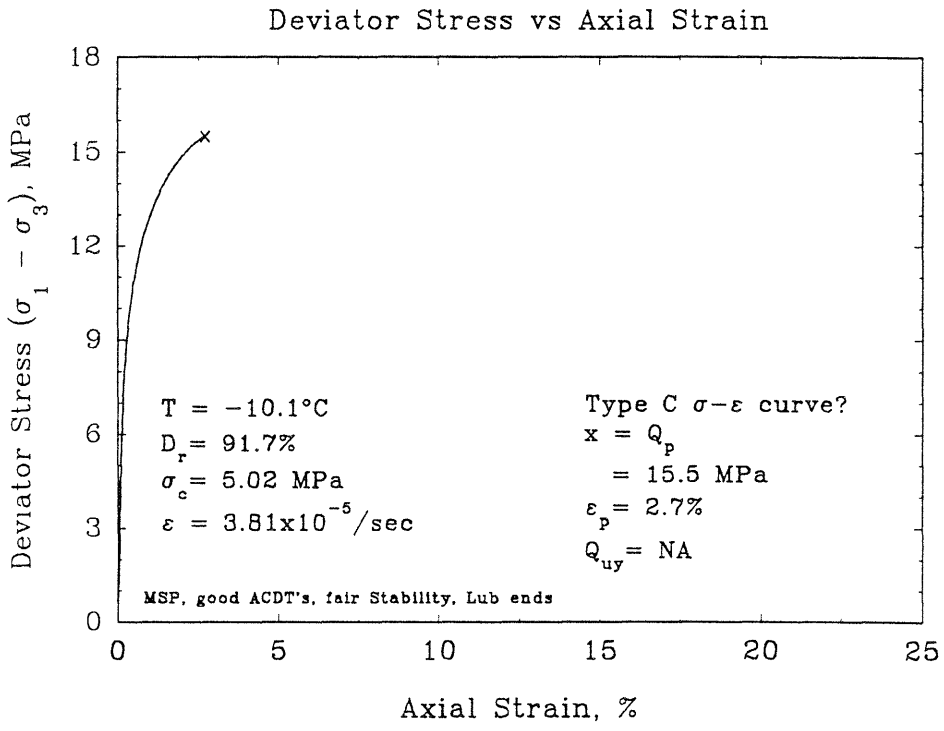
Deviator Stress vs Axial Strain
Deviator Stress ($\sigma_1 - \sigma_3$), MPa
18
15
12
9
6
3
0
0
5
10
15
20
25
Axial Strain, %
T = −10.1°C
D_r= 91.7%
σ_c= 5.02 MPa
$\dot{\varepsilon}$ = 3.81x10^{-5}/sec
Type C σ−ε curve?
x = Q_p
= 15.5 MPa
ε_p= 2.7%
Q_{uy}= NA
MSP, good ACDT's, fair Stability, Lub ends

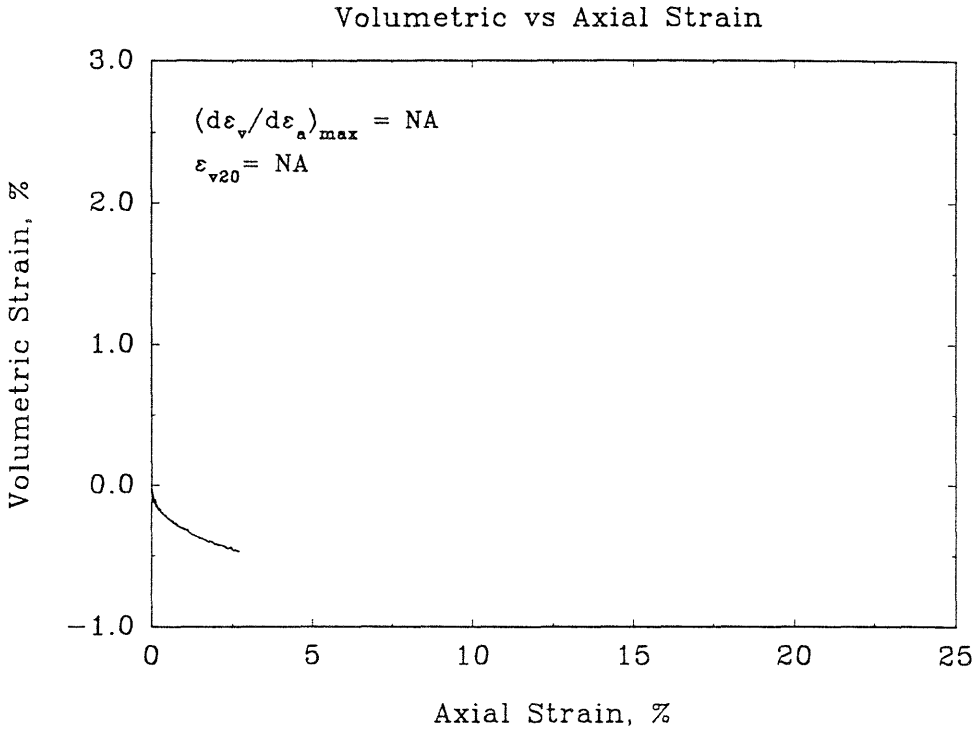
Volumetric vs Axial Strain
Volumetric Strain, %
3.0
2.0
1.0
0.0
−1.0
0
5
10
15
20
25
Axial Strain, %
$(d\varepsilon_v/d\varepsilon_a)_{max}$ = NA
ε_{v20}= NA